EDITED BY

PENELOPE J. BROTHERS • MATHIAS O. SENGE

VOLUMES 1 & 2

FUNDAMENTALS OF PORPHYRIN CHEMISTRY

A 21st CENTURY APPROACH

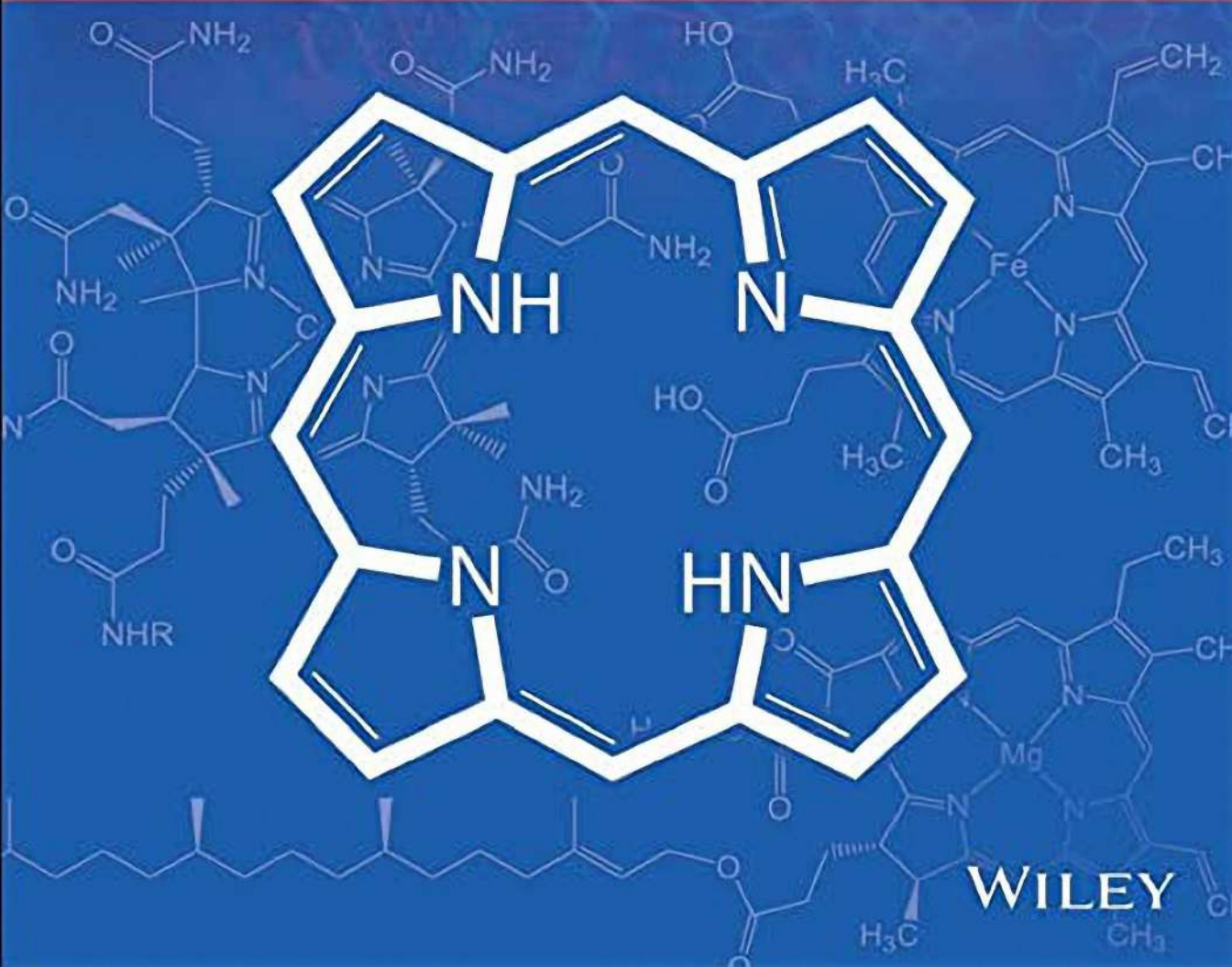

WILEY

Fundamentals of Porphyrin Chemistry

Fundamentals of Porphyrin Chemistry

A 21st Century Approach

Volume 1

Edited by

Penelope J. Brothers
The Australian National University
Canberra, Australia

Mathias O. Senge
Trinity College Dublin
Dublin, Ireland

WILEY

Fundamentals of Porphyrin Chemistry

A 21st Century Approach

Volume 2

Edited by

Penelope J. Brothers
The Australian National University
Canberra, Australia

Mathias O. Senge
Trinity College Dublin
Dublin, Ireland

WILEY

This edition first published 2022
© 2022 John Wiley & Sons Ltd

All rights reserved. No part of this publication may be reproduced, stored in a retrieval system, or transmitted, in any form or by any means, electronic, mechanical, photocopying, recording or otherwise, except as permitted by law. Advice on how to obtain permission to reuse material from this title is available at http://www.wiley.com/go/permissions.

The right of Penelope J. Brothers and Mathias O. Senge to be identified as the authors of the editorial material in this work has been asserted in accordance with law.

Registered Offices
John Wiley & Sons, Inc., 111 River Street, Hoboken, NJ 07030, USA
John Wiley & Sons Ltd, The Atrium, Southern Gate, Chichester, West Sussex, PO19 8SQ, UK

Editorial Office
The Atrium, Southern Gate, Chichester, West Sussex, PO19 8SQ, UK

For details of our global editorial offices, customer services, and more information about Wiley products visit us at www.wiley.com.

Wiley also publishes its books in a variety of electronic formats and by print-on-demand. Some content that appears in standard print versions of this book may not be available in other formats.

Limit of Liability/Disclaimer of Warranty
In view of ongoing research, equipment modifications, changes in governmental regulations, and the constant flow of information relating to the use of experimental reagents, equipment, and devices, the reader is urged to review and evaluate the information provided in the package insert or instructions for each chemical, piece of equipment, reagent, or device for, among other things, any changes in the instructions or indication of usage and for added warnings and precautions. While the publisher and authors have used their best efforts in preparing this work, they make no representations or warranties with respect to the accuracy or completeness of the contents of this work and specifically disclaim all warranties, including without limitation any implied warranties of merchantability or fitness for a particular purpose. No warranty may be created or extended by sales representatives, written sales materials or promotional statements for this work. The fact that an organization, website, or product is referred to in this work as a citation and/or potential source of further information does not mean that the publisher and authors endorse the information or services the organization, website, or product may provide or recommendations it may make. This work is sold with the understanding that the publisher is not engaged in rendering professional services. The advice and strategies contained herein may not be suitable for your situation. You should consult with a specialist where appropriate. Further, readers should be aware that websites listed in this work may have changed or disappeared between when this work was written and when it is read. Neither the publisher nor authors shall be liable for any loss of profit or any other commercial damages, including but not limited to special, incidental, consequential, or other damages.

Library of Congress Cataloging-in-Publication Data

Names: Brothers, Penelope, editor. | Senge, Mathias, 1961- editor.
Title: Fundamentals of porphyrin chemistry : a 21st century approach / edited by Penelope J. Brothers, The Australian National University, Canberra, Australia. Mathias O. Senge, Trinity College Dublin, Dublin, Ireland.
Description: Hoboken, NJ : Wiley, 2022. | Includes bibliographical references and index.
Identifiers: LCCN 2021043864 (print) | LCCN 2021043865 (ebook) | ISBN 9781119129288 (hardback) | ISBN 9781119129295 (adobe pdf) | ISBN 9781119129318 (epub)
Subjects: LCSH: Porphyrins.
Classification: LCC QP671.P6 P683 2022 (print) | LCC QP671.P6 (ebook) | DDC 547/.593–dc23/eng/20211007
LC record available at https://lccn.loc.gov/2021043864
LC ebook record available at https://lccn.loc.gov/2021043865

Cover design: Wiley
Cover image: Volume 1: Courtesy of Penelope J. Brothers, whiteMocca/Shutterstock

Set in 9.5/12.5pt STIXTwoText by Straive, Chennai, India

Contents

Volume 1

Contents

List of Contributors

Sk Amanullah
School of Chemical Sciences
Indian Association for the Cultivation of Science
Kolkata
India

Penelope J. Brothers
Research School of Chemistry
The Australian National University
Canberra, ACT
Australia
and
School of Chemical Sciences
University of Auckland
Auckland
New Zealand

Christian Brückner
Department of Chemistry
University of Connecticut
Storrs, CT
USA

Abhishek Dey
School of Chemical Sciences
Indian Association for the Cultivation of Science
Kolkata
India

Fabienne Dumoulin
Department of Medical Engineering
Faculty of Engineering and Natural Sciences
Acıbadem Mehmet Ali Aydınlar University
Istanbul
Turkey

Eugeny A. Ermilov
Institut für Physik, Photobiophysik
Humboldt-Universität zu Berlin
Berlin
Germany
and
PicoQuant GmbH
Berlin
Germany

Abhik Ghosh
Department of Chemistry
UiT-The Arctic University of Norway
Tromsø
Norway

Chandradeep Ghosh
School of Chemical Sciences
Indian Association for the Cultivation of Science
Kolkata
India

Somdatta Ghosh Dey
School of Chemical Sciences
Indian Association for the Cultivation of Science
Kolkata
India

Daniel T. Gryko
Institute of Organic Chemistry
Polish Academy of Sciences
Warsaw
Poland

Nisansala Hewage
Department of Chemistry
University of Connecticut
Storrs, CT
USA

Ümit Işci
Department of Chemistry
Gebze Technical University
Gebze
Turkey

Bernhard M. Jaun
Laboratory of Organic Chemistry
ETH-Zürich
Zürich
Switzerland

Bernhard Kräutler
Institute of Organic Chemistry & Center of Molecular Biosciences (CMBI)
University of Innsbruck
Innsbruck
Austria

Timothy D. Lash
Department of Chemistry
Illinois State University
Normal, IL
USA

Craig J. Medforth
LAQV-REQUIMTE
Department of Chemistry and Biochemistry
University of Porto
Porto
Portugal

Alina Meindl
School of Chemistry
Trinity Biomedical Sciences Institute
Trinity College Dublin
Dublin
Ireland

Mikio Nakamura
Department of Chemistry
Faculty of Science
Toho University
Chiba
Japan

Nina I. Novikova
School of Chemical Sciences
The University of Auckland
Auckland
New Zealand
and
The Photon Factory
The University of Auckland
Auckland
New Zealand
and
MacDiarmid Institute for Advanced Materials and Nanotechnology
New Zealand
and
Dodd Walls Centre for Photonic and Quantum Technologies
New Zealand

Tebello Nyokong
Institute for Nanotechnology Innovation
Rhodes University
Grahamstown
South Africa

Atsuhiro Osuka
Department of Chemistry
Kyoto University
Kyoto
Japan

Beate Röder
Institut für Physik, Photobiophysik
Humboldt-Universität zu Berlin
Berlin
Germany

W. Robert Scheidt
Department of Chemistry and Biochemistry
University of Notre Dame
Notre Dame, IN
USA

Mathias O. Senge
School of Chemistry
Trinity Biomedical Sciences Institute
Trinity College Dublin
Dublin
Ireland

M. Cather Simpson
Department of Physics
The University of Auckland
Auckland
New Zealand
and
School of Chemical Sciences
The University of Auckland
Auckland
New Zealand
and
The Photon Factory
The University of Auckland
Auckland
New Zealand
and
MacDiarmid Institute for Advanced
Materials and Nanotechnology
New Zealand
and
Dodd Walls Centre for Photonic and
Quantum Technologies
New Zealand

Hitoshi Tamiaki
Graduate School of Life Sciences
Ritsumeikan University
Kusatsu
Shiga
Japan

Takayuki Tanaka
Department of Chemistry
Kyoto University
Kyoto
Japan

Mariusz Tasior
Institute of Organic Chemistry
Polish Academy of Sciences
Warsaw
Poland

1

An Introduction to Porphyrins for the Twenty-First Century

Penelope J. Brothers[1,2] *and Mathias O. Senge*[3]

[1] *Research School of Chemistry, Australian National University, Canberra, ACT, Australia*
[2] *School of Chemical Sciences, University of Auckland, Auckland, New Zealand*
[3] *School of Chemistry, Trinity Biomedical Sciences Institute, Trinity College Dublin, Dublin, Ireland*

1.1 Why Porphyrins?

Why porphyrins? They are in our blood – literally – and give it the red color (Greek πορφύρα, *porphyra*, "purple"). Porphyrin is the ligand that encapsulates iron in heme, the active site of the red blood cell protein hemoglobin. Without hemoproteins, life as we know it on this planet would not exist. With every breath we take, the iron in heme binds dioxygen (O_2) at high partial pressure in our lungs via a delicately balanced cooperative binding process. The oxygenated hemoglobin in red blood cells embarks on a journey through our circulatory system before releasing oxygen from the iron at low partial pressure in the tissues. Humans have understood the importance of blood since the very beginning of their self-awareness, and the quest to understand its properties have been at the heart of the development of both medicine and science. The disciplines of chemistry and biochemistry have given us the tools to understand just how hemoglobin works and the exquisite functions of the porphyrin ligand and iron in controlling the cooperative binding process.

Even more fundamentally, air-breathing organisms would not exist without oxygen and plant food sources. In plants, porphyrins in the form of magnesium complexes are the key players in photosynthesis. As reduced porphyrins, they are green in color and thus are called chlorophylls (greek: χλωρός, *khloros*, "pale green" and φύλλον, *phyllon*, "leaf"). Chlorophylls comprise part of large antenna and reaction center complexes which harvest light and convert light energy into chemical energy and – in oxygenic photosynthesis – also produce oxygen.

Porphyrin is more than just a fundamental unit of physiology. It is one of the tetrads of bioinorganic systems based on cyclic tetrapyrroles – heme, vitamin B_{12}, cofactor F430, and chlorophyll –containing, respectively, iron, cobalt, nickel, and magnesium (Figure 1.1). Their predominant functions are oxygen transport (heme), energy capture (chlorophyll), and metabolic processes (vitamin B_{12} and F430). That these very different systems performing such varied functions in widely differing organisms should have at their core the same ligand based on a tetrapyrrole macrocycle illustrates the evolutionary conservation of a very versatile and efficient chemical entity. The chemistry of this entity is the subject of this book.

Although the discovery of the porphyrin macrocycle and its relevance derive from biology, the modern chemistry of porphyrins lies at the crossroads of many different

Fundamentals of Porphyrin Chemistry: A 21st Century Approach, Volume 1, First Edition.
Edited by Penelope J. Brothers and Mathias O. Senge.
© 2022 John Wiley & Sons Ltd. Published 2022 by John Wiley & Sons Ltd.

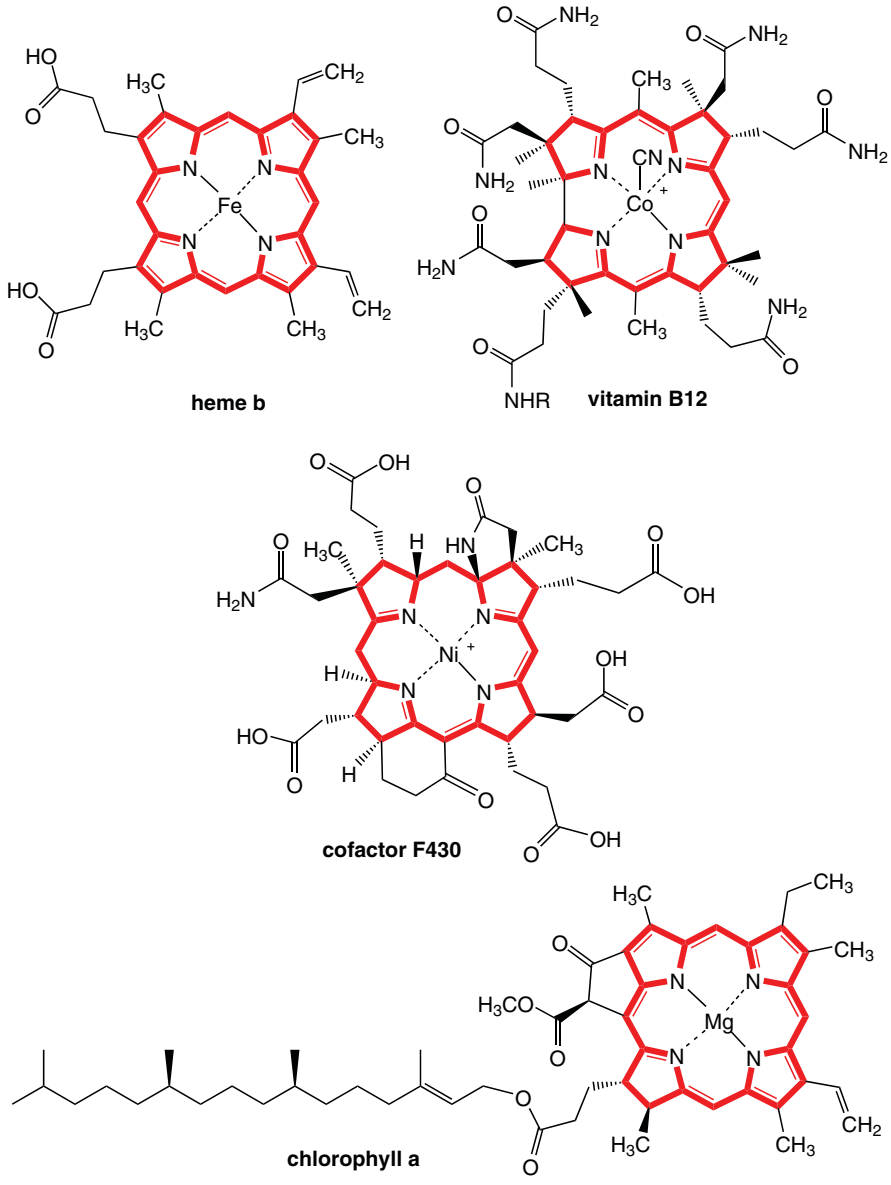

Figure 1.1 Nature's tetrapyrroles heme b, chlorophyll a, vitamin B12, and cofactor F430, with the tetrapyrrole core in each highlighted.

disciplines. The term *porphyrins* is often used as shorthand for a family of polypyrrole macrocycles including phthalocyanines, corroles, porphyrazines, and their expanded, contracted, isomeric, and heteroatom-substituted relatives. Hence, in recent years the term *porphyrinoids* has been more frequently used to illustrate the wide space of compound classes derived from the parent compound. All of these can be conveniently synthesized in the laboratory, and their applications span biochemistry, catalysis, materials, and human health.

1.2 The Natural World of Porphyrins

Porphyrins and chlorophylls are known as the "pigments of life" because they dominate the life processes in organisms ranging from bacteria to the animal and plant worlds. Although the best-known role of the iron porphyrin in heme is its oxygen transport function, iron porphyrins occur in a much larger group of proteins responsible for not only oxygen transport but also for oxygen storage, nitric oxide (NO) synthesis and transport, cytochromes responsible for electron transfer, and enzymes catalyzing a wide range of chemical reactions including oxidases, peroxidases, reductases, dehydrogenases, and catalases. Additional iron complexes contain reduced macrocycles such as the purple siroheme and heme d (isobacteriochlorins), which play a role in the reduction of sulfur and nitrogen.

Chlorophylls, the green pigments in plants, comprise magnesium chlorins clustered in photosystems, essentially antennae for absorbing sunlight energy, which is then used to drive photosynthesis, the chemical process converting CO_2 and H_2O into sugars and O_2. Related bacteriochlorophylls are involved in bacterial photosynthesis and have green chlorin or green-brown bacteriochlorin cores. Vitamin B_{12} has a cherry-red color and is an essential cofactor in many metabolic processes and contains a cobalt corrin core. Nickel is the central metal in cofactor F430, a highly reduced corphin system. Found in archaebacteria, this yellow compound is involved in methanogenesis.

Porphyrin colors are also encountered in daily life. Green gummy bears and other colored foodstuffs are dyed with E140 or E141, which are derived from natural chlorophylls. The brown egg on one's breakfast table contains the rusty brown protoporphyrin, while some avian eggshells contain porphyrin degradation products such as the blue-green biliverdin, yellow-brown bilirubin, and the red-orange tripyrrolic uroerythrin. Porphyrins such as copro-, uro-, and protoporphyrin can be found in some bird feathers, with the red copper uroporphyrin II turacin being the only known natural copper porphyrin. Porphyrins are also found in seashells and demosponges of coral reefs and in the spines of the European hedgehog.

Many colors around us are related to porphyrin biosynthesis and catabolism. Spring is the time of renewed plant growth and increased chlorophyll production, while the beautiful fall colors are related to the breakdown and disappearance of chlorophyll, bringing the colors of other plant pigments such as the carotenoids and flavonoids to light. Similar processes are involved in the ripening (degreening) of bananas. On the red side, degradation of heme results in the formation of the bile pigments. Open-chain (linear) tetrapyrroles like biliverdin and bilirubin are observed in the colorful changes involved in the formation and healing of hematomas, and a significant overproduction of bilirubin gives rise to the yellow color in jaundice.

Linear tetrapyrroles derived from porphyrins are also found in plants, bacteria, and fungi as photoreceptors. These blue phytochromes are sensory pigments which regulate plant growth, germination, and many other aspects of plant development. The structurally related phycobilins serve as accessory photosynthetic pigments in cyanobacteria and some non-green algae. With their red, orange, and blue colors, they close the "green gap" of the chlorophylls and allow light absorption for photosynthesis in the whole visible spectrum.

Lastly, a little-recognized fact is that by far the most abundant porphyrins on earth occur as geoporphyrins, which are found in large quantities in petroleum, oil shales, and other sediments derived from fossilized materials. These geoporphyrins (also known as petroporphyrins), often occurring as their vanadium and nickel complexes, arise from the

chlorophyll and heme deposited from plant and animal matter that have undergone partial decomposition and chemical modification through geological sedimentary processes.

1.3 Brief History of Porphyrins

The early development of the field of porphyrin chemistry and biochemistry, dating back to the mid-nineteenth century, was driven by the quest to understand the components and function of leaf pigments and of blood. Many well-known scientists are associated with this: Berzelius, Hoppe-Seyler, Stokes, Soret, and so on, with seminal contributions from Lecanu, Scherer, Mülder, Thudichum, McMunn, Stokvis, and more. Detailed investigations of the structure and function of vitamin B_{12} followed about a century later, in the mid-twentieth century. Particularly on the heme front, investigations into the fundamental properties of structure and functions occurred in parallel with a developing understanding of the role of biochemical malfunctions which lead to diseases such as the porphyrias and sickle cell anemia.

By the late nineteenth century, it was recognized that the organic parts of both chlorophyll and heme were based on tetrapyrrolic structures. The early twentieth century saw the first golden period of porphyrin research with Willstätter and Fischer's work on the chlorophyll and porphyrin structure, which was first correctly formulated by Küster in 1912. Both natural and synthetic porphyrins such as the 5,10,15,20-tetraarylporphyrins and the phthalocyanines became available, and crucial studies on porphyrias and photodynamic therapy set the stage for clinical porphyrin research.

Major developments in the twentieth century were recognized by the award of Nobel Prizes spanning all the three major areas, heme, chlorophyll, and vitamin B_{12}, and highlighting the major significance of the broader field of porphyrin chemistry and biochemistry. These included awards in 1915 (Willstätter, chlorophyll), 1930 (Hans Fischer, heme and porphyrin synthesis), 1961 (Calvin, photosynthesis), 1962 (Perutz and Kendrew, X-ray crystal structure of hemoglobin), 1964 (Hodgkin, structure of vitamin B_{12}), 1965 (Woodward, total synthesis of chlorophyll and vitamin B_{12}), and 1988 (Deisenhofer, Huber, Michel, structure of the photosynthetic reaction center). One may also consider Finsen's award in 1903 (treatment of Lupus vulgaris, beginning of photomedicine, probably based on the photodynamic action of coproporphyrin III). A complete list of seminal discoveries would comprise several hundred entries and feature contributions from many disciplines.

In the later part of the twentieth century and into the twenty-first century, developments have built on increasing sophistication in synthetic chemistry. In the period after the Second World War, this aided the elucidation of the biosynthetic pathways for tetrapyrroles, and structural, photochemical, and mechanistic investigations. The quest for the total synthesis of the natural tetrapyrroles led to the development of synthetic methodologies for symmetric and unsymmetric porphyrins. Synthetic porphyrins ranging from the very simple to the highly specialized can now be prepared in the laboratory, and coordination chemistry has extended to almost all the elements in the periodic table.

Although the naturally occurring porphyrins, chlorins, and corrins were the original inspiration, pyrrolic macrocycles now encompass expanded, contracted, and isomeric species. Spawned by Vogel's 1986 synthesis of porphycene (a porphyrin isomer), each category of these porphyrinoids has now its own new field of research and applications. In parallel with the developments in synthetic chemistry, physical techniques and instrumentation have

moved forward in leaps and bounds, providing both sophisticated tools for studying new molecules and materials and their reactivity, and new applications where creative scientists have found imaginative uses for porphyrins.

1.4 Practical Applications

Since antiquity porphyrins have practical relevance. Historically, the earliest mention of porphyrins in relation to medicine is by Hippocrates, who in around 460 BCE described a case of acute intermittent porphyria. In the past century, much clinical research has been devoted to porphyrias, hereditary diseases caused by the accumulation of porphyrins in the body because of impairments in the biosynthetic pathway. They can also be induced through toxic substances and drugs, the so-called porphyrinogenic compounds. Among other clinical symptoms, a characteristic feature of porphyria sufferers is their increased photosensitivity. This arises because porphyrins can act as photosensitizers, whereby after photoexcitation long-lived triplet states are formed which can react with oxygen to form toxic reactive oxygen species. This principle can be deliberately exploited to allow the targeted destruction of cells and tissues through photodynamic therapy. This had its origins at the turn of the nineteenth/twentieth century, with much further development in the last 50 years. Now photomedicine is a vibrant and critical area of medicine. Several porphyrin-based drugs are approved for clinical use, and many more are in development.

NO was named Molecule of the Year in 1992, and the 1998 Nobel Prize in Physiology or Medicine was awarded to Furchgott, Ignarro, and Murad for their discoveries concerning NO as a signaling molecule in the cardiovascular system. Heme plays critical roles in both the biosynthesis of NO, as a cofactor of NO synthase, and in the signaling function of NO through its interactions with the heme proteins soluble guanylate cyclase and oxyhemoglobin. Many metabolic disorders arise from problems with the NO biosynthesis pathways.

Natural compounds such as heme and chlorophyll derivatives have found uses as well, mostly as nutritional supplements, although since the middle of the last century interest in this has waned because of lack of scientific proof for the purported benefits. As mentioned earlier, chlorophylls and chlorophyllin are approved food colorants, and emerging studies indicate further medical uses for these. The geoporphyrins described above have been around for billions of years, and in practical terms, analysis of the porphyrin composition in carbon deposits is one means of identifying and analyzing oil and coal.

Synthetic porphyrins are commercially available from several smaller chemical companies. Most of the products find their use in research laboratories or as standards for analytical chemistry or as catalysts. Porphyrins have found use as catalysis in industrial syntheses of drug molecules. Use of porphyrin photosensitizers can also be found frequently in small-scale industrial syntheses. The one class of porphyrins which has found the most use, at least in terms of annual production, is the phthalocyanines. Due to their high (photo)stability and light fastness, they are widely used as pigments and dyes. One can find them as car paints, printing inks, and as dyes for paper and textiles. (Phthalocyaninato)copper(II), known under many trade names such as phthalocyanine blue, is produced at a scale of about 60 000 tons per year. Phthalocyanines were also used in DVDs, and all the applications described for porphyrins – ranging from medicine, synthesis, and catalysis to materials sciences – have been realized using them as well.

If we look at contemporary applications of porphyrins, the list is almost endless. Many of the recent achievements and future challenges for the application of porphyrin systems relate to the critical issues facing the world in the twenty-first century: health, energy, environment, and sustainability. Looking at the chemistry behind these topics, one finds several themes which bridge these areas.

For example, if we look at a theme such as porphyrins as agents for chemical transformations, this is based on the classic function of porphyrins as catalysts. Much of the inspiration for this derives from the action of cytochrome P450, which catalyzes oxygen atom transfer in the oxidation of xenobiotic substances. Many porphyrin-based oxidation catalysts are now in frequent use, some with astonishing catalytic efficiency and selectivity. Catalysis mediated by porphyrins has also been used to tackle some of the big questions in catalysis: dioxygen activation, water oxidation and hydrogen production, and photocatalytic systems where energy transduction is coupled to chemical change. Looking at this list, one immediately sees the relevance of topics such as decarbonization, green chemistry, circular economy, and energy.

Next to the chemical reactivity, one must also consider the three-dimensional structure of porphyrins. Porphyrins are widely used as architectural elements in supramolecular chemistry and materials science. Porphyrin arrays feature prominently in light-harvesting systems and contemporary photonics materials. Porphyrin macrocycles are used as architectural elements in the design of new one-, two-, and three-dimensional assemblies with dimensions approaching the nanometer scale. These encompass nanoparticles and nanoclusters, nanotubes, nanosheets, and elegant three-dimensional framework architectures. Biopolymers such as peptides and DNA have been used as scaffolds for organizing arrays of porphyrins. Other architectural motifs occur as liquid crystals and as two-dimensional, ordered porphyrins on surfaces. Increasingly, one finds combinations of structural and functional engineering in such systems, where the (photo)catalytic properties of porphyrins are altered through molecular engineering and combined with their use as scaffolds. Functional materials based on these are now reaching practical utility for CO_2 fixation, small molecule activation, and more.

Much of the impetus for designing and building complex porphyrin architectures has been to utilize their unique capacity to absorb energy, and this leads to the third theme, the use of porphyrins in energy capture and transduction, and their applications in artificial photosynthesis, photovoltaics, and organic electronics. In terms of practical relevance, one may only recall the rapid developments in dye-sensitized solar cells, where efficiencies of ~13% are reached with push-pull porphyrins. C_{60}, the new carbon allotrope discovered in 1985, nicknamed fullerene and resulting in the award 1996 Nobel Prize in Chemistry to Curl, Kroto, and Smalley, finds its most prominent application in new materials comprising porphyrin-fullerene co-crystallates. The aromatic surfaces of the spherical fullerene and planar porphyrin can interact closely, and the resulting conjugate uses the light-absorbing properties of the porphyrin and the electron-accepting properties of the fullerene as the critical charge separation step in newly developed organic photovoltaic systems.

The history of the discovery and unraveling of heme structure and function is intertwined with a growing understanding of the impact of hemes on human health – as oxygen carriers and as electron- and atom-transfer catalysts in the cytochromes, but also the ways in which malfunctions in heme biosynthesis leads to disorders such as the porphyrias. These questions were asked at the beginning of the study of porphyrins, and they will also lead us into the future. While porphyrias as diseases are reasonably well understood, use of the underlying principle of photosensitization offers means to treat other diseases as well.

Photodynamic cancer therapy is now an established treatment modality for malignant diseases, and current research targets its use as antimicrobials and antifungals. Next to a focus on antiviral applications, it is one means of combating antibiotic resistance. Porphyrins are applied in radioimmunotherapy, and their unique photochemical properties give them a superior role in diagnostics and imaging.

Much in these topics is now well established, at least in terms of basic and translational research. So, if we were to look ahead into the twenty-second century, what role might porphyrins play? Most likely, we will find them in the context of sustainability and environmental control. They will form part of new technologies for fuels and energy, and – at least through their function in photosynthesis – feature in large-scale biorefineries. Ever more complex photonics systems incorporating porphyrins are currently leading to a renaissance in porphyrin photochemistry. The assembly and patterning of optoelectronic 2D materials incorporating porphyrins as catalysts, transporters, conducting, and transducing elements is close to delivering functional materials, and we will see molecular circuitry and memory devices based on them. Current developments in using porphyrins for the sensing of analytes and pollutants will be coupled with their (photo)catalytic properties for the degradation of chemical and biological pollutants in remediation devices. Hopefully, this work will stimulate the next generation of porphyrin researchers to look into yet unrealized areas,

1.5 Porphyrins for the Twenty-First Century

In the 1970s and 1980s, the single-volume book on the shelf of every porphyrin researcher was *Porphyrins and Metalloporphyrins* (J. E. Falk and Kevin M. Smith, Elsevier: 1975, 934 pp). These were complemented by the classics that are still relevant today: *Untersuchungen über Chlorophyll. Ergebnisse und Methoden* [Investigations on Chlorophyll] (R. Willstätter and A. Stoll, Verlag von Julius Springer: 1913, 424 pp) and *Die Chemie des Pyrrols* [The Chemistry of Pyrrole] (H. Fischer and H. Orth, Akademische Verlagsgesellschaft: 1934–1940, 3 volumes). Porphyrin chemistry is now covered in multivolume series, the ever-expanding size of which indicates the growth in the field: *The Porphyrins* (D. Dolphin, Ed., 8 volumes, Academic: 1978); *The Porphyrin Handbook* (K. M. Kadish; K. M. Smith; R. Guilard, Eds., 20 volumes, Academic: 2000–2003); *The Handbook of Porphyrin Science* (K. M. Kadish; K. M. Smith; R. Guilard, Eds., 45 volumes, World Scientific: 2010–2019). The latter series provides a comprehensive resource for researchers in the field and is supplemented by a plethora of review articles in the chemical literature. A search on "subject: porphyrins" filtered by "document type: review" in Web of Science yielded over 2600 such articles published since 2000, while the total number of articles (since 1945) therein on the subject "porphyrin" is 66 100 in the "core collection" and 401 000 in "all databases" (January 2022).

The field will continue to grow and will be rich and relevant for many decades to come, hence the title *Porphyrins for the Twenty-First Century*. It is intended as an approach to the chemistry and properties of porphyrins, whether as a graduate student wishing to learn the basics, a teacher who wishes to incorporate their richness and diversity into a course, or a researcher from outside the immediate field who wishes to use a porphyrin-related compound for a particular application. The focus here on *Fundamentals* comprises a self-contained description of the basics of the chemistry and properties of porphyrins and their close relatives. There is scope for a later volume on *Applications*, which could offer an overview of the current and future roles porphyrins play in chemical transformations,

materials design and synthesis, energy capture and transduction, human health, and the environment. The emphasis will be on coherence across these topics, aiming for breadth rather than depth. Literature citations will focus on leading review articles, compendia such as the *Handbook of Porphyrin Science*, and seminal, landmark papers in each area, rather than on a detailed treatment of the research literature.

The challenge in producing this book is not what to include, but what to leave out. The coverage here is designed to introduce the "porphyrin family," including most of the relevant types of porphyrinoid compounds: naturally occurring and synthetic porphyrins; the free bases and their metallated complexes; expanded, contracted, and isomeric porphyrins; and phthalocyanines and heteroporphyrins. Synthetic approaches to the porphyrin macrocycles and their coordination complexes, their physical properties, and the physical methods used to investigate them will be outlined to give a newcomer in the field an entry into the important literature and techniques used in modern porphyrin synthesis and research. Naturally occurring porphyrinoid systems, comprising hemes (of which there are many more varieties and functions than in hemoglobin), chlorophyll, and vitamin B_{12} will be surveyed to introduce their structure, function, and, briefly, their biochemistry. Much of the history of scientific investigations in the porphyrin area have been focused on replicating the structure and function of the naturally occurring porphyrin systems, either by total synthesis or by the design and synthesis of functional models. These approaches have greatly influenced many other areas. For example, the evolution of the discipline of bioinorganic chemistry owes much to the use of porphyrin scaffolds and the advent of superstructured porphyrinoids.

Even these select topics can only give a glimpse of the fascinating chemistry of porphyrins and their manifold applications. Porphyrins will continue to amaze us and will stay at the forefront of new research areas. One only needs to look at the many developments in photonics and photomedicine which feature porphyrinoids as photoactive pigments and the many supramolecular systems using porphyrin components. Contemporary covalent organic frameworks (COFs) and metal-organic frameworks (MOFs) often contain porphyrin building blocks and increasingly as functional subunits. Likewise, the rapidly expanding field of on-surface chemistry would not be where it is without many seminal contributions based on porphyrin studies. Indeed, maybe the most fascinating aspect of porphyrins is that they are not all around us and in our blood but that – unlike any other class of organic compounds – they continue to serve as test beds for almost any other discipline, new analytical techniques, or possible applications. Porphyrins are the fundament of many groundbreaking developments in modern science, and thus knowledge of their fundamentals is essential.

2

It's All in the Name

Structure, Nomenclature, Numbering, and Isomers of Porphyrins

Mathias O. Senge

School of Chemistry, Trinity Biomedical Sciences Institute, Trinity College Dublin, Dublin, Ireland

2.1 Basic Structure and Nomenclature of Porphyrins

Porphyrin is the name given to a family of compounds whose common structural feature is a tetrapyrrole macrocyclic ring. They are intensely colored compounds, and the name porphyrin is derived from the Greek word *porphura*, which was used to describe the color purple in ancient times. It was first used by Hoppe-Seyler when naming haemato*porphyrin* [1]. The macrocyclic ring is made up of four pyrrole-type ring units linked together by four methine bridging groups whose structure was first proposed by Küster in 1912 [2] and proved by Fischer in 1929 upon his synthesis of heme, the iron porphyrin that occurs in hemoproteins [3–6]. Of the 22 conjugated π-electrons in the parent porphyrin structure, shown in Figure 2.1, only 18 π-electrons take part in the aromatic system, thus obeying Hückel's law for aromaticity $(4n + 2)$. The other four π-electrons possess more double bond character and are not involved in the aromatic system. In fact, much of the chemistry of porphyrins can be rationalized by their relationship with the [7]annulene system **2** [8].

Porphyrins are heteroaromatic compounds and are based on pyrrole condensation products. The parent porphyrin system comprises 24 macrocycle atoms with the pyrrole nitrogen forming the core of the system and the site of metal coordination. To identify any substituent, the 24 atoms are numbered in sequence, beginning with an alpha pyrrole carbon atom numbered as 1 and ending with N21 … N24 for the nitrogen atoms. This gives rise to three different types of carbon atoms: the α (C_a) and β carbon (C_b) atoms of the pyrrole rings and the bridging carbon atoms linking the pyrrole units (C_m) (Figure 2.1). In free base porphyrins, the two pyrrole hydrogen atoms are located at N21 and N23.

The C_m and C_b carbon atoms can undergo various addition and substitution reactions. The inner nitrogen atoms can either lose or gain protons to form dianionic or dicationic species, respectively. Metal ions can insert readily into the porphyrin core to form metalloporphyrins. Porphyrins can undergo many characteristic aromatic nucleophilic or electrophilic substitution reactions. The reactive sites on the porphyrin macrocycle are the C_m and C_b positions, and depending on how electronegative the porphyrin is, either site can be activated. Directing the reactivity to the N, C_b, C_m, or – to a small extent – C_a positions can be achieved through steric effects, the degree of macrocycle reduction, or the type of central metal [9]. In general, based on frontier orbital theory, all electrophilic, nucleophilic, and radical addition reactions should preferentially occur on the meso-positions. Electrophilic addition

Fundamentals of Porphyrin Chemistry: A 21st Century Approach, Volume 1, First Edition.
Edited by Penelope J. Brothers and Mathias O. Senge.
© 2022 John Wiley & Sons Ltd. Published 2022 by John Wiley & Sons Ltd.

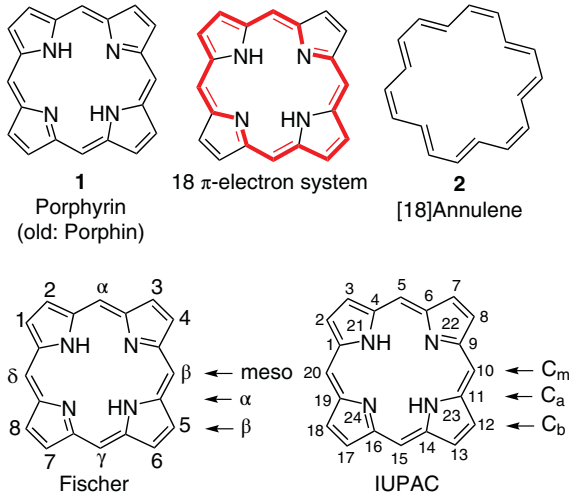

Figure 2.1 The parent porphyrin structure, aromatic character, old Fischer, and contemporary IUPAC atom numbering in porphyrins.

reactions at the β-positions form chlorins and bacteriochlorins, while addition reactions at the meso-positions generate hydroporphyrins (phlorins or porphodimethenes; see below).

The current nomenclature system for porphyrins and related compounds is based on IUPAC-IUB recommendations, the most recent one being from 1986 [10]. While this has brought some order for compounds based on a tetrapyrrolic 18π-electron system and for hemes and chlorophylls, it does not take into account the explosive growth in contracted, expanded, isomeric, and macrocycle-modified systems. Thus, in reality, a mix of "official" and informal systems of naming porphyrins is in use.

The IUPAC system supersedes the older "Fischer" nomenclature, which came into use in the 1920s and is described in his books on pyrrole [4–6]. Here, the C_m positions are called "meso" carbon atoms, and the eight β-pyrrole carbon atoms were numbered 1, …, 8. A cornucopia of trivial names was introduced over time, some of which have been retained in the modern semi-systematic nomenclature, and many of the older names are still used in the biochemical and clinical literature. Even a century after the works of Willstätter and Fischer, an entry into porphyrin chemistry is impossible without studying their seminal works [4–6, 11], all written in German. A full comparison of the two systems has been given by Bonnett [12], and this is also discussed in more detail in the IUPAC recommendations [10]. Wherever appropriate, the older Fischer names are included in brackets "()" with the chemical structures in this chapter, as are colloquial contemporary terms.

The current systematic nomenclature is based on the parent compound porphyrin (**1**) and numbers all macrocycle atoms from 1 to 24. Side-chain positions are then identified by superscripts and metal complexes (chelates) by using the rules for coordination compounds (Figure 2.2). For metalloporphyrins (**4**), this requires that the ligand part (the porphyrin) comes first, followed by the metal with its oxidation number. As dianionic chelates, the macrocycle part is called "porphyrinato," while any axial ligands are placed first in the systematic name. The generic name for neutral porphyrins with two NH units is "free base." The main guiding principle in naming porphyrins is using a semi-systematic approach to keep it simple. Thus, a trivial name is used for the macrocyclic part, which is then modified as appropriate.

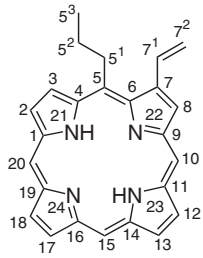

5-Propyl-7-vinylporphyrin **3**

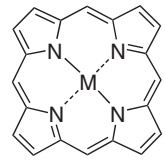

4

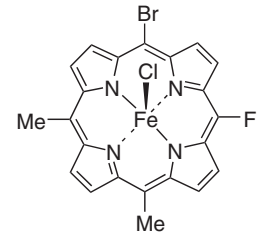

(Chloro)(5-bromo-10-fluoro-15,20-dimethylporphyrinato)iron(III) **5**

Figure 2.2 IUPAC nomenclature for porphyrins and metalloporphyrins.

2.2 General Classes of Porphyrin Systems

The common members of the porphyrin family are derived by modification, replacement, rearrangement, insertion, or deletion of macrocycle atoms in the tetrapyrrole skeleton. Many more possibilities than those illustrated in Figure 2.3 are possible, and systems with various combinations of the skeletal manipulations or multiple instances thereof are known.

2.2.1 Hydroporphyrins

Many of the different types of porphyrins can be classified with regard to their degree of reduction. Based on their relationship with natural systems, the degree of reduction at the C_b positions gives rise to several different parent systems, the most prominent ones being the chlorins and (iso)bacteriochlorins that are present in natural systems (Figure 2.4) [13]. The four structures shown in Figure 2.4 are part of the series of fundamental tetrapyrrole parents identified by IUPAC. The others are porphyrinogen, phthalocyanine, sapphyrin, corrin, corrole, bilane, biline, tripyrrin, and dipyrrin, and will be briefly illustrated below [10].

Likewise, reduction of the meso-positions is possible and results in different types of cyclic tetrapyrroles with interrupted π-electron pathways (Figure 2.5). Many of these are (bio)synthetic intermediates of porphyrins or the products of specific porphyrin derivatization reactions. Note that although they are formally derived from C_m reduction, additional N-hydrogen atoms may be present. Thus, porphyrinogen **9** has four sp^3 hybridized C_m positions, but is a 5,10,15,20,22,24-hexahydroporphyrin.

2.2.2 Calix-Type Systems

One of the oldest known synthetic "porphyrins" is acetone pyrrole **14** [15], which in porphyrin nomenclature would be called 22,24-dihydro-5,5,10,10,15,15,20,20-octamethylporphyrin. Obtained by condensation of pyrrole and acetone, it has become the parent compound for an almost limitless number of cyclic oligopyrrole derivatives. Based on the similarity to calixarene **15**, the respective pyrrole compounds are often colloquially called calixpyrroles or, with partial conjugation, calixphyrins (Figure 2.6) [16]. Formula **16** is a calix[4]pyrrole, where the number "[n]" indicates the number of units linked by methylene groups. Various types are possible, similar to the situation for the hydroporphyrins illustrated in Figure 2.5 [14].

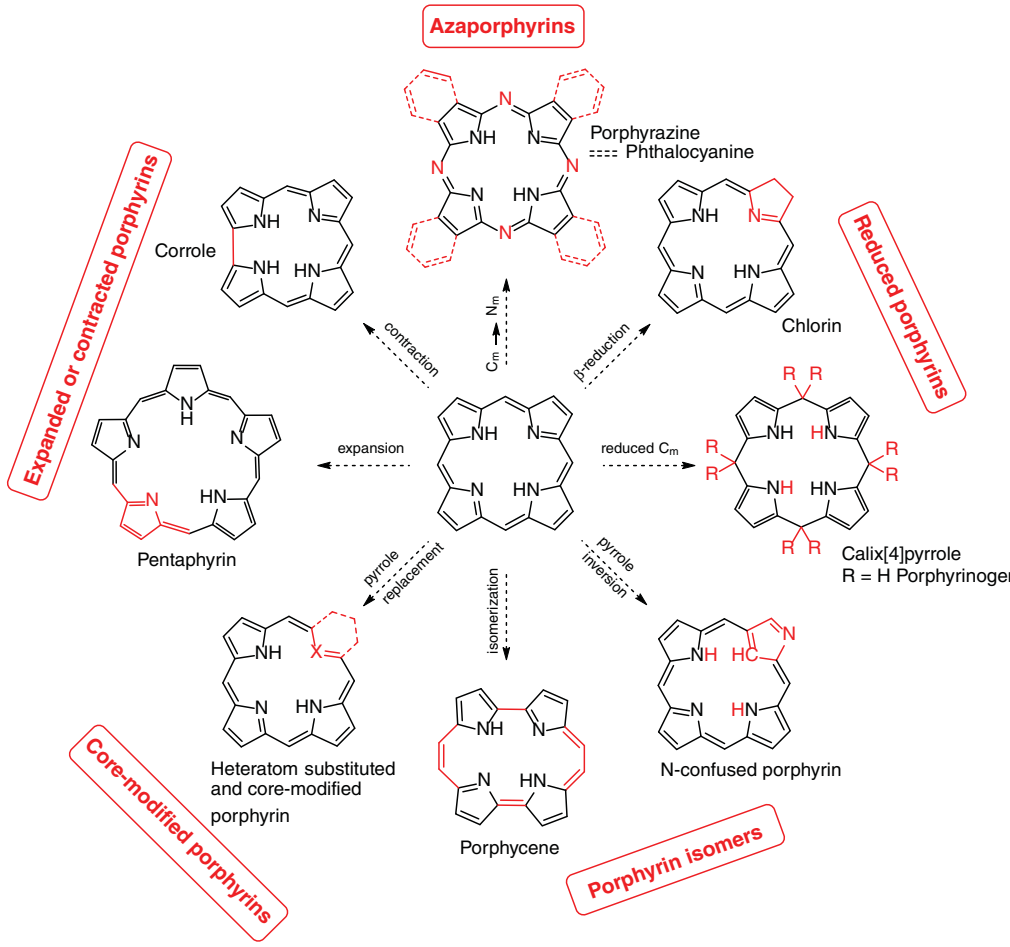

Figure 2.3 Illustration of the main members of the porphyrin family and their relationship with the parent compound.

2.2.3 Isomeric, Expanded, and Contracted Systems

By now there are probably more "porphyrins" that do not conform to the general arrangement of the macrocycle atoms shown in formula **1** than those that do. By convention any compound that is formally derived by rearrangement of the basic 24 macrocycle atoms and with additional or missing atoms in the ring structure is classified as a porphyrin and named as a derivative thereof.

This begins with isomers of porphyrins, for example, the unstable isoporphyrin **21**, and also includes different NH tautomers (Figure 2.7) [17]. Flipping one (or more) pyrrole rings so that the nitrogen atom is on the outside of the macrocycle gives so-called N-confused porphyrins (2-carba-21-azaporphyrin) **22** (red color) and **23** (green color) with an inverted pyrrole ring [7, 18]. A more drastic rearrangement involving the transposition of two methine bridges is present in the constitutional isomer porphycene **24** [19].

The systematic name for N-confused porphyrin also indicates how other derivatives are named. Many heteroatom-substituted and core-modified porphyrins have

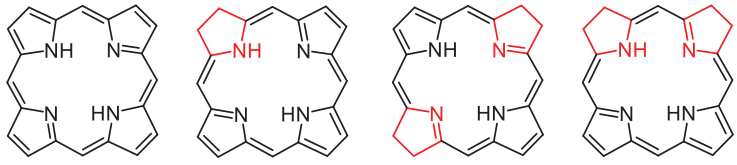

1 Porphyrin (old: porphin)

6 Chlorin 2,3-Dihydroporphyrin

7 Bacteriochlorin 7,8,17,18-Tetrahydroporphyrin

8 Isobacteriochlorin 2,3,7,8-Tetrahydroporphyrin

Figure 2.4 Aromatic hydroporphyrin parent systems. Old names are given in brackets where relevant, in this and subsequent figures.

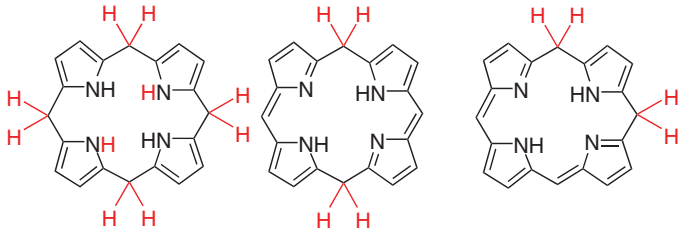

9 Porphyrinogen 5,10,15,20,22,24-Hexahydroporphyrin

10 5,15-Dihydroporphyrin (5,15-porphodimethene)

11 5,10-Dihydroporporphyrin (5,10-porphodimethene)

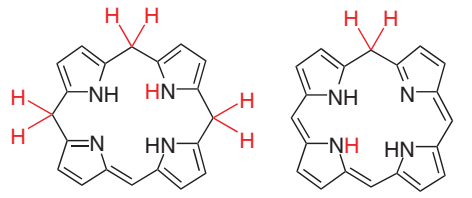

12 5,10,15,22-Tetrahydroporphyrin (porphomethene)

13 5,24-Dihydroporporphyrin (phlorin)

Figure 2.5 Nonaromatic hydroporphyrins with sp^3-hybridized C_m positions.

been reported (Figure 2.8). For example, the "furan analogue" of porphyrin is the 21,22,23,24-tetraoxaporphyrin dication **25** [20], and replacement of individual atoms is indicated by the relevant position and name of substituent atom; for example, as shown for **26** and **27**. Replacement of a whole section of the molecule, for example, a benzene instead of a pyrrole ring in **28**, gives rise to related macrocycles, most of which are identified by trivial names not covered by IUPAC rules [21].

Finally, apart from rearrangement or replacement of parts of the tetrapyrrole macrocycle, additional atoms can be present or missing as well. This defines the class of expanded or contracted porphyrins (Figure 2.9) [22]. The simplest case is the addition or deletion of a bridging carbon atom, giving the nonaromatic homoporphyrin **29** and the aromatic corrole **30**, respectively. Other classic examples are sapphyrin **31**, pentaphyrin **32**, and secochlorin **33**. Each of

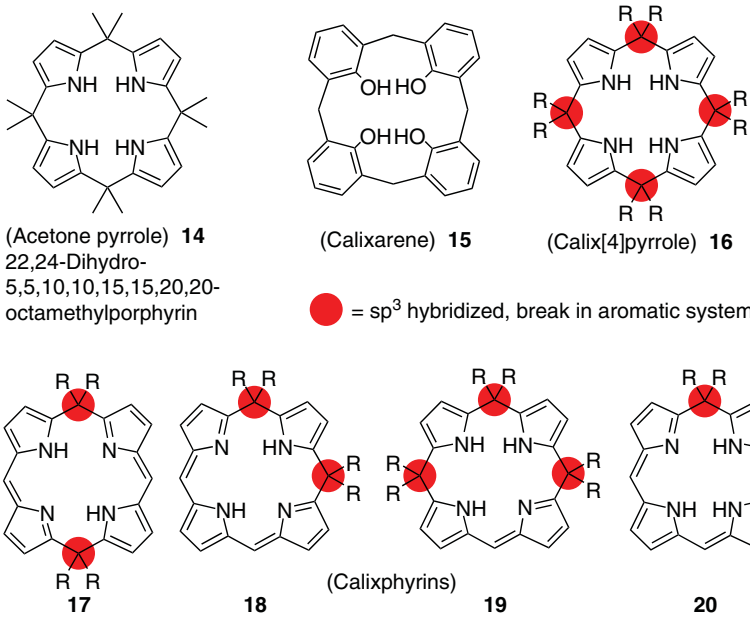

Figure 2.6 Nonaromatic porphyrins with sp^3-hybridized meso carbon positions.

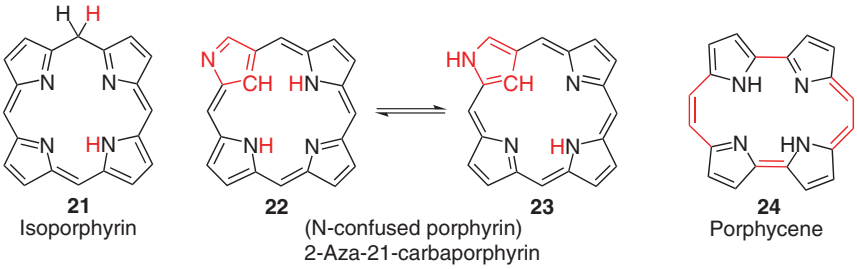

Figure 2.7 Examples of porphyrin isomers.

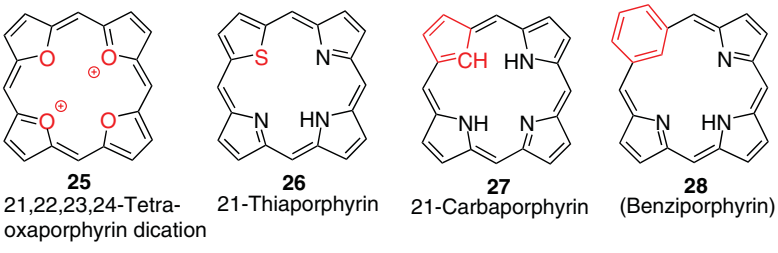

Figure 2.8 Heteroatom-modified and core-substituted porphyrins.

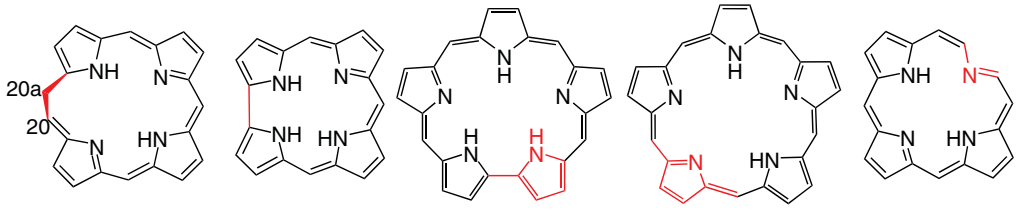

20a-Homoporphyrin **29** Corrole **30** Sapphyrin **31** (Pentaphyrin) **32** (Seccochlorin) **33**

Figure 2.9 Expanded and contracted porphyrins.

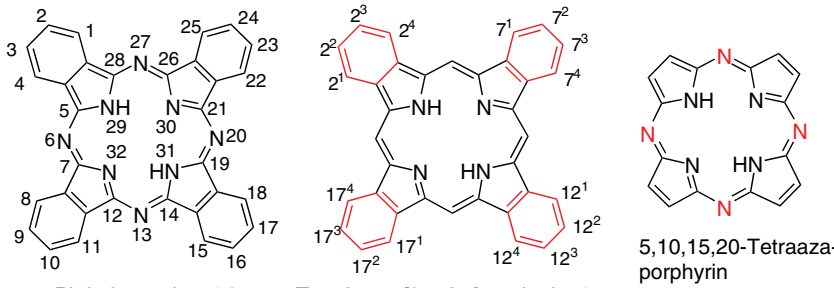

Phthalocyanine **34** Tetrabenzo[*b,g,l,q*]porphyrin **35**

Figure 2.10 Phthalocyanine, tetrabenzoporphyrin, and porphyrazine.

these systems can itself be modified in the form of isomers, substituted derivatives, and as expanded or contracted systems. Reactivity, aromatic character, and metal coordination can differ drastically in each of these different classes of porphyrins. The list of trivial names in this area is legion, with some research groups being especially ingenious (and prolific) in naming their new porphyrin offspring.

2.2.4 Phthalocyanines and Azaporphyrins

Phthalocyanines form a large group of non-natural tetrapyrroles that have found wide industrial use [23]. They can be considered as tetramers of isoindole and due to their very different synthetic chemistry are often considered separate from porphyrins. The parent name phthalocyanine is reserved for structure **34** (Figure 2.10) [10]. In formal terms, they can be envisioned as 5,10,15,20-tetraaza derivatives of tetrabenzoporphyrin **35**. The closely related class of 5,10,15,20-tetraazaporphyrins, which do not contain β-fused benzene rings, are based on a tetrapyrrole instead of a tetraisoindole framework and are also termed porphyrazines **36** [24].

2.3 Naturally Occurring Porphyrins

2.3.1 Porphyrins and Hemes

All naturally occurring porphyrins are cyclic *tetra*pyrroles. In relation to their ubiquitous role in the living world, porphyrins are often termed the pigments of life [25] and labeled as the red (hemes) and green (chlorophylls) colors of life [26]. In practical terms, the various tetrapyrrole classes are distinguished by the degree of reduction and the type of central

metal. Modulation of the peripheral substituents then further fine-tunes the tetrapyrroles for individual biological roles (Figure 2.11) [27, 28].

Several biosynthetic intermediates are common to the different classes, and the most important precursors are shown in Figure 2.12. All natural tetrapyrroles are derived from uroporphyrinogen III **38**, and protoporphyrin **39** is common to hemes and chlorophylls. In fact, the birth, life, and death of the different tetrapyrroles have many similarities [29]. Closer inspection of formula **38** indicates that this is one of four possible isomers, depending on the location of the propionic acid (Cet) and acetic acid (Cme) side groups at the β-positions. To distinguish these, Fischer employed a "type-isomer" nomenclature, labeling the various isomers with Roman numerals [4–6]. Four different combinations of porphobilinogen **37** yield uroporphyrinogen, and subsequently uroporphyrin primary isomers are possible. Uroporphyrinogen III is the precursor of all "normal" porphyrins, while other type isomers can be found in porphyric organisms, that is, those with impairments in porphyrin biosynthesis. For a porphyrin with three different types of β-substituents, for example, protoporphyrin, 15 different secondary type isomers are possible. As only one is found in nature, for these the type nomenclature has been abandoned, and Fischer's protoporphyrin IX **39** is now simply called protoporphyrin in the IUPAC nomenclature.

Most of the early studies were made with degradation products of natural porphyrins, and thus many of the old trivial names for related synthetic porphyrins have been retained in the IUPAC system (Table 2.1). The Roman numeral type designation (I-IV) is only retained for etioporphyrin (Me, Et residues), coproporphyrin (Me, Cet), and uroporphyrin (Cme, Cet).

Iron complexes of porphyrins are called heme (haem), which is derived from the old name hämatin for the material derived from the iron-containing blood pigment [30]. The biochemical nomenclature of hemes is quite complex, and formal rules have only been established for the general systems listed in Table 2.2.

The hemes are essential to the function of cytochromes, P_{450}'s, hemoglobin and myoglobin, and peroxidases, in which they provide the active site where the chemistry takes place. Except for their role in signaling, biologically functional hemes are protein-bound cofactors. In practical terms, the most prominent hemes are based on iron complexes of protoporphyrin (heme b, **42**). Binding to the protein occurs either through axial coordination at the iron center and/or through covalent bonds at C_b or C_m positions, for example, through thioether formation with cysteine residues in heme c **43**. Other side-chain modifications and types of covalent protein attachment are known involving many of the peripheral positions [31–33]. In addition, to make things a bit more complicated, two natural iron complexes of isobacteriochlorins, heme d_1 **44** and siroheme **45**, are known. Figure 2.13 illustrates the current use of heme names for natural iron porphyrin complexes. The informal terminology "heme x" is used almost exclusively as it relates the type of heme to the type of cytochrome it occurs in (e.g., heme c as part of cytochrome c), although there are inevitably exceptions to the rule.

2.3.2 Chlorophylls and Bacteriochlorophylls

Chlorophylls are the reaction center and accessory pigments of photosynthesis [27, 34, 35]. All chlorophyll derivatives are based on the phytochlorin **47** framework, which is a reduced derivative (17,18-dihydro) of phytoporphyrin **46**. The four pyrrole rings and the isocyclic pentanone ring are often differentiated by Roman numerals (I, II, …, V) or letters (A, B, …, E). The two main pigments of oxygenic photosynthesis are the green Chl a **48** and b **50** (Figure 2.14). The ending *–phyll* identifies phytol as the esterified alcohol at $C17^3$, while

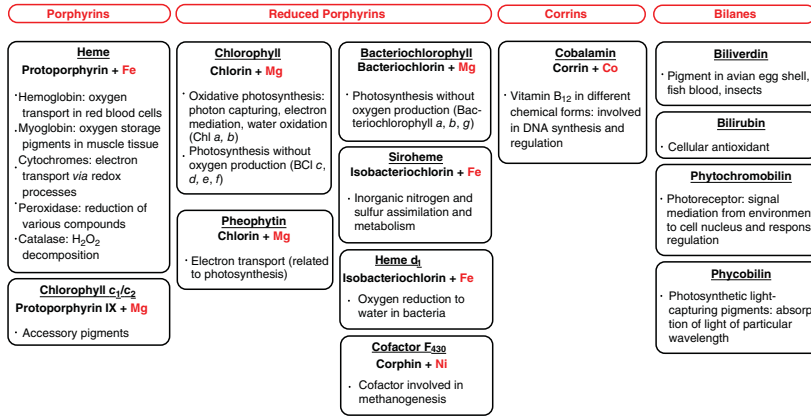

Figure 2.11 Overview of the naturally occurring tetrapyrrole classes and their functions.

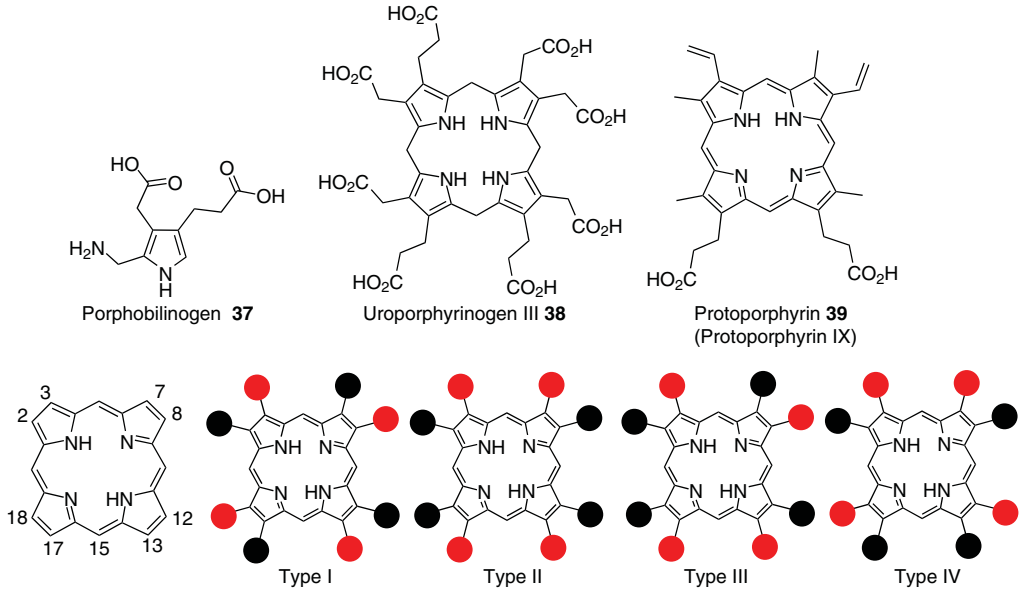

Figure 2.12 Important biosynthetic intermediates of porphyrins and type-isomer nomenclature for uroporphyrin. Red and black circles indicate two different types of substituents.

Table 2.1 List of the IUPAC trivial names for substituted porphyrins.

Trivial name	Substituents and locants ● ●								
	2	3	7	8	12	13	15	17	18
Porphyrins									
Coproporphyrin I	Me	Cet	Me	Cet	Me	Cet	H	Me	Cet
Cytoporphyrin	Me	CH(OH) CH_2Farnesyl	Me	$CH{=}CH_2$	Me	Cet	H	Cet	CHO
Deuteroporphyrin	Me	H	Me	H	Me	Cet	H	Cet	Me
Etioporphyrin I	Me	Et	Me	Et	Me	Et	H	Me	Et
Hematoporphyrin	Me	$CH(OH)CH_3$	Me	$CH(OH)CH_3$	Me	Cet	H	Cet	Me
Mesoporphyrin	Me	Et	Me	Et	Me	Cet	H	Cet	Me
Phylloporphyrin	Me	Et	Me	Et	Me	H	Me	Cet	Me
Protoporphyrin	Me	$CH{=}CH_2$	Me	$CH{=}CH_2$	Me	Cet	H	Cet	Me
Pyrroporphyrin	Me	Et	Me	Et	Me	H	H	Cet	Me
Rhodoporphyrin	Me	Et	Me	Et	Me	COOH	H	Cet	Me
Uroporphyrin I	Cme	Cet	Cme	Cet	Cm	Cet	H	Cme	Cet
Phytoporphyrin	Me	Et	Me	Et	Me	C(O)---CH_2–		Cet	Me
Chlorins (as 17,18-dihydroporphyrins)									
Phyllochlorin	Me	Et	Me	Et	Me	H	Me	Cet	Me
Phytochlorin	Me	Et	Me	Et	Me	C(O)---CH_2–		Cet	Me
Pyrrochlorin	Me	Et	Me	Et	Me	H	H	Cet	Me
Rhodochlorin	Me	Et	Me	Et	Me	COOH	H	Cet	Me

Abbreviations: Cme = CH_2COOH, Cet = CH_2CH_2COOH.

Table 2.2 IUPAC nomenclature for iron complexes of porphyrins.

Term	Definition
Heme	Iron porphyrin complex
Ferroheme	Iron(II) porphyrin complex
Ferriheme	Iron(III) porphyrin complex
Hemochrome	Low-spin iron porphyrin complex with one or more strong field axial ligand (e.g., pyridine)
Ferrohemochrome	Fe(II) complex of a hemochrome
Ferrihemochrome	Fe(III) complex of a hemochrome
Hemin	A chloro(porphyrinato)iron(III) complex [e.g., protohemin = Fe(III)Proto(Cl)]
Hematin	A hydroxo(porphyrinato)iron(III) complex (mostly isolated as μ-oxo dimer)

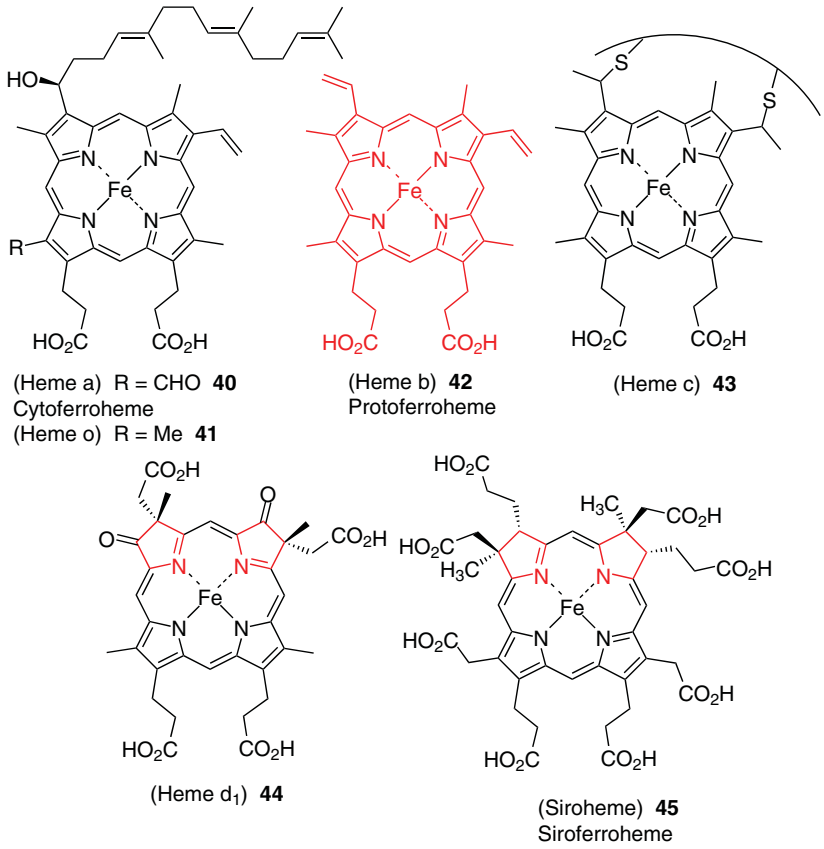

Figure 2.13 The more prominent types of iron porphyrins found in nature.

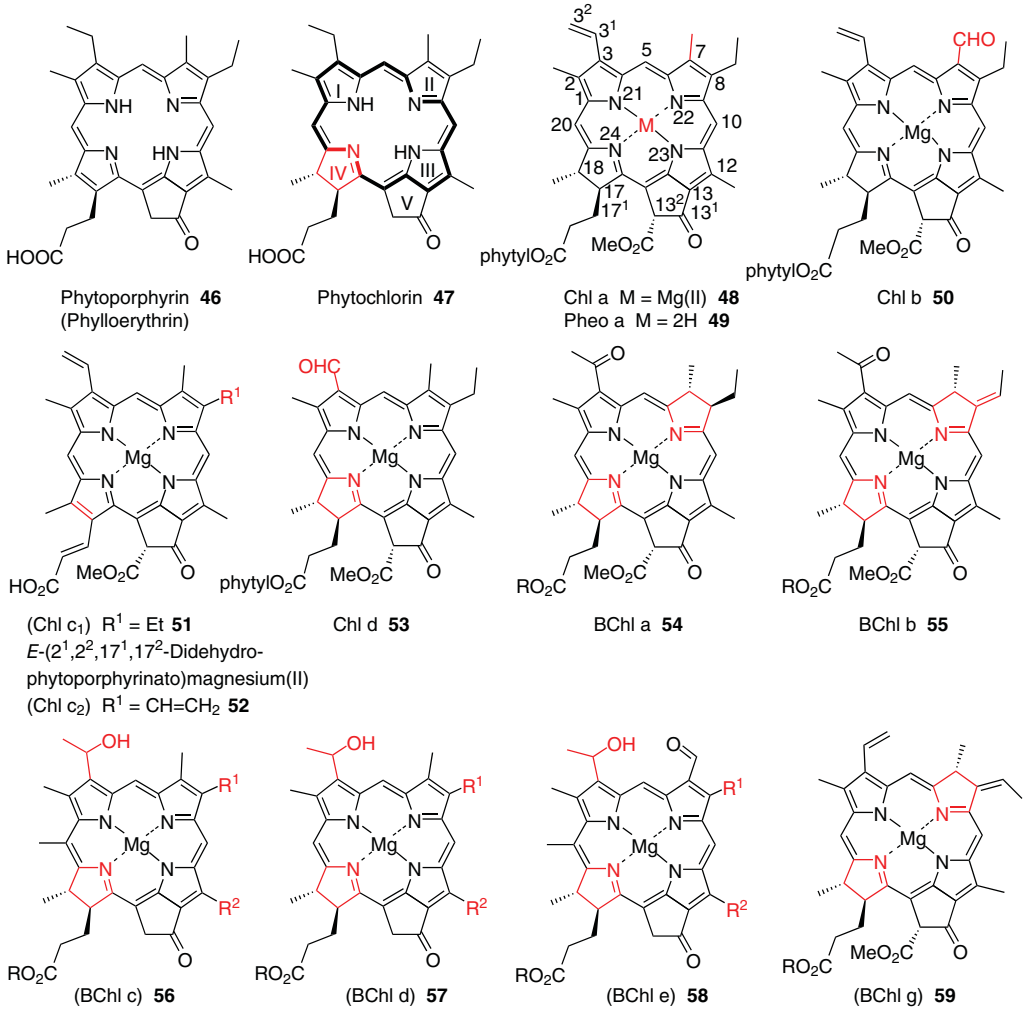

Figure 2.14 Naturally occurring chlorophylls and bacteriochlorophylls. R indicates the different long-chain esterified alcohols. BChl = chlorophyll, Chl = chlorophyll, Pheo = pheophytin.

chloro- indicates a magnesium complex (Table 2.3). Demetalation is identified by the prefix *pheo-*, and *–phorbide* indicates a free carboxylic acid at C17[3].

Other compounds are Chl d **53** from cyanobacteria, the green bacteriochlorophylls c, d, and e (**56**–**58**) (which, despite the name are chlorins, i.e., dihydroporphyrins). They are found in green sulfur bacteria and Chloroflexaceae, and can occur as mixtures of homologs with different peripheral substituents at C8 and C12 and have either *R* or *S* configuration at C3[1] [36]. For practical considerations on naming and distinguishing the various homologues, see Smith [37]. The brownish-purple BChls a **54** and b **55** are bacteriochlorins (7,8,17,18-tetrahydroporphyrins) and are mostly found in photosynthetic purple bacteria. Other examples are BChl g **59** from heliobacteria, and many of the (bacterio)chloro"phylls" occur with different esterified alcohols. To complete the confusing nomenclature, the gold-brownish chlorophylls c (**51**,**52**) are actually porphyrins and magnesium complexes of pheophorbide a, while chlorophyll f is a standard "chlorin-type" chlorophyll

Table 2.3 Terminology for (bacterio)chlorophyll derivatives.

Term	Definition
Bacteriochlorophyll	Magnesium complex of bacteriochlorin with $C17^3$ phytyl ester (note, c–f series are chlorins)
Bacteriopheofarnesin	Free base of bacteriochlorin with $C17^3$ farnesyl ester
Bacteriopheophytin	Free base of bacteriochlorin with $C17^3$ phytyl ester (note, c–f series are chlorins)
Chlorophyll	Magnesium complex of chlorin with $C17^3$ phytyl ester
Chlorophyllide	Magnesium complex of chlorin with $C17^3$ carboxylic acid
Mesochlorophyll	$3^1,3^2$-Dihydrochlorophyll
Pheophorbide	Free base of chlorin with $C17^3$ carboxylic acid
Pheophytin	Free base of chlorin with $C17^3$ phytyl ester
Pheophytin	Free base of chlorin with $C17^3$ phytyl ester

(2-demethyl-2-formyl-chlorophyll a) [38]. Formally, only Chl a, b, d and BChl a and b (and their derivatives as per Table 2.3) are approved trivial names. The other compound should be named systematically or as derivatives of phytochlorin and phytoporphyrin. Synthetic 17,18-dihydroporphyrins may be named using a semi-systematic nomenclature based on the four approved trivial names (phyllo-, phyto-, pyrro-, and rhodochlorin) for chlorins (Table 2.2).

2.3.3 Sirohydrochlorins and Corrins

Only one isobacteriochlorin (2,3,7,8-tetrahydroporphyrin) has been given a trivial name in the IUPAC recommendation [10]. The arrangement of the side chains in sirohydrochlorin **60** indicates uroporphyrinogen III as its biosynthetic precursor, and insertion of iron yields siroheme **45**. One other natural compound is closely related to this structure, albeit derived from "precorrin-2," a biosynthetic precursor of **60**. This compound is commonly called cofactor F_{430} (coenzyme F_{430}) **61** and is the only nickel complex of a tetrapyrrole found in living organisms. It is involved in Archaea and as the active cofactor of methyl coenzyme M reductase functions in the last step of methanogenesis [39]. Thirteen of the 20 macrocycle carbon atoms in this yellow compound are sp^3 hybridized (Figure 2.15).

The corrins **62** form a separate class of porphyrinoids that are both reduced and contracted; that is, they lack C20 and contain 10 sp^3-hybridized centers in the macrocycle. Cobalamins **63** are ubiquitous natural compounds, and their most prominent representative is coenzyme B_{12} (vitamin B_{12}) [40]. They typically contain a central cobalt ion that can form reactive Co—C bonds and are biosynthesized only in microorganisms. There are many different derivatives and cobalt coordination types; an example of an IUPAC trivial name is cobyrinic acid **64**. Others are closely related; for example, the cobyrinic *a,b,c,d,e,g*-hexaamide is called cobyric acid. Specific and detailed rules for their nomenclature, including derivatization and replacement of cobalt by other metals, have been established by the IUPAC-IUB [41].

Note that the structurally related corroles **30** are not natural compounds.

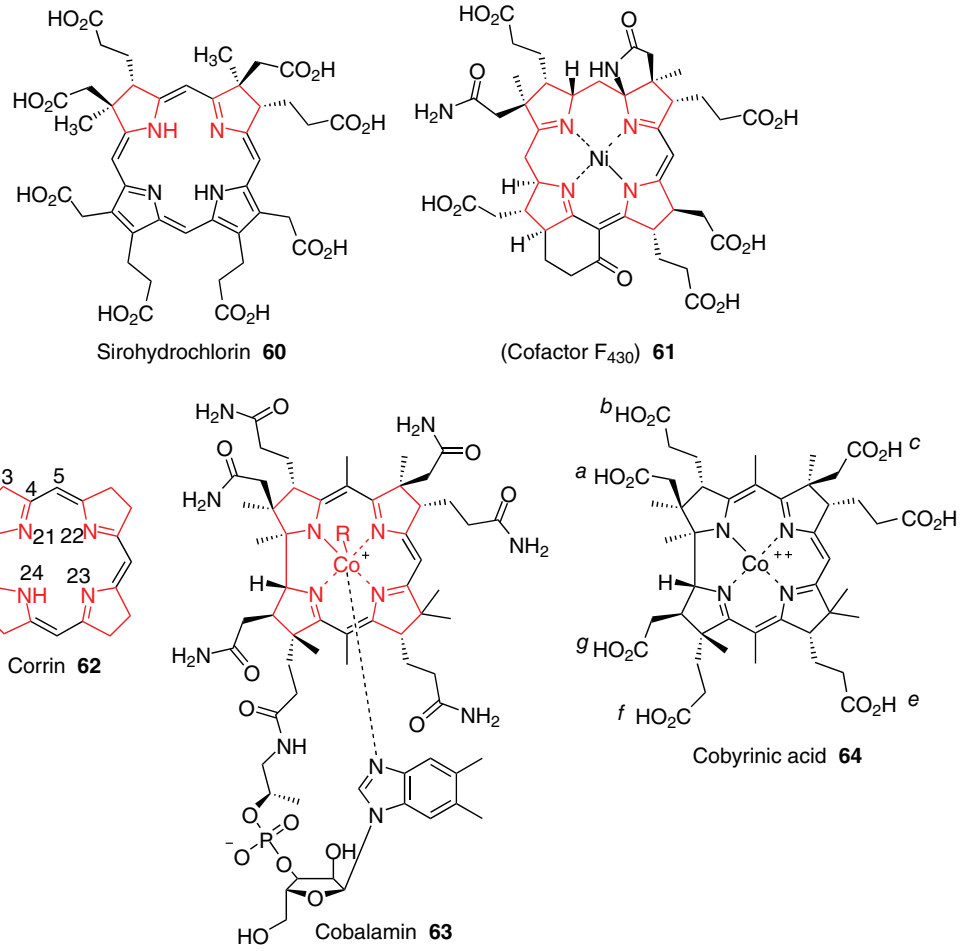

Figure 2.15 Examples of natural products related to sirohydrochlorin and corrin.

2.3.4 Linear Tetrapyrroles

Although not the topic of this book, linear (tetra)pyrroles are closely related to porphyrins. In organic chemistry and biosynthesis, pyrrole building blocks are the assembly units for the macrocyclic compounds. On the other hand, once formed, natural porphyrins are converted in nature to a multitude of important linear tetrapyrroles (Figure 2.16) [25]. The latter are all based on the bilane **70** or bilin skeletons **71**. Their nomenclature is as involved as that of porphyrins [10]. An excellent analysis of the nomenclature of all tetrapyrroles and the idiosyncrasies thereof has been given by Bonnett [12], and a general treatise on their chemistry has been written by Falk [42].

All of them are obtained via ring-opening reactions of either porphyrins or chlorins. In many cases, these catabolic reactions *and* classic examples are the formation of bilirubin **77** and biliverdin **78** as heme catabolites [42, 43] and related reactions in the degradation of chlorophylls to yield various phyllobilins (e.g., **79**) [44]. In addition, photosynthetic organisms contain functional linear tetrapyrrole protein complexes. Examples are

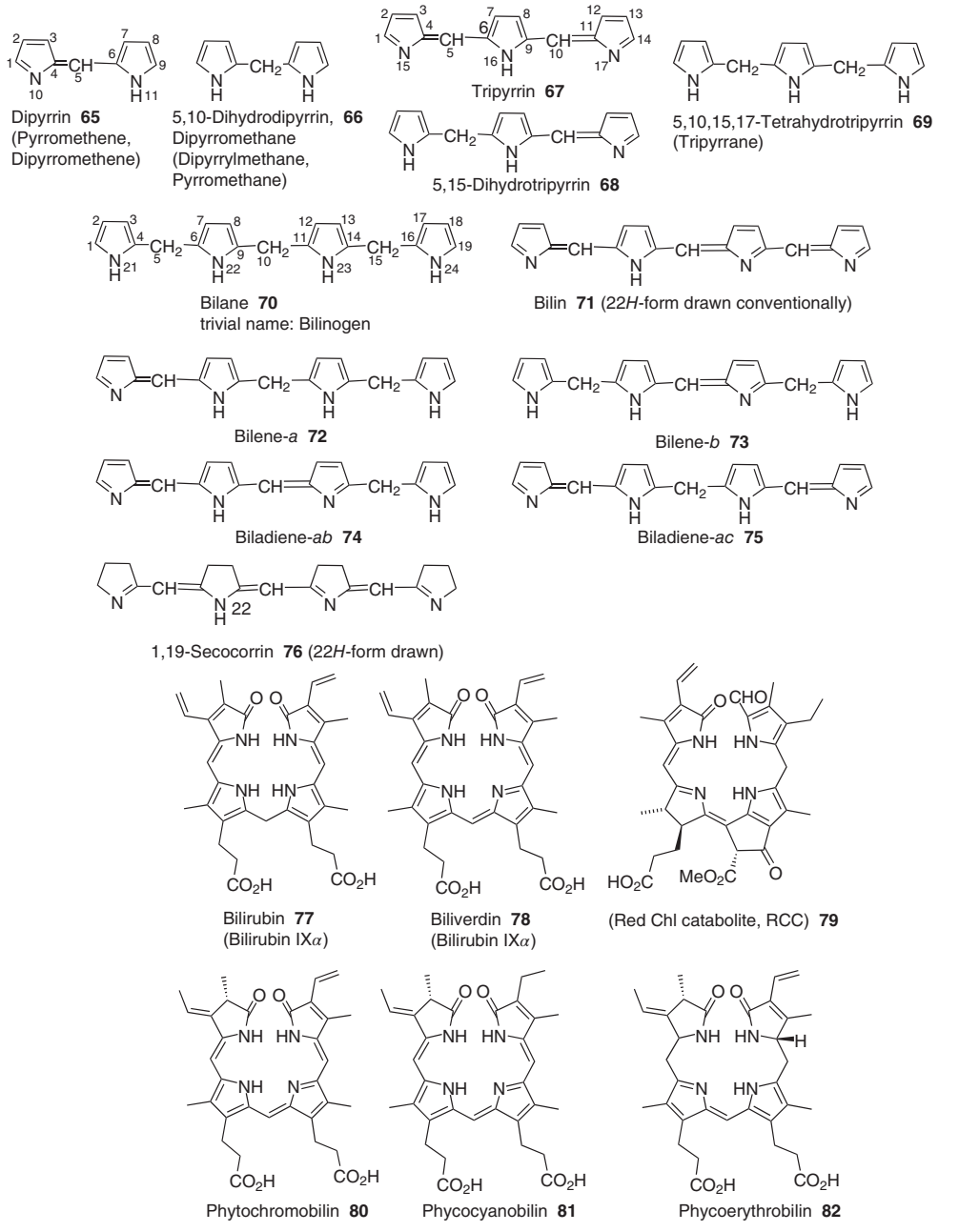

Figure 2.16 Fundamental linear tetrapyrroles and selected natural products.

photochromobilin **80** as the photosensory chromophore of phytochromes and biliverdin **78** as the photoreceptor in two-component sensor histidine kinases (bacteriophytochromes) [45]. Linear tetrapyrroles also function as accessory light-harvesting pigments in photosynthesis. Examples for these phycobilins are phycocyanobilin **81** and phycoerythrobilin **82** [46].

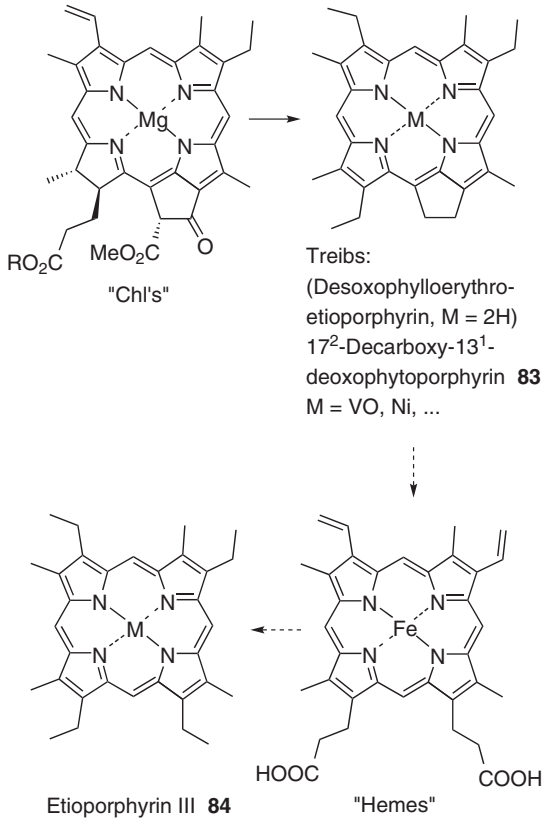

Figure 2.17 Treibs' scheme for the diagenic formation of petroporphyrins from chlorophylls and hemes.

2.3.5 Geoporphyrins

In addition to porphyrins in living organisms, a large number of natural porphyrins exist in geological deposits [47]. These geoporphyrins are formed abiotically over geological time periods in organic sediments. Synonyms are petroporphyrins and sedimentary porphyrins, and their fundamental structure and diagenic formation was established by Treibs [48]. These fossil molecules are derived from the biological chlorophylls and porphyrins under low thermal and oxidative stress, and they often retain a structural resemblance with their biochemical precursors (Figure 2.17). Many of the over 100 known petroporphyrins are related to or derived from phytoporphyrin **46** (more ferns than dinosaurs). Etioporphyrin derivatives are well represented, and much of this organic geochemistry involves side-chain manipulations and thus most can be easily named using the semi-systematic nomenclature based on Table 2.1. Often they occur as metal complexes, mostly with Ni(II) or V(IV)O, but some with Cu, Fe, and Ga are known as well [49].

2.4 Special Aspects of Porphyrin Nomenclature

2.4.1 IUPAC-IUB Nomenclature

By now it is clear that naming porphyrins is not an easy endeavor, as it is confounded by the concomitant use of "old" Fischer nomenclature, IUPAC-IUB nomenclature, and

the constant addition of new trivial names. In some areas, we have the emergence of whole new fields with their own informal sub-nomenclature, notably for the expanded, contracted, and isomeric porphyrins and hydroporphyrins. Although formal rules are all well and good, the often complicated and very long systematic names are too cumbersome for practical use (e.g., the systematic name of phytoporphyrin **46** is 7,12-diethyl-2^1, 22-dihydro-3,8,13,17-tetramethyl-2^1-oxocyclopenta[*at*]porphyrin-1-propionic acid). Thus, in most cases, the semi-systematic nomenclature, that is, using the IUPAC trivial names as a basis, will be more convenient. For example, the compound called "chlorin e_6" by Fischer is semi-systematically 2^1,22-dihydrorhodochlorin-15-acetic acid, an unambiguous name.

Often a subtractive/substitutive nomenclature can be efficient and is recommended by IUPAC. Thus, if one (or more) substituent is changed compared to a parent compound, add the prefix "de-" followed by the name of the substituent to be removed (e.g., compound **83**). In case of substitution, also add the position and name of the new substituent. For example, Fischer's "rhodinporphyrin g_3" is 7-formyl-7-demethyl-phylloporphyrin.

New trivial names abound. Many of the common use names make sense to the specialist and are useful within a laboratory, but can be confusing for other chemists. That said, it is still a requirement to give systematic or semi-systematic names for new compounds, and the naming of new compounds as "complex **XX**,", "dimer **XX**" or such in experimental sections should be a no-no. Some of the ingenuity spent on new catchphrase trivial names could be better devoted to helping to give a more streamlined and organized picture of the variety in the porphyrin world and make the field more accessible for other chemists.

As always, the devil is in the details. Often, multiple ways to name a porphyrin can exist. If in doubt, consult the rank given to the various parent macrocycles in the IUPAC rules [10]. Likewise, some of the IUPAC names (e.g., rhodochlorin, phyllochlorin) are the same as those used by Fischer, but may have different side chains (vinyl vs. Et). For some of the type isomers, the numbers for the β-positions are different from the ones obtained by employing IUPAC/CAS rules.

2.4.2 Metalloporphyrins

The deprotonated, dianionic porphyrinato is a tetradentate ligand where N21, N22, N23, and N24 have been shown to complex or bind almost any element in the periodic table [50]. Naming these "metalloporphyrins," that is, the ligand–metal ion complexes, is relatively simple. In the older literature, they have often been simply called "metal(XX) porphyrin," while today the IUPAC system for coordination compounds [51] requires specific identification of the porphyrin as an anionic ligand (ato), the use of enclosing marks [{()}], and a specific ordering of the various components, as in axial ligand(porphyrinato)metal(ox-#). Additionally, the orientation of axial ligands with regard to the porphyrin plane is identified as **α** (below) or **β** (above) (Figure 2.18).

Metal coordination can also occur at other positions of the macrocycle [52]. Like other aromatic compounds, porphyrins can form π-complexes. Most of the known compounds involve organometallic complexes formed with the π-system of the pyrrole ring(s), for example, similar to ferrocene, or substituent ring systems. Porphyrinogen **85** illustrates that both metal-nitrogen σ-bonds and metal-(η^5-pyrrolyl) π-bonds can occur within one molecule [53]. Transition metals may also be bound to peripheral tetrapyrrole positions, that is, involving a C_m or C_b position, and the various types are also illustrated in Figure 2.18. The

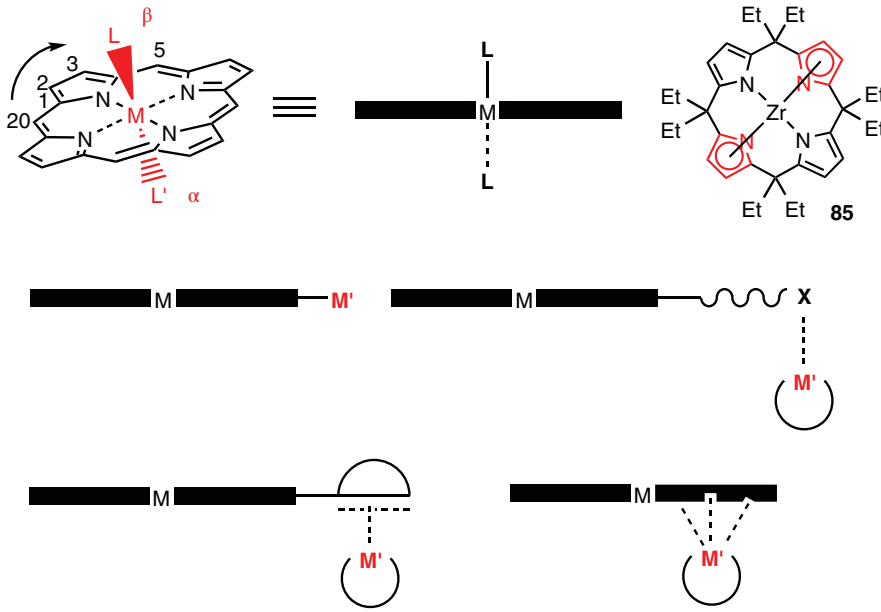

Figure 2.18 Illustration of different types of metal–porphyrin interactions.

standard rules for organometallic compounds (e.g., η^n-nomenclature, where n = number of atoms coordinating to M') and from the "Red Book" apply [51, 54].

2.4.3 Expanded Porphyrins

The variety of expanded/contracted porphyrins and skeletal isomers is best sorted in a formal manner using Vogel's annulene approach [8]. This incorporates the number of electrons involved in the aromatic pathway in the name of the compound. Thus, porphyrin **1** is an [18]annulene, benzene is a [6]annulene, and "subporphyrin" **86** and sapphyrin **31** are[14]- and [22]annulenes, respectively. However, porphycene **24** also has 18 π-electrons but a different arrangement of the skeleton atoms. Thus, the number of meso-positions is appended to the name. Hence, porphyrin is [18]-porphyrin(1.1.1.1), whereas porphycene is [18]-porphyrin(2.0.2.0). The system is quite useful and allows a systematic description of various expanded systems. It is easily used for heteroatom-substituted systems and oligophyrins (a colloquial term for cyclic compounds similar to porphyrins) as well [55]. For example, compound **25** is a 21,22,23,24-tetraoxo[18]porphyrin(1.1.1.1) dication, while the "Figure 8" molecule **87** contains eight pyrrole units and is an octaphyrin(1.1.1.0.1.1.1.0) (Figure 2.19) [56]. Note that the [x]annulene nomenclature conforms to IUPAC rulings, but its use for porphyrin systems is informal.

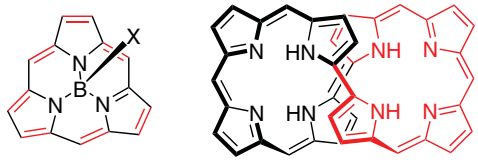

86
(Subporphyrin)

87
Octaphyrin(1.1.1.0.1.1.1.0)

Figure 2.19 Subporphyrin and octaphyrin.

Similar systems are in use for contracted, core-modified, and isomeric porphyrins and can also be found in the literature on calix-type compounds, especially those of the expanded type and those with skeletal rearrangements. For example, compound **12**, a 5,10,15-trihydroporphyrin, might informally be called a calix[4]phyrin-(**1**,*1*,*1*,*1*), where [4] now indicates the number of pyrrole units, bold numbers the number of carbon atoms in bridging conjugated units, and numbers in italics the number of atoms in non-conjugated bridges.

2.4.4 Fused Systems

Porphyrins with fused ring systems are encountered frequently. Classic examples of systems with extra *ortho*-fused rings are phthalocyanine **34** and tetrabenzoporphyin **35**. Porphyrins with cyclic hydrocarbons are named using the standard IUPAC rules for fused compounds and using the porphyrin as the basic component of the semi-systematic name. For example, the geoporphyrin **83** (M = 2H) has the systematic name 7,12,18-triethyl-2^1,2^2-dihydro-3,8,13,17-tetramethylcyclopenta[*at*]porphyrin or can be named semi-systematically based on phytoporphyrin as 17^2-decarboxy-13^1-deoxophytoporphyrin. The fused character can also be highlighted in the semi-systematic name 13^2,15-cycloetioporphyrin III. More detail can be found in the IUPAC recommendations for tetrapyrroles [10]. Figure 2.20 gives some more selected examples of naming porphyrins with fused rings; as shown for compounds **88**–**90**, the fused ring is numbered as a substituent of the lowest possible position of the porphyrin ring.

Many contemporary compounds have fused rings involving both the C_m and C_b positions. Of considerable interest are fused (oligo)porphyrins such as **92** to **94** or porphyrins with other aromatic units fused to the C_m and C_b positions, for example, **95** [57]. According to IUPAC rules, these must be named by selecting the component with a trivial or semi-systematic name (here porphyrin) as the principal component and designating the other components as a prefix. The biporphyrin **91** or compound **96** is technically a ring-assembled system, and the standard rules as outlined in the "blue book" are applicable [58]. Colloquially such systems are known as singly-, doubly-, or triply-linked porphyrins and are often specified as "meso-meso-linked" **XX** or "meso-meso,β-β-linked" **XX** or "meso-meso,β-β,β-β-linked," and so on, systems.

2.4.5 Conformers, Rotamers, and Atropisomers

Like the situation with axial ligands in metalloporphyrins (Figure 2.18), it is sometimes necessary to incorporate information for the stereochemical configuration of substituents or macrocycle atoms. Two typical examples are illustrated in Figure 2.21. Porphyrinogens with meso-substituents can have different relative orientations of the R groups (↑↑↑↑, ↑↑↑↓, ↑↑↓↓, ↑↓↑↓), which are technically optical configurational isomers. These are identified by α and β for up and down, respectively, in the different possibilities. For only two residues, *syn* and *anti* can be used. The same applies to the description of peripheral substituents. For example, Collman's classic picket fence porphyrins **98** can exist as different atropisomers (conformational isomers) due to hindered rotation about the C_m-C_i bond [59]. A similar notation is also used for poly-N-substituted porphyrins to indicate the orientation of the N-substituents and in porphyrinogens to identify the up and down orientation of the pyrrole rings.

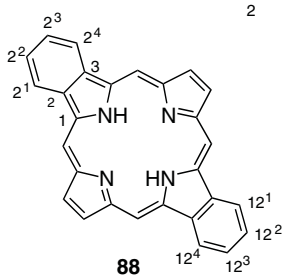

88
Dibenzo[*b,l*]porphyrin

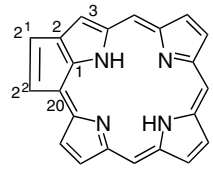

89
Cyclopenta[*at*]porphyrin

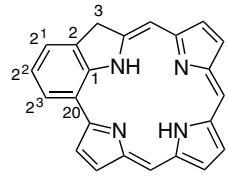

90
3*H*-Benzo[*at*]porphyrin

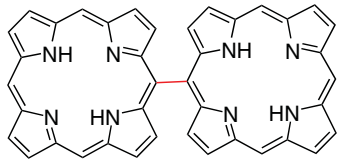

91
5,5'-(Biporphyrinyl)
5,5'-Bi(porphyrin)

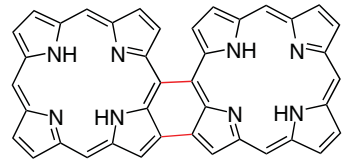

92
2,20-(Porphyrin-2',20'-triyl)porphyrin

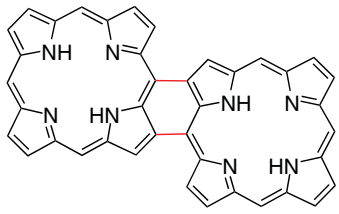

93
2,20-(Porphyrin-2',20'-diyl)porphyrin

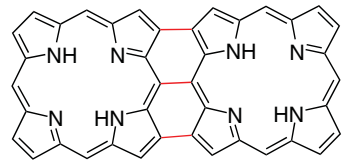

94
2,18,20-(Porphyrin-2',18',20'-triyl)porphyrin

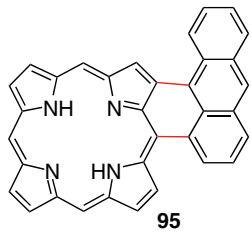

95
2,20-(Anthracen-1,9-diyl)porphyrin

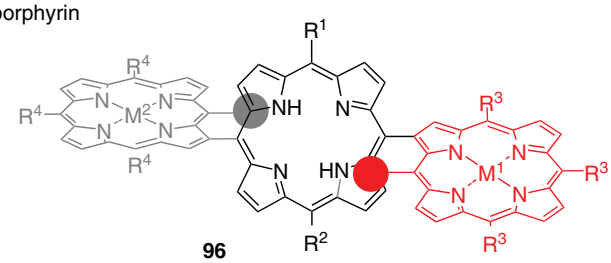

96

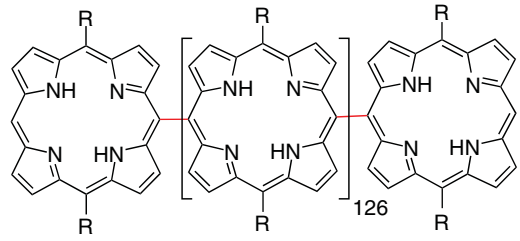

97 R = 3,5-dioctyloxyphenyl

Figure 2.20 Examples of ring-assembled and fused porphyrins.

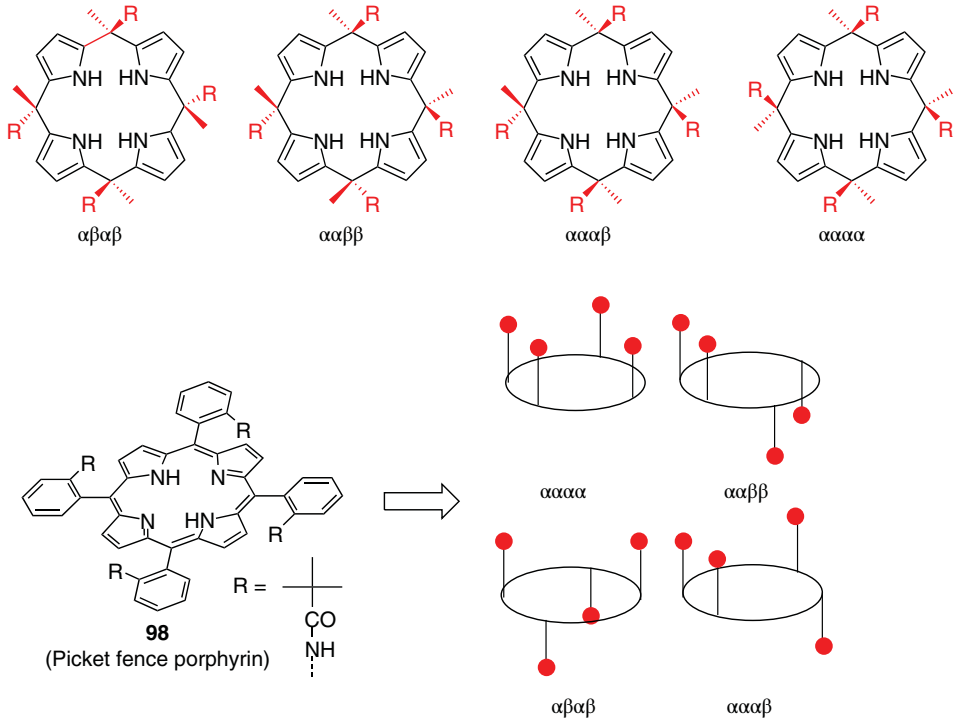

Figure 2.21 Configurational and conformational isomerism in porphyrins.

The larger a porphyrin, the more complicated the situation. Expanded porphyrins become more flexible than [18]porphyrins, and thus the questions of whether a pyrrole ring points inwards or outwards becomes relevant. Likewise, all double bonds in the aromatic (annulene) 18-electron system of a normal porphyrin have a *Z* configuration, whereas in larger systems *E*-configurated double bonds can occur, and this must then be specified.

2.4.6 Chirality

Many porphyrins with stereogenic centers are known. For natural occurring hydroporphyrins such as Chl (and derivatives) or sirohydrochlorin, the stereochemistry at the chiral centers is known and does not need to be expressively stated [27]. For other compounds, the absolute configuration must be indicated by *R* or *S*.

Many special cases of chirality are associated with porphyrins. In the natural environment, all porphyrin cofactors, even the achiral (protoporphyrinato)iron(II), are chiral as ligation occurs at the central metal (giving rise to α/β-forms). Likewise, porphyrins can have inherent chirality (especially in the solid state) due to unsymmetrical nonplanar distortions [28, 60], and many chiral supramolecular complexes are known [61]. Planar chirality may be encountered in metalloporphyrins or bridged porphyrins. Axial chirality is an intriguing topic with systems such as **96**, while large expanded systems such as "octaphyrins" or "helimeric" porphyrins can be chiral due to helicity (axial chirality) [62, 63].

2.5 Porphyrin Stenography

Porphyrins are large organic compounds, and those of current interest (arrays, oligomers, materials, and supramolecular complexes) are even larger. The parent compound **1** has a molecular weight of 310.35, and the molecular weights of the standard workhorses H_2TPP (5,10,15,20-tetraphenylporphyrin) and H_2OEP (2,3,7,8,12,13,17,18-octaethylporphyrin) are 614.74 and 534.78, respectively. Some of the largest and most fascinating porphyrins belong to Osuka's "meso-meso-linked" porphyrin arrays; porphyrin **97**, a 128-mer, has a molecular weight of 132 702 [64]! No wonder that many shorthand notations for porphyrins are in use in day-to-day lab operations and in the literature.

Simple (metallo)porphyrins are often informally abbreviated by using shorthand for the porphyrin ligand and appending information about the metal and axial ligands. For example, Fe(III)(TPP)Cl would be chloro(5,10,15,20-tetraphenylporphyrinato)iron(III), while H_2TPP identifies the respective free base 5,10,15,20-tetraphenylporphyrin. Some of the more widely used abbreviations are tabulated in Table 2.4. These are used

Table 2.4 Abbreviations used for standard porphyrins and derivatives.

Abbreviation	Definition
BChl	Bacteriochlorophyll
Chl	Chlorophyll
Chlide	Chlorophyllide
Pheo	Pheophorbide
Cbl	Cobalamin
Cyt	Cytochrome
H_2Por	Free base porphyrin
M(X)Por	Metalloporphyrin with metal in oxidation state "X"
OBrTPP	2,3,7,8,12,13,17,18-Octabromo-5,10,15,20-tetraphenylporphyrin*ato*
OEP	2,3,7,8,12,13,17,18-Octaethylporphyrin*ato*
OETPP	2,3,7,8,12,13,17,18-Octaethyl-5,10,15,20-tetraphenylporphyrin*ato*
H_1NCP	N-confused porphyrin (**23**)
H_2NCP	N-confused porphyrin (**22**)
NCP	N-confused porphyrin*ato*
H_3Cor	Free base corrole
H_2TBP	Tetrabenzoporphyrin
TBP	Tetrabenzoporphyrin*ato*
Etio	Etioporphyrin*ato*
Hp	Hematoporphyrin*ato*
H_2Pc	Phthalocyanin
Pc	Phthalocyanin*ato*
Por	Porphyrin*ato* (= dianion)
PP	Protoporphyrin*ato*
TPP	5,10,15,20-Tetraphenylporphyrin*ato*

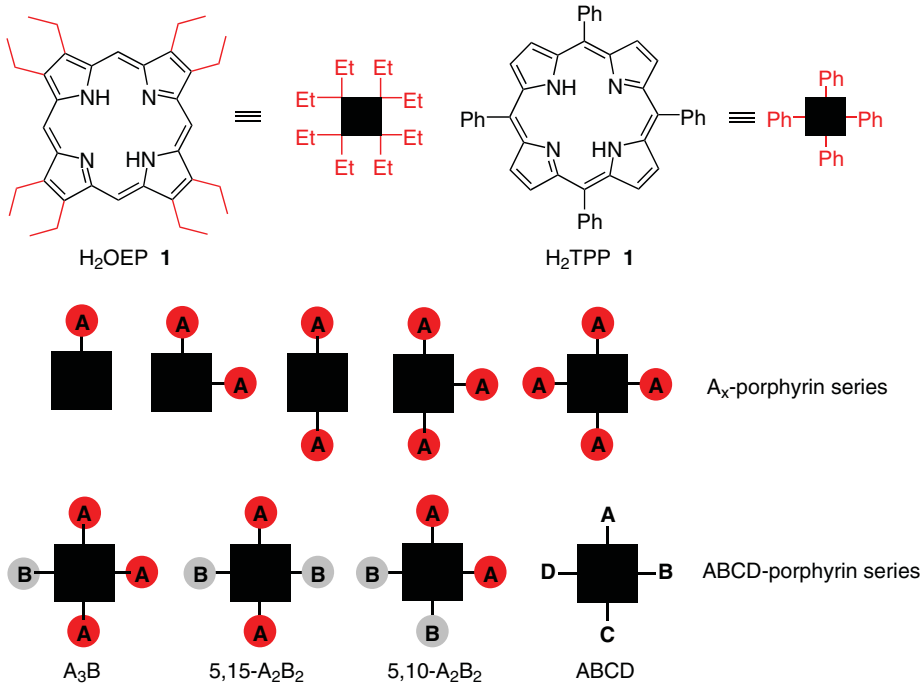

Figure 2.22 Shorthand notation for β-substituted A_x- and ABCD-type porphyrins.

throughout this book too, and allow some scope for logical application. For example, β-octabromination of TPP would give OBrTPP, while combinations of the tetraphenylporphyrin (TPP) and octaethylporphyrin (OEP) substituent pattern would yield OETPP (2,3,7,8,12,13,17,18-octaethyl-5,10,15,20-tetraphenylporphyrinato).

Likewise, the multitude of differently substituted porphyrins that are based on a common macrocycle can be illustrated in simplified form. The classic is the type-isomer notification illustrated in Figure 2.12 for uroporphyrin. The different pyrrole rings are often identified as I, II, III, IV or A, B, C, and D for the pyrroles N21, N22, N23, and N24, respectively. Total syntheses often refer to "geographic" parts of the porphyrin; for example, a [2 + 2] condensation of two dipyrromethanes could involve a combination of southern and northern or eastern and western halves. For 5,10,15,20-tetrasubstituted porphyrins (meso-tetrasubstituted) alone, the porphyrin is simply shown as a square ■ or circle ○ when discussing chemistry that does not involve the macrocycle. Figure 2.22 shows this for the A_x- and ABCD-type porphyrins [65, 66]. None of this is an official nomenclature, but it will be found in many lab notebooks and publications on porphyrin chemistry.

Acknowledgments

Our own work on porphyrins was generously supported over the years by grants from the Detusche Forschungsgemeinschaft (DFG), Fonds der Chemischen Industrie (FCI), Irish Research Council (IRC), Health Research Board (HRB), the European Commission, and Science Foundation Ireland (SFI).

References

1 Hoppe-Seyler, F. (1877–1878). Weitere Mitteilungen über die Eigenschaften des Blutfarbstoffes. *Hoppe-Seylers Zeitschrift für Physiologische Chemie* 1: 121–139.

2 Küster, W. (1912). Über die Konstitution des Haemins. *Berichte der Deutschen Chemischen Gesellschaft* 45: 1935–1946.

3 Fischer, H. and Klarer, J. (1926). Über Ätioporphyrin aus Kryptopyrrol und Hämopyrrol. Synthese des Hämopyrrols. *Justus Liebigs Annalen der Chemie* 450: 181–201.

4 Fischer, H. and Orth, H. (1934). *Die Chemie des Pyrrols*, vol. 1. Leipzig: Akademische Verlagsgesellschaft.

5 Fischer, H. and Orth, H. (1937). *Die Chemie des Pyrrols*, vol. 2, part 1. Leipzig: Akademische Verlagsgesellschaft.

6 Fischer, H. and Stern, A. (1940). *Die Chemie des Pyrrols*, vol. 2, part 2. Leipzig: Akademische Verlagsgesellschaft.

7 Furuta, H., Asano, T., and Ogawa, T. (1994). N-confused porphyrin – a new isomer of tetraphenylporphyrin. *Journal of the American Chemical Society* 116: 767–768.

8 Vogel, E. (1993). The porphyrins from the 'annulene chemist's' perspective. *Pure & Applied Chemistry* 65: 143–152.

9 Fuhrhop, J.-H. (1978). Irreversible reactions on the porphyrin periphery (excluding oxidations, reductions, and photochemical reactions). In: *The Porphyrins*, vol. 1, Part A (ed. D. Dolphin), 131–159. New York: Academic Press.

10 Moss, G.P. (1988). Nomenclature of tetrapyrroles. Recommendations 1986. IUPAC-IUB Joint Commission on Biochemical Nomenclature (JCBN). *European Journal of Biochemistry* 178: 277–328; also published in: (1987) Pure & Applied Chemistry, 59, 779–832.

11 Willstätter, R. and Stoll, A. (1913). *Untersuchungen über Chlorophyll. Ergebnisse und Methoden*. Berlin: Verlag von Julius Springer.

12 Bonnett, R. (1978). Nomenclature. In: *The Porphyrins*, vol. 1, Part A (ed. D. Dolphin), 1–27. New York: Academic Press.

13 Montforts, F.-P., Gerlach, B., and Höper, F. (1994). Discovery and synthesis of less common natural hydroporphyrins. *Chemical Reviews* 94: 327–347.

14 Sessler, J.L., Gale, P.A., and Cho, W.-S. (2006). *Anion Receptor Chemistry*. London: RSC Publishing.

15 Baeyer, A. (1886). Ueber ein Condensationsproduct von Pyrrol mit Aceton. *Berichte der Deutschen Chemischen Gesellschaft* 19: 2184–2185.

16 Gale, P.A., Sessler, J.L., and Král, V. (1998). Calixpyrroles. *Chemical Communications* 1–8.

17 Senge, M.O. (2011). Extroverted confusion – Linus Pauling, Melvin Calvin and porphyrin isomers. *Angewandte Chemie International Edition* 50: 4272–4277.

18 Chmielewski, P.J., Latos-Grazynski, L., Rachlewicz, K., and Glowiak, T. (1994). Tetra-*p*-tolylporphyrin with an inverted pyrrole ring – a novel isomer of porphyrin. *Angewandte Chemie International Edition* 33: 779–781.

19 Vogel, E., Kocher, M., Schmickler, H., and Lex, J. (1986). Porphycene – a novel porphyrin isomer. *Angewandte Chemie International Edition* 25: 257–259.

20 Vogel, E., Haas, W., Knipp, B. et al. (1988). Tetraoxaporphyrin Dication. *Angewandte Chemie International Edition* 27: 406–409.

21 Szyszko, B. and Latos-Grazynski, L. (2015). Core chemistry and skeletal rearrangements of porphyrinoids and metalloporphyrinoids. *Chemical Society Reviews* 44: 3588–3616.

22 Sessler, J.L. and Weghorn, S.J. (1997). *Expanded, Contracted & Isomeric Porphyrins*. Pergamon Press, Oxford.

23 Kadish, K.M., Smith, K.M., and Guilard, R. (ed.) (2010). *The Porphyrin Handbook*, vol. 15. Singapore: World Scientific.

24 Rodriguez-Morgade, M.S. and Stuzhin, P.A. (2004). The chemistry of porphyrazines: an overview. *Journal of Porphyrins and Phthalocyanines* 8: 1129–1265.

25 Battersby, A.R. (2000). Tetrapyrroles: the pigments of life. *Natural Product Reports* 17: 507–526.

26 Milgrom, L.R. (1997). *The Colours of Life: An Introduction to the Chemistry of Porphyrins and Related Compounds*. Oxford University Press.

27 Senge, M.O., Ryan, A.A., Letchford, K.A. et al. (2014). Chlorophylls, symmetry, chirality, and photosynthesis. *Symmetry* 6: 781–843.

28 Senge, M.O., MacGowan, S.A., and O'Brien, J. (2015). Conformational control of cofactors in nature – the influence of protein-induced macrocycle distortion on the biological function of tetrapyrroles. *Chemical Communications* 51: 17031–17063.

29 Warren, M.J. and Smith, A.G. (ed.) (2009). *Tetrapyrroles: Birth, Life and Death*. New York: Springer-Verlag.

30 Mülder, G.H. (1844). Über eisenfreies Hämatin. *Journal für Praktische Chemie* 32: 186–197.

31 Lin, Y.W. (2015). The broad diversity of heme-protein cross-links: an overview. *Biochimica et Biophysica Acta – Proteins and Proteomics* 1854: 844–859.

32 Bowman, S.E.J. and Bren, K.L. (2008). The chemistry and biochemistry of heme c: functional bases for covalent attachment. *Natural Product Reports* 25: 1118–1130.

33 Reedy, C.J., Elvekrog, M.M., and Gibney, B.R. (2008). Development of a heme protein structure-electrochemical function database. *Nucleic Acids Research* 36: D307–D313.

34 Grimm, B., Porra, R.J., Rüdiger, W., and Scheer, H. (ed.) (2006). *Chlorophylls and Bacteriochlorophylls*. Dordrecht: Springer.

35 Scheer, H. (ed.) (1991). *Chlorophylls*. Boca Raton: CRC Press.

36 Senge, M.O. and Smith, K.M. (1995). Structure and biosynthesis of bacteriochlorophylls. In: *Anoxygenic Photosynthetic Bacteria* (ed. R.E. Blankenship, M.T. Madigan and C. Bauer), 137–151. Dordrecht: Kluwer Academic Publ.

37 Smith, K.M. (1994). Nomenclature of the bacteriochlorophylls *c*, *d*, and *e*. *Photosynthesis Research* 41: 23–26.

38 Chen, M., Schliep, M., Willows, R.D. et al. (2010). A red-shifted chlorophyll. *Science* 329: 1318–1319.

39 Pfaltz, A., Jaun, B., Fassler, A. et al. (1982). Zur Kenntnis des Faktors F430 aus methanogenen Bakterien: Struktur des porphinoiden Ligandsystems. *Helvetica Chimica Acta* 65: 828–865.

40 Gruber, K., Puffer, B., and Kräutler, B. (2011). Vitamin B_{12}-derivatives – enzyme cofactors and ligands of proteins and nucleic acids. *Chemical Society Reviews* 40: 4346–4363.

41 IUPAC-IUB Commission on Biochemical Nomenclature (JCBN) (1976). Nomenclature of corrinoids (rules approved 1975). *Pure & Applied Chemistry* 48: 495–502.

42 Falk, H. (1989). *The Chemistry of Oligopyrroles and Bile Pigments*. Wien, New York: Springer Verlag.

43 Lightner, D.A. (2013). *Bilirubin: Jekyll and Hyde Pigment of Life*. Wien: Springer.

44 Kräutler, B. (2014). Phyllobilins – the abundant bilin-type tetrapyrrolic catabolites of the green plant pigment chlorophyll. *Chemical Society Reviews* 43: 6227–6238.

45 Rockwell, N.C., Su, Y.-S., and Lagarias, J.C. (2006). Phytochrome structure and signaling mechanisms. *Annual Review of Plant Biology* 57: 837–858.

46 Scheer, H., Yang, X., and Zhao, K.-H. (2015). Biliproteins and their applications in bioimaging. *Procedia Chemistry* 14: 176–185.

47 Ryan, A.A. and Senge, M.O. (2015). How green is green chemistry? Chlorophylls as a bioresource from biorefineries and their commercial potential in medicine and photovoltaics. *Photochemical & Photobiological Sciences* 14: 638–660.

48 Treibs, A. (1934). Chlorophyll- und Häminderivate in bituminösen Gesteinen, Erdölen, Erdwachsen und Asphalten. Ein Beitrag zur Entstehung des Erdöls. *Liebigs Annalen der Chemie* 510: 42–62.

49 Callot, H.J. (1991). Geochemistry of chlorophylls. In: *Chlorophylls* (ed. H. Scheer), 339–364. Boca Raton: CRC Press.

50 Buchler, J.W. (1978). Synthesis and properties of metalloporphyrins. In: *The Porphyrins*, vol. 1, Part A (ed. D. Dolphin), 389–483. New York: Academic Press.

51 Connelly, N.G. and Damhus, T. (2005). *Nomenclature of Inorganic Chemistry. IUPAC Recommendations 2005*. Cambridge: Royal Society of Chemistry.

52 Senge, M.O. (1996). π-Pyrrole – metal complexes-the missing coordination mode for metal- porphyrin interactions. *Angewandte Chemie International Edition in English* 35: 1923–1925.

53 Floriani, C. (1996). Transition metal complexes as bifunctional carriers of polar organometallics: their application to large molecule modifications and to hydrocarbon activation. *Pure & Applied Chemistry* 68: 1–8.

54 Salzer, A. (1999). Nomenclature of organometallic compounds of the transition elements (IUPAC recommendations 1999). *Pure & Applied Chemistry* 71: 1557–1585.

55 Sessler, J.L. and Seidel, D. Synthetic expanded porphyrin chemistry. *Angewandte Chemie International Edition* 42: 5134–5174.

56 Vogel, E., Bröring, M., Fink, J. et al. From porphyrin isomers to octapyrrolic figure 8 macrocycles. *Angewandte Chemie International Edition in English* 34: 2511–2514.

57 Tanaka, T. and Osuka, A. (2015). Conjugated porphyrin arrays: synthesis, properties and applications for functional materials. *Chemical Society Reviews* 44: 943–969.

58 Favre, H.A. and Powell, W.H. (2014). *Nomenclature of Organic Chemistry : IUPAC Recommendations and Preferred Names 2013*. Cambridge: Royal Society of Chemistry.

59 Collman, J.P., Gagne, R.R., Reed, C.A. et al. (1975). Picket-fence porphyrins – synthetic models for oxygen binding hemoproteins. *Journal of the American Chemical Society* 97: 1427–1439.

60 Senge, M.O. (2006). Exercises in molecular gymnastics – bending, stretching and twisting porphyrins. *Chemical Communications* 243–256.

61 Borovkov, V. (2014). Supramolecular chirality in porphyrin chemistry. *Symmetry* 6: 256–294.

62 Götz, D.C.G., Bruhn, T., Senge, M.O., and Bringmann, G. (2009). Synthesis and stereochemistry of highly unsymmetric beta, meso-linked porphyrin arrays. *Journal of Organic Chemistry* 74: 8005–8020.

63 Brückner, C., Götz, D.C.G., Fox, S.P. et al. (2011). Helimeric porphyrinoids: stereostructure and chiral resolution of meso-tetraarylmorpholinochlorins. *Journal of the American Chemical Society* 133: 8740–8752.

64 Aratani, N., Osuka, A., Kim, Y.H. et al. (2000). Extremely long, discrete meso-meso-coupled porphyrin arrays. *Angewandte Chemie International Edition* 39: 1458–1462.

65 Lindsey, J.S. (2010). Synthetic routes to meso-patterned porphyrins. *Accounts of Chemical Research* 43: 300–311.

66 Senge, M.O. (2011). Stirring the porphyrin alphabet soup--functionalization reactions for porphyrins. *Chemical Communications* 47: 1943–1960.

3

Organic Synthesis and Reactivity of Porphyrins

Mathias O. Senge and Alina Meindl

School of Chemistry, Trinity Biomedical Sciences Institute, Trinity College Dublin, Dublin, Ireland

3.1 Introduction

This chapter aims to briefly survey the organic chemistry of porphyrins with an emphasis on synthetic strategies and functionalization reactions for the main 24-macrocycle atom, 18π-electron system. An overview of the main classes of porphyrins has been given in Chapter 2, and the synthetic aspects of several of the more specialized ones, such as isomers, expanded and contracted systems, hydroporphyrins and natural products, are covered in other chapters of this book.

Even with this limitation, we cannot cover all related literature, nor highlight all worthwhile studies. In early 2022, the Web of Science Database contained >66 000 publications on "porphyrins," and even an arbitrary restriction to those in "organic chemistry" journals yielded an excess of 5800 papers (with another 21 500 in "chemistry multidisciplinary"). This also excludes the classic period of porphyrin chemistry prior to 1945! Thus, we can only give an overview of general strategies and methods, and will highlight selected examples of contemporary research together with key references to facilitate further reading.

Many fine books and reviews have been published on the synthesis and reactivity of porphyrins over the centuries, and some of these remain relevant for today's practitioner of porphyrin chemistry. Next to Fischer and Orth's classic *Die Chemie des Pyrrols* [1], four book(s) series cover almost everything there is to know about past porphyrin chemistry. The most useful single-volume book is still Kevin Smith's *Porphyrins and Metalloporphyrins* from 1975 [2], which also contains a handy laboratory methods section. In conjunction with David Dolphin's definitive six-volume set *The Porphyrins* [3], this covers the literature up to the late 1970s. Both works include many fundamental chapters on reactivity and synthesis that remain pertinent today. Perhaps the last time a comprehensive picture of porphyrin chemistry could be given was at the turn of the millennium with the publication of *The Porphyrin Handbook* [4], a 20-volume series edited by Kadish, Smith, and Guilard. The reader is referred to these works for more detailed descriptions. Other relevant reviews can be found in the more recent (currently at 45 volumes!) *Handbook of Porphyrin Science* and journals and will be referenced below where appropriate.

Dedicated to the memory of Prof. Dr. Teodor Silviu Balaban

Fundamentals of Porphyrin Chemistry: A 21st Century Approach, Volume 1, First Edition.
Edited by Penelope J. Brothers and Mathias O. Senge.
© 2022 John Wiley & Sons Ltd. Published 2022 by John Wiley & Sons Ltd.

The breadth of available primary to tertiary literature on porphyrins indicates the futility – even in the subset context of "organic chemistry" – of covering all of what a porphyrin specialist might consider relevant. The main focus here will be on the synthesis and reactivity of the fundamental porphyrin macrocycle, and we will use historical and contemporary examples to highlight enduring concepts and state-of-the-art organic chemistry of porphyrins.

Fundamentally, the synthesis of porphyrins comes down to symmetry considerations [5], as implied by its basic structure – that of a *tetra*pyrrole (Figure 3.1). If the target structure **1** is symmetrical, then a simple *tetra*merization of the pyrrole precursor(s) will suffice; if not, more elaborate syntheses and starting materials must be employed. The former typically involves the condensation of either four α-substituted pyrroles or (β-substituted) pyrroles with an aldehyde carrying the meso-substituent (**2**). In the latter case, one can employ various approaches, be it the "total" synthesis of a linear tetrapyrrole **3** followed by cyclization, the reaction of smaller building blocks, for example, a tripyrrane and a pyrrole [3 + 1] or of two dipyrrins [2 + 2] (**4**), partial synthesis using preformed porphyrins **5**, or even "mixed" condensations of different pyrroles/aldehydes, provided the reaction preferentially gives the desired regioisomer or the stamina of the chemist is sufficient for the required chromatographic purification.

One hundred and fifty years after the first description of a pure porphyrin by Thudichum in 1867 (see [6] for an excellent article on the history of porphyrin research), porphyrin chemistry remains challenging for the uninitiated. Pyrroles tend to polymerize, pyrrins can undergo side reactions, bilanes may fragment under the reaction conditions and scramble, initial cyclization products can resist oxidation to the aromatic systems, and so on. Yields of condensation reactions may reach 60%, but in reality are mostly in the 10–20% range; at best, porphyrins show good solubility in the millimolar range, limiting the scale-up of reactions.

Similar problems are faced when targeting new systems via functionalization reactions. Even for symmetrical target compounds, one has to deal with the different reactivity of the

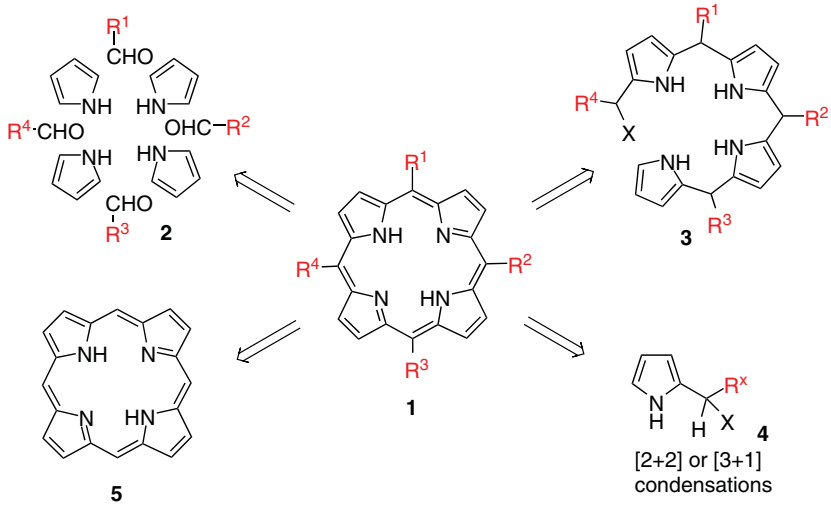

Figure 3.1 Retrosynthetic analysis of porphyrin synthesis. Similar symmetry considerations apply for meso- and β-substituted porphyrins.

α-positions (C_a), meso-positions (C_m), β-positions (C_b), and the reactivity and chelating ability of the nitrogen core, for example, the possibility of metal insertion into a free base porphyrin. For metalloporphyrins, follow-up reactions may involve axial ligation or ligand exchange, or one may encounter low acid stability of the metal complex. And – do not forget – when all is done and dusted, porphyrins are dyes; they do have a rich photochemistry, can photobleach or act as photosensitizers. So, like the synthesis of porphyrins, their reactivity and use as building blocks for complex systems encompasses thousands of different reactions.

3.2 Synthesis of meso-Substituted Porphyrins from Pyrrole Building Blocks

meso-Substituted porphyrins present the most accessible class of tetrapyrroles. Even though they cannot be used as direct counterparts to naturally occurring porphyrins, they still play an integral role in a wide range of applications such as material science, synthetic methods development, and fundamental studies. Various syntheses now exist and enable chemists to attach different substituents to the porphyrin core in a defined manner. In practical terms, their synthesis often necessitates only the use of aldehydes for the C_m part in pyrrole condensation reactions, which gives broad scope to quickly generate systems with alkyl, aryl, heterocyclic, functional, and organometallic groups, or even other porphyrins. This has made meso-substituted porphyrins the standard workhorses of many contemporary studies.

3.2.1 Symmetric A_4-Type Porphyrins

The most easily prepared porphyrins are the symmetric A_4-type systems, and here 5,10,15,20-tetraphenylporphyrin (H_2TPP) stands out as the prime example that we will encounter frequently. Their synthesis was first investigated by Rothemund in 1935. He reacted a range of aliphatic and aromatic aldehydes with pyrrole in methanol and obtained the respective porphyrins in low yields, typically not exceeding 5% [7]. The reactions were performed in sealed tubes, using high concentrations in the absence of an oxidant and required high reaction temperatures. In addition, significant amounts of the corresponding chlorin were isolated as side product, requiring follow-up oxidation. Subsequent modifications included the use of other solvents or metal salts, which benefits reactions with some, but not all, aldehydes and results in the formation of metal complexes. The synthesis of 5,10,15,20-tetramesitylporphyrin is one of the examples of a Rothemund method with a metal salt additive. Newer variants involve the reaction of pyrrole with 1–3 eq. of aldehyde in the presence of metal salts without any solvent, gas phase reactions, or use of acidic solid supports such as silica gel or clay, achieving yields for selected porphyrins in the 10–20% range [8].

3.2.1.1 Adler–Longo Method

A more general method that is still frequently used was developed by Adler, Longo, and co-workers in 1964 [9]. Initially developed for H_2TPP, they used benzaldehyde, pyrrole, and an acidic solvent with heating to reflux under atmospheric conditions. Optimized conditions employing propionic acid and higher concentrations gave improved yields, but the porphyrin is still contaminated with the corresponding chlorin, similar to the Rothemund method.

Contemporary practices of this *Adler–Longo method* involve heating of equimolar amounts of aldehyde and pyrrole in propionic acid for 30 min in air and filtering off the porphyrin after cooling. The chlorin component is often oxidized in the crude reaction mixture with DDQ or chloranil prior to purification, and porphyrins such as H_2TPP can routinely be prepared in >20% yield [10]. Use of other acids, for example acetic acid, can increase the yields to 35–40%, but propionic acid is preferred as it typically allows crystallization of the products directly from the reaction mixture.

The reaction mechanism was investigated in detail by Dolphin, and he proposed the porphyrinogen, that is, the cyclic nonaromatic tetrapyrrole, as the key intermediate in aldehyde-pyrrole condensation reactions. Using UV/vis spectroscopy, he suggested sequential oxidations from the porphyrinogen via porphodimethene to the fully aromatized porphyrin. This was confirmed by isolation of the porphyrinogen and subsequent (photo)chemical oxidation to the porphyrin [11].

The detailed reaction mechanism for the synthesis of H_2TPP is shown in Figure 3.2. In the first step, the oxygen of the benzaldehyde is protonated by the acid, and the pyrrole attacks the carbonyl group. Following deprotonation of the substituted α-position, the aromaticity in the pyrrole is restored. Protonation of the hydroxyl group is then followed by loss of water and formation of a carbocation. This carbocation is then attacked by another pyrrole molecule, and the previous steps are repeated to form the porphyrinogen **7** after the fourth attack of a pyrrole molecule. The preference of cyclotetramerization over simple polymerization can be explained on the basis of steric considerations. In particular, for β-substituted pyrroles (see below), the steric hindrance (see inset in Figure 3.2) between the residues is minimized in a cyclic arrangement as in **6**, which also presents the reactive partners for cyclotetramerization in close vicinity [12]. The porphyrinogen is then subsequently oxidized to the porphomethene **8** and then via the porphodimethene **9** stepwise to the porphyrin **10**.

This method opened the pathway to the widespread use of meso-substituted porphyrins with various substituents, ranging from simple alkyl residues over *p*-, *m*-, or *o*-substituted aryl units to more complex systems such as the "picket fence" porphyrins or capped, strapped, cofacial, and other superstructured systems, some of which we will show below (see Sections 3.8.4 and 3.8.6). The experimental procedure has seen many modifications over the years primarily with regard to solvent and acid catalysis. For example, H_2TPP **10** can be prepared using DMF and $AlCl_3$ as catalyst in 30% yield in 2 h without formation of the chlorin side product. Similar to the synthesis for β-substituted porphyrins, where the C_m carbon atom is often brought into the reaction as a pyrrole α-residue, pyrrole carbinols can be used under Adler–Longo conditions for both alkyl- and arylporphyrin synthesis in low to moderate yields [13].

3.2.1.2 Lindsey Method

The most general and versatile development in this area stems from Lindsey's persistent efforts to develop mild and general conditions for the synthesis of porphyrins [8, 14]. He considered that both pyrrole and benzaldehyde are reactive molecules that should be able to react under milder conditions. Aryl aldehydes tend to react with nucleophiles and an acid catalyst at room temperature. Therefore, this should also work in pyrrole-aldehyde condensations, as pyrrole is very reactive toward S_EAr. Additionally, the biosynthesis of natural porphyrins proceeds via porphyrinogen intermediates with subsequent oxidation to the porphyrin.

Ultimately, these considerations resulted in the development of the "Lindsey method," a two-step, one-flask condensation method for meso-substituted porphyrins that is now a

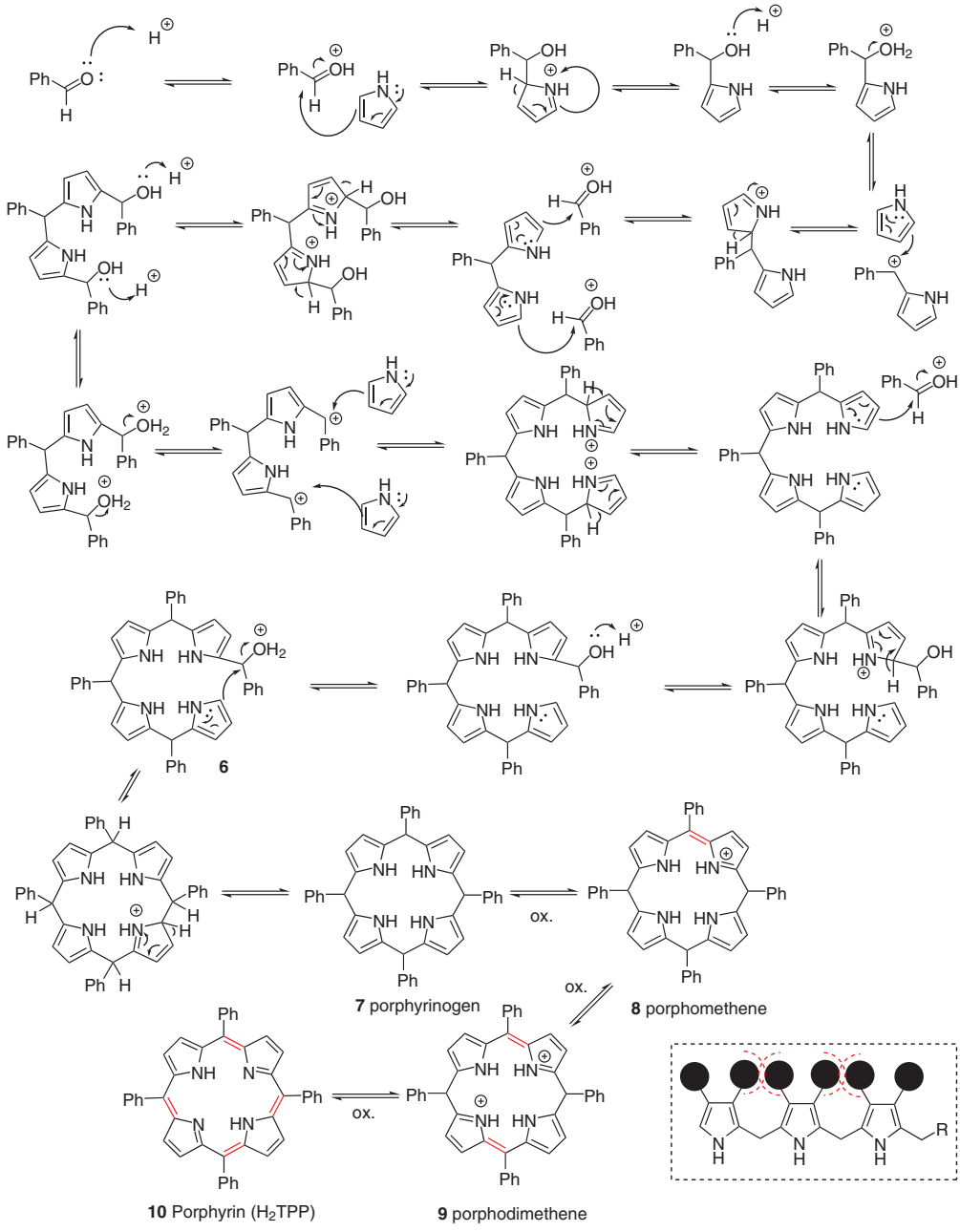

Figure 3.2 Reaction mechanism for the formation of 5,10,15,20-tetraphenylporphyrin (H_2TPP).

cornerstone of the canon of porphyrin chemistry [15]. It consists of the reaction of pyrrole and an aldehyde in CH_2Cl_2 with trifluoroacetic acid (TFA) or BF_3-etherate at room temperature. The final porphyrin is formed through oxidation of the initially formed porphyrinogen in a second step. For example, H_2TPP can be synthesized in 35–40% yield with this method. The reaction is very sensitive to the concentration of the reactants and the acid catalyst.

Typically, a higher concentration of TFA is necessary compared to BF_3-etherate. DDQ is widely used to oxidize porphyrins, and formally three DDQ molecules are necessary to oxidize one porphyrinogen, that is, remove six hydrogen atoms, to a porphyrin. Due to the cost of DDQ, large-scale syntheses often employ the (less effective) *p*-chloranil as an oxidant. This methodology works very well for a broad range of aldehydes due to the mild conditions at room temperature for both condensation and oxidation, and its versatility has made this strategy the standard method for C_m-substituted porphyrins [8]. It is compatible with various benzaldehydes, including sterically hindered ones, organometallic units, protected carbohydrates, and many more; and yields of up to 50% can be achieved.

The reaction is critically dependent on all ingredients and may require adaptation for a specific target material. For example, 2,6-disubstituted aryl aldehydes with electron-donating groups react better with BF_3-etherate and ethanol as co-catalyst. In fact, mesitylaldehyde will not react without the presence of the latter. The concentration of the acid catalyst is crucial as well and needs to balance the maximization of yield of porphyrinogen with minimization of any side products. The latter comprise dipyrromethanes and pyrrole red, among others, and are formed at high acid concentrations.

Many extensions to the Lindsey method have been made over time, too numerous to list here [8]. Examples include the use of aerobic oxidation with catalytic amounts of DDQ or *p*-chloranil in the presence of (phthalocyaninato)iron(II) to activate oxygen, or the design of one-step room-temperature condensations similar to the Rothemund or Adler–Longo methods. Sequential addition of CH_2Cl_2, *p*-chloranil, benzaldehyde, pyrrole, and acid (in this order!) yielded H_2TPP in an 18% yield in less than 2 min. The sequence of the reactants used is critically important; deviations thereof give the often-observed, yet not-well-understood and undesired pyrrole red (pyrrole + acid or oxidant) or pyrrole black (pyrrole + both). Such one-step methods can be beneficial in individual cases, but one needs to consider that parts of the porphyrinogen precursors are inevitably oxidized prior to cyclization, and thus yields are generally lower when compared to the two-step, one-pot procedure.

Another modification involves the use of salts, and the yield of H_2TPP can be doubled via the addition of salts containing Cl^-, Br^-, I^-, or Ph_4B^- as anions [16]. Even though beneficial for some condensation reactions, this does not affect all aldehydes, and no clear predictions can be made. Of more general relevance is the use of clays as catalysts instead of acids. Clays such as Montmorillonite K10 achieve superior yields when compared to acid catalysts, especially in the synthesis of meso-tetraalkylporphyrins [17]. This is believed to be due to a stabilization of the porphyrinogen in the nanospaces of the clay rather than its acidity. Likewise, the use of micelles in aqueous solutions has proved to be beneficial, notably for polar aldehydes, which are insoluble in chlorinated solvents and usually give very low yields with the standard Lindsey method. Here, reactions of aldehyde and pyrrole in an aqueous solution with sodium dodecasulfate and 0.05–0.3 M HCl gave yields of up to 40 to 50% with aldehydes containing carboxy, hydroxy, acetamido, ether, ester groups, and so on [18].

3.2.1.3 Comparison

At this stage, the Rothemund method has no real benefit over other methods. The Adler–Longo method is suitable for condensations with relatively stable aldehydes that can survive boiling propionic acid and for the synthesis of porphyrins on a preparative scale if the product crystallizes easily, but it is not the method of choice for 2,6-disubstituted aryl and aliphatic aldehydes. The Lindsey method uses the mildest reaction conditions of all three methods, can be used with a broad range of aldehydes, and it usually gives superior yields

compared to the other two methods. It works very well for sterically hindered, aliphatic, and sensitive aldehydes. A drawback is the more involved work-up, which normally includes column chromatography.

3.2.1.4 Microwave-Assisted Reactions

Apart from the previously outlined classical synthetic methodologies, new methods such as microwave-assisted syntheses are frequently employed today. Over the last few decades, it was shown that free base porphyrins, as well as metal complexes, can be synthesized in short reaction times and with good yields using microwave conditions. For example, Momenteau and co-workers in their pioneering work used benzaldehyde and pyrrole on silica gel and achieved a yield of almost 10% for H_2TPP in just 10 min [19]. More extensive studies showed that meso-tetraarylporphyrins can easily be prepared in yields of 20–43% and within 3 to 5 min using benzaldehydes, pyrrole, and small amounts of propionic acid [20]. Today, microwave assistance is used in an ever-expanding array of porphyrin syntheses and functionalization reactions [21].

In addition, metal complexes can be synthesized fairly easily under microwave conditions in good yields. This is especially beneficial in the case of metals, which normally require very harsh conditions or long reaction times such as Pd(II), Pt(II), or Ni(II). For example, Brückner and co-workers used pyridine or benzonitrile as solvents in order to metallate free base porphyrins or chlorins in nearly quantitative yields [22]. Ionic liquids have also been used to improve metallation reactions, as have solid-phase reactions. These days microwave-assisted synthesis is also employed in the preparation of porphyrin building blocks such as dipyrromethanes and bilanes and their condensation/cyclization to symmetrical and unsymmetrical porphyrins [23].

3.2.1.5 meso-Tetraalkylporphyrins

meso-Alkylporphyrins have always stood partially in the shadows of their meso-aryl counterparts. Their yields are often low; for example, classic Adler–Longo conditions gave 5,10,15,20-tetra(*n*-propyl)porphyrin in 6% yield, and modifications could improve this to only about 12% for short alkyl chains [24]. Porphyrins with longer alkyl chains are better prepared using Lindsey conditions and can be obtained in up to 25% yield. Porphyrins with hindered alkyl aldehydes (*tert*-butyl, isopropyl, and other branched alkyl aldehydes) can be synthesized using higher BF_3-etherate concentrations [25]. Complementary methods utilize clays and molecular sieves, in particular, for long alkyl chains [26], or the self-condensation of pyrrole carbinols (suitable for perfluoroalkyl porphyrins). More reactive systems such as porphyrins with α,β-unsaturated C_m-substituents may require the use of protecting groups (e.g., TMS-protected alkynyl aldehydes) but, similar to the meso-arylporphyrins, a wide range of porphyrins with aliphatic meso-residues are accessible using condensation reactions [8].

3.2.2 Porphyrins with Different meso-Substituents

The synthesis of porphyrins with a defined number of either identical meso-substituents (A_x-porphyrins) or different ones (e.g., ABCD-porphyrins **14**) requires the skills to introduce the meso-substituents in a controlled manner. Simple pyrrole condensation reactions will yield mixtures, and thus, this area mainly relies on reactions using building blocks with more than one pyrrole unit (Figure 3.3). A typical example is the use of dipyrromethanes **11**,

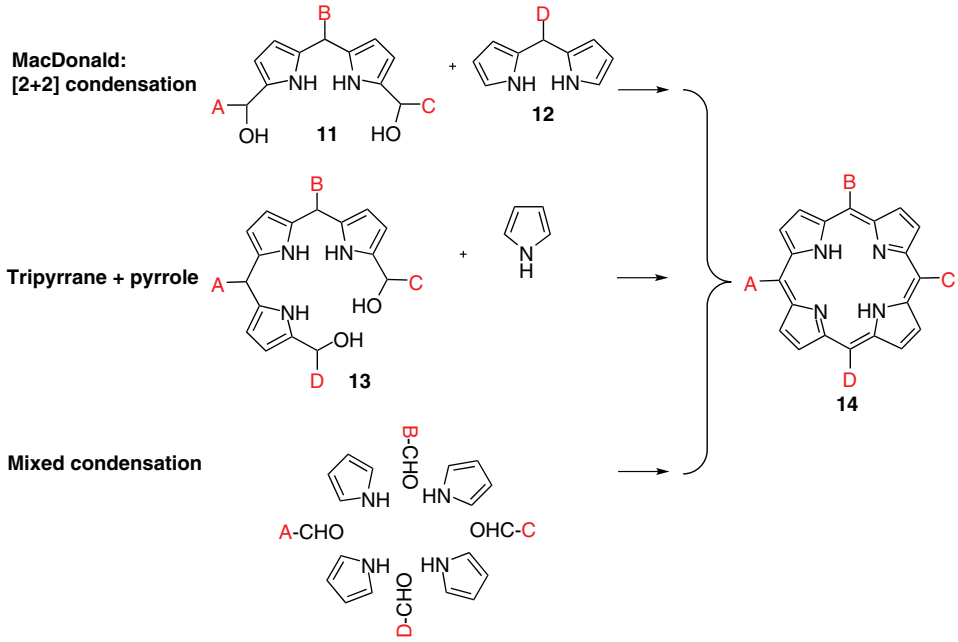

Figure 3.3 Different condensation methodologies toward the synthesis of ABCD-porphyrins.

that is, dipyrrins with two pyrroles. Many of the methods described in the following sections were initially developed for β-substituted porphyrins (see below) [27]. Advancements in this area for meso-substituted porphyrins came late, primarily after 1990, when interest in β-substituted porphyrins waned [8].

3.2.2.1 ABCD-Porphyrins via Condensation Reactions

MacDonald-Type [3 + 1] and [2 + 2] Routes Toward ABCD-Porphyrins A typical synthesis of ABCD-type systems can be achieved through the use of 1,9-diacyldipyrromethanes and goes back to concepts developed in the groundbreaking work of MacDonald and co-workers for β-substituted porphyrins [28, 29]. This compound is reduced with $NaBH_4$ to the dipyrromethane dicarbinol **11**, which is followed by condensation with a dipyrromethane **12** and subsequent oxidation (Figure 3.3). Scrambling, that is, the cleavage of preformed pyrrole systems followed by recondensation in a different arrangement is a troublesome side reaction of many porphyrin condensations, but this could be remedied in many cases, giving access to various ABCD-porphyrins [14].

Condensation with dipyrromethane carbinols can be catalyzed by Lewis acids, which are ineffective in the condensation of aldehydes and pyrrole/dipyrromethanes. But caution must be exercised with the order of substituents when applying this to the condensation of dipyrromethane dicarbinol and dipyrromethane. Substituents on the meso-position of the dipyrromethane dicarbinol should be stable during the acylation and ketone reduction steps, while the substituent on the dipyrromethane has to be stable only during the milder condensation and oxidation steps. Furthermore, scrambling can be addressed in part by the choice of substituents. Thus, alkyl groups or an absence of substituents on the carbinol give the lowest amount of scrambling, while basic heterocycles result in low yields or scrambled products. Even though optimizations were investigated for this method, many aspects of

the optimal conditions are still the original ones introduced by MacDonald. Yields of up to 60% can be achieved, and only very little by-products are formed. Many variants of this strategy have been employed, for example, the acid-catalyzed condensation of functionalized tripyrranes **13** with pyrrole (Figure 3.3).

Mixed Pyrrole Condensation As seen above, pyrrole condensation reactions are a technically simple approach to porphyrins. Hence, pyrrole is often employed in mixed-condensation reactions with different aldehydes. Although this method looks deceptively simple, it has major drawbacks in practical terms for unsymmetrical porphyrins. Mixed condensations tend to yield a mix of various porphyrins with different degrees of substitution, which are often very hard or even impossible to separate. For example, reaction with just two different aldehydes already yields a mixture of six different porphyrins and may serve to illustrate the pitfalls of this approach (Figure 3.4). The product mixture includes the two A_4- and B_4-porphyrins (**15** and **20**, respectively), as well as the A_3B- (**16**), 5,10-A_2B_2- (**17** "*cis*"), 5,15-A_2B_2- (**18** "*trans*") and AB_3-type (**19**) porphyrins. Naturally, separation of this mixture may require elaborate chromatography depending on factors such as the polarity of the two meso-substituents.

Statistically, the porphyrin formation follows a binominal distribution as shown in Figure 3.4 for a 1:1 ratio. The ratio of the expected porphyrins can be tuned by varying the ratio of aldehydes used. For example, the A_3B porphyrin **16** is often the desired compound in mixed condensations and can be maximized with a ratio of 3:1 of aldehyde A and B to give 31.64% A_4-, 42.19% A_3B-, 14.06% 5,10-A_2B_2-, 7.03% 5,15-A_2B_2-, 4.69% AB_3-, and 0.39% B_4-porphyrin. However, these yields are only theoretical, and the actual isolated yield depends on the reactivity of the aldehydes as well as on the ease of separation of the different porphyrins. In reality, isolated yields for A_3B-porphyrin via this route tend to be around 5% compared to an overall porphyrin yield of 20%. In special circumstances, the desired porphyrin can be obtained in high yield due to kinetic control, but this is not a general case. Acid labile groups tend to cause problems as does the use of hindered groups, which can result in the quantitative formation of porphodimethenes [8, 14].

3.2.2.2 "*trans*"-5,15-A_2B_2-Porphyrins

Dipyrromethane and Aldehyde Condensation Route 5,15-Disubstituted A_2-porphyrins are very useful for various applications. Mixed aldehyde condensation gives access to both the

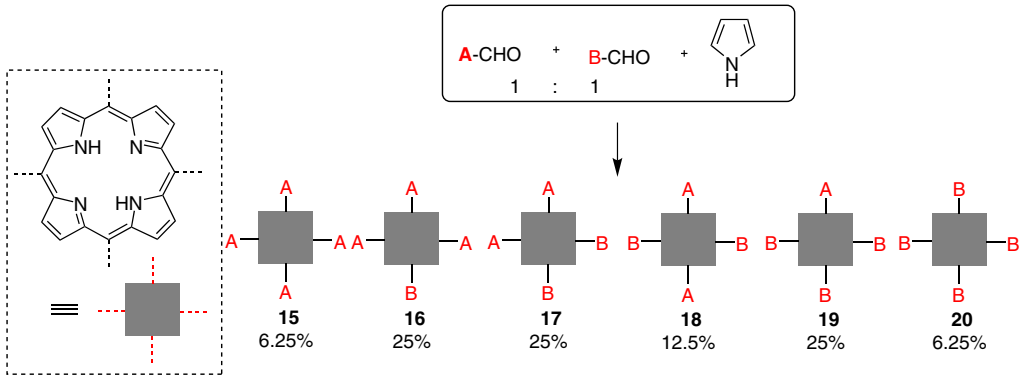

Figure 3.4 Mixed condensation of two aldehydes with pyrrole.

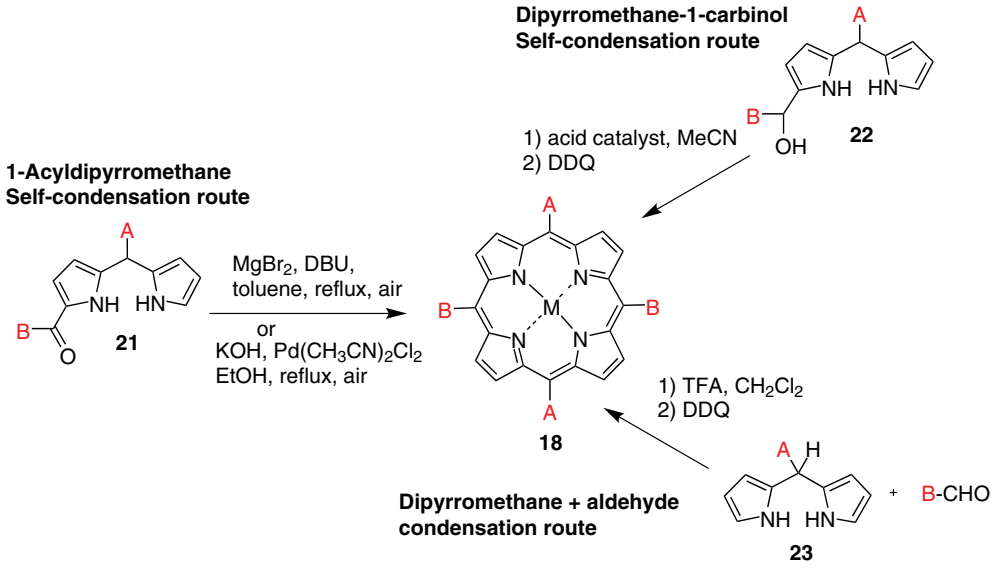

Figure 3.5 Synthesis of "*trans*"-A_2B_2-porphyrins.

5,15- and 5,10-systems, but separation is often very difficult due to the frequently similar polarities of the products. A more strategic and rational synthesis is again a [2 + 2] condensation (Figure 3.5). This reaction involves the condensation of dipyrromethane **23** and an aldehyde under acid-catalyzed conditions, and presents one of the easiest and most often-used strategies toward A_2B_2- **18** (M = 2H) or A_2-porphyrins. Dipyrromethanes are very similar to simple pyrroles in terms of their stability and electrophilicity, although they are prone to oxidation at the C_m bridge to dipyrromethenes or dipyrroketones.

The tendency for scrambling during these reactions depends largely on the meso-substituents used. Whereas *ortho*-aryl-substituents result in hardly any scrambling, non-bulky-aryl or alkyl groups result in a mixture of porphyrins [14]. A_2- or A_2B_2-porphyrins can be synthesized when an α-free dipyrromethane is used with aldehydes. Many of the initial experiments utilized β-substituted dipyrromethanes, as most known procedures for the synthesis of dipyrromethanes were established in the context of studies on naturally occurring porphyrins [27]. Today β-unsubstituted dipyrromethanes are readily available and give strategic access to "*trans*" $A_2(B_2)$-porphyrins. The reaction is suitable for a wide range of aldehydes and can normally be performed under standard conditions. Sometimes exchange reactions occur, resulting in "*cis*"-substituted porphyrins **17**. In general, this happens far less with sterically hindered dipyrromethanes (e.g., 5-mesityldipyrromethane) and is more pronounced for less hindered systems such as 5-phenyldipyrromethane.

Self-Condensation of AB-Substituted Dipyrromethane-Monocarbinols AB-substituted dipyrromethane monocarbinols **22** can be used under the same conditions as in the [2 + 2] approach and yield the A_2B_2-porphyrin **18** (M = 2H, Figure 3.5). A significant benefit is the milder acid-catalyzed condition as compared to the condensation of dipyrromethanes with aldehydes, which results in reduced scrambling. Nevertheless, the reaction has limitations in terms of possible scrambling and requires substituents that tolerate the acylation and ketone reduction steps.

Self-Condensation of 1-Acyldipyrromethane This route was developed when it was realized that the reaction of PdX_2 and 1-acyldipyrromethane **21** in hot basic ethanol gave the palladium-porphyrin in yields close to 50% [30]. While convenient, this method was initially limited to the Ni(II), Cu(II), and Pd(II) porphyrins; which are all metals that are difficult to remove from the porphyrin core. Subsequent studies showed that DBU, toluene, $MgBr_2$ and 1-acyldipyrromethane can also be used to give A_2B_2-porphyrins in about 60% yield, which expanded the scope of this method (Figure 3.5). Magnesium porphyrins can be easily demetallated, and this reaction is also suitable for basic heterocycles such as pyridyl, allowing the preparation of "*trans*"-B_2-porphyrins (**18**, A = H). Furthermore, the preparation of (porphyrinato)magnesium is possible with formyldipyrromethane in 40% yield [31]. The latter presents the only multi-gram scale entry into unsubstituted porphyrin synthesis **5** via condensation reactions and finally facilitated practical access to the parent compound of all porphyrins. Although often studied, other syntheses suffered from low yields and the very low solubility of the target compound (see Section 3.8.1) [32].

In addition, such acyldipyrromethane condensations are a tool that is well suited for combinatorial chemistry. The reaction conditions resemble to some extent the Rothemund reaction of an aldehyde and pyrrole. However, both the reaction temperature and the concentration of reactants are lower, while the yields are notably higher with 60% versus ~5%. The scope is broader and allows for a larger variety of substituents to be used, and the method is generally very efficient. For example, while the dipyrromethane-carbinol condensation requires four distinct steps for reduction, condensation, oxidation, and complexation, the acyldipyrromethane method delivers the same product from a one-flask process [14].

3.2.2.3 "*trans*"-5,15-A_2-Porphyrins

The synthesis of A_2-substituted porphyrins, formally a subgroup of the A_2B_2-porphyrins **18**, is well established, and they are some of the most widely used starting materials in contemporary porphyrin chemistry. They allow a facile entry to strapped porphyrins, polymers and, via functionalization of the unsubstituted meso-positions, give rise to more unsymmetrical A_2BC-type systems. Their synthesis is easy and requires only the reaction of unsubstituted dipyrromethane with various aldehydes under acid-catalyzed conditions; there is also significant scope to utilize other synthetic approaches. The various approaches are exemplified in Figure 3.6 for 5,15-diphenylporphyrin **24**.

A straightforward method uses one equivalent of unsubstituted dipyrromethane **28** with one equivalent of benzaldehyde in CH_2Cl_2 and an acid catalyst at room temperature. 5,15-A_2-porphyrins are obtained in good yields and can easily be isolated via column chromatography. The [2 + 2] methodology is widely used with yields typically in the 20–30% range and allows better control of the C_m-substituents compared to mixed condensations. It is equally amenable to the synthesis of 5,15-dialkylporphyrins. For example, 5,15-dihexylporphyrin has been reported in a yield of 27% with a work-up consisting of just filtration of the compound through silica gel with CH_2Cl_2 and recrystallization [33].

5,15-Diphenylporphyrin was first described by Treibs and Häberle in 1968 [34], and the requirement for two different C_m-positions allows the use of several different [2 + 2] approaches. One pathway is the aforementioned condensation of unsubstituted dipyrromethane **28** with benzaldehyde using TFA as the catalyst (Path 1). Oxidation of the condensation products with chloranil gave yields of about 25–40%. Another option is the condensation of 5-phenyldipyrromethane **25** with formaldehyde (Figure 3.6, Path 2). Initially developed by Baldwin et al. for β-alkyl-substituted diphenylporphyrins, this

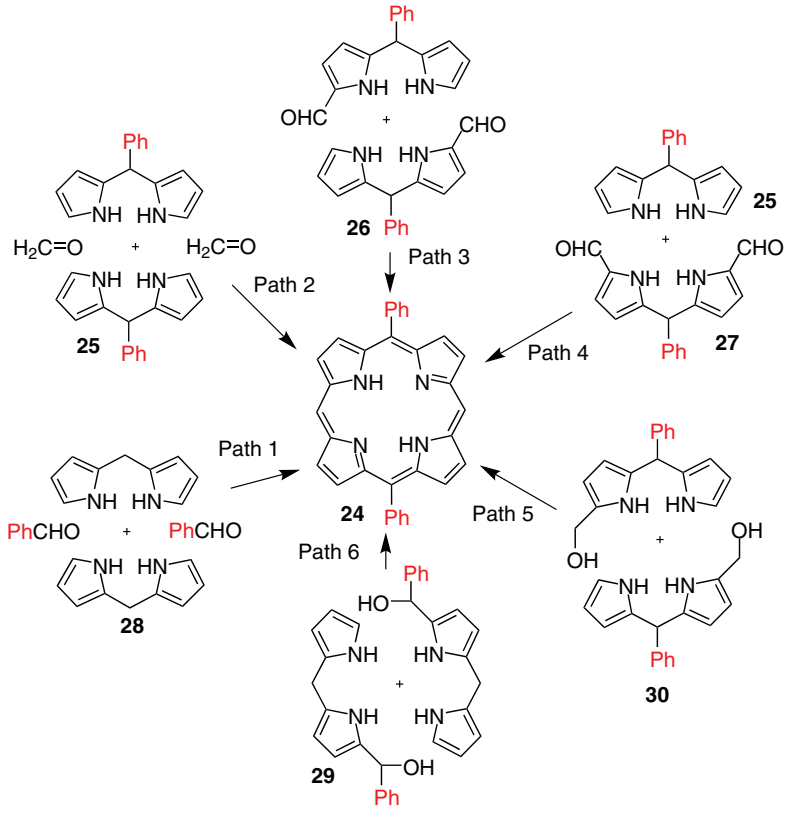

Figure 3.6 Synthesis of 5,15-A_2-porphyrins illustrated for 5,15-diphenylporphyrin **24**.

method used trichloroacetic acid as the catalyst and oxidation with air [35]. The application of this procedure to diphenylporphyrin by Brückner et al. gave yields of about 30% [36]. Tetraphenylporphyrin was obtained as a side product from acid-catalyzed scrambling, but only in yields of <1%.

In other pathways, the dipyrrolic compound with the linking carbon in the condensation carries either a hydroxymethyl substituent (**29**, **30**, Path 5, 6) or a formyl group (**26**, **27**, Path 3, 4). However, these methods require more synthetic steps to form the dipyrromethene species (Path 4–6), as well as reduction of the carbonyl group to form the sensitive hydroxymethyl substituents (Path 5, 6). Path 4 represents a classic MacDonald-type approach, whereas Path 3 and 5 are other options to prepare 5,15-diphenylporphyrin via acid-catalyzed self-condensation.

3.2.2.4 "*trans*"-5,15-AB-Porphyrins

Unsymmetrical 5,15-AB-type porphyrins **33** can also be prepared using such [2 + 2] approaches. However, two newer methods illustrate the current state of the art (Figure 3.7). The iminodipyrromethane route utilizes the formylation of the A-dipyrromethane, followed by the imination with propylamine [37]. This iminodipyrromethane **31** is then reacted with a second dipyrromethane **32** in refluxing ethanol with zinc acetate. This reaction gives the zinc porphyrin in 30% yield without any scrambling. Furthermore, it is suitable for aryl/aryl, aryl/alkyl, and aryl/H substituents.

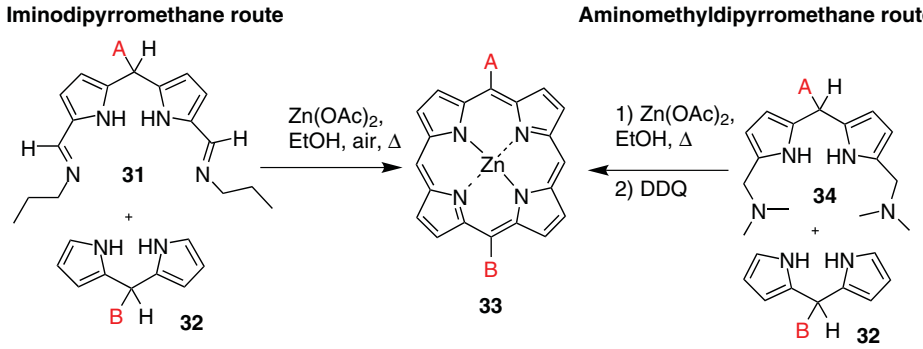

Figure 3.7 Synthesis of 5,15-AB-porphyrins.

In a similar manner, the aminomethyldipyrromethane route [38] requires the reaction of dipyrromethane with Eschenmoser's reagent (*N,N*-dimethylmethyleneiminium iodide) at room temperature to yield 1,9-bis(*N,N*-dimethylaminomethyl)dipyrromethane **34**. This derivative is subjected to a condensation with the B-dipyrromethane unit **32** in refluxing ethanol and zinc acetate. Oxidation with DDQ gave the desired zinc(II) porphyrins in 5–20%. This reaction is applicable for alkyl/alkyl, aryl/alkyl, and alkyl/H combinations [14].

3.2.2.5 A- and 5,10-A_2-Porphyrins

Even though many different methods exist today to synthesize nearly any meso-substituted porphyrin, some are more difficult to obtain than others. One example is the meso-monosubstituted A-porphyrin **35**. Even though this type is often mentioned in publications, it is mostly formed as a side product. On the other hand, less is often more, as such systems represent a superior starting material for the strategic synthesis of unsymmetric porphyrins via stepwise functionalization. One possible synthesis would be the condensation of bilane with an aldehyde. Yet, due to their instability, bilanes are hard to synthesize and handle.

A simpler approach was designed by Wiehe et al. that utilized formylpyrrole **36**, an "A"-aldehyde, and dipyrromethane **28** (Figure 3.8) [39]. Herein, a pyrrole aldehyde is condensed with dipyrromethane and an aldehyde under acid-catalyzed conditions. The so-called [2 + 1 + 1] approach is straightforward, tolerates a broad range of different functional (A) groups, and gives yields between 2% and 15%. Additional products are formed, as in other "mixed condensations," notably the disubstituted porphyrins from scrambling. However, in terms of yields, the electronic properties of the aldehydes are often less significant than the solubility of the products. In this case, the disubstituted porphyrin is by far less

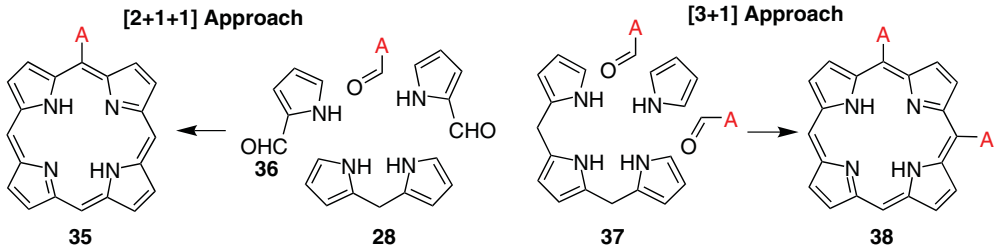

Figure 3.8 Synthesis of A- and "*cis*"-5,10-A_2-porphyrins.

soluble than the monosubstituted compound, which makes separation significantly easier. Sometimes the A-porphyrin can be isolated as the sole product (e.g., A = 4-nitrophenyl, 4-methoxyphenyl, *tert*-butyl), allowing for large-scale synthesis.

A similar situation existed for 5,10-disubstituted porphyrins **38**, where two neighboring meso-residues carry substituents. For 5,10-diphenylporphyrin, that is, the regioisomer of **24**, Briñas and Brückner reported a logical "total synthesis" involving the condensation of dicarbinol-dipyrromethane with dipyrromethane [40]. More general are [3 + 1] condensation reactions using tripyrrane **37** together with an aldehyde and acid as catalyst. Tripyrrane can be obtained via condensation of 2,5-bis(hydroxymethyl)pyrrole and pyrrole, with yields of up to 12%. Similar to the synthesis of monosubstituted porphyrins, here the A-porphyrin **35** is formed as a side product, but can be easily separated from the target compound. This synthesis is amenable to aromatic and aliphatic aldehydes [41]. Alternative methods for **35** and **38** are S_NAr (nucleophilic aromatic substitution) reactions of unsubstituted porphyrin **5** and will be discussed below (Section 3.5.3.2) [42].

3.2.2.6 Synthesis of Porphyrins Through Cyclization of Linear Tetrapyrroles

On paper, the one method suited for the synthesis of any unsymmetrically substituted porphyrin is the cyclization of linear tetrapyrroles. This approach involves the stepwise and controlled linkage of monopyrroles to form open-chain tetrapyrroles, akin to the natural biosynthesis. One quite obvious quintessential feature of these linear tetrapyrroles has to be their ability to undergo cyclization in order to form the desired porphyrin. This must be achieved under relatively mild conditions to avoid the otherwise inevitable ring redistribution "scrambling" reactions, which would lead to a mixture of different porphyrins. And therein lies the crux and often futility of this strategy. It is a true total synthesis, requiring many steps to construct the linear tetrapyrroles, and although many advances have been made, it still remains an art, primarily in the hands of the few "methods-oriented" synthetic organic porphyrin chemists.

Linear tetrapyrroles (the completely saturated parent compound is a bilane) present a fundamental class of pyrrole compounds and natural products (think only of bilirubin, biliverdin, and the phycobilins) in their own right [43]. Thus, their chemistry is almost as involved, albeit somewhat less well studied in modern times, as that of the porphyrins. Many different classes of open-chain tetrapyrroles exist, such as *a*-, and *b*-bilenes, *a, b*-and *a,c*-biladienes or *a,b,c*-bilatrienes (the letter in italics refers to the location of methine bridges) or oxobilanes with bridging carbonyl units. There are various means of constructing them from mono-, di-, and tripyrrolic precursors, and these smaller building blocks are themselves part of the diverse "condensation" strategies to yield porphyrins.

β-Substituted porphyrins such as copro-, etio-, and protoporphyrins were the first targets of synthetic porphyrin chemistry, and different historical periods have seen a varied and shifting focus on the open-chain (tetra)pyrrole building blocks. The multitude of possible strategies, their benefits and pitfalls, have aptly been delineated in many treatises by Kevin Smith, whose laboratory was instrumental in developing many of the modern syntheses for β-substituted porphyrins [2, 5, 12, 27, 44]. The most useful tetrapyrroles for porphyrin formation are bilanes, *b*-bilenes, oxobilanes, and *a,c*-biladienes. To illustrate one such approach, let us now consider the synthesis of an octa-β-substituted porphyrin with one meso-substituent.

Biladiene Route – A Classic for β-Substituted Porphyrins The synthesis of the target compound **42** as outlined in Figure 3.9 represents many related syntheses with various alkyl and/or aryl residues. It features the use of biladienes, which are normally used in their protonated form; for example, as the crystalline dihydrobromide form. They are one of the most frequently used linear tetrapyrroles due to their stability [44]. *a,c*-Biladienes were first synthesized by Johnson's group in the 1960s, who used an acid-catalyzed condensation of two equivalents of 2-formyl-5-methylpyrrole with dipyrromethane-5,5′-dicarboxylic acid or 5-unsubstituted 2-methylpyrrole with 5,5′-diformyldipyrromethane. Cyclization to the porphyrin was achieved with cupric salts and gave the copper porphyrins in 20–30% [46].

The condensation of 1,19-diunsubstituted *a,c*-biladienes **41** with an aldehyde allows the formation of porphyrins with only one meso-substituent, such as **42**. The biladienes can be synthesized utilizing a [2 + 2] condensation of two dipyrromethanes, from the condensation of dipyrromethane with two equivalents of formylpyrrole (e.g., **39** + **40**), or through stepwise condensation of two different formylpyrroles with dipyrromethane, naturally requiring appropriate protecting group chemistry. The latter is also known as a [2 + 1 + 1] approach and is a general entry into unsymmetrical porphyrins [47].

Bilane Route to ABCD-Porphyrins Even though the [2 + 2] approach can be used for the formation of ABCD-type porphyrins, it is plagued with some limitations. These include very low reaction concentrations, yields of just 20–30%, and a requirement for acid catalysis, often resulting in severe scrambling with certain substituents [48]. A method to overcome this is the use of tetrapyrrolic building blocks such as bilanes. As for so many other methods for meso-patterned porphyrins, the most versatile method here stems from Lindsey's laboratory [14].

The methodology consists of two key reactions (Figure 3.9) [45]. In the first step, 1-acyldipyrromethane (**45**, the "CD half") and 9-protected dipyrromethane-1-carbinol **44** are condensed to the 1-protected 19-acylbilane **46**. The next step gives the desired metalloporphyrin in a one-flask reaction. A key problem was the identification of a suitable protecting group for the α-pyrrole that could be easily introduced, prevents side reactions during bilane synthesis, and is easily removed. All criteria were met by using an α-bromine, a pleasing result as it bridges this modern chemistry with Hans Fischer's porphyrin syntheses from the 1920s, which utilized different building blocks, reaction conditions, and targets, but also featured α-bromo residues (see Section 3.3.3).

Bromination of the 1-acyldipyrromethane **43** and subsequent reduction to **44** was easily achieved. The final cyclization involved heating of the bilane **46** in toluene with DBU and $MgBr_2$ at 115 °C for 2 h. This gave the corresponding magnesium porphyrins **47** in about 60% yield. Key advantages of this method are the use of high concentrations for the bilane formation and the mild basic conditions (as opposed to all the other acid-catalyzed cyclizations) for porphyrin formation. In addition, oxidation is accomplished in air, and the magnesium porphyrin can be readily demetallated. This strategy gives access to porphyrins with up to four alkyl or aryl/heterocyclic groups (e.g., pyridyls) that are not accessible via the [2 + 2] route. Some limitations are imposed on the scope of suitable substituents by the reaction conditions for the Grignard-mediated formation of the 1-acyldipyrromethane, the ketone reduction, electrophilic bromination, and the final ring closure.

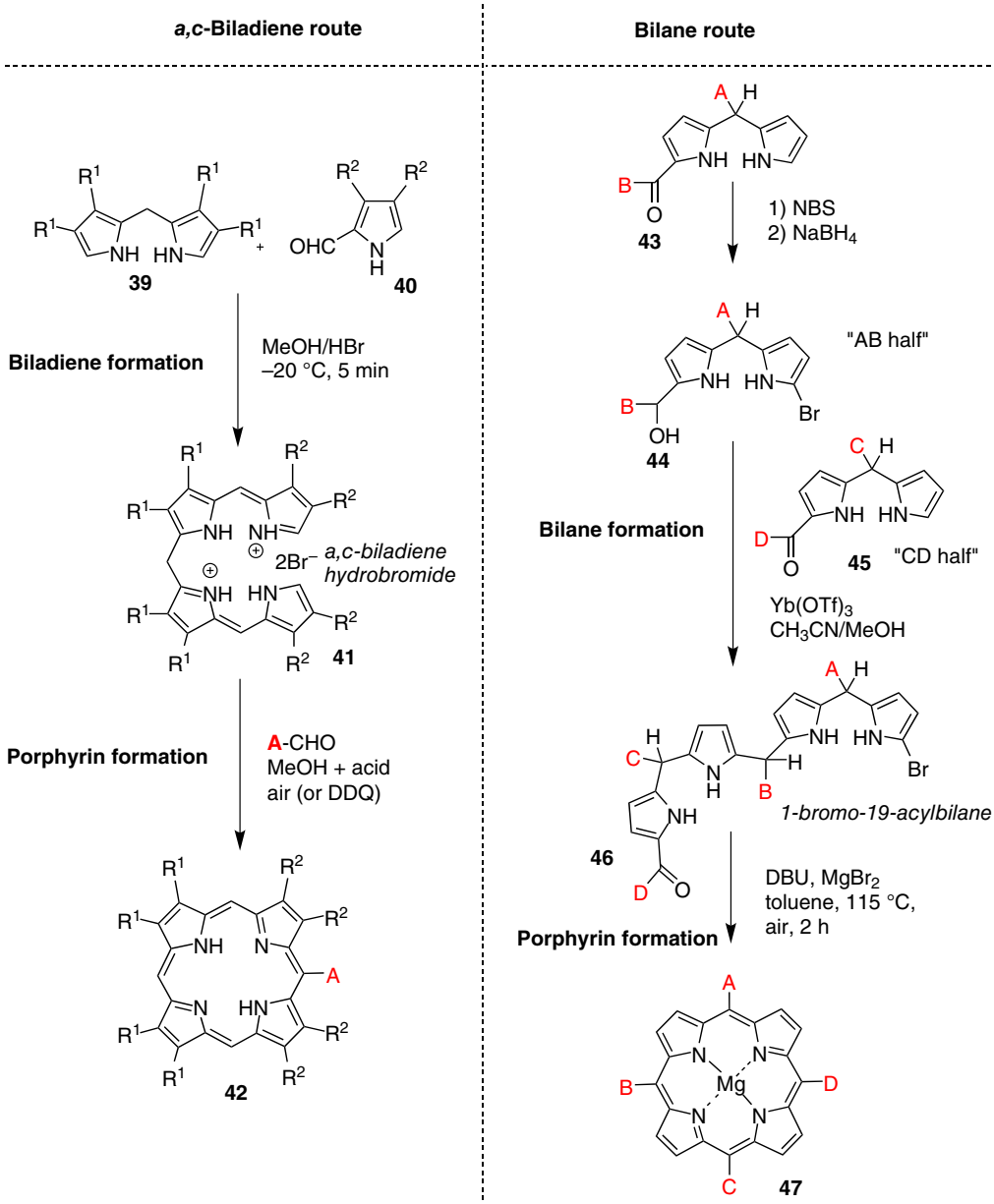

Figure 3.9 Exemplary strategies for the synthesis of unsymmetrical meso-substituted porphyrins from linear tetrapyrroles.

3.3 Synthesis of β-Substituted Porphyrins from Pyrrole Building Blocks

3.3.1 General Strategies

Like everything else in the synthesis of porphyrins, planning of syntheses for β-substituted porphyrins comes down to symmetry considerations. Symmetric porphyrins can be prepared

via pyrrole tetramerization reactions, whereas unsymmetric ones require the use of either [2 + 2] or [3 + 1] condensation methods, or bilane cyclizations [2, 5, 12, 27, 44]. Problems encountered are like the ones described for meso-substituted porphyrins, that is, scrambling, possible formation of isomers, and side reactions, and depend on the type and position of substituents on the pyrrole components.

The classic example is the formation of the so-called type-isomers **49**–**52** when using pyrroles with two different β-substituents **48**. These can be incorporated into the porphyrin framework in two different orientations in each quadrant, and thus four isomers are formed (Figure 3.10). In a related manner, two products are formed when using unsymmetrically substituted dipyrromethanes (**53** + **54**) in [2 + 2] MacDonald condensation reactions. The situation becomes progressively easier the more symmetric the building blocks and target porphyrins are.

The main difference compared to meso-substituted porphyrins is that the synthesis of β-substituted porphyrins allows more leeway in providing the C_m (meso) carbon atoms. This can be done using various α-substituted dipyrromethane and tripyrrane precursors and ranges from methyl units (Fischer, plus Br on other unit), formyl (MacDonald, plus H or COOH on other unit), to one-carbon units, such as orthoformate for symmetric porphyrins. In [3 + 1] condensations using tripyrranes **55**, the meso-carbons are typically introduced via a diformylpyrrole **56** [49] or diaminomethylpyrroles, which limits the use of unsymmetrical pyrroles (Figure 3.10). The [3 + 1] method has been developed to a fine art by Lash, notably for systems where the "fourth" pyrrole unit has been replaced by nonpyrrolic building blocks (Chapter 9) [50]. Similar means are employed for the cyclization of bilanes,

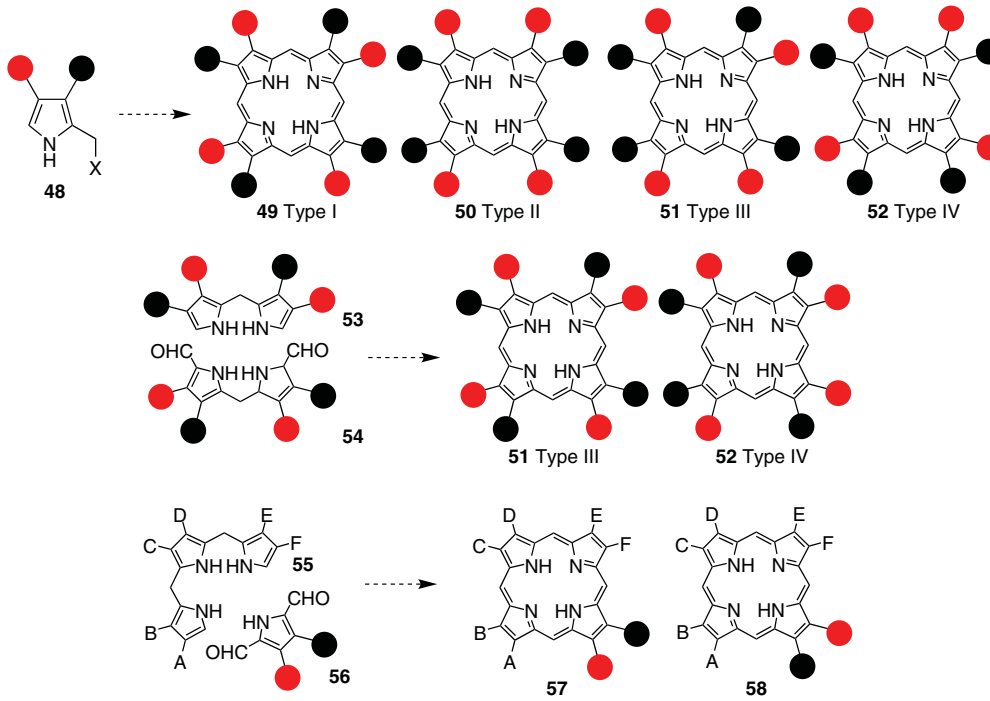

Figure 3.10 Formation of different β-substituted regioisomers during pyrrole, dipyrromethane [2 + 2] or tripyrrane [3 + 1] condensation reactions.

notably the useful *a,c*-biladienes [44]. Classic examples are the copper-assisted reactions of 1,19-dimethylbiladienes or electrochemical cyclizations thereof. These reactions proceed via a 4-methyl-4,5-dihydroporphyrin intermediate, which then loses the 4-methyl group to form the fully aromatic porphyrin [44, 51].

3.3.2 2,3,7,8,12,13,17,18-Octaethylporphyrin

2,3,7,8,12,13,17,18-Octaethylporphyrin (H_2OEP **61**) is the β-substituted counterpart to H_2TPP **10** in terms of fundamental structure and widespread use. It has excellent solubility in organic solvents, and its β-substituent pattern has made it the model compound of choice for mimicking natural porphyrins, which are all β-substituted. Since the first reports by Linstead, Inhoffen, Whitlock, and Dolphin [52, 53], two strategies have been developed for its synthesis (Figure 3.11). Older methods used tetramerization of α-substituted pyrroles, where the α-substituent provides the C_m carbon atom. This required α–CH_2-X units, where X is a suitable leaving group, as in carbinol **63** (or **62**), or dimethylaminomethylene **60** groups. After tetramerization, the porphyrinogen formed is then oxidized to the porphyrin (similar to the sequences shown in Figure 3.2).

The most practical method developed by Sessler et al. uses 3,4-diethylpyrrole **59** and formaldehyde. The two components are reacted under catalysis by *p*-toluenesulfonic acid, followed by oxidation with air. The reaction works very well; often the product crystallizes from the mixture and gives yields between 50% and 70% [54]. This method was greatly facilitated by the development of the Barton–Zard pyrrole synthesis, which gave a general entry into α-unsubstituted 3,4-disubstituted pyrroles from simple nitroolefins [55]. These pyrroles can be used in a similar manner to yield other β-substituted porphyrins. Note that **64** is an intermediate in the synthesis of **59** in the Barton–Zard reaction, but here the C_m carbon is derived from formaldehyde. The last decades have seen a steady decline in the use of OEP derivatives versus meso-aryl-substituted ones. This is partially due to a wider synthetic scope of functionalization reactions for meso-aryl-substituted porphyrins. Other reasons are the mistaken belief that "pyrrole chemistry" of OEPs is too involved, and a shift in applications toward materials sciences with its requirement for cheaper and "easier" starting materials.

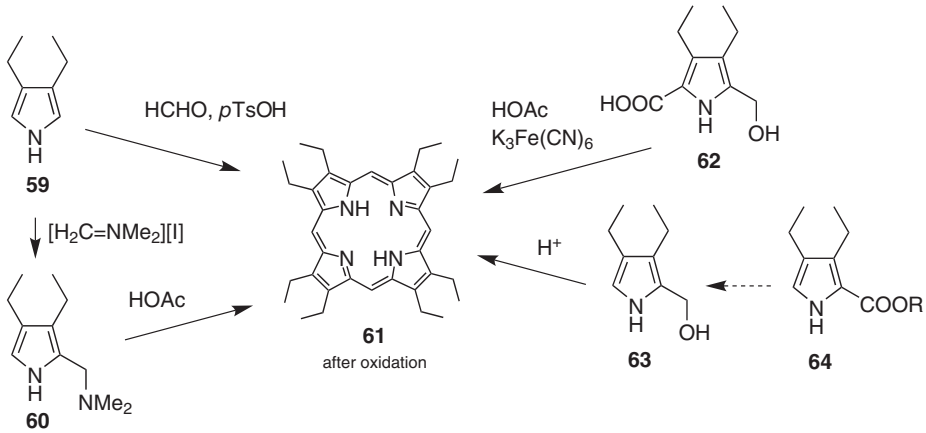

Figure 3.11 Synthetic strategies for the formation of 2,3,7,8,12,13,17,18-octaethylporphyrin.

3.3.3 The Classic: Fischer's Synthesis of Heme

No treatise of porphyrin synthesis would be complete without mentioning the three classic natural porphyrin syntheses: heme **65**, chlorophyll a, and vitamin B_{12}. Their origins go back to the works of Willstätter, Küster, and Fischer, and despite the many advances since, they still stand out as prime examples of planning, logic, and efficiency in total syntheses. The synthesis of chlorophyll (Woodward, 1960, see chapter 18) and vitamin B_{12} (Woodward and Eschenmoser in the 1970's, see chapter 19) present the pinnacles of these achievements and are still largely unsurpassed.

The same holds true for the first total synthesis of a porphyrin, that of hemin **69**, a more stable form of the natural heme **65**. Its synthesis presented a tour de force by Hans Fischer's group in Munich and was completed in 1929 and honored by the award of the Nobel Prize in Chemistry in 1930 [56]. Although synthetic porphyrin chemistry has matured considerably in the intervening 90 years, the fundamental approach adopted by Fischer is still found in many newer developments and illustrates the classic principles.

An outline of Fischer's retrosynthetic analysis (although the term was not used in those times) is given in Figure 3.12. The fundamental problem is similar to that encountered in the

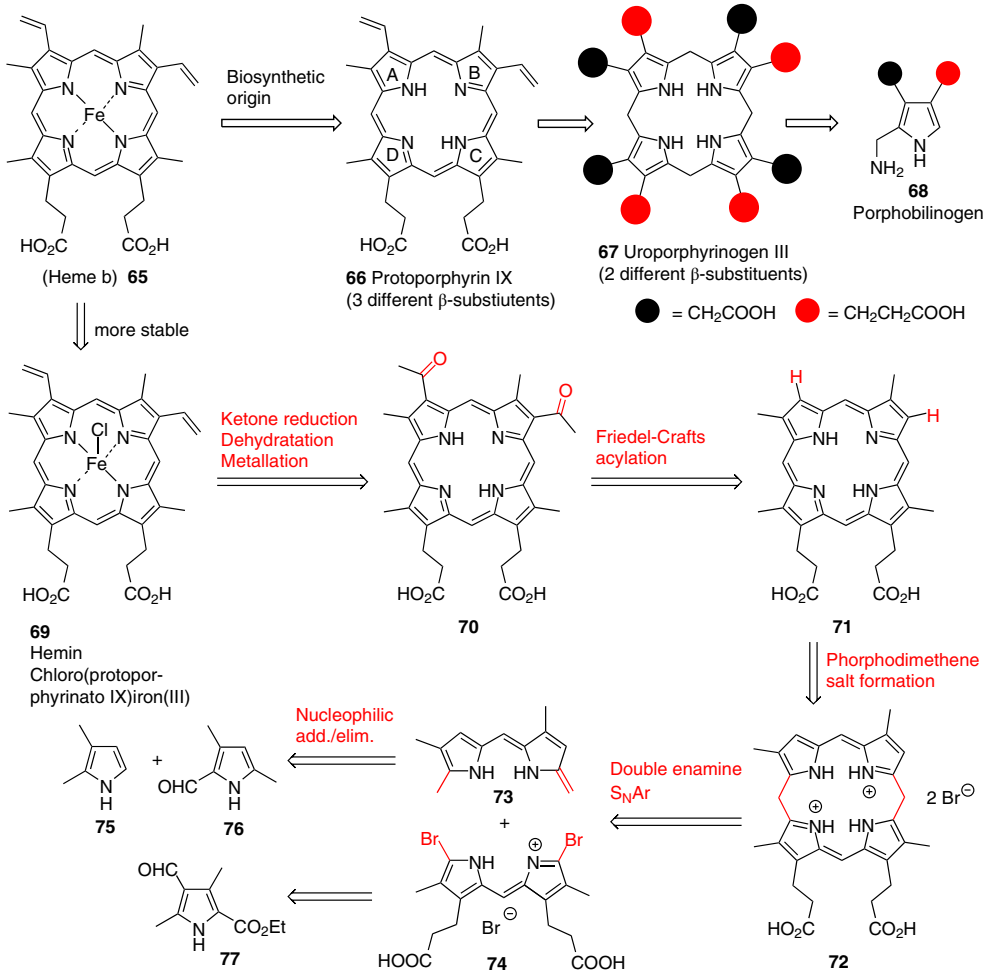

Figure 3.12 Retrosynthetic analysis of heme and biosynthetic origin of the unsymmetric substituent pattern.

synthesis of other natural tetrapyrroles, that is, how to achieve the unsymmetric substitution pattern at the porphyrin periphery. Of the various types of isomers possible, natural heme **65** is a type IX isomer and is formed from protoporphyrin IX **66**. This is a result of the "inverted" positioning in which pyrrole ring D is incorporated in the tetrapyrrole framework of uroporphyrinogen III **67** from porphobilinogen **68** during porphyrin biosynthesis. Fischer planned a "2 + 2" approach by cutting the porphyrin into a top (Northern) and bottom (Southern) half, where a tandem [2 + 2] condensation/cyclization initiated by the enamino vinyl group in **73** would function as the initial nucleophile. Each of these porphyrin halves is a dipyrromethene (**73** and **74**), which were the primary "two pyrrole" units in use at the time. They, in turn, were accessible from standard pyrroles (**75** + **76** → **73** and dimerization of 2 × **77** → **74**).

The use of dipyrromethenes as key construction components also illustrates the limitations of Fischer's approach, which had to rely on strong reagents and very harsh reaction conditions. In those times, dipyrromethanes were considered to be too unstable, yet the dipyrromethenes were still prone to self-condensation by bromination and required heating in acids or melts. All this gave very low yields after lengthy purification, which would challenge most researchers today.

Yet, the synthesis proceeded successfully along these lines (Figure 3.13), but was originally based more on studies from porphyrin derivatization reactions – an important subtopic of

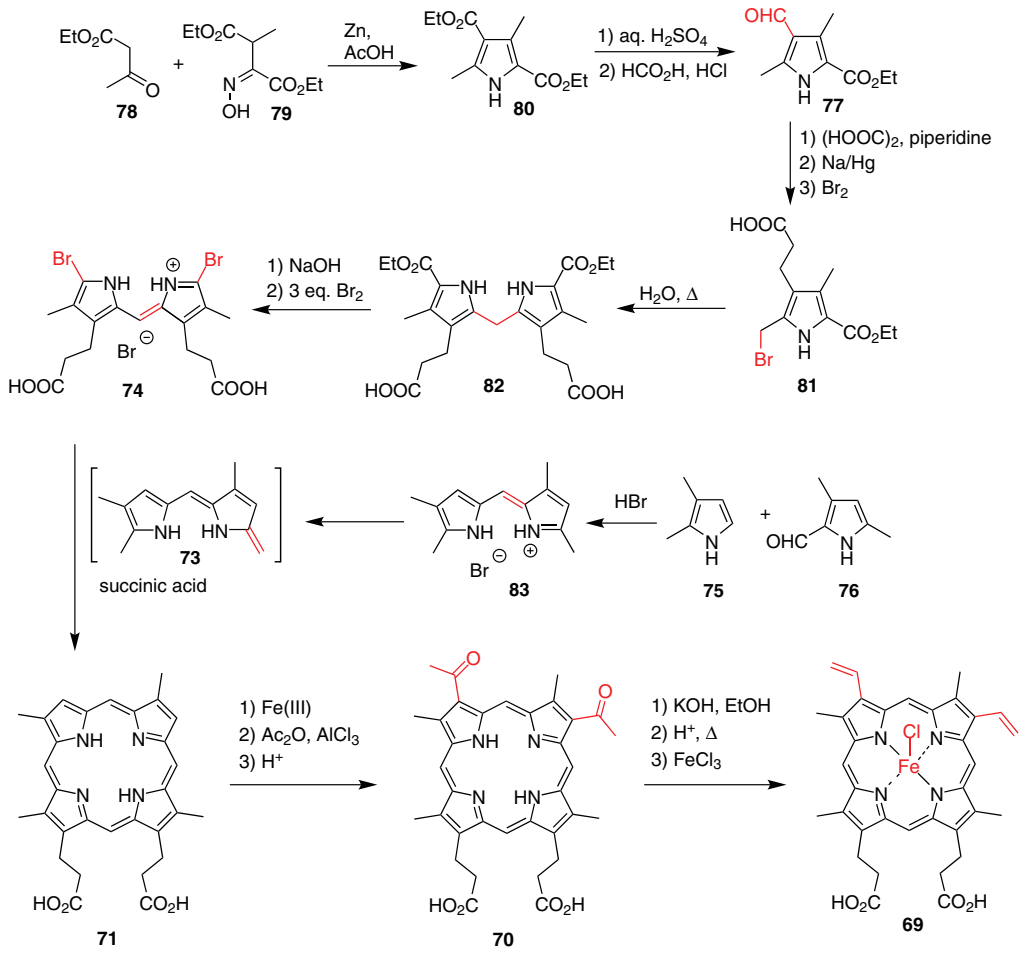

Figure 3.13 Hans Fischer's synthesis of hemin.

porphyrin chemistry on its own – and partial syntheses, then logical forward planning as we perceive it today. For example, a key step is the generation of the vinyl groups in positions 3 and 8. This was made possible by forming the diacetylporphyrin **70** from deuteroporphyrin **71**, a known degradation product of protoporphyrin. Formation of **70** was achieved by a Friedel–Crafts acylation. The acylated porphyrin **70** could then be reduced to the secondary alcohol, which was converted by acid-mediated alcohol elimination to the free base protoporphyrin IX **66**. Finally, iron(III) chelation completed the sequence to hemin **69**.

3.4 Total Synthesis of Other Porphyrin(oid)s

The strategies outlined in the preceding parts can also be applied to other cyclic tetra- and polypyrrole systems. Depending on the target compounds, this requires different starting materials. Exchange of the building blocks for the meso-carbon (or other linkage) or pyrrole (or alternatives thereof) may be necessary as well. Some of these approaches are highlighted in other parts of this book, for example, in Chapters 5, 7, 8, and 9 on porphyrin isomers, porphyrazines, carbaporphyrins, and contracted and expanded porphyrinoids. In the following, we illustrate conceptual approaches to porphyrinogens, dodecasubstituted porphyrins, benzoporphyrins, and chlorins, within the context of the parent [1.1.1.1]-porphyrin system.

3.4.1 Porphyrinogens and Calixpyrroles

We have already encountered the porphyrinogens, that is, nonaromatic hexahydroporphyrins, as the products of the initial condensation reaction in the synthesis of porphyrins (see Figure 3.2). Although these are normally not isolated but oxidized in situ to the target porphyrin (e.g., **7**), related non-oxidizable compounds have burgeoned into a field of their own, notably as anion sensors and receptors [57] and synthons in organometallic chemistry [58]. Modern syntheses and applications of such compounds were developed by Sessler's group [59], but a classic example, acetone pyrrole **84**, is one of the oldest synthetic tetrapyrroles known.

It was prepared in 1886 by Adolf (von) Baeyer [60] and, as the name implies, is derived from the reaction of acetone and pyrrole. The reaction of these two components under acid catalysis will generate high yields of a colorless product, which is a tetrapyrrole where the four pyrrole rings are linked by four dimethylmethylene bridges. The reaction begins with the standard electrophilic α-substitution of pyrrole by acetone, followed by oligomerization and cyclization (Figure 3.14). Cyclization is spontaneous, does not require a template or high dilution, and is preferred over chain elongation or formation of larger rings in this case.

Due to the presence of the bridging CMe_2 units, no aromatization will take place and free rotation about the C_a—C_m bonds is possible. Thus, various relative pyrrole orientations are possible. In the up-down-up-down (↑↓↑↓) example, two pairs of NH units now point outward and can each act as a receptor. Depending on the type of conjugation of the connecting bridge, or lack thereof, various types of calixphyrins (e.g., **85**) can be prepared. Such compounds are called porpho(di)methenes in the older literature, and their stable metal complexes can also be prepared via derivatization of porphyrins; examples include Buchler's reductive alkylation [61] or reactions with organolithium reagents [62].

3.4.2 Dodecasubstituted Porphyrins

If one desires porphyrins with substituents at all peripheral positions, this requires just a combination of the substituted building blocks for a meso-tetrasubstituted and a

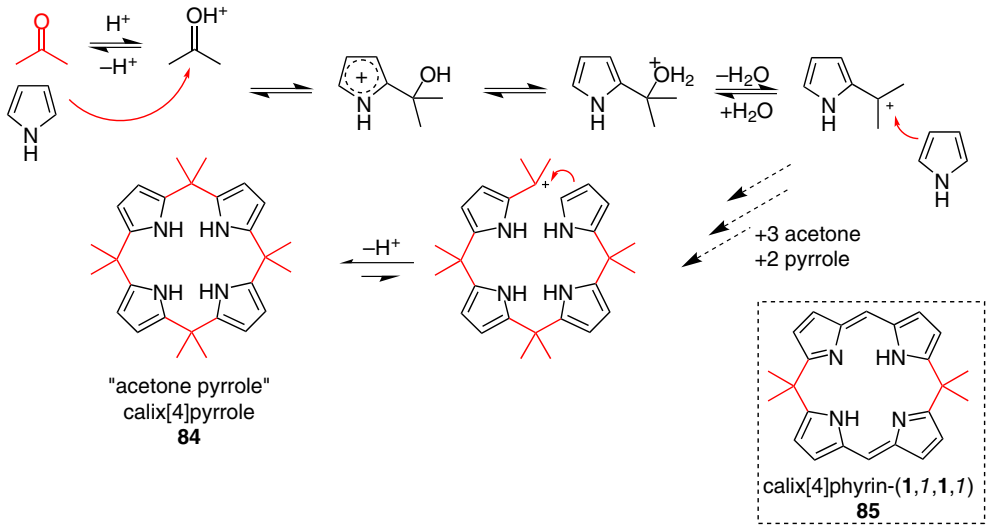

Figure 3.14 Synthesis of acetone pyrrole.

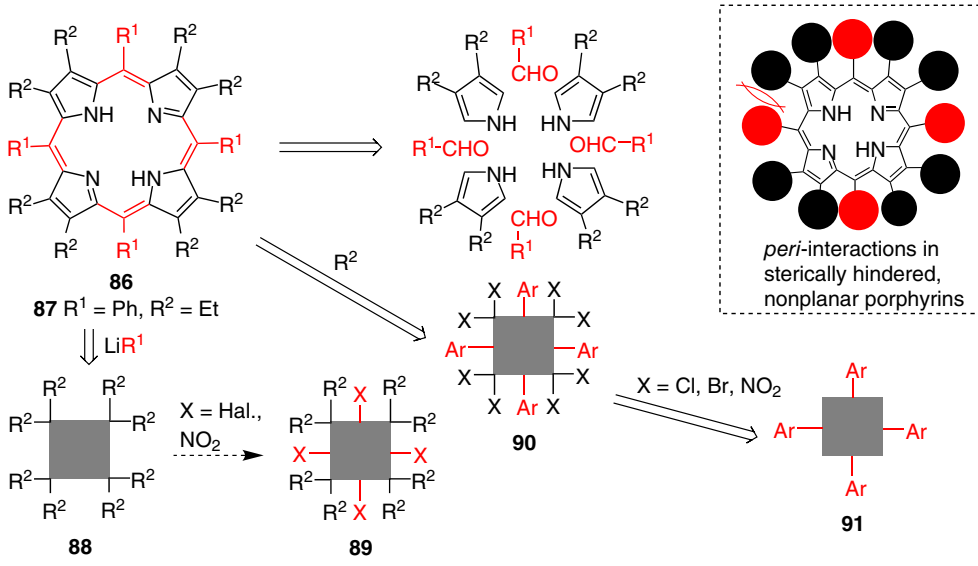

Figure 3.15 Synthetic strategies for dodecasubstituted porphyrins.

β-octasubstituted porphyrin (Figure 3.15). Thus, for S_4-symmetric systems **86**, simple condensation reactions will work well. An illuminating and classic example here is the synthesis of 2,3,7,8,12,13,17,18-octaethyl-5,10,15,20-tetraphenylporphyrin **87**, which is a hybrid of H_2TPP **10** and H_2OEP **61**. Condensation of 3,4-diethylpyrrole and benzaldehyde under Lindsey conditions gave the target compound in 55% yield [63]. These "highly substituted porphyrins" are of interest due to their nonplanar macrocycle conformations arising from *peri*-interactions of R^1 and R^2 [64].

Typically, condensation reactions work well only for meso-aryl systems; with alkyl residues, the intermediary porphyrinogens often can only be partially oxidized. Hence, for nonplanar meso-alkylporphyrins, one uses β-substituted porphyrins such as OEP and introduces the C_m-residue via substitution reactions (see Section 3.5.3.2) [65]. Other meso-functionalization reactions such as halogenation of **88** can be used to give **89**; however, subsequent C—C coupling reactions fail due to steric hindrance. The situation is much easier for β-substituted systems. Here, standard meso-tetraarylporphyrins **91** (but not alkyl) can easily be perhalogenated to **90** and then used in Pd-catalyzed reactions to yield **86** [66].

3.4.3 Benzoporphyrins

Benzoporphyrins **92** are a class of compounds related to the phthalocyanines (see Chapter 5), albeit containing meso carbon atoms instead of nitrogen atoms. Their high stability and interesting optical properties make them appealing for many applications. However, their synthesis is difficult as the unsubstituted benzoporphyrin is a flat molecule and rather insoluble, and one encounters problems similar to those in the synthesis of unsubstituted porphyrins [67].

Originally tetrabenzoporphyrins (TBPs) were synthesized from phthalimides **95** or similar compounds in the presence of metal ions, using template-assisted condensations akin to phthalocyanines [68]. One example is the synthesis of Zn(II)TBP from potassium phthalimide with sodium acetate and $Zn(OAc)_2$ at 340–360 °C, which gave Zn(II)TBP in 26% yield. Another way is to use isoindolinone-3-acetic acid **96** with $Zn(OAc)_2$ or 2-acetylbenzoic acid **93** in aqueous ammonia solution with zinc acetate. In these cases, the $Zn(OAc)_2$ acts as a template to form the desired porphyrin **92** (M = Zn(II)). Other options are a Rothemund-like template reaction with isoindole **97** and formaldehyde. Such reactions require harsh reaction conditions, limiting the introduction of functional groups. Due to this and low yields, a range of improved methods utilizing isoindole precursors have been developed over the years (Figure 3.16) [67].

One alternative is to use an oxidative method in combination with isoindole precursors under milder reaction conditions. This requires stable and easy-to-handle isoindole precursors that are amenable to the use of normal Lindsey, MacDonald, or [3 + 1] condensation conditions. The final TBP is then obtained after oxidation. Often this involves a Barton–Zard reaction, for example, reaction of 1-nitrocyclohexene with ethyl isocyanoacetate, followed by reduction with $LiAlH_4$ and acid-catalyzed cyclization. Subsequent oxidation with chloranil gives the desired porphyrin. 5,15-Disubstituted benzoporphyrins can also be synthesized using isoindole precursors. For example, 4,7-dihydroisoindole can be transformed into the meso-unsubstituted dipyrromethanes and subjected to a condensation reaction with TFA and an aryl-aldehyde, followed by oxidation with DDQ [69].

An intriguing approach toward TBPs was developed by Ono and co-workers in 1998 and circumvents the solubility problems by first constructing a soluble tetra "nonbenzo" porphyrin, followed by a final retro-Diels–Alder reaction to generate the annulated benzene rings [70]. The first synthesis with this methodology involved the reaction of 1,3-cyclohexadiene with β-(phenylsulfonyl)nitroethylene, followed by a Barton–Zard reaction to form the bicyclo[2.2.2]octadiene fused pyrrole **99**. The ethyl ester on the fused pyrrole was reduced with $LiAlH_4$ and the resulting carbinol subjected to an acid-catalyzed cyclotetramerization and oxidation to yield **98** in 30% yield. Heating to facilitate the retro-Diels–Alder reaction then gave the target TBP **92** (M = 2H).

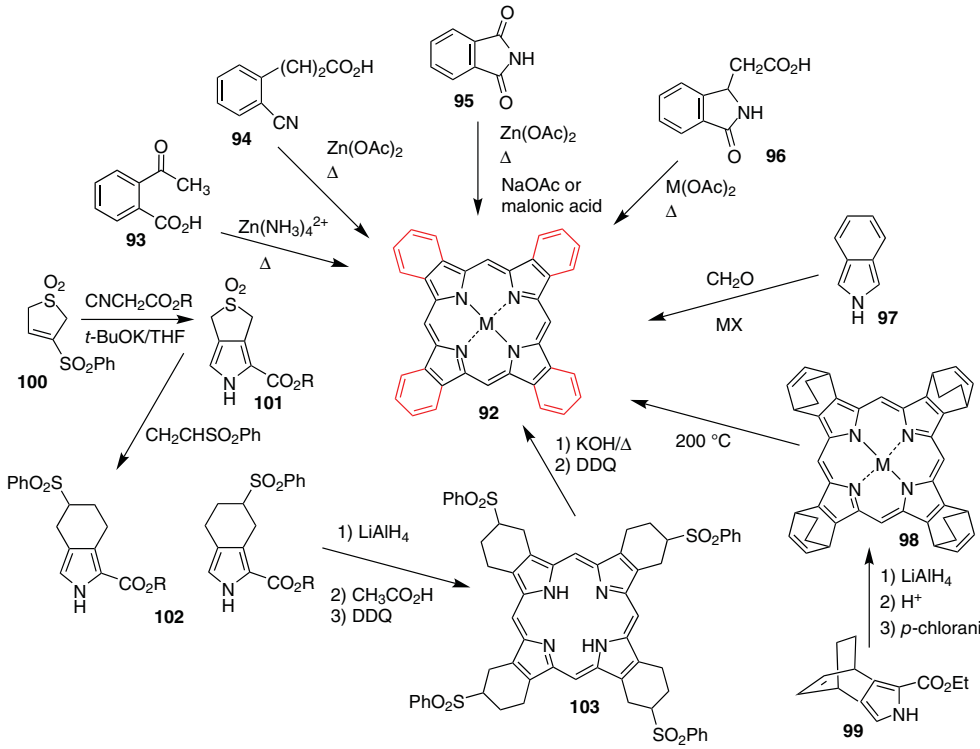

Figure 3.16 Synthetic methods for tetrabenzoporphyrins.

A related approach used the 3-sulfolene **101**, synthesized via a Barton–Zard reaction from **100**. A Diels–Alder-type cycloaddition after elimination of SO_2 furnished the tetrahydroisoindole **102**. Reduction of the ester with $LiAlH_4$ and subsequent cyclotetramerization in acetic acid and oxidation with DDQ formed the phenylsulfonyl-substituted porphyrin **103**. Finally, the TBP **92** (M = 2H) was prepared via elimination of the phenylsulfonate moieties followed by dehydrogenation with DDQ [71]. meso-Tetraaryltetrabenzoporphyrins, that is, systems similar to **86**, were historically synthesized using 3-benzylidenephthalimidine, phthalimide, and phenylacetic acid, or isoindole with aromatic aldehydes and zinc acetate at high temperatures. Here, Ono's approach works as well and makes various meso-substituted TBPs accessible via standard pyrrole tetramerization reactions [70].

3.4.4 Chlorins

3.4.4.1 General Considerations

Chlorins have been a target of research for a long time, going back to the times of Willstätter. This relates to the relevance of the natural chlorophylls and other natural hydroporphyrins [72]. Yet, studies on their total and partial synthesis have remained the purview of few research groups, compared to the vast amount of work published on the synthesis of porphyrins. As reduced porphyrins, they are less symmetric than porphyrins. The reduced pyrrole ring(s) and the sp^3-hybridized centers in the macrocycle (and the isocyclic pentanone ring in (bacterio)chlorophylls **104**) give rise to the presence of chiral centers, further complicating their synthesis, and many chlorophylls are also prone to allomerization reactions [73].

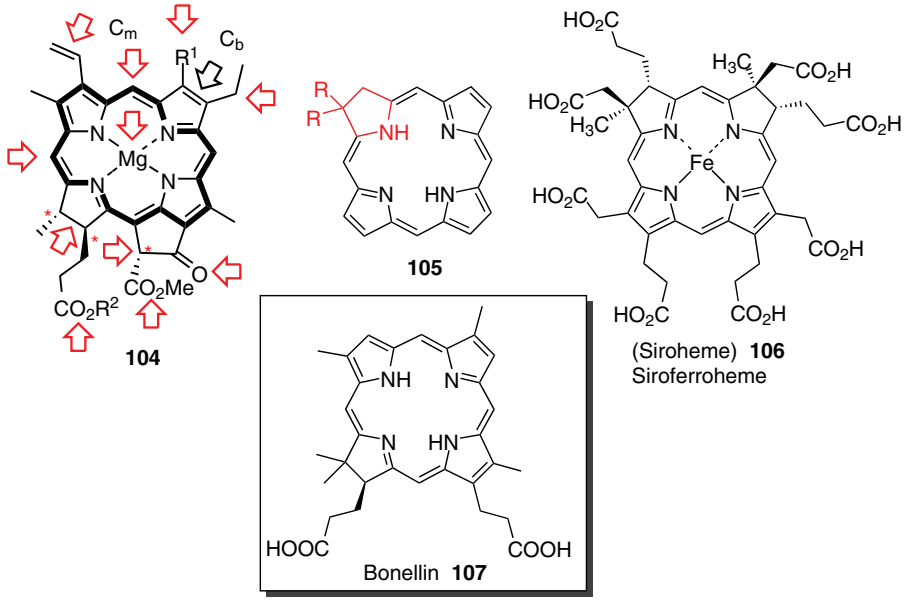

Figure 3.17 General structure of chlorophylls and places of notable chemical reactivity or synthetic challenges; a stable *gem*-disubstituted mimic as found in sirohemes and Bonellin.

Differences in the reactivity of the C_m-positions are more pronounced than in porphyrins, and additional functional groups such as CHO in chlorophyll b can be present. Additionally, the C^{17} and C^{18} positions in chlorophylls are prone to re-oxidation to the porphyrin level, the long-chain esterified alcohols in chlorophylls present a solubility issue, and the Mg center is rather labile, adding other challenging aspects to their chemistry (Figure 3.17). These challenges are amply exemplified in the classic total syntheses of chlorophyll a and vitamin B_{12} [74, 75].

Nevertheless, the fundamental approach to the synthesis from nonaromatic precursors is the same as for porphyrins: construction of appropriate pyrrole building blocks, condensation or cyclization reactions, and oxidation to the aromatic species. Alternative means are their preparation from preformed porphyrins via reduction and addition reactions and are described in Chapter 6.

Different strategies exist to synthesize natural and synthetic chlorins, and their preparation has been extensively discussed in the past [72, 76–78]. One means of simplifying chemical studies on chlorins is to target biomimetic compounds, which are more stable than those in nature. The classic examples here are chlorins with a *gem*-dialkyl C_b-group, as in **105**. These compounds have proved to be more stable than their unsubstituted counterparts as they are resistant to dehydrogenation. Such substitution patterns are also found in nature in sirohemes (**106**), heme d_1, sirohydrochlorins, Faktor I and F430, and corrins (such as in vitamin B_{12}) as biosynthetic intermediates (pre-corrin I), and non-photosynthetic natural product chlorins (such as Bonellin **107** and tolyporphyrin). These *gem*-dialkylchlorins have featured prominently in the works of Battersby, Jacobi, Montforts, and Lindsey, which will be used here as examples for the "*de novo*" synthesis of chlorins. Note that a magisterial account of the strategies used by these groups and others has been given by Lindsey [79], and only a brief overview will be presented here.

3.4.4.2 The Case of *gem*-Dialkylchlorins

gem*-Dimethylchlorins *à la Battersby In an effort to synthesize Bonellin **107** and Faktor I, Battersby and co-workers initiated the synthesis of *C*-methylated chlorins, and his group was the first to propose a rational synthetic pathway toward these systems (Figure 3.18) [80]. Their initial approach used tetrahydrodipyrrin **108** as starting material. It can be synthesized from pyrrole-2-carboxaldehyde in a Henry condensation to yield 2-(2-nitroethyl)pyrrole. The following Michael reaction using mesityl oxide gave nitro-hexanone-pyrrole, reductive cyclization utilizing Zn/acetic acid, and reduction/deoxygenation with $TiCl_3$ resulted in the tetrahydrodipyrrin-ester. Cleavage of the *tert*-butyl group with TFA and decarboxylation then gave the desired compound **108**. This was used in an acid-catalyzed [2 + 2] condensation reaction with formyl-dipyrromethane **109**. The resulting linear 1,19-dimethyltetrapyrrole was oxidatively cyclized with $CuCl_2$ giving the Cu(II)oxochlorin. After removal of Cu(II) with TFA and H_2SO_4, a mixture of two different free base oxochlorins **110**, one containing an acetyl group and one a formyl group, were obtained in low yield [81].

An alternative [2 + 2] approach used the 1-(bromomethyl)-9-bromodipyrrin **111** instead of dipyrromethane [81]. Alkylation on the α-bromomethyl site of the latter compound with tetrahydrodipyrrin **108** gave a 2,3,4,5-tetrahydrobiladiene-*ac* (*seco*-chlorin). Here, oxidation with an excess of copper acetate followed by demetallation with TFA/H_2SO_4 gave the dimethyl oxochlorin **112**. When strictly anaerobic conditions were used during the oxidation with copper acetate, the chlorin **113** was obtained.

Another option investigated used the formyl-dihydrodipyrrinone **114** for the "Western half" and the dipyrromethane **115** with an active methylene unit as the "Eastern half" [82]. The former was prepared via a fluoride-mediated Michael reaction of methyl 3,3-dimethyl acrylate and 2-(2-nitroethyl) pyrrole. The pyrrole-nitropentanoate obtained was transformed into the lactam via two pathways. One route involved ring closure with Zn and acetic acid, followed by treatment with $TiCl_3$, chlorination at the 5-position and dehydrochlorination to give the dihydrodipyrrinone. Another option was to use *tert*-butoxide, followed by treatment with $TiCl_3$, and re-esterification with diazomethane to yield the γ-ketoester. Cyclization with ammonium acetate gave the same dihydrodipyrrinone. In both cases, removal of the *tert*-butoxycarbonyl protecting group was achieved through treatment with TFA and trimethyl orthoformate. Subsequent formylation gave the desired dihydrodipyrrinone **114** with a free α-pyrrole position. The two halves were then reacted in methanolic TFA to yield the *seco*-chlorin. The *seco*-chlorin was then treated with trimethyloxonium tetrafluoroborate to give the 2,3-dihydrobiladiene-*a,b*. Again, cyclization with Cu(II)OAc_2, oxidation with DBU, and demetallation yielded the desired free base chlorin **116**.

Besides [2 + 2] approaches, a [3 + 1] methodology can also be applied. Here, a pyrrole was brominated to yield an α-bromomethyl-substituted pyrrole, which was then reacted with a thiolactam. The resulting thioether was further subjected to standard sulfur extrusion, yielding the tripyrrin **117** with one benzyl ester and two *tert*-butyl ester groups. After removal of the *tert*-butyl esters, the tripyrrin was used in a [3 + 1] condensation reaction with 3,4-dimethylpyrrole-2,5-dicarboxaldehyde **118** to give the free base chlorin **119** upon oxidation with DDQ [82].

A photochemical electrocyclization to form the cyclic macrocycle is possible as well [83, 84]. Here, the dihydrodipyrrin **120** and the dipyrrin **121** were converted into the *seco*-chlorin with TFA. Subsequent irradiation then gave the chlorin **122**. This method has been tested with different building blocks, and the reaction conditions can vary with regard to the reaction medium, the reaction time, and the presence or absence of a metal

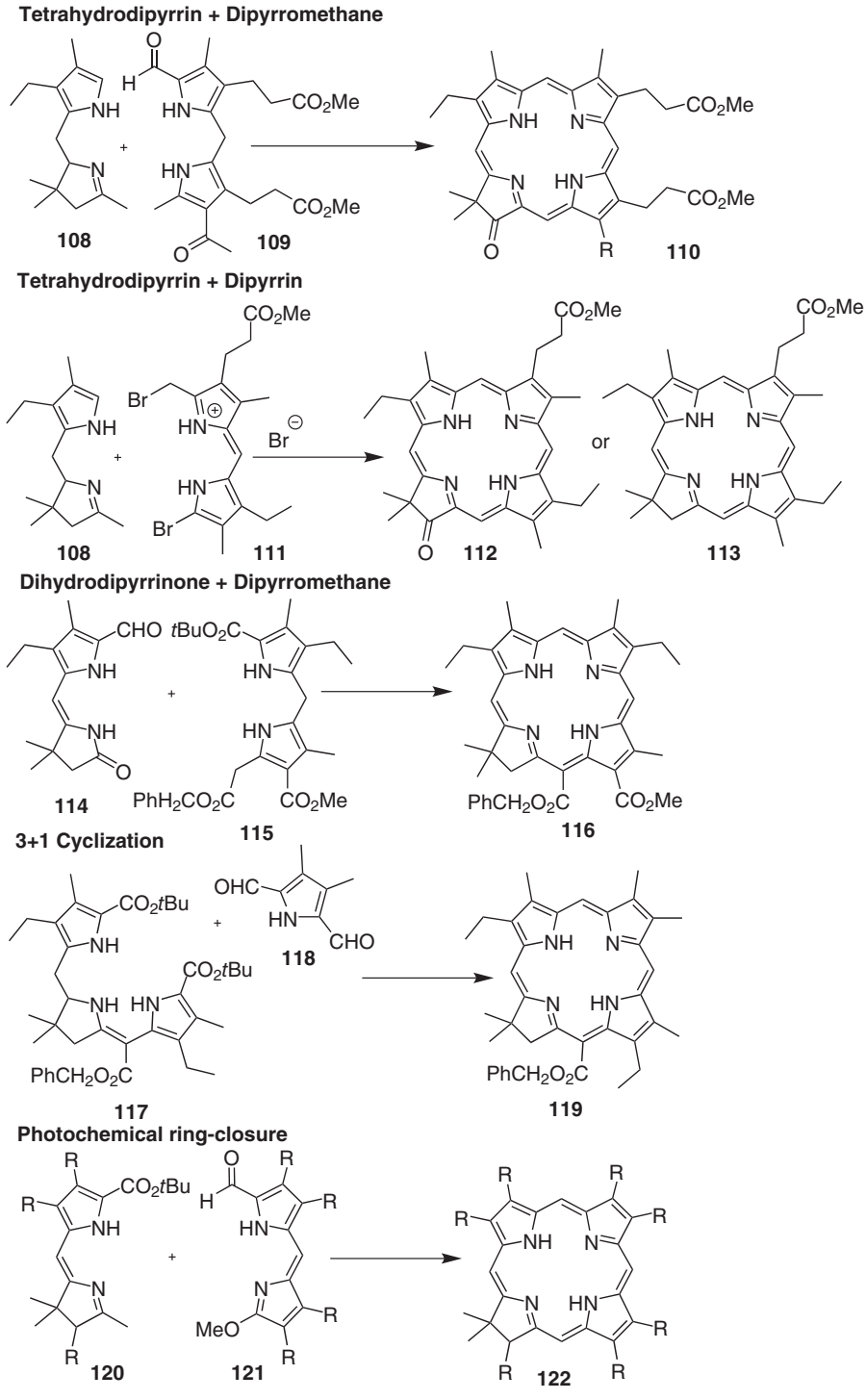

Figure 3.18 Battersby's approaches toward the synthesis of *C*-dimethylated chlorins.

template [85]. One advantage of this method is the milder reaction conditions, allowing the use of alkyl esters. These moieties are important parts in the synthesis of Bonellin and Faktor I, as they can be deprotected to the corresponding alkyl carboxylic acids [86].

Montforts' Approach Montforts and co-workers based their synthesis of dialkylchlorins on the use of a three-pyrrolic building block (Figure 3.19). Preparation of the main parts of the "Eastern half" for their target chlorins used the condensation of a pyrrole-carboxaldehyde with 2-pyrrolinone. This was then reacted with a brominated enamine, giving the sulfide-linked tripyrrin. Following sulfide contraction, tripyrrins containing the BCD-pyrrole units were accessible [88]. However, such tripyrrins are very sensitive to oxygen, and ester saponification can result in de-cyanidation. Montforts' trick here was to metallate the tripyrrin with nickel. The nickel tripyrrin **123** was then subjected to an acid-catalyzed reaction with bromopyrrole-carboxaldehyde **124**. This reaction led to the linear tetrapyrrole after decarboxylation and decomplexation. Ring closure was achieved by treatment of the tetrapyrrole with zinc acetate and base, giving the Zn(II)chlorin **125** [89]. The free base chlorin can then be liberated with a mild acid. Although the synthesis of the tripyrrolic precursor is not for the uninitiated, the variability in the fourth pyrrole synthon makes this a useful method for a variety of different chlorins which are inaccessible by any other method [77, 79]. Similar strategies were also used by this group for their synthesis of (±)-Bonellin dimethyl ester [90].

Jacobi's Strategy Whereas Battersby's and Montforts' main contribution stems from the early to mid-1980s, Jacobi and co-workers began work on a different approach about two decades later, similarly targeting natural corrins and hydroporphyrins. They focused on [2 + 2] reactions combining the "Northern" and "Southern" halves [87] (Figure 3.19). Again, the synthesis of pyrroline-containing precursor molecules presented the key synthetic hurdle. Jacobi's breakthrough here was the synthesis of 4-alkynoic acids bearing *gem*-dimethyl groups, which fed into the synthesis of dihydrodipyrrins [91, 92]. Construction of the chlorin macrocycle followed the MacDonald-type reaction for porphyrins, and thus he used a diformyl-dipyrrolic species **127a** together with a dipyrromethane-1,9-dicarboxylic acid **126a**. Condensation was achieved by simple stirring at room temperature with 5% TFA in CH_2Cl_2, allowing the synthesis of a range of chlorins with this methodology [93].

This method gives high yields and can be used on a reasonable scale, but was limited to symmetrical dipyrromethanes with two identical alkyl substitutions in two C_b-positions and two methyl substituents on the other two β-positions. Therefore, subsequent work targeted less symmetric systems, resulting in three different methods. First, they reacted a dipyrromethane **126b** with one ester and one carboxylic acid group, and a dihydrodipyrrin **127b** with a carboxaldehyde and an ester in 5% TFA. Further treatment with 25% TFA and trimethyl orthoformate gave the desired chlorin. Similarly, the unsymmetrically substituted dipyrromethane **126c** and the dihydrodipyrrin **127c**, each of the two moieties carrying one carboxaldehyde group, gave the desired chlorin without side products. In another variation, dipyrromethane **126d** and dihydrodipyrrin **127d** were used, in which each building block bears one carboxaldehyde and one *tert*-butyl ester group. Differences in the reactivity of the carboxaldehyde group on either the dihydrodipyrrin or the dipyrromethane unit led to the development of a pathway where the dihydrodipyrrin **127e** had two carboxaldehydes and the dipyrromethane **126e** was substituted with one ester and one acid group. Thus, characteristic features of Jacobi's strategy are the absence of any metals for chlorin formation, use of precursors with the same oxidation state as the chlorin, circumvention of the need

for an oxidant, and the production of chlorins with the six pyrrole-β-positions carrying alkyl substituents [94].

Lindsey's Concept Following his many seminal contributions to the synthesis of porphyrins, Lindsey and his group also developed general strategies for the synthesis of chlorins [78, 79]. Although this was based on their interest in mimicking chlorophylls and photosynthesis, attaching auxochromes to tune spectral properties, or introducing functional groups for subsequent modifications and/or bioconjugation, ultimately, their work aimed at the development of a general concept for the synthesis of a range of meso-substituted chlorins (see [78] and [79] for a full account).

To provide the desired stability, they also chose to use *gem*-dimethyl groups (Figure 3.19). The first route they investigated was based on the thermal route from Battersby discussed

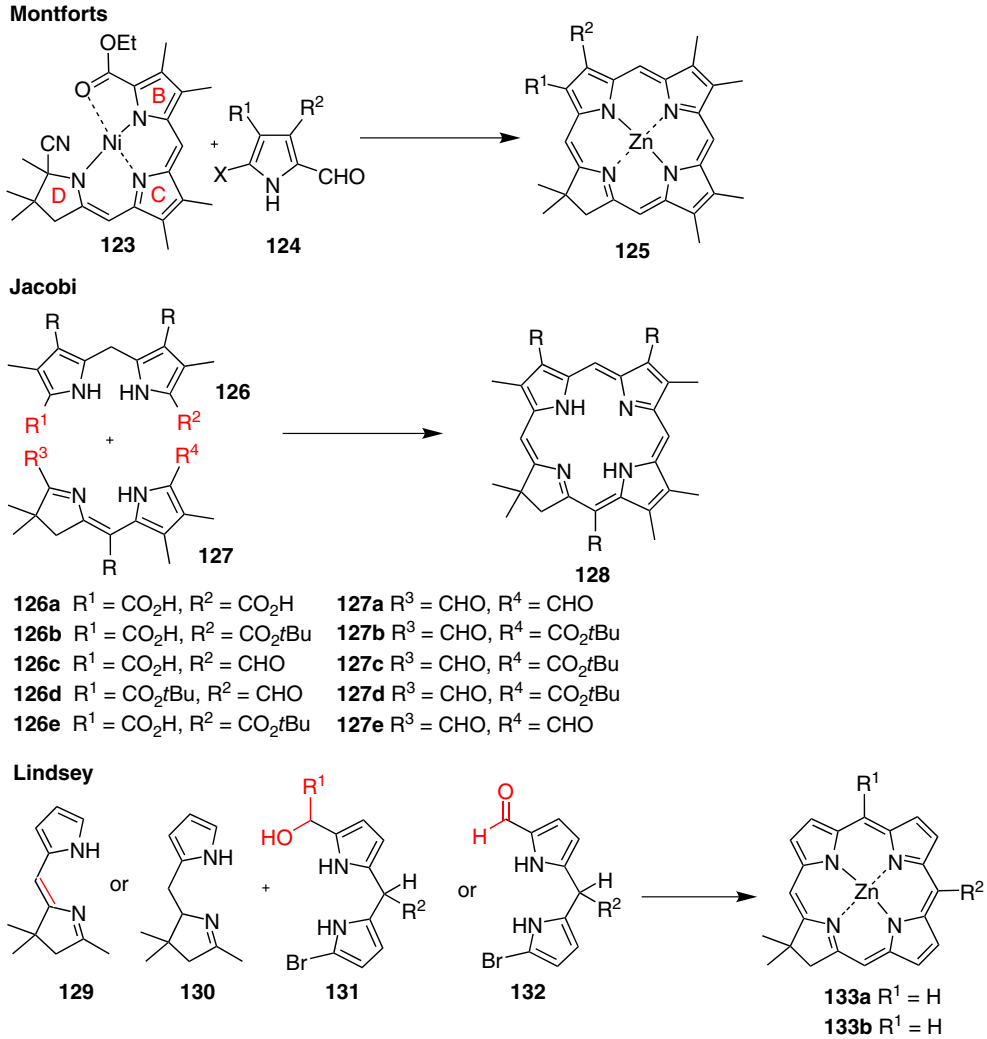

Figure 3.19 Synthetic strategies for *gem*-dimethylchlorins by Montforts, Jacobi, and Lindsey.

above. They used a dipyrromethane **131** with carbinol and bromo substituents as the "Eastern half" rather than dipyrrin and preferred Zn(II) over Cu(II) as the metal template for the cyclization. Characteristically, they utilized compounds with no or only few β-pyrrole substituents but rather with one or two meso-aryl moieties, giving the desired chlorins on a 10–100 mg scale [95, 96]. In a modified route, they used a tetrahydrodipyrrin **130** instead of a dihydrodipyrrin for the "Western half" to provide more stability and reactivity [97]. Furthermore, the use of a carbinol-substituted "Eastern half" required a substituent at C_5 other than hydrogen, which resulted in chlorins with mainly 5-aryl substituted "Eastern halves" **133a**. In their second modification, they used an "Eastern half" **132** that contained a carboxaldehyde instead of the carbinol substituent. This allows access to 5-unsubstituted chlorins **133b** [98]. Aside from free base chlorins, metallochlorins were also synthesized using various strategies. A special feature of Lindsey's strategy is that it yields so-called "sparsely" substituted chlorins, which have proved to be very useful in many applications and for fundamental studies [99]. Naturally, use of the *geminal* dimethyl pattern to provide stability for the reduced pyrrole ring can also be used to access related (iso)bacteriochlorins [78, 100].

3.5 Reactivity of Porphyrins

3.5.1 General Aspects

The reactivity of porphyrins is governed by many factors, ranging from electronic and steric effects to more special features such as macrocycle conformation, coordination state in complexes, aggregation, and more [101, 102]. Much of the fundamental chemistry can be explained by consideration of the electron density distribution in the macrocycle and the effect exerted thereon by core and peripheral substituents and other contributors (Figure 3.20). The C_m are generally more reactive in reactions with nucleophiles, radicals, or electrophiles, as compared to the C_b (**134**). This is counteracted to some extent by sterically hindered residues at neighboring β-positions (**135**), which may shield the meso-position against attack (and vice versa for β). The electronic character of the macrocycle is most easily manipulated by metallation (M, **134**). Metal complexes with Mg(II), Zn(II), and Cd(II) (d^0, d^{10}) have increased electron density and lower oxidation potential. On the other hand, Sn(IV) or Fe(III) (d^1–d^5) complexes have lower electron densities and show high reactivity at the β-positions with nucleophiles. The former complexes are relatively labile toward acid, and other metals are often difficult to remove from the porphyrin core. Thus, Ni(II) and Cu(II) (d^6–d^9) are often the compromise of choice in synthetic reactions,

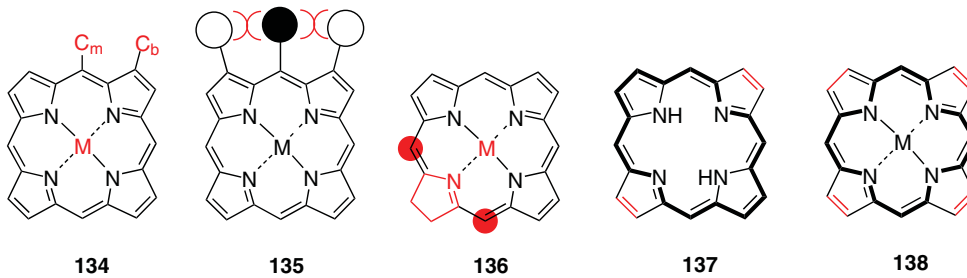

Figure 3.20 Reactivity considerations and aromatic delocalization pathways in porphyrins.

while Zn(II) is preferred over Mg(II) in chlorophyll-related studies. Naturally, the π-system can be modulated via protonation or deprotonation of free base systems. However, many irreversible secondary reactions with acids and bases may occur under these conditions.

Various aspects of porphyrin reactivity can also be illustrated by analysis of the π-delocalization pathways (Figure 3.20). Only 18 of the 22 π-electrons are involved in the aromatic system [Hückel $4n+2$ rule, $n = 4$], and hence, in free base porphyrins, the β-β′-bonds are not equivalent. The two not involved in the delocalization pathway (**137**) have double bond character and will undergo standard addition reactions. This also explains the easy formation of chlorins (2,3-dihydroporphyrins) and bacteriochlorins (2,3,12,13-tetrahydroporphyrins) (see Chapter 6, which also covers oxidation and reduction reactions of porphyrins), which show higher reactivity next to the reduced pyrrole ring (**136**). This gives rise to different N—H tautomers in substituted (hydro)porphyrins, with the N21,N23-tautomer (shown in **137**) being considered thermodynamically more stable. In metalloporphyrins and dications or tetraanions, the various possible tautomeric forms are equivalent (**138**), and thus there is no difference in β-β′ reactivity of the pyrrole units in symmetric porphyrins. Consideration of the delocalization pathway in tautomers also provides a rationale for directive effects in substituted porphyrins, although this is sometimes complicated by steric and macrocycle conformation effects. Reactions at the α-position are rare; they are only found during oxygenation or rearrangement reactions.

3.5.2 Electrophilic Reactions

Historically, electrophilic substitution and addition reactions provided the main entry into functionalized porphyrins. Taking into account the aforementioned influence of central metals and steric effects, substitution reactions can specifically target either the meso- or β-positions. Porphyrins readily undergo deuteration or tritiation at the meso-positions, can be halogenated and nitrated, and participate in Friedel–Crafts and Vilsmeier reactions. Other examples include cyanation, mercuration, methylation, and more [102]. Note that the underlying reaction mechanisms often differ from standard S_EAr reactions, which would require an isoporphyrin carbocation intermediate. Rather, they may involve addition-elimination sequences or intermediary π-cation radical species. In light of their relevance for follow-up chemistry, we will specifically highlight formylation, halogenation, and nitration reactions.

3.5.2.1 Vilsmeier Formylation

Vilsmeier formylation is a classic reaction for the introduction of C-substituents into porphyrins [103]. Developed by Inhoffen [104], the reaction is typically performed with Ni(II) or Cu(II) complexes (stable under acidic conditions) and uses DMF/$POCl_3$ for generation of the Vilsmeier complex, followed by base hydrolysis. Porphyrin or β-substituted systems (**139**) will undergo meso-monoformylation to **140**, while prolonged reaction with excess reagent will result in diformylation to **141** (Figure 3.21). Reaction of meso-substituted porphyrins such as Ni(II)TPP will result in 2-formylporphyrins **142**. Polyformylation is possible, but difficult to control. Synthetically useful transformations are vinylogous formylations to prepare acrolein-substituted porphyrins **143** [105] and Umpolung chemistry, that is, the introduction of masked formyl groups as dithianes **144** via condensation reactions or under basic conditions [106].

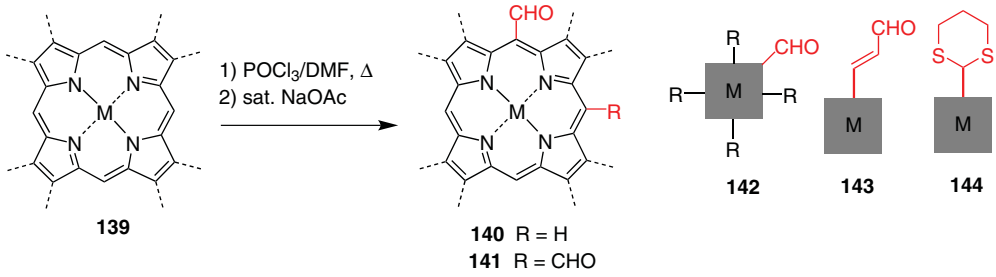

Figure 3.21 Vilsmeier formylation of porphyrins.

Formylporphyrins have been used widely for transformations, although most derivatives thereof are today more easily prepared via organometallic reactions. Examples include oxime formation, reductions and oxidations, Wittig, Petersen, Grignard, and McMurry reactions (to yield -CH=CH-–bridged bisporphyrins [105, 107]) as well as many others [103]. Acroleinylporphyrins **143** undergo acid-catalyzed intramolecular (meso→β) cyclization to benzochlorins [105], while β-CHO porphyrins in strong acid form naphthoporphyrins (see Section 3.7.3) [108].

3.5.2.2 Halogenation

The standard halogens F, Cl, Br, and I can all be introduced at the meso- and/or β-positions. Selectivity and regiochemistry are primarily controlled by steric considerations; for example, iodination is more likely at unhindered β-positions, as is bromination; while fluorination and chlorination preferentially occur at the meso-positions. Over the years, the whole cornucopia of possible halogenation reagents has been used with varying success [12, 109], even in reactions with unsubstituted porphyrin **5** [110]. β-Substituted porphyrins such as H_2OEP **61** can be meso-halogenated (X = F, Cl, Br), although the degree of halogenation is difficult to control, and radical conditions might promote reactions in alkyl side chains [111].

β-Perhalogenated porphyrins **146** are easily prepared for X = Cl and Br via reaction of 5,10,5,20-tetraarylporphyrins **145** with NCS and NBS (Figure 3.22) [112]. Bromine can also be used, but will always give perbromination and can degrade free base porphyrins. These highly electron deficient and often nonplanar systems have found wide use as oxidation catalysts [113]. Contemporary methods [112, 114] allow selective β-halogenations giving access to 5,10,15,20-tetraarylporphyrins with 1, 2, 4, 6, and 8 β-halogen atoms, which in turn serve as precursors for porphyrins with mixed substituent types [115]. The key regiochemical consideration is that halogenation is directed to the pyrrole ring opposite one carrying electron-withdrawing substituents (e.g., other halogen atoms or NO_2); thus, in **147** X^1 is followed by X^2. β-Fluoroporphyrins are better prepared via condensation reactions with fluoropyrroles [116].

Halogenated porphyrins are the most important construction materials in contemporary porphyrin chemistry [117]. This relates to their utility in transition metal-catalyzed reactions (see Section 3.6), and many current syntheses use 5,15-disubstituted porphyrin **149** building blocks. For example, regioselective meso-mono- (**150)** or dibromination (**151)** is possible, as is meso-monoiodination to **152** [118, 119]. Even more selective or complex halogenation patterns are accessible from organometallic compounds, for example, the formation of **152** through a bromo-iodo exchange via an intermediary η^1-palladioporphyrin [120]. The highly

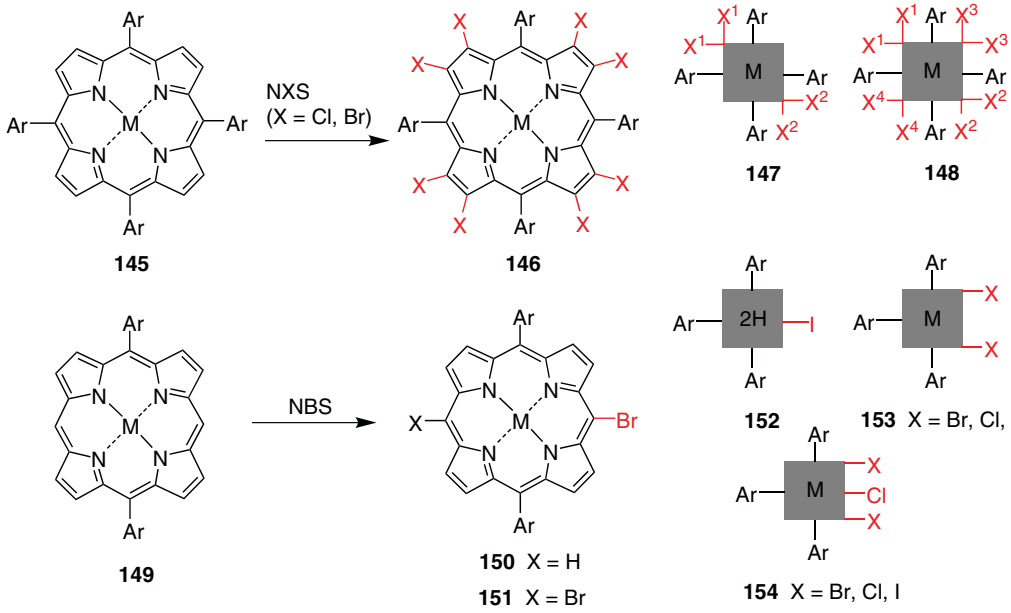

Figure 3.22 Halogenated porphyrins.

useful β-dihaloporphyrins **153** were prepared by Osuka and co-workers through the application of Cu-mediated *ipso*-halogenation of porphyrin boronic acid pinacols [121]. Later, this was extended by the same group to the mixed, oligohaloporphyrins **154** with $PhICl_2$ or, better, with 2-chloro-1,3-bis(methoxycarbonyl)guanidine (Palau'Chlor) [122].

3.5.2.3 Nitration

Similar to other reactions, nitration proceeds preferentially at the meso-position. For example, reaction of H_2OEP **61** with nitric acid in acetic acid gives the mononitrated product **155**, whereas HNO_3 in sulfuric acid gives the mono- to trinitrated products with disubstitution preferring the 5,15-pattern (Figure 3.23) [123]. Complete meso-nitration is achieved with $Zn(NO_3)_2$ to yield the metalloporphyrin **156** [124]. The nitro group in **155** and other porphyrins can be reduced with $SnCl_2$/HCl or $NaBH_4$/Pd/C to the aminoporphyrin [125]. The latter is highly reactive and behaves similar to meso-oxoporphyrins; that is, in acid it forms phlorins such as **157** [126]. Phlorins are easily distinguished from porphyrins by their broad absorption in the 500–600 nm region and orange color. β-Nitration of meso-arylporphyrins is possible as well; notably, compounds with one to eight β-nitro groups **158** have been prepared using $HNO_3/CF_3SO_3H/(CF_3SO_2)_2O$ mixtures [127].

Nitroporphyrins can also be prepared using an oxidizing agent and nitrite, and this illustrates another fundamental reaction of porphyrins. (Metallo)porphyrins are easily oxidized to π-cation radicals **160**, and these electrophiles can be trapped with various nucleophiles [128]. Thus, reaction of Mg(II)OEP with iodine/pyridine/HCl can yield meso-pyridinium salts, whereas 5,15-diarylporphyrins can be meso-nitrated to **161** with $I_2/AgNO_2$ [129]. Such reactions can also be performed at the β-position if the meso-positions are blocked.

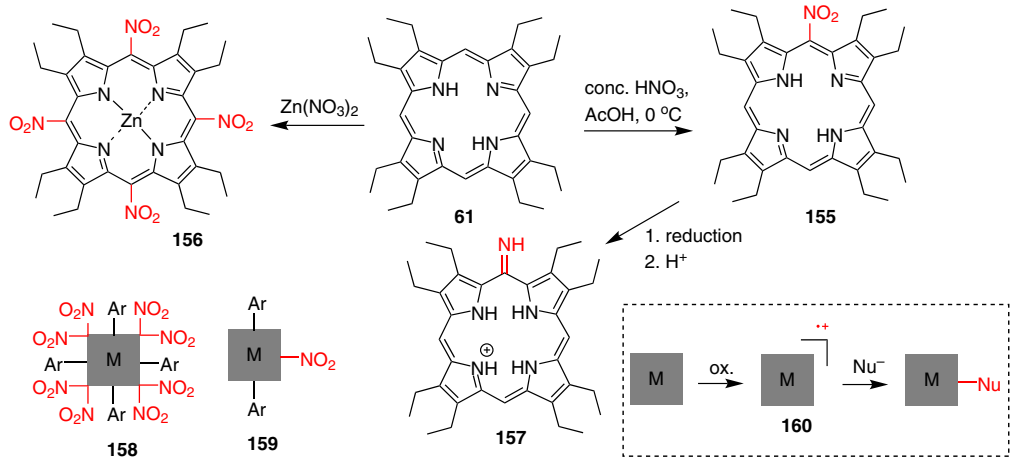

Figure 3.23 Nitration of porphyrins (inset: reaction of porphyrin π-cation radicals).

3.5.3 Nucleophilic Reactions

Porphyrins are known to undergo a range of nucleophilic substitution reactions, again predominantly at the meso-position. A classic approach is the generation of porphyrin π-(di)cation radicals using electrochemical oxidation or chemical oxidants such as iodine and then an in situ reaction with nucleophiles. Typically, these reactions are performed with metalloporphyrins. For example, metallo-β-octaalkylporphyrins can be oxidized with I_2 and then substituted with pyridine, to give pyridinium porphyrin salts [130]. The use of meso-substituted porphyrins gives analogous products, for example, in the reaction of M(II)TPP$^+$ with nitrite to yield 2-nitroporphyrins. Many other possibilities exist [12, 131, 132], but often require activation of the porphyrin system via oxidation, appropriate central metals, steric effects, or the presence of electron-withdrawing substituents [133]. In the following, we will discuss the exemplary and classic case of electron-deficient porphyrins and the use of strong nucleophiles such as RLi reagents for nucleophilic aromatic substitution reactions.

3.5.3.1 Nitroporphyrins and Porphyrin Thioethers

Nitro groups have a highly electron-withdrawing effect and can act as good leaving groups. Thus, compounds such as those described in Section 3.5.2.3 can undergo reactions with nucleophiles. In general, β-nitroporphyrins are more reactive than meso-nitroporphyrins. Depending on whether "hard" or "soft" nucleophiles are used, different substitution mechanisms apply. When 5-nitroporphyrin **161** is treated with "hard" nucleophiles such as methylmagnesium iodide or benzyl oxide, a 5,15-meso-addition ("*trans*") to **166** occurs, whereas "soft" nucleophiles, such as thiolates or benzaldoxime anions, result in an *ipso*-substitution (**162**) followed by denitration to **163** (Figure 3.24) [134]. Similar results were obtained for 2-nitroporphyrins, where the attack of "soft" nucleophiles results in an *ipso*-attack, and the reaction with "hard" nucleophiles results in an attack on the adjacent β-pyrrolic position. This was exemplified in Crossley's reaction of 2-nitro-TPP with Grignard reagents. These first involve a nucleophilic addition, that is, give a 2-substituted-3-nitrochlorin which rapidly eliminates nitrous acid to reform the porphyrin system [136].

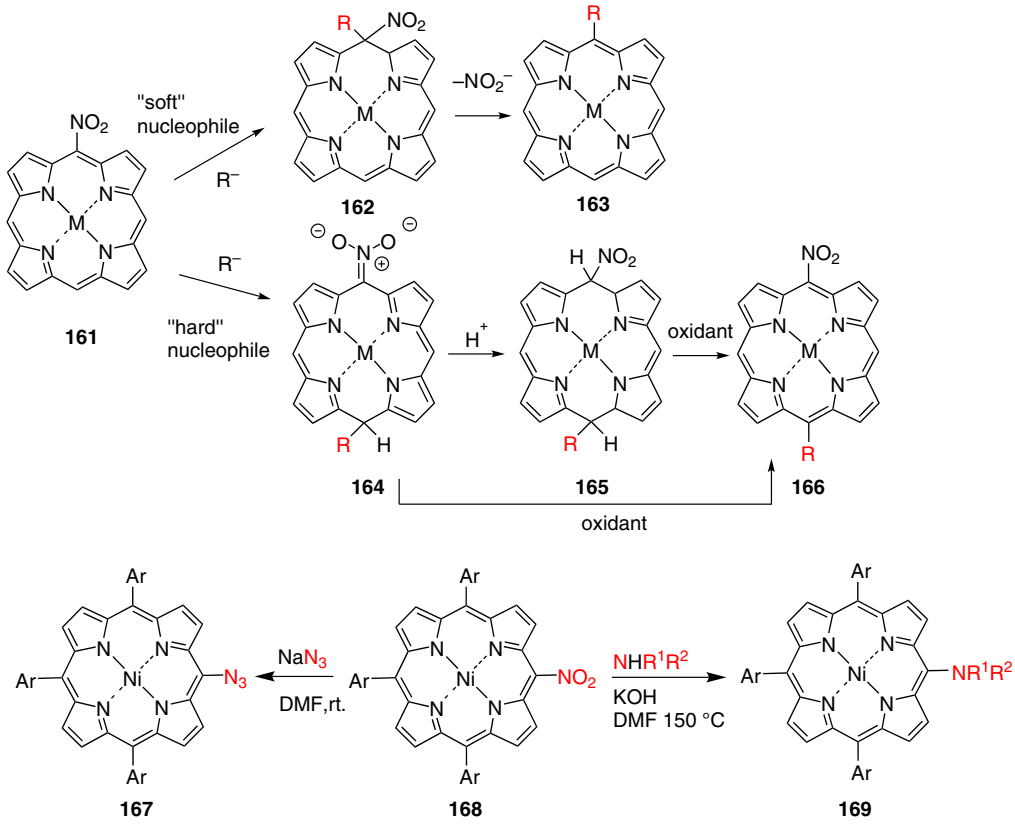

Figure 3.24 Nucleophilic substitution of 5-nitroporphyrin.

The reaction of nickel(II) nitroporphyrins **168** with nitrogen-based nucleophiles such as sodium azide to **167** or primary or secondary aryl- and alkylamines to **169** are of practical utility. As shown by Devillers et al., the use of amines with electron-donating or -withdrawing groups requires a basic catalyst, whereas the azide anion is nucleophilic enough to react without any catalyst (Figure 3.24) [135]. Various compounds could easily be synthesized via this method, including NH-bridged porphyrin dimers.

Such reactions were first observed by Gong and Dolphin, who studied reactions of the free base 2,3,7,8,12,13,17,18-octaethyl-5,10,15,20-tetranitroporphyrin **174** with halides [137] (Figure 3.25). The reaction proceeds via an addition-elimination pathway to form a Jackson-Meisenheimer complex, followed by elimination of the nitro group to yield the *ipso*-substituted products. The degree of substitution could be controlled through variation of the reaction conditions, ranging from replacement of all four nitro groups by halides (**170**) to partial substitution, as in **171** or **172**. More recently *S*-nucleophiles were shown to yield the respective tetrasubstituted thioethers **173** in high yield [138]. Next to substitution, stepwise denitration to **174** was also observed as a competing process under basic conditions.

Another intriguing reaction was the formation of bisporphyrin thioethers via a similar mechanism. Studies on the "unmasking" of porphyrin thioethers with an isooctyl-3-mercaptopropionate group **175**, that is, attempting to generate the free thiol, resulted in the formation of the bisporphyrin thioethers **178** in good yield (Figure 3.26) [139].

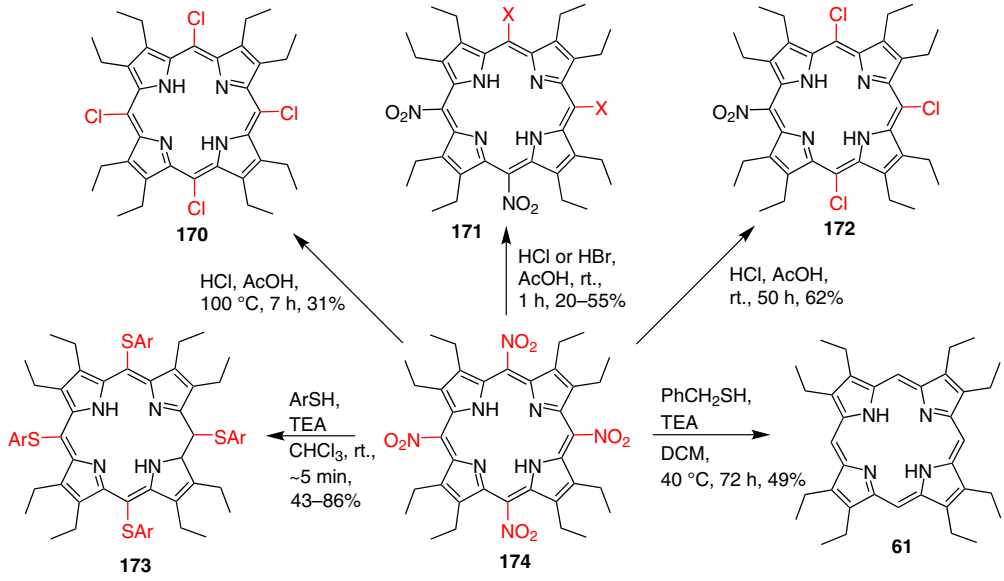

Figure 3.25 Nucleophilic substitution and denitration reactions of 2,3,7,8,12,13,17,18-octaethyl-5,10,15,20-tetranitroporphyrin.

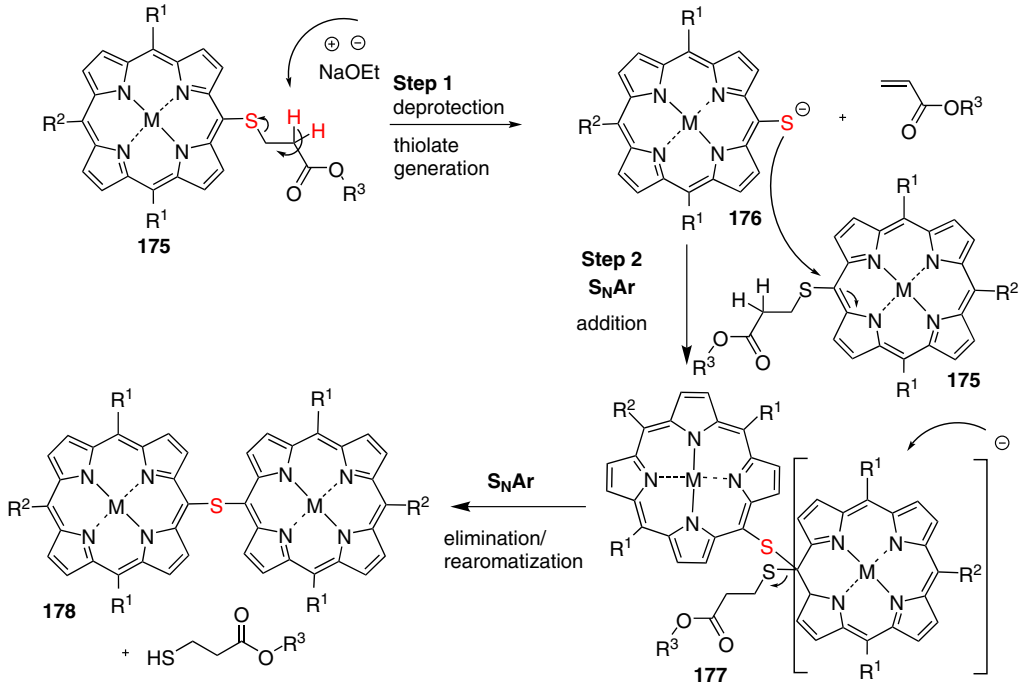

Figure 3.26 Synthesis of bisporphyrin thioethers via thiolate displacement.

Nucleophiles containing sulfur groups often require activation of the system (good leaving groups, strong bases, high temperatures, and metal catalysts). Therefore, it was very surprising that the formation of sulfur-linked dimers could be achieved through simple treatment with base at room temperature. These systems were considered rather inactive, but substitution occurred nevertheless. The reaction mechanism includes a base-mediated deprotection of a porphyrin thiol, followed by a S_NAr reaction. The deprotected porphyrin thiolate **176** acts as a very strong nucleophile and attacks the, as of yet, unreacted starting material to form the bisporphyrin, most likely via a phlorin intermediate **177**.

3.5.3.2 C—H Activation with Organolithium Reagents

A more generally applicable method is the reaction of porphyrins with organolithium reagents. This reaction from our laboratory was developed in 1998 by Kalisch and Senge [65] and gave rise to many follow-up studies [133, 140]. At that time, functionalization on the β-position had been explored more widely, and fewer synthetic methods existed for substitution of the meso-position. S_NAr reactions are often limited to special cases or depend upon activation of the porphyrin core, such as with electron-withdrawing substituents, metals or steric effects, and therefore require synthetic modifications prior to substitution. Thus, although it was perhaps counterintuitive to attack an electron-rich, heteroaromatic system with nucleophiles, surprisingly, "standard" porphyrins submitted readily to reactions with RLi.

As shown in Figure 3.27, Ni(II)OEP **179** underwent direct meso-substitution with alkyl or aryl residues, without activation of the porphyrin, giving excellent and often quantitative yields. This methodology utilizes organolithium reagents to perform a nucleophilic aromatic substitution on the porphyrin core. The reaction gives facile access to a broad spectrum of highly substituted porphyrins with various functional groups (as long as they are tolerated under the conditions used for the preparation of the RLi reagent) without cumbersome

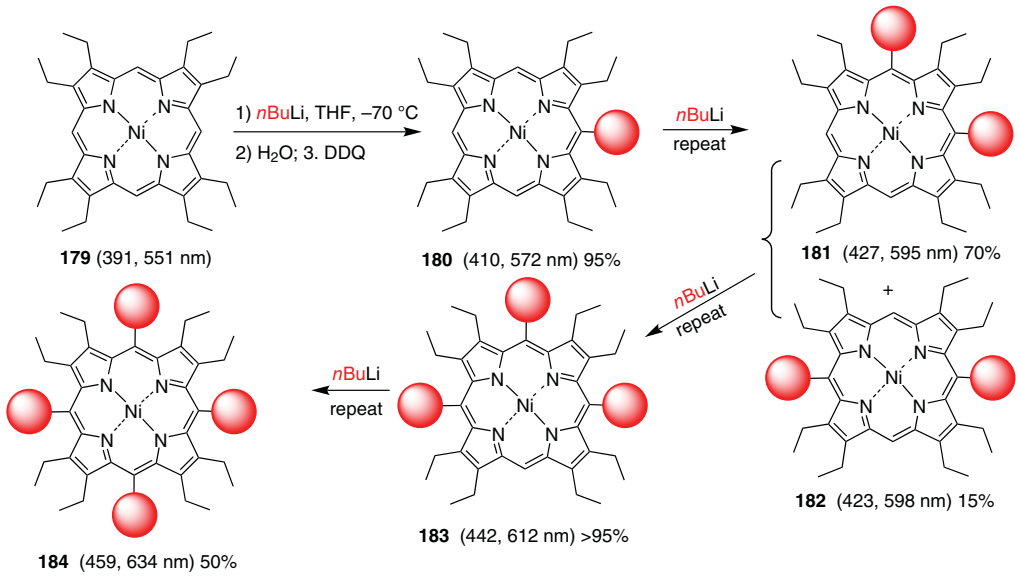

Figure 3.27 Reaction of Ni(II)OEP with *n*BuLi. Numbers in brackets refer to the main absorption maxima in CH_2Cl_2.

multi-step syntheses or mixed-condensation reactions. The reaction is compatible with both free base porphyrins and metal complexes, such as Zn(II), Cu(II), Co(II), and Ni(II). Usually, the trend is that alkyllithium compounds tend to give higher yields with metalloporphyrins, whereas substitutions with aryllithium reagents work better with free base porphyrins [141].

The general reaction mechanism follows an addition-oxidation sequence. The nucleophile attacks the meso-position of a porphyrin, leading to a Meisenheimer-type complex as an intermediate. In the following steps, this complex is hydrolyzed and oxidized to yield the substituted porphyrin. The reaction mechanism can depend on the steric aspects and conformation of the porphyrin, as well as on the steric bulk of the organolithium reagents. Further investigation, using spectroscopic and deuterium labeling studies, showed that the reaction mechanism follows two different pathways, depending on whether either metalloporphyrins or free base porphyrins are being used (Figure 3.28). The metalloporphyrin forms a porphodimethene anion **188**, whereas the free base porphyrin results in a phlorin anion **186** [142]. One limitation is that organolithium reagents are not compatible with very reactive substituents. Usually, these reactions are performed at low temperatures between −100 and −40 °C, depending on the starting material and the organolithium reagent used. However, the reaction can be repeated, giving easy and selective access to porphyrins with one (**180**), two (**181**, **182**), three (**183**), and four (**184**) meso-substituents. Such systems are examples of highly substituted nonplanar porphyrins, as illustrated in Figure 3.15. The impact of increasing the numbers of meso-substituents and the concomitant increase in the macrocycle nonplanarity is clearly shown in the bathochromic shift of the absorption maxima for the porphyrins detailed in Figure 3.27.

The possibility of introducing four meso-substituents in a stepwise manner also allowed the synthesis of porphyrins with four different C_m-residues, that is, OEP-type ABCD-porphyrins **197** utilizing a sequence similar to that shown for **179**→→→→**184** [143]. Here, the predominant localization of the negative charge on the meso-carbon opposite to the one attacked results in a regioselective preference of the second substitution in the 10-position (as in **181**). This was more distinctive for meso-aryl substituents than for meso-alkyl derivatives [133].

This versatile method can be used to synthesize not only mono-, di-, tri-, and tetra-meso-substituted porphyrins with different residues **197**, but also directly meso-meso-linked bisporphyrins **196**, phlorins, porphodimethenes (**192** or **193**), and chlorins (**191**) (Figure 3.29) [133]. The key aspect here is the generation of the anionic intermediate **190** from **189** and how this is used in subsequent transformations. Quenching with water followed by oxidation will yield the porphyrin, while trapping with an organic electrophile

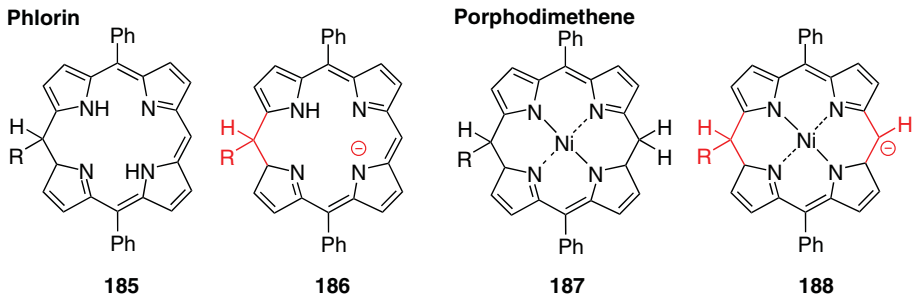

Figure 3.28 Intermediates in the reaction of porphyrins with RLi.

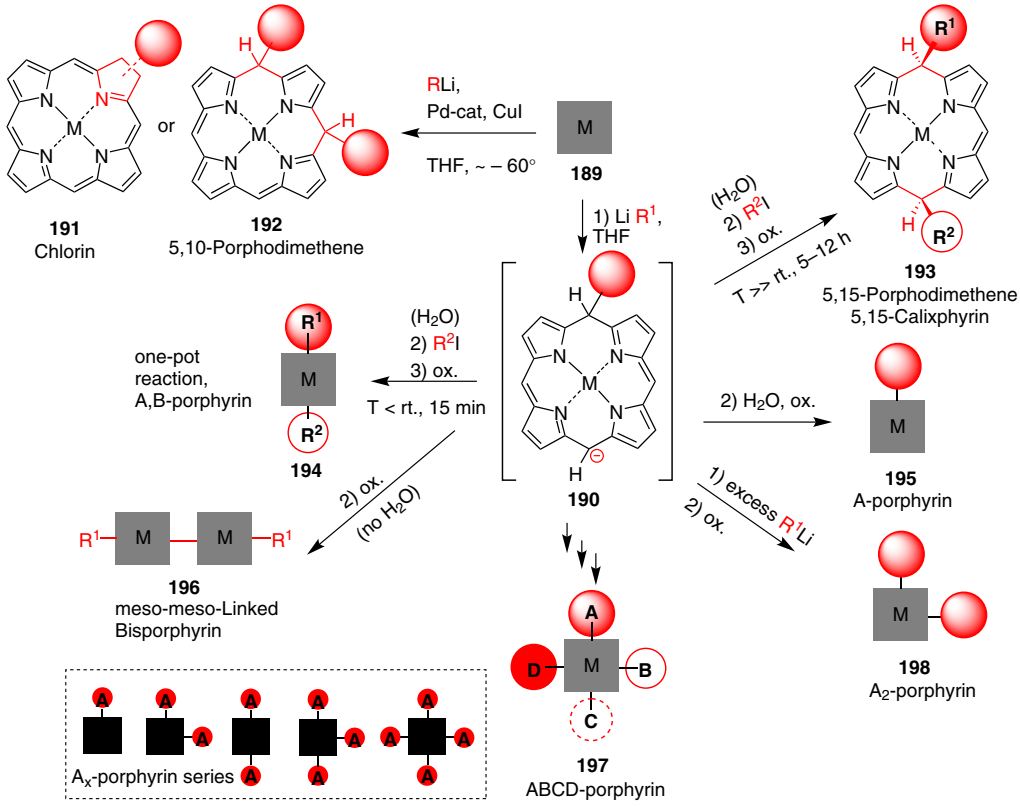

Figure 3.29 Synthetic scope of using organolithium reagents for porphyrin modifications.

at low temperature will yield A,B-disubstituted porphyrins **194** in a one-pot reaction [144]. If the electrophile is added at higher temperatures, then the intermediate becomes locked in a roof-type conformation that cannot be oxidized to the porphyrin level, and 5,15-porphodimethenes **193** are obtained [62, 145]. Skipping the hydrolysis step and instead directly oxidizing the intermediate **190** yields an anion radical that can dimerize to **196** [146].

The use of an organolithium reagent also offered the first rational entry into "less-substituted" porphyrins and the completion of the A_x-type porphyrin series (inset, Figure 3.29) through functionalization of unsubstituted porphyrin **5** (naturally, in practice, the symmetric compounds are more easily prepared by simple condensation reactions). The synthesis and use of porphyrin was cumbersome and plagued by low yields as well as its extremely low solubility (due to π-stacking), and this hampered synthetic advances with it [32, 147]. This was overcome by preparation of the free base **5** via acid-catalyzed thermal dealkylation of the highly nonplanar porphyrin 5,10,15,20-tetra(*tert*-butyl)porphyrin or its β-substituted analogs [148] (see Figure 3.52). Reaction of **5** in situ with RLi as outlined above then gave a high-yielding synthesis of 5-substituted **190** [39] or, with excess RLi, 5,10-disubstituted porphyrin **198** [41, 42]. Formally, these reactions are the initial steps in the synthesis of 5,10,15,20-tetrasubstituted ABCD-type porphyrins **197** from **5** [117, 149].

This method can also be used for substitution of the β-position. This depends on the steric bulk of the RLi reagent, where larger ones such as *t*BuLi undergo nucleophilic β-addition

reactions to yield chlorins **191** [145, 150]. When all meso-positions are blocked, unhindered reagents such as *n*BuLi will attack at the more reactive meso-positions and yield phlorins, porphodimethenes, or even porphyrinogens [141, 150].

3.5.4 Electrophilic Addition and Pericyclic Reactions

Electrophilic addition reactions are also possible. Most of these involve reactions at the β-positions and derive from the 18π-electron delocalization pathway, as shown in formula **137**. Thus, the two C=C "double bonds" have a cryptoolefinic character and can undergo reactions similar to standard double bonds. The most prominent examples are the vast range of oxidation and reduction reactions described in Chapter 6. In terms of introducing carbon substituents, a host of pericyclic reactions, including Diels–Alder and 1,3- or 1,7-dipolar cycloadditions, have been developed over the years [151, 152]. The porphyrin can take the role of diene, dienophile, dipolarophile, or 1,3-dipole, and participate in electrocyclizations and cheleotropic reactions (Figure 3.30) [152]. However, these are not necessarily general reactions for porphyrins, and some only work for specific porphyrin systems, for example, electron-deficient systems such as 5,10,15,20-tetrakis(pentafluorophenyl)porphyrin.

A classic example of a Diels–Alder reaction is Dolphin's synthesis of benzoporphyrin derivative monomethyl ester **199** (better known as Verteporfin, one of the success stories of photodynamic therapy and used for the treatment of age-related macular degeneration [153]), in which a vinylporphyrin such as protoporphyrin IX **66** acts as the diene component. Its chemistry goes back to the initial reaction of tetracyanoethylene with protoporphyrin IX by Johnson to give chlorins such as **200** or isobacteriochlorins [154, 155]. Other examples shown in Figure 3.30 for dipolar cycloadditions are taken from Cavaleiro's pioneering work to yield **202** [156] and a recent study by Pinho e Melo and co-workers using diazafulvenium methides for the generation of **203** [157]. Cheleotropic reactions, such as those with carbenes, can be used for the synthesis of cyclopropanechlorins such as **204** [158]; similar reactions are known for β-alkylporphyrins. An illustrative example of the "flexibility" of the tetrapyrrole macrocycle toward ring transformations is the reaction of H_2OEP with a nitrene. Here, meso-addition occurs with the nitrene to give the ring-expanded meso-homoazaporphyrin **205**, which can be ring-contracted further to the porphyrin **206** [159].

3.5.5 Core Substitution

The prime example of manipulating the porphyrin core is the use of the four nitrogen units as a chelating agent for metals to yield metalloporphyrins (see Chapter 4). Even simpler is the conversion of free base porphyrins to mono- **207** or dicationic **208** species via core protonation (Figure 3.31). In many cases, traces of acid are sufficient; more basic porphyrins can even be protonated by water. As four protons cannot fit inside the core, this protonation results in nonplanar macrocycles and is accompanied by a color change from red to green. Formation of porphyrin acids is often a useful means for purification or the generation of single crystals for X-ray diffraction studies [160, 161].

N-substituted porphyrins were first discovered by McEwen in 1936, and their synthesis and characterization was published in 1946 [162, 163]. Interest in these materials arose due to their role in different biological mechanisms, including the inhibition of ferrochelatase, an important enzyme in the biosynthesis of heme B. After identification of compounds such as *N*-methyl mesoporphyrin as a specific enzyme inhibitor, their role in biological

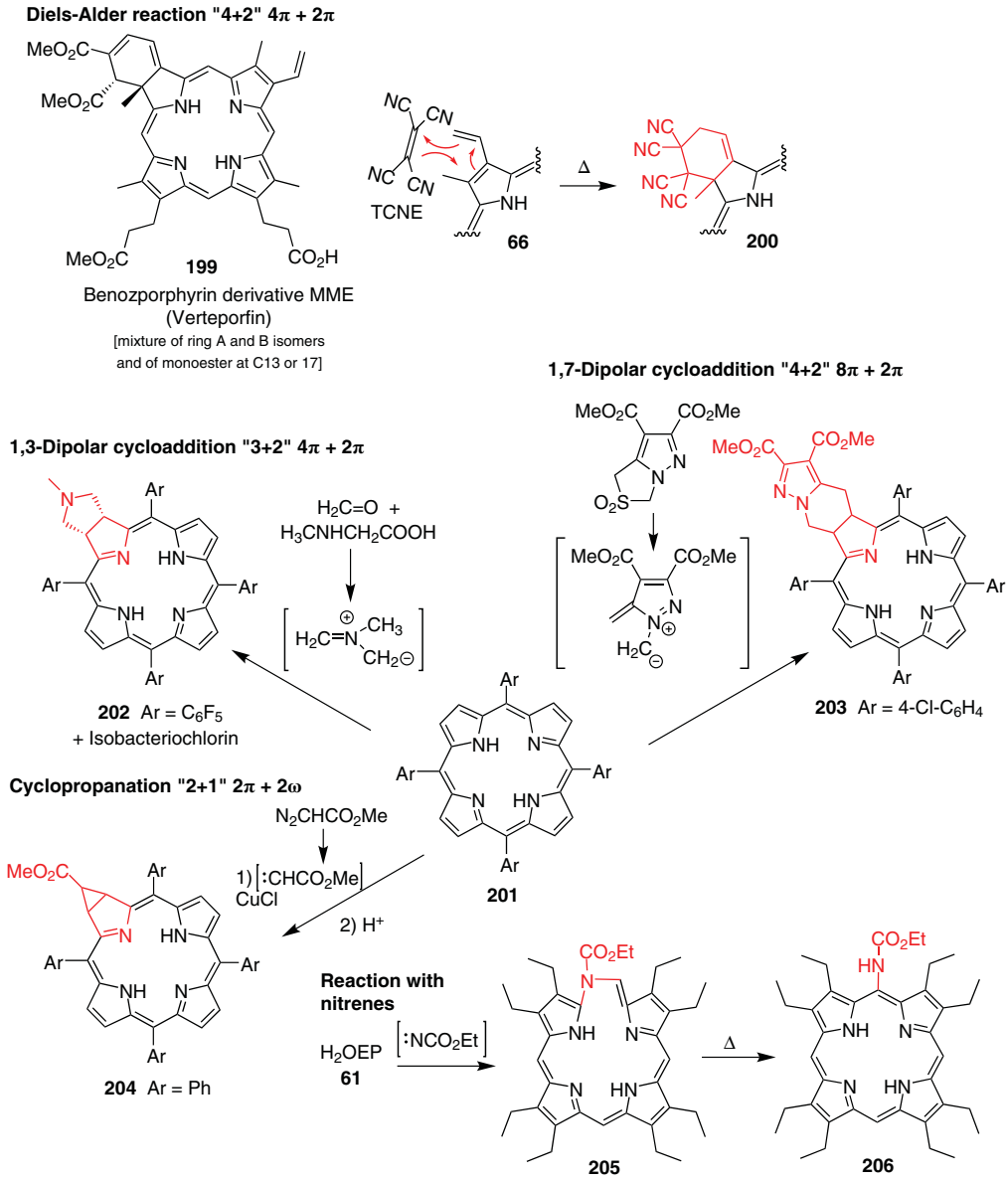

Figure 3.30 Classic examples of pericyclic reactions involving the $C_b = C_b$ in porphyrins and reaction of H_2OEP with nitrenes.

reactions, structural properties, and potential use in medicine has been further investigated. Subsequent to Lavallee's comprehensive account of the chemistry and biochemistry of *N*-substituted porphyrins in 1987 [164], interest has declined, and they remain a neglected class of porphyrins whose full potential has yet to be explored [165].

N-substituted porphyrins have alkyl, vinyl, or aryl groups attached to the pyrrolic nitrogen. This can be achieved by various methods such as the use of alkylating agents or rearrangement reactions. Possible substitution patterns include substitution on the pyrrolic nitrogen

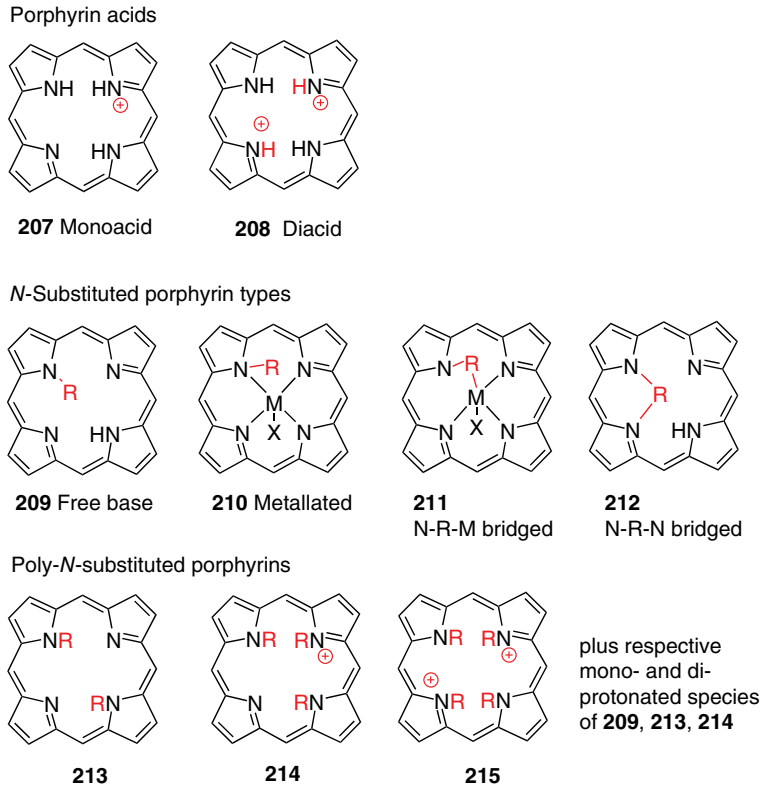

Figure 3.31 Classes of core-substituted porphyrins.

of a free base porphyrin **209** and the use of metallated porphyrins **210**. Furthermore, the formation of molecules in which a moiety bridges one nitrogen and the coordinated metal center **211**, or two pyrrolic nitrogen atoms **212**, is possible.

The synthesis of *N*-alkylporphyrins can be achieved with alkylfluorosulfonates or methyl iodide in one step. Varying the equivalents of the alkylating agent in the reaction can direct the degree of substitution of the inner nitrogen atoms. Use of the agent in a stoichiometric ratio will mainly form the mono-*N*-substituted porphyrin **209**, whereas an excess will lead to further substitution (e.g., **213**–**215**) [166]. The synthesis of *N*-phenyl or -vinyl porphyrins, on the other hand, often requires the formation of iron(III) or cobalt(III) complexes, which are oxidized in the presence of an acid. This leads to the migration of the aryl or vinyl group from the metal to the nitrogen atom and subsequent demetallation [167].

Similar to the porphyrin acids, *N*-substitution introduces steric strain, and this opens the door to a variety of highly distorted porphyrins [168]. Whereas, for example, mono-*N*-methyl-TPP exhibits a comparably small distortion of the macrocyclic ring, the di- or trimethylated compounds display an increasing tilt of the *N*-methyl group out of the macrocycle plane, which can be further increased though peripheral substitution [166]. This loss of planarity is accompanied by a change in reactivity, such as the ease of forming metal complexes and increased basicity and concomitant changes in electronic and optical properties. This in turn, is the reason why *N*-substitution of natural porphyrins inhibits their biosynthesis. Such distorted porphyrins mimic the transition state of the metal-inserting reaction and act as suicide inhibitors of the chelatases [169].

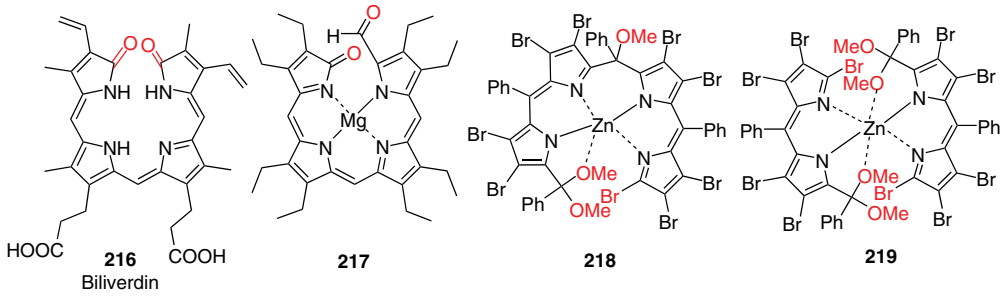

Figure 3.32 Selected porphyrin ring-opening products.

3.5.6 Ring-Opening Reactions

Various methodologies for the ring-opening of porphyrins have been studied over the years to help elucidate the in vivo degradation of heme and chlorophyll [170]. Outside of biological systems, this requires harsh conditions such as strong oxidants. A classic example is chromic acid degradation with CrO_3/H_2SO_4, which produces maleimides in high yields, whereas permanganate degradation leaves the pyrrole rings intact and converts functionalized side chains into carboxylic acids. Conversely, porphyrins can also be deconstructed via reduction (e.g., HI/acetic acid) or thermal decomposition at very high temperatures [102]. More revealing were studies of iron porphyrins, which form biliverdins **216** via an oxophlorin intermediate upon treatment with hydrogen peroxide (H_2O_2) and acid: the so-called "coupled oxidation." This illustrates a key principle of porphyrin ring-opening reactions, the disconnection of a C_a—C_m bond [171] (Figure 3.32).

Similar products can be generated using other oxidations. These include Smith's use of thallium(III) trifluoroacetate to yield meso-trifluoroacetoxy derivatives, followed by ring-opening via an oxophlorin intermediate [172], ozonolysis, and photo-oxygenation. The latter, exemplified here with Mg(II)OEP, gives a C_a-C_m-endoperoxide and forms metallo-formylbiliverdins **217** [173]. More recently, another possibility of ring-opening porphyrins at one or two C_m-positions was discovered during studies on the β-bromination of meso-tetraarylporphyrins [174, 175]. Using excess NBS during the bromination gave the expected β-perbrominated porphyrin, which was then converted into biladienes. The proposed mechanism involves a nucleophilic attack of MeO^-, formed from methanol and NBS, at the meso-position and subsequent ring opening at one **218** [174] or two **219** [175] meso-positions.

3.6 Transition-Metal-Catalyzed Reactions at the Porphyrin Macrocycle

Organometallic reactions are currently the most widely used means of modifying a porphyrin. Initially developed for small molecules, their application in C—C- and C–heteroatom-bond formation on the porphyrin macrocycle has been the main driving force behind the explosion in porphyrin research and applications in recent decades. We have already highlighted the use of organolithium reagents for C—H activation in Section 3.5.3.2 and will focus next on the use of transition metal (catalysts) for transformations aimed directly at the porphyrin ring system. An excellent survey of synthetically

useful organometallic reactions was recently published by Shinokubu and co-workers [176]. It nicely sets the various reactions in the context of their synthetic utility.

3.6.1 C—H Activation

One of the fundamental challenges in organic chemistry is the direct activation of C—H bonds. Ideally, this should be possible in "nonactivated" systems, that is, systems that do not require any special pretreatment of the material. This is in contrast to the case of standard transition metal catalysis, in which typically two "reactive" compounds (e.g., a bromide and a boronic acid in Suzuki couplings) combine to form a C—C or C–Het bond (see below). At present, metallation, borylation, and arylation are possible for porphyrin C—H units.

Porphyrins with C–M σ-bonds are useful precursors for other organometallic reactions and often show unusual coordination geometry. π-Pyrrole-metal complexes are also known, but will not be considered here (177; also see Chapter 4). Likewise, many porphyrins carrying organometallic residues, such as ferrocene substituents, have been described [178]. The first porphyrins with peripheral metal units were obtained using deuteroporphyrins and mercury acetate/NaCl, which yielded porphyrins containing a HgCl unit at the two β- and one meso-position(s). Subsequently, Smith expanded this electrophilic mercuration reaction to prepare a range of *C*-substituted and halogenated derivatives; for example, via subsequent olefination reactions (Mizoroki–Heck) [179]. More recently, mercury(II) trifluoroacetate/NaCl was used with Ni(II)5,15-diarylporphyrins. These underwent regioselective mono-β-mercuration, and after iodination could be used as the halogen partner in Suzuki–Miyaura couplings [180]. All involved nice chemistry, but the respective target compounds are today more easily accessible via other routes that circumvent the requirement for Hg reagents. Ni, Ir, Pt, and Pd centers have also been introduced to the porphyrin periphery; both C_b and C_m binding are possible, depending on the metal and the directing effects in the starting material. The latter are pyridyl or phosphanyl residues, which serve to "flank" the metal center in the products and stabilize the coordination sphere of the metals [181].

More relevant to synthetic chemistry is the catalytic C—H activation of porphyrins developed by Osuka and co-workers [182] (Figure 3.33). It presents one of the latest, but critical, additions to the repertoire of porphyrin chemists. A characteristic experiment used the 5,15-diarylporphyrin **220**, the iridium catalyst $[Ir(OMe)(cod)]_2$, 4,4′-di(*tert*-butyl)-2,2′-bipyridyl (dtbpy) as ligand, and bis(pinacolato)diboron $[(Bpin)_2]$. This gave the tetraborylated product **222** in good yield (>70%) [183]. Depending on the stoichiometry of the reactants, the metal center and/or the presence of other functional groups or meso-substituents, this reaction can be directed to yield the mono- or diborylated products as well, albeit with variations in yield [184]. The beauty of the reaction lies in its complete regioselectivity. The catalyst and reagent are bulky, and C—H activation occurs only at the sterically less hindered porphyrin β-positions. With three C_m-substituents (as in **221**), substitution only occurs in the porphyrin half without any substituents, for example, to yield **223**. With four meso-substituents (**224**) the reaction is directed toward the peripheral aryl rings (if present) and gives **225** or similar, and this recalls the origin of this method as the Ir-catalyzed arene activation developed by Milton Smith III and Hartwig's groups [185, 186].

The borylated products are very useful coupling partners in some of the Pd-catalyzed reactions described below (Section 3.6.2), leading to the respective β-substituted target compounds. However, if the organic residue to be introduced is required in a similar position as those obtained with the borylation just discussed, then the situation

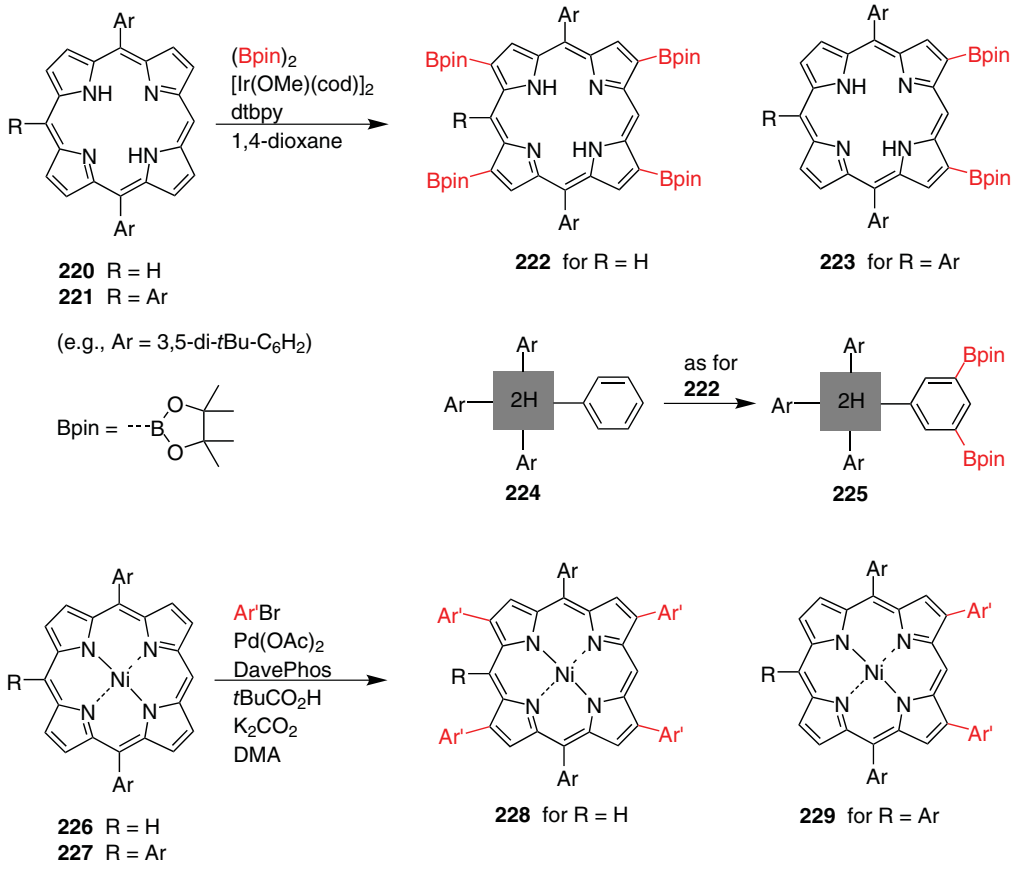

Figure 3.33 Iridium-catalyzed porphyrin-C–H borylation and arylation reactions.

becomes even simpler. Osuka's C—H arylation uses palladium acetate catalysis, DavePhos [2-dicyclohexylphosphino-2′-(*N*,*N*-dimethylamino)biphenyl], pivalic acid, and a respective aryl bromide [187]. Again, steric constraints direct the substitution to the β-position with perfect regioselectivity, as shown in Figure 3.33 for the conversion of **226** or **227** to **228** or **229**, respectively.

C–H activation reactions may also be used for intramolecular cyclization and annulation reactions (Figure 3.34). The former requires the presence of one reactive handle in the porphyrin molecule, for example, a halogen or tosylate as in Boyle's (**230**→**231**) and Cammidge's (**232**→**233**) work [188, 189]. A new C—C bond is formed here from one of the porphyrin's own substituents onto a neighboring β-position in the same porphyrin. We will encounter more of these fused and π-extended porphyrins later (see Section 3.7.3). The fusing structure of the meso-β-linked naphthylporphyrin **233** is also found in the meso-β-doubly-linked bisporphyrin **234**. It was prepared by Sugiura and co-workers via a reductive aryl-coupling of **226** using $TeCl_4$ and involves the tellurium intermediate **235**, which dimerizes by nucleophilic attack of a C_b-C_b double bond at the Te-C_m unit [190].

A more general reaction uses meso-bromoporphyrins as reactants in Pd-catalyzed [3 + 2] annulation reactions. Reaction of **150** (M = Ni(II), Cu(II), Zn(II)) with alkynes

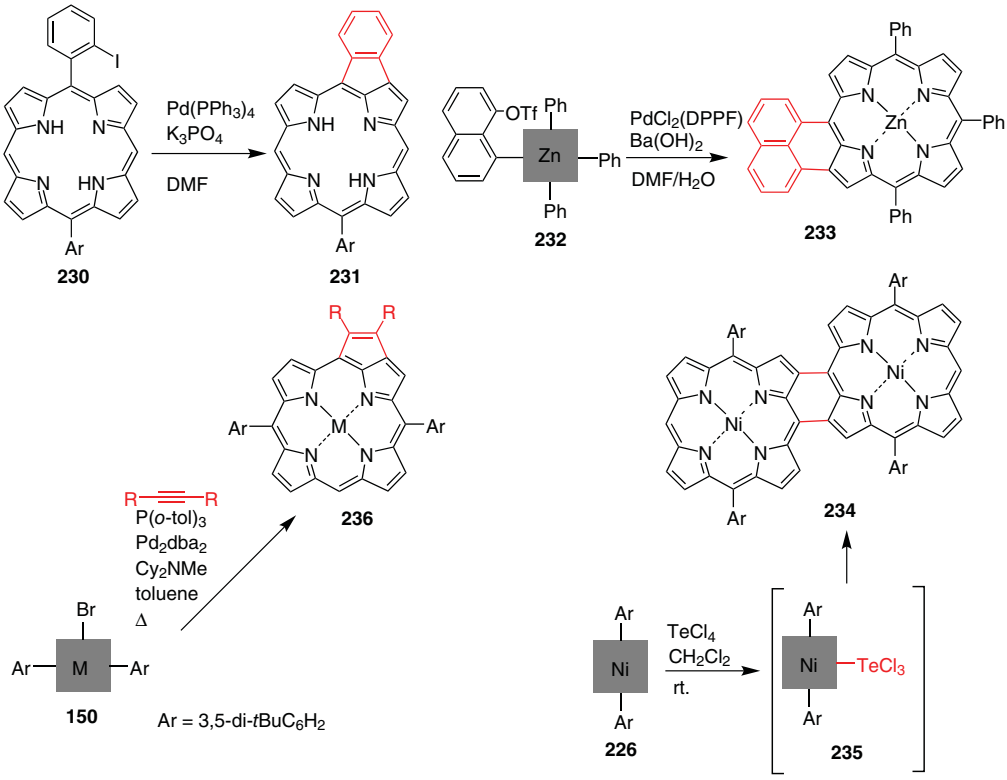

Figure 3.34 Palladium-catalyzed cyclization and annulation reactions.

and Pd_2dba_3/(*o*-Tol)$_3$P generated the cyclopenta[*at*]porphyrin **236** [191]. Mechanistically, this involves an oxidative addition of the porphyrin bromide to Pd(0), carbopalladation of C≡C furnishing a palladacycle via C—H cleavage at the nearby C_b, and finally reductive elimination to the annulated product. Many more applications and variations of the reactions discussed in this part are known and allow for the generation of a diverse set of porphyrinoids [176, 182].

3.6.2 C—C Bond Formation

Since the advent of transition metal-catalyzed reactions in the second half of the last century, C—C bond forming reactions based on them have become a mainstay of synthetic organic chemistry, and most have been subsequently applied to porphyrins. Typically, this involved the transfer and then optimization of reactions initially developed for simple aromatic compounds to porphyrinoids. The most important examples that result in C—C bond formation directly at the macrocycle are grouped according to the metal involved in the catalytic reaction in the following sections.

3.6.2.1 Palladium-Catalyzed Reactions

The central method used to achieve stepwise functionalization of porphyrins is palladium-catalyzed cross-coupling in its many variants, similar to some of those used

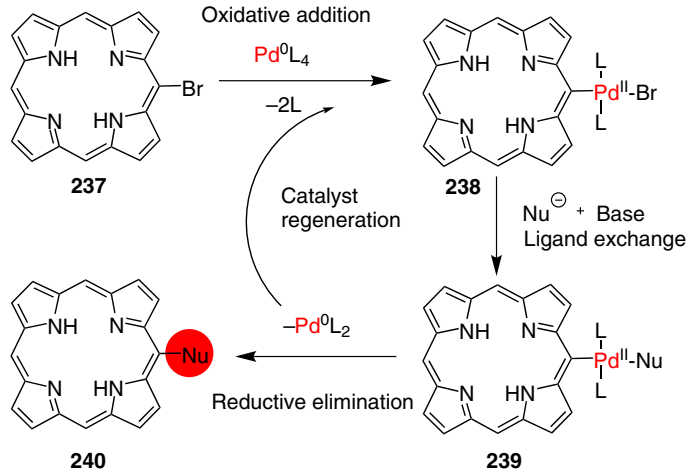

Figure 3.35 General mechanism of Pd catalysis.

for C—H activation (Section 3.6.1) [176, 192]. A functionalization of the aromatic macrocycle, for example, halogenation (**237**), is needed first in most cases. Typically, the reaction mechanism involves an oxidative addition of the Pd(0) complex (**238**), followed by substitution of the halogen by a nucleophile (**239**). The cycle is completed by reductive elimination of the palladium complex, which simultaneously forms the desired coupling product **240** and regenerates the catalyst (Figure 3.35). Porphyrin chemists began to apply such reactions in the 1990s. A host of reaction types are now available, the primary distinction being in what form the second reaction partner (the Nu in Figure 3.35) is fed into the reaction sequence. Therien and co-workers reported the first palladium-catalyzed reaction with porphyrins utilizing organozinc (Negishi coupling) and organotin (Stille reaction) nucleophiles in 1993, and these reactions can be applied to both the meso- and β-positions [193].

Suzuki–Miyaura – Boron One of the best-known palladium-catalyzed coupling reactions is the Suzuki reaction, which has been used in porphyrin chemistry now for two decades [194, 195]. Here, the porphyrin can either be used as the organohalide (i.e., bromoporphyrins) or as the attacking nucleophile. The latter can be achieved by reversing the polarity of the porphyrin via the synthesis of boronyl porphyrins (typically prepared from bromoporphyrins). The mechanism follows the general palladium-catalyzed reaction mechanism (Figure 3.35). In the first step, the organopalladium species is formed via oxidative addition to **241** (Figure 3.36). Next, the complex **242** reacts with a base to yield the intermediate **243**. Meanwhile, the boronic acid **244** is activated with a base to give the boronate complex **245**. This activation is necessary to facilitate transmetallation to the compound **246**. The catalytic cycle is completed with reductive elimination, delivering the desired product **247**.

This strategy can be used to synthesize a broad range of alkyl and aryl meso- and β-substituted porphyrins. The reaction conditions are normally relatively mild, require only hours, and give, depending on the substituents used, excellent yields. Possible variations described in the literature are abundant and include the stepwise or one-pot introduction of residues at all meso- or β-positions using boronic acids or boronates [196], as well as the synthesis of various homo- and hetero-porphyrin-porphyrin combinations and oligomers [176]. Some arbitrary examples are illustrated in Figure 3.37. These include Therien's

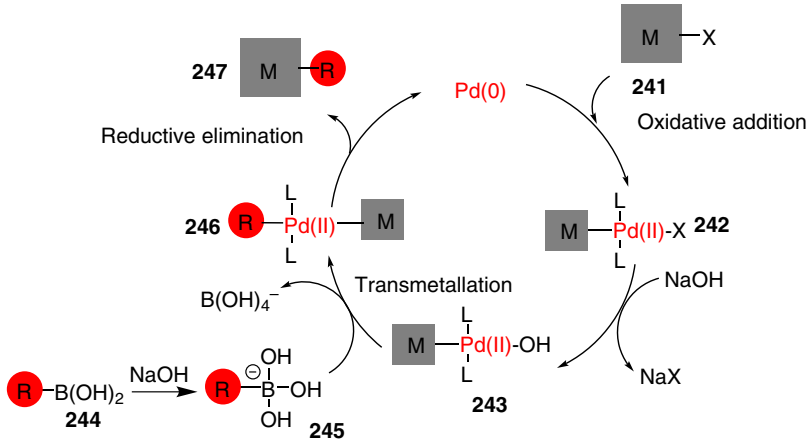

Figure 3.36 Illustration of the Suzuki–Miyaura reaction mechanism with porphyrins. Note that R can also be a porphyrin to be coupled with either another organic residue of a (different) porphyrin.

initial reaction to prepare an amino acid appended porphyrin **249** [195] and one of Osuka's meso-meso-linked bisporphyrins **250** via coupling of two different porphyrins [197]. Two examples from our group are the sequential preparation of a porphyrin trimer **253**, which is an example of Bringmann's porphyrins with axial chirality [198], and the introduction of highly reactive substituents, here an allenyl group **254** [199]. The introduction of eight residues at the β-positions in a one-pot reaction is exemplified by the reaction of the octabromoporphyrin **146** to **255** [194, 200].

Sonogashira – C≡C-R Another coupling reaction using palladium is the Sonogashira cross-coupling reaction. It is the method of choice to generate alkynyl-substituted porphyrins through the introduction of ethynyl compounds. The groups of van Lier and Therien were the first to apply this method to porphyrins in 1994 [201, 202]. Reactions of haloporphyrins using a range of acetylene derivatives worked well with β-alkyl- and meso-arylporphyrins and is now routinely used with all types of halo-, tosyl-, and boronylated porphyrins (**256**→**257**) (Figure 3.38). Porphyrin chemistry is hard to imagine without this versatile method, and numerous compounds have been generated with it, mostly using CuI as a co-catalyst and $Pd(PPh_3)_4$, $PdCl_2(PPh_3)_2$, or $Pd_2(dba)_3$ as catalyst. To avoid metal insertion during the reaction, metallated porphyrins must be used. Even though a few copper-free methods exist, applications for them are still limited. Alkynyl-linked bis- and oligoporphyrins are frequently employed due to the rigid conjugating linker(s) in biomimetic chemistry, photonics, and the synthesis of superstructured molecules [202, 203].

Heck – Alkenyl The Mizoroki–Heck reaction was first used with porphyrins by Gauler and Risch in 1998 [204], but recall Smith's use of mercurated porphyrins in Pd-mediated vinylations [179]. Since then, this reaction type has been used to introduce alkenyl substituents into the meso- or β-positions [205]. Some examples for alkenes which have been applied to Heck reactions are acrylates, styrenes, and acrylonitrile (**256**→**258**). Usually, bromoporphyrins are used as the coupling partner, but vinylporphyrins such as **259** or protoporphyrin IX **66** also react [206], and this method can be used to modify the peripheral positions of a porphyrin. The mechanism of the Heck reaction is slightly different from that of other Pd-catalyzed

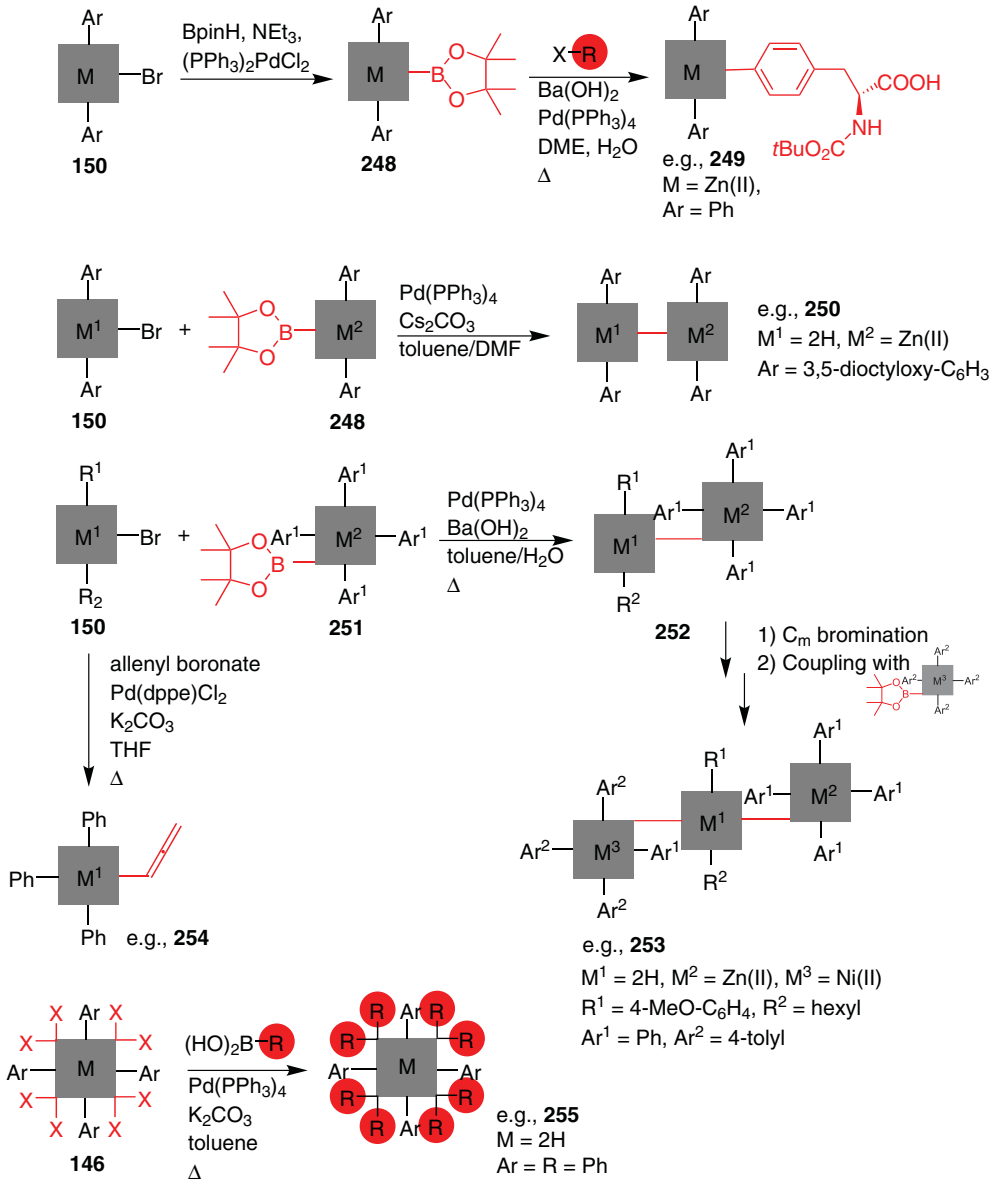

Figure 3.37 Examples of Suzuki coupling reactions with porphyrins.

reactions. The first step is an oxidative addition, followed by coordination and migratory insertion of the olefin to palladium. A subsequent bond rotation moves the two aryl groups *trans* to each other and results in β-hydride elimination to form the desired coupling product. The catalyst is then regained by base-mediated reductive elimination.

Stille, Negishi, and Kumada – Tin, Zinc, Magnesium Further variations of the catalytic Pd cycle are exemplified in the use of organometallic Sn, Zn, and Mg compounds. The Migita–Kosugi–Stille reaction is a coupling between bromoporphyrins and tin reagents with a Pd catalyst (**256**→**261**) [193]. Even though organotin reagents are very cheap to synthesize,

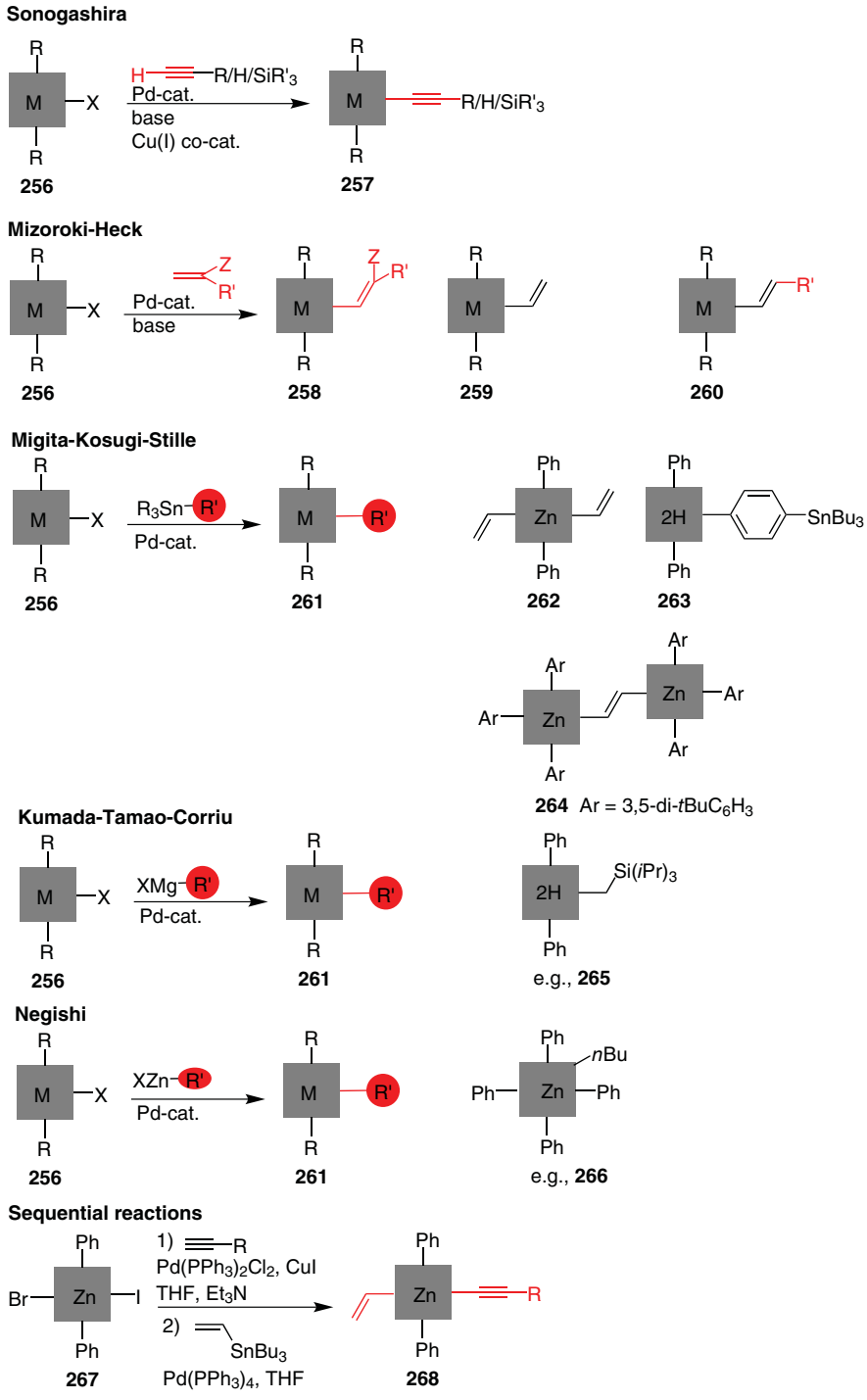

Figure 3.38 Examples of other Pd-catalyzed coupling reactions with porphyrins. Note that various other combinations and use of porphyrin reactants than those shown are possible.

the number of applications with porphyrins is limited [118]. The reaction mechanism is very similar to Suzuki coupling (Figure 3.36), aside from the fact that the boronic acids must be activated with a base, whereas the tin reagents used in the transmetallation step react on their own. First used for the synthesis of vinylporphyrins (**261**) [193], a number of substitution patterns, including those of porphyrin organotin compounds (**263**) [207], are known. Organotin compounds are also a complementary method for introducing alkenyl (**264**) [208] and alkynyl residues [209], the latter up to eight times [210].

Related catalytic reactions include the use of Grignard reagents (Kumada–Tamao–Corriu coupling) (**256→261**). Thus far, this has been used for the synthesis of silylmethyl porphyrins **262** using catalytic $Pd_2dba_3/Ph_2P(O)H$ [210, 211]. In contrast, organozinc reactions (Negishi coupling, **256→261**) have been used for a longer period of time [193], and for both aryl and alkyl residues [212]. Such reactions may also be executed in sequence, for example, by using bis-halogenated porphyrins **267** in consecutive Sonogashira and Stille reactions to give **268** [213]. Many other reactions involving Pd catalysts for C–C-coupling reactions with porphyrinoids are known; for an almost complete list, see Reference [176]. Some of these include homocouplings or intramolecular cyclizations, as for the compound **231** [214], or intramolecular C—H arylations to yield air-stable porphyrin radicals [215].

3.6.2.2 Nickel- and Rhodium-Mediated Reactions

Other metal catalysts can also be employed. Established examples, although lagging in their use in standard organic chemistry, are nickel and rhodium. Nickel catalysts can often be used effectively under mild conditions (Figure 3.39). A synthetically useful example is the $Ni(OAc)_2$-mediated coupling of meso-bromoporphyrins with (di)carbonyl (doubly activated methylene) compounds (**269→270**) [216]. This approach is quite adaptable and was successfully used to generate aryloxyporphyrins and aminoporphyrins; that is, it covers the full spectrum of C—C-, C—O-, and C—N-bond formation (see below). Ni catalysts have also been employed in the generation of directly linked bisporphyrins through Ullmann homocoupling. Thus, the bromoporphyrin **271** gave the meso-meso-linked dimer **272** [217].

Other syntheses of these highly useful systems have already been mentioned, and are illustrated by **250** via Suzuki [197] and **196** via RLi [146]. They were pioneered by Osuka in 1997 through direct oxidative coupling of meso-unsubstituted porphyrins with $AgPF_6$ [218]. This reaction and improvements thereof opened the field of fused and π-extended porphyrinoids [219]. Homocoupling yielding C_b-C_b-linked bisporphyrins is also possible by treating mono-β-borylated 5,15-diarylporphyrins similar to those shown in Figure 3.33 with $Pd(OAc)_2$, DPPP under oxygen [183]. The positioning of the coupling partner on the porphyrin may also affect the selectivity of the coupling reaction. An intriguing example is the use of borylporphyrins in rhodium-catalyzed Heck-type reactions. The β-borylated porphyrin **273** is reacted with a vinyl ester under $[Rh(OH)(COD)]_2$-catalysis to give the vinylated porphyrin **274**. However, positioning of the Bpin at the meso-position (**275**) resulted in the formation of the 1,4-conjugate addition product **276**, presumably due to steric reasons [220].

3.6.3 C-Het Bond Formation

The use of transition-metal-catalyzed reactions not only allows the formation of C—C bonds, but also in recent years we have seen a parallel development of C-Het bond forming methods, mostly using halogenated porphyrins. Again, these methods derive from advances

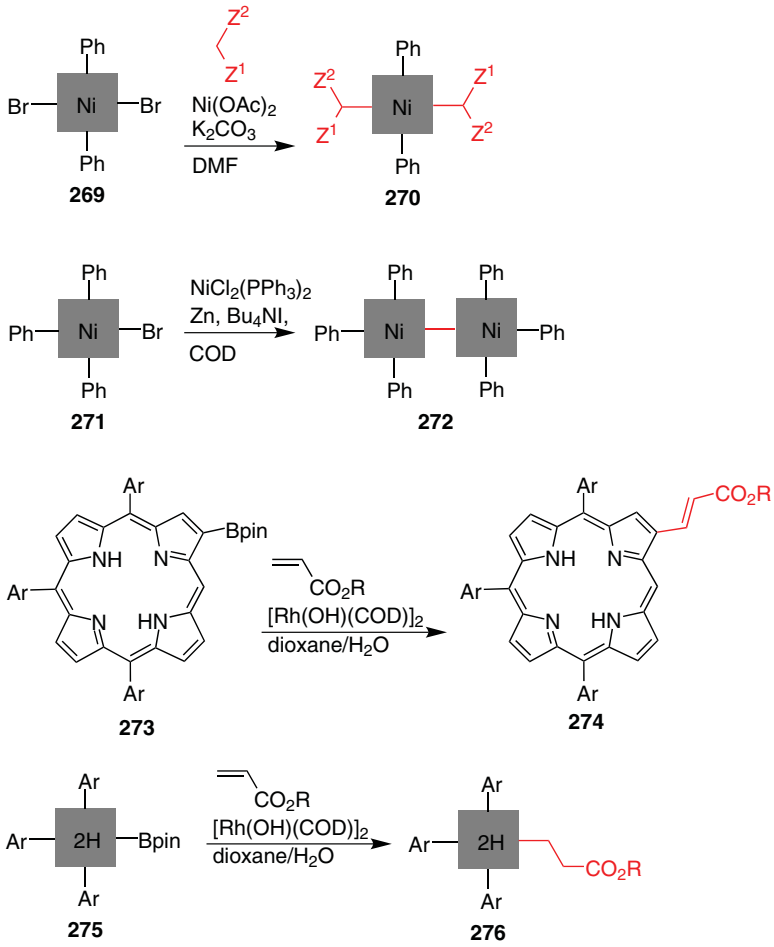

Figure 3.39 Examples of Ni- and Rh-mediated C–C-bond forming reactions.

in the organometallic chemistry of "small" molecules. A wide range of nucleophiles can now be applied to these reactions, such as thiols, amines, or alcohols, resulting in the corresponding C—S, C—N, and C—O bonds.

3.6.3.1 Amination and Amidation, C—N

Amino groups can have a significant impact on the electronic properties of porphyrins and therefore feature prominently in applications such as dye-sensitized solar cells (DSSCs). Historically they were accessible via nitration and reduction or substitution (see Figure 3.34), but the main advance in their use came from the application of the Buchwald–Hartwig reaction (Figure 3.40). In 2003, Chen and Zhang reported a series of palladium-catalyzed amination reactions with bromoporphyrins using Buchwald–Hartwig conditions (e.g., **281**→**283**) [221]. This reaction can be used to synthesize aminoporphyrins with a broad variety of alkyl- and arylamines. Various optimizations and adaptations exist, using different strengths of bases (Cs_2CO_3, NaO*t*Bu), different ligands (DPEphos, BINAP, Xantphos) and palladium catalysts ($Pd(OAc)_2$, $Pd_2(dba)$, etc.) (Figure 3.41). Furthermore, optimized reaction conditions do exist for a variety of amines with bromoporphyrins [222]. Normally both electron-rich

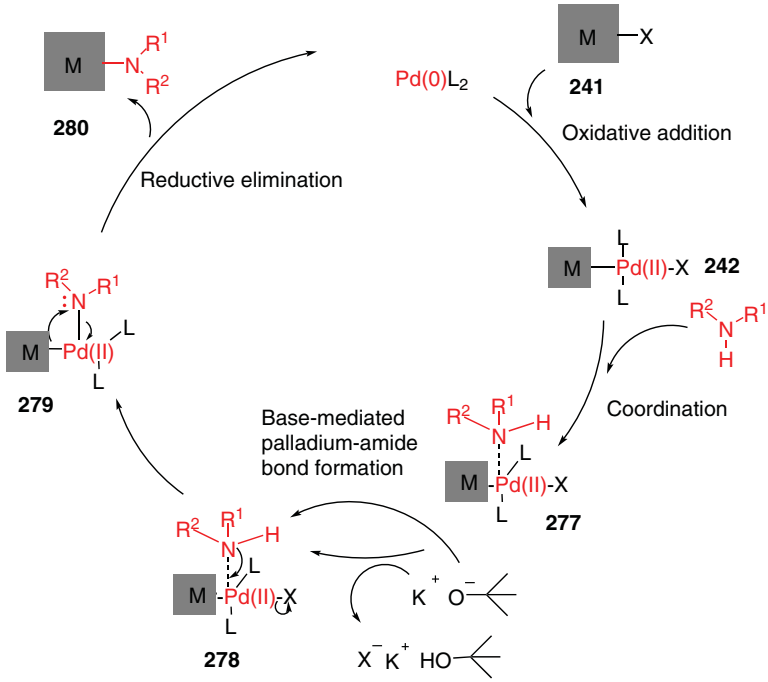

Figure 3.40 Illustration of the Buchwald–Hartwig amination reaction mechanism with porphyrins.

and electron-poor derivatives give moderate to high yields in relatively short reaction times (<24 h), but sterically demanding or aliphatic amines require longer reaction times [223].

The meso-aminoporphyrin **287** was prepared by Arnold and co-workers using unprotected hydrazine sulfate as the ammonia source [224]. Its formation was accompanied by the bisporphyrinylamine **288** and meso-hydroxyporphyrin **289**. C—N amide bonds can also be formed [221, 222]. Although the reactivity and yields of Pd-catalyzed reactions often depend on the central metal, conditions developed by Chen and Zhang allow coupling of free base and zinc porphyrins with primary and secondary amides, as well as acetamide, carbamates, and other alkyl amides [221]. A typical example is the transformation of **284**→**286** using Xantphos [225]. β-Brominated porphyrins have been employed for the generation of β-aminoporphyrins, notably in the pioneering work by van Lier and co-workers [226].

3.6.3.2 Alkoxylation, C—O

Even though alkoxy- and aryloxyporphyrins find application as catalysts or for photo-induced electron transfer studies, few synthetic methods exist for these compounds. They can be synthesized via nucleophilic substitution of pyrroles; this, however, requires multiple steps. More modern syntheses again use readily accessible meso- or β-bromoporphyrins and alcohols in the presence of a palladium catalyst, a ligand, and a base. Various alcohols such as aliphatic or aromatic electron-rich and electron-deficient alcohols, as well as linear or cyclic primary and secondary alcohols, can be applied. Zhang and co-workers investigated this so-called etheration and found that mild conditions and simple bidentate phosphine ligands such as DPEphos and Xantphos worked best [227]. Ligand-free nickel-catalyzed methods are known as well, and a modification of Arnold's reaction shown in Figure 3.41 using a

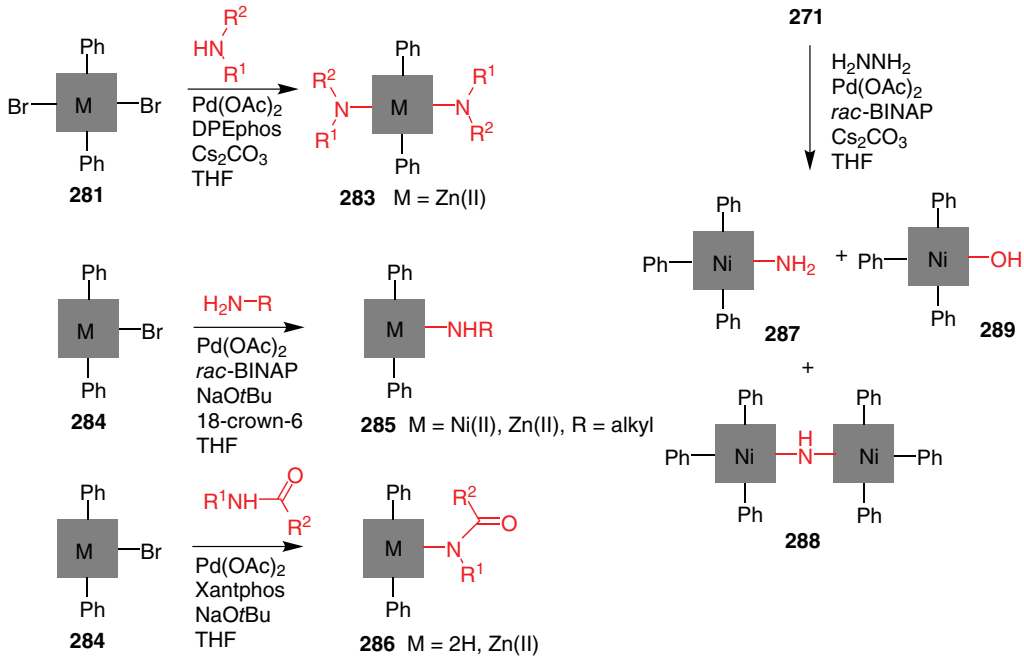

Figure 3.41 Examples of amination and amidation reactions.

palladium-catalyzed hydroxylation with $Pd(OAc)_2$, BINAP, and Cs_2CO_3 in the absence of hydrazine gave **289** as the main product [224].

3.6.3.3 Sulfonylation and Selenation, C–S/Se

Meso- and β-sulfonylation can be achieved in moderate to good yields with alkyl and aryl thiols in the presence of a palladium catalyst, ligand, and Cs_2CO_3 [228, 229]. Several ligands such as mono- and bidentate phosphine ligands were studied over the years with zinc and free base meso-bromoporphyrins. Although all ligands gave good results for free base and zinc porphyrins, some thiols worked better with bidentate ligands such as DPEphos, Xantphos, or BINAP. A selection of different thiols such as sterically hindered aryl thiols, electron-rich aryl thiols, and short-chain aliphatic thiols were tested with β-substituted porphyrins. All derivatives gave low to moderate yields; however, the sterically hindered aromatic thiols required longer reaction times. C—Se bond formation was achieved via palladium-catalyzed cross-coupling of a meso-bromoporphyrin with selenol, similar to the conditions for sulfonylation, giving the first meso-seleno-substituted porphyrin [229].

3.6.3.4 Phosphorylation, C–P

C—P bonds can be formed via transition-metal-catalyzed reactions along similar lines, and today methodologies can synthesize phosphonates, phosphites, phosphine oxides, and phosphines attached to the porphyrin core. For example, in 2006, Arnold and co-workers were able to synthesize the first phosphine-oxide-substituted porphyrin [230]. Diphenylphosphine oxide, $Pd(dppe)_2$, Cs_2CO_3, and meso-bromoporphyrin gave the oxide-substituted porphyrin in 95% yield. Alternatively, diphenylphosphane can be coupled with meso-iodoporphyrins under Pd catalysis [231], and porphyrins with meso-$P(O)(OEt)_2$ have been prepared as well [232]. Matano et al. also published the synthesis of a meso-phosphoryl-substituted

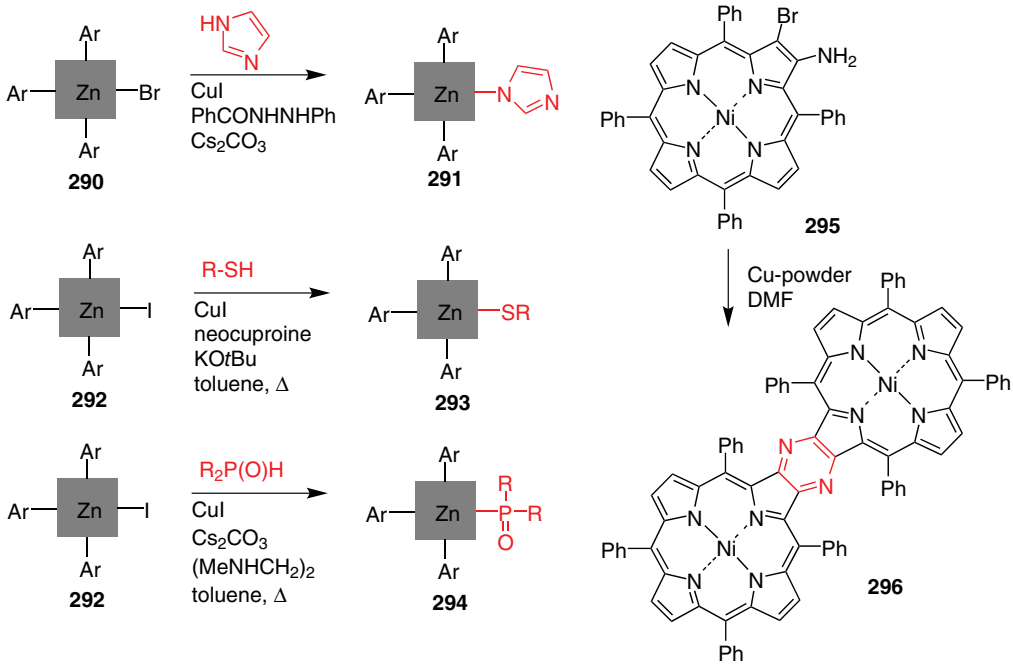

Figure 3.42 Examples of copper-catalyzed porphyrin-C-Het bond forming reactions.

porphyrin using meso-iodoporphyrin with di(*n*-butyl)phosphite and diphenylphosphine, CuI and *N,N′*-ethylenediamine [233]. Phosphanyl systems can also be used to generate β-metal-linked porphyrin dimers utilizing certain palladium or platinum salts [231]. β-Activated systems may also be employed in these reactions. For example, compound **153** (X = I or OTf) was used for the introduction of phosphonyl and phosphanyl residues [121].

Generally speaking, copper- and nickel-mediated C-Het bond forming reactions are beginning to complement the synthetic repertoire, and many newer reactions utilize iodoporphyrins. This is illustrated in Figure 3.42, which gives a few exemplary reactions. These include substitution with imidazole (**291**) via Ullmann coupling [234], the preparation of sulfonylporphyrins (thioethers) **293** [235], the introduction of phosphoryl residues (**294**) [233], and the synthesis of a pyrazine-fused bisporphyrin **296** from the 2-amino-3-bromoporphyrin **295** [236].

3.7 Peripheral Functionalization

Peripheral functionalization of porphyrins refers to reactions at porphyrin substituents already present, that is, those not directly involving transformations at the N, C_a, C_b, or C_m atoms of the 24-atom macrocycle. It also entails functional group interconversions/additions, and so on. As can be expected, the number of possible reactions is almost endless, and many, if not all, of the standard "organic chemistry" reactions have been applied to porphyrins. As long as the aromatic system and/or central metal/4N core is not affected, almost any synthetic procedure may find use in porphyrin chemistry. Typical pitfalls involve unintended metal insertion into free base porphyrins, demetallation of metalloporphyrins under acidic

conditions, or loss of substituents followed by reactions at the porphyrin core. Additionally, one may have to shield reactions from light to prevent photodegradation or other photo-transformations of more reactive porphyrinoids. Again, we have to refer the reader to the more comprehensive treatises mentioned in the introduction.

In the following passages, we will focus on a few selected areas for peripheral functionalization to illustrate what is possible today and to indicate the versatility of porphyrins in a wide range of chemical transformations.

3.7.1 Transition-Metal-Catalyzed Reactions Involving Porphyrin Substituents

Next to the wide range of uncatalyzed FGI (functional group interconversion) and FGA (functional group addition) reactions used for porphyrin modification [12, 102, 132], organometallic reagents and catalysts have been applied to both the porphyrin core (see above) and periphery [176, 237]. All of the reactions detailed in Section 3.6 may also be applied to porphyrins containing suitable coupling partners in the periphery, for example, as bromoaryl residues or phenylboronic acids. Some transition-metal-catalyzed reactions require special precursor molecules, that is, porphyrins with appropriate functional groups, and only the most prominent ones will be illustrated here using transformations involving porphyrins with $-N_3$, $-C\equiv CH$, and $CH=CH_2$ units.

3.7.1.1 Cu-Mediated Functionalization Reactions

Copper-mediated reactions have claimed their role in porphyrin coupling reactions alongside their palladium-catalyzed cousins, especially for coupling with biologically relevant systems. Perhaps the most widely used method is the Cu(I)-catalyzed, the so-called "click" reaction, as developed by Sharpless. Since its discovery, this reaction type has found a broad application and has led to a revitalization of the Huisgen 1,3-dipolar cycloaddition, and has also become an often-used, but atom-inefficient tool in porphyrin chemistry [238]. This reaction relies on the 1,3-dipolar cycloaddition of an azide and alkynyl partner (e.g., **297** + **298**→**299** [239]), either of which can be on the porphyrin, and is typically carried out in the presence of Cu(I) catalysts, although Ru catalysis is also used. A selection of some typical products from our own and Scanlan's group targeting the preparation of water-soluble and amphiphilic bioconjugates for medical studies is shown in Figure 3.43 [240, 241]. These were prepared using microwave-mediated sequential "click" reactions to develop glycoporphyrin analogs [242].

Other representative examples of Cu-catalyzed coupling reactions are the Glaser and Sonogashira couplings (Figure 3.44). The Glaser coupling is an often-used method for the synthesis of porphyrin arrays, as it effectively links dyes in a linear and rigid manner. It enables the coupling of two acetylene bridges and is mostly used for homocouplings. Initially, compounds such as **304** were prepared by Arnold et al. via dehydrobromination of bromovinylporphyrins and oxidative couplings [243, 244]. Transition-metal-catalyzed reactions were pioneered by Anderson's group, who used Glaser–Hay couplings of **303** with Cu(I) to give **304** [245]. Alternative methods are Eglinton couplings with $Cu(OAc)_2$ in pyridine [202] or modifications of the Sonogashira reaction. These reactions have been highly successful in creating large porphyrin arrays, either in 1D or 2D [203, 246]. Examples of the latter are the large polyporphyrin rings beautifully prepared by Anderson using Vernier-template synthesis [247], or the classic porphyrin square **306** synthesized by Sugiura et al. [248].

The Sonogashira reaction was also pioneered in porphyrin chemistry by Arnold's group [249] and is presented here in the example detailing the synthesis of the bisporphyrin **305**

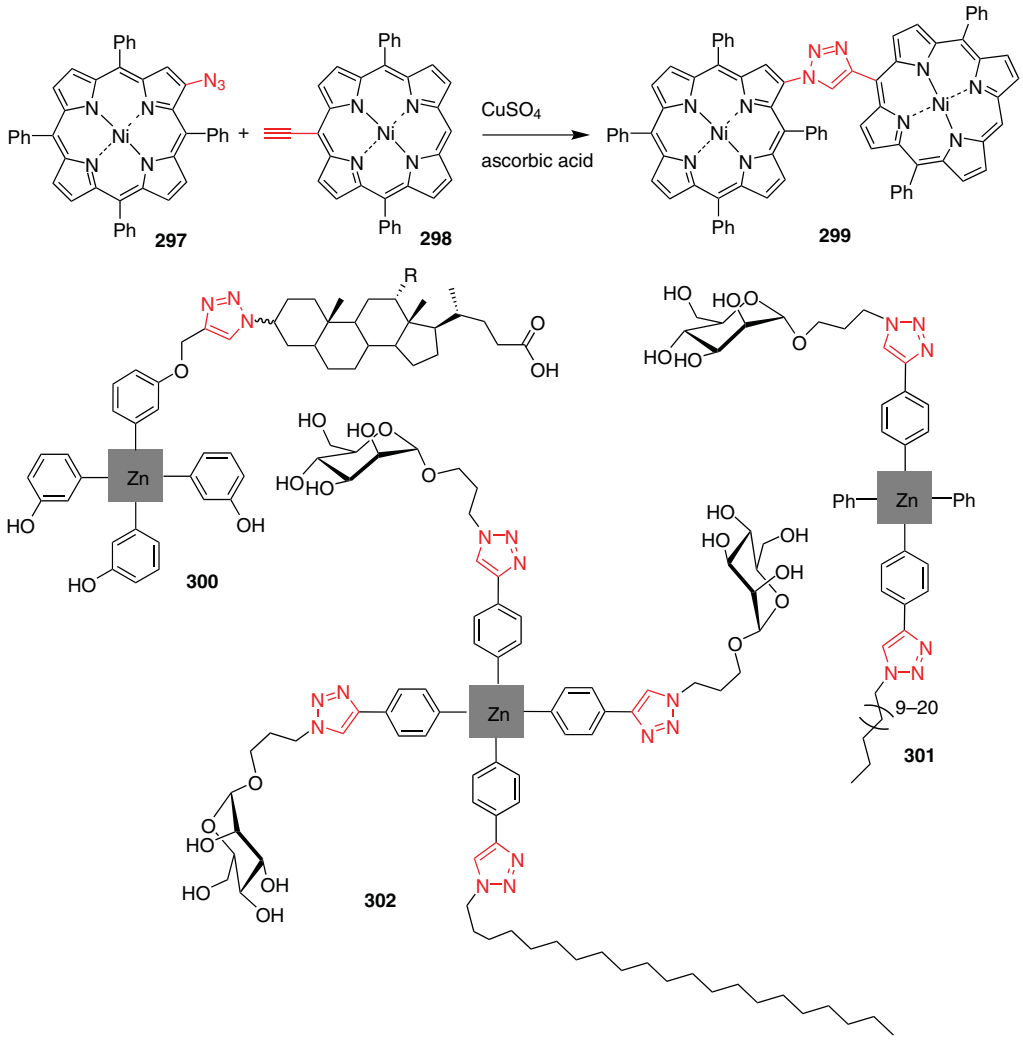

Figure 3.43 Examples of a Huisgen-click reaction with porphyrins and some bioconjugates.

from **303**. Practical uses of this method employ both Cu-containing or Cu-free reactions and can be found in many areas of porphyrin wire and array synthesis.

3.7.1.2 Co-, Ni-, and Ru-Catalyzed Functionalization Reactions

Cobalt is mostly used in the form of $Co_2(CO)_8$ for cyclization reactions such as [2 + 2 + 2] cycloadditions; for example, cyclotrimerizations to yield systems linked by a benzene core. A typical example is the use of an alkynyl-linked bisporphyrin **307** to yield a cofacial porphyrin dimer **308** [250]. The same catalyst is also used in the related Pauson–Khand reaction, where an alkyne, alkene, and CO are reacted in a trimerization reaction to yield cyclopentanone-bridged or appended systems, that is, five-membered rings. The porphyrin component can carry either of the two carbon units, and cyclopentanone-linked or substituted compounds such as **310** have been described [251].

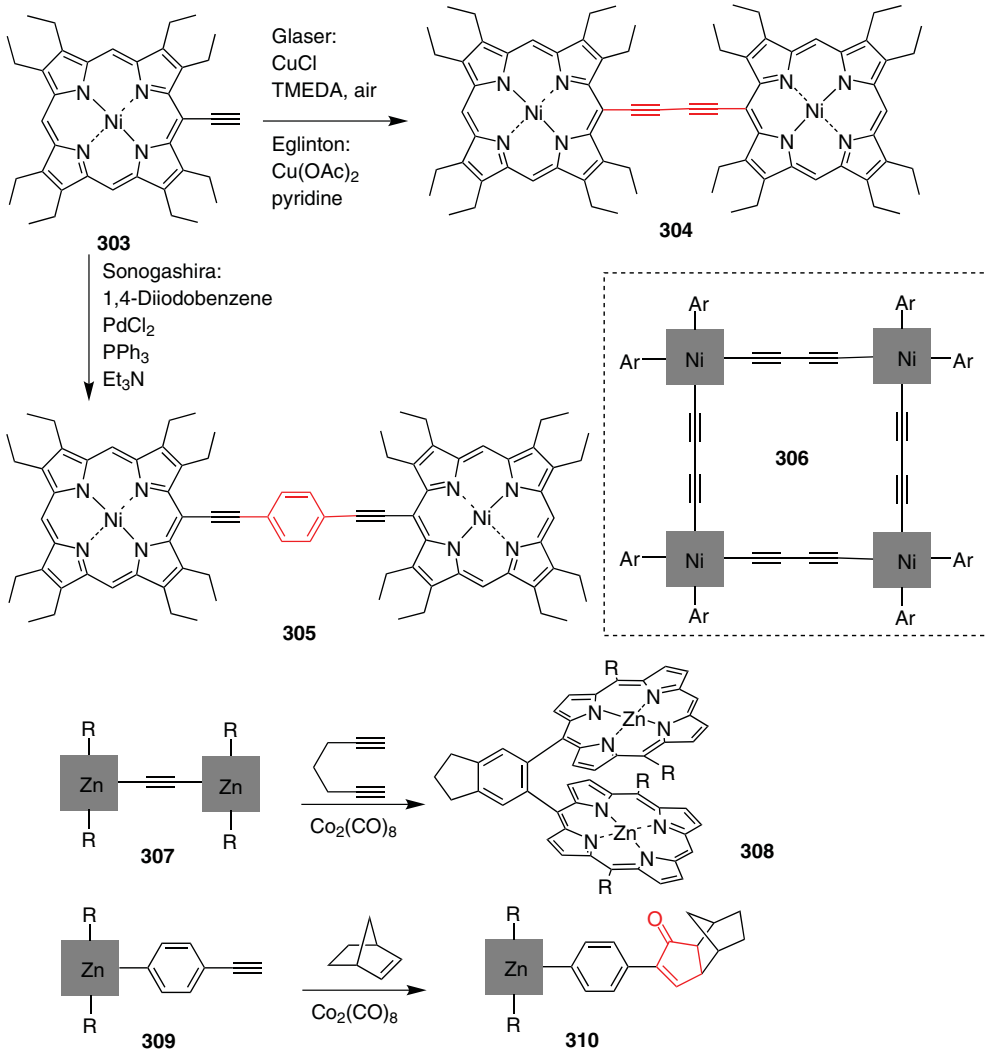

Figure 3.44 Examples of transition-metal-catalyzed reactions involving alkynylporphyrins.

Nickel catalysts have mainly been used as catalysts for reactions such as the examples described above (see Figure 3.39), for example, the coupling of bromoporphyrins or reactions with various carbonyl compounds giving access to a broad range of carbonyl and carboxy porphyrins. A rare case of a nickel-mediated transformation of porphyrins was discovered when studying the reactivity of porphyrin-allyl systems **311**. Reaction with three equivalents of $Ni(OAc)_2$ gave the respective nickel(II) acroleinylporphyrin **312** [252] (Figure 3.45).

Ruthenium catalysts are mostly used for cross-metathesis in porphyrin chemistry. This reaction was first employed by Dolphin and co-workers using vinylporphyrins such as **313** and several olefins to give compounds such as **314** [253]. Prior to this and since, many cross-metathesis reactions linking porphyrins with bioconjugates and acceptor units, or preparing arrays, including ring-closing metathesis and enyne-metathesis [254] transformations, have been reported [176]. Functional groups can also be introduced in this manner. For example, the reaction of allylporphyrins with a pinacolyl ester of vinylboronic acid in the presence of the first-generation Grubbs catalyst gave boronic porphyrin derivatives, or the treatment of allylporphyrins with acrylate ester yielded acrylic porphyrins [255].

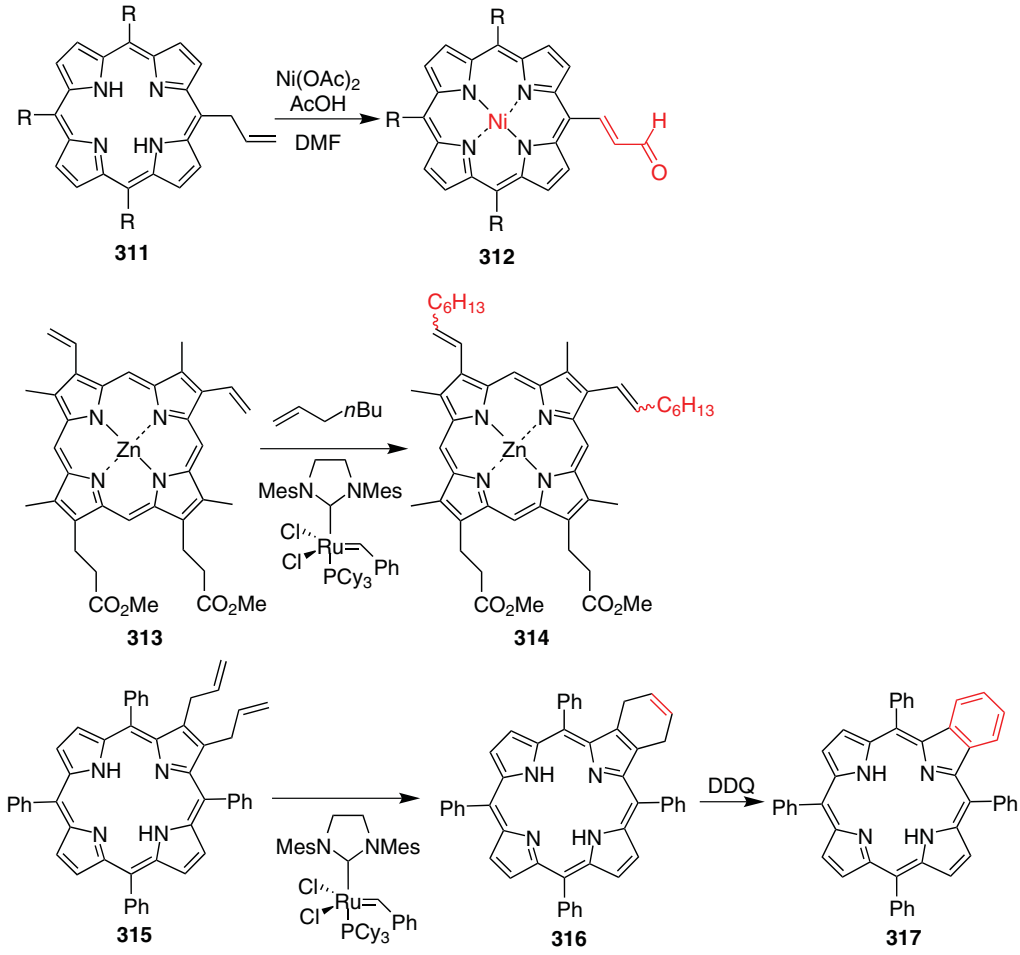

Figure 3.45 Examples of nickel- and ruthenium-mediated reactions of porphyrins.

The power of this reaction in porphyrin chemistry is highlighted in an elegant regioselective synthesis of benzoporphyrins from Smith's group [256]. Compounds such as **317** normally require a total synthesis approach. However, installation of two β-allyl groups (**315**) via Suzuki coupling, followed by intramolecular ring-closing metathesis in the presence of a second-generation Grubbs catalyst, gave excellent yields. The only thing left to do was treatment with DDQ to oxidize **316** to the benzoporphyrin **317** in an almost quantitative yield.

3.7.2 Reactions of Proto- and Deuteroporphyrins

In the past, a significant number of chemical studies were concerned with protoporphyrin IX **66** and compounds related to this natural macrocycle. Initially, this related to Fischer's structural elucidation and synthesis studies (see Section 3.3.3 [1, 56]), and later synthetic methods development studies often used heme as a source for degradation, FGI, and partial synthesis investigations. Although there is no need to recapitulate all studies, these "older" studies can illustrate how to work with natural porphyrins, which only have a limited number of functional groups (alkyl, vinyl, and propionic acids) as synthetic handles (next to the core for metallation or reactions involving the macrocycle) [257]. An up-to-date review on protoporphyrin chemistry has been given by Sitte and Senge [258].

3.7.2.1 Protoporphyrin

Protoporphyrin IX bears a number of easily transformable functional groups, that is, the 3- and 6-vinyl groups, and the 13- and 17-(2-carboxyethyl) groups; but one has to keep in mind that natural porphyrins are unsymmetric systems, and thus, monofunctionalization reactions present a regiochemical problem. Selected transformations that will be discussed are shown in Figure 3.46. For practical reasons (solubility and ease of purification), most of these reactions are initially performed with 13- and 17-ester derivatives (e.g., **318**), with ester saponification (or transesterification) being the last step in any synthetic sequence.

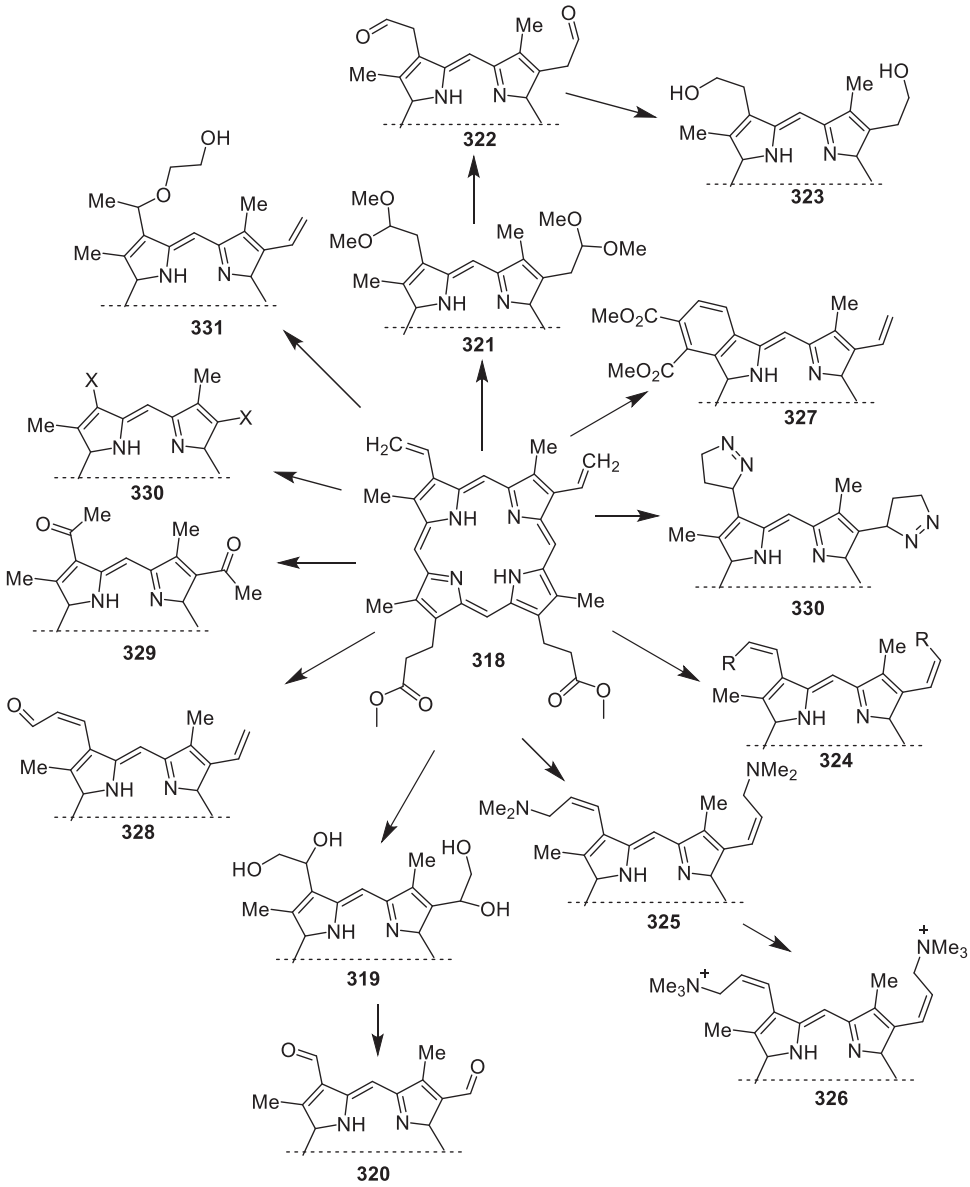

Figure 3.46 Vinyl group transformations in protoporphyrin IX diesters.

Vinyl Groups Due to their high reactivity, the vinyl groups on protoporphyrin IX can take part in a number of reactions such as reduction, oxidation, addition, substitution, electrocyclic reactions, and olefin metathesis. For example, reduction of the vinyl groups can be achieved via rhodium-complex-catalyzed hydroformylation. The outcome of the reaction largely depends on the central metal ion. It was shown that zinc derivatives give a higher yield than the respective nickel compounds [259].

Various methods exist to oxidize the vinyl groups on protoporphyrin IX to formyl substituents. Whereas direct oxidation often results in mixtures of difficult-to-separate monoformyl compounds, treatment of protoporphyrin IX **66** with an OsO_4-methylmorpholine *N*-oxide system readily leads to oxidation of both vinyl groups (**319**). Further reaction of the bis-diol with HIO_4 gives access to the dialdehyde (**320**) [260]. Oxidation of one vinyl group could be achieved by treatment with two equivalents of $Tl(NO_3)_3 \bullet 3H_2O$ [261] in a mixture of methanol and CH_2Cl_2 followed by hydrolysis and reduction of the products using $NaBH_4$ to give the monohydroxy isomers. Using three equivalents of thallium(III)nitrate, the bis-acetal (**321**) can be synthesized. Subsequent acid hydrolysis results in the bis-aldehyde (**322**), which can be further reacted with the diol (**323**) via reaction with $NaBH_4$. The dicarboxylic acid can also be obtained under harsh oxidation conditions with a hot solution of $KMnO_4$ in Me_2CO [258].

One prominent example of substitution reactions of the vinyl groups on protoporphyrin IX with different palladium catalysts is the Heck reaction, briefly described above [206]. One of the initial methods used $LiPdCl_3$ in the presence of aryl halides (**324**) [262]. Furthermore, the reaction with Eschenmoser's salt results in bis-trans-dimethylaminomethyl compounds **325**. This compound can be transformed into the water-soluble ammonium salt **326** by reaction with methyl iodide [263]. It is worth remembering that Diels–Alder reactions are possible with vinylporphyrins (see Section 3.5.4). One example is the synthesis of monobenzoporphyrin **327** via Diels–Alder cycloaddition of protoporphyrin IX dimethyl ester with subsequent elimination of the methyl group in the presence of a base and an excess of dienophile, or via oxidation with *p*-benzoquinone [264]. Another modification of the vinyl groups involves the use of Vilsmeier reaction conditions to yield acrolein derivatives **328** [265].

Another means of functionalizing protoporphyrin IX is to eliminate the vinyl groups by heating in resorcinol, followed by modification of these positions in the deuteroporphyrin form **71**. This is a classic approach toward β-acetylporphyrins. For example, the reaction of protoporphyrin IX after devinylation with acetic anhydride-$SnCl_4$ leads to the formation of either monoacetyl derivatives or diacetylporphyrins **329**, depending on the reaction time [265]. The Vilsmeier formylation of the Pt(II) complex gave entry to monoformyl derivatives. Furthermore, the 3- and 8-positions can be easily halogenated with iodine or bromine using either I_2 and K_2CO_3 or NBS (**330**). Naturally, these materials serve as starting materials for further coupling reactions [204, 266].

Aliphatic amines may be attached to protoporphyrin IX via electrophilic addition upon heating. Additionally, functionalization can be achieved by means of hydrobromination with subsequent replacement of the bromine atoms by nucleophiles. Other methods can include the introduction of alcohols to the vinyl groups (**331**) [267]; olefin metathesis (**313→314**) [253] has been described previously; cycloaddition reactions can occur on either or both of the vinyl groups. For example, a reaction of divinylporphyrins with diazomethane results in a mix of di-and monosubstituted pyrazolylporphyrins **330** [268, 269]. These compounds can be converted into their cyclopropyl counterparts through irradiation with long-wavelength light.

The transformation of vinylporphyrins with ethyl diazoacetate to cyclopropyl porphyrins was historically used by Fischer and Medick to confirm the existence of vinyl groups in natural porphyrins [270].

Modification of the 13- and 17-(2-carboxyethyl) Groups Obviously, standard COOH reactions can be applied here, with esterification being the most used. A typical example is the treatment of protoporphyrin with alcohol and *N,N′*-dicyclohexylcarbodiimide and 4-dimethylaminopyridine [267], and the esters prepared can easily be reduced to the diol and furthermore to propyl side chains [257]. A more recent case is the attachment of fullerenes, first by activation of the carboxy groups with oxalyl chloride, followed by condensation with the fullerene unit in form of an alkyl alcohol in the presence of 4-dimethylaminopyridine [271]. Amidations have also been frequently employed for applications in medicine and biology, and there is a wide range of oligopeptide- and protein-appended protoporphyrin derivatives. The synthesis of deuteroporphyrin amides with aluminum amide for docking studies with apoproteins may serve as a model here [272].

Modification of Methyl Groups Modification of the unactivated methyl residues is more difficult to achieve and has only limited synthetic utility. A classic case involved the heating of protoporphyrin in solvents with MeOD or MeO^- to facilitate electrophilic deuteration of the methyl groups [265], and Smith and co-workers reported a different reactivity for each of the four methyl groups on protoporphyrin [257, 273]. This made it possible to selectively deuterate the 2- and 7-methyl groups via base-catalyzed exchange reactions. Other modifications of the methyl groups include the reaction of porphyrin metal complexes with thionyl chloride [267].

3.7.2.2 Deuteroporphyrin

The 3- and 8-positions of deuteroporphyrin **66** offer convenient places of high reactivity for porphyrin modifications, a prominent example being electrophilic substitution reactions. Older examples are the bromination of deuteroporphyrin IX dimethyl ester with pyridine bromide perbromide in $CHCl_3$ or the synthesis of 3,8-bis(methoxycarbonyl)deuteroporphyrin IX dimethyl ester in acetone with a hot solution of potassium permanganate. Furthermore, 3,8-bis(2-carboxycyclopropyl)deuteroporphyrin can be obtained with ethyl diazoacetate. Another illustrative sequence involved the preparation of 3,8-dioximinodeuteroporphyrin from 2,4-diformyldeuteroporphyrin, and further reaction with 3,8-dicyanodeuteroporphyrin IX dimethyl ester [274].

The aforementioned diformyldeuteroporphyrin is prepared via a Vilsmeier reaction. Classic conditions are those developed in Inhoffen's group [104], for example, formylation of copper(II) deuteroporphyrin dimethyl ester. Nevertheless, it is difficult to control meso- versus β-reactivity and mono- versus diformylation. Later studies improved on this by using *N,N*-diisobutylformamide instead of DMF [275]. The same paper also described the ease of electrophilic meso-deuteration in porphyrins of the proto- and deuteroporphyrin series. More recently, a comparative analysis of Pd-catalyzed reactions of proto- and deuteroporphyrins was given [276].

3.7.3 Fusing Reactions

Porphyrins with peripherally fused ring systems and conjugated porphyrin arrays are currently being widely investigated due to their unique electronic, optical, and electrochemical properties. The synthetic methodologies used to explore annulated, π-extended, and bridged

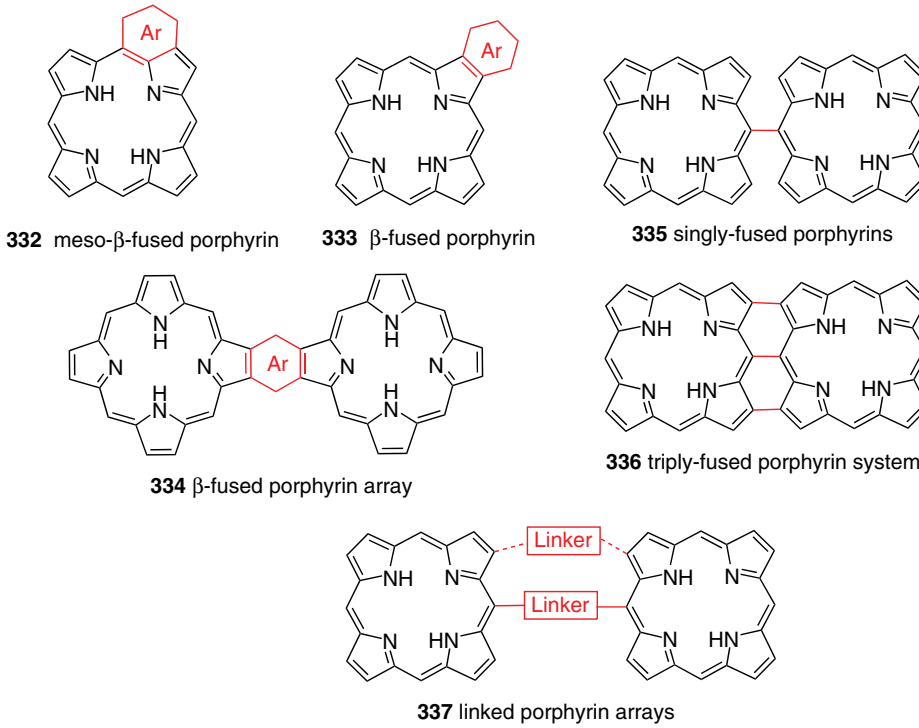

332 meso-β-fused porphyrin

333 β-fused porphyrin

335 singly-fused porphyrins

334 β-fused porphyrin array

336 triply-fused porphyrin systems

337 linked porphyrin arrays

Figure 3.47 Selected types of "fused"-porphyrin systems.

systems span a whole range of reactions from "old" Friedel–Crafts reactions to "modern" transition-metal-catalyzed ones [277]. The number of macrocycles with fused substituents (**332** or **333**) and of porphyrin dimers and arrays prepared through these reactions is ever expanding, as are the types of fused structures (e.g., singly fused **335** versus triply fused **336**) [182]. These structures are complemented by an even larger number of porphyrin arrays whose porphyrin units are linked by bridging linkers (**337**) or fused ring systems (**334**). Some general examples of such systems are shown in Figure 3.47.

Classic examples of porphyrins with fused "extra" ring systems were prepared by intramolecular cyclization reactions. A case in point is the purpurin family (cyclopenta[*at*] porphyrins **338**), in which a five-membered ring system links a meso- and β-position. These compounds are easily recognized as being related to the fundamental structure of chlorophylls. One of the first syntheses was the preparation of the respective bis-C_m-C_b-chloromercurated precursor, followed by a Pd-catalyzed reaction with acrylate and KOH [278]. More facile reactions include the intra- and intermolecular Pd-catalyzed reactions outlined in Section 3.6.1 (e.g., (**230**→**231**) [188]), zinc metal-mediated couplings of 2-bromo-5-arylporphyrins [279], or acid-catalyzed cyclizations of meso-acrylate porphyrins [280].

Fused six-membered ring systems were initially investigated in the form of benzochlorins **339** prepared by intramolecular cyclization of formylvinylporphyrins [105]. We have already encountered (Section 3.4.3) the benzoporphyrins **340**, in which benzene residues are fused to both β-positions of one or more pyrrole rings. These are best prepared via pericyclic reactions. Related compounds are the naphthoporphyrins **341** (where a classic synthesis

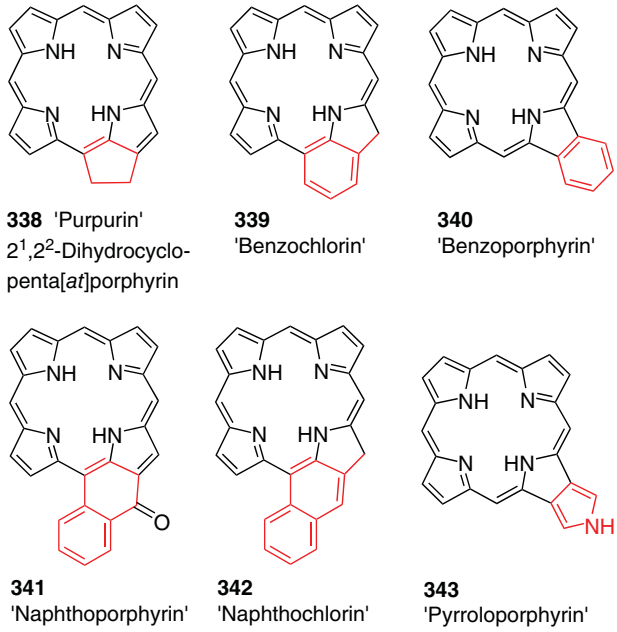

338 'Purpurin'
$2^1,2^2$-Dihydrocyclo-penta[*at*]porphyrin

339
'Benzochlorin'

340
'Benzoporphyrin'

341
'Naphthoporphyrin'

342
'Naphthochlorin'

343
'Pyrroloporphyrin'

Figure 3.48 Porphyrins with fused five- or six-membered rings.

by Callot used a 2-formylporphyrin for an intramolecular acid-catalyzed reaction [281]) and naphthochlorins **342** [282]. For the latter, the easiest access is given by treatment of (5,10,15,20-tetraphenyl-2-vinylporphyrinato)nickel(II) with dilute sulfuric acid [283] (Figure 3.48).

Larger aromatic systems and/or porphyrins can also be fused with or linked to porphyrins. An excellent account of this area has been given by Tanaka and Osuka [284]. This area of research started to take off in the late 1990s with the first reports on singly meso-meso- (e.g., **196** or **250**) and doubly meso-β-linked (**234**) bisporphyrins. Porphyrins can also be fused solely at the β-positions, and this was elegantly demonstrated by Smith and co-workers using pyrroloporphyrins **343** [285, 286]. These are accessible using a 2-nitroporphyrin as the nitroalkene component of a Barton–Zard reaction [55], that is, utilizing the porphyrin as a precursor for a pyrrole. The latter could then be applied to a standard pyrrole condensation reaction to yield directly doubly β-β-fused bisporphyrins such as **344** (Figure 3.49). As a "pyrrole," pyrroloporphyrins can also undergo standard tetramerization reactions to yield a cross-shaped pentaporphyrin with a central porphyrin appended at all four C_b-C_b units by another porphyrin, for example, **346** [287]. However, in this case, the pyrrole unit(s) had to be positioned farther away to minimize steric hindrance, which was achieved by preparing pyrroloporphyrins of type **345**, a 2*H*-dihydroisoindoloporphyrin. This required a [4 + 2] cycloaddition of a 5,10,15,20-tetraarylporphyrin with 1,1-sulfolano[3,4-c]pyrrole [288], acid-catalyzed tetramerization, and exhaustive oxidation with DDQ to assure oxidation of both the porphyrinogen and the cyclohexadiene fragments between the porphyrins.

Apart from fusing porphyrins along the β-position, many porphyrins directly linked at the meso-position have been prepared – ultimately leading to series of bisporphyrins, oligomers, and polymers with meso-meso, meso-β, or meso-β-β fusions [284]. The key development was Osuka's Ag(I)-promoted coupling of porphyrins **347** to yield **348** [218]. These singly

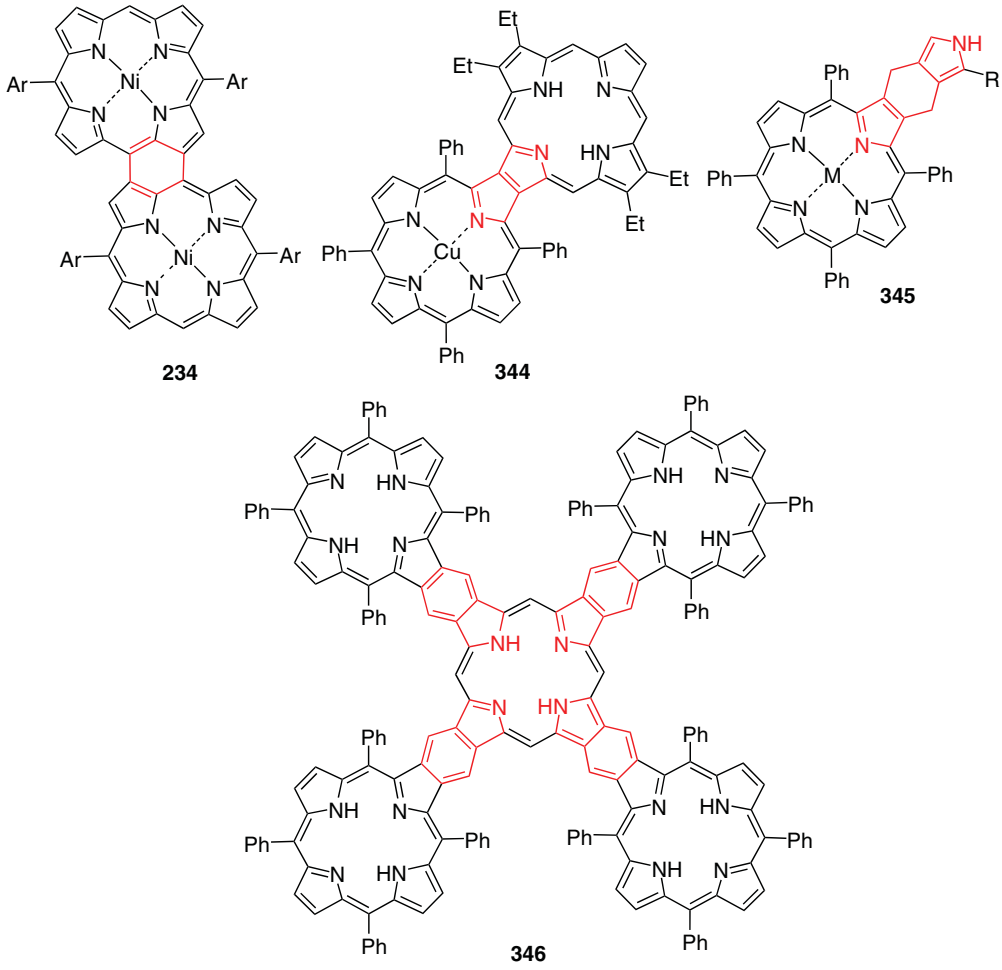

Figure 3.49 Examples of β-fused porphyrin systems.

linked systems could then be oxidized to the triply linked systems **349** [289]. Notably, the meso-meso-linkage could also be achieved in polymerization reactions [290] up to the 128mer, leading to the preparation of fully conjugated porphyrin tapes [291].

Figure 3.50 highlights some key (but not all!) fusing transformations and illustrates the range and type of accessible compounds. These include the formation of the porphyrin-dehydropurpurin dimer **355** [292], an example of the fusion of a meso-substituent onto a β-position, various doubly meso-β-linked bisporphyrins **352** [190] and triply meso-meso-, meso-β-, and β-β-linked porphyrins **349**. Over the years, many improvements have been made with regard to regioselectivity, oxidant (i.e., DDQ, $Sc(OT)_3$ – now often used instead of tris(4-bromophenyl)ammoniumyl hexachloroantimonate) and target systems [284]. Depending on the central metal or the meso-substituents, other types of fusions are possible with zinc(II) complexes leading to triply linked systems and Pd(II) complexes yielding doubly meso-β-linked bisporphyrins [293]. Treatment of porphyrins with meso-hydroxyaryl substituents gave an entry into oxoquinoidal porphyrins **353** [294], while planarization of the porphyrin dimer **353** gave the quinoidal porphyrin dimer **354**,

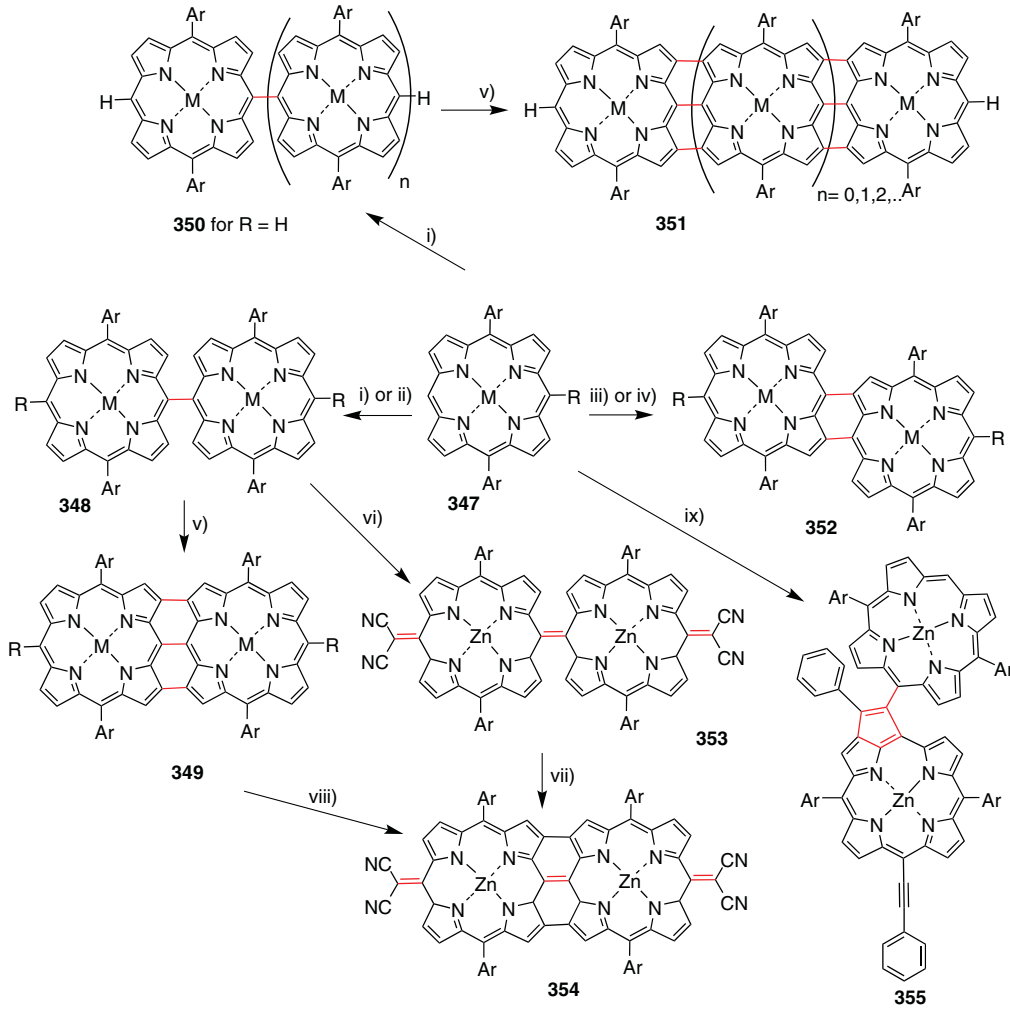

Figure 3.50 Synthesis of meso-meso–, meso-β–, and β-β–fused bisporphyrins. Reaction conditions: (i) R = Ar, M = Zn(II), Ag(I) promoted coupling; ~20–90%. (ii) R = H, M = Ni(II), RLi, THF, –40 °C, DDQ; 60–80%. (iii) M = Pd(II), toluene, 5 eq. DDQ, $Sc(OTf)_3$, 5 eq. 50°C, 12 hours; ~70%. (iv) 1 eq. $TeCl_4$, CH_2Cl_2, rt.; ~30% + oligomers. (v) M = Zn(II), toluene, 5 eq. DDQ, 5 eq. $Sc(OTf)_3$, 50 °C, 30 minutes; ~90%. (vi) M = Zn(II), R = Br; (a) $NaCH(CN)_2$, $Pd_2(dba)_3$, CuI, PPh_3. (vii) DDQ, $Sc(OTf)_3$; ~80%. (viii) R = Br; (vi); ~80%. (ix) R = C≡C-Ph; $AgPF_5$; >30%.

and so on. Larger 2D structures, for example a tetrameric fully fused porphyrin system with a planar cyclooctatetraene core **356**, can be prepared in a similar manner [295]. Note that all of these systems are also accessible via stepwise reactions using transition-metal-catalyzed approaches, for example, **150** + **248** → **250**; **150** + **249** → **252** (**253**); **271** → **272**; or RLi chemistry (**196**). As for monomeric porphyrins, these reactions become progressively more involved if one targets unsymmetrically substituted, fused oligoporphyrinoid systems [296].

If porphyrins can be fused to porphyrins, then it is natural to assume the same for other aromatic units (Figure 3.51). An archetypical case was the fusing of naphthalene to a porphyrin in 2005 via Suzuki coupling (**232→233**) [190]. By now many different aromatic and heteroaromatic residues have been fused to porphyrins, and a convenient review has

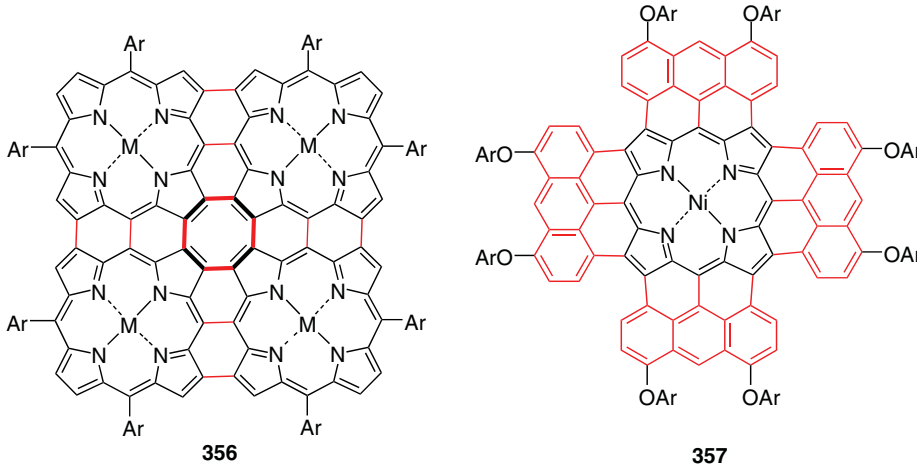

Figure 3.51 Osuka's fully fused porphyrin tetramer and Anderson's fully fused tetraanthracenylporphyrin.

been written by Lewtak and Gryko on this topic [297]. Fusing anthracene proved to be one of the more challenging tasks, and Anderson's synthesis of anthracenyl-triply fused porphyrins, including the tetraanthracenyl-fused system **357**, is a recent highlight in this area [298, 299]. Their syntheses proceed in a similar manner to the preparation of triply linked bisporphyrins; that is, first the substituent is attached by one covalent bond (meso), and this is then followed by oxidative coupling at the remaining neighboring (C_b) positions.

3.8 Examples of Classic and Contemporary Target Systems

3.8.1 Unsubstituted Porphyrin

This book demonstrates the many advances in the synthesis and use of porphyrins and porphyrin arrays. Yet, a closer look at the compounds shown in the figures of this chapter reveals that these examples almost exclusively deal with substituted porphyrins and rarely concern the parent porphyrin **5**, the simplest porphyrin without any peripheral substituents, historically called "porphin(e)" (not a IUPAC name). We have briefly mentioned it twice above (Sections 3.2.1 and 3.5.3.2), indicating that its synthesis eluded organic chemists for a long time [32]. This was not due to any inherent problem in forming the aromatic macrocycle; it has been known since Fischer's times, yet the first "practical" synthesis by Paul Rothemund in 1936 gave only 0.1% yield [300]. The main challenge is the insolubility of this flat, apolar aromatic molecule, which facilitates aggregation and precipitation from solution. As a consequence, some interim improvements used acidified solvent systems, which means the product is initially the water-soluble porphyrin dication (such as **208**), which is nonplanar and thus less prone to aggregation.

The pyrrole components used in the various syntheses (Figure 3.52) ranged from pyrrole, 2-hydroxymethylpyrrole, to 2,5-bis(hydroxymethyl)pyrrole **358**, which was used in a [3 + 1] condensation with tripyrrane **37** under Lindsey conditions [301]. An easier and scalable approach came with Lindsey's magnesium-template-assisted approach for [2 + 2] condensations (see also Figure 3.5). Using 1-formyldipyrromethane **359** under aerobic

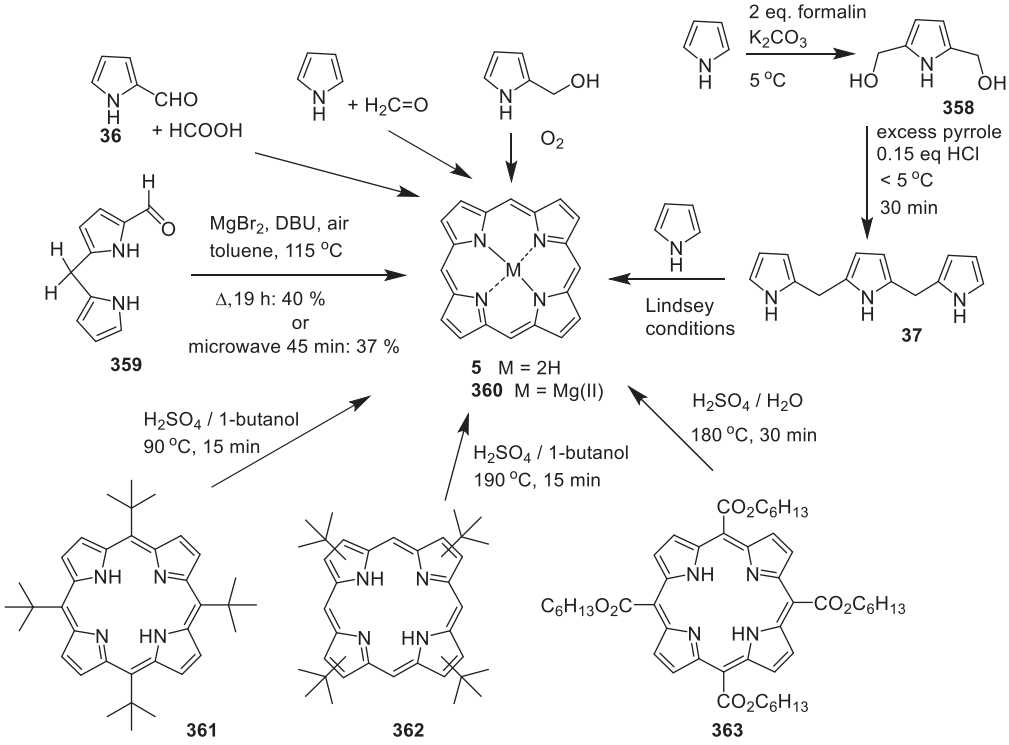

Figure 3.52 Synthesis of unsubstituted porphyrin.

conditions gave the magnesium complex **360** in acceptable yields of 30–40% [31]. Next to simple conditions, scale and ease of purification, again the key was the improved solubility of the magnesium complex as compared to the free base **5**.

The best yields to date are obtained using Neya and Funasaki's dealkylation approach [148]. Akin to the classic dealkylation of *tert*-butylbenzene to benzene, they suggested the use of *tert*-butyl-substituted porphyrins as precursors for the acid-catalyzed reaction. Indeed, use of 5,10,15,20-tetra(*tert*-butyl)porphyrin **361** [25, 302] gave yields of **5** >70%. Compound **361** can easily be prepared by condensation of pyrrole with pivalaldehyde and is a very nonplanar porphyrin due to the bulkiness of the *tert*-butyl groups [303]. Tetra-β-(*tert*-butyl)porphyrin **362** can also be used, but requires higher temperatures for dealkylation as the β-substituents provide less steric hindrance. A related strategy used 5,10,15,20-tetrakis(hexyloxycarbonyl)porphyrin **363**, which was hydrolyzed and thermally decarboxylated to **5** in very good yields as a crystalline material [304].

As a result of the limited and late access to compound **5**, studies on its reactivity remain scarce. Similar to other porphyrins, it undergoes S_EAr reactions. A classic study by Samuels et al. in 1968 [305] looked at halogenations, but yields and regioselectivities were low and depended on the strength of the halogenating agent. Yet, the meso- and β-bromoporphyrins could be identified, and these are examples of true electrophilic substitution reactions with the initial π-complex formation, which collapse to a σ-complex followed by the loss of a proton to restore the aromaticity. Likewise, selective meso-mononitration could be achieved with nitric acid to 5-nitroporphyrin with a second nitration taking place at the 15-position [306]. Fuhrhop later rationalized most of the fundamental reactivity of porphyrin(s) and their metal complexes [307] and also showed that Vilsmeier formylation of **5** preferentially takes place at the meso-position [101].

A wider variety of derivatives only became available much later with the use of nucleophilic substitution reactions as developed by ourselves [133, 308]. In situ generation of free base **5** via dealkylation reactions, directly followed by reaction with organolithium reagents (see Figure 3.29) allowed the facile synthesis of either meso-mono- (“**190**”) [39] or 5,10-disubstituted porphyrins (“**193**”) [41] by simple variation of the number of RLi equivalents used [42]. All of the reactions outlined in Figure 3.29 for substituted porphyrins should, in principle, be applicable here as well.

3.8.2 Water-Soluble and Charged Porphyrins

Many applications in medicine and materials science require water-soluble porphyrins. Depending on the context, one can achieve this through the introduction of polar residues, cleavage of esters to acids, core protonation, conjugation with water-soluble residues such as carbohydrates or amino acids, and more [242]. Here, we will illustrate only very simple systems that can be generated quickly from simple starting materials.

3.8.2.1 Nitration and Further Functionalization of meso-Substituted Arylporphyrins

The simplest way to functionalize meso-aryl residues is through electrophilic substitution reactions, and a classic reaction is the nitration of phenylporphyrins (Figure 3.53) [132]. Typically, this can be achieved via reaction of H_2TPP **10** with nitric acid, nitrate salt, N_2O_4, nitrite ion, or fumic acid. The isolated nitroporphyrins **364** can then be reduced to aminoporphyrins **365**. A method of doing this is to use a 1.5-fold excess of tin dichloride dehydrate in HCl. The reaction is heated to 70–80 °C and results in nearly quantitative conversion to the 5,10,15,20-tetra(aminophenyl)porphyrin [125]. Mono- or disubstituted nitro compounds necessitate milder conditions, for example, room temperature. Another possibility is to subject these compounds to $NaBH_4$ and 10% Pd/C in methanol [309].

Amino groups are very reactive and can be further transformed into diazonium salts **366** [310], for example. These can be obtained via reaction of the aminoporphyrin with sodium nitrite in aqueous solutions of mineral acids. The salts obtained are quite stable, and decomposition through the release of nitrogen is normally observed only at temperatures above room temperature. Diazonium salts can be further modified to a variation

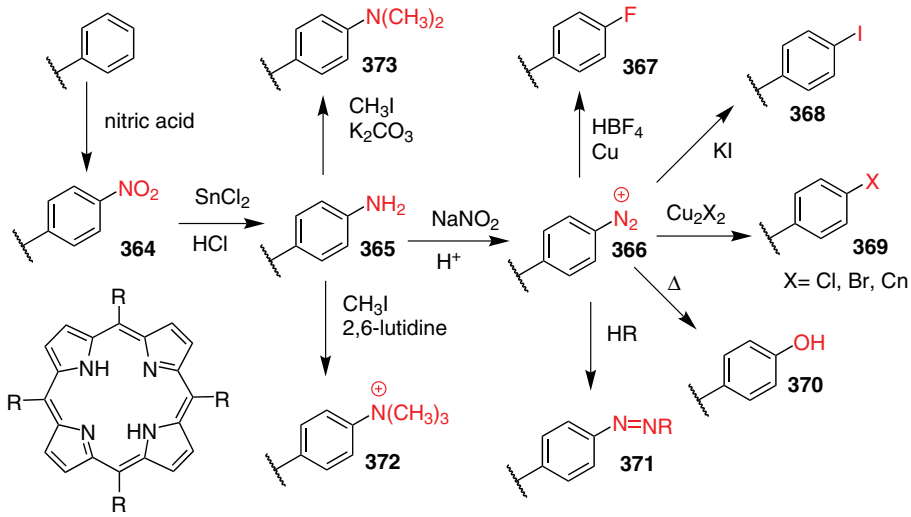

Figure 3.53 Transformations of nitro- and aminophenylporphyrins.

of 5,10,15,20-tetra(halogenophenyl)porphyrins (**367**–**369**), as well as other examples. 5,10,15,20-Tetra(hydroxyphenyl)porphyrins **370** can be synthesized by heating in water. Furthermore, aminoporphyrins can be used in Sandmeyer or azo-coupling reactions to yield **371**. Aminophenyl porphyrins can also be easily methylated with iodomethane. The reaction of **365** with iodomethane in DMFA in the presence of 2,6-lutidine results in the formation of cationic 5,10,15,20-tetrakis(trimethylaminophenyl)porphyrin **372** in very good yields. When potassium carbonate is used as base, the reaction stops at the dimethylaminophenylporphyrin **373**. The tetrakis(*p*- and *m*-trimethylaminophenyl)porphyrin salts are water soluble over a wide pH range. Even simpler is the use of 5,10,15,20-tetra(pentafluorophenyl)porphyrin. This can easily be substituted at the *p*-position, for example, by heating with $Me_2N{\bullet}HCl$ in DMF to yield the *N*,*N*-diamino-2,3,5,6-tetrafluorophenyl derivative, which can be further alkylated (to **376**) [311].

An alternative system, which can be prepared in one step from a simple 5,10,15,20-tetraarylporphyrin, involves *N*-methylation of pyridyl substituents. Hambright and Fleischer prepared the first methylated 5,10,15,20-tetrakis(*N*-methyl-4-pyridyl)porphyrin in 1970 from [5,10,15,20-tetrakis(*N*-4-pyridyl)porphyrinato]zinc(II). They utilized an excess of methyl iodide in $CHCl_3$/ethanol (9/1) solution [311]. Alternatively, methylation can be achieved through the use of methyl *p*-toluenesulfonate in refluxing DMF. Furthermore, trimethyl phosphate in the presence of 2,6-lutidine and methyl *p*-toluenesulfonate has been used to obtain the triflate salt, while 2-chloroethanol can be used to synthesize the ethylated porphyrin.

3.8.2.2 Porphyrin Salts

Aside from the porphyrin (di)cation salts, prepared via protonation/substitution of the core (see Section 3.5.5), many other means exist to prepare "charged" porphyrins, that is, systems with cationic or anionic residues in the periphery. This area has been succinctly detailed by Hambright [312]. Figure 3.54 lists a range of porphyrins with positively charged peripheral substituents. For example, Jin et al. reported the formation of phosphoniumyl (**374**) and ammoniumyl (**375**) cationic porphyrins by the reaction of

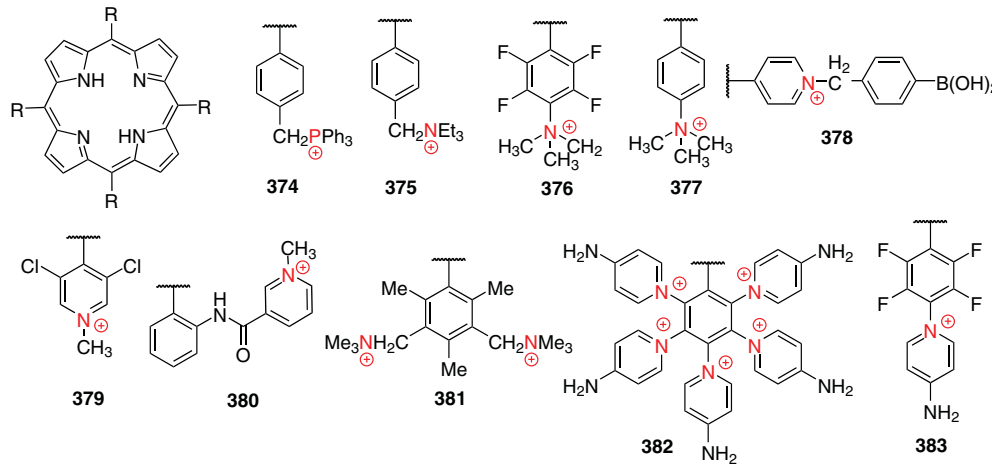

Figure 3.54 Examples of peripherally positively charged porphyrin species.

5,10,15,20-tetrakis(*p*-chloromethylphenyl)porphyrin with either an excess of PPh_3 or NEt_3 in DMF [313]. Other examples are the previously mentioned pentafluorophenyl derivatives **376** and **372**. Many compounds are derived from 4-pyridyl derivatives; for example, **379** was synthesized using Lindsey condensations from pyrrole and 3,5-dichloroisonicotinaldehyde yielding 5,10,15,20-tetrakis(3,5-dichloro-4-pyridyl)porphyrin, which was then methylated with methyl tosylate, while **380** was obtained through the methylation of 5,10,15,20-tetra (nicotinamidophenyl)porphyrin in dry methylphosphate with methyl trifluoromethanesulfonate.

Octacationic species **381** are accessible through bromomethylation of 5,10,15,20-tetramesitylporphyrin followed by replacement of the bromides by trimethylamine. An even more impressive 20-step one-pot synthesis was reported by Weiss et al. to give the cationic porphyrin species **382** with 20 charges [314]. This was achieved via treatment of 5,10,15,20-tetra(pentafluorophenyl)porphyrin with 4-dimethylaminopyridine and Me_3SiOTf in chlorobenzene for four days under heating to reflux. The use of triethylphosphine and heating at reflux for two days gave only the tetrasubstituted porphyrin **383**. The yields in both cases were almost quantitative, and the pure product precipitated directly from the organic solvent!

Besides positively charged systems, negatively charged porphyrins can easily be synthesized as well. The most widely used compounds are derived via sulfonylation (Figure 3.55). The first sulfonation of H_2TPP was reported by Winkelman in 1962 [315]. He used hot sulfuric acid as the sulfonating agent and obtained the meso-tetrakis(4-sulfophenyl)porphyrin **385** in 70% yield. Purification can be difficult, but is possible via sedimentation of the sodium or ammonium salt from a methanol-acetone solution or through the formation of the insoluble potassium salt. A widely followed practical procedure has been reported by Dolphin's group and uses dialysis for purification [316]. When subjected to chlorosulfonic acid at room temperature, the tetrachlorosulfonic derivatives **384** can be formed from H_2TPP. These groups can be easily transformed into free sulfonic acids, sulfonamides, or sulfo-esters upon reaction with water, ammonia, or alcohols (**386**–**388**). Another example is the synthesis of 5,10,15,20-tetrakis(2,6-dichloro-3-sulfonatophenyl)porphyrin **389**. Other examples of

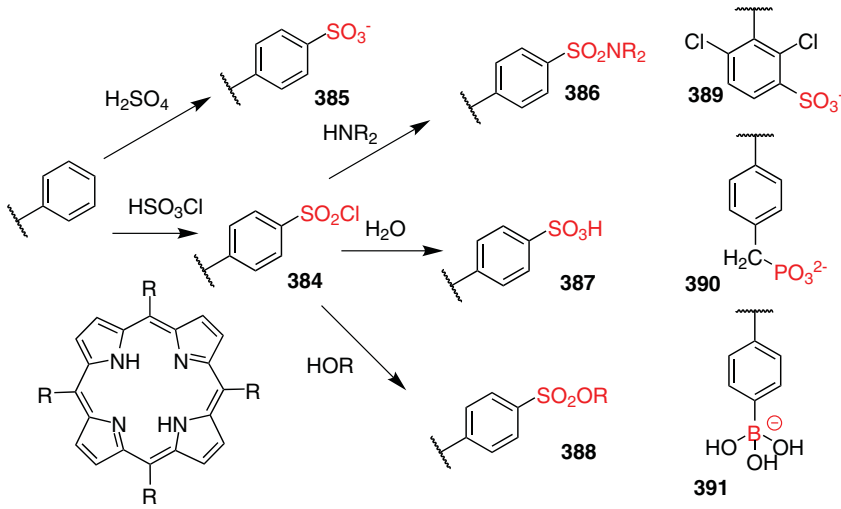

Figure 3.55 Examples of peripherally negatively charged porphyrin species.

negatively charged porphyrins are 5,10,15,20-tetrakis(4-phosphonato-methylphenyl)porphyrin **390** and the phenyl-$B(OH)_3$-substituted porphyrin **391**, which is prepared via condensation of pyrrole with 4-(5,5-dimethyl-1,3-dioxa-2-borinyl)benzaldehyde and subsequent deprotection and substitution [317].

3.8.3 Reactions of meso-Hydroxyphenylporphyrins

Sometimes considerable attention is focused on a specific class of porphyrins due to their relevance in the applied sciences. For example, the tetrahydroxyphenylchlorin **392** (*m*THPC, Temoporfin) is clinically used as a photosensitizer in photodynamic therapy [318], and many derivatives have been prepared in an attempt to improve its clinical use [319, 320]. Naturally, hydroxyphenyl groups on a porphyrin can undergo a variety of reactions, and we will illustrate some of the newer approaches here to help describe how a simple precursor porphyrin **393** can be used to quickly generate a library of related compounds (Figure 3.56).

A simple approach involves the use of Williamson ether reactions, and this can be complemented by a range of more modern reactions. For example, in one of our studies, we investigated the controlled functionalization of the tetrasubstituted hydroxyporphyrin through substitution reactions of **393** (often referred to in the literature as *m*THPP) [321]. Optimization studies showed that **393** was subjected to substitution with propargyl bromide, and the optimum reaction conditions were one eq. of NaH with two eq. of propargyl bromide in DMF for 2 h at room temperature. This gave a 46% yield of the monosubstituted porphyrin **394** and 30% starting material, which could be recovered and reused. To obtain higher substitution,

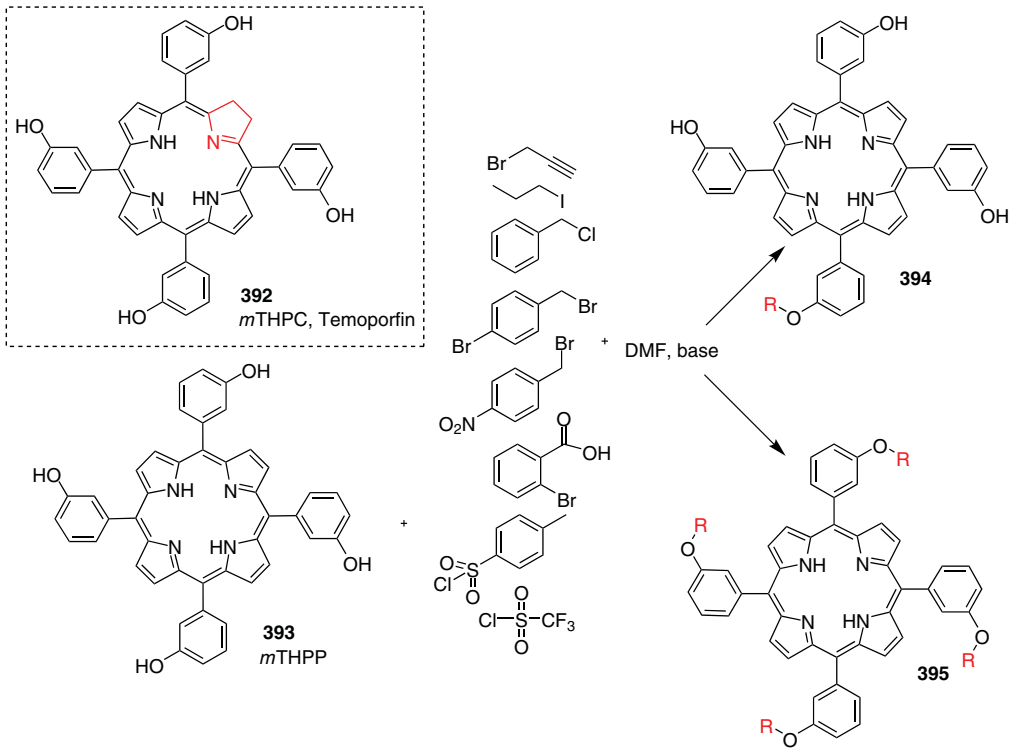

Figure 3.56 Controlled installation of various functional groups in a meso-hydroxyphenylporphyrin.

prolonged reaction times and use of higher amounts of K_2CO_3 and propargyl bromide was necessary, which gave the tetrasubstituted porphyrins **395** in nearly quantitative yields. This method could then be quickly applied to a series of halogenated aryl or alkyl substituents, and a change in the base to pyridine allowed the installation of tosyl or triflyl groups.

Additionally, metal-catalyzed coupling reactions, such as the copper-catalyzed Chan–Lam coupling, were applied to **393**. This enabled the introduction of a variety of boronic acids under very mild conditions. The straightforward and simple substitution reaction could also be used to synthesize A_3B-type picket fence porphyrins, which are normally difficult to generate. Therefore, the reaction of **393** with either 4-*tert*-butylbenzyl bromide or 1-iodohexane is required. The trisubstituted species was then used in a subsequent substitution reaction of the final free OH group with propargyl bromide. Similarly, cofacial bisporphyrins (see Section 3.8.6) were obtained via reaction of the hydroxyphenylporphyrin **393** with 1,4-dibromobutane to give the tetrasubstituted porphyrin, which was then again reacted with another molecule of **393**. Williamson ether syntheses of hydroxyphenylporphyrins generally give good yields; for example, Wada et al. subjected 5-(2-hydroxyphenyl)-10,15,20-triphenylporphyrin to reaction with 3-bromoethylpyridine under basic conditions and obtained the substituted product in 84% yield [322].

Compound **393** can also serve as an illustrative example of photobleaching reactions of porphyrins. While normally not the focus of synthetic studies, porphyrins will photodegrade upon prolonged exposure to light. Although considered an unwanted reaction, when it comes to photodynamic therapy, it still "sheds light" on possible photo-induced reactions of porphyrins. A case study in point was performed by Bonnett and Martínez, who investigated the photobleaching of a series of 5,10,15,20-tetrakis(m-hydroxyphenyl)porphyrin and -(bacterio)chlorin derivatives (Figure 3.57) [323]. They reported the formation of various quinoid porphyrins in which *m*THPP was subjected to irradiation in aqueous methanol. Five new benzoquinonyl porphyrins were formed upon irradiation for 24 h. The major product was 5-(3,4-benzoquinonyl)-10,15,20-tris(3-hydroxyphenyl)porphyrin **394** (25%) accompanied by 5,10-bis(3,4-benzoquinonyl)-15,20-bis(3-hydroxyphenyl)porphyrin **395** (4.8%), 5,15-bis(3,4-benzoquinonyl)-10,20-bis(3-hydroxyphenyl)porphyrin **396** (1%), 5,10,15-tris(3,4-benzoquinonyl)-20-(3-hydroxyphenyl)porphyrin **397** (0.4%), and 5,10,15,20-tetrakis(3,4-benzoquinonyl)porphyrin **398** (0.9%). Unreacted starting material (**361**) was also recovered (32%). When the photooxidation was performed in pure methanol, the reaction was much slower. After 41 h of irradiation, only a small amount of **394** was obtained along with a 53% yield of starting material **393**, 2.5% of 3-hydroxybenzoate **399**, and 1.1% maleimide **400**. Photooxidation of the respective chlorin (*m*THPC, **392**) and bacteriochlorin was much more rapid and also resulted in the formation of a number of macrocycle cleavage products, such as dipyrrins.

3.8.4 Superstructured Biomimetic Porphyrins

A recurring task of a synthetic porphyrin chemist is the synthesis of bimimetic porphyrins that simulate one of the natural functions of porphyrins (e.g., catalysis, electron transfer, or photosynthesis) without the need to analyze the whole holoenzyme. Especially before the advent of modern molecular biology, analysis of cofactors bound to the apoprotein was often too difficult and, in addition, it has always been the desire of chemists to mimic natural processes with simple model compounds and to minimize them to the essential core structural and functional elements. The first-time porphyrin chemists who delivered on this task with

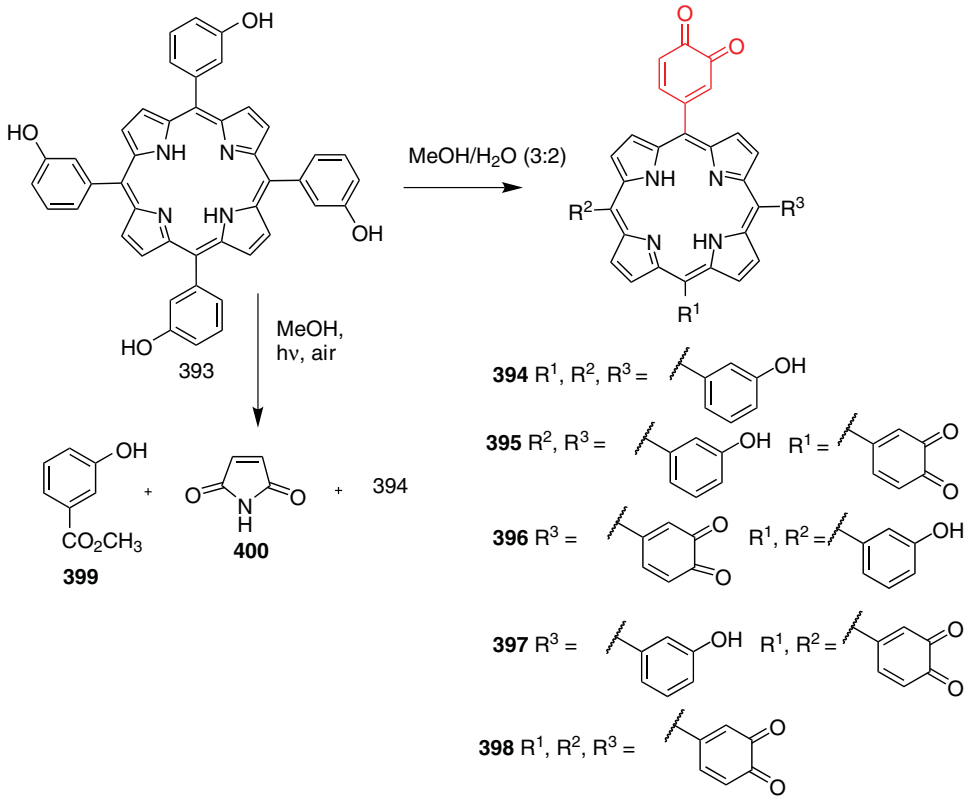

Figure 3.57 Photooxidation reactions of *m*THPP **393**.

admirable aplomb were modeling heme proteins. Part of the function of natural proteins, such as hemoglobin, derives from the protein environment acting as a structural scaffold and steric shield for the cofactor and the metal center therein where the reaction takes place. For example, if one desires to study the binding of oxygen to a simple iron porphyrin, then invariably dimerization to a μ-oxo-bridged bisporphyrin will occur. If one wants to prevent this, then steric shielding of the iron core is necessary.

To achieve this, in the 1970s, chemists began to synthesize and investigate "superstructured" porphyrins, that is, systems in which the apoprotein of the native system was mimicked by suitable porphyrin substituents. Additionally, it is often necessary to position axial ligands on one or two faces of the porphyrin, as protein-bound porphyrins are stabilized and/or activated by axial ligands (e.g., histidine). Thus, both faces of the porphyrin need to be elaborated to assure a function similar to that found in vivo. This required positioning substituents both in functional and structural terms in specific 3D arrangements and using judicious molecular design.

Even for simple heme proteins, a multitude of specifically designed superstructured porphyrin systems have been developed [324]. The naming of these "designer" porphyrins was as ingenious as the chemistry involved in their synthesis. Figure 3.58 illustrates some of the fundamental structures (and there are many more) used as heme protein models. Shielding or blocking of one face of a porphyrin can be achieved by strapping (**401**), creating cyclophane-type arrangements (**402**), using more than one strap (**403**), "crowning"

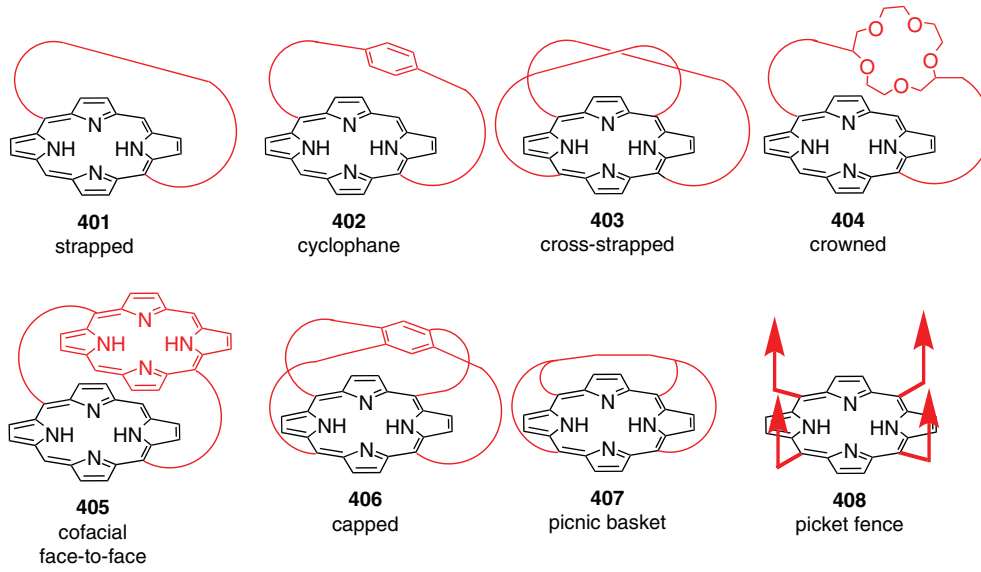

Figure 3.58 Design principles for superstructured biomimetic porphyrins (straps can be either meso- or β-linked).

porphyrins by incorporation of crown ethers in the straps (**404**), using a second porphyrin in cofacial bisporphyrins (**405**; see also Section 3.8.6) as a cap (**406**), attaching handles to create a "picnic basket" porphyrin (**407**) suitable for axial ligand or substrate shopping, or positioning residues around the porphyrin macrocycle to create a picket fence (**408**), where the fence protects the porphyrin core and/or imparts selectivity on binding.

As for any other target, numerous synthetic strategies exist and have been attempted to realize these structures. Even a simple strapped porphyrin can be prepared via aliphatic linkage, esterification, amidation, etherification, substitution reactions, the formation of disulfides or using organometallic reactions, and more. Furthermore, the strap can either be incorporated into starting materials of the porphyrin synthesis or attached/closed afterward.

A typical example of the former is Dolphin's improved synthesis of β-strapped porphyrins **415** (n = 8–11) (Figure 3.59) [325]. Key steps include the use of the linker as an acyl chloride **409** in a pyrrole (**410**) and Friedel–Crafts acylation to yield a building block, in which the strap is appended by two pyrrole units (**411**). **411** is then converted into the pyrrole aldehyde **412** and further to the chloromethyl derivative **413**. This could then be condensed with two equivalents of a second pyrrole to yield a β-β-linked bisdipyrromethane **414**. Further transformations change the α-substituents on dipyrromethane units to H/CHO, which then can undergo acid-catalyzed condensation and oxidation to the porphyrin **415**. Although a laborious multi-step synthesis, the final porphyrin-forming steps could be accomplished in 40–50% yield. Similar strategies have been employed for various other superstructured porphyrins. For example, Traylor and co-workers earlier used the linker **416** to generate the cyclophane porphyrin in **417** in ~5% yield [326].

S_4-symmetric "capped" porphyrins can easily be prepared by providing the cap as a tetraaldehyde that can then be used in pyrrole tetramerization reactions. A classic example is Baldwin's synthesis of the capped porphyrin **419** (Figure 3.60) [327]. Reaction of the tetraaldehyde **418** with pyrrole in propionic acid under heating at reflux for 1.5 h

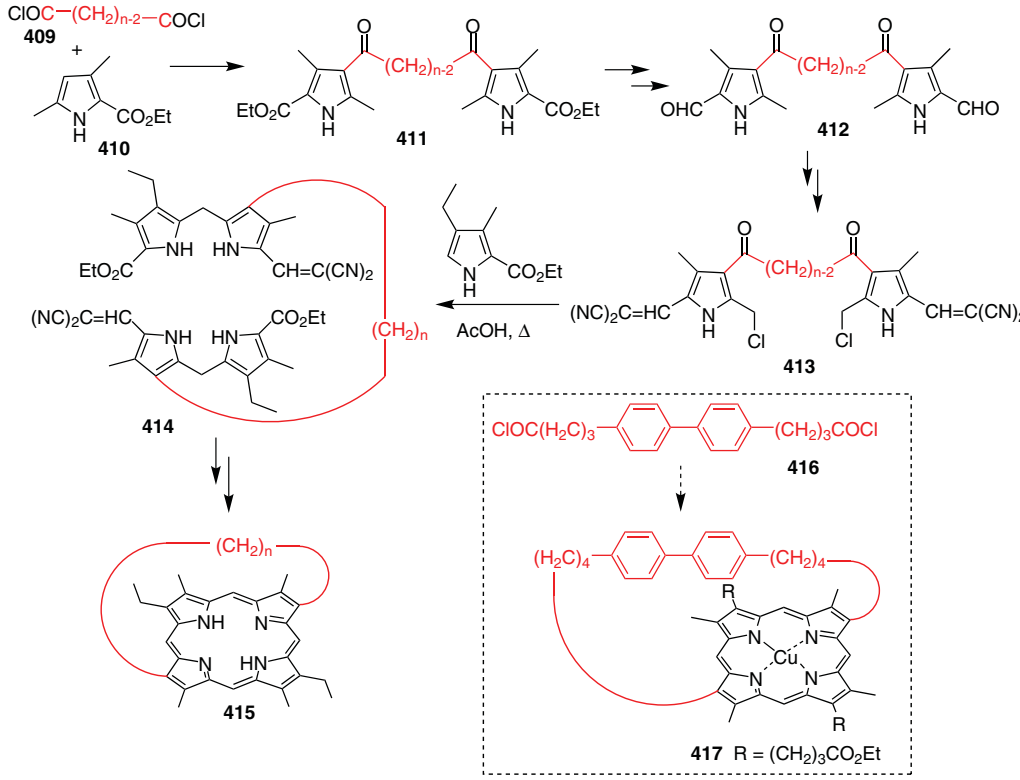

Figure 3.59 Sample syntheses of a strapped and a cyclophane porphyrin.

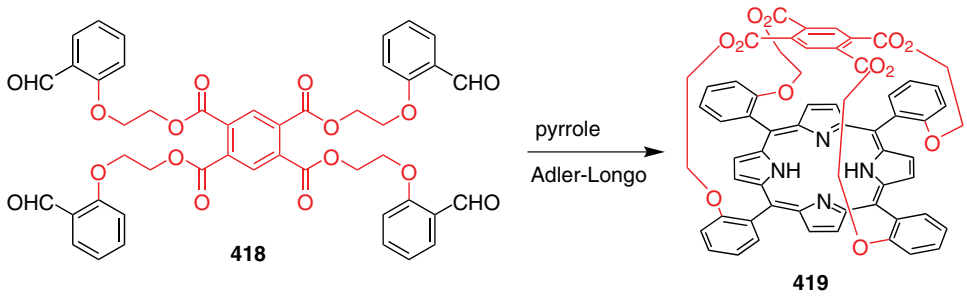

Figure 3.60 Synthesis of a capped porphyrin.

gave a yield of about 2% of the target porphyrin. Alternatively, they used the respective 5,10,15,20-tetrakis(2-hydroxyethoxyphenyl)porphyrin for esterification with pyromellitoyl chloride in boiling methanol and could prepare the same porphyrin in a 15% yield. The use of a linked bisaldehyde in pyrrole condensation reactions allows the generation of porphyrins with two straps, although a mixture of the respective "cross-*trans*"-, "adjacent-*trans*"-, and "adjacent-*cis*"-linked double strapped porphyrins is generated [328].

The most enduring concept to come from these and many other studies [329] was the use of the so-called picket fence porphyrins by Collman in 1977 [330, 331]. This

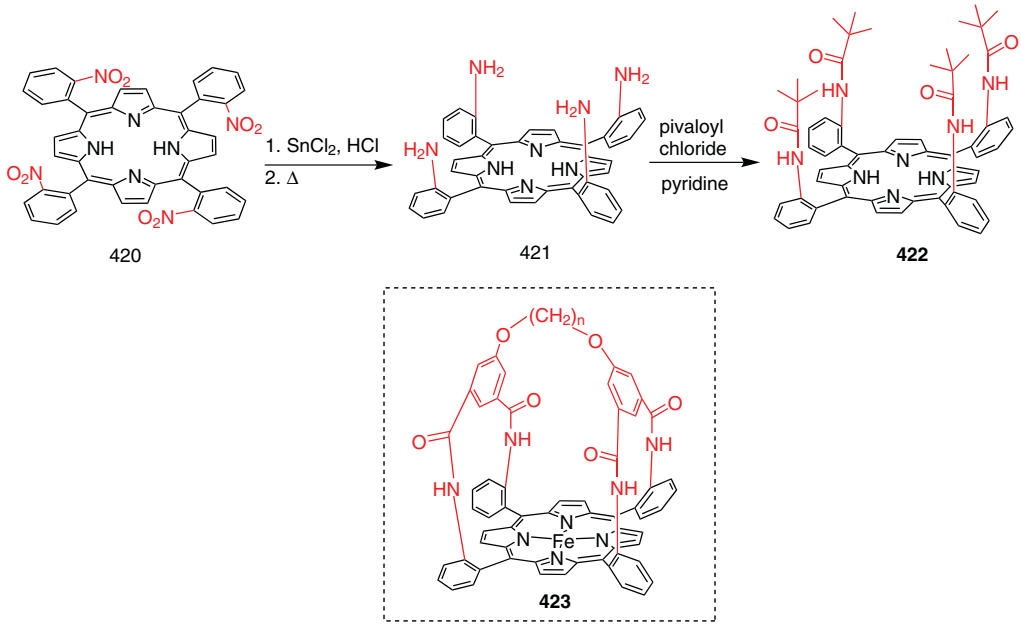

Figure 3.61 Synthesis of a picket fence and picnic basket porphyrin.

relies on using specific atropisomers of porphyrins to position peripheral substituents in a unique relative orientation. The classic synthesis (Figure 3.61) involved preparation of 5,10,15,20-tetrakis(2-nitrophenyl)porphyrin **420**. This was then reduced to the tetraaminophenylporphyrin **421**. As it is derived from a previous nonselective condensation, the amino residues will point in arbitrary directions relative to each other and the porphyrin faces (↑↑↑↑, ↑↑↑↓, ↑↑↓↓, ↑↓↓↑; see Chapter 2, Figure 2.21). However, thermal equilibration (based on rotation about the C_m-C_i bond) allowed the formation of the αααα-atropisomer, in which all four amino groups point in one direction (↑↑↑↑) [332].

Once formed, the atropisomers are relatively stable at room temperature. This allowed the use of αααα-**421** in further reactions; for example, reaction with pivaloyl chloride to give **422**, which, due to steric hindrance, is even more stable toward atropisomerization than **421**. Compound **422** was aptly termed "picket fence porphyrin," and it and related compounds proved highly successful as biomimetic heme-oxygen binding systems or cytochrome models after incorporation of iron and placement of axial ligands [329]. The picket fence porphyrin strategy gave rise to many similar compounds. For example, the reaction of **421** with suitable tetraacid chlorides gave the picnic basket porphyrins **423**, where a linker connects two handles attached to two adjacent meso-residues [332]. Recently, they have emerged again in sensing applications [333].

3.8.5 Chiral Porphyrins

Porphyrin chirality is typically only addressed in the context of catalytic, sensing, or supramolecular studies, and less in the context of synthetic studies. However, a brief look at fundamental chiral porphyrin systems is warranted. A planar porphyrin can be converted into a chiral system via incorporation of suitable substituents and/or out-of-plane distortions, or by selecting specific atropisomers. This class of intrinsically chiral porphyrins does

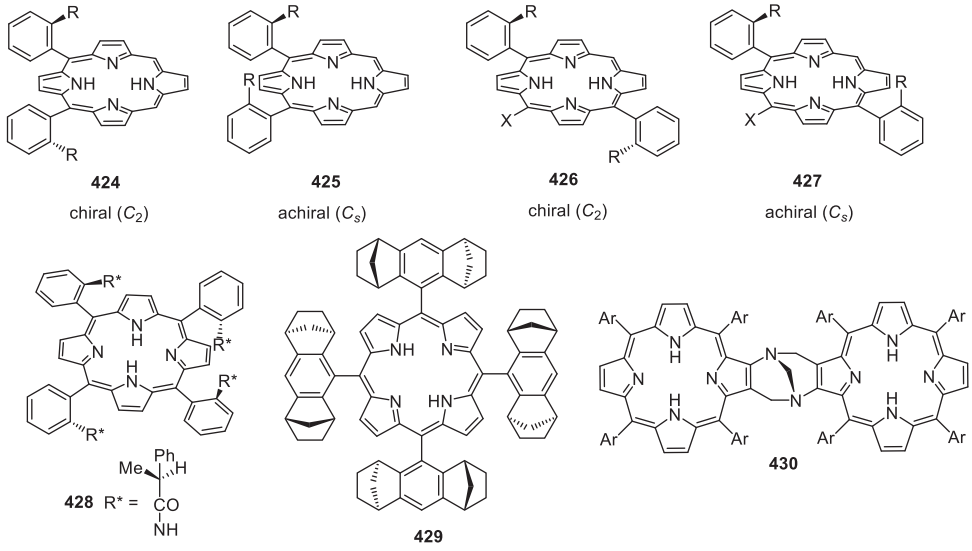

Figure 3.62 Chiral porphyrin systems.

not require chiral auxiliary elements. Classic examples are strapped porphyrins, but even deceptively simple porphyrins can be chiral. For example, the 5,15-, or 5,10-disubstituted porphyrins (Figure 3.62) can be either chiral (**424, 426**) or achiral (**425**, **427**) depending on the orientation of the substituents [334, 335]. This also illustrates the care that has to be taken when working with and analyzing atropisomers.

On the other hand, extrinsically chiral porphyrins are generated by incorporation of chiral substituents. Classic examples are Groves' chiral picket-fence-type porphyrin **428** (prepared by strategies similar to those given in Section 3.8.4) [336] and Halterman's porphyrin (prepared by condensation of pyrrole with the resolved chiral aldehyde) **429** [337] and many more [338]. The next step was the generation of bis- or oligomeric porphyrins with chiral bridges, for example, **430**, as found in Tröger's base, prepared by Crossley et al. [339]. This was then evolved into a whole range of chiral porphyrin tweezers and related systems, which exhibit intricate supramolecular chirality [340]. Note that axial chirality, as in **252**, is another possibility, as is binding of chiral axial ligands, and that many naturally occurring porphyrins, such as the chlorophylls and corrinoids, contain chiral centers [73].

3.8.6 Cofacial Bisporphyrins

How about if one wants to access a very specific three-dimensional arrangement of two porphyrins? The so-called "special pair" is one of the fundamental units in photosynthesis, in which two (bacterio)chlorophylls are situated close to each other in a face-to-face manner with a significant degree of overlap between the two π-systems [73]. This "dimer" is responsible for the charge separation step, the key reaction in the conversion of light energy into (bio)chemical energy.

In terms of molecular design, one needs to bring two porphyrin rings close to each other and hold them in a fixed position relative to each other. Again, there are many avenues to construct such systems – historically many used ester or amide units to create cyclophane-type

structures [341] – so we will only look at simple carbon atom bridged systems held together by one linker unit. A classic approach was to prepare a rigid bisaldehyde linker unit **431**, for example, a bisformylanthracene, and then use this as a component in pyrrole condensation reactions (Figure 3.63, **432**) [342]. We had shown above how to use a linearly linked bisporphyrin **307** to form a related system **308** [250], and one can use appropriate synthons for transition-metal-catalyzed reactions between a linker (**433**) and two porphyrins **434** [343].

Alternatively, one can use the propensity of porphyrins to π-aggregate as a directing tool in synthetic reactions. For example, the -CH_2CH_2-linked bisporphyrin **436** is easily prepared from the hydroxymethyl precursor **435**. This can then be converted into the ethene-bridged dimer. Depending on the reaction conditions, a mixture of *cis*/*trans* isomers (**437**, **438**) could be obtained and separated [344]. Even simpler is the use of meso-formylporphyrins **439** in McMurry couplings [105, 107]. Here, aggregation of the formyl precursors brings them together in the "correct" orientation to allow isolation of the *cis*-bridged systems **438**, despite the *trans*-isomer being thermodynamically favored. The same method could also be used with formylchlorins **440**, allowing the preparation of cofacial bischlorins (albeit more complicated due to the formation of different atropisomers and the presence of chiral elements; see **441** and **442**), which are more related to the situation in natural photosynthesis [345, 346].

3.8.7 *Push-Pull* Porphyrins

Last but not least, we shall take a look at a class of porphyrins more related to practical applications. Many optoelectronic devices for telecommunications, information storage, optical switching, and signal processing require materials with extraordinary nonlinear optical (NLO) responses. Porphyrins have proved to be valuable candidates for such systems due to their thermal and chemical stability. Furthermore, the chemical, physical, and optoelectronic properties of these macrocycles can be easily tailored and fine-tuned through molecular symmetry, metal complexation, strength of the molecular dipole moment, or synthetic modifications. Their strong excited state properties, together with the large library of synthetic methodologies outlined in this chapter, makes porphyrins very suitable for optoelectronic uses [347]. Most of these require *push-pull* porphyrins, which are systems bearing an electron-donor and an electron-acceptor group. In these donor-π-acceptor systems, electrons are transferred from the electron-donating group through a π-spacer to the electron-withdrawing anchoring group. Porphyrins have proved to be very suitable as π-spacer moiety due to their broad and intense absorption properties.

In the simplest terms, *push-pull* porphyrins are unsymmetrically substituted porphyrins, of which there are many. Their specific synthesis for use in NLO was pioneered by Suslick and Therien's groups. Suslick et al. reported the synthesis of a series of difunctionalized tetraarylporphyrins in 1992 [348]. These tetraaryl systems are substituted with nitro groups as electron-acceptor units and amine groups as electron donors. The synthesis involved the partial reduction of 5,10,15,20-tetrakis(4-nitrophenyl)porphyrin **364** to yield porphyrins **443**, **444**, and **445** (Figure 3.64). They studied the electric-field-induced second-harmonic generation for these systems which gave a moderately light NLO response. Therien and co-workers in 1996 synthesized copper and zinc derivatives of 5-[[4-(dimethylamino) phenyl]ethynyl]-15-[(4-nitrophenyl)ethynyl]-10,20-diphenylporphyrin by two stepwise Sonogashira reactions of **281**. The compounds exhibited large first-order hyperpolarizabilities and proved that *push-pull* porphyrins, with their extended conjugation (due to the arylethynyl residues), are excellent candidates for NLO materials [349].

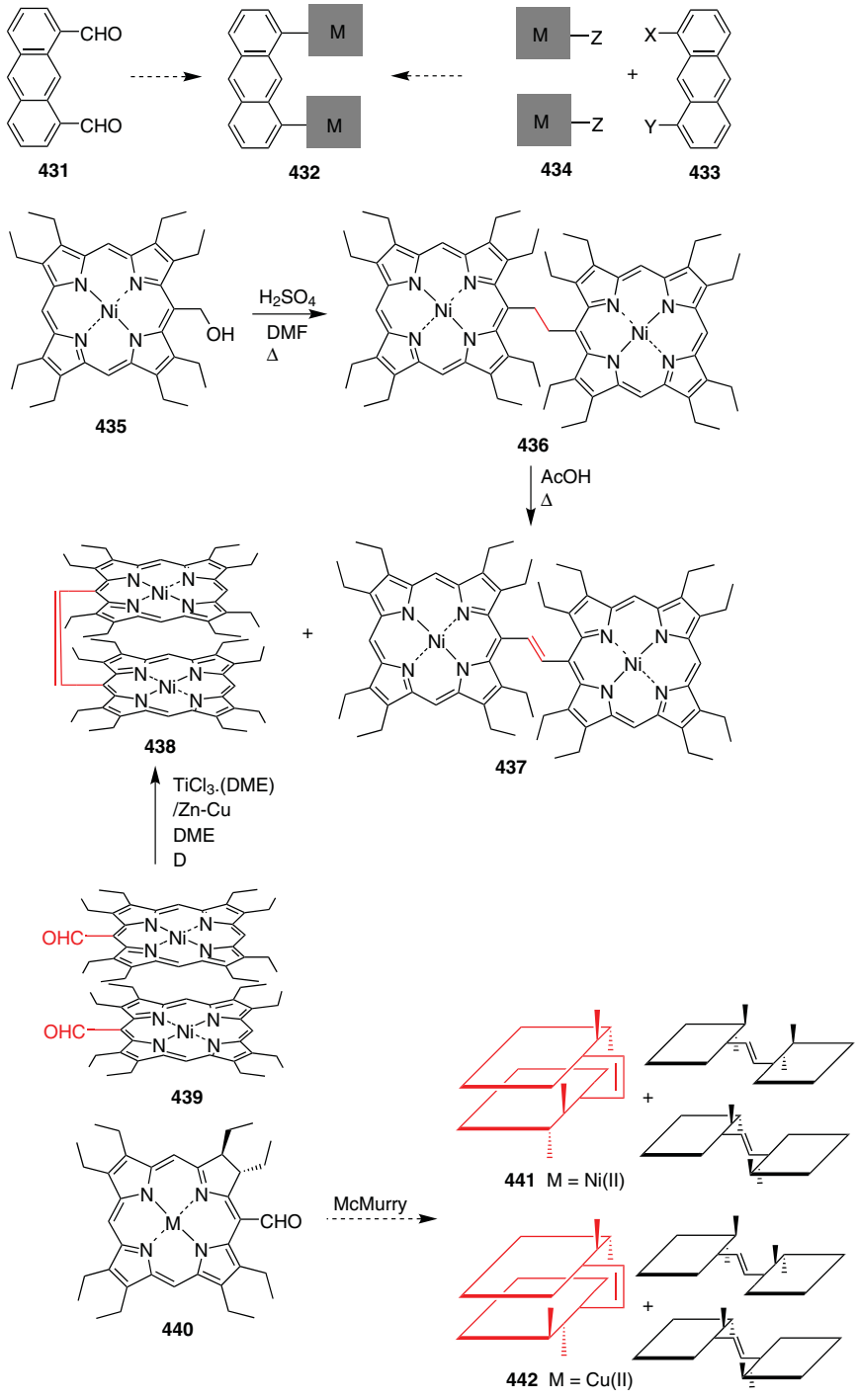

Figure 3.63 Synthetic approaches toward cofacial bisporphyrins.

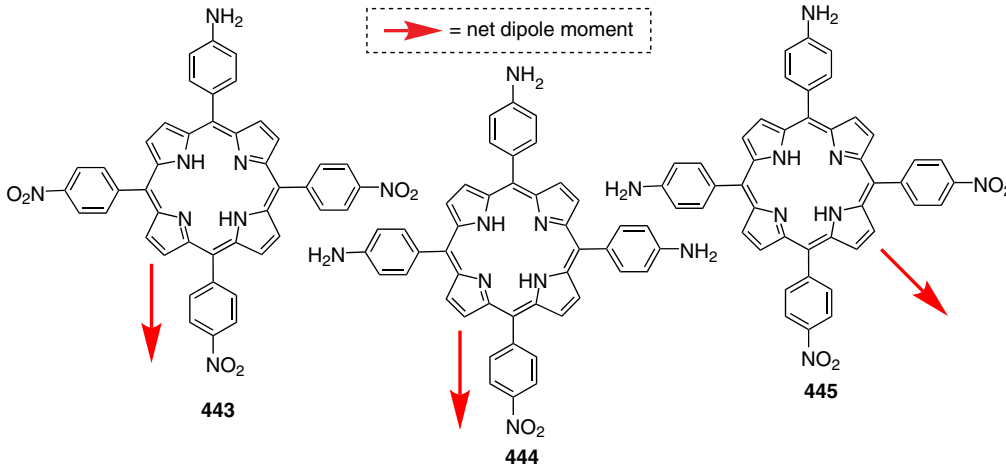

Figure 3.64 First-generation *push-pull* porphyrins.

Although the quest for porphyrin-based NLO materials continues [347], *push-pull* porphyrins have now become a focus of interest as sensitizers in DSSCs, as developed by Grätzel and O'Regan in 1991 [350]. DSSCs are photovoltaic devices that consist of an electrode, an electrolyte, and a dye-sensitized photoanode. The performance of such solar cells strongly depends on the photoactive element, that is, the sensitizer dye. Initially, ruthenium sensitizers were the dyes of choice for DSSCs, owing to their favorable power conversion efficiency (PCE). However, porphyrins became popular as sensitizers with the evolution of the *push-pull* systems, which helped to improve light absorption at the desired wavelengths for DSSCs (for example, via modulation of the π-system through conjugated substituents and linkers) [351].

Grätzel's group has continuously pushed the development of optimized porphyrins as sensitizers for DSSCs and has increased the efficiency from 5.6% PCE in 2005 to >12% in 2011 with compound **446** (Figure 3.65) [352]. Many different acceptor and donor units have been explored, but the use of meso-diarylaminoaryl- and (hetero)aryl-carboxylic acids has been best proved with PCE currently at >13% [353]. For example, Imahori and co-workers used zinc porphyrins with multiple diarylamino groups (**447**) and showed that replacement of one carboxyphenyl group with a carboxyphenylethynyl group and one carboxyphenyl group with a bulkier mesityl group led to an enhancement of the absorption properties [354]. Likewise, dialkylaminophenylethynyl groups have been used, for example, in Pizotti's work, where they compared bis(3,5-*di-tert*-butylphenyl)porphyrins with a dimethylaminophenylethynyl and a carboxyphenylethynyl group (**448**) with similar β-substituted systems [355].

Next to the type of residues used, the positioning of the *push*- and *pull*-substituents is equally important, and this relates to the intramolecular dipole moment (Figure 3.66). Most of the initial work used 5,15-disubstituted porphyrins in which the dipole runs along the meso-meso axis of the porphyrin. These have been shown to give excellent PCEs, as evidenced by **452** (PCE = 13%) [353]. The 5,15-disubstituted porphyrin was obtained through a condensation reaction and then meso-monobromination followed by a zinc insertion. After this, a TIPS acetylene linker was installed via a Sonogashira cross-coupling reaction, followed by another bromination. The electron-donor unit was then introduced via a Buchwald–Hartwig amination, and the acceptor unit was attached in the last step

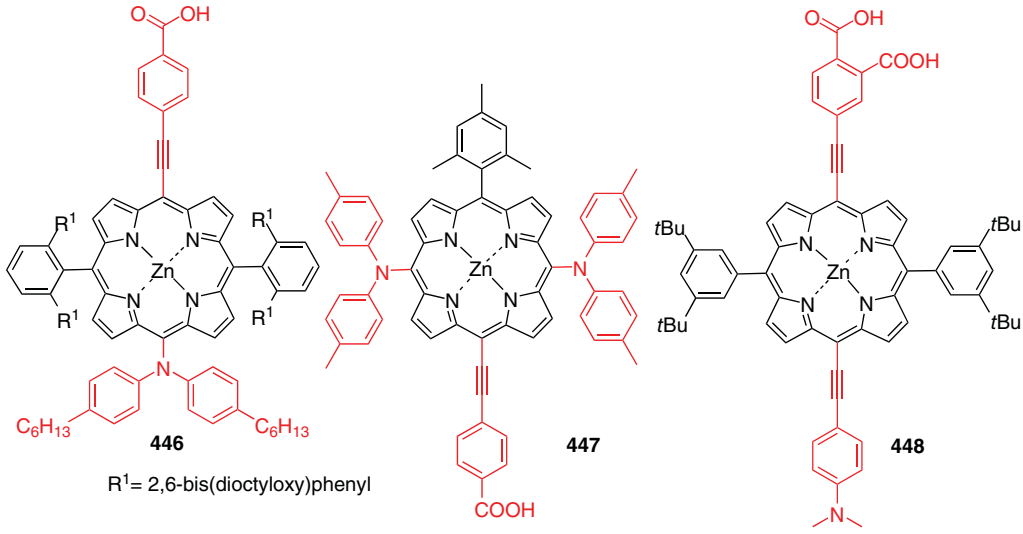

Figure 3.65 *Push-pull* porphyrins used in dye-sensitized solar cells.

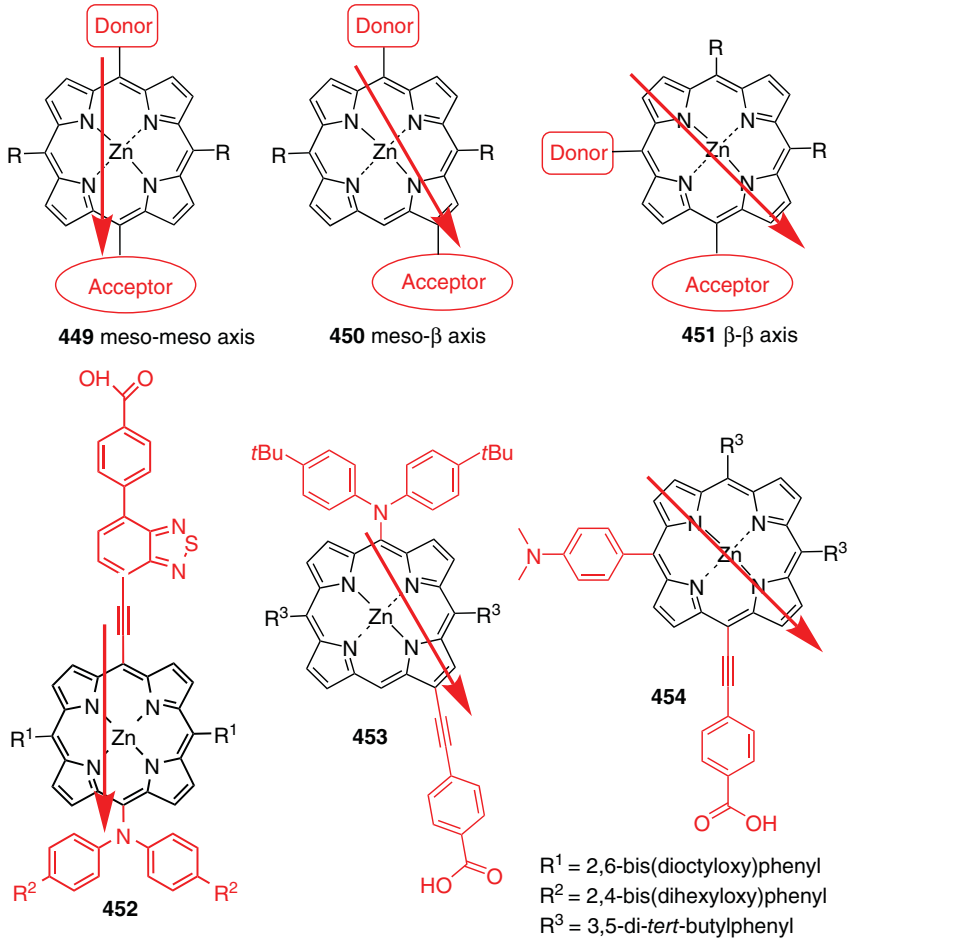

Figure 3.66 *Push-pull* porphyrins with different intramolecular dipole moment orientations.

via a Sonogashira cross-coupling reaction, after deprotection of the TIPS linker. Many other published works follow this synthetic strategy or use slightly modified pathways. Chang et al. reported the synthesis of a 5,15-disubstituted *push-pull* porphyrin with a dimethylaminophenyl-ethynyl group as the donor unit. The 4-ethynyl-*N,N*-dimethylaniline group was attached to the dibromo porphyrin via a Sonogashira reaction and the acceptor unit introduced as 4-ethynyl benzoic acid in one step, rather than in a two-step synthesis [356]. Alternatively, the donor unit can be introduced via an organolithium reaction, as shown by Meindl et al. [357].

Besides *push-pull* porphyrins with a dipole along the meso-meso axis (**449**), Ishida et al. published a series of functionalized porphyrin systems in which the dipole moment goes through the meso-β axis (**450**, for example, compound **453**) [358]. Here, one or two acceptor units were introduced at the β-position of the *push-pull* porphyrins. After bromination and metal insertion of a 5,15-disubstituted porphyrin, the electron-donor unit was attached via a Buchwald–Hartwig amination. Subsequent iridium-catalyzed borylation gave the β-mono- or -difunctionalized porphyrin. In the next step, a series of vinyl esters were attached to the porphyrin via rhodium-catalyzed reactions, or various terminal alkyne derivatives were introduced via palladium-catalyzed reactions.

Alternatively, one can establish a different dipole moment orientation by using 5,10-*push-pull* porphyrins (e.g., **445** or **447**). Their dipole moment goes through the β-β-axis (**451**), and this arrangement has been shown to enhance many electronic properties of porphyrins such as the nonlinear absorption response in 5,10-A_2B_2-type systems **17** [359]. These can be easily prepared from the 5,10-A_2-porphyrins **37** through meso-dihalogenation followed by the respective transition-metal-catalyzed reaction. In Imahori's series with two electron-donor units and one electron-acceptor unit, a porphyrin where the electron-donor units are in a 5,10 conformation was reported. A 5-substituted porphyrin was brominated followed by metal insertion and the introduction of a triisopropylsilylacetylene linker. The amino groups were then either installed directly in the next step utilizing *N,N*-bis(4-methylphenyl)amine, $PhI(OAc)_2$, and $NaAuCl_4 \bullet 2H_2O$, or after further functionalization using a dibrominated porphyrin via Pd-catalyzed reactions [354, 360]. Naturally, mixed condensations can also be used for simple A_xB_y systems to quickly generate libraries of porphyrins with different *push-pull* orientations for comparative analyses, but they do require extensive chromatography [361].

A synthetic study on 5,10-substituted *push-pull* porphyrins **454** and their 5,15-substituted counterparts used the controlled stepwise introduction of one donor and one acceptor group for a comparative analysis of the different synthetic strategies [357]. One pathway involved the bromination and metallation of the porphyrin starting material followed by introduction of *N,N*-bis(4-*tert*-butylphenyl)amine through a Buchwald–Hartwig amination. The electron-acceptor group was then introduced after another bromination in one step as an alkynylphenyl ester via a Sonogashira cross-coupling reaction. The other pathway utilized the versatile organolithium reaction and introduced a 4-*N,N*-dimethylaniline group directly to the porphyrin core without any prior functionalization. Finally, the porphyrin was brominated and metallated and the acceptor unit again introduced via a Sonogashira reaction.

A comparison of the structures shown in the last three figures, and the methods used for their preparation, illustrates how far synthetic porphyrin chemistry has advanced in just 25 years on its way into the twenty-first century! For a more historical view on the

development of synthetic organic chemistry of porphyrins, the reader is referred to a recent tutorial-style review which discusses classic total syntheses and mechanistic organic chemistry of porphyrins in more detail than was possible here [362].

Acknowledgments

Our own work on porphyrins was generously supported over the years by grants from the Deutsche Forschungsgemeinschaft (DFG), Fonds der Chemischen Industrie (FCI), Irish Research Council (IRC), Health Research Board (HRB), the European Commission, and Science Foundation Ireland (SFI).

This article is dedicated to the memory of Silviu Balaban [1958–2016], whom we must miss much too early. M.O.S. gladly acknowledges his many suggestions, insights, enthusiasm, hospitality, and friendship over many years.

References

1 Fischer, H. and Orth, H. (1934–1940). *Die Chemie des Pyrrols*. Leipzig: Akademische Verlagsgesellschaft.
2 Smith, K.M. (ed.) (1975). *Porphyrins and Metalloporphyrins*. New York: Elsevier Scientific Publishing.
3 Dolphin, D. (ed.) (1978–1979). *The Porphyrins*, vol. 1–6. New York: Academic Press.
4 Kadish, K.M., Smith, K.M., and Guilard, R. (ed.) (2000). *The Porphyrin Handbook*, vol. 1–10. New York: Academic Press.
5 Cavaleiro, J.A.S. and Smith, K.M. (1989). Porphyrin synthesis. *Revista portuguesa de química* 31: 29–41.
6 Drabkin, D.L. (1978). Selected landmarks in the history of porphyrins and their biologically functional derivatives. In: *The Porphyrins*, vol. 1 (ed. D. Dolphin), 20–83. New York: Academic Press.
7 Rothemund, P. (1935). Formation of porphyrins from pyrrole and aldehydes. *Journal of the American Chemical Society* 57: 2010–2011.
8 Lindsey, J.S. (2000). Synthesis of *meso*-substituted porphyrins. In: *The Porphyrin Handbook*, vol. 1 (ed. K.M. Kadish, K.M. Smith and R. Guilard), 45–118. New York: Academic Press.
9 Adler, A.D., Longo, F.R., and Shergalis, W. (1964). Mechanistic investigations of porphyrin syntheses. I. Preliminary studies on *ms*-tetraphenylporphin. *Journal of the American Chemical Society* 86: 3145–3149.
10 Adler, A.D., Longo, F.R., Finarelli, J.D. et al. (1967). A simplified synthesis for *meso*-tetraphenylporphine. *The Journal of Organic Chemistry* 32: 476–477.
11 Dolphin, D. (1970). Porphyrinogens and porphodimethenes, intermediates in the synthesis of *meso*-tetraphenylporphyrins from pyrroles and benzaldehyde. *Journal of Heterocyclic Chemistry* 7: 275–283.
12 Vicente, M.G.H. and Smith, K.M. (2014). Syntheses and functionalizations of porphyrin macrocycles. *Current Organic Synthesis* 11: 3–28.

13 Volz, H. and Herb, G. (1983). meso-Tetraalkyl-porphyrine. *Zeitschrift für Naturforschung* 38b: 1240–1242.

14 Lindsey, J.S. (2009). Synthetic routes to *meso*-patterned porphyrins. *Accounts of Chemical Research* 43: 300–311.

15 Lindsey, J.S., Hsu, H.C., and Schreiman, I.C. (1986). Synthesis of tetraphenylporphyrins under very mild conditions. *Tetrahedron Letters* 27: 4969–4970.

16 Li, F., Yang, K., Tyhonas, J.S. et al. (1997). Beneficial effects of salts on an acid-catalyzed condensation leading to porphyrin formation. *Tetrahedron* 53: 12339–12360.

17 Onaka, M., Shinoda, T., Izumi, Y., and Nolen, E. (1993). Porphyrin synthesis in clay nanospaces. *Chemistry Letters* 22: 117–120.

18 Bonar-Law, R.P. (1996). Porphyrin synthesis in surfactant solution: multicomponent assembly in micelles. *The Journal of Organic Chemistry* 61: 3623–3634.

19 Petit, A., Loupy, A., Maillard, P., and Momenteau, M. (1992). Microwave irradiation in dry media: a new and easy method for synthesis of tetrapyrrolic compounds. *Synthetic Communications* 22: 1137–1142.

20 Chauhan, S.M.S., Sahoo, B.B., and Srinivas, K.A. (2001). Microwace-assisted synthesis of 5,10,15,20-tetraarylporphyrins. *Synthetic Communications* 31: 33–37.

21 Horn, S., Dahms, K., and Senge, M.O. (2008). Synthetic transformations of porphyrins – advances 2004-2007. *Journal of Porphyrins and Phthalocyanines* 12: 1053–1077.

22 Dean, M.L., Schmink, J.R., Leadbeater, N.E., and Brückner, C. (2008). Microwave-promoted insertion of group 10 metals into free base porphyrins and chlorins: scope and limitations. *Dalton Transactions* 1341–1345.

23 Pinto, S.M.A., Henriques, C.A., Tomé, V.A. et al. (2016). Synthesis of *meso*-substituted porphyrins using sustainable chemical processes. *Journal of Porphyrins and Phthalocyanines* 20: 45–60.

24 Neya, S. and Funasaki, N.J. (1997). A facile synthesis of the lowest homologues of *meso*-tetraalkylporphyrin. *Journal of Heterocyclic Chemistry* 34: 689–690.

25 Senge, M.O., Bischoff, I., Nelson, N.Y., and Smith, K.M. (1999). Synthesis, reactivity and structural chemistry of 5,10,15,20-tetraalkylporphyrins. *Journal of Porphyrins and Phthalocyanines* 3: 99–116.

26 Plamont, R., Kikkawa, Y., Takahashi, M. et al. (2013). Nanoscopic imaging of *meso*-tetraalkylporphyrins prepared in high yields enabled by Montmorrilonite K10 and 3 Å molecular sieves. *Chemistry – A European Journal* 19: 11293–11300.

27 Smith, K.M. (2000). Strategies for the synthesis of octaalkylporphyrin systems. In: *The Porphyrin Handbook*, vol. 1 (ed. K.M. Kadish, K.M. Smith and R. Guilard), 1–43. New York: Academic Press.

28 Lash, T.D. (2016). What's in a name? The MacDonald condensation. *Journal of Porphyrins and Phthalocyanines* 20: 855–888.

29 Arsenault, G.P., Bullock, E., and MacDonald, S.F. (1960). Pyrromethanes and porphyrins therefrom. *Journal of the American Chemical Society* 82: 4384–4389.

30 Sharada, D.S., Muresan, A.Z., Muthukumaran, K., and Lindsey, J.S. (2005). Direct synthesis of palladium porphyrins from acyldipyrromethanes. *The Journal of Organic Chemistry* 70: 3500–3510.

31 Dogutan, D.K., Ptaszek, M., and Lindsey, J.S. (2007). Direct synthesis of magnesium porphine via 1-formyldipyrromethane. *The Journal of Organic Chemistry* 72: 5008–5011.

32 Senge, M.O. and Davis, M. (2010). Porphyrin (porphine) – a neglected parent compound with potential. *Journal of Porphyrins and Phthalocyanines* 14: 557–567.

33 Wiehe, A., Shaker, Y.M., Brandt, J.C. et al. (2005). Lead structures for applications in photodynamic therapy. Part 1: synthesis and variation of m-THPC (Temoporfin) related amphiphilic A_2BC-type porphyrins. *Tetrahedron* 61: 5535–5564.

34 Treibs, A. and Häberle, N. (1968). Über die synthese und die Elektronenspektren *ms*-substituierter porphine. *Justus Liebigs Annalen der Chemie* 718: 183–207.

35 Baldwin, J.E., Crossley, M.J., Klose, T. et al. (1982). Syntheses and oxygenation of iron(II) "strapped" porphyrin complexes. *Tetrahedron* 38: 27–39.

36 Brückner, C., Posakony, J.J., Johnson, C.K. et al. (1998). Novel and improved synthesis of 5,15-diphenylporphyrin and its dipyrrolic precursors. *Journal of Porphyrins and Phthalocyanines* 2: 455–465.

37 Taniguchi, M., Balakumar, A., Fan, D. et al. (2005). Imine-substituted dipyrromethanes in the synthesis of porphyrins bearing one or two *meso* substituents. *Journal of Porphyrins and Phthalocyanines* 9: 554–574.

38 Fan, D., Taniguchi, M., Yao, Z. et al. (2005). 1,9-Bis(*N,N*-dimethylaminomethyl) dipyrromethanes in the synthesis of porphyrins bearing one or two *meso* substituents. *Tetrahedron* 61: 10291–10302.

39 Wiehe, A., Ryppa, C., and Senge, M.O. (2002). A practical synthesis of meso-monosubstituted, β-unsubstituted porphyrins. *Organic Letters* 4: 3807–3809.

40 Briñas, R.P. and Brückner, C. (2002). Synthesis of 5,10-diphenylporphyrin. *Tetrahedron* 58: 4375–4381.

41 Hatscher, S. and Senge, M.O. (2002). Synthetic access to 5,10-disubstituted porphyrins. *Tetrahedron Letters* 44: 157–160.

42 Ryppa, C., Senge, M.O., Hatscher, S.S. et al. (2005). Synthesis of mono- and disubstituted porphyrins: A- and 5,10-A_2-type systems. *Chemistry – A European Journal* 11: 3427–3442.

43 Falk, H. (1989). *The Chemistry of Oligopyrroles and Bile Pigments*. Wien, New York: Springer Verlag.

44 Smith, K.M. (2000). Cyclizations of a,c-biladiene salts to give porphyrins and their derivatives. In: *The Porphyrin Handbook*, vol. 1 (ed. K.M. Kadish, K.M. Smith and R. Guilard), 119–148. New York: Academic Press.

45 Dogutan, D.K., Zaidi, S.H.H., Thamyongkit, P., and Lindsey, J.S. (2007). New route to ABCD-porphyrins via bilanes. *The Journal of Organic Chemistry* 72: 7701–7714.

46 Johnson, A.W. and Kay, I.T. (1961). The formation of porphyrins by the cyclisation of bilenes. *Journal of the Chemical Society* 2418–2423.

47 Smith, K.M. and Craig, G.W. (1983). Porphyrin synthesis through tripyrrins – an alternate approach. *The Journal of Organic Chemistry* 48: 4302–4306.

48 Wallace, D.M., Leung, S.H., Senge, M.O., and Smith, K.M. (1993). Rational tetraarylporphyrin syntheses: tetraarylporphyrins from the MacDonald route. *The Journal of Organic Chemistry* 58: 1245–1251.

49 Boudif, A. and Momenteau, M. (1994). Synthesis of a porphyrin-2,3-diacrylic acid using a new '3 + 1' type procedure. *Journal of the Chemical Society, Chemical Communications* 2069–2070.

50 Lash, T.D. (1996). Porphyrin synthesis by the "3+1" approach: new applications for an old methodology. *Chemistry – A European Journal* 2: 1197–1200.

51 Jeyakumar, D., Snow, K.M., and Smith, K.M. (1988). Electrosynthesis of porphyrins from *a,c*-biladienes. *Journal of the American Chemical Society* 110: 8562–8564.

52 Inhoffen, H.H., Fuhrhop, J.-H., Voigt, H., and Brockmann, H. (1966). Zur weiteren Kenntnis des Chlorophylls und Hämins. 6. Formylierung der meso-Kohlenstoffatome von Alkyl-substituierten Porphyrinen. *Liebigs Annalen der Chemie* 695: 133–145.

53 Whitlock, H.W. and Hanauer, R. (1968). Octaethylporphyrin. *The Journal of Organic Chemistry* 33: 2169–2171.

54 Sessler, J.L., Mozaffari, A., and Johnson, M.R. (1991). 3,4-Diethylpyrrole and 2,3,7,8,12,13,17,18-octaethylporphyrin. *Organic Syntheses* 70: 68–77.

55 Barton, D.H.R., Kervagoret, J., and Zard, S.Z. (1990). A useful synthesis of pyrroles from nitroolefins. *Tetrahedron* 46: 7587–7598.

56 Fischer, H. and Zeile, K. (1929). Synthese des Hämatoporphyrins, Protoporphyrins und Hämins. *Liebigs Annalen der Chemie* 468: 98–116.

57 Sessler, J.L., Gale, P.A., and Cho, W.-S. (2006). *Anion Receptor Chemistry*. London: RSC Publishing.

58 Floriani, C. (1996). The porphyrinogen-porphyrin relationship: the discovery of artificial porphyrins. *Chemical Communications* 1257–1263.

59 Gale, P.A., Sessler, J.L., and Král, V. (1998). Calixpyrroles. *Chemical Communications* 1–8.

60 Baeyer, A. (1886). Ueber ein Condensationsproduct von Pyrrol mit Aceton. *Berichte der Deutschen Chemischen Gesellschaft* 19: 2184–2185.

61 Dwyer, P.N., Buchler, J.W., and Scheidt, W.R. (1974). Crystal structure and molecular stereochemistry of α,γ-dimethyl- α,γ-dihydrooctaethylporphyrinatonickel(II). *Journal of the American Chemical Society* 96: 2789–2795.

62 Bischoff, I., Feng, X.D., and Senge, M.O. (2001). One-pot synthesis of functionalized, highly substituted porphodimethenes. *Tetrahedron* 57: 5573–5583.

63 Barkigia, K.M., Berber, M.D., Fajer, F. et al. (1990). Nonplanar porphyrins – X-ray structures of (2,3,7,8,12,13,17,18-Octaethyl-5,10,15,20-tetraphenylporphyrinato)zinc(II) and (2,3,7,8,12,13,17,18-octamethyl-5,10,15,20-tetraphenylporphyrinato)zinc(II). *Journal of the American Chemical Society* 112: 8851–8857.

64 Senge, M.O. (2006). Exercises in molecular gymnastics – bending, stretching and twisting porphyrins. *Chemical Communications* 243–256.

65 Kalisch, W.W. and Senge, M.O. (1998). Facile *meso* functionalization of porphyrins by nucleophilic substitution with organolithium reagents. *Angewandte Chemie International Edition* 37: 1107–1109.

66 Senge, M.O. (2000). Highly substituted porphyrins. In: *The Porphyrin Handbook*, vol. 1 (ed. K.M. Kadish, K.M. Smith and R. Guilard), 239–347. New York: Academic Press.

67 Carvalho, C.M.B., Brocksom, T.J., and de Oliveira, K.T. (2013). Tetrabenzoporphyrins: synthetic developments and applications. *Chemical Society Reviews* 42: 3302–3317.

68 Helberger, J.H., von Rebay, A., and Hevér, D.B. (1938). Über die Einwirkung von Metallen auf *o*-Cyanacetophenon sowie auf 3-Methylphtalimidin: Synthese des Tetrabenzoporphins. III. Mitteilung zur Kenntnis der Benzoporphine. *Justus Liebigs Annalen der Chemie* 533: 197–215.

69 Filatov, M.A., Cheprakov, A.V., and Beletskaya, I.P. (2007). A facile and reliable method for the synthesis of tetrabenzoporphyrin from 4,7-dihydroisoindole. *European Journal of Organic Chemistry* 3468–3475.

70 Ito, S., Murashima, T., Uno, H., and Ono, N. (1998). A new synthesis of benzoporphyrins using 4,7-dihydro-4,7-ethano-*2H*-isoindole as a synthon of isoindole. *Chemical Communications* 1661–1662.

71 Lash, T.D. (2000). Synthesis of novel porphyrinoid chromophores. In: *The Porphyrin Handbook*, vol. 2 (ed. K.M. Kadish, K.M. Smith and R. Guilard), 125–199. New York: Academic Press.

72 Scheer, H. (ed.) (1991). *Chlorophylls*. Boca Raton: CRC Press.

73 Senge, M.O., Ryan, A.A., Letchford, K.A. et al. (2014). Chlorophylls, symmetry, chirality, and photosynthesis. *Symmetry* 6: 781–843.

74 Eschenmoser, A. and Wintner, C.E. (1977). Natural product synthesis and vitamin B_{12}. *Science* 196: 1410–1426.

75 Woodward, R.B., Ayer, W.A., Beaton, J.M. et al. (1990). The total synthesis of chlorophyll *a*. *Tetrahedron* 46: 7599–7659.

76 Battersby, A.R. (2000). Tetrapyrroles: the pigments of life. *Natural Product Reports* 17: 507–526.

77 Montforts, F.-P., Gerlach, B., and Hoper, F. (1994). Discovery and synthesis of less common natural hydroporphyrins. *Chemical Reviews* 94: 327–347.

78 Taniguchi, M. and Lindsey, J.S. (2017). Synthetic chlorins, possible surrogates for chlorophylls, prepared by derivatization of porphyrins. *Chemical Reviews* 117: 344–535.

79 Lindsey, J.S. (2015). *De Novo* synthesis of Gem-Dialkyl Chlorophyll analogues for probing and emulating our green world. *Chemical Reviews* 115: 6534–6620.

80 Snow, R.J., Fookes, C.J.R., and Battersby, A.R. (1981). Synthetic routes to C-methylated chlorins. *Journal of the Chemical Society, Chemical Communications* 524–526.

81 Battersby, A.R., Fookes, C.J.R., and Snow, R.J. (1984). Synthetic studies Relevant to biosynthetic research on vitamin B_{12}. Part 1. synthesis of *C*-methylated chlorins based on 1-pyrrolines (3,4-dihydropyrroles). *Journal of the Chemical Society Perkin Transactions* 1: 2725–2732.

82 Battersby, A.R., Fookes, C.J.R., and Snow, R.J. (1984). Synthetic studies relevant to biosynthetic research on vitamin B_{12}. Part 2. synthesis of *C*-methylated chlorins *via* lactams. *Journal of the Chemical Society, Perkin Transactions* 1: 2733–2741.

83 Harrison, P.J., Fookes, C.J.R., and Battersby, A.R. (1981). Synthesis of the Isobacteriochlorin macrocycle – a photochemical approach. *Journal of the Chemical Society, Chemical Communications* 797–799.

84 Battersby, A.R., Dutton, C.J., Fookes, C.J.R., and Turner, S.P.D. (1983). Synthesis of the chlorin macrocycle by a photochemical approach. *Journal of the Chemical Society, Chemical Communications* 1235–1237.

85 Harrison, P.J., Sheng, Z.-C., Fookes, C.J.R., and Battersby, A.R. (1987). Synthetic studies relevant to biosynthetic research on vitamin B_{12}. Part 4. Development of the photochemical route to isobacteriochlorins. *Journal of the Chemical Society, Perkin Transactions* 1: 1667–1678.

86 Battersby, A.R., Dutton, C.J., and Fookes, C.J.R. (1988). Synthetic Studies relevant to biosynthetic research on vitamin B_{12}. Part 7. synthesis of (±)-bonellin dimethyl ester. *Journal of the Chemical Society, Perkin Transactions* 1: 1569–1576.

87 Jacobi, P.A., Lanz, S., Ghosh, I. et al. (2001). A new synthesis of chlorins. *Organic Letters* 3: 831–834.

88 Montforts, F.-P. (1981). A directed synthesis of the chlorin system. *Angewandte Chemie, International Edition in English* 20: 778–779.

89 Montforts, F.P. and Schwartz, U.M. (1985). Ein gezielter Aufbau des Chlorinsystems. *Liebigs Annalen der Chemie* 1228–1253.

90 Montforts, F.-P. and Schwartz, U.M. (1985). Total synthesis of (±)-bonellin dimethyl ester. *Angewandte Chemie, International Edition in English* 24: 775–776.

91 Jacobi, P.A., Brielmann, H.L., Chiu, M. et al. (2011). 4-Alkynoic acids in the synthesis of biologically important tetrapyrroles. *Heterocycles* 82: 1029–1081.

92 O'Neal, W.G., Roberts, W.P., Ghosh, I., and Jacobi, P.A. (2005). Studies in chlorin chemistry. II. A versatile synthesis of dihydrodipyrrins. *The Journal of Organic Chemistry* 70: 7243–7251.

93 O'Neal, W.G., Roberts, W.P., Ghosh, I. et al. (2006). Studies in chlorin chemistry. 3. A practical synthesis of C,D-ring symmetric chlorins of potential utility in photodynamic therapy. *The Journal of Organic Chemistry* 71: 3472–3480.

94 O'Neal, W.G. and Jacobi, P.A. (2008). Toward a general synthesis of chlorins. *Journal of the American Chemical Society* 130: 1102–1108.

95 Strachan, J.P., O'Shea, D.F., Balasubramanian, T., and Lindsey, J.S. (2000). Rational synthesis of meso-substituted chlorin building blocks. *The Journal of Organic Chemistry* 65: 3160–3172.

96 Balasubramanian, T., Strachan, J.-P., Boyle, P.D., and Lindsey, J.S. (2000). Synthesis of *β*-substituted chlorin building blocks. *The Journal of Organic Chemistry* 65: 7919–7929.

97 Taniguchi, M., Ra, D., Mo, G. et al. (2001). Synthesis of meso-substituted chlorins via tetrahydrobilene-*a* Intermediates. *The Journal of Organic Chemistry* 66: 7342–7354.

98 Laha, J.K., Muthiah, C., Taniguchi, M. et al. (2006). Synthetic chlorins bearing auxochromes at the 3- and 13-positions. *The Journal of Organic Chemistry* 71: 4092–4102.

99 Ptaszek, M., McDowell, B.E., Taniguchi, M. et al. (2007). Sparsely substituted chlorins as core constructs in chlorophyll analogue chemistry. Part 1: synthesis. *Tetrahedron* 63: 3826–3839.

100 Taniguchi, M., Cramer, D.L., Bhise, A.D. et al. (2008). Accessing the near-infrared spectral region with stable, synthetic, wavelength-tunable bacteriochlorins. *New Journal of Chemistry* 32: 947–958.

101 Fuhrhop, J.-H. (1978). Irreversible reactions on the porphyrin periphery (excluding oxidations, reductions, and photochemical reactions). In: *The Porphyrins*, vol. 1, Part A (ed. D. Dolphin), 131–159. New York: Academic Press.

102 Vicente, M.G.H. (2000). Reactivity and functionalization of β-substituted porphyrins and chlorins. In: *The Porphyrin Handbook*, vol. 1 (ed. K.M. Kadish, K.M. Smith and R. Guilard), 149–199. New York: Academic Press.

103 Dahms, K., Senge, M.O., and Bakar, M.B. (2007). Exploration of *meso*-substituted formylporphyrins and their Grignard and Wittig reactions. *European Journal of Organic Chemistry* 3833–3848.

104 Brockmann, H. Jr., Bliesener, K.-M., and Inhoffen, H.H. (1968). Zur weiteren Kenntnis des Chlorophylls und des Hämins, XX. Formyl- und Acetyl-substituierte Deuteroporphyrine. *Liebigs Annalen der Chemie* 718: 148–161.

105 Vicente, M.G.H. and Smith, K.M. (1991). Vilsmeier reactions of porphyrins and chlorins with 3-(dimethylamino)acrolein to give *meso*-(2-formylvinyl)porphyrins: new syntheses of benzochlorins, benzoisobacteriochlorins, and benzobacteriochlorins and reductive coupling of porphyrins and chlorins using low-valent titanium complexes. *The Journal of Organic Chemistry* 56: 4407–4418.

106 Senge, M.O., Hatscher, S.S., Wiehe, A. et al. (2004). The dithianyl group as a synthon in porphyrin chemistry: condensation reactions and preparation of formylporphyrins under basic conditions. *Journal of the American Chemical Society* 126: 13634–13635.

107 Senge, M.O., Gerzevske, K.R., Vicente, M.G.H. et al. (1993). Models for the photosynthetic reaction center – synthesis and structure of porphyrin dimers with *cis*-ethene and *trans*-ethene and skewed hydroxylmethylene bridges. *Angewandte Chemie, International Edition in English* 32: 750–753.

108 Barloy, L., Dolphin, D., Dupré, D., and Wijesekera, T.P. (1994). Anomalous double cyclization reactions of *β*-formylporphyrins. *The Journal of Organic Chemistry* 59: 7976–7985.

109 Jin, L.M., Yin, J.J., Chen, L. et al. (2005). Metal-dependent halogenation and/or coupling reactions of porphyrins with $PhIX_2$ (X=Cl, F). *Synlett* 2893–2898.

110 Nudy, L.R., Hutchinson, H.G., Schieber, C., and Longo, F.R. (1984). A study of bromoporphins. *Tetrahedron* 40: 2359–2363.

111 Bonnett, R., Gale, I.A.D., and Stephenson, G.F. (1966). The *meso*-reactivity of porphyrins and related compounds. 2. Halogenation. *Journal of the Chemical Society C* 1600–1604.

112 Bhyrappa, P. and Krishnan, V. (1991). Octabromotetraphenylporphyrin and its metal derivatives – electronic structure and electrochemical properties. *Inorganic Chemistry* 30: 239–245.

113 Dolphin, D., Traylor, T.G., and Lie, L.Y. (1997). Polyhaloporphyrins: unusual ligands for metals and metal-catalyzed oxidations. *Accounts of Chemical Research* 30: 251–259.

114 Chumankov, D.E., Khoroshutin, A.V., Anisimov, A.V., and Kobrakov, K.I. (2009). Bromination of porphyrins (review). *Chemistry of Heterocyclic Compounds* 45: 259–283.

115 Bhyrappa, P. (2016). Recent advances in mixed β-pyrrole substituted *meso*-tetraphenylporphyrins. *Tetrahedron Letters* 57: 5150–5167.

116 Leroy, J. and Bondon, A. (2008). β-Fluorinated porphyrins and related compounds: an overview. *European Journal of Organic Chemistry* 417–433.

117 Senge, M.O. (2011). Stirring the porphyrin alphabet soup – functionalization reactions for porphyrins. *Chemical Communications* 47: 1943–1960.

118 Shanmugathasan, S., Johnson, C.K., Edwards, C. et al. (2000). Regioselective halogenation and palladium-catalysed couplings on 5,15-diphenylporphyrin. *Journal of Porphyrins and Phthalocyanines* 4: 228–232.

119 Nakano, A., Shimidzu, H., and Osuka, A. (1998). Facile regioselective meso-iodination of porphyrins. *Tetrahedron Letters* 39: 9489–9492.

120 Atefi, F., Locos, O.B., Senge, M.O., and Arnold, D.P. (2006). *meso*-Iodo- and *meso*-iodovinylporphyrins via organo-palladium porphyrins and the crystal structure of 5-iodo-10,20-diphenylporphyrin. *Journal of Porphyrins and Phthalocyanines* 10: 176–185.

121 Fujimoto, K., Yorimitsu, H., and Osuka, A. (2014). Facile preparation of *β*-haloporphyrins as useful precursors of *β*-substituted porphyrins. *Organic Letters* 16: 972–975.

122 Fukui, N., Yorimitsu, H., and Osuka, A. (2015). meso,β-oligohaloporphyrins as useful synthetic intermediates of diphenylamine-fused porphyrin and meso-to-meso β-to-β doubly butadiyne-bridged diporphyrin. *Angewandte Chemie International Edition* 54: 6311–6314.

123 Bonnett, R. and Stephens, G.F. (1965). The *meso* reactivity of porphyrins and related compounds. I. Nitration. *The Journal of Organic Chemistry* 30: 2791–2798.

124 Watanabe, T., Nishimura, S., Ogoshi, H., and Yoshida, Z. (1975). Orientation of electrophilic *meso*-substitution in metallooctaethylporphyrins. *Tetrahedron* 31: 1385–1390.

125 Baldwin, J.E. and DeBernardis, J.F. (1977). Efficient peripheral functionalization of capped porphyrins. *The Journal of Organic Chemistry* 42: 3985–3987.

126 Johnson, A.W. and Oldfield, D. (1965). The nitration and hydroxylation of aetioporphyrin I. *Journal of the Chemical Society C* 4303–4312.

127 Palacio, M., Mansuy-Mouries, V., Loire, G. et al. (2000). A new general method for selective β-polynitration of porphyrins; preparation and redox properties of Zn-porphyrins bearing one through to eight β-nitro substituents and X-ray structure of the first Zn β-pernitro porphyrin. *Chemical Communications* 1907–1908.

128 Smith, K.M., Barnett, G.H., Evans, B., and Martynenko, Z. (1979). Novel *Meso*-substitution reactions of metalloporphyrins. *Journal of the American Chemical Society* 101: 5953–5961.

129 Arnold, D.P., Bott, R.C., Eldridge, H. et al. (1997). Functionalization of 5,15-diphenylporphyrin: preparation and X-ray crystal structures of *meso* nitro, bromo, and trimethylsilylethynyl derivatives. *Australian Journal of Chemistry* 50: 495–503.

130 Barnett, G.H., Evans, B., Smith, K.M. et al. (1976). Synthesis of *meso*-pyridinium porphyrin salts. *Tetrahedron Letters* 4009–4012.

131 Barnett, G.H. and Smith, K.M. (1974). Reactions of some metalloporphyrin and metallochlorin π-cation radicals with nitrite. *Journal of the Chemical Society, Chemical Communications* 772–773.

132 Jaquinod, L. (2000). Functionalization of 5,10,15,20-tetra-substituted porphyrins. In: *The Porphyrin Handbook*, vol. 1 (ed. K.M. Kadish, K.M. Smith and R. Guilard), 201–237. New York: Academic Press.

133 Senge, M.O. (2005). Nucleophilic substitution as a tool for the synthesis of unsymmetrical porphyrins. *Accounts of Chemical Research* 38: 733–743.

134 Crossley, M.J., King, L.G., Pyke, S.M., and Tansey, C.W. (2002). Reaction of 5-nitro-octaethylporphyrins with nucleophiles. *Journal of Porphyrins and Phthalocyanines* 6: 685–694.

135 Devillers, C.H., Hebié, S., Lucas, D. et al. (2014). Aromatic nucleophilic substitution (S_NAr) of *meso*-nitroporphyrin with azide and amines as an alternative metal catalyst free synthetic approach to obtain *meso-N*-substituted porphyrins. *The Journal of Organic Chemistry* 79: 6424–6434.

136 Crossley, M.J., Harding, M.M., and Tansey, C.W. (1994). A convenient synthesis of 2-alkyl-5,10,15,20-tetraphenylporphyrins: reaction of metallo-2-nitro-5,10,15,20-tetraphenylporphyrins with grignard and organolithium reagents. *The Journal of Organic Chemistry* 59: 4433–4437.

137 Gong, L.-C. and Dolphin, D. (1985). Nucleophilic substitution of *meso*-nitrooctaethylporphyrins. *Canadian Journal of Chemistry* 63: 406–411.

138 Kielmann, M., Flanagan, K.J., Norvaiša, K. et al. (2017). Synthesis of a family of highly substituted porphyrin thioethers via nitro displacement in 2,3,7,8,12,13,17,18-octaethyl-5,10,15,20-tetranitroporphyrin. *The Journal of Organic Chemistry* 82: 5122–5134.

139 Ryan, A.A., Plunkett, S., Casey, A. et al. (2014). From thioether substituted porphyrins to sulfur linked porphyrin dimers: an unusual S_NAr *via* thiolate displacement? *Chemical Communications* 50: 353–355.

140 Senge, M.O. and Feng, X.D. (2000). Regioselective reaction of 5,15-disubstituted porphyrins with organolithium reagents – synthetic access to 5,10,15-trisubstituted porphyrins and directly *meso*-*meso*-linked bisporphyrins. *Journal of the Chemical Society, Perkin Transactions 1*: 3615–3621.

141 Senge, M.O., Kalisch, W.W., and Bischoff, I. (2000). The reaction of porphyrins with organolithium reagents. *Chemistry – A European Journal* 6: 2721–2738.

142 Feng, X.D., Bischoff, I., and Senge, M.O. (2001). Mechanistic studies on the nucleophilic reaction of porphyrins with organolithium reagents. *The Journal of Organic Chemistry* 66: 8693–8700.

143 Senge, M.O. and Bischoff, I. (2001). Regioselective synthesis of conformationally designed porphyrins with mixed *meso*-substituent types and distortion modes. *European Journal of Organic Chemistry* 1735–1751.

144 Feng, X.D. and Senge, M.O. (2000). One-pot synthesis of functionalized asymmetric 5,10,15,20-substituted porphyrins from 5,15-diaryl- or -dialkyl-porphyrins. *Tetrahedron* 56: 587–590.

145 Sergeeva, N.N., Shaker, Y.M., Finnigan, E.M. et al. (2007). Synthesis of hydroporphyrins based on comparative studies of palladium-catalyzed and non-catalyzed approaches. *Tetrahedron* 63: 12454–12464.

146 Senge, M.O. and Feng, X.D. (1999). Synthesis of directly meso-meso linked bisporphyrins using organolithium reagents. *Tetrahedron Letters* 40: 4165–4168.

147 Chen, B.M.L. and Tulinsky, A. (1972). Redetermination of the structure of porphine. *Journal of the American Chemical Society* 94: 4144–4151.

148 Neya, S. and Funasaki, N. (2002). *meso*-Tetra(*tert*-butyl)porphyrin as a precursor of porphine. *Tetrahedron Letters* 43: 1057–1058.

149 Senge, M.O., Shaker, Y.M., Pintea, M. et al. (2010). Synthesis of *meso*-substituted ABCD-type porphyrins by functionalization reactions. *European Journal of Organic Chemistry* 237–258.

150 Krattinger, B. and Callot, H.J. (1999). Alkylation and reduction of porphyrins and *N*-substituted porphyrins: new routes to chlorins and phlorins. *European Journal of Organic Chemistry* 1857–1867.

151 Galezowski, M. and Gryko, D.T. (2007). Recent advances in the synthesis of hydroporphyrins. *Current Organic Chemistry* 11: 1310–1338.

152 Cavaleiro, J.A.S., Neves, M.G.P.M.S., and Tomé, A.C. (2003). Cycloaddition reactions of porphyrins. *ARKIVOC* 2003: 107–130.

153 Dolphin, D. (1994). 1993 Syntex-award lecture – photomedicine and photodynamic therapy. *Canadian Journal of Chemistry* 72: 1005–1013.

154 Callot, H.J., Johnson, A.W., and Sweeney, A. (1973). Additions to porphins involving formation of new carbon-carbon bonds. *Journal of the Chemical Society, Perkin Transactions 1*: 1424–1427.

155 Pangka, V.S., Morgan, A.R., and Dolphin, D. (1986). Diels-alder reactions of protoporphyrin-IX dimethyl ester with electron-deficient alkynes. *The Journal of Organic Chemistry* 51: 1094–1100.

156 Silva, A.M.G., Tome, A.C., Neves, M.G.P.M.S. et al. (1999). *meso*-Tetraarylporphyrins as dipolarophiles in 1,3-dipolar cycloaddition reactions. *Chemical Communications* 1767–1768.

157 Pereira, N.A.M., Serra, A.C., and Pinho e Melo, T.M.V.D. (2010). Novel approach to chlorins and bacteriochlorins: [8π+2π] cycloaddition of diazafulvenium methides with porphyrins. *European Journal of Organic Chemistry* 2010: 6539–6543.

158 Callot, H.J. (1972). Stereochimie de l'addition de carbenes sur la *meso*-tetraphenylporphine. *Tetrahedron Letters* 1011–1014.

159 Grigg, R. (1971). Ring expansion of porphins with ethoxycarbonylnitrene. *Journal of the Chemical Society C* 3664–3668.

160 Stone, A. and Fleischer, E.B. (1968). The molecular and crystal structure of porphyrin diacids. *Journal of the American Chemical Society* 90: 2735–2748.

161 Senge, M.O., Forsyth, T.P., Nguyen, L.T., and Smith, K.M. (1994). Sterically strained porphyrins – influence of core protonation and peripheral substitution on the conformation of tetra-*meso*-, octa-*β*-, and dodecasubstituted porphyrin dications. *Angewandte Chemie International Edition in English* 33: 2485–2487.

162 McEwen, W.K. (1936). A further study of extremely weak acids. *Journal of the American Chemical Society* 58: 1124–1129.

163 McEwen, W.K. (1946). Steric deformation. the synthesis of N-methyl etioporphyrin I. *Journal of the American Chemical Society* 68: 711–713.

164 Lavallee, D.K. (1987). *The Chemistry and Biochemistry of N-Substituted Porphyrins*. New York: VCH Publishers.

165 Senge, M.O., Kalisch, W.W., and Runge, S. (1997). *N*-Methyl derivatives of highly substituted porphyrins – the combined influence of both core and peripheral substitution on the porphyrin conformation. *Liebigs Annalen – Recueil* 1997: 1345–1352.

166 Roucan, M., Flanagan, K.J., O'Brien, J., and Senge, M.O. (2018). Nonplanar porphyrins by *N*-substitution: a neglected pathway. *European Journal of Organic Chemistry* 6432–6446.

167 Mansuy, D., Battioni, J.-P., Dupré, D., and Sartori, E. (1982). Reversible iron-nitrogen migration of alkyl, aryl, or vinyl groups in iron porphyrins: a possible passage between σ Fe^{III}(porphyrin)(R) and Fe^{II}(*N*-R)(porphyrin) complexes. *Journal of the American Chemical Society* 104: 6159–6161.

168 Al-Hazimi, H.M.G., Jackson, A.H., Johnson, A.W., and Winter, M. (1977). *N*-Methylated tetraphenylporphins. *Journal of the Chemical Society, Perkin Transactions 1*: 98–103.

169 Al-Karadaghi, S., Franco, R., Hansson, M. et al. (2006). Chelatases: distort to select? *Trends in Biochemical Sciences* 31: 135–142.

170 Warren, M.J. and Smith, A.G. (ed.) (2009). *Tetrapyrroles: Birth, Life and Death*. New York: Springer-Verlag.

171 Ortiz de Montellano, P.R. (2000). The mechanism of heme oxygenase. *Current Opinion in Chemical Biology* 4: 221–227.

172 Cavaleiro, J.A.S. and Smith, K.M. (1971). Reactions of trans-octaethylchlorin with thallium(III) trifluoroacetate. *Journal of the Chemical Society D, Chemical Communications* 1384–1385.

173 Fuhrhop, J.-H. and Mauzerall, D. (1971). Photooxygenation of magnesium-octaethylporphin. *Photochemistry and Photobiology* 13: 453–458.

174 Liu, C., Shen, D.-M., and Chen, Q.-Y. (2006). Unexpected bromination ring-opening of tetraarylporphyrins. *Chemical Communications* 770–772.

175 Nandi, G., Titi, H.M., and Goldberg, I. (2014). Pitfalls in bromination reactions of zinc porphyrins: two-sided ring opening of the porphyrin macrocycle. *Inorganic Chemistry* 53: 7894–7900.

176 Hiroto, S., Miyake, Y., and Shinokubo, H. (2017). Synthesis and functionalization of porphyrins through organometallic methodologies. *Chemical Reviews* 117: 2910–3043.

177 Senge, M.O. (1996). π-Pyrrole–metal complexes – the missing coordination mode for metal–porphyrin interactions. *Angewandte Chemie, International Edition in English* 35: 1923–1925.

178 Suijkerbuijk, B.M.J.M. and Gebbink, R.J.M.K. (2008). Merging porphyrins with organometallics: synthesis and applications. *Angewandte Chemie International Edition* 47: 7396–7421.

179 Smith, K.M. and Langry, K.C. (1983). Electrophilic mercuration reactions of derivatives of deuteroporphyrin IX: new syntheses of coproporphyrin III, harderoporphyrin, isoharderoporphyrin, and S-411 porphyrin (dehydrocoproporphyrin). *The Journal of Organic Chemistry* 48: 500–506.

180 Sugiura, K.-I., Kato, A., Iwasaki, K. et al. (2007). Unusual regioselective mercuration of metalloporphyrins and its potential applications. *Chemical Communications* 2046–2047.

181 Yamaguchi, S., Katoh, T., Shinokubo, H., and Osuka, A. (2007). Porphyrin pincer complexes: peripherally cyclometalated porphyrins and their catalytic activities controlled by central metals. *Journal of the American Chemical Society* 129: 6392–6393.

182 Shinokubo, H. and Osuka, A. (2009). Marriage of porphyrin chemistry with metal-catalysed reactions. *Chemical Communications* 1011–1021.

183 Hata, H., Shinokubo, H., and Osuka, A. (2005). Highly regioselective Ir-catalyzed *β*-borylation of porphyrins via C−H bond activation and construction of β−β-linked diporphyrin. *Journal of the American Chemical Society* 127: 8264–8265.

184 Hata, H., Yamaguchi, S., Mori, G. et al. (2007). Regioselective borylation of porphyrins by C−H bond activation under iridium catalysis to afford useful building blocks for porphyrin assemblies. *Chemistry – An Asian Journal* 2: 849–859.

185 Cho, J.Y., Tse, M.K., Holmes, D. et al. (2002). Remarkably selective iridium catalysts for the elaboration of aromatic C-H bonds. *Science* 295: 305–308.

186 Ishiyama, T., Takagi, J., Ishida, K. et al. (2002). Mild iridium-catalyzed borylation of arenes. High turnover numbers, room temperature reactions, and isolation of a potential intermediate. *Journal of the American Chemical Society* 124: 390–391.

187 Kawamata, Y., Tokuji, S., Yorimitsu, H., and Osuka, A. (2011). Palladium-catalyzed *β*-selective direct arylation of porphyrins. *Angewandte Chemie International Edition* 50: 8867–8870.

188 Boyle, R.W. and Fox, S. (2004). First examples of intramolecular Pd(0) catalysed couplings on *ortho*-iodinated *meso*-phenyl porphyrins. *Chemical Communications* 1322–1323.

189 Cammidge, A.N., Scaife, P.J., Berber, G., and Hughes, D.L. (2005). Cofacial porphyrin−ferrocene dyads and a new class of conjugated porphyrin. *Organic Letters* 7: 3413–3416.

190 Sugiura, K.-I., Matsumoto, T., Ohkouchi, S. et al. (1999). Synthesis of the porphyrin-fused porphyrin, [2]porphyracene. *Chemical Communications* 1957–1958.

191 Sahoo, A.K., Mori, S., Shinokubo, H., and Osuka, A. (2006). Facile peripheral functionalization of porphyrins by Pd-catalyzed [3 + 2] annulation with alkynes. *Angewandte Chemie International Edition* 45: 7972–7975.

192 Sharman, W.M. and van Lier, J.E. (2000). Use of palladium catalysis in the synthesis of novel porphyrins and phthalocyanines. *Journal of Porphyrins and Phthalocyanines* 4: 441–453.

193 DiMagno, S.G., Lin, V.S.Y., and Therien, M.J. (1993). Catalytic conversion of simple haloporphyrins into alkyl-substituted, aryl-substituted, pyridyl-substituted, and vinyl-substituted porphyrins. *Journal of the American Chemical Society* 115: 2513–2515.

194 Chan, K.S., Zhou, X., Luo, B., and Mak, T.C.W. (1994). Synthesis of β-aryl substituted porphyrins by palladium-catalysed cross-coupling reactions. *Journal of the Chemical Society, Chemical Communications* 271–272.

195 Hyslop, A.G., Kellet, M.A., Iovine, P.M., and Therien, M.J. (1998). Suzuki porphyrins: new synthons for the fabrication of porphyrin-containing supramolecular assemblies. *Journal of the American Chemical Society* 120: 12676–12677.

196 Horn, S., Cundell, B., and Senge, M.O. (2009). Exploration of the reaction of potassium organotrifluoroborates with porphyrins. *Tetrahedron Letters* 50: 2562–2565.

197 Aratani, N. and Osuka, A. (2001). Synthesis of *meso-meso* linked hybrid porphyrin arrays by Pd-catalyzed cross-coupling reaction. *Organic Letters* 3: 4213–4216.

198 Götz, D.C.G., Bruhn, T., Senge, M.O., and Bringmann, G. (2009). Synthesis and stereochemistry of highly unsymmetric *β,meso*-linked porphyrin arrays. *The Journal of Organic Chemistry* 74: 8005–8020.

199 Plunkett, S., Dahms, K., and Senge, M.O. (2013). Synthesis and reactivity of allenylporphyrins. *European Journal of Organic Chemistry* 1566–1579.

200 Muzzi, C.M., Medforth, C.J., Voss, L. et al. (1999). Novel dodecaarylporphyrins: Synthesis and dynamic properties. *Tetrahedron Letters* 40: 6159–6162.

201 Ali, H. and van Lier, J.E. (1994). Synthesis of *β*-substituted porphyrins using palladium catalysed reactions. *Tetrahedron* 50: 11933–11944.

202 Lin, V.S.-Y., DiMagno, S.G., and Therien, M.J. (1994). Highly conjugated, acetylenyl bridged porphyrins: new models for light-harvesting antenna systems. *Science* 264: 1105–1111.

203 Anderson, H.L. (1999). Building molecular wires from the colours of life: conjugated porphyrin oligomers. *Chemical Communications* 2323–2330.

204 Gauler, R. and Risch, N. (1998). New Heck-type coupling reactions of natural tetrapyrroles – synthesis of porphyrinoligomers bridged by divinyl- and trivinylbenzene. *European Journal of Organic Chemistry* 1193–1200.

205 Locos, O.B. and Arnold, D.P. (2006). The Heck reaction for porphyrin functionalisation: synthesis of *meso*-alkenyl monoporphyrins and palladium-catalysed formation of unprecedented *meso–β* ethene-linked diporphyrins. *Organic and Biomolecular Chemistry* 4: 902–916.

206 Castella, M., Calahorra, F., Sainz, D., and Velasco, D. (2001). New Heck-type reaction applied to the synthesis of protoporphyrin-IX derivatives. *Organic Letters* 3: 541–544.

207 Sergeeva, N.N., Scala, A., Bakar, M.A. et al. (2009). Synthesis of stannyl porphyrins and porphyrin dimers via stille coupling and their ^{119}Sn NMR and fluorescence properties. *The Journal of Organic Chemistry* 74: 7140–7147.

208 Frampton, M.J., Akdas, H., Cowley, A.R. et al. (2005). Synthesis, crystal structure, and nonlinear optical behavior of *β*-unsubstituted *meso–meso E*-Vinylene-linked porphyrin dimers. *Organic Letters* 7: 5365–5368.

209 Aihara, H., Jaquinod, L., Nurco, D.J., and Smith, K.M. (2001). Multicarbocycle formation mediated by arenoporphyrin 1,4-diradicals: synthesis of picenoporphyrins. *Angewandte Chemie International Edition* 40: 3439–3441.

210 Chandra, T., Kraft, B.J., Huffman, J.C., and Zaleski, J.M. (2003). Synthesis and structural characterization of porphyrinic enediynes: geometric and electronic effects on thermal and photochemical reactivity. *Inorganic Chemistry* 42: 5158–5172.

211 Sugita, N., Hayashi, S., Hino, F., and Takanami, T. (2012). Palladium catalysed Kumada coupling reaction of bromoporphyrins with silylmethyl grignard reagents: preparation of silylmethyl-substituted porphyrins as a multipurpose synthon for fabrication of porphyrin systems. *The Journal of Organic Chemistry* 77: 10488–10497.

212 Takanami, T., Yotsukura, M., Inoue, W. et al. (2008). A facil and efficient synthesis of mono- and bisfunctionalized *meso*-substituted porphyrins *via* Palladium-catalyzed Negishi cross-coupling. *Heterocycles* 76: 439–453.

213 DiMagno, S.G., Lin, V.S.-Y., and Therien, M.J. (1993). Facile elaboration of porphyrins *via* metal-mediated cross-coupling. *The Journal of Organic Chemistry* 58: 5983–5993.

214 Shen, D.-M., Liu, C., and Chen, Q.-Y. (2006). A general and efficient palladium-catalyzed intramolecular cyclization reaction of *β*-brominated porphyrins. *The Journal of Organic Chemistry* 71: 6508–6511.

215 Kato, K., Cha, W., Oh, J. et al. (2016). Spontaneous formation of an air-stable radical upon the direct fusion of diphenylmethane to a triarylporphyrin. *Angewandte Chemie International Edition* 55: 8711–8714.

216 Liu, C., Shen, D.-M., and Chen, Q.-Y. (2007). Practical and efficient synthesis of various *meso*-functionalized porphyrins via simple ligand-free nickel-catalyzed C–O, C–N, and C–C cross-coupling reactions. *The Journal of Organic Chemistry* 72: 2732–2736.

217 Lu, X.-Q., Guo, Y., and Chen, Q.-Y. (2011). Efficient synthesis of *meso*–*meso*-linked diporphyrins by Nickel(0)-mediated Ullmann homocoupling. *Synlett* 77–80.

218 Osuka, A. and Shimidzu, H. (1997). *meso*,*meso*-Linked porphyrin arrays. *Angewandte Chemie International Edition* 36: 135–137.

219 Kim, D. and Osuka, A. (2004). Directly linked porphyrin arrays with tunable excitonic interactions. *Accounts of Chemical Research* 37: 735–745.

220 Baba, H., Chen, J., Shinokubo, H., and Osuka, A. (2008). Efficient rhodium-catalyzed installation of unsaturated ester functions onto porphyrins: site-specific heck-type addition versus conjugate addition. *Chemistry – A European Journal* 14: 4256–4262.

221 Chen, Y. and Zhang, X.P. (2003). Facile and efficient synthesis of *meso*-arylamino- and alkylamino-substituted porphyrins via palladium-catalyzed amination. *The Journal of Organic Chemistry* 68: 4432–4438.

222 Takanami, T., Hayashi, M., Hino, F., and Suda, K. (2003). Palladium-catalyzed *meso*-amination and amidation of porphyrins: marked acceleration with the Ni(II) central metal ion. *Tetrahedron Letters* 44: 7353–7357.

223 Kimberly, B.F., Joshua, V.R., Nicole, L.S., and Zhang, X.P. (2010). Porphyrin functionalization via palladium-catalyzed carbon–heteroatom cross-coupling reactions. In: *Handbook of Porphyrin Science*, vol. 3 (ed. K.M. Kadish, K.M. Smith and R. Guilard), 367–427. Singapore: World Scientific Publishing.

224 Esdaile, L.J., Senge, M.O., and Arnold, D.P. (2006). New palladium catalysed reactions of bromoporphyrins: synthesis and crystal structures of nickel(II) complexes of primary 5-aminoporphyrin, 5,5′-bis(porphyrinyl) secondary amine, and 5-hydroxyporphyrin. *Chemical Communications* 4192–4194.

225 Gao, G.-Y., Chen, Y., and Zhang, X.P. (2004). General synthesis of *meso*-amidoporphyrins via palladium-catalyzed amidation. *Organic Letters* 6: 1837–1840.

226 Khan, M.M., Ali, H., and van Lier, J.E. (2001). Synthesis of new aminoporphyrins via palladium-catalysed cross-coupling reaction. *Tetrahedron Letters* 42: 1615–1617.

227 Gao, G.-Y., Colvin, A.J., Chen, Y., and Zhang, X.P. (2003). Versatile synthesis of *meso*-aryloxy- and alkoxy-substituted porphyrins via palladium-catalyzed C–O cross-coupling reactions. *Organic Letters* 5: 3261–3264.

228 Gao, G.-Y., Colvin, A.J., Chen, Y., and Zhang, X.P. (2004). Synthesis of *meso*-arylsulfanyl- and alkylsulfanyl-substituted porphyrins via palladium-mediated C–S bond formation. *The Journal of Organic Chemistry* 69: 8886–8892.

229 Gao, G.-Y., Ruppel, J.V., Allen, B. et al. (2007). Synthesis of *β*-functionalized porphyrins via palladium-catalyzed carbon–heteroatom bond formations: expedient entry into *β*-chiral porphyrins. *The Journal of Organic Chemistry* 72: 9060–9066.

230 Atefi, F., McMurtrie, J.C., Turner, P. et al. (2006). *meso*-Porphyrinylphosphine oxides: mono- and bidentate ligands for supramolecular chemistry and the crystal structures of monomeric {[10,20-diphenylporphyrinatonickel(II)-5,15-diyl]-bis-[$P(O)Ph_2$]} and polymeric self-coordinated {[10,20-diphenylporphyrinatozinc(II)-5,15-diyl]-bis-[$P(O)Ph_2$]}. *Inorganic Chemistry* 45: 6479–6489.

231 Matano, Y., Matsumoto, K., Nakao, Y. et al. (2008). Regioselective *β*-metalation of *meso*-phosphanylporphyrins. Structure and optical properties of porphyrin dimers linked by peripherally fused phosphametallacycles. *Journal of the American Chemical Society* 130: 4588–4589.

232 Enakieva, Y.Y., Bessmertnykh, A.G., Gorbunova, Y.G. et al. (2009). Synthesis of *meso*-polyphosphorylporphyrins and example of self-assembling. *Organic Letters* 11: 3842–3845.

233 Matano, Y., Matsumoto, K., Terasaka, Y. et al. (2007). Synthesis, structures, and properties of *meso*-phosphorylporphyrins: self-organization through P–oxo–zinc coordination. *Chemistry – A European Journal* 13: 891–901.

234 Haumesser, J., Gisselbrecht, J.-P., Weiss, J., and Ruppert, R. (2012). Carbene spacers in bis-porphyrinic scaffolds. *Chemical Communications* 48: 11653–11655.

235 Matano, Y., Shinokura, T., Matsumoto, K. et al. (2007). Synthesis and aggregation behavior of *meso*-sulfinylporphyrins: evaluation of S-chirality effects on the self-organization to S–oxo-tethered cofacial porphyrin dimers. *Chemistry – An Asian Journal* 2: 1417–1429.

236 Bruhn, T., Witterauf, F., Götz, D.C.G. et al. (2014). C,C- and N,C-coupled dimers of 2-aminotetraphenylporphyrins: regiocontrolled synthesis, spectroscopic properties, and quantum-chemical calculations. *Chemistry – A European Journal* 20: 3998–4006.

237 Senge, M.O. and Richter, J. (2004). Synthetic, transformations of porphyrins – advances 2002-2004. *Journal of Porphyrins and Phthalocyanines* 8: 934–953.

238 Ladomenou, K., Nikolaou, V., Charalambidis, G., and Coutsolesos, A.G. (2016). "Click"-reaction: an alternative tool for new architectures of porphyrin based derivatives. *Coordination Chemistry Reviews* 306: 1–42.

239 Shen, D.-M., Liu, C., and Chen, Q.-Y. (2007). Synthesis and versatile reactions of *β*-azidotetraarylporphyrins. *European Journal of Organic Chemistry* 1419–1422.

240 Locos, O.B., Heindl, C.C., Corral, A. et al. (2010). Efficient synthesis of glycoporphyrins by microwave-mediated "Click" reactions. *European Journal of Organic Chemistry* 1026–1028.

241 Moylan, C., Sweed, A.M.K., Shaker, Y.M. et al. (2015). Lead structures for applications in photodynamic therapy 7. Efficient synthesis of amphiphilic glycosylated lipid porphyrin derivatives: refining linker conjugation for potential PDT applications. *Tetrahedron* 71: 4145–4153.

242 Moylan, C., Scanlan, E.M., and Senge, M.O. (2015). Chemical synthesis and medicinal applications of glycoporphyrins. *Current Medicinal Chemistry* 22: 2238–2348.

243 Arnold, D.P., Johnson, A.W., and Mahendran, M. (1978). Some reactions of *meso*-formyloctaethylporphyrin. *Journal of the Chemical Society, Perkin Transactions 1*: 366–370.

244 Arnold, D.P. and Nitschinsk, L.J. (1992). Porphyrin dimers linked by conjugated butadiynes. *Tetrahedron* 48: 8781–8792.

245 Anderson, H.L. (1994). Conjugated porphyrin ladders. *Inorganic Chemistry* 33: 972–981.

246 Anderson, S., Anderson, H.L., Bashall, A. et al. (1995). Assembly and crystal structure of a photoactive array of five porphyrins. *Angewandte Chemie, Internation Edition in English* 34: 1096–1099.

247 O'Sullivan, M.C., Sprafke, J.K., Kondratuk, D.V. et al. (2011). Vernier templating and synthesis of a 12-porphyrin nano-ring. *Nature* 469: 72–75.

248 Sugiura, K.-I., Fujimoto, Y., and Sakata, Y. (2000). A porphyrin square: synthesis of a square-shaped π-conjugated porphyrin tetramer connected by diacetylene linkages. *Chemical Communications* 1105–1106.

249 Arnold, D.P. and Nitschinsk, L.J. (1993). The preparation of novel porphyrins and bis(porphyrins) using palladium catalysed coupling reactions. *Tetrahedron Letters* 34: 693–696.

250 Fletcher, J.T. and Therien, M.J. (2000). Transition-metal-mediated [2 +2 + 2] cycloaddition reactions with ethyne-containing porphyrin templates: new routes to cofacial porphyrin structures and facially-functionalized (porphyrinato)metal species. *Journal of the American Chemical Society* 122: 12393–12394.

251 Horn, S. and Senge, M.O. (2008). The intermolecular Pauson–Khand reaction of *meso*-substituted porphyrins. *European Journal of Organic Chemistry* 4881–4890.

252 Horn, S., Sergeeva, N.N., and Senge, M.O. (2007). Conversion of Ni(II)-allylporphyrins to *α,β*-unsaturated formylporphyrins via a nickel-promoted reaction. *The Journal of Organic Chemistry* 72: 5414–5417.

253 Liu, X., Sternberg, E., and Dolphin, D. (2004). Cross-metathesis reactions of vinyl-chlorins and -porphyrins catalyzed by a "second generation" Grubbs' catalyst. *Chemical Communications* 852–853.

254 Zheng, G., Dougherty, T.J., and Pandey, R.K. (1999). Novel chlorin-diene building block by enyne metathesis: synthesis of chlorin-fullerene dyads. *Chemical Communications* 2469–2470.

255 Sergeeva, N., López Pablo, V., and Senge, M.O. (2008). Synthesis of porphyryl boronates with (un)saturated side–chains. *Journal of Organometallic Chemistry* 693: 2637–2640.

256 Jiao, L., Hao, E., Fronczek, F.R. et al. (2006). Benzoporphyrins *via* an olefin ring-closure metathesis methodology. *Chemical Communications* 3900–3902.

257 Smith, K.M. (1979). Protoporphyrin-IX: some recent research. *Accounts of Chemical Research* 12: 374–381.

258 Sitte, E. and Senge, M.O. (2020). The red color of life transformed – synthetic advances and emerging applications of protoporphyrin IX in chemical biology. *European Journal of Organic Chemistry* 3171–3191.

259 Peixoto, A.F., Pereira, M.M., Sousa, A.F. et al. (2005). Improving regioselectivity in the rhodium catalyzed hydroformylation of protoporphyrin-IX and chlorophyll *a* derivatives. *Journal of Molecular Catalysis A: Chemical* 235: 185–193.

260 Kahl, S.B., Schaeck, J.J., and Koo, M.-S. (1997). Improved methods for the synthesis of porphyrin alcohols and aldehydes from protoporphyrin IX dimethyl ester and their further modification. *The Journal of Organic Chemistry* 62: 1875–1880.

261 Kenner, G.W., McCombie, S.W., and Smith, K.M. (1973). Pyrrole und verwandte Verbindungen, XXI. Schutz der Porphyrinvinylgruppen. Eine Synthese von Koproporphyrin-III aus Protoporphyrin-IX. *Justus Liebigs Annalen der Chemie* 1329–1338.

262 Morris, I.K., Snow, K.M., Smith, N.W., and Smith, K.M. (1990). Syntheses of novel substituted porphyrins by the mercuration and Palladium/Olefin methodology. *The Journal of Organic Chemistry* 55: 1231–1236.

263 Mettath, S., Munson, B.R., and Pandey, R.K. (1999). DNA interaction and photocleavage properties of porphyrins containing cationic substituents at the peripheral position. *Bioconjugate Chemistry* 10: 94–102.

264 Morgan, A.R., Scherrer Pangka, V., and Dolphin, D. (1984). Ready syntheses of benzoporphyrins via Diels-Alder reactions with protoporphyrin IX. *Journal of the Chemical Society, Chemical Communications* 1047–1048.

265 Smith, K.M. and Cavaleiro, J.A.S. (1987). Protoporphyrin-IX: some useful substituent manipulations. *Heterocycles* 26: 1947–1963.

266 Shigeoka, T., Kuwahara, Y., Watanabe, K. et al. (2000). Synthesis of new fluorovinylzinc reagents and their application for synthesis of fluorine analogs of protoporphyrin. *Journal of Flourine Chemistry* 103: 99–103.

267 Pavlov, V.Y. (2007). Modern aspects of the chemistry of protoporphyrin IX. *Russian Journal of Organic Chemistry* 43: 1–34. *Zhurnal Organicheskoi Khimii* (2007), 43:9–36.

268 Desjardins, A., Flemming, J., Sternberg, E.D., and Dolphin, D. (2002). Nitrogen extrusion from pyrazoline-substituted porphyrins and chlorins using long wavelength visible light. *Chemical Communications* 2622–2623.

269 Kozyrev, A.N., Alderfer, J.L., and Robinson, B.C. (2003). Pyrazolinyl and cyclopropyl derivatives of protoporphyrin IX and chlorins related to chlorophyll *a*. *Tetrahedron* 59: 499–504.

270 Fischer, H. and Medick, H. (1935). Über die Einwirkung von Diazoessigester auf einige Chlorophyllderivate. *Justus Liebigs Annalen der Chemie* 517: 245–273.

271 Murakami, H., Matsumoto, R., Okusa, Y. et al. (2002). Design, synthesis and photophysical properties of C_{60}-modified proteins. *Journal of Materials Chemistry* 12: 2026–2033.

272 Liang, Z.-X., Nocek, J.M., Huang, K. et al. (2002). Dynamic docking and electron transfer between Zn-myoglobin and cytochrome b_5. *Journal of the American Chemical Society* 124: 6849–6859.

273 Smith, K.M., Parish, D.W., and Inouye, W.S. (1986). Methyl deuteration reactions in vinylporphyrins: protoporphyrins IX, III, and XIII. *The Journal of Organic Chemistry* 51: 666–671.

274 Caughey, W.S., Alben, J.O., Fujimoto, W.Y., and York, J.L. (1966). Substituted deuteroporphyrins. I. Reactions at the periphery of the porphyrin ring. *The Journal of Organic Chemistry* 31: 2631–2640.

275 Smith, K.M. and Langry, K.C. (1983). Electrophilic substitution reactions of derivatives of deuteroporphyrin-IX: deuteriation and vilsmeier formylation. *Journal of the Chemical Society, Perkin Transactions* 1: 439–444.

276 O'Brien, J.M., Sitte, E., Flanagan, K.J. et al. (2019). Functionalization of deutero- and protoporphyrin ix dimethyl esters via palladium-catalyzed coupling reactions. *The Journal of Organic Chemistry* 84: 6158–6173.

277 Fox, S. and Boyle, R.W. (2006). Synthetic routes to porphyrins bearing fused rings. *Tetrahedron* 62: 10039–10054.

278 Vicente, M.G.H. and Smith, K.M. (2004). Porphyrins with fused exocyclic rings. *Journal of Porphyrins and Phthalocyanines* 8: 26–42.

279 Shen, D.M., Liu, C., and Chen, Q.Y. (2005). A novel and facile Zn-mediated intramolecular five-membered cyclization of β-tetraarylporphyrin radicals from *β*-bromotetraarylporphyrins. *Chemical Communications* 4982–4984.

280 Morgan, A.R., Rampersaud, A., Garbo, G.M. et al. (1989). New sensitizers for photodynamic therapy – controlled synthesis of purpurins and their effect on normal tissue. *Journal of Medicinal Chemistry* 32: 904–908.

281 Callot, H.J., Schaeffer, E., Cromer, R., and Metz, F. (1990). Unexpected routes to naphthoporphyrin derivatives. *Tetrahedron* 46: 5253–5262.

282 Sengupta, D. and Robinson, B.C. (2002). Synthesis of chlorins possessing a fused naphthalene ring. *Tetrahedron* 58: 5497–5502.

283 Faustino, M.A., Neves, M.G.P.M.S., Vicente, M.G.H. et al. (1995). New naphtochlorins from the intramolecular cyclization of *β*-vinyl-*meso*-tetraarylporphyrins. *Tetrahedron Letters* 36: 5977–5978.

284 Tanaka, T. and Osuka, A. (2015). Conjugated porphyrin arrays: synthesis, properties and applications for functional materials. *Chemical Society Reviews* 44: 943–969.

285 Jaquinod, L., Gros, C., Olmstead, M.M. et al. (1996). First syntheses of fused pyrroloporphyrins. *Chemical Communications* 1475–1476.

286 Jaquinod, L., Siri, O., Khoury, R.G., and Smith, K.M. (1998). Linear fused oligoporphyrins: potential molecular wires with enhanced electronic communication between bridged metal ions. *Chemical Communications* 1261–1262.

287 Vicente, M.G.H., Cancilla, M.T., Lebrilla, C.B., and Smith, K.M. (1998). Cruciform porphyrin pentamers. *Chemical Communications* 2355–2356.

288 Vicente, M.G.H., Tomé, A.C., Walter, A., and Cavaleiro, J.A.S. (1997). Synthesis and cycloaddition reactions of pyrrole-fused 3-sulfolenes: a new versatile route to tetrabenzoporphyrins. *Tetrahedron Letters* 38: 3639–3642.

289 Tsuda, A., Furuta, H., and Osuka, A. (2000). Completely Fused Diporphyrins and Triporphyrin. *Angewandte Chemie International Edition* 39: 2549–2552.

290 Yoshia, N., Aratani, N., and Osuka, A. (2000). Poly(zinc(II)-5,15-porphyrinylene) from silver(I)-promoted oxidation of zinc(II)-5,15-diarylporphyrins. *Chemical Communications* 197–198.

291 Tsuda, A. and Osuka, A. (2001). Fully conjugated porphyrin tapes with electronic absorption bands that reach into infrared. *Science* 293: 79–82.

292 Nakano, A., Aratani, N., Furuta, H., and Osuka, A. (2001). Directly linked dehydropurpurin-porphyrin dyads from Ag(I)-promoted oxidation of *meso*-phenylethynyl substituted zinc(II) porphyrins. *Chemical Communications* 1920–1921.

293 Tsuda, A., Furuta, H., and Osuka, A. (2001). Syntheses, structural characterizations, and optical and electrochemical properties of directly fused diporphyrins. *Journal of the American Chemical Society* 123: 10304–10321.

294 Kamo, M., Tsuda, A., Nakamura, Y. et al. (2003). Metal-dependent regioselective oxidative coupling of 5,10,15-triarylporphyrins with DDQ-Sc(OTf)(3) and formation of an oxo-quinoidal porphyrin. *Organic Letters* 5: 2079–2082.

295 Nakamura, Y., Aratani, N., Shinokubo, H. et al. (2006). A directly fused tetrameric porphyrin sheet and its anomalous electronic properties that arise from the planar cyclooctatetraene core. *Journal of the American Chemical Society* 128: 4119–4127.

296 Ryan, A.A. and Senge, M.O. (2013). Synthesis and functionalization of triply fused porphyrin dimers. *European Journal of Organic Chemistry* 3700–3711.

297 Lewtak, J.P. and Gryko, D.T. (2012). Synthesis of π-extended porphyrins *via* intramolecular oxidative coupling. *Chemical Communications* 48: 10069–10086.

298 Davis, N.K.S., Pawlicki, M., and Anderson, H.L. (2008). Expanding the porphyrin π-system by fusion with anthracene. *Organic Letters* 10: 3945–3947.

299 Davis, N.K.S., Thompson, A.L., and Anderson, H.L. (2011). A porphyrin fused to four anthracenes. *Journal of the American Chemical Society* 133: 30–31.

300 Rothemund, P. (1936). A New Porphyrin Synthesis. *Journal of the American Chemical Society* 58: 625–627.

301 Taniguchi, S., Hasegawa, H., Nishimura, M., and Takahashi, M. (1999). A facile route to tripyrrane from 2,5-bis(hydroxymethyl)pyrrole and the improved synthesis of porphine by the "3+1" approach. *Synlett* 73–74.

302 Ema, T., Senge, M.O., Nelson, N.Y. et al. (1994). 5,10,5,20-Tetra-*tert*-butylporphyrin and its remarkable reactivity in the 5- and 15-position. *Angewandte Chemie, International Edition in English* 33: 1879–1881.

303 Senge, M.O., Ema, T., and Smith, K.M. (1995). Crystal structure of a remarkably ruffled nonplanar porphyrin (Pyridine)[5,10,5,20-Tetra(tert-butyl)porphyrinato]zinc(II). *Journal of the Chemical Society, Chemical Communications* 733–734.

304 Neya, S., Quan, J., Hata, M. et al. (2006). A novel and efficient synthesis of porphine. *Tetrahedron Letters* 47: 8731–8732.

305 Samuels, E., Shuttleworth, R., and Stevens, T.S. (1968). Halogenation of porphin and octaethylporphin. *Journal of the Chemical Society* 145–147.

306 Drach, J.E. and Longo, F.R. (1974). Electrophilic substitution on porphin. 1. Nitration. *The Journal of Organic Chemistry* 39: 3282–3284.

307 Fuhrhop, J.-H., Kadish, K.M., and Davis, D.G. (1973). The redox behavior of metallo octaethylporphyrins. *Journal of the American Chemical Society* 95: 5140–5147.

308 Sample, H.C. and Senge, M.O. (2021). Nucleophilic aromatic substitution (S_NAr) and related reactions of porphyrinoids: mechanistic and regiochemical aspects. *European Journal of Organic Chemistry* 7–42.

309 Serra, V.I.V., Pires, S.M.G., Alonso, C.M.A. et al. (2014). *Meso*-Tetraarylporphyrins bearing nitro or amino groups: synthetic strategies and reactivity profiles. *Topics in Heterocyclic Chemistry* 33: 35–78.

310 La, T., Richards, R., and Miskelly, G.M. (1994). Synthesis and characterization of the cationic porphyrin *meso*-tetrakis(2,3,5,6-tetrafluoro-*N*,*N*,*N*-trimethyl-4-aniliniumyl) porphyrin. *Inorganic Chemistry* 33: 3159–3163.

311 Hambright, P. and Fleischer, E.B. (1970). The acid-base equilibria, kinetics of copper ion incorporation, and acid-catalyzed zinc ion displacement from the water-soluble porphyrin α,β,γ,δ-tetra(4-*N*-methylpyridyl)porphine. *Inorganic Chemistry* 9: 1757–1761.

312 Hambright, P. (2000). Chemistry of water soluble porphyrins. In: *The Porphyrin Handbook*, vol. 3 (ed. K.M. Kadish, K.M. Smith and R. Guilard), 129–210. New York: Academic Press.

313 Jin, R.-H., Aoki, S., and Shima, K. (1996). A new route to water soluble porphyrins: phosphonium and ammonium type cationic porphyrins and self-assembly. *Chemical Communications* 1939–1940.

314 Weiss, R., Pühlhofer, F., Jux, N., and Merz, K. (2002). SASAPOS, not sisyphos: highly efficient 20-step one-pot synthesis of a discrete organic-inorganic ion cluster with a porphyrin core. *Angewandte Chemie International Edition* 41: 3815–3817.

315 Winkelman, J. (1962). The distribution of tetraphenylporphinesulfonate in the tumor-bearing rat. *Cancer Research* 22: 589–596.

316 Busby, C.A., Dinello, R.K., and Dolphin, D. (1975). A convenient preparation of *meso*-tetra(4-sulfonatopbenyl)porphyrin. *Canadian Journal of Chemistry* 53: 1554–1555.

317 Imada, T., Murakami, H., and Shinkai, S. (1994). Sugar-induced chiral orientation of a boronic-acid-appended porphyrin stack. Correlation between the absolute configuration and the CD (circular dichroism) Sign. *Chemical Communications* 1557–1558.

318 Ris, H.B., Altermatt, H.J., Inderbitzi, R. et al. (1991). Photodynamic therapy with chlorins for diffuse malignant mesothelioma – initial clinical results. *British Journal of Cancer* 64: 1116–1120.

319 Senge, M.O. and Brandt, J.C. (2011). Temoporfin (Foscan®, 5,10,15,20-tetra(*m*-hydroxyphenyl)chlorin) – a second-generation photosensitizer. *Photochemistry and Photobiology* 87: 1240–1296.

320 Senge, M.O. (2012). *m*THPC – a drug on its way from second to third generation photosensitizer? *Photodiagnosis and Photodynamic Therapy* 9: 170–179.

321 Rogers, L., Burke-Murphy, E., and Senge, M.O. (2014). Simple porphyrin desymmetrization: 5,10,15,20-tetrakis(3-hydroxyphenyl)-porphyrin (*m*THPP) as a gateway molecule for peripheral functionalization. *European Journal of Organic Chemistry* 4283–4294.

322 Wada, K., Mizutani, T., and Kitagawa, S. (2003). Synthesis of functionalized porphyrins as oxygen ligand receptors. *The Journal of Organic Chemistry* 68: 5123–5131.

323 Bonnett, R. and Martínez, G. (2002). Photobleaching of compounds of the 5,10,15,20-tetrakis(*m*-hydroxyphenyl)porphyrin series (*m*-THPP, *m*-THPC, and *m*-THPBC). *Organic Letters* 4: 2013–2016.

324 Momenteau, M. and Reed, C.A. (1994). Synthetic heme dioxygen complexes. *Chemical Reviews* 94: 659–698.

325 Wijesekera, T.P., Paine, J.B. III, and Dolphin, D. (1988). Improved synthesis of covalently strapped porphyrins. Application to highly deformed porphyrin synthesis. *The Journal of Organic Chemistry* 53: 1345–1352.

326 Diekmann, H., Chang, C.K., and Traylor, T.G. (1971). Cyclophane porphyrin. *Journal of the American Chemical Society* 93: 4068–4070.

327 Almog, J., Baldwin, J.E., Dyer, R.L., and Peters, M. (1975). Condensation of tetraaldehydes with pyrrole. Direct synthesis of "Capped" porphyrins. *Journal of the American Chemical Society* 97: 226–227.

328 Momenteau, M., Mispelter, J., Loock, B., and Bisagni, E. (1983). Both-faces hindered porphyrins. Part 1. Synthesis and characterization of basket-handle porphyrins and their iron complexes. *Journal of the Chemical Society, Perkin Transactions 1*: 189–196.

329 Collman, J.P., Boulatov, R., Sunderland, C.J., and Fu, L. (2004). Functional analogues of cytochrome *c* oxidase, myoglobin, and hemoglobin. *Chemical Reviews* 104: 561–588.

330 Collman, J.P., Gagne, R.R., Reed, C.A. et al. (1975). Picket fence porphyrins. Synthetic models for oxygen binding hemoproteins. *Journal of the American Chemical Society* 97: 1427–1439.

331 Collman, J.P. (1977). Synthetic models for oxygen-binding hemoproteins. *Accounts of Chemical Research* 10: 265–272.

332 Collman, J.P., Brauman, J.I., Fitzgerald, J.P. et al. (1988). Synthesis, characterization, and x-ray structure of the Ruthenium "Picnic-Basket" porphyrins. *Journal of the American Chemical Society* 110: 3477–3486.

333 Norvaiša, K., Flanagan, K.J., Gibbons, D., and Senge, M.O. (2019). Conformational Re-engineering of porphyrins as receptors with switchable N–H···X-type binding modes. *Angewandte Chemie, International Edition* 58: 16553–16557.

334 Ogoshi, H. and Mizutani, T. (1998). Multifunctional and chiral porphyrins: model receptors for chiral recognition. *Accounts of Chemical Research* 31: 81–89.

335 Ogoshi, H., Saita, K., Sakurai, K. et al. (1986). Novel chiral porphyrins with C_2 symmetry. *Tetrahedron Letters* 27: 6365–6368.

336 Groves, J.T. and Myers, R.S. (1983). Catalytic asymmetric epoxidations with chiral iron porphyrins. *Journal of the American Chemical Society* 105: 5791–5796.

337 Halterman, R.L. and Jan, S.T. (1991). Catalytic asymmetric epoxidation of unfunctionalized alkenes using the 1st D_4-symmetrical metallotetraphenylporphyrin. *The Journal of Organic Chemistry* 56: 5253–5254.

338 Simonneaux, G. and Le Maux, P. (1991). Optically active ruthenium porphyrins: chiral recognition and asymmetric catalysis. *Coordination Chemistry Reviews* 228: 43–60.

339 Crossley, M.J., Hambley, T.W., Mackay, L.G. et al. (1995). Porphyrin analogues of Tröger's base: large chiral cavities with a bimetallic binding site. *Journal of the Chemical Society, Chemical Communications* 1077–1079.

340 Borovkov, V. (2014). Supramolecular chirality in porphyrin chemistry. *Symmetry* 6: 256–294.

341 Collman, J.P., Wagenknecht, P.S., and Hutchison, J.E. (1994). Molecular catalysts for multielectron redox reactions of small molecules – the cofacial metallodiporphyrin approach. *Angewandte Chemie, International Edition in English* 33: 1537–1554.

342 Chang, C.K. and Abdalmuhdi, I. (1983). Anthracene pillared cofacial diporphyrin. *The Journal of Organic Chemistry* 48: 5388–5390.

343 Burrell, A.K., Officer, D.L., Plieger, P.G., and Reid, D.C.W. (2001). Synthetic routes to multiporphyrin arrays. *Chemical Reviews* 101: 2751–2796.

344 Ponomarev, G.V., Borovkov, V.V., Sugiura, K.-I. et al. (1993). Synthesis and properties of cis-1,2-bis(octaethylporphyrinyl)ethylene. *Tetrahedron letters* 34: 2153–2156.

345 Senge, M.O., Kalisch, W.W., and Ruhlandt-Senge, K. (1996). Synthesis and crystal structures of cofacial bischlorins. Octaethylchlorin-based structural models for the special pair in photosynthesis. *Chemical Communications* 2149–2150.

346 Kalisch, W.W., Senge, M.O., and Ruhlandt-Senge, K. (1998). Synthesis and structural characterization of cofacial bisoctaethylchlorins as models for the special pair. *Photochemistry and Photobiology* 67: 312–323.

347 Senge, M.O., Fazekas, M., Notaras, E.G.A. et al. (2007). Nonlinear optical properties of porphyrins. *Advanced Materials* 19: 2737–2774.

348 Suslick, K.S., Chen, C.T., Meredith, G.R., and Cheng, L.T. (1992). Push-pull porphyrins as nonlinear optical materials. *Journal of the American Chemical Society* 114: 6928–6930.

349 LeCours, S.M., Guan, H.-W., DiMagno, S.G. et al. (1996). Push−pull arylethynyl porphyrins: new chromophores that exhibit large molecular first-order hyperpolarizabilities. *Journal of the American Chemical Society* 118: 1497–1503.

350 O'Regan, B. and Grätzel, M. (1991). A low-cost, high-efficiency solar cell based on dye-sensitized colloidal TiO_2 films. *Nature* 353: 737–740.

351 Li, L.L. and Diau, E.W.G. (2013). Porphyrin-sensitized solar cells. *Chemical Society Reviews* 42: 291–304.

352 Yella, A., Lee, H.-W., Tsao, H.N. et al. (2011). Porphyrin-sensitized solar cells with Cobalt (II/III)–based redox electrolyte exceed 12 percent efficiency. *Science* 334: 629–634.

353 Mathew, S., Yella, A., Gao, P. et al. (2014). Dye-sensitized solar cells with 13% efficiency achieved through the molecular engineering of porphyrin sensitizers. *Nature Chemistry* 6: 242–247.

354 Kurotobi, K., Toude, Y., Kawamoto, K. et al. (2013). Highly asymmetrical porphyrins with enhanced push–pull character for dye-sensitized solar cells. *Chemistry – A European Journal* 19: 17075–17081.

355 Di Carlo, G., Orbelli Biroli, A., Pizzotti, M. et al. (2013). Tetraaryl Zn^{II} porphyrinates substituted at *β*-pyrrolic positions as sensitizers in dye-sensitized solar cells: a comparison with *meso*-disubstituted push–pull Zn^{II} porphyrinates. *Chemistry – A European Journal* 19: 10723–10740.

356 Chang, Y.-C., Wang, C.-L., Pan, T.-Y. et al. (2011). A strategy to design highly efficient porphyrin sensitizers for dye-sensitized solar cells. *Chemical Communications* 47: 8910–8912.

357 Meindl, A., Plunkett, S., Ryan, A.A. et al. (2017). Comparative synthetic strategies for the generation of 5,10- and 5,15-substituted *push-pull* porphyrins. *European Journal of Organic Chemistry* 3565–3583.

358 Ishida, M., Hwang, D., Koo, Y.B. et al. (2013). β-(Ethynylbenzoic acid)-substituted push–pull porphyrins: DSSC dyes prepared by a direct palladium-catalyzed alkynylation reaction. *Chemical Communications* 49: 9164–9166.

359 Notaras, E.G.A., Fazekas, M., Doyle, J.J. et al. (2007). A_2B_2-type *push–pull* porphyrins as reverse saturable and saturable absorbers. *Chemical Communications* 2166–2168.

360 Higashino, T., Kawamoto, K., Sugiura, K. et al. (2016). Effects of bulky substituents of push−pull porphyrins on photovoltaic properties of dye-sensitized solar cells. *ACS Applied Materials & Interfaces* 8: 15379–15390.

361 Ambre, R.B., Mane, S.B., Chang, G.-F., and Hung, C.-H. (2015). Effects of number and position of meta and para carboxyphenyl groups of zinc porphyrins in dye-sensitized solar cells: structure−performance relationship. *ACS Applied Materials & Interfaces* 7: 1879–1891.

362 Senge, M.O., Sergeeva, N.N., and Hale, K.J. (2021). Classic highlights in porphyrin and porphyrinoid total synthesis and biosynthesis. *Chemical Society Reviews* 50: 4730–4789.

4

Coordination Chemistry

Penelope J. Brothers[1,2] *and Abhik Ghosh*[3]

[1] *School of Chemical Sciences, University of Auckland, Auckland, New Zealand*
[2] *Research School of Chemistry, The Australian National University, Canberra, Australia*
[3] *Department of Chemistry, UiT—The Arctic University of Norway, Tromsø, Norway*

Abbreviations

1-MeIm	1-methylimidazole
acac	acetylacetonato ligand
Cor	corrole (unspecified)
Cz	corrolazine
DME	dimethoxyethane
Hb	hemoglobin
Mb	myoglobin
mCPBA	*m*-chloorperbenzoic acid
Nc	naphthalocyanine
NCTPP	N-confused tetraphenylporphyrin
OEC	octaethylcorrole
OEP	octaethylporphyrin
OETPP	octaethyltetraphenylporphyrin
Pc	phthalocyanine (unspecified)
Por	porphyrin (unspecified)
py	pyridine
TEMPO	tetramethylpiperidinyl-N-oxide
THF	tetrahydrofuran
THT	tetrahydrothiophene
TLC	thin layer chromatography
TPC	triphenylcorrole
TpClPP	tetra-*p*-chlorophenylporphyrin
TPFPC	trispentafluorophenylcorrole
TpivPP	tetrapivaloylporphyrin
TPP	tetraphenylporphyrin
TTP	tetra-*p*-tolylporphyrin

Fundamentals of Porphyrin Chemistry: A 21st Century Approach, Volume 1, First Edition.
Edited by Penelope J. Brothers and Mathias O. Senge.
© 2022 John Wiley & Sons Ltd. Published 2022 by John Wiley & Sons Ltd.

4.1 Introduction

The properties of any porphyrin or porphyrinoid species are hugely influenced by the element occupying the coordination site at the center of the macrocycle. In the free-base macrocycle, of course, two protons occupy this site, distributed across the four nitrogens as tautomers. However, once these protons are displaced by a coordinating element – whether a metal, metalloid, or non-metal – then a whole periodic table of possibilities opens up. Despite the apparently simple, idealized square planar arrangement of four nitrogen donors, the resulting complex geometries can be four-, five-, six-, or higher-coordinate, depending on the number of axial ligands. The coordinated element might lie in the plane, be displaced out of the plane, interact with fewer than four of the porphyrin nitrogen atoms, or even avoid the nitrogens altogether and σ- or π-bond to the carbon skeleton of the porphyrin. Porphyrin complexes can be monomeric, dinuclear, or polynuclear depending on the mode of linking. This can encompass direct metal–metal bonding, metal–ligand–metal bridging, multi-decker complexes where the metals are sandwiched between two or more porphyrins, or supramolecular constructs where donor groups on the periphery of one porphyrin complex link to the metal of another. The axial ligands can be simple anionic or neutral heteroatom donors, or carbon-based groups forming organometallic porphyrin complexes. They might be small gaseous molecules like O_2, CO, or NO, or donor atoms that are part of a much larger entity such as a protein or polymer. The coordinated element itself might be able to access several different oxidation states, which in turn might lead to variable spin states and magnetic properties.

The porphyrin ligand (minus its two protons) is a dianion, except when its π-orbitals interact with those of the coordinated element and the porphyrin becomes "non-innocent," complexing in an oxidized or reduced form. The "hole" in the porphyrin ligand (centroid···$N_{pyrrole}$) has a radius close to 2.0 Å. Taking into account the 0.75 Å covalent radius of nitrogen (or more appropriately, 0.70 Å for sp^2 hybridized nitrogen), elements with a covalent radius of around 1.25–1.30 Å should be a good fit for this site. Despite this, porphyrins and related ligands form complexes with many elements, both much larger and much smaller than this ideal size.

A parallel range of possibilities also exists for the other members of the porphyrinoid family – expanded, contracted, isomeric, and hetero-porphyrins. All of this rich chemistry lies under the broad umbrella of coordination chemistry. The multiple functions of porphyrin complexes – in biology, sensing, imaging, catalysis, medicine, electron transfer, energy transduction and supramolecular architecture – are all uniquely governed by the coordination chemistry of each individual porphyrin complex. There is an enormous amount to discuss, several encyclopedias worth, in all likelihood. As a result, the scope of this relatively short chapter on porphyrin coordination chemistry needs to be carefully considered so as to give the best possible overview. What are the essentials a chemist curious about porphyrin coordination chemistry needs to know? A useful list might be how to introduce the desired element into the porphyrin hole (insertion); the stability of the resulting complex toward loss of the coordinated element (demetallation); and how to characterize the resulting complex, including the oxidation state of the central element, ligands, structural niceties, spectroscopy, and any non-innocence on the part of the porphyrin. Depending on the desired function, how to choose which element to use? For example, a porphyrin may be simply required as a large, aromatic, planar chromophore and the identity of the coordinated element might not be critical. In these circumstances, the typical "workhorse" metal ion Zn(II) might be

used – it is cheap, easy to insert, also relatively easy to demetallate, diamagnetic, has no redox chemistry of its own, is a good fit for the porphyrin cavity, and readily coordinates a wide range of ligands with especially good affinity for nitrogen donors. On the other hand, for applications in catalysis or sensing, each particular combination of element, oxidation state, ligands, and tailoring of substituents on the porphyrin periphery will be critical to optimizing the desired function, and the appropriate choice and control of each parameter is essential.

This chapter gives a flavor of the breadth and depth of porphyrin coordination chemistry, beginning with the essentials mentioned above. A brief excursion into other members of the porphyrinoid family (phthalocyanines, corroles, heteroporphyrins, expanded, and contracted porphyrins) will highlight novelties and major similarities and differences. Particular applications of porphyrin complexes where the coordination chemistry plays a critical role will then be considered, with a focus on the principles and features of the chemistry that enable the function.

The chapter begins with a survey of the important members of the porphyrinoid family, beginning with porphyrin itself, focusing on each member's characteristics as ligands. The first step in porphyrin coordination chemistry is inserting the element of interest into the porphyrin macrocycle, generally known as metallation, along with its reverse, demetallation. An overview of typical methods for these processes will be given, followed by a brief survey of useful methods for characterizing the resulting complexes, with a focus on practical applications and tips for those new to the field. Porphyrin coordination complexes are then considered according to a somewhat Mendeleevian march through the periodic table, with elements grouped into sections. The transition metal section is expanded with some extra discussion on metal–metal bonding, ligand non-innocence, and metalloporphyrin-diatomic complexes. A final section considers features particular to the organoelement chemistry of porphyrins.

The introduction above has been careful to be element-neutral with respect to the status of the coordinated element (metal, metalloid, or non-metal). The term "metal" is often used generically to refer to the coordinated element, even when it is a non-metal. For simplicity, the free base of a generic porphyrin (Por) will be denoted H_2(Por) and a complex as M(Por) even if M is actually a non-metal. Other generic usage will be X and L for monodentate anionic and neutral, respectively, ligands, while R (or more specifically, Ar) will refer to alkyl (or aryl) ligands. Generic free-base corrole H_3(Cor) and phthalocyanine H_2(Pc) and the ligands Cor^{3-} and Pc^{2-} will be denoted as shown.

4.2 Overview of the Coordination Chemistry of Porphyrin and its Analogues

The scope of porphyrin coordination chemistry can be mapped through the periodic table – a survey shows that the majority of the elements are known to form porphyrin complexes, where a "complex" is defined for this purpose as an element forming a bond to two or more pyrrole nitrogens. One obvious omission is beryllium, which is intermediate in size between boron and aluminum, both of which form porphyrin complexes. This perhaps simply reflects chemists' reluctance to undertake experimental work with this toxic element. Groups 16 and 17 have only one example, tellurium [1], although other elements of these groups do form coordination complexes with nitrogen donors. Not surprisingly, there are no examples of porphyrin complexes from Group 18 or the more radioactive heavier elements.

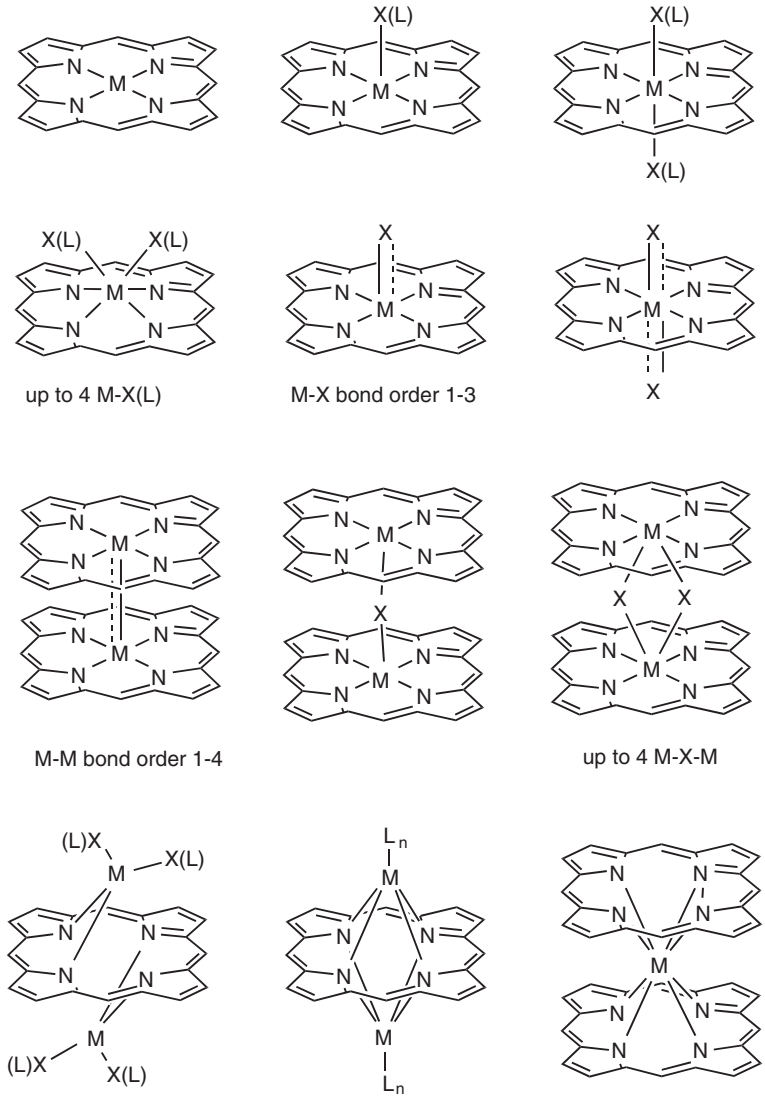

Figure 4.1 Coordination modes observed for porphyrinoid ligands (X is anionic; L is neutral; X(L) can be either).

What is most remarkable is the enormous versatility of the porphyrin macrocycle and its relatives as ligands. Considering the very well-defined 24-atom porphyrin core offering four nitrogen donors in a more or less square planar arrangement, it is remarkable that the ligand can accommodate elements of such varying size, electronegativity, bonding preferences, oxidation states, and geometries. The archetypal metalloporphyrin complex is six-coordinate, with the metal residing in the N_4 plane, with two mutually *trans* neutral or anionic axial ligands. However, the diversity of porphyrin coordination chemistry is such that there are many examples that adopt quite different geometries. Figure 4.1 shows representations of many of the common (and not-so-common) coordination modes for porphyrinoid ligands.

4.2.1 Porphyrin and Porphyrin Relatives

Interest in porphyrin coordination chemistry was originally piqued by the biologically important metals, especially iron (heme), and to a lesser extent cobalt (Vitamin B12) and magnesium (chlorophyll). The first-row transition elements were an obvious place to start, and from there the chemistry spread out to encompass much of the periodic table, with elements from every part of the table featuring as porphyrin complexes with the exception of Groups 17 and 18, encompassing metals, metalloids and nonmetals, and oxidation states from −2 to +8. The availability of good synthetic routes to free-base porphyrins and the continual evolution of separation, purification, and characterization techniques helped to drive this exploration. Even so, examples of the new "firsts" as porphyrin complexes are still being reported, with, for example, tellurium and carbon being recent additions to the periodic table of known porphyrin complexes (Figure 4.2).

In most complexes, the porphyrin can be considered to behave as a dianionic ligand, although there are some examples where this is not the case, particularly for open-shell metal centers like, for example, high-valent iron complexes of biological importance [2]. However, there are recent examples of ligand non-innocence in main group closed-shell complexes. These and other selected examples will be discussed in Section 4.5.5 on ligand non-innocence.

This chapter is not intended to be comprehensive – there are plenty of prior reviews in the area that do have this function, and readers are directed to these for a more encyclopedic approach to looking up particular features and properties of a given element. An excellent example is the section in *The Porphyrin Handbook* (published in 2000) [3], which treats the axial coordination chemistry of porphyrins element by element, and although it is now some 20 years old, it is still an excellent source of the essential information for each

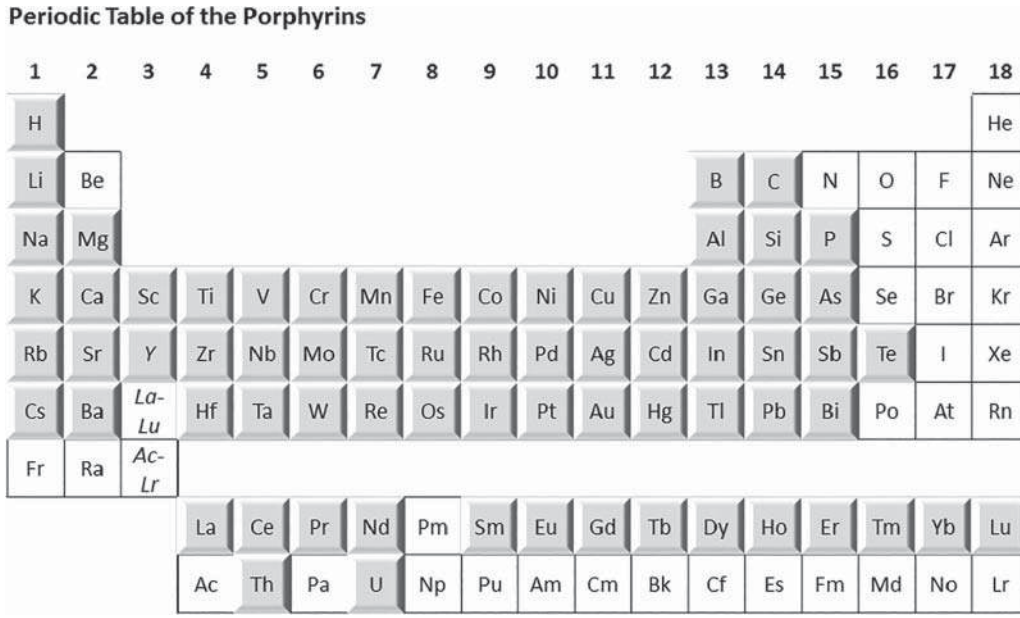

Figure 4.2 The periodic table of known porphyrin complexes.

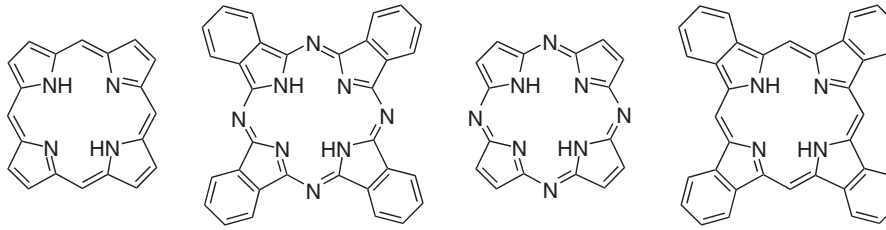

Figure 4.3 Porphyrin, phthalocyanine, porphyrazine, and benzoporphyrin core structures.

element. Reviews on the organoelement chemistry of transition metal and main group porphyrin complexes from the same era give a similar level of detail for organometallic systems [4, 5].

The porphyrin core (Figure 4.3) is the parent of the extended family of porphyrinoid macrocycles. Other members such as phthalocyanines and corroles have been known a long time, and new members, especially expanded porphyrins and heteroporphyrins, are still joining the family regularly. Many of these members have their own chapter in this book. The present chapter on coordination chemistry is mostly focused on porphyrins as the parent, the best-known and most-utilized family member, but others will be touched on as they are relevant. This brief outline will consider the special characteristics relevant to the coordination chemistry of selected members of the wider porphyrinoid family.

4.2.2 Phthalocyanines, Porphyrazines, and Tetrabenzoporphyrins

The coordination chemistry of phthalocyanines (Figure 4.3) has much in common with porphyrins [6–8]. One notable important feature is the use of metal-templated reactions for the synthesis of metallophthalocyanines by high-temperature cyclotetramerization of either phthalonitrile or phthalic anhydride and urea in the presence of a metal salt. Some metal ions (e.g., Cu^{2+}, Zn^{2+}) cannot be removed without destroying the macrocycle, but the free-base phthalocyanine H_2(Pc) can be prepared by the removal of more labile ions such as Li^+ or Mg^{2+}. This is a notable contrast to porphyrins, corroles, expanded porphyrins, and others in the porphyrinoid family for which the free-base macrocycle is first prepared and isolated with metal ion insertion as a subsequent step. Unsubstituted phthalocyanine and its metal complexes have very low solubility, and peripherally substituted derivatives bearing bulky organic groups (e.g., ^{t}Bu) or polar groups (e.g., sulfonate) are often used to confer better solubility in organic solvents or aqueous systems, respectively. The phthalocyanine macrocycle is slightly smaller than a porphyrin, which has consequences for the relative stability of some M(Pc) complexes relative to the corresponding M(Por) complexes [9].

Phthalocyanines differ from porphyrins by virtue of the four nitrogens replacing the four *meso*-carbon atoms, and the benzannulated pyrrole subunits (often referred to as isoindoles). Phthalocyanine/porphyrin hybrids contain one or other, but not both, of these features. Tetrabenzoporphyrins contain the benzannulating groups [10], and porphyrazines (also known as tetraazaporphyrins) have four nitrogens in the *meso*-positions (Figure 4.3) [11–13]. Both have well-developed coordination chemistry, although the latter have probably been more prominent in recent times.

The next categories of porphyrinoids to consider are the contracted, isomeric, and expanded porphyrins – a burgeoning field enabled partly by advances in synthetic methods [14].

4.2.3 Contracted Porphyrins

Notation for expanded, contracted, and isomeric porphyrins uses three parts. The core name shows the number of pyrrole subunits, the number in the prefix (in square brackets) indicates the number of π electrons in the effective macrocyclic conjugation, and the numbers in the suffix (round brackets) indicate the numbers of bridging carbon atoms between the pyrrole groups, starting from the largest unit. Using this notation, porphine is denoted [18]tetraphyrin(1.1.1.1) [15, 16].

Contracted porphyrinoids are those constructed from fewer than four pyrrole subunits linked by four *meso*-carbons (the 24-atom core of porphyrin) [17, 18]. The smallest of the contracted porphyrins contain only three pyrroles, of which the best known are the subphthalocyanines (subPc), produced under the same conditions as the phthalocyanine parent but using the small element boron as the template for the self-assembly (Figure 4.4). The small size of boron coupled with its preference for trigonal planar or tetrahedral geometry supports the formation of the inverted bowl-shaped boron subphthalocyanines. The ligand has a formal 2– charge, and boron sits at the center of the bowl coordinated to three subPc nitrogens and with a fourth, anionic ligand completing the pseudotetrahedral coordination environment. The subPc macrocycles exist only as boron complexes and cannot be demetallated to the free bases [19–21]. More recently, subporphyrins, the true contracted porphyrins [14]triphyrin(1.1.1) have emerged [20, 22, 23], and there are also examples of subbenzoporphyrins [24] and subazaporphyrins (Figure 4.4) [20]. All have the following in common: their formation and existence are templated by boron, the free bases are unknown, and they all have bowl shapes with varying curvatures and boron at the center [17, 18, 22, 23, 25].

4.2.4 Corroles

Of the contracted porphyrinoids bearing four pyrroles, the corroles, formally [18]tetraphyrin(1.1.1.0), have a long history but have only recently come to prominence now that reliable methods of synthesis accessible to non-specialist organic chemists have become available (Figure 4.5) [26–31]. Structurally characterized examples of new element corrole complexes are appearing regularly, and the "Periodic Table of Corroles" has doubled in size

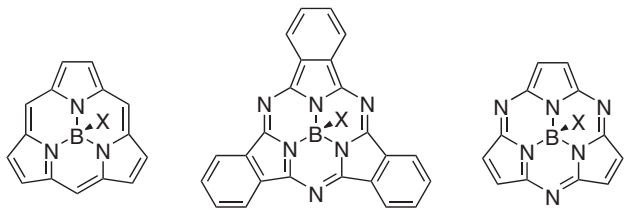

Figure 4.4 Subporphyrin, subphthalocyanine, and subporphyrazine core structures.

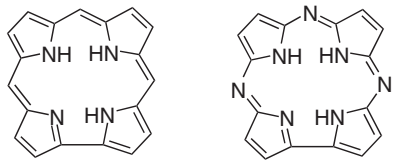

corrole
H_3(Cor)

corrolazine

Figure 4.5 Corrole and corrolazine core structures.

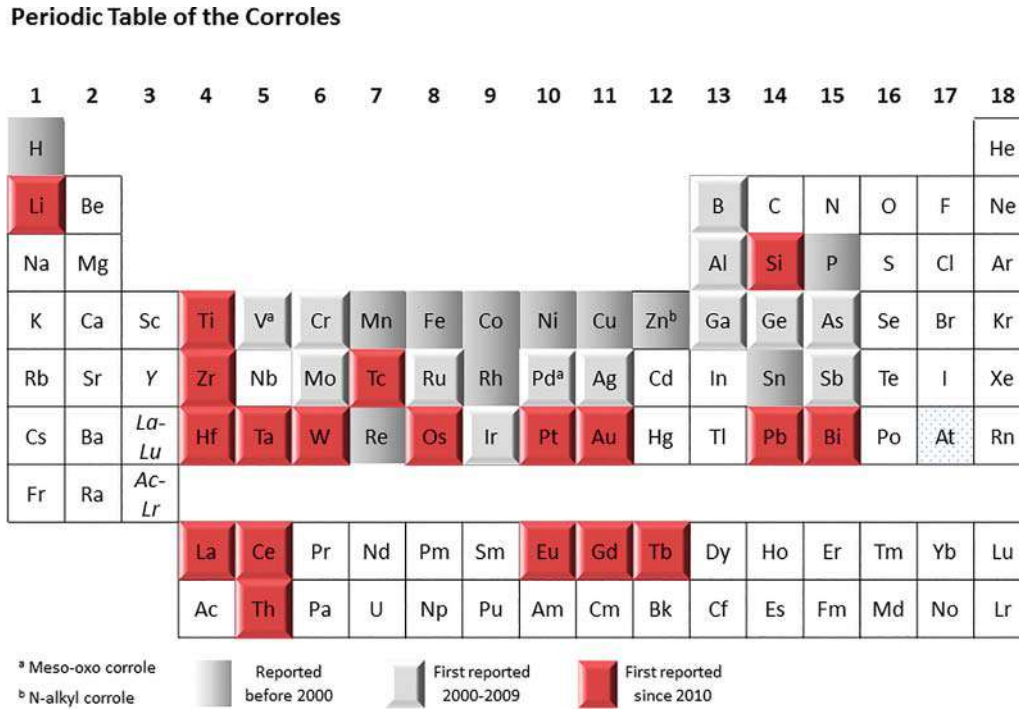

Figure 4.6 The periodic table of known corrole complexes.

since 2010, in part prompted by the availability of Li_2(Cor), which permitted the synthesis of early transition metal, lanthanide, and actinide corroles (Figure 4.6) [32]. The structural chemistry and electronic properties of metallocorrole complexes have both been recently reviewed [33–35].

From a coordination chemistry point of view, there are quite distinct differences between corroles and porphyrins, the most obvious of which are the lower symmetry and the triprotic nature of the free-base corrole, giving rise to a trianionic ligand. The N_4 coordination site in corrole is slightly smaller than in porphyrin, and this, together with the higher formal charge on the corrole anion, suggest that corroles appear to be more effective for stabilizing higher-oxidation-state transition metal ions than porphyrins. However, on closer examination, it is apparent that in these complexes the corrole may be partially oxidized, illustrating a higher tendency for corroles to behave as non-innocent ligands [33–35]. The smaller coordination site in corroles means that the typical geometry is a five-coordinate complex with the metal slightly displaced from the N_4 plane of the macrocycle, which may be planar or slightly

domed, and one anionic or neutral axial ligand. However, as with porphyrins, there are plenty of exceptions [34]. The predominance of five-coordinate corrole complexes demonstrates that for most metals, the affinity for a sixth ligand is surprisingly low, partly for steric reasons with doming of the corrole, and partly because of the strong σ-donation by the trianionic N_4 donor set, which may reduce the Lewis acidity of the central metal. Another consequence is that coordinated metals are particularly electron rich, and this can result in air oxidation of Cr(III), Mn(III), and Fe(III) corroles to formal oxidation states Cr(V), Mn(IV), and Fe(IV). Metallocorroles also tend to be more resistant to demetallation than their porphyrin counterparts [36].

In corrolazines, the three corrole *meso*-carbons are replaced by nitrogens and can be considered the corrole analogues of azaporphyrins (Figure 4.5). Indeed, corrolazines are prepared by a reductive ring contraction reaction performed on a phosphorus azaporphyrin complex followed by removal of phosphorus to give the free base. Corrolazines are also effective for stabilization of high-valent transition metals [37–39].

4.2.5 Porphyrin Isomers

Porphyrin isomers are macrocycles whose core has the same $C_{20}H_{14}N_4$ formula as free-base porphine, but with a different structural constitution [40, 41]. As noted above, if porphyrin is denoted [18]tetraphyrin(1.1.1.1), then the most symmetrical of its other possible isomers is [18]tetraphyrin(2.0.2.0), more commonly known as porphycene [42–44], with the less symmetrical isomers [18]tetraphyrin(2.1.0.1) and [18]tetraphyrin(2.1.1.0) known as corrphycene and hemiporphycene, respectively. Metal complexes of all these isomers are known, with those of the rectangular elongated porphycene being the most prevalent [45].

A more surprising form of porphine isomerism was developed in the early 2000s with the first reports of N-confused porphyrins. An N-confused porphyrin contains one (or more) of the pyrrole rings covalently linked into the macrocycle in an α,β′ manner rather than the α,α′ linkages that occur in regular porphyrin. As a result, the "confused" pyrrole has nitrogen located on the porphyrin periphery and carbon in the core, giving a 2-aza-21-carbaporphyrin (Figure 4.7) [46–48]. The N-H tautomerism operating in porphyrins also occurs for N-confused porphyrins, meaning that one tautomer has the N-H proton residing on the peripheral pyrrole nitrogen [49]. Coordination of a metal to the core of an N-confused porphyrin necessitates the formation of an M-C bond, giving a new type of porphyrin organometallic chemistry. Around 20 transition metal, main group, and lanthanide complexes of N-confused porphyrins are known [47, 50–52]. The landscape is even further confused (no pun intended) when an N-confused porphyrin is heated, or treated with base, undergoing an intramolecular fusion reaction to give an N-fused

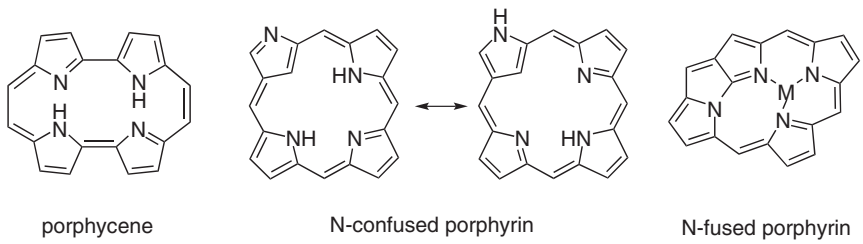

Figure 4.7 Porphycene, N-confused porphyrin, and N-fused porphyrin core structures.

porphyrin (Figure 4.7). These two-electron oxidized porphyrin isomers ($C_{20}H_{12}N_4$) have only three nitrogens available for coordination and can also form complexes. Confusion and fusion can also be combined with expansion to give an even larger and more architecturally complicated array of macrocycles [52].

4.2.6 Expanded Porphyrins

Expanded porphyrins contain a skeleton with five or more pyrroles (Figure 4.8). Of these, the hexaphyrins are the best known, but examples with up to 10 (decaphyrin) and even 16, 20, and 24 pyrroles have been reported in this rapidly developing field [16, 41, 53–55]. All of them are tours de force of synthetic chemistry, and increasingly sophisticated physical and spectroscopic studies are revealing new and interesting properties. The expanded porphyrins are no longer constrained to be planar and may be considerably twisted. Pyrrole rings may rotate within the skeleton, with the result that some rings may have a Möbius-like twist. This has consequences for aromaticity, with molecules in the Möbius configurations showing reversed aromaticity properties relative to those that conform to the Hückel rule [49, 56–58].

Many kinds of isomerism are possible for expanded porphyrins, with pyrrole rings linked through *meso*-carbons, direct pyrrole-pyrrole bonds, N-confused and N-fused links, N-donors other than pyrrole, and carbon and heteroatom donors, all part of the rich tapestry of expanded porphyrins. Simple five pyrrole examples are [22]pentaphyrin(1.1.1.1.1) and [22]pentaphyrin(1.1.1.1.0), given the trivial name sapphyrin (Figure 4.8). Tautomerism and oxidation or reduction to give different π-electron counts for the same skeleton are also possible. All of these form coordination complexes, with the expanded macrocycles offering coordination sites for two or more elements, with each coordinated element able to bond through two, three, or four of the macrocycle donors. Expanded porphyrin complexes of a wide range of elements are known [56], including main group elements (particularly phosphorus and boron) [59, 60], transition metals [61, 62], and the *f*-elements [63].

4.2.7 Heteroporphyrins

The last category of porphyrinoids to be considered are the heteroporphyrins, where one or more of the nitrogen donors is replaced by a different donor atom. If the heteroatom is carbon, then the subcategory carbaporphyrinoids results (Figure 4.9). For example,

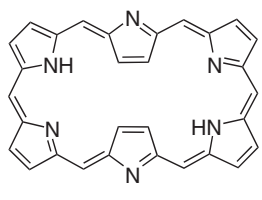

[26]hexaphyrin(1.1.1.1.1.1)

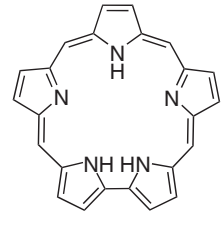

[22]pentaphyrin(1.1.1.1.0)
sapphyrin

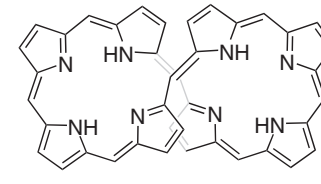

[36]octaphyrin(1.1.1.1.1.1.1.1)

Figure 4.8 Examples of expanded porphyrins: hexaphyrin, sapphyrin, and octaphyrin.

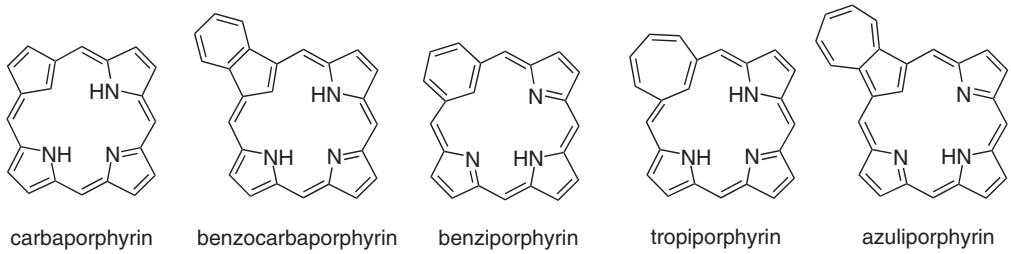

Figure 4.9 Carbaporphyrin, benzocarbaporphyrin, benziporphyrin, tropiporphyrin, and azuliporphyrin core structures.

replacement of one pyrrole unit in the porphyrin core by cyclopentadiene gives the same framework as porphine with one N replaced by C. Other unsaturated organic rings such as indene, benzene, cycloheptatriene, or azulene in place of pyrrole give other modified macrocycles known trivially as benzocarbaporphyrins, benziporphyrins, tropiporphyrins, or azuliporphyrins (Figure 4.9) [64–66]. Many of these systems retain their conjugated aromatic structures, and act as organometallic ligands through C-H activation to form a range of late transition metal complexes [67–69].

Heteroporphyrins are the more general class of core-modified porphyrins where one or more pyrroles are replaced by a five-membered heterocycle such as furan, thiophene, selenophene, tellurophene, phosphole, or silole to give a porphyrinoid containing one or two O, S, Se, Te, P, or Si heteroatoms (Figure 4.10) [70–78]. Heteroporphyrins have limited coordination chemistry relative to tetrapyrroles, for several reasons. The large heteroatoms in the cores may result in nonplanar arrangements of the XNNN or XYNN (X, Y = O, S, Se, Te, P, or Si) donor atoms, and also make the binding cavity more crowded with less space to coordinate a metal. With one neutral heteroatom (XNNN, X = O, S, Se, Te), there is only one ionizable pyrrole NH to give a monoanionic ligand; when two neutral heteroatoms are present (XYNN, X, Y = O, S, Se, Te), no pyrrole NH groups remain, and the ligand becomes a neutral donor. Nevertheless, when heteroporphyrins do from metal complexes, they can stabilize unusually low oxidation states, for example Cu(I), Ni(I), and Pd(I), or unusual spin states such as high-spin organonickel(II) [70, 77]. The monoanionic or neutral charge on the heteroporphyrin ligand means the metal may bear anionic axial ligands, for example Ni^{II}(diaoxaporphyrin)X_2, where X = halide or aryl [77]. There is also some limited coordination chemistry of heterocorroles [70, 74].

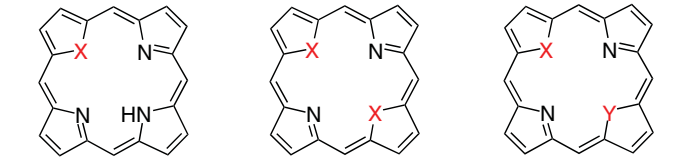

Figure 4.10 Core structures of heteroporphyrins containing one or two heteroatoms.

4.3 Metallation, Demetallation, and Characterization

4.3.1 Metallation and Demetallation

The most general method for element insertion into a porphyrin requires an element salt to be stirred (or heated) with a free-base porphyrin (H_2Por) in a suitable solvent. The choice of salt, solvent (protic/aprotic, polar/nonpolar, coordinating/non-coordinating, acidic/basic), stoichiometry, concentration, reaction time, and temperature are all variables. There is no generic method, and although some elements are remarkably easy to insert, others require a very specific choice of precursor and reaction conditions. The element precursor is often used in considerable excess. The classic Adler and Longo method [79] utilizes a metal salt in refluxing DMF (Eq. 4.1), with the product precipitated by addition of water and subsequent purification by chromatography and/or recrystallization. This method was reported in 1970 to be effective for Mg, Ca, Ba, VO, Mn, Cr, Fe, CO, Ni, Cu, Zn, Pd, Ag, Cd, Hg, Sn, and Pb complexes of TPP using the metal acetates, halides, hydroxides, or carbonates as precursors. The original preparation of Cr(TPP) used 1 L of DMF, 10 g of H_2TPP, and 2–3 g of $CrCl_2$ at reflux for several minutes, with the product precipitated by addition of 1 L of chilled water to the cooled reaction mixture (98% crude yield) [79]. Such quantities are unthinkable in modern times when metallation is often carried out on milligram quantities of bespoke porphyrins painstakingly synthesized for a particular application. Variations on this method use a metal salt with the free-base porphyrin in a range of other organic solvents, ranging from low to high boiling, often with the addition of a base (e.g., 2,6-lutidine) as an acceptor for the protons liberated from the free base (Eq. 4.2). This is to prevent the porphyrin itself from acting as base, forming the $[H_4Por]^{2+}$ salt that inhibits insertion because the metal and protons compete as Lewis acids for the basic porphyrin.

$$MX_n + H_2Por \xrightarrow{DMF} M(Por)X_{2-n} + 2HX \tag{4.1}$$

$$MX_n + H_2Por \xrightarrow[base]{solvent} M(Por)X_{2-n} + 2HX \tag{4.2}$$

$$MX_n + H_2Por \xrightarrow{CH_3CO_2H} M(Por)X_{2-n} + 2HX \tag{4.3}$$

$$MR_n + H_2Por \xrightarrow{solvent} M(Por)R_{2-n} + 2HR \tag{4.4}$$

$$ML_n + H_2Por \xrightarrow{solvent} M(Por)L \tag{4.5}$$

$$MX_n + Li_2Por \xrightarrow{solvent} M(Por)X_{2-n} + 2LiX \tag{4.6}$$

A further classic method is carried out in acidic conditions, using the metal acetate salt in glacial acetic acid as the solvent (Eq. 4.3), reported to be effective for a range of metals including Zr, Hf, Mn, Fe, Co, Ni, Cu, Zn, Pd, Pt, Ag, and Au. Selected metals can be inserted using a different strategy, a metal alkyl precursor MR_n that reacts with the free base porphyrin H_2Por, eliminating the alkane RH to yield MPor (Eq. 4.4), reported for Mg, Al, and Si. The heavier late transition metals can prove challenging to insert, and a metal carbonyl (or other low-oxidation-state organometallic) precursor in a high-boiling solvent is often employed (Eq. 4.5); for example, $Ru_3(CO)_{12}$ with H_2Por in a high-boiling ether gives Ru(Por)(CO)L (where L is a coordinating solvent or ligand). Some insertion methods and subsequent work-ups by precipitation give a relatively pure product directly

that can be purified by crystallization, whereas others require the product to be purified by chromatography.

This is not suitable for less robust M(Por) complexes, which may demetallate on chromatography supports, or for those which are highly oxophilic. An alternative strategy that works in these situations is salt elimination from the lithiated porphyrin Li_2(Por), which itself is produced from the amide $LiN(SiMe_3)_2$ with H_2Por [80, 81]. Treatment of Li_2(Por) with a stoichiometric amount of a salt MX_n then gives the resulting complex M(Por) with elimination of LiX as the only by-product and can typically be removed by filtration (Eq. 4.6) [82]. This method allowed the preparation of very oxophilic early transition metal complexes of the Groups 3, 4, and 5 elements, and was also utilized in the preparation of the first (and only) tellurium porphyrin complex [1]. Preparation of lithium corrole Li_3(Cor) also opened up a similar pathway to early transition metal as well as lanthanide and actinide corrole complexes [32].

One important detail of element insertion chemistry is that the oxidation state of the element precursor is not always the same as the oxidation state in the inserted M(Por) product. When this is the case, the precursor is typically in a lower oxidation state than the product. Iron porphyrins are almost always prepared using an Fe(II) salt, which air oxidizes to the Fe^{III}(Por)X product during workup. Only if oxygen is excluded does the Fe^{II}(Por) product result. The metal carbonyl route gives products in higher oxidation states than the precursors; in the example above, the Ru(0) precursor gives an Ru^{II}(Por) product. Tin is another example; $SnCl_4$ does not appear to insert into H_2Por, but $SnCl_2$ is successful although it gives the Sn^{IV}(Por)X_2 product. These redox processes may arise from an external oxidant (air), disproportionation (as in the use of Ag(OAc) with H_2Por to give Ag^{II}(Por) plus Ag metal), or from mechanistically obscure processes involving reactive fragments under harsh reaction conditions.

The steric constraints of the porphyrin itself can influence the rate of element coordination, with bulky peripheral substituents typically slowing or completely inhibiting the insertion process. On the other hand, carefully designed groups attached to the porphyrin periphery that shepherd the metal into the plane can accelerate the process. A series of porphyrins containing carboxylic acid or ester groups attached to pendant arms or straps was found to accelerate the insertion of Bi(III) and Pb(II) ions, and the process was complete in minutes rather than hours [83, 84].

For some ligand/element combinations, the choice of metal salt, solvent, and conditions might be broad, whereas for others the chemistry is very particular and tricky, requiring patience and persistence on the part of the synthetic chemist. This is true, for example, in recent reports of heavy transition element corroles, and the recently reported examples containing period 6 metals require extremely precise control of the metal precursor, solvent, and reaction conditions [35].

Relatively little is known about the mechanistic process of metal insertion, despite a number of studies during the 1960s–1980s, summarized in a useful review [85]. The prevalent process is believed to be the initial formation of a loosely associated metal/free-base porphyrin conjugate, often referred to as a sitting-atop (SAT) complex as the metal at this stage is well out of the N_4 plane, although these intermediates are very difficult to characterize [86]. The SAT complex is then proposed to collapse to form the metalloporphyrin M(Por) with loss of the porphyrin hydrogens and insertion of the metal into the plane. The kinetics of this sequence of steps has been studied by a number of approaches, and may vary according to the metal and the dissociation constants for the ligands or ions bound to the metal precursor. A

more recent study has investigated the mechanism of metal insertion (specifically Mg(II) and Fe(II)) by theoretical methods, looking at stepwise loss of coordinated H_2O from the metal ions and the protons from the porphyrin [87].

There are also reports that the presence of a heavy metal ion (Cd(II), Hg(II), or Pb(II)) can assist the insertion of a lighter metal (e.g., Cu(II) or Zn(II)), possibly by pre-association of the heavier ion (which is too large to collapse into the N_4 plane) to form a SAT complex, which then accelerates the complexation of a second, lighter element [85, 88]. An update on this work examines double metal–ligand exchange in which two different porphyrin complexes exchange their central metal ions and the corresponding ligands [89]. A phenomenon related to this is also observed in architecturally complex synthetic porphyrins containing two straps, one across each face of the ligand, and each of which positions a carboxylate group that hangs above the face of the porphyrin, providing both hanging atop (HAT) and out-of-plane (OOP) metal binding sites that allowed for coordination of two metals per porphyrin (Figure 4.11). The OOP site involves the metal coordinated to the four porphyrin nitrogens, but is OOP because of the large size of the period 6 metal ions investigated. Several metal exchange processes were identified involving metals swapping between the two sites [90–92].

The recent rise of interest in porphyrins as surface-absorbed species in a range of functional devices has led to a review of methods for metallation of porphyrins on surfaces under

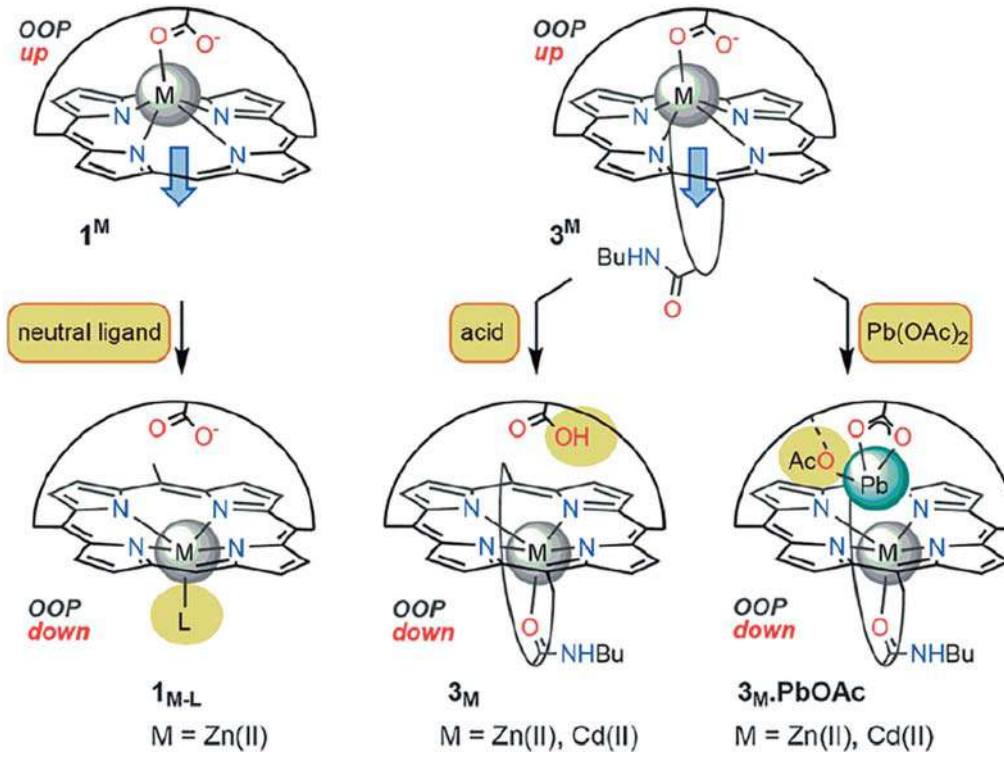

Figure 4.11 Interconversion of metals in the hanging atop (HAT) and out-of-plane (OOP) metal binding sites. Source: Republished with permission of the Royal Society of Chemistry, from Le Gac and Boitrel [90]; scheme 1(b); permission conveyed through Copyright Clearance Center, Inc.

ultra-high vacuum techniques, with the metal introduced by chemical or physical vapor deposition, from the tip of a scanning tunneling microscope, or as atoms from the underlying surface [93].

The stability of metalloporphyrin complexes has been empirically categorized using a stability series devised by Buchler, in decreasing order of stability: Class I, fully resistant to 100% sulfuric acid; Class II, demetallated by 100% sulfuric acid; Class III, demetallated by aqueous hydrochloric acid; Class IV, demetallated by acetic acid; and Class V, demetallated by neutral water [3]. There are many other factors influencing stability, such as ion size with the larger early transition metal and heavier period 6 late transition metal and main group elements residing well out of the N_4 plane, with concomitant higher lability. Oxidation state also influences ion size, so for a given element lower oxidation states mean larger ions and possibly increased lability. The porphyrin ligand itself is a powerful chromophore and photoinduced degradation can also lead to demetallation. Axial ligands coordinated to the metal also have their own stability properties, and binding and exchange constants have been measured in many instances [94].

4.3.2 Characterization

Other chapters in this book give much more detailed descriptions of the physical properties of porphyrins and how they can be used for detailed characterization and analysis of the properties of individual porphyrin complexes. The following is a quick get-started summary for those new to the field.

Element insertion reactions are typically followed by UV–visible absorption spectroscopy and thin layer chromatography. Typical porphyrin complexes follow Gouterman's four-orbital model for their electronic structure [95, 96]. A free-base porphyrin has a characteristic UV–visible spectrum with an intense Soret, or B band, and four Q bands that are typically an order of magnitude less intense. Upon metallation, there is always a distinctive change in the spectrum, with a shift of the Soret and the collapse of the four Q bands to a smaller number of Q bands (Figure 4.12). Insertion reactions can be followed by taking a small aliquot (a drop) of the reaction solution, diluting to a few milliliters in a cuvette, and obtaining the UV–vis spectrum. Absorption spectra are additive, so at first the free base porphyrin is observed, then at later time intervals an admixture of the spectra of the free-base and metallated product are seen, until the reaction can be judged complete when the free base Soret is no longer evident and the new spectrum of the product has emerged with no further changes. One word of caution – the concentration of porphyrin species under these conditions is on the order of 10^{-5} mol L^{-1}, and the concentration of impurities (e.g., water) in the solvent used for spectroscopy can have the same order of magnitude. As a result, this method is less useful for very labile complexes that might undergo hydrolysis or demetallation at the low concentrations utilized for quick UV–visible measurements.

Thin layer chromatography (TLC) can also be useful for following insertion reactions, as the highly colored free-base and metalloporphyrins can be easily discerned by the naked eye. Again, as the insertion reaction proceeds, side-by-side spots of the free-base and reaction mixture on a TLC plate can be a quick method of observing the rate of progress. Both UV–visible spectroscopy and TLC can also be used as quick analytical tools for following the conversion of one metalloporphyrin species into another, so long as each species has sufficient stability under these conditions.

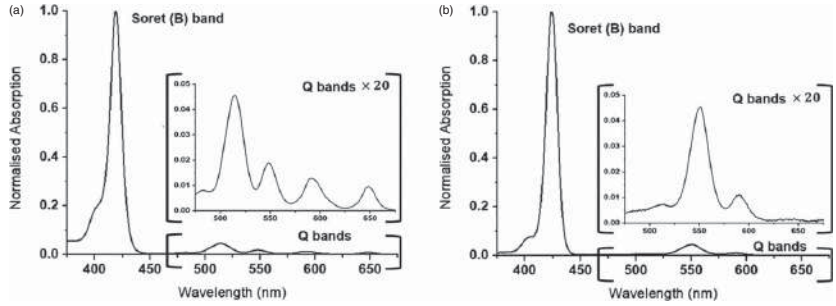

Figure 4.12 UV–visible absorption spectrum of (a) H_2(TTP) and (b) Zn(TTP) in CH_2Cl_2.

Purification is often undertaken by column or flash chromatography (gram to milligram quantities) or, for smaller amounts, preparative HPLC. Handy practical tips on column chromatography can be found in various sources [97], and are often not found in the preparative details in individual research papers. Visualization of the bands is facilitated by the highly colored nature of the compounds, and they also may fluoresce under long-wavelength fluorescent light. Porphyrin compounds can be light sensitive and should be stored in the dark, and prolonged exposure to irradiation should be avoided, particularly for more elaborate free bases and less stable metalloporphyrins. Crystallization is another useful technique for the bulk purification of complexes with good solubility.

NMR spectrometry is a particularly useful technique for checking the purity and composition of diamagnetic metalloporphyrins. The macrocycles are 18π-electron Hückel aromatic systems, and have a marked diamagnetic ring current that dramatically affects the chemical shifts of both the porphyrin and the axial ligands. Protons on the porphyrin periphery show downfield shifts, particularly the β-pyrrolic protons of *meso*-substituted porphyrins, which generally appear around 9 ppm. The high symmetry of simple *meso*-tetra-substituted porphyrins means the β-pyrrolic protons appear as a singlet. The diamagnetic ring current effect means that protons on the axial ligands above and below the porphyrin plane show upfield shifts that can be quite marked, and this is a good, quick, diagnostic tool for the presence of a given ligand (Figure 4.13). Upfield shifts are also observed for the coordinated elements themselves when these are NMR-observable nuclei, of which ^{31}P and ^{29}Si are good examples. The ^{31}P NMR spectrum of $[P(TPP)(OMe)_2]^+$ shows the high symmetry of the system, with the single P atom spin–spin coupled to eight equivalent β-pyrrolic protons and six equivalent OMe protons, giving an overall 63-line multiplet for a single atom (Figure 4.14) [98].

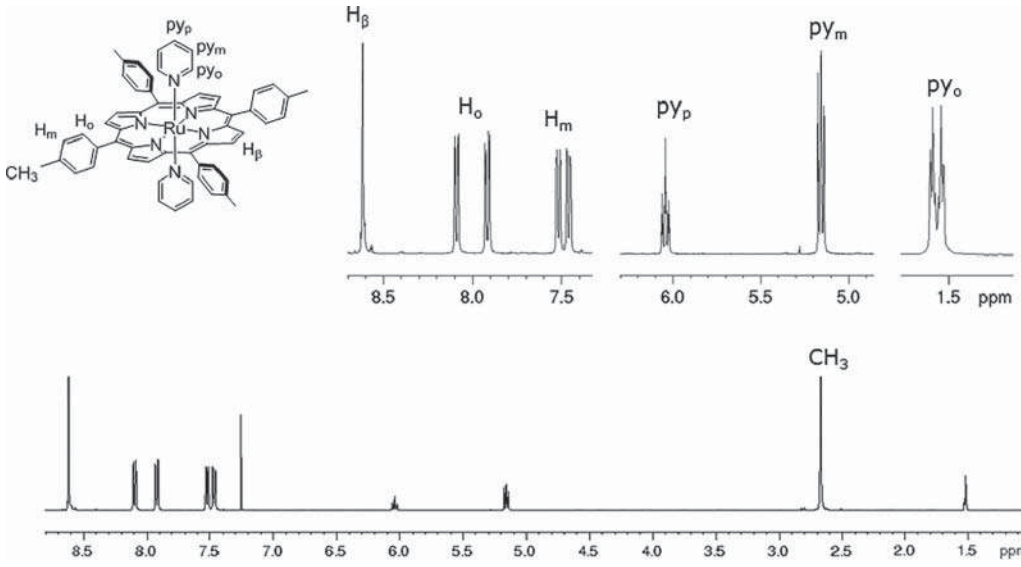

Figure 4.13 ^{1}H NMR spectrum of Ru(TTP)(py)$_2$ in $CDCl_3$; inset shows assignments and upfield-shifted pyridine protons.

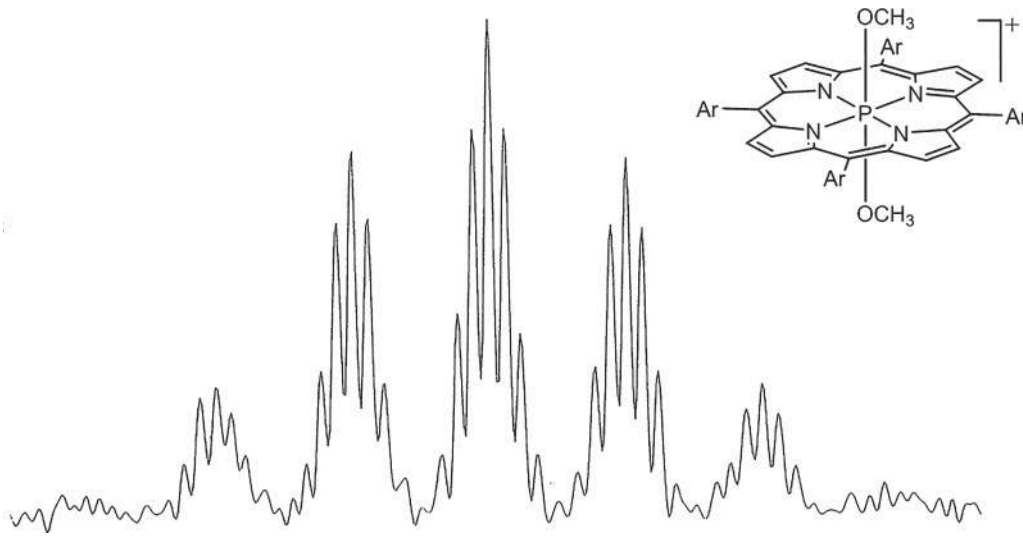

Figure 4.14 Fully proton-coupled ^{31}P NMR spectrum (162 MHz, $CDCl_3$) of $[P(TTP)(OCH_3)_2]Cl$ (Ar = *p*-tolyl); δ −179.93, $^3J_{PH}$ 25.5 Hz, $^4J_{PH}$ = 3 Hz; Source: Reprinted with permission from Barbour et al. [98]; figure 2. Copyright 1992 American Chemical Society.

4.4 Main Group Elements

Describing the porphyrin coordination chemistry of the main group, *s* and *p* block elements, requires traversing the entire range of chemical characteristics in the periodic table, from large electropositive metals that engage in predominantly ionic bonding to small electronegative nonmetals that coordinate to the ligand through much more covalent or hypervalent interactions. These will be briefly considered group by group, with the aim of highlighting particular characteristics and providing an entry point to their use. The heaviest of these elements, mercury, thallium, lead, and bismuth, will be considered together as they have more in common with each other than with their respective group members.

Through a coordination chemistry lens, it is perhaps size that has the most dramatic impact on the structures of porphyrin complexes of the *s* and *p* block elements. The elements in question range from those that are much too small and have the wrong geometrical preferences (e.g., boron) to those that are too large to fit in the N_4 coordination site and may form porphyrin complexes only with the metal in SAT mode, displaced well out of the N_4 plane (e.g., the period 6 elements thallium, lead, and bismuth) (Figure 4.15). Nevertheless, this wide range of elements is documented to form porphyrin complexes with an equally wide range of fascinating structural and chemical properties.

4.4.1 Group 1

A series of papers in the early 1990s on the preparation and characterization of the first porphyrin complexes of the alkali metals Li, Na, and K was a significant advance for a number of reasons [80, 81, 105, 106]. These large electropositive metals form very labile and moisture-sensitive porphyrin complexes with the general formula $M_2(Por)L_n$, where L are

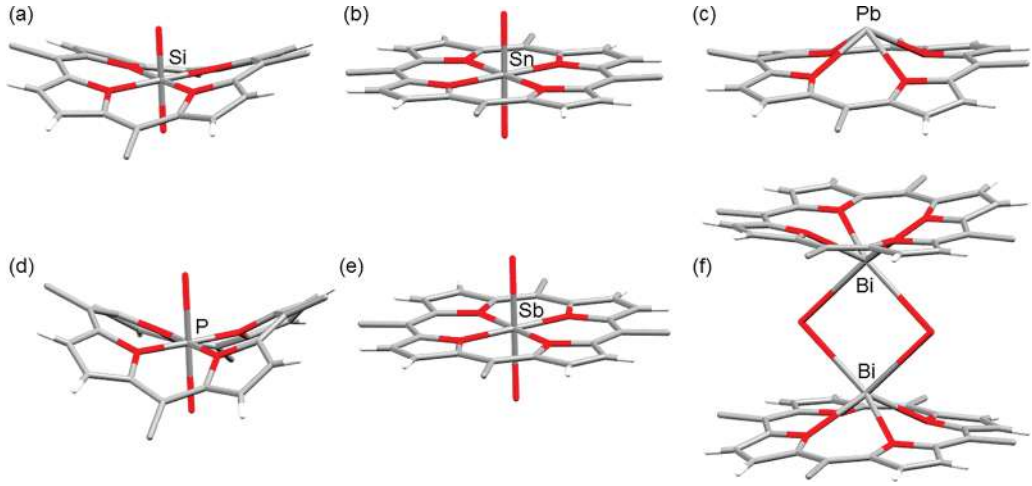

Figure 4.15 Group 14 and 15 porphyrins, showing the effect of element size and oxidation number on coordination: (a) Si(TTP)F_2 [99], (b) Sn(TPP)F_2 [100], (c) Pb(TnPrP) [101], (d) $[P(TPP)Cl_2]^+$ [102], (e) $[Sb(TPP)Cl_2]^+$ [103], (f) $[Bi(TpClPP)Cl]_2$ [104]; *meso*-aryl groups removed except for the *ipso*-C.

typically O- or N-donor solvent molecules. With appropriate care in their handling, they can be used as precursors to porphyrin complexes of other electropositive and oxophilic metals for which the more traditional insertion methods do not work, and also for main group elements [82, 107]. For example, Li_2(Por) was used as the precursor to the first (and only) Te porphyrin complex, and the recent availability of Li_3(Cor) [32] led very shortly thereafter to the preparation of the first examples of corrole complexes of around 10 elements.

The most convenient preparation of the Group 1 porphyrin and corrole complexes is to use the silylamide derivatives M(N($SiMe_3$)$_2$) as the metal source with free base porphyrins or corroles in ether or pyridine (Eqs. 4.7 and 4.8).

$$H_2Por + 2MN(SiMe_3)_2 \longrightarrow M_2(Por)L_n + 2HN(SiMe_3)_2 \tag{4.7}$$

$$H_3Cor + 3MN(SiMe_3)_2 \longrightarrow M_3(Cor)L_n + 3HN(SiMe_3)_2 \tag{4.8}$$

Lithium has a covalent radius of 1.28 Å, which is a relatively good fit for the 2.0 Å hole in the porphyrin in combination with the 0.70 Å covalent radius of sp^2 hybridized nitrogen. Structural studies demonstrated that the complexes adopt an ion pair formulation, for example, $[Li(OEP)]^-[Li(THF)_4]^+$. Sodium and potassium ions are much too large to fit in the N_4 plane, and instead their complexes exist as inverse sandwiches with one metal above and one below the N_4 plane, $L_2M(OEP)ML_2$ (M,L = Na,THF or K,py) (Figure 4.16). Interestingly, lithium can also adopt this structural arrangement as in $(Et_2O)_2Li(TPP)Li(Et_2O)_2$ (Figure 4.16) [106]. In the three structures, the Li, Na, and K ions sit 1.02, 1.38, and 1.84 Å, respectively, above and below the N_4 plane, reflecting the different sizes of the elements. The lithium corrole also adopts this structure, with two Li^+ cations above and below the plane and the third as a solvated counterion in $[(THF)Li(Cor)Li(THF)]^-[Li(THF)_4]^+$ (Cor = Mes_2(p-OMePh)corrole) [32]. The neutral π-radicals of lithium porphyrins $Li^+[Por]^{\cdot-}$ have also been prepared [108], as has an example of the lithium complex of a core-modified 21-thiaporphyrin [109].

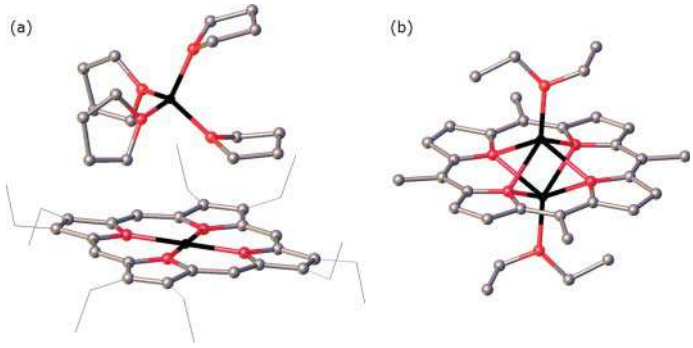

Figure 4.16 Molecular structures of (a) $[Li(OEP)]^-[Li(THF)_4]^+$ and (b) $[Li(OEt_2)]_2(TPP)$ [80, 106]; *meso*-aryl groups removed except for the *ipso*-C.

The lithium porphyrins and corroles are very moisture sensitive and must be prepared and handled using the appropriate techniques. Typical conditions for subsequent salt elimination reactions with other metal halide precursors use $Li_2(Por)$ or $Li_3(Cor)$ in THF, mixed at low temperature and allowed to warm to room temperature. $Li_2(Por)$ was used for the preparation of organo-scandium, -zirconium, -hafnium, and –tantalum porphyrin complexes [110–114], and $Li_3(Cor)$ for the first examples of titanium, zirconium, hafnium, tungsten, lanthanide, and actinide corroles [32, 115–119].

4.4.2 Group 2

Beryllium and magnesium have the exact opposite profiles when it comes to their occurrence in porphyrin coordination chemistry. Beryllium is highly toxic, and has not been reported as a porphyrin complex although it does occur as a phthalocyanine complex with, unusually, square planar and square pyramidal beryllium in Be(Pc) and $Be(Pc)(H_2O)$ [120]. Magnesium, on the other hand, is essential to many forms of life, especially considering its role in chlorophyll. In chlorophyll biosynthesis, the enzyme magnesium chelatase is responsible for the insertion of Mg(II) into protoporphyrin IX in an ATP-dependent process [121]. In synthetic chemistry, magnesium porphyrins and phthalocyanines are well known and moderately stable to demetallation. They can be made by the traditional insertion route using a magnesium salt in DMF, or in a non-coordinating solvent with the addition of a hindered base. Grignard reagents are also used as the source of the metal and react with H_2Por via alkane elimination. However, the insertion of magnesium into porphyrins is not as facile as for zinc, and magnesium porphyrins are more easily demetallated. Mg(Por) typically binds one or two axial ligands, usually O- or N-donors, and has been structurally characterized as six-coordinate complexes or as five-coordinate complexes in which the Mg atom resides slightly out of the porphyrin plane. Magnesium corroles are unknown at present.

The chemistry of the heavier Group 2 elements is relatively undeveloped, most likely owing to their large size and ionic nature, meaning the resulting complexes are likely to be highly labile and moisture sensitive. Two structurally characterized porphyrin complexes are $Ca(Por)py_3$, in which the Ca atom lies considerably OOP and the three pyridine ligands all occupy the same face of the molecule, and the trimetallic double-decker $I(MeCN)_2Ca(Por)Ca(Por)CaI(MeCN)_2$, which contains two porphyrins sandwiched between three Ca^{2+} ions (Por = tetra(tert-butylphenyl)porphyrin) [122].

4.4.3 Group 13

Group 13 elements range from the lightest member, boron, which is too small to form a typical porphyrin complex, through the middle elements, aluminum, gallium, and indium, which all form "normal" porphyrin complexes, and finally the heaviest member, thallium, which forms a range of OOP porphyrin complexes.

For a long time, boron subphthalocyanine was the quintessential boron porphyrinoid, comprising boron at the apex of an inverted bowl with an additional axial anion to give pseudo-tetrahedral coordination [19, 21]. This class of boron subporphyrinoids has now increased to include subporphyrins, subporphyrazines, and subbenzoporphyrins [20, 22, 23, 25]. Boron N-confused- and N-fused-porphyrin complexes utilize only three of the pyrrole nitrogens to bond to boron [123]. BODIPYs are fluorescent boron dipyrrin compounds of typical composition B(dipyrrin)F_2 in which the dipyrrin ligand can be thought of as half a porphyrin [124–126].

The small size of boron (covalent radius 0.82 Å) and its preference for trigonal planar or tetrahedral geometry make it an unlikely prospect for porphyrin coordination; nevertheless, over the last two decades, a rich and unexpected chemistry has developed for boron porphyrins and corroles [127–132]. The characteristic motif is the binding of two borons per macrocycle, each interacting with two pyrrole nitrogens. The two borons may both be in-plane, in-plane/OOP, both OOP cisoid, both OOP transoid, and several examples show B-O-B or B-H-B bridging motifs (Figure 4.17) [17, 18, 133]. Redox chemistry is possible both at boron and at the porphyrin. This occurs when the B-B bonded, formally B(II), complex $[B_2(Por)]^{2+}$ is reduced by two electrons that populate the porphyrin π^* orbital to give $B_2(Por)$, a neutral complex of the reduced, 20 π-electron antiaromatic isophlorin macrocycle [134, 135]. The sterically constrained environment of the porphyrin or corrole macrocycle also influences the chemistry at boron, with spontaneous reductive coupling to give reduced B-B or B-H-B groups coordinated to the porphyrin or corrole, respectively [134–136]. The structural chemistry shows a fine balance, too, with the porphyrin complex $B_2OF_2(Por)$ existing as the *transoid* structure with the N_4 plane markedly elongated (by over 1 Å), while the closely related corrole complex $[B_2OF_2(Cor)]^-$ displays a domed, *cisoid* structure reflecting the smaller coordination pocket (Figure 4.18) [17, 18].

Boron complexes of expanded porphyrins are becoming a prominent motif, in which boron binds to two pyrrole nitrogens in a BODIPY-like arrangement as in the hexapyrrole amethyrin, $(BF_2)_2$(amethyrin), [129] or to one or more sets of three pyrroles to produce

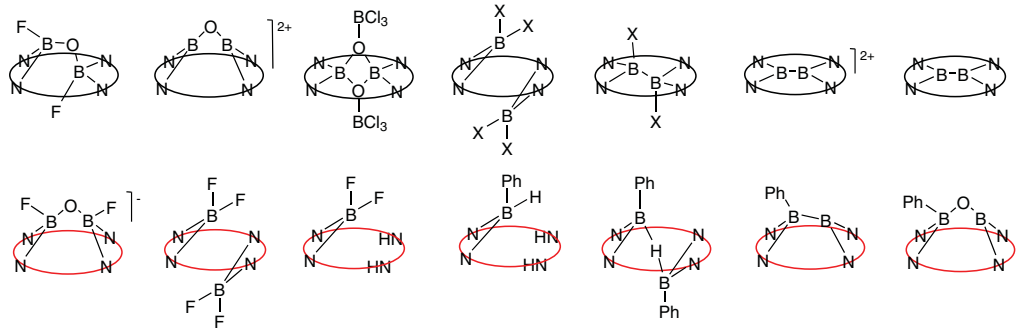

Figure 4.17 Structural motifs exhibited by boron porphyrins (black macrocycle) and corroles (red macrocycle).

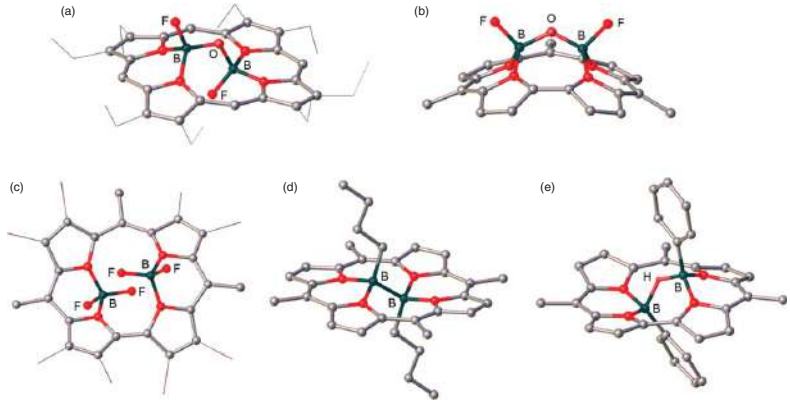

Figure 4.18 Representative boron porphyrin and corrole structures: (a) B_2OF_2(OEP) [129], (b) $[B_2OF_2(TPC)]^-$ [130], (c) $[(BF_2)_2(OBrTPFPC)]^-$ [132], (d) B_2Et_2(TTP) [134] and PhBHBPh(TTC) [136]; *meso*-aryl groups removed except for the *ipso*-C.

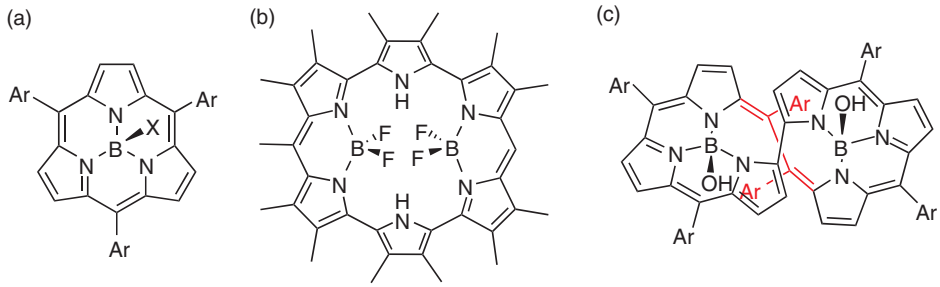

Figure 4.19 Boron complexes of contracted and expanded porphyrins: (a) boron subporphyrin [22], (b) diboron complex of [24]hexaphyrin(1.0.0.1.0.0) (amethyrin) [129], (c) boron complex of [28]hexaphyrin(2.1.1.0.1.1) [137].

boron subporphyrin-like motifs within expanded porphyrins (Figure 4.19) [55, 56, 59]. The incorporation of boron into expanded porphyrins sometimes causes unexpected skeletal rearrangements and bond cleavages. Other expanded macrocycles such as smaragdyrins also form boron complexes [60].

The preparative chemistry of most of the boron subporphyrinoids is macrocycle formation templated by a boron halide, although subporphyrins have been formed beginning with tripyrrolylborane. Boron porphyrins, corroles, and expanded porphyrins are typically prepared from the halide BX_3 or $PhBX_2$ with the free-base macrocycle, often with a bulky base added to absorb the HX by-product.

Aluminum, gallium, and indium porphyrins are typically prepared from the halides MX_3 with H_2Por to give M(Por)X, or, for aluminum, from the alkyl AlR_3 with H_2Por to give Al(Por)R. The halide species Al(Por)X are reactive toward water to give Al(Por)OH, which can be converted to organometallic Al(Por)R or Al(Por)Ar by reaction with RLi or ArLi. The complexes crystallize as five-coordinate species, M(Por)X or M(Por)R, with the metal displaced out of the N_4 plane toward R or X, or as six-coordinate complexes M(Por)XL or $[M(Por)L_2]^+$.

The alkylaluminum complexes Al(Por)R, in particular, are very basic and react with alcohols ROH to give Al(Por)OH. They will also activate other small organic molecules such as CO_2, ketones, lactones, or conjugated esters and catalyze the living anionic polymerization of unsaturated systems [138] and the copolymerization of propylene oxide with carbon dioxide [139, 140].

Recent years have seen big advances in the chemistry of aluminum and gallium corroles, although, curiously, indium corroles remain unexplored, possibly because of the larger size of the indium atom. Gallium is an excellent fit for the corrole cavity (Figure 4.20a), and gallium corrole can be considered to be the closed-shell corrole analogue of zinc porphyrin. It has been used in a similar manner to investigate the intrinsic properties of metallocorroles without interference from coordination of an open-shell metal [141]. The complexes are intensely fluorescent. Aluminum and gallium triarylcorroles can be peripherally functionalized on the pyrroles adjacent to the bipyrrole linkage with one or two -CHO, $-NO_2$, CH=C(CN)(COOH) or $-SO_3H$ groups to give amphiphilic complexes that are proving to have a wide range of uses

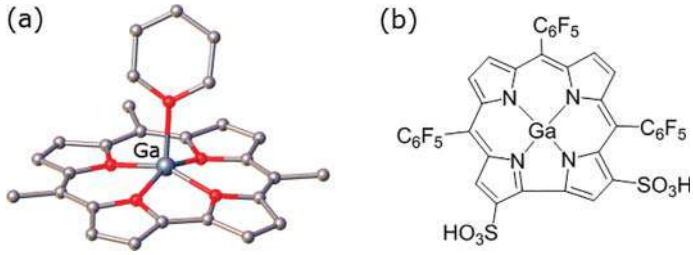

Figure 4.20 (a) Structure of Ga(TPFPC)(py) [141], (b) amphiphilic gallium 2,17-bis-sulfonato-5,10,15 (trispentafluorophenyl)corrole; *meso*-aryl groups removed except for the *ipso*-C.

(Figure 4.20b) [142, 143]. They bind tightly to serum albumins and have been investigated for their biomedical applications. With the aid of appropriate carrier proteins, cell uptake of sulfonated gallium corrole is facile, and it has been shown to have excellent antitumor properties both *in vitro* and *in vivo* against breast cancer cell lines [36, 144]. As a consequence of the intrinsic intense red fluorescence of the gallium corroles, they are effective for tumor imaging as well as tumor elimination with excellent selectivity [145, 146].

4.4.4 Group 14

Porphyrin complexes of all of the Group 14 elements – carbon, silicon, germanium, tin, and lead – are known. In the case of carbon, it possibly stretches the point a little to refer to N-alkylated porphyrins as carbon "complexes," but certainly examples where a carbon group bridges two pyrrole nitrogens would meet the definition adopted for this chapter.

Silicon and germanium porphyrins are generally prepared from MCl_4 with the free-base porphyrins in pyridine or a similar solvent at elevated temperatures, giving the M(IV) products $M(Por)Cl_2$. An alternative route for silicon uses Li_2TPP with $HSiCl_3$ or H_2SiCl_2 to give $Si(TPP)Cl_2$, whereas $MeHSiCl_2$ or Me_2SiHCl yields Si(TPP)MeCl or $Si(TPP)Me_2$. Silicon is small relative to the porphyrin cavity, and the porphyrin is severely ruffled as a result. The silicon complexes are quite labile to hydrolysis and methanolysis, and more prone to demetallation for the TPP complexes than those containing OEP. For both silicon and germanium, $M(Por)Cl_2$ react with Grignard reagents to give the organometallics $M(Por)R_2$. The germanium examples of these are labile toward to both air and light. All of the silicon(IV) and germanium(IV) complexes are six coordinate with the general formula $M(Por)X_2$. Tin(IV) porphyrins are prepared from $SnCl_2$ with H_2Por producing $Sn^{IV}(Por)X_2$ after oxidation during workup. Surprisingly, $SnCl_4$ does not insert into H_2Por [147]. Sn(IV) porphyrins make excellent scaffolds for multiporphyrin assemblies because of their affinity for anionic oxygen ligands such as carboxylates and aryloxides [148].

A tin(II) porphyrin can be isolated if air is excluded from the reaction conditions; it forms a pyramidal complex with the tin atom lying 1.02 Å above the N_4 plane with no axial ligands. It is easily air-oxidized in solution. A recent and unexpected development occurred when silicon and germanium porphyrins and phthalocyanines with the apparent M(II) oxidation state were prepared. The reaction of $GeCl_2$(dioxane) with $K_2(Pc)(DMF)_4$ or $Li_2(TPP)(OEt_2)_2$ yields Ge(Pc) and Ge(TPP). Both dissolve in pyridine to form $Ge(Pc)(py)_2$ and $Ge(TPP)(py)_2$ (Figure 4.21) [149]. Similar chemistry produced the silicon phthalocyanine analogue $Si(Pc)(py)_2$, all of which have an apparent formal M(II) oxidation state [150]. However, ^1H NMR data for $Ge(Pc)(py)_2$, $Ge(TPP)(py)_2$, and $Si(Pc)(py)_2$ show strong paratropic ring

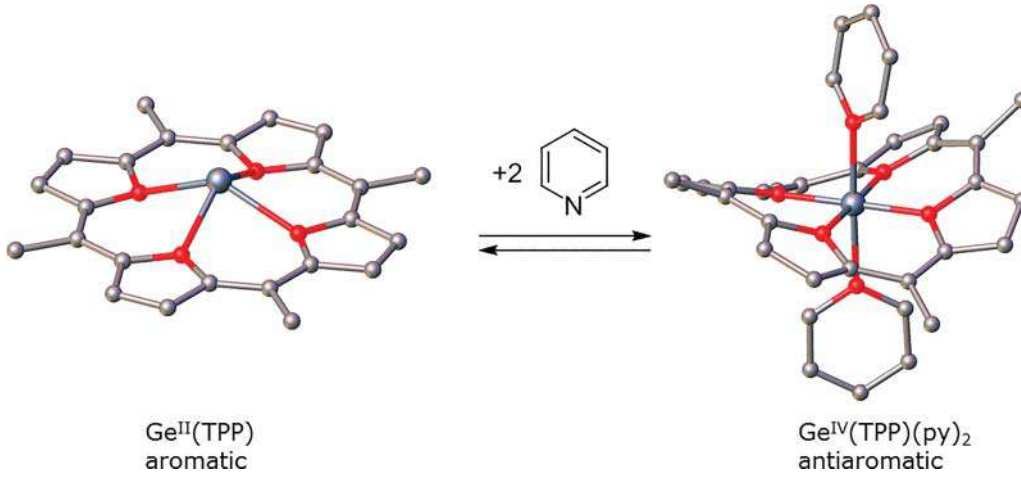

Figure 4.21 Reversible oxidation state change in Ge(TPP) induced by pyridine coordination [149]; *meso*-aryl groups removed except for the *ipso*-C.

currents, supported by nucleus-independent chemical shift (NICS) calculations. All of these are consistent with an antiaromatic electronic structure in which the porphyrin or phthalocyanine rings have been reduced to the 20 π-electron forms and the central element oxidized to M(IV). Remarkably, the formation of $Ge(TPP)(py)_2$ is reversible, and in benzene the pyridine dissociates to form Ge(TPP), which, from UV–visible and ^1H NMR spectroscopy, is an aromatic Ge(II) porphyrin, in contrast to the antiaromatic $Ge(TPP)(py)_2$, which contains Ge(IV) and the two-electron reduced ligand. The formation of $Ge(TPP)(py)_2$ represents an unusual example of an oxidation state change induced by coordination of a donor ligand. Both Ge(TPP) and $GePc(Py)_2$ were structurally characterized, and the latter complex shows significant bond length alternation in the 20-carbon periphery of the reduced porphyrin ring [149, 150]. Two Si(IV) complexes, $Si(TPP)(py)_2$ and $Si(TPP)Cl_2$ (the former bearing the reduced porphyrin ring), have also been studied using static absorption and fluorescence spectroscopy and ultrafast transient absorption measurements [151].

This chemistry is reminiscent of the two-electron reduction of the diboron porphyrin $B_2Cl_2(TTP)$ to $B_2(TTP)$ in which the porphyrin ring rather than the B_2 unit is reduced, also giving a paratropic, 20 π-electron ring in the product [135]. An even closer parallel comes from the preparation of the pair of C_2-containing porphyrins (C=C)(TTP) and $[(C=C)TTP]^{2+}$. NMR spectroscopy, NICS calculations, and the molecular structure of (C=C)TTP indicate that it is antiaromatic with a 20 π-electron ring, whereas the oxidized form $[(C=C)(TTP)]^{2+}$ is aromatic (Scheme 4.1) [152, 153].

Silicon phthalocyanines have proved useful as precursors to arrays in which up to four SiPc units are stacked via [-Si(Pc)-O-Si(Pc)-O-] linkages. GePc can also be included in the arrays, and notable examples have B(subPc) capping the ends [154]. The precursor to these arrays, $Si(Pc)(OH)_2$, is also useful in other architectures created by modifying the hydroxyl substituent with an appropriate alcohol to give $Si(Pc)(OR)_2$ [9].

Group 14 corroles have typical formula $M^{IV}(Cor)X$ reflecting the trianionic corrole ligand but also some interesting spectroscopic and electrochemical properties demonstrating that some examples contain significant spin density on the corrole ligand (see a more detailed discussion in Section 4.7.1.3) [146]. Silicon corroles are the most recent addition to the periodic

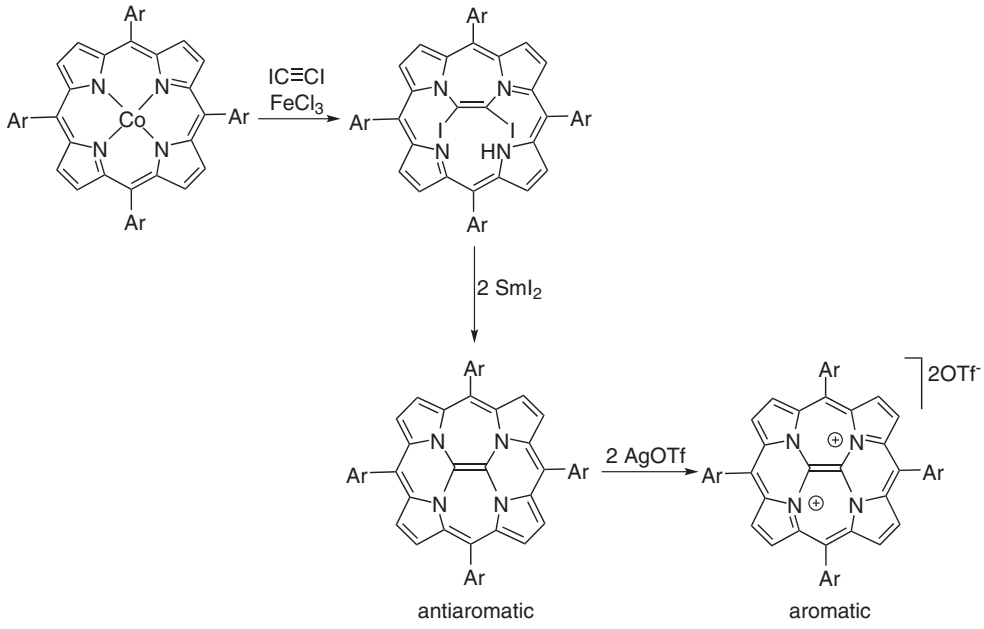

Scheme 4.1 Preparation of antiaromatic (C=C)(TTP) and aromatic $[(C{=}C)TTP]^{2+}$ [152, 153].

table of corroles, and the high affinity of silicon for fluoride ion makes the silicon corrole an interesting material for the naked-eye detection of inorganic fluoride [155, 156].

4.4.5 Groups 15 and 16

The best known of the Group 15 porphyrin complexes are the cationic, six-coordinate phosphorus, arsenic, and antimony complexes $[M(Por)X_2]^+$. The phosphorus and antimony complexes are readily prepared from P(V) or Sb(V) halide precursors with H_2Por in pyridine, but the arsenic examples are more difficult to prepare because of the lack of simple, stable As(V) precursors. $AsCl_3$ in the presence of an added oxidant is used to prepare $[As(Por)X_2]^+$, and this route can also be used for antimony. A range of complexes of all three elements are known, including a rich organometallic chemistry, with typical examples $[M(Por)(OR)_2]^+$, $[M(Por)(R)_2]^+$, $[M(Por)(R)(X)]^+$, and the hydroxo complexes $[M(Por)(R)(OH)]^+$, which, for the P and As examples, show reversible deprotonation to give the neutral oxo species M(Por)(R)(=O) (Scheme 4.2) [157–159]. All of the structurally characterized P, As, and Sb porphyrins are typical six-coordinate complexes with two *trans* axial ligands, although, notably, the porphyrin ligand itself in the phosphorus examples is very strongly ruffled in order to accommodate the small P(V) ion (Figure 4.15). There are some examples of Sb(III) porphyrins, for example Sb(OEP)Cl prepared from H_2OEP with $SbCl_3$, but the P(III) and As(III) porphyrins are less well developed. As(III) precursors give transient As(III) porphyrins identified spectroscopically, and P(III) precursors do not give isolable P(III) porphyrin complexes [157]. This might be due for re-investigation in the light of

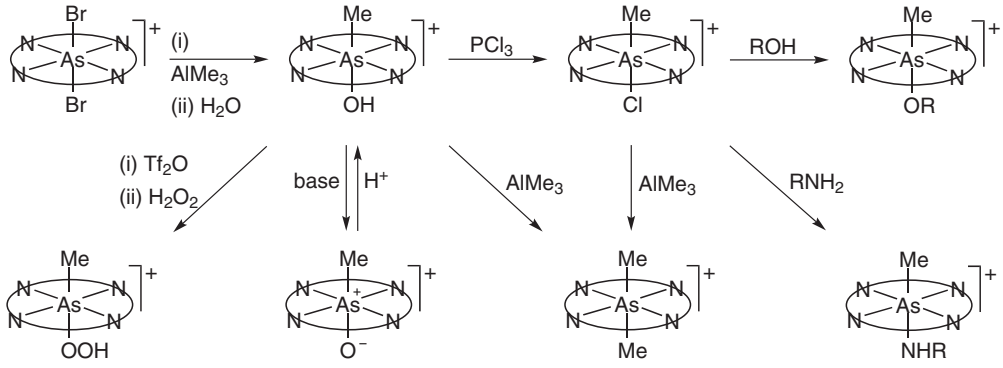

Scheme 4.2 Transformations of arsenic porphyrins [157, 158].

the interesting results with the apparent Si(II) and Ge(II) porphyrin and phthalocyanine species discussed above, which have been shown to contain Si(IV) and Ge(IV) with reduced macrocycles.

The Group 15 M(V) porphyrin complexes $[M(Por)X_2]^+$ are cations; the analogous M(V) corroles are neutral, as in $P(TPFC)(OH)_2$ and $Sb(TPFC)F_2$, with Sb(TPFC)(=O) and the Sb(III) example Sb(TPFC)(py) also known [146, 160]. All three antimony corrole complexes are active as catalysts for photoinduced oxidation of thioanisole by molecular oxygen, with evidence pointing to singlet oxygen as the active species [144, 161]. Antimony porphyrins have also been investigated for their photosensitization and photocatalytic properties [159], and water-solubilized phosphorus and antimony porphyrins have been prepared in order to expand the scope of this application [162].

The P(V) ion is the smallest single ion to form porphyrin complexes in which the central elements are bonded to all four nitrogens. The structures show highly ruffled porphyrin rings, which suggests that the porphyrin ligand is at its limit in terms of accommodating such a small ion (Figure 4.15). In related ring systems, phosphorus has been shown to induce ring contraction or fusion processes that result in smaller macrocycles that are better able to accommodate this small ion. Reaction of N-confused porphyrin with PCl_3 results in a complicated reaction in which the N-confused porphyrin is transformed into a fused porphyrin. This is then two-electron reduced to the fused isophlorin, isolated as its P=O complex in which the four-coordinate phosphorus binds to three pyrrole nitrogens [163].

Attempts to insert phosphorus into phthalocyanine using PBr_3 resulted instead in extrusion of one *meso*-nitrogen to produce the contracted macrocycle triazatetrabenzcorrole, also as its P=O complex [164]. This approach has been exploited to open up a whole new field, the chemistry of corrolazines (Cz) which are the triaza derivatives of corroles in which the three *meso*-carbons are replaced by nitrogen. The reaction of PBr_3 with octaaryl-tetraazaporphyrin resulted in the same kind of ring contraction to give the corrolazine as a cationic P(OH) complex, $[P(Cz)(OH)]^+$. Treatment of this with Na/NH_3 at low temperature resulted in reductive demetallation to produce the free-base corrolazine H_3Cz (Scheme 4.3) [38, 39, 165, 166]. This has been the entry point to the chemistry of a range of transition metal corrolazine complexes, many with reactive high oxidation states [37–39, 167].

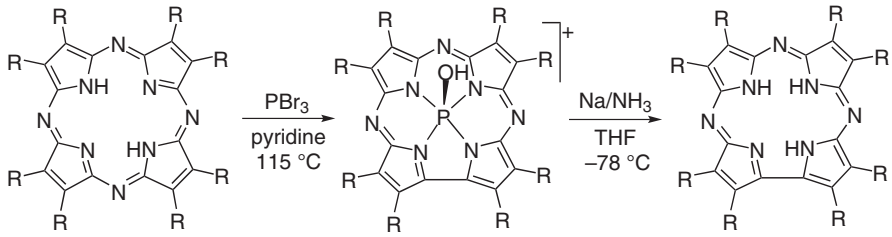

Scheme 4.3 Insertion of phosphorus into tetraazaporphyrin resulting in ring contraction to form phosphorus corrolazine, and reductive demetallation to produce the free base corrolazine (R = 4-C_6H_4-tBu) [38].

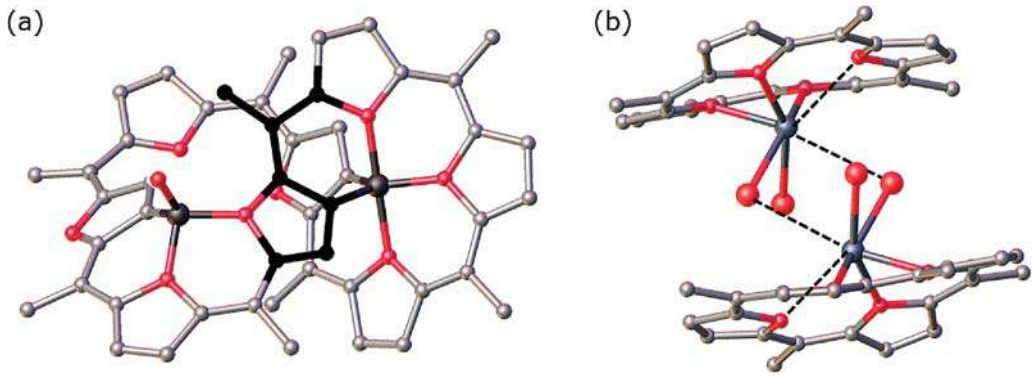

Figure 4.22 Molecular structures of (a) diphosphorus complex of *meso*-C_6F_5 octaphyrin(1.1.1.1.1.1.1.1) [59] and (b) Te(TTP)Cl_2 showing long-range Te···Cl and Te···N interactions [1]; *meso*-aryl groups removed except for the *ipso*-C.

Phosphorus complexes of a selection of expanded porphyrins also show a preference for a lower coordination number than 6 for the phosphorus. Fused pentaphyrins and heptaphyrins have four-coordinate P(V)=O bonded to three pyrrole N- or C-atoms, while octaphyrins have penta-coordinate P(V) bonded to five pyrrole N- or C-atoms (Figure 4.22a). All have interesting properties relating to the aromaticity of the resulting systems [59].

A single example of a Group 16 porphyrin complex contains tellurium and exhibits a dinuclear structure in which the tellurium atom coordinates to only three porphyrin nitrogen atoms, and the two chloro ligands occur on the same face of the porphyrin ligand, reflecting the presence of a lone pair of electrons with predominantly *s* character on the tellurium atom (Figure 4.22b) [1].

4.4.6 Mercury, Thallium, Lead, and Bismuth

The heaviest elements of Groups 12, 13, 14, and 15 are considered separately because they have more in common with each other than with their lighter congeners. Their porphyrin complexes occur as the Hg(II), Tl(I), Tl(III), Pb(II), Pb(IV), and Bi(III) species. These are filled shell configurations ($5d^{10}$ or $5d^{10}6s^2$), and as a result there is no ligand field-driven preference for coordination numbers or geometries. All of the elements are large, and the metal atoms typically sit 0.5–1.5 Å above the N_4 planes. The porphyrin chemistry of these elements has been comprehensively reviewed [83].

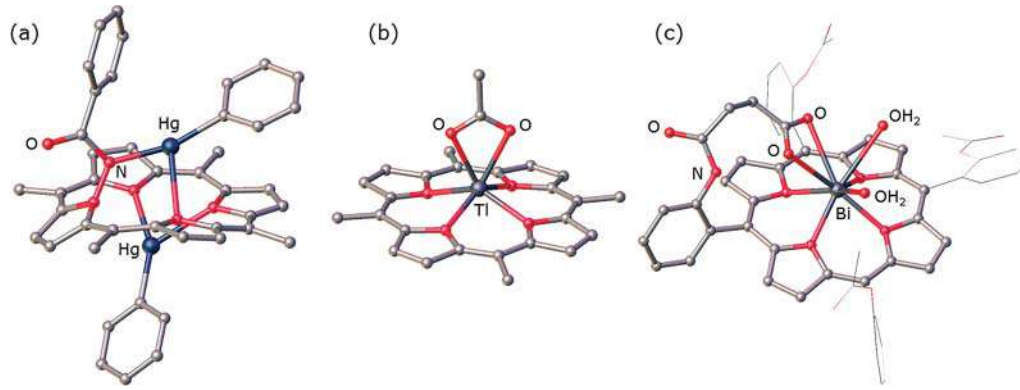

Figure 4.23 Molecular structures of (a) $(HgPh)_2$(N21-benzamido-TPP) [168], (b) Tl(TPP)(O_2CCH_3) [169], and (c) a bismuth tetraarylporphyrin bearing an intramolecular carboxylate picket, Ar = C_6H_4-2-NHC(O)CH_3 [170]; *meso*-aryl groups removed except for the *ipso*-C.

Mercury complexes of simple porphyrins have been prepared from $Hg(OAc)_2$ with H_2Por in THF or pyridine, although there are few structurally characterized examples. More common are complexes of N-functionalized porphyrins that contain a four-coordinate HgX group (X = Cl, Ph) bonded to the three unsubstituted porphyrin nitrogens on the face opposite to the N-substituent (Figure 4.23a) [83].

Tl^{III}(Por)X complexes can be prepared from reaction of a Tl(III) salt with H_2Por; anion metathesis is easily accomplished to afford derivatives with a range of anionic ligands X. Many have been structurally characterized and exhibit five-coordinate, out-of plane geometries in which the displacement of the metal center above the porphyrin plane (ranging from 0.6 to 1.0 Å) correlates with the covalent character in the thallium–ligand bond. Ligands such as acetate or trifluoroacetate are typically bidentate (Figure 4.23b). A few examples of bimetallic thallium(I) complexes have been prepared from TlOEt with H_2TPP or H_2OEP. They have the formulation Tl_2(Por)L_n, and the structure of Tl_2(OEP)$(THF)_2$ demonstrates that each thallium atom lies on one side of the porphyrin plane and forms bonds to three pyrrole nitrogens and one THF molecule [83].

$Pb(OAc)_2$ can be used to form simple lead porphyrins, either Pb^{II}(Por) or Pb^{IV}(Por)X_2 depending on the conditions and presence of an external oxidant. The chemistry of the Pb(II) porphyrin is better developed and features large, OOP lead atoms in the molecular structures.

Bismuth porphyrins are only known as the Bi(III) complexes, originally prepared from the reaction of $Bi(NO_3)_3$ or BiX_3 (X = halide) with H_2Por in refluxing pyridine. They crystallize as dinuclear complexes with bridging anions and large OOP displacements. The metal ions are relatively labile to demetallation [83]. The corrole complex Bi(TPFPC) exhibits a domed corrole and a strongly pyramidalized bismuth center, and the both the Bi–N and Bi–centroid distances are among the longest for any metallocorrole with the exception of the *f*-element corroles [171].

Further bismuth and lead porphyrin chemistry has been developed to investigate the use of the radioisotopes ^{212}Bi and ^{213}Bi as α emitters for radioimmunotherapy [172, 173]. Lead porphyrins are precursors to bismuth complexes via β-emission from ^{212}Pb (half-life 10.6 h) to produce the short half-life (1 h) ^{212}Bi α-emitter. Typical metal insertion conditions for these elements required heating in pyridine for minutes to hours, conditions not compatible with

these short half-life isotopes. Peripherally substituted picket and strapped porphyrins bearing pendant ester or carboxylic acid groups were developed to enhance the kinetics of metal insertion (Figure 4.23c). Metals can be inserted into these porphyrins in a few minutes, and the resulting complexes are much more inert to demetallation. The molecular structures of these "superstructured" lead and bismuth porphyrins show large OOP displacements and interaction with the pendant donors with variable coordination numbers, bond lengths, and geometries, and in some cases evidence for a stereochemically active lone pair [83].

Recent, very elegant work using double strapped porphyrins with one strap on each face has produced a series of bimetallic porphyrins containing Pb, Bi, Hg, and Tl with variable and interesting coordination modes. Genuine bimetallic porphyrin coordination can be observed, as in a dilead(II) complex where each lead resides on one face and interacts with three nitrogens, the carboxylate of the strap, and DMSO molecules. An alternative coordination mode for the bimetallic complexes has one metal coordinated to the porphyrin OOP but with distinct N_4 coordination with the other "hanging atop" (HAT) in which the metal atom is coordinated by the carboxylate on the strap together with added acetate ions but is not actually interacting with the porphyrin nitrogens (Figure 4.11). A variety of bimetallic and heterobimetallic complexes containing Cd(II), Hg(II), Tl(III), Pb(II), and Bi(III) display this behavior [91]. This unusual coordination is not just static; the HAT coordination mode also features in new dynamic processes in the bimetallic porphyrins by which two cations exchange either their locations or their coordination modes or both. Two phenomena are observed in which the metal ions either stay on their respective sides of the macrocycle while exchanging between the HAT and OOP modes, or the metal ions exchange between the two sides of the porphyrin and maintain their OOP or HAT coordination modes. These dynamic processes can be induced or tuned by allosteric effectors, pH, dynamic constitutional evolution, or light exposure [90, 92].

4.5 Transition Metals

4.5.1 Early Transition Metals (Groups 3, 4, and 5)

The early transition metal elements from Groups 3, 4, and 5 feature large ions and strongly oxophilic chemistry, and as such have more in common with the Groups 1 and 2 elements and the lanthanides and actinides. The large ions tend to reside out of the constrained porphyrin plane, leading to complexes with *cisoid* geometry, which is relatively rare for the later transition elements. Their oxophilicity renders them moisture sensitive, and hence they are typically prepared and handled in the absence of air. Complexes generally form with the metals in their highest oxidation states and as such have d^0 configurations. The early transition metal porphyrin chemistry was reviewed some time ago [82], and the corrole chemistry more recently [35, 118], and much of the following summary is taken from these sources.

Complexes can be formed by the traditional method using H_2(Por) with a metal salt in a high-boiling solvent, or by reactions with metal alkyl, alkoxo, or silylamide precursors, driven by elimination of the alkane, alcohol, or amine, respectively, to give complexes such as Y(OEP)($CH(SiMe_3)_2$), Y(OEP)(μ-CH_3)$_2$Li(THF)$_2$, and Y(OEP)(OAr) (Ar = O-2,6-$C_5H_4{}^tBu_2$) [174, 175]. The advent of the Li_2Por precursors allowed much cleaner syntheses. For example,

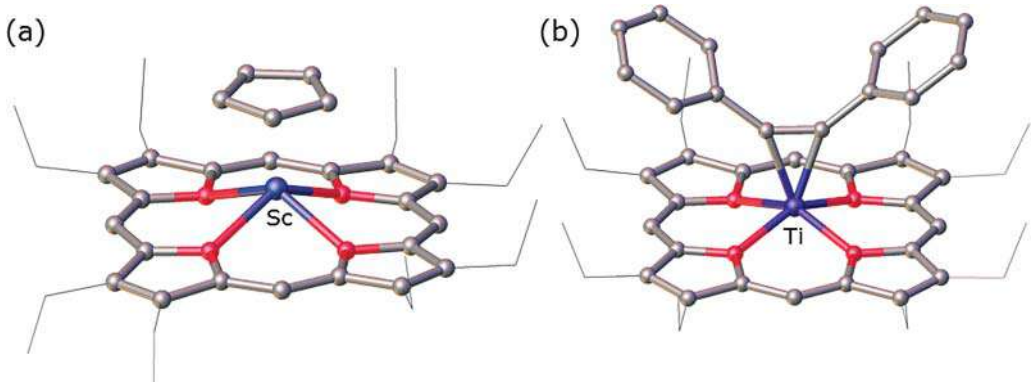

Figure 4.24 Molecular structures showing out-of-plane (OOP), *cisoid* geometries of (a) Sc(OEP)(η^5-C_5H_5) [110] and (b) Ti(OEP)(η^2-PhC≡CPh) [176].

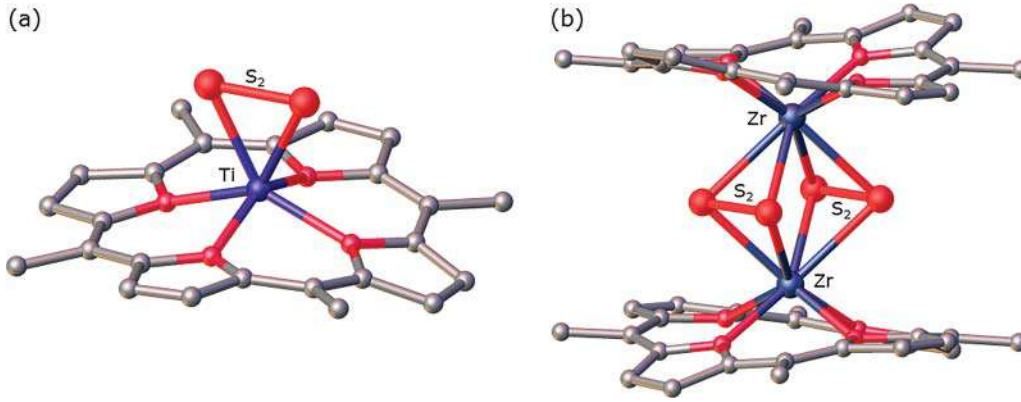

Figure 4.25 Molecular structures contrasting (a) mononuclear Ti(TTP)(S_2) [177] and (b) dinuclear Zr(TPP)-μ-(S_2)$_2$-Zr(TPP) [178]; *meso*-aryl groups removed except for the *ipso*-C.

Li_2OEP reacts with $ScCl_3$ to form Sc(OEP)Cl, which could be derivatized to give a range of Sc(Por)X complexes, including structurally characterized examples where X = acac, OAc, Cl, OH, OR, NR_2, and alkyl. Sc(OEP)(η^5-C_5H_5) is notable as the first example of a porphyrin complex bearing an η^5-cyclopentadienyl ligand (Figure 4.24a) [110]. Yttrium complexes, such as Y(Por)(acac) and the sandwich complex Y(Por)$_2$, have much in common with the lanthanide porphyrins (see Section 4.6), and will be discussed along with these.

Older syntheses of titanium porphyrins used high-temperature reactions of H_2Por with Ti(=O)(acac)$_2$, Cp_2TiCl_2, or $TiCl_4$, all resulting in the titanyl complex Ti(Por)(=O), which exhibits a square pyramidal structure with the Ti atom displaced 0.53 Å above the N_4 plane. Ti(Por)(=O) reacts with HF, HCl, or HBr to give the *transoid* dihalide complexes Ti(Por)X_2. Interesting features of titanium porphyrin chemistry are the dichalcogenide complexes Ti(Por)(η^2-E_2), where E_2 is O_2 (peroxo), S_2, or Se_2 (Figure 4.25a). The peroxo complex is formed from Ti(OEP)(=O) with benzoyl peroxide, whereas the S_2 and Se_2 complexes use $Cp_2Ti(E_5)$ as the source of the E_2 fragment in reactions with Ti(Por)F_2 or Ti(Por)F.

The titanium(IV) porphyrins can be reduced to produce titanium(III) derivatives. Zinc amalgam serves to reduce Ti(Por)F_2 to Ti(Por)F, while sodium anthracenide or electrochemical reduction produces the anion $[Ti(Por)F_2]^{2-}$. Ti(Por)F can coordinate a sixth ligand L (pyridine, imidazole, or phosphine), and both Ti(Por)F and Ti(Por)F(L) undergo air oxidation, the latter more slowly. Other titanium(III) complexes are Ti(Por)(SMe), Ti(Por)(OMe), and Ti(Por)(Ar).

Formally, titanium(II) porphyrins are Ti(Por)(η^2-PhC ≡ CPh) (Figure 4.24b) produced by $LiAlH_4$ reduction of Ti(Por)Cl_2 in the presence of diphenylacetylene, and Ti(Por)$(THF)_2$, which results from $NaBEt_3H$ reduction of Ti(Por)Cl_2 or Ti(Por)Cl. Displacement of diphenylacetylene from Ti(Por)(η^2-PhC ≡ CPh) by pyridine ligands resulted in the *transoid* complex Ti(Por)$(py)_2$.

Harsh conditions, H_2(Por) with M$(acac)_4$ in hot phenol, were used to prepare Zr(OEP)$(acac)_2$ and the hafnium analogue. They are both OOP complexes with two *cisoid*, bidentate acac ligands. Both metals form bis-porphyrin sandwich compounds M$(Por)_2$ using a variety of routes: free-base porphyrin with Zr$(NEt_2)_4$, or Li_2Por with Cp_2MCl_2 or $MCl_4(THT)_2$. Zr(Por)Cl_2 was originally prepared from H_2Por with $ZrCl_4 \cdot L_n$ at high temperature, but a cleaner route uses Li_2Por with $ZrCl_4$(DME). Molecular structures of the Zr or Hf porphyrin dihalides show, variously, coordination numbers 6, 7, and 8 in ZrPorX_2, ZrPorX_2L, and ZrPorX_2L_2, all with the metal displaced from the porphyrin plane and *cisoid* ligands. With a high-yielding route to Zr(Por)Cl_2 available, a host of further derivatives Zr(Por)X_2 were produced including acetato, triflato, alkoxy, alkyl, aryl, and carborane complexes (Figure 4.26). Zr and Hf alkyl complexes can be produced directly from Li_2Por with M$(CH_2SiMe_3)_2Cl_2$. The alkyls Zr(Por)R_2 are reactive toward the insertion of small molecules and catalyze the hydrogenation of alkenes. Zr(OEP)Me_2 reacts with CO and acetone, giving the acetate and t-butoxy complexes as products.

Analogues of the titanium dichalcogenide complexes Ti(Por)(η^2-E_2) also occur for Zr, but the preference of the larger element for higher coordination numbers results in binuclear formulations Zr(Por)-$(E_2)_2$-Zr(Por) (E = S, Se) (Figure 4.25b). Bridging motifs are observed for titanium, as in TiPor-O-TiPor, and are more common for zirconium and hafnium, for which M(Por)-bridge-M(Por) complexes contain O_2, OCl_2, $O(OH)_2$, and $(OH)_4$ groups as the bridges.

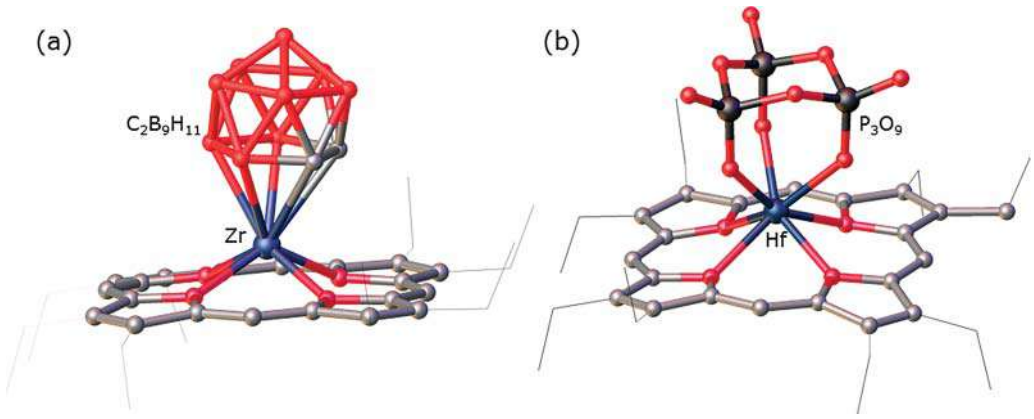

Figure 4.26 Molecular structures of (a) Zr(OEP)(η^5-1,2-$C_2B_9H_{11}$) [179] and (b) $[Hf(OEP)(P_3O_9)]^-$ [180] showing out-of plane geometry and high coordination numbers.

$Zr(OEP)(CH_2SiMe_3)_2$ can be reduced by H_2 to the formally zirconium(III) alkyl with elimination of $SiMe_3$, although the additional electron might not be completely localized on the metal, and the complex may have some porphyrin radical anion character.

Petroporphyrins are found in crude oil extracts and have been determined to be of biogenic origin. The most prevalent of these are vanadium porphyrins [181, 182]. Synthetic vanadium porphyrins bearing the metal in oxidation states V(II) to V(IV) have been described, of which vanadyl porphyrin V(Por)(=O) is the best-known and most-studied of the group 5 porphyrins, and is the most common motif in the structurally characterized vanadium porphyrins. It can be prepared from a myriad of vanadium precursors – vanadyl salts, $V(CO)_6$, V(II) salts, VCl_3 or VCl_4 – and readily coordinates a sixth axial ligand to form V(Por)(=O)L. The lack of V(V) porphyrin complexes has been attributed to the small size of this ion. The oxidized complex $[V(Por)(=O)(H_2O)]^+$ has been established to be a V(IV) porphyrin π-cation radical species [183]. Only a small number of vanadium phthalocyanine species have been structurally characterized, V(Pc′)(=O) and V(Pc′)(=O)(H_2O), in which the Pc′ bears alkyl and fluoroalkyl chains, respectively [184, 185].

Reaction of V(Por)(=O) with $SOCl_2$ gives $V(Por)Cl_2$, which in turn reacts with primary amines to produce the imido species $V(Por)(NR_2)$. Zinc amalgam reduction of $V(Por)Cl_2$ in the presence of neutral ligands produces the V(II) complexes $V(Por)(L)_2$. The V(III) complex V(Por)Cl(THF) is prepared by a simple salt elimination from Li_2Por with VCl_3 [186]. All of the structurally characterized six-coordinate complexes show *transoid* geometry.

Niobium and tantalum porphyrins in the 5+ oxidation state are well known, and for both metals the metal(V) salt MCl_5 with H_2(OEP) followed by HF treatment gave $M(Por)F_3$. Mixed ligand complexes also feature, resulting from hydrolysis of $Nb(Por)F_3$ to $Nb(Por)(\mu\text{-}O)_3Nb(Por)$ followed by a weak acid giving Nb(Por)(=O)X where X is F, OAc, or acac. The large metal ions are displaced from the N_4 plane and six- or seven-coordinate complexes occur with the additional ligands in a *cis* arrangement. The niobium(V) porphyrins Nb(Por)(=O)X and $Nb(Por)X_3$ can be reduced by zinc amalgam to the niobium(IV) complexes Nb(Por)(=O) and $Nb(Por)X_2$. Reaction of Li_2(OEP) with $TaCl_5$ gives the cationic sandwich compound $[Ta(OEP)_2][TaCl_6]$, and with $TaMe_3Cl_5$ produces the organometallic species, $Ta(OEP)Me_3$ which further reacts with HCl as an alternative synthesis of $Ta(OEP)Cl_3$ with subsequent hydrolysis to $Ta(OEP)(\mu\text{-}O)_3Ta(OEP)$.

Groups 3, 4, and 5 phthalocyanine complexes are well known, and as might be expected show similar characteristics to their porphyrin counterparts. The most notable recent advances in the Groups 3, 4, and 5 tetrapyrrole coordination chemistry have occurred with the preparation of the first examples of corrole complexes of these elements. The developments were spurred by the possibilities offered by the availability of the lithium corrole precursor, mirroring the advances in the early transition metal porphyrins some 20 years earlier. Recent reviews offer an excellent summary and useful insights [33, 35, 118].

Of the Group 3 elements, scandium corroles are unknown, and yttrium and lanthanum examples are discussed together with the lanthanides in Section 4.6. The first Groups 4 and 5 corroles to be reported spectroscopically, in 1995, were the titanyl and vanadyl complexes, both containing the M(IV)(=O) moieties. They were formulated as neutral complexes M(CorH)(=O) in which the corrole ligands retained one proton. The Li_3(Cor) precursor proved useful for preparing Ti, Zr, and Hf corroles using the metal salts MCl_4 at room temperature. The M(Cor)Cl products were isolated as a square pyramidal monomer Ti(Cor)Cl for titanium, and bis-chloro-bridged dimers

$[Zr(Cor)(THF)(\mu\text{-}Cl)]_2$ and $[Hf(Cor)(\mu\text{-}Cl)]_2$ for the heavier elements. When cyclopentadienyl complexes Cp^*TiCl_3 and $CpZrCl_3$ were used as the metal sources, the products retained the η^5-ligands in $Ti(Cor)(\eta^5\text{-}Cp^*)$ and $Zr(Cor)(\eta^5\text{-}Cp)$. Reaction of Ti(Cor)Cl with NaCp* produced the same complex, and the Grignard reagent Me_3SiCH_2MgCl gave the titanium alkyl complex $Ti(Cor)(CH_2SiMe_3)$ [117, 118]. Tantalum corroles were prepared from the free base H_3Cor by methane elimination from $TaMe_3Cl_2$ or $TaMe_3(NtBu)$ upon heating in toluene, in contrast to the mild conditions employed for salt elimination for the Group 4 elements with Li_3Cor. The products, $Ta(Cor)Cl_2$ or Ta(Cor)(NtBu), both show markedly OOP tantalum atoms with two *cis* chloro ligands in the former. $Ta(Cor)Cl_2$ reacts with MeLi to give *cis*-$Ta(Cor)Me_2$, which in turn inserts CO to give the bidentate ene-diolate complex $Ta(Cor)(\eta^2\text{-}OC(Me)C(Me)O)$. The imido complex Ta(Cor)(NtBu) reacted with alcohols, resulting in substitution to give $Ta(Cor)(OCH_2\text{-}4\text{-}C_6H_4CH_3)_2$ with $HOCH_2\text{-}4\text{-}C_6H_4CH_3$, and addition to give Ta(Cor)(NHtBu)($OCPh_3$) with the bulker $HOCPh_3$ (Scheme 4.4) [187].

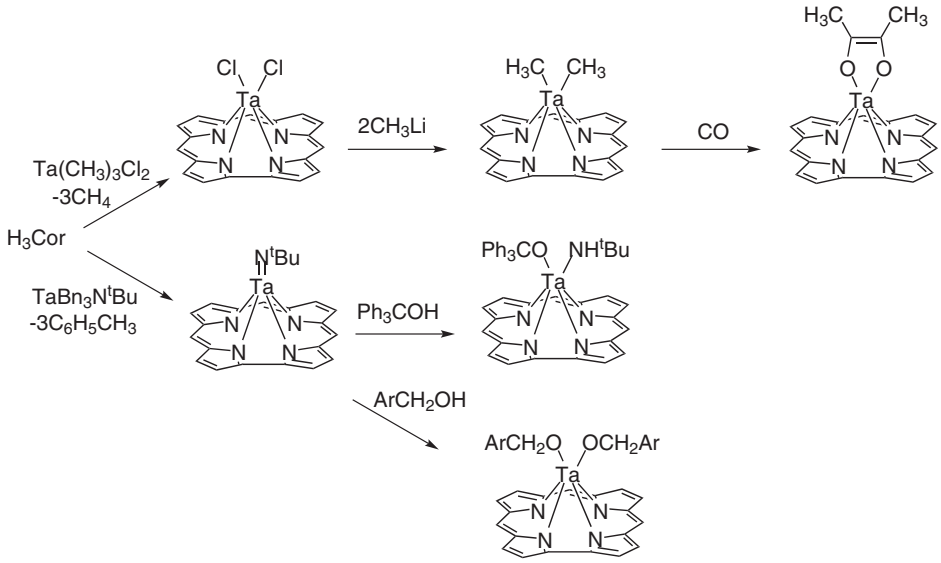

Scheme 4.4 Tantalum corrole chemistry; Cor = $Mes_2(p\text{-}OMePh)$corrole; Ar = $4\text{-}C_6H_4CH_3$ [187].

4.5.2 Middle Transition Elements (Groups 6, 7, 8)

Hemes and other middle transition metal porphyrins arguably epitomize porphyrin chemistry at its most luxuriant. The diversity of chemical behavior is a direct result of the variety of oxidation and spin states accessible to middle transition metals [3, 35, 188].

The three first-row middle transition metals Cr, Mn, and Fe are readily inserted into porphyrins, typically via interaction of a free-base porphyrin with a divalent salt, such as the chloride or acetate, in a high-boiling solvent such as DMF. The $M^{II}(Por)$ derivatives, which are initially formed, autoxidize or may be readily oxidized to a variety of $M^{III}(Por)X$, where X

is one of a wide range of anionic ligands. Standard ligand field theory considerations provide simple rationales for the commonly observed spin states of these complexes:

$Cr^{II}(Por)$	$S = 2$	$Cr^{III}(Por)X$	$S = 3/2$;
$Mn^{II}(Por)$	$S = 5/2$	$Mn^{III}(Por)X$	$S = 2$;
$Fe^{II}(Por)$	$S = 1$	$Fe^{III}(Por)X$	$S = 5/2$.

Chromium(III) porphyrins can be readily oxidized by reagents such as mCPBA or NaOCl to stable, diamagnetic $Cr^{IV}(Por)(=O)$ porphyrins with a d_{xy}^2 electronic configuration. Isoelectronic $Cr^{IV}(Por)(=NAr)$ porphyrins can be prepared via the interaction of $Cr^{II}(Por)$ and aryl azides. In addition, $Cr^{V}(Por)(\equiv N)$ porphyrins can be readily prepared by either photolysis of $Cr^{III}(Por)(N_3)$ or the oxidation of $Cr^{III}(Por)(OH)$ with NH_4OH/NaOCl.

Insertion of molybdenum and tungsten into porphyrins is generally accomplished via exposure to either an inorganic precursor (for example, $MoCl_2$, $MoOCl_3$, WF_5, $K_3W_2Cl_6$) or the hexacarbonyl in a high-boiling solvent such as benzonitrile, phenol, DMF, or decalin. A wide variety of octahedral molybdenum(V) and tungsten(V) porphyrins, with the general formula $M^{V}(Por)(=O)(X)$, have been prepared, where X is one of a wide variety of monoanions. These can be readily reduced to five-coordinate $M^{IV}(Por)(=O)$ complexes. In turn, the $M^{IV}(Por)(=O)$ complexes serve as precursors to a wide range of other complexes, as illustrated in Scheme 4.5. Note the prevalence of both *cis* and *trans* geometries among the various products. The +6 oxidation state is also well represented for the two metals in the form of *cis*-oxoperoxo, *cis*-dioxo, and *trans*-diperoxo complexes.

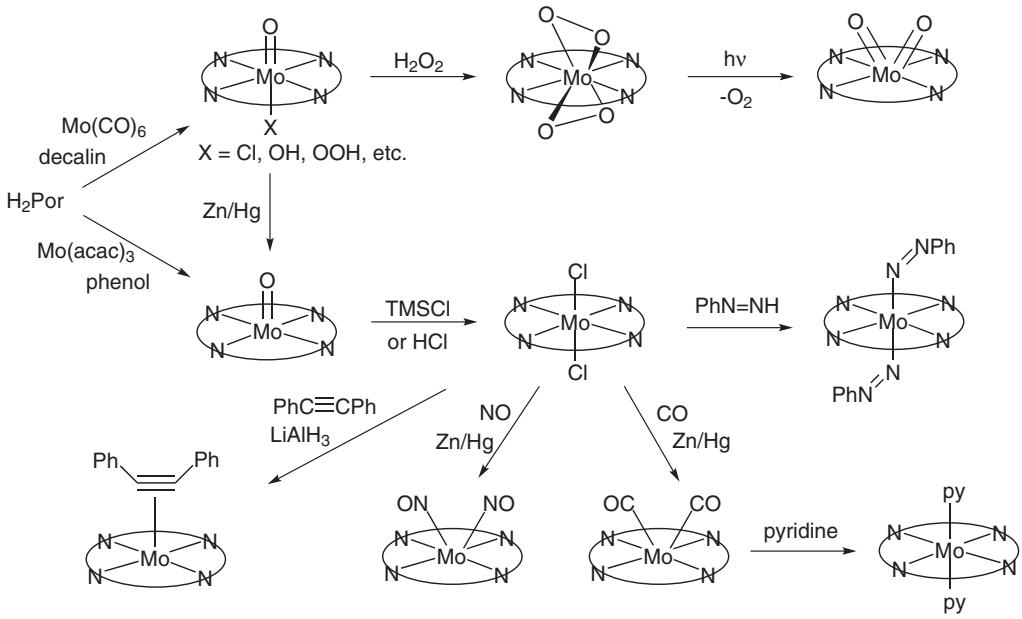

Scheme 4.5 Transformations of molybdenum porphyrin complexes.

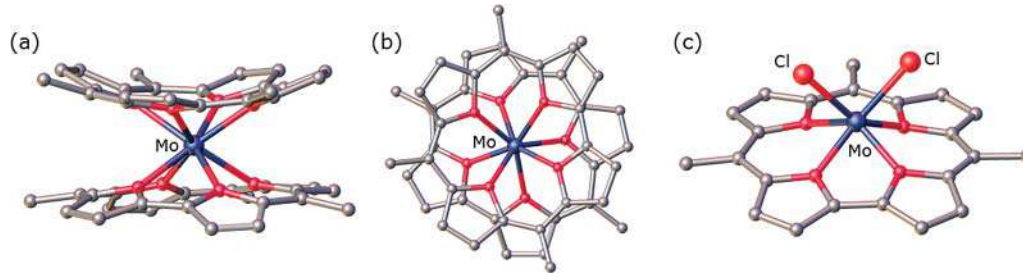

Figure 4.27 Molecular structure of Mo[TTC]$_2$: (a) side and (b) top view of Mo(TTC)$_2$ [191], (c) *cis*-Mo(Cor)Cl$_2$ [192]; *meso*-aryl groups removed except for the *ipso*-C.

The interaction of Cr(CO)$_6$ and Mo(CO)$_6$ with free-base corroles in refluxing decalin affords the corresponding M^{V}(Cor)(=O) complexes, which may be reduced in turn to the [M^{IV}(Cor)(=O)]$^-$ anions [189]. Recently, an analogous reaction with W(CO)$_6$ has been found to afford eight-coordinate W(Cor)$_2$ complexes, the first homoleptic corrole sandwich compounds [190]. Subsequently, under strict exclusion of oxygen, Mo(CO)$_6$ was also shown to yield the analogous M(Cor)$_2$ complexes [191]. Like porphyrin sandwich complexes, these complexes also exhibit rigid square-antiprismatic coordination geometries (Figure 4.27a,b), but because of the lower symmetry of corroles relative to porphyrins, the M(Cor)$_2$ complexes are chiral and have even been resolved and characterized with electronic circular dichroism spectroscopy [193]. Activation of the inert molybdenum-oxido group in M^{V}(Cor)(=O) can be achieved by treatment with SiCl$_4$ to yield *cis*-Mo(Cor)Cl$_2$ [192]. EPR data and DFT calculations are consistent with a Mo^{V} formulation for this paramagnetic complex. The difference in size between the porphyrin and corrole cores is illustrated by the *trans* geometry for *trans*-Mo(Por)Cl$_2$ and *cis* geometry for *cis*-Mo(Cor)Cl$_2$ (Figure 4.27c). Reaction of Na(C$_5$H$_5$) with *cis*-Mo(Cor)Cl$_2$ gives Mo(Cor)(η^5-C$_5$H$_5$) characterized as a diamagnetic Mo^{IV} complex [192].

Manganese(III) porphyrins have been widely studied as catalysts for biomimetic oxygen atom transfer (OAT) processes such as oxygenation of phosphines and sulfides, epoxidation, and C-H activation [194]. This chemistry has recently been applied to effect C-H fluorination [195, 196]. The protocol, illustrated in Scheme 4.6 for the monoterpene bornyl acetate [197], has been shown to work for isolated methylene groups and for unactivated benzylic sites. Mechanistic studies have shown that the reaction proceeds via an Mn^{V}(Por)(=O)F intermediate (with a d_{xy}^2 electronic configuration) as the C-H–abstracting agent and a *trans*-Mn^{IV}(Por)F$_2$ species as the F-transferring agent. The latter species, as well as other $S = 3/2$ Mn(Por)X$_2$ species, have been isolated and structurally characterized.

A wide variety of Mn(V) porphyrinoids have been synthesized and spectroscopically and/or structurally characterized. In general, Mn^{V}(=O) porphyrins and corroles are only generated in solution for subsequent spectroscopic and/or reactivity studies [198–201]. A sterically hindered Mn^{V}(Cz)(=O) corrolazine, however, has even been isolated as a solid and extensively studied [202]. Stable manganese(V)-nitrido porphyrins have been synthesized by treating Mn^{III}(Por)X with iodosobenzene and an excess of ammonia. Both Cr^{V}(Por)(≡N) and Mn^{V}(Por)(≡N) porphyrins exhibit rare, inter-metal nitrogen atom transfer reactivity [203, 204]. Stable M^{V}(Cor)(=NMes) (M = Cr, Mn) corroles have been obtained via the thermal or photochemical reaction of the corresponding M(III) corroles with mesityl azide [205]. In general, these nitrido and imido complexes have all been structurally characterized.

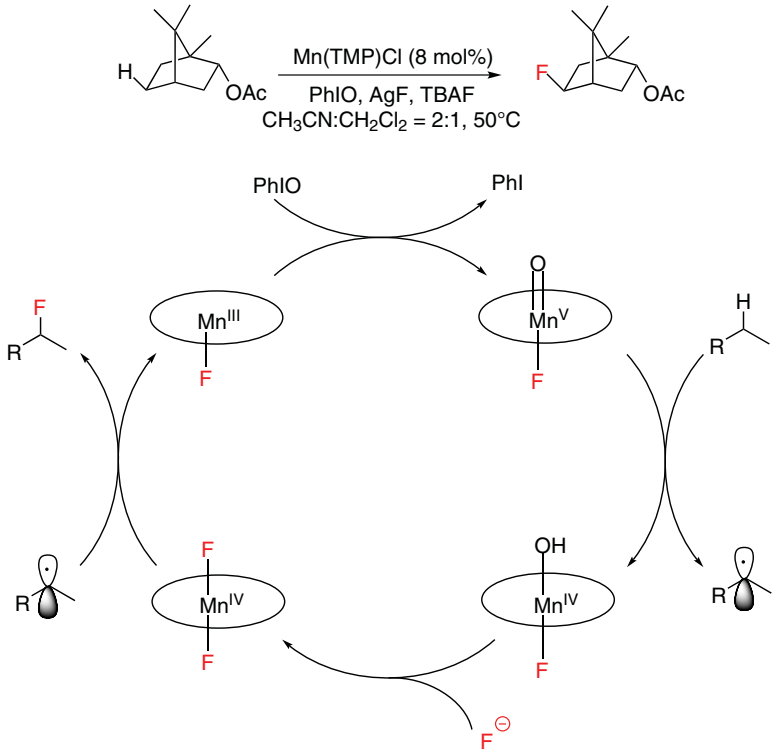

Scheme 4.6 C-H fluorination catalyzed by manganese porphyrin. Source: Adapted from Liu et al. [197].

Compared with manganese, the chemistry of technetium and rhenium porphyrinoids is much less developed. Interaction of free-base porphyrins with $M_2(CO)_{10}$ generally affords SAT mono- and bis-$M^I(Por)(CO)_3$ complexes, in which each $M^I(CO)_3$ fragment is coordinated by only three porphyrin nitrogens (Figure 4.28a) [208]. However, the reaction of *meso*-tetrakis(trifluoromethyl)porphyrin with $Re_2(CO)_{10}$ in refluxing benzonitrile under an inert atmosphere resulted in an unexpected ring contraction, yielding $Re^V(=O)$ *meso*-tris(trifluoromethyl)corrole, $Re^V(TCF_3C)(=O)$, in 9% yield [209]. Recently, rational synthetic routes to both $^{99}Tc^V(Cor)(=O)$ and $Re^V(Cor)(=O)$ corroles have been established (Scheme 4.7) [210, 211], although synthetic routes to analogous medically relevant ^{99m}Tc ($t_{1/2} \approx 6$ h) complexes have yet to be reported.

N-confused porphyrins exhibit rather intricate coordination chemistry with rhenium carbonyls. Thus, in the absence of an added oxidant, *N*-confused tetraphenylporphyrin yields a $Re^I(CO)_3$-coordinated *N*-fused porphyrin [212, 213], whereas *exo*-methylated *N*-confused tetraphenylporphyrin yields the un-rearranged $Re^I(CO)_3$-coordinated product [71]. The $Re^V(NCTPP)(=O)$ complex is obtained by adding an oxidant such as TEMPO to the reaction mixture (Scheme 4.8) [214].

Since iron porphyrins and heme proteins have been discussed at length in several other chapters, only a summary is presented here. A basic rule of thumb is that five-coordinate Fe(II) and Fe(III) porphyrins are generally high spin, whereas six-coordinate complexes with nitrogen ligands (such as imidazole or pyridine) are generally low spin. Like $S = 3/2$ $Mn^{IV}(Por)(=O)$ porphyrins, $S = 1$ $Fe^{IV}(Por)(=O)$ porphyrins are highly reactive; the latter

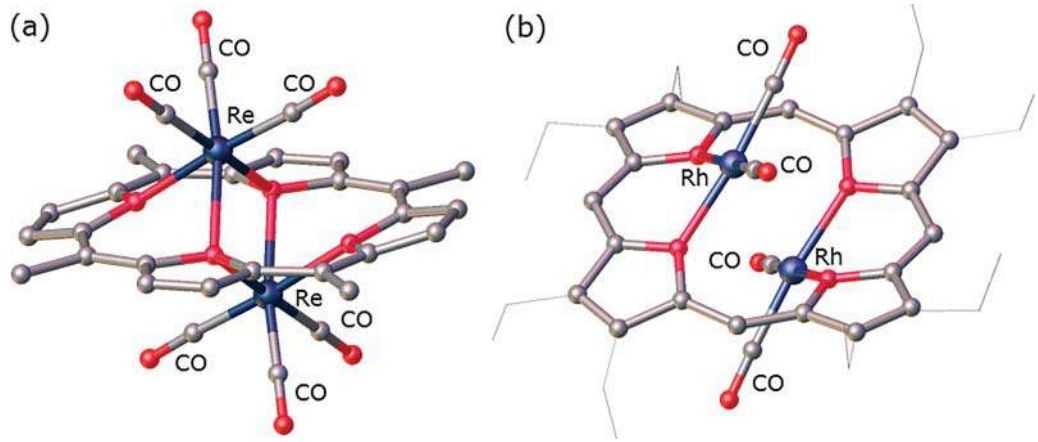

Figure 4.28 "Sitting-atop" complexes: (a) $[Re(CO)_3]_2$(TPP) [206] and (b) $[Rh(CO)_2]_2$(OEP) [207]; *meso*-aryl groups removed except for the *ipso*-C.

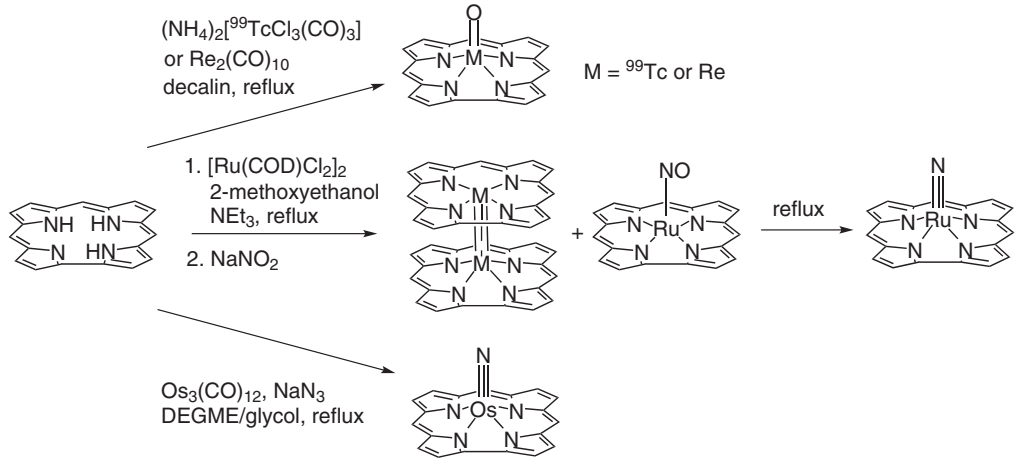

Scheme 4.7 Synthetic strategies for technetium, ruthenium, ruthenium, and osmium corroles.

are, of course, famous as reactive intermediates of heme proteins such as the peroxidases and cytochromes P450 [215]. Much less known are the reduced states $[Fe(Por)]^-$ and $[Fe(Por)]^{2-}$. A combined experimental and theoretical study has recently shown that these anions are best viewed as porphyrin monoanion-radical and dianion-diradical, rather than Fe(I) and Fe(0), respectively [216]. Iron corroles provide a number of interesting examples of ligand non-innocence; these are discussed in Section 4.5.5.

Ruthenium porphyrins exhibit a rich chemistry, with substantial applications to important catalytic transformations. Ruthenium is most commonly inserted into porphyrins via the carbonyl method, through the interaction of a free-base porphyrin with $Ru_3(CO)_{12}$ in a refluxing, high-boiling solvent [188]. The Ru^{II}(Por)(CO)(L) product (L = solvent or other neutral ligand) can then be transformed to a variety of other six-coordinate complexes by treatment with

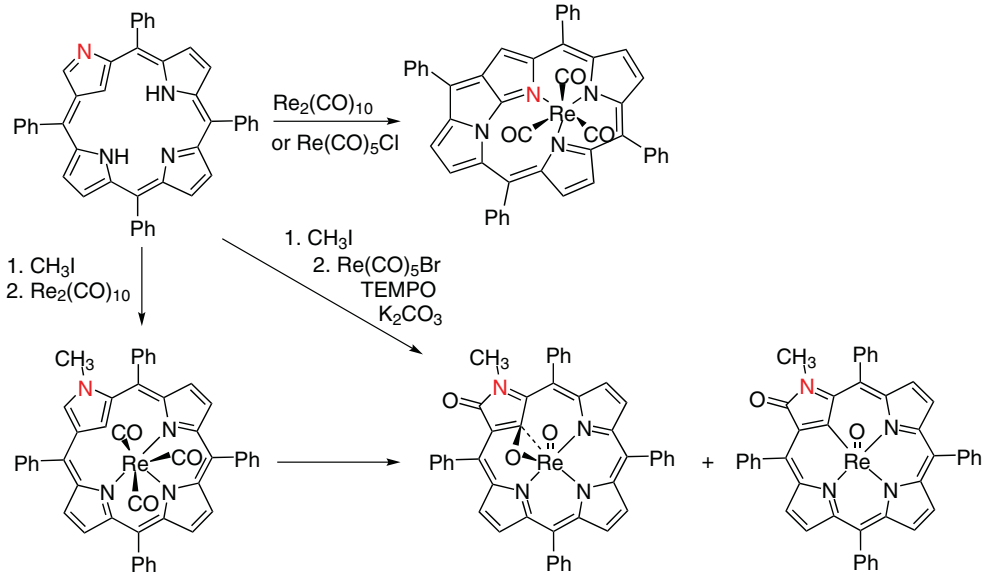

Scheme 4.8 Reaction chemistry of N-confused porphyrin with rhenium carbonyls in the absence and presence of an added oxidant. Source: Modified from Toganoh et al. [212].

the appropriate nucleophile. Thus, photolysis of $Ru^{II}(Por)(CO)(L)$ in the presence of pyridine yields $Ru^{II}(Por)(py)_2$, whereas phosphines yield analogous bisphosphine complexes at room temperature without any photoactivation. Mild oxidation of the $Ru^{II}(Por)(py)_2$ then provides the corresponding Ru(III) cationic species. Vacuum pyrolysis of $Ru^{II}(Por)(L)_2$ (L = THF, CH_3CN, pyridine, etc.) results in 14-electron $Ru^{II}(Por)$ complexes, which readily dimerize to yield metal–metal–bonded $[Ru(Por)]_2$ dimers (discussed in more detail in Section 4.5.4) [217]. Dimerization can be prevented by using a sterically hindered porphyrin such as TMP, which leads to the mononuclear complex $Ru^{II}(TMP)$. These axially unligated Ru(II) porphyrins are generally exceedingly air sensitive.

Ruthenium porphyrins catalyze several important atom and group transfer reactions. Thus, $Ru^{II}(Por)(CO)(L)$ complexes catalyze olefin cyclopropanation with diazoalkanes as the carbene source and olefin aziridination with organic azides as the nitrene source [218–223]. Furthermore, Ru(II) porphyrins can be oxidized by molecular oxygen or an oxygen atom donor reagent such as mCPBA to yield the *trans*-dioxo complexes $Ru^{VI}(Por)(O)_2$, which in turn effect olefin epoxidation with molecular oxygen as the oxidant (Figure 4.29) [218, 221, 224]. The reaction is thought to involve a $Ru^{IV}(=O)$ intermediate, which can also be generated independently as a moderately stable $S = 1$ species.

The carbonyl method also provides access to osmium porphyrin derivatives, with $Os^{II}(Por)(CO)$ acting as the typical entry point [188]. The reactivity of $Os^{II}(Por)(CO)(L)$ derivatives, however, does not quite mirror that of their ruthenium congeners. Osmium engages in much stronger π-backbonding than ruthenium, and accordingly the coordinated CO is not readily displaced by other nucleophiles, although vacuum pyrolysis to produce the $[Os(Por)]_2$ dimers is still effective. Several other differences between ruthenium and osmium porphyrins point to the importance of relativistic effects in the osmium complexes,

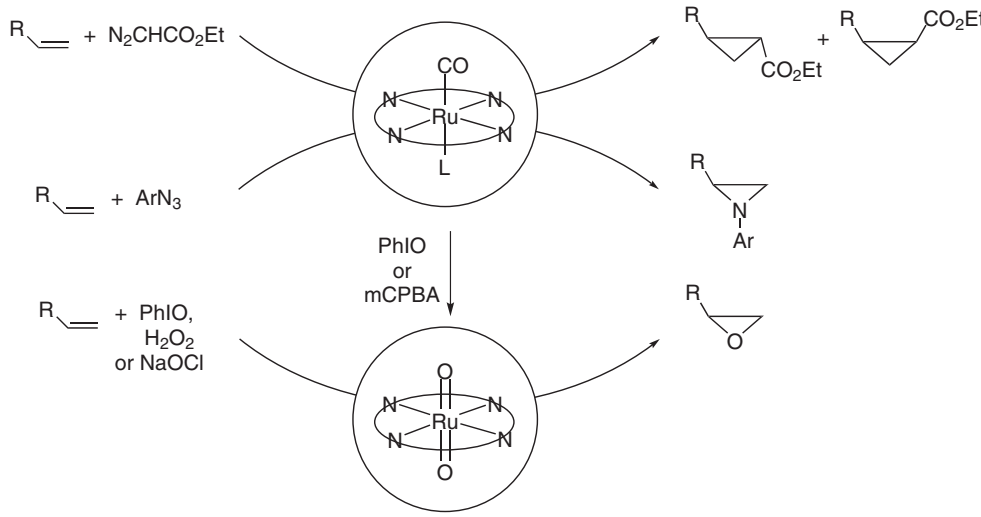

Figure 4.29 Ruthenium porphyrin-catalyzed cyclopropanation, aziridination, and epoxidation.

which result in a substantial destabilization of the Os(5*d*) orbitals relative to Ru(4*d*) orbitals for similar ligand environments.

Ruthenium and osmium corroles illustrate additional differences between the two metals, for example, the experimental conditions for insertion of the two metals (Scheme 4.7) [36, 225, 226]. Ruthenium(III) corroles, which are thought to form initially in the course of ruthenium insertion, readily dimerize to yield $[Ru(Cor)]_2$ dimers, whose air stability may be sharply contrasted with the air-sensitive nature of $[Ru(Por)]_2$ dimers. The putative $Ru^{III}(Cor)$ monomers may, however, be intercepted by a reagent such as NO or nitrite to yield $S = 0$ Ru(Cor)(NO) complexes. Upon prolonged heating, the latter undergo deoxygenation to yield $Ru^{VI}(Cor)(\equiv N)$ complexes [227]. Note that analogous $Os^{VI}(Cor)(\equiv N)$ corroles may be directly obtained with azide as the nitrogen source. Like certain other 5*d* metallocorroles, $Os^{VI}(Cor)(\equiv N)$ corroles have been found to exhibit near-IR phosphorescence at room temperature with applications to oxygen sensing and triplet-triplet upconversion [228].

4.5.3 Late Transition Elements (Groups 9, 10, 11, 12)

The late transitions metals, Groups 9–11 of the periodic table, form a wide range of complexes with porphyrins and related ligands, with metal oxidation states ranging from +1 to +3 [3, 35]. Cobalt and nickel porphyrinoids occur as the important biological cofactors, B_{12} and F_{430}, respectively [229, 230]. Of these, the chemistry of B_{12} is covered in depth in Chapter 18. The Group 9 complexes in particular have been found to act as catalysts for several synthetic transformations. Several of the 4*d* and 5*d* complexes are phosphorescent and are finding applications as oxygen sensors and in photodynamic therapy.

Both Co(II) and Co(III) porphyrins are common. Cobalt(II) porphyrins occur as $S = ½$ four-, five-, and six-coordinate complexes, with the unpaired electron occupying the metal d_{z2} orbital. The d_{z2}^1 occupancy translates to labile axial ligands, and the sixth ligand of six-coordinate Co(II) porphyrins generally dissociates readily. Cobalt(III) porphyrins may be either five- or six-coordinate and are invariably low-spin, with $S = 0$.

Rhodium and iridium porphyrins are commonly prepared from a low-valent organometallic precursor such as $Rh_2(CO)_8$, $[Ir(COD)Cl]_2$, and $[M[CO]_2Cl]_2$.

For both metals, the +3 state is the common oxidation state, and a wide variety of $M^{III}(Por)(X)(L)$ (M = Rh, Ir) complexes have been reported, where X is an anionic ligand such as halide, cyanide, alkyl, or aryl, and L is a neutral ligand such as an amine (including pyridine), phosphine, or CO. The +1 oxidation state is also well known for rhodium and iridium, in the form of OOP complexes $[M(CO)_2]_2(Por)$ (Figure 4.28b) [208]. Oxidation of these SAT M^I complexes causes oxidative collapse into the normal porphyrin coordination mode and formation of the M^{III} complexes M(Por)X (Eq. 4.9).

The +2 oxidation state is largely represented as singly bonded $[M(Por)]_2$ dimers (Section 4.5.4). The metal–metal single bonds in $[M(Por)]_2$ are readily cleaved, and the mononuclear $M^{II}(Por)$ species formed act as metalloradicals toward a variety of organic compounds, including alkyl halides (RX), alkenes, alkynes, and even alkanes (Eqs. 4.10 and 4.11). The hydrides M(Por)H also feature prominently, especially in organometallic transofrmations (see Section 4.7).

$$(Por)[M^I(CO)_2]_2 + X_2 \longrightarrow 2M^{III}(Por)X \tag{4.9}$$

$$[M^{II}(Por)]_2 + RX \longrightarrow M^{III}(Por)R + M^{III}(Por)X \tag{4.10}$$

$$[M^{II}(Por)]_2 + RH \longrightarrow M^{III}(Por)R + M^{III}(Por)H \tag{4.11}$$

Like their isoelectronic Ru(II) counterparts, Ir(Por)Me and even certain six-coordinate Ir(III) porphyrins (that do not have a vacant coordination site) effectively catalyze cyclopropanations (with diazoalkanes as the carbene source) and other carbene transfer reactions [231].

Group 9 metallocorroles with one or two axial ligands (most pyridine or a related nitrogen ligand or triphenylphosphine) have also been widely studied. Both cobalt and rhodium corroles at the formal M(III) oxidation state normally occur as five-coordinate complexes, with the sixth ligand attaching under forcing conditions. Interestingly, five-coordinate Co(Cor)(L) complexes exhibit varying degrees of non-innocent or $Co^{II}(Cor^{\bullet 2-})$ character (see Section 4.5.5 for details). In contrast to cobalt and rhodium corroles, stable Ir(III) corroles exhibit considerably higher affinities for axial ligands and are typically isolated as six-coordinate complexes. Another interesting property of iridium corroles is their unusual electron richness, which is reflected in exceedingly negative reduction potentials and the ability of certain complexes to undergo facile β-octabromination [232, 233].

Interaction of free-base porphyrins with Group 10 metal halides or acetates in refluxing glacial acetic acid or benzonitrile yields highly stable $S = 0$ $M^{II}(Por)$ (M = Ni, Pd, Pt) complexes. The smallest metal ion Ni(II) results in a particular propensity of nickel porphyrins to adopt ruffled geometries, which allows for shorter Ni-N distances. Many nickel porphyrins also bind two amine ligands (but not weaker ligands such as water or alcohols) to yield $S = 1$ Ni(II) complexes, in which Ni-N distances of ~2.0 Å are more natural for porphyrin ligands. Interestingly, chlorin and isobacteriochlorin ligands result in increased ruffling for $S = 0$ Ni(II) complexes, but also increased axial ligand affinities of these complexes. This seemingly paradoxical effect reflects the fact the increased flexibility of these hydroporphyrin ligands, which comfortably accommodate both the small low-spin Ni(II) ion and the larger high-spin Ni(II) ion. Moreover, unlike nickel porphyrins, which undergo ligand-centered reduction, one-electron reduction of Ni(II) octaethylisobacteriochlorin results in a $d_{x2\text{-}y2}{}^1$ Ni(I) state, which provided an early model for Ni^I-F430, the cofactor of methylcoenzyme M reductase

(MCR), which catalyzes the last methane-evolving step of biological methanogenesis. The currently accepted mechanism for the process involves an Ni(I)-mediated homolysis of a thioether as depicted in Scheme 4.9 [234].

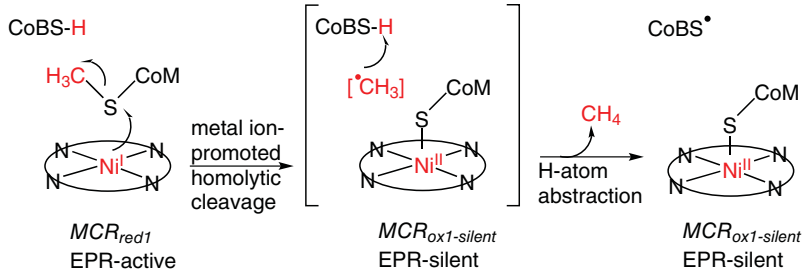

Scheme 4.9 Proposed mechanism for biological methanogenesis by methylcoenzyme M reductase; adapted from [234].

Core-modified porphyrins such as 21-thia- or 21-oxaporphyrins (N_3S or N_3O core) can stabilize nickel in the +1 oxidation state. As an example, 21,23-dioxaporphyrin (N_2O_2 core) can be prepared as its nickel(II) complex and then reduced to the nickel(I) complex (Scheme 4.10) [235].

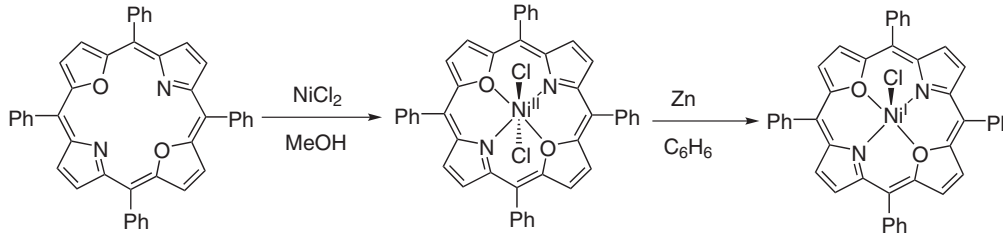

Scheme 4.10 Nickel(II) and nickel(I) complexes of 1,23-dioxaporphyrin [235].

Unlike nickel porphyrinoids, palladium porphyrins exhibit neither any reactivity toward axial ligands nor any metal oxidation states other than +2. Both Pt(II) and a handful of Pt(IV) porphyrins, on the other hand, have been reported. For example, thermally stable $S = 0$ $Pt^{IV}(TPP)Cl_2$ was obtained by oxidizing $Pt^{II}(TPP)$ with H_2O_2 in glacial acetic acid, followed by treatment with gaseous HCl [216].

Surprisingly little is known about the chemistry of Group 10 metallocorroles [35]. There is only a single report of a well-characterized Ni corrole; spectroscopic data indicate a $Ni^{II}(corrole^{\bullet 2-})$ formulation for this species. For palladium corroles, there are no structurally characterized complexes, although solution-phase spectroscopic evidence does indicate the formation of a $[Pd^{II}(CorH)]^-$ complex. Recently, a serendipitous route, involving the interaction of tetranuclear Pt(II) acetate with free-base corroles in benzonitrile, has led to Pt(IV) corroles in low yields (~6%). The initially obtained Pt(IV) corroles arise via C-H activation of the benzonitrile solvent. These complexes could be converted to a series of $Pt^{IV}(corrole^{\bullet 2-})Ar_2$ derivatives, which proved amenable to full structural characterization [236]. As of today, the development of a high-yield route to Pt corroles remains one of the key challenges of corrole coordination chemistry.

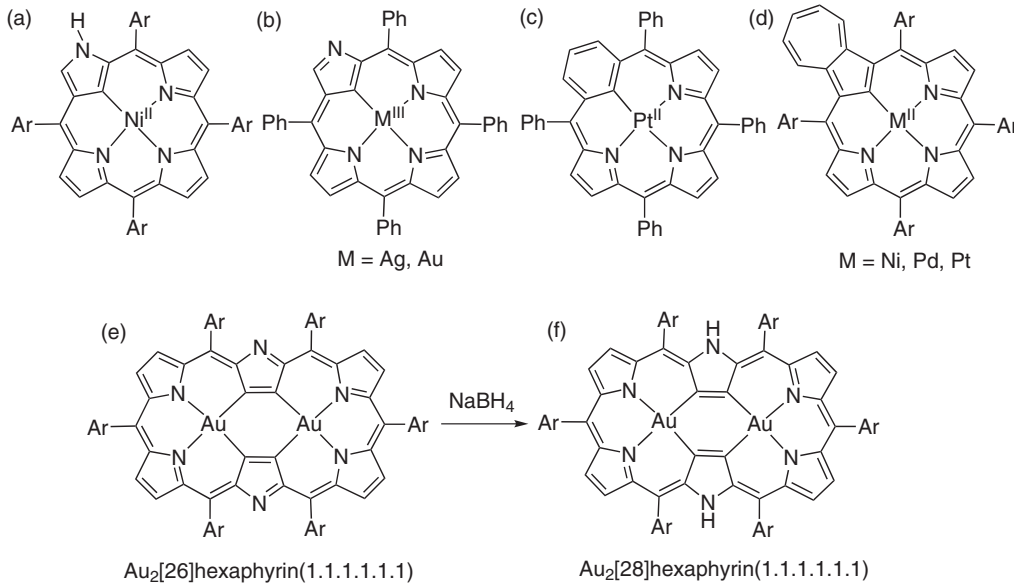

Figure 4.30 Complexes of two different tautomers of N-confused porphyrin: (a) Ni^{II} (diprotic ligand), (b) Ag^{III}, Au^{III} (triprotic ligand), (c) Pt^{II} benziporphyrin, (d) Ni^{II}, Pd^{II}, and Pt^{II} azuliporphyrin, (d) aromatic Au_2[26]hexaphyrin(1.1.1.1.1.1) and its reduction to (e) antiaromatic Au_2[26]hexaphyrin(1.1.1.1.1.1) [64, 67, 239].

The Group 11 coinage metal porphyrins are synthesized via quite traditional protocols. Thus, Cu(II) porphyrins are usually prepared by heating the free bases with Cu(II) acetate (or acetylacetonate) in glacial acetic acid or with Cu(II) halides in DMF. Silver(II) porphyrins are generally synthesized by heating the free bases with Ag(I) acetate in pyridine. Gold(III) porphyrins may be prepared by refluxing free-base porphyrins with $KAuCl_4$ in glacial acetic acid or with $AuCl_3$ in pyridine.

The chemistry of coinage metal porphyrins is somewhat limited on account of their relative lack of interaction with axial ligands. Silver(II) porphyrins are readily demetallated under reductive conditions; they can also be oxidized to diamagnetic Ag(III) porphyrins. A fair number of cationic Au(III) porphyrins are known, and an air-sensitive Au(II) porphyrin has been synthesized and structurally characterized [237]. In contrast, no true Cu(III) porphyrins are known. Thus, one-electron oxidation of Cu(OETPP) leads to the diamagnetic complex Cu^{II}(OETPP$^{\bullet}$), where the strongly saddled geometry allows for symmetry-allowed antiferromagnetic coupling between the Cu $d_{x2\text{-}y2}$ electron and the a_{2u} porphyrin radical [238].

Copper corroles are interesting in this regard in that they are inherently saddled and are best described as antiferromagnetically coupled Cu^{II}(corrole$^{\bullet 2-}$) species. In contrast, gold corroles, Au^{III}(Cor), are essentially planar. See Section 4.5.5 for a more detailed discussion.

The d^8 Group 10 and 11 ions Ni(II), Pd(II) and Au(III) form a variety of highly stable square planar complexes with *N*-confused porphyrins and carbaporphyrins (Figure 4.30, and additional examples in Section 4.7.3) [64, 67]. Expanded porphyrin complexes also feature, for example an Au(III) hexaphyrin, which may have aromatic and antiaromatic forms [239].

Zinc porphyrins are readily synthesized from free-base porphyrins and a zinc salt (typically zinc acetate or chloride) and are also simply and conveniently demetallated. Zinc is often used as the prototype "innocent" metal in applications when the identity of the coordinated

element is not critical. It is cheap, readily available, diamagnetic, exhibits no redox chemistry, is a good fit for the porphyrin cavity, and readily coordinates a wide range of ligands with especially good affinity for nitrogen donors [3]. A zinc porphyrin typically binds one axial ligand to become five-coordinate, but six-coordinate zinc centers are rarely observed in solution ($K_1 = 10^3 - 10^4\ M^{-1}$, $K_2 < 1\ M^{-1}$). A large number of superstructured zinc porphyrins have been synthesized to study ligand binding to the zinc center and the potential for molecular recognition. There are many examples: an elegant recent one is the use of a sixfold symmetric template bearing six pyridines to template the formation of a 6-porphyrin nanoring (Figure 4.31a) [240]. Zinc has also been complexed to an N-alkylcorrole and the resulting complex, which is chiral, has been resolved (Figure 4.31b) [241].

Late transition metal porphyrinoids enjoy a number of applications. Rhodium and iridium porphyrins and rhodium corroles catalyze carbene transfer reactions, in particular olefin cyclopropanations. Several of the heavy element porphyrinoids are phosphorescent and are potentially valuable as oxygen sensors and as sensitizers for photodynamic therapy [242, 243]. Palladium porphyrins are of interest as pressure-sensitive paints for aerofoils [244–246], and water-soluble Au(III) corroles have exhibited significant activity as sensitizers in photodynamic therapy and dye-sensitized solar cells. Iridium(III) corroles exhibit near-IR phosphorescence [243]. Water-soluble porphyrins have also exhibited anticancer activity under non-photochemical conditions [247].

4.5.4 Metal–Metal Multiple Bonding

The emphasis in this section is on metal–metal multiple bonding in metalloporphyrin dimers largely involving the middle 4*d* and 5*d* transition metals. A simple molecular orbital scheme for metal–metal bonding involving *d* orbitals was first provided by Cotton [248]. Subsequently, this scheme was applied to metalloporphyrin dimers, providing a simple method of calculating the metal–metal bond order and accounting for the observed spin states and many other properties of the dimers [217]. Figure 4.32 depicts qualitative MO energy level diagrams for the two limiting-case geometries of a metalloporphyrin homodimer, D_{4h} and D_{4d}, which correspond to the idealized eclipsed and staggered conformations, respectively. If the metal–metal vector defines the *z*-axis, both geometries permit one σ bond involving the d_{z2} orbitals and a pair of π bonds involving the two d_π orbitals (d_{xz} and d_{yz}) at each metal center. The eclipsed D_{4h} geometry further allows the precise alignment of the δ-symmetry orbitals (d_{xy} and d_{x2-y2}), allowing for potential δ-bonding. In practice, only one δ-bond is possible, since the high-energy d_{x2-y2} orbital, whose lobes point toward the porphyrin nitrogens, is never occupied in 4*d* and 5*d* metalloporphyrins. No δ-bonding is possible for the staggered geometry, where the δ-symmetry orbitals do not overlap and are nonbonding [217].

The simple picture outlined above allows the *d* electronic configuration of a metalloporphyrin dimer such as $[Ru^{II}(Por)]_2$ to be described as $\sigma^2\pi^4\delta_{nb}{}^4\pi^{*2}$, and that of $[Ru^{III}(Cor)]_2$ as $\sigma^2\pi^4\delta_{nb}{}^4$. The overall bond order is given by $\frac{1}{2}(n_b - n_a)$, where n_b and n_a are the numbers of bonding and antibonding d electrons, and is thus 2 for $[Ru^{II}(Por)]_2$ and 3 for $[Ru^{III}(Cor)]_2$. Note that the nonbonding electrons do not contribute to the bond order. These bond orders are consistent with significantly different Ru-Ru bond distances in the two classes of

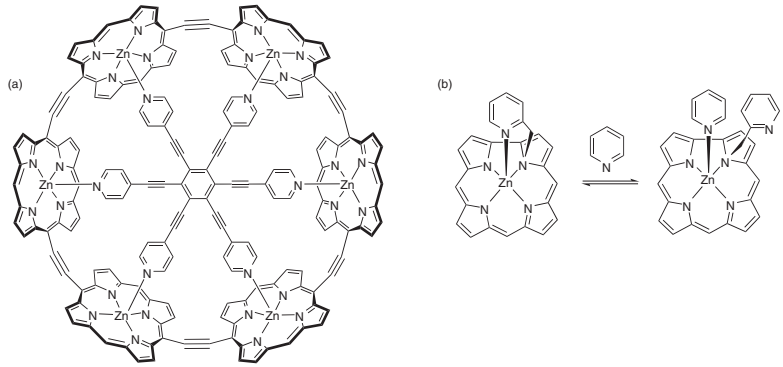

Figure 4.31 (a) Zinc porphyrin nanoring. and (b) chiral zinc N-alkylcorrole. Sources: Adapted from Rickhaus et al. [240]; Gross et al. [241].

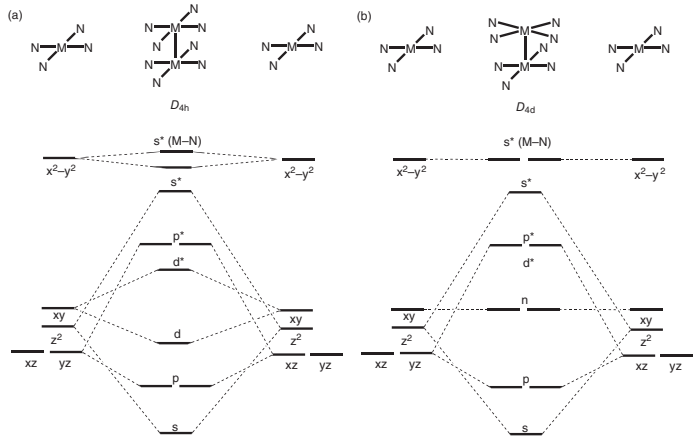

Figure 4.32 Qualitative orbital energy diagram for the (a) D_{4h} eclipsed and (b) D_{4d} staggered conformations of metalloporphyrin homodimers. Source: Diagram adapted from Collman and Arnold [217].

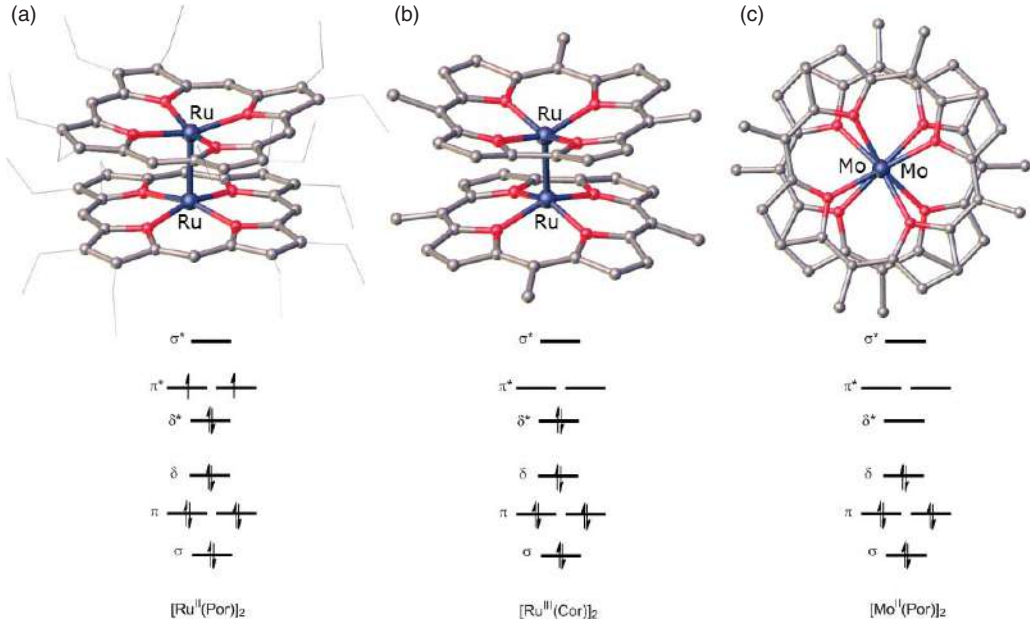

Figure 4.33 Molecular structures of metal–metal bonded homodimers and qualitative MO schemes rationalizing bond orders and spin states: (a) ruthenium porphyrin $[Ru^{II}(OEP)]_2$, $S = 1$, bond order 2 [249]; (b) ruthenium corrole $[Ru^{III}(TPFPC)]_2$, $S = 0$, bond order 3 [225], (c) $[Mo(TPP)]_2$, $S = 0$, bond order 4 [250]; *meso*-aryl groups removed except for the *ipso*-C.

complexes, ~2.4 Å for $[Ru^{II}(Por)]_2$ and ~ 2.2 Å for $[Ru^{III}(Cor)]_2$ (Figure 4.33a,b) [225, 249]. Another notable point is that the π^{*2} configuration of $[Ru^{II}(Por)]_2$ implies that the two degenerate π^* MOs must each be half-occupied, indicating an $S = 1$ ground state, again consistent with experimental observations. Unsurprisingly, the $[Ru^{III}(Cor)]_2$ complexes are $S = 0$ and diamagnetic. Similar considerations account for the observed spin states of a wide variety of metalloporphyrin dimers, involving the 4d elements Mo–Rh and the 5d elements W–Ir.

Besides structural studies (X-ray crystallography and EXAFS, in particular), vibrational spectroscopy can provide valuable information on the strength of the metal–metal bond [251]. Thus, the Ru-Ru stretching frequencies of $[Ru(OEP)]_2$ (285 cm^{-1}), $[Ru(OEP)]_2^+$ (301 cm^{-1}), and $[Ru(OEP)]_2^{2+}$ (310 cm^{-1}) have led to calculated force constants of 2.42, 2.70, and 2.86 mdyn $Å^{-1}$, qualitatively consistent with Ru-Ru bond orders of 2, 2.5, and 3, respectively (Scheme 4.11). Interestingly, analogous data for the isoelectronic osmium complexes $[Os(OEP)]_2$ (233 cm^{-1}), $[Os(OEP)]_2^+$ (254 cm^{-1}), and $[Os(OEP)]_2^{2+}$ (266 cm^{-1}) imply significantly higher force constants – 3.04, 3.46, and 3.96 mdyn $Å^{-1}$, respectively. The stronger bonds in the osmium species, relative to ruthenium, is fairly typical of 5*d* versus 4*d* transition metals and reflects, at least in part, relativistic expansion of the 5*d* orbitals in the osmium case (relativistic effects being much more muted for 4*d* transition series). Electrochemistry highlights another key difference between the ruthenium and osmium porphyrin dimers: the osmium dimers are substantially easier to oxidize, by a margin of 400–500 mV, relative to the ruthenium dimers [217]. Again, thanks substantially

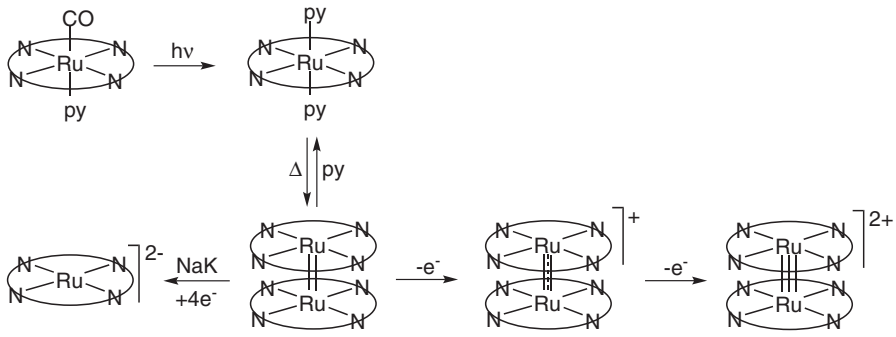

Scheme 4.11 Formation and redox chemistry of ruthenium porphyrin dimer $[Ru(Por)]_2$; Source: Figure adapted from Brothers [4].

to relativistic expansion and destabilization of the osmium 5*d* orbitals, the π^* electrons are significantly more easily lost for the osmium porphyrin dimers.

For neutral molybdenum and tungsten porphyrin dimers, the above MO scheme indicates an $\sigma^2\pi^4\delta^2$ configuration and a metal–metal quadruple bond (Figure 4.33c) [217]. As might be expected, these complexes exhibit an eclipsed molecular geometry as well as a significant energy barrier to torsion about the metal–metal axis; the latter may be thought to provide a rough estimate of the strength of the δ bond. For molybdenum and tungsten porphyrin dimers, this barrier had been found to be about 10–11 and 13 kcal mol^{-1}, respectively. The higher value in the osmium case, once again, reflects stronger Os-Os δ-bonding relative to ruthenium.

Finally, a few words on synthesis and reactivity should be appropriate. A highly general synthetic scheme for metalloporphyrin dimers involves vacuum pyrolysis of mononuclear metalloporphyrins with dissociable neutral ligands such as CO, pyridine, phosphines, and acetylene (Eqs. 4.12 and 4.13). Direct metal insertion into free-base porphyrins (or corroles) provides another fruitful and potentially more convenient approach (Eq. 4.14).

$$(M(Por)(py)2 \xrightarrow[\text{vacuum}]{\Delta} [M(Por)]_2 \quad (M = Ru, Os) \tag{4.12}$$

$$(M(Por)(PhC \equiv CPh) \xrightarrow[\text{vacuum}]{\Delta} [M(Por)]_2 \quad (M = Mo, W) \tag{4.13}$$

$$H_3Cor + Ru_3(CO)_{12} \longrightarrow [Ru(Cor)]_2 \tag{4.14}$$

The π^{*2} configuration of ruthenium and osmium porphyrin dimers translates to relatively high reactivity of these complexes. Thus, exposure to a variety of neutral ligands (L) such as CO, amines, phosphines, ethers, and carbenes results in cleavage of the metal–metal bond, affording access to a variety of six-coordinate complexes of the form $M(Por)L_2$ (M = Ru, Os) (Schemes 4.11 and 4.15 in Section 4.7.2.1) [252]. Triply- and quadruply-bonded dimers such as $[M(Por)]_2$ (M = Re, Mo, W) and $[Ru(Cor)]_2$ are much less readily cleaved.

4.5.5 Ligand Non-Innocence

C. K. Jørgensen first described ligands as *innocent* and *suspect* [253]. Innocent ligands allow a clear determination of the oxidation state of the coordinated metal. Non-innocent (the current preferred term for suspect) ligands do not. Non-innocent ligands are typically

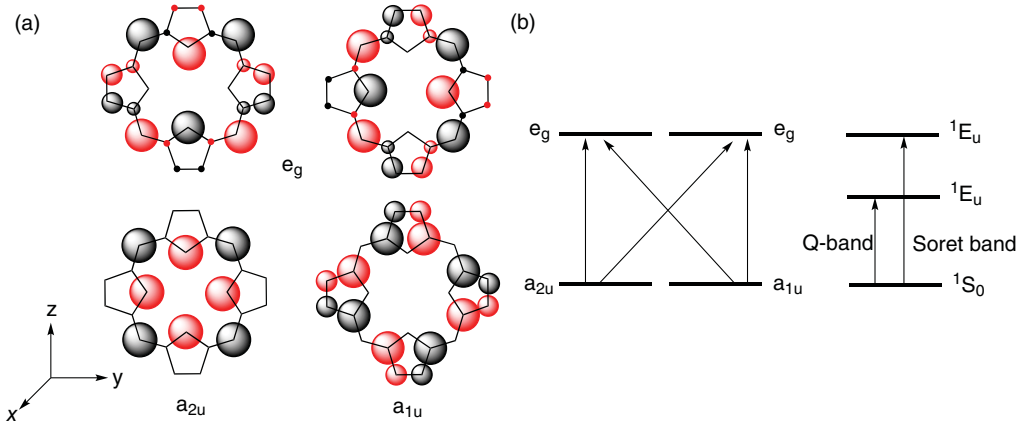

Figure 4.34 (a) Gouterman's four-orbital model for porphyrin frontier orbitals and (b) energy levels and UV–visible absorption transitions.

partially oxidized or reduced and thus have *partial* radical character. Metalloporphyrin-type complexes, especially metallocorroles, afford numerous examples of non-innocent porphyrinoid ligands [35]. Elementary orbital symmetry considerations provide a logical point of entry for a discussion of the wide range of electronic structures of the complexes in question.

Figure 4.34 depicts the topologies of the four frontier π orbitals of a prototypical closed-shell porphyrin such as a zinc porphyrin [96]. The near degeneracy of the two HOMOs (a_{1u} and a_{2u}) naturally raises the question whether a given metalloporphyrin radical should be A_{1u}- or A_{2u}-type. Because of the ability of conjugating substituents such as phenyl groups to stabilize a cation, *meso*-tetraphenylporphyrin derivatives generally give rise to A_{2u}-type radicals. By a similar argument, *β*-octaalkylporphyrin derivatives are expected to form A_{1u}-type radicals. In reality, however, most *β*-octaalkylporphyrin π-cation radicals are thought to undergo a pseudo-Jahn–Teller distortion and exhibit a spin density profile intermediate between those of A_{1u}- or A_{2u}-type radicals [254].

The formally Fe(V) compound I intermediates of heme enzymes such as peroxidases, catalases, and cytochromes P450 provide arguably the most celebrated examples of metalloporphyrin π-cation radicals. A wide range of physical methods, notably EPR and resonance Raman spectroscopies [255], as well as DFT calculations, indicate that these intermediates are $Fe^{IV}O$ porphyrin π-cation radicals. The nature and strength of the spin coupling between the $S = 1$ $Fe^{IV}O$ center and the ligand radical vary and range from moderately strongly antiferromagnetic to weakly ferromagnetic. The formally Fe(IV) compound II intermediates, on the other hand, are not radicals, but true $S = 1$ $Fe^{IV}O$ or Fe^{IV}-OH species [256].

Nonplanar distortions switch on specific orbital interactions between transition metal *d* orbitals and porphyrin π orbitals – most significantly the porphyrin a_{2u} HOMO – that are symmetry forbidden in a planar metalloporphyrin. A few examples are as follows.

Ruffling (alternate up-and-down displacement of the *meso*-carbons) switches on the metal(d_{xy})-porphyrin(a_{2u}) orbital interaction. An excellent example of this orbital interaction is provided by low-spin, six-coordinate Fe(III) porphyrins with π-acceptor axial ligands such as low-basicity pyridines (e.g., 4-cyanopyridine) and isocyanides and the somewhat unusual $(d_{xz},d_{yz})^4 d_{xy}{}^1$ electronic configuration [257]. The electronic imperative for this orbital interaction results in substantial macrocycle ruffling and significant delocalization

of spin density from the iron to the porphyrin *meso*-positions. Because of the latter effect, it is legitimate to view the porphyrin ligand in these complexes as non-innocent and the complexes as a whole as having significant Fe^{II}-$Por^{\bullet-}$ character. Importantly, non-π-acceptor axial ligands such as imidazole and unsubstituted pyridine lead to a $(d_{xz}, d_{yz})^3 d_{xy}{}^2$ configuration for low-spin Fe(III) porphyrins; this is the state commonly observed for biological ferrihemes. As might be expected, these two states are characterized by distinctive EPR parameters and ^{1}H NMR paramagnetic shifts [258].

Saddling (alternate up-and-down displacement of the pyrrole rings), on the other hand, switches on the metal(d_{x2-y2})-porphyrin(a_{2u}) orbital interaction, which is nicely exemplified by saddled, dodecasubstituted copper porphyrins. Thus, pulse EPR studies have confirmed a substantial amount of spin density at the *meso*-carbons of saddled copper *β*-octabromo-tetraarylporphyrin derivatives [259]. Another interesting manifestation of this orbital interaction is provided by strongly saddled Cu(OETPP), which undergoes one-electron oxidation to yield the diamagnetic cation $[Cu^{II}(OETPP^{\bullet})]^+$ [238]. The diamagmetism of this species reflects strong antiferromagnetic coupling between the copper d_{x2-y2} electron and the a_{2u} porphyrin radical.

The frontier orbitals of corroles qualitatively resemble those of porphyrins [260]. Copper corroles, formally Cu(III) complexes, provide fascinating examples of a metal(d_{x2-y2})-corrole ("a_{2u}") orbital interaction. As a result, although metallocorroles are generally exceedingly resistant to ruffling and saddling distortions (because of the rigidity of the direct pyrrole-pyrrole linkage to twisting or pyramidalization), copper corroles are *inherently* saddled [261]. Even sterically unhindered copper *meso*-triarylcorroles exhibit fairly strong saddling with adjacent pyrrole rings tilted 40–50° relative to each other [261], while sterically hindered, undeca-substituted copper corroles exhibit considerably higher degrees of saddling [262]. Saddling permits electron density from the a_{2u}-like corrole HOMO to flow into the copper d_{x2-y2} orbital. Several lines of evidence indicate that copper corroles are best described as antiferromagnetically coupled Cu^{II}-$corrole^{\bullet 2-}$ species, rather than as true Cu(III) complexes. The degree of saddling of Cu corroles can be further enhanced by peripheral substituent effects [263, 264]. A similar metal–ligand orbital interaction does not occur for gold corroles, where the $5d_{x2-y2}$ orbital is much higher in energy than the ligand HOMO, which is reflected in the essentially planar geometries of gold corroles [262, 265]. A dramatic illustration of the difference between copper and gold is provided by their highly sterically hindered *β*-octakis(trifluoromethyl)-*meso*-tetrarylporphyrn complexes. Thus, whereas the copper complex is dramatically saddled with adjacent pyrrole rings nearly orthogonal to each other, the analogous gold corrole is essentially planar (Figure 4.35) [264, 266].

Doming or displacement of the metal out of the porphyrin plane switches on yet a third type of orbital interaction, that between metal d_{z2} orbital and the porphyrin a_{2u} orbital. This orbital interaction is responsible for the delocalization of a large amount of spin density to the *meso*-positions of high-spin five-coordinate Fe(III) porphyrins, which is reflected in characteristic ^{1}H NMR paramagnetic shifts. A similar, if more subtle, orbital interaction is also found in FeCl corroles [267]. These $S = 1$, formally Fe(IV) species also exhibit characteristic ^{1}H NMR paramagnetic shifts, which have been interpreted in terms of an antiferromagnetically coupled Fe($S = 3/2$)– $corrole^{\bullet 2-}$ electronic description, a conclusion that was also supported by DFT calculations. The latter have indicated a $d_{xy}{}^2 d_{xz}{}^1 d_{yz}{}^1 d_{z2}{}^1$ configuration for the intermediate-spin Fe(III) center and an Fe(d_{z2})-corrole("a_{2u}") orbital interaction as mediating the antiferromagnetic coupling. In contrast, for $S = 1$ Fe-aryl corroles, ^{1}H NMR

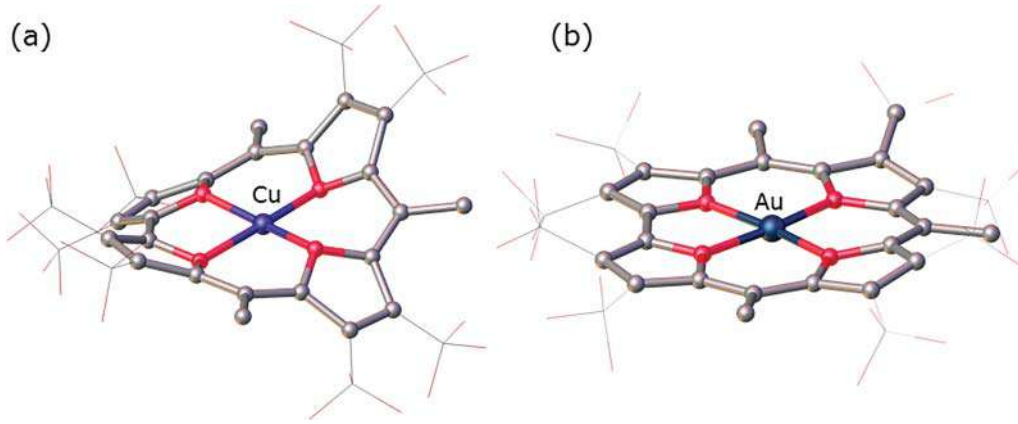

Figure 4.35 Molecular structures of (a) saddled Cu[$(CF_3)_8$T(*p*FP)C] [264] and (b) planar Au[$(CF_3)_8$T(*p*FP)C] [266]; *meso*-aryl groups removed except for the *ipso*-C.

spectroscopy indicates only small quantities of electron spin density on the macrocyle, suggesting an essentially Fe(IV)-like electronic description, again a conclusion supported by DFT calculations.

Interestingly, the metal(d_{z2})–corrole("a_{2u}") orbital interaction is also thought to confer a degree of non-innocent Co^{II}-$corrole^{\bullet 2-}$ character on five-coordinate Co[Cor](L) complexes (L = PPh_3, py). The strength of antiferromagnetic coupling varies, and is thought to be very strong for a PPh_3 axial ligand and much weaker for a pyridine [268, 269].

The optical spectra of metallotriarylcorroles provide a simple probe of ligand non-innocence [35]. For non-innocent metallocorroles with $corrole^{\bullet 2-}$ character, electron-donating *para* substituents on the meso-phenyl groups result in marked redshifts of the Soret band (by some tens of nanometer). The Soret bands of innocent metallocorroles are impervious to such substituent effects. Figure 4.36 illustrates this point by comparing the UV–vis spectra of Au and Cu triarylcorroles [265]. Note that only for the Cu corroles is the Soret maximum sensitive to the *para*-substituent.

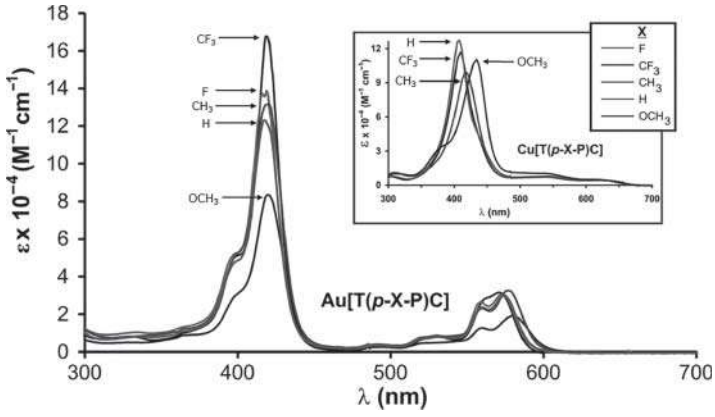

Figure 4.36 Electronic absorption spectra of Au[T(*p*-X-P)C] in CH_2Cl_2; inset: spectra of Cu[T(*p*-X-P)C]. Source: Adapted from Thomas et al. [265]; reprinted with permission. Copyright 2011 American Chemical Society.

Very recently, X-ray absorption spectroscopy (XAS), in particular the pre-edge region of the K-edge (i.e., $1s \rightarrow 3d$) absorption spectra, has also proved to be an excellent probe of the metal electronic configuration in Fe corroles and hence, indirectly, of the innocent or non-innocent character of the corrole macrocycle [270]. There can be little doubt that X-ray spectroscopic methods will play an increasingly important role in delineating many of the electronic-structural subtleties of metalloporphyrinoids in the foreseeable future.

4.5.6 Metalloporphyrin-Diatomic Ligand Complexes

The interaction of hemes with the diatomics CO, NO, and O_2 is a crucial aspect of heme protein function. The key question here is how a given heme protein discriminates among the three ligands and chooses to bind one, either O_2 or CO/NO, selectively. Early structural studies on carbonmonoxymyoglobin (MbCO) suggested that O_2-binding heme proteins employ distal pocket steric interactions to force coordinated CO to adopt an unnaturally bent conformation, thus discriminating against CO in favor of O_2, for which a bent conformation is natural [271]. Subsequent structural studies, however, failed to confirm a strongly bent CO in MbCO. Infrared spectroscopy, in particular a high FeCO bending frequency of $\sim$550 cm^{-1}, suggested that substantial bending of the FeCO unit should be energetically costly. This argument, too, turned out to be essentially incorrect. DFT calculations showed that coupled Fe-C tilting and FeCO bending provide a low-energy path for the FeCO unit to deform substantially, since this mode of deformation does not greatly affect the strength of the Fe-CO backbonding (Figure 4.37) [272, 274]. The modern understanding, which emerged largely in the late 1990s, is that heme proteins do not actively discriminate against CO or NO. Instead, distal pocket hydrogen bonding greatly stabilizes coordinated O_2, which has significant superoxide character, and such stabilization does not occur for coordinated CO or NO. The lack of a suitable hydrogen bond donor in the distal pocket (as in, say, the key NO sensor soluble guanylate synthase, sGC) is thus the key factor that allows a heme protein to selectively bind CO and NO [275].

The great biological importance of heme–NO interactions has resulted in a comprehensive investigation of metalloporphyrin-NO complexes [272, 273, 276, 277]. Because of the highly covalent nature of the MNO units in these complexes, their effective *d* electron counts are commonly described by the Enemark-Feltham notation $\{MNO\}^n$, where n is the sum of number of metal *d* electrons and NO π^* electrons [278]. For example, for adducts of Mn(II)/Fe(III) (d^5), Fe(II) (d^6), and Co(II) (d^7) porphyrins with NO (which has one π^* electron), n = 6, 7, and 8, respectively (Figure 4.38). Synthetic routes to iron porphyrin nitrosyl complexes are shown in Scheme 4.12. Some key highlights of the three electronic configurations are described below.

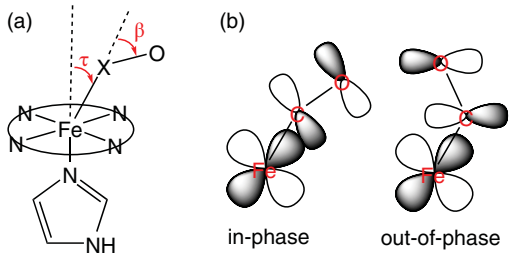

Figure 4.37 (a) Definition of the tilting (τ) and bending (β) angles of the FeCO unit; (b) FeCO backbonding interaction under cooperative tilting and bending [272, 273].

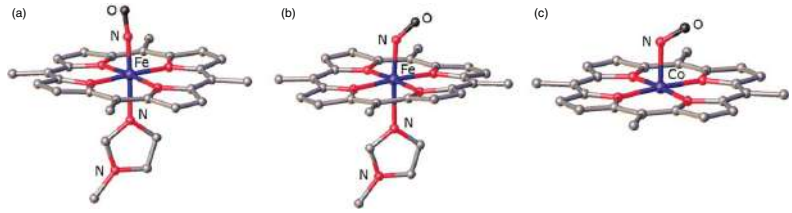

Figure 4.38 Representative molecular structures of metalloporphyrin nitrosyl complexes: (a) $\{FeNO\}^6$, $[Fe(TPP)(NO)(1\text{-MeIm})]^+$, Fe-N = 1.63 Å, Fe-N-O = 176° [279]; (b) $\{FeNO\}^7$, Fe(TpFPP)(NO)(1-MeIm), Fe-N = 1.75 Å, Fe-N-O = 137° [280]; (c) $\{CoNO\}^8$, Co(TPP)(NO), Co-N = 1.83 Å, Fe-N-O = 123° [281]; *meso*-aryl groups removed except for the *ipso*-C.

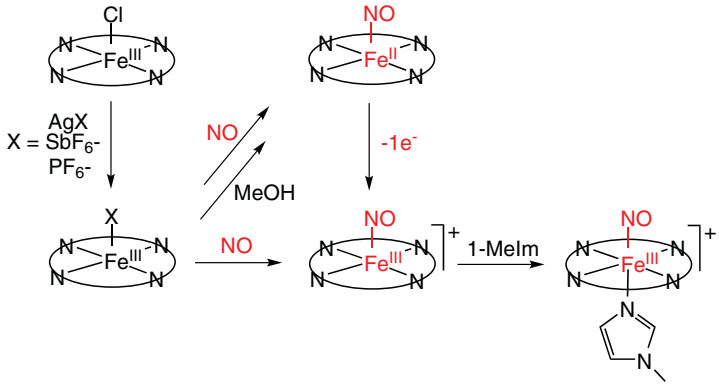

Scheme 4.12 Synthetic routes to iron porphyrin nitrosyl complexes; Source: Adapted from McQuarters et al. [279].

The $S = 0$ $\{MNO\}^6$ electron count is isoelectronic with MbCO (Mb = myoglobin) and is exemplified by several biological and biomimetic $\{FeNO\}^6$ systems, a handful of Mn porphyrins such as Mn(TTP)(NO)(1-MeIm), and by the series M(Por)(NO)(Ar) (M = Fe, Ru, and Os) [282]. For Fe and Mn, the M-N(O) distances hover around 1.65 Å, and the MNO bond is generally linear (Figure 4.38a). Significantly bent $\{MNO\}^6$ units are known, however. Thus, FeNO angles of ~160° have been observed in $\{FeNO\}^6$-thiolate systems such as nitrophorin 4, which occurs in the saliva of the blood-sucking insect *Rhodnius prolixus*, as well as in an Fe(OEP)(SAr)(NO) model complex [283]. The M(Por)(NO)(Ar) (M = Fe, Ru, and Os) series also exemplifies cases of distinctly bent $\{MNO\}^6$ units. Although these bent geometries can be understood in terms of specific orbital interactions involving the thiolate or aryl *trans* ligand, they also make sense in light of the cooperative tilting and bending model (see above) [274].

The $\{MNO\}^7$ electron count is represented by numerous $S = 1/2$ nitrosylhemes (i.e., Fe(II) porphyrin + NO). Compared with $\{FeNO\}^6$ porphyrins, the Fe-N(O) distance in $\{FeNO\}^7$ porphyrins is slightly longer, ~1.72 Å, and the FeNO angle is much more bent, ~140° (Figure 4.38b). These two features are most conveniently explained in terms of an σ-interaction between the Fe d_{z2} orbital and one of the NO π* orbitals. In addition, the Fe-N(O) vector is typically slightly tilted relative to the heme normal [276, 284]. As illustrated in Figure 4.39, this may be viewed as a pseudo-Jahn-Teller distortion, which mixes the d_{z2} and one of the d_p orbitals of the Fe, allowing both to overlap with an NO π* orbital.

Nitric oxide coordination to an Fe(II) porphyrin brings about a strong *trans*-labilizing effect. Thus, for six-coordinate nitrosylhemes, a sixth nitrogenous ligand such as imidazole

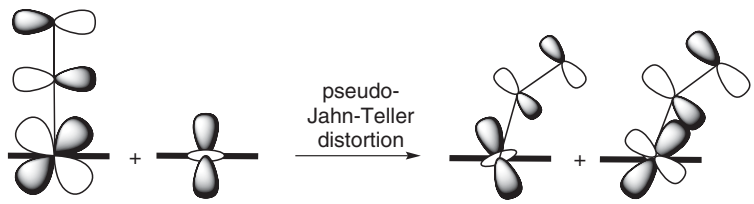

Figure 4.39 Pseudo-Jahn-Teller *d*-orbital mixing in nitrosylhemes that is proposed to lead to Fe-N(O) tilting and NO bending; Source: Figure adapted from Ghosh et al. [273].

or pyridine is very weakly bound, with an Fe-N bond distance of ~2.2 Å. For soluble guanylate cyclase, NO binding leads to uncoupling of the proximal histidine ligand, which acts as a base and sets in motion a cascade of reactions that ultimately brings about vasodilation.

It is worth noting that $S = 1/2$ {FeNO}^{7} complexes with linear FeNO units are known (e.g., $[Fe(CN)_4(NO)]^{2-}$), but not with porphyrins [285]. Nor for that matter are high-spin, $S = 3/2$ {FeNO}^{7} species established for porphyrin systems [286].

Diamagnetic FeNO corroles are fascinating species in this connection. With short Fe-N(O) distances of ~1.65 Å and essentially linear FeNO units, they have long been regarded as classic {FeNO}^{6} complexes [287, 288]. Recent studies, however, indicate that they are better described as {FeNO}^{7}-corrole$^{\bullet 2-}$. Electronic absorption spectra of a series of FeNO *meso*-tris(*p*-X-phenyl)corrole derivatives, Fe(T*p*XPC)(NO), revealed that the Soret maxima redshift sensitively in response to the increasing electron-donating character of the *para*-substituent X. Over a long series of studies, this behavior is now firmly established as a diagnostic for non-innocent corrole$^{\bullet 2-}$ states [289]. Consistent with this picture, the NO stretching frequencies of these compounds (1761–1781 cm^{-1}) are some 100 cm^{-1} lower than those of genuine {FeNO}^{6} porphyrins such as Fe(TpivPP)(NO)(NO$_2$) (1893 cm^{-1}). The FeNO corroles also exhibit skeletal bond length alternations and IR marker bands consistent with corrole radical character. Finally, DFT (B3LYP) calculations yield a broken-symmetry spin density profile (i.e., one where the up-and-down spin densities are spatially separated) best described as an intermediate-spin $S = 3/2$ Fe(III) center antiferromagnetically coupled to an axial $S = 1$ NO$^-$ unit and to the equatorial corrole$^{\bullet 2-}$ radical (Figure 4.40) [289]. Optimum spin coupling between the Fe(d_{z2}) electron and corrole$^{\bullet 2-}$ radical then provides a plausible explanation for the linearity of the {FeNO}^{7} unit. Interestingly, in contrast to FeNO corroles, RuNO corroles are thought to be best described in terms of an innocent corrole ligand, that is, {RuNO}^{6}-corrole^{3-} [227].

Four-coordinate cobalt corroles have been reported to bind CO with a log K ~ 4.5 ± 0.8. The coordinated CO exhibits ν_{CO} values around 2040–2080 cm^{-1}, significantly above those exhibited by five-coordinate heme-CO complexes such as Fe(TPP)(CO) (1969–1972 cm^{-1} in toluene), indicating weaker backbonding and stronger CO bonding. Accordingly,

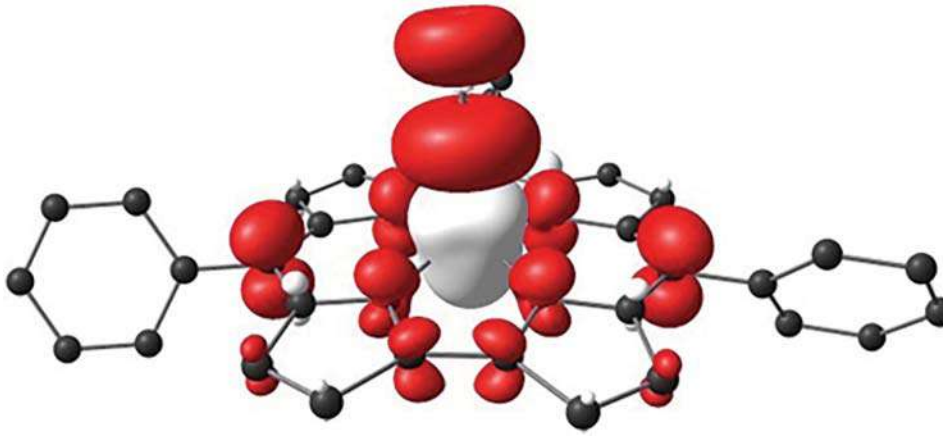

Figure 4.40 Broken-symmetry spin density profile for Fe(TPC)(NO) [289].

a significant amount of effort has been dedicated toward exploiting Co corroles as key components of carbon monoxide sensors [290, 291]. Unfortunately, no experimental structural information is available for these CO adducts. Although DFT calculations (with both pure and hybrid functionals) indicate an $S = 0$ ground state for these species, B3LYP calculations yield a broken-symmetry ($M_S = 0$), antiferromagnetically coupled $Co^{II}(d_{z2}{}^1)$-corrole$^{\bullet 2-}$ description for the lowest-energy solution, with the corresponding ferromagnetically coupled ($M_S = 1$) solution only ~0.3 eV higher in energy. In other words, the CoCO corroles may be partially analogous to the FeNO corroles [292].

Diamagnetic cobalt-NO porphyrins provide some of the best-characterized examples of {MNO}^{8} species. These complexes are characterized by Co-N(O) distances of about 1.8 Å and strongly bent CoNO angles of ~120° (Figure 4.38c) [276, 293]. The electronic configuration may be described as $d_{xy}{}^2 d_{xz}{}^2 d_{yz}{}^2 d_{z2}{}^2$, where the d_{z2} orbital engages in a σ-interaction between the metal d_{z2} orbital and one of the NO π* orbitals (as in the {FeNO}^{7} case). The bonding in these complexes may be described as a simple spin coupling between low-spin Co(II) and NO$^\bullet$.

Formally isoelectronic {FeNO}^{8} intermediates are believed to occur as intermediates for several heme enzymes such as cytochrome c nitrite reductase (ccNIR) [294, 295], fungal cytochrome P450 nitric oxide reductase (P450nor) [296, 297], and hydroxylamine oxidoreductase [298] as well as in a few model complexes. In an important recent development, the first X-ray structure of an {FeNO}^{8} species has been reported; the species in question, the [Fe(Br_8TFPPP)(NO)]$^-$ anion, was found to exhibit an Fe-N(O) distance of ~1.81 Å and an FeNO angle of ~122° [299, 300]. The protonated form of {FeNO}^{8} porphyrins, that is, Fe^{II}-HNO porphyrins, are also important intermediates in biology. While no Fe^{II}-HNO porphyrin has so far been crystallographically characterized, EXAFS measurements on Mb-HNO (Mb = myoglobin) have yielded an Fe-N_{HNO} distance of 1.82 Å [301]. Several HNO complexes involving metals other than iron, however, have been reported in the literature.

A handful of metalloporphyrin dinitrosyl complexes have been reported. Thus, [$Mo(NO)_2$]^6 porphyrins have been structurally characterized and found to exhibit a horseshoe-shaped $Mo(NO)_2$ unit (a so-called *attracto* stereochemistry) as well as a strongly OOP Mo atom. Ford and co-workers have reported unstable *trans*-[$Fe(NO)_2$]^8 and [$Ru(NO)_2$]^8 species [302]. As shown in Figure 4.41, DFT calculations have suggested that such species exhibit a curious *trans-syn* geometry as a result of specific Fe(*d*)-NO(π*) orbital interactions [273, 303]. A dinitrosylheme species has been implicated as a transient intermediate for several NO sensor

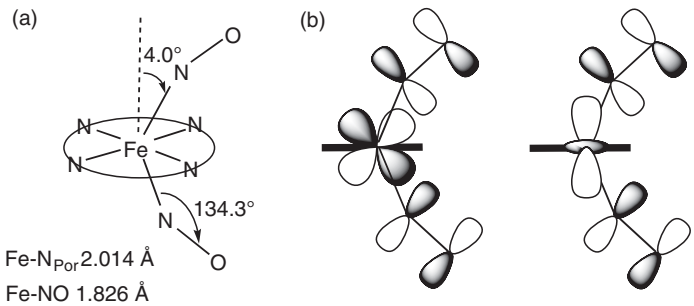

Figure 4.41 (a) Calculated geometry and (b) important Fe(*d*)-NO(π*) orbital interactions for *trans-syn*-Fe(Por)$(NO)_2$; Source: Figure adapted from Ghosh et al. [273].

proteins, including *Alcaligenes xylosoxidans* cytochrome c′ (AXCP), where it was first identified, as well as eukaryotic sGC as well as bacterial H-NOX proteins [304].

It is worth noting in this connection that cobalt corroles bind a variety of inorganic anions, with a strong selectivity for nitrite. In a medically relevant application, optical nitrite sensors based on cobalt corroles have been shown to detect NO emission (NO) from NO-releasing polymers containing *S*-nitroso-*N*-acetyl-*DL*-penicillamine [305].

4.6 Lanthanides and Actinides

Lanthanide tetrapyrrole complexes are a major class of compounds whose importance arises from coupling the magnetic and electronic properties of these elements with the highly conjugated, redox active tetrapyrrole chromophores, offering intriguing possibilities for new functional materials. The best-explored ligands in this context are the phthalocyanines, although there is a wealth of lanthanide porphyrin chemistry as well.

The lanthanide(III) cations are large, and typically form complexes with high coordination numbers and display limited redox chemistry. As a result, the ions usually reside well out of the N_4 plane, and the chemistry features not just simple Ln(Pc)X or Ln(Por)X complexes, but a range of double- and triple-decker complexes $Ln(Mac)_2$ or $Ln_2(Mac)_3$ (where Mac is a porphyrin, phthalocyanine, or naphthalocyanine macrocycle). These multi-decker complexes are what really distinguish lanthanide tetrapyrrole coordination chemistry from that of most of the other elements in the periodic table. Multi-decker complexes are only observed for a handful of other ions such as Ca(II), Zr(IV), Hf(IV), and Ta(V), which have broadly similar chemical characteristics to the lanthanides. The synthesis and properties of lanthanide tetrapyrrole complexes have been comprehensively reviewed, and the following summary is based upon these accounts [306–313].

The monophthalocyanine "single-decker" or "half-sandwich" complexes are generally prepared by template synthesis using a lanthanide salt, often $Ln(acac)_3{\cdot}nH_2O$ with a phthalonitrile precursor at high temperature (typically 200–300 °C) in the presence of a bulky organic base, although this route has the drawbacks of low yields and difficult purification (Scheme 4.13). The alternative approach, which is also how the porphyrin complexes are prepared, is metallation of the free-base macrocycle or its dilithiated salt by $Ln(acac)_3{\cdot}nH_2O$ to give Ln(Pc)(acac) or Ln(Por)(acac), usually in a weakly basic solvent such as quinoline or 1-octanol (Scheme 4.13). The acac substituent is difficult to remove, and as a result these products are less useful as precursors to complexes with other axial ligands. These methods have been applied to both unsubstituted and peripherally substituted phthalocyanines, although the effectiveness and yields can be influenced by bulky substituents, especially in the α-position. There is also an extensive chemistry of lanthanide naphthalocyanines (Nc) that parallels that of the phthalocyanines.

Other lanthanide salt precursors used with H_2Por or Li_2Por are LnR_3 ($R = CH(SiMe_3)_2$), $LnX[N(SiMe_3)_2]_2$, or $LnX_3(THF)$, giving Ln(Por)R or $Ln(Por)(X)(L)_n$ (X = halide, L = ether solvent, $R = CH(SiMe_3)_2$). For the smaller lanthanides ytterbium, erbium, or yttrium, the reaction of $Ln[N(SiMe_3)_2]_3$ with H_2Por in bis(2-methoxyethyl)ether for two days gave the cationic complexes $[Ln(Por)(H_2O)_3]Cl$ in high yield. However, this route did not work for larger lanthanides such as neodymium. The labile cations $[Ln(Por)(H_2O)_3]^+$ formed hydroxo- or chloro-bridged dinuclear complexes when treated with base or HCl. The mononuclear complexes, including even those of the larger cations, could be stabilized

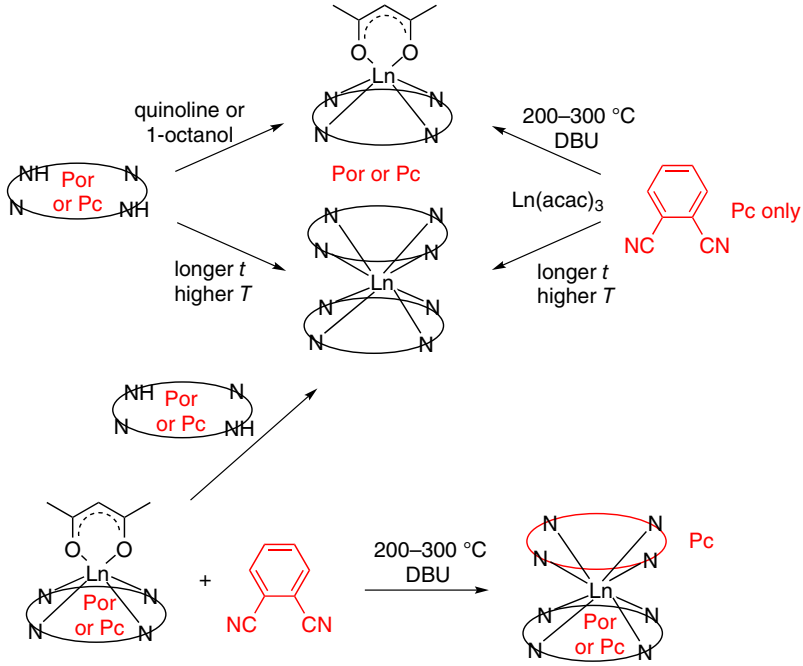

Scheme 4.13 Preparative routes to lanthanide porphyrin and phthalocyanine complexes.

by using tripodal monoanions such as trispyrazolylborate or the Klaui tripod ligand $\{(C_5H_5)Co[(CH_3O)_2PO]_3\}^-$ to give Ln(Por)(tripod) complexes [314]. The Klaui ligand was also used to stabilize ytterbium and erbium complexes of N-confused porphyrin, Ln(NCTPP)(tripod), shown by crystallography to contain an η^2-C–H agostic interaction with the core CH group of the N-confused porphyrin [309].

Double-decker (or sandwich) and triple-decker lanthanide bis- and tris-macrocycle complexes $M(Mac)_2$ and $M_2(Mac)_3$ comprise a major class of compounds in which the macrocycles can be the same (homoleptic) or different (heteroleptic), the latter containing different phthalocyanine ligands or phthalocyanine/porphyrin combinations (Figure 4.42). Synthetic methods range from template synthesis that can give statistical mixtures of products, to carefully designed "raise by one story" sequences that add macrocycles to the stack one at a time (Scheme 4.13). Homoleptic bisphthalocyanine complexes $M(Pc)_2$ can be made using the same method as the monophthalocyanine complexes, by lanthanide salt-templated cyclization of the phthalonitrile precursor using longer reaction times and higher temperatures than for monophthalocyanines, and by the reactions of lanthanide precursors with H_2Pc or Li_2Pc. The cyclization method can also be used for the triple-decker $M_2(Pc)_3$ complexes although with lower yields. A mono-β-substituted phthalonitrile precursor will give four possible isomers of a tetra-β-substituted phthalocyanine and up to 10 isomers of a bisphthalocyanine. This problem disappears when di-β-substituted phthalonitriles are used, resulting in octa-substituted phthalocyanines with no isomeric possibilities. Homoleptic bisporphyrins $M(Por)_2$ can be prepared from $M(acac)_3 \cdot nH_2O$ with H_2Por or Li_2Por in a high-boiling solvent such as 1,2,4-trichlorobenzene (TCB).

Heteroleptic phthalocyanine double-deckers M(Pc)(Pc′) can be made by three possible methods. Cyclization of two different phthalonitrile precursors gives a mixture of differently

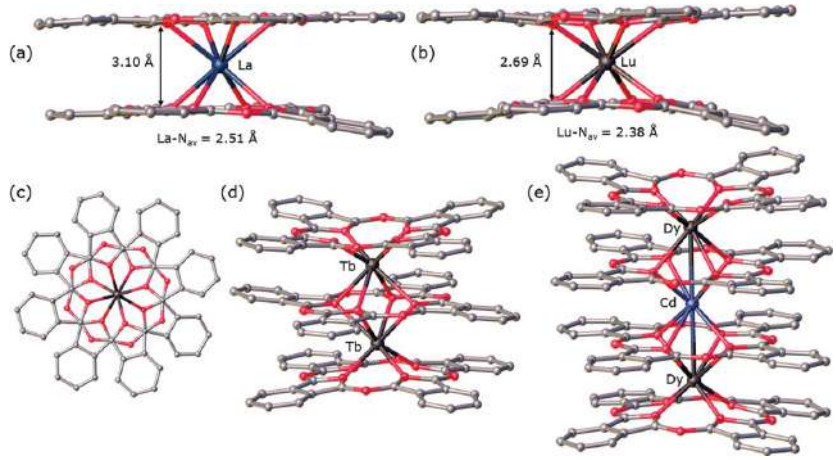

Figure 4.42 Molecular structures of multi-decker lanthanide Pc complexes: (a) $La(Pc)_2$ and (b) $Lu(Pc)_2$ illustrating the effect of size of the central lanthanide ion [315, 316], (c) top view of $Lu(Pc)_2$ showing square-antiprismatic D_{4d} geometry [316], (d) triple-decker $Tb_2[Pc(O^nBu)_8]_3$ [317]; quadruple-decker $Dy_2Cd[Pc(O^nBu)_8]_4$ [318]; O^nBu side chains not shown.

substituted bisphthalocyanine products, while reaction of lanthanide salts with two different lithiated or free-base phthalocyanines will give a mixture of the heteroleptic M(Pc)(Pc′) and homoleptic $M(Pc)_2$ and $M(Pc')_2$ products. The more precise "raise by one story" route uses the single-decker Ln(Pc)(acac) complex as a template for the DBU-promoted cyclization of a second phthalonitrile precursor, giving one desired product with simpler isolation and purification procedures. The reaction of M(Por)(acac) with $Li_2(Por')$ is useful for preparing the heteroleptic bisporphyrins M(Por)(Por′). Mixed porphyrin/phthalocyanine double-deckers can be prepared from M(Pc)(acac) with H_2Por, from M(Por)(acac) with Li_2Pc or by using M(Por)(acac) as the template for phthalonitrile condensation (Scheme 4.13).

Heteroleptic triple-deckers are also produced by the "raise by one story" method, introducing both different macrocycles and different metals to produce heteroleptic bimetallic complexes $MM'(Pc)_2(Pc')$. For example, the series of complexes (Pc)M(Pc′)M′(Pc) were prepared from the reaction of the double-deckers M′(Pc)(Pc′) with M(Pc)(acac) in refluxing TCB (M = M′ = Gd-Lu; M = Lu, M′ = Gd-Yb; Pc′ = Pc(β-$OC_8H_{17})_8$) [311]. Mixed porphyrin/phthalocyanine triple-deckers are synthesized by similar means, or less precisely, as statistical mixtures from the reaction of H_2Por with $M(acac)_3$ in refluxing TCB followed by treatment with Li_2Pc. The number of "decks" continues to increase with examples of four and five rings, for example quadruple-decker (Pc)Dy(Pc)Cd(Pc)Dy(Pc) and Tb–Cd–Tb, Tb–Cd–Y, Y–Cd–Tb and Er-Cd-Er combinations, and a quintuple-decker Tb-Cd-Cd-Tb stack (Figure 4.42) [319].

With similar methods being used to form the single-, double-, and triple-deckers, control of the stoichiometry, solvent, reaction temperature, and time are all important in achieving selectivity for particular products. Long alkyloxo or alkylthio side chains on the phthalocyanine periphery are commonly used to improve solubility and also to impart liquid crystalline properties in the resulting stacks. Crown ether-substituted phthalocyanines also produce compounds with tunable properties, using the crown ethers as secondary coordination sites. The availability of 15 lanthanide elements (or 14, excluding promethium), many porphyrin, phthalocyanine, and naphthalocyanine derivatives, and the double- and triple-decker architectures means the macrocycle π-π interactions and lanthanide metal *f*-*f* interactions can be precisely controlled to give complexes with very specific magnetic and optical properties.

Many complexes have been structurally characterized, some as the complete series of lanthanide ions, for example the unsubstituted $M(Pc)_2$ and mixed naphthalocyanine/porphyrin M(Por)(Nc) double-deckers. These show the expected variation in ring-ring distance as the metal ion radius decreases along the series (Figure 4.42a,b) [312]. The stability of metal bisphthalocyanines increases on going from lanthanum to lutetium [310].

The oxidation states of the single-decker species M(Mac)X and triple-deckers $M_2(Mac)_3$ are clear, with M^{3+} ions and dianionic macrocycles (Pc^{2-}, Nc^{2-}, Por^{2-}). However, the double-deckers $M(Mac)_2$ are anionic when both macrocycles are in their dianionic forms, $[M^{3+}(Mac^{2-})]^-$, and can be isolated as salts, for example $K[M(Pc)_2]$ (M = La, Ce, Pr, Sm, In, Sb, Bi), $[n\text{-}Bu_4N][M(Pc)_2]$ (M = Sc, Y, La, Ce, Pr, Sm, In, Sb), or as the protonated forms $H[M(Pc)_2]$. The neutral complexes $M(Pc)_2$ have more complicated electronic structures and can be formulated as $M(Pc^{2-})(Pc^{\bullet-})$, with evidence obtained from absorption, emission, and vibrational spectroscopy and electrochemistry. For example, the electronic absorption spectra of $[n\text{-}Bu_4N][Sc(Pc)_2]$ in three different ring oxidation states (2-/2-, 2-/1-, and 1-/1-) were

recorded. The full series of unsubstituted $M(Pc)_2$ complexes exhibited weak split Soret bands (ca. 322 and 346 nm), an intense Q band (ca. 680 nm), and two π-radical bands at ca. 460 and 480 nm. With the exception of the π-radical bands, the absorption energies are dependent on the size of the central metal and shift to higher energy along the series as the lanthanide ion becomes smaller, indicating that the π-π interaction between the two rings increases as the ring-to-ring separation decreases [312]. IR spectroscopy shows a band near 1315 nm in the IR that has been identified as a marker band for the neutral, radical $M(Pc)_2$ complexes and also varies linearly with the size of the Ln^{3+} ion. The porphyrin double-deckers $M(TPP)_2$ and $M(OEP)_2$ have similar marker bands at 1225–1265 and 1530–1570 cm^{-1}, respectively. Spectroscopic evidence for the mixed M(Pc)(Por) double-deckers shows the hole to be localized on the Pc ring.

The cerium complex $Ce(Pc)_2$ is a special case as the accessibility of the Ce^{4+} oxidation state means the complex can be formulated as $Ce^{4+}(Pc^{2-})_2$. Consequently, the π-radical bands are absent from the spectrum and the Soret band is not split. The same spectral changes are observed for protonated complexes, for example $H\{M(Pc)[Pc(\alpha\text{-}OR)_8]\}$ (M = Sm, Eu, Gd). The IR marker band near 1380 cm^{-1} is also absent in the cerium and protonated complexes.

Double-decker lanthanide phthalocyanines have proved to be landmark examples of single-molecule magnets (SMMs), important as candidates for data storage and spintronic devices. Most SMMs contain several transition metal ions with coupled spins, but the terbium and dysprosium anions $[Tb(Pc)_2]^-$ and $[Dy(Pc)_2]^-$ show slow magnetization relaxation, opening the possibility of single ion SMMs. SMM behavior is also observed for neutral complexes, for example $Tb(Pc)_2$, with an additional *f*-π interaction arising from the delocalized phthalocyanine radical, in the mixed double-deckers Dy(Pc)(Por) and H[Dy(Pc)(Por)]. SMM effects in the triple-deckers $Tb_2(Pc)_3$ and $TbY(Pc)_3$ (and their quadruple- and quintuple-decker counterparts) involve *f*-*f* interactions as well as the other effects [319–321].

Applications of lanthanide porphyrins have been reviewed [313], including their photophysical properties, especially with respect to near-IR emission. The macrocycle acts as an antenna, absorbing visible light which is then emitted in the near infrared by those *f*-elements that have the correct energy levels – specifically Yb, Nd, and Er [322, 323]. Lanthanide porphyrin complexes stabilized by tripodal monoanions such as trispyrazolylborate or the Klaui tripod ligand {(C5H5)Co[(CH3O)2PO]3}$^-$, Ln(Por)(tripod), are good candidates for near-IR light emitting probes for bioimaging and sensing due to the deep penetration of near-IR light in the biological tissue. Ln(Por)(tripod) complexes with Ln = Yb, Nd, and Er that emit at 980, 900–1300, and 1540 nm, respectively, have been investigated for these applications [314]. Ytterbium porphyrins are possible candidates for photodynamic therapy (PDT) of cancer, and gadolinium porphyrins for PDT and for magnetic resonance imaging [313].

Very recent additions to the lanthanide tetrapyrrole family are the first examples of lanthanide corrole complexes. The 3– charge on the corrole ligand is a good match for the Ln^{3+} cations. The reaction of H_3Cor with $Ln(N(SiMe_3)_2)_3$ gave $Ln(Cor)(DME)_2$ for Ln = La and Tb, while the reaction of $Li_3(Cor)\cdot(THF)_4$ with $GdCl_3$ and Me_3(triazacyclononane) produced Gd(Cor)(Me_3tacn). The molecular structure of the lanthanum complex demonstrated that $La(Cor)(DME)_2$ exhibits the largest metal-N_4 conjugated macrocycle plane distance,

1.469 Å, of any complex so far recorded, in keeping with its large ionic radius [118]. The first triple-deckers containing corroles are also recent additions to this family. They have the formula Pc–M–Cor–M–Pc, where M = Y, Pr, Nd, Sm, Eu, Gd, or Tb. With all metals in the +3 oxidation state, charge balance requires that one of the ligands be a radical. Analysis of the IR markers associated with the radicals indicate that this is most likely to be the corrole, with the triple-deckers formulated as (Pc^{2-})–(M^{3+})–$(Cor^{\cdot 2-})$–(M^{3+})–(Pc^{2-}) [324, 325].

Perhaps not surprisingly, the chemistry of actinides (An) with tetrapyrrole ligands is rather limited [63, 306]. Thorium and uranium monoporphyrin complexes $An(Por)Cl_2$ were prepared from $AnCl_4$ with H_2Por, and subsequent ligand exchange resulted in structurally characterized complexes $Th(OEP)(acac)_2$, $U(TPP)Cl_2(THF)$, and the trimer $[Th(TPP)(\mu\text{-}OH)_2]_3$ (Figure 4.43a). The metal in each complex is displaced from the N_4 plane with the other ligand on one face. The phthalocyanine analogues $An(Pc)(acac)_2$ (An = Th, U) are also known. Reaction of the tetraamides $An(NR_2)_4$ (An = Th, U) with H_2Por and/or H_2Pc gave a series of sandwich compounds $An(por)_2$, $An(Pc)_2$, and $An(Por)(Pc)$, all with the metal in the +4 oxidation state and dianionic ligands (Por = TPP, TTP, OEP). Structures of $Am(Pc)_2$ and $Pa(Pc)_2$ also appear in the database. $Th(TPP)_2$ could be oxidized to the cation $[Th(TPP)_2]^+$ in which the hole resided on the ligand rather than oxidation of the metal.

There were few new examples of actinide tetrapyrroles for nearly two decades, until the recent preparation of the first actinide corroles, the thorium(IV) and uranium(IV) complexes $[An(Cor)Cl(DME)]_2$ (DME = dimethoxyethane), each adopting a binuclear structure bridged through two chloro ligands (Figure 4.43b). They were prepared from $AnCl_4(DME)_n$ plus $[Li_2(Cor)][Li(THF)_4]$. Electrochemistry and absorption spectroscopy suggest that redox processes are ligand-based for the thorium complexes, but have some involvement of the metal for uranium [116, 118].

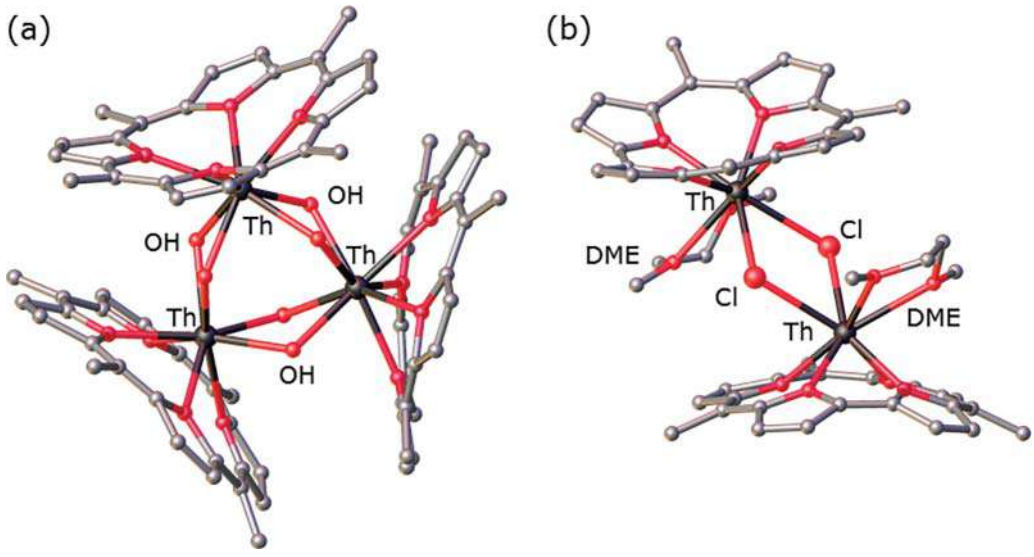

Figure 4.43 Molecular structures of (a) $[Th(TPP)(\mu\text{-}OH)_2]_3$ [326] and (b) $[Th(Cor)Cl(DME)]_2$ (Cor = Mes_2(*p*-OMePh)Cor) [116]; *meso*-aryl groups removed except for the *ipso*-C.

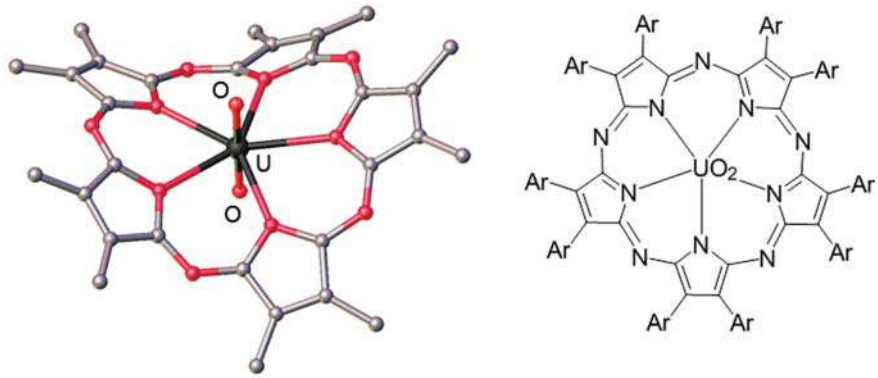

Figure 4.44 Molecular structure of $U(O)_2$(superazaporphyrin), Ar = 4-$C_6H_4OCH_3$ [330]; aryl groups removed except for the *ipso*-C.

Expanded pyrrole macrocycles, with their large coordination cavities, are better suited to the large actinide elements than the tetrapyrroles. The motivation for this chemistry was the development of selective extractants for actinide metals for extraction and separation applications or for remediation of contamination [63, 327, 328]. The first example was the uranyl complex of so-called "superphthalocyanine," prepared from the condensation of phthalonitrile templated by the uranyl cation, UO_2^{2+}, in refluxing DMF. The resulting macrocycle is an expanded phthalocyanine containing five isoindoline subunits with the linear, axial uranyl cation in the center of the pentagonal bipyramid. The structure shows the macrocycle not to be fully planar but somewhat ruffled [329]. A "superazaporphyrin" analogue (an expanded porphyrazine with five subunits) has been more recently reported, again via templated synthesis using $UO_2(OAc)_2{\cdot}(DMF)_2$ (Figure 4.44) [330].

Both of the above azamacrocycles underwent decomposition upon attempts to remove the uranyl cation and isolate the free bases. In contrast, expanded porphyrins are well known as the free bases, which makes the exploration of their coordination chemistry with actinide cations much more accessible [63]. A uranyl complex of [22]-pentaphyrin (1.1.1.1.1) was prepared from the free-base and UO_2Cl_2 ion refluxing isopropanol/pyridine and crystallizes as a pentagonal bipyramidal complex with five equatorial nitrogens and a linear uranyl group [331]. The uranyl cation very readily forms complexes of hexapyrroles in the amethyrin family, the reactions being complete in a few minutes without heating. These include amethyrin, [24]hexaphyrin(1.0.0.1.0.0), dioxamethyrin (an amethyrin analogue containing two furans in place of pyrroles), and isoamethyrin [24]hexaphyrin(1.0.1.0.0.0). Oxidation of the isoamethyrin macrocycle occurs under the reaction conditions for insertion of the uranyl and neptunyl cations, and the complexes feature the oxidized, aromatic [22]hexaphyrin(1.0.1.0.0.0) form. The structures are best described as hexagonal bipyramidal, with the uranyl complex UO_2(isoamethyrin) more distorted from planarity than the neptunyl $[NpO_2(\text{isoamethyrin})]^-$, indicating that the ligand is a better fit for the larger Np^{5+} ion relative to the U^{6+} ion (Figure 4.45) [332]. Spectroscopic evidence was obtained for complexation of the plutonyl ion [333]. Oxidation of the macrocycle during insertion is also observed for complexation of the uranyl cation, introduced as $UO_2[N(SiMe_3)_2]_2{\cdot}2THF$, to cyclo[6]pyrrole, [22]hexaphyrin(0.0.0.0.0.0), to form the antiaromatic, 20 π-electron

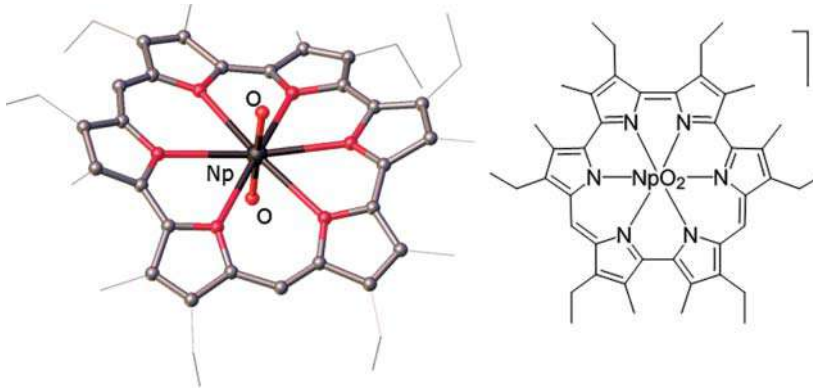

Figure 4.45 Molecular structure of $[Np(O)_2([22]hexaphyrin(1.0.1.0.0.0))]^-$ [332].

ligand [334]. Uranyl cations also complex to hybrid macrocycles containing pyrrole units in combination with, variously, Schiff base donors, pyridine, and furans [335, 336].

4.7 Organometallic Porphyrin Complexes

Through the 1960s and 1970s, there was rapid growth in the two independent fields of metalloporphyrin chemistry and organometallic chemistry. The first explored the coordination chemistry of an expanding number of elements supported by porphyrin and related ligands, while the second developed the chemistry of metal-carbon single, multiple, and π-bonds. For a long time, these two areas barely intersected, despite the obvious point of connection afforded by the Co-C bond in vitamin B12 [229]. A small number of σ-alkyl complexes of Groups 8 and 9 metalloporphyrins had been reported, followed in the late 1970s by the first metalloporphyrin carbene complex, $Fe(TPP)(=CCl_2)$ [337, 338]. From that point on, the field of organometallic porphyrin chemistry grew rapidly, with expansion into other parts of the periodic table and other organometallic ligand types including alkenes, alkynes, hydrides, and π-complexes, documented in several early reviews [339–341], two comprehensive reviews treating transition metal and main group complexes separately [4, 5], and many more focused reviews that will be cited in the appropriate sections.

A useful classification of organometallic porphyrin complexes shown in Figure 4.46 helps to organize the area, modified from previous classifications in the literature [4, 342, 343]. The types are described as follows:

A. one or two metal-carbon single or multiple bonds (alkyl, aryl, carbene), for example: M(Por)R, M(Por)RL, $M(Por)R_2$, $M(Por)(=CR_2)$, $M(Por)(=CR_2)L$, $M(Por)(=CR_2)_2$;
B. π-ligands (η^2-alkene, η^2-alkyne, η^5-Cp);
C. M-R-N bridge between M and N_{Por};
D. carbaporphyrinoids;
E. M′ peripherally coordinated to porphyrin core; and
F. M′ tethered through linker to either central M(Por) or periphery.

The main focus of this section will be types A and B, with types C–E covered briefly, and type F included only to complete the classification. The periodic table of "organometallic metalloporphyrins" of types A–C has some significant gaps, with examples containing vanadium,

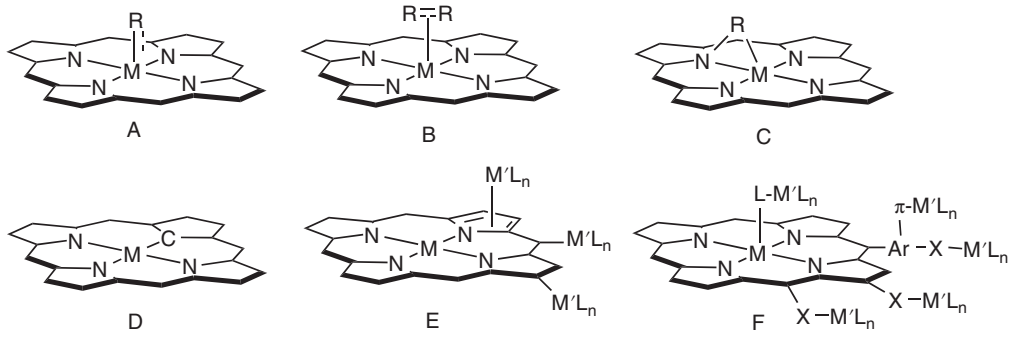

Figure 4.46 Classification of organometallic porphyrin complexes.

niobium, technetium, and rhenium either unknown or not supported by molecular structures. There is little organometallic chemistry for the later transition elements nickel, copper, and zinc, which have stable M^{II}(Por) formulations, although the carbaporphyrinoid complexes (type D) do include some notable examples of these elements. Corrole organometallic chemistry, on the other hand, is growing at a rapid rate following on from the dramatic increase in the number of elements coordinated to corroles, but still lags well behind the porphyrins in breadth and depth.

This section will focus on the porphyrin as a supporting ligand in main group and transition metal organometallic complexes. The porphyrin serves to define the stereochemical and electronic environment of M coordinated in the N_4 site, with the "organometallic" functionality being defined by one or more M-C bonds. The complex types comprise the usual suspects, namely σ-alkyl and σ-aryl (e.g., M(Por)R, M(Por)RL, M(Por)R_2) and carbene/alkylidene (e.g., M(Por)(=CR_2), M(Por)(=CR_2)L, M(Por)(=CR_2)$_2$), all type A in (Figure 4.46), and π-complexes such as η^2-alkene, η^2-alkyne, η^5-Cp, etc. (type B in Figure 4.46). This area is the most developed for porphyrins, with rapid progress in corrole chemistry having occurred in the last few years. In the following discussion, references to earlier work can be found in the comprehensive reviews [4, 5] with only the more recent examples specifically referenced.

A particular feature of six-coordinate organometallic porphyrin complexes with *trans* geometry is the lack of *cis* coordination sites, important in many classical organometallic mechanisms like oxidative addition, reductive elimination, and migratory insertion. Alternative mechanisms for common organometallic processes, including radical pathways sometimes involving non-innocent behavior on the part of the porphyrin ligand, is a notable aspect of this chemistry.

4.7.1 E—C and M—C Single Bonds

4.7.1.1 Synthesis

Porphyrin complexes bearing M-C single bonds contain σ-alkyl or σ–aryl ligands, generally in five-coordinate or six-coordinate geometry, M(Por)R, M(Por)RX, M(Por)RL, or M(Por)R_2. Prototypical examples are shown in Figure 4.47. Examples of these complexes can be prepared almost universally by the reaction of M(Por)X or M(Por)X_2 (X is typically halide, but may be hydroxide or alkoxide) with Grignard or organolithium reagents, where M is from Groups 3–9, 13, and 14. The general route is also effective for phthalocyanines

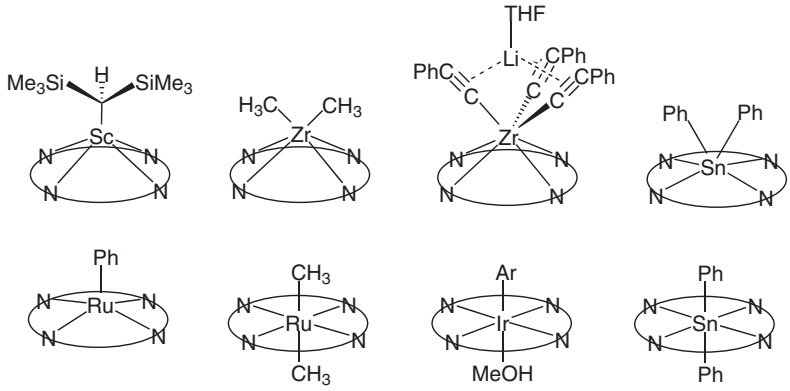

Figure 4.47 Prototypical examples of σ-alkyl or σ–aryl complexes.

(e.g., $Si(Pc)X_2$ + ArMgBr gives $Si(Pc)Ar_2$) and for some corroles, taking into account the generally higher oxidation state of the coordinated element. For example M(OEC)Ph can be prepared from M(OEC)Cl + PhMgBr for M = Fe, Sn, or $Ti(Cor)CH_2SiMe_3$ from Ti(Cor)Cl with Me_3SiCH_2MgCl [117]. Other examples are less straightforward. Treatment of Mn^{III}(Cor) with PhMgX followed by air oxidation yielded the halogenido complexes Mn^{IV}(Cor)X instead of the expected organometallic complexes. However, reaction of these complexes with excess PhMgX or with LiAr did produce the σ-aryl compounds [344]. The salt metathesis route does not work for the Group 15 porphyrins – the reactions of $[M(Por)X_2]^+$ (M = P, As, Sb) with RMgX or RLi results in demetallation or decomposition – but the use of organoaluminum reagents AlR_3 was successful (see Section 4.4.5, Scheme 4.2) [157]. For corroles, Group 15 complexes are again the exception, with P(OEC)=O serving as the precursor to $P(OEC)Ph_2$, $[P(OEC)Me]^+$ or $P(OEC)Me_2$ upon treatment with PhMgBr or MeMgI.

Late transition metals for which low-valent precursors are available open up oxidative addition or nucleophilic displacement pathways. Electrochemically produced $[Fe(Por)]^-$ reacts with RX (R = alkyl, aryl, vinyl, alkynyl, allyl, etc.) to give Fe(Por)R, and the ruthenium and osmium dianions $[M(Por)]^{2-}$ react with RX to give the trans dialkyl complexes $M(Por)R_2$. The monoanions $[M(Por)]^-$ feature all three Group 9 metals and react with RX (R = alkyl, aryl, etc.) to give M(Por)R (M = Co, Rh, Ir). Main group examples featuring oxidative addition are the reaction of RX with the tin(II) porphyrin Sn(Por) or tin(II) corrole $[Sn(TPFC)]^-$ to give Sn(Por)RX or Sn(TPFC)R, and the reaction of arsenic corrole As(OEC) with MeI yielding the cationic complex $[As(OEC)Me]^+I^-$ [345].

The alkali metal porphyrins $M'_2(Por)L_n$ (M′ = Li, Na, K, L = solvent) are useful precursors for reactions with the very oxophilic and moisture-sensitive early transition metal (Groups 3, 4, and 5) and lanthanide halides via transmetallation and salt elimination reactions, and has also been used for Group 14 elements. For example, $Li_2(OEP)(THF)_4$ + $TaMe_3Cl_2$ gives $Ta(OEP)Me_3$, which is notable for having all three methyl groups on the same face of the complex. This route has been more recently extended to corrole examples using $Li_3(Cor)L_n$, for example with $CpZrCl_3$ or Cp^*TiCl_3 to give CpZr(Cor) or Cp*Ti(Cor), respectively.

An alternative route is to use the free-base porphyrin or corrole with an organoelement precursor via alkane elimination. This was first demonstrated for aluminum, for which the

reaction of $AlEt_3$ with H_2TPP gave Al(TPP)Et, and is also useful for Group 15 (E = P, As), for which $PhECl_2$ with H_2OEP produced the cations $[E(OEP)Ph_2]^+$. For early transition metals, alkane elimination occurs with the organoelement precursor, but the organic group is not retained in the product, as in the reaction of $H_3(Cor)$ with $TaMe_3Cl_2$ that gives the halide $Ta(Cor)Cl_2$ (see Section 4.5.1, Scheme 4.4) [187].

Redox reactions can lead to modification of σ-alkyl complexes, as in the reaction of $Zr(OEP)(CH_2SiMe_3)_2$ with H_2 in toluene that gives $Zr^{III}(OEP)(CH_2SiMe_3)$, most likely containing a non-innocent porphyrin ligand. One final example of preparation of an organometallic complex comes from the template synthesis of the ligand around an organoelement precursor, as in the silicon phthalocyanine complexes Si(Pc)(R)Cl (R = Me, Ph), formed from the reactions of $MeSiCl_3$ or $PhSiCl_3$ with 1,3-diiminoisoindoline.

4.7.1.2 Properties

The six-coordinate complexes $M(Por)R_2$ or M(Por)RX are usually *trans,* although *cis* geometries can be observed for early transition metals, of which *cis*-$Zr(OEP)Me_2$ and *cis*-$Ta(Cor)Me_2$ are good examples (see Section 4.5.1, Scheme 4.4). The tin complex $Sn(Por)Ph_2$ is notable for existing in both *cis* and *trans* geometries, the former prepared from $Li_2(OEP)$ with Ph_2SnCl_2 and the latter from $Sn(TPP)Cl_2$ with $MgPh_2$. The corresponding methyl complexes $Sn(Por)Me_2$ also exist in both geometries. Early transition metal, lanthanide, and some main group alkyl and aryl complexes are, as expected, very reactive toward air and water, and their very electrophilic nature is demonstrated by a tendency to form "ate" complexes such as the zirconium complex $Zr(Por)(C\equiv CR)_3Li(THF)$ (R = Ph, $SiMe_3$) in which the three alkynyl ligands are *cisoid* on the same face of the porphyrin. In an yttrium example, Y(OEP) with 2MeLi gives $Y(OEP)(\mu\text{-}Me)_2Li(OEt_2)$, which in turn reacts with $AlMe_3$ to produce $Y(OEP)(\mu\text{-}Me)_2AlMe_2$. Alkyl/aryl exchange in Co(Por)Ar, which reacts with RLi to give Co(Por)R, is postulated to occur through "ate" intermediates $[Co(Por)R_2]^-$.

In the transition metal examples, the energies of *d* orbitals and the porphyrin frontier orbitals are similar, and there are examples where ligand non-innocence is suspected, as in $Zr^{III}(OEP)(CH_2SiMe_3)$ and $Zr^{III}(TPP)(\eta^5\text{-}Cp)$, whereas this is less true for the main group examples. This is reflected in the electrochemistry where for the alkyl or aryl main group element porphyrins ring oxidation and reduction predominates, whereas for the transition metal complexes the lowest-energy redox processes tend to be centered on the coordinated metal. In the UV–visible spectra of the main group complexes, the electronic absorptions are typically shifted to lower energy relative to simple anion (e.g., halide) examples, reflecting the electron-donating character or R or Ar. The group 13 complexes Ga(Por)R and In(Por)R have been used as metal redox-inactive models for Fe(Por)R and Co(Por)R. The difference in redox potentials between M(Por)R and $M(Por)ClO_4$ is <0.17 V for indium but up to 1 V for iron, reflecting the fact that reduction in the indium complexes is at the porphyrin ring and is relatively insensitive to the axial ligand, whereas in iron it is at the metal and hence is very sensitive to the axial ligand. Structures of Ga(Por)R with R = alkyl, vinyl, acetylide have been determined, comprising a series with sp^3, sp^2, and *sp* hybridized carbon. As expected, both the Ga-C and Ga-N(av) bonds shorten as the *s* character in the Ga-C bond increases.

Cobalt porphyrin σ-organometallic complexes attracted close scrutiny because of their relationship with the corrinoid Co-C bond in coenzyme B_{12}, and also because of their role in catalysis of free radical living polymerization of alkenes. The Co-C bond energies in Co(Por)R

were probed via a number techniques and found to fall in the range 18–30 kcal mol^{-1} with a sophisticated understanding of the influence of the porphyrin, the R group, and the presence or absence of a neutral donor ligand.

Not surprisingly, the formally 15-electron d^5 organoiron(III) porphyrin complexes Fe(Por)R can access different spin states depending on R and the porphyrin. If R is aryl or alkyl and Por = TPP, OEP then the complexes are typically low spin, $S = ½$, whereas if R is C_6F_5 or C_6F_4H then the high-spin $S = 5/2$ state is observed. ^1H NMR spectrometry of Fe(Por)R (R = alkyl, aryl) is useful for determining spin states. Low-spin Fe(Por)R is very reactive, light, and thermally sensitive, and undergoes facile Fe-C homolysis with the order of reactivity Fe(Por)(alkyl) > Fe(Por)(aryl) > Fe(Por)(C ≡ CR). The Fe-C bonds have been determined to be 10–15 kcal mol^{-1} weaker than Co-C in Co(Por)R.

The higher apparent oxidation states of the coordinated element in corrole complexes may also mask non-innocent character (Section 4.5.5) [35]. For example, Fe(OEC)Ph is paramagnetic with $S = 1$, consistent with an Fe(IV) center. It can be chemically or electrochemically oxidized to $[Fe(OEC)Ph]^+$, which has $S = ½$ and has been assigned as Fe(IV)($OEC^{\bullet-}$)Ph with antiferromagnetic coupling of the $S = 1$ d^4 Fe(IV center) with the $s = ½$ corrole radical anion. Similarly, Co(OEC)Ph formally contains Co(IV) and can be further oxidized to $[Co(OEC)Ph]^+$, which has non-innocent corrole character.

4.7.1.3 Reactivity

Various of the more reactive and labile σ-organometallic porphyrin and corrole complexes are active toward small molecule activation, either under thermal or photochemical conditions. The Group 14 complexes $M(Por)R_2$ are labile even under ambient light, although the vinyl, alkynyl, and ferrocenyl examples are less photolabile because of the greater e-withdrawing capacity of the ligand compared to alkyl and aryl ligands. The same is true for gallium and indium complexes M(Por)R. Activation of CO_2 by Al(Por)R; CO_2, SO_2 or O_2 by Ga(Por)R; CO_2 or SO_2 by In(Por)R and O_2 by $Ge(Por)R_2$ are all observed via insertion into M-C bond during photolysis, resulting in acetato, sulfinato, or alkylperoxo ligands. $Ta(Cor)Me_2$ inserts and couples two CO molecules under ambient pressure to produce an the enediolate complex containing an $O(CH_3)C{=}C(CH_3)O$ ligand (see Section 4.5.1, Scheme 4.4) [187]. Small molecule activation can be catalytic; for example, $Zr(OEP)(CH_2SiMe_3)_2$ reacts with ethene/H_2 to catalyze production of ethane plus $Zr(OEP)(Et)(CH_2SiMe_3)$ and $Zr(OEP)Et_2$.

The E-C bonds in the Group 15 complexes $[M(Por)R_2]^+$ or $[M(Por)(R)X]^+$ are inert compared to their Groups 13 and 14 counterparts with no photochemical cleavage of E-C bonds observed. Reversible deprotonation of $[E(OEP)(R)(OH)]^+$ gives neutral E(OEP)(R)(=O) for E = P and As but not Sb (see Section 4.4.5, Scheme 4.2).

The role of organo-cobalt porphyrin complexes Co(Por)R in catalyzing the living radical polymerizations of alkyl acrylates, acrylic acid, and vinyl acetate have been extensively studied. This occurs by two different mechanisms: reversible termination and degenerative transfer. Homolysis of the Co-C bond forms a $Co^{II}(Por)^{\bullet}$ metalloradical that reacts with a polymeric radical ($P^{\bullet}$) to produce a quasi-equilibrium with an organometallic complex Co(Por)(P). The polymeric products have relatively low polydispersity and controlled number average molecular weight (based on one polymer chain per cobalt complex) demonstrating the living characters of the process [346–348]. If the organic radical has a β-hydrogen available, then it reacts with the $Co^{II}(Por)^{\bullet}$ radical to produce a cobalt hydride Co(Por)H via β-hydrogen abstraction. The hydride can then add to alkene monomers to form Co(Por)R′ and initiate catalytic chain transfer. The mechanism of alkene insertion

into the Co-H bond of Co(por)H is significant because the complex does not contain any vacant sites *cis* to the hydride, and the usual migratory insertion pathway is not available. The mechanistic study shows that with the low barrier predicted here for the multistep insertion process that even for systems that do have a *cis*-vacant site, the radical insertion might compete with classical migratory insertion [349, 350].

Mechanistic questions have also proved to be very significant for rhodium porphyrins. The Rh(II) porphyrin dimer $[Rh(Por)]_2$ has a relatively low Rh-Rh bond strength (12–16.5 kcal mol^{-1}) and in the presence of H_2 exists in equilibrium with Rh(Por)H. An important reaction observed in 1981 was the insertion of CO into the Rh-H bond of Rh(Por)H to produce a formyl complex, Rh(Por)CHO. This was significant because this reaction had not been observed in classical organometallic chemistry and revealed a new mechanism for the process, a radical chain mechanism for which the balance between Rh-Rh, Rh-C, and Rh-H bond strengths is very important, with the weak Rh-Rh bond and unusually strong Rh-C bond providing the driving force (Eqs. 4.15–4.18). Styrene insertion into the Rh-H bond of Rh(Por)H follows a similar mechanism.

$$2Rh(Por)H \rightleftharpoons [Rh(Por)]_2 + H_2 \tag{4.15}$$

$$[Rh(Por)]_2 \rightleftharpoons 2Rh(Por)^{\bullet} \tag{4.16}$$

$$Rh(Por)^{\bullet} + CO \rightleftharpoons Rh(Por)(CO) \tag{4.17}$$

$$Rh(Por)(CO) + Rh(Por)H \rightleftharpoons Rh(Por)C(O)H + Rh(Por) \tag{4.18}$$

The $Rh^{II}(Por)^{\bullet}$ monomer, like $Co^{II}(Por)^{\bullet}$, is an odd-electron species and can initiate many radical reactions. Use of the sterically constrained TMP ligand allows access to the $Rh(TMP)^{\bullet}$ radical without going through the dimer. Rh(TMP) reversibly reacts with CH_4 to produce Rh(TMP)H and $Rh(TMP)CH_3$. The intermolecular stoichiometric and catalytic activation of both strained and unstrained aliphatic C-C bonds by $Rh^{II}(Por)^{\bullet}$ complexes began with the serendipitous discovery of activation of one of the C-CH_3 bonds in the radical TEMPO. This was extended to activation of C-C bonds in nitriles, non-enolizable ketones, esters, and amides to produce rhodium(III) porphyrin alkyls, $Rh^{III}(Por)R$ with no associated C-H bond activation via homolytic radical substitution of a C(sp^3)-C(sp^3) bond by with a $Rh^{II}(Por)^{\bullet}$ radical. $Rh^{III}(Por)OH$ generated in situ can selectively activate the $C_{\alpha}-C_{\beta}$ bond in ethers and the C_{α}-CO bond in ketones via σ-bond metathesis of a C-C bond with the Rh-OH bond in Rh(Por)OH [351]. New reactivity continues to be developed. As a recent example, catalytic intramolecular H-X addition (X = O, NR, CR_2) to allylphenols to form heterocyclic compounds mediated by rhodium(III) porphyrin complexes involves both hydride and alkyl species in the cycle [352].

Radical chemistry has also been noted for the diethyl ruthenium porphyrin $Ru^{IV}(OEP)Et_2$ that converts to a 1:2 mixture of the ethylidene $Ru(OEP)=CHCH_3$ and Ru(OEP)Et together with ethane and ethane. Kinetic studies using TEMPO as a radical trap showed that Ru-C bond homolysis was the first step.

Both heterolytic and homolytic processes leading to useful and interesting chemistry are observed for main group porphyrins. For example, organo-aluminum porphyrins Al(Por)R undergo photolytic Al-R homolysis and can add to α,β- unsaturated ketones and act as catalysts for living polymerization. In an intriguing sequence of reactions shown in Scheme 4.14, a germanium corrole hydride, Ge(TPFC)H, is produced by $NaBH_4$ reduction of $Ge(TPFC)OCH_3$ and reacts with aldehydes, alkenes, and alkyl halides to

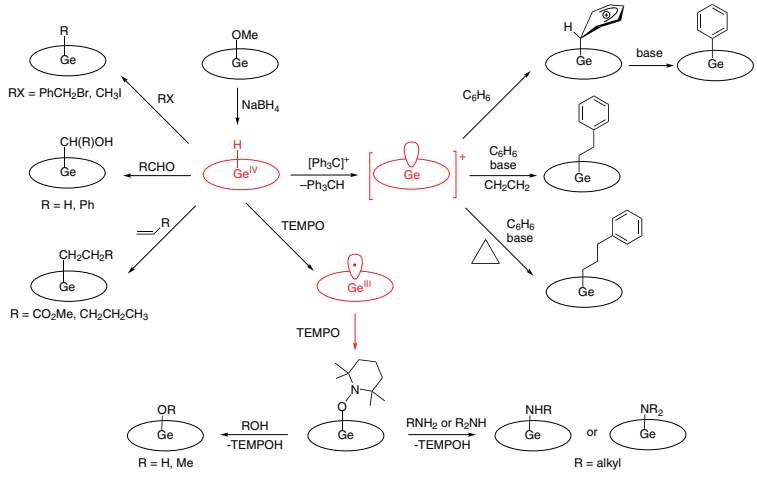

Scheme 4.14 Reactivity of a germanium corrole hydride (Cor = TPFPC).

produce α-hydroxyalkyl and alkyl complexes [353]. Hydride abstraction from Ge(TPFC)H using the trityl cation produced a highly reactive cation, $[Ge(TPFC)]^+$, which reacted with benzene to form (TPFC)GePh through an intriguing σ-type germylium-benzene adduct, $[(TPFC)Ge(\eta^1\text{-}C_6H_6)]^+$. The cation also reacts with ethene and cyclopropane to form germanium alkyl products [354]. A different reactive germanium corrole intermediate is the $Ge^{III}(TPFPC)^\bullet$ formed by homolysis of a Ge(TPFPC)(TEMPO) adduct. Under visible light irradiation, the radical reacts with O-H and N-H bonds in alcohols and amines [355, 356].

A particular feature of some late transition metal porphyrins M(Por)R is oxidatively induced migration of the R group from the metal to a pyrrole nitrogen. One-electron oxidation of Fe(Por)Ph produces $[Fe(Por)R]^+$, which then undergoes migration of the phenyl group to give $[Fe(Por\text{-}N\text{-}Ph)]^+$. The process is reversible, and one-electron reduction induces the reverse migration. The phenomenon also occurs for Co(Por)R, but the initial oxidation for iron is at the metal, whereas initial oxidation for Co is at the ring. Interestingly, Group 13 porphyrins Ga(Por)R and In(Por)R, often considered to be metal redox-inactive models for transition metal porphyrins, do not undergo the oxidatively induced migration.

4.7.2 Metal-Carbon Multiple Bonds

4.7.2.1 Carbene

Prototypical metalloporphyrin carbenoid complexes are shown in Figure 4.48.

In the late 1970s, the iron complex $Fe(TPP) = CCl_2$, prepared from the reaction of Fe(Por) with CCl_4 in the presence of a reductant (Fe powder or dithionite), was the first transition metal dihalocarbene to be reported [357], and also the first example of a metalloporphyrin carbene [337, 338]. The reaction was more general, and use of CX_3Y as the carbene source gave $Fe(Por) = CXY$, CI_4 produced the bridging carbide complex $(Por)Fe = C{=}Fe(por)$, and Cl_3CCHAr_2 yielded the vinylidene $Fe(Por) = C{=}CAr_2$.

Through the 1980s, metalloporphyrin carbene chemistry was extended to ruthenium and osmium, and more varied and versatile synthetic routes were established [4, 219, 341, 358]. Diazoalkane or diazoester reagents N_2CR_2 or N_2CRR' (R = H, allyl, aryl, CO_2Et) proved to be

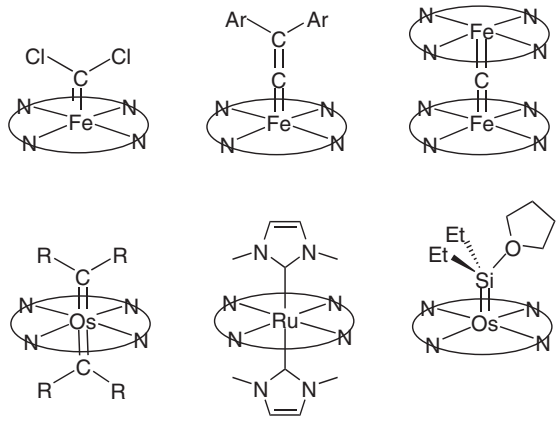

Figure 4.48 Prototypical metalloporphyrin carbenoid complexes.

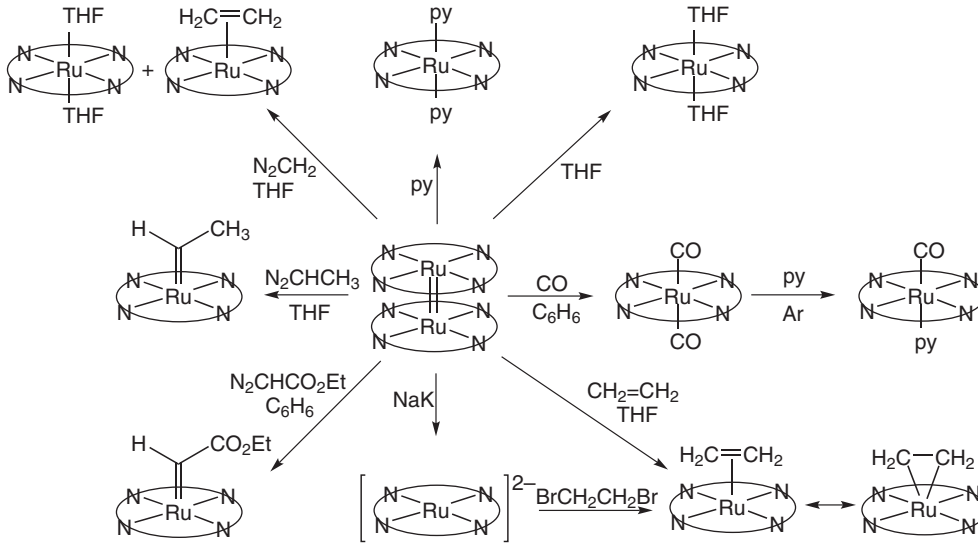

Scheme 4.15 Reactivity and cleavage of Ru porphyrin dimers. Source: Figure adapted from Collman et al. [252].

useful sources of the carbene fragment through reaction with suitable Ru(II) or Os(II) precursors, $[M(Por)]_2$, Ru(Por)(CO)L, or the sterically encumbered Ru(TMP), giving products such as M(Por) = CAr_2, M(Por) = $C(H)CO_2Et$, M(Por) = $C(Me)CO_2Et$, and M(Por) = $C(CO_2Et)_2$. Reduction of the dimers $[M(Por)]_2$ afforded the formally zero-valent dianions $[M(Por)]^{2-}$, which in turn reacted with germinal dihalides X_2CRR' as an alternative route to carbene complexes (Scheme 4.15), for example Ru(Por) = $C(H)CH_3$, Ru(Por) = $C(H)SiMe_3$, and Ru(Por) = $C{=}CAr_2$. In the case of osmium, the use of Cl_2SiR_2 (R = Me, Et, iPr) allowed the preparation of the base-stabilized silylenes Os(Por)(=SiR_2·L). The vinylidene complex Ru(Por) = $C{=}CAr_2$ could also be prepared by insertion of $Ru_3(CO)_{12}$ into a modified porphyrin N-($CCAr_2$)-N containing the vinylidene moiety bridged between two adjacent pyrrole nitrogens as the N-$C(CAr_2)$-N motif. Most of the carbene complexes are six-coordinate with a neutral donor ligand coordinated *trans* to the carbene ligand, which can even be a second carbene. When Os(Por) = CAr_2 (Por = TTP, TPFPP; Ar = Ph, *p*-$C_6H_4CH_3$) was treated with excess N_2CAr_2, the bis-carbene Os(TTP)(=CAr_2)$_2$ could be isolated. Treatment of Ru(Por)(CO)L with an imidazolium or benzimidazolium salt and *t*-BuOK allowed the preparation of a series of *bis*-NHC carbene complexes Ru(Por)$(NHC)_2$ [223]. The reaction of Os(Por)(CO) with N_2CPh_2 in air resulted in the μ-oxo-bridged complexes $[Os(Por)(=CPh_2)]_2(\mu\text{-}O)$ [358]. Os(TTP)(=$C(H)CO_2Et$) reacts with *para*-substituted pyridines to form ylides Os(TTP)(=$C(H)CO_2Et$·py)(py). The diazo precursor route has also been shown to work for iron porphyrins containing F_{20}TPP, with Fe(F_{20}-TPP) reacting with N_2CPh_2 $N_2C(Ph)(CO_2R)$ to give the corresponding carbenes [358].

The ruthenium and osmium carbenes M(Por)(=CR_2)L are diamagnetic but very air sensitive, with the exception of the ruthenium NHC carbene complexes, which are air stable. NMR and UV–visible spectroscopic data and structural data are comprehensively tabulated in a review along with a commentary on the electronic and structural effects of the porphyrin and carbene substituents. The ruthenium porphyrin carbene complexes have Ru=C distances of 1.806–1.877 Å and R–C–R′ angles 108–117°, with the shorter Ru=C distances

on five-coordinate complexes associated with electron-withdrawing carbene or porphyrin substituents [358].

The ruthenium and osmium porphyrin carbenes have become most notable for their ability to catalyze cycloproanation of alkenes by diazoesters, and carbene C-H insertion (Scheme 4.16). This area is quite mature and has been well reviewed, and only a brief summary is given here [219, 222, 358–361].

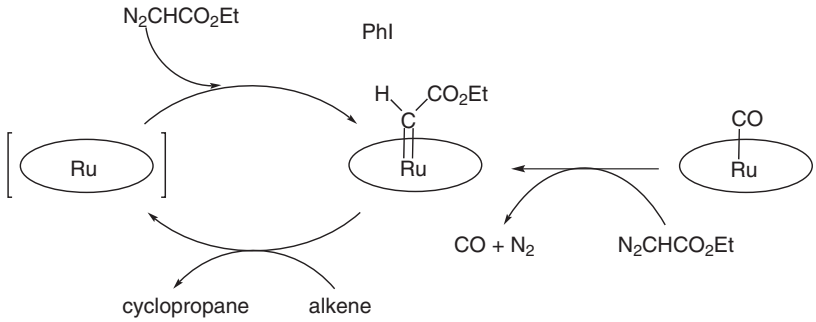

Scheme 4.16 Proposed catalytic cycle for ruthenium porphyrin-catalyzed cyclopropanation of alkenes with ethyl diazoacetate. Source: Diagram adapted from Che and Huang [219].

A useful timeline describes the landmarks in this reactivity, from the first observation of intermolecular coupling of a diazo compound in 1993 through cyclopropanations; C-H, N-H, O-H, and S-H bond insertions; inter- and intramolecular reactivity; asymmetric cyclopropanation and insertions; ylide formation in combination with [2,3]-sigmatropic rearrangements or 1,3-dipolar cycloadditions; and extension to aqueous media [222]. Activity was first observed as stoichiometric reactions of Os(Por) = CR_2 and Ru(Por) = CR_2 with styrenes to form cyclopropanes in which the yields and stereochemistry of the organic products depended on the features of the porphyrin in M(Por) = CR_2 are R groups in the carbenes. Os(TPFPP)(=CPh_2)$_2$ was then noted to react with unfunctionalized alkenes such as cyclohexene to yield C-H insertion products. The cyclopropanation reactions, which almost all featured N_2CHCO_2Et as the carbene source, were then extended to catalytic systems, in which the pre-catalysts included Os(Por)(CO)(py), [Os(Por)]$_2$, Os(Por)(=CHR), Ru(Por)(CO)L, Ru(TMP)O_2, and Ru(Por)(=CR_2) but with ruthenium or osmium porphyrin carbene complexes proposed to be the active intermediates in the catalytic cycles and high *trans* selectivity in intermolecular cyclopropanations. The use of porphyrin ligands with chiral *meso*-substituents extended the chemistry to catalytic asymmetric reactions. Overall, the metalloporphyrin-catalyzed saturated C–H bond functionalization reactions feature high regio-, diastereo-, or enantioselectivity and in some cases high product turnover numbers [362]. A recent development is the use of the Ru(Por)(NHC)$_2$ complexes that display unprecedentedly high catalytic activity toward alkene cyclopropanation, carbene X-H insertion (X = C, N, S, O), alkene aziridination, and nitrene C-H insertion with turnover frequencies up to 1950 min^{-1}. The strong σ-donor strength of the *trans* NHC ligand leads to a lower activation barrier for the decomposition of the diazo and aryl azide precursors [223]. Finally, the chemistry has also been extended to iron, demonstrating alkene cyclopropanation by an iron F_{20}-TPP carbene complex without photolysis as well as reactions with cyclohexene, THF, and cumene to give C-H insertion products [358, 360].

The Group 8 porphyrin carbene reactivity has many parallels with the reactivity of corresponding oxo M(Por) = O and imido (nitrene) M(Por) = NR complexes that are variously active for hydroxylation, epoxidation, amination, and aziridination reactions (Scheme 4.17). The mechanistic details and factors influencing the reactivity deriving from the porphyrin ligand, metal, and axial ligand on this related suite of transformations has been examined [222, 362].

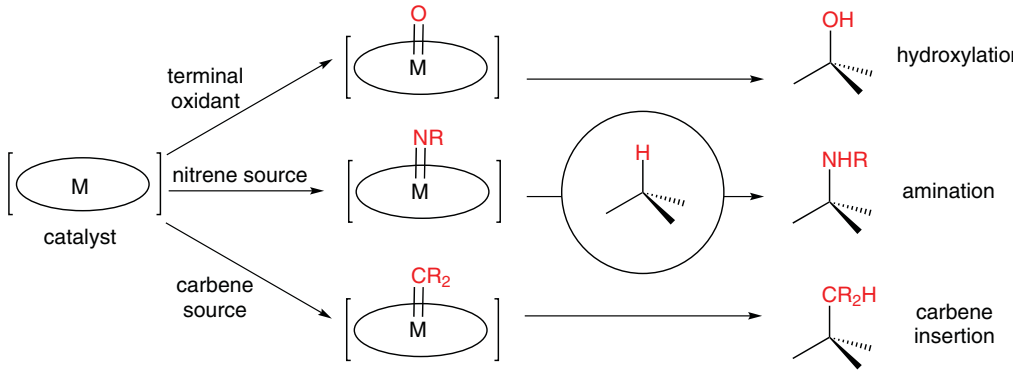

Scheme 4.17 Parallels between hydroxylation, amination, and carbene insertion catalyzed by metalloporphyrins. Source: Scheme adapted from Che et al. [362].

Metal carbene chemistry is less well established for the Group 9 elements cobalt, rhodium, and iridium than for their group 8 counterparts. No cobalt porphyrin carbenes are known, but a $C(H)(SiMe_3)$ or $C(CO_2Et)_2$ carbenoid fragment is observed to bridge the metal and one pyrrole nitrogen in cobalt(III) complexes. This is also observed for nickel. Although $Fe^{II}(Por)=CR_2$ and $Co^{II}(Por)=CR_2$ complexes are formally isoelectronic, they have different formulations, the former being a true metal carbene and the latter a Co,N bridged structure. One-electron oxidation of $Fe^{II}(Por)=C=CAr_2$ causes the vinylidene to bridge C and N.

Rh(Por)I catalyzes the reaction between ethyl diazoacetate and alkenes to give cyclopropanes with *cis*-selective stereochemistry in contrast to the *trans*-selective reactions catalyzed by ruthenium and osmium porphyrins. Rh(Por)I also catalyzes carbene insertion into the O-H bonds of alcohols, again using N_2CHCO_2Et as the carbene source. Rhodium porphyrin carbene species are implicated as reaction intermediates, but there are few examples of isolated and characterized carbenes. The cationic isocyanide complex $[Rh(Por)(CNR)]^+$ reacts with MeOH to give $Rh(TPP)(=C(NHR)_2)(CNR)$ ($R = CH_2Ph$).

Using ethyl diazoacetate as the carbene source, iron and rhodium corroles such as Fe(TPFC)Cl and $Rh(TPFC)(PPh_3)$ are effective catalysts for cyclopropanation of alkenes, although for iron the formation of carbene dimerization products is a competing reaction. The corrole-catalyzed reactions were more effective than those catalyzed by analogous porphyrins. Rhodium and iron corroles also catalyze carbene insertion into C-H and N-H bonds, respectively, and iron corroles are excellent catalysts for aziridination of alkenes using PhI=NTs as the nitrene source [36, 144].

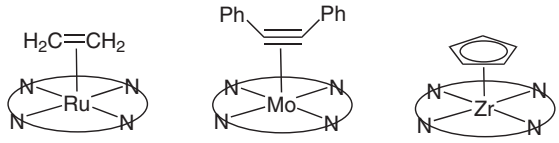

Figure 4.49 Examples of metalloporphyrin π-complexes.

4.7.2.2 π-Complexes

Some prototypical examples of metalloporphyrin π-complexes (type B in Figure 4.46) are shown in Figure 4.49. Molecular structures of some have already been shown – see Section 4.5.1, Figures 4.24 and 4.26 for Sc(OEP)(η^5-Cp), Ti(OEP)(η^2-PhC≡CPh) and Zr(OEP)(η^5-1,2-$C_2B_9H_{11}$), and Section 4.7.2.1, Scheme 4.15 for Ru(Por)(η^2-$CH_2=CH_2$). A small number of η^2-alkyne complexes have been reported for Groups 4 and 6, with a variety of routes leading to Ti(Por)(η^2-RC≡CR) (R = Ph, Me, Et). Reduction of Ti(Por)Cl_2 or TiPorCl by $LiAlH_4$ or $NaBEt_3H$, respectively, in the presence of RC≡CR or the direct reaction of Ti(Por)$(THF)_2$ with RC≡CR all giving the same product. Ready displacement of the alkyne ligand means that Ti(Por)(η^2-RC≡CR) essentially serves as a source of the "Ti(Por)" fragment, which reacts with a variety of reagents to produce many other titanium porphyrin complexes. A similar reductive route was used to prepare alkyne complexes Zr(OEP)(η^2-PhC≡CPh), Mo(Por)(η^2-PhC≡CPh), and W(Por)(η^2-PhC≡CPh) from the M(Por)Cl_2 precursor with Mg (Zr) or $LiAlH_4$ (Mo, W) as the reductant. The η^2-RC≡CR coordinates on one face of the complexes, as illustrated in the molecular structure of Ti(OEP)(η^2-PhC≡CPh).

As described above, one route to ruthenium or osmium porphyrin dialkyl complexes M(Por)R_2 is the reaction of the dianions $[M(Por)]^{2-}$ with alkyl halides, RX. When 1,2-dibromoethane was used, the resulting product could be formulated either as the M(IV) metallacyclopropane or as the M(II) ethene complex M(Por)($CH_2=CH_2$) (Scheme 4.15). The reaction of the Ru(II) dimer $[Ru(Por)]_2$ with CH_2CH_2 gave the same product, Ru(Por)(η^2-$CH_2=CH_2$). The ethane protons appear at −4 ppm in the ^{1}H NMR spectrum, an upfield shift or 9 ppm relative to free ethane. Even more complexity arises from the reactions of $[Ru(Por)]^{2-}$ with CH_2Cl_2 or $[Ru(Por)]_2$ with N_2CH_2 in THF. Both were anticipated to give the methylidene product Ru(Por) = CH_2, which was not observed, but gave instead a 1:1 mixture of Ru(Por)($CH_2=CH_2$) and Ru(Por)$(THF)_2$ through bimolecular coupling of a Ru(Por) = CH_2 intermediate (Scheme 4.15).

The weakly coordinating dinitrogen ligands in the sterically encumbered Ru(TMP)$(N_2)_2$ monomers can be displaced by ethene, cyclohexene, PhC≡CH, and PhC≡CPh, with upfield shifts observed in the ^{1}H NMR spectra as evidence of coordination. ON the other hand, photolysis is required for the reaction of ethyne, HC≡CH, with Ru(TMP)$(N_2)_2$, and a downfield shift for the ethynyl proton indicated a carbenoid product identified as the bridging bis-carbene (TMP)Ru = CH-CH = Ru(TMP). This contrasts with the reaction of the rhodium(II) dimer $[Rh(OEP)]_2$ with ethyne, which gives instead a bridging alkenyl complex, (OEP)Rh-CH=CH-Rh(OEP).

The four nitrogen donors of the porphyrin ligand mean that for later transition metal complexes the electron count of the metal is close to saturated. Not surprisingly, then,

the small number of higher-hapticity organo-ligands occur for the Group 3 and 4 metals with examples Sc(Por)(η^5-Cp′) (Cp′ = Cp, Cp*, C_5H_4Me, η^5-indenyl), Zr^{III}(TPP)(η^5-Cp), Zr(OEP)(η^8-cyclooctatetraene), and Zr(OEP)(η^5-1,2-$C_2B_9H_{11}$). An example of a corrole complex is provided by Zr^{IV}(Cor)(η^5-Cp) [118].

4.7.3 Metallation of Core-Modified Carbaporphyrinoids

A further category of organometallic porphyrin complexes are those in which the porphyrin core itself is modified to contain at least one carbon in place of nitrogen (type D in Figure 4.46). Metallation of these carbaporphyrinoids necessarily involves formation of an M-C bond, and the resulting complexes may have unusual oxidation states, spin states, and geometries resulting from the combination of the properties of the porphyrinoid ligand and organometallic fragment, for example organometallic high-spin nickel(II) or copper(II) derivatives [77]. Again, this is an extensive area of chemistry that has already been considered in Section 4.2.7 in which a core pyrrole group has been replaced by unsaturated organic rings such as benzene, cycloheptatriene, indene, or azulene to give other modified macrocycles known trivially as benziporphyrins, tropiporphyrins, carbaporphyrins, or azuliporphyrins [64–66, 69, 363, 364]. Many of these systems retain their conjugated aromatic structures, and act as organometallic ligands through C-H activation to form a range of late transition metal complexes [67–71, 365]. N-confused porphyrins (Section 4.2.5) also present a carbon atom within the porphyrin core, and metallation of these produces organometallic compounds. A selection of transition metal, main group, and lanthanide complexes of N-confused porphyrins are known [47, 50–52]. As examples, metal complexes of benzocarbaporphyrin are shown in Scheme 4.18, and additional examples of rhenium N-confused porphyrin can be found in Section 4.5.2,

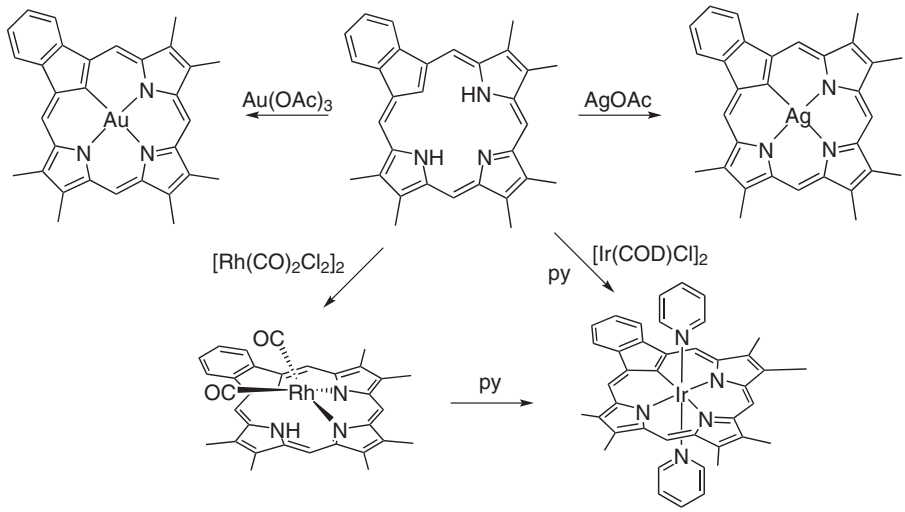

Scheme 4.18 Metallation of benzocarbaporphyrin. Source: Adapted from Lash [64].

Scheme 4.8. C-metallated examples of nickel, palladium, platinum, and gold in N-confused porphyrin, benziporphyrin, azuliporphyrin, and hexaphyrin are shown in Section 4.5.3, Figure 4.30.

4.7.4 Peripheral Metallation of Porphyrins

Compounds in which the organometallic M-C bond does not involve the centrally coordinated metal, but rather a metal bonded through carbon to the macrocycle periphery, form an important class of organometallic porphyrins. Important functions of this class are (i) their utility in functionalization of the porphyrin periphery, for example, Li, Si, Pd, B, and so on; (ii) appending groups that have important electrochemical or electronic functions in their own right, for example, ferrocenyl; and (iii) as building blocks or linkers for porphyrin arrays. Each of these topics is worthy of a chapter of its own, and only a brief overview is given here.

Peripherally metallated porphyrins comprise types E and F from Figure 4.46. The chemistry is covered in a selection of useful reviews, some of which focus on peripherally metallated porphyrins in their own right [343, 366, 367], whereas others describe organometallic reactions for porphyrin functionalization, generally via C-C coupling reactions, some of which involve peripherally metallated porphyrins in the reaction pathways [368–374]. Synthons for palladium-catalyzed cross-coupling reactions are a good example of this latter application of peripherally metallated porphyrins.

Metallation at the periphery through M-C σ-bonds can occur directly at the porphyrin β- or *meso*-positions, or through a linker, and many examples of each type are known for a range of transitional metal and main group elements. Not surprisingly, those which are best documented are those that are significant in functionalization chemistry and coupling reactions – for example boron, silicon, palladium, and mercury. The porphyrin may also serve as an π-ligand through the porphyrin core, for example when a pyrrole ring serves as an η^5-ligand, or through the periphery, for example *meso*-C_5H_5 substituents appending metallocenes, or a *meso*-C_6H_5 ring as an η^6-arene ligand.

The synthesis of peripherally metallated porphyrins can be very broadly grouped into three categories, each of which will have particular requirements in terms of reaction conditions [366]. A preformed organometallic complex can be attached to the porphyrin periphery, most likely by a metal-mediated coupling reaction. This route may require that both substrates be stable under basic conditions. The most common route for the synthesis of the porphyrin core is acid-catalyzed condensation of pyrrole or polypyrroles with aldehydes. The use of an organometallic building block bearing an aldehyde group can be employed, so long as the building block is resistant toward Lewis or Brønsted acids. Finally, a porphyrin can be modified by attaching a ligand to the periphery designed to coordinate a second metal, in which case the order of metallation in the porphyrin N_4 site versus the peripheral site needs to be considered carefully.

A selection of examples of complexes exhibiting different peripheral metallation types, chosen simply because they are either classic or very aesthetically pleasing, are shown in Figure 4.50. References can be found in the reviews [343, 366, 367].

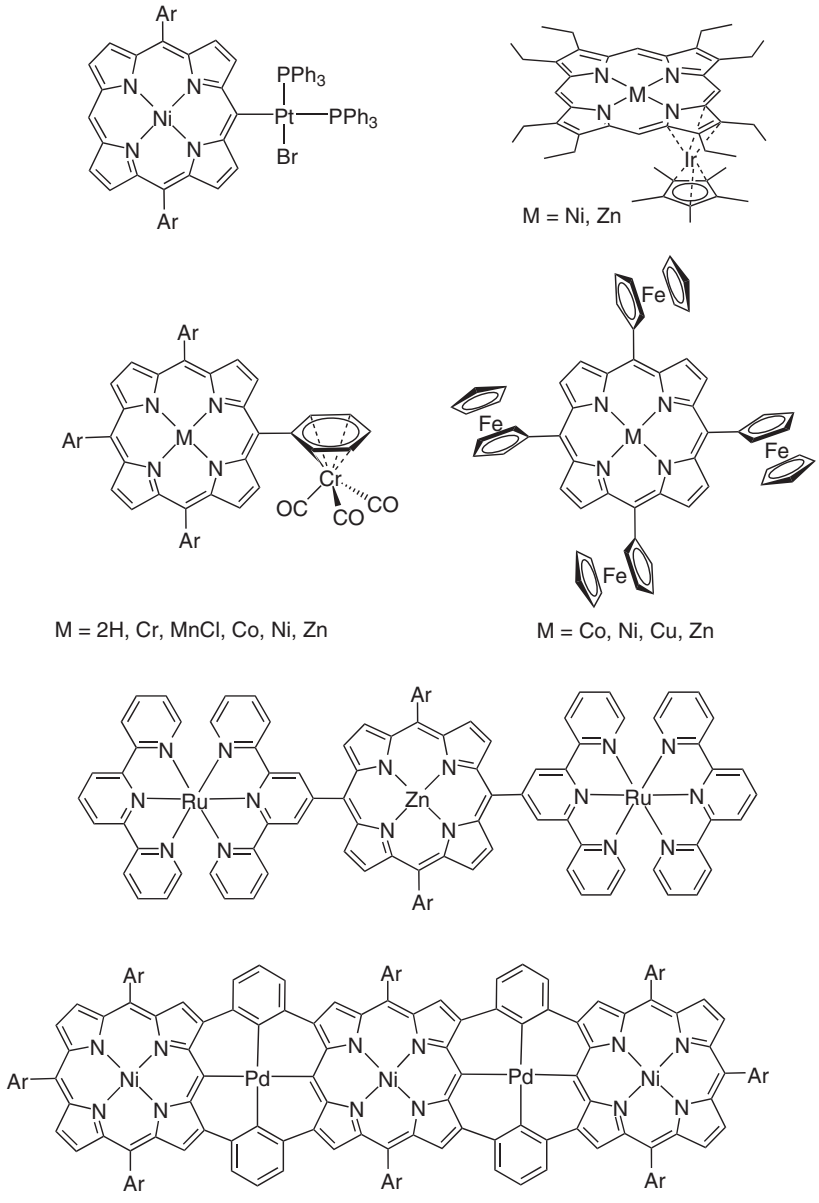

Figure 4.50 Examples of peripherally metallated porphyrin complexes [343, 366, 367].

Acknowledgments

Thanks to Dr. Nina Novikova and Dr. Aaron Chin-Yit Tay for assistance with the preparation of diagrams.

References

1 Grubisha, D.S., Guzei, I.A., Al-Salim, N. et al. (2001). Novel coordination in the first tellurium porphyrin complex: synthesis and crystal structure of [Te(ttp)Cl_2]. *Angewandte Chemie, International Edition* 40: 4743–4745.

2 Ghosh, A. and Steene, E. (2001). High-valent transition metal centers and noninnocent ligands in metalloporphyrins and related molecules: a broad overview based on quantum chemical calculations. *Journal of Biological Inorganic Chemistry* 6: 739–752.

3 Sanders, J.K.M., Bampos, N., Clyde-Watson, Z. et al. (2000). Axial coordination chemistry of metalloporphyrins. In: *The Porphyrin Handbook*, vol. 3 (ed. K.M. Kadish, K.M. Smith and R. Guilard), 1–40. Academic Press, Ch. 15.

4 Brothers, P.J. (2000). Organometallic chemistry of transition metal porphyrin complexes. *Advances in Organometallic Chemistry* 46: 223–321.

5 Brothers, P.J. (2001). Organoelement chemistry of main-group porphyrin complexes. *Advances in Organometallic Chemistry* 48: 289–342.

6 McKeown, N.B. (2003). The synthesis of symmetrical phthalocyanines. In: *The Porphyrin Handbook*, vol. 15 (ed. K.M. Kadish, K.M. Smith and R. Guilard), 61–124. Amsterdam, Ch. 98: Academic Press.

7 McKeown, N.B. (2004). Product Class 9: Phthalocyanines and Related Compounds. In: *Science of Synthesis*, vol. 17, 1237–1368. Georg Thieme Verlag, Ch. pp.

8 Sakamoto, K. and Ohno-Okumura, E. (2009). Syntheses and functional properties of phthalocyanines. *Materials* 2: 1127–1179.

9 de la Torre, G., Claessens, C.G., and Torres, T. (2007). Phthalocyanines: old dyes, new materials. Putting color in nanotechnology. *Chemical Communications* 2000–2015.

10 Carvalho, C.M.B., Brocksom, T.J., and Thiago de Oliveira, K. (2013). Tetrabenzoporphyrins: synthetic developments and applications. *Chemical Society Reviews* 42: 3302–3317.

11 Fuchter, M.J., Zhong, C., Zong, H. et al. (2008). Porphyrazines: designer macrocycles by peripheral substituent change. *Australian Journal of Chemistry* 61: 235–255.

12 Rodriguez-Morgade, M.S. and Stuzhin, P.A. (2004). The chemistry of porphyrazines: an overview. *Journal of Porphyrins and Phthalocyanines* 8: 1129–1165.

13 Michel, S.L.J., Hoffman, B.M., Baum, S.M., and Barrett, A.G.M. (2001). Peripherally functionalized porphyrazines: novel metallomacrocycles with broad, untapped potential. *Progress in Inorganic Chemistry* 50: 473–590.

14 Mack, J. (2017). Expanded, contracted, and isomeric porphyrins: theoretical aspects. *Chemical Reviews* 117: 3444–3478.

15 Franck, B. and Nonn, A. (1995). Novel porphyrinoids for chemistry and medicine by biomimetic syntheses. *Angewandte Chemie (International Ed. in English)* 34: 1795–1811.

16 Saito, S. and Osuka, A. (2011). Expanded porphyrins: intriguing structures, electronic properties, and reactivities. *Angewandte Chemie, International Edition* 50: 4342–4373.

17 Brothers, P.J. (2008). Boron complexes of porphyrins and related polypyrrole ligands: unexpected chemistry for both boron and the porphyrin. *Chemical Communications* 2090–2102.

18 Brothers, P.J. (2011). Boron complexes of pyrrolyl ligands. *Inorganic Chemistry* 50: 12374–12386.

19 Medina, A. and Claessens, C.G. (2009). Subphthalocyanines:: synthesis, self-organization, properties and applications. *Journal of Porphyrins and Phthalocyanines* 13: 446–454.

20 Claessens, C.G., Gonzalez-Rodriguez, D., Rodriguez-Morgade, M.S. et al. (2014). Subphthalocyanines, subporphyrazines, and subporphyrins: singular nonplanar aromatic systems. *Chemical Reviews* 114: 2192–2277.

21 Shimizu, S. and Kobayashi, N. (2014). Structurally-modified subphthalocyanines: molecular design towards realization of expected properties from the electronic structure and structural features of subphthalocyanine. *Chemical Communications* 50: 6949–6966.

22 Inokuma, Y. and Osuka, A. (2008). Subporphyrins: emerging contracted porphyrins with aromatic 14π-electronic systems and bowl-shaped structures: rational and unexpected synthetic routes. *Dalton Transactions* 2517–2526.

23 Shimizu, S. (2017). Recent advances in subporphyrins and triphyrin analogues: contracted porphyrins comprising three pyrrole rings. *Chemical Reviews* 117: 2730–2784.

24 Torres, T. (2006). From subphthalocyanines to subporphyrins. *Angewandte Chemie, International Edition* 45: 2834–2837.

25 Osuka, A., Tsurumaki, E., and Tanaka, T. (2011). Subporphyrins: a legitimate ring-contracted porphyrin with versatile electronic and optical properties. *Bulletin of the Chemical Society of Japan* 84: 679–697.

26 Gross, Z., Galili, N., and Saltsman, I. (1999). The first direct synthesis of corroles from pyrrole. *Angewandte Chemie, International Edition* 38: 1427–1429.

27 Paolesse, R., Mini, S., Sagone, F. et al. (1999). 5,10,15-Triphenylcorrole: a product from a modified Rothemund reaction. *Chemical Communications* 1307–1308.

28 Gryko, D.T. (2002). Recent advances in the synthesis of corroles and core-modified corroles. *European Journal of Organic Chemistry* 2002: 1735–1743.

29 Ghosh, A. (2004). A perspective of one-pot pyrrole-aldehyde condensations as versatile self-assembly processes. *Angewandte Chemie, International Edition* 43: 1918–1931.

30 Koszarna, B. and Gryko, D.T. (2006). Efficient synthesis of *meso*-substituted corroles in a H_2O–MeOH mixture. *The Journal of Organic Chemistry* 71: 3707–3717.

31 Gryko, D.T. (2008). Adventures in the synthesis of meso-substituted corroles. *Journal of Porphyrins and Phthalocyanines* 12: 906–917.

32 Buckley, H.L., Chomitz, W.A., Koszarna, B. et al. (2012). Synthesis of lithium corrole and its use as a reagent for the preparation of cyclopentadienyl zirconium and titanium corrole complexes. *Chemical Communications* 48: 10766–10768.

33 Palmer, J.H. (2012). Transition metal corrole coordination chemistry. A review focusing on electronic structural studies. *Structure and Bonding* 142: 49–90.

34 Thomas, K.E., Alemayehu, A.B., Conradie, J. et al. (2012). The structural chemistry of metallocorroles: combined X-ray crystallography and quantum chemistry studies afford unique insights. *Accounts of Chemical Research* 45: 1203–1214.

35 Ghosh, A. (2017). Electronic structure of corrole derivatives: insights from molecular structures, spectroscopy, electrochemistry, and quantum chemical calculations. *Chemical Reviews* 117: 3798–3881.

36 Aviv-Harel, I. and Gross, Z. (2009). Aura of corroles. *Chemistry - A European Journal* 15: 8382–8394.

37 McGown, A.J., Badiei, Y.M., Leeladee, P. et al. (2011). Synthesis and reactivity of high-valent transition metal corroles and corrolazines. In: *Handbook of Porphyrin Science*, vol. 14 (ed. K.M. Kadish, K.M. Smith and R. Guilard), 525–599. World Scientific Publishing Co. Pte. Ltd., Ch. 66.

38 Goldberg, D.P. (2007). Corrolazines: new frontiers in high-valent metalloporphyrinoid stability and reactivity. *Accounts of Chemical Research* 40: 626–634.

39 Kerber, W.D. and Goldberg, D.P. (2006). High-valent transition metal corrolazines. *Journal of Inorganic Biochemistry* 100: 838–857.

40 Sessler, J.L., Gebauer, A., and Vogel, E. (2000). Porphyrin isomers. In: *The Porphyrin Handbook*, vol. 2 (ed. K.M. Kadish, K.M. Smith and R. Guilard), 1–54. Amsterdam, Ch. 8: Academic Press.

41 Roznyatovskiy, V.V., Lee, C.-H., and Sessler, J.L. (2013). π-Extended isomeric and expanded porphyrins. *Chemical Society Reviews* 42: 1921–1933.

42 Sanchez-Garcia, D. and Sessler, J.L. (2008). Porphycenes: synthesis and derivatives. *Chemical Society Reviews* 37: 215–232.

43 Anguera, G. and Sanchez-Garcia, D. (2017). Porphycenes and related isomers: synthetic aspects. *Chemical Reviews* 117: 2481–2516.

44 Waluk, J. (2017). Spectroscopy and tautomerization studies of porphycenes. *Chemical Reviews* 117: 2447–2480.

45 Fowler, C.J., Sessler, J.L., Lynch, V.M. et al. (2002). Metal complexes of porphycene, corrphycene, and hemiporphycene: stability and coordination chemistry. *Chemistry - A European Journal* 8: 3485–3496.

46 Furuta, H., Maeda, H., and Osuka, A. (2002). Confusion, inversion, and creation-a new spring from porphyrin chemistry. *Chemical Communications* 1795–1804.

47 Srinivasan, A. and Furuta, H. (2005). Confusion approach to porphyrinoid chemistry. *Accounts of Chemical Research* 38: 10–20.

48 Maeda, H. and Furuta, H. (2006). A dozen years of N-confusion: from synthesis to supramolecular chemistry. *Pure and Applied Chemistry* 78: 29–44.

49 Stepien, M. and Latos-Grazynski, L. (2009). Aromaticity and tautomerism in porphyrins and porphyrinoids. *Topics in Heterocyclic Chemistry* 19: 83–153.

50 Harvey, J.D. and Ziegler, C.J. (2003). Developments in the metal chemistry of N-confused porphyrin. *Coordination Chemistry Reviews* 247: 1–19.

51 Harvey, J.D. and Ziegler, C.J. (2006). The metal complexes of N-confused porphyrin as heme model compounds. *Journal of Inorganic Biochemistry* 100: 869–880.

52 Toganoh, M. and Furuta, H. (2012). Blooming of confused porphyrinoids - fusion, expansion, contraction, and more confusion. *Chemical Communications* 48: 937–954.

53 Sessler, J.L. and Seidel, D. (2003). Synthetic expanded porphyrin chemistry. *Angewandte Chemie, International Edition* 42: 5134–5175.

54 Misra, R. and Chandrashekar, T.K. (2008). Structural diversity in expanded porphyrins. *Accounts of Chemical Research* 41: 265–279.

55 Szyszko, B., Bialek, M.J., Pacholska-Dudziak, E., and Latos-Grazynski, L. (2017). Flexible porphyrinoids. *Chemical Reviews* 117: 2839–2909.

56 Tanaka, T. and Osuka, A. (2017). Chemistry of *meso*-aryl-substituted expanded porphyrins: aromaticity and molecular twist. *Chemical Reviews* 117: 2584–2640.

57 Moebius, K., Savitsky, A., Lubitz, W., and Plato, M. (2016). Mobius-huckel topology switching in expanded porphyrins: EPR, ENDOR, and DFT studies of doublet and triplet open-shell systems. *Applied Magnetic Resonance* 47: 757–780.

58 Pawlicki, M. and Latos-Grazynski, L. (2015). Aromaticity switching in porphyrinoids. *Chemistry - An Asian Journal* 10: 1438–1451.

59 Higashino, T. and Osuka, A. (2013). Boron and phosphorus complexes of meso-aryl expanded porphyrins. *Heterocycles* 87: 31–54.

60 Chatterjee, T., Srinivasan, A., Ravikanth, M., and Chandrashekar, T.K. (2017). Smaragdyrins and sapphyrins analogues. *Chemical Reviews* 117: 3329–3376.

61 Shimizu, S. and Osuka, A. (2006). Metalation chemistry of meso-aryl-substituted expanded porphyrins. *European Journal of Inorganic Chemistry* 1319–1335.

62 Sessler, J.L. and Tomat, E. (2007). Transition-metal complexes of expanded porphyrins. *Accounts of Chemical Research* 40: 371–379.

63 Sessler, J.L., Vivian, A.E., Seidel, D. et al. (2001). Actinide expanded porphyrin complexes. *Coordination Chemistry Reviews* 216-217: 411–434.

64 Lash, T.D. (2017). Carbaporphyrinoid systems. *Chemical Reviews* 117: 2313–2446.

65 Lash, T.D. (2016). Out of the blue! Azuliporphyrins and related carbaporphyrinoid systems. *Accounts of Chemical Research* 49: 471–482.

66 Stepien, M. and Latos-Grazynski, L. (2005). Benziporphyrins: exploring arene chemistry in a macrocyclic environment. *Accounts of Chemical Research* 38: 88–98.

67 Lash, T.D. (2014). Metal complexes of carbaporphyrinoid systems. *Chemistry – An Asian Journal* 9: 682–705.

68 Pawlicki, M. and Latos-Grazynski, L. (2010). Carbaporphyrinoids. Synthesis and coordination properties. In: *Handbook of Porphyrin Science*, vol. 2 (ed. K.M. Kadish, K.M. Smith and R. Guilard), 103–192. World Scientific Publishing Co. Pte. Ltd., Ch. 8.

69 Ziegler, C.J. (2009). Studies into the metal chemistry of the carbaporphyrinoids: insights into the biological choice of porphyrin. *ACS Symposium Series* 1012: 115–131.

70 Chatterjee, T., Shetti, V.S., Sharma, R., and Ravikanth, M. (2017). Heteroatom-containing porphyrin analogues. *Chemical Reviews* 117: 3254–3328.

71 Szyszko, B. and Latos-Grazynski, L. (2015). Core chemistry and skeletal rearrangements of porphyrinoids and metalloporphyrinoids. *Chemical Society Reviews* 44: 3588–3616.

72 Pareek, Y. and Ravikanth, M. (2014). Thiaporphyrins: from building blocks to multiporphyrin arrays. *RSC Advances* 4: 7851–7880.

73 Yedukondalu, M. and Ravikanth, M. (2011). Core-modified porphyrin based assemblies. *Coordination Chemistry Reviews* 255: 547–573.

74 Matano, Y., Nakabuchi, T., and Imahori, H. (2010). Synthesis, structures, and aromaticity of phosphole-containing porphyrins and their metal complexes. *Pure and Applied Chemistry* 82: 583–593.

75 Matano, Y. and Imahori, H. (2009). Phosphole-containing calixpyrroles, calixphyrins, and porphyrins: synthesis and coordination chemistry. *Accounts of Chemical Research* 42: 1193–1204.

76 Gupta, I. and Ravikanth, M. (2006). Recent developments in heteroporphyrins and their analogues. *Coordination Chemistry Reviews* 250: 468–518.

77 Chmielewski, P.J. and Latos-Grazynski, L. (2005). Core modified porphyrins - a macrocyclic platform for organometallic chemistry. *Coordination Chemistry Reviews* 249: 2510–2533.

78 Latos-Grazynski, L. (2000). Core-modified heteroanalogues of porphyrins and metalloporphyrins. In: *The Porphyrin Handbook*, vol. 2 (ed. K.M. Kadish, K.M. Smith and R. Guilard), 361–416. Amsterdam, Ch. 14: Academic Press.

79 Adler, A.D., Longo, F.R., Kampas, F., and Kim, J. (1970). On the preparation of metalloporphyrins. *Journal of Inorganic and Nuclear Chemistry* 32: 2443–2445.

80 Arnold, J. (1990). The first structurally characterized alkali metal porphyrin: lithium-7 NMR behavior and X-ray crystal structure of the dilithium salt of octaethylporphyrin(2-). *Journal of the Chemical Society, Chemical Communications* 976–978.

81 Arnold, J., Dawson, D.Y., and Hoffman, C.G. (1993). Synthesis and characterization of lithium, sodium, and potassium porphyrin complexes. X-ray crystal structures of $Li_2(C_6H_{12}O_2)_2$TMPP, $Na_2(THF)_4$OEP, and $K_2(pyridine)_4$OEP. *Journal of the American Chemical Society* 115: 2707–2713.

82 Brand, H. and Arnold, J. (1995). Recent developments in the chemistry of early transition metal porphyrin compounds. *Coordination Chemistry Reviews* 140: 137–168.

83 Lemon, C.M., Brothers, P.J., and Boitrel, B. (2011). Porphyrin complexes of the period 6 main group and late transition metals. *Dalton Transactions* 40: 6591–6609.

84 Le Gac, S. and Boitrel, B. (2012). The overhanging carboxylic acid strategy: an alternative route to the porphyrin core expansion/modification for the coordination of large metal ions. *Journal of Porphyrins and Phthalocyanines* 16: 537–544.

85 Lavallee, D.K. (1985). Kinetics and mechanisms of metalloporphyrin reactions. *Coordination Chemistry Reviews* 61: 55–96.

86 Funahashi, S., Inada, Y., and Inamo, M. (2001). Dynamic study of metal-ion incorporation into porphyrins based on the dynamic characterization of metal ions and on sitting-atop complex formation. *Analytical Sciences* 17: 917–927.

87 Shen, Y. and Ryde, U. (2005). Reaction mechanism of porphyrin metallation studied by theoretical methods. *Chemistry - A European Journal* 11: 1549–1564.

88 Tabata, M. (1995). Kinetic evidence for short-lived intermediates in metalloporphyrin formation. *Journal of Molecular Liquids* 65/66: 221–228.

89 Berezin, B.D., Zvezdina, S.V., and Berezin, M.B. (2013). Double metal-ligand exchange in solvate complex-metal porphyrin systems. *Russian Journal of General Chemistry* 83: 1410–1418.

90 Le Gac, S. and Boitrel, B. (2016). Compartmentalized vs. non-compartmentalized translocations in metal porphyrin complexes. *New Journal of Chemistry* 40: 5650–5655.

91 Le Gac, S. and Boitrel, B. (2016). Structurally characterized bimetallic porphyrin complexes of Pb, Bi, Hg and Tl based on unusual coordination modes. *Journal of Porphyrins and Phthalocyanines* 20: 117–133.

92 Le Gac, S., Fusaro, L., Roisnel, T., and Boitrel, B. (2014). Heterobimetallic porphyrin complexes displaying triple dynamics: coupled metal motions controlled by constitutional evolution. *Journal of the American Chemical Society* 136: 6698–6715.

93 Diller, K., Papageorgiou, A.C., Klappenberger, F. et al. (2016). In vacuo interfacial tetrapyrrole metallation. *Chemical Society Reviews* 45: 1629–1656.

94 Tabata, M. and Nishimoto, J. (2000). Equilibrium data of porphyrins and metalloporphyrins. In: *The Porphyrin Handbook*, vol. 9 (ed. K.M. Kadish, K.M. Smith and R. Guilard), 221–419. Amsterdam, Ch. 60: Academic Press.

95 Gouterman, M., Wagniere, G., and Snyder, L.C. (1963). Spectra of porphyrins. II. Four-orbital model. *Journal of Molecular Spectroscopy* 11: 108–127.

96 Gouterman, M. (1978). Optical spectra and electronic structure of porphyrins and related rings. In: *The Porphyrins. Part A*, vol. III (ed. D. Dolphin), 1–165. London: Academic.

97 Bommer, J.C. and Hambright, P. (2002). General laboratory methods for tetrapyrroles. In: *Heme, Chlorophyll, and Bilins - Methods and Protocols* (ed. A.G. Smith and M. Witty), 39–67. Totowa, New Jersey: Humana Press.

98 Barbour, T., Belcher, W.J., Brothers, P.J. et al. (1992). Preparation of group 15 (phosphorus, antimony, and bismuth) complexes of *meso*-tetra-p-tolylporphyrin (TTP) andX-ray crystal structure of $[Sb(TTP)(OCH(CH_3)_2)_2]Cl$. *Inorganic Chemistry* 31: 746–754.

99 Kane, K.M., Lemke, F.R., and Petersen, J.L. (1997). *trans*-Difluorosilicon(IV) complexes of tetra-*p*-tolylporphyrin and tetrakis(*p*-(trifluoromethyl)phenyl)porphyrin: crystal structures and unprecedented reactivity in hexacoordinate difluorosilanes. *Inorganic Chemistry* 36: 1354.

100 Arnold, D.P. and Tiekink, E.R.T. (1995). Tin(IV) porphyrin complexes—VII. Crystal structures of meso-tetraphenylporphyrinatotin(IV) difluoride and dinitrate, and the correlation of spectroscopic data with core size for tin(IV) porphyrin complexes. *Polyhedron* 14: 1785.

101 Barkigia, K.M., Fajer, J., Adler, A.D., and Williams, G.J.B. (1980). Crystal and molecular structure of (5,10,15,20-tetra-N-propylporphinato)lead(II): a "roof" porphyrin. *Inorganic Chemistry* 19: 2057.

102 Guo, J.L., Sun, F., and Li, Y. (1995). Molecular and crystal structure of dichloro (5,10,15,20-tetraphenylporphinato)phosphorus(V) chloride dichloromethane solvate. *Polyhedron* 14: 1471.

103 Soury, R., Belkhiria, M.S., Giorgi, M., and Nasri, H. (2014). Dichlorido(5,10,15,20-tetraphenylporphyrinato-κ^4N)antimony(V) hexachloridoantimonate(V). *Acta Crystallographica Section E: Structure Reports Online* 70: m256.

104 Boitrel, B., Breede, M., Brothers, P.J. et al. (2003). Bismuth porphyrin complexes: syntheses and structural studies. *Dalton Transactions* 1803.

105 Brand, H., Capriotti, J.A., and Arnold, J. (1994). New lithium porphyrin derivatives: synthesis of $Li_2(P)(Et_2O)_2$ (P = TTP, TBPP) and solution structure of $Li_2(TTP)(Et_2O)_2$ by ^7Li and ^{15}N NMR. *Inorganic Chemistry* 33: 4334–4337.

106 Dawson, D.Y. and Arnold, J. (1997). Ionic versus covalent bonding in dilithium porphyrins: x-ray structure of dilithium tetraphenylporphyrin bis(etherate). *Journal of Porphyrins and Phthalocyanines* 1: 121–124.

107 Arnold, J. (2000). Alkali metal porphyrins. In: *The Porphyrin Handbook*, vol. 3 (ed. K.M. Kadish, K.M. Smith and R. Guilard), 113–127. Amsterdam, Ch. 17: Academic Press.

108 Gebauer, A., Dawson, D.Y., and Arnold, J. (2000). Neutral π-radicals of lithium porphyrins: synthesis and characterization. *Dalton Transactions* 111–112.

109 Gebauer, A., Schmidt, J.A.R., and Arnold, J. (2000). Synthesis, characterization, and properties of a lithium 21-thiaporphyrin complex. *Inorganic Chemistry* 39: 3424–3427.

110 Arnold, J. and Hoffman, C.G. (1990). A novel synthetic route to scandium porphyrin derivatives and the first structurally characterized metalloporphyrin-η^5-cyclopentadienyl sandwich compound. *Journal of the American Chemical Society* 112: 8620–8621.

111 Brand, H. and Arnold, J. (1992). Early transition metal porphyrins. Synthesis and reactivity of some novel zirconium derivatives and the X-ray crystal structure of the first metalloporphyrin cis-dialkyl: $(OEP)Zr(CH_2SiMe_3)_2$. *Journal of the American Chemical Society* 114: 2266–2267.

112 Brand, H. and Arnold, J. (1993). Early transition metal porphyrins: synthesis, characterization, and reactivity of novel out-of-plane cis-ligated zirconium porphyrin derivatives. *Organometallics* 12: 3655–3665.

113 Brand, H., Capriotti, J.A., and Arnold, J. (1994). New early transition metal porphyrins: a new route to diorgano complexes of zirconium and hafnium and the preparation of cationic derivatives. *Organometallics* 13: 4469–4473.

114 Dawson, D.Y., Brand, H., and Arnold, J. (1994). Tantalum porphyrin chemistry. Synthesis and reactivity of organometallic derivatives and the X-ray crystal structure of the sandwich compound $[Ta(OEP)_2][TaCl_6]$. *Journal of the American Chemical Society* 116: 9797–9798.

115 Buckley, H.L., Anstey, M.R., Gryko, D.T., and Arnold, J. (2013). Lanthanide corroles: a new class of macrocyclic lanthanide complexes. *Chemical Communications* 49: 3104–3106.

116 Ward, A.L., Buckley, H.L., Lukens, W.W., and Arnold, J. (2013). Synthesis and characterization of thorium(IV) and uranium(IV) corrole complexes. *Journal of the American Chemical Society* 135: 13965–13971.

117 Padilla, R., Buckley, H.L., Ward, A.L., and Arnold, J. (2014). Synthesis, structure and reactivity of group 4 corrole complexes. *Chemical Communications* 50: 2922–2924.

118 Buckley, H.L. and Arnold, J. (2015). Recent developments in out-of-plane metallocorrole chemistry across the periodic table. *Dalton Transactions* 44: 30–36.

119 Padilla, R., Buckley, H.L., Ward, A.L., and Arnold, J. (2015). Preparation and characterization of a tungsten(V) corrole dichloride complex. *Journal of Porphyrins and Phthalocyanines* 19: 150–153.

120 Kubiak, R., Waśkowska, A., Śledź, M., and Jezierski, A. (2006). Synthesis, X-ray structures and characterization of beryllium phthalocyanine and (2-ethoxyethanol)-aqua-beryllium phthalocyanine. *Inorganica Chimica Acta* 359: 1344–1350.

121 Kannangara, C.G. and von Wettstein, D. (2010). Magnesium chelatase. *Advances in Photosynthesis and Respiration* 31: 79–88.

122 Bonomo, L., Lehaire, M.-L., Solari, E. et al. (2001). The first crystalline calcium porphyrin and tetrakis(tert-butylphenyl)porphyrinato calcium(II): its synthesis, structure, and binding properties towards alkali and alkaline earth metal salts. *Angewandte Chemie, International Edition* 40: 771–774.

123 Mlodzianowska, A., Latos-Grazynski, L., Szterenberg, L., and Stepien, M. (2007). Single-boron complexes of N-confused and N-fused porphyrins. *Inorganic Chemistry* 46: 6950–6957.

124 Wood, T.E. and Thompson, A. (2007). Advances in the chemistry of dipyrrins and their complexes. *Chemical Reviews* 107: 1831–1861.

125 Loudet, A. and Burgess, K. (2010). BODIPY dyes and their derivatives: syntheses and spectroscopic properties. In: *Handbook of Porphyrin Science*, vol. 8 (ed. K.M. Kadish, K.M. Smith and R. Guilard), 1–164. World Scientific Publishing Co. Pte. Ltd.

126 Boens, N., Leen, V., and Dehaen, W. (2012). Fluorescent indicators based on BODIPY. *Chemical Society Reviews* 41: 1130–1172.

127 Belcher, W.J., Boyd, P.D.W., Brothers, P.J. et al. (1994). New coordination mode for the porphyrin ligand in the boron porphyrin complex $B_2OF_2(TTP)$. *Journal of the American Chemical Society* 116: 8416–8417.

128 Belcher, W.J., Breede, M., Brothers, P.J., and Rickard, C.E.F. (1998). A porphyrin as a binucleating ligand: preparation and crystal structure of a porphyrin complex

containing a coordinated B_2O_2 ring. *Angewandte Chemie (International Ed. in English)* 37: 1112–1114.

129 Koehler, T., Hodgson, M.C., Seidel, D. et al. (2004). Octaethylporphyrin and expanded porphyrin complexes containing coordinated BF2 groups. *Chemical Communications* 1060–1061.

130 Albrett, A.M., Conradie, J., Boyd, P.D.W. et al. (2008). Corrole as a binucleating ligand: preparation, molecular structure and density functional theory study of diboron corroles. *Journal of the American Chemical Society* 130: 2888–2889.

131 Belcher, W.J., Hodgson, M.C., Sumida, K. et al. (2008). Porphyrin complexes containing coordinated BOB groups: synthesis, chemical reactivity and the structure of [BOB(tpClpp)]2+. *Dalton Transactions* 1602–1614.

132 Albrett, A.M., Thomas, K.E., Maslek, S. et al. (2014). Mono- and diboron corroles: factors controlling stoichiometry and hydrolytic reactivity. *Inorganic Chemistry* 53: 5486–5493.

133 Albrett, A.M., Conradie, J., Ghosh, A., and Brothers, P.J. (2008). DFT survey of monoboron and diboron corroles: regio- and stereochemical preferences for a constrained, low-symmetry macrocycle. *Dalton Transactions* 4464–4473.

134 Weiss, A., Pritzkow, H., Brothers, P.J., and Siebert, W. (2001). Coordinated B_2 bridges in porphyrins - unexpected formation of a diborane(4)- from a diborylporphyrin. *Angewandte Chemie, International Edition* 40: 4182–4184.

135 Weiss, A., Hodgson, M.C., Boyd, P.D.W. et al. (2007). Diboryl and diboranyl porphyrin complexes: synthesis, structural motifs, and redox chemistry: diborenyl porphyrin or diboranyl isophlorin? *Chemistry - A European Jouranl* 13: 5982–5993.

136 Albrett, A.M., Boyd, P.D.W., Clark, G.R. et al. (2010). Reductive coupling and protonation leading to diboron corroles with a B-H-B bridge. *Dalton Transactions* 39: 4032–4034.

137 Moriya, K., Saito, S., and Osuka, A. (2010). Boron(III) induced skeletal rearrangement of hexaphyrin(1.1.1.1.1.1) to hexaphyrin(2.1.1.0.1.1). *Angewandte Chemie, International Edition* 49: 4297–4300.

138 Boffa, L.S. (2000). The organometallic polymerization of (meth)acrylates: an overview. *ACS Symposium Series* 760: 1–21.

139 Ikpo, N., Flogeras, J.C., and Kerton, F.M. (2013). Aluminium coordination complexes in copolymerization reactions of carbon dioxide and epoxides. *Dalton Transactions* 42: 8998–9006.

140 Sheng, X., Wu, W., Qin, Y. et al. (2015). Efficient synthesis and stabilization of poly(propylene carbonate) from delicately designed bifunctional aluminum porphyrin complexes. *Polymer Chemistry* 6: 4719–4724.

141 Bendix, J., Dmochowski, I.J., Gray, H.B. et al. (2000). Structural, electrochemical, and photophysical properties of gallium(III) 5,10,15-tris(pentafluorophenyl)corrole. *Angewandte Chemie, International Edition* 39: 4048–4051.

142 Weaver, J.J., Sorasaenee, K., Sheikh, M. et al. (2004). Gallium(III) corroles. *Journal of Porphyrins and Phthalocyanines* 8: 76–81.

143 Sorasaenee, K., Taqavi, P., Henling, L.M. et al. (2007). Amphiphilic aluminum(III) and gallium(III) corroles. *Journal of Porphyrins and Phthalocyanines* 11: 189–197.

144 Aviv, I. and Gross, Z. (2007). Corrole-based applications. *Chemical Communications* 1987–1999.

145 Agadjanian, H., Ma, J., Rentsendorj, A. et al. (2009). Tumor detection and elimination by a targeted gallium corrole. *Proceedings of the National Academy of Sciences of the United States of America* 106: 6105–6110.

146 Aviv-Harel, I. and Gross, Z. (2011). Coordination chemistry of corroles with focus on main group elements. *Coordination Chemistry Reviews* 255: 717–736.

147 Arnold, D.P. and Blok, J. (2004). The coordination chemistry of tin porphyrin complexes. *Coordination Chemistry Reviews* 248: 299–319.

148 Shetti, V.S., Pareek, Y., and Ravikanth, M. (2012). Sn(IV) porphyrin scaffold for multiporphyrin arrays. *Coordination Chemistry Reviews* 256: 2816–2842.

149 Cissell, J.A., Vaid, T.P., and Yap, G.P.A. (2007). Reversible oxidation state change in germanium(tetraphenylporphyrin) induced by a dative ligand: aromatic GeII(TPP) and antiaromatic GeIV(TPP)(pyridine)$_2$. *Journal of the American Chemical Society* 129: 7841–7847.

150 Cissell, J.A., Vaid, T.P., DiPasquale, A.G., and Rheingold, A.L. (2007). Germanium phthalocyanine, GePc, and the reduced complexes SiPc(pyridine)$_2$ and GePc(pyridine)$_2$ containing antiaromatic π-electron circuits. *Inorganic Chemistry* 46: 7713–7715.

151 Song, H.-E., Cissell, J.A., Vaid, T.P., and Holten, D. (2007). Photophysics of reduced silicon tetraphenylporphyrin. *The Journal of Physical Chemistry B* 111: 2138–2142.

152 Vaid, T.P. (2011). A porphyrin with a C=C unit at its center. *Journal of the American Chemical Society* 133: 15838–15841.

153 Sung, Y.M., Vasiliu, M., Dixon, D.A. et al. (2013). Electronic structure and photophysics of (C=C)tetra-p-tolylporphyrin^{2+}. *Photochemical & Photobiological Sciences* 12: 1774–1779.

154 Cammidge, A.N., Nekelson, F., Hughes, D.L. et al. (2010). Stepwise syntheses of complex μ-oxo-linked heterochromophore arrays containing phthalocyanine, porphyrin and subphthalocyanine ligands. *Journal of Porphyrins and Phthalocyanines* 14: 1001–1011.

155 Pomarico, G., Monti, D., Bischetti, M. et al. (2018). Silicon (IV) corroles. *Chemistry - A European Jouranl* http://dx.doi.org/10.1002/chem.201801246.

156 Ueta, K., Fukuda, M., Kim, G. et al. (2018). The first silicon(IV) corrole complexes: synthesis, structures, properties, and formation of a μ-oxo dimer. *Chemistry - A European Jouranl* 24: 7637–7646.

157 Yamamoto, Y. and Akiba, K.-Y. (2000). The chemistry of group 15 element porphyrins bearing element-carbon bonds: synthesis and properties. *Journal of Organometallic Chemistry* 611: 200–209.

158 Brothers, P.J. (2002). Recent developments in the coordination chemistry of porphyrin complexes containing non-metallic and semi-metallic elements. *Journal of Porphyrins and Phthalocyanines* 6: 259–267.

159 Shiragami, T., Matsumoto, J., Inoue, H., and Yasuda, M. (2005). Antimony porphyrin complexes as visible-light driven photocatalyst. *Journal of Photochemistry and Photobiology, C: Photochemistry Reviews* 6: 227–248.

160 Vestfrid, J., Kothari, R., Kostenko, A. et al. (2016). Intriguing physical and chemical properties of phosphorus corroles. *Inorganic Chemistry* 55: 6061–6067.

161 Luobeznova, I., Raizman, M., Goldberg, I., and Gross, Z. (2006). Synthesis and full characterization of molybdenum and antimony corroles and utilization of the latter complexes as very efficient catalysts for highly selective aerobic oxygenation reactions. *Inorganic Chemistry* 45: 386–394.

162 Matsumoto, J., Shiragami, T., Hirakawa, K., and Yasuda, M. (2015). Water-solubilization of P(V) and Sb(V) porphyrins and their photobiological application. *International Journal of Photoenergy* 148964. https://doi.org/10.1155/2015/148964.

163 Młodzianowska, A., Latos-Grażyński, L., and Szterenberg, L. (2008). Phosphorus complexes of N-fused porphyrin and its reduced derivatives: new isomers of porphyrin stabilized via coordination. *Inorganic Chemistry* 47: 6364–6374.

164 Li, J., Subramanian, L.R., and Hanack, M. (1998). Studies on phosphorus phthalocyanines and triazatetrabenzcorroles. *European Journal of Organic Chemistry* 1998: 2759–2767.

165 Gryko, D.T., Fox, J.P., and Goldberg, D.P. (2004). Recent advances in the chemistry of corroles and core-modified corroles. *Journal of Porphyrins and Phthalocyanines* 8: 1091–1105.

166 Orlowski, R., Gryko, D., and Gryko, D.T. (2017). Synthesis of corroles and their heteroanalogs. *Chemical Reviews* 117: 3102–3137.

167 Neu, H.M., Baglia, R.A., and Goldberg, D.P. (2015). A balancing act: stability versus reactivity of Mn(O) complexes. *Accounts of Chemical Research* 48: 2754–2764.

168 Chen, K.-T., Yang, F.-A., Chen, J.-H. et al. (2008). A novel bismercury(II) complex of bidentate N^{21},N^{22}-bridged porphyrin. *Polyhedron* 27: 2216.

169 Suen, S.-C., Lee, W.-B., Hong, F.-E. et al. (1992). (Acetato-O,O')-*meso*-tetraphenylporphyrinato-thallium(III). *Polyhedron* 11: 3025.

170 Boitrel, B., Halime, Z., Michaudet, L. et al. (2003). Structural characterisation of the first mononuclear bismuth porphyrin. *Chemical Communications* 2670–2671.

171 Reith, L.M., Stiftinger, M., Monkowius, U. et al. (2011). Synthesis and characterization of a stable bismuth(III) A_3–corrole. *Inorganic Chemistry* 50: 6788–6797.

172 Boitrel, B. (2011). Bismuth complexes of porphyrins and their potential in medical applications. In: *Biological Chemistry of Arsenic, Antimony and Bismuth* (ed. H. Sun), 209–240. Chichester, Ch. 9: Wiley.

173 Halime, Z., Lachkar, M., and Boitrel, B. (2009). Coordination of bismuth and lead in porphyrins: towards an in-situ generator for α-radiotherapy? *Biochimie* 91: 1318–1320.

174 Schaverien, C.J. (1991). Octaethylporphyrin-yttrium-methyl chemistry: preparation and selective activation of dioxygen by (oep)Y(μ-Me)2AlMe2. *Journal of the Chemical Society, Chemical Communications* 458–460.

175 Schaverien, C.J. and Orpen, A.G. (1991). Chemistry of (octaethylporphyrinato)lutetium and -yttrium complexes: synthesis and reactivity of (OEP)MX derivatives and the selective activation of O_2 by (OEP)Y(μ-Me)$_2$AlMe$_2$. *Inorganic Chemistry* 30: 4968–4978.

176 Woo, L.K., Hays, J.A., Jacobson, R.A., and Day, C.L. (1991). Low-valent titanium porphyrin complexes. Synthesis and structural characterization of the first titanium(II) porphyrin complex, (η^{2-}diphenylacetylene)titanium octaethylporphyrin. *Organometallics* 10: 2102.

177 Ratti, C., Richard, P., Tabard, A., and Guilard, R. (1989). Synthesis and characterization of a new series of titanium(IV) porphyrins co-ordinated to a disulphur or a diselenium ligand. *Journal of the Chemical Society, Chemical Communications* 69.

178 Ryu, S., Whang, D., Kim, H.-J. et al. (1997). Novel disulfido- and diselenido-bridged zirconium and hafnium porphyrin dimers with unusual coordination geometries: [M(TPP)]$_2$(μ-η^2-Q$_2$)$_2$ (M = Zr, Hf; Q = S, Se). *Inorganic Chemistry* 36: 4607.

179 Arnold, J., Johnson, S.E., Knobler, C.B., and Hawthorne, M.F. (1992). A metalloporphyrin-carborane sandwich compound: synthesis and x-ray crystal

structure of (OEP)Zr(η^5-1,2-$C_2B_9H_{11}$). *Journal of the American Chemical Society* 114: 3996–3997.

180 Ryu, S., Whang, D., Kim, J. et al. (1993). Synthesis, characterization and crystal structures of novel hafnium porphyrins. *Journal of the Chemical Society, Dalton Transactions* 205.

181 Lesage, S., Xu, H., and Durham, L. (1993). The occurrence and roles of porphyrins in the environment: possible implications for bioremediation. *Hydrological Sciences Journal* 38: 343–354.

182 Dechaine, G.P. and Gray, M.R. (2010). Chemistry and association of vanadium compounds in heavy oil and bitumen, and implications for their selective removal. *Energy & Fuels* 24: 2795–2808.

183 Schulz, C.E., Song, H., Lee, Y.J. et al. (1994). Metalloporphyrin π-cation radicals. Molecular structure and spin coupling in a vanadyl octaethylporphyrinate derivative. An unexpected spin coupling path. *Journal of the American Chemical Society* 116: 7196–7203.

184 Łapok, Ł., Lener, M., Tsaryova, O. et al. (2011). Structures and redox characteristics of electron-deficient vanadyl phthalocyanines. *Inorganic Chemistry* 50: 4086–4091.

185 Dong, S., Tian, H., Huang, L. et al. (2011). Non-peripheral tetrahexyl-substituted vanadyl phthalocyanines with intermolecular cofacial π–π stacking for solution-processed organic field-effect transistors. *Advanced Materials* 23: 2850–2854.

186 Berreau, L.M., Hays, J.A., Young, V.G., and Woo, L.K. (1994). Synthesis of early transition metal porphyrin halide complexes: first structural characterization of a vanadium(III) porphyrin complex. *Inorganic Chemistry* 33: 105–108.

187 Ziegler, J.A., Buckley, H.L., and Arnold, J. (2017). Synthesis and reactivity of tantalum corrole complexes. *Dalton Transactions* 46: 780–785.

188 Buchler, J.W., Dreher, C., and Kuenzel, F.M. (1995). Synthesis and coordination chemistry of noble metal porphyrins. *Structure and Bonding* 84: 1–69.

189 Johansen, I., Norheim, H.-K., Larsen, S. et al. (2011). Substituent effects on metallocorrole spectra: insights from chromium-oxo and molybdenum-oxo triarylcorroles. *Journal of Porphyrins and Phthalocyanines* 15: 1335–1344.

190 Alemayehu, A.B., Vazquez-Lima, H., Gagnon, K.J., and Ghosh, A. (2016). Tungsten biscorroles: new chiral sandwich compounds. *Chemistry - A European Jouranl* 22: 6914–6920.

191 Alemayehu, A.B., Vazquez-Lima, H., McCormick, L.J., and Ghosh, A. (2017). Relativistic effects in metallocorroles: comparison of molybdenum and tungsten biscorroles. *Chemical Communications* 53: 5830.

192 Schweyen, P., Brandhorst, K., Hoffmann, M. et al. (2017). Viking helmet corroles: activating inert oxidometal corroles. *Chemistry - A European Journal* 23: 13897.

193 Schies, C., Alemayehu, A.B., Vazquez-Lima, H. et al. (2017). Metallocorroles as inherently chiral chromophores: resolution and electronic circular dichroism spectroscopy of a tungsten biscorrole. *Chemical Communications* 53: 6121–6124.

194 Meunier, B. (1992). Metalloporphyrins as versatile catalysts for oxidation reactions and oxidative DNA cleavage. *Chemical Reviews* 92: 1411–1456.

195 Liu, W., Huang, X., Cheng, M.-J. et al. (2012). Oxidative aliphatic C-H fluorination with fluoride ion catalyzed by a manganese porphyrin. *Science* 337: 1322–1325.

196 Liu, W. and Groves, J.T. (2015). Manganese catalyzed C–H halogenation. *Accounts of Chemical Research* 48: 1727–1735.

197 Liu, W., Huang, X., and Groves, J.T. (2013). Oxidative aliphatic C-H fluorination with manganese catalysts and fluoride ion. *Nature Protocols* 8: 2348.

198 Groves, J.T., Kruper, W.J., and Haushalter, R.C. (1980). Hydrocarbon oxidations with oxometalloporphinates. Isolation and reactions of a (porphinato)manganese(V) complex. *Journal of the American Chemical Society* 102: 6375–6377.

199 Huang, X. and Groves, J.T. (2018). Oxygen activation and radical transformations in heme proteins and metalloporphyrins. *Chemical Reviews* 118: 2491–2553.

200 Arasasingham, R.D., He, G.X., and Bruice, T.C. (1993). Mechanism of manganese porphyrin-catalyzed oxidation of alkenes. Role of manganese(IV)-oxo species. *Journal of the American Chemical Society* 115: 7985–7991.

201 Song, W.J., Seo, M.S., DeBeer George, S. et al. (2007). Synthesis, characterization, and reactivities of manganese(V)−oxo porphyrin complexes. *Journal of the American Chemical Society* 129: 1268–1277.

202 Mandimutsira, B.S., Ramdhanie, B., Todd, R.C. et al. (2002). A stable manganese(V)-oxo corrolazine complex. *Journal of the American Chemical Society* 124: 15170–15171.

203 Groves, J.T., Takahashi, T., and Butler, W.M. (1983). Synthesis and molecular structure of a nitrido(porphyrinato)chromium(V) complex. *Inorganic Chemistry* 22: 884–887.

204 Bottomley, L.A. and Neely, F.L. (1989). The nitrogen atom transfer reactivity of nitrido-manganese(V) porphyrins with chromium(III) porphyrins. *Journal of the American Chemical Society* 111: 5955–5957.

205 Abu-Omar, M.M. (2011). High-valent iron and manganese complexes of corrole and porphyrin in atom transfer and dioxygen evolving catalysis. *Dalton Transactions* 40: 3435–3444.

206 Tsutsui, M., Hrung, C.P., Ostfeld, D. et al. (1975). Unusual metalloporphyrins. XXIII. Unusual metalloporphyrin complexes of rhenium and technetium. *Journal of the American Chemical Society* 97: 3952.

207 Takenaka, A., Sasada, Y., Ogoshi, H. et al. (1975). The crystal and molecular structure of μ-1,2,3,4,5,6,7,8-octaethylporphinatobis[dicarbonylrhodium(I)]. *Acta Crystallographica. Section B: Structural Science* 31: 1.

208 Tatsumi, K. and Hoffmann, R. (1981). Metalloporphyrins with unusual geometries. 2. Slipped and skewed bimetallic structures, carbene and oxo complexes, and insertions into metal-porphyrin bonds. *Inorganic Chemistry* 20: 3771–3784.

209 Kin Tse, M., Zhang, Z., and Shing Chan, K. (1998). Synthesis of an oxorhenium(V) corrolate from porphyrin with detrifluoromethylation and ring contraction. *Chemical Communications* 1199–1200.

210 Einrem, R.F., Gagnon, K., Alemayehu, A.B., and Ghosh, A. (2015). Metal–ligand misfits: facile access to rhenium–oxo corroles by oxidative metalation. *Chemistry - A European Jouranl* 22: 517–520.

211 Einrem, R.F., Braband, H., Fox, T. et al. (2016). Synthesis and molecular structure of ^{99}Tc corroles. *Chemistry - A European Jouranl* 22: 18747–18751.

212 Toganoh, M., Ishizuka, T., and Furuta, H. (2004). Synthesis and properties of rhenium tricarbonyl complex bearing N-fused tetraphenylporphyrin ligand. *Chemical Communications* 2464–2465.

213 Yamamoto, T., Toganoh, M., Mori, S. et al. (2012). Rhenium complexes of peripherally π-extended N-confused porphyrins. *Chemical Science* 3: 3241–3248.

214 Yamamoto, T., Toganoh, M., and Furuta, H. (2012). Cooperation between metal and ligand in oxygen atom transport by N-confused porphyrin oxorhenium(V) complexes. *Dalton Transactions* 41: 9154–9157.

215 Groves, J.T. (2006). High-valent iron in chemical and biological oxidations. *Journal of Inorganic Biochemistry* 100: 434–447.

216 Römelt, C., Song, J., Tarrago, M. et al. (2017). Electronic structure of a formal iron(0) porphyrin complex relevant to CO_2 reduction. *Inorganic Chemistry* 56: 4745–4750.

217 Collman, J.P. and Arnold, H.J. (1993). Multiple metal-metal bonds in 4*d* and 5*d* metal-porphyrin dimers. *Accounts of Chemical Research* 26: 586–592.

218 Che, C.-M. and Yu, W.-Y. (1999). Ruthenium-oxo and -tosylimido porphyrin complexes for epoxidation and aziridination of alkenes. *Pure and Applied Chemistry* 71: 281–288.

219 Che, C.-M. and Huang, J.-S. (2002). Ruthenium and osmium porphyrin carbene complexes: synthesis, structure, and connection to the metal-mediated cyclopropanation of alkenes. *Coordination Chemistry Reviews* 231: 151–164.

220 Che, C.-M., Huang, J.-S., and Zhang, J.-L. (2003). Dendritic metalloporphyrins as catalysts for organic transformations. *Comptes Rendus de l' Academie des Sciences Serie IIc:Chemie* 6: 1105–1115.

221 Che, C.-M. and Huang, J.-S. (2009). Metalloporphyrin-based oxidation systems: from biomimetic reactions to application in organic synthesis. *Chemical Communications* 3996–4015.

222 Zhou, C.-Y., Huang, J.-S., and Che, C.-M. (2010). Ruthenium-porphyrin-catalyzed carbenoid transfer reactions. *Synlett* 2681–2700.

223 Chan, K.-H., Guan, X., Lo, V.K.-Y., and Che, C.-M. (2014). Elevated catalytic activity of ruthenium(II)–porphyrin-catalyzed carbene/nitrene transfer and insertion reactions with N-heterocyclic carbene ligands. *Angewandte Chemie, International Edition* 53: 2982–2987.

224 Rose, E., Andrioletti, B., Zrig, S., and Quelquejeu-Etheve, M. (2005). Enantioselective epoxidation of olefins with chiral metalloporphyrin catalysts. *Chemical Society Reviews* 34: 573–583.

225 Simkhovich, L., Luobeznova, I., Goldberg, I., and Gross, Z. (2003). Mono- and binuclear ruthenium corroles: synthesis, spectroscopy, electrochemistry, and structural characterization. *Chemistry - A European Jouranl* 9: 201.

226 Alemayehu, A.B., Gagnon, K.J., Terner, J., and Ghosh, A. (2014). Oxidative metalation as a route to size-mismatched macrocyclic complexes: osmium corroles. *Angewandte Chemie, International Edition* 53: 14411–14414.

227 Alemayehu, A.B., Vazquez-Lima, H., Gagnon, K.J., and Ghosh, A. (2017). Stepwise deoxygenation of nitrite as a route to two families of ruthenium corroles: group 8 periodic trends and relativistic effects. *Inorganic Chemistry* 56: 5285–5294.

228 Borisov, S.M., Alemayehu, A., and Ghosh, A. (2016). Osmium-nitrido corroles as NIR indicators for oxygen sensors and triplet sensitizers for organic upconversion and singlet oxygen generation. *Journal of Materials Chemistry C* 4: 5822–5828.

229 Krautler, B. and Puffer, B. (2012). Vitamin B12-derivatives: organometallic catalysts, cofactors and ligands of bio-macromolecules. In: *Handbook of Porphyrin Science*, vol. 25 (ed. K.M. Kadish, K.M. Smith and R. Guilard), 131–263. World Scientific Publishing Co. Pte. Ltd.

230 Ragsdale, S.W. (2014). Biochemistry of methyl-coenzyme M reductase: the nickel metalloenzyme that catalyzes the final step in synthesis and the first step in anaerobic oxidation of the greenhouse gas methane. *Metal Ions in Life Sciences* 14: 125–145.

231 Anding, B.J., Ellern, A., and Woo, L.K. (2012). Olefin cyclopropanation catalyzed by iridium(III) porphyrin complexes. *Organometallics* 31: 3628–3635.

232 Palmer, J.H., Day, M.W., Wilson, A.D. et al. (2008). Iridium corroles. *Journal of the American Chemical Society* 130: 7786–7787.

233 Palmer, J.H., Mahammed, A., Lancaster, K.M. et al. (2009). Structures and reactivity patterns of group 9 metallocorroles. *Inorganic Chemistry* 48: 9308–9315.

234 Wongnate, T., Sliwa, D., Ginovska, B. et al. (2016). The radical mechanism of biological methane synthesis by methyl-coenzyme M reductase. *Science* 352: 953–958.

235 Chmielewski, P.J., Latos-Grażyński, L., Olmstead, M.M., and Balch, A.L. (1997). Nickel complexes of 21-oxaporphyrin and 21, 23-dioxaporphyrin. *Chemistry - A European Jouranl* 3: 268–278.

236 Alemayehu, A.B., Vazquez-Lima, H., Beavers, C.M. et al. (2014). Platinum corroles. *Chemical Communications* 50: 11093–11096.

237 Preiß, S., Förster, C., Otto, S. et al. (2017). Structure and reactivity of a mononuclear gold(II) complex. *Nature Chemistry* 9: 1249.

238 Renner, M.W., Barkigia, K.M., Zhang, Y. et al. (1994). Consequences of oxidation in nonplanar porphyrins: molecular structure and diamagnetism of the π cation radical of copper(II) octaethyltetraphenylporphyrin. *Journal of the American Chemical Society* 116: 8582–8592.

239 Mori, S. and Osuka, A. (2005). Aromatic and antiaromatic gold(III) hexaphyrins with multiple gold–carbon bonds. *Journal of the American Chemical Society* 127: 8030–8031.

240 Rickhaus, M., Vargas Jentzsch, A., Tejerina, L. et al. (2017). Single-acetylene linked porphyrin nanorings. *Journal of the American Chemical Society* 139: 16502–16505.

241 Gross, Z. and Galili, N. (1999). N-Substituted corroles: a novel class of chiral ligands. *Angewandte Chemie, International Edition* 38: 2366–2369.

242 Lemon, C.M., Powers, D.C., Brothers, P.J., and Nocera, D.G. (2017). Gold corroles as near-IR phosphors for oxygen sensing. *Inorganic Chemistry* 56: 10991–10997.

243 Palmer, J.H., Durrell, A.C., Gross, Z. et al. (2010). Near-IR phosphorescence of iridium(III) corroles at ambient temperature. *Journal of the American Chemical Society* 132: 9230–9231.

244 Gouterman, M. (1997). Oxygen quenching of luminescence of pressure sensitive paint for wind tunnel research. *Journal of Chemical Education* 74: 697.

245 Yutaka, A., Keisuke, A., Tokuji, M., and Ichiro, O. (1999). Novel optical oxygen pressure sensing materials: platinum porphyrin-styrene-trifluoroethylmethacrylate copolymer film. *Chemistry Letters* 28: 1031–1032.

246 Grenoble, S., Gouterman, M., Khalil, G. et al. (2005). Pressure-sensitive paint (PSP): concentration quenching of platinum and magnesium porphyrin dyes in polymeric films. *Journal of Luminescence* 113: 33–44.

247 Alemayehu, A.B., Day, N.U., Mani, T. et al. (2016). Gold tris(carboxyphenyl)corroles as multifunctional materials: room temperature near-IR phosphorescence and applications to photodynamic therapy and dye-sensitized solar cells. *ACS Applied Materials & Interfaces* 8: 18935–18942.

248 Cotton, F.A. (1965). Metal-metal bonding in $[Re_2X_8]^{2-}$ ions and other metal atom clusters. *Inorganic Chemistry* 4: 334–336.

249 Collman, J.P., Barnes, C.E., Swepston, P.N., and Ibers, J.A. (1984). Synthesis, proton NMR, and structural characterization of binuclear ruthenium porphyrin dimers. *Journal of the American Chemical Society* 106: 3500.

250 Yang, C.-H., Dzugan, S.J., and Goedken, V.L. (1986). Synthesis and structural characterization of the metalloporphyrin dimer, $[Mo(TPP)]_2$. *Journal of the Chemical Society, Chemical Communications* 1313.

251 Tait, C.D., Garner, J.M., Collman, J.P. et al. (1989). Vibrational study of multiply metal-metal bonded ruthenium porphyrin dimers. *Journal of the American Chemical Society* 111: 7806–7811.

252 Collman, J.P., Brothers, P.J., McElwee-White, L. et al. (1985). Cleavage of ruthenium and osmium porphyrin dimers: formation of organometallic ruthenium porphyrin complexes and highly reduced metalloporphyrin species. *Journal of the American Chemical Society* 107: 4570–4571.

253 Jørgensen, C.K. (1966). Differences between the four halide ligands, and discussion remarks on trigonal-bipyramidal complexes, on oxidation states, and on diagonal elements of one-electron energy. *Coordination Chemistry Reviews* 1: 164–178.

254 Vangberg, T., Lie, R., and Ghosh, A. (2002). Symmetry-breaking phenomena in metalloporphyrin π-cation radicals. *Journal of the American Chemical Society* 124: 8122–8130.

255 Terner, J., Palaniappan, V., Gold, A. et al. (2006). Resonance Raman spectroscopy of oxoiron(IV) porphyrin π-cation radical and oxoiron(IV) hemes in peroxidase intermediates. *Journal of Inorganic Biochemistry* 100: 480–501.

256 Yosca, T.H., Ledray, A.P., Ngo, J., and Green, M.T. (2017). A new look at the role of thiolate ligation in cytochrome P450. *Journal of Biological Inorganic Chemistry* 22: 209–220.

257 Nakamura, M., Ohgo, Y., and Ikezaki, A. (2008). Electronic ground states of low-spin iron(III) porphyrinoids. *Journal of Inorganic Biochemistry* 102: 433–445.

258 Walker, F.A. (2010). NMR and EPR spectroscopy of paramagnetic metalloporphyrins and heme proteins. In: *Handbook of Porphyrin Science*, vol. 6 (ed. K.M. Kadish, K.M. Smith and R. Guilard), 1–337. World Scientific Publishing Co. Pte. Ltd.

259 Shao, J., Steene, E., Hoffman, B.M., and Ghosh, A. (2005). EPR, ENDOR, and DFT studies on (β-octahalo-meso-tetraarylporphyrin)copper complexes: characterization of the metal(d_x2-_y2)–porphyrin(a_{2u}) orbital interaction. *European Journal of Inorganic Chemistry* 2005: 1609–1615.

260 Ghosh, A., Wondimagegn, T., and Parusel, A.B.J. (2000). Electronic structure of gallium, copper, and nickel complexes of corrole. High-valent transition metal centers versus noninnocent ligands. *Journal of the American Chemical Society* 122: 5100–5104.

261 Alemayehu, A.B., Gonzalez, E., Hansen, L.K., and Ghosh, A. (2009). Copper corroles are inherently saddled. *Inorganic Chemistry* 48: 7794–7799.

262 Thomas, K.E., Vazquez-Lima, H., Fang, Y. et al. (2015). Ligand noninnocence in coinage metal corroles: a silver knife-edge. *Chemistry - A European Jouranl* 21: 16839–16847.

263 Alemayehu, A.B., Hansen, L.K., and Ghosh, A. (2010). Nonplanar, noninnocent, and chiral: a strongly saddled metallocorrole. *Inorganic Chemistry* 49: 7608–7610.

264 Thomas, K.E., Conradie, J., Hansen, L.K., and Ghosh, A. (2011). A mtallocorrole with orthogonal pyrrole rings. *European Journal of Inorganic Chemistry* 1865.

265 Thomas, K.E., Alemayehu, A.B., Conradie, J. et al. (2011). Synthesis and molecular structure of gold triarylcorroles. *Inorganic Chemistry* 50: 12844–12851.

266 Thomas, K.E., Beavers, C.M., and Ghosh, A. (2012). Molecular structure of a gold β-octakis(trifluoromethyl)-meso-triarylcorrole: an 85° difference in saddling dihedral relative to copper. *Molecular Physics* 110: 2439.

267 Walker, F.A., Licoccia, S., and Paolesse, R. (2006). Iron corrolates: unambiguous chloroiron(III) (corrolate)$^{2-}$ π-cation radicals. *Journal of Inorganic Biochemistry* 100: 810–837.

268 Ganguly, S., Renz, D., Giles, L.J. et al. (2017). Cobalt- and rhodium-corrole-triphenylphosphine complexes revisited: the question of a noninnocent corrole. *Inorganic Chemistry* 56: 14788–14800.

269 Ganguly, S., Conradie, J., Bendix, J. et al. (2017). Electronic structure of cobalt–corrole–pyridine complexes: noninnocent five-coordinate Co(II) corrole–radical states. *The Journal of Physical Chemistry. A* 121: 9589–9598.

270 Ganguly, S., Giles, L.J., Thomas, K.E. et al. (2017). Ligand noninnocence in iron corroles: insights from optical and X-ray absorption spectroscopies and electrochemical redox potentials. *Chemistry - A European Jouranl* 23: 15098–15106.

271 Springer, B.A., Sligar, S.G., Olson, J.S., and Phillips, G.N. Jr., (1994). Mechanisms of ligand recognition in myoglobin. *Chemical Reviews* 94: 699–714.

272 Ghosh, A. (2005). Metalloporphyrin-NO bonding: building bridges with organometallic chemistry. *Accounts of Chemical Research* 38: 943–954.

273 Ghosh, A., Hopmann, K.H., and Conradie, J. (2009). Electronic structure calculations: Transition metal – NO complexes. In: *Encyclopedia of Inorganic Chemistry* [Internet]. Wiley Available from: https://onlinelibrary.wiley.com/doi/abs/10.1002/0470862106.ia628.

274 Ghosh, A. and Bocian, D.F. (1996). Carbonyl tilting and bending potential energy surface of carbon Monoxyhemes. *The Journal of Physical Chemistry* 100: 6363–6367.

275 Boon, E.M. and Marletta, M.A. (2005). Ligand specificity of H-NOX domains: from sGC to bacterial NO sensors. *Journal of Inorganic Biochemistry* 99: 892–902.

276 Wyllie, G.R.A. and Scheidt, W.R. (2002). Solid-state structures of metalloporphyrin NO_x compounds. *Chemical Reviews* 102: 1067–1089.

277 Goodrich, L.E., Paulat, F., Praneeth, V.K.K., and Lehnert, N. (2010). Electronic structure of heme-nitrosyls and its significance for nitric oxide reactivity, sensing, transport, and toxicity in biological systems. *Inorganic Chemistry* 49: 6293–6316.

278 Enemark, J.H. and Feltham, R.D. (1974). Principles of structure, bonding, and reactivity for metal nitrosyl complexes. *Coordination Chemistry Reviews* 13: 339–406.

279 McQuarters, A.B., Kampf, J.W., Alp, E.E. et al. (2017). Ferric heme-nitrosyl complexes: kinetically robust or unstable intermediates? *Inorganic Chemistry* 56: 10513–10528.

280 Silvernail, N.J., Barabanschikov, A., Pavlik, J.W. et al. (2007). Interplay of structure and vibrational dynamics in six-coordinate heme nitrosyls. *Journal of the American Chemical Society* 129: 2200.

281 Grande, L.M., Noll, B.C., Oliver, A.G., and Scheidt, W.R. (2010). Dynamics of NO motion in solid-state [Co(tetraphenylporphinato)(NO)]. *Inorganic Chemistry* 49: 6552.

282 Richter-Addo, G.B., Wheeler, R.A., Hixson, C.A. et al. (2001). Unexpected nitrosyl-group bending in six-coordinate {M(NO)}^{6} σ-bonded aryl(iron) and -(ruthenium) porphyrins. *Journal of the American Chemical Society* 123: 6314–6326.

283 Xu, N., Powell, D.R., Cheng, L., and Richter-Addo, G.B. (2006). The first structurally characterized nitrosyl heme thiolate model complex. *Chemical Communications* 2030–2032.

284 Ellison, M.K. and Scheidt, W.R. (1997). Structural distortion in five-coordinate nitrosyl iron porphyrins. Axial ligand tilting and its effect on equatorial geometry. *Journal of the American Chemical Society* 119: 7404–7405.

285 Tangen, E., Conradie, J., and Ghosh, A. (2005). The challenge of being straight: explaining the linearity of a low-spin {FeNO}^{7} unit in a tropocoronand complex. *Inorganic Chemistry* 44: 8699–8706.

286 Conradie, J., Quarless, D.A., Hsu, H.-F. et al. (2007). Electronic structure and FeNO conformation of nonheme iron–thiolate–NO complexes: an experimental and DFT study. *Journal of the American Chemical Society* 129: 10446–10456.

287 Vogel, E., Will, S., Tilling, A.S. et al. (1994). Metallocorroles with formally tetravalent iron. *Angewandte Chemie (International Ed. in English)* 33: 731–735.

288 Joseph, C.A., Lee, M.S., Iretskii, A.V. et al. (2006). Substituent effects on nitrosyl iron corrole complexes Fe(Ar_3C)(NO). *Inorganic Chemistry* 45: 2075–2082.

289 Vazquez-Lima, H., Norheim, H.-K., Einrem, R.F., and Ghosh, A. (2015). Cryptic noninnocence: FeNO corroles in a new light. *Dalton Transactions* 44: 10146–10151.

290 Barbe, J.-M., Canard, G., Brandes, S. et al. (2004). Metallocorroles as sensing components for gas sensors: remarkable affinity and selectivity of cobalt(III) corroles for CO vs. O_2 and N_2. *Dalton Transactions* 1208–1214.

291 Barbe, J.-M., Canard, G., Brandès, S., and Guilard, R. (2005). Organic–inorganic hybrid sol–gel materials incorporating functionalized cobalt(III) corroles for the selective detection of CO. *Angewandte Chemie, International Edition* 44: 3103–3106.

292 Vazquez-Lima, H., Conradie, J., and Ghosh, A. (2016). Metallocorrole interactions with carbon monoxide, nitric oxide, and nitroxyl—a DFT study of low-energy bound states. *Inorganic Chemistry* 55: 8248–8250.

293 Ellison, M.K. and Scheidt, W.R. (1998). Tilt/asymmetry in nitrosyl metalloporphyrin complexes: the cobalt case. *Inorganic Chemistry* 37: 382–383.

294 Einsle, O., Messerschmidt, A., Huber, R. et al. (2002). Mechanism of the six-electron reduction of nitrite to ammonia by cytochrome *c* nitrite reductase. *Journal of the American Chemical Society* 124: 11737–11745.

295 Bykov, D. and Neese, F. (2015). Six-electron reduction of nitrite to ammonia by cytochrome *c* nitrite reductase: insights from density functional theory studies. *Inorganic Chemistry* 54: 9303–9316.

296 Daiber, A., Shoun, H., and Ullrich, V. (2005). Nitric oxide reductase ($P450_{nor}$) from *Fusarium oxysporum*. *Journal of Inorganic Biochemistry* 99: 185–193.

297 Krámos, B., Menyhárd, D.K., and Oláh, J. (2012). Direct hydride shift mechanism and stereoselectivity of $P450_{nor}$ confirmed by QM/MM calculations. *The Journal of Physical Chemistry B* 116: 872–885.

298 Cabail, M.Z., Kostera, J., and Pacheco, A.A. (2005). Laser photoinitiated nitrosylation of 3-electron reduced *Nm europaea* hydroxylamine oxidoreductase: kinetic and thermodynamic properties of the nitrosylated enzyme. *Inorganic Chemistry* 44: 225–231.

299 Hu, B. and Li, J. (2015). One electron makes differences: from heme {FeNO}7 to {FeNO}8. *Angewandte Chemie, International Edition* 54: 10579–10582.

300 Conradie, J. and Ghosh, A. (2016). Metalloporphyrin–nitroxyl interactions: the low-energy states of reduced manganese, iron, and cobalt porphyrin nitrosyls. *The Journal of Physical Chemistry B* 120: 4972–4979.

301 Immoos, C.E., Sulc, F., Farmer, P.J. et al. (2005). Bonding in HNO-myoglobin as characterized by X-ray absorption and resonance Raman spectroscopies. *Journal of the American Chemical Society* 127: 814–815.

302 Lorković, I. and Ford, P.C. (2000). Nitric oxide addition to the ferrous nitrosyl porphyrins Fe(P)(NO) gives *trans*-Fe(P)$(NO)_2$ in low-temperature solutions. *Journal of the American Chemical Society* 122: 6516–6517.

303 Conradie, J., Wondimagegn, T., and Ghosh, A. (2003). Molecular structure and conformation of dinitrosylheme. *Journal of the American Chemical Society* 125: 4968–4969.

304 Kekilli, D., Petersen, C.A., Pixton, D.A. et al. (2017). Engineering proximal vs. distal heme-NO coordination via dinitrosyl dynamics: implications for NO sensor design. *Chemical Science* 8: 1986–1994.

305 Yang, S., Wo, Y., and Meyerhoff, M.E. (2014). Polymeric optical sensors for selective and sensitive nitrite detection using cobalt(III) corrole and rhodium(III) porphyrin as ionophores. *Analytica Chimica Acta* 843: 89–96.

306 Nemykin, V.N. and Volkov, S.V. (2000). Mixed-ligand complexes of lanthanides with phthalocyanine and its analogues: synthesis, structure, and spectroscopic properties. *Russian Journal of Coordination Chemistry* 26: 436–450.

307 Buchler, J.W. and Ng, D.K.P. (2000). Metal tetrapyrrole double- and triple-deckers with special emphasis on porphyrin systems. In: *The Porphyrin Handbook*, vol. 3 (ed. K.M. Kadish, K.M. Smith and R. Guilard), 245–294. Amsterdam, Ch. 20: Academic Press.

308 Weiss, R. and Fischer, J. (2003). Lanthanide phthalocyanine complexes. In: *The Porphyrin Handbook*, vol. 16 (ed. K.M. Kadish, K.M. Smith and R. Guilard), 171–246. Amsterdam, Ch. 105: Academic Press.

309 Wong, W.-K., Zhu, X., and Wong, W.-Y. (2007). Synthesis, structure, reactivity and photoluminescence of lanthanide(III) monoporphyrinate complexes. *Coordination Chemistry Reviews* 251: 2386–2399.

310 Pushkarev, V.E., Tomilova, L.G., and Tomilov, Y.V. (2008). Synthetic approaches to lanthanide complexes with tetrapyrrole type ligands. *Russian Chemical Reviews* 77: 875–907.

311 Jiang, J. and Ng, D.K.P. (2009). A decade journey in the chemistry of sandwich-type tetrapyrrolato-rare earth complexes. *Accounts of Chemical Research* 42: 79–88.

312 Bian, Y., Zhang, Y., Ou, Z., and Jiang, J. (2011). Chemistry of sandwich tetrapyrrole rare earth complexes. In: *Handbook of Porphyrin Science*, vol. 14 (ed. K.M. Kadish, K.M. Smith and R. Guilard), 249–460. World Scientific Publishing Co. Pte. Ltd., Ch. 64.

313 Mironov, A.F. (2013). Lanthanide porphyrin complexes. *Russian Chemical Reviews* 82: 333–351, 319 pp.

314 He, H. (2014). Near-infrared emitting lanthanide complexes of porphyrin and BODIPY dyes. *Coordination Chemistry Reviews* 273-274: 87–99.

315 Ostendorp, G. and Homborg, H. (1995). bis(Phthalocyaninato)-lanthanum(III) dichloromethane solvate. *Zeitschrift fur Naturforschung B: Journal of Chemical Sciences* 50: 1200.

316 De Cian, A., Moussavi, M., Fischer, J., and Weiss, R. (1985). Synthesis, structure, and spectroscopic and magnetic properties of lutetium(III) phthalocyanine derivatives: $LuPc_2 \cdot CH_2Cl_2$ and $[LuPc(OAc)(H_2O)_2] \cdot H_2O \cdot {}^2CH_3OH$. *Inorganic Chemistry* 24: 3162.

317 Katoh, K., Kajiwara, T., Nakano, M. et al. (2011). Magnetic relaxation of single-molecule magnets in an external magnetic field: an ising dimer of a terbium(III)–phthalocyaninate triple-decker complex. *Chemistry - A European Jouranl* 17: 117.

318 Wang, H., Qian, K., Wang, K. et al. (2011). Sandwich-type tetrakis(phthalocyaninato) dysprosium–cadmium quadruple-decker SMM. *Chemical Communications* 47: 9624.

319 Wang, H., Wang, B.-W., Bian, Y. et al. (2016). Single-molecule magnetism of tetrapyrrole lanthanide compounds with sandwich multiple-decker structures. *Coordination Chemistry Reviews* 306: 195–216.

320 Ishikawa, N., Sugita, M., Ishikawa, T. et al. (2003). Lanthanide double-decker complexes functioning as magnets at the single-molecular level. *Journal of the American Chemical Society* 125: 8694–8695.

321 Ishikawa, N., Sugita, M., and Wernsdorfer, W. (2005). Quantum tunneling of magnetization in lanthanide single-molecule magnets: bis(phthalocyaninato)terbium and bis(phthalocyaninato)dysprosium anions. *Angewandte Chemie, International Edition* 44: 2931–2935.

322 Bulach, V., Sguerra, F., and Hosseini, M.W. (2012). Porphyrin lanthanide complexes for NIR emission. *Coordination Chemistry Reviews* 256: 1468–1478.

323 Zhu, X., Wong, W.-K., Wong, W.-Y., and Yang, X. (2011). Design and synthesis of near-infrared emissive lanthanide complexes based on macrocyclic ligands. *European Journal of Inorganic Chemistry* 2011: 4651–4674.

324 Lu, G., Yan, S., Shi, M. et al. (2015). A new class of rare earth tetrapyrrole sandwich complexes containing corrole and phthalocyanine macrocycles: synthesis, physicochemical characterization and X-ray analysis. *Chemical Communications* 51: 2411–2413.

325 Lu, G., Li, J., Yan, S. et al. (2015). Synthesis and characterization of rare earth corrole–phthalocyanine heteroleptic triple-decker complexes. *Inorganic Chemistry* 54: 5795–5805.

326 Kadish, K.M., Liu, Y.H., Anderson, J.E. et al. (1988). First example of a trimeric metalloporphyrin. Synthesis, electrochemical, and spectroelectrochemical studies of $[(P)Th(OH)_2]_3$ where P is the dianion of octaethyl- or tetraphenylporphyrin. *Journal of the American Chemical Society* 110: 6455.

327 Gorden, A.E.V., DeVore, M.A., and Maynard, B.A. (2013). Coordination chemistry with f-element complexes for an improved understanding of factors that contribute to extraction selectivity. *Inorganic Chemistry* 52: 3445–3458.

328 Jones, M.B. and Gaunt, A.J. (2013). Recent developments in synthesis and structural chemistry of nonaqueous actinide complexes. *Chemical Reviews* 113: 1137–1198.

329 Day, V.W., Marks, T.J., and Wachter, W.A. (1975). Large metal ion-centered template reactions. Uranyl complex of cyclopentakis(2-iminoisoindoline). *Journal of the American Chemical Society* 97: 4519–4527.

330 Furuyama, T., Ogura, Y., Yoza, K., and Kobayashi, N. (2012). Superazaporphyrins: meso-pentaazapentaphyrins and one of their low-symmetry derivatives. *Angewandte Chemie, International Edition* 51: 11110–11114.

331 Burrell, A.K., Hemmi, G., Lynch, V., and Sessler, J.L. (1991). Uranylpentaphyrin: an actinide complex of an expanded porphyrin. *Journal of the American Chemical Society* 113: 4690–4692.

332 Sessler, J.L., Seidel, D., Vivian, A.E. et al. (2001). Hexaphyrin(1.0.1.0.0.0): an expanded porphyrin ligand for the actinide cations uranyl (UO22+) and neptunyl (NpO2+). *Angewandte Chemie, International Edition* 40: 591–594.

333 Sessler, J.L., Gorden, A.E.V., Seidel, D. et al. (2002). Characterization of the interactions between neptunyl and plutonyl cations and expanded porphyrins. *Inorganica Chimica Acta* 341: 54–70.

334 Melfi, P.J., Kim, S.K., Lee, J.T. et al. (2007). Redox behavior of cyclo[6]pyrrole in the formation of a uranyl complex. *Inorganic Chemistry* 46: 5143–5145.

335 Ho, I.T., Zhang, Z., Ishida, M. et al. (2014). A hybrid macrocycle with a pyridine subunit displays aromatic character upon uranyl cation complexation. *Journal of the American Chemical Society* 136: 4281–4286.

336 Yang, M., Ding, W., and Wang, D. (2017). Characterization of the binding of six actinyls $AnO_2^{2+/+}$ (An = U/Np/Pu) with three expanded porphyrins by density functional theory. *New Journal of Chemistry* 41: 63–74.

337 Mansuy, D., Lange, M., Chottard, J.-C. et al. (1977). Reaction of carbon tetrachloride with 5,10,15,20-tetraphenyl-porphinatoiron(II)[(TPP)Fe]: evidence for the formation of the carbene complex [(TPP)Fe(CCl_2)]. *Journal of the Chemical Society, Chemical Communications* 648–649.

338 Mansuy, D., Lange, M., Chottard, J.C. et al. (1978). Dichlorocarbene complexes of iron(II)-porphyrins–crystal and molecular structure of Fe(TPP)(CCl_2)(H_2O). *Angewandte Chemie (International Ed. in English)* 17: 781–782.

339 Guilard, R., Lecomte, C., and Kadish, K.M. (1987). Synthesis, electrochemistry, and structural properties of porphyrins with metal-carbon single bonds and metal-metal bonds. In: *Metal Complexes with Tetrapyrrole Ligands I* (ed. J.W. Buchler), 205–268. Berlin Ch: Springer.

340 Guilard, R. and Kadish, K.M. (1988). Some aspects of organometallic chemistry in metalloporphyrin chemistry: synthesis, chemical reactivity, and electrochemical behavior of porphyrins with metal-carbon bonds. *Chemical Reviews* 88: 1121–1146.

341 Brothers, P.J. and Collman, J.P. (1986). The organometallic chemistry of transition-metal porphyrin complexes. *Accounts of Chemical Research* 19: 209–215.

342 Cheng, L., Chen, L., Chung, H.-S. et al. (1998). Synthesis and characterization of osmium nitrosyl porphyrins containing organo, halogeno, and μ-oxo ligands, and extensions to the first organometallic thionitrosyl porphyrin. *Organometallics* 17: 3853–3864.

343 Atefi, F. and Arnold, D.P. (2008). Porphyrins with metal, metalloid or phosphorus atoms directly bonded to the carbon periphery. *Journal of Porphyrins and Phthalocyanines* 12: 801–831.

344 Bröring, M., Cordes, M., and Köhler, S. (2008). Manganese(IV) corroles with σ-aryl ligands. *Zeitschrift für Anorganische und Allgemeine Chemie* 634: 125–130.

345 Yun, L., Vazquez-Lima, H., Fang, H. et al. (2014). Synthesis and reactivity studies of a tin(II) corrole complex. *Inorganic Chemistry* 53: 7047–7054.

346 Wayland, B.B., Fu, X., Peng, C.-H. et al. (2006). Living radical polymerizations mediated by metallo-radical and organo-transition metal complexes. *ACS Symposium Series* 944: 358–371.

347 Peng, C.-H., Li, S., and Wayland, B.B. (2009). Aspects of living radical polymerization mediated by cobalt porphyrin complexes. *Journal of the Chinese Chemical Society* 56: 219–233.

348 Peng, C.-H., Yang, T.-Y., Zhao, Y., and Fu, X. (2014). Reversible deactivation radical polymerization mediated by cobalt complexes: recent progress and perspectives. *Organic & Biomolecular Chemistry* 12: 8580–8587.

349 Peng, C.-H., Li, S., and Wayland, B.B. (2009). Formation, dissociation, and radical exchange of organo-cobalt complexes in mediating living radical polymerization. *ACS Symposium Series* 1024: 115–129.

350 de Bruin, B., Dzik, W.I., Li, S., and Wayland, B.B. (2009). Hydrogen-atom transfer in reactions of organic radicals with [CoII(por)]· (por=porphyrinato) and in subsequent addition of [Co(H)(por)] to olefins. *Chemistry - A European Jouranl* 15: 4312–4320.

351 To, C.T. and Chan, K.S. (2017). Selective aliphatic carbon–carbon bond activation by rhodium porphyrin complexes. *Accounts of Chemical Research* 50: 1702–1711.

352 Liu, X., Liu, L., Wang, Z., and Fu, X. (2015). Visible light promoted hydration of alkynes catalyzed by rhodium(III) porphyrins. *Chemical Communications* 51: 11896–11898.

353 Fang, H., Ling, Z., Brothers, P.J., and Fu, X. (2011). Reactivity studies of a corrole germanium hydride complex with aldehydes, olefins and alkyl halides. *Chemical Communications* 47: 11677–11679.

354 Fang, H., Jing, H., Zhang, A. et al. (2016). Synthesis, electronic structure, and reactivity studies of a 4-coordinate square planar germanium(IV) cation. *Journal of the American Chemical Society* 138: 7705–7710.

355 Fang, H., Ling, Z., Lang, K. et al. (2014). Germanium(III) corrole complex: reactivity and mechanistic studies of visible-light promoted N-H bond activations. *Chemical Science* 5: 916–921.

356 Fang, H., Jing, H., Ge, H. et al. (2015). The mechanism of E-H (E = N, O) bond activation by a germanium corrole complex: a combined experimental and computational study. *Journal of the American Chemical Society* 137: 7122–7127.

357 Brothers, P.J. and Roper, W.R. (1988). Transition-metal dihalocarbene complexes. *Chemical Reviews* 88: 1293–1326.

358 Che, C.-M., Ho, C.-M., and Huang, J.-S. (2007). Metal-carbon multiple bonded complexes. *Coordination Chemistry Reviews* 251: 2145–2166.

359 Maas, G. (2004). Ruthenium-catalysed carbenoid cyclopropanation reactions with diazo compounds. *Chemical Society Reviews* 33: 183–190.

360 Che, C.-M., Zhou, C.-Y., and Wong, E.L.-M. (2011). Catalysis by Fe=X complexes (X = NR, CR2). *Topics in Organometallic Chemistry* 33: 111–138.

361 Zhou, C.-Y., Lo, V.K.-Y., and Che, C.-M. (2012). Metalloporphyrin-catalyzed C-C bond formation. In: *Handbook of Porphyrin Science*, vol. 21 (ed. K.M. Kadish, K.M. Smith and R. Guilard), 321–376. World Scientific Publishing Co. Pte. Ltd.

362 Che, C.-M., Lo, V.K.-Y., Zhou, C.-Y., and Huang, J.-S. (2011). Selective functionalisation of saturated C-H bonds with metalloporphyrin catalysts. *Chemical Society Reviews* 40: 1950–1975.

363 Lash, T.D. (2007). Recent advances on the synthesis and chemistry of carbaporphyrins and related porphyrinoid systems. *European Journal of Organic Chemistry* 5461–5481.

364 Pacholska-Dudziak, E. and Latos-Grazynski, L. (2007). NMR studies of paramagnetic metallocarbaporphyrinoids. *European Journal of Inorganic Chemistry* 2594–2608.

365 Lash, T.D. (2015). Benziporphyrins, a unique platform for exploring the aromatic characteristics of porphyrinoid systems. *Organic & Biomolecular Chemistry* 13: 7846–7878.

366 Suijkerbuijk, B.M.J.M. and Klein Gebbink, R.J.M. (2008). Merging porphyrins with organometallics: synthesis and applications. *Angewandte Chemie, International Edition* 47: 7396–7421.

367 Vecchi, A., Galloni, P., Floris, B. et al. (2015). Metallocenes meet porphyrinoids: consequences of a "fusion". *Coordination Chemistry Reviews* 291: 95–171.

368 Shinokubo, H. and Osuka, A. (2009). Marriage of porphyrin chemistry with metal-catalysed reactions. *Chemical Communications* 1011–1021.

369 Sergeeva, N.N., Senge, M.O., and Ryan, A. (2010). Organometallic C-C coupling reactions for porphyrins. In: *Handbook of Porphyrin Science*, vol. 3 (ed. K.M. Kadish, K.M. Smith and R. Guilard), 325–365. World Scientific Publishing Co. Pte. Ltd., Ch. 12.

370 Senge, M.O. (2011). Stirring the porphyrin alphabet soup-functionalization reactions for porphyrins. *Chemical Communications* 47: 1943–1960.

371 Beletskaya, I.P., Tyurin, V.S., Uglov, A. et al. (2012). Survey of synthetic routes for synthesis and substitution in porphyrins. In: *Handbook of Porphyrin Science*, vol. 23 (ed. K.M. Kadish, K.M. Smith and R. Guilard), 81–279. World Scientific Publishing Co. Pte. Ltd.

372 Takanami, T. (2013). Functionalization of porphyrins through C-C bond formation reactions with functional group-bearing organometallic reagents. *Heterocycles* 87: 1659–1689.

373 Yorimitsu, H. and Osuka, A. (2013). Organometallic approaches for direct modification of peripheral C-H bonds in porphyrin cores. *Asian Journal of Organic Chemistry* 2: 356–373.

374 Hiroto, S., Miyake, Y., and Shinokubo, H. (2017). Synthesis and functionalization of porphyrins through organometallic methodologies. *Chemical Reviews* 117: 2910–3043.

5

Phthalocyanines and Porphyrazines

Ümit İşci[1] *and Fabienne Dumoulin*[2]

[1]*Department of Chemistry, Gebze Technical University, Gebze, Turkey*
[2]*Department of Medical Engineering, Faculty of Engineering and Natural Sciences, Acıbadem Mehmet Ali Aydınlar University, Istanbul, Turkey*

5.1 Phthalocyanines and Porphyrazines: Structures and Syntheses of Peculiar Members of the Porphyrin Family

5.1.1 Structural Variability

Phthalocyanines (routinely abbreviated as Pc) and porphyrazines (Pz) are tetrapyrrolic derivatives with a tetraazaporphyrin core structure, containing eight nitrogen atoms within the 18 π-electron system. The term *porphyrazine* either has a strict meaning describing the porphyrazine core itself, substituted or not, or, more broadly interpreted, describes all derivatives with this core (including phthalocyanines), possibly composed of subunits of different types.

Phthalocyanines and porphyrazines are tetrapyrrolic structures with a wide range of structural variability, in particular, regarding the nature of the metals and pseudo-metals likely to be coordinated at the center of the macrocycle. They comprise four isoindole or pyrrole subunits, respectively, giving parent macrocycles with closely related structures. The members of the family described below are shown in Figure 5.1.

Phthalocyanines are tetrabenzoporphyrazines. Contracted phthalocyanines and porphyrazines are commonly named subphthalocyanines (subPc) and subporphyrazines (subPz), and comprise three subunits coordinating a central boron atom [1]. The presence of one (either in the α or β position) or two (in the β position) additional nitrogen atoms on the benzene ring of phthalocyanine corresponds, respectively, to tetrapyridinoporphyrazines or tetrapyrazinoporphyrazines, the latter being more commonly called azaphthalocyanines. Superphthalocyanines have a uranium atom (as a UO_2 group) coordinated by five isoindole subunits [2]. Rare related "norcorroles of superphthalocyanines," although called pentabenzotriazasmaragdyrins, have also been reported [3]. There are three types of multi-decker structures. Two macrocycles may be coordinated by a single metal atom, usually from the lanthanide series (Ln double-decker) although other metals are reported as well. On the other hand, the metal atoms of two metallated macrocycles can be bridged by oxygen, nitrogen, or carbon atoms, giving μ-oxo, μ-nitrido or μ-carbido compounds. Alternatively, the metals of two macrocycles can establish a direct metal–metal bond. Finally, azaphenalene

Fundamentals of Porphyrin Chemistry: A 21st Century Approach, Volume 1, First Edition.
Edited by Penelope J. Brothers and Mathias O. Senge.
© 2022 John Wiley & Sons Ltd. Published 2022 by John Wiley & Sons Ltd.

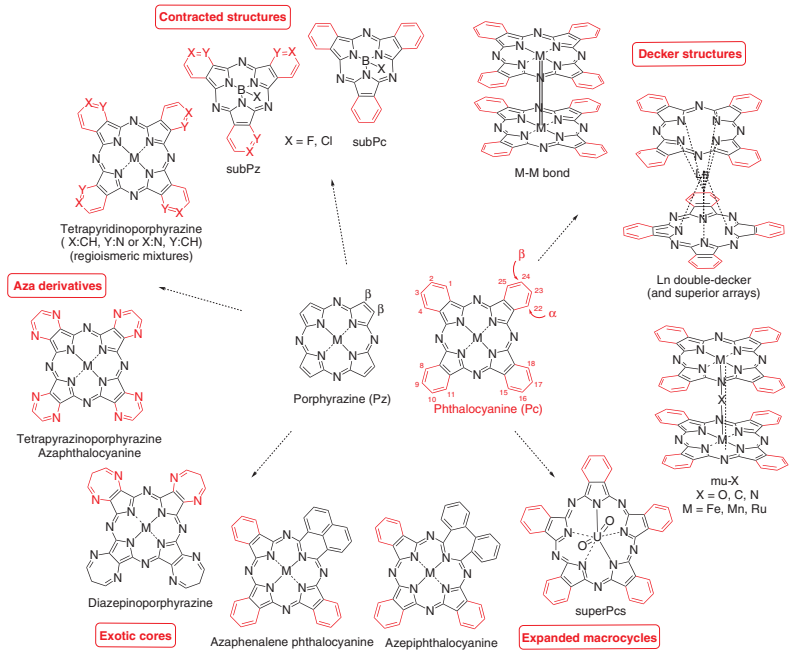

Figure 5.1 Porphyrazine (black) and phthalocyanine (black + blue) cores and related structures.

phthalocyanine [4] and azepiphthalocyanine [5] are more exotic structures with asymmetric substitution patterns, mixing isoindole and π-expanded subunits.

The designation of the different positions hosting substituents is quite simple for porphyrazine macrocycles, with the notation β-pyrrole positions being the same as those used for porphyrins. In the case of phthalocyanines, several notations are observed. The most external positions of the macrocycle are said to be peripheral, designated as β, and correspond to the positions 2, 3, 9, 10, 16, 17, 23, and 24. The more inner positions of the macrocycle are said to be non-peripheral, designated as α, and correspond to the positions 1, 4, 8, 11, 15, 18, 22, and 25.

The substitution of the subunits of these macrocycles is another source of structural variability. Porphyrazines can be substituted on their peripheral β-carbon atoms. For other derivatives, all carbons of each isoindole subunit (and the related nitrogenated derivatives) that are not fused to the pyrrole ring are likely to be substituted by one, two, or four substituents, of the same or different nature, possibly fused (thereby inducing an extension of the electronic delocalization), and in different positions. The nature of the grafting function, the number, size, and position of the substituents will affect the properties of the phthalocyanine. The substitution of a fused ring on the subunit extends the structural variability.

5.1.2 Symmetric and Asymmetric Substitution Patterns

Macrocycles bearing the same substituents on each subunit have a symmetric substitution pattern, whereas for asymmetric substitution some subunits bear different substituents. Among all the possible combinations, the largest number of substitution patterns (six) is reported for phthalocyanines (Figure 5.2); other combinations are yet to be reported. Only some of these combinations are reported for other macrocycle cores.

5.1.3 Isomeric Mixtures

For the special case of tetrasubstituted derivatives with symmetric substitution where the substituents are in peripheral (β) or non-peripheral (α) positions, they are obtained as mixtures of four regioisomers with C_{2v}, C_{4h}, D_{2h}, and C_s symmetries (Figure 5.3).

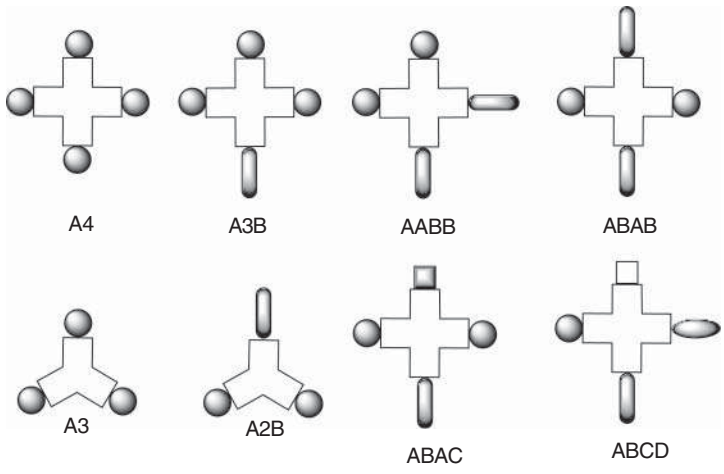

Figure 5.2 Symmetric and asymmetric substitution patterns. ✚ represents tetrapyrrolic cores and ⏃ represents contracted tripyrrolic cores.

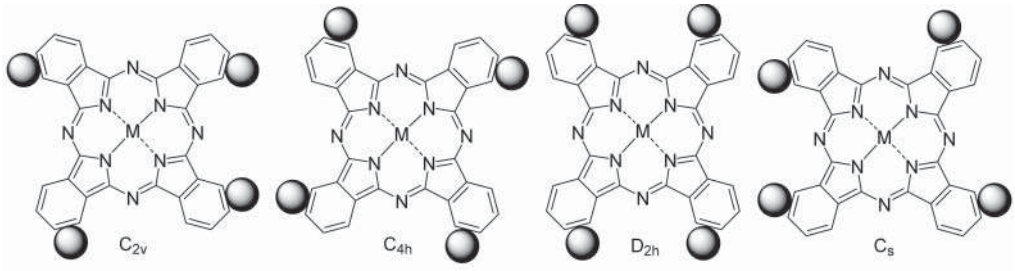

Figure 5.3 The different symmetries of isomeric mixtures.

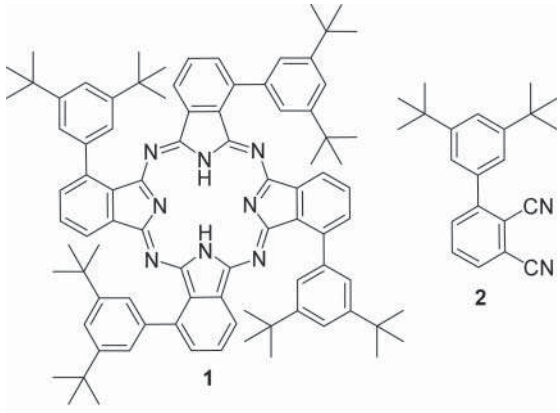

Figure 5.4 Tetra non-peripherally (α) substituted phthalocyanine **1** obtained as a single regioisomer due to the steric hindrance of the substituent on the starting phthalonitrile **2**. Source: Modified from Ranta et al. [6].

The relative ratio of the isomers can be modulated by the steric hindrance of some substituents in non-peripheral (α) position. The phthalocyanine **1** (Figure 5.4) obtained from a phthalonitrile bearing very bulky substituents **2** led exclusively to one regioisomer, whereas less hindered phthalonitriles led to mixtures of only two or three regioisomers [6]. Tetrapyridinoporphyrazines are regioisomeric mixtures even without substituents, and thus can exhibit the same symmetries as tetrasubstituted derivatives.

Examples of more complex isomeric mixtures are given in Figure 5.5 [7, 8]. Some fused precursors produce regioisomeric mixtures (compounds **3** and **4**). Octasubstituted derivatives are usually regioisomerically pure. Anyway, precursors disubstituted in positions other than 4,5- or 3,6- lead to regioisomeric mixtures of octasubstituted derivatives (compounds **5** and **6**). Other derivatives with symmetrical substitution patterns are also regioisomeric mixtures, such as compounds **7** and **8** (Figure 5.5).

Asymmetric substitution patterns with monosubstituted subunits increase the number of possible regioisomers. Eight regioisomers were reported in the case of an asymmetric A3B substitution pattern (Figure 5.6) [9].

Finally, one may note that asymmetric structures of the A3B type prepared from 4,5- or 3,6-disubstituted A-precursor and a monosubstituted B-precursor give isomerically pure derivatives (Figure 5.7) [11], whereas the ABAB derivative prepared from the same precursors have two regioisomers (Figure 5.7) [10].

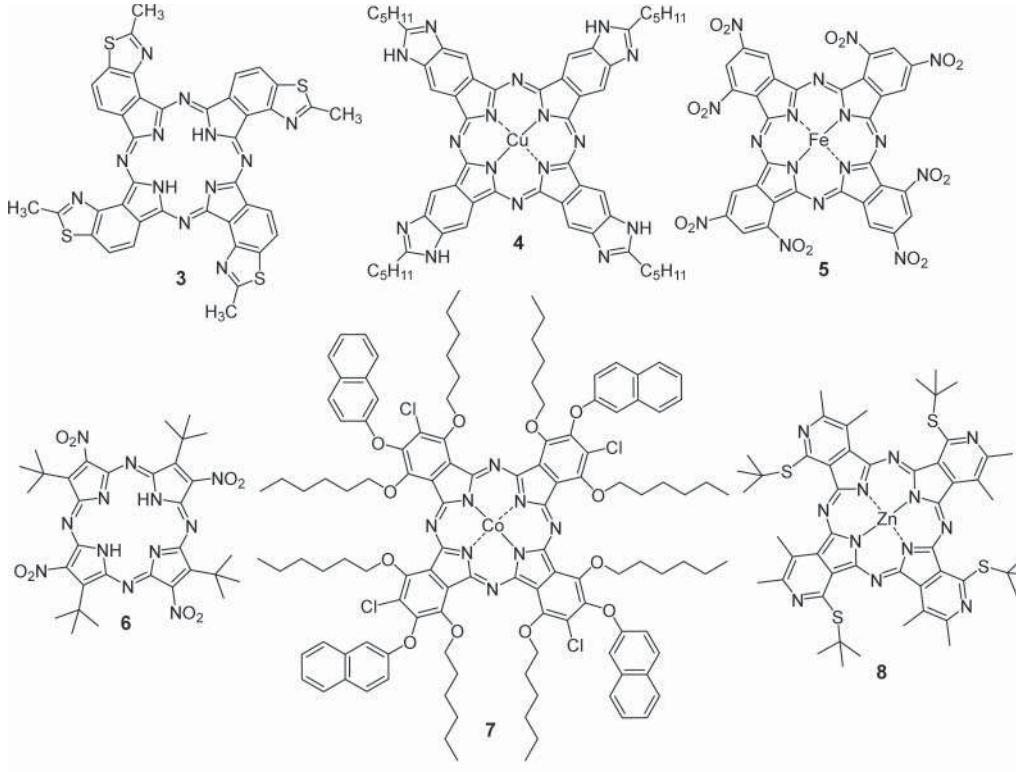

Figure 5.5 Symmetrically substituted porphyrazines being regioisomeric mixtures. Among the possible regioisomers, only the C_{4h} is shown. Based on Necedová et al. [7]; Kobayashi et al. [8].

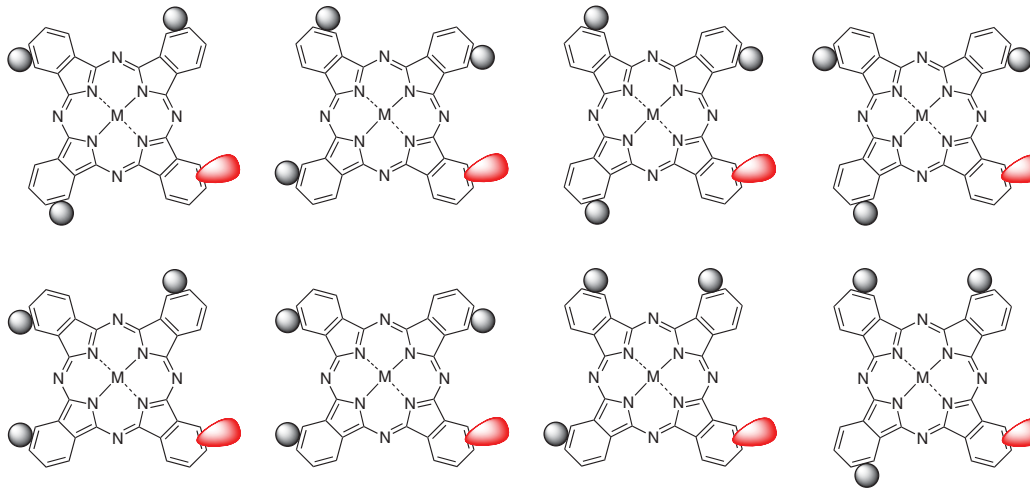

Figure 5.6 The possible symmetries of an isomeric mixture of A3B phthalocyanines. Based on Tejerina et al. [9].

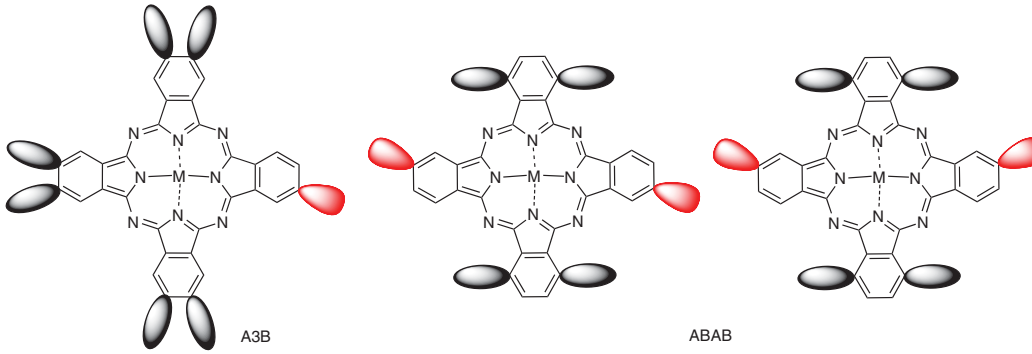

Figure 5.7 A3B and ABAB derivatives prepared from disubstituted A-precursors and monosubstituted B-precursors. Based on Fazio et al. [10].

5.1.4 Properties and Applications

One last detail to add in this section would be a sentence about how unsubstituted Pc compounds can be very insoluble because of aggregation.

As can be guessed from their highly conjugated structures, phthalocyanines, porphyrazines, and related derivatives are intensely colored and possess outstanding optical and electronic properties. Subsequently, they have been historically widely used as dyes, but also became crucial in the last decades for technological applications, hence being designated as "old dyes, new materials" [12].

The properties of these fascinating compounds are affected by structural and external effects. All the structural variations on the parent macrocycle, the number, position, and nature of substituents, and the metal itself allow tailoring of their properties. In their electronic adsorption spectra, the maximum absorption wavelengths for subphthalocyanines and phthalocyanines are around 565 and 700 nm, respectively, depending on the substituent and metallation pattern. External effects such as the solvent, concentration, temperature, aggregation, incorporation into nanoparticles, organization into films or monolayers, and/or the presence of other molecules can also modify their properties.

Aggregation is the coplanar stacking of macrocycles from monomer to dimer and higher-order edifices, promoted by van der Waals interactions [13]. The electronic structure of aggregated macrocycles is modified, which in turn alters their ground and excited electronic states, and results in shifted or even quenched fluorescence, singlet oxygen generation, redox properties, second- or third-order nonlinear optical properties, electrochemical behavior, and the ability to participate in energy or electron transfer, which are among the most commonly desired properties.

The properties are exploited in multiple applications: singlet oxygen generation can be used in photodynamic therapy to destroy cancer cells or remedy infections, in synthetic oxidation catalysis, or for environmental purposes such as wastewaters treatment or destruction of pollutants. Nonlinear properties are necessary for optical limiting in telecommunications transmissions. Light harvesting is used in various technologies to convert solar energy into electricity, such as dye-sensitive or bulk heterojunction solar cells. Their sensitivity to the presence of external molecules also makes them an ideal molecular basis for various sensor devices.

5.2 Synthetic Methods and Strategies

5.2.1 Key Steps, Template Effect, and Final Metallation, Choice of the Metal and Demetallation

The structural variability is at two main levels: the substitution pattern and the metallation. Their nature determines the synthetic strategy, the different options being summarized in Figure 5.8. Porphyrazines and phthalocyanines, like other porphyrinoids, are tetrapyrrolic derivatives. Macrocycle formation can be generally considered a cyclotetramerization (cyclotrimerization for contracted derivatives) that requires four precursor units to come close enough to each other to establish covalent bonds. The template effect is the use of a metal salt to coordinate the precursors – thus spatially pre-arranging them – to facilitate the reaction. Intramolecular reactions are favored compared to intermolecular reactions, and the template effect facilitates this. The simplest case is when the starting precursor units react with the desired metal salt to give the metallated macrocycle in one step (route a).

Non-metallated free bases are very rarely obtained without using a metal salt (route b) as the absence of a template effect lowers the yields. The free bases are typically prepared via the demetallation of corresponding metallated macrocycles (route a + c, with or without isolation of the metallated derivative). Metals used for this sequence are usually lithium, magnesium, and sometimes zinc. On the other hand, it is possible to prepare the free bases (by route b or a + c) and to subsequently insert a metal (route d).

Finally, when targeted substituents are not compatible with macrocycle formation conditions, further reactions on pre-formed macrocycles – metallated or not – may be necessary (route e or h). Final metallation (route f) or demetallation (route g) may complete the synthetic sequence.

The tentative mechanism of the formation of a phthalocyanine, starting from phthalonitrile in the presence of a base (generated in situ, as when lithium is added to butanol), is represented in Figure 5.9. The alkoxide anion is therefore important [15].

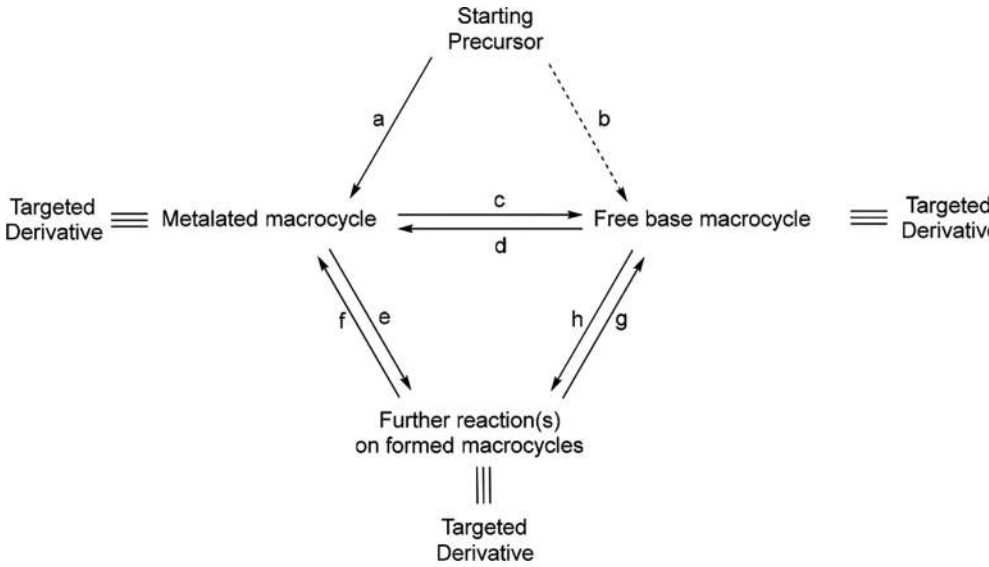

Figure 5.8 Key steps and different synthetic pathways.

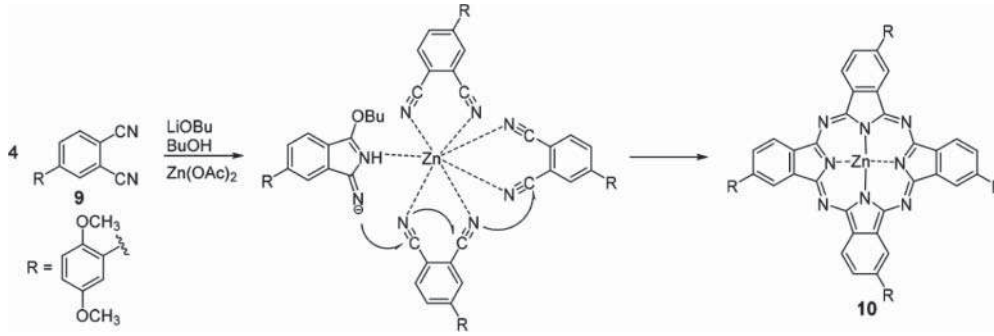

Figure 5.9 Proposed mechanism of the template-assisted formation of a phthalocyanine. Based on Aranyos et al. [14].

Metals that can easily be removed but are not desired in the final structure are useful as templates, for example, lithium, magnesium, or cerium [16]. They are removed following the formation of the phthalocyanine (route a + c) by a quick acidic treatment, and the resulting free-base phthalocyanine can be metallated as desired (route a + c + d). This sequence is particularly appropriate when a study aims to investigate the effect of different metals at the center of the macrocycle, as metallation reactions are often high yielding, whereas the direct template formation of macrocycle is less efficient and may have purification problems. It is also a useful approach for metals that induce aggregation and/or insolubility.

Other demetallations can occur without being targeted. For example, removal of zinc from the center of Zn Pc was serendipitously discovered [17]. Metals with a large ionic size (such as lead [18]) are easily released. Obtaining and purifying these metallated derivatives requires specific precautions, as even the mildest acidic media, including silica gel for chromatography, or even water, must be avoided. The formation of double-deckers (or superior arrays) with one metal coordinating two macrocycles is specific and will be treated in Section 5.6.

5.2.2 Choice of Precursors

The choice of precursors is determined by a range of factors including their chemical feasibility, their suitability for achieving the desired substitution pattern, the conditions to be used during the macrocycle formation, and their possible selective reactivity for the preparation of asymmetric derivatives.

The smallest precursor is fumaronitrile. All other precursors of phthalocyanines and related derivatives are of the phthalic type (except for some very exotic structures). Most phthalic acids, phthalic anhydrides, and other phthalic derivatives can be used (Figure 5.10), although over the last two decades it is predominantly phthalonitriles that have been used as precursors to phthalocyanines. Fused phthalonitriles (e.g., naphthalonitriles), 5- or 6-membered aromatic heterocycles (pyridine dicarbonitriles and pyrazine-2,3-dicarbonitrile), possibly fused as well, are also reported (Figure 5.11). Their activated diiminoisoindoline form may be used when the substituent lowers the phthalonitrile reactivity or if the metal used has only a weak templating effect (see below). Dibromobenzene can be used only as precursors of Cu derivatives using CuCN as the salt, as they are converted into phthalonitriles during the course of the reaction [19].

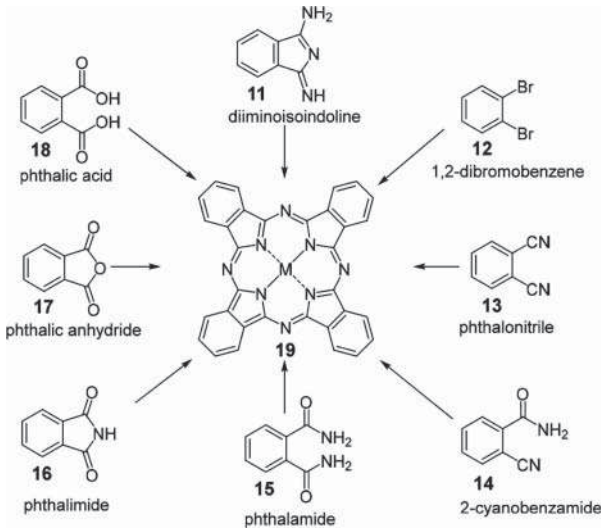

Figure 5.10 The different possible precursors of phthalocyanine.

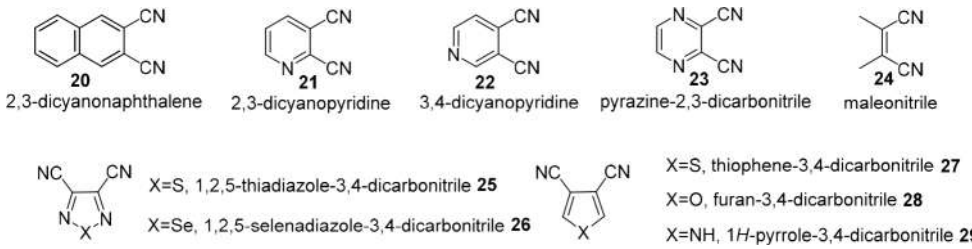

Figure 5.11 Common precursors of other porphyrazines.

Other precursors can be annulated, contain heteroatoms, be 5- or 6-membered, or be smaller maleonitrile derivatives. Fumaronitriles, phthalonitriles, and diiminoisoindolines already contain all the nitrogen atoms required in the final tetrameric structure. Other precursors require the use of an additional nitrogen source, often urea in the presence of ammonium salts.

5.2.3 Choice of Reaction Solvent and Other Reagents

Reactions are commonly performed at high temperature using high-boiling solvents, and usually in basic and/or reducing conditions. Alcohols with C4-C8 chains and non-nucleophilic bases such as 1,8-diazabicyclo[5.4.0]undec-7-ene (DBU) are widely used. In situ generated alcoholates (Li/alcohol) are also used and intrinsically basic dimethylaminoethanol (DMAE) is also convenient. The solvent should not interfere with the substituents on the precursors. Carboxylated phthalonitriles are extremely likely to be esterified when alcohols are used as solvents in basic conditions, requiring a subsequent hydrolysis step [20]. Alcoholates are nucleophiles and can attack some substituents such as sulfonyl functions [21]. The use of hexamethyldisilazane (HMDS) in DMF comprises mild conditions allowing phthalocyanines to be obtained from phthalonitriles [22], phthalimides, and phthalic anhydride [23].

In more rare cases, the preparation of phthalocyanines at room temperature can be achieved. This requires the use of a stronger base than usual with an appropriate solvent, for example, lithium 2-*N,N*-dimethylaminoethoxide in DMAE [24] or diisopropylamide anion [25]. Some phthalocyanines can also be prepared in solvent-free conditions simply by heating and melting a mixture of phthalonitriles and metal salt [26]. These conditions are suitable for a limited numbers of precursors that do not degrade at high temperature.

Porphyrazines and azaphthalocyanines can almost all be prepared by using the template method with magnesium, which is easily removed afterward in acidic conditions. Whenever possible, the alcohol corresponding to the substituent is used as the solvent to avoid scrambling [27]. In some cases, more chemically inert solvents having no other role than their high boiling point can be used, such as DMF/1,2-dichlorobenzene (the latter avoiding side reactions [28]). In line with green chemistry requirements, ionic liquids can also be used as solvents [29]. Finally, macrocycle formation under microwave irradiation has proved to be efficient [30].

5.2.4 Metallation

Metallation reactions are typically performed made using metal chloride or metal acetate salts, commonly with a polar, aprotic solvent such as DMF. Chloroform/methanol mixtures are a good alternative. Chapter 4 (on coordination chemistry) gives much more information on metallation procedures for tetrapyrroles in general.

5.2.5 Purification Methods

The removal of the solvent and excess metal salt is the first step of the reaction work-up. Ideally, the solvent can be removed by distillation and the metal salt removed by washing with water. Precipitating the crude product by adding another solvent (water and/or ethanol) is also convenient. Nonetheless, one must be careful that this treatment has no side effect such as undesired demetallation. Crude products from reactions performed in large quantities can be pre-purified using Soxhlet extraction. Hot ethyl acetate is especially suitable to remove undesired imides formed during the course of phthalocyanine formation. Chromatographic purifications are often the final steps, and reverse-phase columns are useful to purify water-soluble derivatives.

5.3 Preparation and Characterization of Precursors

As outlined in the previous section, the precursors to porphyrazines can be of widely different natures and can be prepared by various synthetic pathways – indeed, an entire book could be devoted to this topic. The purpose here is to summarize the different synthetic options. For more details, the reader is invited to refer to available reviews [31] and chapters [32]. Nowadays, the most common phthalocyanine precursors are phthalonitriles. First, a short remark on nomenclature. Although the IUPAC-approved names are 1,2-dicyanobenzene or phthalonitrile, the terms *o*-cyanobenzonitrile or *o*-phthalodinitrile are often used as well. The synthesis of other precursors of phthalocyanines and porphyrazines is also discussed.

5.3.1 Functionalized Phthalonitriles as Synthons

Most of the phthalonitriles in this section are commercially available, but it may be more economical to prepare them from cheaper precursors.

Nitrophthalonitriles. Whereas 3-nitrophthalimide (**33**) is commercially available, 4-nitrophthalimide (**30**) is obtained by the nitration of phthalimide in one step (Scheme 5.1). In the last step of the synthesis, DMF is not only the solvent but also a reagent, reacting with thionyl chloride to form *N,N*-dimethylchlorosulfitemethaniminium chloride, which is the dehydrating agent (Vilsmeier agent, Scheme 5.1 inset) [33]. Nitrophthalonitriles are intermediates for the synthesis of other functionalized phthalonitriles (see below). Finally, nitronaphthalene-2,3-dicarbonitrile (**39**) can be obtained via a rather different sequence [34] (Scheme 5.2).

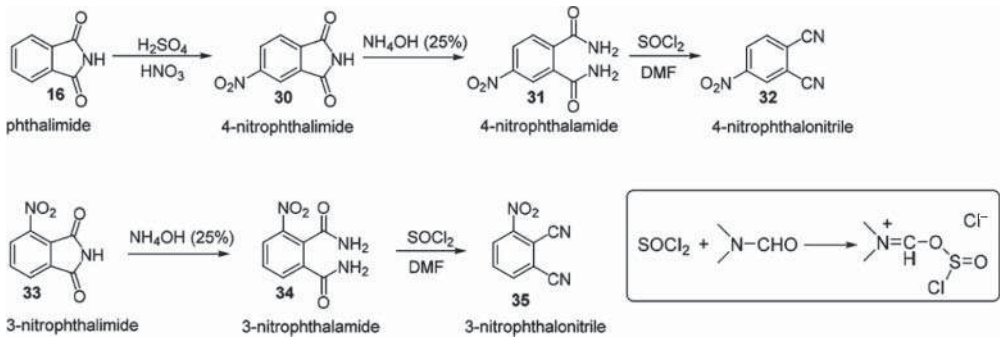

Scheme 5.1 Syntheses of 4-nitrophthalonitrile (**32**) and 3-nitrophthalonitrile (**35**). Based on Arrieta et al. [33].

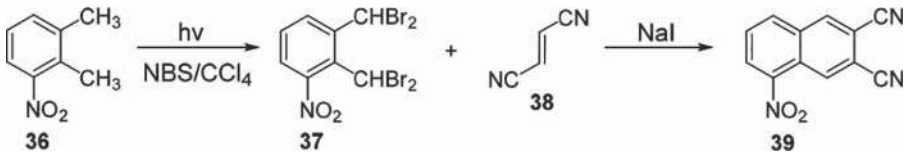

Scheme 5.2 Synthesis of nitronaphthalene-2,3-dicarbonitrile (**39**). Source: Leznoff et al. [34].

Aminophthalonitriles. Reduction of nitrophthalonitriles (**32** or **35**) gives 4- and 3-aminophthalonitriles (**40** or **41**) [34] (Scheme 5.3).

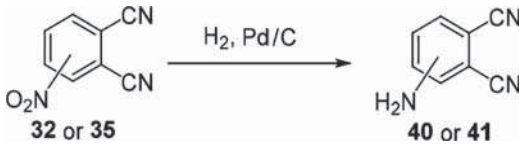

Scheme 5.3 Reduction of nitrophthalonitriles (**32** or **35**) to give 4- or 3-aminophthalonitriles (**40** or **41**). Source: Leznoff et al. [34].

Four routes are possible to synthesize 4,5-diaminophthalonitrile (**46**), with different starting compounds (Scheme 5.4). Three routes, starting either from 1,2-dibromobenzene (**12**) [35], 1,2-diaminobenzene (**42**) [36], or 1,2-dinitrobenzene (**47**) [37], occur via the

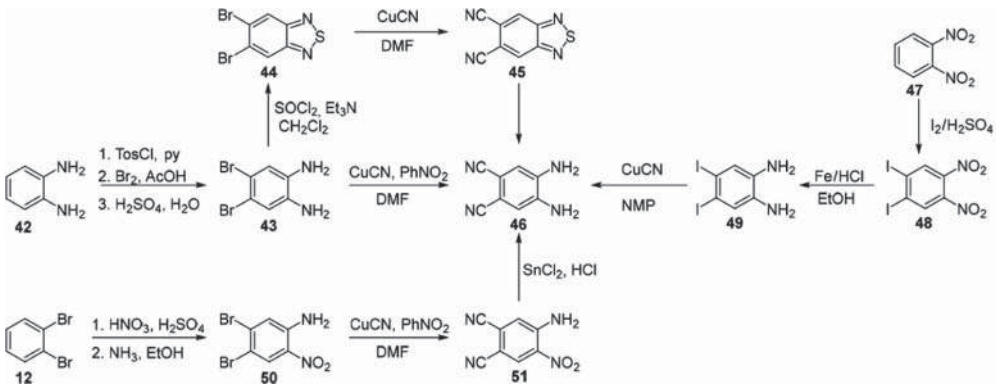

Scheme 5.4 Four routes to synthesize 4,5-diaminophthalonitrile (**46**).

Rosenmund-von Braun nitrilation of an aminated intermediate. Tedious removal of metal salts coordinating the amine functions were overcome in the most recent synthetic sequence, called the 2,1,3-benzothiadiazole route [38], in which the diamino function is generated at the last step.

Halogenated phthalonitriles. The Sandmeyer reaction applied to 3- or 4-aminophthalonitriles (**40** or **41**) yields the corresponding iodophthalonitriles (**52** or **53**) (Scheme 5.5). 5-Iodonaphthalene-2,3-dicarbonitrile was obtained using the same synthetic sequence starting from nitronaphthalene-2,3-dicarbonitrile (**39**) [34].

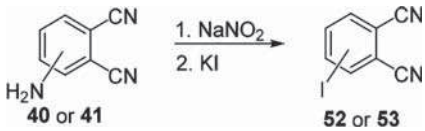

Scheme 5.5 Syntheses of iodophthalonitriles (**52** or **53**) from 3- or 4-aminophthalonitriles (**40** or **41**). Based on Leznoff et al. [34].

The preparation of 3,6-diiodophthalonitrile via a two-step nitrile-directed ortho-lithiation has been reported [39], but remains very rarely used in phthalocyanine chemistry. 4,5-Diiodophthalonitrile (**59**) is prepared via an initial iodination reaction in quite harsh conditions. Tedious separations are necessary at the end of the synthetic sequence (Scheme 5.6) [40].

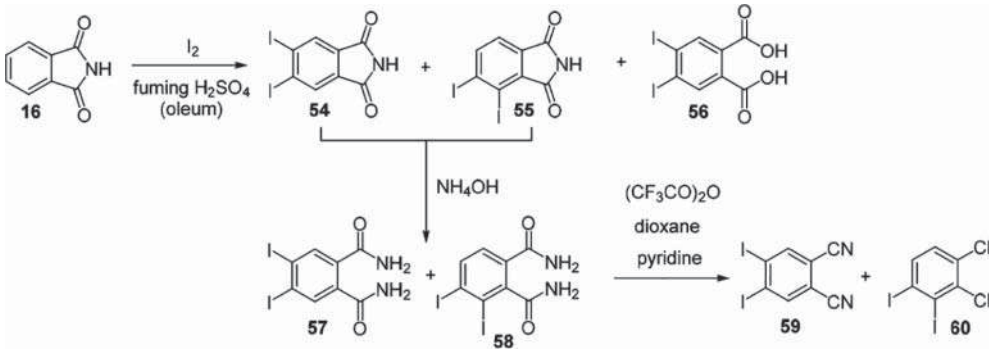

Scheme 5.6 Synthesis of 4,5-diiodophthalonitrile (**59**). Source: Terekhov et al. [40].

4,5-Dibromophthalonitrile (**65**) is a convenient substitute for 4,5-diiodophthalonitrile. Its synthesis was first reported by the direct bromination of phthalonitrile by *N,N*-dibromoisocyanuric acid (DBI) and led to a mixture of mono- and dibrominated derivatives (**61**–**65**) [41]. A key inexpensive, mild, and environmentally benign iodination of dibromobenzene followed by the selective dinitrilation of the iodines proved to be the best synthetic pathway reported so far (Scheme 5.7) [42]. Mono- and dibromomethylated (**71**, **72**, and **74**) phthalonitrile are also reported. Methylated phthalonitriles are brominated by N-bromosuccinimide (Scheme 5.8).

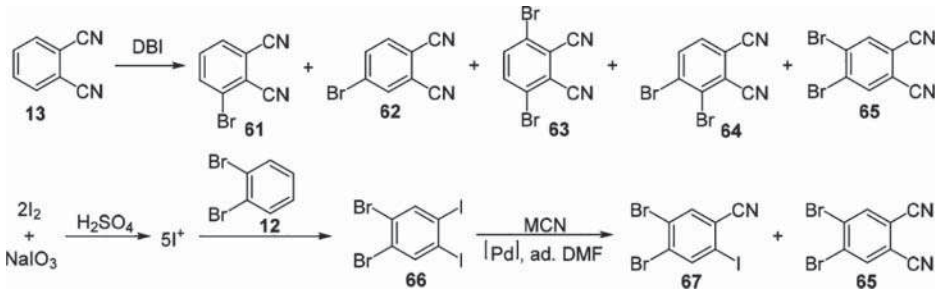

Scheme 5.7 Best synthetic pathway to 4,5-dibromophthalonitrile (**65**). Based on Juricek et al. [42].

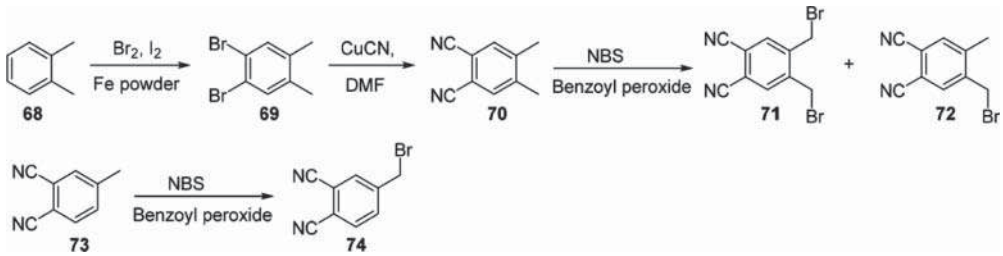

Scheme 5.8 Syntheses of mono- and dibromomethylated (**71**, **72** and **74**) phthalonitriles.

As for nitrophthalonitriles, 4,5-dichlorophthalimide (**77**) obtained in two steps from 4,5-dichlorophthalic acid (**75**) via the corresponding phthalic anhydride intermediate **(76)** gives 4,5-dichlorophthalonitrile (**79**) (Scheme 5.9). 3,4,5,6-Tetrafluorophthalonitrile, another

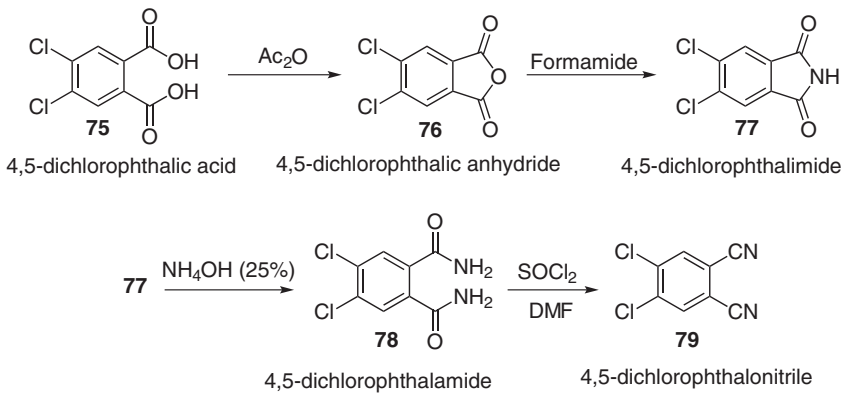

Scheme 5.9 Synthesis of 4,5-dichlorophthalonitrile (**79**).

useful building block, is commercially available. It is also widely used by itself to prepare perfluorinated phthalocyanine [43].

Hydroxyphthalonitriles. Nitrophthalonitriles give hydroxyphthalonitriles by reaction with sodium nitrite (Scheme 5.10) [44, 45]. Alternatively, benzyl alcohol can react with nitrophthalonitriles; then the benzyl group is removed in reducing conditions [46].

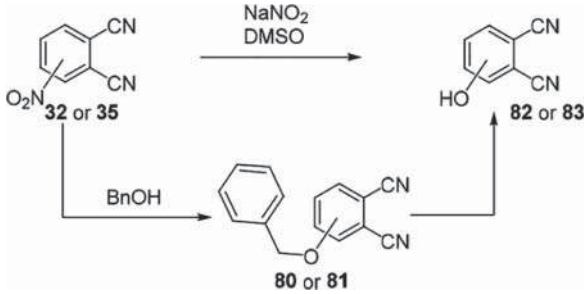

Scheme 5.10 Syntheses of hydroxyphthalonitriles (**82** or **83**). Based on Wöhrle and Knothe [44]; Leznoff and Drew [45].

Two major ways are reported to access to 4,5-dihydroxyphthalonitrile (**88**), both starting from dibromocatechol (**85**), with the hydroxyls protected either by acetal formation (**89**) [47] or by benzyl groups (**86**) [28] prior to nitrilation, and removal of the protecting groups as the final step (Scheme 5.11). Hydroxyphthalonitriles and 3,6-dihydroxyphthalonitrile (also known as 2,3-dicyanohydroquinone) are commercially available.

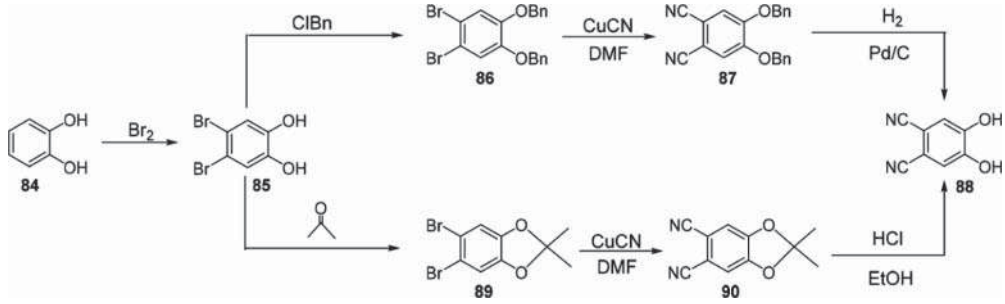

Scheme 5.11 Two synthetic routes to 4,5-dihydroxyphthalonitrile (**88**). Based on Cha and Lim [47]; Cabezon et al. [28].

Miscellaneous. Phthalonitriles activated in the 3,6-positions can be prepared as described in Scheme 5.12. Either 3,6-bis(4′-methylphenylsulfonyloxy)phthalonitrile (**91**) [48] or its more reactive triflate derivative (**93**) [49] are prepared from 3,6-dihydroxyphthalonitrile (**92**), while 4,5-dichloro-3,6-dihydroxyphthalonitrile (**95**) is obtained by the reduction of 2,3-dichloro-5,6-dicyano-1,4-benzoquinone (**94**, DDQ) [50].

5.3.2 Substituted Phthalonitriles

Substituted phthalonitriles can be obtained by reactions on the convenient phthalonitrile precursors described above. Another possibility is the nitrilation of suitable precursors.

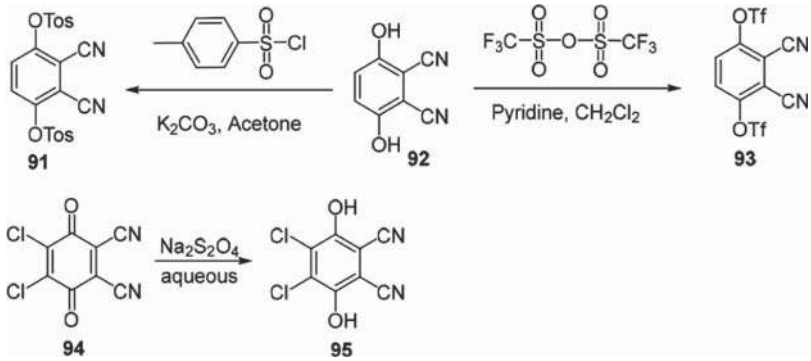

Scheme 5.12 Synthesis of phthalonitriles activated in the 3,6-positions.

Nitrilation. Cyanation of aromatic halides by CuCN, also known as the Rosenmund-von Braun reaction [51], is generally applied to dibromobenzenes. Diiodobenzenes are more reactive, and dibromophthalonitrile can be obtained from dibromodiiodobenzene under finely optimized conditions (Scheme 5.7) [42]. Nitrilations that are difficult or even impossible [52] under classical conditions are performed using microwaves [53]. The use of $Zn(CN)_2$ as the cyanide source, in the presence of a palladium catalyst, improves the yields [54].

Nucleophilic substitutions. Nitrophthalonitriles [55] can undergo nucleophilic substitutions with alcoholates, phenolates, and thiolates by reacting with the corresponding alcohol/thiol/phenol in an aprotic polar solvent in rather mild conditions (commonly DMF or DMSO) in the presence of a carbonate base at room temperature. Tetrafluorophthalonitrile substitution by alcohols is most commonly performed using NaH in THF or toluene [56], whereas thiolates react in the presence of K_2CO_3 in DMF [57]. Less common nucleophiles such as sodium alkanesulfinates reacting with nitrophthalonitriles can lead directly to alkylsulfonylphthalonitriles [58], but the limited availability of the starting sulfonyl chloride limits the number of possible derivatives. 4,5-Dichlorophthalonitrile is less reactive and can be substituted by thiolates [59] and phenolates [60], but not by alcoholates (unless strongly activated by fluorines [61]). It may also happen that only one chlorine atom is substituted, leading to 4-chloro-5-substituted derivatives [62]. Extensive studies of the sequential substitution of the chlorine atoms on tetrachlorophthalonitrile by different nucleophiles have been performed as well [63].

The specific case of a phthalonitrile alkene-functionalized can be highlighted. As pent-4-ene-1-thiol is not available, 4,5-dimercaptophthalonitrile (**97**) [64] was first prepared and subsequently reacted with bromopentene [65] (Scheme 5.13).

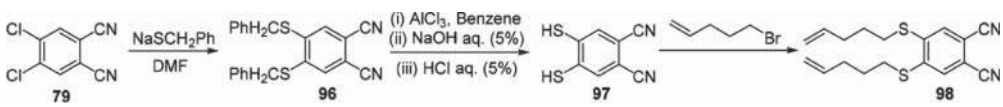

Scheme 5.13 Synthesis of an alkene-functionalized phthalonitrile. Based on Hota et al. [65].

Organometallic couplings. 4,5-Dibromophthalonitrile, 4,5-diiodophthalonitrile, and tosyl or triflate-activated 3,6-dicyanohydroquinones can undergo organometallic couplings with alkynes (Sonogashira) [42, 66] or with boronic acids (Suzuki–Miyaura) [10] (Scheme 5.14).

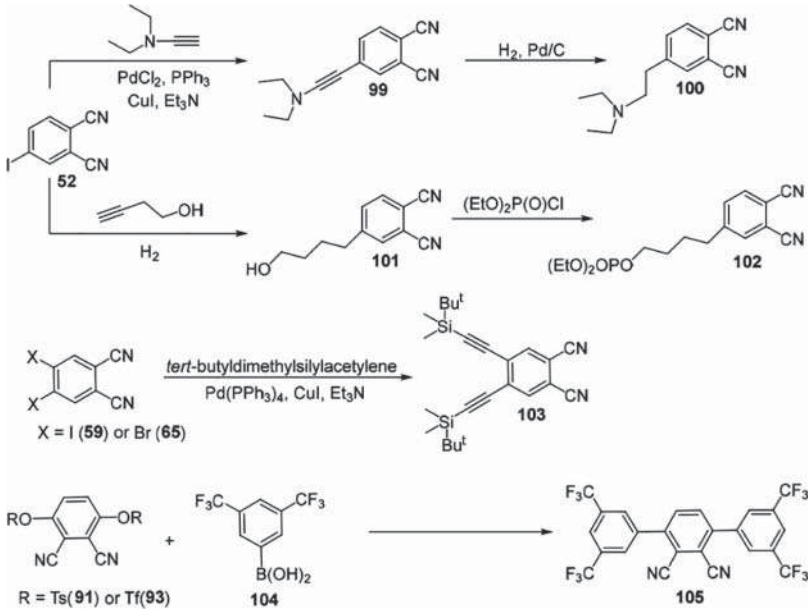

Scheme 5.14 Examples of organometallic couplings with alkynes (Sonogashira) [42, 66] or boronic acids (Suzuki–Miyaura). Based on Juricek et al. [42]; Lexnoff et al. [66]; Fazio et al. [10].

Successive organometallic couplings, first Migita–Kosugi–Stille cross-coupling then Suzuki–Miyaura (with ratio adjustment of the boronic ester used) after a bromination step led to an asymmetrically substituted phthalonitrile (Scheme 5.15) [67].

Phosphorylation of 4-iodophthalonitrile with diethyl phosphite in the presence of Pd catalyst and triethylamine leads to phosphonate groups after final deprotection [68].

Oxidation. The oxidation of sulfanyl derivatives, either by *meta*-chloroperbenzoic acid (mCPBA) in dichloromethane or by hydrogen peroxide in refluxing acetic acid, led to corresponding sulfonyl derivatives [69].

Diels–Alder reaction. Even though it is not the final step, the Diels–Alder reaction is crucial to prepare 3,6-alkylphthalonitriles. 2,5-Dialkylthiophene (**114**) is oxidized to the sulfone (**115**), which acts as the diene in a Diels–Alder reaction, fumaronitrile (**38**) being the dienophile [70]. 2,5-Dialkylfurans can be used instead of 2,5-dialkylthiophenes (Scheme 5.16) [71].

Miscellaneous. The Mitsunobu reaction is another synthetic tool to prepare phthalonitriles, such as tetrasubstituted derivatives from 4,5-dichloro-3,6-dihydroxyphthalonitrile (**118**), followed by a nucleophilic substitution by phenols (Scheme 5.17) [50].

It is tedious to purify anionic sulfonated phthalocyanines. The use of protected functional groups allowing classical chromatographic purifications has been developed by using phthalonitriles **124–126** (Scheme 5.18) [72]. Final removal of the protecting group can be done after isolation of the desired asymmetric derivative [73].

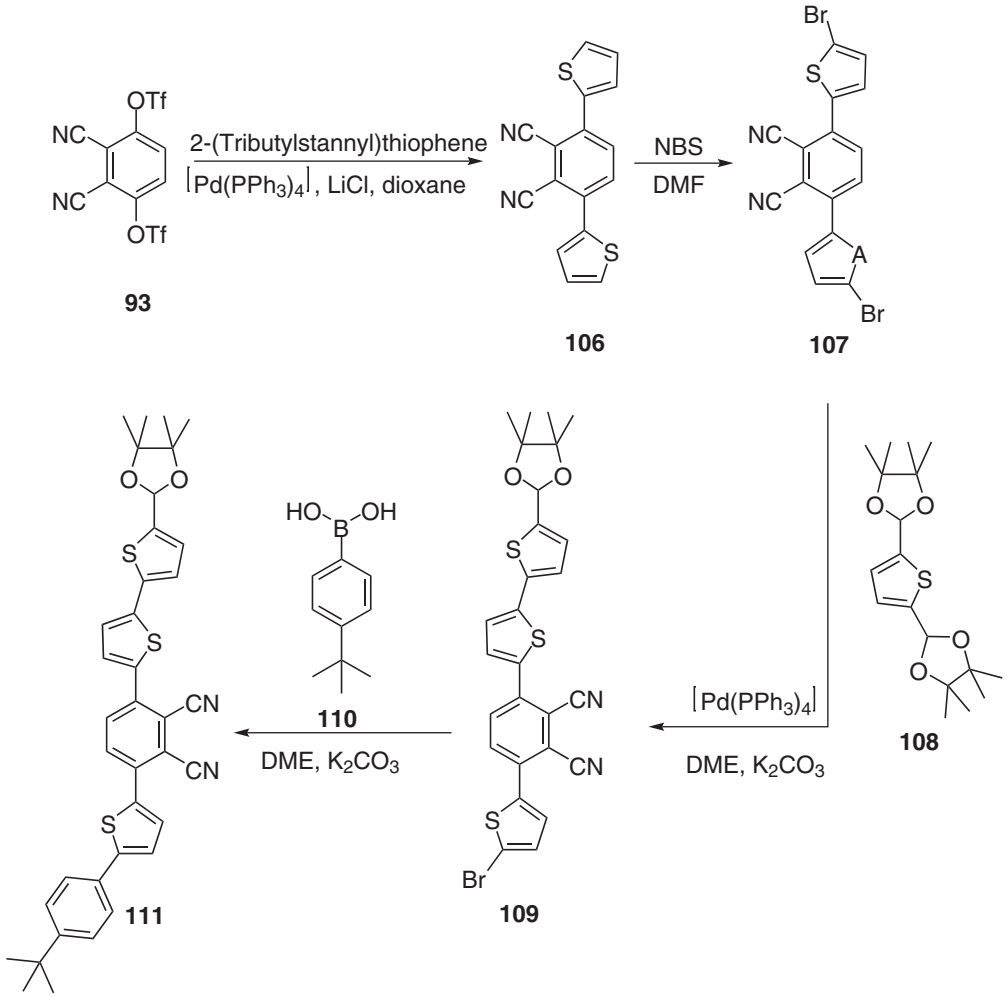

Scheme 5.15 Asymmetrically substituted phthalonitrile prepared via successive organometallic couplings. Source: Modified from Yamamoto et al. [67].

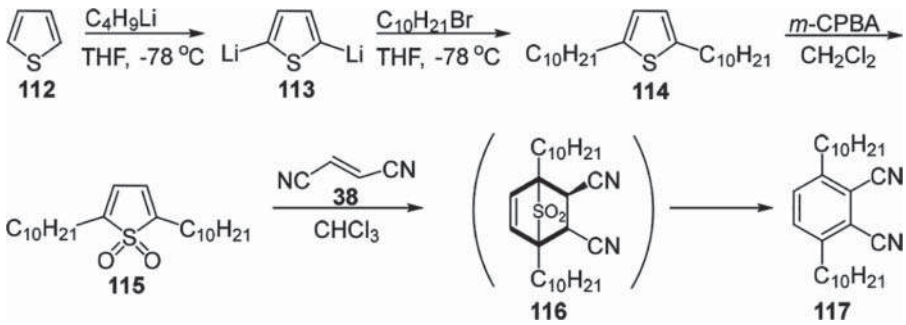

Scheme 5.16 3,6-Alkylphthalonitriles prepared via a Diels-Alder reaction. Based on Cook and Cracknell [71].

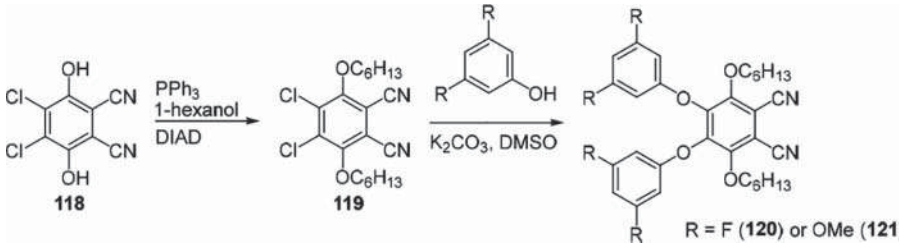

Scheme 5.17 Phthalonitriles prepared via the Mitsunobu reaction. Source: Modified from Al-Raqa [50].

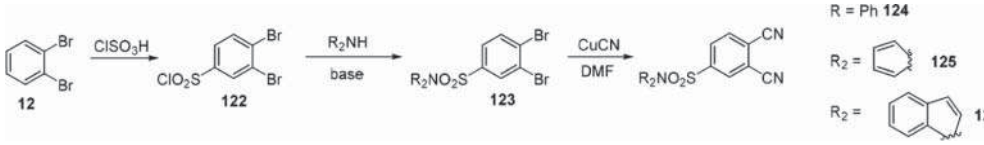

Scheme 5.18 Syntheses of protected sulfonated phthalonitriles. Based on Li et al. [72].

Finally, *tert*-butylphthalonitrile is widely used and commercially available, although its synthesis is reported by different routes [74].

5.3.3 Diiminoisoindolines

These derivatives are prepared by refluxing the corresponding phthalonitrile in methanol with ammonia bubbling in the presence of sodium methoxide. Their preparation is thus limited to derivatives that do not carry ammonia- or base-sensitive substituents. The resulting diiminoisoindoline has two tautomeric forms (Scheme 5.19), both of which could be isolated for the non-substituted derivative [75]. Their crystallographic structures showed different conformations and polymorphism.

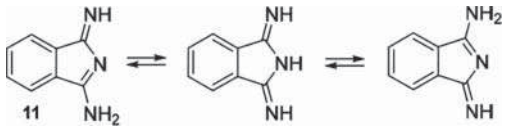

Scheme 5.19 Tautomeric forms of diiminoisoindoline (**11**). Based on Zhang et al. [75].

The high reactivity of the diiminoisoindolines prevents chromatographic purification, and the reaction is considered to be quantitative. Most diiminoisoindoline products precipitate when the reaction mixture is cooled down and can be isolated by a simple filtration. For other derivatives, evaporation of the methanol and re-dissolution of the diiminoisoindoline in an organic solvent allow its recovery it with elimination of the salts [76].

5.3.4 Trichloroisoindolenines

Trichloroisoindolenines are probably the only phthalocyanine precursors that do not react with themselves. They are prepared from corresponding phthalamides in refluxing *o*-dichlorobenzene in the presence of freshly sublimated PCl_5 (Scheme 5.20a). These harsh conditions limit the preparation to derivatives with substituents that are unlikely to be chlorinated. So far, only the derivatives (**127**–**129**) represented in Scheme 5.20b are reported. Trichloroisoindolenines are very sensitive to oxidation and are isolated by distillation followed by sublimation whenever possible. This latter technique resulted in obtaining suitable crystals of 1,3,3-trichloroisoindolenine (**128**) [77] and of 1,3,3,6,7-pentachloroisoindolenine (**128**) [78].

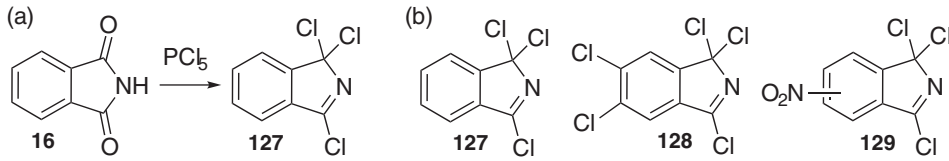

Scheme 5.20 Preparation of (a) trichloroisoindolenines; (b) three trichloroisoindolenine derivatives.

5.3.5 Porphyrazine Precursors

Sodium maleonitriledithiolate (**130**) can perform nucleophilic substitutions to yield substituted maleonitriles, for example, the preparation of **131** (Scheme 5.21) [79]. Macrocyclic-substituted compounds (**133** and **134**) can also be obtained [80, 81].

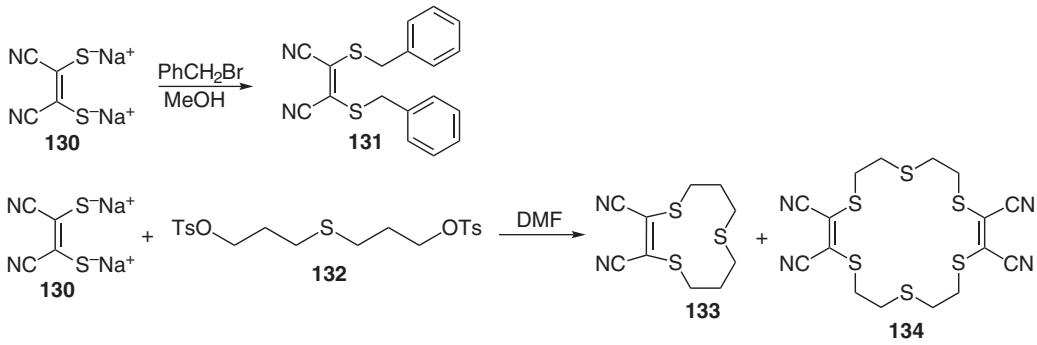

Scheme 5.21 Preparations of substituted maleonitriles via nucleophilic substitution on sodium maleonitriledithiolate (**130**). Based on Veliizquez et al. [79].

Benzonitriles react with sodium methoxide and iodine, following Linstead's procedure for the oxidative coupling of substituted acetonitriles [82], to yield substituted maleonitriles (**137**) (Scheme 5.22) [83].

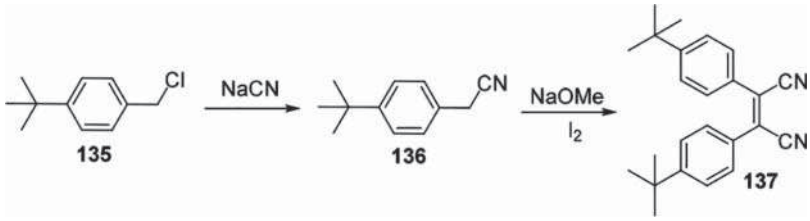

Scheme 5.22 Preparation of substituted maleonitrile via Linstead's procedure. Based on Baumann et al. [83].

Spiro-substituted derivatives (**142**) can be obtained from L-(+)-dimethyl tartrate (Scheme 5.23) [84].

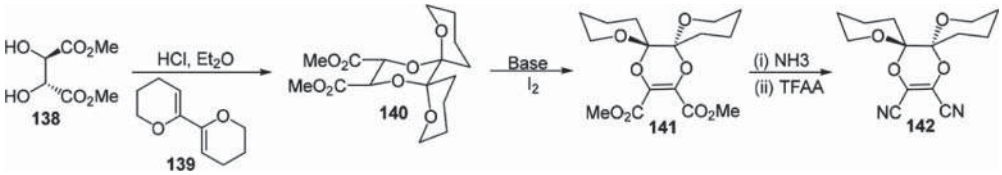

Scheme 5.23 Preparation of spiro-substituted maleonitrile. Source: Cook et al. [84].

2,3-Diaminomaleonitrile can undergo successive reactions such as for derivative **148** (Scheme 5.24) [85].

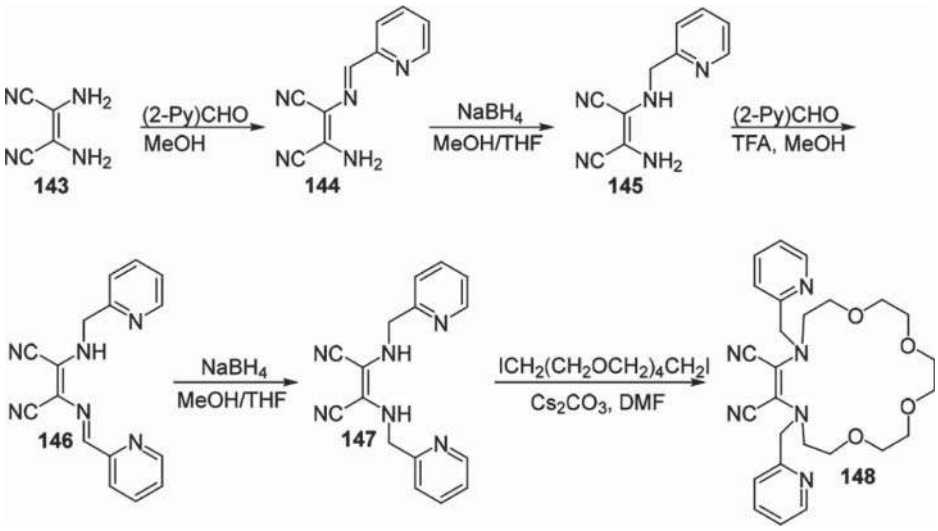

Scheme 5.24 Reactions of 2,3-diaminomaleonitrile. Source: Modified from Beall et al. [85].

5.3.6 Tetrapyridinoporphyrazine Precursors: Dicyanopyridines

Tetrapyridinoporphyrazines are obtained by the cyclotetramerization of commercially available pyridine-3,4-dicarbonitrile (**22**) or pyridine-2,3-dicarbonitrile. They are quite expensive and can instead be prepared, respectively, from cinchomeronic acid (**149**) [70]

(Scheme 5.25) or quinolinic acid [86]. The synthetic sequence is similar to the synthesis of 4,5-dichlorophthalonitrile.

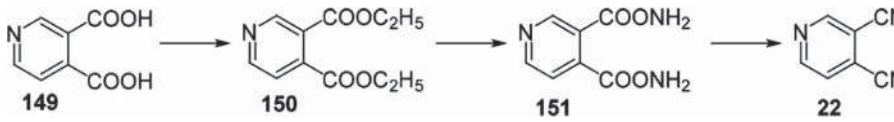

Scheme 5.25 Synthesis of pyridine-3,4-dicarbonitrile (**22**). Source: Sakamoto et al. [86].

Quasi-unique substituted derivatives were prepared from the dimethylated chlorinated synthon **154** (Scheme 5.26) [87].

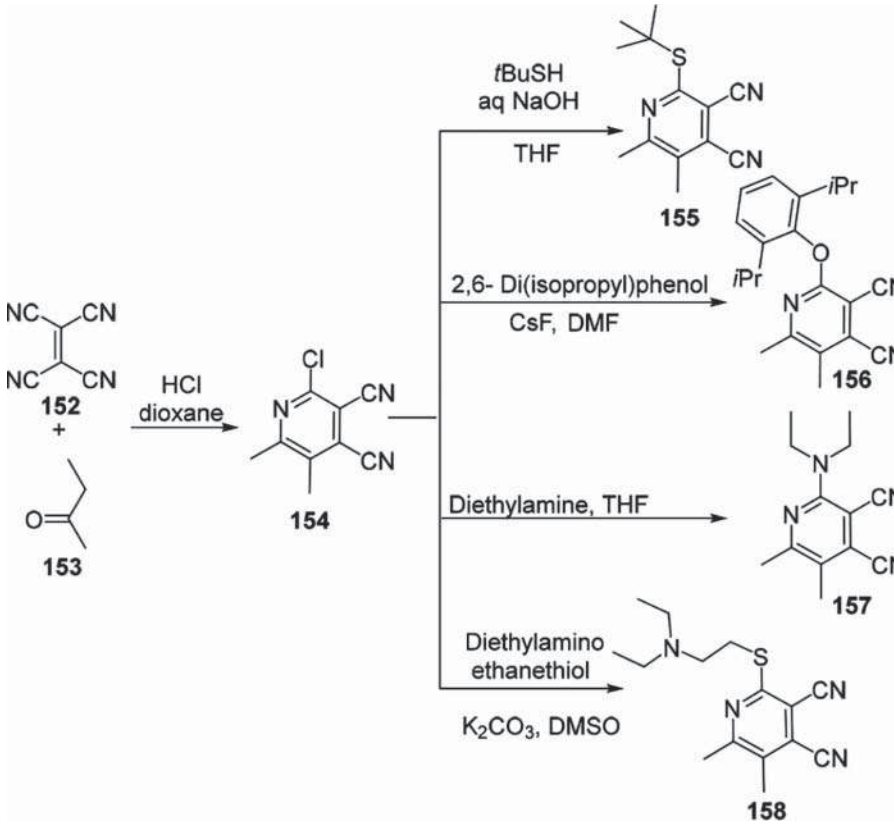

Scheme 5.26 The use of synthon (**154**) to prepare several substituted pyridine-3,4-dicarbonitriles. Source: Modified from Vachova et al. [87].

5.3.7 Azaphthalocyanine Precursors

Precursors of azaphthalocyanines are substituted pyrazine-2,3-dicarbonitriles that have two important preparative routes. First of these is the reaction of 2,3-diaminomaleonitrile (**143**) with diketones (**159**) (Scheme 5.27) [88] in which the acetal-protected diketone can be regenerated in situ [89], possibly with asymmetrically substituted diketones [90].

The alternative is nucleophilic substitution of 5,6-dichloro-pyrazine-2,3-dicarbonitrile (**162**), which is strongly activated due to the electron-withdrawing character of the nitrile,

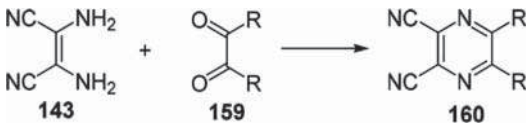

Scheme 5.27 Synthesis of substituted pyrazine-2,3-dicarbonitriles from the reaction of 2,3-diaminomaleonitrile (**143**) with diketones. Based on Mohr et al. [88].

by primary and secondary amines, alcoholates, or thiolates. 5,6-Dichloro-pyrazine-2,3-dicarbonitrile (**162**) is itself prepared in two steps by the condensation of oxalyl chloride with 2,3-dioxo-1,2,3,4-tetrahydropyrazine-5,6-dicarbonitrile (**161**) followed by halogenation using thionyl chloride (Scheme 5.28) [27].

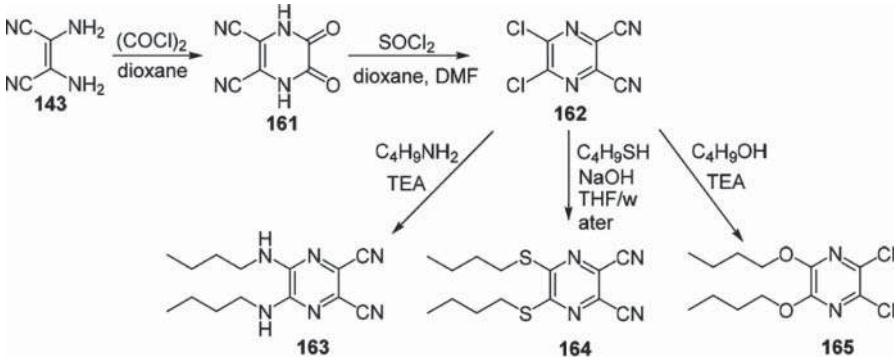

Scheme 5.28 Synthesis of substituted pyrazine-2,3-dicarbonitriles via nucleophilic substitution of 5,6-dichloro-pyrazine-2,3-dicarbonitrile (**162**). Source: Modified from Zimcik et al. [27].

Similarly, the protected ketones of compound **166** can be first hydrolyzed and then reacted with diaminomalonitrile to produce dicarbonitrile **167**.

5.4 Formation of Macrocycles with Asymmetric Substitution Patterns

The preparation of phthalocyanines and porphyrazines with asymmetric substitution patterns quickly became a goal after the first soluble phthalocyanines were obtained. Many reviews were written at regular intervals [91]. Asymmetrically substituted macrocycles can be prepared, in theory, by mixing two (or more) different precursors. The main problem is then the separation and the identification of the several derivatives obtained. The formation of the desired compound can be favored by adjusting the relative amount of the precursors utilized in the macrocycle formation. More selective methods have been developed to increase the yields and facilitate the purification.

5.4.1 Statistical Mixtures of Precursors for Asymmetric Substitution Patterns

The ratio of mixed substitution patterns is directly related to the statistical ratio of the mixture of precursors engaged in the reaction. Mathematically expected ratios of different mixed

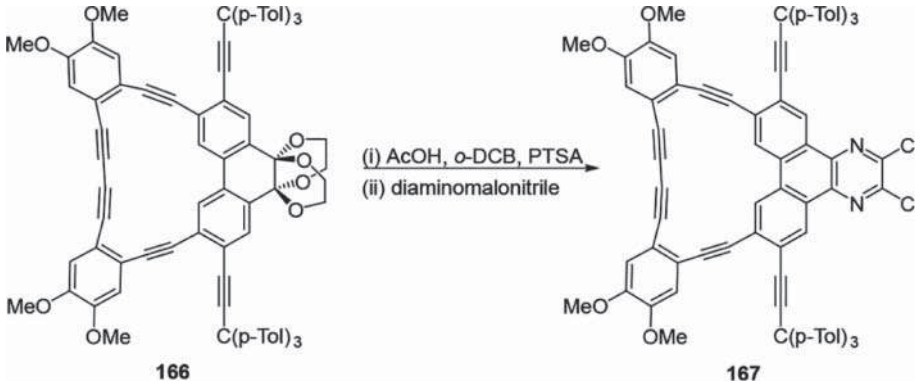

Scheme 5.29 Synthesis of an elaborate substituted pyrazine-2,3-dicarbonitrile (**167**) via a protected ketone.

Table 5.1 Mathematically expected ratios of resulting substitution patterns when mixing two precursors A and B.

A/B ratio	AAAA	AAAB	AABB	ABAB	ABBB	BBBB
1:1	6.25	25	25	12.5	25	6.25
3:1	31.6	42.2	14.1	7.0	4.7	0.4
9:1	65.6	29.2	3.2	1.6	0.4	0.01

substitution patterns obtained by mixing two precursors having the same reactivity are summarized in Table 5.1.

For more complicated mixtures, Lindsey and co-workers developed the *PorphyrinViLiGe* [92] and *Cyclaplex* [93] programs, which are designed to "simulate combinatorial processes and to enumerate products and isomers in the domain of porphyrins (and other tetrapyrrole macrocycles)" and to "simulate combinatorial processes that give rise to linear and cyclic oligomers," respectively [94].

Asymmetrically substituted subphthalocyanines have been prepared by the same statistical methods, either to yield fused dimeric structures (A2B-BA2) such as the perfluoro derivatives **170** (*cis* and *trans*) concomitantly reported by Torres [95] and Kobayashi and Durfee [96] (Scheme 5.30), or A2B derivatives [97]. Trimeric structures have been reported as well [98]. When a linked B-B precursor such as 1,2,4 5-tetracyanobenzene **169** is used, obtaining only A3B-BA3 requires increasing the relative quantity of A (phthalonitrile **168** in Scheme 5.30) [99]. It is possible to use a mixture of precursors of different types [100].

Bisphthalonitriles with longer and rigid spacers (such as 1,8-naphthalene) are used to prepare clam-shell dimeric phthalocyanines [101], while flexible spacers allowed the preparation of ball-type phthalocyanines (Figure 5.12) [102].

5.4.2 Selective Preparation of A3B

Subphthalocyanine expansion. Kobayashi et al. reported in 1990 the ring expansion of an A-substituted subphthalocyanine by reacting it with a B-substituted diiminoisoindoline to lead selectively to A3B type asymmetrically substituted phthalocyanines (Figure 5.13) [103].

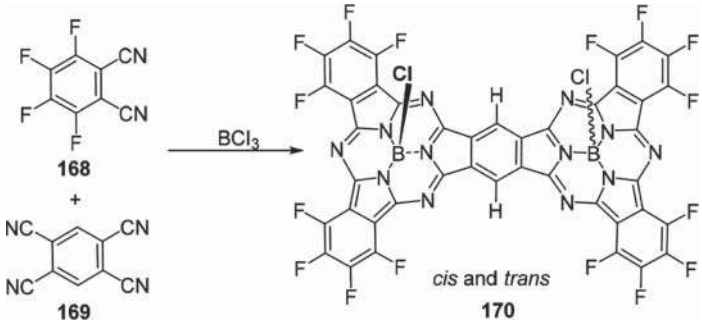

Scheme 5.30 Synthesis of a fused, isomeric bis-subphthalocyanines (**170**). Based on Fukuda et al. [96].

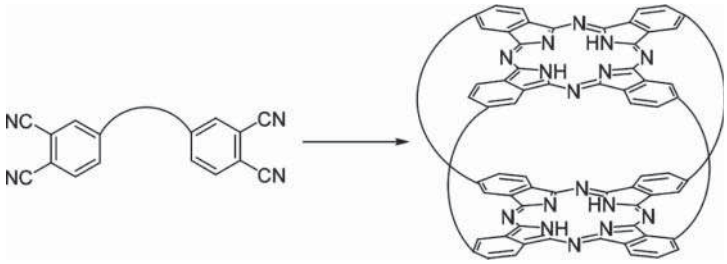

Figure 5.12 Generic representation of the synthesis of ball-type phthalocyanines. Based on Tolbin et al. and Ceyhan et al. [102].

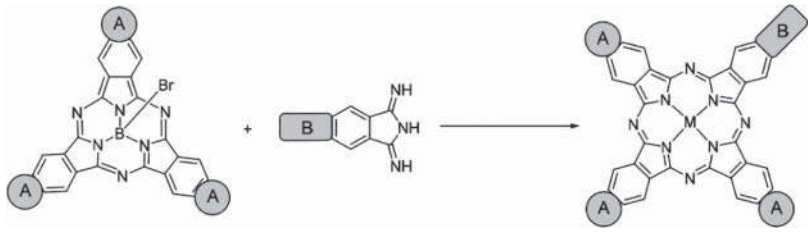

Figure 5.13 Selective preparation of A3B by the subphthalocyanine expansion method. Based on Kobayashi et al. [103].

Spectrophotometric studies showed that the subphthalocyanine ring first opens, then undergoes a statistical reaction with the diiminoisoindoline, the reaction having a first-order rate (based on the subphthalocyanine). Consequently, the reaction is not entirely selective, and other asymmetrically substituted phthalocyanines are also obtained in small amounts.

Polymer-supported synthesis of A3B. Two methods using polymer supports are reported to prepare A3B derivatives in which B bears a chemical function XH. Their interest is to facilitate the separation of the desired A3B derivatives from the others inevitably formed when two precursors are used. Rather than chromatographic separation, polymer-assisted methods require at some point of the synthesis to have the A3B derivative bound to a polymer while A4 is free and removed by washing, followed by the cleavage of the desired A3B derivative from the polymer. Two methods have been developed and are schematically represented in Figure 5.14 while their successive steps are reported in Table 5.2.

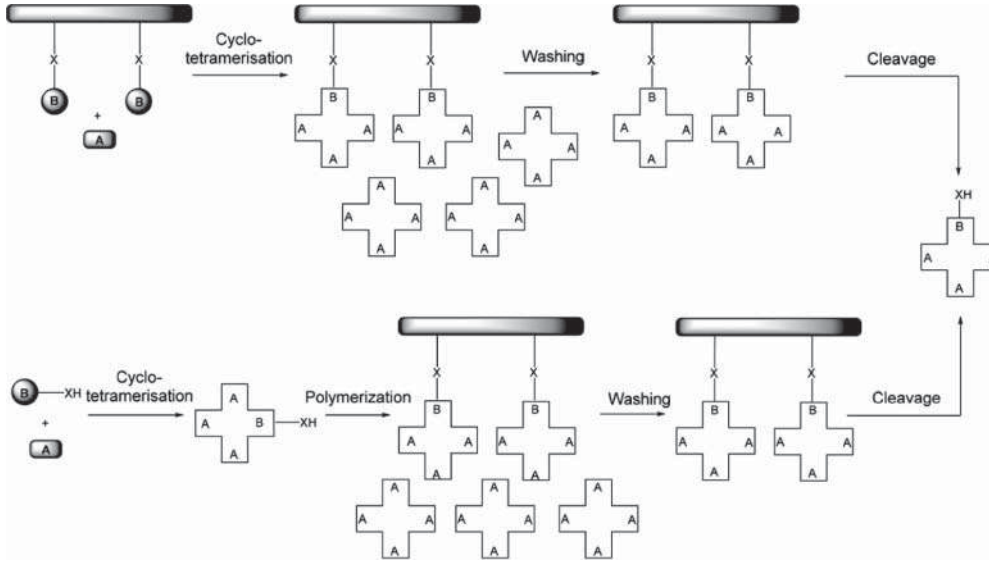

Figure 5.14 The two different methods of polymer-supported syntheses of A3B derivatives.

Table 5.2 The different steps of the two polymer-supported methods for the synthesis of A3B derivatives.

Step #	Method 1	Method 2
1	Preparation of resin-X-B	Cyclotetramerization of a mixture of B-XH and A-precursors
2	Cyclotetramerization and formation of resin-X-BA3 + A4	Binding of A3B-XH to the polymer
3	Removal of A4 by washings	Removal of A4 by washings
4	Cleavage from resin and release of A3B-XH	Cleavage from resin and release of A3B-XH

In the first method, precursor B is first bound to a poly(ethylene glycol) (PEG)-based support with a Wang-type X linker [104]. The cyclotetramerization is then made with a large excess of A-precursor, giving a mixture of free A4 and A3B derivatives bound to the polymer. Free symmetrically substituted A4 derivatives are easily eliminated, and the desired XH-functionalized A3B derivative is cleaved from the polymer.

The second method is based on the use of the ring-opening metathesis polymerization (ROMP)-Capture-Release sequence [105]. Precursor B with an XH function reacts with a large excess of precursor A. The resulting mixture (A4 + A3B-XH) reacts with the polymer that binds the A3B derivative. A4 is then eliminated, and the desired A3B-XH is finally cleaved.

5.4.3 Selective Preparation of ABAB

Two methods are available for the selective preparation of ABAB phthalocyanines: the trichloroisoindolenenine-based chemoselective method and the steric-directed method.

The trichloroisoindolenenine-based chemoselective method. This is based on the fact that trichloroisoindolenenines cannot react with themselves, but do react with diiminoisoindolines. Slow addition of an A-substituted diiminoisoindoline (**171–173)** in the presence of triethylamine to a solution of B-substituted tricloroisoindolenine (**129**) (or the opposite) is performed at 0 °C, followed by stirring at room temperature for a few hours. The reaction proceeds under very mild conditions (refluxing THF in the presence of hydroquinone and sodium methoxide). The reaction mixture is then filtered to eliminate salts, being kept as much as possible under inert atmosphere during this step. After addition of sodium methoxide and hydroquinone to the filtered solution, the reaction mixture is refluxed overnight. The desired compound (**174–176**) is then obtained (Scheme 5.31) with possible contamination by A3B and A4 derivatives. The scope of the reaction is limited by the number of available trichloroisoindolenenines but remains useful for preparing compounds of high interest [106].

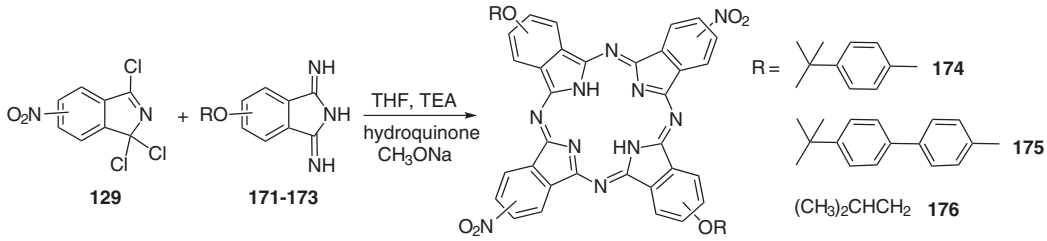

Scheme 5.31 Preparation of an ABAB phthalocyanine by the trichloroisoindolenenine-based chemo-selective method.

Selective preparation of ABAB by the steric-directed method. This method is based on the fact that phthalonitriles bearing sterically demanding substituents do not tend to get close to each other. Indeed, two molecules of phthalonitrile **105** (formed by the reaction of boronic acid **104** on activated precursor **91** or **93**) cannot come close to each other. A mixture of phthalonitrile **105** and phthalonitrile **52** (or **59**) will produce preferentially derivatives **177**, **178**, or **179**, but not the derivatives in which the steric substituents would be adjacent (Scheme 5.32) [10]. The same method has been applied to the preparation of amphiphilic porphyrazines [86]. The reported yield of ABAB obtained by mixing nearly 9 equivalents of phthalonitrile with 1 equivalent of 3,6-didedocyloxyphthalonitrile [107] is therefore questionable as one would expect to obtain mainly the A3B derivative as shown by the mathematically expected ratio in Table 5.2.

5.4.4 Selective Preparation of Adjacent AABB

AABB phthalocyanines are prepared by three selective methods, in addition to the statistical method: the so-called bridge method, the Leznoff method, and the post-adjacent disubstitution method. Each has been applied in only a few instances, and their versatility still has to be assessed with the preparation of more numerous structures.

The bridge method. This is based on the use of dimeric precursors reacting with a second monomeric precursor. In most cases, the precursors are phthalonitriles, but their more reactive diiminoisoindoline forms can be used as well. The first example reported by Leznoff used a propanediol spacer (phthalonitrile **181** prepared from **35** and **180**) that underwent the cyclotetramerization reaction to give phthalocyanine **182**. After optimization, the use of

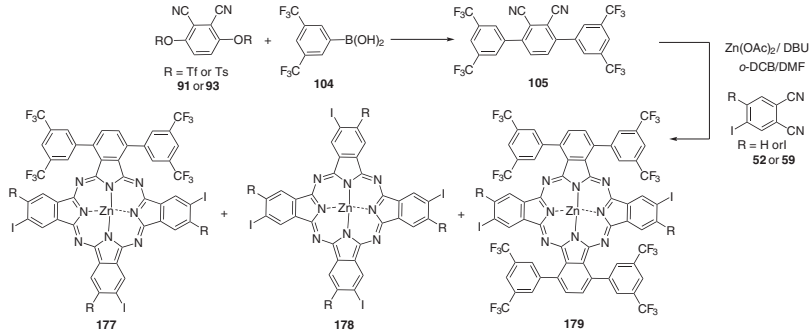

Scheme 5.32 Preparation of an ABAB phthalocyanine by the steric-directed method. Source: Fazio et al. [10].

dilute conditions and the Li/octanol base proved to be the best method [108]. It actually gives the AABB derivative **182** in which AA = BB (Scheme 5.33).

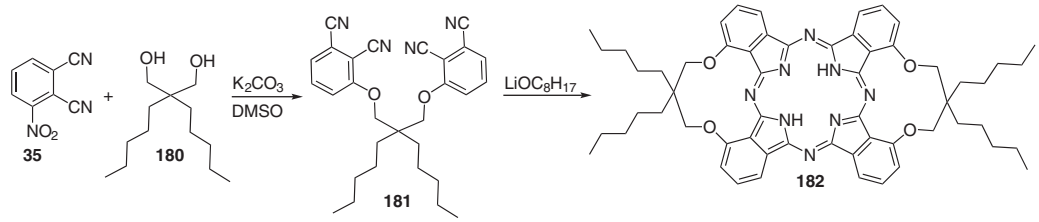

Scheme 5.33 Preparation of an adjacent AABB phthalocyanine by the bridge method.

The same principle was applied to a mixture of a dimeric diiminoisoindoline and a monomeric diiminoisoindoline, the spacer of the dimeric derivative being a rigid unit [109]. Other derivatives (**183–185**), including non-centrosymmetric structures have also been obtained (Figure 5.15) [110].

Using different precursors leads to hybrid derivatives, such as adjacent dibenzotetraazaporphyrin, which is a structural intermediate between tetraazaporphyrin and phthalocyanine [111].

Leznoff method. A half-phthalocyanine intermediate bearing H (**188**) or 3,3-dibutynyl (**187**) substituents can react with phthalonitriles to produce AABB-type phthalocyanines (**189**) (Scheme 5.34). Unless previously stated [15, 112], the scope of the reaction was not limited to the use of electron-withdrawing substituents to form the half-phthalocyanine intermediate.

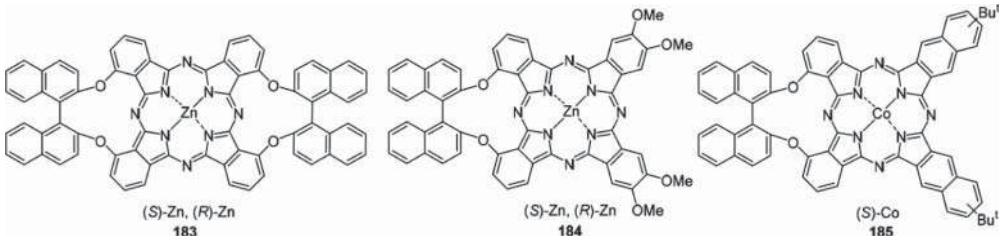

Figure 5.15 Examples of AABB phthalocyanines prepared by the bridge method.

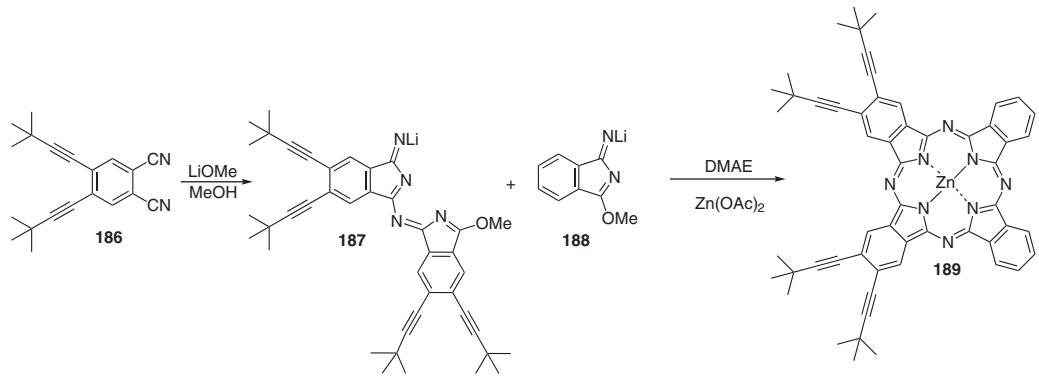

Scheme 5.34 Preparation of an adjacent AABB phthalocyanine by the Leznoff method.

Post-adjacent disubstitution method. Finally, an amphiphilic water-soluble phthalocyanine (**194–196**) was prepared by reacting cyclodextrins (**191–193**) with hexadecafluorophthalocyanine (**190**), which is sensitive to nucleophilic substitutions, in this case performed by the cyclodextrin (Scheme 5.35) [113].

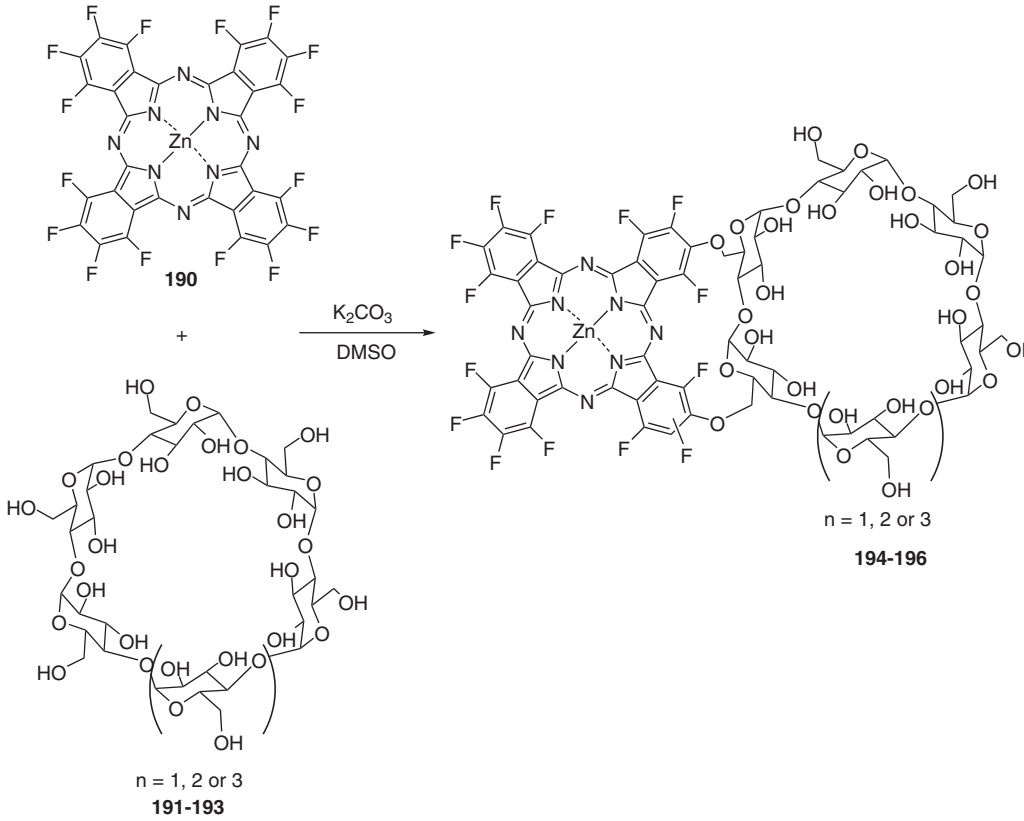

Scheme 5.35 Preparation of an adjacent AABB phthalocyanine by the post-adjacent disubstitution method. Based on Lourenço et al. [113].

5.4.5 ABAC

The expansion of an A2B subphthalocyanine (**197**, **198**) by a C-substituted diiminoisoindoline (**199**) led to several phthalocyanines (**200–203**) bearing three different substituents, the resulting substitution pattern being ABAC or AABC (Scheme 5.36) [97].

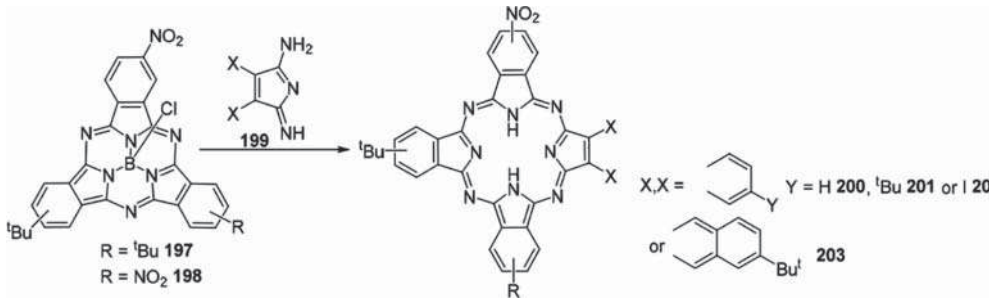

Scheme 5.36 Preparation of ABAC or AABC phthalocyanines by expansion of A2B subphthalocyanine. Source: Modified from Ali et al. [97].

A more selective method based on the diversion of the trichloroisoindolenenine (**127**)-based chemoselective method to prepared ABAB phthalocyanines (**206**) was used to obtain an ABAC derivative, using a mixture of two diiminoisoindolines (**204** and **205**) with the trichloroisoindolenenine **127** (Scheme 5.37) [76].

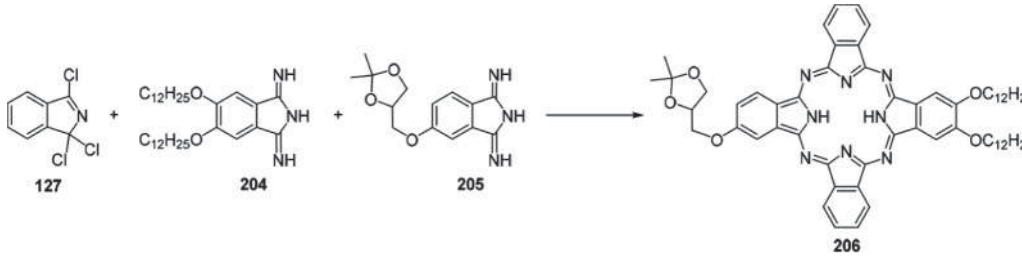

Scheme 5.37 Preparation of an ABAB phthalocyanine from a trichloroisoindolenenine precursor. Source: Dumoulin et al. [76].

With an entirely different synthetic strategy, triazolephthalocyanines with an ABAC pattern, such as derivative **212**, can be prepared by reacting 3,5-diamino-1,2,4-triazole **207** (guanazole) with two diiminoisoindoline units (**208**), followed by metallation and reaction with another diiminoisoindoline unit (**211**) (Scheme 5.38) [28, 114].

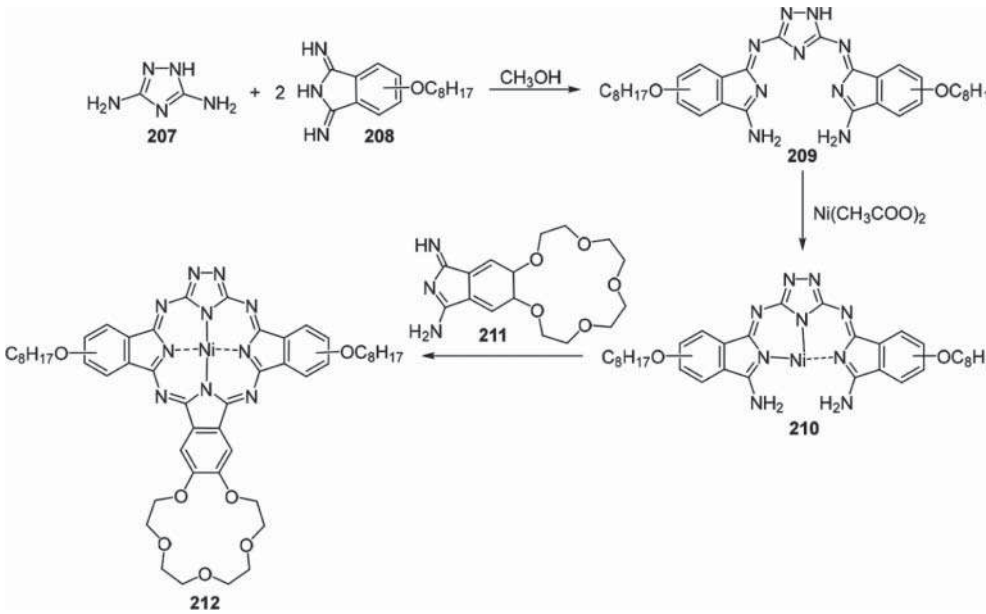

Scheme 5.38 Syntheses of triazolephthalocyanines with an ABAC pattern. Based on Cabezon et al. [28]; Cabezon et al. [114].

5.4.6 ABCD

The elegant and selective synthesis of phthalocyanines in which each isoindole subunit has different substituents – ABCD derivative – was reported by Ng et al. (Scheme 5.39) [115]. It is

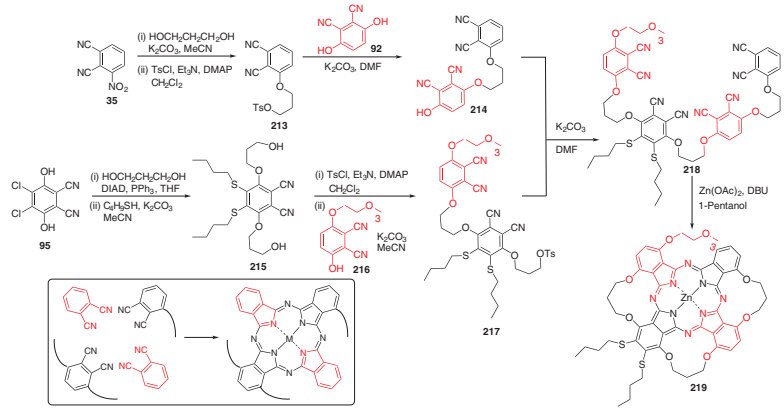

Scheme 5.39 An elegant and selective synthesis of the first ABCD phthalocyanine. Source: Chow and Ng [115].

based on the pre-linkage of four phthalonitriles, which subsequently undergo an intramolecular cyclization reaction. Tosylated phthalonitrile **213** prepared in two steps from **35** reacts with an excess of dicyanohydroquinone **92**, yielding monohydroxylated diphthalonitrile **214**. The reported yield of 7.2% is outstandingly high for such a complicated, multi-step synthesis. On the other hand, dihydroxylated phthalonitrile **215** prepared from **95** is ditosylated and then reacted with one equivalent of monohydroxylated phthalonitrile **216** to yield monotosylated diphthalonitrile **217**. Compounds **214** and **217** react with each other, giving the tetraphthalonitrile **218**, which then undergoes an intramolecular cyclotetramerization (schematically represented in the inset of Scheme 5.39), producing the first ABCD phthalocyanine **219** ever reported.

5.5 Lanthanide Double- and Multi-Decker Derivatives

5.5.1 Structural Variations: Homoleptic and Heteroleptic, Homometallic and Heterometallic Complexes

Metals from the lanthanide series (Ln, rare-earths) can coordinate two porphyrinoid macrocycles. Such complexes are called double-deckers. The same porphyrinoid macrocycle can also participate in the coordination of two metal atoms (same or different), leading to triple or multi-deckers. Compared to monomeric "mono-decker" derivatives, the number of theoretically possible structural variations is multiplied by the number of macrocycles involved. In addition, triple-decker and superior arrays may coordinate different metal atoms, which also increases the possible variations. These different structural variations are schematically represented in Figure 5.16.

When the substitution pattern (symmetric or asymmetric) of each porphyrinoid macrocycle is identical, the complex is homoleptic. In the case of triple-deckers, if the metal atoms involved in these complexes are identical, the complexes are homoleptic and homometallic. In the vast majority of the cases, homoleptic double-decker complexes comprise phthalocyanines, although a few homoleptic complexes containing porphyrins [116] have been reported.

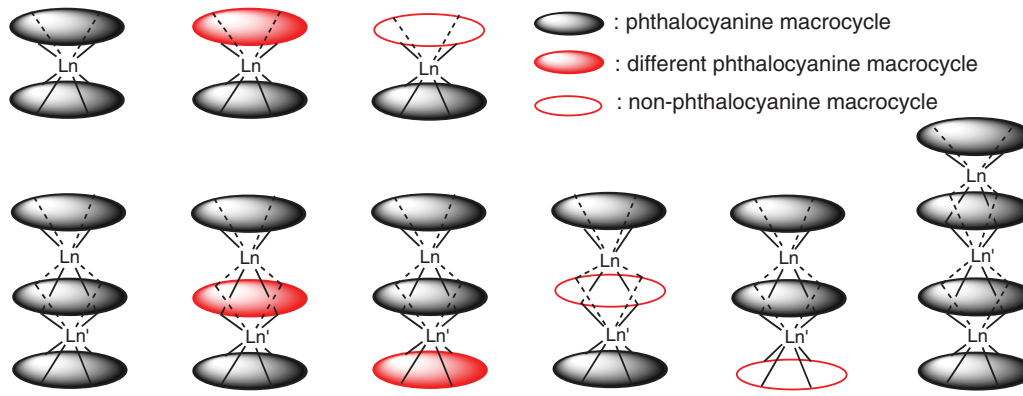

Figure 5.16 The different types of lanthanide (Ln) double and multiple deckers involving phthalocyanines.

Heteroleptic complexes are made of two (or more) porphyrinoids of different nature, either two different phthalocyanines, or one phthalocyanine and another porphyrinoid. Double-decker complexes made of one phthalocyanine and one other porphyrinoid (frequently a porphyrin) are quite common, such as triple-deckers made of two phthalocyanines and a different porphyrinoid. In this latter case, the other porphyrinoid can be intercalated between the two phthalocyanines or be at one end of the sequence. Triple-deckers can be homo- or heterometallic, increasing the number of possibilities. Quadruple-deckers are reported as well. Such complexes have multiple oxidations states; see Chapter 4.

5.5.2 Pc-Pc Homoleptic Lanthanide Double-Decker Complexes from Precursors

These complexes contain macrocycles with a symmetric substitution pattern, and bear only one type of substituent. Heating phthalonitriles (**13**) in the presence of a base and a lanthanide salt (chloride, acetate, or acac) leads to the formation of the corresponding double-decker (**222**) or triple-decker complex (**223**), depending on the salt/phthalonitrile ratio. Free-base (**220**) and monomeric Ln-metallated (**221**) phthalocyanines can be observed as well (Figure 5.17). The yields depend on the metal, and more precisely on its size. Metal atoms with small or large ionic size are obtained in lower yields than when a metal from the middle of the lanthanide series is used.

5.5.3 Pc-Pc Heteroleptic Lanthanide Double-Decker Complexes from Precursors

Rare attempts to use mixture of two different phthalonitriles have led to mixtures of asymmetrically functionalized double-deckers that are difficult to separate and are formed in low yields [117]. This has been then rationalized with a careful optimization of the phthalonitrile mixture (**224** and **225**), to obtain heteroleptic double-decker complexes functionalized on only one isoindole subunit – and hence named A7B **226** – and the symmetrically substituted **227** (Scheme 5.40).

Mixtures of diiminoisoindoline (**228**) and phthalonitrile (**229**) have been reported as well to yield an unusual bridged structure (**230**) (Scheme 5.41) [118].

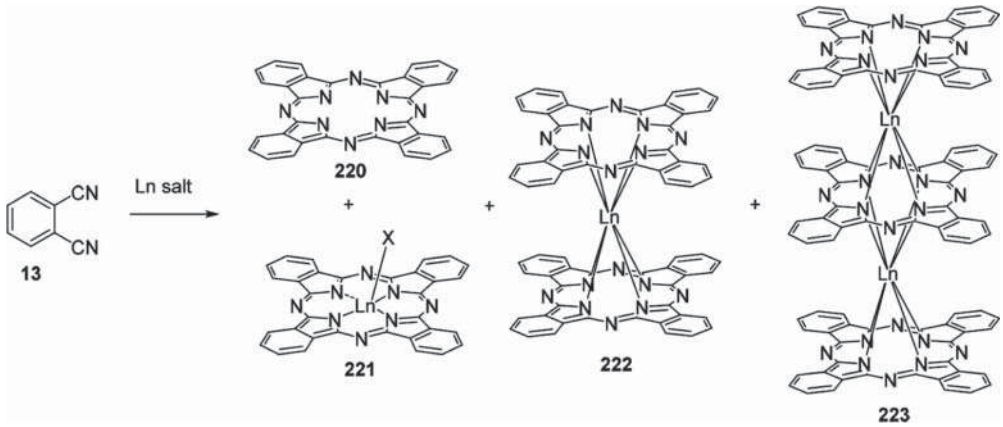

Figure 5.17 The different species obtainable when reacting a single phthalonitrile with a lanthanide salt.

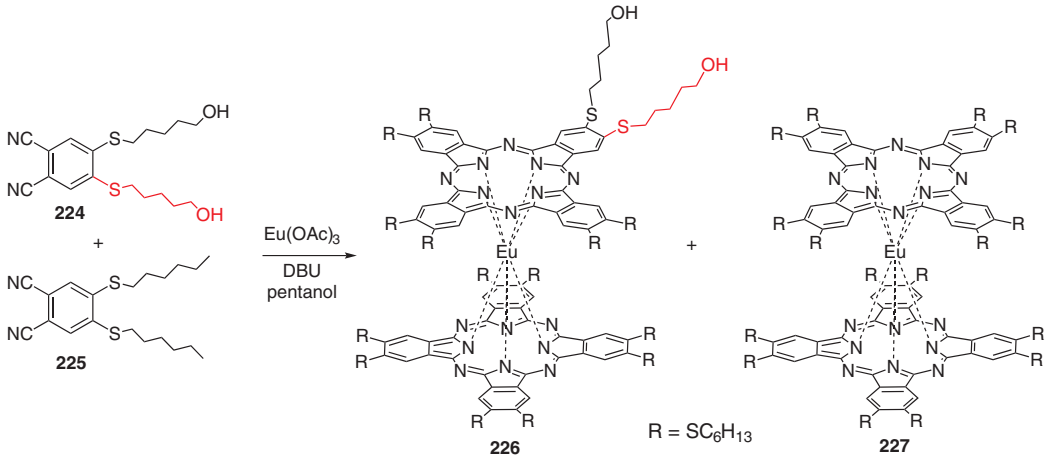

Scheme 5.40 Preparation of a heteroleptic lanthanide double-decker complexe A7B (**226**) and it's homoleptic relative (**227**).

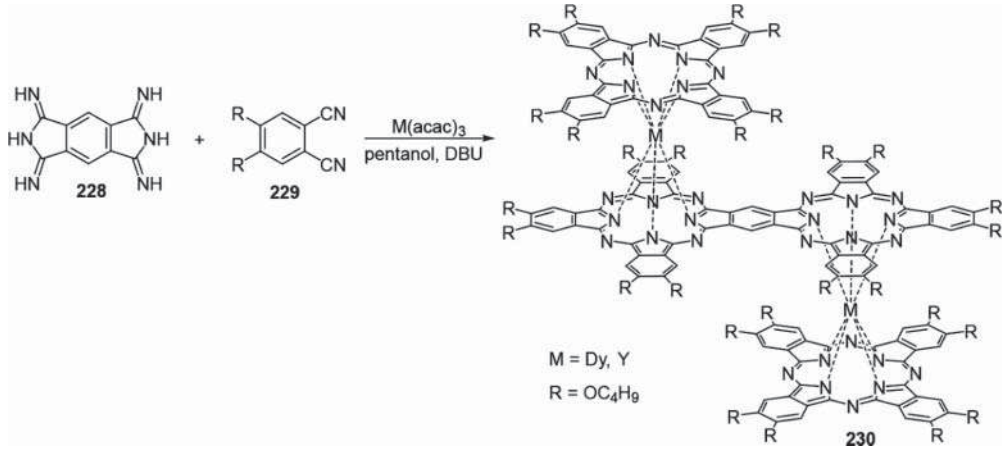

Scheme 5.41 Synthesis of a bis double-decker phthalocyanine complex. Source: Modified from Wang et al. [118].

5.5.4 Pc-Pc Homoleptic Lanthanide Double-Decker Complexes from Pre-Formed Macrocycles

Free-base phthalocyanines, when heated at high temperature (frequently >180 °C, usually in chloronaphthalene) in the presence of lanthanide salts, lead to double or multi-decker complexes. Double-decker **232** was obtained by this method from unmetallated phthalocyanine **231** (Scheme 5.42) [106]. The quantity of lanthanide salt must be carefully adjusted depending on the target molecule. This method can also be applied to exotic derivatives such as diazepinoporphyrazines [119].

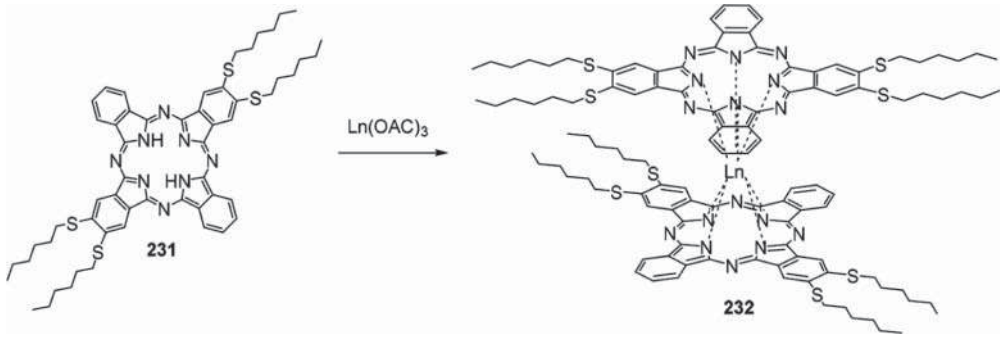

Scheme 5.42 Synthesis of a double-decker phthalocyanine. Based on Ayhan et al. [106].

5.5.5 Pc-Por Heteroleptic Lanthanide Double and Triple-Deckers from Formed Macrocycles

Pc-Por heteroleptic lanthanide double and triple-deckers can be obtained by heating a mixture of Ln-porphyrin and Li_2(Pc) (**234**). The porphyrin (**233**) is first metallated by the lanthanide and then reacted with Li_2Pc. The resulting mixtures (**235**–**239**) can be separated by thorough chromatographic purifications, the order of elution being indicated in Scheme 5.43 [120].

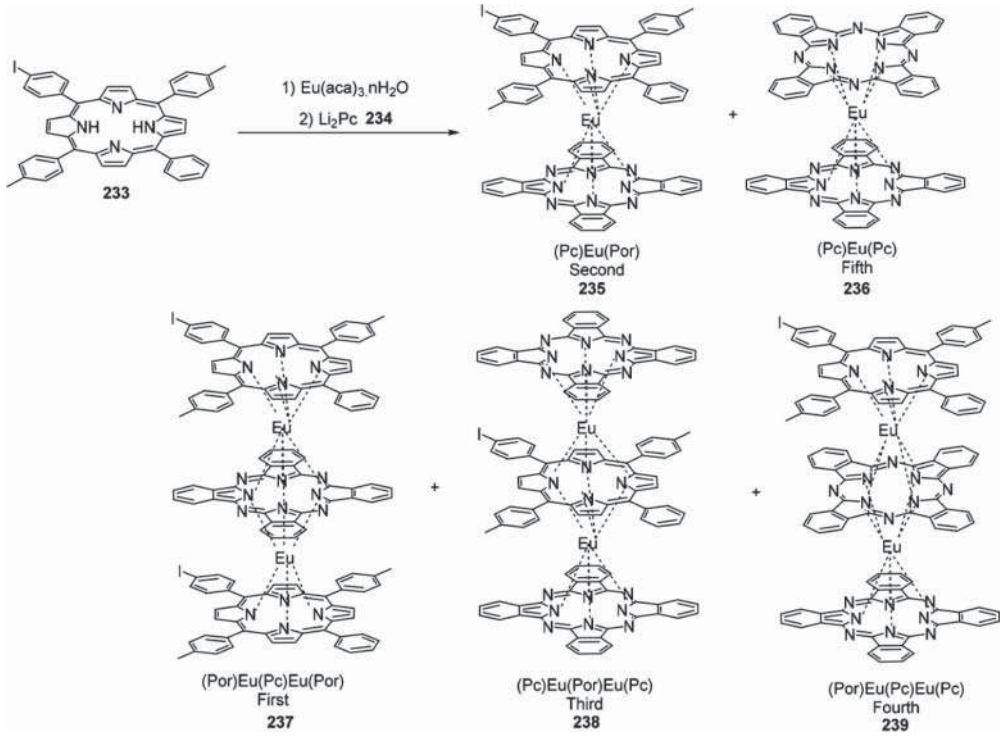

Scheme 5.43 Synthesis of lanthanide double- and triple-decker phthalocyanines. Source: Modified from Li et al. [120].

Conversely, corrole-Pc heteroleptic complexes are obtained by first preparing Ln-metallated phthalocyanine and then reacting then with corrole [121]. Playing with the stoichiometry and the reaction duration allows the composition of the mixture to be optimized for a majority of the desired derivative [122].

5.5.6 Sequential Preparation of Pc-Por and Pc-Pc Double-Deckers

Ln-metallated porphyrin (**241**) made from **240** reacts with phthalonitrile (**242**) to form Por-Pc heteroleptic double-deckers (**243**) (Scheme 5.44) [123].

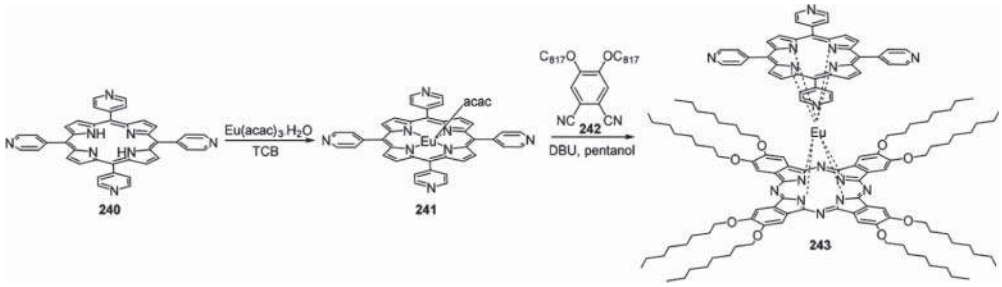

Scheme 5.44 Synthesis of a heteroleptic porphyrin-phthalocyanine double-decker. Source: Modified from Zhu et al. [123].

Li-metallated phthalocyanine (**244**) is formed in situ and react with another Li_2Pc (**234**) to yield double-decker **245** (Scheme 5.45) [124]. It is also possible to Ln-metallate a phthalocyanine and to introduce a phthalonitrile to obtain heteroleptic Pc-Pc double-deckers.

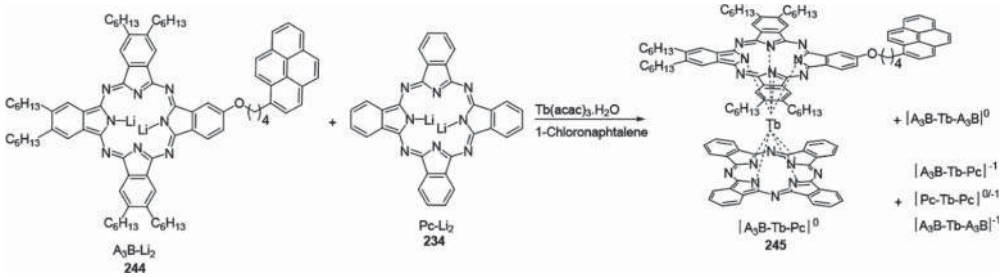

Scheme 5.45 Synthesis of a heteroleptic phthalocyanine double-decker from a lithium phthalocyanine precursor. Source: Modified from Kyatskaya et al. [124].

5.6 Other Double- and Multi-Decker Derivatives

5.6.1 Phthalocyanine-Based N- (μ-Nitrido), O- (μ-Oxo), and C- (μ-Carbido) Bridged Complexes

Porphyrinoids (phthalocyanines in most of the cases) metallated by Fe, Ru, or Mn can be axially bridged by a single nitrogen, resulting in μ-nitrido dimeric complexes. When the two macrocycles are the same, they are said to be homoleptic, and when they are different (should their substitution pattern or the macrocycle be different), they are described as heteroleptic.

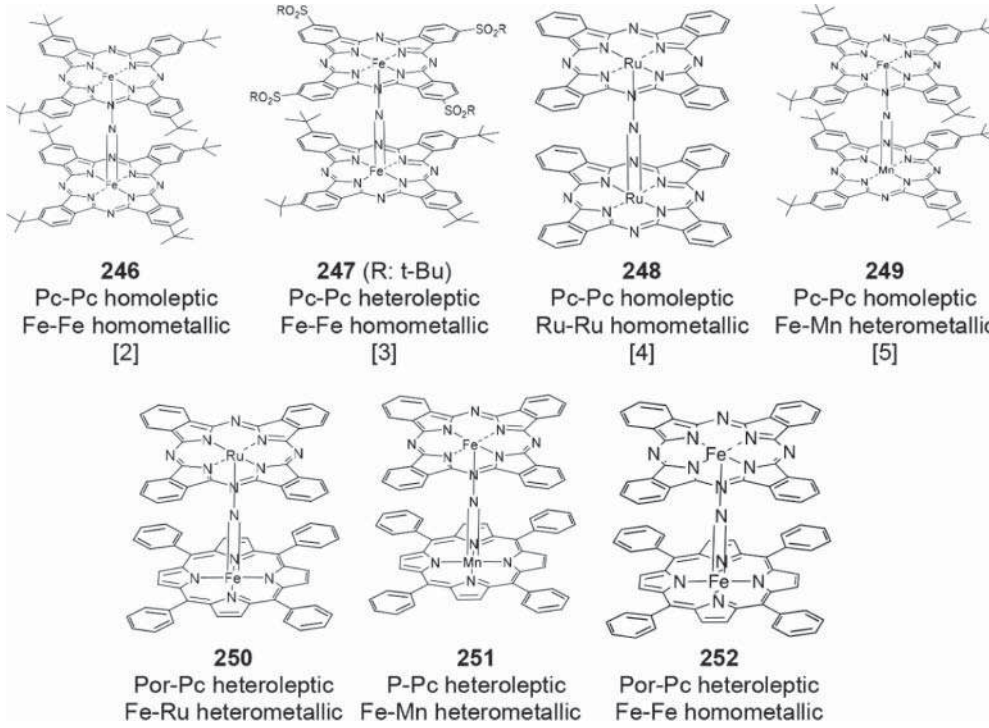

Figure 5.18 Examples of μ-nitrido complexes. **246** Pc-Pc homoleptic Fe-Fe homometallic [129], **247** (R: t-Bu) Pc-Pc heteroleptic Fe-Fe homometallic [130], **248** Pc-Pc homoleptic Ru-Ru homometallic [131], **249** Pc-Pc homoleptic Fe-Mn heterometallic [132], **250** Por-Pc heteroleptic Fe-Ru heterometallic, **251** P-Pc heteroleptic Fe-Mn heterometallic, **252** Por-Pc heteroleptic Fe-Fe homometallic. Based on Sorokin et al. [129]; İşçi [130]; Rossi et al. [131]; Kudrik et al. [132].

In addition, the complexes can be homo- or heterometallic (Figure 5.18). The first derivatives were unsubstituted and were the subject of extensive work [125]. The main field of applications is based on their powerful catalytic redox properties [126]. The synthesis depends on the nature of the targeted complex: homo- or heteroleptic and homo- or heterometallic.

Usually, the straightforward reaction of one (or two) Fe or Ru phthalocyanines in the presence of sodium azide leads to homoleptic (or heteroleptic) complexes such as **246**, **247**, or **248** in 50–60% yield. Depending on the solubility of the starting phthalocyanine, α-chloronaphthalene, or xylene are used as the solvent. The thermal decomposition of μ-oxo complexes in the presence of sodium azide is also reported [125b].

In the case of manganese metallation, initially a Mn—N_3 or Mn≡N complex is formed, and then a second reaction with an appropriately metallated tetrapyrrole macrocycle is performed. For example, for the homoleptic heterometallic complex **249**, Mn(^{t}BuPc)(N_3) is first prepared, which is then reacted with Fe^{t}BuPc.

Similarly, heteroleptic complexes **250** [127], **251** [127a] and **252** [128] were prepared by the preliminary formation of the Fe(TPP)(N_3) or Mn(TPP)(N_3) that were reacted afterward with RuPc or FePc.

Fe(II) phthalocyanines are sensitive to dioxygen [133] and can form μ-oxo complexes with two possible geometries, either linear or bent [134], similar to the extensive μ-oxo chemistry observed for iron porphyrins. μ-Carbido dinuclear complexes (μ-C)[Fe(Pc)]$_2$ are obtained by

reacting Fe(Pc) with CI_4 in chloronaphthalene at 140–150 °C in the presence of reducing reagents such as sodium dithionite or iron powder [135]. Similarly, μ-oxo (**255**), μ-nitrido (**256**), and μ-carbido (**257**) dimers of iron octapropylporphyrazine (**254**) have been prepared (Scheme 5.46) [136].

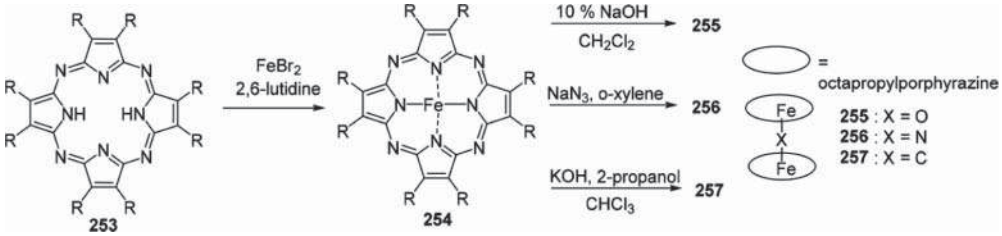

Scheme 5.46 Synthesis of μ-oxo (**255**), μ-nitrido (**256**) and μ-carbido (**257**) dimers of iron octapropylporphyrazine (**254**). Source: Colomban et al. [136].

5.6.2 Metal–Metal Bridged Derivatives

Similar to the lanthanide double-decker complexes, two phthalocyanine macrocycles can complex a single atom of trivalent or tetravalent metal such as titanium, scandium, or tin, among others. Such $M(Pc)_2$ complexes are easily oxidized into their $[M(Pc)_2]^+$ form [137]. Cadmium can form double- or triple-deckers complexes [138], and one atom of cadmium can complex two lanthanide double-decker phthalocyanines, leading to quadruple-deckers [139]. Two ruthenium phthalocyanines can dimerize and are then linked via their respective metal atoms with an Ru=Ru bond [140].

5.7 Reactions on Phthalocyanines and Porphyrazines

There are several reasons to engage pre-formed phthalocyanines and porphyrazines in further reactions. Obviously, axial substitution at the metal center of the macrocycle can be performed only on existing metallated macrocycles. Further derivatization cannot be avoided when a part of the final targeted structure is not chemically compatible with the quite stringent conditions used for the macrocycle formation. Often, the final reactions in a sequence consist of protecting group removal. The macrocycle formation step may be yield-limiting, so when a series of molecules is desired it is more fruitful to prepare an appropriately functionalized common intermediate and to introduce the different moieties to be compared (e.g., different carbohydrates) at the end of the synthetic sequence. This section aims at summarizing the range of reactions on pre-formed compounds, but does not pretend to be exhaustive. Metallation of the free bases is treated in Section 5.2.1.

5.7.1 Electrophilic Aromatic Reactions

The first attempts to obtain a water-soluble phthalocyanine were made by sulfonating unsubstituted, variously metallated phthalocyanines [141]. They led to mixtures of phthalocyanines with different degrees of sulfonation, requiring tedious purifications by reverse-phase chromatographies. Similarly, a nitration reaction was achieved on tetra-*tert*-butyl substituted porphyrazine [31].

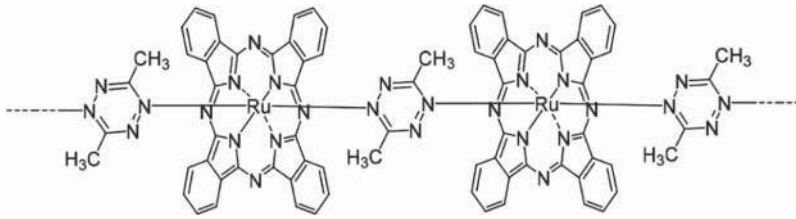

Figure 5.19 Kebab-like linear chains of Ru(Pc). Source: Modified from Hanack et al. [143].

5.7.2 Axial Substitutions

Depending on the propensity of the metal at the center of macrocycle to coordinate ligands, one or two axial substituents may be present. Axial ligand bonds strengths may vary widely. For example, coordination of the 1,4-diazabicyclo[2.2.2]octane (DABCO) nitrogen atom to Zn phthalocyanines [142] is very weak and hence reversible. In contrast, nitrogen ligand coordination to ruthenium is much stronger and kebab-like linear chains of Ru(Pc) can be obtained (Figure 5.19) [143].

As examples of more exotic ligand substitution, using a C2-type axial ligand (**259**) lowers the symmetry of a Ti=O phthalocyanine (**258**) (Scheme 5.47) [144]. ScCl phthalocyanines have also been converted into metallophthalocyaninocenes after coordination of an η^5-cyclopentadienyl ligand [145].

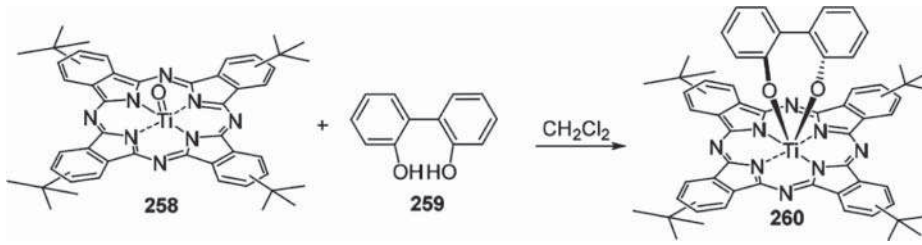

Scheme 5.47 Reaction of a Ti=O phthalocyanine (**258**) to form a complex containing a C2 type axial ligand (**259**). Source: Kobayashi et al. [144].

The introduction of axial substituents is a major part of the chemistry of SiPc (**261**). Different conditions can be used [146], and two different moieties (**262** and **263**) can be grafted, leading to another type of asymmetry, this time in the axial positions (Scheme 5.48) [147].

Boron SubPc's such as **265** have an axial B—Cl substituent that can undergo nucleophilic substitution (**266**) or organometallic couplings (**268**), with further couplings yielding, for example, **267** or **269** (Scheme 5.49) [148]. It may be necessary to replace the chloride ion by triflate to allow more difficult substitutions [149].

5.7.3 Protecting Group Removal

Protecting groups are used to introduce chemical functions that are not compatible with macrocycle formation conditions and/or to provide the necessary solubility to the protected derivative before its deprotection, which is ideally quantitative without the need for chromatographic purification.

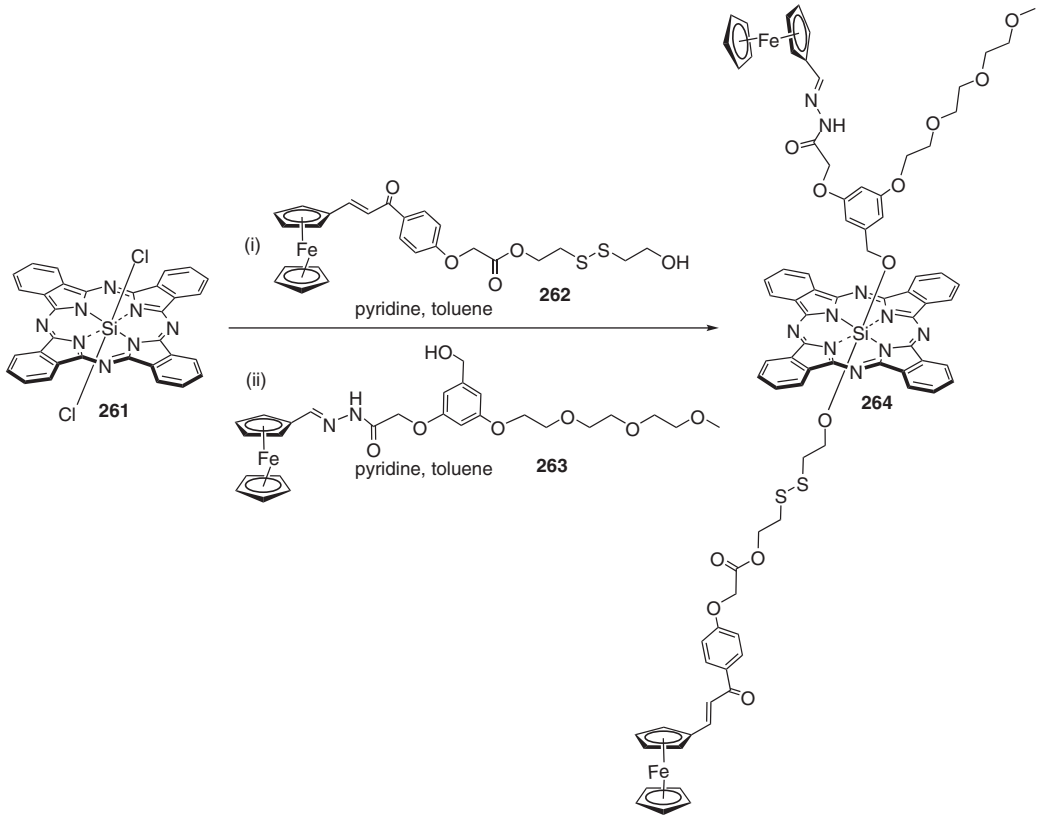

Scheme 5.48 Synthesis of a silicon phthalocyanine containing two different axial ligands. Source: Lau et al. [147].

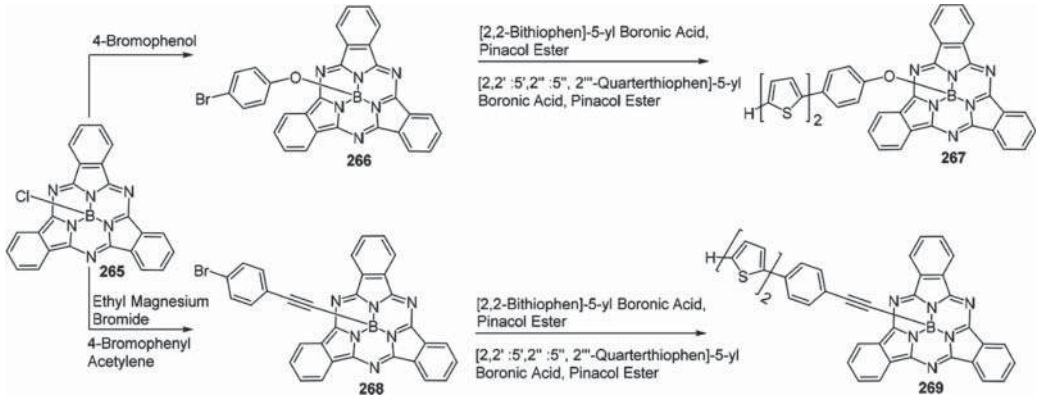

Scheme 5.49 Axial substitution reactions of boron subphthalocyanines. Source: Mauldin et al. [148].

The case of octasilylated phthalocyanine (**272**) (Scheme 5.50) is quite different as the *tert*-butyldimethylsilyl (TBDMS) groups were introduced into the pre-formed (octahydroxy)phthalocyanine (**273**) (itself obtained by demethylation of the corresponding octamethoxyphthalocyanine (**270**)), to increase its solubility [150]. The octahydroxylated phthalocyanine (**271**) is then regenerated with HF.

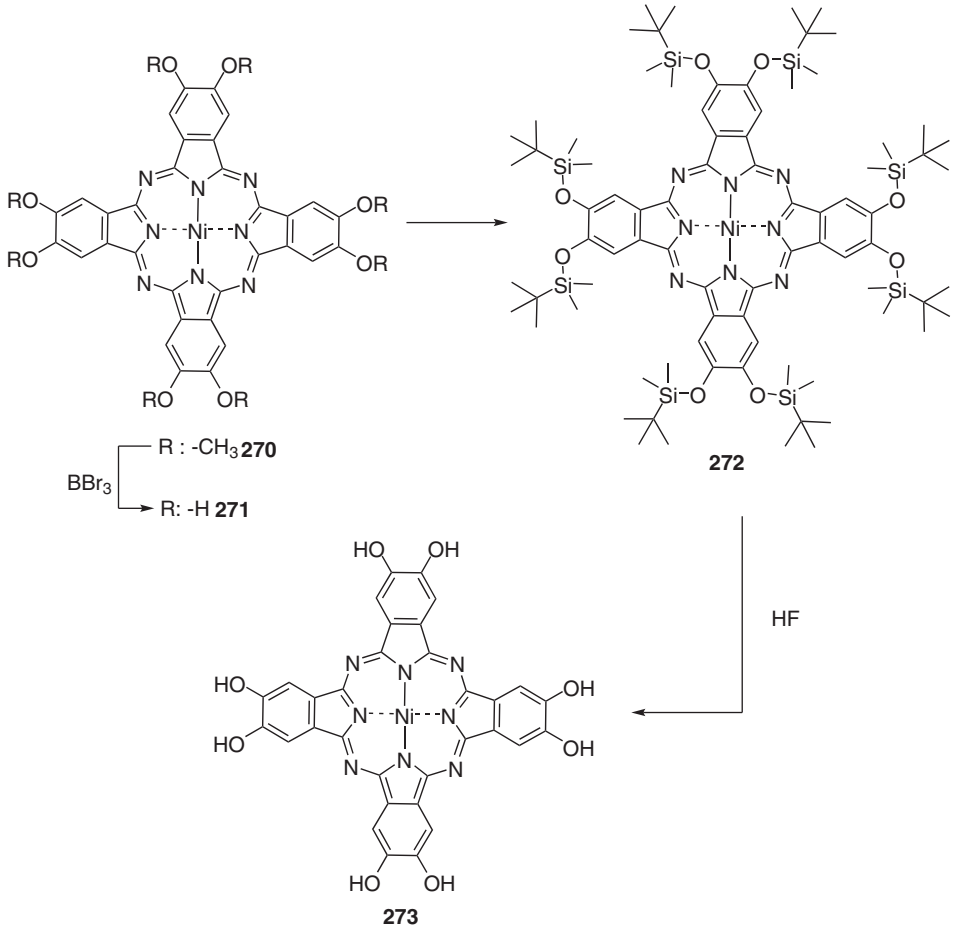

Scheme 5.50 Preparation of an octa-hydroxylated phthalocyanine. Based on Ruf et al. [150].

Since macrocycle sulfonation requires tedious purification steps, organosoluble phthalocyanines with sulfonic acid functions protected by aryl sulfonamides groups (**274**) were prepared. The sulfonic acid functions are removed at the last step from the formed phthalocyanine in basic conditions such as lithium 2-*N*,*N*-dimethylaminoethoxide or lithium methoxide, yielding **275** (Scheme 5.51) [72]. With the same goal of avoiding tedious purifications using reverse-phase chromatography, acetal groups of the numerous reported solketal-substituted phthalocyanines are removed at the end of the synthetic sequence [151–153]. Trimethylsilyl groups that protect terminal alkynes functions are often removed on pre-formed phthalocyanines [154].

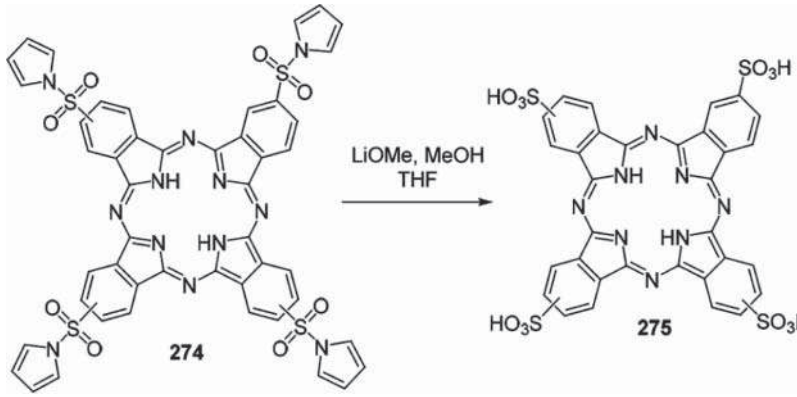

Scheme 5.51 Aryl sulfonamides as protecting groups for the synthesis of a sulfonic-acid substituted phthalocyanine. Based on Li et al. [72].

5.7.4 Click Reactions

Click chemistry [155], and in particular the copper-catalyzed Huisgen 1,3-dipolar cycloaddition between azides and terminal alkynes, is a powerful synthetic tool that is now widely used in porphyrinoid chemistry [156, 157]. The first report of the use of click chemistry [158] readily prompted chemists to optimize the conditions and scope of the reaction. Rather than the click reaction itself, the synthetic challenge arose from the introduction of alkynyl or azide functions onto the macrocycle. Phthalocyanine **277** could be obtained from phthalocyanine **276** but not from **278** which was too insoluble to react (Scheme 5.52) [42]. Converting a hydroxylated phthalocyanine into its azido analogues via an intermediate mesylation appears to be one of the best options [159].

The introduction via click chemistry of triethoxysilyl groups allowed the preparation phthalocyanine-bridged silsesquioxane nanoparticles for the first time [160]. When the azide function is on the phthalocyanine, it is often introduced on the pre-formed macrocycle, as it is quite sensitive to phthalocyanine formation conditions, although there are exceptions [161]. Azidophthalocyanines have been clicked onto various alkynyl-functionalized molecules or polymers, for example poly(3-hexylthiophene) (P3HT)-based copolymer, to prepare solar energy harvesting systems [162] and (Gd-DOTA) to yield theranostic agents combining photodynamic and MRI imaging properties [163], among others.

The less known thiol-ene click reaction was applied to olefin-functionalized Zn Pc (**279**) with 1,2-ethanedithiol, giving covalently linked, hollow phthalocyanine nanospheres (**281** and **282**) (Scheme 5.53) [65].

5.7.5 Quaternization

Quaternization is a widely used method to produce water-soluble derivatives [164]. Phthalocyanine **283** was inversely quaternized, as it is a halogenated derivative that reacts with a trisubstituted amine (DMAE) (Scheme 5.54) [165]. The outer nitrogen on pyridinoporphyrazines can also be quaternized [166].

Less commonly, the quaternization of the sulfur atom of thioether substituents has been reported as well. It was used to make the nanoparticles described above water soluble. The

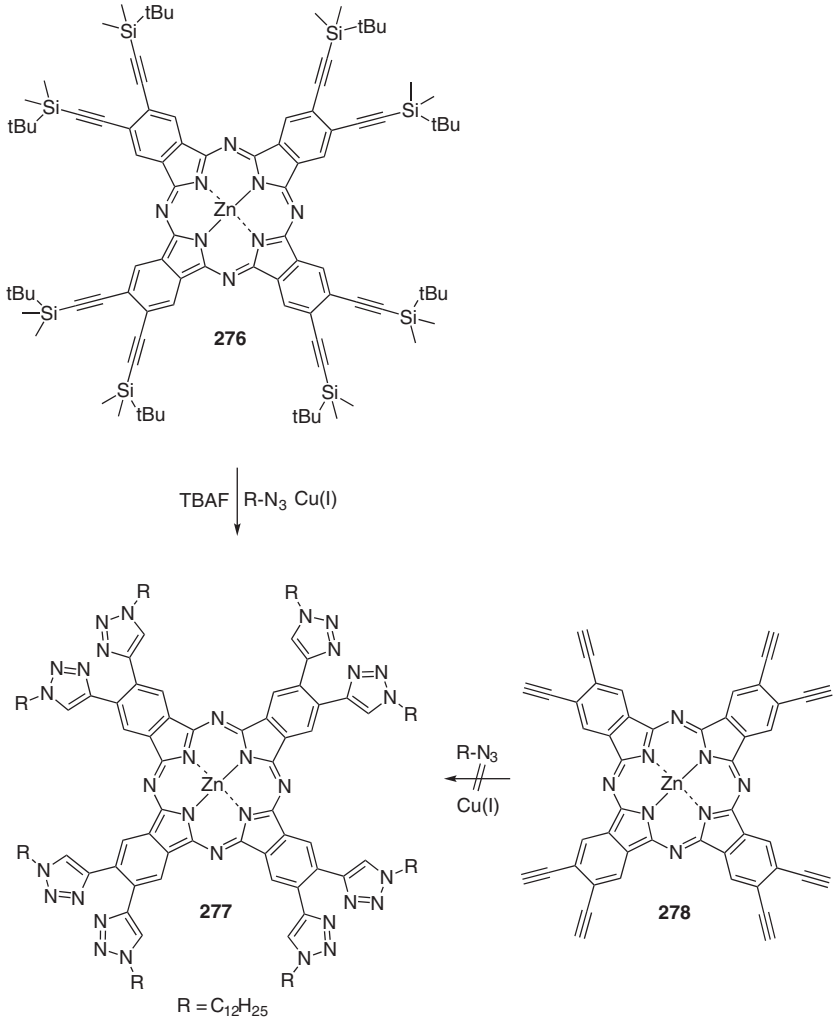

Scheme 5.52 Alkyne/azide click chemistry as a method of phthalocyanine functionalization. Source: Juricek et al. [42].

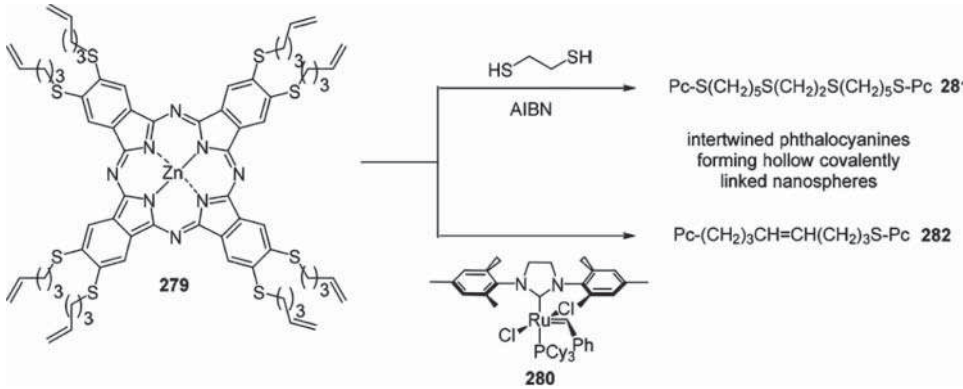

Scheme 5.53 Thiol-ene click chemistry as a method of phthalocyanine functionalization. Source: Hota et al. [65].

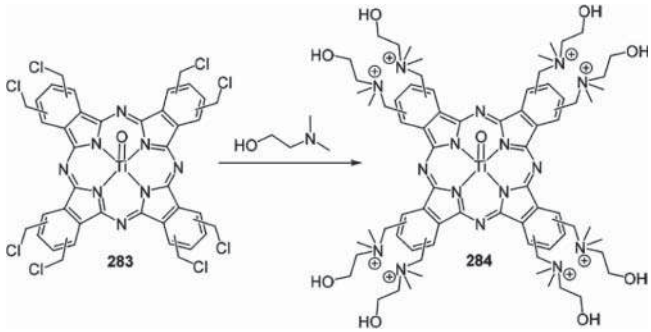

Scheme 5.54 Amine quaternization to produce a water-soluble, cationic phthalocyanine. Source: Modified from Kuznetsova et al. [165].

related subphthalocyanine **285** was, for its part, quaternized prior to the formation of the nanoparticles (Scheme 5.55) [167].

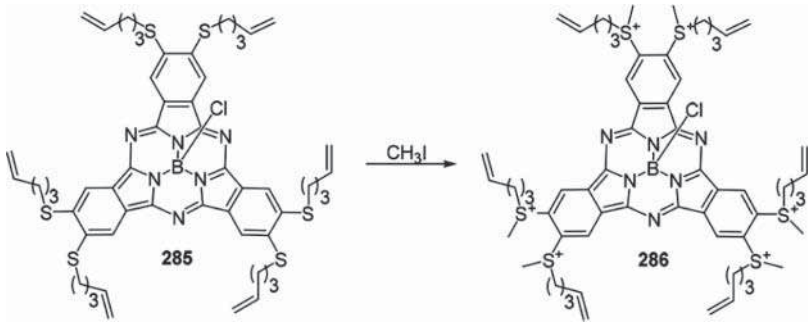

Scheme 5.55 Thioether alkylation to produce a water-soluble, cationic phthalocyanine. Source: Modified from Roy et al. [167].

5.7.6 Organometallic Couplings

A large range of organometallic couplings have been performed on pre-formed macrocycles, for various purposes: introduction of new functions, formation of dinuclear or multinuclear structures, preparation of nano-objects, among others. Organometallic couplings must be considered as a powerful synthetic tool to increase the structural variations on porphyrazines and phthalocyanines [168].

The carboxyl function is commonly formed directly on phthalocyanine macrocycle by the oxidation of hydroxymethyl phthalocyanine [169], a method applicable only in the absence of oxidation-sensitive substituents on other subunits, unlike sulfanyl substituents. The carboxyl function was therefore introduced on **287** by a palladium-catalyzed hydroxycarbonylation, using chloroform and aqueous alkali as the carbon source rather than carbon monoxide, which is more difficult to handle, and finally yielding **288** (Scheme 5.56) [170].

An alternative method of producing monocarboxylated phthalocyanine (**291**) is the palladium-catalyzed cyanation reaction, with a final step allowing concomitant removal of alkaline-sensitive protecting groups and alkaline hydrolysis of the nitrile moiety (**290**) into the desired carboxylic acid function (**291**) (Scheme 5.57) [171].

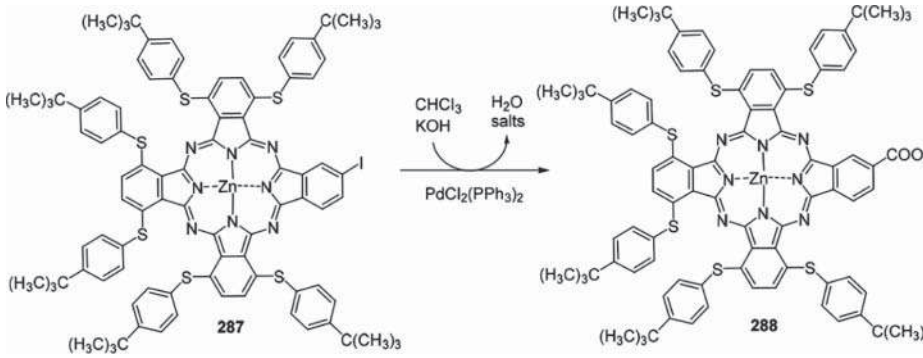

Scheme 5.56 Preparation of a monocarboxyphthalocyanine by hydroxycarbonylation of the corresponding iodo precursor. Source: de Carcer García et al. [170].

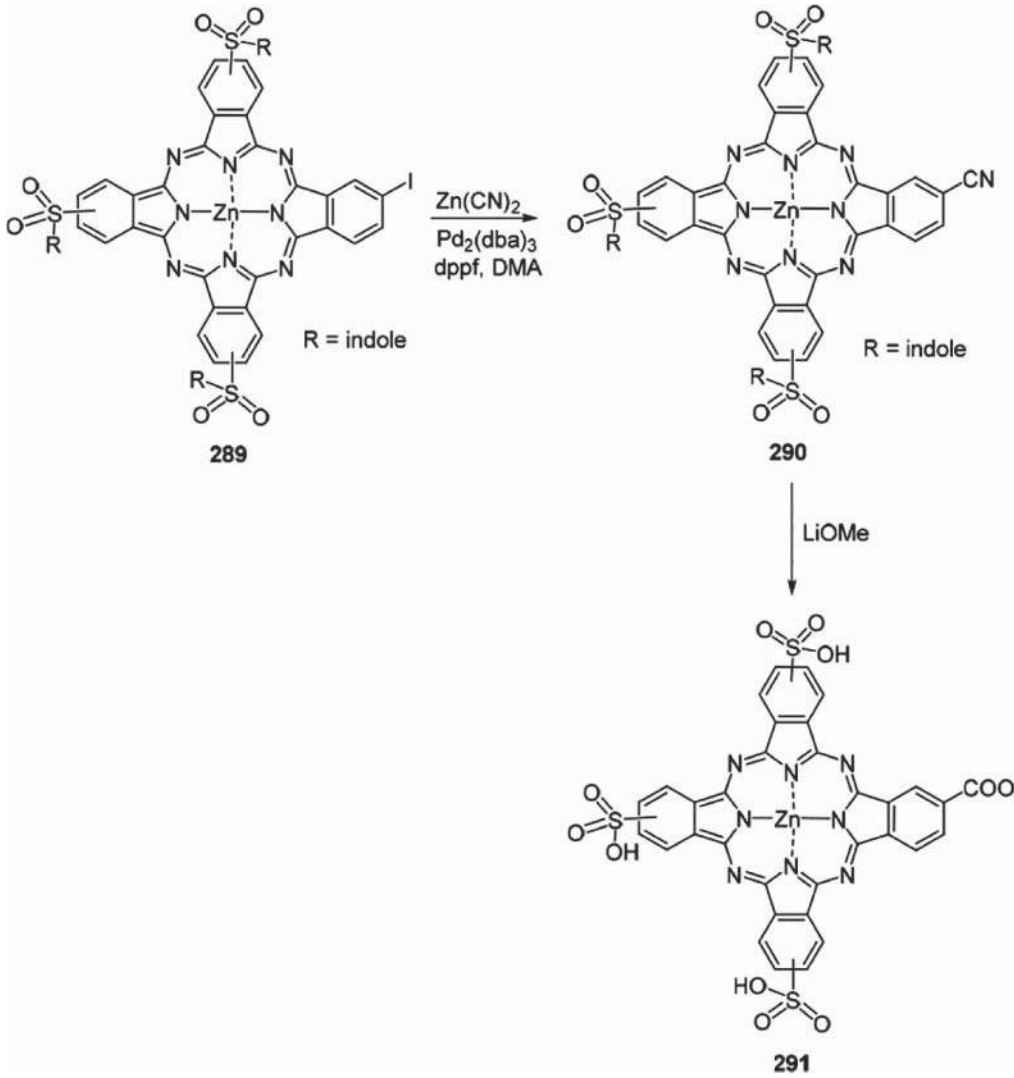

Scheme 5.57 Preparation of a monocarboxyphthalocyanine via palladium-catalyzed cyanation. Source: Modified from Mutyala and Park [171].

Sonogashira, Heck, and Suzuki couplings have been used to prepare series of derivatives with different amphiphilicities, an important parameter in the application of phthalocyanine derivatives in photodynamic therapy. These couplings were performed in aqueous media for monoiodo trisulfonated water-soluble derivatives [172]. Similar structures were obtained by performing the coupling in organic solvents on protected derivatives and regenerating the water-solubilizing function at the last step of the synthetic sequence [173]. A porphyrazine with a naphtha subunit proved to be particularly photoactive [73]. The palladium-catalyzed Buchwald amination reaction was also used to produce monoaminated derivatives (**293**) from **289**. **289** could also undergo Sonogashira coupling to produce derivative **292** (Scheme 5.58).

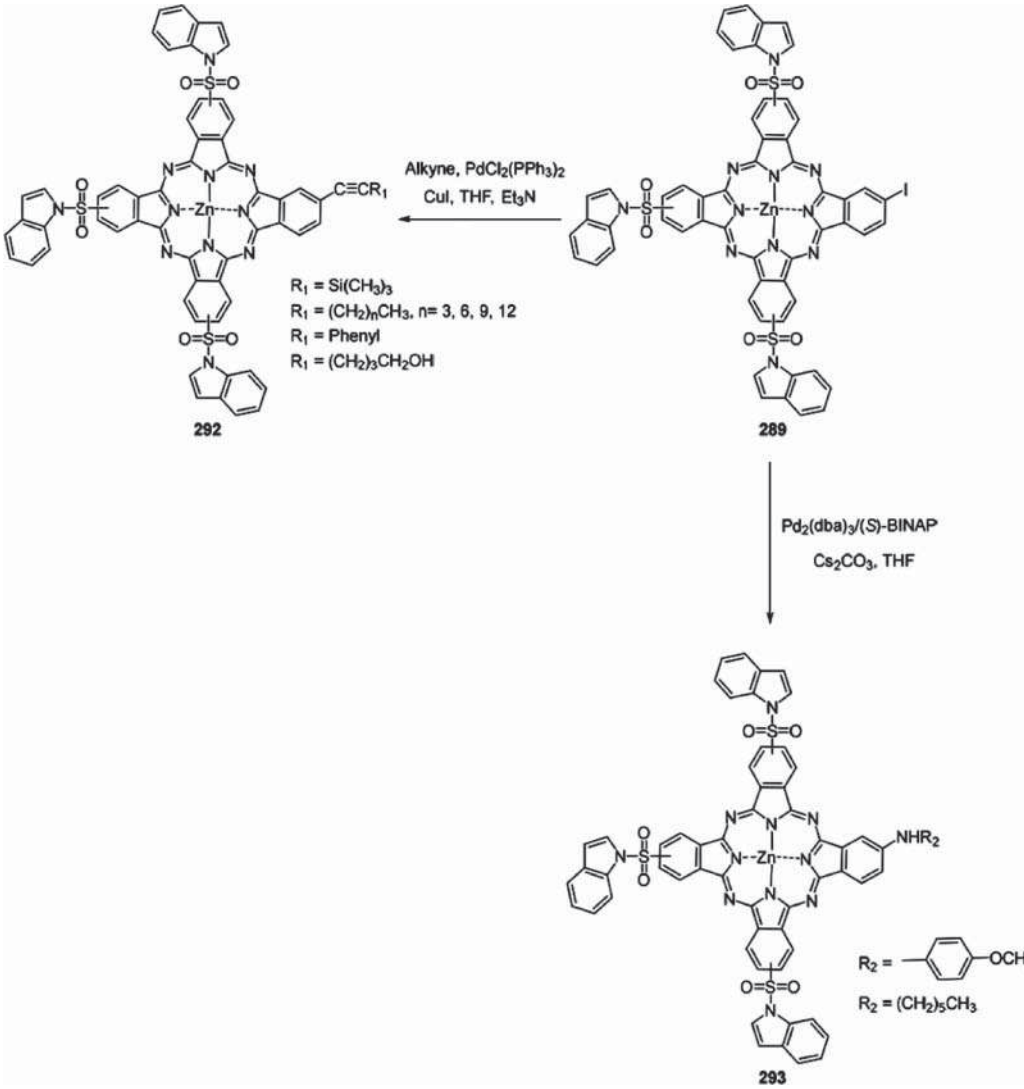

Scheme 5.58 Phthalocyanine substitution reactions using Sonogashira coupling to produce **292**, and a palladium-catalysed Buchwald amination reaction to produce **293**. Based on Tian et al. [173].

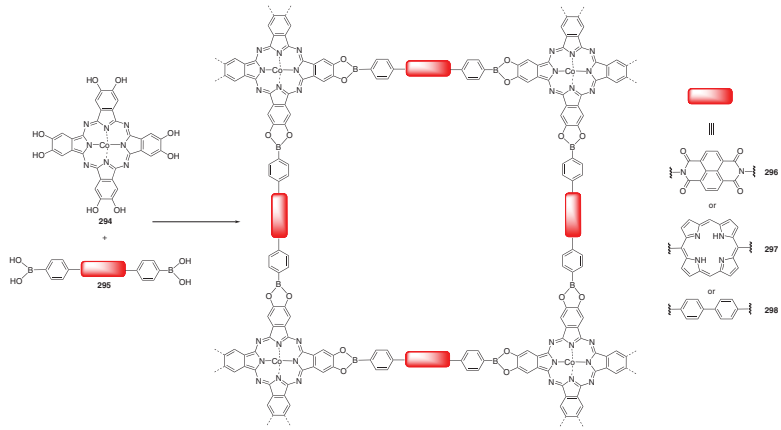

Scheme 5.59 Phthalocyanine-based covalent organic frameworks. Based on Neti et al.; Jin et al.; Neti et al. [175].

Finally, and unlike for the olefin-phthalocyanine above, hollow nanospheres were made from a quaternized subphthalocyanine undergoing an olefin cross-metathesis reaction catalyzed by the second-generation Grubbs' catalyst [167].

5.7.7 Miscellaneous Derivatives

Perfluorinated derivatives are sensitive to nucleophilic attacks by alcohols or thiols, a property widely used to introduce substituents on the pre-formed derivative (Scheme 5.35) or dendrimeric structures [174]. Formation of boronic esters between various rigid diboronic acids (**295**) and octahydroxyphthalocyanines (**294**) led to the formation of a phthalocyanine-based covalent organic framework with different types of units between each phthalocyanine (**296**–**298**) (Scheme 5.59) [175]. Phthalocyanines, and more generally porphyrazines with functional groups such as hydroxyls, can act as glycosylation acceptors [176], for example, boronic acids [177].

As another example of reactions on pre-formed macrocycles, the dienophile outer C=C bonds of the unsubstituted porphyrazine (**299**) macrocycle that are partially excluded from the overall aromaticity, as one can consider that there is an internal 16-membered macrocycle, or the 18-membered system including $C_\beta = C_\beta$ bonds of pyrrole rings [178], and can act as such in Diels–Alder cycloaddition with activated dienes such as anthracene (**300**). Derivatives **301**, **302**, and **303** were obtained with remarkable atom economy (Scheme 5.60).

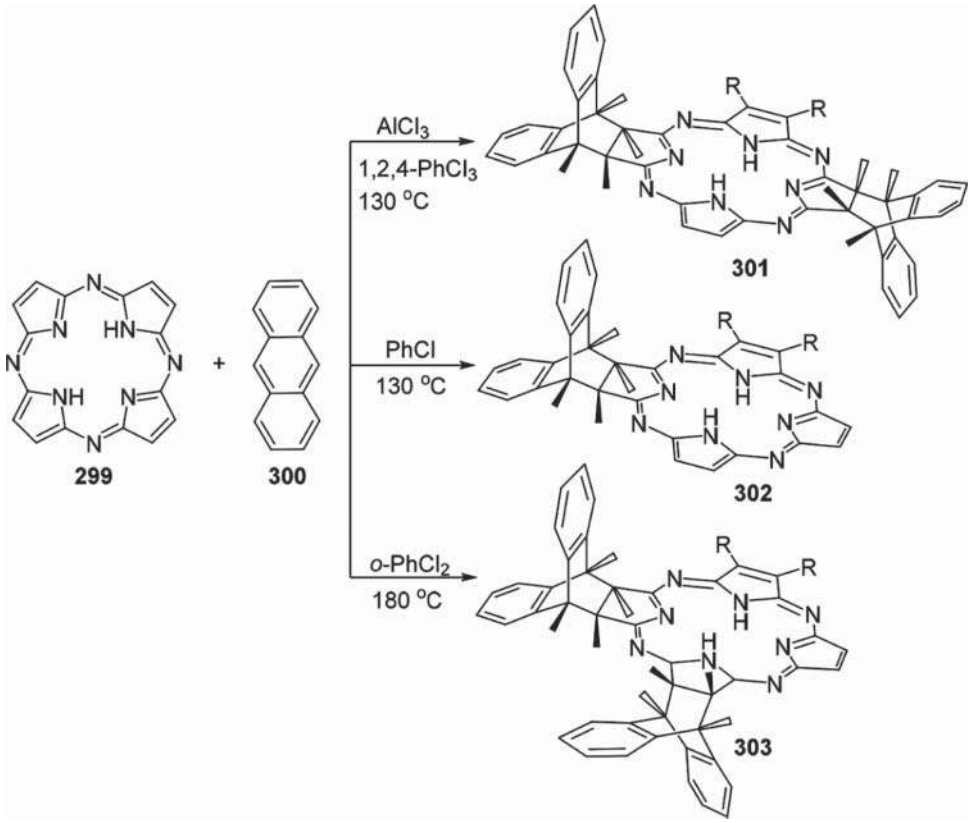

Scheme 5.60 Phthalocyanine derivatives formed from Diels-Alder cycloaddition with anthracene. Source: Rodríguez-Morgade and Stuzhin [178].

5.8 Conclusion

This chapter summarizes the different synthetic pathways to phthalocyanines, porphyrazines, and related molecules, and highlights the infinite possibilities offered by their versatility. Much work is still required to fully understand the structure–property relationships of this family of molecules, which will be possible thanks to the synthesis of more compounds. Finally, specific synthetic pathways to asymmetric substitution patterns are still needed and are yet to be discovered.

References

1 Claessens, C.G., González-Rodríguez, D., Rodríguez-Morgade, M.S. et al. (2014). Subphthalocyanines, subporphyrazines, and subporphyrins: singular nonplanar aromatic systems. *Chemical Reviews* 114: 2192–2277.

2 Marks, T.J. and Stojakovic, D.R. (1978). Large metal ion-centered template reactions. Chemical and spectral studies of the "superphthalocyanine" dioxocyclopentakis (1-iminoisoindolinato) uranium (VI) and its derivatives. *Journal of the American Chemical Society* 100: 1695–1705.

3 Furuyama, T., Sato, T., and Kobayashi, N. (2015). A bottom-up synthesis of Antiaromatic expanded phthalocyanines: pentabenzotriazasmaragdyrins, i.e. norcorroles of superphthalocyanines. *Journal of the American Chemical Society* 137: 13788–13791.

4 Shimizu, S., Zhu, H., and Kobayashi, N. (2010). Azaphenalene phthalocyanines: phthalocyanine analogues with six-membered-ring units instead of five-membered-ring units. *Chemistry – A European Journal* 16: 11151–11159.

5 Shimizu, S., Zhu, H., and Kobayashi, N. (2011). Azepiphthalocyanine-an unprecedented large twist of a π-conjugation system upon core-modification with a seven-membered ring unit. *Chemical Communications* 47: 3072–3074.

6 Ranta, J., Kumpulainen, T., Lemmetyinen, H., and Efimov, A. (2010). Synthesis and characterization of monoisomeric 1,8,15,22-substituted (A3B and A2B2) phthalocyanines and phthalocyanine-fullerene dyads. *The Journal of Organic Chemistry* 75: 5178–5194.

7 Necedová, M., Magdolen, P., Novakova, V. et al. (2015). Synthesis and photophysical, electrochemical and theoretical study of thiazole-annelated phthalocyanines. *European Journal of Organic Chemistry* 7053–7068.

8 Kobayashi, N., Nakajima, S., and Osa, T. (1992). Spectroscopy, electrochemistry, and spectroelectrochemistry of tetra-tert-butylated and octaphenylated tetraazaporphyrins. *Chemistry Letters* 2415–2418.

9 Tejerina, L., Martínez-Díaz, M.V., and Torres, T. (2015). Convergent strategy for the regioselective synthesis of nonaggregated α-triaryl-β-carboxy zinc phthalocyanines. *Organic Letters* 17: 552–555.

10 Fazio, E., Jaramillo-García, J., de la Torre, G., and Torres, T. (2014). Efficient synthesis of ABAB functionalized phthalocyanines. *Organic Letters* 16: 4706–4709.

11 Tarakci, D.K., Berber, S., Zorlu, Y. et al. (2015). Synthesis of an octasubstituted monohydroxylated phthalocyanine designed to investigate the effect of the presence of active moieties. *New Journal of Chemistry* 39: 3929–3935.

12 de la Torre, G., Claessens, C.G., and Torres, T. (2007). Phthalocyanines: old dyes, new materials. Putting color in nanotechnology. *Chemical Communications* 2000–2015.

13 Snow, A.W. (2003). Phthalocyanine aggregation. In: *The Porphyrin Handbook*, vol. 17 (ed. K.M. Kadish, K.M. Smith and R. Guilard), 129–176. San Diego: Academic Press.

14 Aranyos, V., Castano, A.M., and Grennberg, H. (1999). An application of the Stille coupling for the preparation of arylated phthalonitriles and phthalocyanines. *Acta Chemica Scandinavica* 53: 714–720.

15 Oliver, S.W. and Smith, T.D. (1987). Oligomeric cyclization of dinitriles in the synthesis of phthalocyanines and related compounds: the role of the alkoxide anion. *Journal of the Chemical Society, Perkin Transactions 1* 11: 1579–1582.

16 Lee, C.H. and Ng, D.K.P. (2002). Cerium-promoted formation of metal-free phthalocyanines. *Tetrahedron Letters* 43: 4211–4214.

17 Alzeer, J., Roth, P.J.C., and Luedtke, N.W. (2009). An efficient two-step synthesis of metal-free phthalocyanines using a Zn(II) template. *Chemical Communications* 1970–1971.

18 Tuncel, S., Banimuslem, H.A.J., Durmus, M. et al. (2012). Liquid crystalline octasubstituted lead(II) phthalocyanines: effects of alkoxy and alkylthio substituents on film alignment and electrical properties. *New Journal of Chemistry* 36: 1665–1672.

19 Gürek, A.G., Ahsen, V., Gül, A., and Bekaroğlu, Ö. (1991). Synthesis and characterization of a new copper(II) phthalocyaninate substituted with four 15-membered tetraazamacrocycles and its water-soluble pentanuclear complexes. *Journal of the Chemical Society, Dalton Transactions* 3367–3371.

20 Zimcik, P., Miletin, M., Novakova, V. et al. (2009). Effective monofunctional azaphthalocyanine photosensitizers for photodynamic therapy. *Australian Journal of Chemistry* 62: 425–433.

21 Tylleman, B., Gbabode, G., Amato, C. et al. (2009). Metal-free phthalocyanines bearing eight alkylsulfonyl substituents: design, synthesis, electronic structure, and mesomorphism of new electron-deficient mesogens. *Chemistry of Materials* 21: 2789–2797.

22 Uchida, H., Tanaka, H., Yoshiyama, H. et al. (2002). Novel synthesis of phthalocyanines from phthalonitriles under mild conditions. *Synlett* 1649–1652.

23 Uchida, H., Reddy, P.Y., Nakamura, S., and Toru, T. (2003). Novel efficient preparative method for phthalocyanines from phthalimides and phthalic anhydride with HMDS. *The Journal of Organic Chemistry* 68: 8736–8738.

24 Leznoff, C.C., Hu, M., and Nolan, K.J.M. (1996). The synthesis of phthalocyanines at room temperature. *Chemical Communications* 1245–1246.

25 Zheng, W., Wan, C.Z., Zhang, J.X. et al. (2015). Facile synthesis of phthalocyanine at low temperature with diisopropylamide anion as nucleophile. *Tetrahedron Letters* 56: 4459–4462.

26 Mayukh, M., Sema, C.M., Roberts, J.M., and McGrath, D.V. (2010). Solvent-free synthesis of soluble, near-IR absorbing titanyl phthalocyanine derivatives. *The Journal of Organic Chemistry* 75: 7893–7896.

27 Zimcik, P., Miletin, M., Kostka, M. et al. (2004). Synthesis and comparison of photodynamic activity of alkylheteroatom substituted azaphthalocyanines. *Journal of Photochemistry and Photobiology A: Chemistry* 163: 21–28.

28 Cabezon, B., Quesada, E., Esperanza, S., and Torres, T. (2000). Synthesis of crowned triazolephthalocyanines. *European Journal of Organic Chemistry* 2767–2775.

29 Gürek, A.G. and Hirel, C. (2011). Recent developments of synthetic techniques for porphyrins, phthalocyanines and related systems. In: *Photosensitizers in Medicine, Environment, and Security* (ed. T. Nyokong and V. Ahsen), 47–120. Dordrecht: Springer.

30 Burczyk, A., Loupy, A., Bogdala, D., and Petit, A. (2005). Improvement in the synthesis of metallophthalocyanines using microwave irradiation. *Tetrahedron* 61: 179–188.

31 Lukyanets, E.A. and Nemykin, V.N. (2010). The key role of peripheral substituents in the chemistry of phthalocyanines and their analogs. *Journal of Porphyrins and Phthalocyanines* 14: 1–40.

32 Sharman, W.M. and Van Lier, J.E. (2003). Synthesis of phthalocyanine precursors. In: *The Porphyrin Handbook*, vol. 15 (ed. K. Kadish, R. Guilard and K.M. Smith), 1–60.

33 Arrieta, T., Aizpurun, J.M., and Palomo, C. (1984). N,N-dimethylchlorosulfite-methaniminium chloride ($SOCl_2$-DMF) – a versatile dehydrating reagent. *Tetrahedron Letters* 25: 3365–3368.

34 Leznoff, C.C., Terekhov, D.S., McArthur, C.R. et al. (1995). Multisubstituted phthalonitriles, naphthalenedicarbonitriles, and phenanthrenetetracarbonitriles as precursors for phthalocyanine syntheses. *Canadian Journal of Chemistry* 73: 435–443.

35 Mitzel, F., FitzGerald, S., Beeby, A., and Faust, R. (2003). Acetylenic quinoxalinoporphyrazines as photosensitisers for photodynamic therapy. *Chemistry – A European Journal* 9: 1233–1241.

36 (a) Kudrik, E.V., Shaposhnikov, G.P., and Balakirev, A.E. (1999). Synthesis and properties of 5,6-dicyanobenzimidazole and porphyrazines derived from it. *Russian Journal of General Chemistry* 691: 321–1324. (b) Mikhalenko, S.A., Derkacheva, V.M., and Luk'yanets, E.A. (1981). Phthalocyanines and related compounds. XIX. Tetra- and octaamino-substituted phthalocyanines. *Russian Journal of General Chemistry* 51: 1405–1411. (c) Rusanova, J., Pilkington, M., and Decurtins, S. (2002). A novel fully conjugated phenanthroline-appended phthalocyanine: synthesis and characterisation. *Chemical Communications* 2236–2237.

37 Youngblood, W.J. (2006). Synthesis of a new trans-A2B2 phthalocyanine motif as a building block for rodlike phthalocyanine polymers. *The Journal of Organic Chemistry* 71: 3345–3356.

38 Burmester, C. and Faust, R. (2008). A reliable route to 1,2-diamino-4,5-phthalodinitrile. *Synthesis* 8: 1179–1181.

39 Pletnev, A.A., Tian, Q., and – Larock, R. C. (2002). Carbopalladation of nitriles: synthesis of 2,3-diarylindenones and polycyclic aromatic ketones by the Pd-catalyzed annulation of alkynes and bicyclic alkenes by 2-iodoarenenitriles. *The Journal of Organic Chemistry* 67: 9276–9287.

40 Terekhov, D.S., Nolan, K.J.M., McArthur, C.R., and Leznoff, C.C. (1996). Synthesis of 2,3,9,10,16,17,23,24-octaalkynylphthalocyanines and the effects of concentration and temperature on their 1H NMR spectra. *The Journal of Organic Chemistry* 61: 3034–3040.

41 Leznoff, C.C., Li, Z., Isago, H. et al. (1999). Syntheses of octaalkynylphthalocyanines from halophthalonitriles. *Journal of Porphyrins and Phthalocyanines* 3: 406–416.

42 Juricek, M., Kouwer, P.H.J., Rehak, J. et al. (2009). Novel modular approach to triazole-functionalized phthalocyanines using click chemistry. *The Journal of Organic Chemistry* 74: 21–25.

43 Jones, J.G. and Twigg, M.V. (1969). Fluorinated iron phthalocyanine. *Inorganic Chemistry* 8: 2018–2019.

44 Wöhrle, D. and Knothe, G. (1989). Reaction of 4-nitrophthalonitrile with carbonate, nitrite, and fluoride. *Synthetic Communications* 19: 3231–3239.

45 Leznoff, C.C. and Drew, D.M. (1996). The use of bisphthalonitriles in the synthesis of side-strapped 1, 11, 15, 25-tetrasubstituted phthalocyanines. *Canadian Journal of Chemistry* 74: 307–318.

46 Álvarez-Micó, X., Calvete, M.J.F., Hanack, M., and Ziegler, T. (2007). Expeditious synthesis of glycosylated phthalocyanines. *Synthesis* 14: 2186–2192.

47 Cha, I. and Lim, Y. (1988). Synthesis and morphology of new discogenic phthalocyanine derivatives. *Molecular Crystals and Liquid Crystals Incorporating Nonlinear Optics* 154: 9–26.

48 Mbambisa, G., Tau, P., Antunes, E., and Nyokong, T. (2007). Synthesis and electrochemical properties of purple manganese(III) and red titanium(IV) phthalocyanine complexes octa-substituted at non-peripheral positions with pentylthio groups. *Polyhedron* 26: 5355–5364.

49 Burnham, P.M., Cook, M.J., Gerrard, L.A. et al. (2003). Structural characterisation of a red phthalocyanine. *Chemical Communications* 2064–2065.

50 Al-Raqa, S.Y. (2008). The synthesis and photophysical properties of novel, symmetrical, hexadecasubstituted Zn phthalocyanines and related unsymmetrical derivatives. *Dyes and Pigments* 77: 259–265.

51 Ellis, G.P. and Romney-Alexander, T.M. (1987). Cyanation of aromatic halides. *Chemical Reviews* 87: 779–794.

52 Pardo, C., Yuste, M., and Elguero, J. (2000). Tetraimidazophthalocyanines. *Journal of Porphyrins and Phthalocyanines* 4: 505–509.

53 Önal, E., Dumoulin, F., and Hirel, C. (2009). Tetraimidazophthalocyanines: influence of protonation and aggregation on spectroscopic observations. *Journal of Porphyrins and Phthalocyanines* 13: 702–711.

54 Iqbal, Z., Lyubimtsev, A., and Hanack, M. (2008). Synthesis of phthalonitriles using a palladium catalyst. *Synlett* 15: 2287–2290.

55 George, R.D. and Snow, A.W. (1995). Synthesis of 3-nitrophthalonitrile and tetra-α-substituted phthalocyanines. *Journal of Heterocyclic Chemistry* 32: 495–498.

56 Ribeiro, A.O., Tomé, J.P.C., Neves, M.G.P.M.S. et al. (2006). [1,2,3,4-tetrakis (a/b-D galactopyranos-6-yl)-phthalocyaninato] zinc(II): a water-soluble phthalocyanine. *Tetrahedron Letters* 47: 9177–9180.

57 Zorlu, Y., İşci, Ü., Ün, İ. et al. (2013). Comparative structural analysis of 4,5- and 3,6-dialkylsulfanylphthalonitriles of different bulkiness. *Structural Chemistry* 24: 1027–1038.

58 İşci, Ü., Dumoulin, F., Ahsen, V., and Sorokin, A.B. (2010). Preparation of N-bridged diiron phthalocyanines bearing bulky or small electron-withdrawing substituents. *Journal of Porphyrins and Phthalocyanines* 14: 324–334.

59 Gürek, A.G. and Bekâroğlu, Ö. (1994). Octakis(alkylthio)-substituted phthalocyanines and their interactions with silver(I) and palladium(II) ions. *Journal of the Chemical Society, Dalton Transactions* 1419–1423.

60 Wöhrle, D., Eskes, M., Shigehara, K., and Yamada, A. (1993). A simple synthesis of 4,5-disubstituted 1,2-dicyanobenzenes and 2,3,9,10,16,17,23,24-octasubstituted phthalocyanines. *Synthesis* 194–196.

61 Gürol, İ., Gümüs, G., and Ahsen, V. (2012). Synthesis and characterization of novel fluoroether-substituted phthalocyanines. *Journal of Fluorine Chemistry* 142: 60–66.

62 Gürek, A.G., Durmuş, M., and Ahsen, V. (2004). Synthesis and mesomorphic properties of tetra- and octa-substituted phthalocyanines. *New Journal of Chemistry* 28: 693–699.

63 Volkov, K.A., Negrimovsky, V.M., Avramenko, G.V., and Lukyanets, E.A. (2008). Phthalocyanines and related compounds: XLVIII. Stepwise nucleophilic substitution in tetrachlorophthalonitrile: synthesis of polysubstituted phthalonitriles. *Russian Journal of General Chemistry* 78: 1794–1801.

64 Simao, D., Alves, H., Belo, D. et al. (2001). Synthesis, structure and physical properties of tetrabutylammonium salts of nickel complexes with the new ligand dcbdt 5 4,5-dicyanobenzene-1,2-dithiolate, $[Ni(dcbdt)_2]^{z-}$ (z = 0.4,1,2). *European Journal of Inorganic Chemistry* 3119–3126.

65 Hota, R., Baek, K., Yun, G. et al. (2013). Self-assembled, covalently linked, hollow phthalocyanine nanospheres. *Chemical Science* 4: 339–344.

66 Leznoff, C.C., Vigh, S., Svirskaya, P.I. et al. (1989). Synthesis and photocytotoxicity of some new substituted phthalocyanines. *Photochemistry and Photobiology* 49: 279–284.

67 Yamamoto, S., Zhang, A., Stillman, M.J. et al. (2016). Low-symmetry W-shaped zinc phthalocyanine sensitizers with panchromatic light-harvesting properties for dye-sensitized solar cells. *Chemistry – A European Journal* 22: 18760–18768.

68 Sharman, W.M., Kudrevich, S.V., and van Lier, J.E. (1996). Novel water-soluble phthalocyanines substituted with phosphonate moieties on the benzo rings. *Tetrahedron Letters* 37: 5831–5834.

69 Önal, E., Okyay, T.M., Ekineker, G. et al. (2017). Sulfanyl vs sulfonyl, 4,5- vs 3,6- position. How structural variations in phthalonitrile substitution affect their infra-red, crystallographic and Hirshfeld surface analyses. *Journal of Molecular Structure* 1155: 310–319.

70 Sakamato, K., Kato, T., and Cook, M.J. (2001). Position isomer separation of non-peripheral substituted zinc dibenzo-di(3,4-pyrido)porphyrazines. *Journal of Porphyrins and Phthalocyanines* 5: 742–750.

71 Cook, M.J. and Cracknell, S.J. (1994). The Diels-Alder reaction of 2,5-dialkylfurans and fumaronitrile revisited. *Tetrahedron* 50: 12125–12132.

72 Li, Z., van Lier, J., and Leznoff, C.C. (1999). Heterocyclic aromatic amide protecting groups for aryl and phthalocyaninesulfonic acids. *Canadian Journal of Chemistry* 77: 138–145.

73 van Lier, J.E., Tian, H., Ali, H. et al. (2009). Trisulfonated porphyrazines: new photosensitizers for the treatment of retinal and subretinal edema. *Journal of Medicinal Chemistry* 52: 4107–4110.

74 Cook, M.J., Dunn, A.J., Gold, A.A. et al. (1988). Association and orientation of copper(II) tetra-t-butylphthalocyaninate in multilayer Langmuir–Blodgett films as determined by electron paramagnetic resonance spectroscopy. *Journal of the Chemical Society, Dalton Transactions* 1583–1589.

75 Zhang, Z., Njus, J.M., Sandman, D.J. et al. (2004). Diiminoisoindoline: tautomerism, conformations, and polymorphism. *Chemical Communications* 886–887.

76 Dumoulin, F., Zorlu, Y., Ayhan, M.M. et al. (2009). A first ABAC phthalocyanine. *Journal of Porphyrins and Phthalocyanines* 13: 161–165.

77 Engle, J.T., Allison, A.N., Standard, J.M. et al. (2013). The structures of several modified isoindolines, the building blocks of phthalocyanines. *Journal of Porphyrins and Phthalocyanines* 17: 712–721.

78 Ayhan, M.M., Zorlu, Y., Gökdemir, Ö. et al. (2014). Optimized synthesis and crystal growth by sublimation of 1,3,3-trichloroisoindolenines, key building blocks for crosswise phthalocyanines. *CrystEngComm* 16: 6556–6563.

79 Veliizquez, C.S., Fox, G.A., Broderick, W.E. et al. (1992). Star-porphyrazines: synthetic, structural, and spectral investigation of complexes of the polynucleating porphyrazineoctathiolato ligand. *Journal of the American Chemical Society* 114: 7416–7424.

80 Lange, S.J., Sibert, J.W., Stern, C.L. et al. (1995). Macrocyclic dithiomaleonitrile derivatives containing sulfur and nitrogen heteroatoms. *Tetrahedron* 51: 8175–8188.

81 Pullen, A.E., Faulmann, C., and Cassoux, P. (1999). Synthesis and investigation of chalcogen atom substituted dinitriles and porphyrazines. *European Journal of Inorganic Chemistry* 2: 269–276.

82 Cook, A.H. and Linstead, R.P. (1937). Phthalocyanines. Part XI. The preparation of octaphenylporphyrazines from diphenylmaleinitrile. *Journal of the Chemical Society* 929–932.

83 Baumann, T.F., Barrett, A.G.M., and Hoffman, B.M. (1997). Porphyrazine binaries: synthesis, characterization, and spectroscopy of a metal-linked trinuclear porphyrazine dimer. *Inorganic Chemistry* 36: 5661–5665.

84 Cook, A.S., Williams, D.B.G., White, D.A.J.P. et al. (1997). Enantiomerically pure "Winged" spirane porphyrazinoctaols. *Angewandte Chemie International Edition in English* 36: 760–761.

85 Beall, L.S., Mani, N.S., White, A.J.P. et al. (1998). Porphyrazines and norphthalocyanines bearing nitrogen donor pockets: metal sensor properties. *The Journal of Organic Chemistry* 63: 5806–5817.

86 Sakamoto, K., Okumura, E.O., Kato, T. et al. (2008). Investigation of zinc bis(1,4-didecylbenzo)-bis(2,3-pyrido) porphyrazine as an efficient photosensitizer by cyclic voltammetry. *Dyes and Pigments* 78: 213–218.

87 Vachova, L., Machacek, M., Kucera, R. et al. (2015). Heteroatom-substituted tetra(3,4-pyrido)- porphyrazines: a stride toward near-infraredabsorbing macrocycles. *Organic & Biomolecular Chemistry* 13: 5608–5612.

88 Mohr, B., Wegnera, G., and Ohta, K. (1995). Synthesis of triphenylene-based porphyrazinato metal(II) complexes which display discotic columnar mesomorphism. *Journal of the Chemical Society, Chemical Communications* 995–996.

89 Körte, F., Bruhn, C., and Faust, R. (2015). A fourfold benzodehydroannuleno-fused porphyrazine. *Synlett* 26: 1620–1624.

90 Lee, B.H. and Jaung, J.Y. (2003). Synthesis and characteristics of dicyanopyrazine dyes containing spiropyran group. *Dyes and Pigments* 59: 135–142.

91 (a) Mack, J. and Kobayashi, N. (2011). Low symmetry phthalocyanines and their analogues. *Chemical Reviews* 111: 281–321. (b) Wang, A., Long, L., and Zhang, C. (2012). Synthesis of unsymmetrical phthalocyanines: a brief overview. *Tetrahedron* 68: 2433–2451. (c) de la Torre, G. and Torres, T. (2002). Synthetic advances in phthalocyanine chemistry. *Journal of Porphyrins and Phthalocyanines* 6: 274–284. (d) de la Torre, G., Claessens, C.G., and Torres, T. (2000). Phthalocyanines: the need for selective synthetic approaches. *European Journal of Organic Chemistry* 2821–2830. (e) Nemykin, V.N., Dudkin, S.V., Dumoulin, F. et al. (2014). An introduction to synthetic methods for preparation of asymmetric phthalocyanines and their analogues. *Arkivoc* 142–204.

92 Taniguchi, M., Du, H., and Lindsey, J.S. (2011). Virtual libraries of tetrapyrrole macrocycles. Combinatorics, isomers, product distributions, and data mining. *Journal of Chemical Information and Modeling* 51: 2233–2247.

93 Taniguchi, M., Du, H., and Lindsey, J.S. (2013). Enumeration of virtual libraries of combinatorial modular macrocyclic (bracelet, necklace) architectures and their linear counterparts. *Journal of Chemical Information and Modeling* 53: 2203–2216.

94 http://www.photochemcad.com (accessed 17 November 2021).

95 Claessens, C.G. and Torres, T. (2002). Synthesis, separation, and characterization of the topoisomers of fused bicyclic subphthalocyanine dimers. *Angewandte Chemie International Edition* 114: 2673–2677.

96 Fukuda, T., Stork, J.R., Potucek, R.J. et al. (2002). Cis and trans forms of a binuclear subphthalocyanine. *Angewandte Chemie International Edition* 114: 2677–2680.

97 Ali, H., Kim, S.K., and van Lier, J.E. (1999). Synthesis of highly unsymmetrical phthalocyanines. *Journal of Chemical Research, Synopses* 496–497.

98 Iglesias, R.S., Claessens, C.G., Torres, T. et al. (2007). Subphthalocyanine-fused dimers and trimers: synthetic, electrochemical, and theoretical studies. *The Journal of Organic Chemistry* 72: 2967–2977.

99 Köç, M., Gürek, A.G., Dumoulin, F., and Ahsen, V. (2012). Symmetric, twinned, and double-decker phthalocyanines substituted by trialkylated pentaerythritol. *Turkish Journal of Chemistry* 36: 493–502.

100 Kimura, T., Murakami, N., Suzuki, E. et al. (2016). Preparation, optical and electrochemical properties, and molecular orbital calculations of tetraazaporphyrinato ruthenium (II) bis(4-methylpyridine) fused with one to four diphenylthiophene units. *Journal of Inorganic Biochemistry* 158: 35–44.

101 Leznoff, C.C., Lam, H., Nevin, W.A. et al. (1987). 1,8-naphthalene-linked cofacial dimeric phthalocyanines. *Angewandte Chemie International Edition* 26: 1021–1023.

102 (a) Tolbin, A.Y., Ivanov, A.V., Tomilova, L.G., and Zefirov, N.S. (2002). Preparation of 1,2-bis(3,4-dicyanophenoxymethyl)benzene and the binuclear zinc phthalocyanine derived from it. *Mendeleev Communications* 12 (3): 96–97. (b) Ceyhan, T., Altindal, A., Özkaya, A.R., et al. (2006). Synthesis, characterization, and electrical, electrochemical and gas sensing properties of a novel ball-type four t-butylcalix[4]arene bridged binuclear zinc(II) phthalocyanine. *Chem. Commun.* 320–322.

103 Kobayashi, N., Kondo, R., Nakajima, S., and Osa, T. (1990). New route to unsymmetrical phthalocyanine analogues by the use of structurally distorted subphthalocyanines. *Journal of the American Chemical Society* 112: 9640–9641.

104 Erdem, S.S., Nesterova, I.V., Soper, S.A., and Hammer, R.P. (2008). Solid-phase synthesis of asymmetrically substituted "AB3-type" phthalocyanines. *The Journal of Organic Chemistry* 73 (13): 5003–5007.

105 Chen, X., Salmon, T.R., and McGrath, D.V. (2009). Asymmetric phthalocyanine synthesis by ROMP-capture release. *Organic Letters* 11: 2061–2064.

106 (a) Ayhan, M.M., Singh, A., Hirel, C. et al. (2014). ABAB homoleptic bis(phthalocyaninato) lanthanide(III) complexes: original octupolar design leading to giant quadratic hyperpolarizability. *Inorganic Chemistry* 53: 4359–4370. (b) Ayhan, M.M., Singh, A., Hirel, C. et al. (2012). ABAB homoleptic bis(phthalocyaninato)lutetium(III) complex: toward the real octupolar cube and giant quadratic hyperpolarizability. *Journal of the American Chemical Society* 134: 3655–3658.

107 Kudrik, E.V., Nikolaev, I.Y., and Shaposhnikov, G.P. (2000). 3,6- didecyloxyphthalonitrile as a starting compound for the selective synthesis of phthalocyanines of the ABAB type. *Russian Chemical Bulletin, International Edition* 49 (12): 2027–2030.

108 Drew, D.M. and Leznoff, C.C. (1994). The synthesis of pure 1,11,15,25-tetrasubstitutedphthalocyanines as single isomers using bisphthlonitriles. *Synlett* 623–624.

109 Mokhosi, I.S. and Nyokong, T. (2005). Photophysical properties of a water-soluble adjacently substituted bisnaphthalophthalocyanine. *Journal of Porphyrins and Phthalocyanines* 9: 476–483.

110 Kobayashi, N. (1998). Optically active 'adjacent' type non-centrosymmetrically substituted phthalocyanines. *Chemical Communications* 487–488.

111 Kobayashi, N., Miwa, H., Isago, H., and Tomura, T. (1999). An adjacent dibenzotetraazaporphyrin: a structural intermediate between tetraazaporphyrin and phthalocyanine. *Inorganic Chemistry* 38: 479–485.

112 Hurley, T.J., Robinson, M.A., and Trotz, S. (1967). Complexes derived from 1,3-diiminoisoindoline-containing ligands. II. Stepwise formation of nickel phthalocyanine. *Inorganic Chemistry* 6: 389–392.

113 Lourenço, L.M.O., Pereira, P.M.R., Maciel, E. et al. (2014). Amphiphilic phthalocyanine-cyclodextrin conjugates for cancer photodynamic therapy. *Chemical Communications* 50: 8363–8366.

114 Cabezon, B., Nicolau, M., Barbera, T., and T. (2000). Synthesis and liquid-crystal behavior of triazolephthalocyanines. *Chemistry of Materials* 12: 776–781.

115 Chow, S.Y.S. and Ng, D.K.P. (2016). Synthesis of an ABCD-type phthalocyanine by intramolecular cyclization reaction. *Organic Letters* 18 (13): 3234–3237.

116 Pan, N., Bian, Y., Fukuda, T. et al. (2004). Homoleptic lanthanide triple-deckers of 5,15-diazaporphyrin with D2h symmetry. *Inorganic Chemistry* 43: 8242–8244.

117 (a) Ishikawa, N. and Kaizu, Y. (2002). Synthetic, spectroscopic and theoretical study of novel supramolecular structures composed of lanthanide phthalocyanine double-decker complexes. *Coordination Chemistry Reviews* 226: 93–101. (b) Liu, Y., Shigehara, K., Hara, M., and Yamada, A. (1991). Electrochemistry and electrochromic behavior of Langmuir–Blodgett films of octakis-substituted rare-earth metal diphthalocyanines. *Journal of the American Chemical Society* 113: 440–443.

118 Wang, K., Qi, D., Wang, H. et al. (2013). Binuclear phthalocyanine-based sandwich-type rare earth complexes: unprecedented two p-bridged biradical-metal integrated SMMs. *Chemistry – A European Journal* 19: 11162–11166.

119 Tarakanovaa, E.N., Tarakanova, P.A., Pushkareva, V.E., and Tomilova, L.G. (2014). The first synthesis of sandwich-type complex based on tetradiazepinoporphyrazine ligand. *Journal of Porphyrins and Phthalocyanines* 18: 149–154.

120 Li, J., Gryko, D., Dabke, R.B. et al. (2000). Synthesis of thiol-derivatized europium porphyrinic triple-decker sandwich complexes for multibit molecular information storage. *The Journal of Organic Chemistry* 65: 7379–7390.

121 Lu, G., Li, J., Yan, S. et al. (2015). Synthesis and characterization of rare earth corrole-phthalocyanine heteroleptic triple-decker complexes. *Inorganic Chemistry* 54: 5795–5805.

122 Birin, K.P., Gorbunova, Y.G., and Tsivadze, A.Y. (2012). Efficient scrambling-free synthesis of heteroleptic terbium triple-decker (porphyrinato)(crown-phthalocyaninates). *Dalton Transactions* 41: 9672–9681.

123 Zhu, P., Wang, Y., Ma, P. et al. (2017). Highly ordered sandwich-type (phthalocyaninato) (porphyrinato) europium double-decker nanotubes and room temperature NO2 sensitive properties. *Dalton Transactions* 46: 1531–1538.

124 Kyatskaya, S., Mascaros, J.R.G., Bogani, L. et al. (2009). Anchoring of rare-earth-based single-molecule magnets on single-walled carbon nanotubes. *Journal of the American Chemical Society* 131: 15143–15151.

125 (a) Goedkent, V.L. and Ercolani, C. (1984). *Nitrido-Bridged Iron Phthalocyanine Dimers: Synthesis and Characterization*, 378–379. Chemical Communications: *Journal of the Chemical Society*. (b) Bottomlev, L.A., Gorce, J.N., Goedken, V.L., and Ercolani, C. (1985). Spectroelectrochemistry of a mu nitrido-bridged iron phthalocyanine dimer. *Inorganic Chemistry* 24: 3733–3737. (c) Kennedy, B.J., Murray, K.S., Homborg, H., and Kalz, W. (1987). Iron(IV)phthalocyanines. Magnetic and spectral features of μ-nitrido-iron-phthalocyanine, (FePc)2N and of some oxidized derivatives. *Inorganica Chimica Acta* 134: 19–21. (d) Ercolani, C., Gardini, M., Pennesi, G. et al. (1988). High-valent iron phthalocyanine mu nitrido dimers. *Inorganic Chemistry* 27: 422–424. (e) Moubaraki, M., Benlian, D., Baldy, A., and Pierrot, M. (1989). [mu]-nitruro-bis[bromo(phtalocyaninato)fer], (BrFePc)2 N. *Acta Crystallographica Section C* 45: 393–394.

126 Afanasiev, P. and Sorokin, A.B. (2016). μ-nitrido diiron macrocyclic platform: particular structure for particular catalysis. *Accounts of Chemical Research* 49: 583–593.

127 (a) Ercolani, C., Jubb, J., Pennesi, G. et al. (1995). (mu-nitrido)((tetraphenylporphyrinato) iron)((phthalocyaninato)iron) and its Fe-Ru analog: redox behavior and characterization of new Fe(IV)-containing species. X-ray crystal structure of [(THF)(TPP)Fe-N-FePc(H2O)](I5).Cntdot.2THF. *Inorganic Chemistry* 34: 2535–2541. (b) Ercolani, C., Hewage, S., Heucher, R., and Rowill, G. (1993). First example of a mixed-ligand bimetallic (Fe-Fe) N-bridged dimer: (mu-nitrido) [((tetraphenylporphyrinato) iron) (phthalocyaninato) iron]. *Inorganic Chemistry* 32: 2975–2977.

128 a) Donzello, M.P., Ercolani, C., Kadish, K.M. et al. (1998). Synthesis, chemical–physical characterization, and redox properties of a new mixed-ligand Heterobimetallic N-bridged dimer: (μ-nitrido) [((tetraphenylporphyrinato) manganese) ((phthalocyaninato)iron)]. *Inorganic Chemistry* 37: 3682–3688. b) Donzello, M.P., Ercolani, C., Russo, U. et al. (2001). Metal- and ligand-centered Monoelectronic oxidation of μ-nitrido [((tetraphenylporphyrinato)manganese) (phthalocyaninatoiron)], [(TPP)Mn−N−FePc]. X-ray crystal structure of the Fe(IV)-containing species [(THF) (TPP) Mn−N−FePc(H2O)](I5)·2THF. *Inorganic Chemistry* 40: 2963–2967.

129 Sorokin, A.B., Kudrik, E.V., and Bouchu, D. (2008). Bio-inspired oxidation of methane in water catalyzed by N-bridged diiron phthalocyanine complex. *Chemical Communications* 2562–2564.

130 İşci, Ü. (2013). The first push-pull μ-nitrido iron phthalocyanine dimer. *Journal of Porphyrins and Phthalocyanines* 17: 1022–1026.

131 Rossi, G., Gardini, M., Pennesi, G. et al. (1989). Ruthenium phthalocyanine chemistry: synthesis and properties of a mixed-valence nitrido-bridged ruthenium phthalocyanine dimer. *Journal of the Chemical Society, Dalton Transactions* 193–195.

132 Kudrik, E.V., Afanasiev, P., and Sorokin, A.B. (2010). Synthesis and properties of FeIII-N=MnIV heterometallic complex with tetra-tert-butylphthalocyanine ligands. *Macroheterocycles* 3: 19–22.

133 Floris, B., Donzello, M.P., and Ercolani, C. (2003). Single-atom bridged dinuclear metal complexes with emphasis on phthalocyanine systems. In: *The Porphyrin Handbook*, vol. 18 (ed. K.M. Kadish, K.M. Smith and R. Guilard), 1–62. San Diego, CA: Elsevier Science.

134 Ercolani, C., Rossi, G., and Monacelli, F. (1980). Synthesis and characterization of a μ-oxo dimer formed by the interaction of phthalocyanine iron(II) with dioxygen. *Inorganica Chimica Acta* 44: 215–216.

135 (a) Rossi, G., Goedken, L., and Ercolani, C. (1988). μ-Carbido-bridged iron phthalocyanine dimers: synthesis and characterization. *Journal of the Chemical Society, Chemical Communications* 46–47. (b) Ercolani, C., Gardini, M., Goedken, V.L. et al. (1989). High-valent iron phthalocyanine five- and six-coordinated p-carbido dimers. *Inorganic Chemistry* 28: 3097–3099.

136 Colomban, C., Kudrik, E.V., Tyurin, D.V. et al. (2015). Synthesis and characterization of μ-nitrido,μ-carbido and μ-oxo dimers of iron octapropylporphyrazine. *Dalton Transactions* 44: 2240–2251.

137 Sumimoto, M., Kawashima, Y., Horia, K., and Fujimoto, H. (2015). Theoretical study on the stability of double-decker type metal phthalocyanines, M(Pc)2 and M(Pc)2+ (M = Ti, Sn and Sc): a critical assessment on the performance of density functionals. *Physical Chemistry Chemical Physics* 17: 6478–6483.

138 Chambrier, I., Hughes, D.H., Swarts, J.C. et al. (2006). First example of a di-cadmium tris-phthalocyanine triple-decker sandwich complex. *Chemical Communications* 3504–3506.

139 Fukuda, T., Biyajima, T., and Kobayashi, N. (2010). A discrete quadruple-Decker phthalocyanine. *Journal of the American Chemical Society* 132: 6278–6279.

140 Ebadi, M. (2003). Electrocatalytic oxidation of hydroxylamine by (RuPc)2 graphite modified electrode. *Electrochimica Acta* 48: 4233–4238.

141 (a) Ali, H., Langlois, R., Wagner, J.R. et al. (1988). Biological activities of phthalocyanines-X. syntheses and analyses of sulfonated phthalocyanines. *Photochemistry and Photobiology* 47 (5): 713–717. (b) Spikes, J.D. (1986). Phthalocyanines as photosensitizers in biological systems and for the photodynamic therapy of tumors. *Photochemistry and Photobiology* 43 (6): 691–699.

142 Lebedeva, N.S., Kumeev, R.S., Alper, G.A. et al. (2007). Dimerization and coordination properties of zinc(II)tetra-4-alkoxybenzoyloxi phthalocyanine in relation to DABCO in o-xylene and chloroform. *Journal of Solution Chemistry* 36: 793–801.

143 Hanack, M., Lange, A., and Grosshans, R. (1991). Tetrazine-bridged phthalocyaninato-metal complexes as semiconducting material. *Synthetic Metals* 45: 59–70.

144 Kobayashi, N., Muranaka, A., and Ishii, K. (2000). Symmetry-lowering of the phthalocyanine chromophore by a C2 type axial ligand. *Inorganic Chemistry* 39: 2256–2257.

145 Platel, R.H., Tasso, T.T., Zhou, W. et al. (2015). Metallophthalocyanin-ocenes: scandium phthalocyanines with an η5-bound Cp ring. *Chemical Communications* 51: 5986–5989.

146 Taşkın, G.C., Durmuş, M., Yüksel, F. et al. (2015). Axially paraben substituted silicon(IV) phthalocyanines towards dental pathogen *Streptococcus mutans*: synthesis, photophysical, photochemical and in vitro properties. *Journal of Photochemistry and Photobiology A: Chemistry* 306: 31–40.

147 Lau, J.T.F., Lo, P.C., Jiang, X.J. et al. (2014). A dual Activatable photosensitizer toward targeted photodynamic therapy. *Journal of Medicinal Chemistry* 57: 4088–4097.

148 Mauldin, C.E., Piliego, C., Poulsen, D. et al. (2010). Axial thiophene-boron (subphthalocyanine) dyads and their application in organic photovoltaics. *ACS Applied Materials & Interfaces* 2: 2833–2838.

149 Romero-Nieto, C., Guilleme, J., Fernandez-Ariza, J. et al. (2012). Ultrafast photoinduced processes in subphthalocyanine electron donor acceptor conjugates linked by a single BN bond. *Organic Letters* 14: 5656–5659.

150 Ruf, M., Lawrence, A.M., Noll, B.C., and Pierpont, C.G. (1998). Silicon and zinc coordination to peripheral catechol sites of (2,3,9,10,16,17,23,24-octahydroxyphthalocyaninato)nickel(II). Phthalocyanine coordination chemistry at the edge. *Inorganic Chemistry* 37: 1992–1999.

151 Kimura, M., Muto, T., Takimoto, H. et al. (2000). Fibrous assemblies made of amphiphilic metallophthalocyanines. *Langmuir* 16: 2078–2082.

152 Liu, J.Y., Lo, P.C., Jiang, X.J. et al. (2009). Synthesis and in vitro photodynamic activities of di-α-substituted zinc(II)phthalocyanine derivatives. *Dalton Transactions* 4129–4135.

153 Zorlu, Y., Ermeydan, M.A., Dumoulin, F. et al. (2009). Glycerol and galactose substituted zinc phthalocyanines. Synthesis and photodynamic activity. *Photochemical and Photobiological Sciences* 8: 312–318.

154 Dumoulin, F., Ali, H., Ahsen, V., and van Lier, J.E. (2011). Preparation of amphiphilic glycerol-substituted zinc phthalocyanines using copper-free Sonogashira cross-coupling in aqueous medium. *Tetrahedron Letters* 52: 4395–4397.

155 Kolb, H.C., Finn, M.G., and Sharpless, K.B. (2001). Click chemistry: diverse chemical function from a few good reactions. *Angewandte Chemie International Edition* 40: 2004–2021.

156 Dumoulin, F. and Ahsen, V. (2011). Click chemistry: the emerging role of the azide-alkyne Huisgen dipolar addition in the preparation of substituted tetrapyrrolic derivatives. *Journal of Porphyrins and Phthalocyanines* 15: 502–504.

157 Acherar, S., Colombeau, L., Frochot, C., and Vanderesse, R. (2015). Synthesis of porphyrin, chlorin and phthalocyanine derivatives by azide-alkyne click chemistry. *Current Medicinal Chemistry* 22 (28): 3217–3254.

158 Campidelli, S., Ballesteros, B., Filoramo, A. et al. (2008). Facile decoration of functionalized single-wall carbon nanotubes with phthalocyanines via click chemistry. *Journal of the American Chemical Society* 130: 11503–11509.

159 Zorlu, Y., Dumoulin, F., Bouchu, D. et al. (2010). Monoglycoconjugated water-soluble phthalocyanines. Design and synthesis of potential selectively targeting PDT photosensitisers. *Tetrahedron Letters* 51: 6615–6618.

160 Jimenez, C.M., Henry, M., Aggad, D. et al. (2017). Porphyrin- or phthalocyanine-bridged silsesquioxane nanoparticles for two-photon photodynamic therapy or photoacoustic imaging. *Nanoscale* 9: 16622–16626.

161 Giuntini, F., Dumoulin, F., Daly, R. et al. (2012). Orthogonally bifunctionalised polyacrylamide nanoparticles: a support for the assembly of multifunctional nanodevices. *Nanoscale* 4: 2034–2045.

162 Campo, B.J., Duchateau, J., Ganivet, C.R. et al. (2011). Broadening the absorption of conjugated polymers by "click" functionalization with phthalocyanines. *Dalton Transactions* 40: 3979–3988.

163 Tekdas, D.A., Garifullin, R., Şentürk, B. et al. (2014). Design of a Gd-DOTA-phthalocyanine conjugate combining MRI contrast imaging and photosensitization properties as a potential molecular theranostic. *Photochemistry and Photobiology* 90: 1376–1386.

164 Dumoulin, F., Durmus, M., Ahsen, V., and Nyokong, T. (2010). Synthetic pathways to water-soluble phthalocyanines and close analogs. *Coordination Chemistry Reviews* 254: 2792–2847.

165 Kuznetsova, N., Makarov, D., Yuzhakova, O. et al. (2009). Photophysical properties and photodynamic activity of octacationic oxotitanium(IV) phthalocyanines. *Photochemical and Photobiological Sciences* 8: 1724–1733.

166 Machacek, M., Demuth, J., Cermak, P. et al. (2016). Tetra(3,4-pyrido)porphyrazines caught in the cationic cage: toward nanomolar active photosensitizers. *Journal of Medicinal Chemistry* 59: 9443–9456.

167 Roy, I., Shetty, D., Hota, R. et al. (2015). A multifunctional subphthalocyanine nanosphere for targeting, labeling, and killing of antibiotic-resistant bacteria. *Angewandte Chemie International Edition* 54: 15152–15155.

168 Martínez-Díaz, M.V., Quintiliani, M., and Torres, T. (2008). Functionalisation of phthalocyanines and subphthalocyanines by transition-metal-catalysed reactions. *Synlett* 1: 1–20.

169 Cid, J.J., Yum, J.H., Jang, S.R. et al. (2007). Molecular cosensitization for efficient panchromatic dye-sensitized solar cells. *Angewandte Chemie International Edition* 46: 8358–8362.

170 de Carcer García, I.A., Sevim, A.M., de la Escosura, A., and Torres, T. (2013). Synthesis of unsymmetrical carboxyphthalocyanines by palladium-catalyzed hydroxycarbonylation of iodo-substituted precursors. *Organic and Biomolecular Chemistry* 11: 2237–2240.

171 Mutyala, A.K. and Park, J.S. (2016). Synthesis of highly water-soluble trisulfonated phthalocyanine with single carboxylic acid via palladium-catalyzed cyanation reaction. *Tetrahedron Letters* 571: 109–1112.

172 Ali, H., St-Jean, O., Tremblay-Morin, J.P., and van Lier, J.E. (2006). Functionalization of sulfophthalocyanines in aqueous medium by palladium-catalyzed cross-coupling reactions. *Tetrahedron Letters* 47: 8275–8278.

173 Tian, H., Ali, H., and van Lier, J.E. (2000). Synthesis of water soluble trisulfonated phthalocyanines via palladium-catalysed cross coupling reactions. *Tetrahedron Letters* 41: 8435–8438.

174 Silva, S., Pereira, P.M.R., Silva, P. et al. (2012). Porphyrin and phthalocyanine glycodendritic conjugates: synthesis, photophysical and photochemical properties. *Chemical Communications* 48: 3608–3610.

175 (a) Neti, V.S.P.K., Wu, X., Deng, S., and Echegoyen, L. (2013). Synthesis of a phthalocyanine and porphyrin 2D covalent organic framework. *CrystEngComm* 15: 6892–6895. (b) Jin, S., Ding, X., Feng, X. et al. (2013). Charge dynamics in a donor-acceptor covalent organic framework with periodically ordered bicontinuous heterojunctions. *Angewandte Chemie International Edition* 52: 2017–2021. (c) Neti, V.S.P.K., Wu, X., Hosseini, M. et al. (2013). Synthesis of a phthalocyanine 2D covalent organic framework. *CrystEngComm* 15: 7157–7160.

176 Lafont, D., Zorlu, Y., Savoie, H. et al. (2013). Monoglycoconjugated phthalocyanines. Effect of sugar and linkage on photodynamic activity. *Photodiagnosis and Photodynamic Therapy* 10: 252–259.

177 Başeren, Ş.C., Özçelik, Ş., and Gül, A. (2011). Boronic esters of a porphyrazine and its precursor. *Journal of Porphyrins and Phthalocyanines* 15: 742–747.

178 Rodríguez-Morgade, M.S. and Stuzhin, P.A. (2004). The chemistry of porphyrazines: an overview. *Journal of Porphyrins and Phthalocyanines* 8: 1129–1165.

6

Oxidation and Reduction of Porphyrins

Christian Brückner and Nisansala Hewage

Department of Chemistry, University of Connecticut, Storrs, CT, USA

6.1 Introduction: Scope and Limits of This Chapter

Porphyrins are fully unsaturated tetrapyrrolic macrocycles linked by methylene carbons and enclosing an 18+4 π-system, that is, an aromatic 18 π-electron system cross-conjugated with two additional β,β′-double bonds (Figure 6.1). Summarized here are the redox reactions that directly alter this porphyrinic π-system. We focus on the formation and some physical properties of the reduction and oxidation products, but not on their chemical reactivity. Redox reactions of peripheral substituents, such as the reduction/oxidation of a β-vinyl group to an ethyl/acetyl group, are ignored, even if they affect the π-system through inductive or resonance effects. Likewise, many electrophilic aromatic substitution reactions on the porphyrin *meso*- or β-positions are technically oxidations (halogenation, nitration, etc.), but are not included here. We refer to other reviews summarizing the functionalization of porphyrins [2, 3].

The most prominent oxidation and reduction reactions of porphyrins take place at the β-positions, followed by those at the *meso*-positions. Reactions at the α-positions occur only rarely, are not observed under mild reaction conditions, and thus are ignored. For sake of convenience, we will discuss the oxidation and reduction reactions of the porphyrins separately from each other, organized by the positions oxidized or reduced. Metal-centered and macrocycle-centered resonance-stabilized reversible redox events of the (metallo)porphyrins are discussed together, reflecting the non-innocent nature of the porphyrinic ligand.

Generally, we are limiting the discussion to representative and well-documented examples; a complete treatment of the subjects is not attempted. Comprehensive reviews on related topics, such as the syntheses and occurrence of synthetic and natural hydroporphyrins [4, 5], the conversion of porphyrins to hydroporphyrins and porphyrin analogues [5–8], chlorophylls and its oxidative degradation products [9–12], metal-centered and macrocycle-centered resonance-stabilized redox events [13], and exploitation of the redox properties of porphyrins in devices [14], are available. The redox reactions of the porphyrazines [15], phthalocyanines [16], contracted [17] or expanded [18–21] porphyrins, carbaporphyrins [22–24], and other porphyrin analogues [6, 7, 25] will also not be included here; instead, we refer the reader to dedicated reviews.

Fundamentals of Porphyrin Chemistry: A 21st Century Approach, Volume 1, First Edition.
Edited by Penelope J. Brothers and Mathias O. Senge.
© 2022 John Wiley & Sons Ltd. Published 2022 by John Wiley & Sons Ltd.

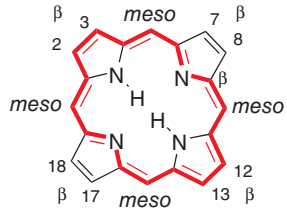

Figure 6.1 Porphyrin macrocycle structure, including the position numbering used, showing the macrocycle-aromatic 18 π-system inherent to all chromophores in red and bold. For a detailed account of the naming conventions, see Senge [1]. Source: Senge [1].

6.2 Reductions of Porphyrins

6.2.1 Reduction of the β,β′-Bonds: Hydroporphyrins

The β-hydroporphyrins include the chlorins (7,8-dihydroporphyrins), bacteriochlorins (7,8,17,18-tetrahydroporphyrins), and their tautomers, the isobacteriochlorins (7,8,12, 13-tetrahydroporphyrins (Figure 6.2) [26]. This naming suggests that they are formed along reduction pathways; however, the cross-conjugated β,β′-double bonds can also be removed from conjugation with the 18 π-electron system along addition or oxidation pathways. In fact, the spectroscopic properties of some porphyrin oxidation and reduction products are very similar to each other; the number and position of the modifications have a much larger impact on the optical properties of the resulting macrocycle than the formal type of conversion. In accordance with the established nomenclature rules for the tetrapyrroles [2, 27], we will refer to any chromophore containing an 18+2 π-system as a chlorin, and 18 π-systems, depending on the relative position of their "reduction" sites, as bacteriochlorins or isobacteriochlorins.

The four principal porphyrin/hydroporphyrin chromophore classes each possess diagnostic UV-vis spectra (Figure 6.3) [29]. As expected for principally $\pi \rightarrow \pi^*$ transitions, the band position and intensities observed find their qualitative and quantitative explanation in the relative position and symmetry of the associated chromophore frontier orbitals [29]. The spectra of regular porphyrins are characterized by an intense band around 400 nm (the so-called Soret band), followed by four so-called side bands (the so-called Q bands) in descending order of intensity. These possess extinction coefficients that are at least an order lower than those of the Soret band. Owing to an increase of the chromophore symmetry, the porphyrin and chlorin metal complexes possess a reduced number of Q bands. The UV-vis spectrum of a

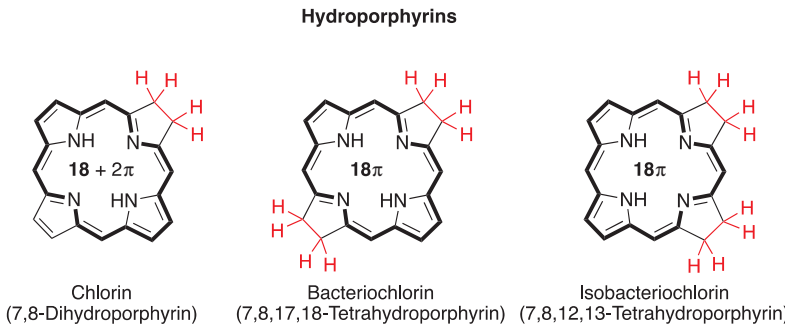

Figure 6.2 β-Hydroporphyrin macrocycle structures, showing the inherent macrocycle-aromatic 18 π-system in bold. For a detailed account of the naming conventions, based on Ref. [1, 26].

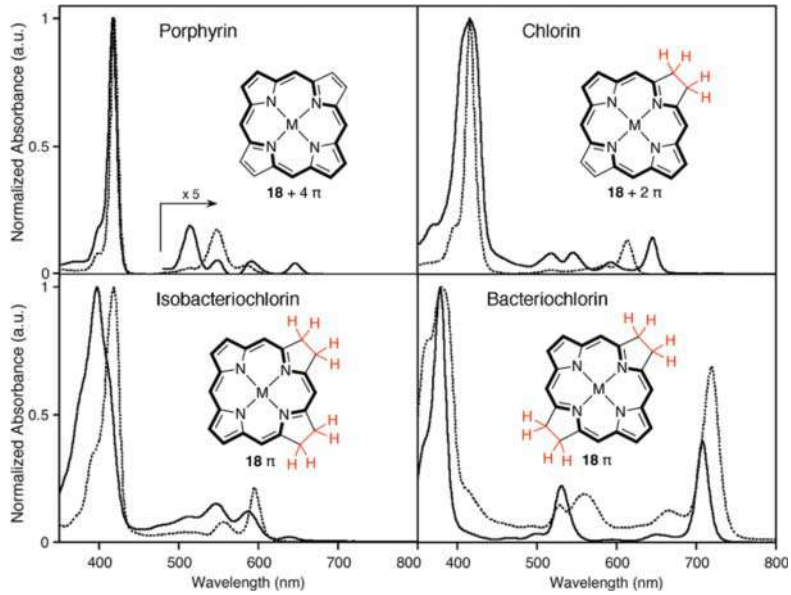

Figure 6.3 Comparison of the UV-vis spectra (in CH_2Cl_2) of the four principal porphyrin and hydroporphyrin classes, in their free-base (solid trace) and metalated form (M = Zn; broken trace), as illustrated by their hydroxylated *meso*-tetraphenyl derivatives. The spectra of the hydroxylated hydrochlorins are hypsochromically shifted compared to the spectra of the non-hydroxylate chromophores, but the overall shapes of the spectra are representative of their chromophore classes; the spectra of the *cis*- and *trans*-isomers of the tetrahydroxy-bacteriochlorin and -isobacteriochlorin are shown, respectively, but the spectra of the corresponding isomers are essentially identical [28]. Source: Based on Brückner and Dolphin [29].

free-base chlorin is similar of that of a porphyrin in that it also exhibits a Soret band and four Q bands, but the λ_{max} band is now the most intense Q band, and the spectrum tends to be generally broadened; λ_{max} may or may not be bathochromically shifted compared to the parent porphyrin. The Soret band of an isobacteriochlorin is hypsochromically shifted compared to that of a chlorin, the spectrum is chlorin-like broadened, the Q-band intensity distribution is altered, and the λ_{max} is hypsochromically shifted. The highly diagnostic spectra of free-base bacteriochlorins are characterized by large hypsochromic shifts in the Soret band along with a significantly bathochromically shifted λ_{max} (Q-) band. The intensity of the latter band has the same order of magnitude as the intensity of the Soret band, even though, in absolute terms, the extinction coefficient of the Soret band of a bacteriochlorin can be an order of magnitude lower than that of a porphyrin or chlorin. The optical spectra are modulated by β- and *meso*-substituents.

Increasing degrees of reduction of the macrocycle also lead to increased conformational flexibility. Broadly generalized, the porphyrinoid absorption spectra broaden with increasing conformational flexibility and red-shift with increasing deviation from planarity [30, 31]. As a consequence of the multiple electronic and conformational factors influencing the spectra of the hydroporphyrin chromophores, the spectra of each type may span a considerable wavelength range.

The intrinsically basic imine-type nitrogen atoms of porphyrins are sterically protected from protonation since protonation brings a total of three (or four) hydrogen atoms into the macrocycle cavity, a sterically untenable situation for a planar macrocycle. Given a strong

enough acid, however, mono-protonation can be enforced, leading to a saddled distortion of the macrocyle (two opposing pyrroles tilt up, two opposing pyrroles tilt down). Although it alleviates this steric clash between the inner hydrogens, this distortion comes with a steric (Pitzer strain) and electronic (reduction of π-overlap) energy penalty. Once the saddled conformation is induced by protonation of the first imine nitrogen, the second imine nitrogen loses the steric protection of the planar conformation and thus becomes much more basic. This effect is dramatic, leading to the observation that the basicity of the second imine is higher than that of the first. Therefore, mono-protonated porphyrins are, outside of special cases, not observed [32].

Increasing reduction decreases the basicity of the inner imine-type nitrogen atoms significantly. Thus, planar bacteriochlorins are less basic than chlorins, which, in turn, are less basic than porphyrins [33]. This indicates that the intrinsic electronic effect of the π-system overrides the expected increase in basicity of the hydroporphyrins because of their increased conformational flexibility [34]. On account of their β-substitution with electron-withdrawing substituents (ketones, lactones), some oxidation products have been shown to possess reduced basicity [35].

6.2.1.1 Diimide Reduction

Diimide (HN=NH), generated in situ from *p*-toluenesulfonylhydrazide in hot pyridine or picoline in the presence of K_2CO_3, is an excellent – and the most general – reductant for the *syn*-reduction of porphyrin β,β′-double bonds. First reported by Whitlock et al. [33], it has been applied to *meso*-aryl- (Scheme 6.1) and octaalkyl-porphyrins (Scheme 6.2) (and the corresponding chlorins) with equal success [33, 36–38]. The diimide reduction of porphyrins can also be performed on a number of particularly stable *meso*-tetraarylporphyrins $\mathbf{1^{Ar}}$ under solvent-free conditions in a *p*-toluenesulfonylhydrazide melt [36, 39]. The diimide reduction is characterized by a high degree of regioselectivity. The reduction of free-base porphyrins $\mathbf{1^{Ar}}$/**5** generates the chlorins **2**/**6** and the bacteriochlorins **3**/**7** in high yields, while the reduction of a metalloporphyrin, such as $\mathbf{1^{Ar}Zn}$, generates a metallochlorin **2Zn** and selectively a metalloisobacteriochlorin **4Zn**. This switch of regioselectivity is typical for most other reduction or oxidation methods and could be deduced to be primarily a kinetic effect [40].

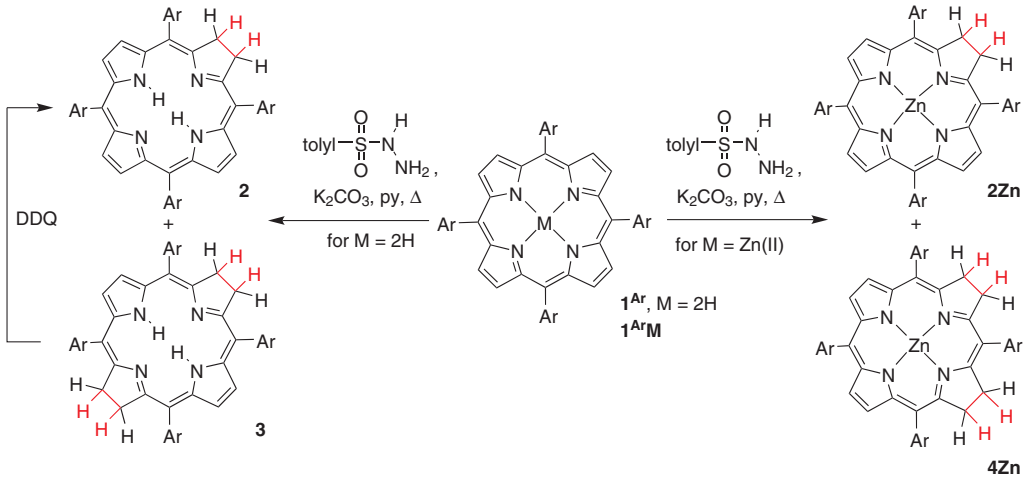

Scheme 6.1 Diimide reduction of *meso*-tetraaryl-porphyrins $\mathbf{1^{Ar}}$ and –metalloporphyrins $\mathbf{1^{Ar}M}$. Based on Whitlock et al. [33].

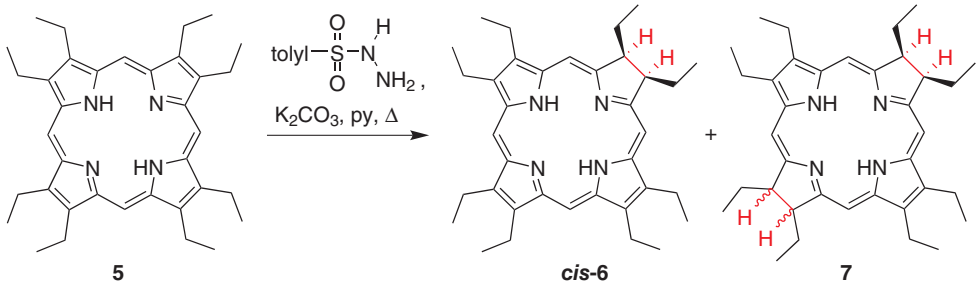

Scheme 6.2 Diimide reduction of octaethylporphyrin **5**. Based on [33].

The diimide reduction stops at the bacteriochlorin/isobacteriochlorin stage, even in the presence of a large excess of the reductant (or precursor) [33, 36, 39]. The separation of the two products is frequently nontrivial, requiring extractions with acids of different concentrations, thus utilizing the different Brønsted basicities of the hydroporphyrins (see above) [33]. In some cases, a bacteriochlorin can be specifically oxidized back to the corresponding chlorin, as the oxidation of the tetrahydroporphyrin to the dihydroporphyrin is faster than the subsequent oxidation of the dihydroporphyrin to the porphyrin [33, 37, 38, 41].

6.2.1.2 Miscellaneous Reductions

Hydrazine (H_2N-NH_2) has also been shown to be an efficient reductant of porphyrins and porphyrinoids to the corresponding hydroporphyrins, but its use is not widespread, presumably due to its lack of reaction selectivity and low reactivity [42, 43]. Conceptually, the most straightforward access to hydroporphyrins might be the reduction of porphyrins using any of many known metal (Na/alcohol) [44] or metal-catalyzed reduction (such as Raney-Ni [45], H_2/Pt or Pd-C [46]) methodologies; however, these reactions are complicated by their unfavorable regioselectivity: they tend to reduce double bonds at the *meso*-positions [47], and may quickly reduce a porphyrin to a non-aromatic porphyrinogen (a hexahydroporphyrin) [46]. A number of other non-general and often hard-to-control methods are known to convert porphyrins to hydroporphyrins [48–52].

6.2.1.3 Cycloadditions to Porphyrin β,β′-Double Bonds

The β,β′-bonds of porphyrins and chlorins can participate in cycloaddition reactions: Diels–Alder reactions and 1,3-dipolar cycloadditions are the most prominent among them, yielding hydroporphyrin derivatives [53–56].

Diels–Alder reactions can take place in two different ways [56–58]: The β,β′-bonds of porphyrins and chlorins can participate as the dienophile (Scheme 6.3A) or a β-vinyl group and the associated β,β′-double bond may constitute a diene, capable of undergoing a Diels–Alder reaction with an electron-poor dienophile (Scheme 6.3B). Both reactions remove the β,β′-double bond from cross-conjugation with the central 18 π-system, thus forming hydroporphyrin chromophores. Because of this outcome, we classify these reactions as reductions. It should be noted that this metric for the classification of a reaction as a reduction is ambiguous, at best. To highlight this, the cycloadditions involving OsO_4 or O_3 are best classified as oxidations, although they also lead to the formation of chlorins or chlorin analogues, respectively (see Section 6.3.1).

Early examples of porphyrin β,β′-double bonds acting as dienophiles relied on the reaction of a *meso*-tetraarylporphyrin with the highly reactive diene *o*-benzoquino–dimethane,

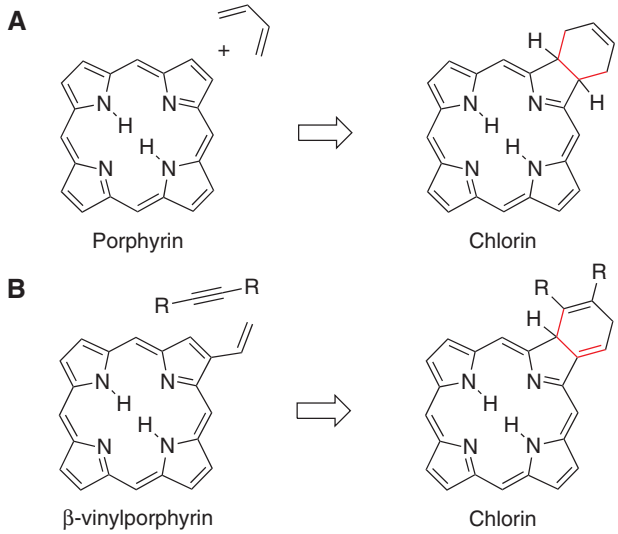

Scheme 6.3 Generalized reaction schemes for (a) the reactivity of a porphyrin to act as a dienophile in Diels–Alder reactions, or (b) the reactivity of a β-vinylporphyrin to act as a diene in Diels–Alder reactions, generating in either case a hydroporphyrin derivative.

generated in situ by thermal extrusion of SO_2 from a sulfone. The outcomes of the reaction were much dependent on the nature of the *meso*-aryl groups [58, 59]. When the *meso*-pentafluorophenylporphyrin $\mathbf{1^F}$ is used as the dienophile, a chlorin mono-adduct **8** and two stereoisomeric bacteriochlorin bis-adducts **9** are isolated (Scheme 6.4). Less electron-deficient *meso*-arylporphyrin derivatives result only in the formation of mono-adducts. Diels–Alder reactions of porphyrins can also be induced with stable dienes, such as naphthacene and pentacene under classic thermal or, preferably, microwave (MW) heating conditions [59, 60].

The most readily accessible β-vinylporphyrin is protoporphyrin IX (or its dimethyl ester) **10**. The most common dienophiles used in the reaction with **10** are dimethyl acetylenedicarboxylate (DMAD) and tetracyanoethylene (TCNE) [61, 62]. Reaction of **10** with DMAD generates chlorin **11** as a mixture of the stereoisomers resulting from the DMAD attack from either above or below the plane of the porphyrin (Figure 6.4). Similarly, compound **12** (as a mixture of isomers) is afforded from **10** and TCNE. Neither the iron(III) nor the nickel(II) complexes of porphyrin **10** react with either dienophile (DMAD or TCNE) [61]. The primary addition products are subject to isomerization reactions, shifting the position of the double bonds in the annulated ring [61, 62].

A 1,3-dipolar cycloaddition to a porphyrin β,β′-double bond also removes it from conjugation and thus generates a chlorin (Scheme 6.5) [53, 63–68]. Likewise, two subsequent cycloadditions can generate bacteriochlorins or isobacteriochlorins, whereby the regioselectivity of these reactions does not always follow the rules of the traditional reductions (see Section 6.2.1). The bis-addition reactions are further complicated by the possible formation of multiple regio- and stereoisomers resulting from the relative orientation and plane of attack of the two 1,3-dipoles.

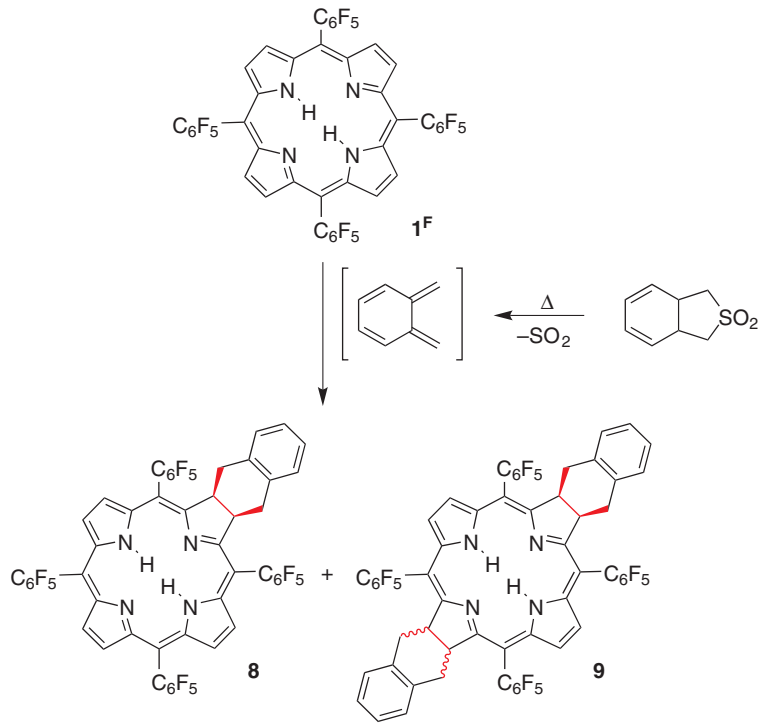

Scheme 6.4 Porphyrin $\mathbf{1^F}$ involved in a Diels–Alder reaction acting as a dienophile.

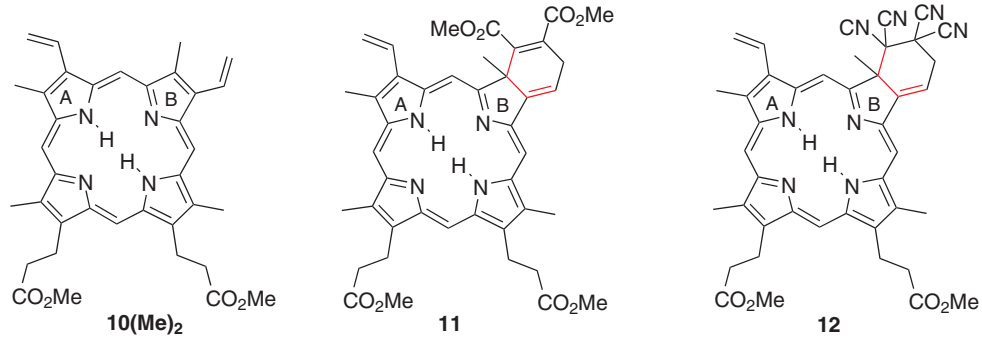

Figure 6.4 Dimethyl acetylenedicarboxylate (DMDA) addition product **11** and tetracyanoethylene (TCNE) addition product **12** of protoporphyrin IX dimethyl ester $\mathbf{10(Me)_2}$.

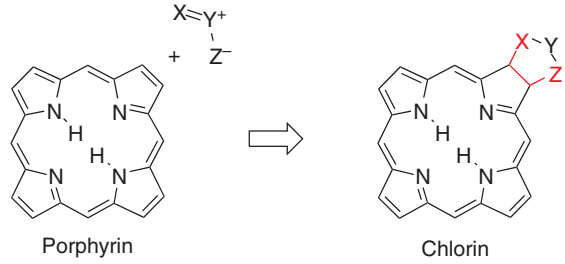

Scheme 6.5 Generalized reaction scheme for the reactivity of a β,β′-bond of porphyrins to undergo a 1,3-dipolar cycloaddition, resulting in the formation of a hydroporphyrin. Based on [53, 63–68].

The cycloaddition of azomethine ylide, generated in situ, with tetraphenylporphyrin **1**^{Ph} (Scheme 6.6), forming chlorin mono-adduct **13** and (iso)bacteriochlorin bis-adducts, is representative for a range of related ylide addition reactions [63, 64, 66, 69]. Regio- and stereochemical control is not always achieved, and is dependent on the ylide and the *meso*-aryl groups. Other 1,3-dipoles, such as carbonyl ylides [70], nitrile oxides [71–74], nitrones [67], nitrile imines [53], and carbonyl ylides [70], have been examined for the conversion of porphyrins into hydroporphyrins. Functionally related reactions are the additions of diazomethane [65, 75] or malononitrile [76], respectively, to one or two porphyrin β,β′-double bonds.

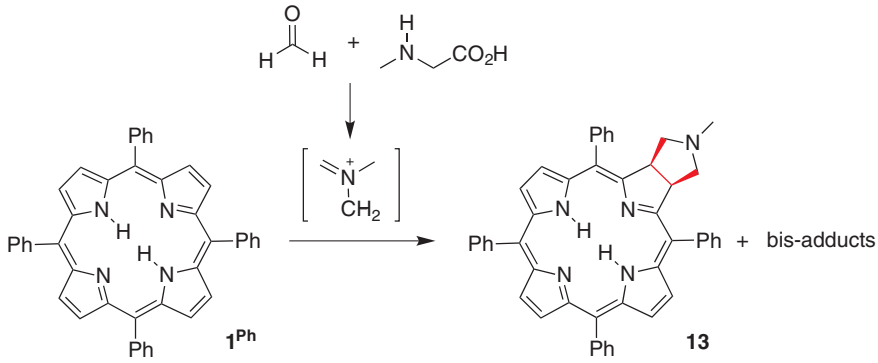

Scheme 6.6 Representative ylide addition to a the porphyrin β,β′-double bond of **1**^{Ph}, forming chlorin **13** and the corresponding bis-adducts. Based on [63, 64, 66, 69].

6.2.2 Reductions of the *meso*-Position: Phlorins

The *meso*-positions of porphyrin may also be reduced (or oxidized, see Section 6.3.2), forming phlorins or the fully *meso*-reduced macrocycle porphyrinogen (Figure 6.5). Phlorins and porphomethenes may be intermediates in classic porphyrin syntheses or products of porphyrin modification reactions [77–79]. Chlorins, phlorins, and porphomethenes are isomers of each other that, in rare cases, can be interconverted [80, 81].

The presence of the sp^3-hybridized *meso*-positions disrupts the π-conjugation in the phlorin and porphomethene macrocycles and distorts the macrocycle structure from planarity. Thus, the electronic properties of these reduced derivatives are significantly different from those of the chlorins and resemble those of the corresponding open-chain bilins and dipyrrins, respectively (cf. to Section 6.3.2). Porphyrinogens are the fully reduced, colorless, *leuco*-form of porphyrins. They are generally formed by the condensation reactions of pyrroles or dipyrromethanes and are intermediates in a range of porphyrin syntheses. Air or other chemical oxidants, typically 2,3-dichloro-5,6-dicyano-1,4-benzoquinone (DDQ) or 2,3,5,6-tetrachloro-1,4-benzoquinone (TCQ), convert porphyrinogens to porphyrins [78, 79, 82, 83]. Their generation by reduction or addition reactions from porphyrins is much less common [84].

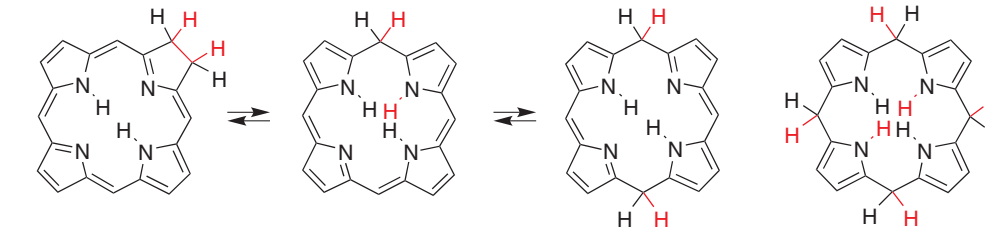

Figure 6.5 Structures of key *meso*-hydroporphyrin classes.

Phlorins are also generally found as intermediates in some porphyrin syntheses [85, 86]. Though their intermediacy in the catalytic cycle of haem P460 of the hydroxylamine oxidoreductases has been suggested [87]. Their oxidation to porphyrins is generally facile [88], but the insertion of a metal ion (such as Au^{III}) [89] or the addition of bulky *meso*-mesityl substituents were found to enhance their stability [90, 91]. One-flask syntheses of phlorins carrying alkyl groups at the *meso*-positions preventing their formation to porphyrins have been reported [92]. The primary formation of phlorins **15** involves the chemical and electrochemical reduction [90, 93–96] and nucleophilic addition of organometallic reagents to the *meso*-position of porphyrins, such as triarylporphyrin **14** (Scheme 6.7) [78, 79, 97–99].

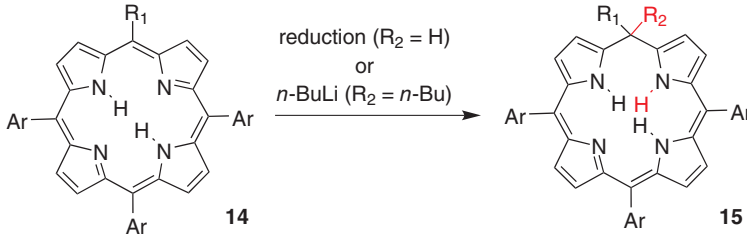

Scheme 6.7 Generation of phlorins **15** from porphyrins **14** through reduction or addition of an organometallic reagent to the *meso*-position. Based on [78, 79, 97–99].

6.3 Oxidations of Porphyrins

6.3.1 Oxidations at the β-Positions

6.3.1.1 OsO_4-Mediated Dihydroxylations: Dihydroxyhydroporphyrins

The β,β′-double bonds of porphyrins and chlorins are susceptible to oxidations that also generate chlorins and bacteriochlorins/isobacteriochlorins. One such oxidant is osmium tetroxide (OsO_4). This leads to the formation of a β,β′-osmate ester **16** that can be isolated and subsequently reduced, typically using hydrogen sulfide (H_2S) or sodium bisulfite

($NaHSO_3$) [100], to a *vic-cis*-diol functionality in chlorin **17** (Scheme 6.8). The possibility for such an OsO_4-mediated dihydroxylation of one or two β,β′-bonds of porphyrins highlights their pseudo-olefinic nature; it also reflects the general finding that OsO_4 selectively attacks the double bond that results in the least loss of resonance energy [101]. Compared to the OsO_4-mediated dihydroxylation of true olefins, however, the reaction is slow, requiring a stoichiometric quantity or even a stoichiometric excess of OsO_4 in the presence of pyridine (as co-solvent and accelerator of the osmylation reaction) [102], and up to a week of reaction time [103, 104].

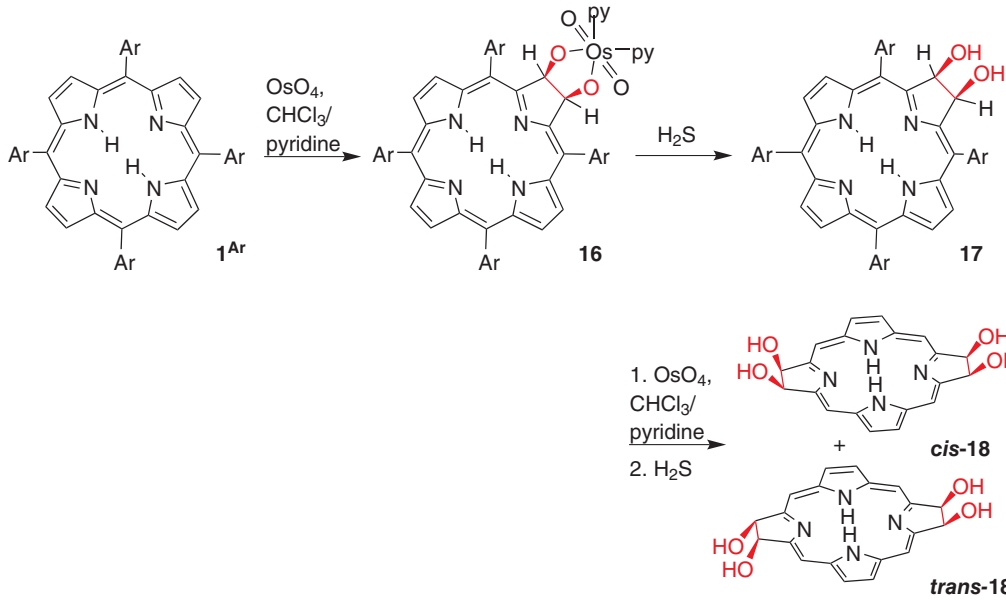

Scheme 6.8 Formation of chlorin diol **17** upon OsO_4-mediated *cis*-dihydroxylation of porphyrin $\mathbf{1^{Ar}}$ and formation of the two stereoisomers of bacteriochlorin tetraol **18** upon OsO_4-mediated *cis*-dihydroxylation of chlorin **17**. *meso*-Aryl substituents removed from the bacteriochlorins for clarity.

This OsO_4-mediated dihydroxylation is highly regioselective [29, 40, 104]: The dihydroxylation of free-base chlorins generates bacteriochlorins as a mixture of two isomeric tetrahydroxybacteriochlorins, ***cis*-** and ***trans*-18**, while the dihydroxylation of metallochlorins generates metalloisobacteriochlorins also as a mixture of stereoisomers (cf. to the corresponding outcomes of the diimide reduction and some of the cycloaddition reactions, Section 6.2.1) [105]. In non-symmetrically β-substituted porphyrins, the osmylation reaction is in select cases subject to directing effects, allowing their regioselective dihydroxylation [106–108].

The OsO_4-mediated dihydroxylation reaction has found widespread use in the formation of β-alkyl- and *meso*-aryl-dihydroxychlorins [29, 103, 104, 109, 110], tetrahydroxybacteriochlorins, and -isobacteriochlorins with a wide variety of framework structures, including 2,3,7,8,12,13,17,18-octaethylhydrochlorin derivatives, such as **19** [111, 112], phytochlorin derivatives, such as **20** [106, 113, 114] azahydroporphyrins [115], bacteriopurpurins **23** and bacteriopurpurinimides **22** [116], benzoporphyrin derivatives **21** [117, 118], and bacteriochlorin analogues such as **24** (Figure 6.6) [105, 119, 120].

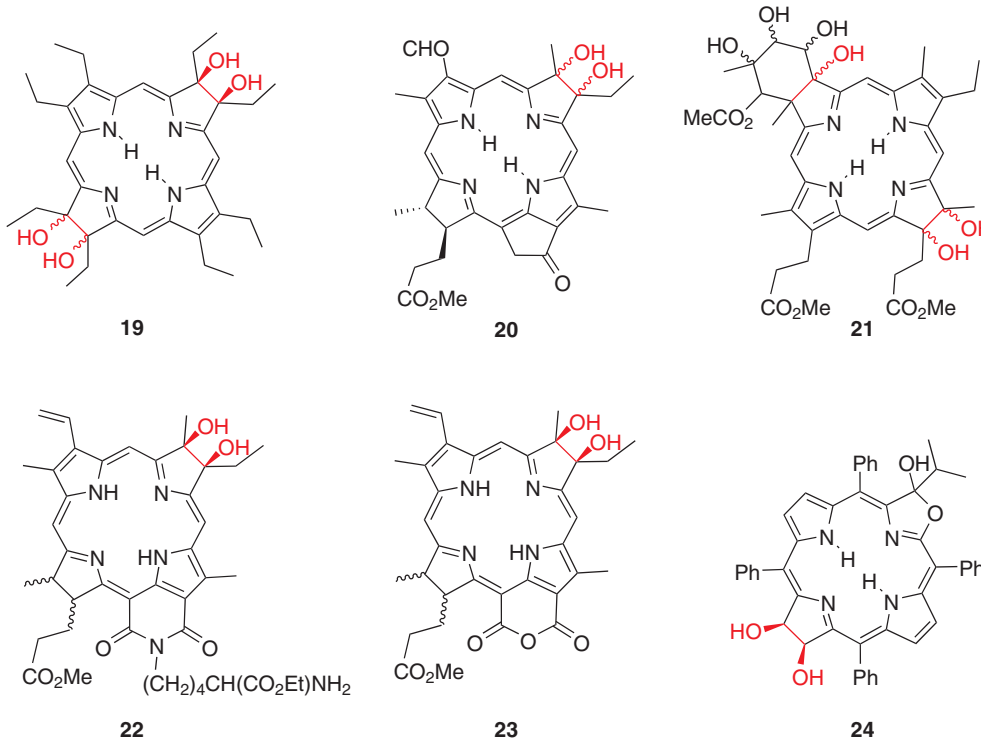

Figure 6.6 Select examples of β,β′-hydroxy-chlorins and -bacteriochlorins generated by OsO_4-mediated *cis*-dihydroxylation of the corresponding porphyrins and chlorins. Based on Ogikubo, J. et al [119].

The resulting dihydroxy-chlorins and di- or tetrahydroxybacteriochlorins tend to possess hypsochromically shifted optical spectra when compared to the corresponding all-hydro-compounds [104]. They are also characterized by significantly higher chemical stabilities toward oxidation, although they may dehydrate under certain conditions [104, 121]. β-Alkylhydroxyhydroporphyrins can undergo acid-induced pinacol-pinacolone rearrangements to the corresponding oxochlorins (cf. to Section 6.3.1) [104, 121]. Furthermore, the β,β′-diol moieties of the diol/tetraolbacteriochlorins allow facile functional group transformations that result in the conversion of the pyrroline diol to a variety of non-pyrrolic heterocycles [6, 8].

6.3.1.2 Oxochlorins and Oxobacteriochlorins

The β,β′-bond of octaethylporphyrin (**5**) is susceptible to epoxidation by treatment with conc. H_2SO_4/H_2O_2; however, the intermediate epoxide **25** and *trans*-diol **26** can only be inferred. Evidently, under the reaction conditions, the epoxide is ring-opened to the corresponding putative *trans*-diol that subsequently undergoes a pinacol-pinacolone rearrangement to provide the isolated main product, oxochlorin **25** (Scheme 6.9). This reaction is long known [122], though the *gem*-diethyl-keto-structure connectivity of the products was recognized much later [123]. The reaction does not halt at the oxochlorin **25** stage; it is further oxidized and all possible isomeric dioxobacteriochlorins **26** and dioxoisobacteriochlorins **27** form in greatly varying yields (suggesting that the reaction is not merely controlled by statistics), in addition to (likely non-macrocycle aromatic) trioxoporphyrins [124–126].

A number of octaalkylporphyrin-derived oxochlorins and dioxobacterio/isobacteriochlorins can also be obtained by pinacol-pinacolone rearrangements of the corresponding dihydroxychlorins and tetrahydroxybacterio/isobacteriochlorins, respectively [111, 127–130]. The ease of insertion of nickel(II) into the dioxobacteriochlorins and dioxoisobacteriochlorins is noted to vary, likely reflecting their varying basicity [128]. The regular ketone reactivity of the oxochlorins was demonstrated [129, 131].

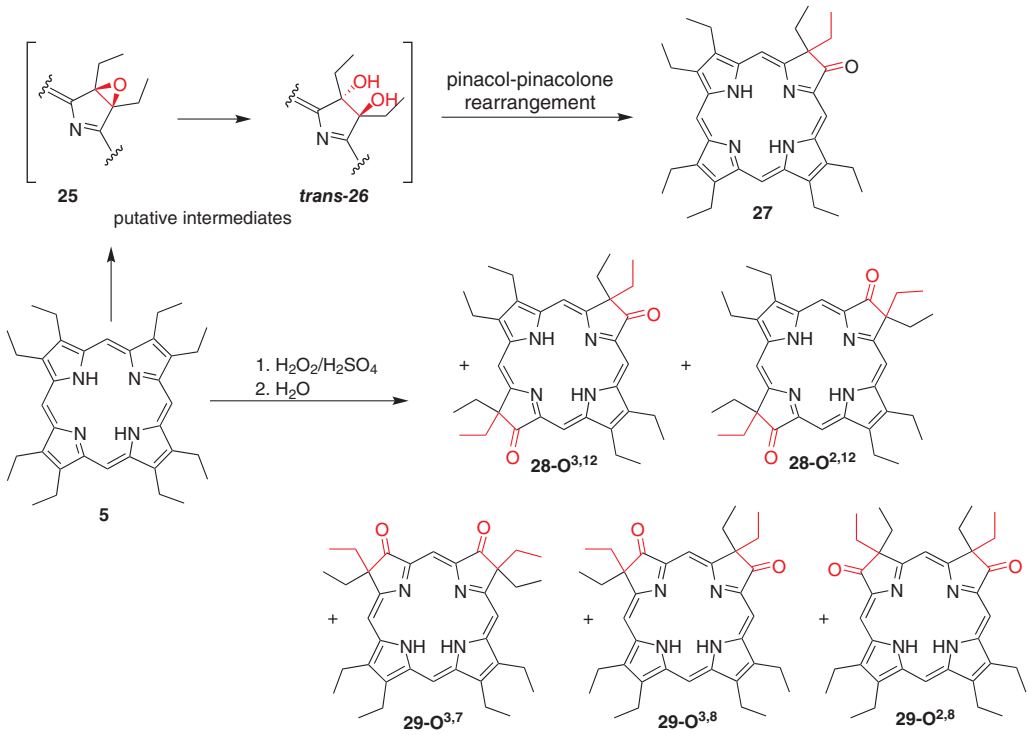

Scheme 6.9 Formation of oxochlorins **27**, dioxobacteriochlorinisomers **28**, and dioxoisobacteriochlorin isomers **29** by treatment of octaethylporphyrin **5** under epoxidizing conditions.

In the context of the synthesis of the natural product tolyporphin **31** (which contains an 8,18-dioxobacteriochlorin chromophore), or model complexes thereof, the groups of Kishi and Lindsey developed (stepwise) oxidation methodologies of *gem*-β-dialkyl-substituted bacteriochlorins **30** or **32** using a range of strong inorganic oxidants to generate the corresponding oxobacteriochlorins **33** and dioxobacteriochlorins **31**/**34**, respectively (Scheme 6.10) [132–134].

meso-Aryl-β,β′-diones of type **38** are available via a number of oxidations of β-substituted porphyrins or chlorins (Scheme 6.11). For instance, β-nitration of a 5,10,15,20-tetraarylmetalloporphyrin $\mathbf{1^{Ar}Cu}$, followed by demetalation and reduction to the β-aminoporphyrin **36** and singlet oxygen or SeO_2-mediated oxidation, leads to β,β′-dione **38** [135]. A similar pathway is available via β-hydroxyporphyrin **35M**, itself available along an oxidation route from metalloporphyrins $\mathbf{1^{Ar}M}$ [136, 137]. Likewise, β-hydroxychlorin **37**, generated by oxidation of the chlorin on silica gel, is susceptible to oxidation to dione **38** [138]. Perhaps the conceptually

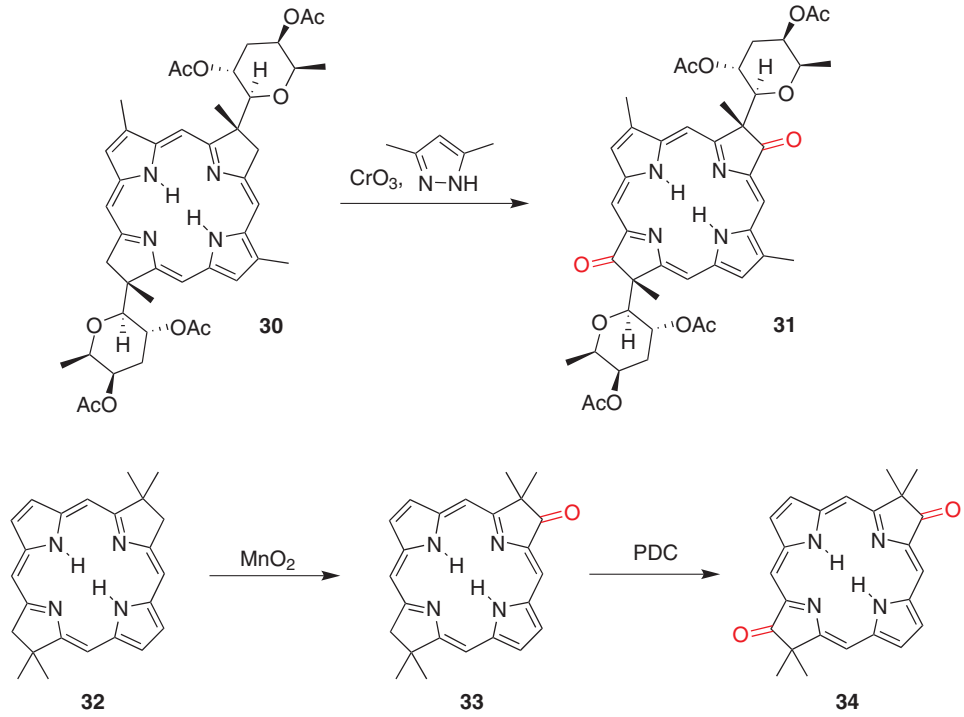

Scheme 6.10 Oxidation of *gem*-β-dialkyl-substituted bacteriochlorins to the corresponding oxobacteriochlorins. PDC = pyridinium dichromate. Based on [132–134].

most straightforward synthesis of the dione is by oxidation of the corresponding diolchlorin **17**, using a number of possible oxidants [139, 140]. Select oxidation pathways have also been demonstrated for the synthesis of 7,8,17,18- (**39**) and 7,8,12,13-tetraones (**40**) [110, 141]. Owing to the presence of the π-conjugated dione functionality, the *meso*-aryl-β,β′-diones of type **38** possess greatly perturbed UV-vis spectra compared to porphyrins or chlorins [142]. The dione functionality shows typical carbonyl reactivity, and the porphyrin diones have been converted to the corresponding anhydrides [143, 144], oximes [145, 146], dialkoxy-α-oxochlorins [147], and diazo-α-oxochlorins [148].

6.3.1.3 Porpholactones

Porpholactones **42** are 5,10,15,20-tetraaryl-substituted porphyrins in which a porphyrin β,β′-bond is replaced by a lactone moiety [6]. On account of the presence of the sp^2-lactone carbon atom, porpholactones possess porphyrin-like optical properties [149]. Porpholactones were discovered as a fortuitous oxidative degradation product [143, 150]. Since this discovery, a number of oxidative pathways to generate porpholactones from β-derivatized (**35**, **36**, **38**, or **41**) and β-underivatized porphyrins (**1**$^{\mathbf{F}}$) and chlorins (**17**) have been described (Scheme 6.12) [151–153]. In fact, the porpholactones appear to be fairly common products when the β-positions of *meso*-arylporphyrins are being oxidized, suggesting that porpholactones might be a thermodynamic sink in the β,β′-oxidative degradation pathway of porphyrins, irrespective of the starting material [149]. The porpholactone analogues of carbaporphyrins [154, 155], dithiaporphyrins [156, 157], and porphyrin-*N*-oxides

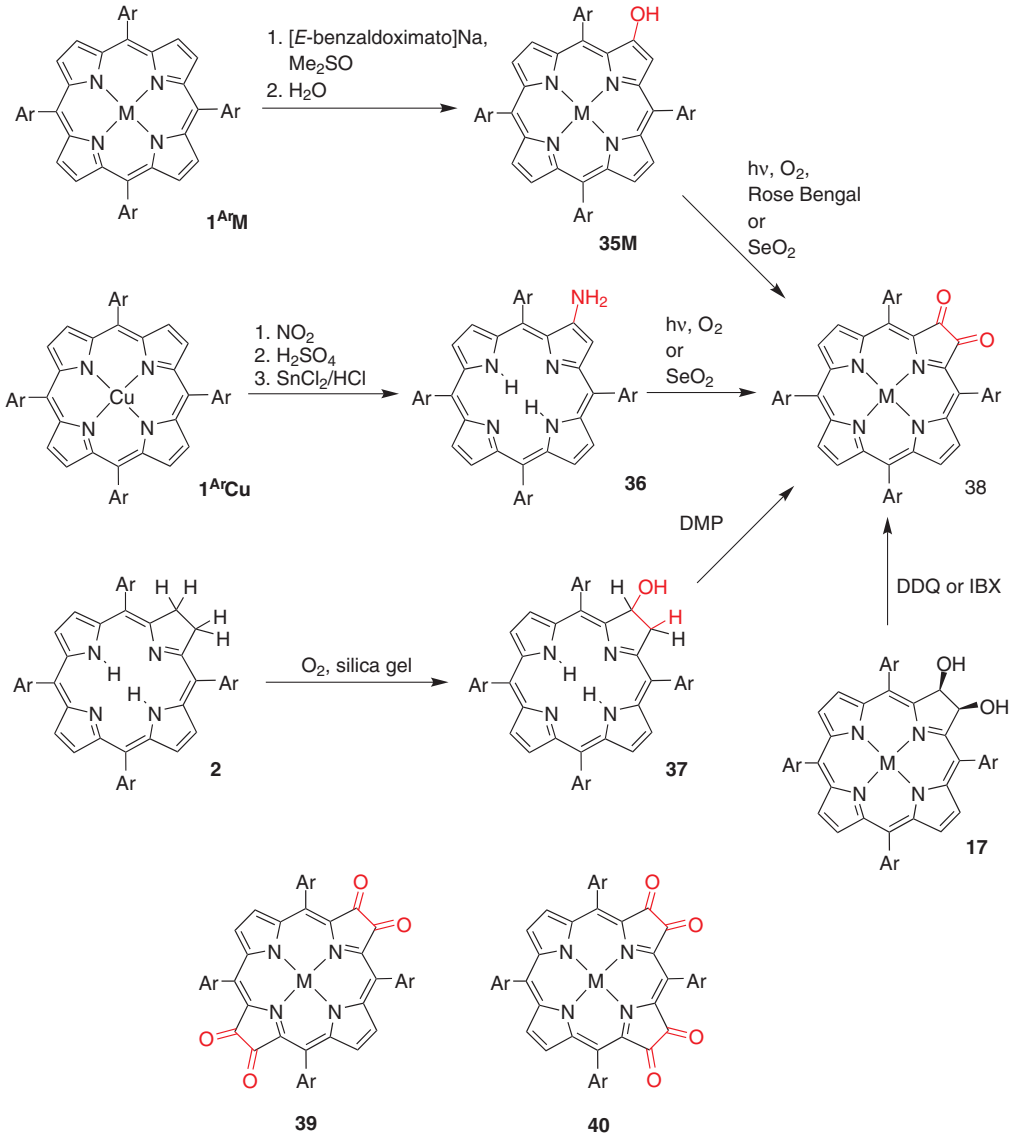

Scheme 6.11 Formation of β,β′-dioxoporphyrin **38** along a number of complementary oxidation routes, ultimately all resting on the conversion of 5,10,15,20-tetraarylporphyrin $\mathbf{1^{Ar}M}$ [M = 2H or Cu(II), Ni(II), Zn(II)]; note that chlorins **2** and **17** are also derived from $\mathbf{1^{Ar}M}$ (M = 2H) (Sections 6.2.1.1 and 6.3.1.1, respectively). DMP = Dess–Martin periodinane; IBX = 2-iodoxybenzoic acid; DDQ = 2,3-dichloro-5,6-dicyano-1,4-benzoquinone.

have also been reported, all invariably formed by the oxidation of suitably activated precursors [144, 158].

The syntheses of porpholactones fall broadly into two categories: In one category a β-activated porphyrinoid is the direct precursor, forming selectively a single porpholactone, and in the other category 5,10,15,20-tetrakis(pentafluorophenyl)porphyrin $\mathbf{1^F}$ (the only

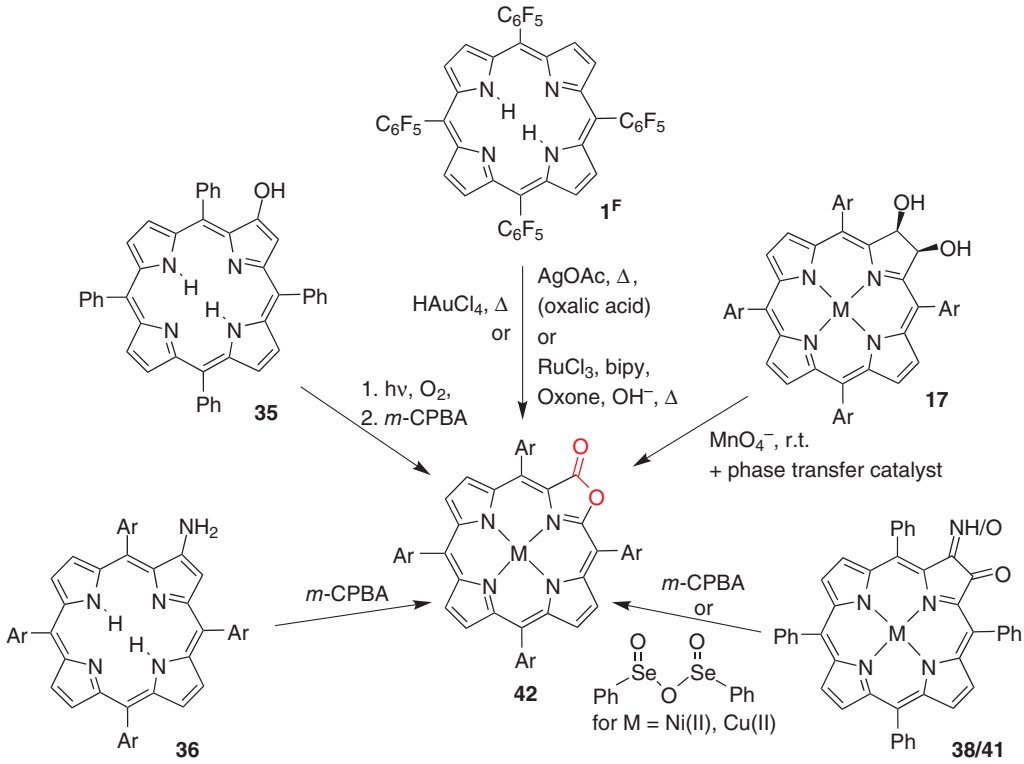

Scheme 6.12 Representative oxidative pathways leading from variously β-substituted porphyrins and chlorins to porpholactones **42**. Based on [132–134].

porphyrin shown to be readily susceptible to these conversions) is oxidized in a non-selective fashion, forming monoporpholactone **42**, all isomers of the bacteriochlorin-type **43**, and isobacteriochlorin-type **44** dilactones (in varying yields) (Scheme 6.13) [152, 159, 160]. The separation of the dilactone isomers is challenging [152, 159, 161, 162].

Porpholactones, in their free-base form or as their metal complexes, have found varied uses [159] as model compounds for naturally occurring chlorin-type prosthetic groups [151] in nitrogen transfer [163], sulfoxidation [164], epoxidation [165], hydrogen evolution reaction catalysis [166], and photocatalysis for oxidative C-H activation [167]; as oxygen-sensing [168], high-pH-sensing [35, 169–171], or cyanide-sensing chromophores [172]; in phototheranostics [173]; and as near-infrared (NIR) emitters [174] and lanthanide sensitizers [175]. The lactone moiety was also shown to enhance the cellular uptake and intracellular localization selectivity of photosensitizers [176].

Porpholactones **42** also show rich chemistry [8, 159, 177]. It is relevant in the context of this chapter that porpholactones are susceptible to reductions, whereby either the lactone moiety can be reduced in a stepwise fashion and/or alkylated [149, 174, 178], generating chlorin-like chromophores (oxazolochlorins **47**, **48**, or **49**). Alternatively, and controlled by the reductant used, the pyrrole adjacent to or opposite the oxazolone is reduced, creating chlorolactone isomers **45** or **46**, respectively, chlorin analogues with bathochromically shifted chlorin-like optical spectra (Scheme 6.14) [43, 179].

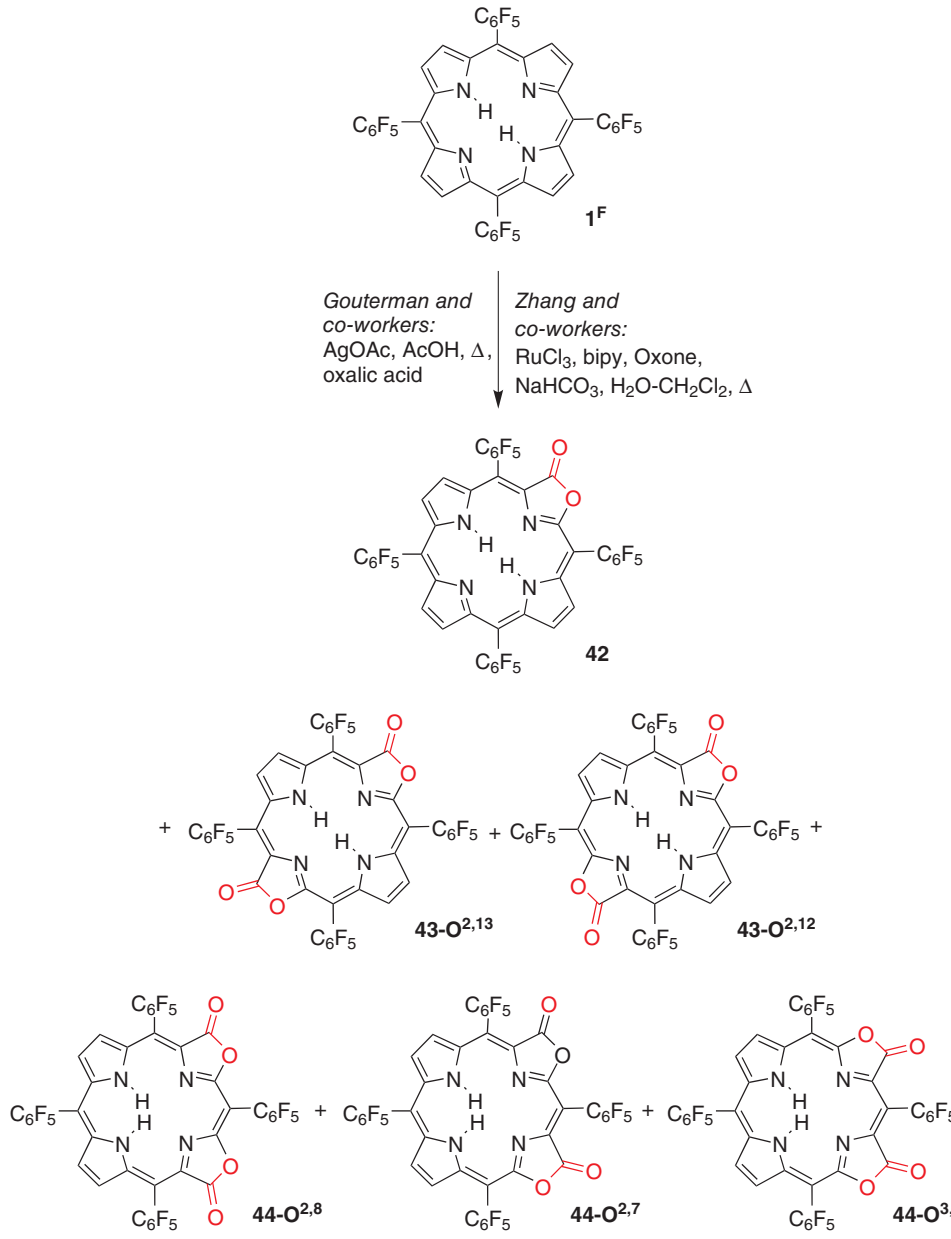

Scheme 6.13 Conversion of 5,10,15,20-tetrakis(pentafluorophenyl)porphyrins **1^F** to porpholactone **42** and porphodilactone isomers **43**/**44**. The naming of the isomers is derived from the formal numbering of porphyrins, with the numbers characterizing the isomers indicating the position of their oxo groups [152, 159, 160].

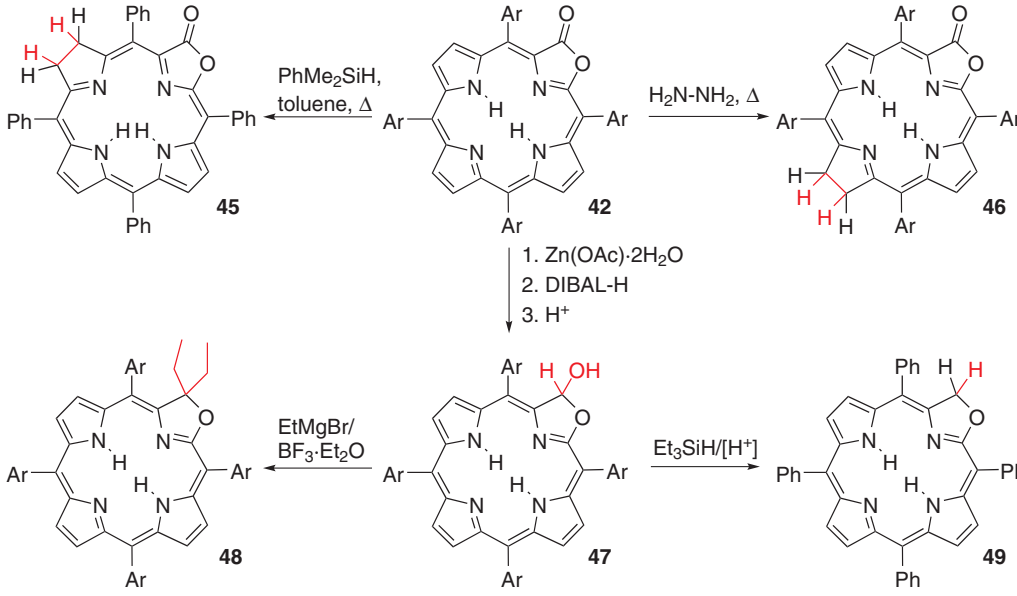

Scheme 6.14 Select reduction reactions of porpholactones **41**. Based on [43, 179].

The β-alkyl analogue to the *meso*-substituted porpholactones, hexaethylporpholactone, accessible along a non-general and little-understood oxidation pathway, was recently reported [180].

6.3.1.4 Cycloadditions Involving Oxygen and Ozone

One special case of a 4+2 cycloaddition involving β-vinylporphyrins **10(Me)$_2$** is the addition of singlet oxygen ($^1O_2$), frequently generated by photosensitization of triplet oxygen ($^3O_2$) by the porphyrin itself (Scheme 6.15). The long-known conversion of protoporphyrin dimethyl ester **10** to photoprotoporphyrin dimethyl ester **47** is an example of this reaction [61, 62, 181, 182]. The initially formed endoperoxide **46** can be reduced to the final product, chlorin **47**. Again, we like to point out that a formal oxidation has led to the formation of a chlorin chromophore, formally a hydroporphyrin.

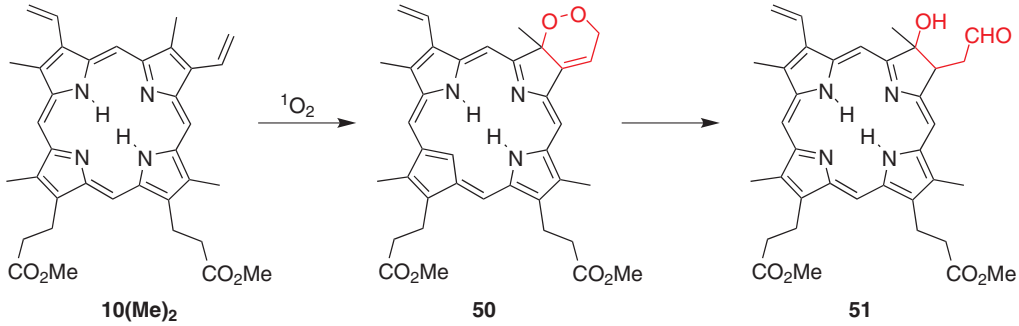

Scheme 6.15 Formation of photoprotoporphyrin **51** via singlet oxygen cycloaddition to protoporphyrin dimethyl ester **10(Me)$_2$**, and reduction of the endoperoxide **50** formed.

In fact, the generation of hydroporphyrins through oxidative methods has been known for a long time. Fischer and Deželić reported, in 1933, that the careful oxidation of β-octaalkylporphyrins **5** (such as etioporphyrin I) with ozone generates chlorin-like chromophores, but the proposed "chlorin ozonides" could not be verified [183]. In 1977, Shul'ga et al. found that the chlorin-like chromophores were heptaalkyloxazolochlorin hemiacetals, such as **55**, in which a pyrrolic subunit of the porphyrins was replaced by an oxazoline moiety (Scheme 6.16) [184]. Thus, a pyrrolic β-carbon with its alkyl substituent was excised and replaced by an oxygen atom, and the neighboring β-carbon was hydroxylated. A mechanism resting on the typical 3+2 cycloaddition reaction for ozone with the porphyrin β,β′-bond was proposed [184]. The synthesis of **55** was later optimized, and the chemistry of this oxazolochlorin hemiacetals studied (e.g., conversion to alkyl acetals **56** that are chemically more stable than the hemiacetal or alkylation to form *gem*-dialkyl derivatives) [180]. An oxidation reaction generated a unique tetrahydrofuran-linked oxazolochlorin dimer and eventually hexaethylporpholactone [180]. Some of the reactivity of **55** resembled the chemistry of the *meso*-aryloxazolochlorins made by chemical reduction of the corresponding porpholactones **35** [149, 177, 185].

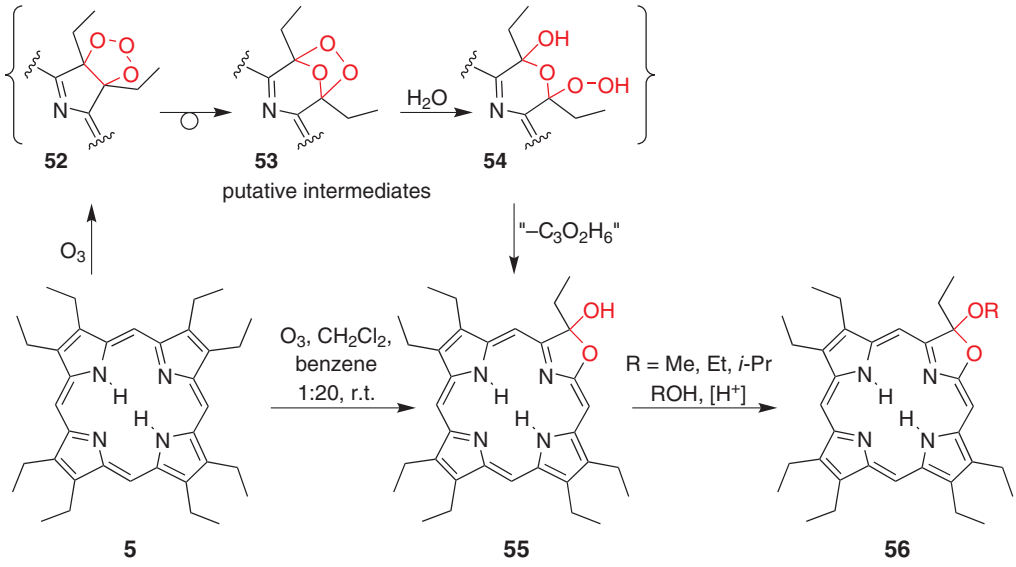

Scheme 6.16 Ozonation of OEP (**5**), according the mechanistic proposal by Shul'ga et al. [180, 184], including the putative mechanism of formation of oxazolochlorin **55**.

6.3.1.5 β,β′-Bond Breaking Reactions: Secochlorins and Chlorophins

No naturally occurring porphyrinic compound is known that carries a building block derived from a pyrrole that is cleaved at the β,β′-position, not even among the porphyrin and chlorophyll degradation products [186]. However, a number of discoveries have shown that the cleavage of β,β′-bonds or even the complete removal of β-carbons is readily possible [6–8, 187]. Porphyrins containing a cleaved β,β′-bond are generally referred to as secochlorins; in chlorophins, one or both β-carbon atoms were entirely removed from the macrocycle; this nomenclature is commonly used in the literature, but was not formalized [2, 27].

Conceptually the most straightforward access to secochlorins is by oxidative cleavage of an activated β,β′-bond of a porphyrin or chlorin. For instance, the cleavage of a chlorin diol (for its formation, see below) by sodium periodate ($NaIO_4$, generally heterogenized on silica gel) or lead tetraacetate [$Pb(OAc)_4$] provides, depending on whether a β-alkylated (***cis*-26**) or non-alkylated chlorin diols (such as **17**) were oxidized, the secochlorin diketone **57** or the secochlorin dialdehyde **58**, respectively (Scheme 6.17) [188, 189].

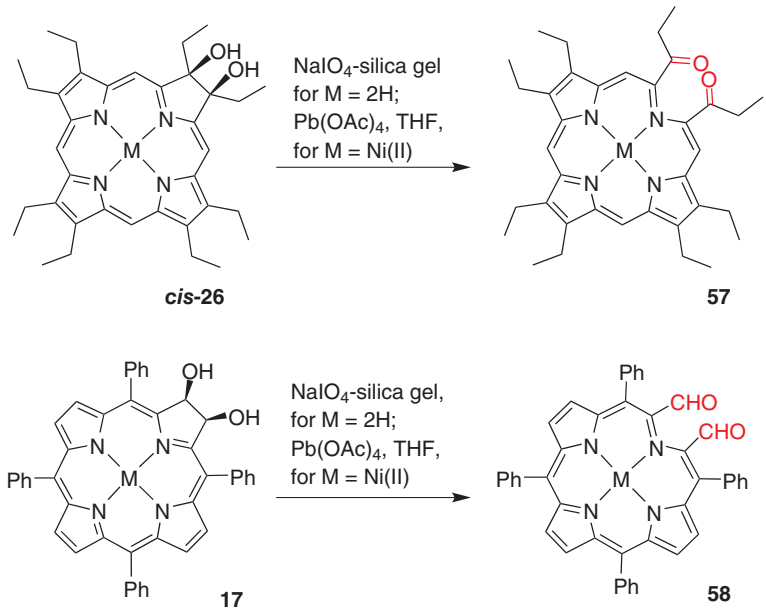

Scheme 6.17 Oxidative ring-cleavage reactions of chlorin diols. Based on [188, 189].

Other secochlorin formation reactions have become known, including the reaction of β-hexaalkyl-β,β′-dimethoxyporphyrins with singlet oxygen [190], or the (diacetoxy) iodobenzene [$PhI(OAc)_2$]-mediated cleavage of {β,β′-diaminoporphyrinato}M(II) complexes, generating [secochlorinato]M(II) dicyanides (with M = Ni(II), Zn(II)) [191]. Secobacteriochlorins, chromophores derived by diol cleavage of both sets of diols of tetrahydroxybacteriochlorins (such as **18**), have also become available, but they are highly sensitive to degradation, and thus are preferably prepared and reacted away in situ [120, 192]. Similar to the related β,β′-dioxochlorins, the optical properties of the secochlorins are drastically different from those of porphyrins or chlorins [6].

Importantly, the secochlorin dialdehydes are versatile starting materials for a range of porphyrinoids containing non-pyrrolic building blocks along with a range of ring-closing reactions [6–8, 187]. The stepwise deformylations of the secochlorin dialdehyde nickel complex **58** generates chlorophins **59** and **60** (Scheme 6.18) [193, 194]. An alternative and efficient method of influencing the degradation of the porphyrin framework is treatment of the β-tetrabromoporphyrin nickel complex **61** with the anion of *E*-benzaldoxime at elevated temperatures in the presence of a copper(I) catalyst [195]. The reaction generates the intermediate chlorophin **62** (of different stages of bromination) and the final product {bacteriophinato}Ni(II) complex **63.**

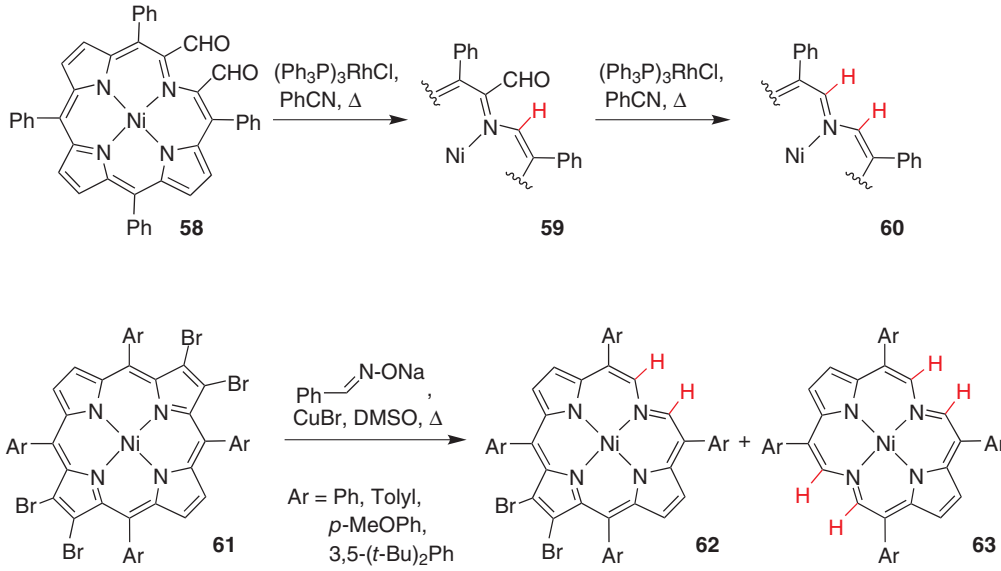

Scheme 6.18 Oxidative degradation pathways of a porphyrin to chlorophins **60** and **62**, and bacteriophin **63**. Based on [193, 194].

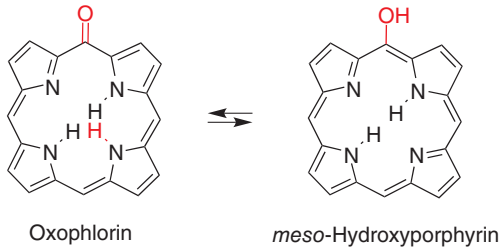

Figure 6.7 Structures of key *meso*-oxidized porphyrin macrocycle classes.

6.3.2 Oxidations of the *meso*-Positions

6.3.2.1 Oxophlorins and Related Macrocycles

Oxophlorins are a class of porphyrinoid macrocycles derived from oxidation of (metallo)porphyrins at a single *meso*-position (Figure 6.7). Oxophlorins may exist in either the keto- (**58-I**) or enol-tautomer (**58-II**), whereby the position of the equilibrium is determined by their metalation, the solvent, or the acidity/basicity of the environment [196].

The oxidation of a porphyrin, such as octaethylporphyrin **5**, to the corresponding oxophlorin **64** can be accomplished, for instance, using peroxide-based oxidants or Tl(III)-based hydroxylation methods (Scheme 6.19) [197]. The chemistry of oxophlorins has been investigated in detail as the natural heme degradation process begins with a *meso*-hydroxylation reaction (see also below) [198]. The redox characteristics of the β-octaalkyloxophlorins were studied and compared against those of 2,3,7,8,12,13,17,18-octaethylporphyrin [199]. In general, oxophlorins are more readily oxidized to the corresponding π-radicals than porphyrins. Crystal structures investigations of the keto- (**64-I**) and enol-(**64-II**) tautomers suggest that the two forms possess considerably different macrocycle

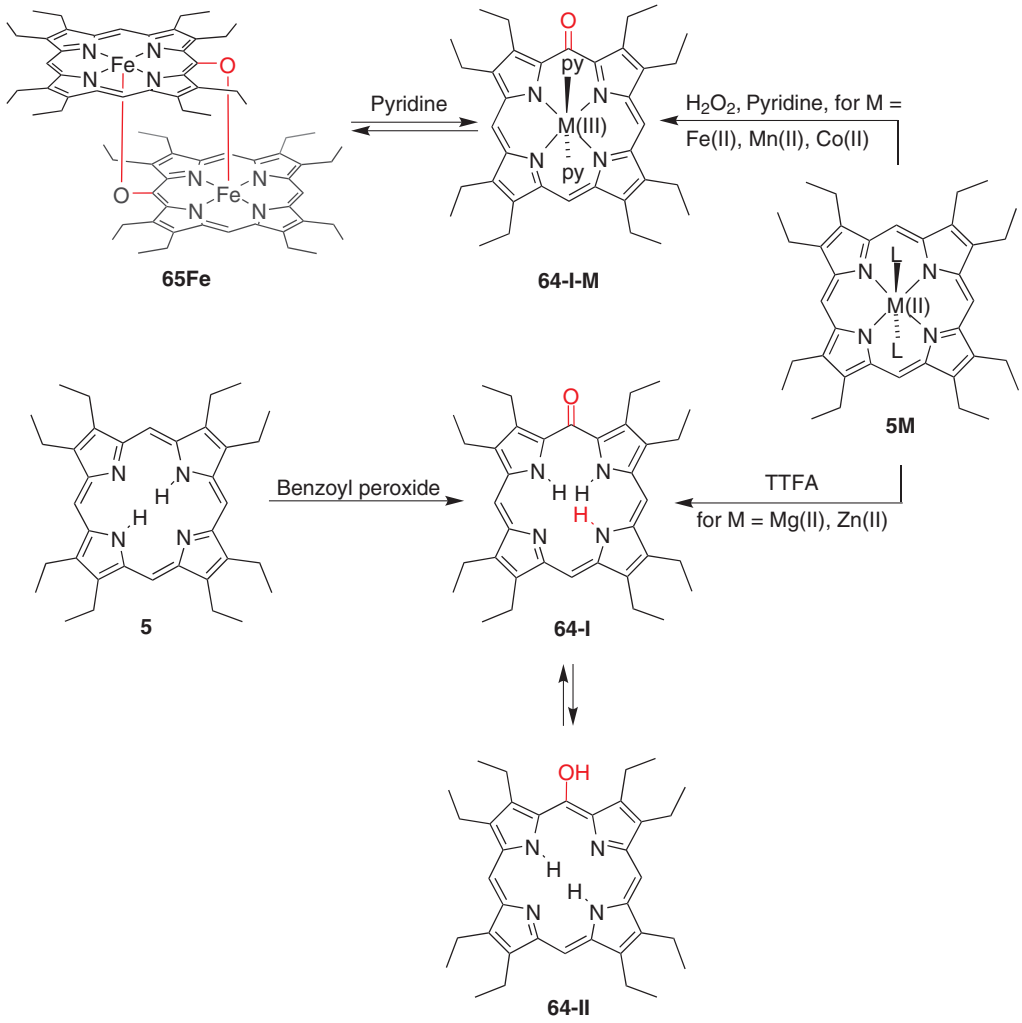

Scheme 6.19 Synthesis of oxophlorins by oxidation of porphyrin. TTFA = thallium(III) trifluoroacetate. Based on [197].

conformations. This switching of conformations and the associated facilitated oxidations of oxophlorins were proposed to be the functional basis for the natural breakdown mechanism of heme [200].

Oxophlorins made by total synthesis served as key intermediates in the synthesis of porphyrins; their reduction resulted in the formation of the corresponding porphyrins [196].

The coordination chemistry of octaethyloxophlorinato complexes varies from that of the corresponding octaethylporphyrins in that the *meso*-OH group of one complex can act as an axial ligand for another, as in complex **65Fe** [201, 202]. These complexes show a rich (reversible) redox chemistry. Ligand- and metal-based redox events can be distinguished that retain the dimeric forms of the complexes, or monomeric units are formed, before bilins are irreversibly formed by oxidation [202–209].

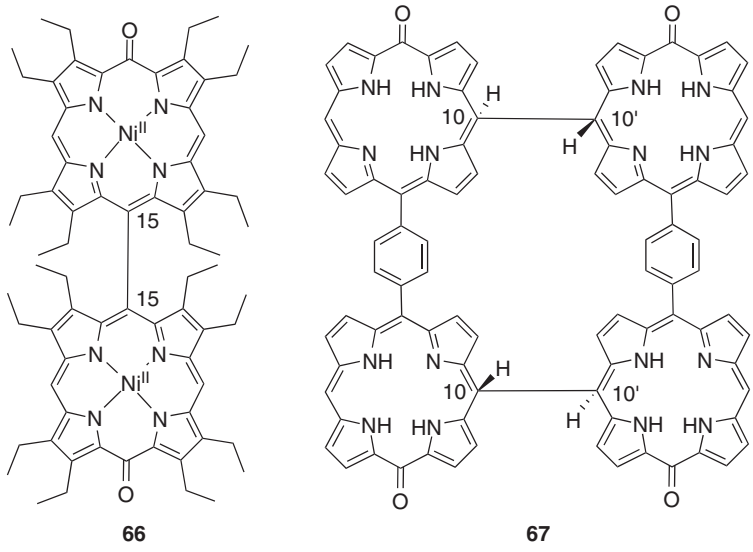

66 67

Figure 6.8 Structure of oxophlorin oxidative *meso-meso*-addition products. Based on Fuhrhop [210].

Octaethyloxophlorin metal complexes may also undergo one-electron oxidations in air, forming neutral π-radicals that may dimerize regiospecifically at the *meso*-position opposite the *meso*-oxo functionality, for instance forming dimer **66** (Figure 6.8) [210, 211]. The regiochemical preference can be altered by substitution, as the formation of a regio- and stereochemically pure tetramer of oxophlorins **67** highlights [198].

All four *meso*-positions can be converted to oxo-functionalities via a nitration [212, 213] and substitution strategy [214], thus generating octaethylxanthoporphyrinogen **69** via octanitroporphyrin **68** (Scheme 6.20).

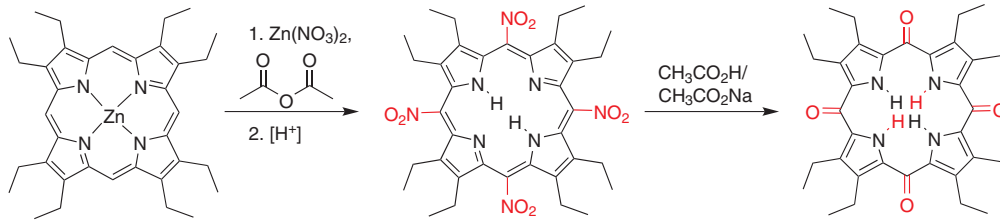

5Zn 68 69

Scheme 6.20 The formation of octaethylxanthoporphyrinogen **69** by a nitration/replacement sequence of **5Zn**. Based on [212–214].

6.3.2.2 Oxidative Macrocycle-Opening Reactions: Biliverdins

Distinct from the macrocycle-aromatic tetrapyrrolic compounds are their ring-opened congeners, the bilins (Figure 6.9). Bilins can be made by total synthesis or by oxidative ring

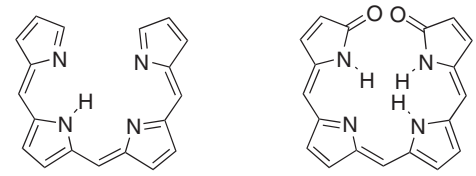

Figure 6.9 Structures of key *meso*-ring-opened porphyrin classes.

cleavage of porphyrins [215]. When formed by oxidation of a porphyrin, they generally carry oxo-functionalities at the cleavage positions, and the respective *meso*-carbon is lost. Their optical properties reflect the presence of conjugated but non-macrocycle-aromatic chromophores. The chemistry and optical properties of the ring-opened oligopyrrolic pigments have been reviewed [216].

Ring-opening reactions of porphyrins and hydroporphyrins as a result of oxidative attacks at the *meso*-positions are common in biology. For instance, heme from senescent erythrocytes is, when catalyzed by the enzyme heme oxygenase, regioselectively degraded along a *meso*-ring-opening pathway. The mechanism is known (Scheme 6.21) [217, 218]: *meso*-hydroxylation generating **10Fe** is followed by iron reduction and excision of the *meso*-carbon as CO, forming the intermediate verdoheme **71**. This product is subsequently ring-opened to the green open-chain tetrapyrrolic pigment biliverdin **72**, whereupon the metal is also lost. In the next step, biliverdin is reduced to the yellow tetrapyrrolic pigment bilirubin **73**, which is further metabolized, or used as a precursor for the many functional bilins in photosynthetic organisms [219]. Abiotic oxidative ring openings of heme are not regiospecific and result in the formation of all four possible biliverdin regioisomers [220].

Many of the early-stage degradation products from senescent chlorophyll (such as chlorophyll *a* **74**) are also derived from ring-cleavage reactions at the *meso*-position, with the distinct difference being that the *meso*-carbon is frequently not lost and remains on the open-ring tetrapyrrolic pigment, such as in the form of an aldehyde functionality in the red Chl catabolite **75** (Scheme 6.22). Multiple examples also exist in which the *meso*-position adjacent to the pyrroline moiety is cleaved [221, 222].

The heme degradation process can also be mimicked *in vitro*, albeit this uncatalyzed cleavage reaction is not regiospecific, and up to four products (denoted α through δ) resulting from ring cleavage at all possible nonequivalent *meso*-carbons of non-symmetric porphyrins are formed [220]. Oxidation occurs preferentially at the most electron-rich *meso*-position. Only a single tetrapyrrolic product is formed when ring-opening symmetric porphyrins, such as the iron complex of 2,3,7,8,12,13,17,18-octaethylporphyrin **5Fe** (Scheme 6.23) [205, 223]. The yields of these reactions are mostly low, as the oxidation conditions needed to cleave the aromatic ring are generally also potent enough to further degrade the linear tetrapyrrolic product.

The oxidative ring-opening reaction of the iron complex of octaethylporphyrin **5M** proceeds via an isolable verdoheme intermediate containing iron in either the oxidation state +II or +III. The ring opening of verdoheme is possible along either hydrolytic or oxidative

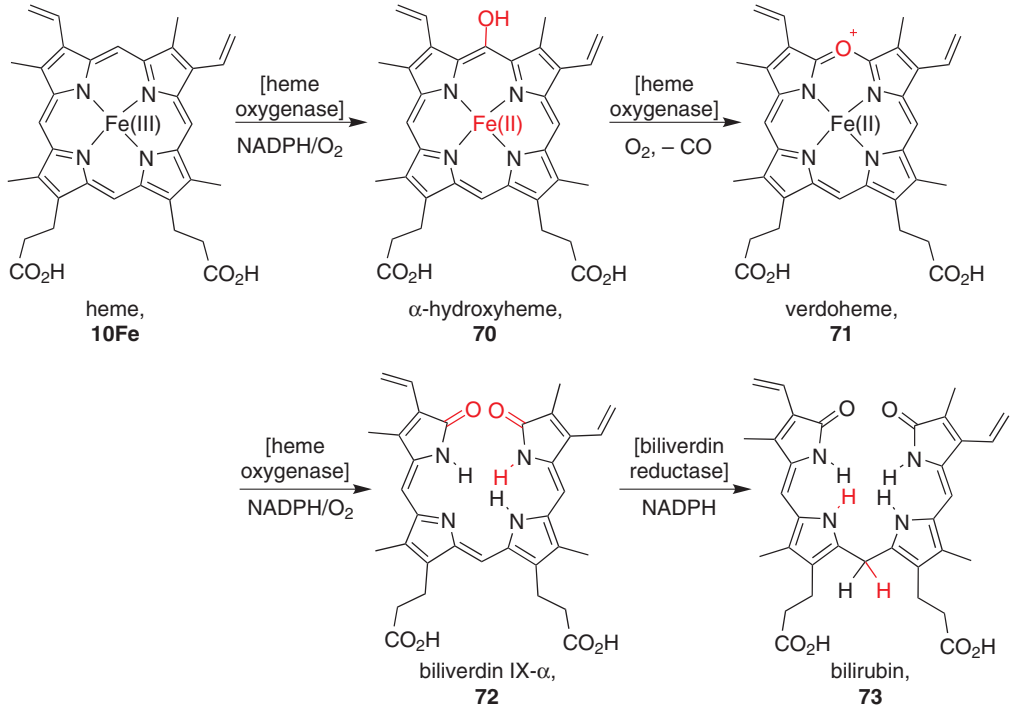

Scheme 6.21 Heme oxygenase-catalyzed heme metabolic pathway toward biliverdin **72** and bilirubin **73**. Based on [217, 218].

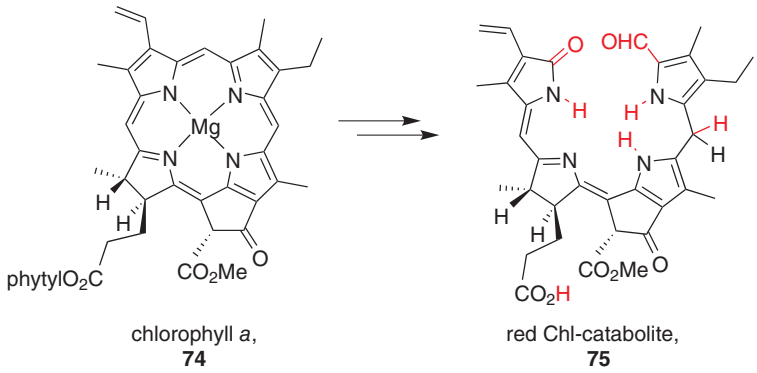

Scheme 6.22 First steps of a representative chlorophyll degradation pathway during green leaf senescence.

pathways, forming either **76**, **77**, or **77Fe** [223–227]. In addition to the oxidations via the verdoheme intermediate, the iron complexes of 5-amino-2,3,7,8,12,13,17,18-octaethylporphyrin (**78**) also undergoes rapid oxidative ring-opening reactions under a number of conditions that retain the *meso*-carbon in the bilins, such as in α-esterbiliverdin **79**, and α-cyanobiliverdin **80** (Scheme 6.24) [228, 229].

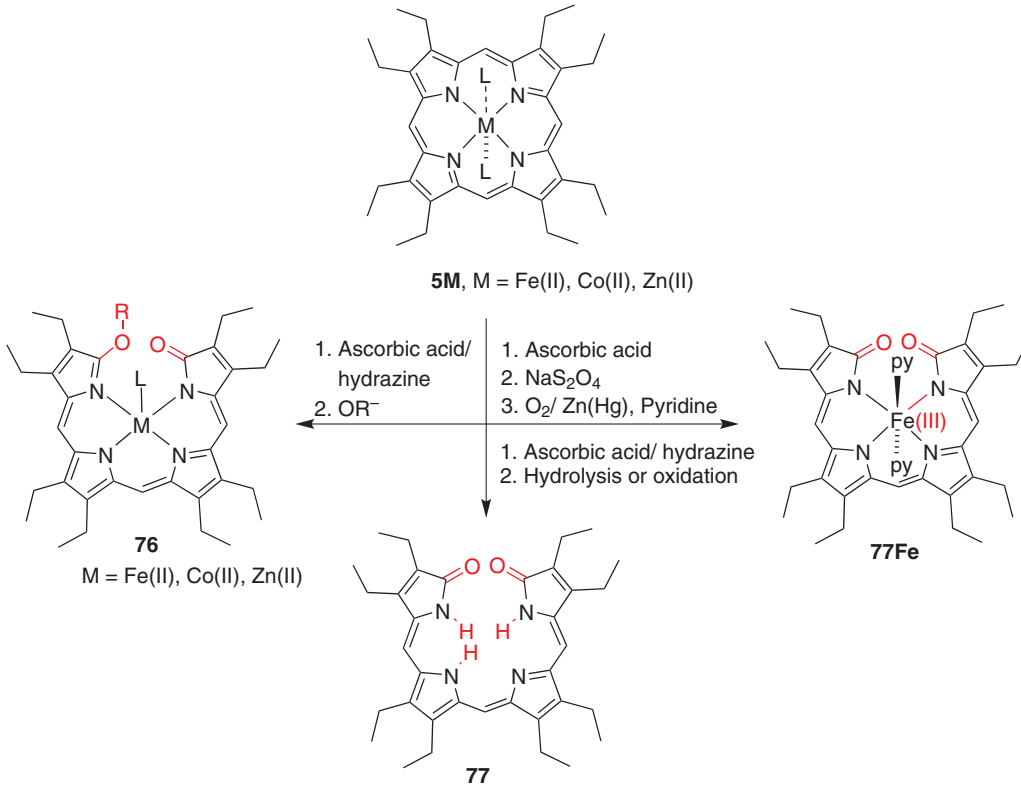

Scheme 6.23 Bilin-forming pathways of (2,3,7,8,12,13,17,18-octaethylporphyrinato)metal **5M** complexes. Based on [205, 223].

The singlet oxygen-driven photo-oxygenation of metallooctaethylporphyrins [M = Zn(II), Mg(II)] also leads to the formation of metallo-formylbilins **81** [230]. Surprisingly, the corresponding oxidation of metallochlorins ***trans*-6Zn** leads to a *meso*-ring cleavage before oxidation of the pyrroline moiety of the chlorin to a pyrrole, thus forming the two isomeric formyldihydrobiliverdin isomers **82-I** and **82-II** (Scheme 6.25) [231].

Asymmetric synthetic porphyrins and chlorins may also be regioselectively ring-opened if the cleavage reaction is preceded by a regioselective activation step. One example is the preparation of a synthetic bilin model **84**, derived from the *meso*-trifluoroacetoxylated octaethyloxochlorin zinc complex **83** (Scheme 6.26) [232]. Curiously, this compound adopts a stretched near-planar conformation with the central double bond in the *E*-configuration. This finding is attributed to the facile isomerization of the central double bond that is in conjugation with the β-oxo functionality.

6.3.3 Oxidations at the Nitrogen Atoms

The oxidation of porphyrins under certain conditions may also lead to the formation of porphyrin *N*-oxides, such as 2,3,7,8,12,14,17,18-octaethylporphyrin-*N*-oxide **85** (Scheme 6.27)

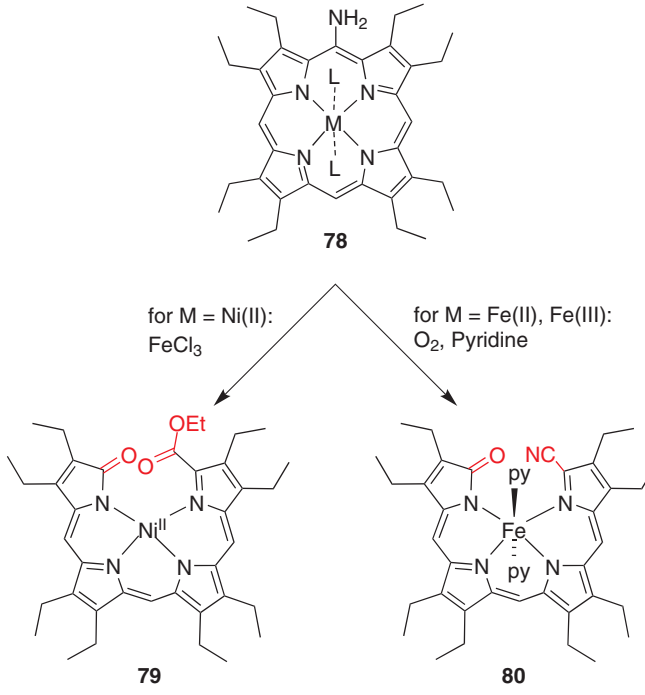

Scheme 6.24 Ring-opening pathways of 5-amino-[2,3,7,8,12,13,17,18-octaethylporphyrinato]metal **78** complexes producing bilins that retain the *meso*-carbon at the cleavage site. Based on [228, 229].

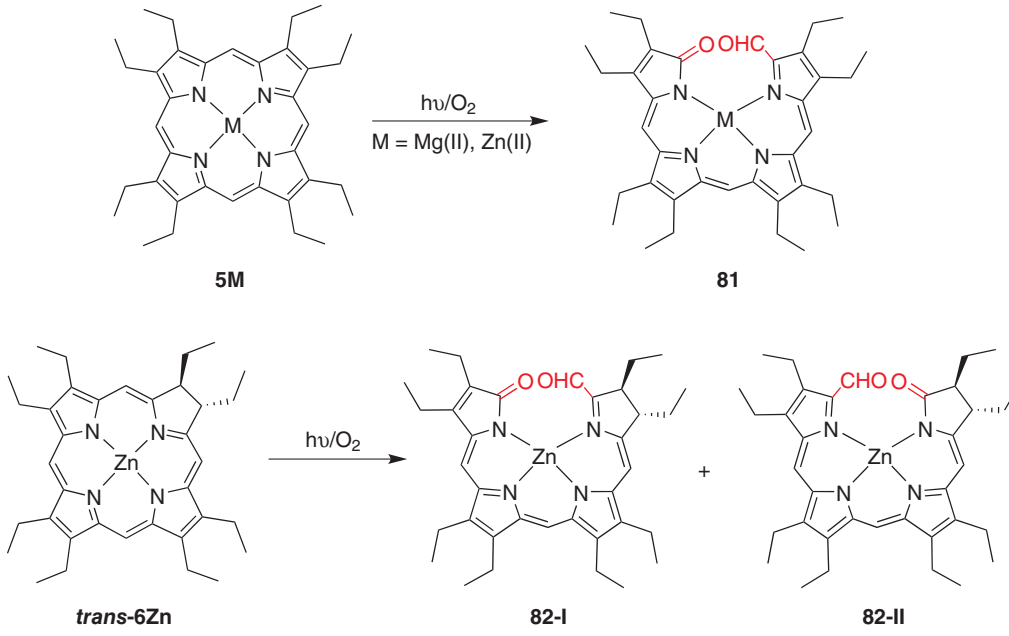

Scheme 6.25 Formation of formylbilins **81**/**82** by singlet oxygen-mediated oxidation of metalloporphyrins **5M** and metallochlorins ***trans*-6Zn**. Based on [231].

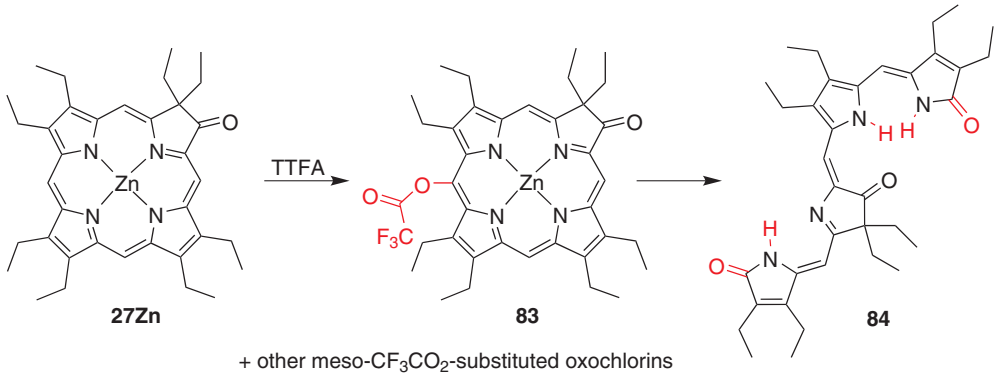

Scheme 6.26 Formation of octaethyloxochlorin-derived biliverdin **84**. TTFA = thallium(III) trifluoroacetate. Based on [232].

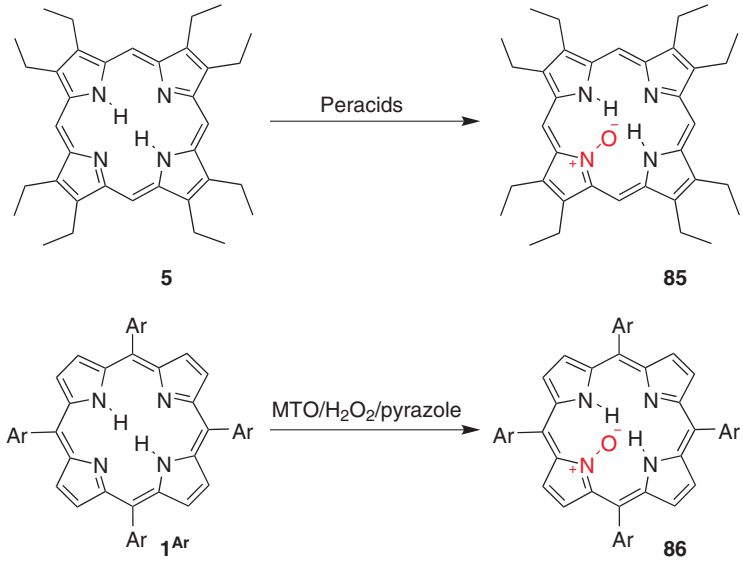

Scheme 6.27 Formation of porphyrin *N*-oxides by oxidation of the corresponding free-base porphyrins. MTO = methyltrioxorhenium. Based on [233].

[233]. Surprisingly, porphyrin *N*-oxides still can form metal complexes with Ni(II), Cu(II), Zn(II), Fe(III), and Tl(III) in which the oxygen bridges one N-M bond [233–235]. The significance of the porphyrin *N*-oxide Fe(III)-complexes with respect to possible heme degradation products or suicide reactions of the heme-based mono-oxygenation enzyme P-450 has been discussed [236–239].

The 5,10,15,20-tetraarylporphyrin *N*-oxide analogs, such as **82**, can be synthesized from their corresponding porphyrins by oxidation using either hypofluorous acid or organic acid peroxides, such as peracetic, permaleic acid, or *m*-CPBA [234, 237, 240]. More recently, the

use of methyltrioxorhenium/H_2O_2/pyrazole has also been described to be suitable for the high-yield *N*-oxidation of porphyrins and thiaporphyrins [241]. In addition, the *N*-oxide of octaethyloxochlorin has been reported to form by treatment of the parent oxochlorin **27** with peracids [242].

6.4 Metal-Centered and Resonance-Stabilized π-System Redox Events

The redox chemistry of free-base porphyrins is rich [13]. A multitude of chemical and electrochemical methods can generate single- or multi-electron reduced or oxidized porphyrins species. The primary radical anion and cation species formed upon single electron reduction and oxidation events are resonance-stabilized by the porphyrinic π-system. Their formation and stabilization is greatly influenced by the type of porphyrinic chromophore and its substituents [243, 244]. The importance of porphyrin π-cation radicals in nature has been recognized [245]. For instance, they have been observed as short-lived intermediates in the photo-excited photosynthetic pigments, or π-cation radical porphyrins coordinating Fe(IV) have been proposed to be the reactive species in the catalytic cycles of catalases and horseradish peroxidases.

Porphyrins also undergo rich photo-induced redox events [246]. The ability to readily eject a photo-excited electron is what allows hydroporphyrins to act as the primary light-harvesting pigments in nature [247]. The study of redox events controlling the utilization of porphyrins and hydroporphyrins as artificial light harvesters [248, 249], photocatalysts for water splitting [250] or to generate solar fuels [251], building blocks in electronic devices [14], metalloenzyme mimics [244], and molecular wires [252] are currently some of the most actively investigated areas in porphyrin-related research.

The redox chemistry of metalloporphyrins is more complex than that of their corresponding free bases [13, 244]. The most common redox behavior of a (transition) metal complex involves the chemical or electrochemical oxidation or reduction of the metal, leaving the ligand unaffected. However, the redox activity of the free-base porphyrins extends to their metal complexes. Thus, porphyrinic ligands are so-called non-innocent ligands. The situations between a redox-active transition metal $M^{y/y+1}$ and a non-innocent porphyrinic ligand $Por^{x/x-1}$ can be described as being either a resonance situation with delocalized valences in a single minimum or an equilibrium between two different valence tautomeric species with a double minimum (Scheme 6.28) [253, 254]. Spin- and additional metal ligand equilibria may be layered on top of these valence isomerizations [13].

$$[Por]^{x}M^{y} \overset{\text{barrier-less resonance}}{\rightleftharpoons} [Por]^{x-1}M^{y+1}$$

$$[Por]^{x}M^{y} \overset{\text{redox equilibrium}}{\rightleftharpoons} [Por]^{x-1}M^{y+1}$$

Scheme 6.28 Varying descriptions of the interaction between a non-innocent porphyrinic ligand and a redox-active transition metal. Based on [253, 254].

The non-innocence of porphyrinic ligands is one of the major factors in the ubiquitous use of hemes as prosthetic groups in enzymes catalyzing either oxidations, reductions, electron transfers, or oxygen transports, as this allows the generation of, for example, high-oxidation iron species capable of C-H group activation [254, 255] or DNA cleavage [256].

The resonance stabilization of cation radicals of free base and metalloporphyrinoids does not imply that they do not lead to numerous β,β-, *meso*-β-, and *meso*-*meso*-coupling reactions, many of which are regiochemically very well controlled. Oxidative coupling strategies resulted in the preparation of conjugated porphyrin arrays that hold promise as functional materials [257].

Acknowledgments

This work was supported by the US National Science Foundation through grants CHE-1465133 and CHE-1800361.

References

1 Senge, M.O. (2022). It's all in the name: structure, nomenclature, numbering and isomers of porphyrins. In: *Porphyrins for the 21st Century* (ed. P. Brothers and M.O. Senge). Wiley.
2 Vicente, M.D.G.H. (2000). Reactivity and functionalization of β-substituted porphyrins and chlorins. In: *The Porphyrin Handbook*, vol. 1 (ed. K.M. Kadish, K.M. Smith and R. Guilard), 149–199. San Diego, CA: Academic Press.
3 Vincente, M.G.H. and Smith, K.M. (2000). Porphyrins and derivatives: synthetic strategies and reactivity profiles. *Current Organic Chemistry* 4: 139–174.
4 Lindsey, J.S. (2015). De novo synthesis of gem-dialkyl chlorophyll analogues for probing and emulating our green world. *Chemical Reviews* 115: 6534–6620.
5 Taniguchi, M. and Lindsey, J.S. (2017). Synthetic chlorins, possible surrogates for chlorophylls, prepared by derivatization of porphyrins. *Chemical Reviews* 117: 344–535.
6 Brückner, C., Akhigbe, J., and Samankumara, L. (2014). Syntheses and structures of porphyrin analogues containing non-pyrrolic heterocycles. In: *Handbook of Porphyrin Science*, vol. 31 (ed. K.M. Kadish, K.M. Smith and R. Guilard), 1–276. Singapore: World Scientific Publishing.
7 Costa, L.D., Costa, J.I., and Tomé, A.C. (2016). Porphyrin macrocycle modification: pyrrole ring-contracted or -expanded porphyrinoids. *Molecules* 21: 320.
8 Brückner, C. (2016). The breaking and mending of *meso*-tetraarylporphyrins: transmuting the pyrrolic building blocks. *Accounts of Chemical Research* 49: 1080–1092.
9 Kräutler, B. and Matile, P. (1999). Solving the riddle of chlorophyll breakdown. *Accounts of Chemical Research* 32: 35–43.
10 Kadish, K.M., Smith, K.M., and Guilard, R. (ed.) (2003). *The Porphyrin Handbook*. vol. 13. San Diego, CA: Academic Press.

11 Hörtensteiner, S. (2006). Chlorophyll degradation during senescence. *Annual Review of Plant Biology* 57: 55–77.

12 Kräutler, B. (2014). Phyllobilins - the abundant bilin-type tetrapyrrolic catabolites of the green plant pigment chlorophyll. *Chemical Society Reviews* 43: 6227–6238.

13 Kadish, K.M., van Caemelbecke, E., and Royal, G. (2000). Electrochemistry of metalloporphyrins in nonaqueous media. In: *The Porphyrin Handbook*, vol. 8 (ed. K.M. Kadish, K.M. Smith and R. Guilard), 1–114. San Diego, CA: Academic Press.

14 Jurow, M., Schuckman, A.E., Batteas, J.D., and Drain, C.M. (2010). Porphyrins as molecular electronic components of functional devices. *Coordination Chemistry Reviews* 254: 2297–2310.

15 Fuchter, M.J., Zhong, C., Zong, H. et al. (2008). Porphyrazines: designer macrocycles by peripheral substituent change. *Australian Journal of Chemistry* 61: 235–255.

16 Kadish, K.M., Smith, K.M., and Guilard, R. (ed.) (2003). *The Porphyrin Handbook*, vol. 15–20. San Diego, CA: Academic Press.

17 Inokuma, Y. and Osuka, A. (2008). Sub-porphyrins: emerging contracted porphyrins with aromatic 14π-electronic systems and bowl-shaped structures: rational and unexpected synthetic routes. *Dalton Transactions* 2517–2526.

18 Sessler, J.L. and Tomat, E. (2007). Transition-metal complexes of expanded porphyrins. *Accounts of Chemical Research* 40: 371–379.

19 Misra, R. and Chandrashekar, T.K. (2008). Structural diversity in expanded porphyrins. *Accounts of Chemical Research* 41: 265–279.

20 Saito, S. and Osuka, A. (2011). Expanded porphyrins: intriguing structures, electronic properties, and reactivities. *Angewandte Chemie, International Edition in English* 50: 4342–4373.

21 Pareek, Y., Ravikanth, M., and Chandrashekar, T.K. (2012). Smaragdyrins: emeralds of expanded porphyrin family. *Accounts of Chemical Research* 45: 1801–1816.

22 Lash, T.D. (2016). Out of the blue! Azuliporphyrins and related carbaporphyrinoid systems. *Accounts of Chemical Research* 49: 471–482.

23 Lash, T.D. (2012). Carbaporphyrins and related systems. Synthesis, characterization, reactivity and insights into Porphyrinoid aromaticity. In: *Handbook of Porphyrin Science*, vol. 16 (ed. K.M. Kadish, K.M. Smith and R. Guilard), 1–329. Singapore: World Scientific Publishing.

24 Pawlicki, M. and Latos-Grażyński, L. (2010). Carbaporphyrinoids. Synthesis and coordination properties. In: *Handbook of Porphyrin Science*, vol. 2 (ed. K.M. Kadish, K.M. Smith and R. Guilard), 103–192. Singapore: World Scientific Publishing.

25 Furuta, H., Maeda, H., and Osuka, A. (2002). Confusion, inversion, and creation–a new spring from porphyrin chemistry. *Chemical Communications* 1795–1804.

26 Flitsch, W. (1988). Hydrogenated porphyrin derivatives: hydroporphyrins. *Advances in Heterocyclic Chemistry* 43: 73–126.

27 IUPAC-IUB Joint Commission on Biochemical Nomenclature (1987). Nomenclature of tetrapyrroles. *Pure and Applied Chemistry* 59: 779–832.

28 Gouterman, M. (1978). Optical spectra and electronic structure of porphyrins and related rings. In: *The Porphyrins*, vol. 3 (ed. D. Dolphin), 1–165. New York, NY: Academic Press.

29 Brückner, C. and Dolphin, D. (1995). β,β′-Dihydroxylation of *meso*-tetraphenylchlorins and metallochlorins. *Tetrahedron Letters* 36: 9425–9428.

30 Parusel, A.B., Wondimagegn, T., and Ghosh, A. (2000). Do nonplanar porphyrins have red-shifted electronic spectra? A DFT/SCI study and reinvestigation of a recent proposal. *Journal of the American Chemical Society* 122: 6371–6374.

31 Ryeng, H. and Ghosh, A. (2002). Do nonplanar distortions of porphyrins bring about strongly red-shifted electronic spectra? Controversy, consensus, new developments, and relevance to chelatases. *Journal of the American Chemical Society* 124: 8099–8103.

32 Fleischer, E.B. (1970). The structure of porphyrins and metalloporphyrins. *Accounts of Chemical Research* 3: 105–112.

33 Whitlock, H.W. Jr., Hanauer, R., Oester, M.Y., and Bower, B.K. (1969). Diimide reduction of porphyrins. *Journal of the American Chemical Society* 91: 7485–7489.

34 Wondimagegn, T. and Ghosh, A. (2000). Ruffling deformations of nickel(II) and zinc(II) hydroporphyrin and chlorophin complexes: implications for F430, the nickel tetrapyrrole cofactor of methylcoenzyme M reductase. *Journal of Physical Chemistry B* 104: 10858–10862.

35 Worlinsky, J.L., Halepas, S., Ghandehari, M. et al. (2015). High pH sensing with water-soluble porpholactone derivatives and their incorporation into a Nafion® Optode membrane. *Analyst* 140: 190–196.

36 Pereira, M.M., Monteiro, C.J.P., Simoes, A.V.C. et al. (2010). Synthesis and photophysical characterization of a library of photostable halogenated bacteriochlorins: an access to near infrared chemistry. *Tetrahedron* 66: 9545–9551.

37 Bonnett, R., White, R.D., Winfield, U.J., and Berenbaum, M.C. (1989). Hydroporphyrins of the *meso*-tetra(hydroxyphenyl)porphyrin series as tumour photosensitizers. *Biochemistry Journal* 261: 277–280.

38 Wang, T.Y., Chen, J.R., and Ma, J.S. (2002). Diphenylchlorin and diphenylbacteriochlorin: synthesis, spectroscopy and photosensitizing properties. *Dyes and Pigments* 52: 199–208.

39 Dąbrowski, J.M., Arnaut, L.G., Pereira, M.M. et al. (2010). New halogenated water-soluble chlorin and bacteriochlorin as photostable PDT sensitizers: synthesis, spectroscopy, photophysics, and *in vitro* photosensitizing efficacy. *ChemMedChem* 5: 1770–1780.

40 Bruhn, T. and Brückner, C. (2015). Origin of the regioselective reduction of chlorins. *The Journal of Organic Chemistry* 80: 4861–4868.

41 Wang, T.Y., Chen, J.R., and Ma, J.S. (2001). Synthesis and photochemistry of diphenylchlorin and diphenylbacteriochlorin. *Chinese Chemical Letters* 12: 671–674.

42 Genady, A.R. and Gabel, D. (2003). Synthesis of triazole- and pyridine-bridged porphyrin–chlorin and porphyrin dimers. *Tetrahedron Letters* 44: 2915–2917.

43 Akhigbe, J., Haskoor, J.P., Krause, J.A. et al. (2013). Formation, structure and reactivity of *meso*-tetraaryl-chlorolactones, -porpholactames, and chlorolactames, porphyrin and chlorin analogues incorporating oxazolone or imidazolone moieties. *Organic & Biomolecular Chemistry* 11: 3616–3628.

44 Eisner, U. (1957). Some novel hydroporphyrins. *Journal of the Chemical Society* 3461–3469.

45 Renner, M.W., Furenlid, L.R., Barkigia, K.M. et al. (1991). Models of factor 430. Structural and spectroscopic studies of nickel(II) and nickel(I) hydroporphyrins. *Journal of the American Chemical Society* 113: 6891–6898.

46 Bergonia, H.A., Phillips, J.D., and Kushner, J.P. (2009). Reduction of porphyrins to porphyrinogens with palladium on carbon. *Analytical Biochemistry* 384: 74–78.

47 Naab, P., Lattmann, R., Angst, C., and Eschenmoser, A. (1980). Synthesis and transformations of 5-cyano-2,2,8,8,12,13,17,18-octamethylisobacteriochlorin. *Angewandte Chemie International Edition in English* 19: 143–145.

48 Krasnovskii, A.A. and Voinovskaya, K.K. (1954). Reversible photochemical reduction of porphyrin to chlorin and bacteriochlorin. *Doklady Akademii Nauk SSSR (Proceedings of the Academy of Sciences of the USSR)* 96: 1209–1212.

49 Whitten, D.G., Yau, J.C.N., and Carroll, F.A. (1971). Photochemistry and oxidation-reduction reactions of tin porphyrins. *Journal of the American Chemical Society* 93: 2291–2296.

50 Harel, Y. and Manassen, J. (1978). Photoreduction of tetraphenylporphyrins by amines in the visible. Photochemical syntheses of reduced tetraphenylporphyrins and the mechanism of photoreduction. *Journal of the American Chemical Society* 100: 6228–6234.

51 Iakovides, P., Simpson, D.J., and Smith, K.M. (1991). Regioselective photoreduction of zinc(II) porphyrins to give chlorins. *Photochemistry and Photobiology* 54: 335–343.

52 Fuhrhop, J.-H., Lumbantobing, T., and Ullrich, J. (1970). Chloroform adduct of octaethylporphin tin(IV) dihydroxides and their conversion to 1-methyl-2-hydro-octaethyl porphin. *Tetrahedron Letters* 11: 3771–3772.

53 Moura, N.M.M., Giuntini, F., Faustino, M.A.F. et al. (2010). 1,3-Dipolar cycloaddition of nitrile imines to *meso*-tetraarylporphyrins. *ARKIVOC* 24–33.

54 Cavaleiro, J.A.S., Neves, M.G.P.M.S., and Tomé, A.C. (2003). Cycloaddition reactions of porphyrins. *ARKIVOC* 107–130.

55 Tomé, A.C., Neves, M.G.P.M.S., and Cavaleiro, J.A.S. (2009). Porphyrins and other pyrrolic macrocycles in cycloaddition reactions. *Journal of Porphyrins and Phthalocyanines* 13: 408–414.

56 Silva, A.M.G. and Cavaleiro, J.A.S. (2008). Porphyrins in Diels-Alder and 1,3-dipolar cycloaddition reactions. *Progress in Heterocyclic Chemistry* 19: 44–69.

57 Pangka, V.S., Morgan, A.R., and Dolphin, D. (1986). The Diels-Alder reactions of protoporphyrin IX dimethyl ester with electron-deficient alkynes. *The Journal of Organic Chemistry* 51: 1094–1100.

58 Tomé, A.C., Lacerda, P.S.S., Neves, M.G.P.M.S., and Cavaleiro, J.A.S. (1997). *meso*-Arylporphyrins as dienophiles in Diels-Alder reactions: a novel approach to the synthesis of chlorins, bacteriochlorins and naphthoporphyrins. *Chemical Communications* 1199–1200.

59 Tomé, A.C., Lacerda, P.S.S., Silva, A.M.G. et al. (2000). Synthesis of new tetrapyrrolic derivatives-porphyrins as dienophiles or dipolarophiles. *Journal of Porphyrins and Phthalocyanines* 4: 532–537.

60 Silva, A.M.G., Tomé, A.C., Neves, M.G.P.M.S. et al. (2005). Porphyrins in Diels-Alder reactions. Improvements on the synthesis of Barrelene-fused chlorins using microwave irradiation. *Tetrahedron Letters* 46: 4723–4726.

61 Callott, H.J., Johnson, A.W., and Sweeney, A. (1973). Additions to porphins involving the formation of new carbon-carbon bonds. *Journal of the Chemical Society, Perkin Transactions* 1: 1424–1427.

62 DiNello, R.K. and Dolphin, D. (1980). Reactions of protoporphyrin with tetracyanoethylene. *The Journal of Organic Chemistry* 45: 5196–5204.

63 Silva, A.M.G., Lacerda, P.S.S., Tomé, A.C. et al. (2006). Porphyrins in 1,3-dipolar cycloaddition reactions. Synthesis of new porphyrin-chlorin and porphyrin-tetraazachlorin dyads. *The Journal of Organic Chemistry* 71: 8352–8356.

64 Silva, A.M.G., Tomé, A.C., Neves, M.G.P.M.S. et al. (2005). 1,3-Dipolar cycloaddition reactions of porphyrins with azomethine ylides. *The Journal of Organic Chemistry* 70: 2306–2314.

65 Silva, A.M.G., Tomé, A.C., Neves, G.P.M.S., and Cavaleiro, J.A.S. (2002). Porphyrins in 1,3-dipolar cycloaddition reactions: synthesis of a novel pyrazoline-fused chlorin and a pyrazole-fused porphyrin. *Synlett* 1155–1157.

66 Silva, A.M.G., Tomé, A.C., Neves, M.G.P.M.S. et al. (2005). Porphyrins in 1,3-dipolar cycloadditions with sugar azomethine ylides. Synthesis of pyrrolidinoporphyrin glycoconjugates. *Synlett* 857–859.

67 Silva, A.M.G., Tomé, A.C., Neves, M.G.P.M.S. et al. (2002). Porphyrins in 1,3-dipolar cycloaddition reactions with sugar nitrones. Synthesis of glycoconjugated isoxazolidine-fused chlorins and bacteriochlorins. *Tetrahedron Letters* 43: 603–605.

68 Zhao, S., Neves, M.G.P.M.S., Tomé, A.C. et al. (2005). Novel porphyrin-quinone architectures via 1,3-dipolar cycloaddition reactions. *Tetrahedron Letters* 46: 5487–5490.

69 Silva, A.M.G., Tomé, A.C., Neves, M.G.P.M.S. et al. (1999). *meso*-Tetraarylporphyrins as dipolarophiles in 1,3-dipolar cycloaddition reactions. *Chemical Communications* 1767–1768.

70 Flemming, J. and Dolphin, D. (2002). Carbonyl ylide 1,3-dipolar cycloadditions with porphyrins. *Tetrahedron Letters* 43: 7281–7283.

71 Li, X., Zhuang, J., Li, Y. et al. (2005). Synthesis of isoxazoline-fused chlorins and bacteriochlorins by 1,3-dipolar cycloaddition reaction of porphyrin with nitrile oxide. *Tetrahedron Letters* 46: 1555–1559.

72 Liu, X., Feng, Y., Chen, X. et al. (2005). Porphyrins as dipolarophiles in 1,3-dipolar cycloaddition reactions with nitrile oxide. *Synlett* 1030–1032.

73 Galezowski, M. and Gryko, D.T. (2006). Synthesis of locked *meso*-β-substituted chlorins via 1,3-dipolar cycloaddition. *The Journal of Organic Chemistry* 71: 5942–5950.

74 Ostrowski, S., Wyrebek, P., and Mikus, A. (2006). Synthesis of isoxazoline-fused chlorins by 1,3-dipolar cycloaddition reaction of porphyrins with alkyl nitrile oxides. *Heterocycles* 68: 885–888.

75 Desjardins, A., Flemming, J., Sternberg, E.D., and Dolphin, D. (2002). Nitrogen extrusion from pyrazoline-substituted porphyrins and chlorins using long wavelength visible light. *Chemical Communications* 2622–2623.

76 Shea, K.M., Jaquinod, L., Khoury, R.G., and Smith, K.M. (2000). Functionalization of 2,3-disubstituted-2,3-dihydro-5,10,15,20-tetraphenylporphyrins. *Tetrahedron* 56: 3139–3144.

77 Krattinger, B. and Callot, H.J. (1999). Alkylation and reduction of porphyrins and *N* substituted porphyrins. New routes to chlorins and phlorins. *European Journal of Organic Chemistry* 1857–1867.

78 Senge, M.O., Kalisch, W.W., and Bischoff, I. (2000). The reaction of porphyrins with organolithium reagents. *Chemistry—a European Journal* 6: 2721–2738.

79 Feng, X., Bischoff, I., and Senge, M.O. (2001). Mechanistic studies on the nucleophilic reaction of porphyrins with organolithium reagents. *The Journal of Organic Chemistry* 66: 8693–8700.

80 Fuhrhop, J.H. and Mauzerall, D. (1968). The one-electron oxidation of magnesium octaethylporphin. *Journal of the American Chemical Society* 90: 3875–3876.

81 Pistner, A.J., Yap, G.P.A., and Rosenthal, J. (2012). A tetrapyrrole macrocycle displaying a multielectron redox chemistry and tunable absorbance profile. *Journal of Physical Chemistry C* 116: 16918–16924.

82 Kim, J.B., Adler, A.D., and Longo, F.R. (1978). Synthesis of Porphyrins from Monopyrroles. In: *The Porphyrins*, vol. 1 (ed. D. Dolphin), 85–100. New York, NY: Academic Press.

83 Lindsey, J.S. (2000). Synthesis of *meso*-substituted porphyrins. In: *The Porphyrin Handbook*, vol. 1 (ed. K.M. Kadish, K.M. Smith and R. Guilard), 45–118. San Diego, CA: Academic Press.

84 Jeandon, C., Krattinger, B., Ruppert, R., and Callot, H.J. (2001). Biladienones from the photooxidation of a *meso-gem*-disubstituted phlorin: crystal and molecular structures of the 3N + O coordinated nickel(II) and copper(II) complexes. *Inorganic Chemistry* 40: 3149–3153.

85 Pistner, A.J., Lutterman, D.A., Ghidiu, M.J. et al. (2013). Synthesis, electrochemistry, and photophysics of a family of phlorin macrocycles that display cooperative fluoride binding. *Journal of the American Chemical Society* 135: 6601–6607.

86 Bruce, A.M., Weyburne, E.S., Engle, J.T. et al. (2014). Phlorins bearing different substituents at the sp^3-hybridized *meso*-position. *The Journal of Organic Chemistry* 79: 5664–5672.

87 Arciero, D.M. and Hooper, A.B. (1998). Consideration of a phlorin structure for heme P 460 of hydroxylamine oxidoreductase and its implications regarding reaction mechanism. *Biochemical Society Transactions* 26: 385–389.

88 Ka, J.W. and Lee, C.H. (2001). Unusual phlorins from the oxidative coupling of pentapyrromethanes: their facile conversion to *meso*-substituted porphyrins. *Tetrahedron Letters* 42: 4527–4529.

89 Sugimoto, H. (1982). Phlorin complex of gold(III). *Journal of the Chemical Society, Dalton Transactions* 1169–1171.

90 LeSaulnier, T.D., Graham, B.W., and Geier, G.R. (2005). Enhancement of phlorin stability by the incorporation of *meso*-mesityl substituents. *Tetrahedron Letters* 46: 5633–5637.

91 O'Brien, A.Y., McGann, J.P., and Geier, G.R. III, (2007). Dipyrromethane + dipyrromethanedicarbinol routes to an electron deficient *meso*-substituted phlorin with enhanced stability. *The Journal of Organic Chemistry* 72: 4084–4092.

92 Kim, D., Chun, H.-J., Donnelly, C.C., and Geier, G.R. (2016). Two-step, one-flask synthesis of a *meso*-substituted phlorin. *The Journal of Organic Chemistry* 81: 5021–5031.

93 Lanese, J.G. and Wilson, G.S. (1972). Electrochemical studies of zinc tetraphenylporphine. *Journal of the Electrochemical Society* 119: 1039–1043.

94 Langhus, D.L. and Wilson, G.S. (1979). Spectroelectrochemistry and cyclic voltammetry of the EE mechanism in a porphyrin diacid reduction. *Analytical Chemistry* 51: 1139–1144.

95 Marrese, C.A. and Carrano, C.J. (1984). Mechanism of electrochemical reduction of the (5,10,15,20-tetraphenylporphinato)dihydroxophosphorus(V) cation. *Inorganic Chemistry* 23: 3961–3968.

96 Sutter, T.P.G., Rahimi, R., Hambright, P. et al. (1993). Steric and inductive effects on the basicity of porphyrins and on the site of protonation of porphyrin dianions: radiolytic reduction of porphyrins and metalloporphyrins to chlorins or phlorins. *Journal of the Chemical Society, Faraday Transactions* 89: 495–502.

97 Pandian, R.P., Chandrashekar, T.K., and Chandrasekhar, V. (1991). Nonmetal porphyrins – reactions of trichlorophosphine, phosphoryl chloride, and phenylphosphonic dichloride with tetraphenylporphyrin: spectroscopic and electrochemical studies. *Indian Journal of Chemistry, Section A: Inorganic, Bio-inorganic, Physical, Theoretical, and Analytical Chemistry* 30A: 579–583.

98 Segawa, H., Azumi, R., and Shimidzu, T. (1992). Direct hydroxylation at the *meso*-position of gold(III) tetraphenylporphyrin by nucleophilic addition: novel hydroxyphlorin derivatives. *Journal of the American Chemical Society* 114: 7564–7565.

99 Jiang, X., Nurco, D.J., and Smith, K.M. (1996). Direct *meso*-alkylation of *meso*-formylporphyrins using grignard reagents. *Chemical Communications* 1759–1760.

100 Baran, J. (1960). Method for the cleavage of osmate esters. *The Journal of Organic Chemistry* 25: 257.

101 Kolb, H.C., Van Nieuwenhze, M.S., and Sharpless, K.B. (1994). Catalytic asymmetric dihydroxylation. *Chemical Reviews* 94: 2483–2547.

102 Berrisford, D.J., Bolm, C., and Sharpless, K.B. (1995). Ligand-accelerated catalysis. *Angewandte Chemie International Edition in English* 34: 1059–1070.

103 Brückner, C., Rettig, S.J., and Dolphin, D. (1998). Formation of a *meso*-tetraphenylsecochlorin and a homoporphyrin with a twist. *The Journal of Organic Chemistry* 63: 2094–2098.

104 Samankumara, L.P., Zeller, M., Krause, J.A., and Brückner, C. (2010). Syntheses, structures, modification, and optical properties of *meso*-tetraaryl-2,3-dimethoxychlorin, and two isomeric *meso*-tetraaryl-2,3,12,13-tetrahydroxybacteriochlorins. *Organic & Biomolecular Chemistry* 8: 1951–1965.

105 Samankumara, L., Dorazio, S., Akhigbe, J. et al. (2015). Indachlorins: nonplanar indanone-annulated chlorin analogues with panchromatic absorption spectra between 300 and 900 nm. *Chemistry—a European Journal* 21: 11118–11128.

106 Pandey, R.K., Shiau, F.Y., Isaac, M. et al. (1992). Substituent effects in tetrapyrrole subunit reactivity and pinacol-pinacolone rearrangements: *vic*-dihydroxychlorins and *vic*-dihydroxybacteriochlorins. *Tetrahedron Letters* 33: 7815–7818.

107 Kozyrev, A.N., Dougherty, T.J., and Pandey, R.K. (1996). Effect of substituents in OsO_4 reactions of metallochlorins regioselective synthesis of isobacteriochlorins and bacteriochlorins. *Tetrahedron Letters* 37: 3781–3784.

108 Akhigbe, J., Yang, M., Luciano, M., and Brückner, C. (2016). Quinoline-annulated chlorins and chlorin-analogues. *Journal of Porphyrins and Phthalocyanines* 20: 265–273.

109 Brückner, C. and Dolphin, D. (1995). 2,3-*vic*-Dihydroxy-*meso*-tetraphenylchlorins from the osmium tetroxide oxidation of *meso*-tetraphenylporphyrin. *Tetrahedron Letters* 36: 3295–3298.

110 Starnes, S.D., Rudkevich, D.M., and Rebek, J. Jr., (2001). Cavitand-porphyrins. *Journal of the American Chemical Society* 123: 4659–4669.

111 Adams, K.R., Berenbaum, M.C., Bonnett, R. et al. (1992). Second generation tumour photosensitisers: the synthesis and biological activity of octaalkyl chlorins and bacteriochlorins with graded amphiphilic character. *Journal of the Chemical Society, Perkin Transactions* 1: 1465–1470.

112 Bonnett, R., Nizhnik, A.N., White, S.G., and Berenbaum, M.C. (1990). Porphyrin sensitizers in tumour phototherapy. Novel sensitizers of the chlorin and bacteriochlorin class with amphiphilic properties. *Journal of Photochemistry and Photobiology B: Biology* 6: 29–37.

113 Pandey, R.K. (1992). Improved photosensitizers for photodynamic therapy. *Proceedings of the Society of Photo-Optical Instrumentation Engineers* 1645: 264–273.

114 Zheng, G., Dougherty, T.J., and Pandey, R.K. (1999). A simple and short synthesis of divinyl chlorophyll derivatives. *The Journal of Organic Chemistry* 64: 3751–3754.

115 Gerzevske, K.R., Pandey, R.K., and Smith, K.M. (1994). Synthesis of *meso*-azachlorins and *meso*-azabacteriochlorins. *Heterocycles* 39: 439–443.

116 Pandey, R.K., Shiau, F.-Y., Sumlin, A.B. et al. (1994). Synthesis of new bacteriochlorins and their antitumor activity. *Bioorganic and Medicinal Chemistry Letters* 4: 1263–1267.

117 Meunier, I., Pandey, R.K., Walker, M.M. et al. (1992). New syntheses of benzoporphyrin derivatives and analogues for use in photodynamic therapy. *Bioorganic and Medicinal Chemistry Letters* 2: 1575–1580.

118 Chen, Y., Medforth, C.J., Smith, K.M. et al. (2001). Effect of *meso*-substituents on the osmium tetraoxide reaction and pinacol-pinacolone rearrangement of the corresponding *vic*-dihydroxyporphyrins. *The Journal of Organic Chemistry* 66: 3930–3939.

119 Ogikubo, J. and Brückner, C. (2011). Tunable *meso*-tetraphenylalkyloxazolo-chlorins and –bacteriochlorins. *Organic Letters* 13: 2380–2383.

120 Samankumara, L.P., Wells, S., Zeller, M. et al. (2012). Expanded bacteriochlorins. *Angewandte Chemie International Edition* 51: 5757–5760.

121 Hyland, M.A., Hewage, N., Walton, K. et al. (2016). Chromene-annulated bacteriochlorins. *Journal of Organic Chemistry* 81: 3603–3618.

122 Fischer, H. and Orth, H. (1937) *Die Chemie des Pyrrols*. Akademische Verlagsgesellschaft, Leipzig (Johnson Reprint, New York, NY, 1968).

123 Bonnett, R., Dolphin, D., Johnson, A.W. et al. (1964). Oxidation of porphyrins with H_2O_2 in H_2SO_4. *Proceedings of the Chemical Society* 371–372.

124 Inhoffen, H.H. and Nolte, W. (1967). Umwandlungen des octaethylporphyrins in octaethyl-geminiporphyrin-polyketone. *Tetrahedron Letters* 23: 2185–2187.

125 Inhoffen, H.H. and Nolte, W. (1969). Oxidative Umlagerungen am Octaäthylporphyrin zu Geminiporphin-polyketonen. *Liebigs Annalen der Chemie* 725: 167–176.

126 Bonnett, R., Dimsdale, M.J., and Stephenson, G.F. (1969). *meso*-Reactivity of porphyrins and related compounds. IV. Introduction of oxygen functions. *Journal of the Chemical Society C* 564–570.

127 Connick, P.A., Haller, K.J., and Macor, K.A. (1993). X-ray structural and imidazole-binding studies of nickel β-oxoporphyrins. *Inorganic Chemistry* 32: 3256–3264.

128 Connick, P.A. and Macor, K.A. (1991). Spectroscopic and electrochemical characterization of nickel β-oxoporphyrins: identification of nickel(III) oxidation products. *Inorganic Chemistry* 30: 4654–4663.

129 Stolzenberg, A.M., Glazer, P.A., and Foxman, B.M. (1986). Structure, reactivity, and electrochemistry of free-base β-oxoporphyrins and metallo-β-oxoporphyrin. *Inorganic Chemistry* 25: 983–991.

130 Barkigia, K.M., Chang, C.K., Fajer, J., and Renner, M.W. (1992). Models of heme d1. Molecular structure and NMR characterization of an iron(III) dioxoisobacteriochlorin (porphyrindione). *Journal of the American Chemical Society* 114: 1701–1707.

131 Chang, C.K. (1980). Synthesis and characterization of alkylated isobacteriochlorins, models of siroheme and sirohydrochlorin. *Biochemistry* 19: 1971–1976.

132 Minehan, T.G. and Kishi, Y. (1999). Total synthesis of the proposed structure of (+) tolyporphin A *O,O*-diacetate. *Angewandte Chemie International Edition* 38: 923–925.

133 Wang, W. and Kishi, Y. (1999). Synthesis and structure of tolyporphin A *O,O*-diacetate. *Organic Letters* 1: 1129–1132.

134 Liu, M., Chen, C.-Y., Hood, D. et al. (2017). Synthesis, photophysics and electronic structure of oxobacteriochlorins. *New Journal of Chemistry* 41: 3732–3744.

135 Crossley, M.J., Burn, P.L., Langford, S.J. et al. (1991). A new method for the synthesis of porphyrin-β-diones that is applicable to the synthesis of trans-annular extended porphyrin systems. *Journal of the Chemical Society, Chemical Communications* 1567–1568.

136 Crossley, M.J., Harding, M.M., and Sternhell, S. (1986). Tautomerism in 2-substituted 5,10,15,20-tetraphenylporphyrins. *Journal of the American Chemical Society* 108: 3608–3613.

137 Crossley, M.J., Harding, M.M., and Sternhell, S. (1988). Tautomerism in 2-hydroxy-5,10,15,20-tetraphenylporphyrin: an equilibrium between enol, keto, and aromatic hydroxyl tautomers. *The Journal of Organic Chemistry* 53: 1132–1137.

138 Wicks, M.N. and Burn, P.L. (2005). A short route to chlorin β-diones. *Journal of Porphyrins and Phthalocyanines* 9: 444–450.

139 Daniell, H.W., Williams, S.C., Jenkins, H.A., and Brückner, C. (2003). Oxidation of *meso*-tetraphenyl-2,3-dihydroxychlorin: simplified synthesis of β,β′-dioxochlorins. *Tetrahedron Letters* 44: 4045–4049.

140 Hewage, N., Zeller, M., and Brückner, C. (2017). Oxidations of chromene-annulated chlorins. *Organic & Biomolecular Chemistry* 15: 396–407.

141 Crossley, M.J., Govenlock, L.J., and Prashar, J.K. (1995). Synthesis of porphyrin-2,3,12,13- and −2,3,7,8-tetraones: building blocks for the synthesis of extended porphyrin arrays. *Journal of the Chemical Society, Chemical Communications* 2379–2380.

142 Brückner, C., McCarthy, J.R., Daniell, H.W. et al. (2003). A spectroscopic and computational study of the singlet and triplet excited states of synthetic β-functionalized chlorins. *Chemical Physics* 294: 285–303.

143 Crossley, M.J. and King, L.G. (1984). Novel heterocyclic systems from selective oxidation at the β-pyrrolic position of porphyrins. *Journal of the Chemical Society, Chemical Communications* 920–922.

144 Banerjee, S., Zeller, M., and Brückner, C. (2010). OsO_4-mediated dihydroxylation of *meso*-tetraphenylporphyrin-*N*-oxide, and transformation of the resulting diolchlorin-*N*-oxide regioisomers. *Journal of Organic Chemistry* 75: 1179–1187.

145 Akhigbe, J. and Brückner, C. (2013). Expansion of a pyrrole in *meso*-tetraphenylporphyrin to a pyrazine imide moiety using a Beckmann rearrangement. *European Journal of Organic Chemistry* 3876–3884.

146 Akhigbe, J., Luciano, M., Zeller, M., and Brückner, C. (2015). Mono- and bisquinoline-annulated porphyrins from porphyrin β,β′-dione oximes. *The Journal of Organic Chemistry* 80: 499–511.

147 Köpke, T., Pink, M., and Zaleski, J.M. (2008). Efficient silver-mediated acetalation of β,β′-functionalized chlorins. *Synlett* 1882–1888.

148 Köpke, T., Pink, M., and Zaleski, J.M. (2006). Photochemical preparation of pyrrole ring-contracted chlorins by the Wolff rearrangement. *Organic & Biomolecular Chemistry* 4: 4059–4062.

149 Brückner, C., Ogikubo, J., McCarthy, J.R. et al. (2012). *meso*-Arylporpholactones and their reduction products. *The Journal of Organic Chemistry* 77: 6480–6494.

150 Gouterman, M., Hall, R.J., Khalil, G.E. et al. (1989). Tetrakis(pentafluorophenyl) porpholactone. *Journal of the American Chemical Society* 111: 3702–3707.

151 Jayaraj, K., Gold, A., Austin, R.N. et al. (1997). Compound I and compound II analogues from porpholactones. *Inorganic Chemistry* 36: 4555–4566.

152 Hewage, N., Daddario, P., Lau, K.S.F. et al. Bacterio- and isobacterio-dilactones by stepwise or direct oxidations of *meso*-tetrakis(pentafluorophenyl)porphyrin. *The Journal of Organic Chemistry* 84: 239–256.

153 Köpke, T., Pink, M., and Zaleski, J.M. (2006). Elucidation of the extraordinary 4-membered pyrrole ring-contracted azeteoporphyrinoid as an intermediate in chlorin oxidation. *Chemical Communications* 4940–4942.

154 Grzegorzek, N., Pawlicki, M., and Latos-Grażyński, L. (2009). Regioselective amination of carbaporpholactone and N-confused porphyrin. *The Journal of Organic Chemistry* 74: 8547–8553.

155 Grzegorzek, N., Pawlicki, M., Szterenberg, L., and Latos-Grażyński, L. (2009). Organocopper(II) complex of 21-diphenylphosphoryl-carbaporpholactone hybrid: a side-on coordination mode of copper(II). *Journal of the American Chemical Society* 131: 7224–7225.

156 Lara, K.K., Rinaldo, C.R., and Brückner, C. (2003). *meso*-Tetraaryl-7,8-dihydroxydithiachlorins: first examples of heterochlorins. *Tetrahedron Letters* 44: 7793–7797.

157 Lara, K.K., Rinaldo, C.K., and Brückner, C. (2005). *meso*-Tetraaryl-7,8-diol-dithiachlorins and their pyrrole-modified derivatives: synthesis and spectroscopic comparison to their aza-analogues. *Tetrahedron* 61: 2529–2539.

158 Zeller, M., Banerjee, S., and Brückner, C. (2014). 8-Oxo-5,10,15,20-tetraphenyl-7-oxaporphyrin-24-*N*-oxide. *Acta Crystallographica, Section C: Crystal Structure Communications* 70: 707–711.

159 Ning, Y., Jin, G.-Q., and Zhang, J.-L. (2019). Porpholactone chemistry: an emerging approach to bioinspired photosensitizers with tunable near-infrared photophysical properties. *Accounts of Chemical Research* 52: 2620–2633.

160 Khalil, G., Gouterman, M., Ching, S. et al. (2002). Synthesis and spectroscopic characterization of Ni, Zn, Pd and Pt tetra(pentafluorophenyl)porpholactone with comparison to mg, Zn, Y, Pd and Pt metal complexes of tetra(pentafluorophenyl)porphine. *Journal of Porphyrins and Phthalocyanines* 6: 135–145.

161 Wan, J.R., Gouterman, M., Green, E., and Khalil, G.E. (1994). High performance liquid chromatography separation and analysis of metallotetra(pentafluorophenyl) porpholactone. *Journal of Liquid Chromatography* 17: 2045–2056.

162 Ke, X.-S., Chang, Y., Chen, J.-Z. et al. (2014). Porphodilactones as synthetic chlorophylls: relative orientation of β substituents on a pyrrolic ring tunes NIR absorption. *Journal of the American Chemical Society* 136: 9598–9607.

163 Liang, L., Lv, H., Yu, Y. et al. (2012). Iron(III) tetrakis(pentafluorophenyl)porpholactone catalyzes nitrogen atom transfer to C=C and C-H bonds with organic azides. *Dalton Transactions* 41: 1457–1460.

164 Rahimi, R., Tehrani, A.A., Fard, M.A. et al. (2009). First catalytic application of metal complexes of porpholactone and dihydroxychlorin in the sulfoxidation reaction. *Catalysis Communications* 11: 232–235.

165 Cetin, A. and Ziegler, C.J. (2005). Structure and catalytic activity of a manganese(III) tetraphenylporpholactone. *Dalton Transactions* 25–26.

166 Wu, Z.-Y., Xue, H., Wang, T. et al. (2020). Mimicking of tunichlorin: deciphering the importance of a β-hydroxyl substituent on boosting the hydrogen evolution reaction. *ACS Catalysis* 10: 2177–2188.

167 To, W.-P., Liu, Y., Lau, T.-C., and Che, C.-M. (2013). A robust palladium(II)–porphyrin complex as catalyst for visible light induced oxidative C-H functionalization. *Chemistry—a European Journal* 19: 5654–5664.

168 Gouterman, M., Callis, J., Dalton, L. et al. (2004). Dual luminophor pressure-sensitive paint: III. Application to automotive model testing. *Measurement Science and Technology* 15: 1986–1994.

169 Khalil, G.E., Daddario, P., Lau, K.S.F. et al. (2010). *meso*-Tetraarylporpholactones as high pH sensors. *Analyst* 135: 2125–2131.

170 Liu, E., Ghandehari, M., Brückner, C. et al. (2017). Mapping high pH levels in hydrated calcium silicates. *Cement & Concrete Research* 95: 232–239.

171 Yu, Y., Czepukojc, B., Jacob, C. et al. (2013). Porphothionolactones: synthesis, structure, physical, and chemical properties of a chemidosimeter for hypochlorite. *Organic & Biomolecular Chemistry* 11: 4613–4621.

172 Worlinsky, J.L., Halepas, S., and Brückner, C. (2014). PEGylated meso-arylporpholactone metal complexes as optical cyanide sensors in water. *Organic & Biomolecular Chemistry* 12: 3991–4001.

173 Yang, Z.-S., Yao, Y., Sedgwick, A.C. et al. (2020). Rational design of an "all-in-one" phototheranostic. *Chemical Sciences* 11: 8204–8213.

174 Ke, X.S., Yang, B.Y., Cheng, X. et al. (2014). Ytterbium (III) porpholactones: β lactonization of porphyrin ligands enhances sensitization efficiency of lanthanide near-infrared luminescence. *Chemistry—a European Journal* 20: 4324–4333.

175 Ning, Y., Ke, X.-S., Hu, J.-Y. et al. (2017). Bioinspired orientation of β substituents on porphyrin antenna ligands switches ytterbium(III) NIR emission with thermosensitivity. *Inorganic Chemistry* 56: 1897–1905.

176 Tang, J., Chen, J.-J., Jing, J. et al. (2014). β Lactonization of fluorinated porphyrin enhances LDL binding affinity, cellular uptake with selective intracellular localization. *Chemical Sciences* 5: 558–566.

177 Yao, Y., Rao, Y., Liu, Y. et al. (2019). Aromaticity versus regioisomeric effect of β-substituents in porphyrinoids. *Physical Chemistry, Chemical Physics* 21: 10152–10162.

178 Ogikubo, J., Meehan, E., Engle, J.T. et al. (2012). *meso*-Aryl-3-alkyl-2-oxachlorins. *The Journal of Organic Chemistry* 77: 6199–6207.

179 Yu, Y., Furuyama, T., Tang, J. et al. (2015). Stable iso-bacteriochlorin mimics from porpholactone: effect of a β oxazolone moiety on the frontier π-molecular orbitals. *Inorganic Chemistry Frontiers* 2: 671–677.

180 Sharma, M., Meehan, E., Mercado, B.Q., and Brückner, C. (2016). β Alkyloxazolochlorins: revisiting the ozonation of octaalkylporphyrins, and beyond. *Chemistry—a European Journal* 22: 11706–11718.

181 Inhoffen, H.H., Brockmann, H. Jr., and Bliesener, K.-M. (1969). Photoprotoporphyrine und ihre umwandlung in spirographis- sowie isospirographis-porphyrin. *Liebigs Annalen der Chemie* 730: 173–185.

182 Cox, G.S. and Whitten, D.G. (1982). Mechanisms for the photooxidation of protoporphyrin IX in solution. *Journal of the American Chemical Society* 104: 516–521.

183 Fischer, H. and Mladen, D. (1933). Über die Einwirkung von Ozon auf Porphyrine. *Hoppe-Seyler's Zeitschrift für Physiologische Chemie* 222: 270–278.

184 Shul'ga, A.M., Byteva, I.M., Gurinovich, I.F. et al. (1977). Oxidation of porphyrins. Structure of the products of octaethylporphine ozonization. *Biofizika* 22: 771–776.

185 Ogikubo, J., Meehan, E., Engle, J.T. et al. (2013). *meso*-Tetraphenyl-2-oxabacteriochlorins and *meso*-tetraphenyl-2,12/13-dioxabacteriochlorins. *The Journal of Organic Chemistry* 78: 2840–2852.

186 Hortensteiner, S. and Kräutler, B. (2011). Chlorophyll breakdown in higher plants. *Biochimica et Biophysica Acta* 1807: 977–988.

187 Arnold, L. and Müllen, K. (2011). Modifying the porphyrin core—a chemist's jigsaw. *Journal of Porphyrins and Phthalocyanines* 15: 757–779.

188 Adams, K.R., Bonnett, R., Burke, P.J. et al. (1993). The 2,3-secochlorin-2,3-dione system. *Journal of the Chemical Society, Chemical Communications* 1860–1861.

189 Adams, K.R., Bonnett, R., Burke, P.J. et al. (1997). Cleavage of (octaethyl-2,3-dihydroxychlorinato)nickel(II) to give the novel 2,3-dioxo-2,3-secochlorin system. *Journal of the Chemical Society, Perkin Transactions* 1: 1769–1772.

190 Sessler, J.L., Shevchuk, S.V., Callaway, W., and Lynch, V. (2001). A one-step synthesis of a free base secochlorin from a 2,3-dimethoxy porphyrin. *Chemical Communications* 968–969.

191 Lo, M., Lefebvre, J.-F., Marcotte, N. et al. (2012). Synthesis of stable free base secochlorins and their corresponding metal complexes from *meso*-tetraarylporphyrin derivatives. *Chemical Communications* 48: 3460–3462.

192 Ryppa, C., Niedzwiedzki, D., Morozowich, N.L. et al. (2009). Stepwise conversion of two pyrrole moieties of octaethylporphyrin to pyridin-3-ones: synthesis, mass spectral, and photophysical properties of mono- and bis(oxypyri)porphyrins. *Chemistry—a European Journal* 15: 5749–5762.

193 Brückner, C., Sternberg, E.D., MacAlpine, J.K. et al. (1999). A novel stepwise degradation of porphyrins. Synthesis and structural characterization of *meso*-tetraphenylchlorophinato nickel(II) and *meso*-tetraphenylsecochlorinato nickel(II). *Journal of the American Chemical Society* 121: 2609–2610.

194 Brückner, C., Hyland, M.A., Sternberg, E.D. et al. (2005). Preparation of [*meso*-tetraphenylchlorophinato]nickel(II) by stepwise deformylation of [*meso*-tetraphenyl-2,3-diformylsecochlorinato]nickel(II): conformational consequences of breaking the structural integrity of nickel porphyrins. *Inorganica Chimica Acta* 358: 2943–2953.

195 Li, K.-L., Guo, C.-C., and Chen, Q.-Y. (2009). Unprecedented degradation of nickel(II) 2,3,12,13-tetrabromo-5,10,15,20-tetraarylporphyrins by the anion of *E*-benzaldoxime: a novel approach to nickel(III) chlorophins and bacteriophins. *Organic Letters* 11: 2724–2727.

196 Clezy, P.S. (1978). Oxophlorins (oxyporphyrins). In: *Porphyrins*, vol. 2 (ed. D. Dolphin), 103–130. New York, NY: Academic Press.

197 Barnett, G.H., Hudson, M.F., McCombie, S.W., and Smith, K.M. (1973). Synthesis of oxophlorines (oxyporphyrines) from magnesium and zinc porphyrin chelates. *Journal of the Chemical Society, Perkin Transactions* 1: 691–696.

198 De Montellano, P.R.O. and Auclair, K. (2003). Heme oxygenase structure and mechanism. In: *The Porphyrin Handbook*, vol. 12 (ed. K.M. Kadish, K.M. Smith and R. Guilard), 183–210. San Diego, CA: Academic Press.

199 Khoury, R.G., Jaquinod, L., Paolesse, R., and Smith, K.M. (1999). New chemistry of oxophlorins (oxyporphyrins) and their π-radicals. *Tetrahedron* 55: 6713–6732.

200 Senge, M.O. and Smith, K.M. (1992). Structural evidence for nonplanar keto- and planar enol-forms of oxophlorins. *Journal of the Chemical Society, Chemical Communications* 1108–1109.

201 Balch, A.L., Noll, B.C., and Zovinka, E.P. (1992). Structural characterization of zinc(II) complexes of octaethyloxophlorin dianion and octaethyloxophlorin radical anion. *Journal of the American Chemical Society* 114: 3380–3385.

202 Balch, A.L., Noll, B.C., Reid, S.M., and Zovinka, E.P. (1993). Coordination patterns for oxophlorin ligands. Pyridine-induced cleavage of dimeric manganese(III) and iron(III) octaethyloxophlorin complexes. *Inorganic Chemistry* 32: 2610–2611.

203 Masuoka, N. and Itano, H.A. (1987). Radical intermediates in the oxidation of octaethylheme to octaethylverdoheme. *Biochemistry* 26: 3672–3680.

204 Balch, A.L., Latos-Grażyński, L., Noll, B.C. et al. (1992). Chemistry of iron oxophlorins. 1. Proton NMR and structural studies of five-coordinate iron(III) complexes. *Inorganic Chemistry* 31: 2248–2255.

205 Balch, A.L., Latos-Grażyński, L., Noll, B.C. et al. (1993). Chemistry of iron oxophlorins. 2. Oxidation of the iron(III) octaethyloxophlorin dimer and observation of stepwise, two-electron oxidation of the oxophlorin macrocycle. *Journal of the American Chemical Society* 115: 11846–11854.

206 Balch, A.L., Latos-Grażyński, L., and St. Claire, T.N. (1995). Chemistry of iron oxophlorins. 3. Reversible, one-electron oxidation of the iron(III) octaethyloxophlorin dimer. *Inorganic Chemistry* 34: 1395–1401.

207 Balch, A.L., Koerner, R., Latos-Grażyński, L. et al. (1997). Coupled oxidation of heme without pyridine. Formation of cyano complexes of iron oxophlorin and 5-oxaporphyrin (verdoheme) from octaethylheme. *Inorganic Chemistry* 36: 3892–3897.

208 Garcia, T.Y., Olmstead, M.M., Fettinger, J.C., and Balch, A.L. (2008). Cleavage of the indium(III) octaethyloxophlorin dimer, $\{In^{III}(OEPO)\}_2$, with Lewis bases. Importance of outer-sphere hydrogen bonding in adduct structures. *Inorganic Chemistry* 47: 11417–11422.

209 Shimizu, D., Oh, J., Furukawa, K. et al. (2015). Triarylporphyrin *meso*-oxy radicals: remarkable chemical stabilities and oxidation to oxophlorin π-cations. *Journal of the American Chemical Society* 137: 15584–15594.

210 Fuhrhop, J.-H., Besecke, S., Subramanian, J. et al. (1975). Reactions of oxophlorines and their π-radicals. *Journal of the American Chemical Society* 97: 7141–7152.

211 Balch, A.L., Noll, B.C., Reid, S.M., and Zovinka, E.P. (1993). Carbon-carbon bond formation in the dimerization of (octaethyloxophlorin radical)nickel(II). *Journal of the American Chemical Society* 115: 2531–2532.

212 Watanabe, E., Nishimura, S., Ogoshi, H., and Yoshida, Z. (1975). Orientation of electrophilic *meso*-substitution in metallooctaethylporphyrins. *Tetrahedron* 31: 1385–1390.

213 Gong, L.C. and Dolphin, D. (1985). Nitrooctaethylporphyrins: synthesis, optical and redox properties. *Canadian Journal of Chemistry* 63: 401–405.

214 Gong, L.C. and Dolphin, D. (1985). Nucleophilic substitution of meso-nitrooctaethylporphyrins. *Canadian Journal of Chemistry* 63: 406–411.

215 Gossauer, A. (2003). Synthesis of bilines. In: *The Porphyrin Handbook*, vol. 13 (ed. K.M. Kadish, K.M. Smith and R. Guilard), 237–274. San Diego, CA: Academic Press.

216 Falk, H. (1989). *The Chemistry of Linear Oligopyrroles and Bile Pigments*. Wien, New York, NY: Springer Verlag.

217 Frydman, R.B. and Frydman, B. (1987). Heme catabolism: a new look at substrates and enzymes. *Accounts of Chemical Research* 20: 250–256.

218 McDonagh, A.F. (2001). Turning green to gold. *Nature Structural Biology* 8: 198–200.

219 Frankenberg, N. and Lagarias, J.C. (2003). Biosynthesis and biological functions of bilins. In: *The Porphyrin Handbook*, vol. 13 (ed. K.M. Kadish, K.M. Smith and R. Guilard), 211–235. San Diego, CA: Academic Press.

220 Bonnett, R. and McDonagh, A.F. (1973). The meso-reactivity of porphyrins and related compounds. VI. Oxidative cleavage of the haem system. The four isomeric biliverdins of the IX series. *Journal of the Chemical Society, Perkin Transactions* 1 (9): 881–888.

221 Gossauer, A. and Engel, J. (1978). Linear polypyrrolic compounds. In: *The Porphyrins*, vol. 2 (ed. D. Dolphin), 197–253. New York, NY: Academic Press.

222 Gossauer, A. and Plieninger, H. (1979). Synthesis, purification, and characterization of bile pigments and related compounds. In: *The Porphyrins*, vol. 6 (ed. D. Dolphin), 585–650. New York, NY: Academic Press.

223 Balch, A.L., Latos-Grażyński, L., Noll, B.C. et al. (1993). Isolation and characterization of an iron biliverdin-type complex that is formed along with verdohemochrome during

the coupled oxidation of iron(II) octaethylporphyrin. *Journal of the American Chemical Society* 115: 9056–9061.

224 Koerner, R., Latos-Grażyński, L., and Balch, A.L. (1998). Models for verdoheme hydrolysis. Paramagnetic products from the ring opening of verdohemes, 5-oxaporphyrin complexes of iron(II), with methoxide ion. *Journal of the American Chemical Society* 120: 9246–9255.

225 Latos-Grażyński, L., Johnson, J., Attar, S. et al. (1998). Reactivity of the verdoheme analogs, 5-oxaporphyrin complexes of cobalt(II) and zinc(II), with nucleophiles: opening of the planar macrocycle by alkoxide addition to form helical complexes. *Inorganic Chemistry* 37: 4493–4499.

226 Balch, A.L., Latos-Grażyński, L., Noll, B.C. et al. (1993). Structural characterization of verdoheme analogs. Iron complexes of octaethyloxoporphyrin. *Journal of the American Chemical Society* 115: 1422–1429.

227 Nguyen, K.T., Rath, S.P., Latos-Grażyński, L. et al. (2004). Formation of a highly oxidized iron biliverdin complex upon treatment of a five-coordinate verdoheme with dioxygen. *Journal of the American Chemical Society* 126: 6210–6211.

228 Sprutta, N., Rath, S.P., Olmstead, M.M., and Balch, A.L. (2005). Metal complexes of *meso*-amino-octaethylporphyrin and the oxidation of Ni^{II}(*meso*-amino-octaethylporphyrin). *Inorganic Chemistry* 44: 1452–1459.

229 Koerner, R., Olmstead, M.M., Ozarowski, A. et al. (1998). Possible intermediates in biological metalloporphyrin oxidative degradation. Nickel, copper, and cobalt complexes of octaethylformybiliverdin and their conversion to a verdoheme. *Journal of the American Chemical Society* 120: 1274–1284.

230 Fuhrhop, J.H. and Mauzerall, D. (1971). The photooxygenation of magnesium-octaethylporphyrin. *Photochemistry and Photobiology* 13: 453–458.

231 Wasser, P.K.W. and Fuhrhop, J.-H. (1973). The photooxygenation of metalloporphyrins and metallochlorins. *Annals of the New York Academy of Sciences* 206: 533–548.

232 Isaac, M., Senge, M.O., and Smith, K.M. (1995). Synthesis and characterization of models for the bilin catabolites of chlorophylls using metallo-β-oxochlorins and benzo[at]chlorins: comparison of macrocycle cleavage versus *meso*-oxochlorin formation. *Journal of the Chemical Society, Perkin Transactions* 1: 705–714.

233 Andrews, L.E., Bonnett, R., Ridge, R.J., and Appelman, E.H. (1983). The preparation and reactions of porphyrin *N*-oxides. *Journal of the Chemical Society, Perkin Transactions* 1: 103–107.

234 Balch, A.L., Chan, Y.-W., and Olmstead, M.M. (1985). A complex containing a Ni-O unit at the center of a porphyrin. The X-ray crystal and molecular structure of the nickel(II) complex of octaethylporphyrin *N*-oxide dianion. *Journal of the American Chemical Society* 107: 6510–6514.

235 Yang, F.-A., Guo, C.-W., Chen, Y.-J. et al. (2007). ESR, zero-field splitting, and magnetic exchange of exchange-coupled copper(II)–copper(II) pairs in copper(II) tetraphenylporphyrin *N*-oxide. *Inorganic Chemistry* 46: 578–585.

236 Balch, A.L., Chan, Y.W., Olmstead, M., and Renner, M.W. (1985). Structure of octaethylporphyrin *N*-oxide and the characterization of its nickel(II) and copper(II) complexes. *Journal of the American Chemical Society* 107: 2393–2398.

237 Groves, J.T. and Watanabe, Y. (1986). Preparation and characterization of an iron(III) porphyrin *N*-oxide. *Journal of the American Chemical Society* 108: 7836–7837.

238 Groves, J.T. and Watanabe, Y. (1988). Reactive iron porphyrin derivatives related to the catalytic cycles of cytochrome P-450 and peroxidase. Studies of the mechanism of oxygen activation. *Journal of the American Chemical Society* 110: 8443–8452.

239 Mizutani, Y., Watanabe, Y., and Kitagawa, T. (1994). Resonance Raman characterization of iron(III) porphyrin *N*-oxide: evidence for an Fe-O-N bridged structure. *Journal of the American Chemical Society* 116: 3439–3441.

240 Arasasingham, R.D., Balch, A.L., Olmstead, M.M., and Renner, M.W. (1987). Insertion of manganese and cobalt into octaethylporphyrin *N*-oxide. Formation of layered diporphyrin structures joined through M-O-N links. *Inorganic Chemistry* 26: 3562–3568.

241 Banerjee, S., Zeller, M., and Brückner, C. (2009). MTO//H_2O_2/Pyrazole-mediated *N* oxidation of *meso*-tetraarylporphyrins and -chlorins, and *S*-oxidation of a *meso*-tetraaryldithiaporphyrin and -chlorin. *The Journal of Organic Chemistry* 74: 4283–4288.

242 Li, R., Zeller, M., and Brückner, C. (2017). Surprising outcomes of classic ring-expansion conditions applied to octaethyloxochlorin, 1. Baeyer–Villiger-oxidation conditions. *European Journal of Organic Chemistry* 1820–1825.

243 Dolphin, D., Traylor, T.G., and Xie, L.Y. (1997). Polyhaloporphyrins: unusual ligands for metals and metal-catalyzed oxidations. *Accounts of Chemical Research* 30: 251–259.

244 Fujii, H. (2002). Electronic structure and reactivity of high-valent oxo iron porphyrins. *Coordination Chemistry Reviews* 226: 51–60.

245 Dolphin, D. and Felton, R.H. (1974). Biochemical significance of porphyrin π-cation radicals. *Accounts of Chemical Research* 7: 26–32.

246 Sergeeva, N.N. and Senge, M.O. (2012). Photochemical transformations involving porphyrins and phthalocyanines. In: *CRC Handbook of Organic Photochemistry and Photobiology*, vol. 1 (ed. W.M. Horspool and F. Lenci), 831–879. Boca Raton, FL: CRC Press.

247 Blankenship, R.E. (2008). *Molecular Mechanisms of Photosynthesis*. London, UK: Wiley Blackwell.

248 Li, L.-L. and Diau, E.W.-G. (2013). Porphyrin-sensitized solar cells. *Chemical Society Reviews* 42: 291–304.

249 Urbani, M., Grätzel, M., Nazeeruddin, M.K., and Torres, T. (2014). *Meso*-substituted porphyrins for dye-sensitized solar cells. *Chemical Reviews* 114: 12330–12396.

250 Kärkäs, M.D., Verho, O., Johnston, E.V., and Åkermark, B. (2014). Artificial photosynthesis: molecular systems for catalytic water oxidation. *Chemical Reviews* 114: 11863–12001.

251 Gust, D., Moore, T.A., and Moore, A.L. (2009). Solar fuels via artificial photosynthesis. *Accounts of Chemical Research* 42: 1890–1898.

252 Gilbert, M. and Albinsson, B. (2015). Photoinduced charge and energy transfer in molecular wires. *Chemical Society Reviews* 44: 845–862.

253 Kaim, W. and Schwederski, B. (2010). Non-innocent ligands in bioinorganic chemistry—an overview. *Coordination Chemistry Reviews* 254: 1580–1588.

254 Meunier, B., de Visser, S.P., and Shaik, S. (2004). Mechanism of oxidation reactions catalyzed by cytochrome P450 enzymes. *Chemical Reviews* 104: 3947–3980.

255 Poulos, T.L. (2014). Heme enzyme structure and function. *Chemical Reviews* 114: 3919–3962.

256 Meunier, B., Robert, A., Pratviel, G., and Bernadou, J. (2000). Metalloporphyrins in catalytic oxidations and oxidative DNA cleavage. In: *The Porphyrin Handbook*, vol. 4 (ed. K.M. Kadish, K.M. Smith and R. Guilard), 119–187. San Diego, CA: Academic Press.

257 Tanaka, T. and Osuka, A. (2015). Conjugated porphyrin arrays: synthesis, properties and applications for functional materials. *Chemical Society Reviews* 44: 943–969.

7

Corroles and Contracted Porphyrins

Daniel T. Gryko and Mariusz Tasior

Institute of Organic Chemistry, Polish Academy of Sciences, Warsaw, Poland

7.1 Introduction

It is difficult to determine exactly when the concept of contracted porphyrins was born. They are defined as macrocycles composed of four pyrrole units and the equivalent of three or fewer methine bridges. The pyrrole moieties can be replaced with furan or thiophene, whereas the carbon atoms linking them can be replaced by heteroatoms (typically by nitrogen or oxygen). Contracted porphyrins are typically fully conjugated, with some exceptions. Although in principle many structures fit this definition, we shall focus in this chapter on the existing structures. Moreover, the proportion of the description will roughly reflect the number of papers published. That means that the lion's share of the chapter will be devoted to corroles (Figure 7.1). Many contracted porphyrins that were presented in the literature just once and usually long ago will be only shown as generic structures (Figure 7.1), and they will not be further described. The structures that may exist in the future but have not yet been synthesized will also only be presented in Figure 7.1. Instead, attention will be given to some recent discoveries that hold potential for further development extending beyond basic characterization.

7.2 Corroles

7.2.1 General Information

Among the many existing contracted porphyrins, the one scaffold that clearly stands out is the corrole [1–3]. Corroles were discovered more than 50 years ago (1964) [4] and their straightforward synthetic methodology made it possible not only to study their basic properties, but also to perform numerous more sophisticated studies. After porphyrins and phthalocyanines, corroles are the third most often investigated group of porphyrinoids, and more than 100 papers were published in 2015 alone. The skeleton of a corrole consists of four pyrrole units and three methine bridges; that is, it possesses one direct pyrrole-pyrrole link. A smaller cavity that results from this configuration is accompanied by reduced symmetry from D_{4h} (in the case of porphyrins) to C_{2v}. Numerous X-ray structures obtained to date confirmed that bonds of the corrole core are intermediate between C—C single and double bonds. Corroles, however, are not planar. The presence of three "pyrrole-type" nitrogen atoms and one

Fundamentals of Porphyrin Chemistry: A 21st Century Approach, Volume 1, First Edition.
Edited by Penelope J. Brothers and Mathias O. Senge.
© 2022 John Wiley & Sons Ltd. Published 2022 by John Wiley & Sons Ltd.

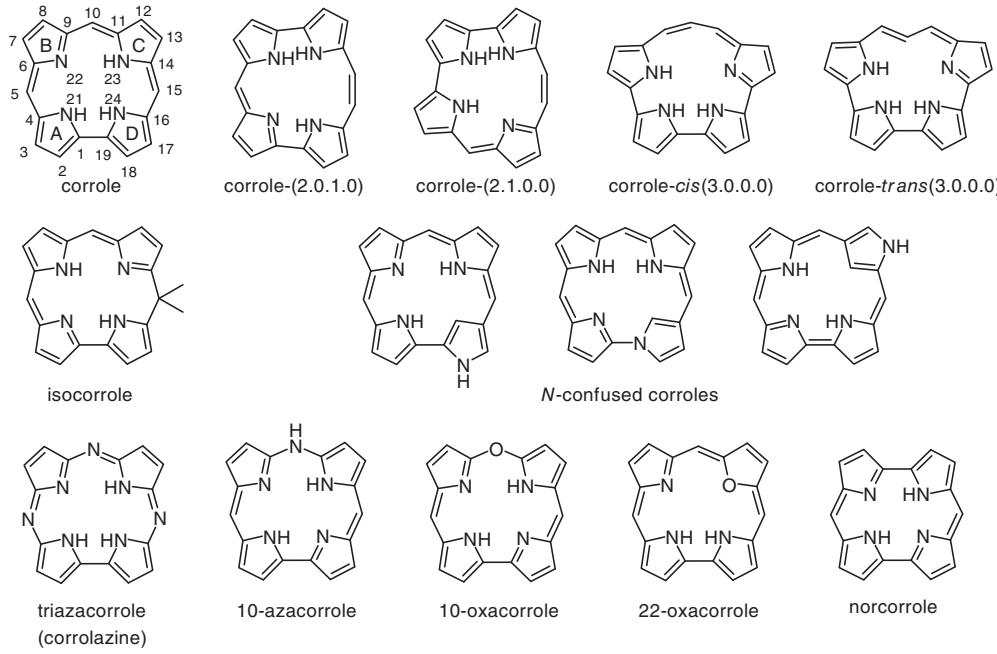

Figure 7.1 The contracted porphyrins.

"pyridine–type" nitrogen atom results in crowding of three protons inside the cavity. Eventually, this arrangement leads to tilting of one of the pyrrole units out of the plane. Both this observation and ^{1}H NMR studies fully confirmed that corroles are aromatic. Corroles are significantly more acidic than porphyrins; their anion can form in the presence of Et_3N in organic solvents. They can also be easily protonated. Two main tautomers of corroles exist, and the related tautomerization process, which is very rapid even below 200 K, involves the engagement of the proton in an unsymmetrical proton sponge unit formed by two pyrrole ring atoms (rings A and B, Figure 7.1) [5]. The overall picture is, however, more complex, and some tautomerization processes are intermolecular (in solution). The smaller cavity is a consequence of the absence of one carbon-based methine bridge and has multiple consequences, the most important being the preference for metal cations with higher oxidation states, which have smaller radii.

7.2.2 Synthesis

The synthesis of corroles has been reviewed several times [6–8]. From the early work of Johnson and Kay until the late 1990s, the synthesis of corroles conceptually followed the Fisher approach toward β-substituted porphyrins. The strategies began with preparation of 2-formylpyrroles substituted at positions 3 and 4 with alkyl or aryl groups (such as **1**) and corresponding dipyrranes (dipyrromethanes) possessing two carboxylic groups at positions 2 and 8 (such as **2**) (Scheme 7.1). The Friedel–Crafts reaction followed by dehydration led to the biladiene salt, which underwent macrocyclization in the presence of *p*-chloranil, leading to corrole **3** [9]. The yields of the final macrocyclization varied from case to case. However, the most important problem in these syntheses is the preparation of precursors, which usually comprised ~10 steps. Although various modifications have been investigated over the

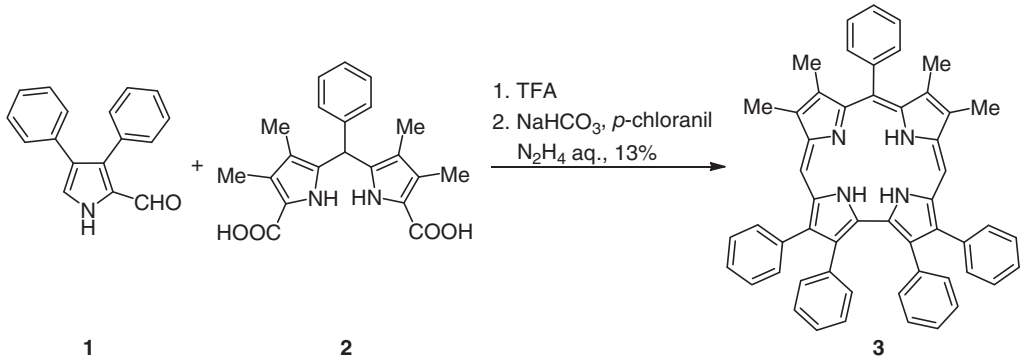

Scheme 7.1 Example of the most versatile synthesis of β-substituted corroles developed before 1999.

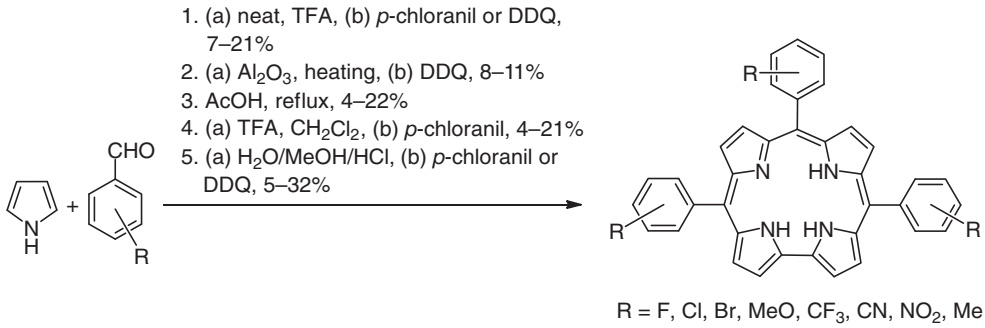

Scheme 7.2 One-pot synthesis of A_3-corroles directly from aldehydes and pyrrole.

decades, most of them differ in the order of steps leading toward biladiene. It is worth noting that historically the first synthesis of undecasubstituted corrole was performed by Paolesse and co-workers in 1994 [10]. The tetra-substituted pyrrole derivative was transformed into porphyrinogen, which was subjected to treatment by $Co(OAc)_2$ and triphenylphosphine, giving rise to Co-complex of corrole (possessing PPh_3 as the axial ligand) in 25% yield.

Although discovered in 1964, corroles did not really hit the headlines until the late 1990s, when Vogel observed that they stabilized higher oxidation states of metals [11]. Although this claim was proved partially wrong by later studies, it certainly brought attention to the subject. Three years later, the groups of Paolesse [12] and Gross [13] discovered a one-step methodology to synthesize A_3-corroles (i.e., corroles bearing identical substituents at all three *meso*-positions) directly from pyrrole and aromatic aldehydes (Scheme 7.2). With respect to this point, we should not overlook earlier reports by Rose and Andrioletti [14] as well as by Loim [15], who discovered the formation of A_3-corroles while using very specific aldehydes in reaction with pyrrole. Apart from the observations of these research groups, Gross and Paolesse noted the great potential of corroles, and they immediately followed their discoveries by expanding the chemistry of these macrocycles in various directions.

The pioneering studies by Gross and co-workers have demonstrated that no catalyst is required to induce reaction between pyrrole and pentafluorobenzaldehyde under neat conditions. Oxidation of mixtures of oligocondensates (containing tetrapyrrane) with 2,3-dichloro-5,6-dicyanobenzoquinone (DDQ) led to the 5,10,15-tris(pentafluorophenyl)

corrole (**TPFC**) in 13% yield. Modifications led to the use of Al_2O_3 as a solid support for the first step, which maintained the yield even with an increase in the scale [13]. At the same time, Paolesse and co-workers discovered that simply changing the ratio of pyrrole to aldehyde from 1:1 to 3:1 under classical Adler–Longo conditions altered the ratio of formed porphyrinogen to bilane (tetrapyrrane), so that 5,10,15-triarylcorroles formed with acceptable yields (Scheme 7.2) [16]. Once the door was opened, many researchers tried to optimize the yields by employing CH_2Cl_2 as a solvent or by fine-tuning the reaction conditions in the neat solvent to the reactivity of aldehyde, by altering the ratio of substrates and concentration of trifluoroacetic acid (TFA) [17, 18]. In 2006, Gryko and Koszarna published a new approach, in which the first step is performed in H_2O/MeOH mixture (1:1) and is catalyzed by HCl (Scheme 7.2). With the notable exception of **TPFC**, the yields of all attempted A_3-corroles have been improved significantly to reach typically 15–27%, with a miniscule amount of A_4-porphyrin (~1%) [19]. The yield of 5,10,15-tris(pentafluorophenyl)corrole was eventually increased to 17% by the joint efforts of Virgil, Grubbs, and Gray [20]. The most electron-poor corrole, that is, 2,3,7,8,12,13,17,18-octafluoro-5,10,15-tris(pentafluorophenyl)corrole, has been synthesized by Chang and co-workers in 5% yield [21].

The synthesis of *meso*-substituted corroles evolved quickly during the first seven years after Paolesse's and Gross's discovery. The methodology which led to *trans*-A_2B-corroles (i.e., corroles bearing substituents A at positions 5 and 15 and substituent B at position 10) from dipyrranes and aldehydes was discovered in 2000 [22] and optimized several times [23–26] prior to 2006, when Gryko and Koszarna discovered that as long as aldehydes and dipyrranes were relatively small and/or hydrophilic, performing this reaction in a mixture of water and methanol in the presence of HCl allowed the yields to increase from 6–30% to ~55% (Scheme 7.3) [19].The importance of the latter discovery lies in the fact that with such high yields, gram quantities became available either via simplified chromatography or in some cases via crystallization directly from the reaction mixture. The knowledge obtained from Lindsey's papers on the synthesis of *meso*-substituted porphyrins possessing two, three, or four different substituents (mostly awareness of scrambling) helped to accelerate the development of corrole chemistry, influencing attempted reaction conditions.

Thanks to the work of various research groups, numerous conditions exist for the synthesis of *trans*-A_2B-corroles possessing various substituents. These reaction conditions have been collected in Table 7.1, so as to assist in planning syntheses.

Corroles can be either synthesized from aldehydes/dipyrranes/dipyrrane-diols already modified with the required substituents or they can be modified after assembling the macrocycle ring. Both options are viable, and significant work has focused on investigation of the reactivity of the corrole ring (Schemes 7.4 and 7.5). Over the years, it was discovered

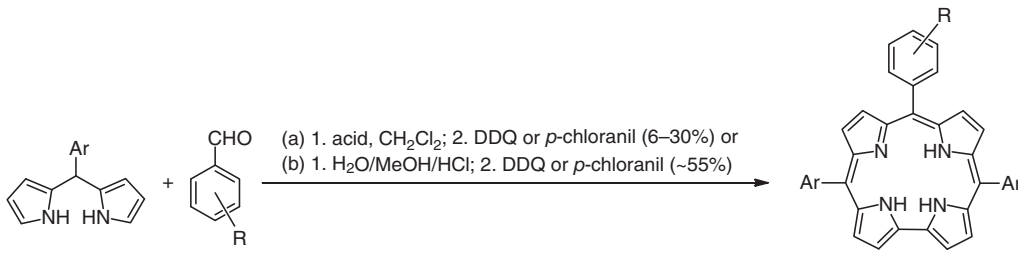

Scheme 7.3 Synthesis of *trans*-A_2B-corroles from aldehydes and dipyrranes.

Table 7.1 Guide to the synthesis of *trans*-A_2B-corroles from various types of aldehydes with dipyrranes.

Aldehyde type	Dipyrrane type	Ald./mM	Acid/mM	Yields (%)	References
Aromatic	Hindered	17	TFA/1.3	3–30	[24]
Aromatic	Unhindered	67	TFA/0.26	6–10	[24]
Aromatic	Electron-withdrawing	17	TFA/13	9–21	[25]
Bearing basic nitrogen atom	Hindered	17	TFA/50	3–28	[27]
Bearing basic nitrogen atom	Unhindered	17	TFA/17	4–9	[27]
Bearing basic nitrogen atom, hindered	Hindered	2.84	$BF_3{\cdot}Et_2O$/0.12	19	[28]
Aromatic	Hindered, bearing basic nitrogen atom, hindered	1.52	$BF_3{\cdot}Et_2O$/0.07	9–28	[29]
Electron-withdrawing	Hindered	4.3	$BF_3{\cdot}Et_2O$/1.6	22	[30]
		11.1	TCA/0.16	17	
Aromatic	Unhindered, bearing basic nitrogen atom	17	TFA/67	2–11	[27]
Dialdehydes	Hindered	4.4	TFA/6.3	12–19	[31]
Aromatic	Hindered	3.3	HCl/200	27–30	[19]
Aromatic	Unhindered	5	HCl/300	45–56	[19]

that corroles undergo multiple electrophilic aromatic substitution reactions, initially at positions 2 or 3 since they are the most electron-rich sites. Clearly, the most influential studies from the point of view of future medicine-related applications were Gross's papers showing that chlorosulfonation of **TPFC** occurs regioselectively in almost quantitative yield leading to **TPFC(SO$_2$Cl)$_2$** and, after hydrolysis, to **TPFC(SO$_3$H)$_2$** (Scheme 7.4) [32]. The importance of this reaction stems from a combination of three conditions: (i) adding additional electron-withdrawing substituents results in higher stability; (ii) SO_2Cl groups are very reactive and allow construction of various derivatives; and (iii) **TPFC(SO$_3$H)$_2$** is hydrophilic enough to be soluble in water and in DMSO. It is worth noting that the same reaction does not work with any other corroles, always leading to inseparable mixtures of regioisomers. The complexity of the corrole core such as reduced symmetry, differences in electron density at various positions, the influence of *meso*-substituents, and overall higher electron density versus porphyrins account for the differences in products from reaction to reaction. The comparison of nitration and formylation of **TPFC** are good examples of this trend (Scheme 7.4, only formylation is shown) [33]. Both reactions require inserting the gallium cation, and the products have different substitution patterns: 3 and 17 in the case of nitration, and 2 and 17 in the case of formylation. The relative ratio of the mono- and bis-substituted products can be controlled by varying the amount of $POCl_3$ or the oxidant.

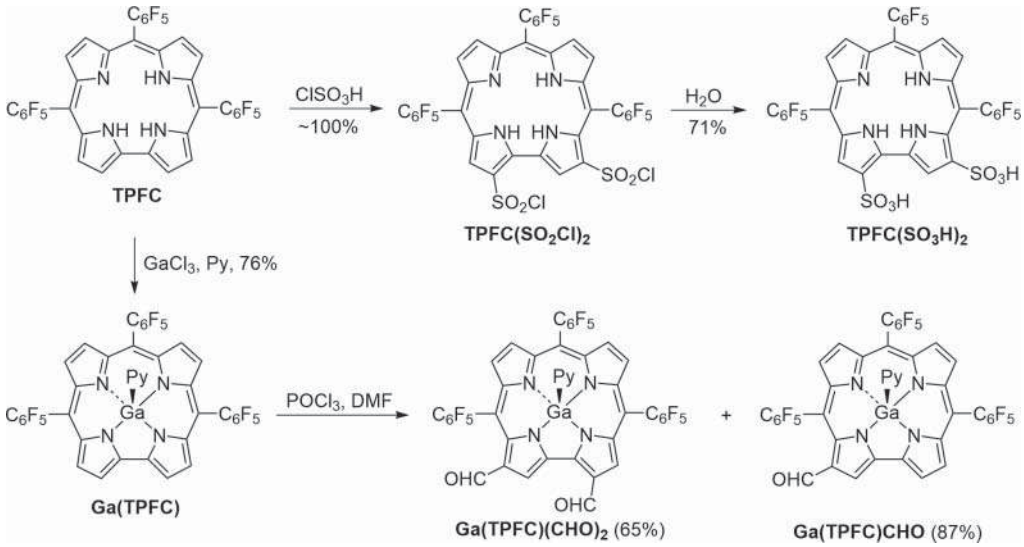

Scheme 7.4 Functionalization of **TPFC** and its gallium complex.

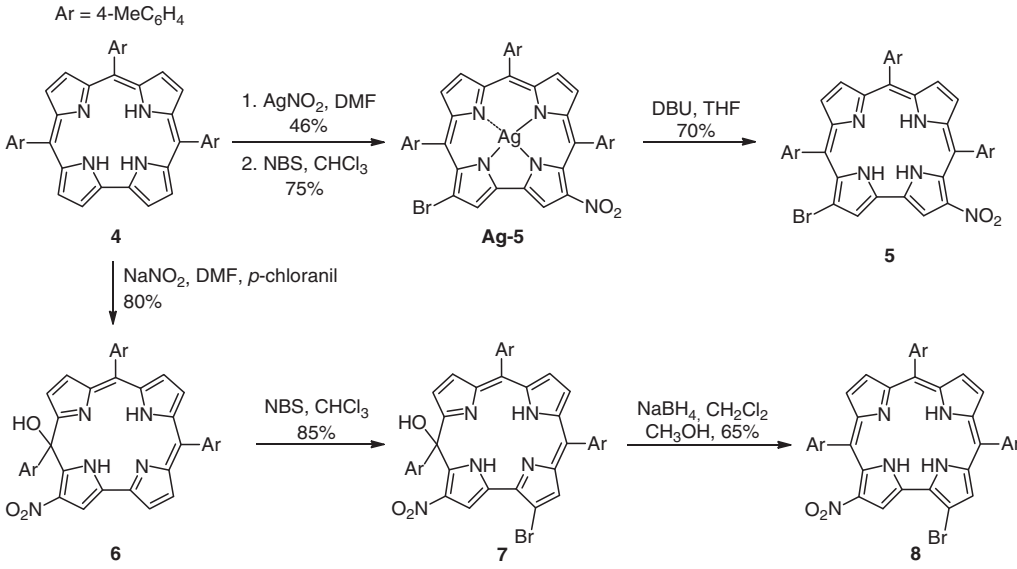

Scheme 7.5 Exemplary functionalization of *meso*-substituted corroles.

In parallel, Paolesse and co-workers and Ghosh's group investigated functionalization of other A_3-corroles (Scheme 7.5). The transformations of corrole **4** are perhaps the most representative to show both the possibilities and the challenges of this chemistry. The nitration of corrole **4** as a free base was achieved with a highly unusual nitrating reagent, $AgNO_2$, leading to a silver complex of 3-nitrocorrole [34]. This corrole can be further brominated to afford the silver complex of 3-bromo-17-nitrocorrole **Ag-5**. Final demetallation gives rise to free-base corrole **5** (Scheme 7.5). Different regioselectivity has been achieved starting with the same substrate and changing the nitration conditions. Because the whole

process proceeds through the isocorrole, the final product is 2-bromo-17-nitrocorrole **8**. Easy oxidation of corroles lacking electron-withdrawing substituents to isocorroles is often problematic, but as shown by Paolesse, this reaction can be beneficial.

One of the important aspects of corrole reactivity is bromination in all eight β-positions. This transformation could not be achieved with free-base corroles, but it has been in some of their metal complexes. Such octa-bromo A_3-corroles turned out to be more stable and are applicable in coordination chemistry and catalysis.

The corrole core can be extended via various strategies, the most important being oxidative aromatic coupling. One of the most interesting examples in this direction of research has been published by Osuka [35]. The regioselective borylation of **TPFC** followed by palladium-catalyzed oxidative coupling afforded the β,β'-linked dimer. Subsequent intramolecular oxidative aromatic coupling led to closure of the eight-membered ring and the formation of an oxidized corrole dimer that showed (as the Zn(II) complex) biradical character, but can be reduced to the corrole dimer **9** (Scheme 7.6).

Following the long-time trend observed for porphyrins, an expansion of the corrole macrocycle has become a challenging branch of research. The most important structures **10**–**12** have been presented in Figure 7.2 [36–38].

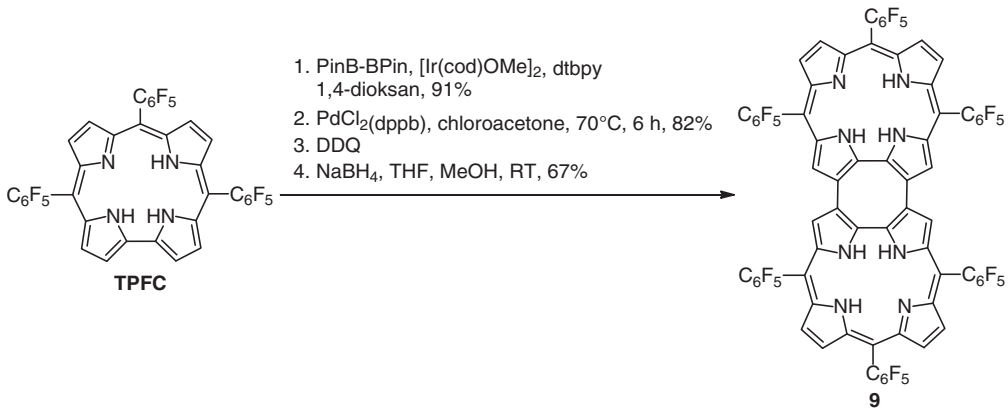

Scheme 7.6 The synthesis of doubly-linked corrole dimer.

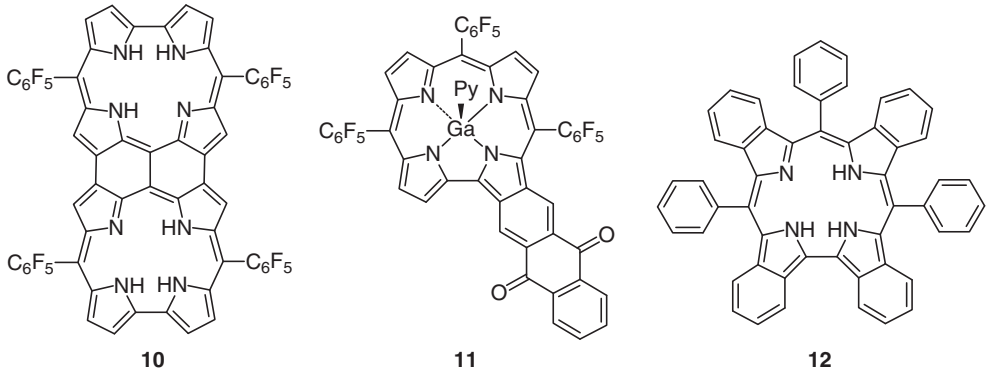

Figure 7.2 Exemplary π-extended corroles. Source: Adapted from Pomarico et al. [36]; Ooi et al. [37]; Vale et al. [38].

Among the many reactions that occur not on the core (β-positions) but on preexisting aryl substituents, the most important is nucleophilic aromatic substitution of the fluorine atoms located at position 4 of pentafluorophenyl substituents. At the free-base level, they react with primary and cyclic secondary amines [39], and also with some alcohols. After complexation with highly nucleophilic bismuth, fluorine can be replaced also by thiols, alcohols, and deactivated amines (NaH, DMSO) in high yields [40]. In both cases, substituents at positions 5 and 15 were found to be more reactive than the one located at position 10.

One of the critical issues that plays a formidable role in the chemistry of corroles is their stability. This is especially important for free-base corroles, but since corroles are almost always obtained originally in this form, it is worth mentioning this aspect. Given that the same number of π-electrons are delocalized over one less carbon atom, the first oxidation potential of corroles is lower than for porphyrins possessing identical substituents. As a result, in the presence of light and oxygen, corroles undergo quick decomposition, with ring opening leading to various conjugated linear dyes. The presence of electron-withdrawing groups is beneficial in this regard since they increase the first oxidation potential of corroles. Among many such groups, C_6F_5 plays the most important role, which stems from – in addition to its electron-withdrawing effect – the combination of its availability in the form of the aldehyde and the historical aspect. A_3-Corrole possessing three C_6F_5 substituents (i.e., **TPFC**) was one of the first free-base corroles prepared, and it is still the most frequently studied because of its excellent stability under ambient conditions. Very recently, the stabilizing effect of C_6F_5 has been surpassed by ester groups located directly at positions 5 and 15 (the first oxidation potential of 5,15-bis(CO_2Et)-10-(pentafluorophenyl)corrole is 0.14 V higher than that of **TPFC**) [41].

Corroles lacking electron-withdrawing groups undergo decomposition in the combined presence of oxygen and light. The detailed pathway of decomposition depends on the substituents (both steric and electronic effects). Typically, an isocorrole bearing the OH group (Figure 7.1) is one of the products, accompanied by various biliverdin-type dyes. Additionally, the in-depth study by Gryko, Danikiewicz, and co-workers has proved that (i) decomposition of corroles occurs the fastest in CH_3CN, and this solvent should be avoided; and (ii) among the many mass spectrometry ionization techniques, field-desorption (FD) is the best for evaluation of corrole purity. The use of electrospray induces the formation of the hydroxy-isocorrole and consequently is not reliable [42].

7.2.3 Electrochemistry

Electrochemical properties constitute one of the cornerstones critical in various more detailed studies. The most comprehensive study performed on free-base corroles revealed that, depending on the specific pattern of substituents, the first oxidation potential lies in the range 0.38–0.86 V (vs. SCE) [43]. The typical pathway is an irreversible one-electron oxidation $[(^{\bullet}Cor)H_3]^+$ followed by rapid loss of a proton to generate $(^{\bullet}Cor)H_2$. Irreversibility also characterizes the first reduction step (−1.02/−1.36) V vs. SCE, and it leads to $[(Cor)H_2]^-$. Obviously, the electrochemistry of metal complexes of corroles is more complex, and it has been described many times [44, 45].

7.2.4 Photophysical Properties

The general spectroscopic features of corroles resemble these of porphyrins; that is, the Soret-type band is located at 400–430 nm and Q bands around 500–680 nm (Figure 7.3)

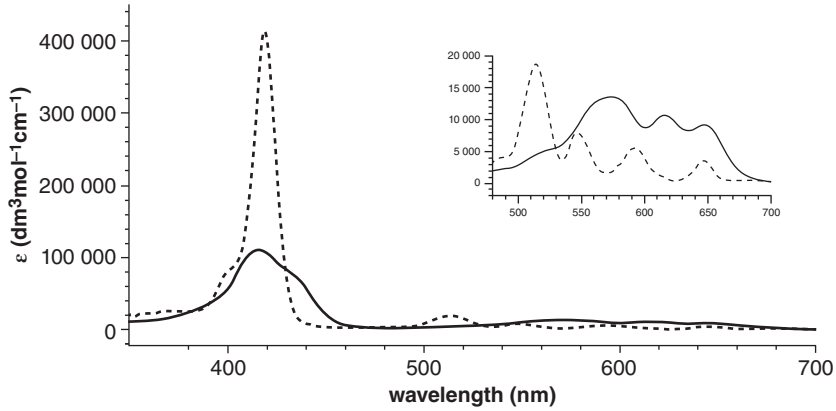

Figure 7.3 Optical spectra of triphenylcorrole (solid line) and tetraphenylporphyrin (dashed line) and the distribution of their Q bands (inset) in toluene. Source: Adapted from Ventura et al. [46]; Flamigni and Gryko [47].

[46, 47]. The Soret band is markedly broader than for porphyrins, which is reflected in lower molar absorption coefficient (120 000). At the same time, the lowest-energy Q-band (being less shaped and wider) has higher intensity than the lowest-energy Q-band for porphyrins. The notable feature is that corroles exhibit more intense fluorescence than porphyrins. The fluorescence quantum yield (Φ_{fl}) is around 0.2 for many studied free bases of A_3-corroles and *trans*-A_2B-corroles [46]. Indeed, this is the highest Φ_{fl} among major porphyrinoids. Interestingly, this value is even higher for gallium complexes (0.37–0.47, depending on the number of coordinated pyridines) and reaches 0.76 for the aluminum complex. The plausible reason for this enhancement of Φ_{fl} is planarization of the macrocycle. For **TPFC**, the mean plane deviation is 0.202 Å, whereas for **Ga(TPFC)(Py)**, it is 0.136 Å and for **Ga(TPFC)(Py)$_2$** only 0.063 Å. Although phosphorus corroles have been known since 1998, only very recently Ravikanth and co-workers have discovered that hexa-coordinated complexes of P(V) with *meso*-substituted corroles possess very high Φ_{fl} (0.33–0.67) with $\lambda_{em} \sim 610$ nm [48]. This feature has been already used for *in vivo* imaging of living cells [49]. Both singlet and triplet excited states of corroles react with oxygen, and sensitization of singlet oxygen has an efficiency comparable to that of porphyrins [46].

The rigid structure of the corrole core is responsible for the very small Stokes shift, so that the luminescence spectrum displays two vibronic bands. In-depth studies of the photophysical properties of corroles have been performed by Kruk, Dehaen, and Maes [50]. The most important finding is that the long-wavelength (typically ~650 nm) tautomer dominates the emission at RT, while at low temperature the majority of emission comes from the shorter-wavelength tautomer (typically ~600 nm).

Phosphorescence of free-base corroles has been quite elusive, and only recently Kruk and co-workers revealed that for halogenated corroles, λ_{ph} (at 77 K) is at 890–950 nm (with the second band located around 1050 nm) [51]. They also found that the S_1-T_1 energy gap is unusually large (5300–5000 cm^{-1}) and that Φ_{ISC} is close to unity when six chlorine atoms are present in the structure, and even for **TPFC** Φ_{ISC} is still 72%.

Two-photon absorption of mono-corroles was investigated by Rebane, Gryko, and co-workers [52]. It was found that the Soret band is allowed for two-photon transitions, which results from lowering of the symmetry, hence relaxing parity selection rules. The

distinct peaks are located ~850 nm, and the two-photon absorption cross-section values are 60–130 GM; that is, they are much higher than for tetra-aryl porphyrins. Surprisingly high values were obtained using the Z-scan technique for very similar *meso*-substituted corroles [53].

7.2.5 Coordination Chemistry

The coordination chemistry of corroles has developed in three phases and has been reviewed several times [45, 46, 54–56]. The small amount of material available between 1964 and 1998 resulted in preparation of corroles into which only transition metals of the first row were inserted, and their fundamental (structural, optical, electrochemical) properties were investigated. Between 1999 and 2007, attention was devoted to the study of more advanced properties of these complexes (mostly iron, copper, and manganese) and their use in materials and medicine-oriented research. Additionally, the first complexes with some other metals such as gallium [57] and aluminum [58] were prepared. Since 2008, the groups of Arnold, Ghosh, Gross/Gray, and Schoefberger vastly expanded the periodic table of corroles (Figure 7.4), with all of them having the same idea, namely, insertion of larger metal cations of transition and main group elements.

Despite the fact that the cavity of corroles is smaller than that of porphyrins, the apparently dubious idea of inserting large metal cations turned out to be very fruitful. Within just a few years, complexes of ~15 new metals have been synthesized and characterized for the first time. Needless to say, some of them were unstable and required great care in handling. Due to space limitations, the most essential and useful facts about these complexes will be presented in the form of a table, organized by increasing atomic number (Table 7.2). Special attention will be devoted to only the two most important topics: corrole innocence and demetallation.

There is a strong coupling of π and d electrons in many corrole complexes. Consequently, the innocence of the corrole core in various metal complexes and especially in iron complexes has been the subject of considerable debate [54]. Finally, based on much evidence deriving from various physicochemical techniques, it was established that corroles are often non-innocent ligands; that is, their complexes with many metals should be described as radical cations of the corrole and the metal at oxidation states higher than for the porphyrins,

H																	He
Li *2012*	Be											**B** *2008*	C	N	O	F	Ne
Na	Mg											**Al** *2002*	**Si** *2018*	**P** *1998*	S	Cl	Ar
K	Ca	Sc	**Ti** *1995 2012*	**V** *1995*	**Cr** *1980 2001*	**Mn** *1990*	**Fe** *1994 2002*	**Co** *1965*	**Ni** *1965 1997*	**Cu** *1965*	Zn	**Ga** *2000*	**Ge** *1990 2001*	**As** *2000*	Se	Br	Kr
Rb	Sr	Y	**Zr** *2012*	**Nb** *1979*	**Mo** *1977 2006*	**Tc** *2016*	**Ru** *2000*	**Rh** *1990*	Pd	**Ag** *2003*	Cd	**In** *1990*	**Sn** *1990 2001*	**Sb** *2000 2006*	Te	I	Xe
Cs	Ba	**La** *2013*	**Hf** *2014*	**Ta** *2017*	**W** *2012*	**Re** *1998, 2016*	**Os** *2014*	**Ir** *2008*	**Pt** *2014*	**Au** *2011*	Hg	Tl	**Pb** *2010*	**Bi** *2000 2011*	Po	At	Rn
Fr	Ra	Ac															
				Ce *2017*	Pr	Nd	Pm	Sm	**Eu** *2018*	**Gd** *2013*	**Tb** *2013*	Dy	Ho	Er	Tm	Yb	Lu
				Th *2013*	Pa	**U** *2013*	Np	Pu	Am	Cm	Bk	Cf	Es	Fm	Md	No	Lr

Figure 7.4 Periodic table of corroles (year of discovery is assigned, and in special cases the year when significant development has been made).

Table 7.2 Overview of coordination chemistry of corroles.

Metal	Axial ligand	Synthesis	Type	Formal oxidation state and innocence	Remarks	References
Li	2 THF	$Li[N(TMS)_2]_3$, −40 °C, THF, 74%	Sitting atop	Li^{I}, innocent	$[Li_2Cor(THF)_2]^-$ $[Li(THF_4)]^+$, useful synthetic precursors to many other complexes	[59]
B	F	$BF_3{\cdot}Et_2O$, $(i\text{-}Pr)_2NEt$, 40%	Sitting atop	B^{III}, innocent	Two boron atoms inside of cavity, $[(cor)FBOBF]^-$ $[NR_3H]^+$	[60]
Al	2 Py	$AlMe_3$, pyridine	Planar	Al^{III}, innocent	Diamagnetic, the record high fluorescence quantum yield (0.76), moderately stable	[58]
Si	OH, μ-oxo	Si_2Cl_6, pyridine, reflux or $SiCl_4$, DIPEA, DCE	Square-pyramidal	Si^{IV}, nd	Penta-coordinated square-pyramidal coordination, fluorescence quantum yield 0.13–0.50	[61, 62]
P	2 OH or 2 protic solvents	$POCl_3$, pyridine, reflux, ~80%	Planar	P^{III} and P^{V}, planar, innocent	Hexacoordinated P^{V} – high fluorescence quantum yield (0.33–0.62), inactivation of mold fungi spores	[44, 48]
Ti	Cp* or oxo	Li-corrole, Cp^*TiCl_3, THF, −40 °C, 78% or Li-corrole, $TiCl_4$, or $TiO(acac)_2$, phenol, 180 °C, 60–70%	Lopsided "sandwich" complex with the Cp* or TiO(Hcor)	Ti^{IV}, nd	In the case of TiO(Hcor), corrole macrocycle does not act as trianionic ligand. Only N21 and N24 nitrogen atoms are involved in metal complexing. In the presence of base, TiO(Hcor) exists in an anion $TiO(cor)^-$ form	[44, 63]

(*continued*)

Table 7.2 (Continued)

Metal	Axial ligand	Synthesis	Type	Formal oxidation state and innocence	Remarks	References
V	oxo	$VO(acac)_2$, phenol, 180 °C, 60–70%	VO(Hcor)	V^{IV}, nd	In the case of VO(Hcor), corrole macrocycle does not act as a trianionic ligand. Only N21 and N24 nitrogen atoms are involved in metal complexing. In the presence of base, VO(Hcor) exists in an anion $VO(Hcor)^-$ form	[44]
Cr	Oxo (Cr^V), 2 $OPPh_3$, 2 Py (Cr^{III})	$CrCl_2$, NaOAc, DMF, or $CrCl_2$, pyridine, 54–59%	Planar	Cr^V and Cr^{III}, nd	Hexacoordinated Cr^{III} can be obtained from Cr^V(oxo) complexes by reaction with PPh_3. Existence in four oxidation states (III-VI).	[64, 65]
Mn	1 solvent (Mn^{III}), halogen anion (Mn^{IV}), oxo, imido (Mn^V) or nitrido ($Mn^{V/VI}$)	$Mn(OAc)_2$, DMF, MeOH or $Mn_2(CO)_{10}$, toluene or Mn^{II} assisted cyclization of biladienes or bisdipyrrins	Planar	Mn^{III}, Mn^{IV}, Mn^V, Mn^{VI}, innocent or non-innocent	Imido manganese(V) complexes, catalysis, decomposition of reactive oxygen species, decomposition of reactive nitrogen species, electrocatalyst $OH^- \rightarrow O_2$	[44, 66]
Fe	μ-oxo, Cl, Ph, NO, 2 Py	$Fe_2(CO)_9$, toluene	Planar	Fe^{IV}, non-innocent	Discussions on the innocence of ligand in complexes, decomposition of reactive oxygen species, decomposition of reactive nitrogen species, catalysis	[67, 68]

Table 7.2 (Continued)

Metal	Axial ligand	Synthesis	Type	Formal oxidation state and innocence	Remarks	References
Co	None or PPh_3, 2 Py, CO, isonitrile (Co^{III}), or Ph (Co^{IV})	$Co(OAc)_2 \cdot 4H_2O$, $CHCl_3$/MeOH, 10–48% or Co^{II} assisted cyclization of biladienes or condensation of dipyrranes and aldehydes in presence of Co^{II} and PPh_3	Planar	Co^{III}, innocent or Co^{IV}, non-innocent	Carbon monoxide detection, electrocatalyst in oxygen reduction, electrocatalyst in H_2O oxidation to O_2	[9, 10, 44]
Ni	None	$Ni(OAc)_2$, DMF, air, 60 °C, 10 min	Planar	Ni^{II}, non-innocent	Paramagnetic, short Ni—N distances in the range of 1.829–1.859 Å *meso*-Aryl substituted corroles do not form stable Ni-complexes	[11]
Cu	None	$Cu(OAc)_2$, various solvents	Planar	Cu^{II}, non-innocent	The energy of π-cation radical of Cu^{II}corrole is only slightly higher than the energy of Cu^{III}corrole	[44, 69]
Ga	Py or 2 Py	$GaCl_3$, pyridine, reflux	Almost planar	Ga^{III}, innocent	Diamagnetic, highly fluorescent, studies on fluorescent imaging (including whole body imaging), tumor elimination, and photophysics	[3, 57]
Ge	OH, OMe, Cl, H, μ-oxo	$GeCl_4$, pyridine/DMF, or $GeCl_4$ assisted cyclization of biladienes	Domed	Ge^{IV}, nd	Labile chloro and hydroxo axial ligand, photochemical NH bond activation by radical pathway, hydride complex reacts with aldehydes, olefins and alkyl halides to form hydroxyalkyl and alkyl complexes	[44, 45]

(*continued*)

Table 7.2 (Continued)

Metal	Axial ligand	Synthesis	Type	Formal oxidation state and innocence	Remarks	References
As	None or Me	$AsCl_3$, pyridine, 94%	nd	As^{III}, nd	Unstable, slowly oxidized, especially when exposed to light	[44, 45]
Zr	Cp*	Li-corrole, Cp^*ZrCl_3, THF, −40 °C, 81%	Lopsided "sandwich" complex with the Cp*	Zr^{IV}, nd		[59, 63]
Nb	oxo/AcO^-	$NbCl_5$, NaOAc, decalin	nd	Nb^{V}, nd		[44]
Mo	oxo	$MoCl_5$ or $Mo(CO)_6$, decalin, 65–73%	Domed	Mo^{V}, nd	Very large out-of-plane metal displacement (0.73 Å)	[44, 70]
Tc	oxo	$[NEt_4]_2[^{99}TcCl_3(CO)_3]$, decalin, 170 °C, 8 h	Domed	Tc^{V}, innocent	Very large out-of-plane metal displacement (0.681 Å)	[71]
Ru	None	$[Ru(cod)Cl_2]_2$, 2-methoxy-ethanol, Et_3N, reflux, 72%	Sandwich dimer	Ru^{III}, nd	Diamagnetic, Ru—Ru bond	[72]
Rh	2 amine	$[Rh(cod)_2Cl]_2$, CH_2Cl_2, RT, Et_3N, 60–90%	Planar	Rh^{III},	Diamagnetic	[44]
Ag	None	AgOAc, Py, 80 °C, 70–80%	Saddled	Ag^{III}, innocent or non-innocent	Diamagnetic	[73, 74]
In	None	$InCl_3$ or In^{III} assisted cyclization of biladienes	nd	In^{III}, nd	Highly unstable	[75]
Sn	Cl, OH	$SnCl_4$, pyridine/DMF, or $SnCl_4$ assisted cyclization of biladienes	Domed	Sn^{IV}, nd	Labile chloro and hydroxo axial ligand	[44, 45]
Sb	oxo, F, Py	$SbCl_3$, pyridine, 95%	Planar	Sb^{V}, nd	Catalytic activity in photoinduced oxygenation of thioanisole by O_2, photo-catalyst in oxidation of hydrocarbons, inactivation of mold fungi spores	[44, 45]

Table 7.2 (Continued)

Metal	Axial ligand	Synthesis	Type	Formal oxidation state and innocence	Remarks	References
La	DME	Li-corrole, $La[N(TMS)_2]_3$, RT, 12 h, 58%	Domed	La^{III}, nd	Oxophilic, air-sensitive	[76]
Gd	$TACNMe_3$	Li-corrole, $GdCl_3$, THF, RT, 12 h, 72%	Domed	Gd^{III}, nd	Oxophilic, air-sensitive	[76]
Tb	DME	Li-corrole, $La[N(TMS)_2]_3$, RT, 12 h, 73%	Domed	Tb^{III}, nd	Oxophilic, air-sensitive	[76]
Hf	Cl	Li-corrole, $HfCl_4$, 25 °C, 12 h	Sandwich $Cor_2Hf_2Cl_2$	Hf^{IV}, nd	Oxophilic, air-sensitive	[63]
W	trioxo	WCl_6, decalin, 180 °C, 40 min, 35%	Sandwich, domed	W^{VI}, nd	Diamagnetic, $[W(tpfc)]_2O_3$	[77]
Re	oxo	$[Re_2(CO)_{10}]$, decalin, 190 °C, 60–85%	Slightly domed	Re^{V}, innocent	Diamagnetic	[78]
Os	nitrido	$[Os_3(CO)_{12}]$, NaN3, DEGME, reflux, 43–60%	Square-pyramidal	Os^{VI}, innocent	Diamagnetic	[79]
Ir	2 NH_3	(1)$Ir[(cod)Cl]_2$, K_2CO_3, THF, reflux; (2) NH_3, air, 27%	Almost planar	Ir^{III}, nd	Diamagnetic, phosphorescence in NIR ($\lambda_{ph} \sim 800$ nm, $\Phi_{ph} \sim 4.0 \times 10^{-3}$, at RT)	[80]
Pt	C_6H_5CN	$[Pt(OAc)_2]_4$ •2HOAc, C_6H_5CN, 150 °C, microwave, 6%	Square planar	Pt^{IV}, non-innocent	Formally $Pt^{IV}(corrole^{\bullet 2-})$, diamagnetic	[81]
Au	PPh_3 (Au^{I}), – (Au^{III})	Au(III): $HAuCl_4$, CH_2Cl_2, Et_3N, 54–65% or $Au(OAc)_3$, Py, ~30% or [ClAu(tht)], RT, 88%; Au(I): $[ClAu(PPh_3)]$, RT, toluene, 70%	Au^{I} – saddled; Au^{III} – planar	Au^{I} and Au^{III}, innocent	Au^{III} – diamagnetic, phosphorescence in NIR, cytotoxic and cytostatic; Au^{I} – octabromo-corrole only, diamagnetic	[82–84]
Pb	nd	$Pb(NO_3)_2$, Bu_4NBF_6, EtOH, 15 h, 45 °C	Domed	Pb^{II}, nd	Very unstable, photo-oxidation to Pb^{IV}	[85]

(*continued*)

Table 7.2 (Continued)

Metal	Axial ligand	Synthesis	Type	Formal oxidation state and innocence	Remarks	References
Bi	None	$Bi\{N(SiMe_3)_2\}_3$, THF, RT, 73%	Domed	Bi^{III}, nd	Out-of-plane displacement and significant doming, useful in synthesis	[86, 87]
Th	Cl, DME	Li-corrole, $ThCl_4(DME)_2$, RT, 93%	Domed, sandwich	Th^{IV}, nd	$(cor)_2Th_2Cl_2(DME)_2$, diamagnetic,	[88]
U	Cl, DME	Li-corrole, UCl_4, RT, 83%	Domed	U^{IV}, nd	$(cor)_2U_2Cl_2(DME)_2$, paramagnetic	[88]

DEGME, diethylene glycol monomethyl ether; DME, ethylene glycol dimethyl ether; $TACNMe_3$, 1,4,7-trimethyl-1,4,7-triazacyclononane; nd, not determined.

for example, the iron(III)/radical cation of corrole and not the iron(IV)/corrole^{3-}. Recently, Ghosh and co-workers ventured the hypothesis that corroles are innocent in their complexes if both of the following conditions are fulfilled: (i) the Soret maxima of the complexes are not sensitive to the *para* substituent located on *meso*-aryl substituents, and (ii) the electrochemical HOMO–LUMO gaps are large (approximately 2.24 ± 0.02 eV), which is essentially equal to the π–π^* gap of a typical porphyrin or corrole macrocycle. Studies on gold(III) (innocent), osmium (innocent), and copper (non-innocent) corroles support this hypothesis. Silver represents an interesting case, being essentially in the middle; that is, innocence of the corrole ligand in its complexes can be manipulated by bromination of the core [73].

Although the periodic table of corroles has expanded considerably in recent years, the complexes with the most classical metals are the most often studied. These include copper, cobalt, iron, and manganese. Copper corroles, synthesized for the first time in 1965, have never stopped attracting the attention of researchers, mostly because of their intriguing electronic structure. The question whether they are copper(II) or copper(III) puzzled a few groups that studied their structure via various physicochemical methods. It was Bröring who first suggested, based on a DFT/XRD study, that copper complexes in corroles should be described as Cu^{II} rather than as Cu^{III} [89]. This finding was corroborated by Ghosh's DFT calculations [73], and finally Nocera [90] and co-workers confirmed that these complexes should be described as antiferromagnetically coupled Cu^{II} corrole radical cation. Their research was based mainly on X-ray photoelectron spectroscopy, EPR, and magnetometry. The interesting aspect of copper corroles is their inherently (i.e., regardless of the steric hindrance) saddled conformation [91]. In complexes with all other metals, the corrole core is planar or almost planar.

It is interesting that all attempts to obtain stable nickel complexes of corroles have failed. After insertion of the nickel cation into the cavity, the transformation of the macrocyclic ring occurs, leading either to oxo-corroles [69] or to unidentified species. The same holds true for palladium. Very recently, Kadish and co-workers have proved that corroles

can also form triple-decker complexes with phthalocyanines (the corrole ring is in the middle) [92].

To summarize, corrole complexes can be divided in two groups: (i) synthesized once and characterized and (ii) corrole metal complexes that have become the object of intense studies. In this second group of complexes, special emphasis should be given to gallium(III), iron(III), and manganese(III) since each of them has been published in >20 papers and utilized in various research applications.

Finally, the problem of demetallation of corroles is worth mentioning. Unlike porphyrin chemistry, in the case of corroles, demetallation is a particularly difficult problem. The following treatments have been developed over the years to demetallate corrole complexes:

a) Copper – $H_2SO_4/CHCl_3$ [93]
b) Copper – (i) $SnCl_2$, CH_3CN, CH_2Cl_2; (ii) HCl, 20–96% [94]
c) Manganese – conc. H_2SO_4, $FeCl_2$, 40 °C ~80% [95]
d) Silver – $NaBH_4$ or DBU, 45–55% [96]
e) Bismuth – HCl (0.01 M), ~100% [40]

7.2.6 Applications in Research

As mentioned before, the key element of Paolesse's and especially Gross's influence on corrole chemistry was the realization (from the very beginning) of the potential of these macrocycles in modern science. This subject has been reviewed several times [3, 97], and only the most significant examples will be detailed here. Although initial studies were focused on catalysis with complexes of Mn, Fe, and Cr corroles, it was quickly realized that the stability of such macrocycles and their performance were similar or worse when compared to analogous complexes of porphyrins [97].

Guilard and co-workers have discovered that cobalt(III)corroles possess high affinity and infinite selectivity for CO over O_2 and N_2 [98], and these investigators subsequently were able to incorporate suitably functionalized complexes into silica matrices. Such hybrid composite material maintained its CO-recognizing property while possessing enhanced long-term stability [99].

The fact that corroles combine easy oxidation with relatively easy reduction inspired studies on photo-active molecular arrays containing corroles, performed mainly by Flamigni and Gryko [47]. Combining corroles with electron-deficient imides resulted in the formation of dyads and triads, with electron transfer from the corrole macrocycle to, for example, perylene bisimide [100]. Comprehensive studies embraced the combination of corroles with various counterparts such as naphthalene imides and coumarins. It has been proved that corroles act as electron donors and that the lifetime of charge-separated states can reach 24 ns for perylene-bisimide as an acceptor and 4.5 μs if fullerene is an acceptor [47].

Guilard and co-workers were the first to synthesize face-to-face bis-corroles and their complexes [101]. A subsequent comprehensive study compared the efficiency of cobalt complexes of (i) "monocorroles"; (ii) face-to-face bis-corroles (**13**, Figure 7.5); and (iii) face-to-face Co(II)porphyrin linked with cobalt(III)corrole to serve as electrocatalysts in reduction of O_2 [102]. All face-to-face complexes provided a direct four-electron pathway for the reduction of O_2 to H_2O in acidic pH, with H_2O being the predominant product. On the other hand, the same experiments performed with rotating ring-disk electrode voltammetry have shown that Co(III) complexes of monocorroles were electrocatalysts for the reduction of oxygen, but the

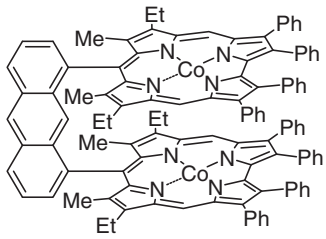

13

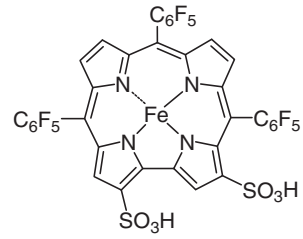

Fe(TPFC)(SO$_3$H)$_2$

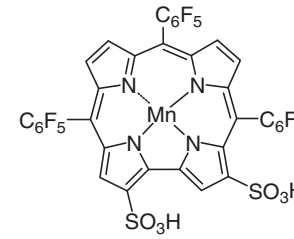

Mn(TPFC)(SO$_3$H)$_2$

Figure 7.5 Corrole complexes used as catalysts in electrochemical reduction of O_2 to H_2O (**13**) and for superoxide radical and peroxynitrite decomposition studies (**Fe(TPFC)(SO$_3$H)$_2$** and **Mn(TPFC)(SO$_3$H)$_2$**).

final products contained H_2O and H_2O_2 in a 1:1 ratio. The latter observation was later confirmed by Collman, who also found that iron corroles catalyzed O_2 reduction via parallel two- and four-electron pathways [103].

Interestingly, structurally related hangman Co(III)corroles possessing a xanthene unit (with the carboxylic group located directly above the corrole core) were found to be excellent electrocatalysts in the reverse process, that is, water oxidation to O_2 [104]. Nocera and co-workers revealed that increasing the oxidation potential by incorporation of eight fluorine atoms at all β-positions gave the best-performing catalyst, stable under operating conditions. The superior activity of this catalyst was attributed to the ability of the COOH group to preorganize H_2O within the hangman cleft.

Undoubtedly, one of the most important aspects of corrole chemistry in recent years has been related to cell biology and medicine. Two amphiphilic corrole complexes **Fe(TPFC)(SO$_3$H)$_2$** and **Mn(TPFC)(SO$_3$H)$_2$** were found to possess truly exceptional activity in decomposition of reactive oxygen species (ROS) and reactive nitrogen species (RNS) (Figure 7.5). This effect, initially discovered in 2006 [105], was the key subject of in-depth research performed by the Gross group. A 10-year study has led to remarkable results. Importantly, the role of the combination of water solubility and amphiphilic structure has been elucidated. The following advantages of these complexes have been discovered: (i) the stability of their oxo-metal complexes is surprisingly high; (ii) they are very strong reductants; (iii) demetallation under biologically relevant conditions is not observed; and (iv) weak pro-oxidant activity leads to less bleaching. Relevant experiments established the catalytic cycles for decomposition of both ROS and RNS. In the case of ROS, the rate limiting step is reduction of $O_2^{\bullet-}$, and the metallocorroles shuttle between +3 and +4 oxidation states (formally). Interestingly, **Mn(TPFC)(SO$_3$H)$_2$** and some other manganese corroles are able to decompose peroxynitrite without any reducing additive. The catalytic cycle for RNS depends on the particular metal. For example, the manganese complex starts from heterolytic cleavage of the peroxynitrite O—O bond, which leads to the formation of nitrite and the (O)Mn(V) intermediate. Many of these investigations were confirmed by *in vivo* studies with mice models. Overall, **Fe(TPFC)(SO$_3$H)$_2$** was found to be the most active in decomposition of ROS, and **Mn(TPFC)(SO$_3$H)$_2$** was the most active in decomposition of RNS. The reasons for the spectacular results of **Fe(TPFC)(SO$_3$H)$_2$** can be summarized as follows: (i) high bioavailability to organs; (ii) protection of biomolecules against oxidative stress; (iii) accumulation within cells to a significant amount; (iv) protection of cells against both direct and indirect oxidative stress; (v) a broad range of independent catalytic

antioxidants (ICA) for efficient decomposition of O_2, ONOOH, and H_2O_2; (vi) not cytotoxic, not mutagenic, not cardiotoxic, well tolerated by animals at and beyond therapeutic doses; and (vii) highly potent for attenuating the development of atherosclerosis and diabetic complications in animals.

The well-known photodynamic aspect of porphyrin chemistry was probably the motivation for studying corroles and their metal complexes in this regard. This line of research led to rather unexpected findings. Gallium corroles, particularly **Ga(TPFC)$(SO_3H)_2$**, were the favorite objects of study since their localization in the cell could be easily detected through their strong fluorescence. A ground-breaking study has shown that **Ga(TPFC)$(SO_3H)_2$** spontaneously forms conjugates with the breast-cancer-targeted cell penetrating protein (HerPBK10). In addition to fluorescence imaging through the excellent targeting properties to heregulin-positive cancer cells, it was also revealed that this conjugate displays strong dark phototoxicity, that is, not arising from the photodynamic effect. Later studies have shown that (i) the complex of **Ga(TPFC)$(SO_3H)_2$** alone is enough to display cytotoxicity [106] as well as to induce shrinkage of tumor [107] and (ii) the conjugate disrupts the mitochondrial potential, thus acting as a pro-oxidant [108]. The perplexing aspect of all above studies is that the negative charge of the complexes of **TPFC** should, in principle, disrupt cell membrane penetration. Other studies using **Ga(TPFC)$(SO_3H)_2$** as the exemplary fluorescent complex revealed that this compound is internalized in many eukaryotic cells (e.g., neuroblastoma cells) [109] and accumulates in the cytoplasm. The most probable hypothesis is that the ability of these complexes to penetrate cell membranes via an endocytosis pathway is related to the formation of non-covalent conjugates with various serum proteins [106].

Parallel studies have shown that **Fe(TPFC)$(SO_3H)_2$** and positively charged manganese complexes of corroles significantly increase cell nervous cell survival (neurorescue activity) with the parkinsonism-related neurotoxin, 6-hydroxydopamine, increasing cell survival [110]. Encouraged by these results, Gross and collaborators also investigated metallocorroles in models of diabetes [111] and in animal models of atherosclerosis [112]. Significant activity was found in each cases, although the performance of negatively charged and positively charge complexes varied from case to case.

In a recent study, Gray and co-workers presented a study showing that amphiphilic complexes of corroles with gallium possess high cytotoxicity against cell lines derived from nine tumor types. The values of IC_{50} ranged from 4.8 to >200 μM [113]. A strong correlation between ic50 values and (i) rates of uptake; (ii) the extent of intracellular accumulation; and (iii) lipophilicity has been found. The gallium(III) complex possessing the aminocaproate side chain was found to possess the highest cytotoxic effect.

Röder and Gross found that mold fungi spores can be inactivated by a complex of cationic or anionic corroles with P(V) and Sb(V). The critical factors for their efficiency are that they are water soluble, photostable, and they generate singlet oxygen with high quantum yield. This photodynamic effect is particularly strong for cationic complexes [114]. This observation is a very important discovery since the applications of photodynamic therapy (PDT) to the treatment of human cancer have thus far been limited, and this result opens new horizons for PDT.

Corroles have been shown to form strong hydrogen bonds both in solutions and in the solid state engaging cavity N—H [115]. This property has been very recently utilized to design bichromophoric molecule, in which the pyrrole NH groups of the corrole, the carbonyls of the perylenediimide, and four amino acids provide a hydrogen-bonding network that can mediate electron transfer with unusually high efficiencies [116]. Finally, corroles have been

incorporated into a two-dimensional corrole-based covalent organic framework (COF) by reacting the T-shaped 5,10,15-tris(4-aminophenyl)corrole with terephthalaldehyde. This COF exhibits high crystallinity and excellent chemical stability. It adopts desymmetrized ***hcb*** topology and consists of a staggered AB stacking structure with elliptical pores [117].

7.3 Isocorroles

Isocorroles (Figure 7.1) are non-aromatic corrole-type macrocycles in which one of the *meso* carbon atoms is sp^3 hybridized. Only a limited number of synthetic methods allows preparation of these rarely seen heterocycles, including a condensation of 5,5-dialkyldipyrranes with pyrrole-2-carboxyaldeyde and subsequent Ni(II)-assisted cyclization of the resulting linear *ac*-biladiene, affording the Ni(II) complex of the 10-isocorrole [118]. 5-Isocorrole **16** was obtained in 37% yield by $InCl_3$-catalyzed condensation of 5,5-dimethyldipyrrane-carbinol **15** with dipyrrane **14** followed by DDQ oxidation (Scheme 7.7). Alternatively, dipyrrane **18** and dipyrrane-carbinol **17** can be applied, although the yields do not exceed 8% [119]. The formation of isocorroles as unexpected products also occurred during peripheral functionalization of the corrole macrocycle, as, for example, in bromination of 3-nitro-tris-(tolyl)corrole (80% yield of 2-bromo-15-hydroxy-17-nitro-tris(tolyl)corrole, single isomer) [34]. Alkoxy- or alkyl-substituted triarylisocorroles can also be prepared directly from corroles by mixing them with DDQ in methanol [120], or by oxidation of corroles with DDQ in the absence of a nucleophilic solvent, followed by treatment with EtMgBr, respectively [121].

10-Alkylisocorroles form stable four-coordinate Ni(II) and Cu(II) complexes, five-coordinate (chloro)Fe(III) (chloro)Mn(III) complexes, and six-coordinate (chloro) (pyridinato)Rh(III) complexes. The dinuclear μ-oxo-diiron(III) complex was also synthesized and characterized [122]. However, interesting behavior of 5- and 10- alkoxyisocorroles was observed when they were treated with $Co(OAc)_2$ and $MnCl_2$. Unexpected corrole complexes were isolated in both cases as a result of the loss of the alkoxy group [123]. The Zn(II) complex was found to undergo demetallation. These complexes, in general, exhibit broad absorption bands in the NIR region and the presence of sp^3 hybridized *meso*-carbon introduces more conformational lability, so they can adapt more easily to changes in the metal coordination geometries.

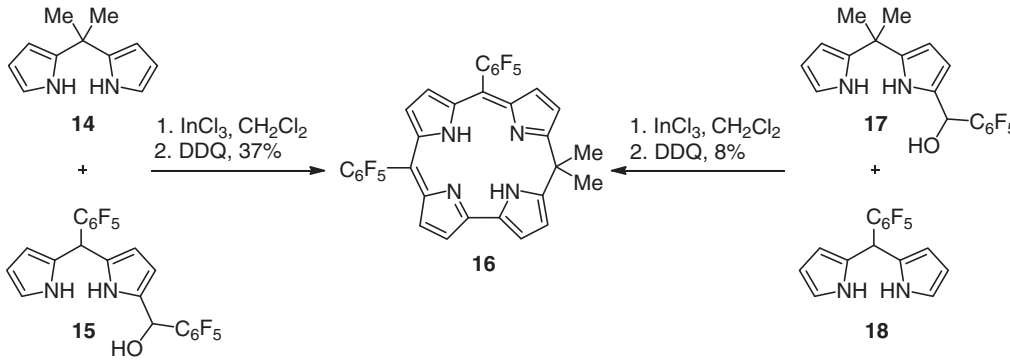

Scheme 7.7 The synthesis of 5-isocorroles.

7.4 *N*-Confused Corroles

In 2011, Furuta and co-workers developed the synthesis of unique *N*-confused corroles [124]. In perhaps the most original synthesis, the key starting material was the appropriate 2-aza-21-carbabilane **19**, which upon oxidation with DDQ in refluxing acetonitrile gave *N*-confused corroles **20** and **21** (Scheme 7.8). The NMR data suggest that all *N*-confused corroles are aromatic (albeit to various degrees) and adopt the inner-3H-form, which was further confirmed by X-ray analysis. The confused pyrrole rings are significantly tilted from the plane composed by the remaining tripyrrole moiety, which is an indication of lower aromaticity, when compared to regular corroles. Strong bathochromic shifts of both absorption and emission maxima were also observed for **20** and **21**, together with reduced fluorescence quantum yields (1.4% and 5.7%, respectively, measured in CH_2Cl_2), comparing to corroles. High flexibility of the new macrocycles was also reflected in the relatively high Stokes shifts of 800–1500 cm^{-1}.

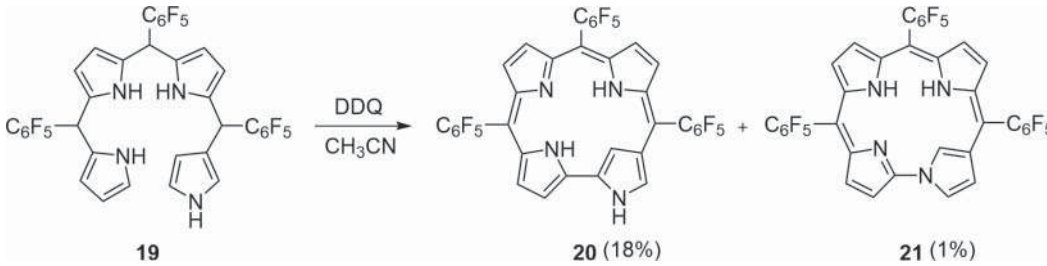

Scheme 7.8 The synthesis of *N*-confused corroles.

7.5 Heteroanalogues of Corroles

Incorporation of a heteroatom directly on the aromatic π-system of corroles results in significant changes of their spectroscopic properties, as well as in the modification of the coordination behavior of their macrocyclic cavity. Such transformations were realized by exchange of carbon atoms in either *meso*-positions or in pyrrole rings. Fine-tuning of photophysical properties of corroles might be crucial for their future applications; therefore, several heteroanalogues of corroles have been synthesized to date.

7.5.1 10-Heterocorroles

The simplest modification of the corrole core at the *meso*-position can be achieved by a replacement of one of the *meso*-carbons by a heteroatom such as nitrogen, sulfur, oxygen, and so on. With regard to corrole C_{2v} symmetry, the existence of at least two isomers of such corroles can be predicted; however, due to the synthetic difficulties, the family of contracted porphyrins embraces only 10-heterocorroles, while 5(15)-heterocorrole isomers are still undiscovered. 10-Heterocorroles have, in fact, been known since 1960 [125]; however, the procedure described in the literature to synthesize these macrocycles was long and tedious. As a result, 10-heterocorroles remained almost unexplored for over 40 years, despite the relatively simple structure. Recently, the research groups of Bröring and Shinokubo independently developed much more convenient routes toward these macrocycles and

their metal complexes. These new synthetic strategies rely mostly on the cyclization of α,α′-dihalogenodipyrrins or their complexes under appropriate conditions.

Shinokubo and co-workers found that treatment of α,α′-dichlorodipyrrin Ni(II) complex **22** with benzylamine under Buchwald–Hartwig amination conditions leads to nickel azacorrole **23** and *N*-benzylazacorrole **24** in 27% and 8% yield, respectively (Scheme 7.9) [126]. By modifying the catalytic system and changing the starting material to α,α′-dibromodipyrrin, the same authors were able to further improve the total yields of the desired azacorroles, however, the reaction sequence was one step longer and occurred via aminodipyrrins, which cyclize in the presence of nickel or aluminum salts [127]. The chosen metal ion seemed to be crucial, since it plays the role of template in the macrocyclization process. Interestingly, although two possible tautomers of 10-azacorrole can be drawn (Scheme 7.9, Structures I and II), the spectroscopic behavior of **23** clearly shows that the outer nitrogen is an amine type, with the lone electron pair participating in the aromatic 18 π-electron [17]triazaannulene system. The observed chemical shift of the outer proton of **23** was 11.39 ppm, and its UV/Vis spectra exhibited distinct Soret and Q-like bands, resembling those of typical corroles, which suggested that **23** has a strong aromatic character. Moreover, azacorrole **23** is highly planar and exhibits a surprisingly low oxidation potential when compared to that of diazaporphyrins.

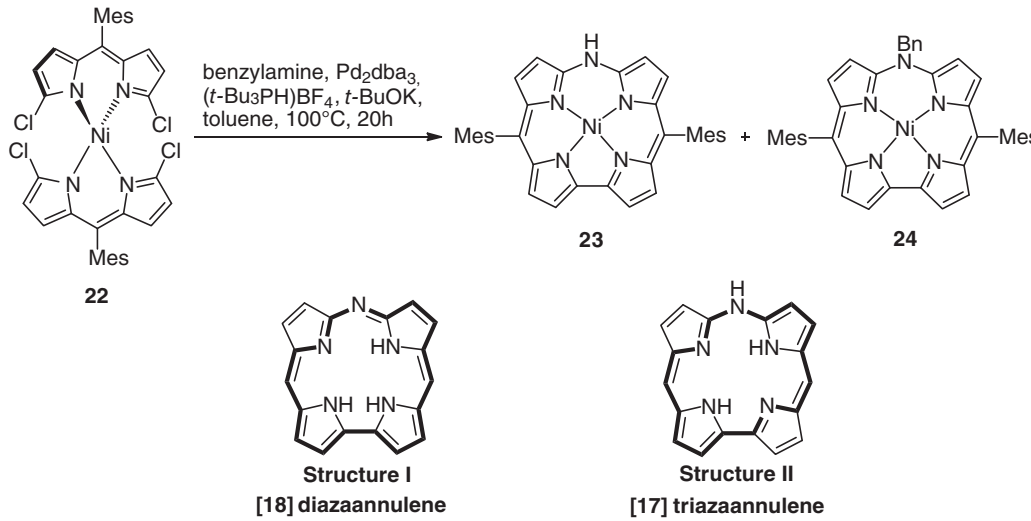

Scheme 7.9 The synthesis of nickel complex of 10-azacorrole by cyclization of α,α′-dichlorodipyrrin. Mes = mesityl. Source: Based on Horie et al. [126].

Closely related 10-heterocorroles with group 16 elements (O, S, Se) in the backbone were synthesized by Bröring and co-workers using the same strategy [128]. The cyclization of α,α′-dibromodipyrrin **25** in wet DMF in the presence of copper(II) acetate gave 10-oxacorrole **26** in the form of its copper complex, which was subsequently demetallated under reductive conditions (Scheme 7.10). Similarly, 10-thia- and 10-selenacorroles were synthesized by treatment of **25** with sodium sulfide or potassium selenocyanate, respectively, followed by demetallation. The mechanism of formation of the 10-thiacorrole is particularly intriguing and was an object of deeper studies. It is believed to proceed via 5,15-dithiaporphyrin, which undergoes thermal sulfur extrusion [129]. This reaction takes place only for Cu(II)

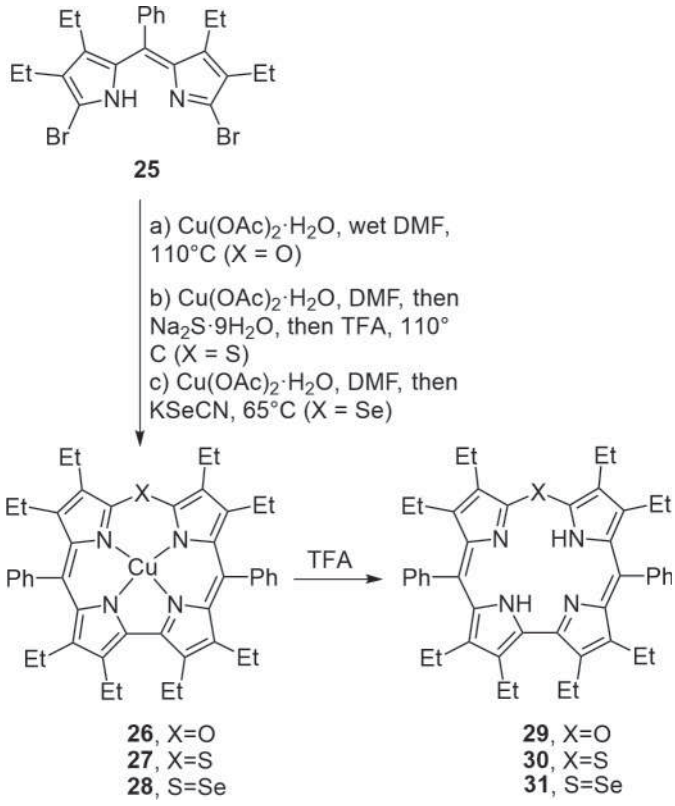

Scheme 7.10 The synthesis of 10-oxa- 10-thia- and 10-selenacorrole by cyclization of α,α′-dibromodipyrrin, followed by demetallation.

and Ni(II) complexes, whereas free-base, Zn(II), Pd(II), and Pt(II) dithiaporphyrins do not exhibit similar reactivity. All macrocycles **29**–**31** are almost perfectly planar, with only small saddle-shaped distortions and, as can be expected, the macrocyclic cavity size increases from **29** to **30** to **31**. Interestingly, **30** and **31** exhibit typical porphyrinoid UV–Vis spectra, whereas for **29**, unusual broadening of the Q bands, together with a blue-shift and an increase in relative intensity were observed, suggesting lower aromatic character of 10-oxacorroles. This assumption was further supported by NMR and NICS calculations, showing that the aromaticity increases in the order O ≪Se < S.

7.5.2 Corrolazines

A replacement of all three *meso*-carbons in corroles with nitrogen atoms gives birth to a very interesting class of macrocycles, namely, corrolazines (triazacorroles, Cz). These heterocycles can be obtained by a simple ring contraction of porphyrazines, which are very convenient starting materials available in multi-gram quantities (Scheme 7.11) [130]. The reaction takes place in the presence of a large excess of PBr_3 and leads to phosphorous corrolazines, which are converted into free bases by treatment with Na/NH_3, followed by protonation.

Corrolazine **34** exhibits photophysical properties characteristic of typical porphyrazines, with well-conserved aromaticity confirmed by the presence of the Soret and Q bands at 467 and 668 nm, respectively (measured in pyridine) [130]. Corrolazines form trianionic

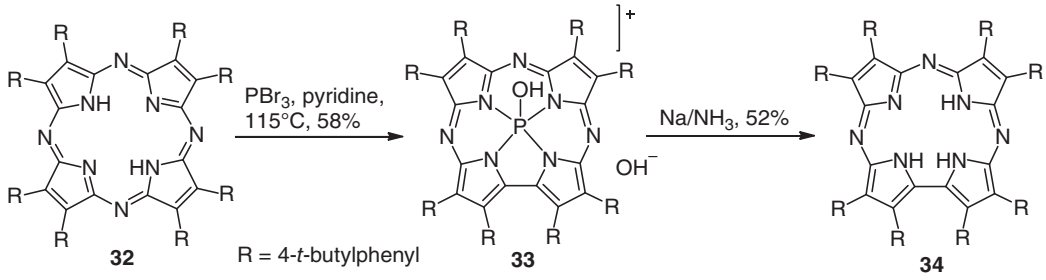

Scheme 7.11 The synthesis of corrolazines by PBr_3-induced ring contraction of porphyrazines or condensation of indolines. Source: Ramdhanie et al. [130].

ligands, and their core size is the smallest among 18-π electron aromatic porphyrinoids (3.54 Å). Despite the small cavity size, they are able to bind transition metal ions and form stable Mn(III), Fe(III), Co(III), and Cu(III) complexes, similarly to corroles. However, in spite of structural resemblance, striking differences in properties between complexes of both macrocycles are sometimes observed. For example, pyridine binding to CzCo(III) showed that the Co(III) center is significantly more Lewis acidic than analogous Co(III) corroles, which can be explained by the electron-withdrawing effect of the *meso*-nitrogen atoms in corrolazine. Moreover, $[CzCo(II)(py)]^-$ complexes exhibit reversible O_2 binding, which has not been observed for analogous complexes of corroles [131]. Interestingly, manganese (III) corrolazines have been reported as efficient photocatalysts used in the oxidation of hexamethylbenzene and thioanisole by O_2 to the corresponding alcohol and sulfoxide, respectively [132, 133]. The detailed analysis of the reaction mechanism revealed that it is very complex and involves photoinduced electron transfer from the catalyst to molecular oxygen, and the reactivity of the catalyst strongly depends on the binding of the external acid to the manganese metal center. Corrolazines are also known to stabilize metal cations in high oxidation states, such as high-valent metal-oxo and metal–imido complexes [134]. These complexes have likewise been shown to possess a broad range of catalytic activity. It should be pointed out that in many cases they are sufficiently stable, even at room temperature, to allow their isolation, characterization, and better analysis of the catalytic process. A high-valent iron-oxo corrolazine has been shown to activate the C—H bond and oxidize a range of C—H substrates, for example, 9,10-dihydroanthracene to anthracene, and xanthene to xanthydrol or 9,9′-bixanthene [135]. The proposed mechanism assumes a hydrogen atom transfer from the C—H substrate to the iron(IV)(O)corrolazine$^{\bullet+}$, which results in formation of a hydrocarbon radical and iron(IV)(OH)corrolazine. The subsequent rebound step yields an expected alcohol, although products of a radical dimerization have also been observed. Epoxidation reactions catalyzed by oxo- and imido- Mn(V) complexes have also been described [136]. These reactions use ArIO as an oxidant and proceed via an oxidant-metal-oxo/imido species. Analogous corrole complexes are also capable of aziridination, an activity that was not observed for iron corrolazines.

7.5.3 Heteroanalogues of Corroles Modified in Pyrrole Ring

Another way to modify the aromatic π-system of corroles is by replacing the pyrrole ring with other heterocycles. A few such oxa-analogues of corroles have been synthesized by coupling of 16-oxatripyrrane **35** with 5-phenyldipyrrane (apparently by acid-catalyzed

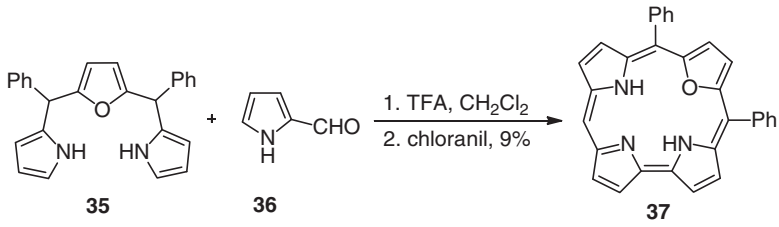

Scheme 7.12 The synthesis of 22-oxacorrole. Source: Based on Sankar et al. [138].

rearrangement/fragmentation of poly-pyrrole species) [137] or pyrrole-2-carboxaldehyde (**36**) (Scheme 7.12) [138], while dioxacorroles were obtained through condensation of hydroxymethylfurans with pyrrole [139].

22-Oxacorroles as well as dioxacorroles fully retain the aromatic character of typical corroles, which is expressed by the presence of characteristic Soret and Q bands in the UV–Vis spectra and the appearance of signals at −2.5 ppm in the ^{1}H NMR spectra, which originate from highly shielded inner protons. Oxacorroles easily form stable four-coordinate Ni(II), Cu(II), and Co(II) complexes, while in Rh(I) complexes, metal cation binds only to the N23 and N24 nitrogen atoms.

7.6 Norcorroles

Over the years of research, a question has been raised whether the second *meso*-carbon be removed from the core of porphyrin, leading to the macrocycle in which two pairs of directly linked pyrroles can occur? The existence of such a molecule was predicted theoretically in 2005, a few years before it was actually synthesized [140]. According to DFT calculations, the new macrocycle was expected to have polyenic rather than antiaromatic character. The first observation of norcorroles was made by Bröring and co-workers, who confirmed the formation of the new macrocycle by NMR and MALDI-TOF analysis of the crude reaction mixture from the oxidation of the iron complex of 2,2′-bidipyrrin **38** (Scheme 7.13). However, **39** could not be isolated due to its very high instability and rapid dimerization [141].

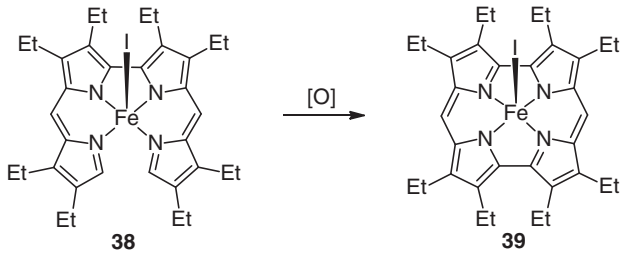

Scheme 7.13 The synthesis of norcorrole by oxidation of iron complex of 2,2′-bidipyrrin.

The gram-scale synthesis and unambiguous characterization of the Ni^{II}-norcorrole complex was finally achieved in 2012 by Kobayashi and Shinokubo [142]. The key step to the successful preparation of **41** was the Ni(II) templated reductive homocoupling of α,α′-dibromodipyrrin (Scheme 7.14). The expected product was isolated in remarkable 90%

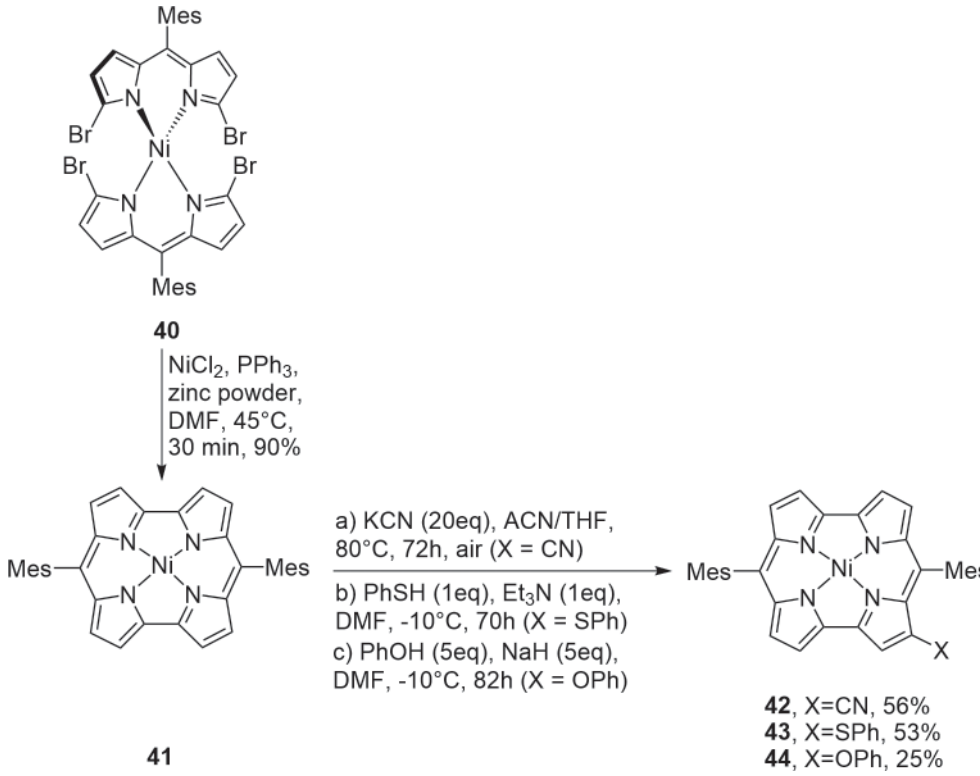

Scheme 7.14 The synthesis of norcorrole by reductive homocoupling of α,α′-dibromodipyrrin.

yield as a stable green solid. X-ray diffraction analysis showed that the skeleton of **41** is perfectly planar, while NMR and NICS studies confirmed that its 16 π-electron system is strongly antiaromatic. The UV–Vis spectrum of **41** exhibited a broad absorption band at 431 nm and weak absorption bands in the 600–1000 nm region, characteristic of antiaromatic porphyrinoids.

Norcorrole **41** can also be easily functionalized by highly regioselective nucleophilic substitution with cyanide, phenol, or thiophenol (Scheme 7.14) [143]. This reaction clearly proceeds through oxidative hydride substitution, and allows the synthesis of multisubstituted phenylthio-norcorroles. Interestingly, norcorrole **41** has been used as an electrode-active material in rechargeable batteries, showing high discharge capacity even after 100 cycles when examined with a Li metal anode. Moreover, the bipolar redox character of the Ni(II) norcorrole allowed the construction of a Li metal-free rechargeable battery. The reason for the high performance of **41** was its facile conversion involving four electrons per molecule, leading to an aromatic, stabilized species [144].

7.7 Outlook

In 1996, it would have been impossible to imagine that only 25 years later the chemistry of one of the contracted porphyrins – corrole – would expand to create an independent field of study. The synthetic revolution made it possible to try risky ideas in diverse areas of

materials chemistry and in various biology- and medicine-oriented applications. On a somewhat smaller scale, triazacorroles followed a similar history. One can venture to hypothesize that any of the other contracted porphyrins could witness such rapid development, if only preparative aspects could progress at an analogous rate. This indeed may happen in the future for norcorroles since the Shinokubo method gives access to gram quantities of these macrocycles. Although an inevitable consequence of contraction is a decrease in the size of the cavity of the rigid macrocyclic compounds, the periodic table of corroles has reached the third row of transition metals, lanthanides, and actinides. All these complexes display unique properties, which can, in turn, lead to unique applications. The analysis of research performed within the last 20 years suggests that the variety of future compounds will be limited only by our imagination.

Very recently complexes of corroles with novel metals were revealed: Ta [145], Ce [146] and Eu [147, 148]. Moreover long-sought after corrole lacking any substituents was finally synthesized [149].

References

1 Paolesse, R. (2000). *The Porphyrin Handbook*, vol. 2 (ed. K.M. Kadish, K.M. Smith and R. Guilard), 201–232. New-York: Academic Press.

2 Gryko, D.T. (2002). Recent advances in the synthesis of *meso*-substituted corroles and core-modified corroles. *European Journal of Organic Chemistry* 1735–1743.

3 Aviv-Harel, I. and Gross, Z. (2009). Aura of corroles. *Chemistry – A European Journal* 15: 8382–8394.

4 Johnson, A.W. and Kay, I.T. (1964). *The Pentadehydrocorrin (Corrole) Ring System*, 89–90. London: Proceedings of the Chemical Society.

5 Szymański, S., Paluch, P., Gryko, D.T. et al. (2014). Insights into the Tautomerism in meso-substituted corroles: a variable-temperature ^{1}H, ^{13}C, ^{15}N, and ^{19}F NMR Spectroscopy Study. *Chemistry - A European Journal* 20: 1720–1730.

6 Gryko, D.T., Fox, J.P., and Goldberg, D.P. (2004). The recent advances in the synthesis of corroles and core-modified corroles. *Journal of Porphyrins and Phthalocyanines* 8: 1091–1105.

7 Gryko, D.T. (2008). Adventures in the synthesis of *meso*-substituted corroles. *Journal of Porphyrins and Phthalocyanines* 12: 906–917.

8 Nardis, S., Monti, D., and Paolesse, R. (2005). Novel aspects of corrole chemistry. *Mini-Reviews in Organic Chemistry* 2: 355–372.

9 Guilard, R., Gros, C.P., Bolze, F. et al. (2001). Alkyl and aryl substituted corroles. 1. Synthesis and characterization of free base and cobalt containing derivatives. X-ray structure of $(Me_4Ph_5Cor)Co(py)_2$. *Inorganic Chemistry* 40: 4845–4855.

10 Paolesse, R., Licoccia, S., Bandoli, G. et al. (1994). First direct synthesis of a corrole ring from a monopyrrolic precursor. Crystal and molecular structure of (triphenylphosphine)(5,10,15-triphenyl-2,3,7,8,12,13,17,18-octamethylcorrolato)cobalt(III)-dichloromethane. *Inorganic Chemistry* 33: 1171–1176.

11 Will, S., Lex, J., Vogel, E. et al. (1997). Nickel and copper corroles: well-known complexes in a new light. *Angewandte Chemie International Edition* 36: 357–361.

12 Paolesse, R., Jaquinod, L., Nurco, D.J. et al. (1997). 5,10,15-Triphenylcorrole: a product from a modified Rothemund reaction. *Chemical Communications* 1307–1308.

13 Gross, Z., Galili, N., and Saltsman, I. (1999). The first direct synthesis of corroles from pyrrole. *Angewandte Chemie International Edition* 38: 1427–1429.

14 Rose, E., Kossanyi, A., Quelquejeu, M. et al. (1996). Synthesis of biomimetic heme precursors: the "double picket fence" 5,10,15,20-tetrakis(2′,6′-dinitro-4′-*tert*-butylphenyl)porphyrin. *Journal of American Chemical Society* 118: 1567–1568.

15 Loim, N.M., Grishko, E.V., Pyshnograeva, N.I. et al. (1994). 5,10,15,20-Tetracymantrenylporphyrin and 5,10,15-tricymantrenylcorrole. *Izvestiia Akademiia Nauk Seriia Khimicheskaia* 5: 925. *Chemical Abstracts* 1995, 122: 187733; *Izvestiia Akademiia Nauk Seriia Khimicheskaia*, 5: 925; *Chemical Abstracts* 1995, 122: 187733.

16 Paolesse, R., Nardis, S., Sagone, F., and Khoury, R.G. (2001). Synthesis and functionalization of *meso*-aryl-substituted corroles. *Journal of Organic Chemistry* 66: 550–556.

17 Gryko, D.T. and Koszarna, B. (2003). Refined methods for the synthesis of *meso*-substituted A_3- and *trans*-A_2B-corroles. *Organic and Biomolecular Chemistry* 1: 350–357.

18 Paolesse, R., Marini, A., Nardis, S. et al. (2003). Novel routes to substituted 5,10,15-triarylcorroles. *Journal of Porphyrins and Phthalocyanines* 7: 25–36.

19 Koszarna, B. and Gryko, D.T. (2006). Efficient synthesis of *meso*-substituted corroles in a H_2O-MeOH mixture. *Journal of Organic Chemistry* 71: 3707–3717.

20 Blumenfeld, C., Fisher, K.J., Henling, L.M. et al. (2015). Control of oligomerization and oxidation steps in the synthesis tris(pentafluorophenyl)corrole. *European Journal of Organic Chemistry* 3022–3025.

21 Liu, H.-Y., Lai, T.-S., Yeung, L.-L., and Chang, C.K. (2003). First synthesis of perfluorinated corrole and its Mn=O complex. *Organic Letters* 5: 617–620.

22 Gryko, D.T. (2000). A simple, rational synthesis of *meso*-substituted A_2B-corroles. *Chemical Communications* 2243–2244.

23 Briñas, R.P. and Brückner, C. (2001). Triarylcorroles by oxidative coupling of triaryltetrapyrranes. *Synlett* 442–444.

24 Gryko, D.T. and Jadach, K. (2001). A simple and versatile one-pot synthesis of *meso*-substituted *trans*-A_2B-corroles. *Journal of Organic Chemistry* 66: 4267–4275.

25 Gryko, D.T. and Koszarna, B. (2004). Refined synthesis of *meso*-substituted *trans*-A_2B-corroles bearing electron-withdrawing groups. *Synthesis* 13: 2205–2209.

26 Asokan, C.V., Smeets, S., and Dehaen, W. (2001). Sterically encumbered triarylcorroles from aryldipyrromethanes and aromatic aldehydes. *Tetrahedron Letters* 42: 4483–4485.

27 Gryko, D.T. and Piechota, K.E. (2002). Synthesis of *meso*-substituted *trans*-A_2B-corroles bearing basic nitrogen groups. *Journal of Porphyrins and Phthalocyanines* 6: 81–97.

28 Maes, W., Ngo, T.H., Vanderhaeghen, J., and Dehaen, W. (2007). meso-Pyrimidinyl-substituted A_2B-corroles. *Organic Letters* 9: 3165–3168.

29 Ngo, T.H., Nastasi, F., Puntoriero, F. et al. (2010). *meso*-Pyrimidinyl-substituted A_2B- and A_3-corroles. *Journal of Organic Chemistry* 75: 2127–2130.

30 Rohand, T., Dolusic, E., Ngo, T.H. et al. (2007). Efficient synthesis of aryldipyrromethanes in water and their application in the synthesis of corroles and dipyrromethenes. *Archivoc* 10: 307–324.

31 El Ojaimi, M., Gros, C.P., and Barbe, J.-M. (2008). Efficient two-step synthesis of face-to-face *meso*-substituted Bis(corrole) dyads. *European Journal of Organic Chemistry* 1181–1186.

32 Mahammed, A., Goldberg, I., and Gross, Z. (2001). Highly selective chlorosulfonation of tris(pentafluorophenyl)corrole as a synthetic tool for the preparation of amphiphilic corroles and metal complexes of planar chirality. *Organic Letters* 3: 3443–3446.

33 Saltsman, I., Mahammed, A., Goldberg, I. et al. (2002). Selective substitution of corroles: nitration, hydroformylation, and chlorosulfonation. *Journal of American Chemical Society* 124: 7411–7420.

34 Tortora, L., Nardis, S., Fronczek, F.R. et al. (2011). Functionalization of the corrole ring: the role of isocorrole intermediates. *Chemical Communications* 47: 4243–4245.

35 Hiroto, S., Furukawa, K., Shinokubo, H., and Osuka, A. (2006). Synthesis and biradicaloid character of doubly linked corrole dimers. *Journal of American Chemical Society* 128: 12380–12381.

36 Pomarico, G., Nardis, S., Stefanelli, M. et al. (2013). Synthesis and characterization of functionalized *meso*-triaryltetrabenzocorroles. *Inorganic Chemistry* 52: 8834–8844.

37 Ooi, S., Tanaka, T., Park, K.H. et al. (2016). Triply linked corrole dimers. *Angewandte Chemie International Edition* 55: 6535–6539.

38 Vale, L.S.H.P., Barata, J.F.B., Neves, M.G.P.M.S. et al. (2007). Novel quinone-fused corroles. *Tetrahedron Letters* 48: 8904–8908.

39 Hori, T. and Osuka, A. (2010). Nucleophilic substitution reactions of *meso*-5,10,15-tris(pentafluorophenyl)corrole; synthesis of ABC-type corroles and corrole-based organogels. *European Journal of Organic Chemistry* 2379–2386.

40 Faschinger, F., Aichhorn, S., Himmelsbach, M., and Schoefberger, W. (2014). Bismuth A_3-corroles: useful precursors for the development of *meso*-substituted free-base corroles. *Synthesis* 46: 3085–3096.

41 Canard, G., Gao, D., D'Aléo, A. et al. (2015). *meso*-Ester corroles. *Chemistry – A European Journal* 21: 7760–7771.

42 Świder, P., Nowak-Król, A., Voloshchuk, R. et al. (2010). Mass spectrometry studies on meso-substituted corroles and their decomposition products. *Journal of Mass Spectrometry* 45: 1443–1451.

43 Shen, J., Shao, J., Ou, Z.E.W. et al. (2006). Electrochemistry and spectroelectrochemistry of *meso*-substituted free base corroles in nonaqueous media. Reactions of $(Cor)H_3$, $[(Cor)H_4]^+$ and $[(Cor)H_2]^-$. *Inorganic Chemistry* 45: 2251–2265.

44 Erben, C., Will, S., and Kadish, K.M. (2000). *The Porphyrin Handbook*, vol. 2 (ed. K.M. Kadish, K.M. Smith and R. Guilard), 233–300. New York: Academic Press (Chapter 12).

45 Aviv-Harel, I. and Gross, Z. (2011). Coordination chemistry of corroles with focus on main group elements. *Coordination Chemistry Reviews* 255: 717–736.

46 Ventura, B., Esposti, A.D., Koszarna, B. et al. (2005). Photophysical characterization of free-base corroles, promising chromophores for light-energy conversion and singlet oxygen generation. *New Journal of Chemistry* 29: 1559–1566.

47 Flamigni, L. and Gryko, D.T. (2009). Photoactive corrole-based arrays. *Chemical Society Reviews* 38: 1635–1646.

48 Ghosh, A. and Ravikanth, M. (2012). Synthesis, structure, spectroscopic, and electrochemical properties of highly fluorescent phosphorus(V)–*meso*-triarylcorroles. *Chemistry – A European Journal* 18: 6386–6396.

49 Liang, X., Mack, J., Zheng, L.-M. et al. (2014). Phosphorus(V)-corrole: synthesis, spectroscopic properties, theoretical calculations, and potential utility for *in vivo* applications in living cells. *Inorganic Chemistry* 53: 2797–2802.

50 Kruk, M., Ngo, T.H., Verstappen, P. et al. (2012). Unraveling the fluorescence features of individual corrole NH tautomers. *Journal of Physical Chemistry A* 116: 10695–10703.

51 Knyukshto, V.N., Ngo, T.H., Dehaen, W. et al. (2016). Phosphorescence of free base corroles. *RSC Advances* 6: 43911–43915.

52 Rebane, A., Drobizhev, M., Makarov, N.S. et al. (2008). Two-photon absorption properties of *meso*-substituted A_3-corroles. *Chemical Physics Letters* 462: 246–250.

53 Anusha, P.T., Swain, D., Hamad, S. et al. (2012). Ultrafast excited-state dynamics and dispersion studies of third-order optical nonlinearities in novel corroles. *Journal of Physical Chemistry C* 116: 17828–17837.

54 Palmer, J.H. (2012). Transition Metal Corrole Coordination Chemistry. In: *Molecular Electronic Structures of Transition Metal Complexes I*, Structure and Bonding, vol. 142, 49–90. Berlin: Springer https://doi.org/10.1007/430_2011_52.

55 Buckley, H.L. and Arnold, J. (2015). Recent developments in out-of-plane metallocorrole chemistry across the periodic table. *Dalton Transactions* 44: 30–36.

56 Thomas, K.E., Alemayehu, A., Conradie, J. et al. (2012). The structural chemistry of metallocorroles: combined X-ray crystallography and quantum chemistry studies afford unique insights. *Accounts of Chemical Research* 45: 1203–1214.

57 Bendix, J., Dmochowski, I.J., Gray, H.B. et al. (2000). Structural, electrochemical, and photophysical properties of Gallium(III) 5,10,15-tris(pentafluorophenyl)corrole. *Angewandte Chemie International Edition* 39: 4048–4051.

58 Mahammed, A. and Gross, Z. (2002). Aluminum corrolin, a novel chlorophyll analogue. *Journal of Inorganic Biochemistry* 88: 305–309.

59 Buckley, H.L., Chomitz, W.A., Koszarna, B. et al. (2012). Synthesis of a lithium corrole and its use as a reagent for the preparation of cyclopentadienyl zirconium and titanium corrole complexes. *Chemical Communications* 48: 10766–10768.

60 Albrett, A.M., Conradie, J., Boyd, P.D.W. et al. (2008). Corrole as a binucleating ligand: preparation, molecular structure and density functional theory study of diboron corroles. *Journal of American Chemical Society* 130: 2888–2889.

61 Ueta, K., Fukuda, M., Kim, G. et al. (2018). The first silicon(IV) corrole complexes: synthesis, structures, properties, and formation of a μ-oxo dimer. *Chemistry – A European Journal* 24: 7637–7646.

62 Pomarico, G., Monti, D., Bischetti, M. et al. (2018). Silicon(IV) corroles. *Chemistry – A European Journal* 24: 8438–8446.

63 Padilla, R., Buckley, H.L., Ward, A.L., and Arnold, J. (2014). Synthesis, structure and reactivity of group 4 corrole complexes. *Chemical Communications* 50: 2922–2924.

64 Matsuda, Y., Yamada, S., and Murakami, Y. (1980). Preparation and characterization of an oxochromium (V) complex with a macrocyclic N_4-ligand: oxo(2,3,17,18-tetramethyl-7,8,12,13-tetraethylcorrolato)chromium(V). *Inorganica Chimica Acta* 44: L309–L311.

65 Meier-Callahan, A.E., Di Bilio, A.J., Simkhovich, L. et al. (2001). Chromium corroles in four oxidation states. *Inorganic Chemistry* 40: 6788–6793.

66 Boschi, T., Licoccia, S., Paolesse, R. et al. (1990). Synthesis and characterization of novel metal(III) complexes of corrole. Crystal and molecular structure of (2,3,7,8,12,13,17,18-octamethylcorrolato)(triphenylarsine)rhodium(III). *Journal of Chemical Society, Dalton Transactions* 463–468.

67 Vogel, E., Will, S., Tilling, A.S. et al. (1994). Metallocorroles with formally tetravalent iron. *Angewandte Chemie* 106: 771–775; *Angewandte Chemie International Edition*, 33: 731–735.

68 Simkhovich, L., Goldberg, I., and Gross, Z. (2002). Iron(III) and iron(IV) corroles: synthesis, spectroscopy, structures, and no indications for corrole radicals. *Inorganic Chemistry* 41: 5433–5439.

69 Jérôme, F., Barbe, J.-M., Gros, C.P. et al. (2001). Peculiar reactivity of face to face biscorrole and porphyrin-corrole with a nickel(II) salt. X-Ray structural characterization of a new nickel(II) bisoxocorrole. *New Journal of Chemistry* 25: 93–101.

70 Luobeznova, I., Raizman, M., Goldberg, I., and Gross, Z. (2006). Synthesis and full characterization of molybdenum and antimony corroles and utilization of the latter complexes as very efficient catalysts for highly selective aerobic oxygenation reactions. *Inorganic Chemistry* 45: 386–394.

71 Einrem, R.F., Braband, H., Fox, T. et al. (2016). Synthesis and molecular structure of ^{99}Tc corroles. *Chemistry – A European Journal* 22: 18747–18751.

72 Jérôme, F., Billier, B., Barbe, J.-M. et al. (2000). Evidence for the formation of a Ru^{III}–Ru^{III} bond in a ruthenium corrole homodimer. *Angewandte Chemie International Edition* 39: 4051–4053.

73 Thomas, K.E., Vazquez-Lima, H., Fang, Y. et al. (2015). Ligand noninnocence in coinage metal corroles: a silver knife-edge. *Chemistry – A European Journal* 21: 16839–16847.

74 Brückner, C., Barta, C.A., Briñas, R.P., and Bauer, J.A.K. (2003). Synthesis and structure of [*meso*-triarylcorrolato]silver(III). *Inorganic Chemistry* 42: 1673–1680.

75 Paolesse, R., Licoccia, S., and Boschi, T. (1990). Towards the periodic table of metallocorrolates: synthesis and characterization of main group metal complexes of octamethylcorrole. *Inorganica Chimica Acta* 178: 9–12.

76 Buckley, H.L., Anstey, M.R., Gryko, D.T., and Arnold, J. (2013). Lanthanide corroles: a new class of aromatic macrocyclic lanthanide complexes. *Chemical Communications* 49: 3104–3106.

77 Nigel-Etinger, I., Goldberg, I., and Gross, Z. (2012). 5d Early-transition-metal corroles: a trioxo-bridged binuclear tungsten(VI) derivative. *Inorganic Chemistry* 51: 1983–1985.

78 Einrem, R.F., Gagnon, K.J., Alemayehu, A.B., and Ghosh, A. (2016). Metal-ligand misfits: facile access to rhenium-oxo corroles by oxidative metalation. *Chemistry – A European Journal* 22: 517–520.

79 Alemayehu, A.B., Gagnon, K.J., Terner, J., and Ghosh, A. (2014). Oxidative metalation as a route to size-mismatched macrocyclic complexes: osmium corroles. *Angewandte Chemie International Edition* 53: 14411–14414.

80 Palmer, J.H., Durrell, A.C., Gross, Z. et al. (2010). Near-IR phosphorescence of iridium(III) corroles at ambient temperature. *Journal of American Chemical Society* 132: 9230–9231.

81 Alemayehu, A.B., Vazquez-Lima, H., Beavers, C.M. et al. (2014). Platinum corroles. *Chemical Communications* 50: 11093–11096.

82 Alemayehu, A.B. and Ghosh, A. (2011). Gold corroles. *Journal of Porphyrins and Phthalocyanines* 15: 106–110.

83 Rabinovich, E., Goldberg, I., and Gross, Z. (2011). Gold(I) and gold(III) corroles. *Chemistry – A European Journal* 17: 12294–12301.

84 Thomas, K.E., Alemayehu, A.B., Conradie, J. et al. (2011). Synthesis and molecular structure of gold triarylcorroles. *Inorganic Chemistry* 50: 12844–12851.

85 Schöfberger, W., Lengwin, F., Reith, L.M. et al. (2010). Lead corrole complexes in solution: powerful multielectron transfer reagents for redox catalysis. *Inorganic Chemistry Communications* 13: 1187–1190.

86 Reith, L.M., Himmelsbach, M., Schoefberger, W., and Knör, G. (2011). Electronic spectra and photochemical reactivity of bismuth corrole complexes. *Journal of Photochemistry and Photobiology A: Chemistry* 218: 247–253.

87 Reith, L.M., Stiftinger, M., Monkowius, U. et al. (2011). Synthesis and characterization of a stable bismuth(III) A3-corrole. *Inorganic Chemistry* 50: 6788–6797.

88 Ward, A.L., Buckley, H.L., Lukens, W.W., and Arnold, J. (2013). Synthesis and characterization of thorium(IV) and uranium(IV) corrole complexes. *Journal of American Chemical Society* 135: 13965–13971.

89 Bröring, M., Brégier, F., Tejero, E.C. et al. (2007). Revisiting the electronic ground state of copper corroles. *Angewandte Chemie International Edition* 46: 445–448.

90 Lemon, C.M., Huynh, M., Maher, A.G. et al. (2016). Electronic structure of copper corroles. *Angewandte Chemie International Edition* 55: 2176–2180.

91 Alemayehu, A.B., Gonzalez, E., Hansen, L.K., and Ghosh, A. (2009). Copper corroles are inherently saddled. *Inorganic Chemistry* 48: 7794–7799.

92 Lu, G., Yan, S., Shi, M. et al. (2015). A new class of rare earth tetrapyrrole sandwich complexes containing corrole and phthalocyanine macrocycles: synthesis, physicochemical characterization and X-ray analysis. *Chemical Communications* 51: 2411–2413.

93 Mandoj, F., Nardis, S., Pomarico, G., and Paolesse, R. (2008). Demetalation of corrole complexes: an old dream turning into reality. *Journal of Porphyrins and Phthalocyanines* 12: 19–26.

94 Ngo, T.H., Van Rossom, W., Dehaen, W., and Maes, W. (2009). Reductive demetallation of Cu-corroles – a new protective strategy towards functional free-base corroles. *Organic and Biomolecular Chemistry* 7: 439–443.

95 Capar, C., Hansen, L.-K., Conradie, J., and Ghosh, A. (2010). Reductive demetalation of copper corroles: first simple route to free-base β-octabromocorroles. *Journal of Porphyrins and Phthalocyanines* 14: 509–512.

96 Stefanelli, M., Shen, J., Zhu, W. et al. (2009). Demetalation of silver(III) corrolates. *Inorganic Chemistry* 48: 6879–6887.

97 Aviv, I. and Gross, Z. (2007). Corrole-based applications. *Chemical Communications* 48: 1987–1999.

98 Barbe, J.-M., Canard, G., Brandès, S. et al. (2004). Metallocorroles as sensing components for gas sensors: remarkable affinity and selectivity of cobalt(III) corroles for CO *vs.* O_2 and N_2. *Dalton Transactions* 1208–1214.

99 Barbe, J.-M., Canard, G., Brandès, S., and Guilard, R. (2005). Organic-inorganic hybrid sol-gel materials incorporating functionalized cobalt(III) corroles for the selective detection of CO. *Angewandte Chemie International Edition* 44: 3103–3106.

100 Flamigni, L., Ventura, B., Tasior, M. et al. (2008). New and efficient arrays for photoinduced charge separation based on perylene bisimide and corroles. *Chemistry – A European Journal* 14: 169–183.

101 Jérôme, F., Gross, C.P., Tardieux, C. et al. (1998). First synthesis of sterically hindered cofacial bis(corroles) and their bis(cobalt) complexes. *Chemical Communications* 2007–2008.

102 Kadish, K.M., Frémond, L., Ou, Z. et al. (2005). Cobalt(III) corroles as electrocatalysts for the reduction of dioxygen: reactivity of a monocorrole, biscorroles, and porphyrin-corrole dyads. *Journal of American Chemical Society* 127: 5625–5631.

103 Collman, J.P., Kaplun, M., and Decréau, R.A. (2006). Metal corroles as electrocatalysts for oxygen reduction. *Dalton Transactions* 554–559.

104 Dogutan, D.K., Stoian, S.A., McGuire, R. Jr., et al. (2011). Hangman corroles: efficient synthesis and oxygen reaction chemistry. *Journal of American Chemical Society* 133: 131–140.

105 Mahammed, A. and Gross, Z. (2006). Iron and manganese corroles are potent catalysts for the decomposition of peroxynitrite. *Angewandte Chemie International Edition* 45: 6544–6547.

106 Lim, P., Mahammed, A., Okun, Z. et al. (2011). Differential cytostatic and cytotoxic action of metallocorroles against human cancer cells: potential platforms for anticancer drug development. *Chemical Research in Toxicology* 25: 400–409.

107 Agadjanian, H., Ma, J., Rentsendorj, A. et al. (2009). Tumor detection and elimination by a targeted gallium corrole. *Proceedings of the National Academy of Sciences* 106: 6105–6110.

108 Hwang, J.Y., Lubow, J., Chu, D. et al. (2001). A mechanistic study of tumor-targeted corrole toxicity. *Molecular Pharmaceutics* 8: 2233–2243.

109 Okun, Z., Kupershmidt, L., Youdim, M.B.H., and Gross, Z. (2011). Cellular uptake and organ accumulation of amphipolar metallocorroles with cytoprotective and cytotoxic properties. *Anti-Cancer Agents in Medicinal Chemistry* 11: 380–384.

110 Kupershmidt, L., Okun, Z., Amit, T. et al. (2010). Metallocorroles as cytoprotective agents against oxidative and nitrative stress in cellular models of neurodegeneration. *Journal of Neurochemistry* 113: 363–373.

111 Okun, Z., Kupershmidt, L., Amit, T. et al. (2009). Manganese corroles prevent intracellular nitration and subsequent death of insulin-producing cells. *ACS Chemical Biology* 4: 910–914.

112 Haber, A., Mahammed, A., Fuhrman, B. et al. (2008). Amphiphilic/bipolar metallocorroles that catalyze the decomposition of reactive oxygen and nitrogen species, rescue lipoproteins from oxidative damage, and attenuate atherosclerosis in mice. *Angewandte Chemie International Edition* 47: 7896–7900.

113 Pribisko, M., Palmer, J., Grubbs, R.H. et al. (2016). Cellular uptake and anticancer activity of carboxylated gallium corroles. *Proceedings of the National Academy of Sciences* 113: 2258–2266.

114 Preuß, A., Saltsman, I., Mahammed, A. et al. (2014). Photodynamic inactivation of mold fungi spores by newly developed charged corroles. *Journal of Photochemistry and Photobiology B: Biology* 133: 39–46.

115 Orłowski, R., Vakuliuk, O., Gullo, M.P. et al. (2015). Self-assembling corroles. *Chemical Communications* 51: 8284–8287.

116 Orłowski, R., Clark, J.A., Derr, J.B. et al. (2021). Role of intramolecular hydrogen bonds in promoting electron flow through amino-acid and oligopeptide conjugates. *Proceedings of the National Academy of Sciences* 118: e2026462118.

117 Zhao, Y., Dai, W., Peng, Y. et al. (2020). A Corrole-Based Covalent Organic Framework Featuring Desymmetrized Topology. *Angewandte Chemie International Edition* 59: 4354–4359.

118 Hohlneicher, G., Bremm, D., Wytko, J. et al. (2003). Spiroconjugation in spirodicorrolato-dinickel(II). *Chemistry – A European Journal* 9: 5636–5642.

119 Flint, D.L., Fowler, R.L., LeSaulnier, T.D. et al. (2010). Investigation of complementary reactions of a dipyrromethane with a dipyrromethanemonocarbinol leading to a 5-isocorrole. *Journal of Organic Chemistry* 75: 553–563.

120 Nardis, S., Pomarico, G., Fronczek, F.R. et al. (2007). One-step synthesis of isocorroles. *Tetrahedron Letters* 48: 8643–8646.

121 Nardis, S., Pomarico, G., Mandoj, F. et al. (2010). One-pot synthesis of *meso*-alkyl substituted isocorroles: the reaction of a triarylcorrole with Grignard reagent. *Journal of Porphyrins and Phthalocyanines* 14: 752–757.

122 Setsune, J.-I., Tsukajima, A., and Okazaki, N. (2009). Synthesis and structure of isocorrole metal complexes. *Journal of Porphyrins and Phthalocyanines* 13: 256–265.

123 Pomarico, G., Xiao, X., Nardis, S. et al. (2010). Synthesis and characterization of free-base, copper, and nickel isocorroles. *Inorganic Chemistry* 49: 5766–5774.

124 Fujino, K., Hirata, Y., Kawabe, Y. et al. (2011). Confusion and neo-confusion: corrole isomers with an NNNC core. *Angewandte Chemie International Edition* 50: 6855–6859.

125 Johnson, A.W., Kay, I.T., and Rodrigo, R. (1963). 2,2′-Bipyrrolic macrocyclic ring systems. *Journal of Chemical Society* 2336–2342.

126 Horie, M., Hayashi, Y., Yamaguchi, S., and Shinokubo, H. (2012). Synthesis of nickel(II) azacorroles by Pd-catalyzed amination of α,α'-dichlorodipyrrin Ni^{II} complex and their properties. *Chemistry – A European Journal* 18: 5919–5923.

127 Omori, H., Hiroto, S., and Shinokubo, H. (2016). The synthesis of Ni^{II} and Al^{III} 10-azacorroles through coordination-induced cyclisation involving 1,2-migration. *Chemical Communications* 52: 3540–3543.

128 Sakow, D., Böker, B., Brandhorst, K. et al. (2013). 10-Heterocorroles: ring-contracted porphyrinoids with fine-tuned aromatic and metal-binding properties. *Angewandte Chemie International Edition* 52: 4912–4915.

129 Kamiya, H., Kondo, T., Sakida, T. et al. (2012). *meso*-Thiaporphyrinoids revisited: missing of sulfur by small metals. *Chemistry – A European Journal* 18: 16129–16135.

130 Ramdhanie, B., Stern, C.L., and Goldberg, D.P. (2001). Synthesis of the first corrolazine: a new member of the porphyrinoid family. *Journal of American Chemical Society* 123: 9447–9448.

131 Ramdhanie, B., Telser, J., Caneschi, A. et al. (2004). An example of O_2 binding in a cobalt(II) corrole system and high-valent cobalt-cyano and cobalt-alkynyl complexes. *Journal of American Chemical Society* 126: 2515–2525.

132 Jung, J., Neu, H.M., Leeladee, P. et al. (2016). Photocatalytic oxygenation of substrates by dioxygen with protonated manganese(III) corrolazine. *Inorganic Chemistry* 55: 3218–3228.

133 Neu, H.M., Baglia, R.A., and Goldberg, D.P. (2015). A balancing act: stability versus reactivity of Mn(O) complexes. *Accounts of Chemical Research* 48: 2754–2764.

134 Goldberg, D.P. (2007). Corrolazines: new frontiers in high-valent metalloporphyrinoid stability and reactivity. *Accounts of Chemical Research* 40: 626–634.

135 Cho, K., Leeladee, P., McGown, A.J. et al. (2012). A high-valent iron–oxo corrolazine activates C-H bonds via hydrogen-atom transfer. *Journal of American Chemical Society* 134: 7392–7399.

136 Leeladee, P. and Goldberg, D.P. (2010). Epoxidations catalyzed by manganese(V) oxo and imido complexes: role of the oxidant-Mn-oxo (imido) intermediate. *Inorganic Chemistry* 49: 3083–3085.

137 Sridevi, B., Narayanan, S.J., Chandrashekar, T.K. et al. (2000). Core modified *meso*-aryl corrole: first examples of Cu^{II}, Ni^{II}, Co^{II} and Rh^{I} complexes. *Chemistry – A European Journal* 6: 2554–2563.

138 Sankar, J., Anand, V.G., Venkatraman, S. et al. (2002). Modified corroles with one meso-free carbon: synthesis and characterization. *Organic Letters* 4: 4233–4235.

139 Pawlicki, M., Latos-Grażyński, L., and Szterenberg, L. (2002). 5,10,15-Triaryl-21,23-dioxacorrole and its isomer with a protruding furan ring. *Journal of Organic Chemistry* 67: 5644–5653.

140 Ghosh, A., Wasbotten, I.H., Davis, W., and Swarts, J.C. (2005). Norcorrole and dihydronorcorrole: a predictive quantum chemical study. *European Journal of Inorganic Chemistry* 22: 4479–4485.

141 Bröring, M., Köhler, S., and Kleeberg, C. (2008). Norcorrole: observation of the smallest porphyrin variant with a N_4 core. *Angewandte Chemie* 120: 5740–5743; *Angewandte Chemie International Edition* 47: 5658–5660.

142 Ito, T., Hayashi, Y., Shimizu, S. et al. (2012). Gram-scale synthesis of nickel(II) norcorrole: the smallest antiaromatic porphyrinoid. *Angewandte Chemie International Edition* 51: 8542–8545.

143 Nozawa, R., Yamamoto, K., Shin, J.-Y. et al. (2015). Regioselective nucleophilic functionalization of antiaromatic nickel(II) norcorroles. *Angewandte Chemie International Edition* 54: 8454–8457.

144 Shin, J.-Y., Yamada, T., Yoshikawa, H. et al. (2014). An antiaromatic electrode-active material enabling high capacity and stable performance of rechargeable batteries. *Angewandte Chemie International Edition* 53: 3096–3101.

145 Ziegler, J.A., Buckley, H.L., Arnold, J. (2017). Synthesis and reactivity of tantalum corrole complexes. *Dalton Transations* 46:780–785.

146 Armstrong, K.C., Hohloch, S., Lohrey, T.D. et al. (2016). Control of clustering behavior in anionic cerium(III) corrole complexes: from oligomers to monomers. *Dalton Transactions* 45: 18653–18660.

147 Lu, G., He, C., Fang, Y. et al. (2018). Construction of mixed corrole–phthalocyanine europium triple-decker complexes involving *meso*-substituted *trans*-A_2B-corrole. *New Journal of Chemistry* 42: 2498–2503.

148 Nardis, S., Mandoj, F., Stefanelli M. (2019). Metal complexes of corrole. *Coordination Chemistry Reviews* 388: 360–405.

149 Kumar, A., Yadav, P., Majdoub, M. (2021). Corroles: The Hitherto Elusive Parent Macrocycle and its Metal Complexes. *Angewandte Chemie International Edition* 60: 25097–25103.

8

Heteroporphyrins and Carbaporphyrins

Timothy D. Lash

Department of Chemistry, Illinois State University, Normal, IL, USA

8.1 Introduction

The widespread interest in porphyrins and related tetrapyrrolic systems led to investigations into further modified macrocyclic structures [1]. The porphyrin macrocycle can be altered by expanding or contracting the core, by introducing nitrogen bridges such as those found in the porphyrazines and phthalocyanines, or by exchanging the usual pyrrolic subunits with other heterocyclic or carbocyclic rings [2, 3]. Porphyrin analogues that have one or more of the nitrogen atoms replaced by heteroatoms such as oxygen or sulfur are known as heteroporphyrins (e.g., **1** and **2**), whereas the introduction of carbon atoms produces carbaporphyrins (e.g., **3**) (Chart 8.1).

Investigations into heteroporphyrins and carbaporphyrins have been carried out not only to find new applications of porphyrinoid systems, but also to probe the fundamental properties of these types of conjugated systems. Porphyrins are remarkably versatile ligands, but variations in the coordination core can lead to the formation of unusual metalated derivatives that differ considerably from metalloporphyrins [4]. The porphyrin nucleus is also strongly aromatic, and modifications to the macrocyclic scaffold can provide important insights into the origins of these properties [5]. It has long been recognized that porphyrins have a diaza[18]annulene substructure, which is commonly highlighted in bold (structure **4**, Chart 8.1), and it has been proposed that this feature is responsible for the observed aromatic characteristics. However, theoretical studies have questioned the validity of this model, and indeed a number of factors must be considered to explain the properties of porphyrinoid systems. Even so, the presence of aromatic conjugation pathways within a porphyrinoid system is often used to predict their properties. Furthermore, this model has been particularly valuable in helping to design synthetic routes to porphyrin analogues and was popularized in particular by Vogel for the synthesis of porphyrin isomers [6]. When additional factors are taken into account, such as accessible resonance contributors, the [18]annulene model remains a powerful tool [5]. Metalloporphyrins **5** can be considered to be derivatives of a bridged tetraaza[16]annulene dication **5**, while diprotonated porphyrins **4**H_2^{2+} are better viewed as [20]annulene dications **4′**H_2^{2+}, but in both cases these descriptions correspond to 18π electron delocalization pathways. Clearly, models of this type are oversimplifications, but they are self-consistent and can easily be applied to diverse porphyrinoid structures.

Fundamentals of Porphyrin Chemistry: A 21st Century Approach, Volume 1, First Edition.
Edited by Penelope J. Brothers and Mathias O. Senge.
© 2022 John Wiley & Sons Ltd. Published 2022 by John Wiley & Sons Ltd.

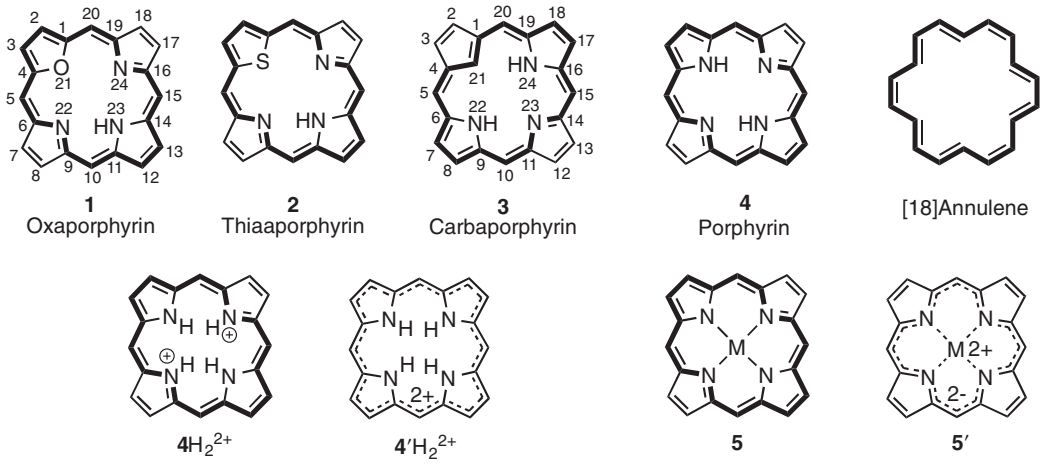

Chart 8.1 Porphyrins, heteroporphyrins, and carbaporphyrins.

The aromatic characteristics of porphyrinoids are commonly assessed using proton NMR spectroscopy and related computational methods such as nucleus-independent chemical shifts (NICS). The aromatic ring current associated with porphyrins leads to strong deshielding at the periphery of the macrocycle, and the *meso*-protons typically show up downfield near 10 ppm. The internal NH protons fall into the shielding zone and are shifted upfield to between −3 and −4 ppm. Although other factors may affect these shifts, the marked differences between the internal and external protons provide a reliable measure of diatropic character. Nonaromatic porphyrinoids do not show these effects, while antiaromatic systems display paratropic ring currents. Therefore, the NMR spectra of antiaromatic porphyrinoids show shielding to the external protons and deshielding to the internal protons [6]. The electronic spectra of porphyrin analogues can also be insightful. Porphyrins have a strong absorption band near 400 nm known as the Soret band and several small absorptions known as Q bands between 500 and 650 nm. Analogues that have similar UV–vis spectra are likely to be aromatic porphyrinoids, and nonaromatic systems generally have very different spectroscopic properties.

8.2 Mono- and Diheteroporphyrins (O, S, Se, Te)

Heteroporphyrins were first reported by Johnson and co-workers using a "3 + 1" variant on the MacDonald condensation [1, 7]. Tripyrrane **6a** was condensed with furan or thiophene dialdehydes **7** under acidic conditions (HBr in acetic acid) to give oxa- and thiaporphyrins **8a** and **8b** (Scheme 8.1). Similarly, tripyrrane analogues **6b** and **6c** reacted with **7a** and **7b** to give dioxaporphyrin **8c**, dithiaporphyrin **8d**, and oxathiaporphyrin **8e**. A synthesis of a 21,22-dioxaporphyrin **9** using the "2 + 2" MacDonald approach was also noted (Scheme 8.1). These analogues all gave proton NMR spectra that were consistent with strongly aromatic compounds. The UV–vis spectra were also very porphyrin-like, showing strong Soret bands between 369 and 412 nm and a series of Q bands at higher wavelengths. Porphyrins with *meso*-hydroxy substituents **10a** favor the keto form **10b** and are generally known as oxophlorins. Clezy synthesized analogous macrocycles **11** by reacting dipyrrylketone **12a** with furylmethylpyrrole **13a** or thienylmethylpyrrole **13b** in a "2 + 2" fashion

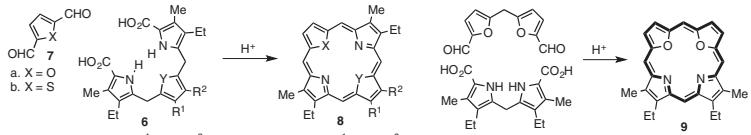

For **8**, a. X = O, Y = NH, R^1 = Me, R^2 = Et; b. X = S, Y = NH, R^1 = Me, R^2 = Et; c. X = Y = O, $R^1 = R^2$ = H; d. X = Y = S, $R^1 = R^2$ = H; e. X = O, Y = S, $R^1 = R^2$ = H

Scheme 8.1 MacDonald-type syntheses of heteroporphyrins.

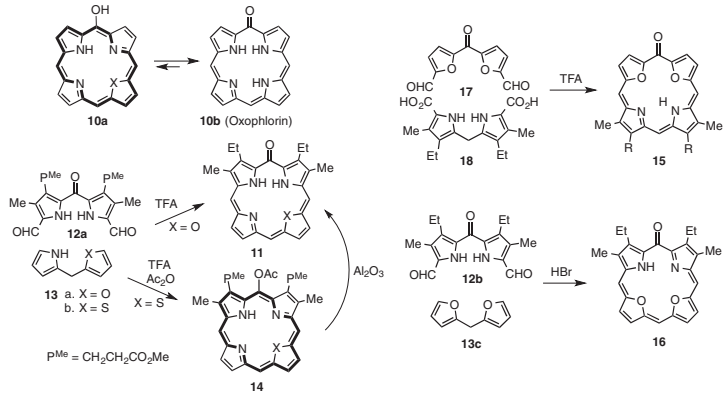

Scheme 8.2 Synthesis of oxophlorin analogues. Based on [2].

(Scheme 8.2) [2]. Dialdehyde **12a** reacted with **13a** in the presence of trifluoroacetic acid to give oxophlorin analogue **11a**. However, **12a** and **13b** were reacted with trifluoroacetic acid and acetic anhydride to afford the acetoxy-thiaporphyrin **14**. This hydrolyzed on alumina to give the related oxothiaphlorin **11b**. Later studies demonstrated that oxodioxaphlorins **15** and **16** could easily be prepared by reacting difurylketone dialdehyde **17** with dipyrrylmethanes **18** or by condensing difurylmethane **13c** with dipyrrylketone **12b**. These macrocycles all favor the keto forms **11**, **15**, and **16** over the corresponding hydroxyheteroporphyrin tautomers. Oxophlorin analogues of this type are quite stable even though they have greatly reduced aromatic character, although protonation leads to the formation of fully aromatic hydroxyporphyrinoid dications.

Syntheses of *meso*-tetrasubstituted heteroporphyrins were first reported by Ulman and Manassen (Scheme 8.3) [8]. Thiophene dicarbinol **19a** reacted with one equivalent of pyrrole in toluene containing 2% chloroacetic acid to give tetraphenyl-21,23-dithiaporphyrin **20a** in 10% yield. A stepwise route to less symmetrical derivatives was accomplished by reacting **19b** with two equivalents of pyrrole to form thiatripyrrins **21a**. These in turn reacted with a differently substituted dicarbinol **19c** to give the dithiaporphyrin **20b**. This approach was also used to prepare tetraphenyl 21,23-diselenaporphyrin **20c**, 21,23-thiaselenaporphyrin **20d**, and 21-tellura-23-thiaporphyrin **20e**. Although **20c** and **20d** were generated in 6% and 10% yields, respectively, **20e** was isolated in less than 0.1% yield.

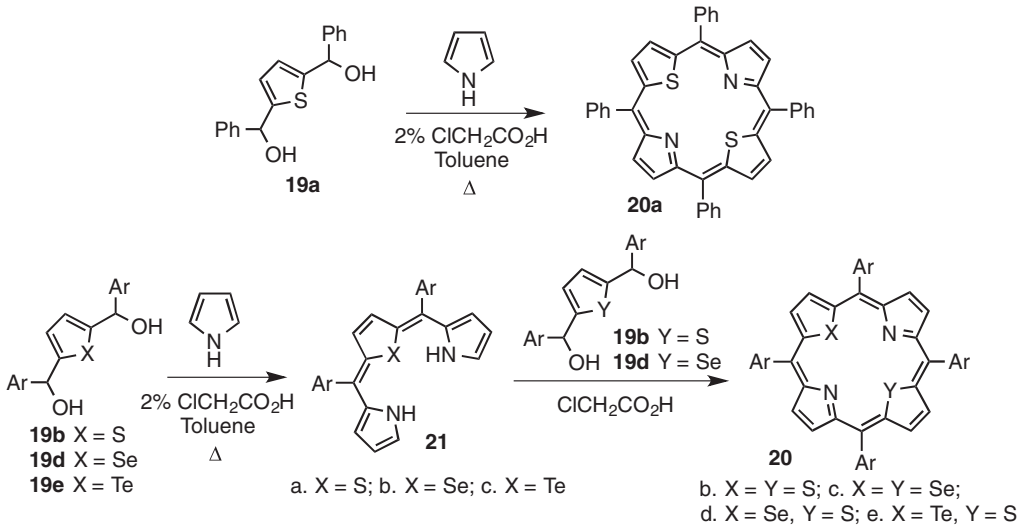

Scheme 8.3 Synthesis of tetraaryl thia-, selena-, and telluraporphyrins. Based on [8].

Subsequent studies have improved upon these syntheses [2, 9]. Furan dicarbinol **22** reacted with one equivalent of pyrrole in the presence of boron trifluoride etherate to give, following oxidation with chloranil, 21,23-dioxaporphyrin **23** in 10% yield (Scheme 8.4). However, when **22** was reacted with three equivalents of pyrrole and two equivalents of an aromatic aldehyde with catalytic boron trifluoride etherate, oxaporphyrins **24** were generated following an oxidation step. The latter approach has been successfully applied to the synthesis of thia-, selena-, and telluraporphyrins **25a–c**, while the former method allows the generation of dithia-, diselena-, and ditelluraporphyrins **20a**, **20c**, and **26**, respectively (Scheme 8.4). Ditelluraporphyrin **26**, which could be isolated in 11% yield, proved to be particularly interesting

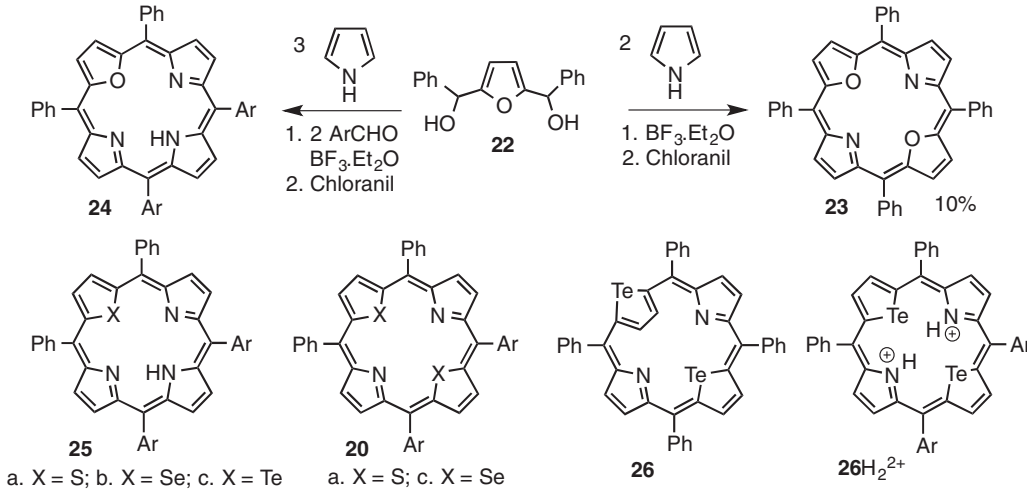

Scheme 8.4 Syntheses of heteroporphyrins from pyrrole and heterocyclic dicarbinols.

as the larger tellurium atoms could not be accommodated by the macrocyclic core, and for this reason one of the tellurophene rings is inverted. In fact, the macrocycle is severely distorted, and the dihedral angle for the inverted ring relative to the mean plane defined by the four *meso*-carbons is 123.0°. Unsurprisingly, the proton NMR spectrum for **26** shows a greatly reduced ring current, and the UV–vis spectrum gave broad relatively low-intensity absorptions at 348, 464, and 668 nm. Addition of trifluoroacetic acid gave a dicationic species **26**H_2^{2+} that had rotated the tellurophene ring back into a more conventional orientation, although the presence of two tellurium atoms caused substantial distortion. The dication also regained significant aromatic character, and the proton NMR spectrum showed the internal NH resonance at −0.7 ppm, while the external pyrrolic and tellurophene protons showed up at 8.03 and 8.71 ppm, respectively. Stepwise syntheses of heteroporphyrins include the "3 + 1" reaction of oxa- and thiatripyrranes **27** with dicarbinols **19a** or **22** in the presence of TFA, followed by oxidation with DDQ, to give dioxa-, dithia-, and oxathiaporphyrins **28** (Scheme 8.5). Similarly, difurylmethane and dithienylmethane dicarbinols **29** condensed with dipyrrylmethanes **30** to give, following an oxidation step, *adj*-dioxa-, and dithiaporphyrins **31**. Hence, a wide range of *meso*-tetrasubstituted porphyrin analogues are available.

Modified heteroporphyrins with carbazole subunits have been prepared. For instance, the butadiyne-linked dicarbazole **32** reacted with sodium sulfide to give the dithiaporphyrinoid **33** (Scheme 8.6). Although this system does not possess overall aromatic character, oxidation with manganese dioxide afforded the aromatic system **34**. The proton NMR spectrum for **34** showed the thiophene protons downfield at 9.90 ppm, while the benzene protons were observed at 8.87 and 9.44 ppm. The UV–vis spectrum also implied the presence of extensive conjugation as strong Q-like bands were observed at 845, 934, and 1049 nm. This fused ring dithiaporphyrin has 18π, 26π, and 34π electron delocalization pathways that are believed to be responsible for the aromatic characteristics of this system. Dioxa- and diselenaporphyrinoids of this type have also been described.

Porphyrins are excellent ligands for transition metal ions and commonly act as dianionic ligands due to the presence of two internal hydrogen atoms [10]. As monoheteroporphyrins only have one internal hydrogen, and diheteroporphyrins have none, the incorporation of

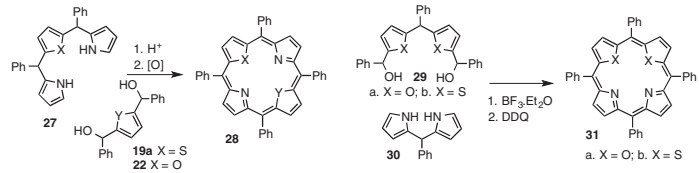

Scheme 8.5 Stepwise syntheses of heteroporphyrins.

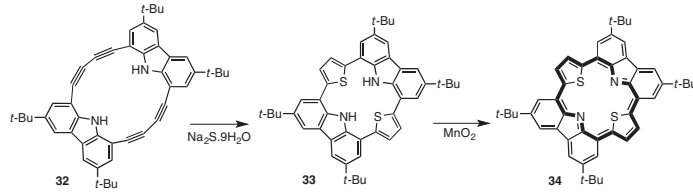

Scheme 8.6 Synthesis of a dithiaporphyrin with embedded carbazole subunits.

metal cations may lead to charged complexes. For instance, thiaporphyrin **25a** reacted with palladium(II) to give the corresponding metalloheteroporphyrin cation **35** (Scheme 8.7). This species readily undergoes a one-electron reduction of the corresponding neutral π-radical **36**. Similar complexes of thiaporphyrins with nickel, copper, and rhodium have been described. Complexes with rhenium(I) are neutral (e.g., **36a** and **36b**), but in these cases one of the heteroatoms or the pyrrolic nitrogens are not involved in coordination to the metal ion. The formation of nickel(II) complexes have proved to be particularly versatile. Not only have nickel(II) complexes of oxa-, thia-, and selenaporphyrins been prepared, but nickel(II) derivatives **37** of dioxaporphyrins are also known. Iron complexes of oxaporphyrins have also been well explored.

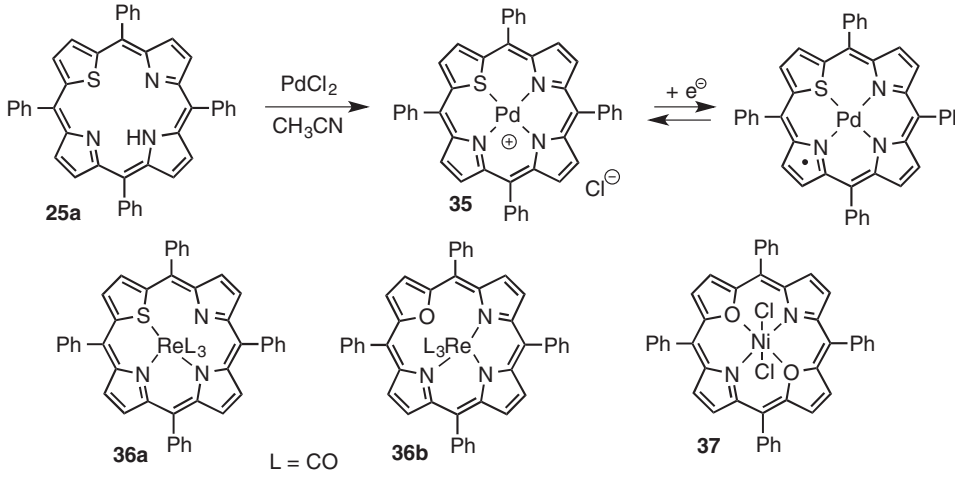

Scheme 8.7 Metalation of oxa-, thia-, and dioxaporphyrins.

Dithiaporphyrins **20** have been converted into the corresponding dithiachlorins **38** and dithiabacteriochlorins **39** (Scheme 8.8) [9]. Reaction of **19** with osmium tetroxide in pyridine furnished dihydroxychlorin analogue **38** and a diastereomeric mixture of bacteriodithiachlorins **39**. As is the case for true chlorins, the UV–vis spectrum for dithiachlorin **38** showed a relatively strong absorption at longer wavelengths. This band, which appears at 687 nm, is bathochromically shifted compared to tetrapyrrolic chlorins. Furthermore, dithiabacterochlorins **39** produced a long wavelength absorption at 734 nm, which is at a significantly higher wavelength than regular bacteriochlorins.

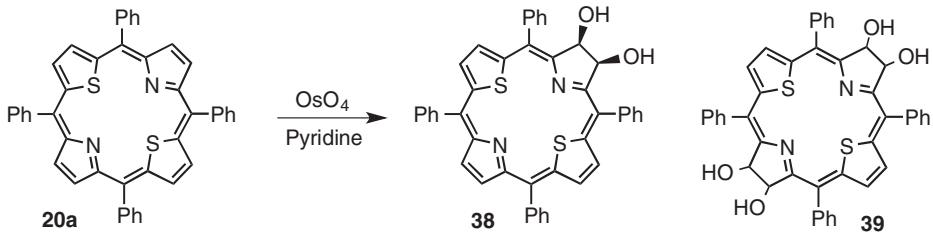

Scheme 8.8 Synthesis and dithiachlorins and dithiabacteriochlorins. Based on [9].

Telluraporphyrins proved to have particularly interesting reactivity. Monotelluraporphyrin **25c** is somewhat air sensitive and can be readily oxidized by molecular oxygen or *m*-chloroperbenzoic acid to give the corresponding 21-oxaporphyrin **24** (Scheme 8.9).

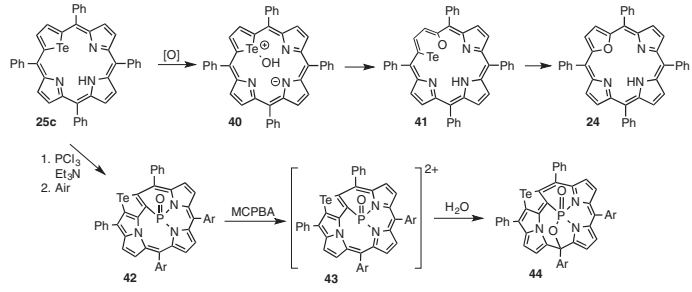

MCPBA = *m*-chloroperbenzoic acid

Scheme 8.9 Reactions of tetraphenyltelluraporphyrin.

Initially, a hydroxytellurium derivative **40** was formed, and this species was sufficiently stable to be isolated. The hydroxy compound could also be reduced with zinc amalgam to regenerate telluraporphyrin **25c**. It was proposed that the tellurophene ring in **40** rearranged to form a transient six-membered ring structure **41** before eliminating tellurium to form **24**. Telluraporphyrin **25c** also reacted with phosphorus trichloride and triethylamine to give, following air oxidation, the antiaromatic N-fused telluraporphyrin **42** (Scheme 8.9). Although compound **42** can be oxidized to an aromatic dication **43**, this species is prone to nucleophilic attack and reacts with water to give a nonaromatic derivative **44**. Treatment of **25c** with hydrochloric acid at 180 °C resulted in loss of tellurium to give a deazaporphyrin **45** called "vacataporphyrin" (Scheme 8.10). This structure can be considered to be a hybrid of [18]annulene and porphyrin. The system retains 18π electron delocalization pathways and is strongly aromatic. Vacataporphyrin has a porphyrin-like UV–vis spectrum with a strong Soret band at 433 nm and Q bands between 489 and 742 nm. The proton NMR spectrum showed the inner CH protons at −2.50 ppm and the NH as an upfield resonance at 0.01 ppm. Addition of TFA led to the formation of a related dication **45**H_2^{2+} that exhibited a substantially enhanced diamagnetic ring current.

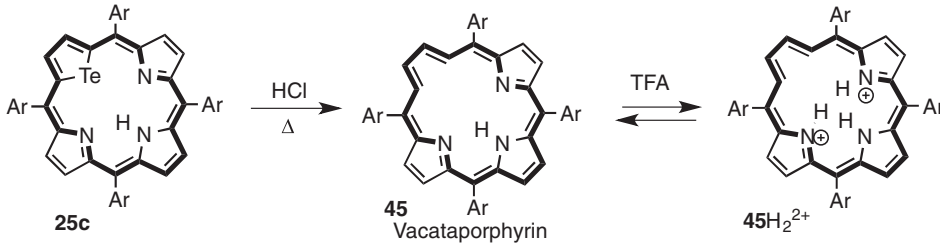

Scheme 8.10 Synthesis and protonation of vacataporphyrin.

In a theoretical study, the aromatic properties of porphyrins were attributed to the lone pair electrons on two of the pyrrole units in addition to 18π electrons from the remaining macrocycle. As one of these nitrogen atoms is missing in vacataporphyrin, but the structure still retains a porphyrin-like electronic spectrum and a substantial ring current effect as assessed by proton NMR spectroscopy, these results seem to contradict this model. In order to further assess this issue, the synthesis of a porphyrin analogue **46** that had lost both of these core nitrogens was targeted for study [5]. The synthesis was accomplished by carrying out a McMurry coupling of stretched pyrroledialdehyde **47** using titanium tetrachloride and a zinc-copper couple (Scheme 8.11). Initially, a reduced form of the structure would be expected, but this underwent a spontaneous oxidation to generate dideazaporphyrin **46**. The UV–vis spectrum for this compound was still somewhat porphyrin-like, showing a Soret band at 401 nm, and the proton NMR spectrum demonstrated that the macrocycle was strongly aromatic in nature. The internal CHs were shifted upfield to −2.52 ppm, while the external protons gave downfield resonances near 9.9 ppm. Addition of TFA produced the corresponding dication **46**H_2^{2+}, which gave an enhanced Soret band at 422 nm and a series of Q bands at 602, 669, and 747 nm. The ring current effect was also increased for the diprotonated species, showing the internal CH protons at −5.45 ppm and the external protons downfield at 11.07 and 11.11 ppm. The results demonstrate that the designated nitrogen atoms are not required to retain aromatic character or to produce porphyrin-like electronic spectra. Nevertheless,

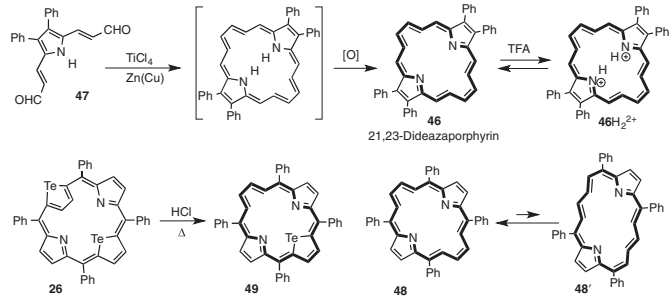

Scheme 8.11 Syntheses of dideazaporphyrins.

the [18]annulene model is too simplistic to explain all of the properties of porphyrins and is strongly disputed in a number of computational papers. Further studies are needed to fully reconcile the observed properties of porphyrin-like macrocycles with theoretical studies. Subsequent to this study, dideazaporphyrin **48**, called divacataporphyrin, was obtained in variable yields by heating ditelluraporphyrin **26** with hydrochloric acid (Scheme 8.11). The major product from these reactions was telluravacataporphyrin **49**. Interestingly, the proton NMR spectrum of divacataporphyrin showed that this structure was in equilibrium with an aromatic species **48′** possessing an alternative conformation (more properly, this is a stereoisomer that has undergone two *cis*/*trans* isomerizations).

8.3 Tetraoxa-, Tetrathia-, and Tetraselenaporphyrin Dications

In the 1980s, Emanuel Vogel initiated a program that was designed to probe porphyrin-like systems from an annulene chemist's perspective [6]. This groundbreaking work led to the synthesis of porphyrin isomers such as porphycene, but also probed new classes of heteroporphyrins. He speculated that all four of the nitrogen atoms in the porphyrin nucleus could be replaced with oxygen atoms to give dicationic species while retaining the aromatic properties of the macrocycle. In the first of these studies, difurylmethane **13c** was condensed with the related dialdehyde **50** in the presence of trifluoroacetic acid, and following oxidation with nitric acid the tetraoxaporphyrin dication **51a** was isolated as a perchlorate salt (Scheme 8.12) [11]. Alternatively, **13c** could be reacted with formaldehyde, or furfuryl alcohol could be self-condensed with zinc chloride and HCl, to produce tetraoxaporphyrinogen **52a**, and further oxidation gave **51a**. The dication is planar, and the proton NMR spectrum for this species demonstrates that it possesses a strong ring current that shifts the *meso*- and β-protons downfield to 12.13 and 11.17 ppm, respectively. The UV–vis spectrum of **51a** in 96% sulfuric acid gave a very strong Soret band at 370 nm ($\varepsilon > 10^6$), together with a series of Q bands between 370 and 569 nm. The more soluble octaethyltetraoxaporphyrin dication **51b** was prepared similarly via the tetraoxaporphyrinogen **52b**.

Treatment of tetrafuran **52a** with hydrogen sulfide gave the corresponding tetrathiaporphyrinogen **53a**, while reaction with acid and hydrogen selenide afforded the tetraselenophene structure **53b** (Scheme 8.12). Oxidation with DDQ then yielded the related tetrathia- and tetraselenaporphyrin dications **54a** and **54b**. Alternatively, diethyl hydroxymethylthiophene **55a** and the related selenophene **55b** underwent cyclotetramerization in the presence of *p*-toluenesulfonic acid to give the porphyrinogen analogues **56** (Scheme 8.12). Oxidation with DDQ yielded the corresponding tetrathia- or tetraselenaporphyrin dications **57**. The X-ray crystal structure for tetrathiaporphyrin dication **57a** showed that two of the thiophene subunits were twisted in opposite directions by 22.8° relative to the mean macrocyclic plane. The remaining thiophenes were only tilted by 3.7°. In the analogous tetraselena-dication **57b**, the structure is further distorted, and the selenophene rings exhibited twist angles of 24.3° and 30.5°. Nevertheless, the proton NMR spectra for these dications show that they retain virtually all of their diatropic characteristics.

Treatment of dication **51a** with potassium in THF led to a four-electron reduction to give dianion **58**, which could be air-oxidized at low temperatures to give the neutral tetraoxaisophlorin **59** (Scheme 8.13). This species proved to be air sensitive and had to be stored at low temperatures (−78 °C). The proton NMR spectrum for **59** in d_6-benzene demonstrated that this 20π electron system is antiaromatic as the *meso*- and β-protons

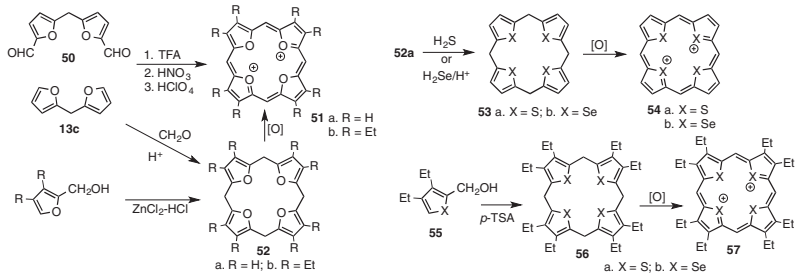

Scheme 8.12 Syntheses of tetraoxa-, tetrathia-, and tetraselenaporphyrin dications. Based on [11].

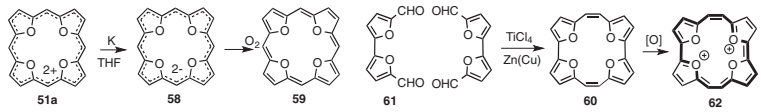

51a 58 59 61 60 62

Scheme 8.13 Reduction of the tetraoxaporphyrin dication and synthesis of a tetraoxaporphycene dication.

appear at −0.64 and 1.98 ppm due to shielding by the paratropic ring current. The isophlorin analogue can be oxidized back to the aromatic dication with silver(I) in perchloric acid. A related antiaromatic macrocycle **60** was prepared by McMurry coupling of bifuran dialdehyde **61** (Scheme 8.13), but this compound proved to be reasonably stable. In the proton NMR spectrum for **60**, the paratropic ring current shifted the furan protons upfield to give two doublets at 4.90 and 4.94 ppm, while the *meso*-protons appeared at 4.19 ppm. Clearly, these shifts are far smaller than the ones reported for **59**. Oxidation with bromine and treatment with perchloric acid gave the aromatic tetraoxaporphycene dication **62** [2, 6].

8.4 Phosphaporphyrins

Although the possibility of replacing a nitrogen with a phosphorus atom within the porphyrin framework is intriguing, it was not until relatively recently that porphyrin analogues of this type have been described [12]. One difficulty that is encountered is that simple phosphole intermediates are highly reactive and too unstable to be used as synthetic intermediates. This consideration led to the use of phosphole sulfides as reasonably robust intermediates. Phosphole diester **63** was reduced with diisobutylaluminum hydride and then reacted with elemental sulfur to give the phosphole dicarbinol **64** (Scheme 8.14). Condensation with excess pyrrole in the presence of boron trifluoride etherate then gave phosphatripyrrane **65** in 32% yield. Further reaction with pyrrole or thiophene dicarbinols **19 g** and **19a** in the presence of boron trifluoride etherate gave phosphaporphyrinogen **66a** and the corresponding thiaphosphaporphyrinogen **66b** in 43% and 36% yield, respectively. Desulfurization with $P(NMe_2)_3$ gave porphyrinogen analogues **67**, and subsequent treatment with DDQ afforded the phosphaporphyrin **68a** and thiaphosphaporphyrin **68b**. In the synthesis of **68a**, further oxidation took place to give **69** as a side product. Porphyrin analogues **68a** and **68b** were quite aromatic and gave porphyrin-like UV–vis spectra with Soret bands at 431 and 440 nm, respectively. The proton NMR spectrum for **68a** showed the external pyrrole protons between 8.35 and 8.67 ppm and the *meso*-protons at a doublet due to coupling with ^{31}P at 10.18 ppm. The NH signal was shifted upfield to −0.59 ppm, while the internal phenyl unit afforded resonances between 2.43 and 5.68 ppm. Treatment of **68a** with *m*-chloroperbenzoic acid, followed by oxidation with DDQ, gave the 22π electron delocalized phosphaporphyrin **69**. In this structure, the aromatic pathway has been relocated through the fused five-membered ring. The external *meso*- and pyrrolic protons appeared at 9.21 and 7.94–8.19 ppm, respectively, while the NH resonance appeared at 5.40 ppm and the internal phenyl unit gave multiplets between 5.60 and 6.92 ppm. These results indicate that **69** has reduced diatropicity compared to phosphaporphyrin **68a**. The X-ray crystal structure of **68a** showed that the structure was ruffled and the phosphole ring was tilted by 9.6° relative to the mean macrocyclic plane. However, **69** is highly distorted, which explains the reduced diatropic ring current associated with this species. Phosphaporphyrin **68a** could also be oxidized to **69** with hydrogen peroxide, although the thia-analogue reacted under these conditions to give the 20π electron porphyrinoid **70**. The proton NMR spectrum for the latter species indicates that this has a weak paratropic ring current. Nevertheless, this antiaromatic derivative proved to be quite stable. Attempts to prepare fully conjugated oxaphosphaporphyrins were unsuccessful, but a phosphaporphyrin with a fused six-membered ring has been prepared. Partially oxidized phosphacalixphyrins have also been described [9, 12].

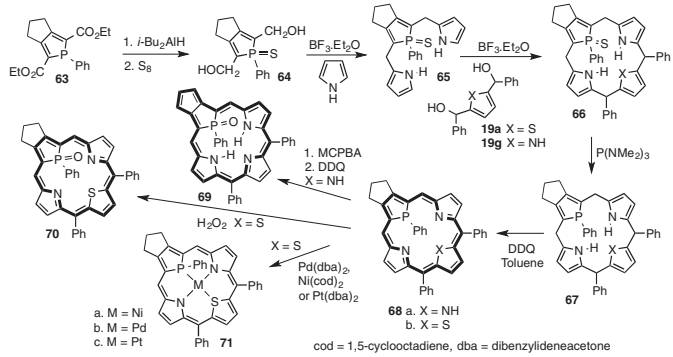

Scheme 8.14 Synthesis and reactions of phosphaporphyrins.

Thiaphosphaporphyrin **68b** readily reacted with zero valent group 10 reactants to give metalated derivatives **71** (Scheme 8.14). For instance, treatment of **68b** with $Pd(dba)_2$ in dichloromethane gave palladium(II) complex **71b** within 1 min at room temperature. Similarly, **68b** reacted with $Ni(cod)_2$ or $Pt(dba)_2$ to afford **71a** and **71c**, respectively. These metalation reactions occur with reduction of the porphyrinoid macrocycle to form isophlorin derivatives. Hence, the aromatic π-system of **68b** is lost to produce a 20π electron delocalization pathway. The proton NMR spectrum for the palladium complex **71b** showed the *meso*-protons as a doublet at 6.01 ppm, and the pyrrolic protons appeared between 5.58 and 6.13 ppm. In addition, the inner phenyl group gave rise to multiplets between 7.65 and 8.37 ppm. These results indicate that the macrocycle is essentially nonaromatic as there is no apparent diatropic or paratropic ring current effect. Similar results were reported for **71a** and **71c**. The macrocycle for **71b** is somewhat distorted as the phosphorus and sulfur atoms are displaced from the mean macrocyclic plane by 0.95 and 0.93 Å, respectively [12].

8.5 Carbaporphyrinoid Systems

Carbaporphyrinoid systems are porphyrin analogues with one or more carbons in place of the usual core nitrogens [13–16]. In early work on the synthesis of *meso*-tetraarylporphyrins from aldehydes and pyrrole using the Rothemund reaction, numerous unidentified porphyrin-like byproducts were noted. In 1943, Calvin and Aronoff speculated about the identity of these byproducts and proposed that a series of macrocycles **72** and **73a–e** (Chart 8.2) with one or two inverted pyrrole subunits might have been generated (other less plausible structures were also put forward). The authors proposed the name "carboporphines" for porphyrin isomers of this type [17]. In unpublished work from around the same time, Pauling also speculated about the possibility of synthesizing structures of this type [18]. However, no progress was made in this area for the following 50 years, and it was not until 1994 that two groups independently discovered the formation of a porphyrin isomer **71** with an inverted pyrrole ring [19]. This system, which is commonly known as N-confused porphyrin, is an example of a carbaporphyrin. Very soon after this discovery, carbaporphyrinoids such as true carbaporphyrins (e.g., **78** and **81**) [20], azuliporphyrins [21, 22], benziporphyrins [23], and oxybenziporphyrins [24] were described. These structures were initially obtained by application of the "3 + 1" variant on the MacDonald condensation (Scheme 8.15) [25]. Hence, tripyrrane **74** can be condensed with suitable dialdehydes in the presence of an acid (usually TFA), and following oxidation with DDQ or aqueous ferric chloride, diverse porphyrin analogues are generated (Scheme 8.15). Reaction of pyrrole-2,4-dicarbaldehydes **75** with **74** gave N-confused porphyrins **76**, while indene dialdehyde **77** gave benzocarbaporphyrins **78** and the related cyclopentene derivative **79** afforded a carbachlorin **80** that could be oxidized to carbaporphyrin **81**. Furthermore, azulene dialdehydes **82** produced azuliporphyrins **83**, isophthalaldehyde **84** afforded benziporphyrins **85**, and the phenolic dialdehyde **86** yielded oxybenziporphyrin **87**. These reactions are reproducible, generally give good yields, and afford a wide range of porphyrinoid systems in addition to the ones shown in Scheme 8.15. The properties of these carbaporphyrinoids are discussed in the following sections.

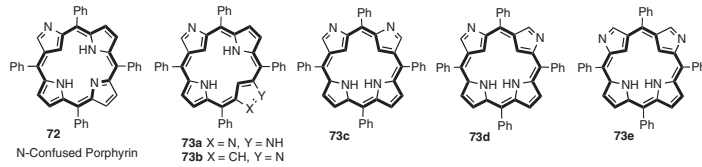

Chart 8.2 Proposed porphyrin analogues with inverted pyrrolic subunits.

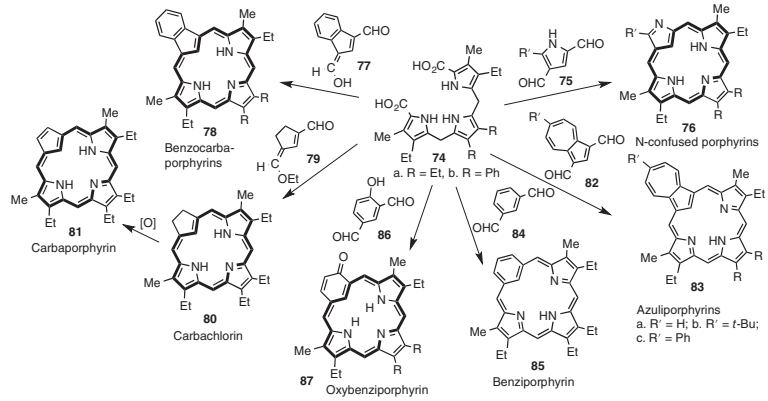

Scheme 8.15 Syntheses of carbaporphyrinoid systems using the "3 + 1" variant of the MacDonald condensation.

8.6 True Carbaporphyrins

In carbaporphyrins, one of the nitrogen atoms in the porphyrin macrocycle has been replaced with carbon [13–16]. Many examples of carbaporphyrins are now known, but much of the work in this area has been performed on porphyrinoids **78** with fused benzene rings. Benzocarbaporphyrins of this type are more easily synthesized and have proved to be robust compounds that have unique chemical reactivity. Carbaporphyrins such as **78** and **81** are fully aromatic compounds, and their proton NMR spectra show the presence of strong diamagnetic ring currents. For **78a**, the internal CH and NH resonances are shifted upfield to −6.74 and −4.0 ppm, respectively, while the external *meso*-protons are strongly deshielded, giving rise to two 2H singlets at 9.82 and 10.10 ppm (Figure 8.1) [20]. The UV–vis spectrum for **78a** is also very porphyrin-like, giving a strong Soret band at 424 nm and Q bands at 510, 544, 602, and 662 nm (Figure 8.2). In addition, as is generally the case for carbaporphyrins, a secondary medium-sized band was noted at shorter wavelengths (376 nm for **78a**). The proton NMR spectrum for carbaporphyrin **81** also confirmed that this compound is highly diatropic, and the internal CH and NH protons gave rise to peaks at −6.91 and −3.92 ppm, respectively. As would be expected, the *meso*-protons are strongly shifted downfield to give two 2H singlets at 9.77 and 9.83 ppm. The external cyclopentadiene protons gave a resonance at 8.15 ppm, indicating that the associated double bond is not involved in the aromatic delocalization pathway [26]. However, the UV–vis spectrum for **81** does not closely resemble the spectra for porphyrins as two weakened bands appear in the Soret region at 377 and 421 nm and only two broadened Q bands were noted at 510 and 585 nm. In principle, carbaporphyrins could exist in several tautomeric forms that could possess aromatic characteristics (Scheme 8.16 illustrates these tautomers for **78**). However, DFT calculations have shown that tautomers with internal methylene units such as **78″** and **78‴** are less favored and are also inconsistent with the spectroscopic data. In addition **78** is favored over **78′**, in part because the NHs are better situated for hydrogen bonding interactions. Variable temperature NMR studies confirm that a single symmetrical tautomer **78** predominates in solution. The X-ray structure for a diphenylbenzocarbaporphyrin **78b** showed that the indene subunit was significantly canted from the mean macrocyclic plane by 15.5° due to steric crowding within the macrocyclic cavity.

Addition of trace amounts of TFA to solutions of **78a** gave the related monocation **78a**H^+ (Scheme 8.17). This species retained its aromatic characteristics and the proton NMR spectrum showed the internal CH at −6.78 ppm, while the NHs gave rise to peaks at −4.61 (1H) and −3.22 ppm (2H). Further addition of TFA to the solution led to messy NMR spectra presumably due to the presence of mixtures of different species. However, in 50% TFA-$CDCl_3$, an aromatic *C*-protonated dication **78a**H_2^{2+} was generated (Scheme 8.17). The internal methylene unit gave a 2H resonance at −5.21 ppm and showed two broad peaks for the NH resonances near −1.6 ppm. The *meso*-protons were shifted further downfield and showed up at 10.46 and 11.07 ppm. In this species, the 18π electron delocalization pathway has been relocated through the fused benzene unit, as a result of which the benzo-protons appear as two downfield multiplets at 8.95 and 10.15 ppm. The dication can be considered to be a bridged benzo[18]annulene, although this species shows considerably more aromatic character than the parent system **79** [3]. Addition of deuterated TFA to solutions of **78a** resulted in rapid exchange of the NH and 21-CH protons, but slow exchange also occurred at the *meso*-positions. This was attributed to *meso*-protonated species being present in equilibrium with **78a**H^+ and **78a**H_2^{2+}. The UV–vis spectrum of **78a**H_2^{2+} in 50%

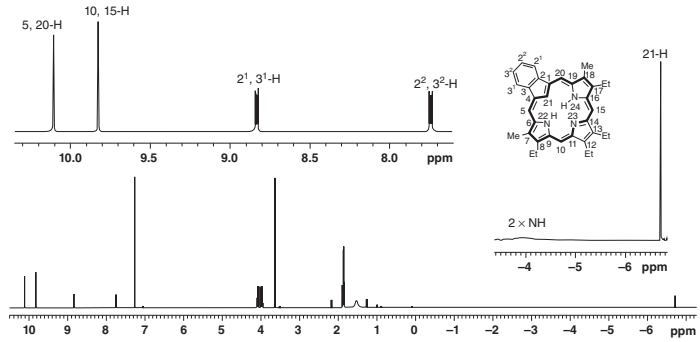

Figure 8.1 500 MHz proton NMR spectrum of benzocarbaporphyrin **78a** in $CDCl_3$.

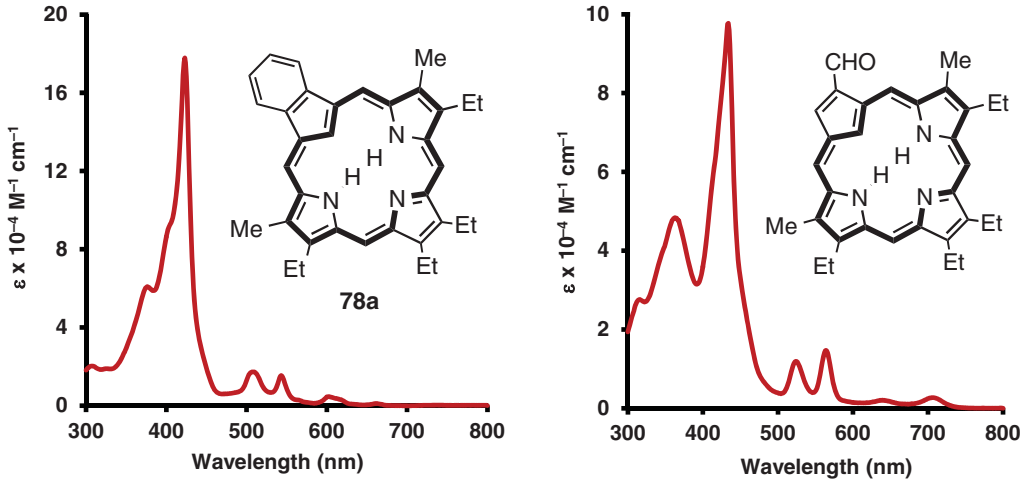

Figure 8.2 UV–vis spectra of benzocarbaporphyrin **78a** (left) and a formylcarbaporphyrin (right) in CH_2Cl_2 showing the presence of strong Soret bands and a series of Q bands.

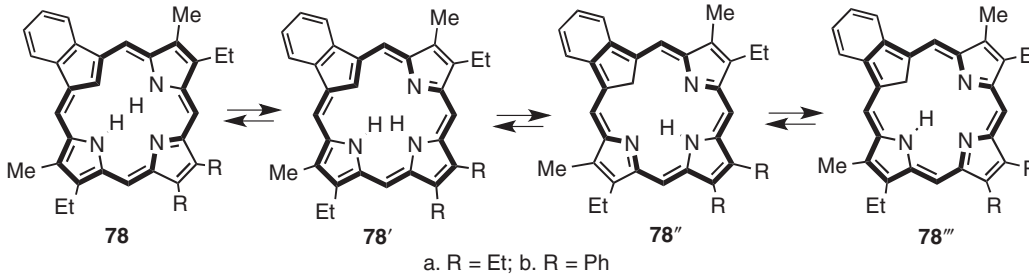

Scheme 8.16 Potential aromatic tautomers of a benzocarbapophyrin.

TFA-$CHCl_3$ gave two Soret bands at 410 and 426 nm and Q bands at 548, 600, and 664 nm. Carbaporphyrin **81** also underwent sequential protonations to give monocation **81**H^+ and dication **81**H_2^{2+} (Scheme 8.17). The dication was fully formed in 10% TFA-$CDCl_3$, and the proton NMR spectrum showed the presence of a very strong diamagnetic ring current. The internal CH_2 gave rise to a resonance at −8.27 ppm, while the *meso*-protons afforded two 2H singlets at 11.00 and 11.45 ppm. As the cyclopentadiene is fully integrated into the aromatic delocalization pathway, the protons at positions 2 and 3 gave a downfield singlet at 11.11 ppm [26].

Benzocarbaporphyrins **78** reacted with silver(I) acetate at room temperature to give good yields of the corresponding silver(III) derivatives **88** (Scheme 8.18). These organometallic complexes were stable, nonpolar compounds that gave orange-colored solutions and afforded porphyrin-like UV–vis spectra with a Soret band near 437 nm. The proton NMR spectra also demonstrated that these are fully aromatic derivatives, and **88a** showed the *meso*-protons downfield at 9.89 and 10.06 ppm. The X-ray structure for the related diphenyl-substituted complex demonstrated that the structure is near planar and the indene unit is only tilted from the mean macrocyclic plane by 5.1°. Tetraarylcarbaporphyrins **89**, derived from azuliporphyrins (see the next section), also reacted with silver(I) acetate to form silver(III) complexes **90a** (Scheme 8.18). In addition, *meso*-tetrasubstituted porphyrinoids **89** were metalated

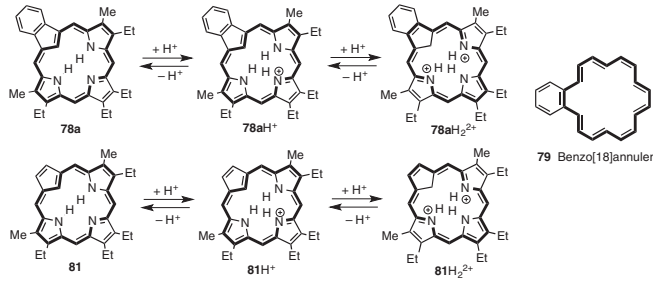

79 Benzo[18]annulene

Scheme 8.17 Protonation of carbaporphyrins.

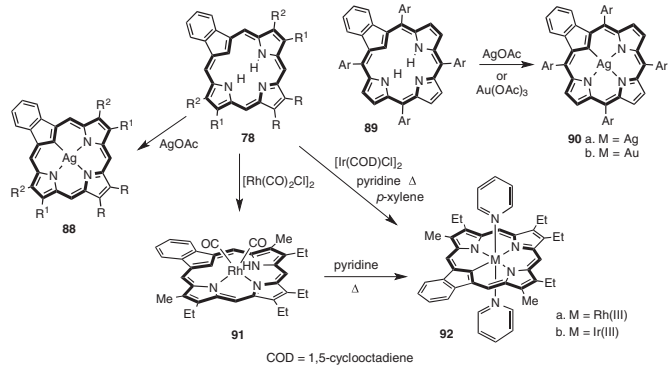

Scheme 8.18 Metalation of benzocarbaporphyrins. Based on [27].

with gold(III) acetate to generate gold(III) organometallic complexes **90b**. However, *meso*-unsubstituted benzocarbaporphyrins **78** only gave very poor yields of metalated derivatives with gold(III) acetate, and these reactions primarily resulted in decomposition [16]. Recently, benzocarbaporphyrin **78a** has been shown to react with $[Rh(CO)_2Cl]_2$ to give the rhodium(I) complex **91**, which was converted into rhodium(III) derivative **92a** upon heating in pyridine (Scheme 8.18) [27]. In addition, benzocarbaporphyrin **78a** reacted with $[Ir(COD)Cl]_2$ and pyridine in refluxing *p*-xylene to afford the related iridium(III) complex **92b**. All three metalated derivatives retained strongly aromatic properties [27].

Reaction of benzocarbaporphyrins **78** with ferric chloride in the presence of alcohol cosolvents led to the formation of carbaporphyrin ketals **93** (Scheme 8.19). When **78a** was refluxed with 500–600 equivalents of $FeCl_3$ in chloroform-methanol, the corresponding dimethoxy derivative was isolated in 94% yield as the hydrochloride salt **93a**·HCl. Similar ketals were generated using ethanol, isopropyl alcohol, or ethylene glycol. This remarkably chemistry enables the regioselective oxidation of carbaporphyrins to give polar derivatives that possess strong absorptions in the far red. The UV–vis spectrum for **93a** showed a Soret band at 422 nm and two additional strong absorptions at 751 and 832 nm (Figure 8.3). Addition of TFA resulted in the formation of a dication **93a**H_2^{2+} that gave a Soret band at 434 nm and Q bands at 633, 683, and 748 nm. The free-base form of **93** proved to be highly unstable. The proton NMR spectrum for **93a**HCl in $CDCl_3$ confirmed that the macrocycle is highly diatropic, and the internal methoxy groups gave rise to a 6H singlet at −1.34 ppm. The *meso*-protons afforded two 2H singlets at 9.68 and 10.93 ppm, and importantly the benzo-unit produced two 2H multiplets at 8.93 and 10.48 ppm, confirming that the aromatic delocalization pathway runs through the benzene ring. Again, carbaporphyrin ketals **93** can be considered to be derivatives of benzo[18]annulene. Dications **93**H_2^{2+} were also fully aromatic species. When **78a** was heated with $FeCl_3$ in dichloromethane-water for 3 h, 21-chlorocarbaporphyrin **94** was generated, although a nonaromatic dioxo-derivative **95** was formed as a by-product when the reaction time was extended to 16 h. The X-ray crystal structure of **94** demonstrated that the indene unit was pivoted by 29.6° relative to the mean macrocyclic plane, although the

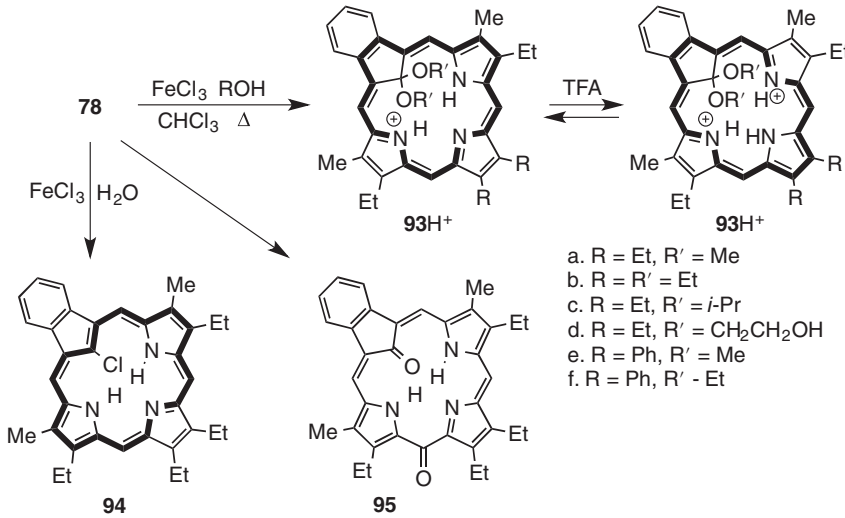

Scheme 8.19 Reactions of benzocarbaporphyrins with ferric chloride.

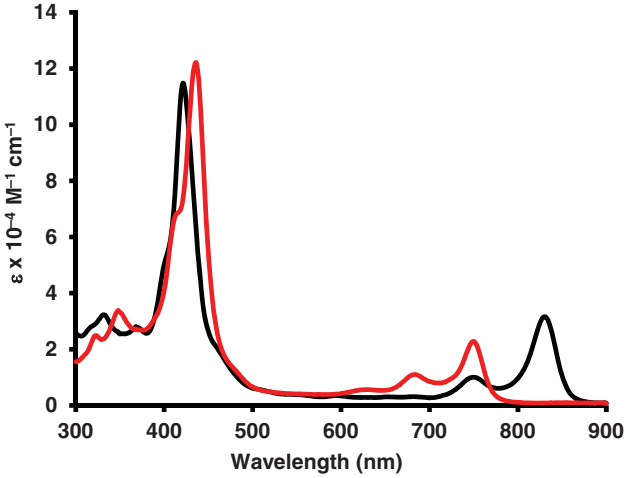

Figure 8.3 UV–vis spectra of carbaporphyrin ketal **93a**.HCl in CH_2Cl_2 (black line, monocation) and 5% TFA-CH_2Cl_2 (red line, dication **93a**H_2^{2+}).

proton NMR spectrum for this compound showed that its diatropic character had not been diminished.

Reaction of **78a** with methyl or ethyl iodide and potassium carbonate in refluxing acetone gave the *N*-alkylated derivatives **96** as major products together with the *C*-alkylated products **97** (Scheme 8.20). Although direct reaction of **78a** with palladium salts failed to give an identifiable metalated derivative, **96** reacted with palladium(II) acetate in refluxing acetonitrile to afford palladium(II) complexes **98**. Initially, the *N*-alkyl complexes **99** appear to be formed, but an alkyl group migration ensues to form the observed products **98**. The proton NMR spectra for **98** demonstrated that the macrocycle remains fully aromatic and the internal methyl resonance for **98a** appeared upfield at −3.21 ppm, while the *meso*-protons produced two downfield singlets at 9.56 and 10.27 ppm. The aromatic conjugation pathway for these derivatives runs through the benzene rings, and as a result the benzo-protons are shifted downfield to give two 2H multiplets at 8.24 and 9.41 ppm.

Carbachlorins such as **80a**, **80b**, and **100** have also been investigated (Scheme 8.21). These dihydroporphyrinoids are fully aromatic and give porphyrin-like UV–vis spectra. For instance, the UV–vis spectrum of **80a** gave a Soret band at 401 nm and Q bands at 495, 526, 593, and 651 nm (Figure 8.4). As is the case for true chlorins, the longest wavelength absorption was relatively strong. The proton NMR spectra for these carbachlorins show that they possess strong diatropic ring currents. Protonation of **80a** with TFA gave the corresponding cation **80a**H^+, which also showed highly diatropic characteristics. The UV–vis spectrum for **80a**H^+ in 1% TFA-CH_2Cl_2 gave a split Soret band at 409 and 426 nm and Q bands at 552, 582, and 636 nm (Figure 8.4). When **80a** was heated with methyl iodide and potassium carbonate in refluxing acetone, the related *N*-methyl carbachlorin **80b** was generated in 34% yield. The UV–vis spectrum for **80b** was somewhat broadened compared to **80a** and showed a weakened Soret band at 407 nm. Nevertheless, the macrocycle retained most of its diatropic character, and the proton NMR spectrum showed the inner CH and methyl groups at −6.31 and −4.27 ppm, respectively. These resonances were shifted further upfield in the corresponding cation **80b**H^+. Reaction of **80b** with palladium(II) acetate in refluxing acetonitrile led to a metalation-oxidation-alkyl group migration cascade that

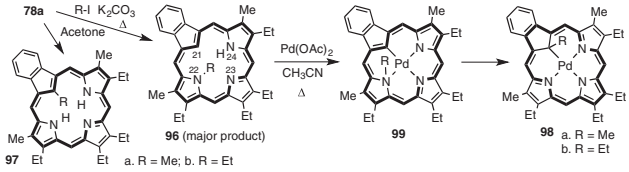

Scheme 8.20 Alkylation of a benzocarbaporphyrin and the formation of palladium(II) derivatives.

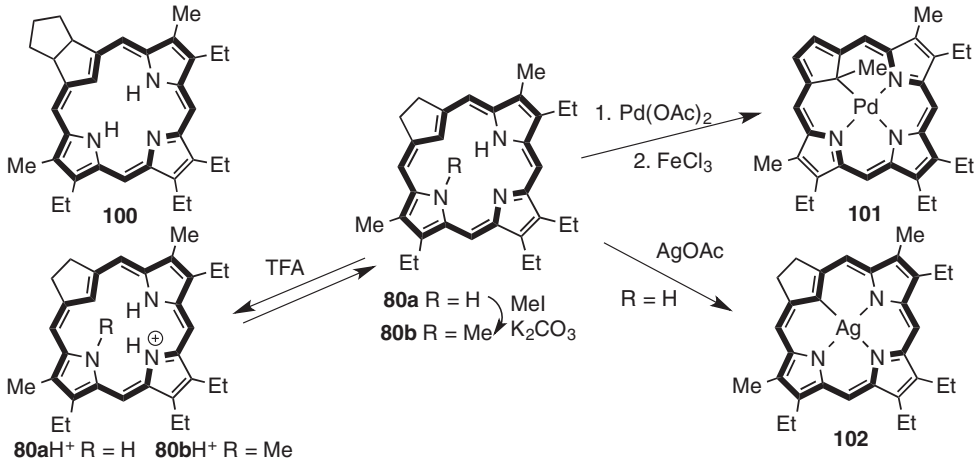

Scheme 8.21 Alkylation and metalation of carbachlorins.

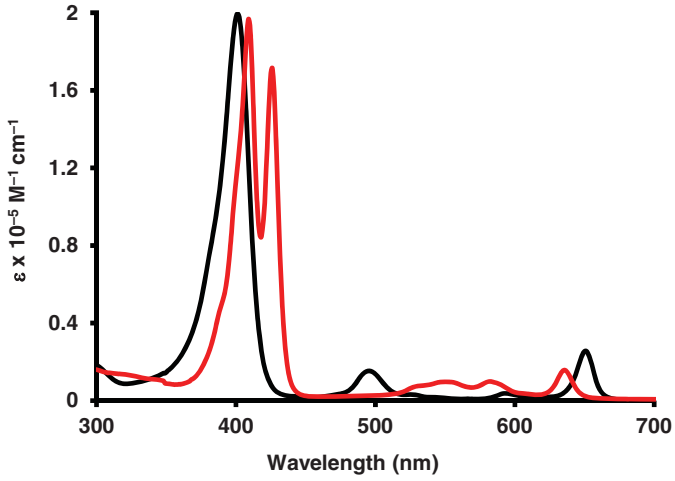

Figure 8.4 UV–vis spectra of carbachlorin **80a** in CH_2Cl_2 (black line, free base) and 1% TFA-CH_2Cl_2 (red line, cation **80a**H^+).

afforded palladium(II) carbaporphyrin **101**. Yields were raised to 34% when the crude product was oxidized with an aqueous solution of ferric chloride. A silver(III) carbachlorin **102** was also prepared in 31% by reacting **80a** with 3.5 equivalents of silver(I) acetate at room temperature. Reactions with a further excess of silver acetate primarily led to decomposition, although low yields of the related silver(III) carbaporphyrin were noted. Silver chlorin **102** gave a porphyrin-like UV–vis spectrum with a Soret band at 411 nm and Q bands at 492, 524, 553, and 599 nm, and exhibited strongly diatropic characteristics [26].

MacDonald-type syntheses of oxa- and thiacarbaporphyrins **103a,b** were reported (Scheme 8.22), and again these macrocycles exhibited aromatic properties [3, 13, 16]. Oxa-, thia-, and selenacarbaporphyrins **103a–c** were also available from the ring contraction of heteroazuliporphyrins (see the next section). Addition of TFA to **103a–c** afforded the corresponding aromatic cations **103**H^+, and evidence for the formation of dicationic species

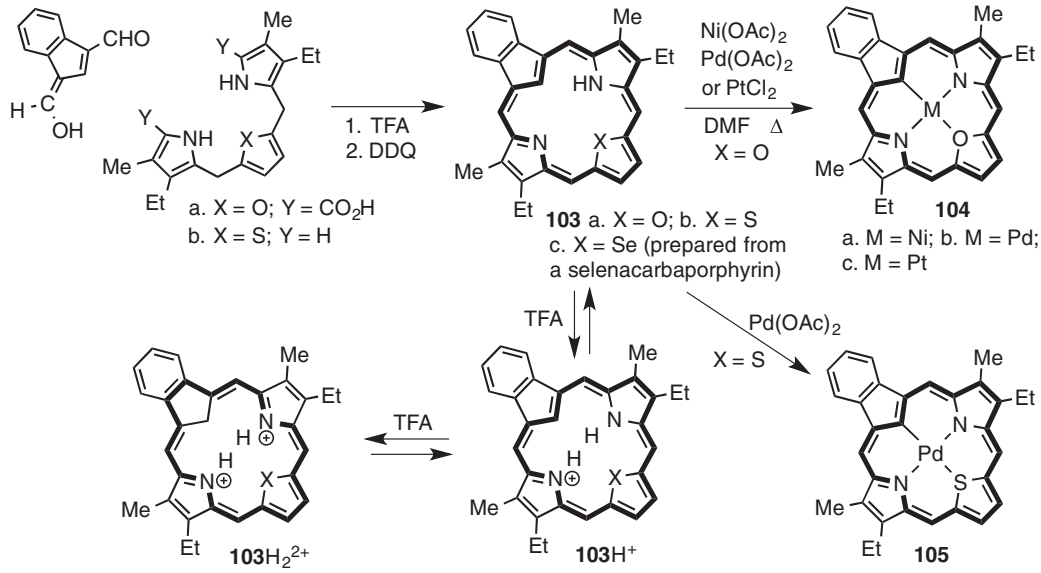

Scheme 8.22 Syntheses and metalation of 23-oxa- and 23-thiacarbaporphyrins.

103H_2^{2+} in equilibrium with the monocations was obtained at higher acid concentrations. Oxacarbaporphyrin **103a** reacted with nickel(II) acetate and palladium(II) acetate in refluxing DMF to give the related metalloporphyrinoids **104a** and **104b** in 53% and 70% yield, respectively. Low yields of the related platinum(II) complex **104c** were also obtained by reacting **103a** with platinum(II) chloride under these conditions. The X-ray structure of **104b** showed that the macrocycle was nearly planar. Thiacarbaporphyrin **103b** also acted as a dianionic ligand and rapidly reacted with palladium(II) acetate to give the palladium(II) organometallic derivative **105** in 92% yield.

A 22-oxa-21-carbaporphyrin **106** was prepared by a MacDonald-type "2 + 2" condensation between fulvene dialdehyde **107** and dipyrrylmethane **18a** (Scheme 8.23). As the fulvene unit is conjugated, no oxidation step was required. The UV–vis spectrum for this heterocarbaporphyrin was again porphyrin-like, and the NMR spectrum demonstrated that this system was highly diatropic. Addition of TFA gave the corresponding monocation **106**H^+, and in neat TFA a *C*-protonated dication **106**H_2^{2+} was generated. The proton NMR spectrum for dication **106**H_2^{2+} in HCl-TFA showed that this species had a very strong aromatic ring current as the *meso*-protons appeared as four 1H singlets between 11.13 and 11.92 ppm, while the interior CH_2 gave rise to a resonance at −5.67 ppm. Reaction of **106** with palladium(II) acetate in refluxing DMF gave the palladium(II) complex **108** in 80% yield. The proton NMR spectrum of **108** indicated that this species had a slightly reduced diatropic ring current compared to **106**, although single crystal X-ray diffraction analyses for **106** and **108** indicated that both of these structures were near planar.

An alternative route to carbaporphyrins and heterocarbaporphyrins has been developed using carbatripyrrin **109** as the key intermediate (Scheme 8.24) [28]. Indene reacted with pyrrole-2-carbaldehyde (**110**) in the presence of KOH in refluxing ethanol to give fulvene **111**, which was reduced with lithium aluminum hydride to generate the related dihydrofulvene **112**. At higher concentrations, when **112** and **110** were reacted in refluxing ethanol

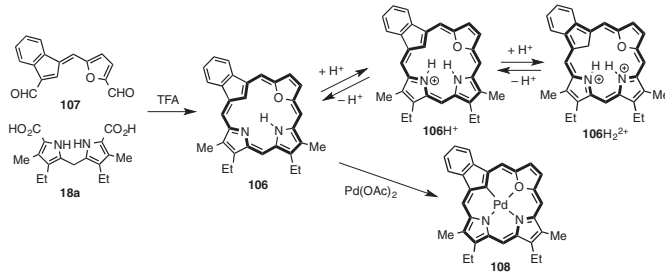

Scheme 8.23 Synthesis and metalation of a 22-oxacarbaporphyrin.

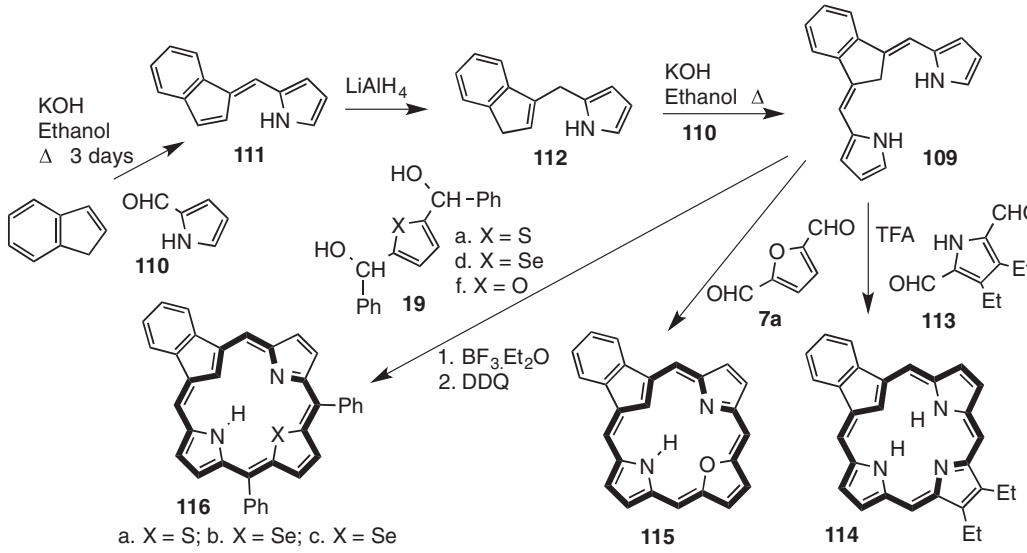

Scheme 8.24 Synthesis of carbaporphyrins and heterocarbaporphyrins from a carbatripyrrin.

containing KOH, carbatripyrrin **109** precipitated out from the reaction mixtures in 75% yield. Condensation of **109** with pyrrole dialdehydes such as **113** in the presence of TFA afforded carbaporphyrins (e.g., **114**) in up to 51% yield. Similarly, furan dialdehyde **7a** reacted with **109** to give the unsubstituted oxacarbaporphyrin **115**. In addition, **109** reacted with thiophene, selenophene, and furan dicarbinols **19a**, **19d**, and **19f** in the presence of boron trifluoride etherate to afford, following oxidation with DDQ, a series of heterocarbaporphyrins **116a–c** in 24–25% yield [28]. Reaction of a cyclopentadienyl analogue **117** of the tripyrranes with thiophene dicarbinol **19b** and $BF_3.Et_2O$ gave a thiacarbachlorin **118**, albeit in only 5% yield (Scheme 8.25) [29]. Oxidation with one equivalent of DDQ gave the corresponding thiacarbaporphyrin **119** in 25% yield. Both **118** and **119** proved to be fully aromatic species. Reaction of **118** and **119** with palladium(II) acetate in refluxing toluene afforded the related palladium(II) complexes **120a** and **120b**.

8.7 Azuliporphyrins

Azuliporphyrins are closely related porphyrin analogues in which an azulene unit has replaced one of the pyrrolic rings [22]. This system was originally synthesized by reacting azulene dialdehydes with tripyrranes using the "3 + 1" methodology described above [21]. The presence of an azulene moiety within the porphyrinoid framework essentially interrupts the conjugation in the system by introducing a cross-conjugated element. However, the proton NMR spectrum for azuliporphyrin **83a** (Scheme 8.26) in $CDCl_3$ showed the *meso*-protons near 8 and 9 ppm, suggesting that this system has some diatropic character. Many azuliporphyrins are somewhat insoluble, which prevented high-quality proton NMR spectra from being obtained. However, azuliporphyrins with substituents on the azulene ring, such as *tert*-butylazuliporphyrin **83b**, are far more soluble, which allows the resonances for the internal protons to be identified. For **83b**, the NH and CH protons were noted near 3 ppm. These values are shifted significantly upfield, although the observed shifts

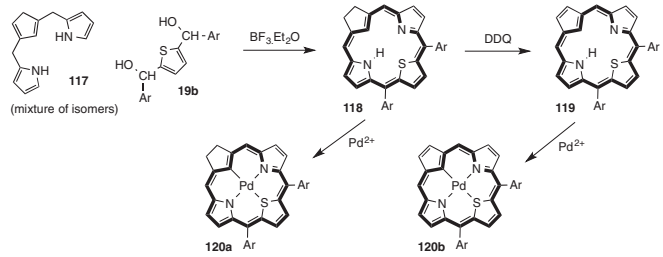

Scheme 8.25 Synthesis and metalation of a thiacarbachlorin and a related thiacarbaporphyrin. Based on [29].

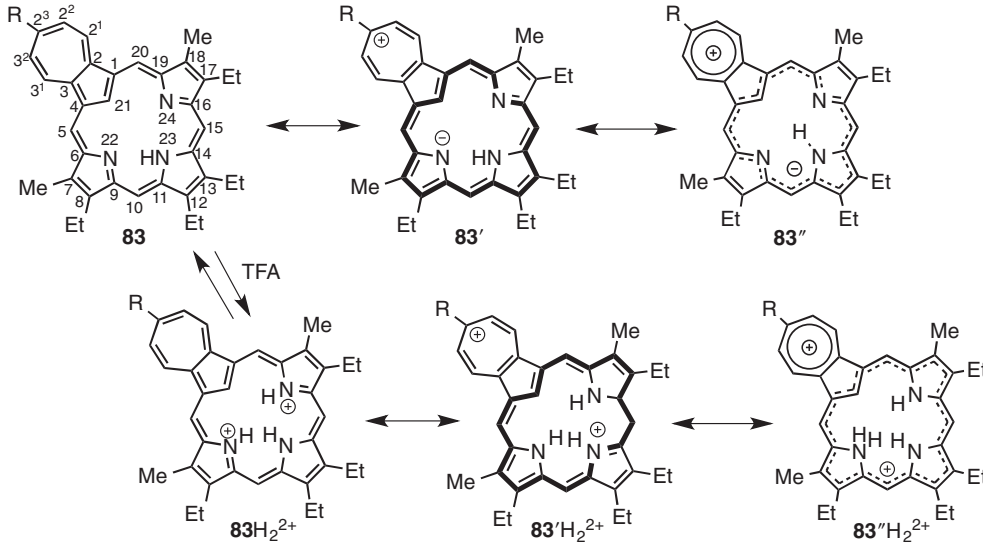

Scheme 8.26 Resonance contributors and protonation of azuliporphyrins.

are relatively small compared to those seen for true carbaporphyrins. The intermediary aromatic characteristics of azuliporphyrins were initially explained as being due to dipolar resonance contributors such as **83′** that have 18π electron delocalization pathways. This type of contribution is limited due to the need for charge separation. An analysis of the bond lengths for **83b** obtained from single crystal X-ray diffraction suggested that a dipolar species **83″** with a 17-atom 18π electron delocalization pathway provided a better explanation for the properties of this system. Azuliporphyrins readily protonate to give dications **83**H_2^{2+}, and these show greatly increased diatropicity (Scheme 8.26). For **83a** in TFA-$CDCl_3$, the proton NMR spectrum showed the inner CH at −2.56 ppm, and the external *meso*-protons shifted further downfield to give two 2H singlets at 9.42 and 9.95 ppm. The increase in aromatic character can be attributed to canonical forms such as **83′**H_2^{2+} and **83″**H_2^{2+} that are relatively favorable because they facilitate charge delocalization. The UV–vis spectra of azuliporphyrins generally show four medium-sized absorptions between 350 and 500 nm and a very broad peak between 500 and 800 nm (Figure 8.5). The diprotonated forms **83**H_2^{2+} afforded more porphyrin-like spectra in that they exhibited a Soret-like band near 500 nm and several Q-like bands at longer wavelengths [22].

Several alternative routes to azuliporphyrins have been developed [22]. A back-to-front "3 + 1" synthesis was accomplished by reacting azulenes with acetoxymethylpyrroles **121** in the presence of an acid catalyst to afford azulitripyrranes **122** (Scheme 8.27). The *tert*-butyl ester groups could be cleaved with trifluoroacetic acid, and subsequent condensation with a pyrrole dialdehyde such as **113** gave azuliporphyrins **123** following an oxidation step. Heteroazuliporphyrins **124–126** could also be prepared by this approach. Condensation of **122** with dialdehydes **7a–c** gave the corresponding oxa-, thia-, and selenaazuliporphyrins

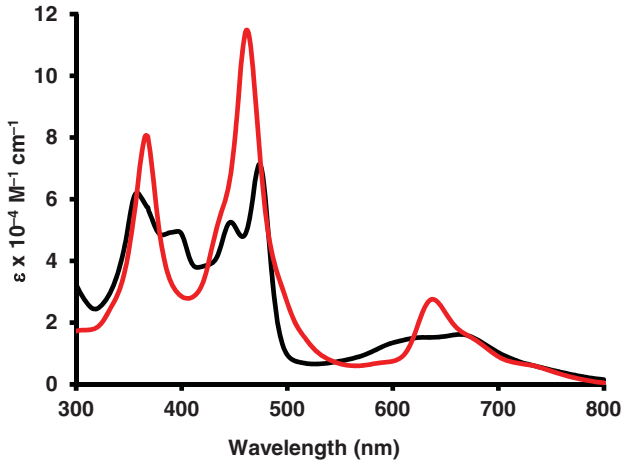

Figure 8.5 UV–vis spectra of azuliporphyrin **83b** in 1% Et_3N-$CHCl_3$ (free base, black line) and 1% TFA-$CHCl_3$ (dication **83b**H_2^{2+}, red line).

(Scheme 8.27). An oxidation step was required in each case, which was generally accomplished with either DDQ or aqueous ferric chloride. In reactions with furan dialdehyde **7a**, a mixture of benzo-oxacarbaporphyrins **127** was obtained when the oxidation was conducted using DDQ, but the somewhat unstable oxaazuliporphyrins **124** could be isolated when aqueous ferric chloride was used instead. A "2 + 2" method for preparing azuliporphyrins has also been reported. A remarkable one-pot route to *meso*-tetrasubstituted azuliporphyrins **128** was developed where azulenes were reacted with three equivalents of pyrrole and four equivalents of an aromatic aldehyde in the presence of boron trifluoride etherate, followed by oxidation with DDQ (Scheme 8.28). In these reactions, it was crucial to use chloroform rather than dichloromethane as a solvent, and it was suggested that the ethanol present in this solvent as a stabilizer modified the selectivity of the Lewis acid catalyst. Benzaldehyde reacted with azulene and pyrrole to give tetraphenylazuliporphyrin **123a** in 13% yield, but in some cases yields as high as 26% were obtained [22].

Addition of excess pyrrolidine to solutions of azuliporphyrins such as **83a** and **128a** led to the formation of carbaporphyrin adducts **129** and **130** where nucleophilic attack had occurred preferentially at the 2^3-position (Scheme 8.29). However, when the pyrrolidine was removed, the original azuliporphyrin was regenerated. Similar adducts were noted with thiophenol, benzylamine, and hydrazine. When solutions of azuliporphyrins **83a** and **128a** were treated with *tert*-butyl hydroperoxide and potassium hydroxide, a ring contraction occurred to give benzocarbaporphyrins **78a** and **89a** together with the related aldehydes **131a,b** and **132**, respectively. The mechanism proposed to explain these results involves initial nucleophilic attack from the *tert*-butyl peroxide anion (Scheme 8.30). Subsequent Cope rearrangement would give the norcaradiene-fused structure **133**, which could eliminate *tert*-butyl alcohol to afford aldehyde **131a** or cyclopropanone **134**. Extrusion of CO would then yield benzocarbaporphyrin **78**. Initial nucleophilic attack at a different position on the seven-membered ring explains the formation of minor aldehyde product **131b**. Surprisingly, 2^3-substituted azuliporphyrins also underwent facile ring contraction reactions to give car-

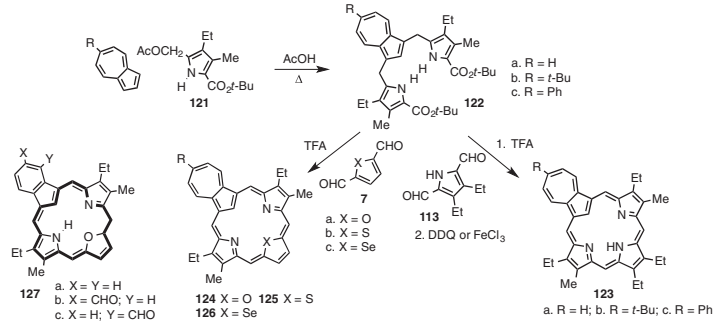

Scheme 8.27 Alternative "3 + 1" syntheses of azuliporphyrins and heteroazuliporphyrins.

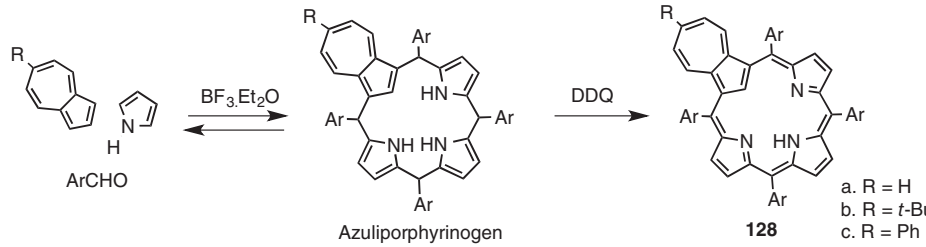

Scheme 8.28 One-pot synthesis of tetraarylazuliporphyrins.

baporphyrin products. This chemistry provides the only available method for synthesizing tetraaryl benzocarbaporphyrins **89**. Heteroazuliporphyrins similarly undergo oxidative ring contractions to give benzoheterocarbaporphyrin products **103** (see Scheme 8.22).

6-Methoxyazulene reacted with acetoxymethylpyrrole **121** in the presence of acetic acid to give azulitripyrrane **135** (Scheme 8.31). Following cleavage of the protective groups with TFA, the tripyrrane analogue was condensed with pyrrole dialdehyde **113**, but instead of the expected methoxy derivative **136**, tropone-fused azuliporphyrin **137** was isolated instead. This appears to be due to an S_N2 displacement where **137** is effectively the leaving group. The tropone-fused system is fully aromatic, although the Soret band region in its UV–vis spectrum resembled the spectra obtained for azuliporphyrins. Reaction of **137** with silver(I) acetate gave the corresponding silver complex **138**. Condensation of azulitripyrrane **135** with thiophene dialdehyde **7b** gave the related thiacarbaporphyrin **139** [22].

Azuliporphyrins **83** and **128** are dianionic ligands and react with nickel(II), palladium(II), and platinum(II) salts to give the related organometallic derivatives **140** and **141** (Scheme 8.32). *meso*-Unsubstituted azuliporphyrins also reacted with $[Ir(COD)Cl]_2$ and $[Rh(CO)_2Cl]_2$ in refluxing xylenes to give the iridium(III) and rhodium(III) complexes **142** and **143**, respectively. In addition, tetraphenylazuliporphyrin **128a** reacted with $Ru_2(CO)_{12}$ to give ruthenium(II) complex **144**. When an excess of the ruthenium(0) reagent was used, a cluster complex **145a** was obtained. Similar bimetallic derivatives **145b–d** were also generated by reacting **141a–c** with $Ru_2(CO)_{12}$ [22].

Treatment of tetraarylazuliporphyrins **128** with copper(II) acetate led to an oxidative metalation that gave copper(II) complexes **146** in moderate yields (Scheme 8.33). These could be demetalated with 10% TFA-chloroform to afford 21-oxyazuliporphyrins **147**. In addition, treatment of **128** with silver(I) acetate in refluxing chloroform-acetonitrile also generated oxyazuliporphyrins **147**. DFT calculations demonstrated that this system strongly favors the keto form **147** over the hydroxy tautomer **147′**, and this assignment was confirmed by X-ray crystallography. Although porphyrinoids **147** formally have a 24π electron delocalization pathway, the macrocycle is weakly diatropic. However, the proton NMR spectra for **147** show the seven-membered ring proton resonances between 5 and 6 ppm, and these values are consistent with this unit having olefinic character. Metalation of **147** with nickel(II) acetate, palladium(II) acetate, or platinum(II) chloride yielded the corresponding metal complexes **148** [22].

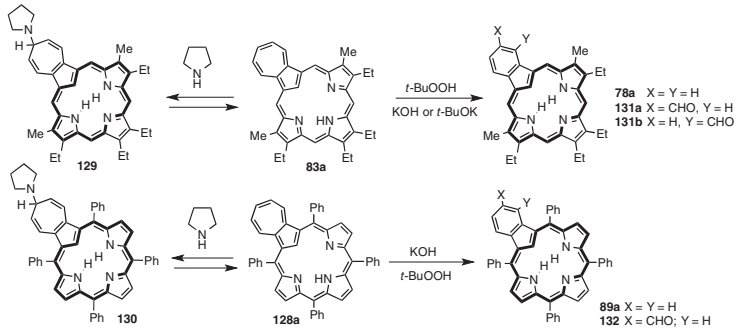

Scheme 8.29 Pyrrolidine adducts and oxidative ring contractions of azuliporphyrins.

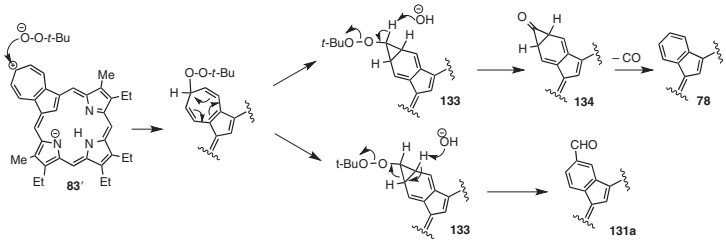

Scheme 8.30 Proposed mechanism for the oxidative ring contraction of azuliporphyrins to give benzocarbaporphyrins.

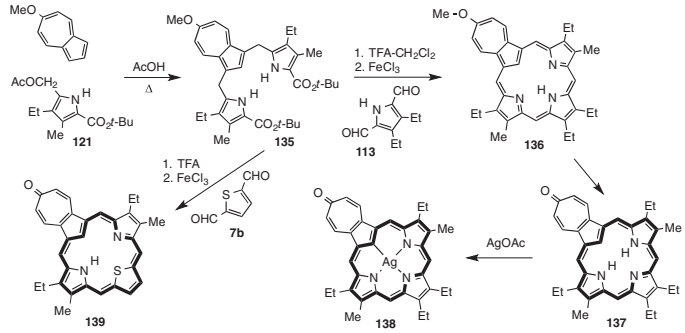

Scheme 8.31 Synthesis of a tropone-fused carbaporphyrin and a related thiacarbaporphyrin.

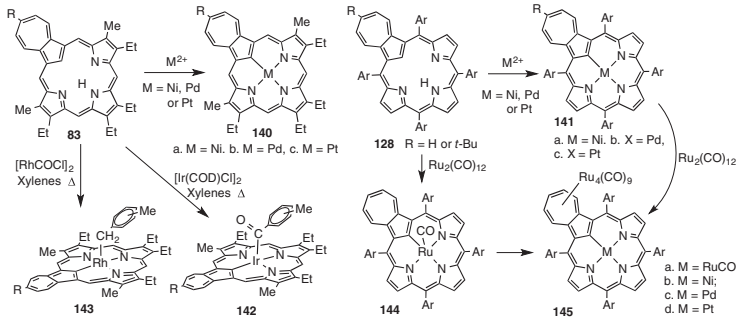

Scheme 8.32 Metalation of azuliporphyrins.

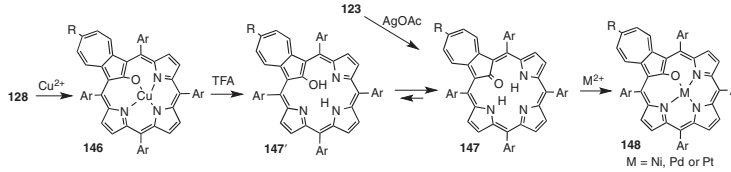

Scheme 8.33 Oxidation of azuliporphyrins to 21-oxyazuliporphyrins and related metalated derivatives.

8.8 Neo-Confused Porphyrins

Neo-confused porphyrins (e.g., **149** and **150**) are a new family of porphyrin analogues where one of the pyrrole units is connected in a 1,3-fashion so that the nitrogen is linked to a bridging carbon atom [30]. This system was prepared by using "2 + 2" MacDonald condensations of 1,2′-dipyrrylmethane dialdehydes such as **151** and **152** with dipyrrylmethanes **18** in the presence of *p*-toluenesulfonic acid (Scheme 8.34). Following oxidation of the phlorin intermediates with aqueous ferric chloride solutions, good yields of the neo-confused porphyrins **149** and **150** could be isolated. As a carbon atom has been placed within the porphyrinoid cavity, neo-confused porphyrins can be considered to be carbaporphyrinoid systems. They exhibit macrocyclic aromaticity, and the proton NMR spectrum for **149a** showed the internal NH and CH resonances at −0.33 and −0.74 ppm, respectively. Nevertheless, these shifts are considerably smaller than those due to porphyrins or true carbaporphyrins. The aromatic character associated with neo-confused porphyrins can be attributed to the presence of a 17-atom 18π electron delocalization pathway, but this appears to be less effective than the [18]annulene-type conjugation pathways in other porphyrinoid systems. The UV–vis spectra for neo-confused porphyrins closely resemble the spectra for porphyrins, and **149a** shows a strong Soret band at 407 nm and Q bands at 503, 537, 567, and 615 nm. Neo-confused porphyrins **149** and **150** reacted with nickel(II) acetate and palladium(II) acetate in refluxing acetonitrile to yield the corresponding organometallic derivatives **153** and **154**. X-ray crystallography for metal complexes **153a**, **153b**, **154a**, and **154b** and free-base neo-confused porphyrin **149a** demonstrated that these porphyrinoids all take on essentially planar conformations.

8.9 Benziporphyrins

In benziporphyrins, a benzene ring replaces one of the pyrrole units within the porphyrin framework [23]. The arene moiety is usually connected in a 1,3- or *meta*-fashion. Etio-type benziporphyrins **85** can be prepared by reacting 1,3-benzenedicarbaldehydes with tripyrranes using the MacDonald "3 + 1" approach (Scheme 8.15). Naphthiporphyrin **155** (Scheme 8.35) can be prepared similarly. Benziporphyrin **85** is nonaromatic, and the proton NMR spectra demonstrate that the internal and external benzene protons have essentially the same chemical shifts (7.7–8.0 ppm). Naphthiporphyrin **155** gave similar results. However, in the presence of trifluoroacetic acid, the corresponding dications **85**H_2^{2+} and **155**H_2^{2+} gave proton NMR spectra that showed the emergence of a weak diatropic ring current. For **85**H_2^{2+}, the *meso*-proton signals shifted downfield while the internal CH produced an upfield resonance near 5.0 ppm. Reaction of **85** with nickel(II) acetate in DMF or palladium(II) acetate in acetonitrile afforded the stable organometallic complexes **156a** and **156b**, and naphthiporphyrin **155** reacted similarly with palladium(II) acetate to give the palladium complex **157** (Scheme 35) [23].

Tetraarylbenziporphyrins **158** have been prepared by reacting benzene dicarbinols **159** with pyrrole and aromatic aldehydes in the presence of boron trifluoride etherate, followed by oxidation with DDQ (Scheme 8.36) [31]. The proton NMR spectra for free-base *meso*-substituted benziporphyrins **158** also gave no indication of diatropic character, but the related dications again showed the presence of a weak diamagnetic ring current [23]. Benziporphyrins **158** were shown to form nickel(II), palladium(II), and platinum(II) complexes

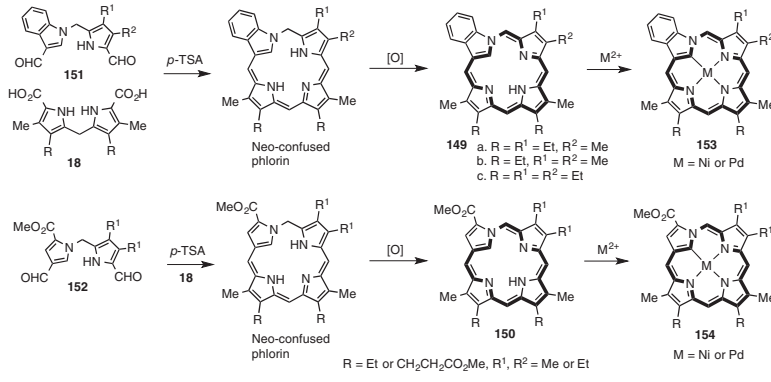

Scheme 8.34 Synthesis and metalation of neo-confused porphyrins.

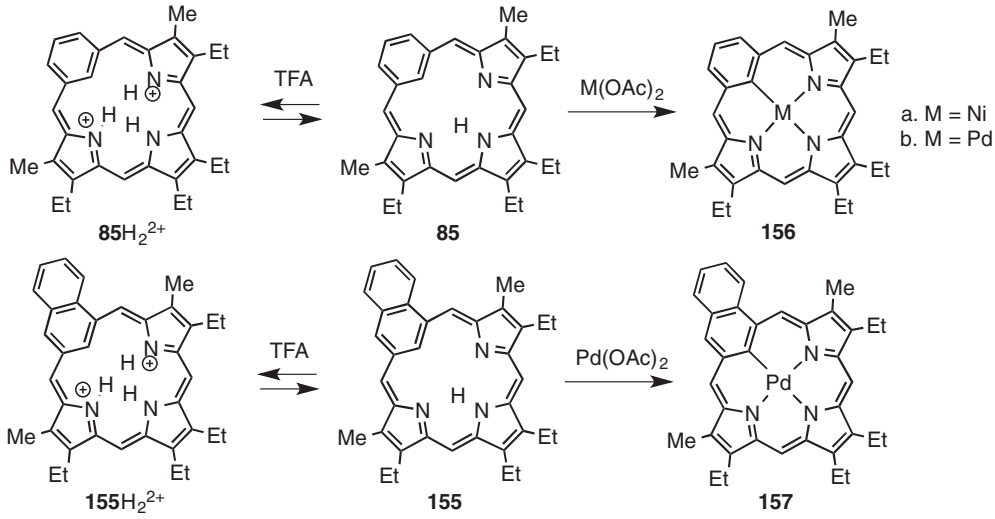

Scheme 8.35 Protonation and metalation of *meso*-unsubstituted benzi- and naphthiporphyrins.

160a–c [31, 32]. Reaction with nickel(II) chloride initially gave partial complexation to form **161**, and this derivative could be closed to afford the organometallic derivative **160a** in the presence of base. Reaction of **158** with silver(I) acetate led to a selective oxidation to form the 22-acetoxybenziporphyrins **162**. Similarly, copper(II) chloride reacted with **158** to produce a dimeric complex **163** where the internal carbon atoms had undergone an oxidative chlorination [31, 32].

Hydrolysis of acetoxybenziporphyrin **162** with hydrochloric acid, followed by treatment with sodium hydroxide, gave the unstable hydroxybenziporphyrin **164** (Scheme 8.37) [33]. At low temperatures, **164** was shown to be in equilibrium with keto tautomer **164′**. The proton NMR spectrum for **164′** showed the external pyrrolic resonances between 5.0 and 5.5 ppm, while the benzene unit afforded peaks at 3.9 (2H) and 5.1 ppm (1H). These upfield shifts indicate that **164′** has a paratropic ring current due to the presence of a 20π electron delocalization pathway.

2,4-Dimethoxybenziporphyrins **165** and **166** (Scheme 8.38) were prepared using the same synthetic approaches. These substituted benziporphyrins showed weak diatropic characteristics that were magnified upon protonation. These observations were attributed to the electron-donating methoxy substituents making accessible resonance contributors such as **165′** and **166′** that possess porphyrin-like delocalization pathways. *meso*-Tetrasubstituted benziporphyrins **166** readily formed the corresponding nickel(II) and palladium(II) complexes **167** and reacted with silver(I) acetate to give the acetoxy-derivatives **168** [23].

Syntheses of heterobenziporphyrins have been developed using benzitripyrrane intermediates **169** (Scheme 8.39). Benzene dicarbinols **159** and **170** were reacted with excess pyrrole in the presence of boron trifluoride etherate to give the required tripyrrane analogues **169**. Acid-catalyzed condensation of **169** with pyrrole dialdehyde **113** gave the corresponding benziporphyrins **171** in good yields. Alternatively, reactions of **169** with furan or thiophene dicarbinols **19a** and **22** in the presence of $BF_3.Et_2O$ afforded oxa- and thiabenziporphyrins **172**. Heterobenziporphyrins are nonaromatic and like benziporphyrins show some aromatic character upon protonation. As would be expected, this effect is enhanced by the presence of

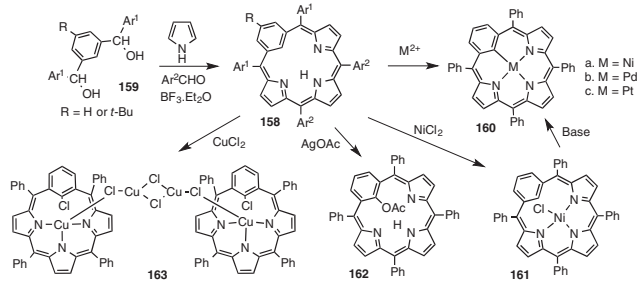

Scheme 8.36 Synthesis, metalation, and oxidation of *meso*-tetraarylbenziporphyrins.

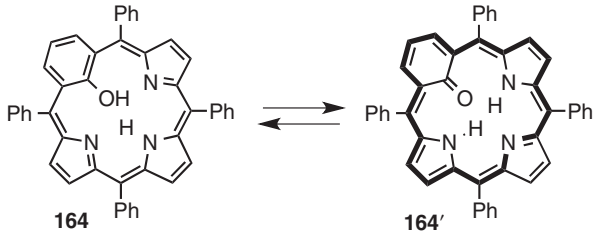

Scheme 8.37 Tautomeric equilibrium of 22-hydroxybenziporphyrin **164** with its antiaromatic keto tautomer **164′**.

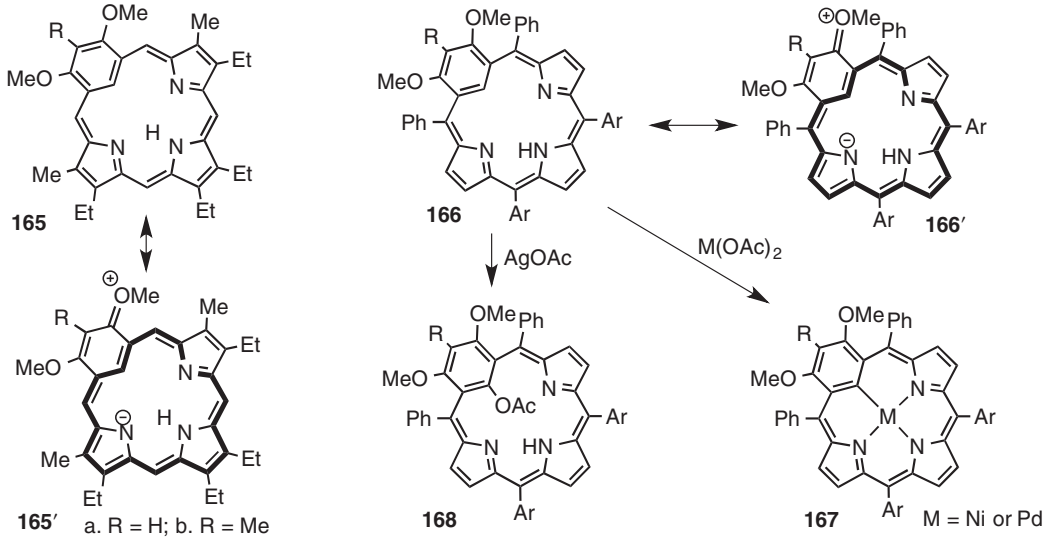

Scheme 8.38 Synthesis and reactions of dimethoxybenziporphyrins.

methoxy substituents. Metalation of dimethoxythiabenziporphyrins **172c** or **172d** with palladium(II) acetate triggered loss of a methyl group to afford the aromatic oxybenziporphyrin derivatives **173** [23].

Reaction of 4-hydroxyisophthalaldehyde **86** with tripyrranes afforded oxybenziporphyrins **87** (Scheme 8.15) [24]. It had been hypothesized that 2-hydroxybenziporphyrin **174** would tautomerize to a keto form **87** that possesses a porphyrin-like conjugation pathway (Scheme 8.40), and this speculation was subsequently supported by DFT calculations. Oxynaphthiporphyrins **175** were prepared similarly, and these also strongly favor the keto form. Oxybenzi- and oxynaphthiporphyrins **87** and **175** are strongly diatropic, and their proton NMR spectra showed the resonance for the inner CH upfield near −7 ppm. The UV–vis spectra of oxybenziporphyrins are also porphyrin-like, showing strong Soret bands and a series of Q bands (Figure 8.6). Tetraaryloxybenziporphyrins **176** have also been prepared, and these retain aromatic characteristics, although these are reduced due to steric crowding at the macrocyclic periphery. These porphyrinoids commonly act as trianionic ligands and react with silver(I) acetate to give the silver(III) complexes **177**, **178**, and **179a**. The *meso*-substituted porphyrinoid **176** could also be metalated with gold(III) acetate to yield the corresponding gold(III) complexes **179b**. A palladium(II) complex **180** of

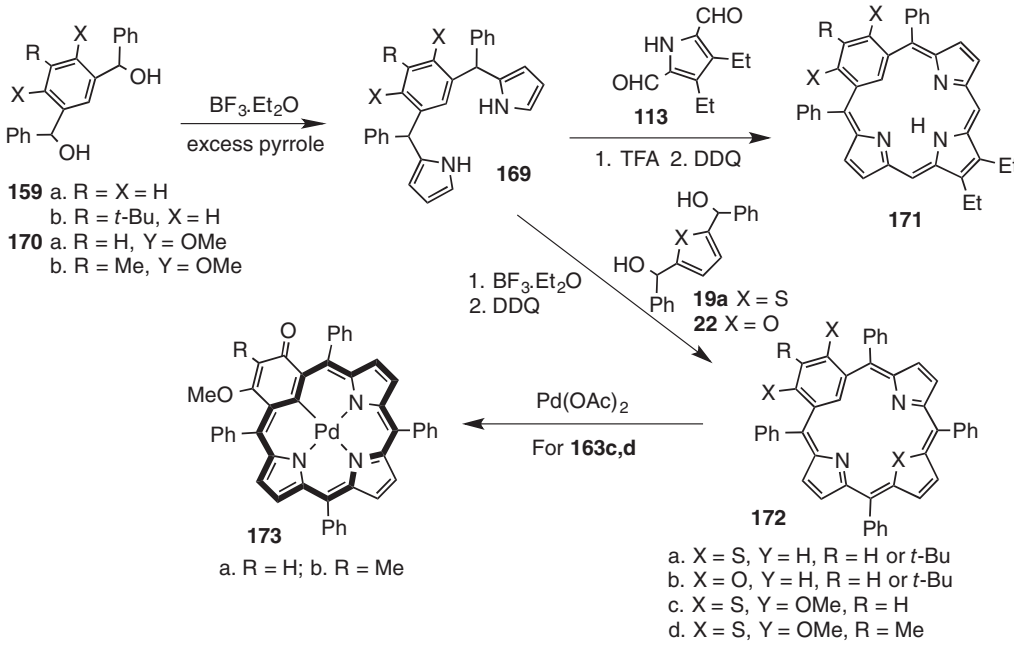

Scheme 8.39 Stepwise syntheses of diarylbenziporphyrins and tetraarylheterobenziporphyrins and the formation of palladium(II) thiaoxybenziporphyrins.

oxybenziporphyrin **87** has also been reported. Dimesityl oxa- and thiaoxybenziporphyrins **181a** and **181b** were prepared using the "3 + 1" methodology from heterotripyrrane **182** (Scheme 8.41). Metalation of **182a** with palladium(II) chloride in refluxing benzonitrile gave the corresponding palladium complex **183**. Oxa- and thiaoxybenziporphyrins **184a** and **184b** were also obtained from tripyrrane analogues **185** (Scheme 8.41), and thiaporphyrinoid **184b** was shown to react with palladium(II) acetate in acetonitrile to give the related palladium(II) complex **186** [23].

Resorcinol and 2-methylresorcinol reacted with acetoxymethylpyrrole **187** in the presence of *p*-toluenesulfonic acid and calcium chloride to give tripyrrane analogues **188** (Scheme 8.42) Following hydrogenolysis of the benzyl ester protective groups to give dicarboxylic acids **189**, the tripyrranes were reacted with pyrrole dialdehyde **113** in the presence of TFA, followed by oxidation with ferric chloride, to produce hydroxyoxybenziporphyrins **190**. The methyl-substituted version **190b** proved to be somewhat unstable, but could be efficiently oxidized with $PhI(OCOCF_3)_2$ to give the further modified benziporphyrin **191**. This derivative was very stable and possessed a strong diatropic ring current. Depending on concentration, the proton NMR spectra showed the internal CH resonance between −7 and −8 ppm. Reaction with silver(I) acetate gave the related silver(III) complex **192**. Benzitripyrrane **189b** also reacted with furan, thiophene, and selenophene dialdehydes **7a–c** to give analogous diketones **193a–c**, all of which proved to be highly aromatic structures [23].

p-Benziporphyrins **194** have been prepared, albeit in low yields, by reacting dicarbinols **195** with pyrrole and aromatic aldehydes in the presence of $BF_3.Et_2O$ (Scheme 8.43). The *p*-phenylene unit is tilted relative to the porphyrinoid plane and undergoes a teeter-tottering motion that averages out the environments for the inner and outer protons. However, at low temperatures, the proton NMR spectrum showed the inner protons at 2.32 ppm and the outer

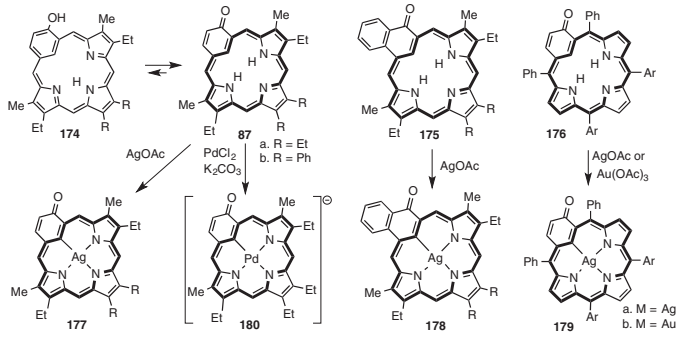

Scheme 8.40 Metalation of oxybenzi- and oxynaphthiporphyrins.

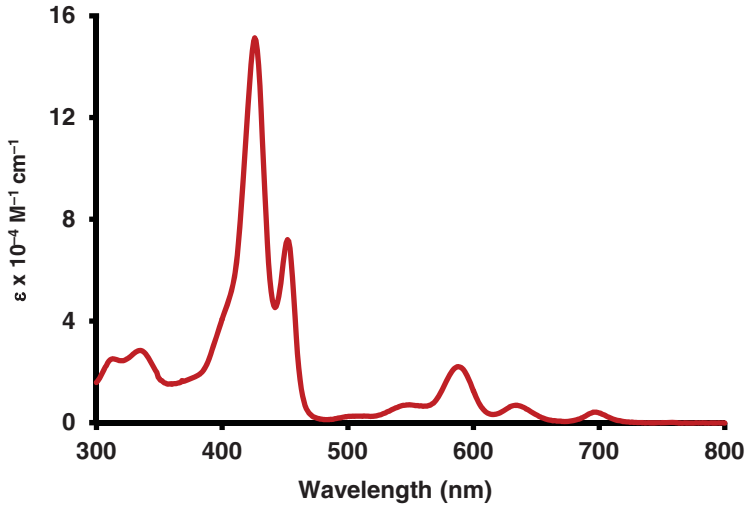

Figure 8.6 UV–vis spectrum of oxybenziporphyrin **87a** in CH_2Cl_2.

protons at 7.68 ppm, which confirmed the presence of an aromatic ring current within this system. *p*-Benziporphyrin reacted with palladium(II) chloride to give a metal complex **196** that underwent a ring contraction reaction in the presence of potassium carbonate to generate palladium(II) carbaporphyrin complexes **197**. Similar ring contraction reactions have also been reported using gold and rhodium reagents [32, 34].

8.10 Miscellaneous Carbaporphyrinoid Systems

The same types of synthetic strategies have been used to prepare a number of other carbaporphyrinoid systems. Cycloheptatriene dialdehyde **198** reacted with tripyrranes under standard "3 + 1" conditions to give tropiporphyrins **199** (Scheme 8.44). This system is aromatic, and the proton NMR spectrum of **199a** showed the inner CH at 7.3 ppm. However, the *meso*-protons appeared at 8.0 and 9.2 ppm, values that are nowhere near as far downfield as those reported for aromatic porphyrinoids such as carbaporphyrins **78** and **81**. This is due to strain from the seven-membered ring that prevents the macrocycle from being planar. Tropiporphyrins **199** reacted with silver(I) acetate and DBU in refluxing pyridine to give silver(III) derivatives **200**. The diene component of the seven-membered ring for **199** underwent a cycloaddition reaction with dimethyl acetylenedicarboxylate in refluxing xylenes to give a Diels–Alder adduct **201**. Interestingly, this cage structure exhibited greatly increased aromatic characteristics, and the proton NMR spectrum showed the inner CH resonance at −9.2 ppm while the *meso*-protons appeared at 9.47 and 9.86 ppm. Reduction with diimide afforded the related strongly diatropic dihydroporphyrinoid **202** [14, 16].

Pyrazole dialdehydes **203** condensed with tripyrrane **74a** in the presence of TFA to give pyrazolophlorins **204**, and these could be oxidized with ferric chloride or silver acetate to produce the fully conjugated porphyrinoids **205** (Scheme 8.45). This system is cross-conjugated and only shows weak diatropic character. Reaction with nickel(II) or palladium(II) acetate gave good yields of the corresponding metal complexes **206** [16, 32].

Carbaporphyrinoid structures with pyridine subunits have been described (Scheme 8.46) [16]. Pyritripyrranes **207** were reacted with pyrrole and benzaldehyde in the presence of

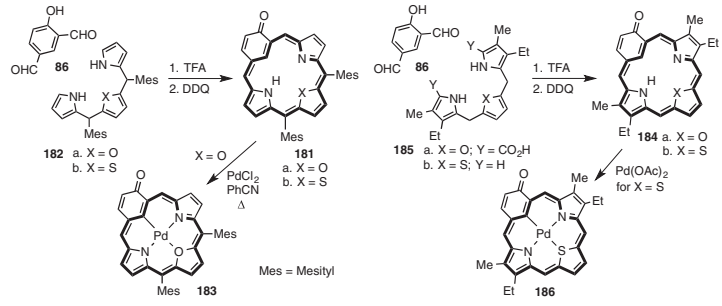

Scheme 8.41 Synthesis and metalation of hetero-oxybenziporphyrins.

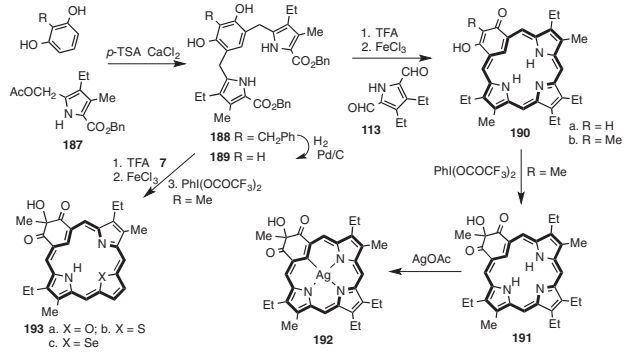

Scheme 8.42 Synthesis and metalation of oxidized benziporphyrins.

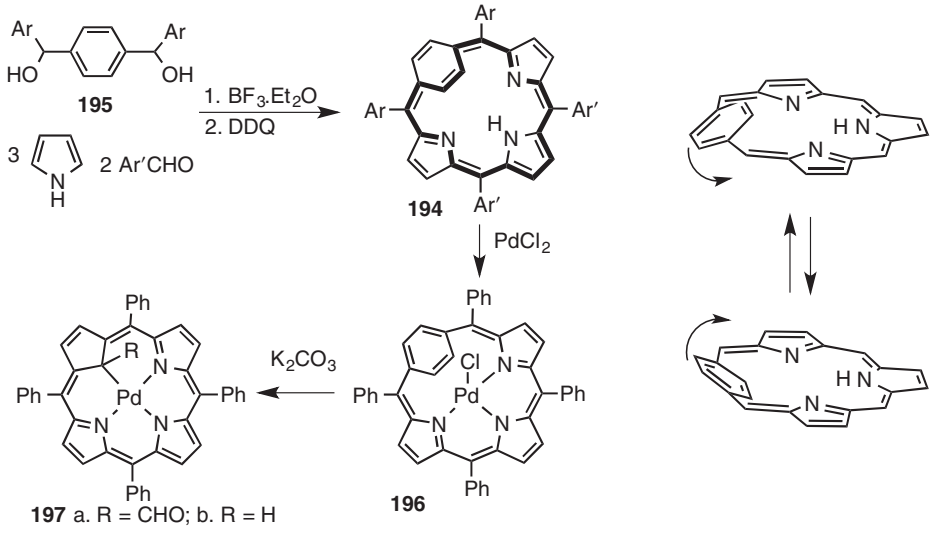

Scheme 8.43 Synthesis, conformation, and palladium(II)-mediated ring contraction of *p*-benziporphyrins.

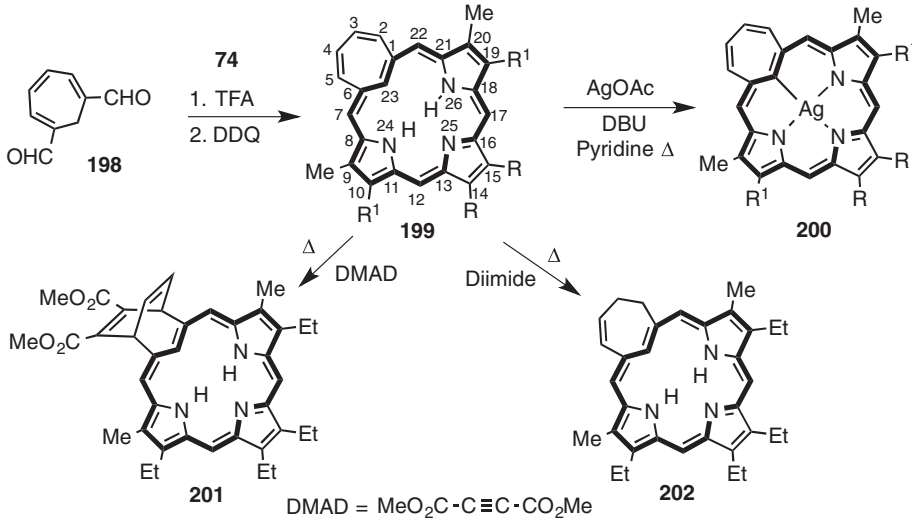

Scheme 8.44 Synthesis and reactions of tropiporphyrins.

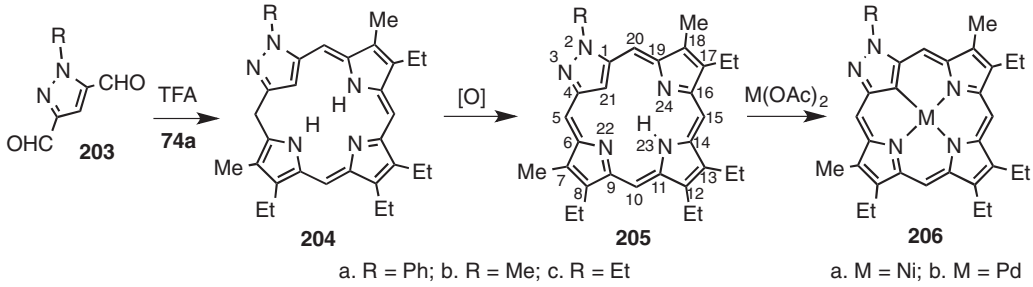

Scheme 8.45 Synthesis and metalation of pyrazoloporphyrins.

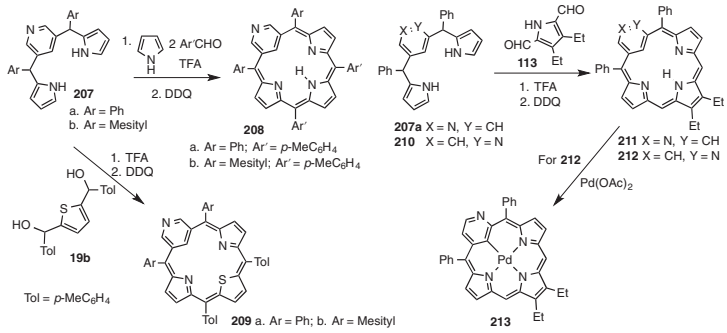

Scheme 8.46 Synthesis and metalation of N-confused pyriporphyrins.

TFA, and following oxidation with DDQ, nonaromatic pyriporphyrins **208** were generated. Reaction of **207** with thiophene dicarbinol **19b** similarly afforded thiapyriporphyrins **209**. Pyritripyrranes **207a** and **210** condensed with pyrrole dialdehyde **113** in the presence of TFA to give, following oxidation with DDQ, the N-confused pyriporphyrins **211** and **212**, respectively. Pyriporphyrin **212** reacted with palladium(II) acetate to give the corresponding palladium complex **213**. An aromatic pyriporphyrin **214** was obtained by reacting pyridine dialdehyde **215** with tripyrrane **74a** in the presence of TFA, followed by *N*-substitution with phenyl chloroformate (Scheme 8.47). The proton NMR spectrum for **214** gave a peak at −6.66 ppm for the internal CH, and the *meso*-protons gave signals between 8.53 and 9.56 ppm. The UV–vis-spectrum was also very porphyrin-like with a strong Soret band at 431 nm.

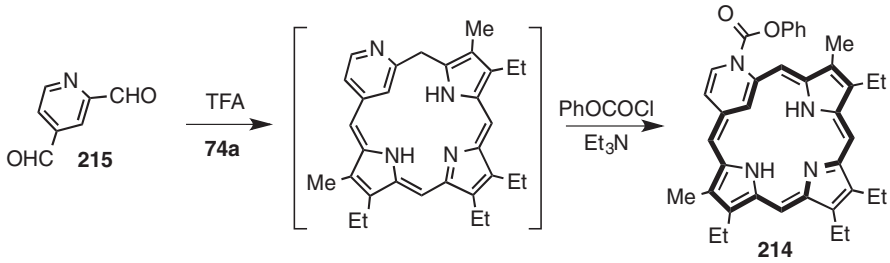

Scheme 8.47 Synthesis of an aromatic dihydropyriporphyrin.

Carbaporphyrinoids with exocyclic double bonds have been synthesized [35]. For instance, Knoevenagel condensation of diethyl malonate with isophthalaldehyde gave **216**, which reacted with pyrrole in the presence of an acid catalyst to afford benzitripyrrane **217** (Scheme 8.48). Condensation with furan or thiophene dicarbinols gave benziporphyrin products **218** that favor tautomers with cross-conjugated exocyclic double bonds. Expanded porphyrinoids were also generated in these reactions [35].

Heteroporphyrins with inverted furan and thiophene rings have also been investigated [15, 16]. Thiophene dicarbinol **219** reacted with pyrrole and benzaldehyde in the presence of $BF_3.Et_2O$ to give, following oxidation with *p*-chloranil, the S-confused thiaporphyrin **220** (Scheme 8.49). The proton NMR spectrum for **220** showed that the system is only slightly diatropic. Further oxidation of **220** gave the aromatic thiolactone **221**. Reaction of furan dicarbinol **222** with pyrrole and *p*-tolualdehyde gave rise to pyrrole-appended O-confused chlorin **223**, but when the reaction was carried out in the presence of ethanol the related ethoxy-derivative **224** was isolated instead (Scheme 8.50). Both of these carbaporphyrinoids exhibited strongly aromatic characteristics. Metalation of **224** with silver(I) acetate gave the silver(III) complex **225**. Treatment with TFA led to demetalation to give a cationic species that slowly converted into carbaporpholactone **226**. This could then be remetalated with silver(I) acetate to afford **227**. Interestingly, silver(III) complex **227** reacted with methyl or dimethylamine to afford amino-substituted porphyrinoids **228**, and oxidation of **228b** with DDQ afforded the unusual ring fused products **229** and **230**.

8.11 Dicarbaporphyrinoids

Porphyrin analogues with two carbons within the macrocyclic cavity have been prepared. The first example of this type was obtained by reacting 3,4-diethylpyrrole with indene dialdehyde

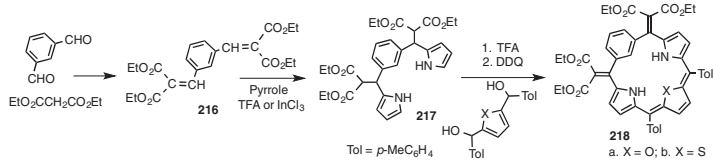

Scheme 8.48 Synthesis of heterobenziporphyrins with exocyclic double bonds.

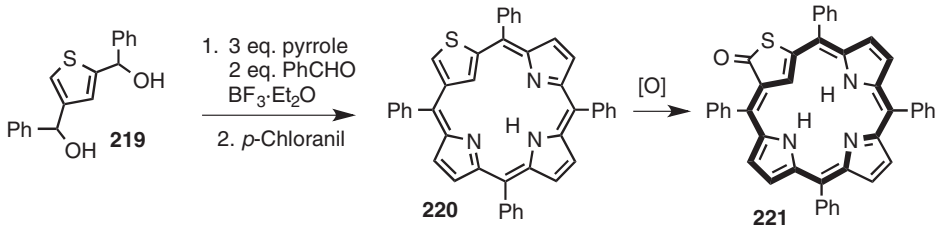

Scheme 8.49 Synthesis of tetraphenyl S-confused thiaporphyrin and its oxidation to an aromatic thiolactone.

231 in the presence of TFA. Following oxidation with ferric chloride, dicarbaporphyrin **232** was isolated (Scheme 8.51). The dicarbaporphyrin was somewhat unstable but proved to be strongly diatropic, and the proton NMR spectrum showed the internal CH and NH resonances at −5.68 and −4.82 ppm, respectively, while the *meso*-protons afforded a 4H singlet at 9.79 ppm. Addition of TFA produced an aromatic *C*-protonated cation **232**H^+. The related *adj*-dicarbaporphyrin **233** was generated by reacting diindenylmethane **234** with dipyrrylmethane dialdehyde **235** and potassium hydroxide in refluxing ethanol [36]. The proton NMR spectrum for **233** also showed the presence of a strong diamagnetic ring current (Figure 8.7). This aromatic system underwent *C*-protonation to afford monocation **233**H^+ and in neat TFA produced a dicationic species **233**$H_2^{2+}$with two internal methylene units. Reaction of **233** with palladium(II) acetate afforded an unprecedented palladium(IV) sandwich complex **236** between two palladium(II) dicarbaporphyrin units [36]. Dipentadienylmethane **237** also reacted with dialdehyde **235** under basic conditions to give the aromatic dicarbachlorin **238** (Scheme 8.51). This system represents the first free-base carbaporphyrinoid to be described with an internal methylene unit [37]. The UV–vis spectrum for **238** was still very porphyrin-like (Figure 8.8), giving a Soret band at 398 nm and four Q bands between 500 and 700 nm.

Chart 8.3 shows the structures of a selection of dicarbaporphyrinoid systems [16]. 23-Carbaazuliporphyrin **239** proved to be somewhat unstable, but exhibited significant diatropic character. The proton NMR spectrum showed the inner indene, azulene, and NH protons at 0.52, 1.25, and 1.99 ppm, respectively. An isomeric system **240** with adjacent indene and azulene units proved to be far more robust and again exhibited significant aromatic character. In the presence of excess TFA, the dicarbaporphyrinoids both gave *C*-protonated dications **239**H_2^{2+} and **240**H_2^{2+} with enhanced diatropic properties. Dicarbaporphyrinoid **240** reacted with silver(I) acetate in the presence of methanol to give a nonaromatic dimethoxy derivative **241**. Fully aromatic dicarbaporphyrinoids **242** with resorcinol subunits have been described, although these proved to be rather insoluble in solvents other than DMSO. *adj*-Diazuliporphyrins **243** have been prepared that show significant aromatic character, but these could only be isolated in the cationic form shown. Metalation of **243** with palladium(II) acetate afforded a zwitterionic palladium(II) complex **244**. The proton NMR spectrum of the palladium complex in d_6-DMSO indicated that the macrocycle retained diatropic character. Nonaromatic dioxa- and dithiadiazuliporphyrins **245** have been reported, and these can be oxidized with excess DDQ to afford aromatic dications **246**. Dioxadicarbaporphyrins **247** have also been prepared by the cyclization of dicarbadioxobilins **248** with TFA-paraformaldehyde or aromatic aldehydes with $BF_3.Et_2O$.

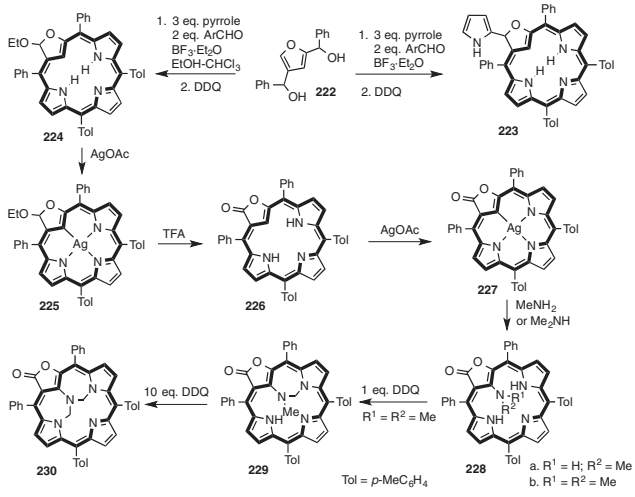

Scheme 8.50 Synthesis and reactions of O-confused oxaporphyrins.

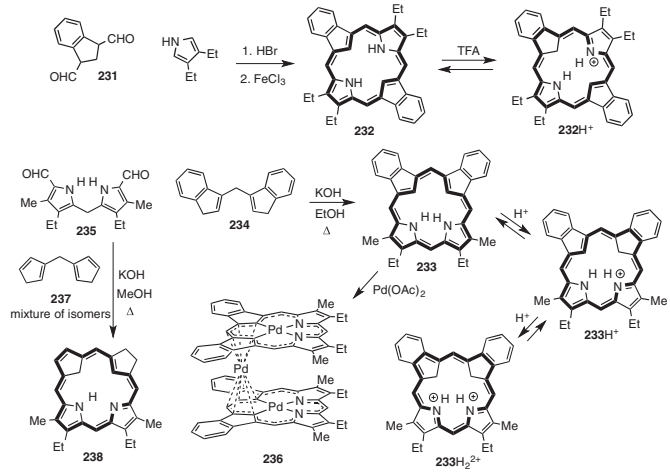

Scheme 8.51 Synthesis and metalation of dicarbaporphyrins and a dicarbachlorin.

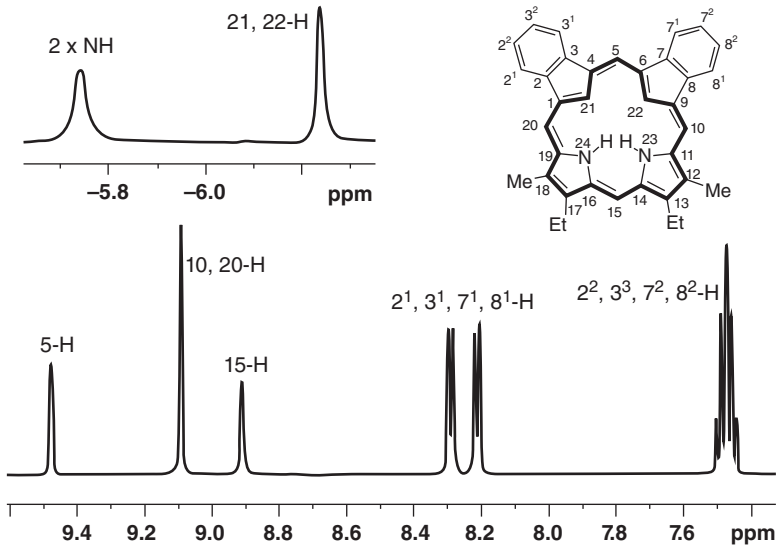

Figure 8.7 Partial 500 MHz proton NMR spectrum of *adj*-dibenzodicarbaporphyrin **233** in $CDCl_3$ showing the upfield and downfield regions.

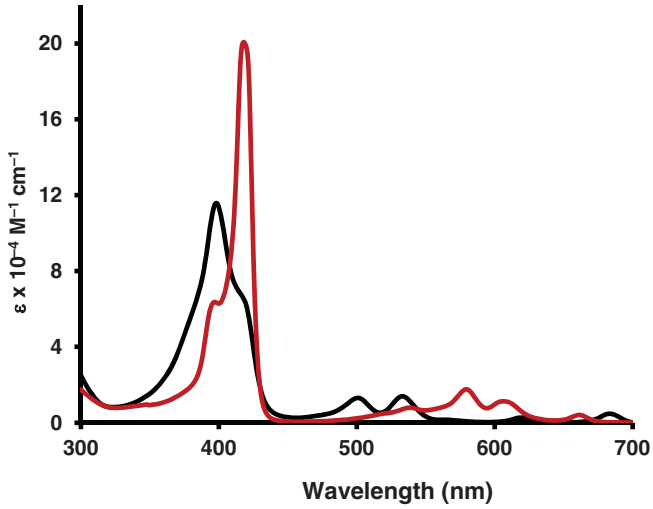

Figure 8.8 UV–vis spectra of *adj*-dicarbachlorin **238** in 1% Et_3N-$CHCl_3$ (black line, free base) and 0.05% TFA-$CHCl_3$ (monocation **238**H^+).

These porphyrinoids have strong aromatic ring currents, and the proton NMR spectrum for **247a** gave a resonance for the internal indene protons at −3.87 ppm. Nonaromatic oxodibenziphlorins **249** and dibenziporphyrins **250** have also been described [38]. Hence, a wide range of dicarbaporphyrinoid systems have been reported that show diverse reactivity and spectroscopic characteristics [15, 16].

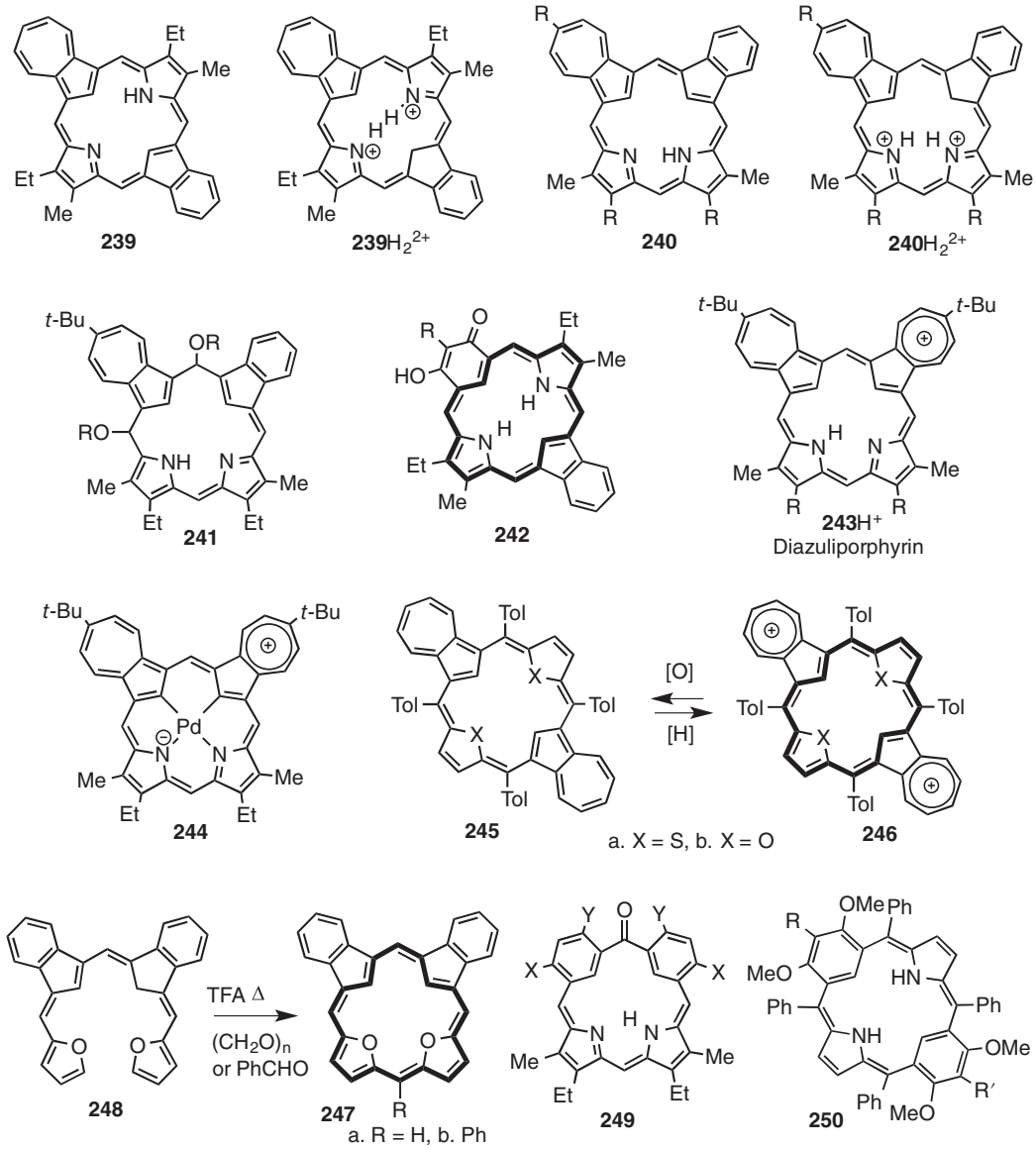

Chart 8.3 Selected dicarbaporphyrinoid systems.

8.12 Tetracarbaporphyrinoids

Attempts to extend these investigations into the synthesis of tetracarbaporphyrins have been far less successful. Quatyrin (**251**), the theoretically important hydrocarbon analogue of the porphyrins, remains elusive although DFT and NICS calculations indicate that this structure is planar and strongly aromatic [39]. The carbon skeleton for quatyrin is present in calix[4]azulenes **252**, which can be prepared by reacting azulenes with paraformaldehyde in the presence of Florisil® (Scheme 8.52). Treatment of **252b** with triphenylcarbenium hexafluorophosphate afforded a partially conjugated dication **253** that can be considered to be

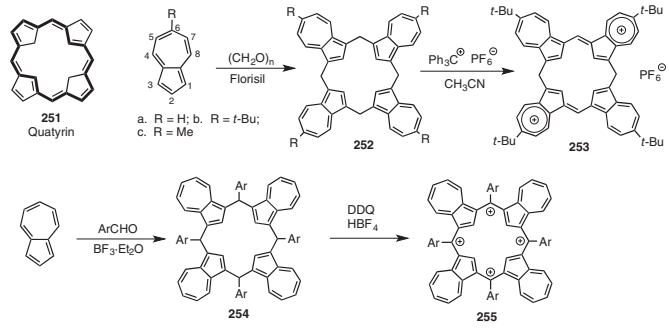

Scheme 8.52 Tetracarbaporphyrinoids.

a dihydroquatyrin. This species gave dark blue solutions and showed a strong absorption at 616 nm in its UV–vis spectrum. Oxidation of tetraarylcalix[4]azulenes **254** with DDQ in the presence of tetrafluoroboric acid gave the tetraazuliporphyrin tetracations **255**. Although these tetracations can be considered to be didehydroquatyrins, DFT calculations demonstrate that they have severely distorted conformations, and the macrocycles do not possess the paratropic ring current that would be expected for the conjugated species [22].

8.13 Related Porphyrin Analogues

Many other modifications to the porphyrin core have been investigated [9, 15, 16]. In an attempt to prepare silaporphyrins, silole dicarbinol **256** was reacted with pyrrole and *p*-tolualdehyde in the presence of $BF_3.Et_2O$ (Scheme 8.53). Following oxidation with DDQ, a tetrahydrosilaporphyrin **257** and the related phlorin **258** were isolated. Further oxidation of **258** led to a complex rearrangement that afforded a low yield of isocarbacorrole **259**. Metalation with silver tetrafluoroborate or copper(II) acetate afforded the aromatic silver(III) and copper(III) carbacorrole complexes **260a** and **260b** [15, 16].

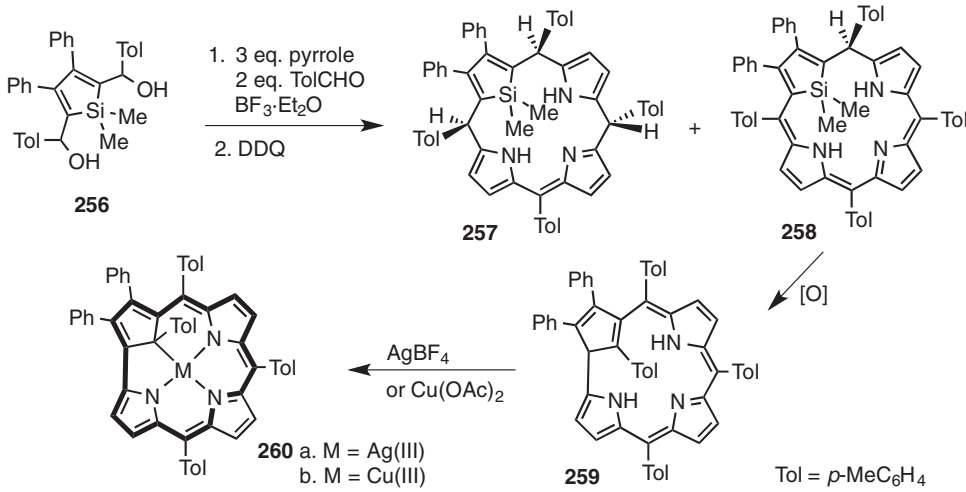

Scheme 8.53 Synthesis of silaporphyrinoids and metallocarbacorroles.

Modifications to preformed porphyrins (e.g., *meso*-tetraphenylporphyrin) can be used to prepare numerous analogue systems including porpholactones **261** and morpholinochlorins **262** (Chart 8.4) [40]. Oxypyriporphyrins **263** provide another example of a porphyrinoid system that can be prepared by modification of porphyrin precursors, although it is also readily accessible by the "3 + 1" variant on the MacDonald condensation [16]. Porphyrinoids **261**–**263** are all fully aromatic systems and have been the topic of many investigations. A full discussion of these types of structures is given in Chapter 6. Metallocenoporphyrins such as **264–266** provide another variation on the theme. Even though ferrocene or ruthenocene units have replaced a pyrrole ring, the macrocycles still retain a degree of aromatic or antiaromatic character, which indicates that π-delocalization can be transferred through the d-orbitals of the metallocene [9, 15, 16]. Many examples of expanded porphyrins with heterocyclic or

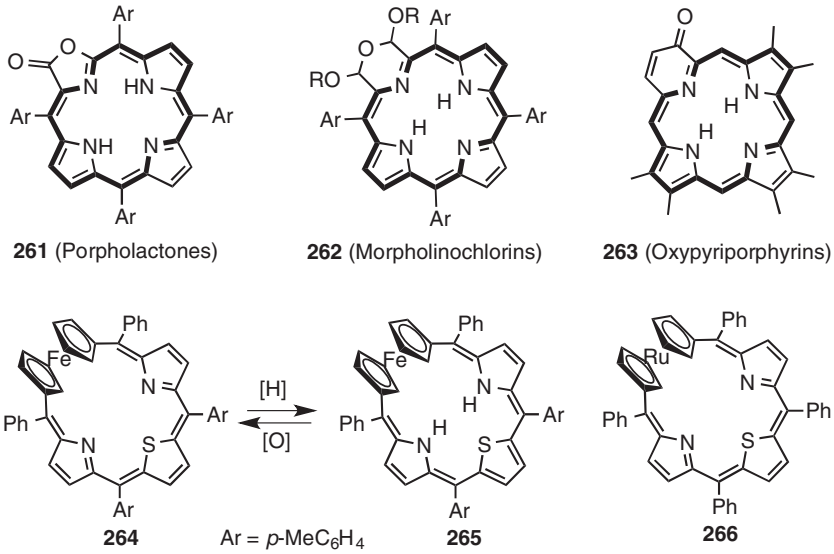

Chart 8.4 Selected porphyrin analogues with nonpyrrolic subunits.

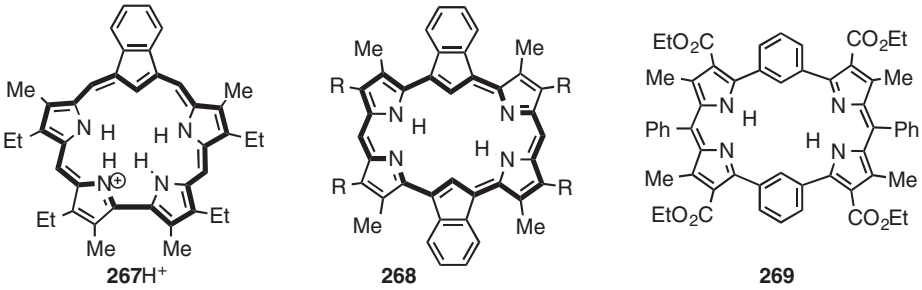

Chart 8.5 Selected expanded carbaporphyrinoid systems.

carbocyclic subunits have been described, such as carbasapphyrin **267**, dicarbahexaphyrin **268**, and dibenzihexaphyrins **269** (Chart 8.5), but these types of systems are not considered in this review [16, 41, 42].

8.14 Conclusions

Core modification of the porphyrin framework provides access to a multitude of macrocyclic systems whose properties vary considerably. Replacement of nitrogen atoms with oxygen, sulfur, selenium, tellurium, phosphorus, and carbon afford porphyrin-like structures with greatly altered coordination chemistry and varying degrees of aromatic character. The reactivity of these analogues is often vastly modified, and many intriguing chemical transformations have been observed. Furthermore, these systems are being investigated for many types of applications including uses as photosensitizers in photodynamic therapy, as agents for the treatment of leishmaniasis, and in molecular recognition studies. Metalated derivatives have been shown to have catalytic activity and also have promise as colorimetric and fluorescent

chemosensors [43]. The remarkable range of porphyrin analogues that can be generated while retaining the original framework is astounding, and this area is likely to remain a fertile area of study for many years to come.

Acknowledgments

The author's work in this area has been supported by the National Science Foundation, most recently under grant no. CHE-1465049, and the Petroleum Research Fund, administered by the American Chemical Society.

References

1 Johnson, A.W. (1975). Structural analogs of porphyrins. In: *Porphyrins and Metalloporphyrins* (ed. K.M. Smith), 729–754. Amsterdam: Elsevier.
2 Latos-Grażyński, L. (2000). Core-modified heteroanalogues of porphyrins and Metalloporphyrins. In: *The Porphyrin Handbook*, vol. 2 (ed. K.M. Kadish, K.M. Smith and R. Guilard), 361–416. San Diego: Academic Press.
3 Lash, T.D. (2000). Syntheses of novel porphyrinoid chromophores. In: *The Porphyrin Handbook*, vol. 2 (ed. K.M. Kadish, K.M. Smith and R. Guilard), 125–199. San Diego: Academic Press.
4 Gupta, I. and Ravikanth, M. (2006). Recent developments in heteroporphyrins and their analogues. *Coordination Chemistry Reviews* 250: 468–518.
5 Lash, T.D. (2011). Origin of aromatic character in porphyrinoid systems. *Journal of Porphyrins and Phthalocyanines* 15: 1093–1115.
6 a. Vogel, E. (1993). The porphyrins from the 'Annulene Chemist's' perspective. *Pure and Applied Chemistry* 65: 143–152. b. Vogel, E. (1996). Porphyrinoid macrocycles: a cornucopia of novel chromophores. *Pure and Applied Chemistry* 68: 1355–1360.
7 Broadhurst, M.J., Grigg, R., and Johnson, A.W. (1971). Synthesis of Porphin analogues containing furan and/or thiophen rings. *Journal of the Chemical Society C* 2681–2690.
8 a. Ulman, A. and Manassen, J. (1975). Synthesis of new tetraphenylporphyrin molecules containing heteroatoms other than nitrogen. I. tetraphenyl-21,23-dithiaporphyrin. *Journal of the American Chemical Society* 97: 6540–6544. b. Ulman, J. and Manassen, J. (1979). Synthesis of tetraphenylporphyrin molecules containing heteroatoms other than nitrogen. Part 4. Symmetrically and unsymmetrically substituted tetraphenyl-21,23-dithiaporphyrins. *Journal of the Chemical Society, Perkin Transactions* 1: 1066–1069.
9 Brückner, C., Akhigbe, J., and Samankumara, L.P. (2014). Porphyrin analogs containing non-Pyrrolic heterocycles. In: *Handbook of Porphyrin Science – With Applications to Chemistry, Physics, Material Science, Engineering, Biology and Medicine*, vol. 31 (ed. K.M. Kadish, K.M. Smith and R. Guilard), 1–275. Singapore: World Scientific Publishing.
10 Minonov, A. (2012). Transition metal complexes of porphyrins and porphyrinoids. In: *Handbook of Porphyrin Science – With Applications to Chemistry, Physics, Material Science, Engineering, Biology and Medicine*, vol. 18 (ed. K.M. Kadish, K.M. Smith and R. Guilard), 303–413. Singapore: World Scientific Publishing.
11 Vogel, E., Haas, W., Knipp, B. et al. (1988). Tetraoxaporphyrin Dication. *Angewandte Chemie, International Edition in English* 27: 406–409.

12 Matano, Y. and Imahori, H. (2009). Phosphole-containing calixpyrroles, calixphyrins, and porphyrins: synthesis and coordination chemistry. *Accounts of Chemical Research* 42: 1193–1204.

13 Lash, T.D. (2000). Carbaporphyrinoids: taking the heterocycle out of nature's [18]annulene. *Synlett* 279–295.

14 Lash, T.D. (2007). Recent advances on the synthesis and chemistry of carbaporphyrins and related porphyrinoid systems. *European Journal of Organic Chemistry* 5461–5481.

15 Pawlicki, M. and Latos-Grażyński, L. (2010). Carbaporphyrinoids – synthesis and coordination properties. In: *Handbook of Porphyrin Science – with Applications to Chemistry, Physics, Material Science, Engineering, Biology and Medicine*, vol. 2 (ed. K.M. Kadish, K.M. Smith and R. Guilard), 104–192. Singapore: World Scientific Publishing.

16 Lash, T.D. (2012). Carbaporphyrins and related systems. Synthesis, characterization, reactivity and insights into the nature of Porphyrinoid aromaticity. In: *Handbook of Porphyrin Science – With Applications to Chemistry, Physics, Material Science, Engineering, Biology and Medicine*, vol. 16 (ed. K.M. Kadish, K.M. Smith and R. Guilard), 1–329. Singapore: World Scientific Publishing.

17 Aronoff, S. and Calvin, M. (1943). The porphyrin-like products of the reaction of pyrrole with benzaldehyde. *Journal of Organic Chemistry* 8: 205–223.

18 Senge, M.O. (2011). Extroverted confusion – Linus Pauling, Melvin Calvin, and porphyrin isomers. *Angewandte Chemie International Edition* 50: 4272–4277.

19 a. Srinivasan, A. and Furuta, H. (2005). Confusion approach to porphyrinoid chemistry. *Accounts of Chemical Research* 38: 10–20. b. Toganoh, M. and Furuta, H. (2012). Blooming of confused porphyrinoids – fusion, expansion, and more confusion. *Chemical Communications* 48: 937–954.

20 Lash, T.D. and Hayes, M.J. (1997). Carbaporphyrins. *Angewandte Chemie, International Edition in English* 36: 840–842.

21 Lash, T.D. and Chaney, S.T. (1997). Azuliporphyrin, a case of borderline Porphyrinoid aromaticity. *Angewandte Chemie, International Edition in English* 36: 839–840.

22 Lash, T.D. (2016). Out of the blue! azuliporphyrins and related carbaporphyrinoid systems. *Accounts of Chemical Research* 49: 471–482.

23 Lash, T.D. (2015). Benziporphyrins, a unique platform for exploring the aromatic characteristics of porphyrinoid systems. *Organic & Biomolecular Chemistry* 13: 7846–7878.

24 Lash, T.D. (1995). Oxybenziporphyrin, an aromatic semiquinone porphyrin analog with pathways for 18π-electron delocalization. *Angewandte Chemie, International Edition in English* 34: 2533–2535.

25 Lash, T.D. (1996). Porphyrin synthesis by the "3 + 1" approach: new applications for an old methodology. *Chemistry – A European Journal* 2: 1197–1200.

26 Li, D. and Lash, T.D. (2014). Synthesis and reactivity of carbachlorins and carbaporphyrins. *Journal of Organic Chemistry* 79: 7112–7121.

27 Adiraju, V.A.K., Ferrence, G.M., and Lash, T.D. (2016). Rhodium(I), rhodium(III) and iridium(III) Carbaporphyrins. *Dalton Transactions* 45: https://doi.org/10.1039/C6DT03093A.

28 Stateman, L.M. and Lash, T.D. (2015). Syntheses of carbaporphyrinoid systems using a carbatripyrrin methodology. *Organic Letters* 17: 4530–4533.

29 Berlicka, A., Dutka, P., Szterenberg, L., and Latos-Grażyński, L. (2014). Towards true carbaporphyrinoids: synthesis of 21-Carba-23-thiaporphyrin. *Angewandte Chemie International Edition* 53: 4885–4889.

30 a. Lash, T.D., Lammer, A.D., and Ferrence, G.M. (2011). Neo-confused porphyrins, a new class of porphyrin isomers. *Angewandte Chemie International Edition* 50: 9718–9721. b. Li, R., Lammer, A.D., Ferrence, G.M., and Lash, T.D. (2014). Synthesis, structural characterization, aromatic properties and metalation of neo-confused porphyrins, a newly discovered class of porphyrin isomers. *Journal of Organic Chemistry* 79: 4078–4093.

31 Stępień, M. and Latos-Grażyński, L. (2005). Benziporphyrins: exploring arene chemistry in macrocyclic environment. *Accounts of Chemical Research* 38: 88–98.

32 Lash, T.D. (2014). Metal complexes of carbaporphyrinoid systems. *Chemistry – An Asian Journal* 9: 682–705.

33 Stępień, M., Latos-Grażyński, L., and Szterenberg, L. (2007). 22-hydroxybenziporphyrin: switching of antiaromaticity by phenol-keto tautomerization. *Journal of Organic Chemistry* 72: 2259–2270.

34 Szyszko, B. and Latos-Grażyński, L. (2015). Core chemistry and skeletal rearrangements of porphyrinoids and metalloporphyrinoids. *Chemical Society Reviews* 44: 3588–3616.

35 Singh, K., Abebayehu, A., Mulugeta, E. et al. (2016). Recent advances in *meso*-alkylidenyl carbaporphyrinoids. *Journal of Porphyrins and Phthalocyanines* 20: 21–34.

36 AbuSalim, D.I., Ferrence, G.M., and Lash, T.D. (2014). Synthesis of an *adj*-dicarbaporphyrin and the formation of an unprecedented tripalladium sandwich complex. *Journal of the American Chemical Society* 136: 6763–6772.

37 Lash, T.D., AbuSalim, D.I., and Ferrence, G.M. (2015). *Adj*-dicarbachlorin, the first example of a free base carbaporphyrinoid system with an internal methylene unit. *Chemical Communications* 51: 15952–15955.

38 Fosu, S.C., Ferrence, G.M., and Lash, T.D. (2014). Synthesis and metalation of dimethoxy-benziporphyrins, thiabenziporphyrins and dibenziporphyrins. *Journal of Organic Chemistry* 79: 11061–11074.

39 AbuSalim, D.I. and Lash, T.D. (2013). Relative stability and diatropic character of carbaporphyrin, dicarbaporphyrin, tricarbaporphyrin and quatyrin tautomers. *Journal of Organic Chemistry* 78: 11535–11548.

40 Brückner, C. (2016). The breaking and mending of *meso*-tetraarylporphyrins: transmuting the pyrrole building blocks. *Accounts of Chemical Research* 49: 1080–1092.

41 Sessler, J.L. and Seidel, D. (2003). Synthetic expanded porphyrin chemistry. *Angewandte Chemie International Edition* 42: 5134–5175.

42 a. Chandrashekar, T.K. and Venkatramin, S. (2003). Core-modified expanded porphyrins: new generation organic materials. *Accounts of Chemical Research* 36: 676–691. b. Misra, R. and Chandrashekar, T.K. (2008). Structural diversity in expanded porphyrins. *Accounts of Chemical Research* 41: 265–279.

43 Ding, Y., Zhu, W.-H., and Xie, Y. (2017). Development of ion chemosensors based on porphyrin analogues. *Chemical Reviews* 116: 2203–2256.

9

Expanded Porphyrins

Atsuhiro Osuka and Takayuki Tanaka

Department of Chemistry, Kyoto University, Kyoto, Japan

9.1 Historical Background

The origin of expanded porphyrin can be traced back to R.B. Woodward's serendipitous discovery of sapphyrin **1**, a pentapyrrolic macrocycle having one direct linkage between two pyrrole units (i.e., [22]pentaphyrin(1.1.1.1.0)), while he was working on the synthesis of vitamin B_{12} in 1966 (Figure 9.1) [1]. Another pioneering study on its synthesis was reported by Johnson and co-workers in 1972 [2]. However, it was not until 1990 when an improved and rational synthesis of sapphyrin was described by Sessler and co-workers [3]. Next to this, vinylogous porphyrins were extensively explored by LeGoff and Franck [4, 5]. One example is platyrin **2** (i.e., [22]porphyrin(3.1.3.1)), reported in 1978. Gossauer and co-workers first synthesized [22]pentaphyrin(1.1.1.1.1) and [26]hexaphyrin(1.1.1.1.1.1), and prepared the first metal complexes of [26]hexaphyrin such as **3** in 1993 [6]. These earlier examples all possess β-alkyl substituents that serve to stabilize the expanded porphyrins to some extent. Another important example, texaphyrin **4**, constituted a new class of expanded porphyrins containing Schiff-base coordination sites. Developed by Sesser et al. in 1988, its lanthanide metal complexes have been actively studied [7, 8]. Notably, the water-soluble texaphyrin Gd(III) complex **5**, called motexafin gadolinium (**MGd**) in the medicinal field, is a promising anticancer reagent, and has motivated many chemists to enter this field [9]. Larger expanded porphyrins having more than six pyrrolic subunits were also reported in the middle of 1990s. Undoubtedly, X-ray diffraction analyses helped significantly to reveal the unambiguous structures of large expanded porphyrins. In some cases, the solid-state structure exhibits nonplanar or highly twisted macrocycles. As a beautiful example, figure-eight octaphyrin **6** was reported by Vogel et al. in 1995 [10]. Since then, the relationship between molecular twist and conjugation (aromaticity) has become one of the most interesting topics in this field.

The *meso*-aryl-substituted sapphyrin **7** was first isolated in a low yield by Latos-Grażyński and co-workers in 1995 through simple condensation of pyrrole with benzaldehyde (Figure 9.2) [11]. In 1999, Cavaleiro and co-workers reported the isolation and solid-state structure of [26]hexaphyrin(1.1.1.1.1.1) **8** from the reaction mixture of pyrrole and pentafluorobenzaldehyde under modified reaction conditions [12]. In 2001, Osuka and co-workers reported the one-pot synthesis of expanded porphyrins, which was conducted simply by condensation of pyrrole and pentafluorobenzaldehyde each at ca. 67 mM in CH_2Cl_2 [13]. This concentration is about a 10-fold excess of that recommended for the synthesis of

Fundamentals of Porphyrin Chemistry: A 21st Century Approach, Volume 1, First Edition.
Edited by Penelope J. Brothers and Mathias O. Senge.
© 2022 John Wiley & Sons Ltd. Published 2022 by John Wiley & Sons Ltd.

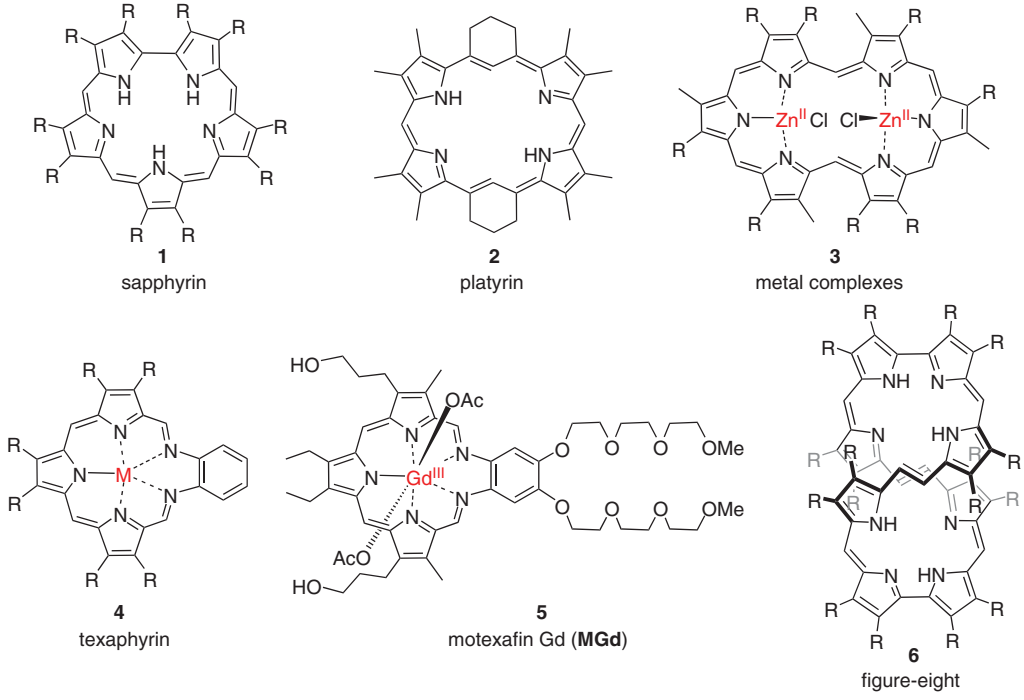

Figure 9.1 β-Alkyl-type expanded porphyrins reported until 1995.

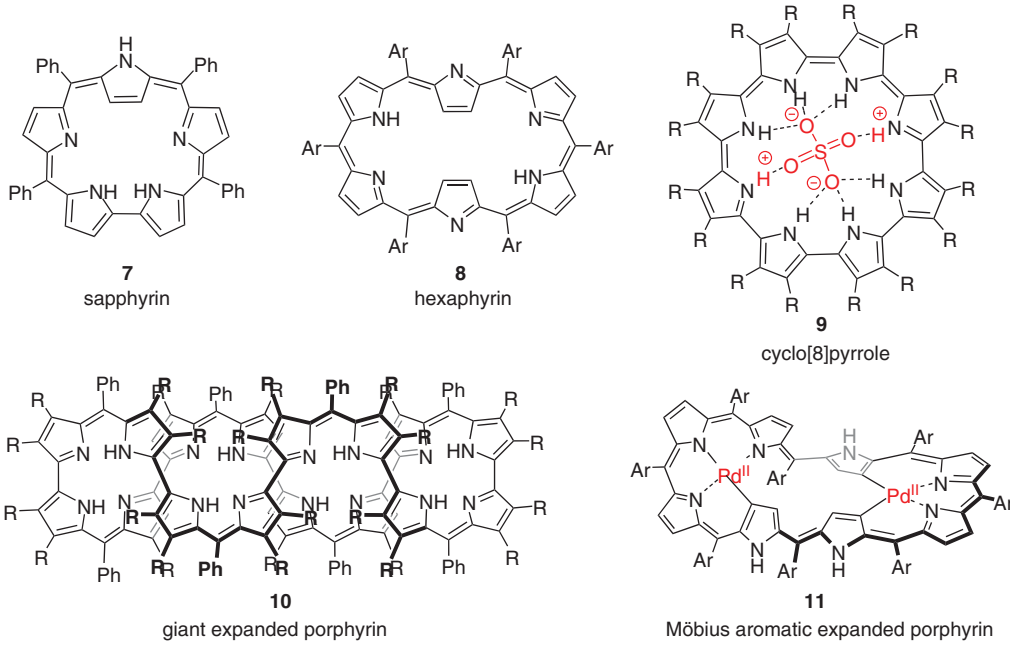

Figure 9.2 *meso*-Aryl-type expanded porphyrins reported after 1999.

tetraarylporphyrins [14]. This efficient synthetic protocol allowed the synthesis of a series of *meso*-(pentafluorophenyl)-substituted expanded porphyrins such as *N*-fused pentaphyrin **12**, hexaphyrin **8**, heptaphyrin **13**, octaphyrin **14**, nonaphyrin **15**, decaphyrin **16**, and even larger expanded porphyrins. Giant expanded porphyrins such as hexadecaphyrin(1.0.1.0.1.0.1.0.1.0.1.0.1.0.1.0) **10** were reported by Setsune et al. in 1999 using similar acid-catalyzed condensation reactions of a β-alkyl bipyrrole with benzaldehyde [15, 16]. Another unique expanded porphyrin, [30]octaphyrin(0.0.0.0.0.0.0.0) **9**, called cyclo[8]pyrrole, was reported in 2003 by Sessler and co-workers [17]. Cyclo[8]pyrroles and their derivatives have been actively used for anion binding studies [18]. Following the development of efficient syntheses for expanded porphyrins, their metal coordination chemistry has also been studied [19]. Metal ions in the expanded porphyrin cavities often serve to lock in conformations depending on the metal-coordination modes. The Möbius-twisted [36]octaphyrin(1.1.1.1.1.1.1.1) di-Pd(II) complex **11** was one of the first reported examples of Möbius aromatic expanded porphyrins with distinct Möbius aromaticity [20]. Subsequently, many expanded porphyrins with [4n] π-electrons have been converted to Möbius aromatic molecules using suitable stimuli [21–23].

9.2 One-Pot Synthesis of Expanded Porphyrins

In 2001 Osuka and co-workers reported that *meso*-pentafluorophenyl-substituted expanded porphyrins could be obtained in yields of 5–20% with a one-pot reaction sequence including acid-catalyzed condensation reaction of pyrrole with pentafluorobenzaldehyde, and subsequent oxidation with 2,3-dichloro-5,6-dicyano-1,4-benzoquinone (DDQ) (Figure 9.3). Although the separation of expanded porphyrins by silica-gel column chromatography was tedious, a series of expanded porphyrins were obtained as stable compounds, and all structures of the expanded porphyrins were characterized by single crystal X-ray diffraction analysis (Figure 9.4). *meso*-Aryl-substituted pentaphyrins yielded *N*-fused pentaphyrins, whereas non-fused pentaphyrins were not isolated [24]. [26]Hexaphyrin **8** exhibited a planar rectangular shape, whereas [32]heptaphyrin **13**, [36]octaphyrin **14**, [40]nonaphyrin **15**, and [44]decaphyrin **16** showed nonplanar conformations.

9.2.1 *meso*-Aryl-Substituted Expanded Porphyrins

Although the one-pot synthesis of *meso*-aryl-substituted expanded porphyrins was effective for 2,6-disubstituted electron-deficient aryl aldehydes such as 2,6-dichlorobenzaldehyde and 2,4,6-trifluorobenzaldehyde, neither 2-substituted nor 2,6-unsubstituted aryl aldehydes produced expanded porphyrins. Recently, similar acid-catalyzed condensation reactions of 1-formyl-2,6-dichloropyrimidine and 3,5-bis(trifluoromethyl)benzaldehyde with pyrrole were reported to give corresponding *meso*-aryl-substituted expanded porphyrins [25, 26].

Unlike standard porphyrins, which can take only an 18π-electronic state, expanded porphyrins can adopt several oxidation states by interconverting imine-type and amine-type pyrroles while keeping the molecule neutral. Naturally, expanded porphyrins display different conformational and electronic properties depending upon their oxidation states. For instance, [26]hexaphyrin(1.1.1.1.1.1) **8** was quantitatively reduced with $NaBH_4$ to [28]hexaphyrin(1.1.1.1.1.1) **17**, which was oxidized back to **8** upon treatment with DDQ. [26]Hexaphyrin **8** is a rectangular molecule with distinct Hückel aromaticity, while

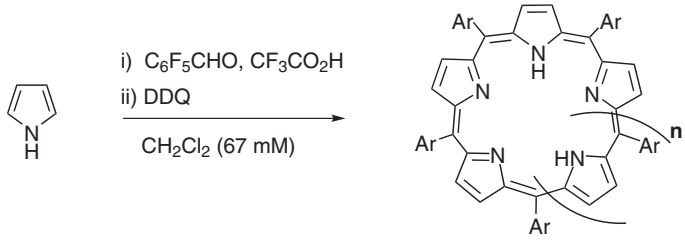

Figure 9.3 One-pot synthesis of *meso*-aryl-substituted expanded porphyrins.

N-fused [22]pentaphyrin(1.1.1.1.1)

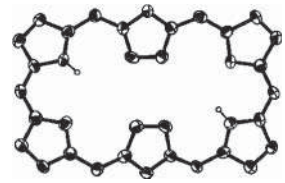

[26]hexaphyrin(1.1.1.1.1.1)

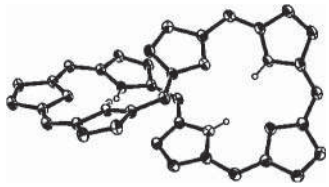

[32]heptaphyrin(1.1.1.1.1.1.1)

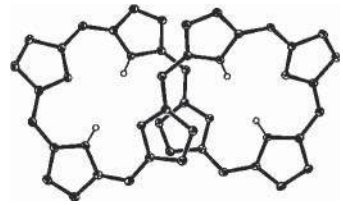

[36]octaphyrin(1.1.1.1.1.1.1.1)

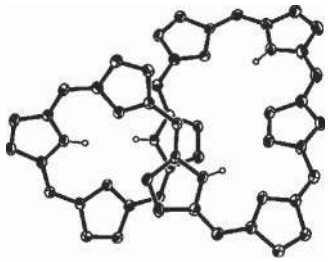

[40]nonaphyrin(1.1.1.1.1.1.1.1.1)

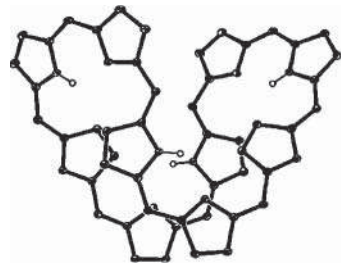

[44]decaphyrin(1.1.1.1.1.1.1.1.1.1.1)

*meso-C_6F_5 substituents were omitted for clarity

Figure 9.4 X-ray crystal structures of *N*-fused [22]pentaphyrin **12**, [26]hexaphyrin **8**, [32]heptaphyrin **13**, [36]octaphyrin **14**, [40]nonaphyrin **15**, and [44]decaphyrin **16**.

[28]hexaphyrin **17** shows fast conformational dynamics in solution involving twisted Möbius aromatic conformers and a planar Hückel antiaromatic conformer [27]. In the case of di-Au(III) complexes of hexaphyrin, the hexaphyrin framework was rigidly held to be a rectangular shape by double Au(III) metalation, and thus a distinct aromatic-antiaromatic switching was observed upon reduction from the di-Au(III) complex of [26]hexaphyrin **18** to the corresponding [28]hexaphyrin complex **19** [28] (Figure 9.5).

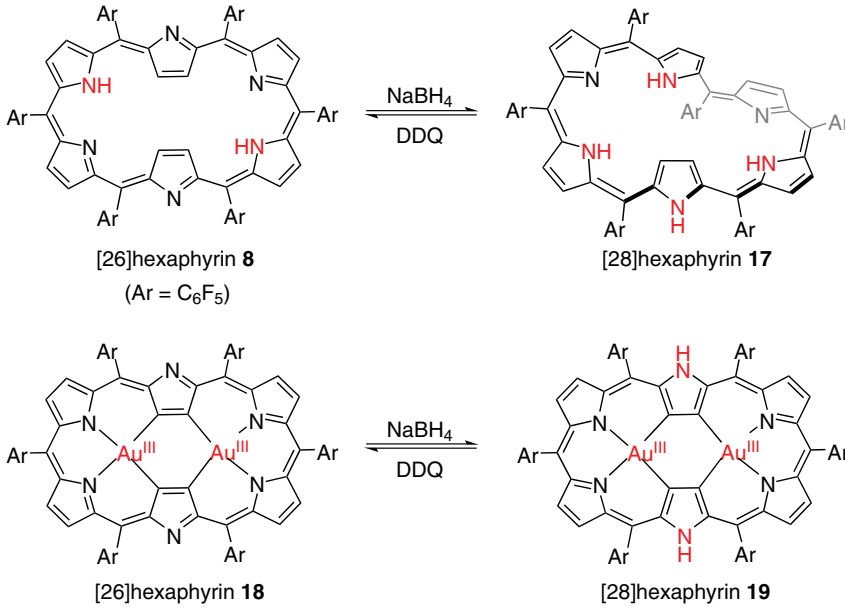

Figure 9.5 Redox interconversions of [26]hexaphyrins and [28]hexaphyrins.

Similar stable redox pairs were characterized for *N*-fused [22]/[24]pentaphyrins (**12** and **20**), [36]/[38]octaphyrins (**14** and **21**), [40]/[42]nonaphyrins (**15** and **22**), and [44]/[46]decaphyrins (**16** and **23**). *N*-Fused [22]pentaphyrin **12** is a Hückel aromatic molecule, and *N*-fused [24]pentaphyrin **20** is a weakly Hückel antiaromatic molecule. [36]Octaphyrin **14** is a nonaromatic molecule, while [38]octaphyrin **21** is a Hückel aromatic molecule (Figure 9.6).

9.2.2 *β*-Substituted Expanded Porphyrins

β-Perfluoro-*meso*-aryl-substituted expanded porphyrins were synthesized in moderate yields by the condensation of pentafluorobenzaldehyde with 3,4-difluoropyrrole using $BF_3 \cdot OEt_2$ as acid catalyst (Figure 9.7) [29]. *β*-Perfluoro-[26]hexaphyrin **24** and [28]hexaphyrin **25** are interconvertible via redox reactions. Although both **24** and **25** show similar figure-eight conformations, they have been assigned to be aromatic and nonaromatic, respectively, on the basis of their absorption and ^{1}H NMR spectra. *β*-Perfluoro-[36]/[38]octaphyrins (**26** and **27**) are also interconvertible, albeit with larger structural changes. Solid-state structures of **26** and **27** are different from those of the parent octaphyrins (**14** and **21**) due to the presence of *β*-fluoro substituents.

9.2.3 Modified Syntheses

meso-Pentafluorophenyl-substituted hexaphyrin(1.1.0.1.1.0), called rubyrin, and its homologues were synthesized by TFA-catalyzed coupling of tripyrrane **28** and subsequent oxidation with *p*-chloranil. [26]Hexaphyrin(1.1.0.1.1.0) **29**, [38]nonaphyrin (1.1.0.1.1.0.1.1.0) **30**, [52]dodecaphyrin(1.1.0.1.1.0.1.1.0.1.1.0) **31**, and [62]pentadecaphyrin(1.1.0.1.1.0.1.1.0.1.1.0.1.1.0) **32** were obtained and fully characterized by HR-MS, ^{1}H NMR, UV/Vis, and X-ray diffraction analysis (Figure 9.8) [30]. [26]Rubyrin **29** proved to be a

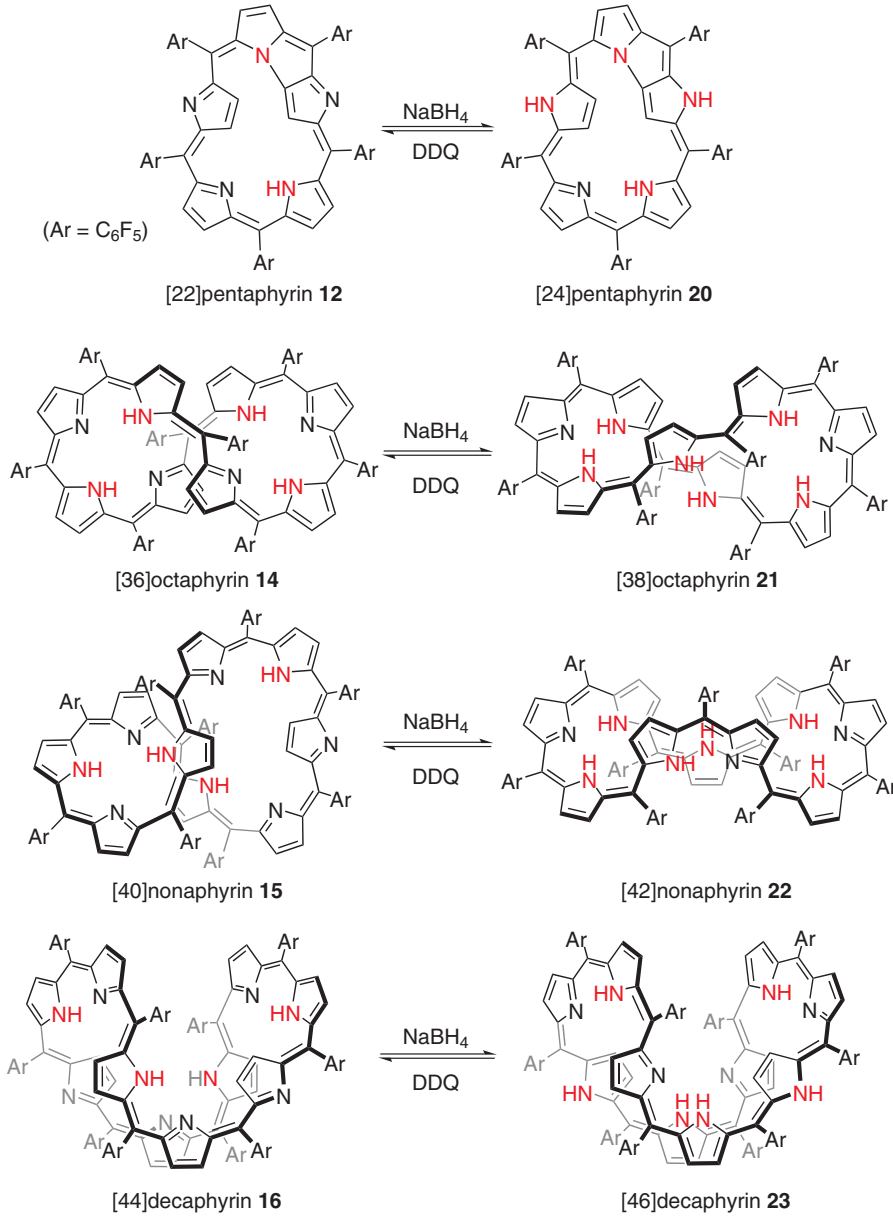

Figure 9.6 Redox interconversions of *N*-fused pentaphyrins, heptaphyrins, octaphyrins, nonaphyrins, and decaphyrins.

planar aromatic molecule with a distinct diatropic ring current. [38]Nonaphyrin **30** showed a distorted figure-eight structure, while [52]dodecaphyrin **31** and [62]pentadecaphyrin **32** exhibited significantly distorted structures due to multiple intramolecular hydrogen bonding interactions.

[30]Heptaphyrin(1.1.1.1.0.0.0) **33**, [30]heptaphyrin(1.1.1.1.1.1.0) **34**, and [34]octaphyrin(1.1.1.1.1.1.1.0) **35** were obtained with the $Sc(OTf)_3$-catalyzed reaction of pyrrole with pentafluorobenzaldehyde in an aqueous micellar system (Figure 9.9) [31]. Electrospray

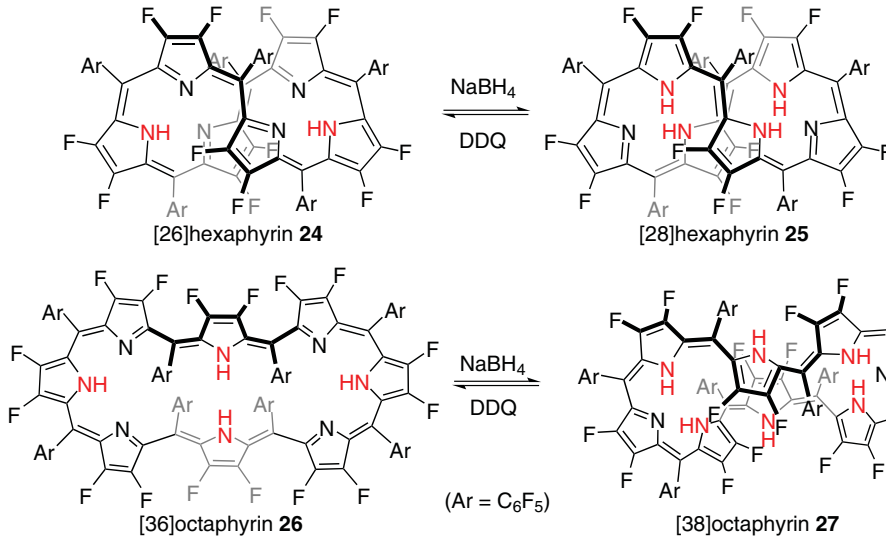

Figure 9.7 β-Perfluoro-substituted expanded porphyrins.

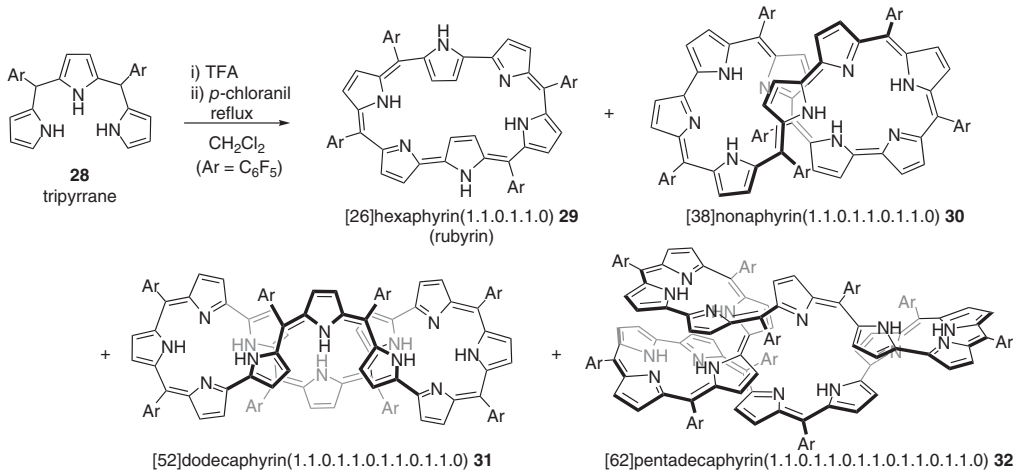

Figure 9.8 Oxidative coupling of tripyrrane.

ionization–time-of-flight (ESI-TOF) mass analysis of the reaction mixture prior to oxidation showed a series of mass peaks assignable to linear oligopyrroles. These results underlined the importance of the reaction media for the formation of expanded porphyrins because the reaction intermediates prior to the final oxidation may be in equilibrium of several cyclic or non-cyclic oligomers.

9.2.4 Core-Modified Expanded Porphyrins

Core modification by replacement of one or more pyrrolic units by other heterocycles such as furan, thiophene, and selenophene has led to a new class of expanded porphyrins. Notably, Chandrashekar and co-workers reported the synthesis of core-modified [22]smaragdyrin **36**,

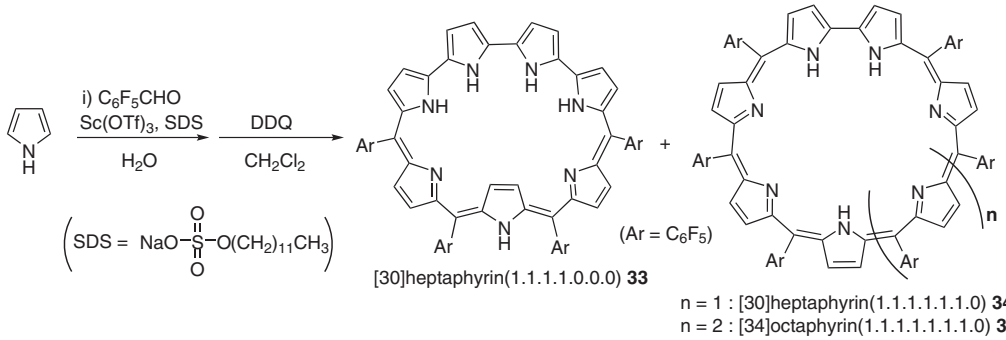

Figure 9.9 One-pot synthesis of *meso*-aryl-substituted expanded porphyrins in water.

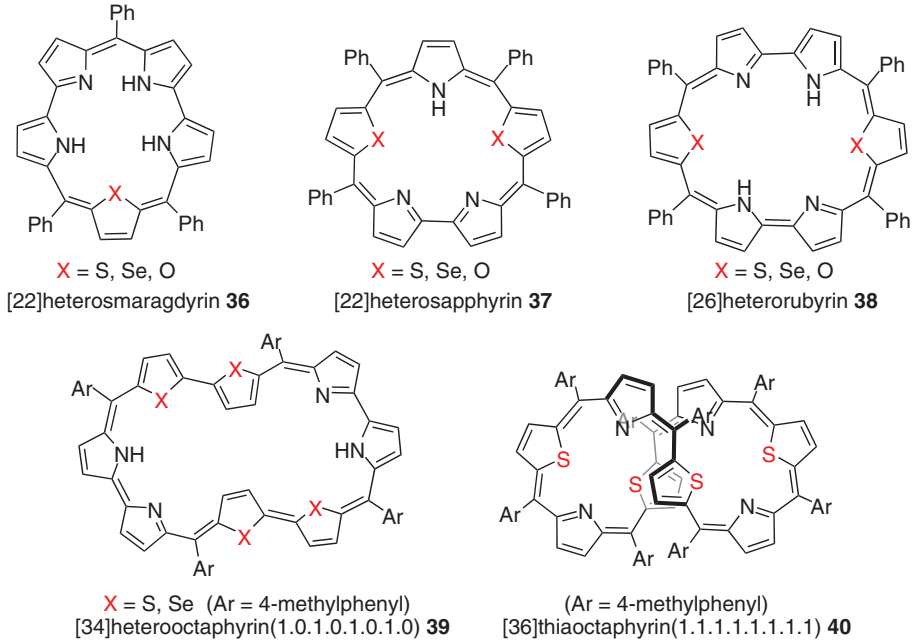

Figure 9.10 Core-modified expanded porphyrins.

[22]sapphyrin **37**, and [26]rubyrin **38** by oxidative coupling of the corresponding tripyrrane precursor in moderate to good yields (Figure 9.10) [32]. Later, a variety of modified syntheses as well as the coordination chemistry of these core-modified expanded porphyrins were studied, which is not fully discussed in this chapter due to space constraints [33]. Important examples are [34]heterooctaphyrin(1.0.1.0.1.0.1.0) **39** reported by Chandrashekar and co-workers and [36]tetrathiaoctaphyrin(1.1.1.1.1.1.1.1) **40** described by Sprutta and Latos-Grażyński [34, 35]. The former exhibited an aromatic character due to its planar structure, while the latter showed a figure-eight form with nonaromatic features.

9.3 Size-Selective Syntheses of Expanded Porphyrins

Size-selective syntheses of *meso*-aryl-substituted expanded porphyrins were achieved by employing dipyrromethane or tripyrrane as starting materials. Condensation of dipyrromethane and pentafluorobenzaldehyde (33 mM) with the aid of methanesulfonic acid (MSA)-catalysis in CH_2Cl_2 gave [18]porphyrin (10%), [26]hexaphyrin **8** (16%), [36]octaphyrin **14** (8%), and [44]decaphyrin **16** (3%) with suppression of the formation of expanded porphyrins bearing odd numbers of pyrrolic units. An analogous acid-catalyzed condensation of tripyrrane **28** with pentafluorobenzaldehyde gave [26]hexaphyrin **8** (30%) and [40]nonaphyrin **15** (15%), and a small amount of dodecaphyrin. Thus, by using appropriate starting materials, exclusive syntheses with defined size were achieved, as shown in the following section.

9.3.1 Pentaphyrins

Pentapyrrolic macrocycles can be constructed in a [3 + 2] manner. For example, [20]pentaphyrin(1.1.1.0.0) **43** was synthesized from diformyldipyrromethane **41** and terpyrrole **42** as HCl salts in good yields (Figure 9.11) [36]. However, a combination of diformylated terpyrrole and dipyrromethane did not afford the same pentaphyrin. *N*-Fused [22]pentaphyrin(1.1.1.1.1) **12** was synthesized by TFA-catalyzed condensation of tripyrrane **28** with dipyrromethane dicarbinol **44** followed by oxidation with DDQ in 28% yield almost exclusively [37].

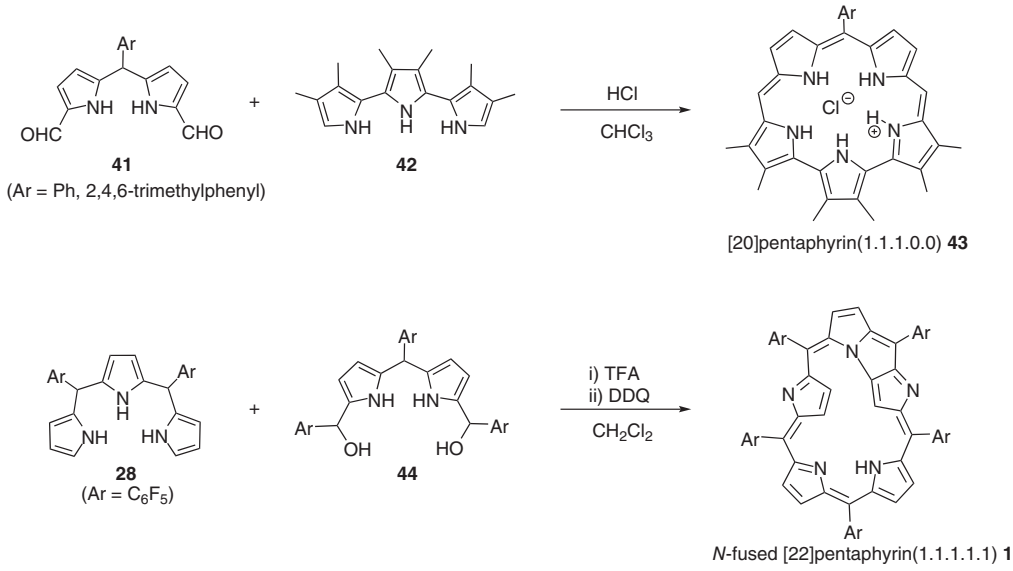

Figure 9.11 [2 + 3]-Type synthesis of pentaphyrins.

9.3.2 Hexaphyrins

Although [26]hexaphyrin(1.1.1.1.1.1) was obtained simply by acid-catalyzed condensation of arylaldehyde with dipyrromethane or tripyrrane, selective syntheses of various hexaphyrins have been performed in a [3 + 3] manner. Condensation of diformylterpyrrole **46** with tripyrrane **45** under appropriate conditions followed by neutralization gave [26]hexaphyrin(1.1.1.1.0.0) **47** in 46% yield (Figure 9.12) [38]. In other cases, A_2B_4-type hexaphyrins were obtained from tripyrrane **28** in low to moderate yields. The studies on A_2B_4-type hexaphyrins led to the conclusion that, depending on the *meso*-aryl substituents, hexaphyrins can adopt different conformations, either the Type-I dumbbell-like form or the Type-II rectangular form [39]. For example, 5,20-di(2-thienyl)- and 5,20-di(3-thienyl)-substituted hexaphyrins (**51** and **52**) prefer a dumbbell conformation (Type-I) due to the relatively small *meso*-aryl groups located at the inward-pointing 5,20-positions, while 5,20-diphenyl-, 5,20-di(2,4,6-trifluorophenyl)-, and 5,20-di(3-methyl-2-thienyl)-substituted hexaphyrins (**48**, **49**, and **50**) have been revealed to have a rectangular conformer (Type-II) in the solid state. A series of [26]hexaphyrins bearing two α-oligothienyl substituents, **53**, were prepared, all of which have Type-I conformers, in a similar manner to **51** [40]. Conjugative perturbation by the oligothienyl substituents significantly alters the optical properties and excited-state dynamics of [26]hexaphyrins.

Various hexaphyrins with functional *meso*-aryl substituents have also been developed (Figure 9.13). Two 2-pyridyl groups introduced at the 5,20-positions in [28]hexaphyrin **54** served as an effective hydrogen bonding motif, helping to give a planar dumbbell shape to its structure and hence imparting antiaromatic character to its electronic system [41]. The [28]hexaphyrin **54** was complexed with metal ions to produce the di-Pd(II) complexes

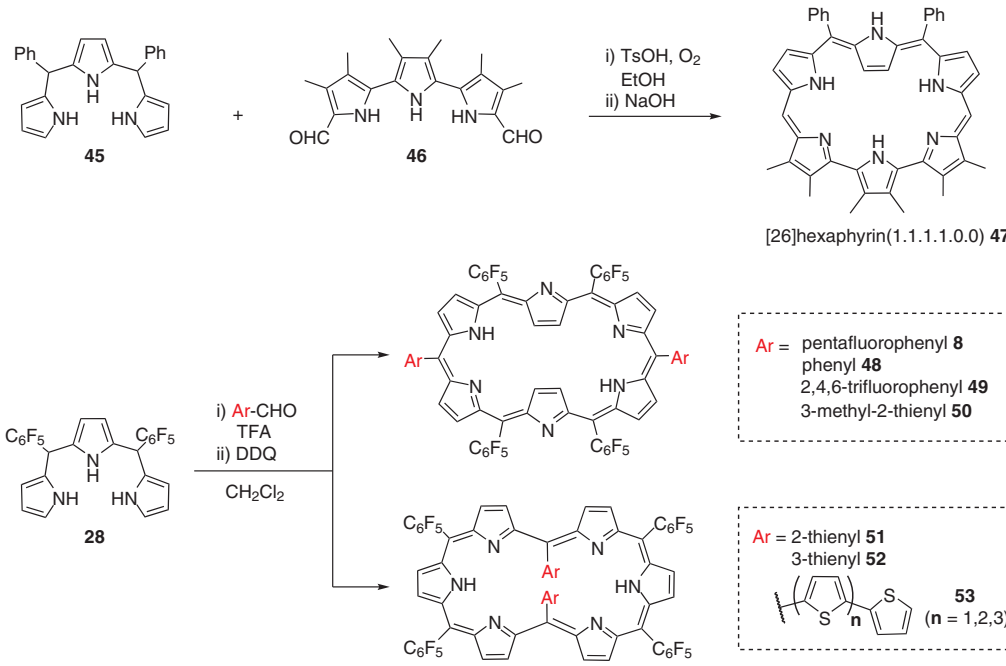

Figure 9.12 [3 + 3]-Type synthesis of hexaphyrins.

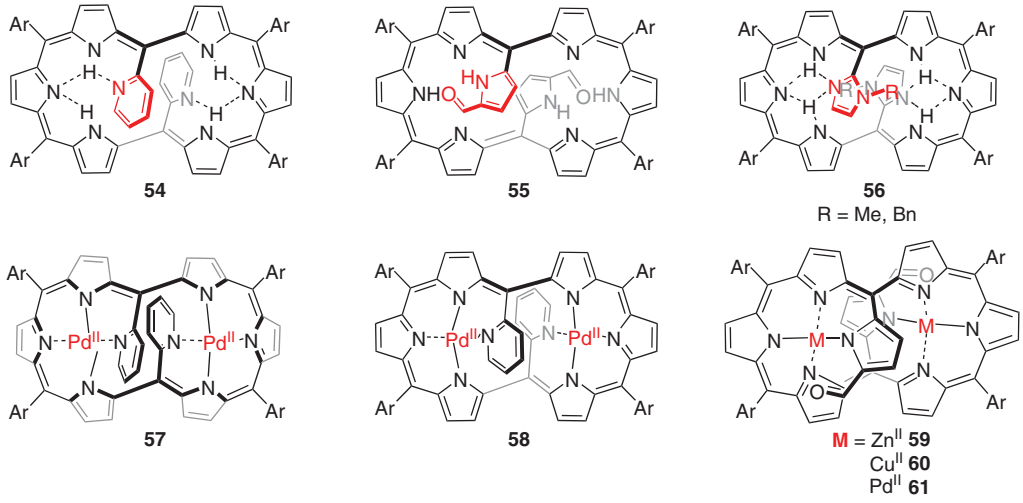

Figure 9.13 Peripherally functionalized hexaphyrins.

57 and **58**. Two 5-formyl-2-pyrryl groups at the 5,20-positions in [26]hexaphyrin **55** were hydrogen-bonded with the amino-type pyrroles to keep this molecule as a Hückel aromatic molecule with a dumbbell conformation [42]. Di-Zn(II), di-Cu(II), and di-Pd(II) complexes (**59**, **60**, and **61**) prepared from **55** exhibited near-infrared (NIR) absorption bands. *meso*-Aryl substituted [28]hexaphyrin **56** was prepared as well [43]. The two *meso*-2-imidazolyl groups stabilize 28π antiaromatic electronic networks through effective intramolecular hydrogen bonding interactions.

9.3.3 Heptaphyrins

For the synthesis of heptaphyrins, a [3 + 4] strategy has been employed. [30]Heptaphyrin(1.1.1.1.1.0.0) **63** was obtained from tetrapyrrane **62** and diformylterpyrrole **46** in 16% yield (Figure 9.14) [44]. X-ray diffraction analysis revealed a figure-eight twisted structure of **63**, while the ^{1}H NMR spectra suggested a more symmetric structure, indicating conformational dynamics faster than the ^{1}H NMR time scale. [32]Heptaphyrin(1.1.1.1.1.1.1) **13** was synthesized from tetrapyrrane **64** and tripyrrane dicarbinol **65** in 39% yield [45]. This method is useful to prepare non-*N*-fused heptaphyrins, as [32]heptaphyrin(1.1.1.1.1.1.1) **13** undergoes facile *N*-fusion reaction to give singly *N*-fused heptaphyrin **66** even during separation by silica-gel column chromatography (Figure 9.15). Successive *N*-fusion reactions proceeded by refluxing a toluene solution of **66** for 12 h to give doubly *N*-fused heptaphyrin quantitatively. Furthermore, upon treatment with NaH in DMF at 60 °C for 4 h, the quadruply *N*-fused heptaphyrin **67** was obtained in 71% yield.

9.3.4 Octaphyrins

To conduct [4 + 4]-type synthesis of octaphyrins, tetrapyrrane precursors were efficiently synthesized. Quaterpyrrole **68** was easily prepared in two steps from 2,2-bipyrroles. Then [32]octaphyrin(1.0.0.0.1.0.0.0) **70** was synthesized in 33% yield via condensation of quaterpyrrole **68** and its diformylated derivative **69** (Figure 9.16) [46]. On the other hand, tetrapyrrane

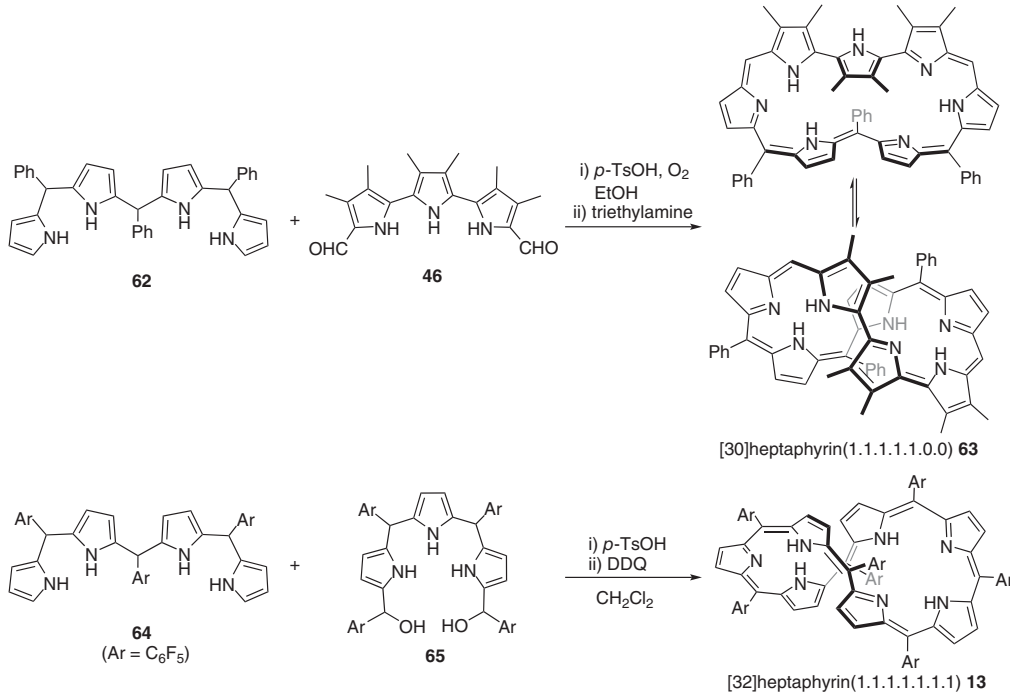

Figure 9.14 [3 + 4]-Type synthesis of heptaphyrins.

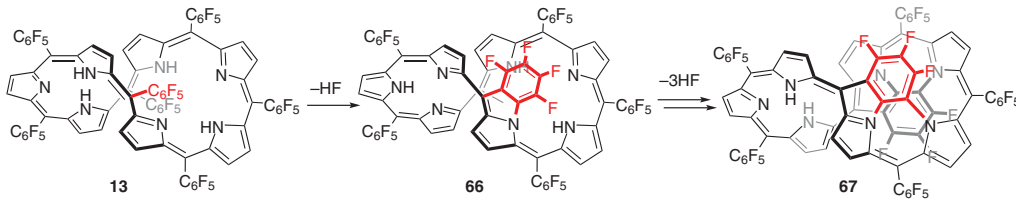

Figure 9.15 *N*-Fusion reactions of heptaphyrins.

64 was prepared from dipyrromethane dicarbinol **44**, and was used to synthesize [36]octaphyrin(1.1.1.1.1.1.1.1) **14**. Acid-catalyzed condensation of tetrapyrrane **64** with arylaldehydes afforded various A_2B_6-type octaphyrins (**71**–**74**) in moderate yields [47].

Shinokubo and co-workers reported a beautiful metal-template synthesis of [32]octaphyrin(1.0.1.0.1.0.1.0) di-Pd(II) complex **76** in 35% yield using a Ni(0)-mediated reductive coupling reaction of the α,α'-dibromodipyrrin Pd(II) complex **75** (Figure 9.17) [48]. Demetalation of this di-Pd(II) complex was accomplished by treatment with *p*-tolylmagnesium bromide at 80 °C to give free-base [32]octaphyrin(1.0.1.0.1.0.1.0) **77** in 38% yield.

9.3.5 Internally Bridged Expanded Porphyrins

Conformational control of large expanded porphyrins is an important tool for tuning their electronic properties, especially when the ring size of expanded porphyrin becomes large. To restrict the conformational flexibility of large expanded porphyrins,

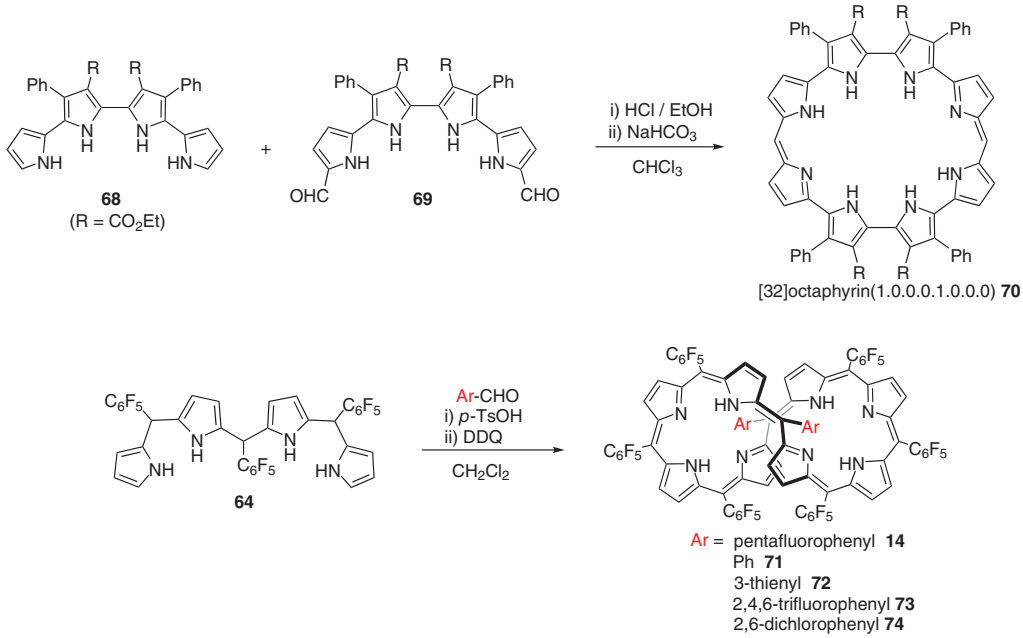

Figure 9.16 [4 + 4]-Type synthesis of octaphyrins.

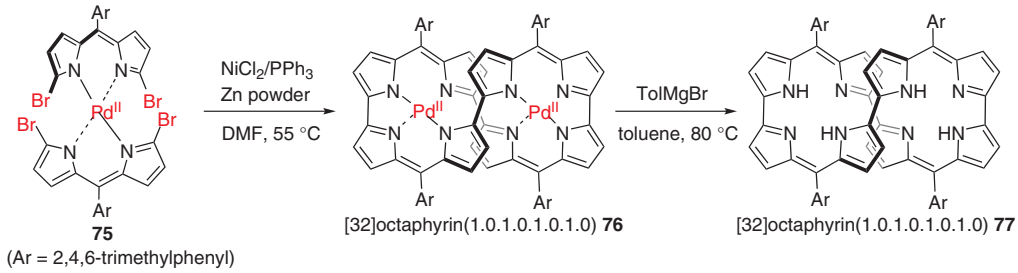

Figure 9.17 Template synthesis of [32]octaphyrin(1.0.1.0.1.0.1.0).

the synthesis of internally bridged expanded porphyrins was attempted. 1,4-Phenylene bridged [46]decaphyrin **78** was thus synthesized and displayed a nonplanar and C_2 symmetric structure (Figure 9.18) [49]. A ^{1}H NMR signal due to the protons of the 1,4-phenylene bridge was shifted upfield, indicating a diatropic ring current effect of the global conjugated network. [46]Decaphyrin **78** was quantitatively oxidized with MnO_2 to the nonaromatic [44]decaphyrin **79**. The structure of **79** was elucidated to be a twisted form with two inverted pyrroles pointing outward. As a similar, but more systematic case, 1,3-phenylene-, 2,5-thienylene-, and 2,5-pyrrylene-strapped [26]hexaphyrins (**80**, **81**, and **82**) were prepared by MSA-catalyzed condensation of tripyrrane **28** with 1,3-diformylbenzene, 2,5-diformylthiophene, and 2,5-diformylpyrrole, respectively [50]. Detailed spectroscopic investigations revealed that the [26]hexaphyrin conjugation was predominantly important for **80**, while active involvement of the 2,5-thienylene and 2,5-pyrrylene straps in the macrocyclic conjugation caused a dual conjugation pathway of [26]hexaphyrin and

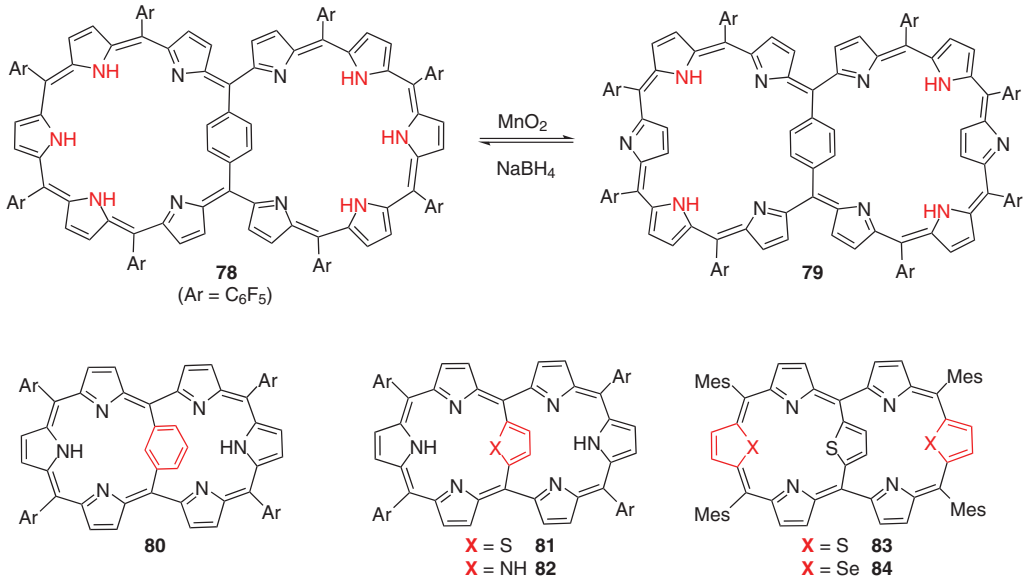

Figure 9.18 Internally bridged expanded porphyrins.

[18]thiaporphyrin for **81** and a predominant conjugation pathway of [18]porphyrin for **82**. 2,5-Thienylene-bridged core-modified hexaphyrins **83** and **84** were reported by Chandrashekar's group [51]. These internally bridged core-modified hexaphyrins showed a dual conjugation pathway of core-modified [18]porphyrins and [26]hexaphyrins.

9.4 Möbius Aromatic Expanded Porphyrins

The concept of Möbius aromaticity, first suggested by Heilbronner in 1964 [52], states that aromatic characteristics will be observed for [4n]annulenes when lying in a twisted Möbius strip. This time-honored concept has been fascinating from both the theoretical and experimental standpoints, since it provides a natural complement to the well-recognized idea of Hückel aromaticity that governs the properties of planar [4n + 2]annulenes (Figure 9.19). For a long time, real Möbius aromatic systems remained elusive until the seminal report by Herges and co-workers in 2003, wherein the first example of a Möbius twisted hydrocarbon was disclosed [53]. However, the diatropic ring current effects of the molecules were only modest, indicating that the aromatic character was weak. Recently, expanded porphyrins have emerged as an effective platform for realizing distinct Möbius aromatic molecules through mitigation of the distortion associated with molecular twists by virtue of the intrinsic conformational flexibilities [54]. Several successful examples of Möbius aromatic and Möbius antiaromatic expanded porphyrins will be introduced in this section.

9.4.1 Metal Complexes

In 2008, Osuka and co-workers discovered the spontaneous formation of Möbius aromatic molecules upon metalation of *meso*-aryl-substituted expanded porphyrins [20]. The first examples were [28]hexaphyrin(1.1.1.1.1.1) Ni(II), Pd(II), and Pt(II) complexes (**85**, **86**, and

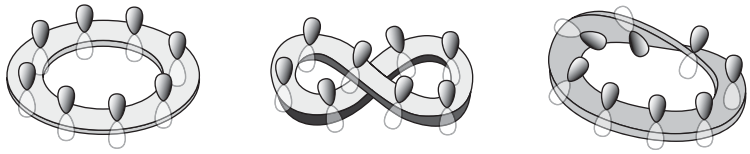

Figure 9.19 Schematic representations of the topologies of π-conjugated electron systems.

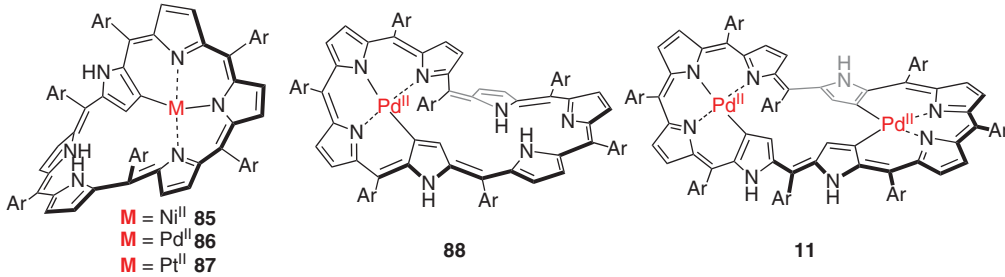

[28]hexaphyrin(1.1.1.1.1.1) Ni(II), Pd(II), Pt(II) complexes

[32]heptaphyrin(1.1.1.1.1.1.1.1) Pd(II) complex

[36]octaphyrin(1.1.1.1.1.1.1.1.1) Pd(II) complex

Figure 9.20 Möbius aromatic expanded porphyrin metal complexes.

87), [32]heptaphyrin(1.1.1.1.1.1.1.1) Pd(II) complex **88**, and [36]octaphyrin(1.1.1.1.1.1.1.1.1) di-Pd(II) complex **11** (Figure 9.20). These Möbius aromatic molecules were obtained as stable compounds, and exhibited distinct diatropic ring current effects in their ^{1}H NMR spectra. The incorporated metal ions worked to lock in twisted Möbius topology. Structural locking has also been effected by incorporation of typical elements (Figure 9.21). Si(IV), Ge(IV), and Sn(IV) complexes of [28]hexaphyrin(1.1.1.1.1.1) (**89**, **90**, and **91**) were obtained, where the incorporated group XIV elements took a typical trigonal bipyramidal coordination to induce a Möbius twist [55, 56]. As another example, the [28]hexaphyrin mono-phosphorus complex **92** exhibited moderate Möbius aromaticity [57]. Its structure revealed a phosphamide moiety being bound to the NNC-cavity to moderately rigidify the hexaphyrin framework. Si(IV) incorporation was also accomplished in the pentaphyrin cavity. Treatment of *N*-fused [24]pentaphyrin(1.1.1.1.1) **20** with trichloromethylsilane in the presence of diisopropylethylamine afforded doubly *N*-fused pentaphyrin **93** and its silicon complex **94**. These molecules showed distinct Möbius aromatic character, and addition of fluoride ion to **94** led to the formation of the six-coordinated silicate **95** with enhanced Möbius aromatic character [58]. The *N*-fused [24]pentaphyrin(1.1.1.1.1) Rh(I) complex **96** was also revealed to be a Möbius aromatic molecule with large two-photon absorption (TPA) properties [59] (Figure 9.22). These are examples of the smallest size of Möbius twisted expanded porphyrins. In contrast, the largest Möbius aromatic expanded porphyrin, at the time of writing this book, is the [44]decaphyrin(1.1.1.1.1.1.1.1.1.1) Pd(II) complex **97**. This complex was obtained by slow isomerization of the corresponding Hückel antiaromatic [44]decaphyrin complex [60]. Importantly, the largest dihedral angle is only 23°–24° in **97**, allowing relatively smooth conjugation. This favorable structural feature may derive from its pseudo-triangular shape, which is enabled by the larger-sized expanded porphyrin framework.

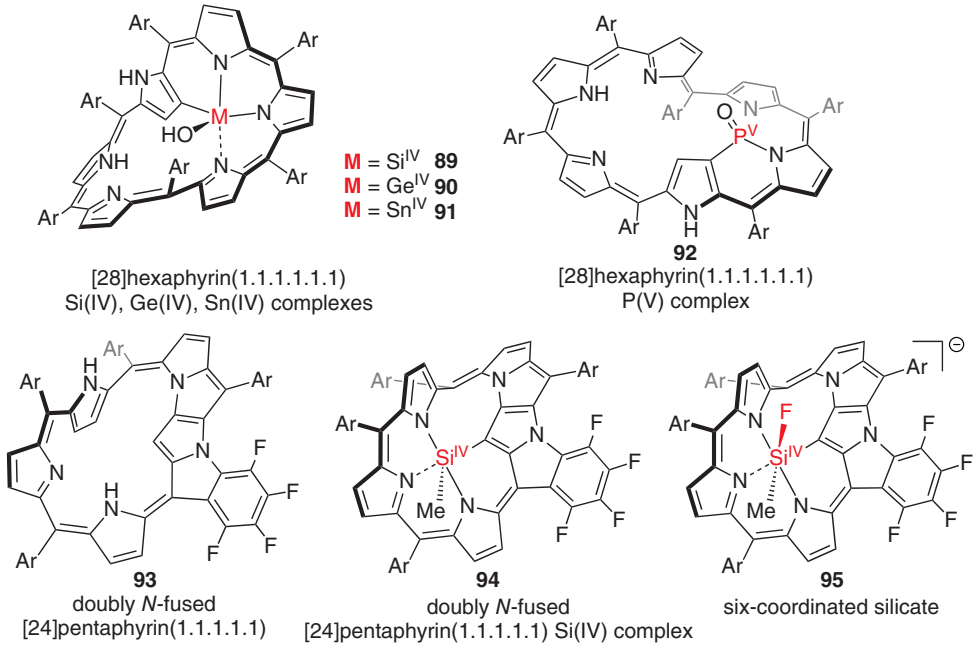

Figure 9.21 Möbius aromatic expanded porphyrin typical element complexes.

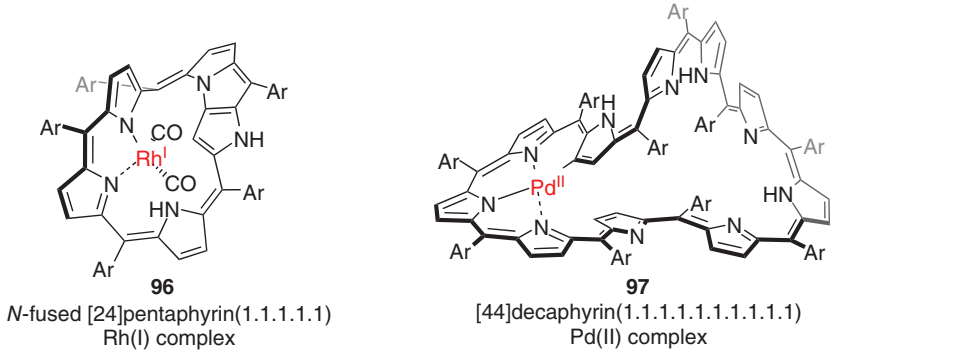

Figure 9.22 The smallest and largest Möbius aromatic expanded porphyrins.

9.4.2 Peripherally Fused Expanded Porphyrins

Möbius aromatic molecules without metal coordination are highly desirable for elucidating their intrinsic properties both in the ground state and in the excited state. In 2009, Osuka and co-workers reported the facile formation of peripherally benzopyrane-fused [28]hexaphyrin **98** by simple heating of [26]hexaphyrin **8** in acetic acid (Figure 9.23) [61]. [28]Hexaphyrin **98** displayed a distinct diamagnetic ring current effect at room temperature, which was largely retained over a wide temperature range from −100 to 100 °C. Compared to the metal complexes, the conjugation was relatively smooth, the largest dihedral angle being only 36° in the solid state. The singlet (π-π*) excited-state lifetime of **98** was determined to be ~40 ps by femtosecond transient absorption spectroscopy. This lifetime was shorter than that of the parent [28]hexaphyrin **17** (183 ps), probably due to conformational flexibility. In addition, the

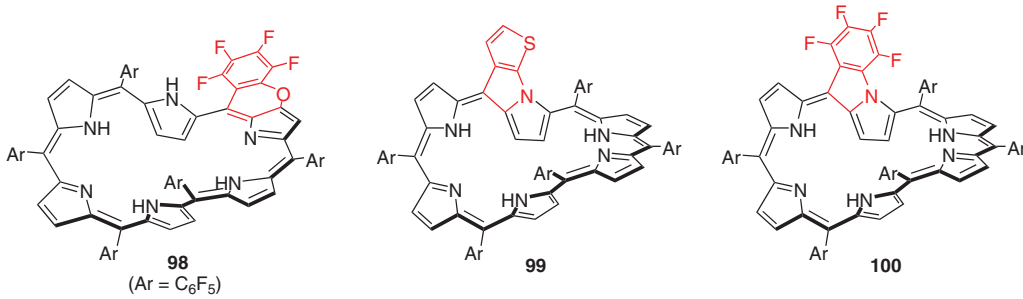

Figure 9.23 Peripherally fused expanded porphyrins with Möbius aromaticity.

NIR fluorescence spectrum was observed at 1058 nm with a vibronic structure. In a similar case, heating of mono-(3-thienyl)-substituted [26]hexaphyrin in toluene led to the formation of the peripherally thienyl-fused [28]hexaphyrin **99** possessing a distinct aromatic character [62]. Differing from these successful examples, a singly *N*-fused [28]hexaphyrin **100** was revealed to show rather complicated features reflecting conformational changes in the various Hückel and Möbius forms; however, its Pd(II) complex displayed clear Möbius aromatic character [63].

9.4.3 Protonated Expanded Porphyrins

Protonation is a very effective means of switching [4n]π expanded porphyrins from Hückel antiaromatic species to Möbius aromatic species by disrupting intramolecular hydrogen bonding networks. Thus, protonation of [28]hexaphyrin, [32]heptaphyrin, and [36]octaphyrin has been examined in detail (Figure 9.24). In the initial attempt in 2009, protonation of [32]heptaphyrins **13** with TFA allowed the formation of several protonated species, one of which was revealed to be a Möbius aromatic mono-protonated [32]heptaphyrin, **102** [64]. A similar behavior was observed for [36]octaphyrin **14**, which was protonated with MSA to give the diprotonated Möbius twisted [36]octaphyrin, **103** [65]. In both cases, ^{1}H NMR titration experiments with TFA or MSA supported the appearance of Möbius aromatic species. The protonation behavior of [28]hexaphyrins was more complicated. For 2,3,17,18-tetraphenyl-[28]hexaphyrin, a clear structural change from the figure-eight form in the neutral state to the Möbius twisted form **101** was shown upon protonation with TFA [66].

9.4.4 Dynamic Equilibrium

The existence of Möbius aromatic species can also be shown in the dynamic equilibrium of some specific molecules that are flexible in solution. In other words, the electronic properties of flexible expanded porphyrins with [4n]π electron systems can be occasionally understood by considering an equilibrium between Hückel antiaromatic species and Möbius aromatic species. In 2007, Latos-Grażyński and co-workers reported that A,D-di-*p*-benzi[28]hexaphyrin **104** showed a conformational switch between Möbius and Hückel topologies in solution by rotating the 1,4-phenylene rings located at the intersection (Figure 9.25) [67]. Temperature-dependent ^{1}H NMR spectroscopy confirmed this assignment.

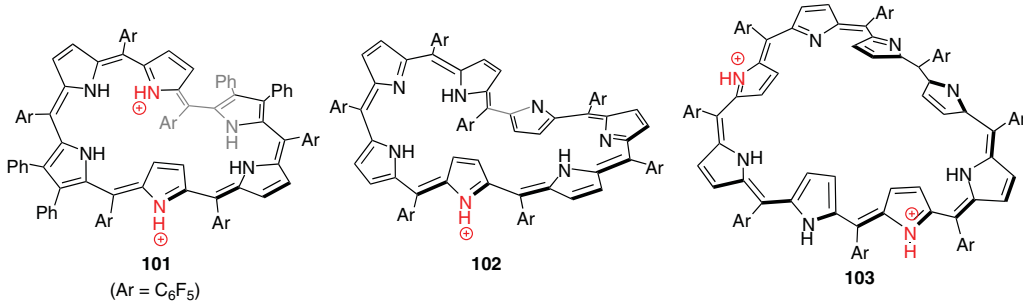

Figure 9.24 Protonated expanded porphyrins with Möbius aromaticity. Counter anions were omitted for clarity.

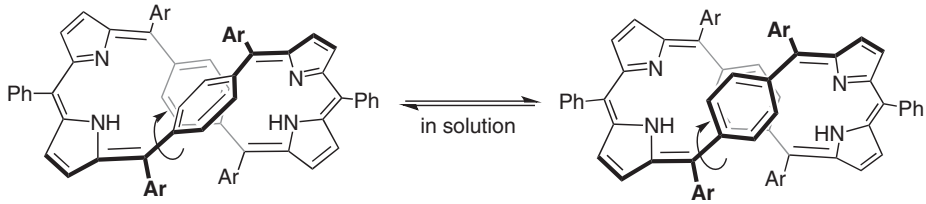

Figure 9.25 Dynamic equilibrium of *p*-benzi-A,D-[28]hexaphyrin(1.1.1.1.1.1).

The ^{1}H NMR spectra of [28]hexaphyrin(1.1.1.1.1.1) was also shown to be temperature dependent [27]. At room temperature, the ^{1}H NMR spectrum of [28]hexaphyrin **17** indicated a D_{2h} symmetry likely assignable to the rectangular Hückel topology, which was later understood to be an averaged spectrum of Möbius and Hückel topologies due to the conformational dynamics being faster than the ^{1}H NMR time scale (Figure 9.26). Low-temperature ^{1}H NMR analysis revealed a predominant population of the non-symmetric Möbius aromatic species, which was energetically lower (3.7 kcal/mol) than the corresponding Hückel antiaromatic species. Following the use of this dynamic behavior to elucidate the character of [4n]π expanded porphyrins, various other observations such as solvent-polarity-dependent conformational changes were noted [68].

9.4.5 Möbius Antiaromatic Expanded Porphyrins

In the course of studies on phosphorus insertion into expanded porphyrins, Osuka and co-workers found that [30]hexaphyrin diphosphorus(V) complex **105** exhibited a paratropic ring current by displaying downfield shifted signals due to the inner-β protons (Figure 9.27) [57]. The X-ray crystal structure of **105** showed a Möbius twisted structure in which the phosphamide moieties were bound to the NNN- or NNC-cavity. These data clearly verified the 30π Möbius antiaromaticity of **105**, making it the first structurally characterized Möbius antiaromatic compound. The highly reduced [30]hexaphyrin system was stabilized by the presence of two electron-withdrawing phosphamide moieties, which also contributed to structural rigidification of the molecule. Phosphorus insertion into a 2,6-dichlorophenyl-substituted [32]heptaphyrin furnished the Möbius antiaromatic monophosphorus(V) complex **106**

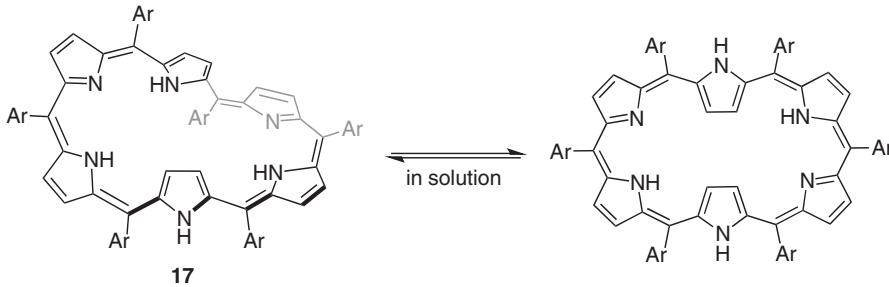

Figure 9.26 Dynamic equilibrium of [28]hexaphyrin(1.1.1.1.1.1).

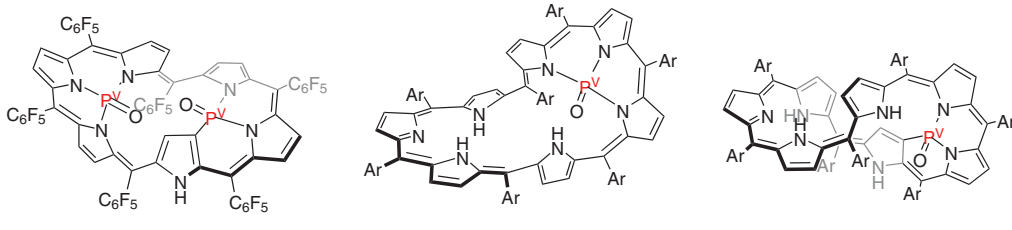

Figure 9.27 Möbius antiaromatic expanded porphyrin phosphorus complexes.

as a kinetically controlled product. This molecule underwent quantitatively a thermal rearrangement to a more stable Hückel aromatic complex **107** [69].

9.5 Giant Expanded Porphyrins

With increasing size, the yields of expanded porphyrins decrease and their characterization becomes increasingly difficult due to the existence of several conformations close in energy. When the acid-catalyzed condensation reaction of pentafluorophenyldipyrromethane with pentafluorobenzaldehyde was conducted at high concentration (ca. 100 mM) at 0 °C, [52]dodecaphyrin, [62]tetradecaphyrin, [72]hexadecaphyrin, and [80]octadecaphyrin were isolated. Although these expanded porphyrins have been characterized by ^{1}H NMR, MALDI-TOF MS, and UV/Vis absorption spectra [70], only [62]tetradecaphyrin **108** has been structurally characterized to be a highly twisted C_1-symmetric conformation with an intricate intramolecular hydrogen bonding network [71]. These giant expanded porphyrins have large π-conjugated networks, which can undergo multiple reversible redox processes.

Structurally well-defined expanded porphyrins bearing more than 50π-conjugated circuits are limited (Figure 9.28). Only four reports have been published up to 2016. Setsune and Maeda reported [96]tetracosaphyrin(1.0.1.0.1.0.1.0.1.0.1.0.1.0.1.0.1.0.1.0.1.0.1.0) **110**, which has a square pillar structure with a tetragonal cut end [16]. Osuka and co-workers described *meso*-trifluoromethyl-substituted [56]dodecaphyrin(1.1.1.1.1.1.1.1.1.1.1.1) **109**,

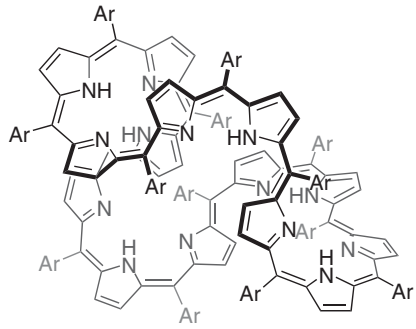

108
[62]tetradecaphyrin(1.1.1.1.1.1.1.1.1.1.1.1.1.1)
(Ar = C_6F_5)

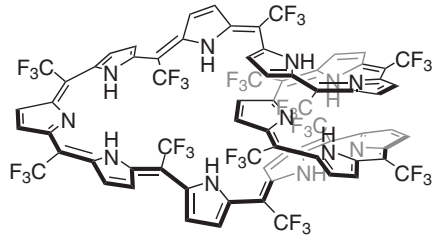

109
[56]dodecaphyrin(1.1.1.1.1.1.1.1.1.1.1.1)

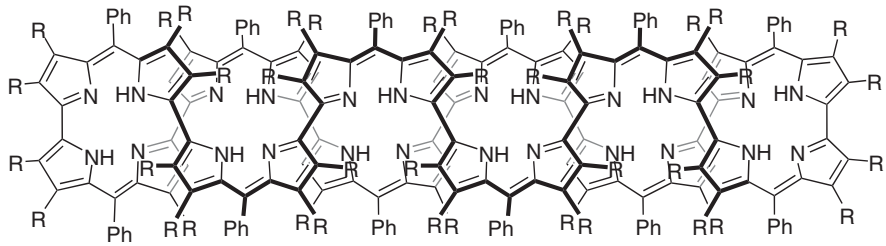

110
[96]tetracosaphyrin(1.1.1.1.1.1.1.1.1.1.1.1.1.1.1.1.1.1.1.1.1.1.1.1)
(R = Et)

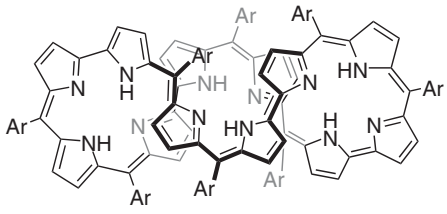

111
[50]dodecaphyrin(1.1.0.1.1.0.1.1.0.1.1.0)

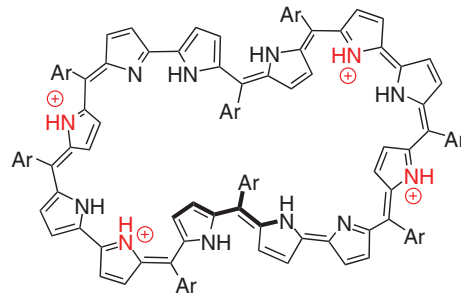

112
[50]dodecaphyrin(1.1.0.1.1.0.1.1.0.1.1.0)

Figure 9.28 Giant expanded porphyrins.

which was synthesized via one-pot condensation of 2-(2,2,2-trifluoro-1-hydroxyethyl) pyrrole followed by oxidation with DDQ [72]. As introduced above, [52]dodecaphyrin(1.1.0.1.1.0.1.1.0.1.1.0) **31** and [62]pentadecaphyrin(1.1.0.1.1.0.1.1.0.1.1.0.1.1.0) **32** were obtained by oxidative coupling of tripyrrane **28** (Figure 9.8) [73]. [52]Dodecaphyrin **31** was oxidized with DDQ to give [50]dodecaphyrin **111**, and further oxidation of **111** with MnO_2 gave [48]dodecaphyrin [74]. [50]Dodecaphyrin **111** is weakly aromatic in spite of its twisted structure, while [48]dodecaphyrin has been proved to be nonaromatic. Interestingly, protonation of **111** with MSA furnished the tetraprotonated species **112**. Its structure was shown to be planar, and the ^{1}H NMR and UV/Vis/NIR absorption spectra indicated its distinct Hückel aromatic character arising from the 50π electron circuit.

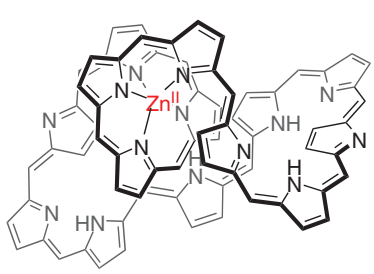

113
[62]tetradecaphyrin(1.1.1.1.1.1.1.1.1.1.1.1.1.1)
mono-Zn(II) complex

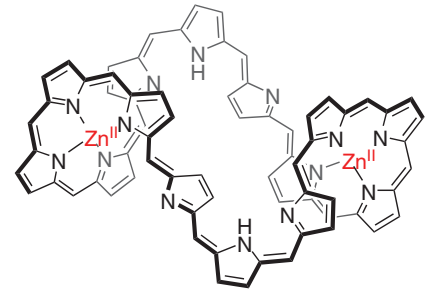

114
[62]tetradecaphyrin(1.1.1.1.1.1.1.1.1.1.1.1.1.1)
di-Zn(II) complex

*meso-C_6F_5 substitutents were omitted for clarity

Figure 9.29 Zn(II) complexes of [62]tetradecaphyrin(1.1.1.1.1.1.1.1.1.1.1.1.1.1).

In 2016, Zn(II) complexes of tetradecaphyrin(1.1.1.1.1.1.1.1.1.1.1.1.1.1) were reported (Figure 9.29) [71]. The mono-Zn(II) complex **113** was revealed to be a 720° twisted structure with a pentacoordinated Zn(II) ion in the coiled cavity. This complex displayed multiple reversible redox waves in electrochemical measurement. Di-Zn(II) complex **114** was also structurally characterized as a topologically untwisted structure with two tetracoordinated Zn(II) ions. The largest torsional angle in the π-conjugated circuit was relatively small (22°), which is favorable to maintain smooth conjugation over the 62π macrocycle. Actually, the ^{1}H NMR spectrum of **114** in acetone-d_6 indicated a moderate diatropic ring current effect for the whole macrocycle. At the time of writing this book, this is the largest expanded porphyrin showing distinct Hückel aromaticity. In spite of the extraordinary progress as described here, the chemistry of expanded porphyrins is still in its infancy. In particular, *meso*-aryl-substituted expanded porphyrins may be promising candidates to surpass the limits for the experimental observation of Hückel and Möbius (anti)aromaticity.

References

1 (a) Woodward, R.B. (1966). *Aromaticity: An International Symposium*. Sheffield, U.K.; Special publication no. 21; The Chemical Society London. Later publication; (b) Bauer, V.J., Clive, D.L.J., Dolphin, D. et al. (1983). Sapphyrins: Novel Aromatic Pentapyrrolic Macrocycles. *Journal of the American Chemical Society* 105: 6429–6436.

2 Broadhurst, M.J., Grigg, R., and Johnson, A.W. (1972). Sulphur extrusion reactions applied to the synthesis of corroles and related systems. *J. Chem. Soc. Perkin Trans.* 1: 1124–1135.

3 Sessler, J.L., Cyr, M.J., and Lynch, V. (1990). Synthetic and structural studies of Sapphyrin, a 22-π-electron Pentapyrrolic "expanded porphyrin". *J. Am. Chem. Soc.* 112: 2810–2813.

4 Berger, R.A. and LeGoff, E. (1978). The synthesis of A 22π-electron tetrapyrrolic macrocycle [1,3,1,3] platyrin. *Tetrahedron Lett.* 44: 4225–4228.

5 König, H., Eickmeier, C., Möller, M. et al. (1990). Synthesis of a bisvinylogous octaethylporphyrin. *Angew. Chem. Int. Ed. Engl.* 29: 1393–1395.

6 Charrière, R., Jenny, T.A., Rexhausen, H., and Gossauer, A. (1993). The chemistry of polyphyrins 2. Syntheses of hexaphyrins and their metal complexes. *Heterocycles* 36: 1561–1575.

7 Sessler, J.L., Murai, T., Lynch, V., and Cyr, M. (1988). An "expanded porphyrin": the synthesis and structure of a new aromatic pentadentate ligand. *J. Am. Chem. Soc.* 110: 5586–5588.

8 Sessler, J.L., Hemmi, G., Mody, T.D. et al. (1994). Texaphyrins: synthesis and applications. *Acc. Chem. Res.* 27: 43–50.

9 Sessler, J.L. and Mody, T.D. (1999). *Supramolecular Materials and Technologies*. Chichester: Wiley.

10 Vogel, E., Bröring, M., Fink, J. et al. (1995). From porphyrin isomers to octapyrrolic "figure eight" macrocycles. *Angew. Chem. Int. Ed. Engl.* 34: 2511–2514.

11 Chmielewski, P.J., Latos-Grażyński, L., and Rachlewicz, K. (1995). 5,10,15,20-Tetraphenylsapphyrin-identification of a Pentapyrrolic expanded porphyrin in the Rothemund synthesis. *Chem. A Eur. J.* 1: 68–73.

12 Neves, M.G.P.M.S., Martins, R.M., Tomé, A.C. et al. (1999). *Meso*-substituted expanded porphyrins: new and stable hexaphyrins. *Chem. Commun.* 385–386.

13 Shin, J.-Y., Furuta, H., Yoza, K. et al. (2001). *Meso*-aryl-substituted expanded porphyrins. *J. Am. Chem. Soc.* 123: 7190–7191.

14 Lindsey, J.S., Schreiman, I.C., Hsu, H.C. et al. (1987). Rothemund and Adler-Longo reactions revisited: synthesis of Tetraphenylporphyrins under equilibrium conditions. *J. Org. Chem.* 52: 827–836.

15 Setsune, J.-i., Katakami, Y., and Iizuna, N. (1999). [48]Dodecaphyrin-(1.0.1.0.1.0.1.0.1.0.1.0) and [64]Hexadecaphyrin-(1.0.1.0.1.0.1.0.1.0.1.0.1.0.1.0): the largest cyclopolypyrroles. *J. Am. Chem. Soc.* 121: 8957–8958.

16 Setsune, J.-i. and Maeda, S. (2000). Bis(azafulvene) as a versatile building block for giant cyclopolypyrroles: X-ray crystal structure of [64]Hexadecaphyrin(1.0.1.0.1.0.1.0.1.0.1.0.1.0.1.0). *J. Am. Chem. Soc.* 122: 12405–12406.

17 Seidel, D., Lynch, V., and Sessler, J.L. (2002). Cyclo[8]pyrrole: a simple-to-make expanded porphyrin with no Meso bridges. *Angew. Chem. Int. Ed.* 41: 1422–1425.

18 Eller, L.R., Stępień, M., Fowler, C.J. et al. (2007). Octamethyl-octaundecylcyclo[8]pyrrole: a promising sulfate anion extractant. *J. Am. Chem. Soc.* 129: 11020–11021.

19 Shimizu, S. and Osuka, A. (2006). Metalation chemistry of *meso*-aryl-substituted expanded porphyrins. *Eur. J. Inorg. Chem.* 1319–1335.

20 Tanaka, Y., Saito, S., Mori, S. et al. (2008). Metalation of expanded porphyrins: a chemical trigger used to produce molecular twisting and Möbius aromaticity. *Angew. Chem. Int. Ed.* 47: 681–684.

21 Stępień, M., Sprutta, N., and Latos-Grażyński, L. (2011). Figure eights, Möbius bands, and more: conformation and aromaticity of porphyrinoids. *Angew. Chem. Int. Ed.* 50: 4288–4340.

22 Saito, S. and Osuka, A. (2011). Expanded porphyrins: intriguing structures, electronic properties, and reactivities. *Angew. Chem. Int. Ed.* 50: 4342–4373.

23 Osuka, A. and Saito, S. (2011). Expanded porphyrins and aromaticity. *Chem. Commun.* 47: 4330–4339.

24 Shin, J.-Y., Furuta, H., and Osuka, A. (2001). *N*-fused Pentaphyrin. A. *Angew. Chem. Int. Ed.* 40: 619–621.

25 Maes, W., Vanderhaeghen, J., and Dehaen, W. (2005). *Meso*-dichloropyrimidinyl substituted expanded porphyrins. *Chem. Commun.* 2612–2614.

26 Kang, S., Hayashi, H., Umeyama, T. et al. (2008). *Meso*-3,5-Bis(trifluoromethyl)phenyl-substituted expanded porphyrins: synthesis, characterization, and optical, electrochemical, and photophysical properties. *Chem. Asian J.* 3: 2065–2074.

27 Sankar, J., Mori, S., Saito, S. et al. (2008). Unambiguous identification of Möbius aromaticity for *meso*-aryl-substituted [28]Hexaphyrins(1.1.1.1.1.1). *J. Am. Chem. Soc.* 130: 13568–13579.

28 Mori, S. and Osuka, A. (2005). Aromatic and antiaromatic gold(III) Hexaphyrins with multiple gold-carbon bonds. *J. Am. Chem. Soc.* 127: 8030–8031.

29 Shimizu, S., Shin, J.-Y., Furuta, H. et al. (2003). Perfluorinated *meso*-aryl-substituted expanded porphyrins. *Angew. Chem. Int. Ed.* 42: 78–82.

30 Shimizu, S., Taniguchi, R., and Osuka, A. (2005). *Meso*-aryl-substituted [26]Hexaphyrin(1.1.0.1.1.0) and [38]Nonaphyrin(1.1.0.1.1.0.1.1.0) from oxidative coupling of a Tripyrrane. *Angew. Chem. Int. Ed.* 44: 2225–2229.

31 Hiroto, S., Shinokubo, H., and Osuka, A. (2006). Porphyrin synthesis in water provides new expanded porphyrins with direct bipyrrole linkages: isolation and characterization of two heptaphyrins. *J. Am. Chem. Soc.* 128: 6568–6569.

32 Narayanan, S.J., Sridevi, B., Chandrashekar, T.K. et al. (1999). Novel core-modified expanded porphyrins with *meso*-aryl substituents: synthesis, spectral and structural characterization. *J. Am. Chem. Soc.* 121: 9053–9068.

33 Misra, R. and Chandrashekar, T.K. (2008). Structural diversity in expanded porphyrins. *Acc. Chem. Res.* 41: 265–279.

34 Anand, V.G., Pushpan, S.K., Venkatraman, S. et al. (2001). 34π Octaphyrin: first structural characterization of a planar, aromatic [1.0.1.0.1.0.1.0] Octaphyrin with inverted heterocyclic rings. *J. Am. Chem. Soc.* 123: 8620–8621.

35 Sprutta, N. and Latos-Grażyński, L. (2001). Figure-eight tetrathiaoctaphyrin and dihydrotetrathiaoctaphyrin. *Chem. A Eur. J.* 7: 5099–5112.

36 Sessler, J.L., Seidel, D., Bucher, C., and Lynch, V. (2001). Novel terpyrrole-containing aromatic expanded porphyrins. *Tetrahedron* 57: 3743–3752.

37 Mori, S., Shin, J.-Y., Shimizu, S. et al. (2005). *N*-fused Pentaphyrins and their rhodium complexes: oxidation-induced rhodium rearrangement. *Chem. A Eur. J.* 11: 2417–2425.

38 Sessler, J.L., Seidel, D., Bucher, C., and Lynch, V. (2000). [26]Hexaphyrin(1.1.1.1.0.0): an all-aza isomer of rubyrin with an inverted pyrrole subunit. *Chem. Commun.* 1473–1474.

39 Suzuki, M. and Osuka, A. (2007). Conformational control of [26]Hexaphyrins(1.1.1.1.1.1) by *meso*-Thienyl substituents. *Chem. A Eur. J.* 13: 196–202.

40 Mori, H., Suzuki, M., Kim, W. et al. (2015). 5,20-Bis(*α*-oligothienyl)-substituted [26]hexaphyrins possessing electronic circuits strongly perturbed by *meso*-oligothienyl substituents. *Chem. Sci.* 6: 1696–1700.

41 Naoda, K., Mori, H., Oh, J. et al. (2015). 5,20-Di(pyridin-2-yl)-[28]hexaphyrin(1.1.1.1.1.1): A stable Hückel antiaromatic Hexaphyrin stabilized by intramolecular hydrogen bonding and protonation-induced conformational twist to gain Möbius aromaticity. *J. Org. Chem.* 80: 11726–11733.

42 Mori, H. and Osuka, A. (2015). Bismetal complexes of 5,20-Bis(5-formyl-2-pyrrolyl)-[26]hexaphyrin(1.1.1.1.1.1) exhibiting strong near-infrared region absorptions. *Chem. A Eur. J.* 21: 7007–7011.

43 Mori, H., Sung, Y.M., Lee, B.S. et al. (2012). Antiaromatic Hexaphyrins and Octaphyrins stabilized by the hydrogen-bonding interactions of *meso*-imidazolyl groups. *Angew. Chem. Int. Ed.* 51: 12459–12463.

44 Bucher, C., Seidel, D., Lynch, V., and Sessler, J.L. (2002). [30]Heptaphyrin(1.1.1.1.1.0.0): an aromatic expanded porphyrin with a 'figure eight' like structure. *Chem. Commun.* 328–329.

45 Saito, S. and Osuka, A. (2006). *N*-fusion reaction sequence of Heptaphyrin(1.1.1.1.1.1.1): singly, doubly, and quadruply *N*-fused Heptaphyrins. *Chem. A Eur. J.* 12: 9095–9102.

46 Anguera, G., Kauffmann, B., Borrell, J.I. et al. (2015). Quaterpyrroles as building blocks for the synthesis of expanded porphyrins. *Org. Lett.* 17: 2194–2197.

47 Mori, H., Aratani, N., and Osuka, A. (2012). Synthesis of A_2B_6-type [36]Octaphyrins: copper(II)-metalation-induced fragmentation reactions to porphyrins and *N*-fusion reactions of *meso*-(3-Thienyl) substituents. *Chem. Asian J.* 7: 1340–1346.

48 Kido, H., Shin, J.-Y., and Shinokubo, H. (2013). Selective synthesis of a [32]Octaphyrin(1.0.1.0.1.0.1.0) bis(palladium) complex by a metal-templated strategy. *Angew. Chem. Int. Ed.* 52: 13727–13730.

49 Anand, V.G., Saito, S., Shimizu, S., and Osuka, A. (2005). Internally 1,4-phenylene-bridged meso aryl-substituted expanded porphyrins: the Decaphyrin and Octaphyrin cases. *Angew. Chem. Int. Ed.* 44: 7244–7248.

50 Mori, H., Lim, J.M., Kim, D., and Osuka, A. (2013). Modulation of dual electronic circuits of [26]Hexaphyrins using internal aromatic straps. *Angew. Chem. Int. Ed.* 52: 12997–13001.

51 Karthik, G., Sneha, M., Raja, V.P. et al. (2013). Core-modified *meso*-aryl hexaphyrins with an internal thiophene bridge: structure, aromaticity, and photodynamics. *Chem. A Eur. J.* 19: 1886–1890.

52 Heilbronner, E. (1964). Hückel molecular orbitals of Möbius-type conformations of annulenes. *Tetrahedron Lett.* 5: 1923–1928.

53 Ajami, D., Oeckler, O., Simon, A., and Herges, R. (2003). Synthesis of a Möbius aromatic hydrocarbon. *Nature* 426: 819–821.

54 Akasaka, T., Osuka, A., Fukuzumi, S. et al. (2015). *Chemical Science of π-Electron Systems*. Tokyo: Springer.

55 Ishida, S.-i., Tanaka, T., Lim, J.M. et al. (2014). Si^{IV} incorporation into a [28]Hexaphyrin that triggered formation of Möbius aromatic molecules. *Chem. A Eur. J.* 20: 8274–8278.

56 Ishida, S.-i. and Osuka, A. (2015). *Meso*-aryl [28]Hexaphyrin silicon complexes bearing various Si-substituents and 1,16-dihydrohexaphyrin bis-Chlorosilicon. *Chem. Asian J.* 10: 2200–2206.

57 Higashino, T., Lim, J.M., Miura, T. et al. (2010). Möbius antiaromatic bisphosphorus complexes of [30]Hexaphyrins. *Angew. Chem. Int. Ed.* 49: 4950–4954.

58 Ishida, S.-i., Kim, J.O., Kim, D., and Osuka, A. (2016). Doubly *N*-fused [24]Pentaphyrin silicon complex and its fluorosilicate: enhanced Möbius aromaticity in the fluorosilicate. *Chem. A Eur. J.* 22: 16554–16561.

59 Park, J.K., Yoon, Z.S., Yoon, M.-C. et al. (2008). Möbius aromaticity in *N*-fused [24]Pentaphyrin upon Rh(I) metalation. *J. Am. Chem. Soc.* 130: 1824–1825.

60 Yoneda, T., Sung, Y.M., Lim, J.M. et al. (2014). Pd^{II} complexes of [44]- and [46]Decaphyrins: the largest Hückel aromatic and antiaromatic, and Möbius aromatic macrocycles. *Angew. Chem. Int. Ed.* 53: 13169–13173.

61 Tokuji, S., Shin, J.-Y., Kim, K.S. et al. (2009). Facile formation of a benzopyrane-fused [28]Hexaphyrin that exhibits distinct Möbius aromaticity. *J. Am. Chem. Soc.* 131: 7240–7241.

62 Inoue, M., Kim, K.S., Suzuki, M. et al. (2009). Thermal fusion reactions of *meso*-(3-Thienyl) groups in [26]Hexaphyrins to produce Möbius aromatic molecules. *Angew. Chem. Int. Ed.* 48: 6687–6690.

63 Higashino, T., Inoue, M., and Osuka, A. (2010). Singly *N*-fused Möbius aromatic [28]Hexaphyrins(1.1.1.1.1.1). *J. Org. Chem.* 75: 7958–7961.

64 Saito, S., Shin, J.-Y., Lim, J.M. et al. (2008). Protonation-triggered conformational changes to Möbius aromatic [32]Heptaphyrins(1.1.1.1.1.1.1). *Angew. Chem. Int. Ed.* 47: 9657–9660.

65 Lim, J.M., Shin, J.-Y., Tanaka, Y. et al. (2010). Protonated [4n]π and [4n+2]π octaphyrins choose their Möbius/Hückel aromatic topology. *J. Am. Chem. Soc.* 132: 3105–3114.

66 Koide, T., Youfu, K., Saito, S., and Osuka, A. (2009). Multiple conformational changes of *β*-tetraphenyl *meso*-hexakis(pentafluorophenyl) substituted [26] and [28]hexaphyrins(1.1.1.1.1.1). *Chem. Commun.* 6047–6049.

67 Stępień, M., Latos-Grażyński, L., Sprutta, N. et al. (2007). Expanded porphyrin with a split personality: A Hückel–Möbius aromaticity switch. *Angew. Chem. Int. Ed.* 46: 7869–7873.

68 Yoon, M.-C., Shin, J.-Y., Lim, J.M. et al. (2011). Solvent-dependent aromatic versus antiaromatic conformational switching in *meso*-(Heptakis)pentafluorophenyl [32]Heptaphyrin. *Chem. A Eur. J.* 17: 6707–6715.

69 Higashino, T., Lee, B.S., Lim, J.M. et al. (2012). A Möbius antiaromatic complex as a kinetically controlled product in phosphorus insertion to a [32]Heptaphyrin. *Angew. Chem. Int. Ed.* 51: 13105–13108.

70 Tanaka, Y., Shin, J.-Y., and Osuka, A. (2008). Facile synthesis of large *meso*-pentafluorophenyl-substituted expanded porphyrins. *Eur. J. Org. Chem.* 2008: 1341–1349.

71 Yoneda, T., Soya, T., Neya, S., and Osuka, A. (2016). [62]Tetradecaphyrin and its mono- and Bis-Zn^{II} complexes. *Chem. A Eur. J.* 22: 14518–14522.

72 Shimizu, S., Aratani, N., and Osuka, A. (2006). *Meso*-Trifluoromethyl-substituted expanded porphyrins. *Chemistry A European Journal* 12: 4909–4918.

73 Shimizu, S., Cho, W.-S., Sessler, J.L. et al. (2008). *Meso*-aryl substituted Rubyrin and its higher homologues: structural characterization and chemical properties. *Chem. A Eur. J.* 14: 2668–2678.

74 Soya, T., Kim, W., Kim, D., and Osuka, A. (2015). Stable [48]-, [50]-, and [52]Dodecaphyrins(1.1.0.1.1.0.1.1.0.1.1.0): the largest Hückel aromatic molecules. *Chem. A Eur. J.* 21: 8341–8346.

10

Fundamentals of Porphyrin and Metalloporphyrin Stereochemistry

W. Robert Scheidt

Department of Chemistry and Biochemistry, University of Notre Dame, Notre Dame, IN, USA

Abbreviations

Porphyrins

OEP	dianion of octaethylporphyrin;
Piv_2C_8	dianion of α,α,5,15-[2,2′-(octanediamido)diphenyl]-α,α,10–20-bis(o-pivalamido-phenyl)porphyrin;
TCHP	dianion of *meso*-tetracyclohexylporhyrin;
TMP	dianion of tetramestylporphyrion;
T*p*-OCH_3PP	dianion of *meso*-tetra-*p*-methoxyphenylporphyrin;
TpivPP	dianion of $\alpha,\alpha,\alpha,\alpha$-tetrakis(*o*-pivalamidophenyl)porphyrin; TPrP, dianion of mesotetra-propylporphyrin;
TPP	dianion of *meso*-tetraphenylporphyrin;
TiPrP	dianion of *meso*-tetra-*iso*propylporphyrin;
TTP	dianion of *meso*-tetratolylporphyrin.
Ligands	Him, imidazole; 5-MeHIm, 5-methylimidazole; 2-MeHIm, 2-methylimidazole; 2-MeBzHIm, 2-methylbenzimidazole; Hind-Im, generic hinder imidazole; 4-CNPy, 4-cyanopyridine; 3-ClPy, 3-chloropyridine.
Other	N_p, porphinato nitrogen atom; EPR, electron paramagnetic resonance; *sad*; saddling; *ruf*, ruffling; *dom*, doming; *wav*, waving; *pro*, propellering.

10.1 General Introduction

Porphyrins are complex molecules in which four pyrrole groups are connected to form a macrocyclic ring. These materials have wide application across chemistry and biology. The formal diagrams of the macrocyclic frameworks of free-base porphyrin and its metalloderivatives are shown in Figure 10.1. The Kekule formulas would suggest that these strongly conjugated molecules should be very rigid and planar; hence, the stereochemical

Fundamentals of Porphyrin Chemistry: A 21st Century Approach, Volume 2, First Edition.
Edited by Penelope J. Brothers and Mathias O. Senge.
© 2022 John Wiley & Sons Ltd. Published 2022 by John Wiley & Sons Ltd.

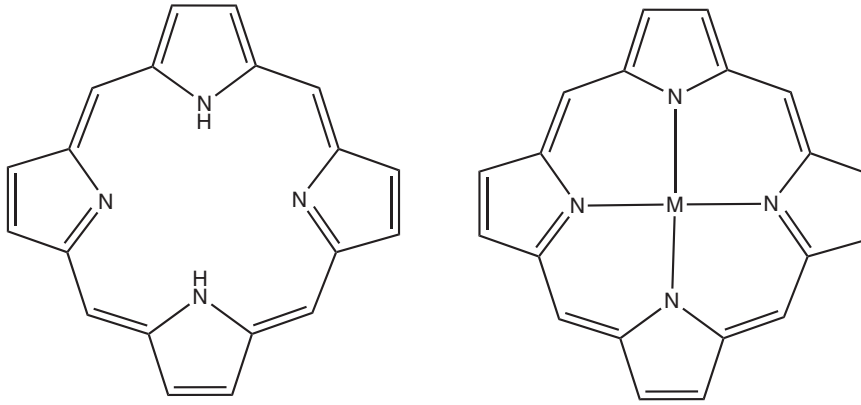

Figure 10.1 Diagrams of the core framework of the parent porphyrin trivially known as porphine. The free base is shown on the left, and a metalloporphyrin is shown at the right. Most characterized porphyrin species have peripheral substituents at either the β-positions or the *meso*-positions. Note that the carbon and nitrogen atoms in the ring center form a 16-membered ring.

variation of the complete set of species would be quite limited. Thus, this chapter should be a few paragraphs long – and boring. Fortunately, the opposite is true, and the stereochemical features of porphyrin systems are rich and diverse. Experimentally, substantial stereochemical variation of porphyrins and metalloporphyrins are known and need to be systematically understood. The adaptations can be simply stated in terms of the radial expansion of the central hole of the porphyrin and a number of distinct deformations or conformations of the nominally planar porphyrin ring. These stereochemical variations can occur separately or in combinations. This chapter will try to emphasize just the principles. More detailed reviews of porphyrin stereochemistry and correlations with physical properties will be found in [1–4].

This chapter will review the features of porphyrin molecules that lead to stereochemical/conformational variation. The first systems considered are the metalloderivatives. The coordination of a central metal ion replaces the two central hydrogens (Figure 10.1), typically with an increase in the molecular symmetry. Almost all metals of the periodic table are known to form metalloporphyrins. This vast array of metal ions encompasses a large range of ionic sizes (as given by their ionic radii, with a large set of experimental values available [5]). The coordination number of the metal ion coordinated by the porphyrin ligand ranges from four upward and primarily reflects the metal ion size. The fundamentals of metalloporphyrin stereochemistry are best framed in terms of the coordination number of the central metal ion.

Four-coordinate derivatives provide a useful framework for detailing the variety of porphyrin core conformations. In these species, the metal ion is coordinated solely to the four porphyrin nitrogen atoms, hereafter denoted as N_p [6]. With rare exceptions, these four-coordinate derivatives have the metal ion centered in the central hole of the ring. In these derivatives, the porphyrin macrocycle has enough flexibility to radially expand or contract the central hole to accommodate metal ions of varying sizes. The size of the central hole is conveniently expressed in terms of half of the transannular $N_p \cdots N_p$ distance. Much of this radial variation is accomplished with a planar porphyrin core, but in addition there can be contributions from nonplanar conformations that we will describe in the next sections. The range of observed transannular distances is about 3.8–4.2 Å. The modification

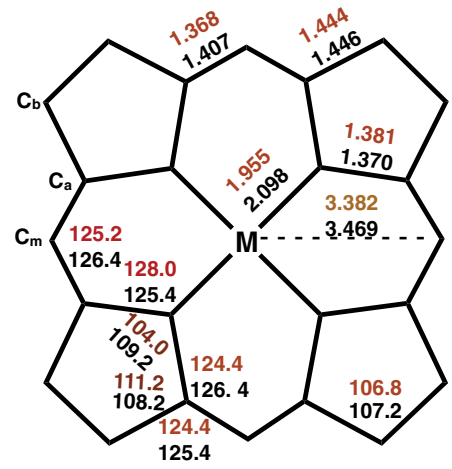

Figure 10.2 Formal diagrams of the core framework of two porphyrin derivatives. The top number of each pair is from planar nickel derivatives (blue) and the lower number is from $[Sn(TPP)(Cl)_2]$. Source: Adapted from a diagram originally given by Collins et al. [8].

in the hole size must lead to variation in ring strain for the central 16-membered ring. Of course, changes in ring strain can be accommodated by the gain in energy from the bonding interactions of the metal ion with the porphyrin. There is an optimum size for the central hole; Hoard suggested the term "hole size of least strain" and gave a value of 2.01 Å [7].

The limits of porphyrin core contraction and expansion were established early. Planar Ni(II) derivatives established the lower end of the scale at Ni–N_p of 1.955 Å, and the structure of the radially expanded core of $[Sn(TPP)(Cl)_2]$ set the upper limit at 2.098 Å. The large Sn ion was expected to remain in the porphyrin plane owing to the two axial chloride ligands. Figure 10.2 displays a number of bond distance and angles observed for the two limiting cases. The largest changes involve angles at the porphyrin nitrogen and the alpha carbons C_a. Note, however, that the sum of the angles subtended at the porphyrin nitrogen and alpha C_a atoms remain at 360°, consistent with rigorous planarity at these atoms.

10.2 Porphyrin Core Conformations and Four-Coordinate Species

The porphyrin ring displays substantial flexibility not only through radial expansion or contraction from an optimum hole size, but also with movement of core atoms perpendicular to the mean porphyrin plane (conventionally the *z* direction). It should be noted that in all of these distortions that the pyrrole rings themselves always remain completely planar. These distortions are illustrated in their symmetric form in Figure 10.3 and were systematically described in an early review by Scheidt and Lee [2]. The distortions are ruffling, *ruf*; saddling, *sad*; doming, *dom*; stepping, also described as waving; and the much less common propellering, *pro*. Stepping, or waving, can have components in either of two orthogonal directions (*wav(x)* or *wav(y)*). The figures illustrate the direction of atom motions from a perfectly planar core. In each of these, the displacement magnitude can show a substantial range of values; however, the requirements of the macrocyclic connectivity clearly demand that the individual values be substantially correlated. The term *pla* will be used for planar porphyrin cores. An insightful advance was set forth by Shelnutt and co-workers [9],

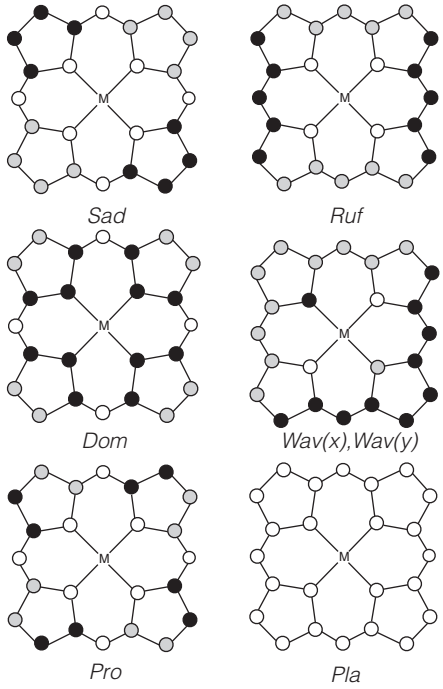

Figure 10.3 Diagrams illustrating porphyrin core distortions in directions perpendicular to the mean plane of the ring. KEY: open circles = at or near the mean porphyrin plane, black filled circles = positive displacements, gray filled circles = negative displacements. The illustrated core deformations represent the lowest-frequency out-of-plane normal coordinates needed to characterize core distortions observed in solid-state structures. (See Section 10.2.5 for a description of the combining of distortions.)

who correctly noted that many nonplanar porphyrins exhibit varying combinations of the components illustrated in Figure 10.3. This is discussed in more detail in Section 10.2.5.

10.2.1 Core Ruffling

The most common distortion from planarity is ring ruffling. In this deformation, the pyrrole rings rotate around the metal–N_p axes with alternating sign (direction). This leads to the methine carbon atoms having the largest displacements from the mean core and alternating up and down around the ring. The idealized symmetry of this distortion has all of the symmetry elements of the D_{4h} point group.

One of the two main mechanisms leading to ring ruffling is a consequence of the incorporation of small metal ions at the ring center. Although many examples might be given, the periodic variation in the M–N_p bond distances for several divalent first-row transition metal ions and three different porphyrin systems, along with considering ring conformations, clearly illustrate the effects. The simplest series are those with unsubstituted porphyrin, trivially known as porphine, which is the most truncated, with examples for the last four members of the first transition series, including zinc. For the porphine series and succeeding series, we give the M–N_p bond distance and the core conformation: Co (*pla*, 1.973 Å), > -Ni (*pla*, 1.951 Å), <Cu (*pla*, 1.999 Å), <Zn (*pla*, 2.037 Å) [10, 11].

Values of M–N_p for a series of octaethylporphyrin derivatives, all of which have planar cores, are as follows: Fe (1.972 Å) [12], >Co (1.971 Å) [13], >Ni (1.952 Å) [14] <Cu (1.998 Å) [15], <Zn (2.036 Å) [16]. The above [M(OEP)] series is a set of isomorphous crystal structures that are a 1-D stack of porphyrin molecules. There are two additional crystalline polymorphs of [Ni(OEP)], a tetragonal form with a ruffled porphyrin core and Ni–N_p = 1.929 Å [17] and a second form with a planar core and Ni–N_p = 1.958 Å [18]. It was this pair of derivatives that

led Hoard to quantitatively examine the effects of ring ruffling on the M–N_p bond distances [7]. As an amusing sidenote, it appears that this planar polymorph of [Ni(OEP)] only results when the crystallizing solution contains a small amount (~3%) of the free-base H_2OEP as an impurity.

The most extensive set of first-row divalent transition ions are those found with the porphyrin ligand tetraphenylporphyrin, several of which have ruffled porphyrin cores. The series of metal ions begins with Cr(II) and ends with Zn(II): Cr (*pla*, 2.033 Å) [19], <Mn (*pla*, 2.084 Å) [20], >Fe (*ruf*, 1.972 Å) [21], >Co (*ruf*, 1.949 Å) [22], >Ni (*ruf*, 1.928 Å) [23], <Cu (*ruf*, 1.981 Å) [24], <Zn (*pla*, 2.037 Å) [25]. The same ordering of bond distances is seen in all three porphyrin ligand series. The M–N_p values for planar sets for octaethylporphyrin (OEP) and porphine are nearly identical between elements, whereas the TPP set (except for Zn) has a bond distance difference of ~0.02 Å; the M–N_p bond distances in ruffled derivatives are always shorter.

A final comment concerns the structure of [Mn(TPP)] with the very large Mn(II) ion. It is likely that the Mn(II) ion is not quite centered in the porphyrin core but is displaced slightly above the porphyrin plane. Crystallographic limitations do not allow an assessment of the exact position. Note that the radial expansion observed in [Mn(TPP)] is near the limit of such expansion. No additional four-coordinate Mn(II) structures have been reported. There are however, four-coordinate main group derivatives with a metal ion that is substantially displaced out of the central four nitrogen atom plane. These include [Ge(TPP)] with a domed core and [Sn(OEP)] and [Pb(TPrP)] with roof-like folded cores. All have metal ions displaced from the porphyrin plane by about 1.0 Å and M–N_p distances ≥ 2.20 Å.

The other major mechanism leading to ring ruffling is an increase in the bulk of the four substituents at the *meso*-carbon positions. This was clearly demonstrated through a combination of structural observations and molecular mechanics calculations [26]. The effect of increasing the bulkiness of the *meso*-group substitutions leads to an increase in the magnitude of the ring ruffling. Nickel porphinato derivatives with *meso*-alkyl substituents such as *iso*-propyl [27] and cyclohexyl [28] displayed much stronger ruffling than that of tetraphenylporphyrin. Increased ruffling leads to shorter Ni–N_p bond distances, as might be expected. A capped stick diagram of [Ni(TiPrP)] is given in Figure 10.4 illustrating the ring ruffling.

Ring ruffling is also observed in many six-coordinate derivatives; the same general principles apply to the six-coordinate species as to the four-coordinate species. Some phosphorus(V) derivatives have the shortest M–N_p bonds at 1.83 Å [29].

10.2.2 Core Saddling

The appearance of saddled core conformations was originally somewhat mysterious. Although a saddled core has the same symmetry elements as that of a ruffled core, it is the β-carbon atoms – and not the methine carbon atoms – that undergo the largest displacements from the mean porphyrin plane. This conformation was first noted in the structures of a number of π-cation radical derivatives that had especially large out-of-plane displacements of the β-carbon atoms. Porphyrin π-cation radical derivatives are species that have been oxidized by the removal of an electron from the porphyrin and not the metal. Such radical species provide oxidizing equivalents for a number of oxidative biological processes. Although other explanations were originally offered, steric effects are the most probable explanation for the core conformation. The saddled structure of the π-cation radical $[Cu(TPP^{\cdot})]^+$ [30] is shown in the top diagram of Figure 10.5. In addition to the

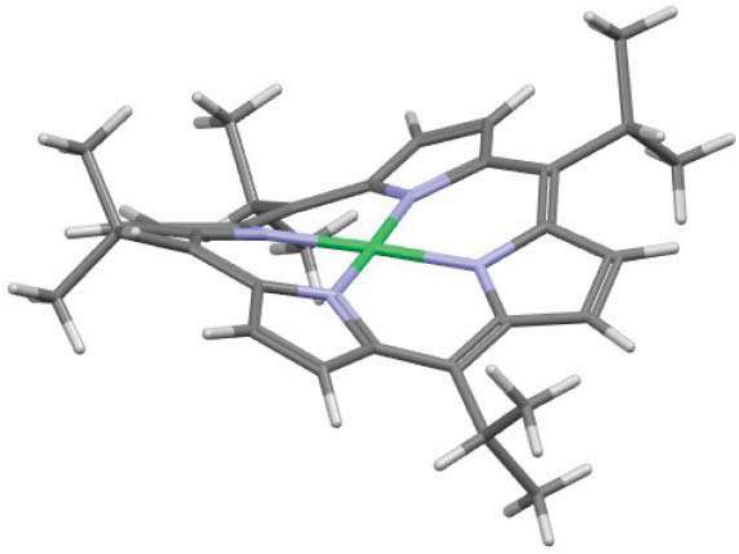

Figure 10.4 Diagram of the ruffling observed for the core conformation of [Ni(TiPrP)]. Source: Drawn from the coordinates reported in Ema et al. [27], CCDC refcode HETDAL. The average Ni–N_p bond distance is 1.896 Å.

strong saddling, the peripheral phenyl rings are more nearly coplanar with the porphyrin core; that is, the dihedral angles are much smaller than usual in order to form the dimeric structure shown in bottom diagram of Figure 10.5. The two porphyrin rings "cup" into each other as shown in the bottom diagram of Figure 10.5. The phenyl rings must form smaller dihedral angles to allow the close approach of the two cores. It is the steric effects of these small phenyl ring to core dihedral angles that also lead to the up-down motion of adjacent pyrrole rings, which is apparent for the two phenyl rings shown in the front of the top

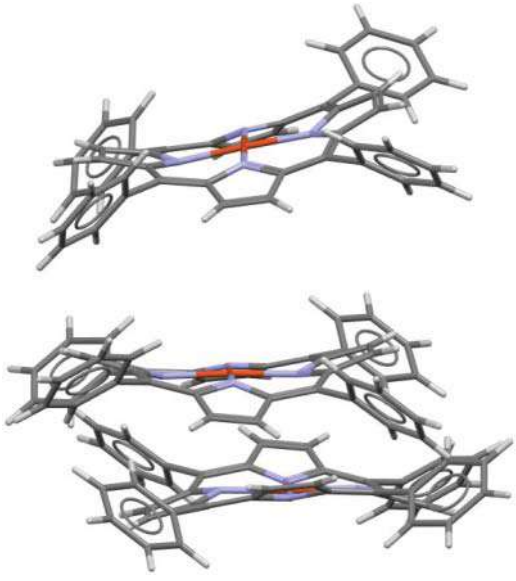

Figure 10.5 Diagrams of the saddling observed for the core conformation of the radical $[Cu(TPP^{\cdot})]^{+}$. Source: Drawn from the coordinates reported in Scholz et al. and Erler et al. [30], CCDC refcode BOSRAM10.

diagram of Figure 10.5. Similar features are seen in other π-cation derivatives formed from tetraarylporphyrins.

Highly substituted porphyrins, for example, dodecaphenylporphyrin or octaethyltetraphenylporphyrin, each with 12 peripheral substituents often lead to highly saddled structures including those of Ni, Co, and Cu. The Ni–N_p distance is extremely short at 1.906 Å [31]. However, it is to be noted that larger metal ions coordinated to these sterically congested porphyrins do tend toward more planar structures. Highly halogenated porphyrins are electron poor, stabilize lower oxidation states of metals, and have strongly saddled cores.

10.2.3 Core Doming

Porphyrin core doming is not typically observed in four-coordinate systems. But it is often seen in five-coordinate species in which the metal is found above the four nitrogens and toward the axial (fifth) ligand. Core doming is especially likely for complexes with larger metal ions, for example zinc or five-coordinate high-spin iron(II), and will be discussed in more detail later.

10.2.4 Core Waving

Waved conformations result from a folding of the porphyrin core along an M–N_p line given by a pair of diagonal porphyrin nitrogen atoms. Clearly two such foldings are possible. In some instances, the two orthogonal foldings may both contribute to the core conformation. Metallo derivatives where the metal ion is located at an inversion center often lead to relatively pure *wav* core conformations. An interesting example is found for the zinc derivative of mesotetracyclohexylporphyrin. In the nickel derivative, the crowded porphyrin periphery leads to strong ruffling, but in the zinc derivative, a stepped or waved conformation is observed with a modest core expansion [28]. The average Zn–N_p distance of 2.029 Å is in the normal range of values for four-coordinate zinc; the structure is illustrated in Figure 10.6.

10.2.5 Combining Deformations

Many observed core conformations cannot be described by a single deformation such as ruffling, doming, and so on, as described above. Moreover, it has long been clear the some

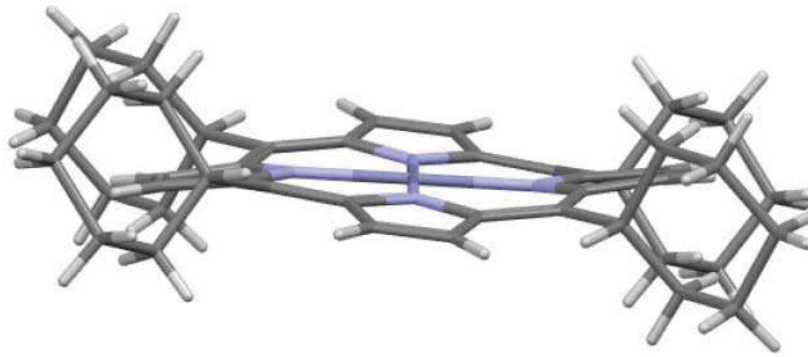

Figure 10.6 Diagram of the waved conformation observed for the core of [Zn(TCHP)]. Source: Drawn from the coordinates reported in Veyrat et al. [28], CCDC refcode ZULMIC. The average Zn–N_p bond distance is 2.029 Å.

core deformations are readily described as combinations. For example, the roof-like folding observed for [Sn(OEP)] is the combination of core doming and core ruffling. But many other core deformations are more difficult to describe. Shelnutt and co-workers proposed that all core conformations could be simulated by using only the six lowest-frequency out-of-plane normal coordinates; the procedure was called normal-coordinate structural decomposition (NSD). The NSD procedure can be used to determine the amounts of *sad*, *ruf*, *dom*, *wav*(*x*), *wav*(*y*), and *pro* that are required to simulate the observed out-of-plane distortions. The NSD procedure often shows a dominant deformation that is less (or not) evident from a simple examination of atomic displacements.

Although it is beyond the scope or this chapter, heme distortions and patterns of distortions have been suggested as important in a number of biological roles of hemes [32].

10.2.6 Structures of Dimers and Aggregates

The original reason for the synthesis of tetraphenylporphyrin and other tetraarylporphyrins was to provide porphyrin molecules with sufficiently bulky groups to prevent the aggregation phenomena that can plague solution studies of the natural porphyrins with alkyl substituents at the molecular periphery. These aggregation phenomena are presumed to result, at least in part, from porphyrin ring–ring interactions. The solid-state structures of porphyrin derivatives with nonbulky peripheral groups and at least one open face provide insight into the ring–ring interactions and were surveyed by Scheidt and Lee [2]. Almost all derivatives of this type exhibit an apparent aromatic interaction between pyrrole rings. Two limiting structural types were found: one in which porphyrin rings interact in an extended stacked arrangement and a second type in which porphyrin rings interact in pairs, both with similar inter-ring interactions. Scheidt and Lee posited that these features were driven by intermolecular π–π interactions and not crystal packing influences.

The stereochemical parameters for defining these structures are given in Figure 10.7, where M.P.S. is the mean separation between adjacent 24-atom mean planes, L.S. is the lateral shift measured between ring centers, and Ct· · ·Ct is the distance between ring centers. This survey suggested classification into three groups that are clustered depending on the observed lateral shift between ring centers. The first group, "S," had small lateral shifts of ~1.50 Å, and a second group, "I," had moderate lateral shifts clustered around 3.5 Å. This pattern of lateral shifts suggests that the most stable π–π interactions are confined to a narrow range of overlap

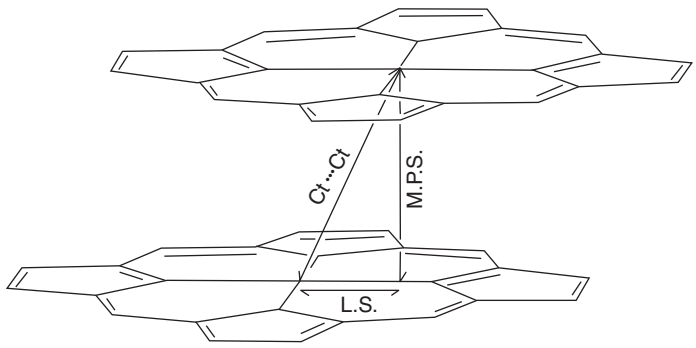

Figure 10.7 Diagram illustrating the geometric parameters used to describe the dimers formed by two porphyrin rings.

areas. The third group, "W," is more diffuse and has a large range of lateral shifts, but with mean plane separations of 3.4–3.6 Å. Some group W members, but probably not all, may result from the need to achieve efficient packing in crystalline solids. Note that the "special pair" of photosynthetic reaction centers has an overlap area that falls within group W. Further details concerning inter-ring parameters may be found in the original review [2].

10.2.7 Other Observations

Spin state issues (the number of unpaired electrons in the complex) are important in porphyrin stereochemistry. This feature is especially significant in complexes with coordination numbers greater than four where, depending on the nature and number of the additional ligands, more than one spin state is possible. The differing spin states have distinctly different stereochemical features. For the four-coordinate species, the spin state of the observed complex is typically low spin; only the iron derivatives have a spin state that is not low spin. Changes in spin state affect the size of the metal ion and have substantial consequences for the radial expansion of the core; these issues will be detailed in the successive sections.

The effects of asymmetric substitution at the porphyrin periphery have been little explored, at least in part because of synthetic challenges in porphyrin preparation. In one pioneering study, it was shown that the addition of two, four (either *cis* or *trans*), or six β-ethyl groups to tetraphenylporphyrin led to varying degrees of nonsymmetric porphyrin distortion. Both the free-base and metal (Cu and Zn) derivatives displayed mostly saddled cores, with nickel derivatives also showing ruffled cores [33].

10.3 Introduction to Five- and Six-Coordinate Species

The spin state of the metal ion is an important component of the stereochemistry of the five- and six-coordinate derivatives. For many metal ions, only two states (high and low spin) need to be considered, but in the iron systems the intermediate spin state must also be considered. Given the biological importance of iron derivatives (hemes), we will concentrate on iron systems that also serve as the stereochemical pattern expected for other metals. The main oxidation states of iron porphyrins are the +2 and + 3 states, and each will be considered separately.

An early review by Scheidt and Reed clearly demonstrated the tight connection between iron spin state and molecular structure [34]. Simple ligand field theory shows that the three orbitals whose lobes are directly between the porphyrin nitrogen atoms (d_{xz}, d_{yz}, and d_{xy}) are lower in energy that those pointing directly at the ligands (porphyrin nitrogen atoms and the axial ligand(s)) $\left(d_{z^2},\ d_{x^2-y^2}\right)$. These latter two orbitals are the stereochemically active orbitals, whose population always leads to longer bonds compared to low-spin complexes, where these two orbitals are unoccupied.

10.4 Iron(III) Derivatives

Under aerobic conditions, the stable oxidation state of iron porphyrin is the +3 (ferric) state, and we consider the complexes in this oxidation state first.

10.4.1 High-Spin (S = 5/2) Systems

The classical high-spin iron(III) complex is a pyramidal five-coordinate species with an anionic ligand such as chloride as the fifth ligand. This is schematically illustrated in Figure 10.8. There is a large variety of axial ligands beyond the halides that include pseudohalides, nitrate, sulfate, thiolates, carboxylates, alkoxides, and phenoxides that lead to high-spin five-coordinate complexes. A five-coordinate structure with a hindered imidazole is also known.

Core conformations for the large number of known iron(III) species include planar, *sad*, *ruf*, and *dom*. The appearance of the *sad* and *ruf* conformations is largely, if not entirely, the result of sterically congested porphyrins. The iron(III) is typically displaced by 0.48–0.52 Å from the 24-atom porphyrin mean plane, the axial bond distance is commensurate with the ligand, and average Fe–N_p distances are 2.055–2.070 Å. This pyramidal structure is due to the large size of the d^5 ion with the singly populated $d_{x^2-y^2}$ orbital, which is the crucial orbital for this stereochemistry. Population of this orbital in any five-coordinate species will lead to similar metal atoms displacements, for example, high-spin Mn(II) derivatives.

A related set of high-spin species are binuclear μ-oxo iron(III) complexes, where the two iron centers are bridged by a single oxygen atom (O^{2-}, oxo). The first structure determined, ([Fe(TPP)$_2$O]) [35], showed that the bulk of the two porphyrin ligands leads to an unusually large Fe–O–Fe bond angle of 174.5°, much larger that the ~150° observed in other binuclear iron(III) complexes with sterically undemanding ligands. Iron(III) is displaced by 0.50 Å from the 24-atom porphyrin plane. A number of additional μ-oxo examples have also been characterized; all have axial Fe–O bond distances of 1.75–1.78 Å. These are significantly shorter than the 1.81–1.84 Å-values for alkoxide and phenoxide iron porphyrinate derivatives. The oxo bridge can be protonated to form a μ-hydroxo species; the Fe–O(H)–Fe bond angle decreases to 146.2° along with increased Fe–O(H) bond distances of 1.92–1.95 Å [36].

The stereochemistry of high-spin six-coordinate derivatives is characterized by a substantial radial expansion to ~2.04 Å when the two axial ligands are neutral and to ~2.06 Å when the ligands are anions. In both cases, the iron is centered in the porphyrin plane. Core constraints clearly limit the radial expansion and that of the Fe–N_p bond lengths. Typically, the two axial ligands are identical; only a small number have an anion and neutral ligand. Only these mixed ligand systems have the iron atom displaced from the porphyrin ring center, where the displacement of iron can be up to about 0.25 Å toward the anionic ligand. Relatively weak field ligands are required to form these high-spin complexes; typical ligands include H_2O, O-bound sulfoxides, and fluoride ion.

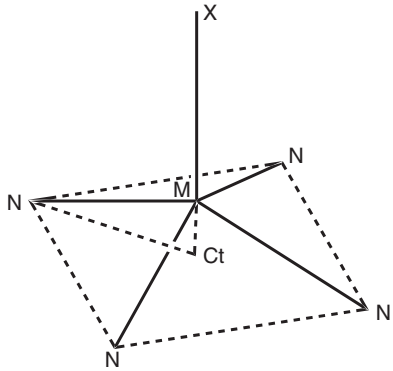

Figure 10.8 A schematic diagram of the square-pyramidal coordination group for five-coordinate metalloporphyrin species. Only the four nitrogen atoms of the porphyrin ligand are shown. X is a variety of anionic ligands that is briefly described in the text.

10.4.2 Intermediate-Spin (S = 3/2) Systems

Five-coordinate intermediate-spin species differ from the high-spin analogs in that the single axial ligand is one that is both more weakly binding and with a weaker ligand field, for example, that of a perchlorate or triflate ion. The resulting species have both smaller ion displacements (0.10–0.30 Å) and shorter Fe–N_p bonds (~2.00 Å). These are the expected structural features of any five-coordinate iron(III) derivative with all d-orbitals except $d_{x^2-y^2}$ occupied.

An unusual case arises when the energy difference between the "pure" S = 3/2 state and the S = 5/2 state is comparable in magnitude to the spin-orbit coupling constant. In this case, the two states can couple to form a new quantum mechanically admixed-intermediate spin state (S = 3/2, 5/2 state) [37]. The amount of the admixture leads to varying structures between the limits of high spin and intermediate spin, and those with a large component of the S = 5/2 state present structural features not too different from those of high-spin complexes. Further details may be found in a review [4].

There are relatively few six-coordinate intermediate-spin complexes. Stereochemically, they are characterized by short equatorial bonds and long axial bonds. Of course, short and long can be considered relative terms, but short Fe–N_p means short compared to that observed for high-spin species, and long axial distances means compared to those of low-spin species. This geometric pattern is the result of populating the stereochemically significant d_{z^2} orbital and would be expected for other metallo species with this electronic configuration. Ligands leading to these intermediate-spin species are weak field ligands such as alcohols, ethers (tetrahydrofuran, THF), or weakly σ-donating, π accepting ligands such as 4-cyanopyridine, especially in porphyrin systems with saddled porphyrin cores. A final unusual case is one in which the relative ligand orientation requires long axial bonds. Many of the six-coordinate intermediate-spin species are quantum-admixed (3/2,5/2) systems, which has a substantial effect on the value of the equatorial Fe–N_p bond distances, but not the axial bond lengths, which all remain long.

10.4.3 Low-Spin (S = 1/2) Systems

There are a limited number of five-coordinate low-spin iron(III) derivatives, all with small iron out-of-plane displacements of ~0.10–0.25 Å, and Fe–N_p distances of 1.96–1.99 Å. The ligands needed to form these species are high on the spectrochemical series with σ-bonded aryls and alkyl ligands, and nitric oxide. The iron atom displacements may reflect nonbonded contacts between porphyrin atoms and the axial ligand atoms; these close contacts are owing to short Fe–Ax bonds distance (1.65 Å in the case of NO).

Six-coordinate iron(III) species are predominantly low spin, and most have two identical axial ligands; mixed axial ligands are typically those of a neutral ligand and an anion, with small or no iron atom displacements. The iron is always effectively centered in the porphyrin plane. The axial bond distances are always short. The Fe–N_p bond distances are found in a relatively narrow range, with generally modest effects from the overall charge on the complex and core conformation issues. The range is on the order of 1.97–2.01 Å. Finally, there are important issues of the relative axial ligand orientation of the two planar ligands that have a real effect on stereochemical and electronic structure. These effects are described below.

Perhaps surprisingly, there are a number of variations of the S = 1/2 electron structure of iron in the six-coordinate species, which also have stereochemical consequences.

Fortunately, these electronic structures are readily characterized by electron paramagnetic resonance (EPR) spectroscopy. The most common EPR spectrum observed is a rhombic spectrum with three observed g values at $g_1 \approx 1.5–1.6$, $g_2 \approx 2.2–2.4$, and $g_3 \approx 2.8–3.0$ and closely satisfying the relationship $\sum g^2 = 16$. This type of spectrum is also observed in heme-based proteins. This particular EPR spectral type is relatively easily observed with strong signals.

The origin of the rhombic EPR spectrum can be understood with the aid of the diagram in Figure 10.9. The figure illustrates the d-orbital energy pattern for the three lowest energy orbitals, the only ones populated in low-spin iron(III). The difference between the average energy of the d_{xz} and d_{yz} orbitals and d_{xy} (the orbital in the porphyrin plane) is the tetragonal splitting, while the energy difference between the two d_π (d_{xz} and d_{yz}) orbitals is the rhombic splitting. These can be evaluated in terms of the magnitude of the spin-orbit coupling constant (approximate value 400 cm^{-1}) according to a procedure given by Taylor [38]. The tetragonal splitting can be on the order of three to four times that of the spin-orbit value and that of the rhombic splitting up can be twice that of the spin-orbit constant.

Is there a stereochemical basis for these splittings? What leads to rhombic splitting when the two ligands are identical? The tetragonal energy splitting is readily understood as the result of differing axial versus equatorial ligand fields. However, the energy differences in the two d_π orbitals (rhombic splitting) result from the axial ligand orientation effects. Ligand orientation effects can result from both relative and absolute orientations. The relative ligand orientation of two planar axial ligands is given by the dihedral angle of the two ligands, which are often exactly parallel. When the two ligand planes have a parallel, or close to parallel relative orientation, a rhombic EPR spectrum is observed, and the electronic structure depicted in Figure 10.9 results. Typical axial ligands for this class include two imidazoles or basic pyridines where the axial Fe–N_{Ax} distances are slightly shorter (1.96–1.98 Å) than the Fe–N_p distances. A number of species with an anionic ligand along with a neutral imidazole or pyridine also show this pattern.

Absolute ligand orientation, frequently denoted by φ, can be understood from Figure 10.10 and is the angle between the projection of the ligand plane and closest Fe–N_p vector. Values range between 0° and 45°. In the rhombic species, the absolute ligand orientation has modest but real effects. The best example is that found in the crystal of [Fe(TPP)$(HIm)_2$]Cl, which has two independent molecules in the solid [39]. One molecule has two φ angles of ~0° and rhombically distorted Fe–N_p distances (1.985 and 2.002 Å), whereas the second has two ligand φ angles near 45° and two equal distances (1.995 and 1.990 Å); the two have modest differences in their rhombic EPR spectra.

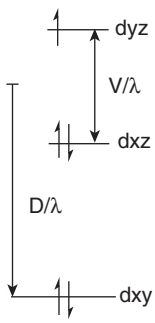

Figure 10.9 Diagram illustrating the orbital splitting pattern of low-spin iron(III) showing a rhombic electron paramagnetic resonance (EPR) spectrum. By convention the d_{yz} orbital is at higher energy than the d_{xz} orbital. The relative energies (in terms of the spin-orbit coupling constant λ) can be derived from the EPR spectrum.

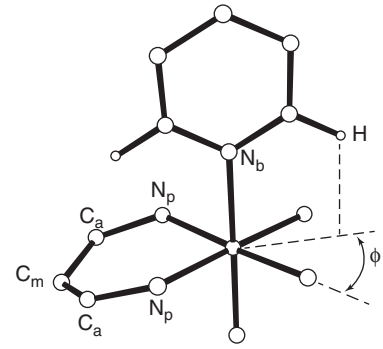

Figure 10.10 Diagram illustrating the steric interactions between an axial ligand and the core of a metalloporphyrin. The dihedral angle φ is between the plane of the ligand and the plane defined by a porphyrinato nitrogen atom, the metal, and the ligand nitrogen atom, N_b.

In a series of studies, Walker and Scheidt showed that a combination of modestly sterically hindered axial ligands and tetraarylporphyrins with bulky 2,6-substituents (e.g., TMP) leads to the two axial ligands having a relative perpendicular arrangement [40]. This orientation of the two axial ligands leads to a distinctly different type of EPR spectrum called, inter alia, HALS, strong g_{max} or large g_{max}. The signal in these systems is weak and only observed at low T (<20 K). Usually only the largest g value is observed with a value >3.20. The perpendicular orientation leads to equivalent energies of the two d_π orbital sand and hence a zero or very small rhombic splitting value. It became clear that moderately weak σ-donating ligands such as unsubstituted pyridine also gave systems with perpendicular orientations, even with unhindered porphyrins such as TPP. Such unusual EPR signals are also observed in some bis histidine-ligated electron transport proteins. The difference between the two states with limiting relative orientations of parallel and perpendicular may be very close. Indeed, in one derivative, $[Fe(TMP)(5\text{-MeHIm})_2]^+$, both parallel and perpendicular forms are known, each with its characteristic EPR spectrum of rhombic or g_{max} [41]. Other examples are now also known.

Porphyrin core conformations have an important effect on orbital energies. The iron(III) systems with perpendicular ligand orientations are seen to have both a strongly ruffled core and a smaller tetragonal splitting energy. A system with substantially enhanced ruffling, very short Fe–N_p bonds of 1.915 Å, and sterically demanding axial ligands, $[Fe(TiPrP)(2\text{-MeBzHIm})_2]^+$, is found to lead to a still different electronic structure where the two d_π orbitals are lower in energy than the d_{xy} orbital and give the orbital configuration $(d_{xz}, d_{yz})^4 (d_{xy})^1$ [42]. This unusual state was first found for complexes where the two axial ligands were extremely weak σ donors, but good π acceptors. Ligand examples include 4-CNPy, isocyanides, and phosphines. Ruffling is observed in all of these $(d_{xy})^1$ species; the strong ruffling allows electron donation from the porphyrin $3a_{2u}(\pi)$ orbital to the Fe d_{xy} [43]. These species give rise to axial EPR spectra with $g_\perp = 2.2–2.3$ and $g_\parallel = 1.8–1.9$. An extensive table of stereochemical and EPR parameters is given in a review [4].

There are a limited number of spin crossover complexes, including a system $(Fe(OEP)(3\text{-ClPy})_2]^+$) where the structures of the two states could be crystallographically resolved [44]. Stereochemical features from all systems, where known, follow the patterns of the particular spin state.

In summary, the stereochemical features of the iron(III) porphyrinates strongly follow the electronic structure, with population of the $d_{x^2-y^2}$ orbital leading to core expansion in

six-coordinate complexes and large out-of-plane displacements in five-coordinate complexes. Population of the d_{z^2} orbital will lead to long axial bond distances being expressed.

Many of the patterns reported here, save that of ligand orientation effects, are found for other six-coordinate species across the periodic table. Values of $M–N_p$ will reflect ionic radii of the central metal, and as described below, very large metal ions will have coordination geometries with coordination numbers greater than six.

10.4.4 Diatomic Ligands in Iron(III)

Heme complexes with diatomic ligands are an important feature of heme biochemistry. Although most of the important derivatives are iron(II) species, there a few iron(III) complexes that should be considered. Iron(III) species are known with two of the common heme diatomic ligands, NO (nitric oxide) and CN^- (cyanide). All cyanide derivatives are six-coordinate complexes, whereas NO forms both five- and six-coordinate complexes, even though the five-coordinate species readily add another ligand. All are known to be low-spin complexes with stereochemical features appropriate to low-spin species.

The Fe–NO bond is very short in the five-coordinate species at 1.65 Å with $Fe–N_p = 1.994$ and an out-of-plane displacement of 0.30 Å for iron. Addition of a *trans*-ligand does not substantially change the Fe–NO bond distance when the axial ligands are water, imidazole, or other nitrogen heterocycles and the Fe–N–O group is essentially linear. The situation is quite different when the *trans*-ligand is a σ-bonded phenyl [45] or thiolate. In those systems, the Fe–N–O group displays substantial changes, with the Fe–N–O angle increasing to 157–159°, along with lengthening of the Fe–NO bond; this change is related to strong σ donors trans to the NO.

The cyanide ion is a potent inhibitor to iron(III) heme proteins and forms low-spin heme complexes that are used as EPR probes. The Fe–CN bond distances are in the range of 1.91–1.93 Å with neutral nitrogen ligands as the *trans*-ligand. Bis-cyanide complexes are also known, with the Fe–CN bond distances slightly longer at 1.97–1.98 Å.

10.5 Iron(II) Derivatives

Stereochemical features of iron(II) follow those of the preceding iron(III) species with some differences resulting from the smaller energy gaps between d-orbitals favoring low-spin species. Assigning electronic structure is more challenging because fewer spectroscopic tools can be employed; Mössbauer spectroscopy is the most powerful tool.

10.5.1 High-Spin (S = 2) Systems

High-spin five-coordinate iron(II) hemes, especially with an imidazole as the fifth ligand, is one of the most important spin state/coordination number combinations and which represents the coordination group found in a large number of heme proteins. Obtaining these FeN_5 species is synthetically challenging, as the binding affinity for the sixth ligand is usually greater than that for the fifth ligand and leads to isolation of a six-coordinate species. The solution to this problem, as originally conceived by Collman and Reed, was to employ a sterically hindered imidazole. Sterically hindered imidazoles do not affect binding of the

fifth ligand, but are sterically inhibitory toward binding of the sixth ligand. The structure of the first five-coordinate derivative that utilized this strategy, [Fe(TPP)(2-MeHIm)], was never completely reported, but important details are available. In that structure, the Fe–N_p bonds are quite long at 2.086 Å, the iron(II) center is displaced by 0.55 Å from the 24-atom porphyrin mean plane, but only 0.42 Å from the plane of the four nitrogen atoms. This difference in iron displacements is consistent for a domed core.

However, in a series of structure determinations of related [Fe(Porph)(Hind-Im)] complexes, an apparent variety of core conformations are found. These are presented in Figure 10.11 as "shoestring" diagrams that also present the Fe–N_p distances. The original Collman/Reed complex is labeled as [Fe(TPP)(2-MeHIm)](2-fold) to distinguish it from a crystalline polymorph. The diagrams clearly show a variety of core conformations. The use of the Shelnutt NSD program showed that although the *dom* conformation is the dominant in all but one of the complexes, a number of different additional and varying components of core conformation contributions are found. A complete analysis is found in Table 3 of [47]. Also shown in Figure 10.11 is a porphyrin designed to block one face of the porphyrin from coordinating ligands ([Fe(Piv_2C_8)(1-MeIm)]). This structure is of somewhat reduced

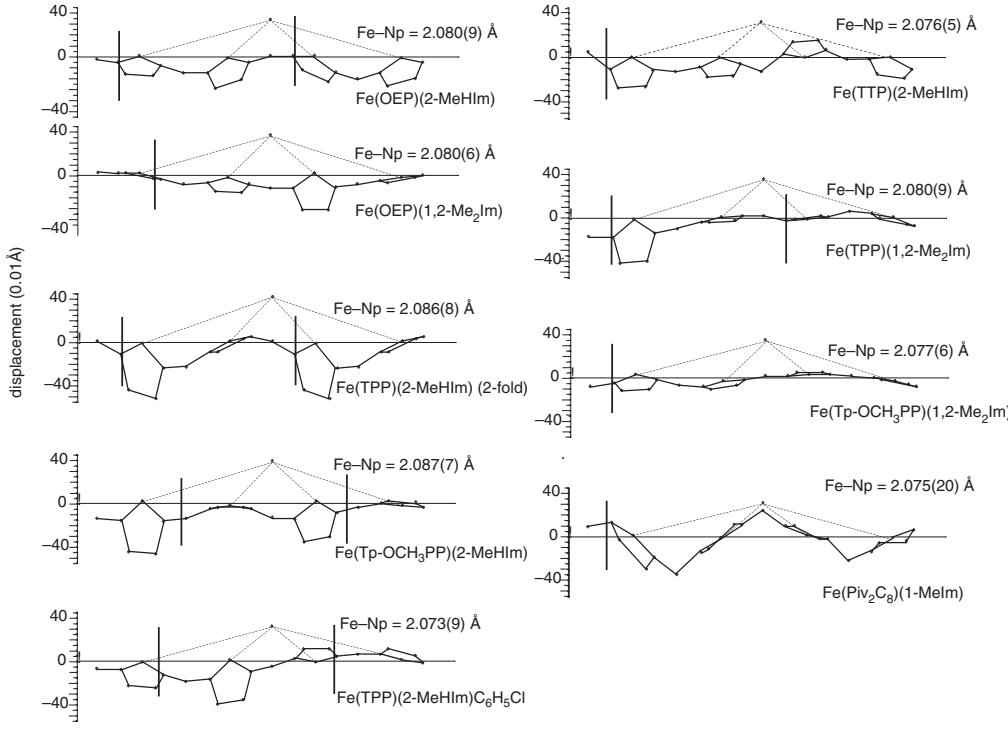

Figure 10.11 "Shoestring" diagrams illustrating the core conformation and iron displacement for nine imidazole-ligated high-spin iron(II) porphyrinates. The mean plane defined by the four porphyrin nitrogens is the horizontal line, and the cyclic porphyrin molecule is displayed in a linear fashion. The perpendicular displacement of the iron and other atoms of the core are shown from this four nitrogen plane. Bonds from the iron to the nitrogens are shown, and the position of the imidazole ligand with respect to directions defined by the Fe–N_p directions is shown by the vertical line (or lines when the imidazole has two positions). Source: Reproduced from Hu et al. [46] with permission from the Royal Society of Chemistry.

resolution, but the unhindered imidazole has a similar axial bond length (average of all Fe–N_{Ax} = 2.147 Å).

In all of these iron(II) derivatives, the large size of the iron is accommodated not only by the large displacements and long Fe–N_p bonds, but also by a substantial radial expansion of the porphyrin core; the Ct· · ·N_p distances are generally 2.046–2.047 Å.

There is one additional important feature of the five-coordinate high-spin iron(II) species, namely, that there are two distinct electronic configurations with stereochemical consequences [46]. Figure 10.12 displays the structural differences between the average coordinate geometry of iron ligated by imidazole versus that ligated by imidazolate. The differences are sufficiently large to suggest that the iron(II) displays a different "size" with a larger iron displacement and longer Fe–N_p bonds in the imidazolate. This stereochemical pattern is also seen in all other five-coordinate derivatives with a variety of anionic axial ligands. High-spin iron(II) with its d^6 state requires that one d-orbital be doubly occupied. In the imidazole-ligated iron(II), this orbital is a low-symmetry orbital comprising the d_{xz} (in the plane of the imidazole) strongly mixed with a porphyrin E(g) orbital. This orbital must be oblique to the heme plane. In the complexes with an anionic ligand, the doubly occupied orbital is the symmetric d_{xy} orbital in the heme plane. This orbital occupancy distinction can be experimentally verified by a number of physical properties, most notably by Mössbauer spectroscopy with the two classes having opposite signs of the quadrupole splitting. Analysis of core conformations in the anionic ligated systems by NSD shows that doming is even more prevalent in these systems.

A limited number of six-coordinate high-spin iron(II) complexes are known. The requirements to form these are very stringent: very weak field axial ligand, for example,

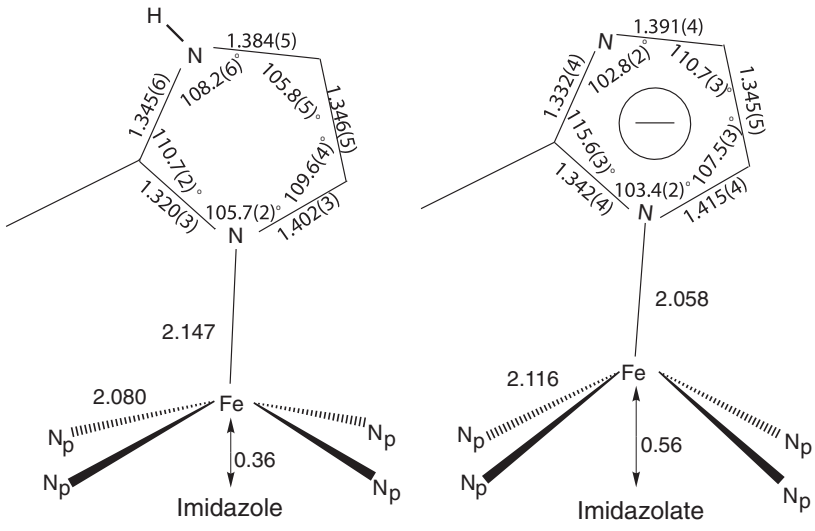

Figure 10.12 Diagram illustrating the differences in the coordination group structure and the five-membered ring geometry between imidazole and imidazolate species. The number to the left in each diagram is the average F–N_p distance, the middle number is the iron displacement from the four nitrogen plane, and the top number is the value of the axial bond distance. Distances and angles for the ligand ring are also displayed. Source: Reproduced from Hu et al. [46] with permission from the Royal Society of Chemistry.

[Fe(TPP)$(THF)_2$], which has an expanded core (Fe–N_p = 2.057 Å) or very electron-poor porphyrins also with very weak field ligands with even more expanded cores.

10.5.2 Intermediate-Spin (S = 1) Systems

There are no intermediate-spin species other than the four-coordinate species already described.

10.5.3 Low-Spin (S = 0) Systems

The majority of iron(II) porphyrinates are found in the low-spin (diamagnetic) state. In five-coordination, the axial ligands are almost exclusively diatomic ligands that will be considered in the next section. Most of the six-coordinate species with differing axial ligands have a diatomic ligand trans to another ligand; a few have a ligand that is a surrogate for the diatomic including nitroso and isocyanide ligands. All complexes follow the same stereochemical pattern described in the next section.

Most low-spin iron(II) species have two identical axial ligands. In addition to a large number with pairs of neutral nitrogen donors, there are species with a number of phosphines, a few alkyl amines, nitrosobenzene, a thioether, and an S-bound sulfoxide. The vast majority have iron at an inversion center that requires iron to be located exactly at the ring center. Planar cores are predominant. The iron is effectively centered even in those derivatives where it is not required by crystallographic symmetry. The Fe–N_p bond distances are slightly longer (~0.01 Å) than those for the iron(III) derivatives with the same core conformation.

A comparison of axial bond distances with the analogous low-spin iron(III) derivatives does reveal some interesting differences. The distances to the donor atom of ligands like isocyanides or phosphines are seen to be shorter in the iron(II) complexes, while the distances to neutral nitrogen donors like imidazoles or pyridines are longer in the iron(II) complexes. Distances to neutral sulfur donors are the same in the two oxidation states. It can be presumed that these patterns reflect differences in π-bonding in the two oxidation states with stronger interactions with the d^6 iron(II) and good π acids.

Almost all of the complexes with planar neutral nitrogen axial donors have the two ligands in relative parallel planes. Surprisingly, the strategies used to force relative perpendicular orientations of axial ligands in iron(III) were unsuccessful for iron(II) derivatives [48]. A comparison of the binding constants of various pyridines with varying basicities shows that the values are similar for all iron(II) but not for iron(III). This leads to the conclusion that there is little to be gained from iron(II) to ligand π-back-bonding; that is, the dπ orbitals are relatively non-interacting. Moreover, theoretical calculations suggest that ring ruffling is much less favored for iron(II) relative to iron(III) species. All of this leads to the expectation of structures with parallel ligand orientations for iron(II) and possible effects on the iron II/III redox potentials.

The few iron(II) cases that do not have relative parallel orientations of the two axial ligands appear to be special cases, including several derivatives with electron-poor porphyrins; these species have *sad* core conformations. The one known case of strong ring ruffling is found for the bis(2-methylimidazole) complex with Fe(TMP) where the Mössbauer parameters are unique among bis(ligated) iron(II) porphyrinates. This is consistent with the very much shortened Fe–N_p bonds of 1.96 Å that are about 0.04 Å shorter than usual and with expected changes in d-orbital energies.

In summary, the stereochemical features of the iron(II) are less varied, but otherwise similar. The major difference is the importance of diatomic ligand complexes in iron(II) as described in the following section.

10.5.4 Diatomic Ligands in Iron(II)

Diatomic ligands with iron(II) porphyrinates are a prominent feature of biological heme proteins with a phenomenal variety of reactivities and functions. Hemes of hemoproteins interact with diatomic molecules to transport, utilize, and sense them. Sensing a diatomic generally leads to some further action: control of enzyme activity, protein synthesis, or other cellular processes. The major diatomic ligands in sensing are O_2, NO, CO, and perhaps H_2S (a recent addition), which is found as HS^- in the biological environment.

With rare exceptions, both the five- and six-coordinate heme complexes with diatomics are low-spin species and follow the expected stereochemical patterns with equatorial Fe–N_p bonds of 1.99–2.00 Å and very small displacements of iron in the six-coordinate derivatives of less than 0.10 Å. In the five-coordinate species, the iron displacements are larger, in the range of 0.20–0.30 Å.

CO. Although CO is best known in biology for its toxicity, it does have roles in sensing. Moreover, the study of CO as a ligand with heme is utilized for the insight it provides for structure/function in the heme proteins. The FeCO vibrational behavior is responsive to the *trans*-ligand and the protein environment of the CO ligand. A most important component of the vibrational behavior is the correlation between the Fe–CO and C–O stretching frequencies. Strengthening the F–C bond leads to weakening of the C–O bond and is the basis for the well-known π-back-bonding correlation that is readily followed with vibrational spectra. The changes in the vibrational frequencies should, in principle, also be observable in changing bond distances. Although the bond distance differences are small, they have been observed in a series of [Fe(TPP)(imidazole)(CO)] complexes. The inverse relation between bond distances is seen with Fe–CO distances of 1.764–1.740 and C–O distances of 1.138–1.149 Å, respectively. These distances are well within the range observed for a large number of six-coordinate CO complexes. The precision of the structures required to demonstrate the correlation is considerably better than the norm. The data are available in [49]. Most of the *trans*-ligands are a variety of neutral nitrogen donors, including sterically hindered imidazoles. The trans Fe–N_{Ax} distance ranges from 2.04 to 2.14 Å. A limited number of other *trans*-ligands have been structurally characterized, including thiolates and THF.

Although it is expected that the *trans*-ligand in CO complexes, when it is a good σ-donor, enhances the Fe–CO bond, there are hemes coordinated solely by CO. [Fe(OEP)(CO)] has an Fe–CO bond of 1.714 Å, slightly shorter than those found in the six-coordinate species with a trans σ-donor. A six-coordinate bis-CO complex has also been structurally characterized. In that complex, the two CO ligands complete for iron π density, and the (two) Fe–CO bonds lengthen to 1.856 Å.

The diatomic CS ligand, an analogue of CO, is known from organometallic chemistry to be a better π-acceptor ligand than CO. This is indeed realized, for the Fe–CS bonds are found to be ~0.06 Å shorter compared to the analogous five- and six-coordinate CO complexes.

O_2. Stereochemical characterization of heme complexes coordinated to a dioxygen molecule is challenging. Although the proteins that reversibly carry dioxygen, most prominently myoglobin and hemoglobin, do so without autoxidation, simpler iron(II) porphyrinate systems are just oxidized to iron(III) when attempts to coordinate O_2 are

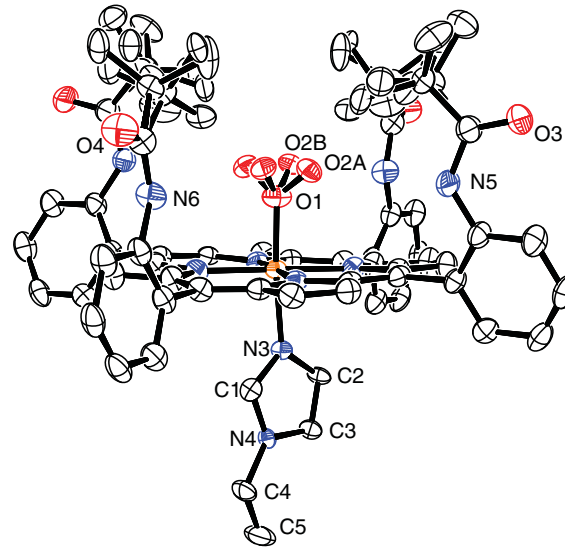

Figure 10.13 ORTEP diagram illustrating the pocket of picket fence porphyrin and the disordered O_2 ligand. The two positions of O_2, labeled O2A and O2B, can have differing atomic occupancies. Only one of the two orientations of the 1-ethylimidazole is shown.

made. The only solution that has led to crystallizable iron(II) dioxygen complexes is the picket fence porphyrin devised by Collman. In this derivative, four pivalamide groups form a ligand binding pocket that prevents binuclear reactions involving the dioxygen ligand, as illustrated in Figure 10.13. The figure also illustrates the difficulties encountered. The molecule has crystallographically demanded twofold symmetry, which leads to disorder of the *trans*-imidazole group and the dioxygen ligand. The dioxygen ligand is further disordered in the pocket into four positions. This clearly limited the precision of the early (room temperature) structure determinations. However, those structures clearly solved one contentious structural problem, namely, that the dioxygen is bonded end on with a nonlinear Fe–O–O group [50]. Later multitemperature structure determinations improved the precision. In one structure, that of [Fe(TpivPP)(O_2)(2-MeHIm)], some ordering of the dioxygen ligand could be induced at 80 K [50]. The structural parameters from that determination are Fe–O_2 = 1.811 Å, Fe–O–O = 118.2°, and O–O = 1.281 Å. An off-axis tilt of the Fe–O_2 bond is also noted.

It should be noted that the name picket fence porphyrin suggests a totally noninteracting set of groups that define the ligand binding pocket. This is not correct; the amide groups clearly provide some polarity to the pocket. However, the N–H groups of the pivalamides are too distant to form hydrogen bonds with the O_2 ligand.

NO. The nitric oxide ligand is the most non-innocent ligand of the diatomics. In recognition of this and the strongly covalent nature of the Fe–NO bond, the notation $\{FeNO\}^n$ is often used as a descriptor, where n is the number of metal d electrons plus the number of π^* electrons of NO. Heme complexes exists in three distinct states, the first of which, ($\{FeNO\}^6$), has been described in the iron(III) section.

Although NO was originally recognized as a toxic gas, it is now recognized as important biologically, with significant roles in signaling, neurotransmission, and in immune defense against pathogens. The $\{FeNO\}^7$ species are important components and include both five- and six-coordinate species. Early characterization of five-coordinate species was hampered by disorder in the position of the NO ligand, but more recent studies with completely ordered NO groups revealed unexpected stereochemical features. These include an off-axis tilt of the

Fe–NO bond and induced equatorial bond inequivalences of ~0.02 Å that are correlated with the NO orientation. The Fe–N–O group is "half-bent" with an angle of 142–144°, and the Fe–NO distance of 1.72–1.73 Å is about 0.10 Å longer than those of the $\{FeNO\}^6$ derivatives. More complete details are found in two reviews [51, 52].

The addition of a sixth neutral nitrogen ligand to form six-coordinate complexes occurs, but the trans bond distance was found to be much longer than expected. The 0.15 Å or longer increase in the Fe–N_{Ax} distance is the result of a large trans effect by NO, which is also reflected in small binding constants for the addition of the *trans*-ligand. This trans effect also leads to the ready loss of the sixth ligand, a feature of probable biochemical significance.

Later structural characterization of several six-coordinate $\{FeNO\}^7$ nitrosyls revealed another important feature, the relatively easy and reversible rotation of the NO group about the Fe–N(NO) bond with completely ordered NO groups at 100 K and disordered NO groups at higher temperatures [53, 54]. The easy rotation of the NO is also consistent with the disordered NO frequently found in both the five- and six-coordinate structures.

One electron reduction of five-coordinate $\{FeNO\}^7$ nitrosyls yields derivatives with major changes in the Fe–NO bond length (to 1.81–1.82 Å) and Fe–N–O bond angle (to 122–127°) [55].

CN^-. Cyanide ion and carbon monoxide are isoelectronic and isosteric diatomics. However, CN^- is a much poorer π-acceptor than CO as demonstrated by the stereochemical parameters for analogous iron(II) species with CN^- and CO. Perhaps the most dramatic difference is found for the five-coordinate cyanide species. The ligand field strength of cyanide is insufficient to yield a low-spin complex under all conditions. Rather, $[Fe(TPP)(CN)]^-$ is a spin crossover complex that is low spin at low temperature, but begins a gradual crossover to a high-spin state at ~200 K. The low-spin Fe–(CN) bond distance is 0.17 Å longer that the Fe–C distance in the five-coordinate CO. The difference in the high-spin form is larger still. Similar differences in the Fe–C are seen in the six-coordinate species with imidazole as the *trans*-ligand. In the bis-CN versus the bis-CO, the difference in 0.11, with the distance being larger than in the five-coordinate species. All in all, the differences give a clear indication of the weaker π-bonding capability of cyanide. But in all other aspects, the stereochemistry of the CO and CN^- species is quite similar.

HS^-. The diatomic anion HS^- is the most probable physiological form of H_2S for which evidence as a biological messenger continues to increase. HS^- reduces iron(III), and hence iron(II) species have been characterized. The species are high spin, unlike the other diatomic species, and have similar stereochemical parameters as other five-coordinate high-spin iron(II) complexes [56].

10.6 Higher Coordination Number States

Metalloporphyrin complexes with higher coordination numbers, that is, greater than six, are represented by examples of early transition metals, especially those of the second and third row and lanthanide and actinide elements. In these species, the metal ion is typically much above the four nitrogen porphyrin plane and with other ligand(s) that provide three or more additional donor atoms. The additional ligand(s) reflect the charge/size demands of the metal ion. Metal ion displacements from the porphyrin plane are large, and the M–N_p

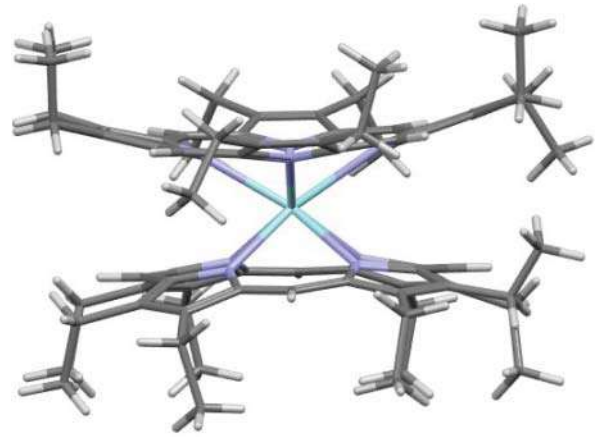

Figure 10.14 Diagram of the domed core conformations of $[Zr(OEP)_2]$. Source: Drawn from the coordinates reported in [57], CCDC refcode KORGIH. The Zr ion is displaced by 1.27 Å, and the average $Zr-N_p$ bond distance is 2.394 Å.

bond distances are also large. Many of these molecules can be described as half-sandwiches, with the additional ligands typically being oxygen donors. Additionally, there are many double- and triple-decker sandwiches, many with combinations of phthalocyanine and porphyrin rings. The structure of one such derivative, $[Zr(OEP)_2]$ is shown in Figure 10.14. Note that both cores are domed toward the central Zr ion and the two rings define a square antiprism.

10.7 Porphyrin Free Bases

The porphyrin molecule, trivially called free-base porphyrin, has two inner hydrogen atoms bonded to opposite nitrogen atoms and is intrinsically less symmetric than the typical metalloporphyrin. The geometries of the two pyrrole rings are distinct, with large differences seen at the C_a–N_p–C_a angle; the N–H substituted pyrrole rings have bond angles that are 3°–5° larger. The symmetrically substituted molecules with substituents at either the *meso*- or the β-positions are mostly planar, whereas the dodecasubstituted molecules have saddled core conformations, much like their metallated derivatives. Free-base species with 8 substituents can be either symmetric or asymmetric, whereas those with 6 or 10 substituents are asymmetric. The symmetric species have planar cores, whereas those that are asymmetric have more distorted cores.

However, in all cases, the two hydrogen atoms do lead to steric crowding with differing N···N transannular distances between the two pairs of pyrrole rings, that is, rhombic distortions. The differences between the two transannular distances can be as large as 0.44 Å, although most are on the order of 0.2 Å or even less. Despite wide variation in the two N···N distances, it is notable that the average of the two transannular distances clusters around a common value of 4.11 ± 0.02 Å. The near constancy of the ring hole size suggests that ring strain can be differently distributed depending on the substituents and their location on the ring.

A few solid-state derivatives do not show localized N–H pyrrole rings, and their pyrrole ring geometries are between those of the two ring types. Whether this N–H disorder is the result of static or dynamic effects cannot be ascertained from the structures.

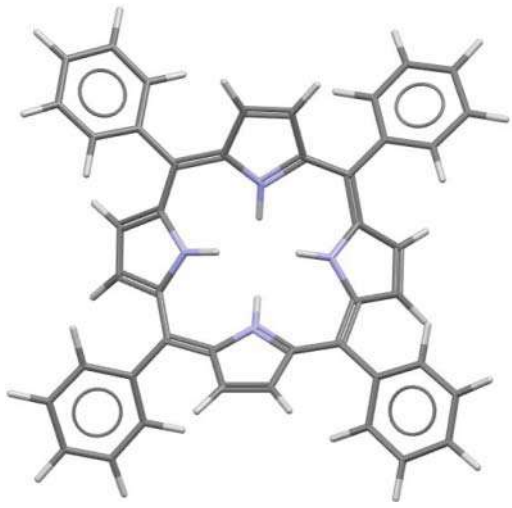

Figure 10.15 Diagram of the saddled core conformations of $[H_4TPP]^{2+}$. The two vertical pyrrole rings have the N—H groups tilted down from the mean plane, whereas the horizontal pyrrole rings are tilted up. Source: Drawn from the coordinates reported in Stone and Fleischer [58], CCDC refcode TPPFEC.

10.8 Porphyrin "Acids"

One or two protons can be added to the porphyrin molecule to form the so-called porphyrin "acids." The addition of two protons leads to diacids or dications that have long been known [58]. The steric crowding of four protons at the ring center typically leads to saddled core conformations. The saddling distortions are large, but there are substantial differences in the degree of ring saddling that depend on both the substituent location and the crystalline environment. Sizes of the ring hole are ~0.10 Å larger than those of the neutral precursors. The extreme ruffling of $[H_4TPP]^{2+}$ is shown in Figure 10.15. In the perspective shown, the molecule appears to be almost flat as the dihedral angles of the phenyl groups with the porphyrin core mean plane are small: ~27°. The tilt of the pyrrole rings lead to hydrogen atoms that are displaced by 0.5–0.7 Å from the mean plane of the porphyrin core.

Monoacid derivatives are much rarer. In the structure of $[H_3OEP]^{+}$, the protonated pyrrole ring opposite the unique pyrrole ring is tilted up, thus allowing easy access for the second protonation. Such structures suggest why the second protonation step is more favorable than the first.

References

1 Scheidt, W.R. and Gouterman, M. (1983). Ligands, spin state and geometry in hemes and related metalloporphyrins. In: *Review Article in Iron Porphyrins, Part One* (ed. A.B.P. Lever and H.B. Gray), 89–139. Reading, MA: Addison-Wesley.

2 Scheidt, W.R. and Lee, Y.J. (1987). Recent advances in the stereochemistry of metallotetrapyrroles. *Struct. Bonding (Berlin)* 64: 1–70.

3 Scheidt, W.R. (2000). Systematics of the stereochemistry of porphyrins and metalloporphyrins. In: *The Porphyrin Handbook*, vol. 3 (ed. K.M. Kadish, K. Smith and R. Guilard). San Diego, CA and Burlington, MA: Academic Press Chapter 16.

4 Scheidt, W.R. (2012). Stereochemical systematics for porphyrins and metalloporphyrins. In: *Handbook of Porphyrin Science*, Coordination Chemistry and Materials, vol. 24

(ed. K.M. Kadish, K. Smith and R. Guilard), 1–180. Singapore and Hackensack, NJ: World Scientific.

5 Shannon, R.D. and Prewitt, C.T. (1969). Effective ionic radii in oxides and fluorides. *Acta Crystallogr.* B25: 925–946.

6 A complete list of abbreviations is given at the beginning of the chapter.

7 (a) Hoard, J.L. (1971). Stereochemistry of hemes and other metalloporphyrins. *Science* 174: 1295–1302. (b) Hoard, J.L. (1973). Some aspects of metalloporphyrin stereochemistry. *Ann. N. Y. Acad. Sci.* 206: 18–31.

8 Collins, D.M., Scheidt, W.R., and Hoard, J.L. (1972). Crystal structure and molecular stereochemistry of $\alpha,\beta,\gamma,\delta$-tetraphenylporphinatodichlorotin(IV). *J. Am. Chem. Soc.* 94: 6689–6696.

9 Jentzen, W., Song, X.Z., and Shelnutt, J.A. (1997). Structural characterization of synthetic and protein-bound porphyrins in terms of the lowest-frequency normal coordinates of the macrocycle. *J. Phys. Chem. B* 101: 1684–1699.

10 Jentzen, W., Turowska-Tyrk, I., Scheidt, W.R., and Shelnutt, J.A. (1996). Planar solid-state and solution structures of (Porphinato)nickel(II) as determined by X-ray diffraction and resonance Raman spectroscopy. *Inorg. Chem.* 35: 3559–3567.

11 Jentzen, W., Shelnutt, J.A., and Scheidt, W.R. (2016). Metalloporphines: dimers and trimers. *Inorg. Chem.* 55: 6294–6299.

12 Straus, S.H., Silver, M.E., Long, K.M. et al. (1985). Comparison of the molecular and electronic structures of (2,3,7,8,12,13,17,18-Octaethylporphyrinato)iron(II) and (*trans*-7,8-34 Dihydro-2,3,7,8,12,13,17,18-octaethylporphyrinato)iron(II). *J. Am. Chem. Soc.* 107: 4207–4215.

13 Scheidt, W.R. and Turowska-Tyrk, I. (1994). Crystal and molecular structure of (Octaethylporphinato) cobalt(II). Comparison of the structures of four-coordinate M(TPP) and M(OEP) derivatives (M = Fe–cu). Use of area detector data. *Inorg. Chem.* 33: 1314.

14 Brennan, T.D., Scheidt, W.R., and Shelnutt, J.A. (1988). New crystalline phase of (octaethylporphinato) nickel(II). Effects of π-π interactions on molecular structure and resonance Raman spectra. *J. Am. Chem. Soc.* 110: 3919–3924.

15 Pak, R. and Scheidt, W.R. (1991). Structure of (2,3,7,8,12,13,17,18-octaethylporphinato) copper(II). *Acta Crystallogr. Sect. C* C47: 431–433.

16 Ozarowski, A., Lee, H.M., and Balch, A.L. (2003). Crystal environments probed by EPR spectroscopy. Variations in the EPR spectra of CoII(octaethylporphyrin) doped in crystalline diamagnetic hosts and a reassessment of the electronic structure of four-coordinate cobalt(II). *J. Am. Chem. Soc.* 125: 12606–12614.

17 Meyer, E.F. Jr., (1972). The crystal and molecular structure of nickel(II)octaethylporphyrin. *Acta Crystallogr. Sect B* B28: 2162–2167.

18 Cullen, D.L. and Meyer, E.F. Jr., (1974). Crystal and molecular structure of the triclinic form of 1,2,3,4,5,6,7,8-octaethylporphinatonickel(II). *J. Am. Chem. Soc.* 96: 2095–2102.

19 Scheidt, W.R. and Reed, C.A. (1978). Stereochemistry of the toluene solvate of $\alpha,\beta,\gamma,\delta$-tetrapheylporphinatochromium(II). *Inorg. Chem.* 17: 710–714.

20 Kirner, J.F., Reed, C.A., and Scheidt, W.R. (1977). Stereochemistry of manganese porphyrins. 2. The toluene solvate of $\alpha,\beta,\gamma,\delta$-tetraphenylporphinatomanganese(II) at 20° and −175 °C. *J. Am. Chem. Soc.* 99: 1093–1101.

21 Collman, J.P., Hoard, J.L., Kim, N. et al. (1975). Synthesis, stereochemistry, and structure-related properties of α, β, γ, δ-tetraphenylporphinatoiron(II). *J. Am. Chem. Soc.* 97: 2676–2681.

22 Madura, P. and Scheidt, W.R. (1976). Stereochemistry of low-spin cobalt porphyrins. VIII. $\alpha,\beta,\gamma,\delta$-tetraphenylporphinatocobalt(II). *Inorg. Chem.* 15: 3182–3184.

23 (a) Jentzen, W., Song, X.-Z., Turowska-Tyrk, I., et al. In preparation. During the preparation of this paper, the crystal structure of Ni(TPP) was obtained independently and reported, see: (b) Maclean, A.L., Foran, G.J., Kennedy, B.J. et al. (1996). Structural characterization of nickel(II) tetraphenylporphyrin. *Aust. J. Chem.* 49: 1273–1278.

24 Fleischer, E.B., Miller, C.K., and Webb, L.E. (1964). Crystal and molecular structures of some metal tetraphenylporphines. *J. Am. Chem. Soc.* 86: 2342–2347.

25 Scheidt, W.R., Kastner, M.E., and Hatano, K. (1978). Stereochemistry of the toluene solvate of $\alpha,\beta,\gamma,\delta$-tetraphenylporphinatozinc(II). *Inorg. Chem.* 17: 706–710.

26 Jentzen, W., Simpson, M.C., Hobbs, J.D. et al. (1995). Ruffling in a series of nickel(II) mesotetrasubstituted porphyrins as a model for the conserved ruffling of the heme of cytochromes c. *J. Am. Chem. Soc.* 117: 11085–11097.

27 Ema, T., Senge, M.O., Nelson, N.Y. et al. (1994). 5,10,15,20-tetra-tert-butylporphyrin and its remarkable reactivity in the 5- and 15-positions. *Angew. Chem. Int. Ed. Engl.* 33: 1879–1881.

28 Veyrat, M., Ramasseul, R., Marchon, J.-C. et al. (1995). Nickel(II) and zinc(II) complexes of *meso*-tetrakis(cyclohexyl)porphyrin: distinct types of porphyrin distortion in response to steric crowding. *New J. Chem.* 19: 1199–1202.

29 Yamamoto, Y., Nadano, R., Itagaki, M., and Akiba, K. (1995). Synthesis and structure of phosphorus(V) octaethylporphyrins that contain a σ-bonded element-carbon bond: characterization of a porphyrin bearing an R-P:O bond and relation of the ruffling of the porphyrin core with the electronegativity of the axial ligands. *J. Am. Chem. Soc.* 117: 8287–8288.

30 (a) Scholz, W.F., Reed, C.A., Lee, Y.J. et al. (1982). Magnetic interactions in metalloporphyrin π-radical cations. *J. Am. Chem. Soc.* 104: 6791–6793. (b) Erler, B.S., Scholz, W.F., Lee, Y.J. et al. (1987). Spin coupling in metalloporphyrin π-cation radicals. *J. Am. Chem. Soc.* 109: 2644–2652.

31 (a) Sparks, L.D., Medforth, C.J., Park, J.R. et al. (1993). Metal dependence of the nonplanar distortion of Octaalkyltetraphenylporphyrins. *J. Am. Chem. Soc.* 115: 581–592. (b) Barkigia, K.M., Renner, M.W., Furenlid, L.R. et al. (1993). Crystallographic and EXAFS studies of conformationally designed nonplanar nickel(11) porphyrins. *J. Am. Chem. Soc.* 115: 3627–3635.

32 See for example: (a) Shelnutt, J.A., Song, X.-Z., Ma, J.-G. et al. (1998). Nonplanar porphyrins and their significance in proteins. *Chem. Soc. Rev.* 27: 31–41. (b) Senge, M.O., MacGowan, S.A., and OBrien, J.M. (2015). Conformational control of cofactors in nature the influence of protein-induced macrocycle distortion on the biological function of tetrapyrroles. *Chem. Commun.* 51: 17031–17063.

33 Senge, M.O. and Kalisch, W.W. (1997). Synthesis and structural characterization of nonplanar tetraphenylporphyrins and their metal complexes with graded degrees of β-ethyl substitution. *Inorg. Chem.* 36: 6103–6116.

34 Scheidt, W.R. and Reed, C.A. (1981). Spin state/stereochemical relationships in iron porphyrins: implications for the hemoproteins. *Chem. Rev.* 81: 543–555.

35 Hoffman, A.B., Collins, D.M., Day, V.W. et al. (1972). The crystal structure and molecular stereochemistry of μ-Oxo-bis[α, β, γ, δ-tetraphenylporphinatoiron(III)]. *J. Am. Chem. Soc.* 94: 3620–3626.

36 Scheidt, W.R., Cheng, B., Safo, M.K. et al. (1992). A new class of bridged diiron(III) complexes with a single hydroxo bridge. The preparation and structure of μ-hydroxobis ((octaethylporphinato) iron(III)) perchlorate. *J. Am. Chem. Soc.* 114: 4420–4421.

37 Reed, C.A., Mashiko, T., Bentley, S.P. et al. (1979). The missing heme spin state and a model for cytochrome c'. The mixed 3/2, 5/2 intermediate-spin ferric porphyrin: perchlorato(*meso*-tetraphenylporphinato)iron(III). *J. Am. Chem. Soc.* 101: 2948–2958.

38 Taylor, C.P.S. (1977). The EPR of low spin heme complexes. Relation of the τ_{2g} hole model to the directional properties of the g tensor, and a new method for calculating the ligand field parameters. *Biochim. Biophys. Acta* 491: 137.

39 Scheidt, W.R., Osvath, S.R., and Lee, Y.J. (1987). Crystal and molecular structure of bis(imidazole)(meso-tetraphenylporphinato)iron(III) chloride. A classic molecule revisited. *J. Am. Chem. Soc.* 109: 1958–1963.

40 (a) Safo, M.K., Gupta, G.P., Walker, F.A., and Scheidt, W.R. (1991). Models of the cytochromes *b*. control of axial ligand orientation with a "hindered" porphyrin system. *J. Am. Chem. Soc.* 113: 5497–5510. (b) Walker, F.A. (2004). Models of the bis-histidine-ligated electron-transferring cytochromes. Comparative geometric and electronic structure of low-spin Ferro- and Ferrihemes. *Chem. Rev.* 104: 589–616.

41 Munro, O.Q., Serth-Guzzo, J.A., Turowska-Tyrk, I. et al. (1999). Two crystalline forms of low-spin $[Fe(TMP)(5\text{-}MeHIm)_2]ClO_4$ relative parallel and perpendicular axial ligand orientations. *J. Am. Chem. Soc.* 121: 11144–11155.

42 Ikezakia, A. and Nakamura, M. (2011). Formation and characterization of a six-coordinate iron(III) complex with the most ruffled porphyrin ring. *Dalton Trans.* 40: 3455–3458.

43 Walker, F.A., Nasri, H., Turowska-Tyrk, I. et al. (1996). π-Aci ligands in iron(III) porphyrinates. Characterization of low-spin bis(*t*-butyl isocyanide)(porphinato)iron(III) complexes having $(d_{xz}, d_{yz})^4$ $(d_{xy})^1$ ground states. *J. Am. Chem. Soc.* 118: 12109–12118.

44 Scheidt, W.R., Geiger, D.K., and Haller, K.J. (1982). Structural characterization of a variable-spin porphinatoiron(III) complex. Molecular stereochemistry of Bis(3-chloropyridine)octaethylporphinatoiron(III) perchlorate at 98 K (S = 1/2) and 293 K (S = 1/2, S = 5/2). *J. Am. Chem. Soc.* 104: 495–499.

45 Richter-Addo, G.B., Wheeler, R.A., Hixson, C.A. et al. (2001). Unexpected nitrosyl group bending in six-coordinate $\{M(NO)\}^6$ σ-bonded aryl(iron) and -(ruthenium) porphyrins. *J. Am. Chem. Soc.* 123: 6314–6326.

46 Hu, C., Schulz, C.E., and Scheidt, W.R. (2015). All high-spin ($S = 2$) iron(II) Hemes are NOT alike. *Dalton Trans.* 44: 18301–18310.

47 Hu, C., An, J., Noll, B.C. et al. (2006). Electronic configuration of high-spin imidazole-ligated iron(II) octaethylporphyrinates. *Inorg. Chem.* 45: 4177–4185.

48 Safo, M.K., Nesset, M.J.M., Walker, F.A. et al. (1997). Models of the cytochromes. Axial ligand orientation and complex stability in iron(II) porphyrinates: the case of the noninteracting d_π orbitals. *J. Am. Chem. Soc.* 119: 9438–9448.

49 Silvernail, N.J., Roth, A., Schulz, C.E. et al. (2005). Heme carbonyls: environmental effects on ν_{C-O} and Fe–C/C–O bond length correlations. *J. Am. Chem. Soc.* 127: 14422–14433.

50 (a) Collman, J.P., Gagne, R.R., Halbert, T.R. et al. (1973). Reversible oxygen adduct formation in ferrous complexes derived from a picket fence porphyrin. Model for oxymyoglobin. *J. Am. Chem. Soc.* 95: 7868–7870. (b) Li, J., Noll, B.C., Oliver, A.G. et al. (2013). Correlated ligand dynamics in Oxyiron picket fence porphyrins: structural and Mössbauer investigations. *J. Am. Chem. Soc.* 135: 15627–15641.

51 Scheidt, W.R. and Ellison, M.K. (1999). The synthetic and structural chemistry of Heme derivatives with nitric oxide ligands. *Acc. Chem. Res.* 32: 350–359.

52 Wyllie, G.R.A. and Scheidt, W.R. (2002). Solid-state structures of metalloporphyrin NO_x compounds. *Chem. Rev.* 102: 1067–1089.

53 Silvernail, N.J., Pavlik, J.W., Noll, B.C. et al. (2008). Reversible NO motion in crystalline [Fe(Porph)(1-MeIm)(NO)] derivatives. *Inorg. Chem.* 47: 912–920.

54 Silvernail, N.J., Barabanschikov, A., Sage, J.T. et al. (2009). Mapping NO movements in crystalline [Fe(Porph)(NO)(1-MeIm)]. *J. Am. Chem. Soc.* 131: 2131–2140.

55 (a) Kundakarla, N., Lindeman, S., Rahman, M.H., and Ryan, M.D. (2016). X-ray structure and properties of the ferrous octaethylporphyrin nitroxyl complex. *Inorg. Chem* 55: 20702075. (b) Hu, B. and Li, J. (2015). One electron makes differences: from heme $FeNO^7$ to $FeNO^8$. *Angew. Chem. Int. Ed. Engl.* 54: 10579–10582.

56 Pavlik, J.W., Noll, B.C., Oliver, A.G. et al. (2010). Hydrosulfide (HS^-) coordination in iron porphyrinates. *Inorg. Chem.* 49: 1017–1026.

57 Buchler, J.W., De Cian, C., Elschner, S. et al. (1992). Structure and products of electrochemical oxidation of zirconium(1V) and hafnium(1V) bisporphyrinate double-deckers. *Chem. Ber.* 125: 107–115.

58 Stone, A. and Fleischer, E.B. (1968). The molecular and crystal structure of porphyrin diacids. *J. Am. Chem. Soc.* 90: 2735–2748.

11

Porphyrins: Electronic Structure and Ultraviolet/Visible Absorption Spectroscopy

M. Cather Simpson[1,2,3,4,5] *and Nina I. Novikova*[2,3,4,5]

[1] *Department of Physics, The University of Auckland, Auckland, New Zealand*
[2] *School of Chemical Sciences, The University of Auckland, Auckland, New Zealand*
[3] *The Photon Factory, The University of Auckland, Auckland, New Zealand*
[4] *MacDiarmid Institute for Advanced Materials and Nanotechnology, New Zealand*
[5] *Dodd Walls Centre for Photonic and Quantum Technologies, New Zealand*

11.1 Introduction

Metalloporphyrins constitute a class of large, π-conjugated macrocycles that act as catalytic and/or ligand-binding active sites in many diverse bacterial, plant, and animal proteins. In addition, because of their structural variability and functional utility, metalloporphyrins are exploited as the active components in technological applications such as fuel cells, biosensors, molecular switches, and as sensitisers for solar energy harvesting and chemotherapeutics. Porphyrins also provide an excellent test bed for probing ideas such as aromaticity and vibronic coupling, and for testing new theoretical and computational chemistry approaches.

A key feature of metalloporphyrins, and a significant reason for their widespread presence in biology, technology, and the research literature, is their very strong absorption of light in the near-infrared (NIR), visible (Vis), and ultraviolet (UV) regions of the spectrum. The mixing of two π-π* transitions originating from the highly delocalised porphyrin ligand leads to multiple strong, characteristic absorption bands that are exquisitely sensitive to the details of the metalloporphyrin structure and environment. These intense, readily identifiable transitions can be spectroscopically isolated to act as beacons that reflect what is happening at the molecular level. Alternatively, they can provide a mechanism, through photoexcitation, to stimulate the metalloporphyrin into activity. As a result, over 50 years of extensive photochemical and photophysical probing of metalloporphyrins has provided significant insight into our fundamental understanding of how light and matter interact, how molecular structure affects function, and how molecules convert light into more useful forms of energy.

Central to this extraordinary optical behaviour is the electronic structure of the porphyrin ligand. This macrocycle consists of four pyrrole rings joined by methine bridges, with nitrogens pointing inwards to form a four-pronged, highly symmetric, coordinating core (Figure 11.1). The atom or atoms bound in the tetradentate core of the porphyrin form the functional heart of the compound. The structural details of the surrounding porphyrin ligand, the presence (or absence) of axial ligands above and below the porphyrin plane, and the wider environment (protein, solid matrix, solvent, etc.) in which the porphyrin resides tune its functional properties. Those same factors affect the porphyrin's interaction with

Fundamentals of Porphyrin Chemistry: A 21st Century Approach, Volume 2, First Edition.
Edited by Penelope J. Brothers and Mathias O. Senge.
© 2022 John Wiley & Sons Ltd. Published 2022 by John Wiley & Sons Ltd.

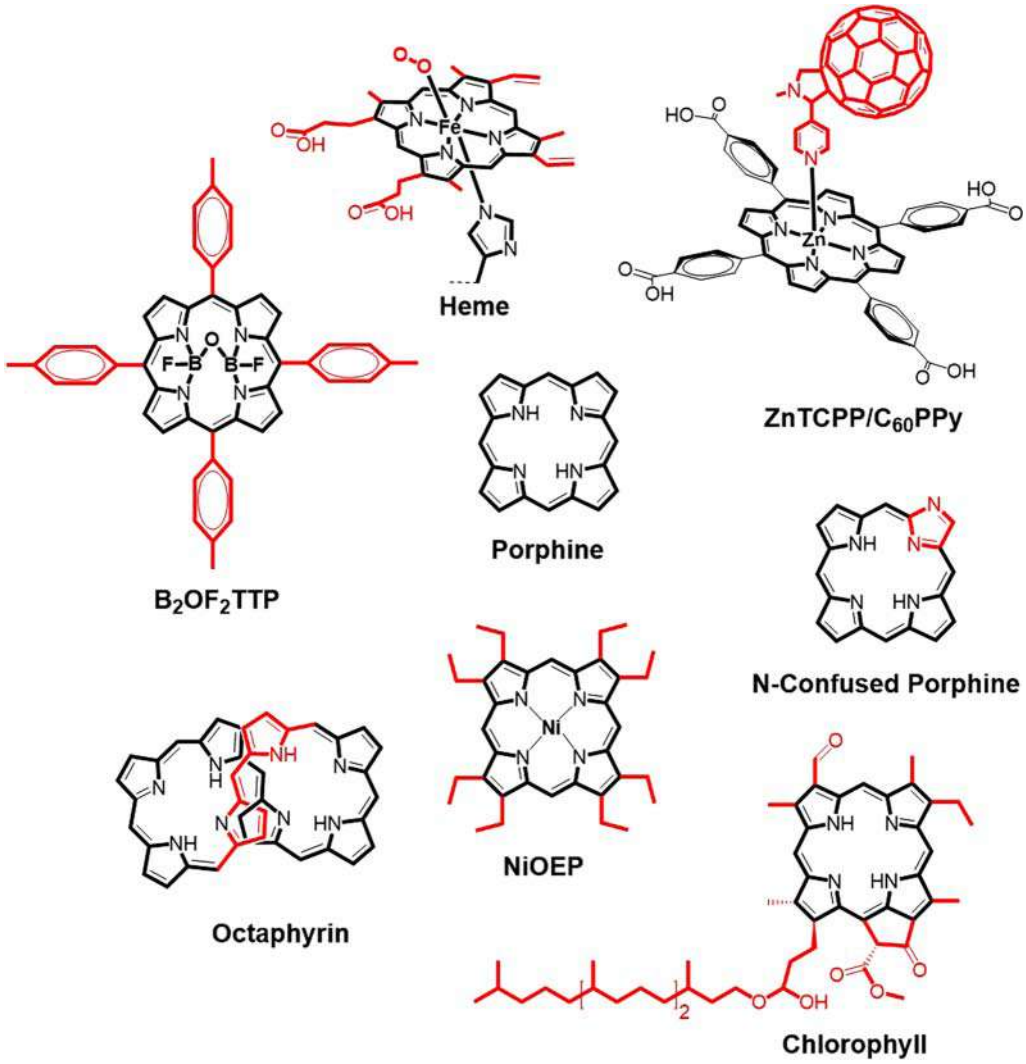

Figure 11.1 Examples of porphyrins with different axial ligands and central metal ions. TTP = tetratolyl porphyrin; TCPP = tetra(4-carboxyphenyl) porphyrin; OEP = octaethyl porphyrin; C_{60}PPy = N-methyl-2-(4′-pyridyl)-3,4-fulleropyrrolidine [1].

light, sometimes quite dramatically, so that the UV/Vis spectrum can be used as a sensitive probe for understanding the details of the electronic structure, and thereby lend direct insight into molecular function. This intense interaction with light makes porphyrins the quintessential system for illustrating the structure–spectrum–function relationship.

The porphyrin macrocycle can hold one or two coordinated elements that can be axially ligated as well, depending upon the metal and the availability of suitable ligands. Substituents may be covalently bound to any of the 12 positions on the periphery of the macrocycle, and in any pattern. The large macrocycle is relatively flexible itself; it may be planar or may adopt a symmetric or asymmetric out-of-plane conformation. Figure 11.1 shows some examples of free base and metalloporphyrins.

Fortunately for chemists, photochemists, and photophysicists, the electronic structure of the porphyrin class of molecules is dominated by the large, conjugated system that possesses nominal D_{4h} (square-planar) symmetry. This conjugated porphyrin ring system gives rise to the intense porphyrin colour, the absorption bands in the UV/Vis spectrum. The positions, shapes, and intensities of these absorptions are modulated by the porphyrin's structural and environmental details. Consequently, with a thorough understanding of the electronic behaviour of a very simple porphyrin, valuable information can be extracted from the spectroscopic signatures of thousands of porphyrin derivatives. Fundamental chemical intuition goes quite a long way for porphyrin structure–spectrum–function insights.

In this chapter, a thorough understanding of the porphyrin electronic structure and its impact on the UV/Vis spectrum is developed. Simple treatments accessible to undergraduate chemistry students are explored, followed by increasingly more rigorous and complex models, and finally to computational quantum chemistry approaches. The goal is to provide the keen undergraduate, the new graduate student, or any curious porphyrin novice with the intuitive foundation to both understand the basics of porphyrin electronic structures and to build new knowledge on that foundation.

First, a very fundamental, intuitive understanding of the porphyrin electronic structure is developed using basic quantum mechanics, π-orbitals, and group theory. Because porphyrins are so highly coloured, and so chemically and biochemically important, this class of molecules has frequently been used as a test case for developing and benchmarking these important quantum chemistry approaches in the 1940s, 1950s, and 1960s. The two basic starting points are the idealised D_{2h} free-base porphine (H_2P) and D_{4h} planar metalloporphine, with a generic central metal ion M and hydrogen substituents at all 12 peripheral sites (Figure 11.2). Basic group theory and quantum mechanics will not be covered here; the reader is referred to several useful textbooks [2–8].

This section begins with a simple particle-on-a-ring model that predicts basic porphyrin frontier states and absorption bands surprisingly well. The next model includes the molecular structure and a more sophisticated approach that applies linear combinations of atomic orbitals to create molecular orbitals (LCAO-MO), which are then used to describe porphyrin ground and excited states. The section concludes with the well-known Gouterman's four-orbital model, which arose from the recognition in the late 1950s that it was difficult to understand the behaviour of unsaturated systems, in particular, if one described the electronic excited states as single electronic configurations (e.g. resulting from exciting a single electron from one filled molecular orbital to an unfilled one). In Gouterman's model,

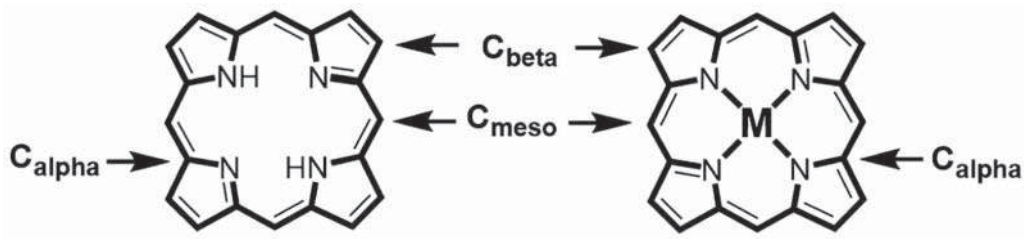

Figure 11.2 Idealised porphyrin macrocycles: (left) H_2-porphine (H_2P) also called free-base porphine; (right) metalloporphine. Both idealised macrocycles are planar and possess high symmetry: H_2P (D_{2h}) and metalloporphine (D_{4h}).

two doubly degenerate, E_u symmetry π-π* transitions mix via configuration interaction to give rise to the major UV/Vis absorption bands in the porphyrin spectrum.

From this basic understanding of metalloporphine's electronic states, the next step is to examine the types of patterns and perturbations on the dominant underlying electronic structure that are commonly observed. For example, symmetry breaking in plane or out of plane gives rise to predictable changes in the electronic states that are reflected in the ground state absorption spectrum. The symmetry and type of peripheral substitution, substituent size and electronic character, and many other variables exert similarly predictable consequences.

The advent of computational chemistry and the improvements in computational algorithms and processing speeds means that it is now relatively easy to directly compute structural and spectral properties of porphyrins using classical mechanics, quantum mechanics, or a combination of both. Unfortunately, the same electronic features that make porphyrins so interesting as a platform for structure–spectrum–function intuition also lead to significant challenges when calculating electronic structures. Factors including electronic delocalisation and correlation, configuration interaction and vibronic coupling, low-energy distortions from planarity, and the impact of the ring and metal electronic states upon each other mean that computational treatments can provide poor and misleading answers – the novice computational chemist must be wary when exploring porphyrins. When applied correctly, however, modern quantum chemistry provides a very powerful tool for probing and understanding porphyrins. The significantly better performance that density functional theory (DFT) affords over Hartree–Fock-based methods will be discussed, and traditional and more modern DFT functionals will be compared for their advantages and disadvantages in calculating porphyrin electronic states.

The final section will focus upon porphyrin aromaticity, a central feature of the porphyrin ground state that influences structure, spectrum, and function. The impact of out-of-plane distortions upon the electronic states and absorption spectrum is presented here. The characterisation of porphyrin aromaticity, Möbius aromaticity, and aromaticity switching will also be discussed. These areas are current 'hot topics' for both porphyrin and aromaticity chemists and physicists, partly because of the potential for important applications like molecular switches. Once again, porphyrins are providing fertile ground for exploring new ideas and understanding about aromaticity. This is entirely in keeping with the historical role of porphyrins and porphyrinoids as powerful test beds for exploring new theories and experimental methods.

11.2 Modelling the Porphyrin Electronic Structure

11.2.1 Ground State Absorption Spectrum

The ground state absorption spectrum of a metalloporphyrin provides a framework within which to discuss its electronic structure. Metalloporphyrins are large, symmetric, π-conjugated macrocycles with one or more atoms coordinated in the centre. Several electronic transitions apparent in the UV/Vis absorption spectrum are characteristic of this class of molecules (Figure 11.3). The most intense feature is usually the B band, also called the Soret band, which occurs in the region from approximately 370 to 450 nm. Generally weaker, overlapping N, L, and M bands are seen at higher energies. The Q band usually observed in the 500–650 nm region is also weaker than the B band. The Q band generally

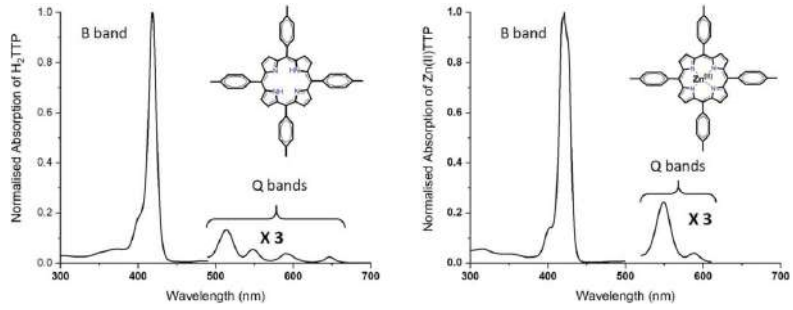

Figure 11.3 UV/Vis spectra of H_2TTP (left) and Zn(II)TTP (right). H_2TTP peak positions: B band (418 nm), Q bands (514, 548, 590, and 645 nm); Zn(II)TTP peak positions: B band (421 nm), Q bands (549 and 588 nm).

comprises 2–4 transitions – it can look quite complicated. These bands (N, L, M, B, and Q) all are assigned to porphyrin-ring-based π-π* transitions of various sub-types. Other features can appear in porphyrin absorption spectra as well, including vibronic contributions most readily apparent in the Q band region, and weak charge transfer transitions in the NIR.

The generic names for porphyrin absorptions were established by Platt in the 1950s [9–11]. He was particularly keen to bring order to the nomenclature of large molecule absorption spectra and provide intuition to experimental and theoretical chemists alike. Platt noted that, in contrast to the field of atomic spectroscopy, the 'glittering successes of quantum mechanics' had undermined the usual progress of 'first, instrumentation and measurement; then, rule-of-thumb regularities; and finally synthesis' of ideas and understanding for large molecule spectroscopy. He lamented that being able to calculate states accurately does not necessarily lead to the chemical insight and intuition that experimentally observed patterns provide.

The classification system we still use for porphyrins today was developed for cata-condensed hydrocarbons [9, 10, 12, 13]. It relies upon the types of orbitals involved in the one-electron excitation (π-π*, n-π*), the parity, and the magnitude of the associated angular momentum change. Subscripts denote polarisation, the measurement of which was in its infancy at the time; superscripts identify the spin multiplicity (e.g. singlet, triplet). The ground state (even parity, zero momentum) is ^{1}A.

The most intense porphyrin absorption band is assigned as a B band because it is a π-π* transition with odd parity and low momentum. These states have symbols ^1B_x, ^1B_y, ^3B_x, and ^3B_y for singlet and triplet states that are x- or y-polarised, as indicated. The weaker visible transitions of porphyrins would be called L states because they arise from π-π* transitions with odd parity and higher angular momentum. However, they receive a special label of Q (^1Q_x, ^1Q_y, ^3Q_x, and ^3Q_y) because, unlike the analogous L bands in benzene, for example, the porphyrin Q bands cannot be distinguished by whether nodes occur through bonds or atoms. The M and N bands have even higher angular momenta than the Q and L bands; N bands have odd parity, and M bands even.

The porphyrin B band is also commonly called the Soret band. This name honours the Swiss chemist Jacques-Louis Soret, who in 1878 first noted haemoglobin's very strong absorption band in the violet region of the spectrum (between the Fraunhofer G and H lines) [14–16]. Soret also observed a colour change when the dilute solution was saturated with CO. This shift upon CO ligation to the iron core of the heme is the origin of the 'cherry red' sign of CO poisoning and is a key spectroscopic tool for understanding the structural and functional dynamics that occur when ligands bind and release from the iron core of hemes [14].

The B (Soret) and Q bands are the most important of the typical metalloporphyrin transitions, in most cases. These frontier states will occupy most of our attention in this chapter.

11.2.2 The Porphyrin as a Free Particle on a Ring

One of the earliest theoretical approaches that led to understanding of the electronic states of porphyrins approximated the porphyrin as a polyene ring with 18 π-electrons that are free to travel as an electron gas (Figure 11.4) [9, 17–20]. This approach was first outlined by Simpson, Kuhn, and Platt in the late 1940s, adapted from the free-electron model originally introduced by O. Schmidt several years earlier. It reduces the system to a two-dimensional problem whose Schrödinger equation can be solved exactly. Transitions between the simple ground and excited states created by this solution occur in the correct part of the spectrum, broadly speaking, and exhibit the correct angular momentum behaviour.

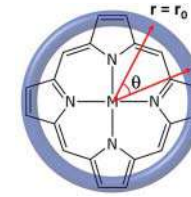

Figure 11.4 Modelling the porphyrin as an 18-electron system on a ring of radius r_0. For $r_0 = 4.0$ Å, a reasonable estimate for a porphyrin, the calculated UV/Vis absorption wavelength is 580 nm.

For a particle on a circular ring of radius $r = r_0$, the potential energy (V) is zero and constant. Outside the ring ($r \neq r_0$), the potential V becomes infinite. These conditions confine the particle to the circle described by $r = r_0$. The Hamiltonian then can be written relatively simply, in terms of the kinetic energy of the electron.

In the most convenient coordinates, plane polar *(r, θ)*, the one-electron Schrödinger equation becomes

$$-\frac{\hbar^2}{2m}\left[\frac{1}{r}\frac{\partial}{\partial r} + \frac{\partial^2}{\partial r^2} - \frac{1}{r^2}\frac{\partial^2}{\partial \theta^2}\right]\psi(r,\theta) = E\,\psi(r,\theta) \tag{11.1}$$

in which $\hbar$ is Planck's constant, and m is the mass of an electron. We can separate the variables so that $\psi(r, \theta) = R(r)\Theta(\theta)$, where $R(r)$ is the radial part of the wavefunction, and $\Theta(\theta)$ is the angular part. The problem is further simplified by recalling from above that by confining the electron to the circular ring, r becomes a constant $(r = r_0)$ and the derivatives with respect to r all equal zero. The eigenvalue equation to be solved depends only upon the angular part of the wavefunction:

$$\frac{\hbar^2}{2mr_0^2}\frac{\partial^2}{\partial \theta^2}\Theta(\theta) = E\,\Theta(\theta) \tag{11.2}$$

The general set of solutions is given by

$$\Theta_n(\theta) = a\,e^{in\theta}\ n = 0, \pm 1, \pm 2 \ldots \tag{11.3}$$

where a is a normalisation constant that will be ignored, and n is an integer quantum number. The accompanying energy levels are given by

$$E_n = \frac{\hbar^2 n^2}{2\,m\,r_0^2} \tag{11.4}$$

These solutions represent the allowed (very simple) orbitals and orbital energies of the particle on a ring (Figure 11.5). The energy levels are doubly degenerate, except for the $n = 0$ level, and are quadratically spaced. This double degeneracy can be thought of as the electron travelling clockwise or counter-clockwise in the pairs of $\pm n$ orbitals. As the energy level increases, the number of nodes in the electronic wavefunction also increases.

When this model is applied to the 18 π-electron porphyrin, the highest filled orbitals have quantum numbers $n = \pm 4$ and the lowest unfilled orbitals have quantum numbers $n = \pm 5$. The states in this simple system can be described by electron configurations; two electrons per orbital. The closed-shell, ground electronic state is given by

$$\Psi_0 = (e^{i0\theta})^2(e^{i1\theta})^2(e^{-i1\theta})^2(e^{i2\theta})^2(e^{-i2\theta})^2(e^{i3\theta})^2(e^{-i3\theta})^2(e^{i4\theta})^2(e^{-i4\theta})^2 \tag{11.5}$$

A useful shorthand focuses only upon the frontier orbitals, labels the frontier electrons (1) to (4), and ignores their indistinguishability. In this notation, the ground state becomes

$$\Psi_0 = e^{i4\theta}(1)\,e^{i4\theta}(2)\,e^{-i4\theta}(3)\,e^{-i4\theta}(4) \tag{11.6}$$

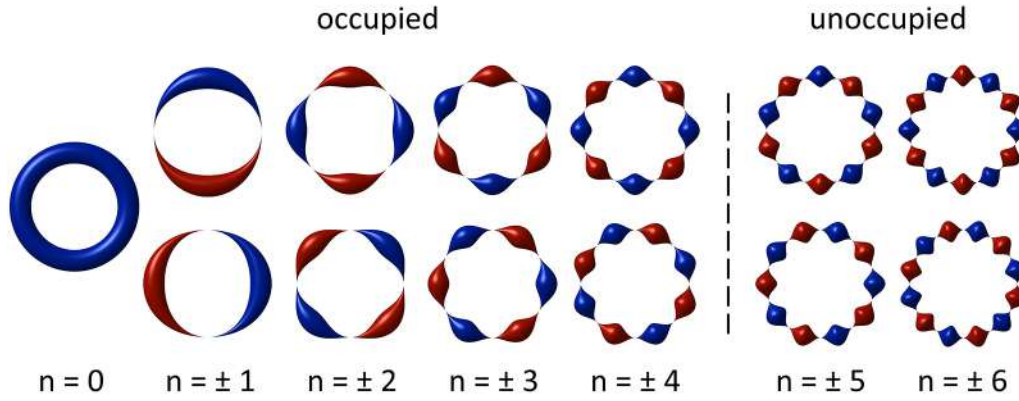

Figure 11.5 Orbital solutions to the free particle on the ring problem, as defined by the Schrödinger equation – Eq. (11.1). The colous indicates the phase.

Excitations of the π-electrons from the highest filled to lowest unfilled levels results in the following excited states:

$$\Psi_{+1} = e^{i4\theta}(1)\, e^{i5\theta}(2)\, e^{-i4\theta}(3)\, e^{-i4\theta}(4) \tag{11.7a}$$

$$\Psi_{-1} = e^{i4\theta}(1)\, e^{i4\theta}(2)\, e^{-i4\theta}(3)\, e^{-i5\theta}(4) \tag{11.7b}$$

$$\Psi_{+9} = e^{i4\theta}(1)\, e^{i4\theta}(2)\, e^{-i4\theta}(3)\, e^{i5\theta}(4) \tag{11.7c}$$

$$\Psi_{-9} = e^{i4\theta}(1)\, e^{-i5\theta}(2)\, e^{-i4\theta}(3)\, e^{-i4\theta}(4) \tag{11.7d}$$

The Ψ_{+1} state (Eq. 11.7a) has one electron promoted from the $n = +4$ orbital to the $n = +5$ orbital, and so on. The subscripts 0, ±1, and ± 9 represent the sum of the quantum numbers n for each state. The four lowest-energy π-π* transitions are the ones that go from Ψ_0 (Eq. 6) to each of these four excited states (Eqs. 11.7a–d). The model predicts that all four of these excitations should have identical energies. Including the electron spin means that each of the states above consists of a singlet and three triplet states; we will not distinguish these here.

If one takes the average C—C bond in a porphyrin to be 1.4 Å, the radius of an 18-membered ring is approximately 4.0 Å. The four electronic transitions from Ψ_0 to each of these states will have the same energy (3.43×10^{-19} J), which corresponds to an absorption wavelength of 580 nm, clearly in the right region of the spectrum.

Application of Hund's rules to these results gives us a bit more agreement between model and experiment. Since the Hamiltonian and the z-component of the orbital angular momentum operator commute, the sums of these quantum numbers also reflect the total orbital angular momenta (L_z) of each state, in units of $\hbar$. The closed-shell ground state Ψ_0 has a total orbital angular momentum of $L_z = 0$. The excited states Ψ_{+1} and Ψ_{-1} have low orbital angular momenta $L_z = \pm 1$, and the states Ψ_{+9} and Ψ_{-9} have high orbital angular momenta $L_z = \pm 9$.

For a given spin multiplicity, the state with the largest value of total orbital angular momentum will have the lower energy. Hence, the $L_z = \pm 9$ states will be lower in energy than the $L_z = \pm 1$ states. Their relative intensities are predicted by selection rules that dictate that only transitions involving $\Delta L_z = \pm 1$ are formally allowed. Therefore, $\Psi_0 \rightarrow \Psi_{+1}$ and $\Psi_0 \rightarrow \Psi_{-1}$ are allowed transitions, and $\Psi_0 \rightarrow \Psi_{+9}$ and $\Psi_0 \rightarrow \Psi_{-9}$ are forbidden.

With this additional information, these states can be assigned to the Q and B states, respectively, and the predicted UV-Vis absorption spectrum now has two sets of absorptions

with a centre of gravity at 580 nm. The higher-energy, formally allowed, doubly degenerate $\Psi_0 \rightarrow \Psi_{\pm 1}$ transitions can be assigned to the more intense B band (Soret), and the formally forbidden, doubly degenerate $\Psi_0 \rightarrow \Psi_{\pm 9}$ transitions to the lower-energy, lower-intensity Q band. These assignments are supported further by studies of the Zeeman effect in several porphyrins, in which the angular momentum of the Q band state is found to be approximately $9\hbar$ and that of the B band (Soret) less than $1.3\ \hbar$. The simple particle-on-a-ring model agrees surprisingly well with experiment.

Although the qualitative correlations between the Simpson particle-on-a-ring model and observed porphyrin spectra are quite useful at providing a basic intuitive understanding of porphyrin excited states and the UV/Vis spectrum, this simple model is insufficient for predicting much more detail. Importantly, it does not directly address the structure of the porphyrin – there are no atoms in this model. Nor does it provide avenues for understanding the observed behaviour of different porphyrins. A more sophisticated model is required, with explicit treatment of the atoms and states that involve conceptual 'handles' such as molecular orbitals.

11.2.3 Hückel Molecular Orbital Approach to Porphyrins

The Hückel LCAO-MO method is the simplest molecular orbital treatment of porphyrins that provides a useful, intuitive picture of the frontier molecular orbitals and the major bands in the UV/Vis spectrum. This approach was originally derived to describe delocalised π-orbitals in molecules that have extended π-systems [20–23]. Here, the UV/Vis absorption bands are assumed to arise entirely from π-π* electronic transitions. The first step is to create molecular orbitals as linear combinations of the atomic p_z-orbitals across the molecule. The resultant ground and excited electronic states are assumed to be well-described single-electron configurations; excited states are described by the promotion of a single electron from an occupied into an unoccupied molecular orbital.

In the Hückel LCAO-MO approach, the wavefunctions $\{\Psi\}$ that describe the ground and excited states are products of one-electron molecular orbitals $\{\psi_i\}$, which are formed in turn by linear combinations of the p_z atomic orbitals $\{\phi_j\}$:

$$\Psi = \prod_{i=1}^{n} \psi_i = \prod_{i=1}^{n} \sum_{j=1}^{n} c_{ij} \phi_j \tag{11.8}$$

where n is the number of orbitals in the basis set. For the basic treatment of porphine, $n = 24$ as there are 24 atoms that contribute p_z atomic orbitals to the basis set. The coefficients $\{c_{ij}\}$ represent the contribution of the jth atomic orbital to the ith molecular orbital.

The relevant Hamiltonian is a sum of one-electron operators $\{\hat{h}(i)\}$

$$\hat{H}_\pi = \sum_{i=1}^{n} \hat{h}(i) \tag{11.9}$$

and the set of molecular orbitals $\{\psi_i\}$ are eigenfunctions of these:

$$\hat{h}(i)\psi_i = \varepsilon_i \psi_i \tag{11.10}$$

The eigenvalues $\{\varepsilon_i\}$ are the molecular orbital energies. The total energy for a given state is the sum of the occupied molecular orbital energies.

Figure 11.6 The molecular orbitals that make up the basis set for the Hückel treatment of porphine are the 24 p_z atomic orbitals, one for each atom in the macrocycle.

Application of the variation principle yields the set of equations

$$\sum_{i=1}^{n} c_{ij}(h_{ij} - \varepsilon_j S_{ij}) = 0 \quad j = 1,2,3 \ldots n \tag{11.11}$$

The set of $\{c_{ij}\}$ comprises weighting coefficients from Eq. (11.8). In the Hückel LCAO-MO approach, knowledge of the forms of the operators $\hat{H}_\pi$ and $\hat{h}(i)$ is not needed to solve the equations. Rather, empirical values are assigned to the Coulomb integrals (h_{ii}), the resonance integrals (h_{ij}), and the overlap integrals (S_{ij}); where $i \neq j$ for the latter two terms.

In the simplest approach, the integrals are treated as follows (in bra-ket notation, for convenience):

$$\begin{aligned} h_{ij} = \langle \phi_i | \hat{h} | \phi_j \rangle &= \alpha \quad \text{for } i = j \\ &= \beta \text{ for } i = j + 1 \\ &= 0 \text{ otherwise} \end{aligned} \tag{11.12a}$$

$$S_{ij} = \langle \phi_i \mid \phi_j \rangle = \delta_{ij} \tag{11.12b}$$

Simplification means that only interactions between atomic orbitals on adjacent atoms ($i = j \pm 1$) contribute to the system's behaviour. The overlap integral condition means that the atomic orbital basis functions are orthogonal to one another and are normalised; the resultant molecular orbitals also are orthogonal and normalised.

When Hückel LCAO-MO theory was applied to porphyrins, the UV/Vis transition energies were predicted with relatively good accuracy [24]. Porphyrins were treated as a 26 π electron, 24 atom conjugated ring, with each atom contributing one p_z atomic orbital perpendicular to the plane of the macrocycle (Figure 11.6). By symmetry, this collection of 24 p_z atomic orbitals transforms into the following set of π-orbitals: {6 e_g, 2 a_{1u}, 4 a_{2u}, 3 b_{1u}, and 3 b_{2u}}.

The molecular orbital energy level diagram is given in Figure 11.7, for various values of the Hückel parameters α and β. In the early, basic Hückel model by Longuet-Higgins and co-workers [24], the carbon and nitrogen atoms were treated as identical; the values of α all were set equal, as were the values of β (Figure 11.7a).

Longuet-Higgins et al. [24] and later studies [25, 27–29], including the Gouterman's four-orbital model (vide infra), took into account the differences between carbon and nitrogen, and between carbon–carbon and carbon-nitrogen bonds, by scaling their α and β integrals, respectively. A few examples of other relationships and their effect upon the molecular orbitals is shown in panels (b)–(e) in Figure 11.7.

The highest-energy occupied molecular orbitals (HOMOs) were found to be the $1a_{1u}(\pi)$ and $3a_{2u}(\pi)$ orbitals, and the lowest-energy unoccupied molecular orbitals (LUMOs) the doubly degenerate $4e_g(\pi^*)$ (Figure 11.8); these are often referred to in this chapter and in the literature without the prefix (e.g. a_{1u}, a_{2u}, and e_g). Initially, electronic transitions between the HOMOs and LUMOs were assigned to the B (Soret) and Q bands, respectively, in one-to-one correspondence.

In order to compare the basic Hückel LCAO-MO results (Figure 11.7a) with the experimental UV/Vis spectrum, Longuet-Higgins et al. first empirically corrected the overlap between

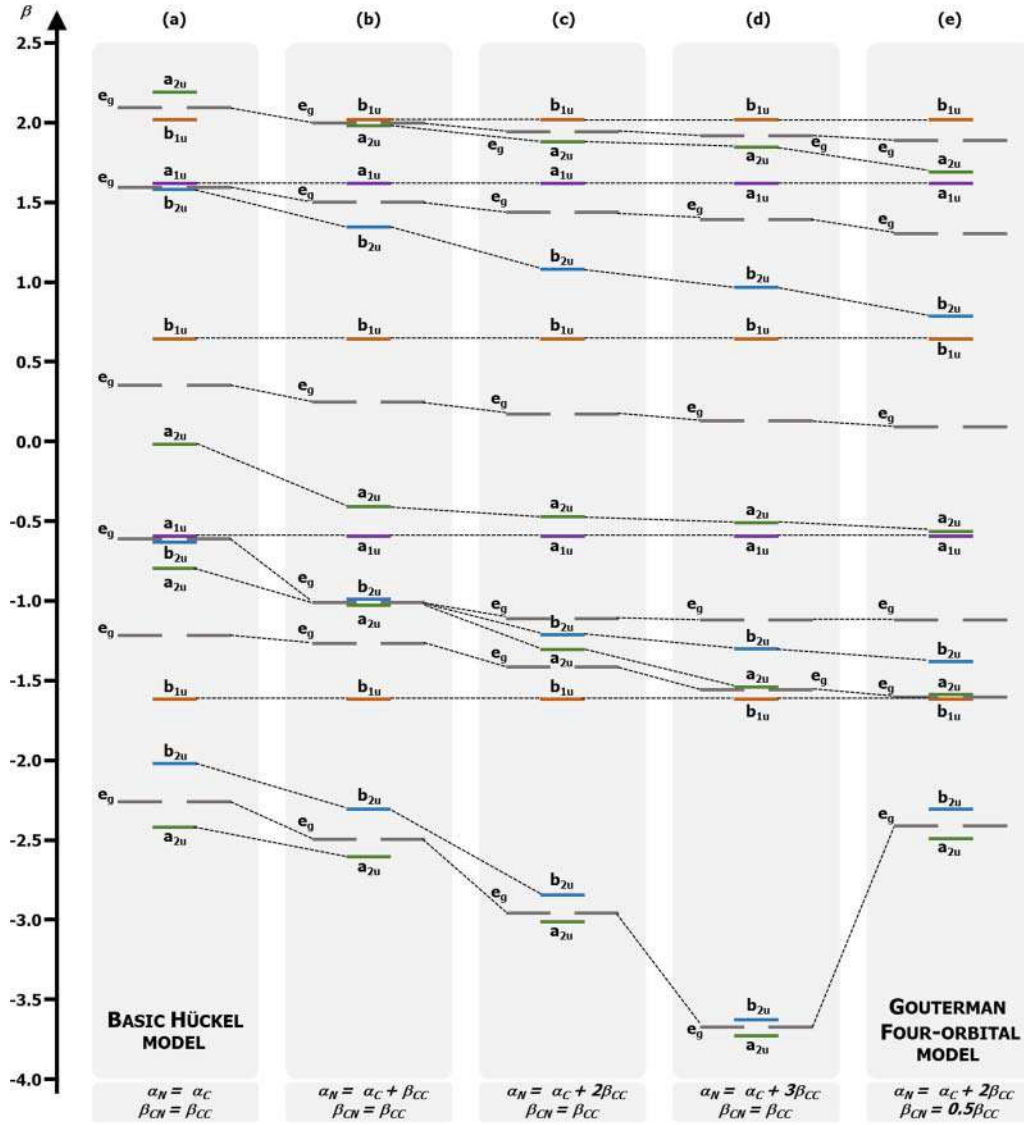

Figure 11.7 Molecular orbital energy level diagram for porphine derived using the Hückel LCAO-MO method and all 24 atomic p_z-orbitals as a basis set. The energy scale is in units of β and relative values of α_N and α_C and of β_{CN} and β_{CC} for each set of molecular orbitals is indicated. The diagram illustrates the sensitivity of the orbitals, particularly the frontier occupied orbitals, to the values of α_N and β_{CN}. Source: Adapted from [24–26].

adjacent atoms to $S_{ij} = 0.25$ for $j = i + 1$ and then examined the transition energies associated with the HOMO → LUMO and HOMO-1 → LUMO excitations [24].

For porphine, the energy of the B band (Soret) transition ($1a_{1u} \rightarrow 4e_g$) was calculated to be 21 300 cm^{-1} and that of the Q band ($3a_{2u} \rightarrow 4e_g$) to be 9000 cm^{-1}. These energies translate to absorptions near 470 nm (B) and 1100 nm (Q), compared to the experimentally observed absorptions at 23 200 cm^{-1} (431 nm) and 16 000 cm^{-1} (625 nm), respectively [24]. Although this very simple Hückel theory approach gives the right energy ordering, and the major

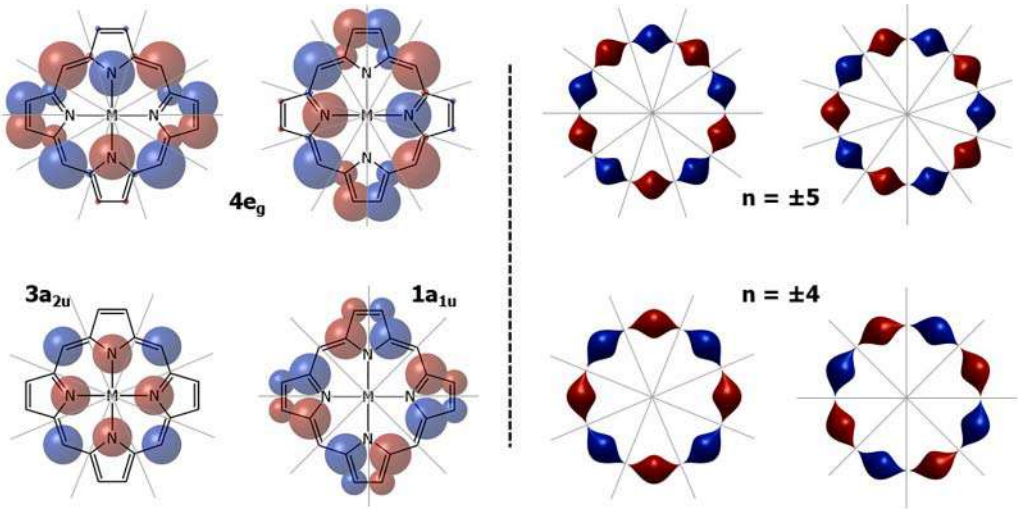

Figure 11.8 Frontier molecular orbitals (left) for the D_{4h} metalloporphine (coefficients from [24]; HOMOs $3a_{2u}$ and $1a_{1u}$ and LUMO $4e_g$) compared to the analogous particle on a ring state (right) (HOMOs (n = ±4) and LUMOs (n = ±5)). Grey lines guide comparison of node structures between the two models.

UV/Vis absorptions are in approximately the correct region of the spectrum, the positions are predicted to be at lower energy than are experimentally observed.

The errors in prediction are lessened somewhat by accounting empirically for the differences between the carbon and nitrogen atoms (e.g. Figure 11.7b). Including adjustments based upon the relative electronegativities of these atoms lowers the energies of both the $3a_{2u}$ and $4e_g$ orbitals, but not of the $1a_{1u}$ orbital as it has nodes at the pyrrole nitrogen positions. This correction leads to a decrease in the predicted B (Soret) band transition energy and an increase in the Q band energy. The predicted Q band became a bit more accurate (only 1500 cm^{-1} too low) and the Soret band a bit less accurate (now 6700 cm^{-1} too low). Overall, however, distinguishing the carbon and nitrogen atoms provides improvement [24].

The Hückel LCAO-MO method does an adequate job of predicting the Soret and Q band transition energies. In addition, the treatment directly addresses the molecular structure of the porphyrin, rather than treating it as a circular ring or polyene, and as a result this approach can be used to correlate spectral changes with molecular structure changes, including symmetry breaking and substitution with electron-donating or -withdrawing groups. Unfortunately, the transition energies of the B and Q bands are not accurate at a predictive level, and the intensity differences between the two are challenging to explain within this model.

These discrepancies can be accounted for by noting that (i) the two HOMOs are nearly (accidentally) degenerate and the LUMOs are degenerate by symmetry (Figure 11.7b–e), and (ii) the transitions have the same E_u symmetry. In this situation, configuration interaction should be important for calculating accurate transition energies and relative intensities. That observation is what led Gouterman to develop the four-orbital model.

11.2.4 Gouterman's Four-Orbital Model

The four-orbital model, developed in the 1960s, is a very powerful approach to modelling the porphyrin electronic structure, and to predicting how alterations to this basic D_{4h} structure affect porphyrin spectroscopy and reactivity. Martin Gouterman, who passed away in 2020, published his model for understanding porphyrin electronic structure in a series of papers from 1959 to 1963 that have been cited well over 3000 times [25, 27, 28, 30]. The extraordinary influence of this work continues today; Gouterman's work is cited over 420 times per year, on average, for the last 10 years (Web of Science) [30]. He and many, many others have used, and continue to use, the four-orbital model to understand and explain the behaviour of hundreds of porphyrins and related classes of molecules.

The Gouterman approach harnesses the strengths of the electron-on-a-ring method that account for the intensity differences of the B and Q bands, and the Hückel LCAO-MO method that relate these transitions more directly to the porphyrin molecular structure. In essence, the molecular orbital transitions generated by the Hückel MO-LCAO method are allowed to mix according to Simpson free-electron-on-a-ring selection rules [27]. The Soret and Q electronic absorption bands are treated as entirely π-π* in nature, and the porphyrin as having D_{4h} symmetry [24, 25, 27, 28]. The excitations themselves ($a_{1u} \rightarrow e_g$ and $a_{2u} \rightarrow e_g$) have E_u symmetry, with equivalence in the x- and y-polarisations. Gouterman's model allows these excitations to couple through configuration interaction. As shown in Figure 11.7, the energy separation between the HOMO (a_{1u}) and HOMO-1 (a_{2u}) orbitals is sensitive to the values of α_N and β_{CN} [24, 25] The values $\alpha_N = \alpha_C + 2\beta_{CC}$ and $\beta_{CN} = 0.5\ \beta_{CC}$ are reasonable ones, and they bring the frontier a_{1u} and a_{2u} orbitals into near complete accidental degeneracy (Figure 11.7e) [25, 28]. This condition formed the start of Gouterman's four-orbital model.

11.2.4.1 Configuration Interaction

This brief section describes the basics of configuration interaction used to describe Gouterman's four-orbital model. Configuration interaction is a method for approximating a solution to the Schrödinger equation by allowing different electronic configurations to interact with one another, to provide a better description of the state and its properties (see, for example, [6, 31]). Configuration provides an additional level of sophistication – and accuracy – over the LCAO-MO method. In the LCAO-MO method, atomic orbitals mix through weighted linear combinations to form molecular orbitals, then products of those molecular orbitals are used to form states. The ground electronic state has an electron configuration with all electrons paired up in the lowest-energy molecular orbitals. Excited states are then the electron configurations in which one or more electrons have been promoted from occupied molecular orbitals into unoccupied ones. Each electronic state is described by a single-electron configuration.

As a simple illustration, consider the N_2 molecule. The atomic orbitals $\{\phi_i\}$ are the 1s, 2s, 2p, 3s, 3p, etc. one-electron wavefunctions that are the solutions to the hydrogen atom Schrödinger equation, centred on each of the N-atoms in the molecule. The molecular orbitals $\{\psi_i\}$ are linear combinations of these. For example, the lowest-energy molecular orbital is the bonding σ_{1s} orbital, which can be expressed as a linear combination of the 1 s atomic orbitals on each of the N-atoms: $\psi_1 = \frac{1}{\sqrt{2}}[\phi_1 + \phi_2] = \sigma_{1s}$. The rest of the molecular

orbitals are likewise created using this LCAO-MO approach. The ground electronic state is then given by the single-electron configuration

$$\begin{aligned}\Psi_0 &= \psi_1(2)\,\psi_2(2)\,\psi_3(2)\psi_4(2)\psi_5(2)\,\psi_6(2)\,\psi_7(2)\\ &= \sigma_{1s}(2)\sigma^*_{1s}(2)\sigma_{2s}(2)\sigma^*_{2s}(2)\,\pi_{2px}(2)\pi_{2py}(2)\,\sigma_{2pz}(2)\end{aligned} \tag{11.13}$$

in which the number of electrons in each molecular orbital is in parentheses. There are four degenerate low-lying π-π* excitations in N_2. Their excited state configurations are given by

$$\Psi_1 = \sigma_{1s}(2)\sigma^*_{1s}(2)\sigma_{2s}(2)\sigma^*_{2s}(2)\,\pi_{2px}(2)\pi_{2py}(1)\,\sigma_{2pz}(2)\,\pi^*_{2py}(1) \tag{11.14a}$$

$$\Psi_2 = \sigma_{1s}(2)\sigma^*_{1s}(2)\sigma_{2s}(2)\sigma^*_{2s}(2)\,\pi_{2px}(1)\pi_{2py}(2)\,\sigma_{2pz}(2)\,\pi^*_{2py}(1) \tag{11.14b}$$

$$\Psi_3 = \sigma_{1s}(2)\sigma^*_{1s}(2)\sigma_{2s}(2)\sigma^*_{2s}(2)\,\pi_{2px}(2)\pi_{2py}(1)\,\sigma_{2pz}(2)\,\pi^*_{2px}(1) \tag{11.14c}$$

$$\Psi_4 = \sigma_{1s}(2)\sigma^*_{1s}(2)\sigma_{2s}(2)\sigma^*_{2s}(2)\,\pi_{2px}(1)\pi_{2py}(2)\,\sigma_{2pz}(2)\,\pi^*_{2px}(1) \tag{11.14d}$$

Configuration interaction takes this one step further by treating the set of the electron configurations as a basis set of zero-order electronic states and forming a new set of multi-configurational wavefunctions through the interactions of these zero-order states with one another. The strength of the interaction between the zero-order states depends upon their symmetry and the energy separation between them. Hence, the ground state configuration is not usually a significant contributor to the new set of excited states. The resultant multi-configurational wavefunctions provide better descriptions of the manifold of excited states of the molecule.

The coupling of zero-order states in configuration interaction occurs through the Hamiltonian for many-electron molecules. The major challenge to solving the electronic Schrödinger equation for these systems is electron–electron correlation. The full electronic Hamiltonian can be written (in atomic units):

$$\hat{H}_{el} = \sum_{i}^{N} -\nabla_i^2 + \sum_{i}^{N}\sum_{A}^{M}\left(-\frac{Z_A}{|r_i - r_A|}\right) + \sum_{i}^{N}\sum_{j>i}^{N}\left(\frac{1}{|r_i - r_j|}\right) \tag{11.15}$$

in which N is the total number of electrons (labelled i, j), and M is the total number of nuclei (labelled A with charge Z_A), respectively. Electron–nucleus and electron–electron distances are in the denominators of the second and third terms, respectively, where r is a generalised electronic (lower case subscript) or nuclear (upper case subscript) coordinate in this expression.

The first term on the right-hand side represents the kinetic energy of each electron. The more complete form of this equation would also have a term for the kinetic energy of the nuclei. Here, an assumption is made that the electrons move about the structure determined by the static nuclei by setting the nuclear kinetic energy is zero.

The second term accounts for the Coulombic attraction between electrons and nuclei. This term allows states to couple through vibronic interactions. Vibronic coupling can be a significant contributor to complexity in the porphyrin UV/Vis absorption spectrum, particularly in the Q band; vibronic coupling will be discussed in more detail later.

The third term, often referred to in shorthand as the $1/r_{ij}$ term, describes the Coulombic repulsion between electrons. It is this term that makes the Schrödinger eigenvalue problem formally insoluble for systems with more than one electron. Approximations to the integrals that involve this term must be made in order to include the effects of electron–electron correlation. One very successful approximation approach is to include configuration interaction.

Before going further, a note on wavefunctions is needed. In the Hückel LCAO-MO method described above, the electronic state wavefunctions $\{\Psi\}$ were described as simple products of molecular orbitals, and the only concession to electron spin was to occupy each one with no more than two electrons. The examples for N_2 above (Eqs. (11.13) and (11.14a–d)) illustrate this approach. Product wavefunctions like these are mathematically suitable for solving the Schrödinger equation to find energies, and this approach works well for simple treatments like the Hückel LCAO-MO one above.

Electrons, however, are fermions, particles with half-integer spins. Therefore, wavefunctions that satisfy the Hamiltonian must have both spatial and spin components, and they must be antisymmetric with respect to exchanging two electrons. That is, if the spatial and spin components of one electron are exchanged with those of another, the wavefunction will change sign. This way of stating the Pauli exclusion principle is equivalent to saying that no two electrons in a system can have the same set of quantum numbers. The consequence is the high-school or first-year chemistry rule that each spatial orbital can contain a maximum of two electrons and they must have opposite spins.

An orbital that includes both the spatial and spin components is called a spin-orbital. A mathematical tool for making wavefunctions antisymmetric with respect to electron exchange is to use a determinant. The mathematics of determinants means that the resultant linear combination of products of spin-orbitals is inherently antisymmetric with respect to electron exchange.

In the configuration interaction method, then, the N-electron problem is solved using a collection of determinants as a basis set and allowing them to couple through the third term in Eq. (11.15). The basis set consists of the ground electronic state configuration and excitations of one or more electrons from occupied spin-orbitals to unoccupied spin-orbitals. Unoccupied spin-orbitals also are called virtual spin-orbitals.

In bra-ket notation, the determinant that describes the zero-order ground electronic state $|\Psi_0>$ of an N-electron system can be written in shorthand as

$$|\Psi_0> = |\psi_1 \psi_2 \ldots \psi_a \psi_b \psi_c \ldots \psi_N> \tag{11.16}$$

where the $\{\psi_i\}$ are all occupied molecular spin-orbitals. Each molecular orbital is described as a weighted linear combination of one-electron spin-orbital functions, analogous to atomic orbitals in the LCAO-MO approach. Promotion of an electron from the ψ_a molecular spin-orbital to the ψ_r molecular spin-orbital results in a single determinant describing that zero-order electronic excited state:

$$|\Psi_a^r> = |\psi_1 \psi_2 \ldots \psi_r \psi_b \psi_c \ldots \psi_N> \tag{11.17a}$$

Excitations involving two electrons or more yield determinants like

$$|\Psi_{ab}^{rs}> = |\psi_1 \psi_2 \ldots \psi_r \psi_s \psi_c \ldots \psi_N> \tag{11.17b}$$

$$|\Psi_{abc}^{rst}> = |\psi_1 \psi_2 \ldots \psi_r \psi_s \psi_t \ldots \psi_N> \tag{11.17c}$$

and so on. These ground state and excited state determinants make up the infinitely large, zero-order basis set used in configuration interaction.

Finally, a configuration interaction wavefunction $|\Phi_i>$ is created by expanding in this basis set of single determinant electron configurations

$$|\Phi_i> = c_0|\Psi_0> + \sum_{a,r} c_a^r |\Psi_a^r> + \sum_{a,b>a} \sum_{r,s>r} c_{ab}^{rs} |\Psi_{ab}^{rs}> + \sum_{a,b>a,c>b} \sum_{r,s>r,t>s} c_{abc}^{rst} |\Psi_{abc}^{rst}> + \ldots \tag{11.18}$$

The collection of $\{c_0, c_a^r, c_{ab}^{rs}, c_{abc}^{rst}, \ldots\}$ coefficients represent the mathematical contribution of each of the associated configurations to the state. For example, for electronic excited states, c_0 is usually very close to zero because the ground electronic state configuration contributes very little to the excited state character. The single-electron excitation configurations (second term on the right-hand side of Eq. (11.18)) usually dominate double, triple, and higher multiple electron excitation contributions to the low-lying excited states.

Solving the configuration interaction problem involves diagonalising the full electronic Hamiltonian matrix, containing the $1/r_{ij}$ term, in this configuration interaction basis set. In theory, this approach could yield an exact solution to the Schrödinger equation. However, in practice the basis set of ground and excited electronic state configurations is never complete, so the solution gives an approximation. Truncating the basis set in some logical manner is key to obtaining high-quality results. Gouterman truncated the number of configuration interaction basis functions to four.

11.2.4.2 Configuration Interaction and Porphyrins

The high symmetry of the idealised D_{4h} porphyrin macrocycle leads to energy levels for the frontier molecular spin-orbital energy levels that are nearly or exactly degenerate (Figure 11.7) [24, 25]. The HOMOs ($3a_{2u}$ and $1a_{1u}$) derived from the LCAO-MO Hückel approach are close in energy, and the LUMOs ($4e_g$) are formally degenerate by symmetry. HOMO-LUMO transitions among them have the same E_u symmetry. These π and π* orbitals also bear similar node structures to the n = ±4 and n = ±5 frontier states from the particle-on-a-ring model (Figure 11.8). These insights are what Gouterman exploited in truncating the configuration interaction basis set to create his four-orbital model. This section lays out some of the basics of Gouterman's four-orbital model; see [25–29, 32] for more detail.

Gouterman modified the LCAO-MO Hückel method to force the $3a_{2u}$ and $1a_{1u}$ orbitals to be accidentally degenerate, or very nearly so, by assuming in the Hückel calculations that $\alpha_N = \alpha_C + 2\,\beta_{CC}$ and $\beta_{CN} = 0.5\,\beta_{CC}$ (see Eq. [11.12] above) (Figure 11.7e). These changes lower the orbital energies of the $3a_{2u}$ and $4e_g$ orbitals, but not of the $1a_{1u}$ orbital, which has nodes at the nitrogen positions. Now, the single-electron excitations from these two HOMOs to the doubly degenerate $4e_g$ LUMO form a set of four (accidentally) degenerate, E_u symmetry transitions.

Gouterman's model assumes that this pair of doubly degenerate transitions dominates the configuration interaction, and that other energetically nearby configurations can be ignored, based upon the following argument. The ($a_{2u} \rightarrow e_g$) and ($a_{1u} \rightarrow e_g$) excitations are analogous to the $e^{\pm i4\theta} \rightarrow e^{\pm i5\theta}$ transitions of the Simpson particle on a ring, which can be seen clearly in the node structures of the HOMOs and LUMOs for the two models in Figure 11.8. Other π-π* configurations ($b_{1u} \rightarrow e_g$) and ($b_{2u} \rightarrow e_g$) are nearby in energy and are also allowed by x- and y-polarised light; they have E_u symmetry. However, the b_{1u} and b_{2u} orbitals have different nodal properties. Thus, in Gouterman's four-orbital model, it is assumed that only the ($a_{2u} \rightarrow e_g$) and ($a_{1u} \rightarrow e_g$) pair of doubly degenerate configurations mix to yield the observed B and Q bands.

The Hamiltonian for this system can be written

$$\hat{H} = \hat{H}^0 + \hat{H}' \tag{11.19}$$

where $\hat{H}^0$ contains the first two terms in Eq. (11.15) above, the ones that involve only one-electron terms. $\hat{H}' = \sum_i^N \sum_{j>i}^N \left(\frac{1}{|r_i - r_j|}\right)$ is the troublesome two-electron $1/r_{ij}$ term that

prevents analytical solution. The LCAO-MO Hückel calculations are performed using only $\hat{H}^0$. The resulting molecular spin-orbitals $\{\psi_i\}$ and determinantal zero-order wavefunctions $\{|\Psi_i>\}$ are thus eigenfunctions of the sum of one-electron operators. The four configurations that are allowed to mix in Gouterman's model via $\hat{H}'$ are one-electron excitations written in shorthand as (a_{1u} e_{gx}), (a_{1u} e_{gy}), (a_{2u} e_{gx}), and (a_{2u} e_{gy}):

$$\text{ground state} = |\Psi_0> = |\psi_1(2)\,\psi_2(2)\ldots\psi_{a_{1u}}(2)\,\psi_{a_{2u}}(2)> \tag{11.20a}$$

$$(a_{1u}\ e_{gx}) = |\Psi^{e_{gx}}_{a_{1u}}> = |\psi_1(2)\,\psi_2(2)\ldots\psi_{a_{1u}}(1)\,\psi_{e_{gx}}(1)\,\psi_{a_{2u}}(2)> \tag{11.20b}$$

$$(a_{2u}\ e_{gx}) = |\Psi^{e_{gx}}_{a_{1u}}> = |\psi_1(2)\,\psi_2(2)\ldots\psi_{a_{1u}}(2)\,\psi_{e_{gx}}(1)\,\psi_{a_{2u}}(1)> \tag{11.20c}$$

$$(a_{1u}\ e_{gy}) = |\Psi^{e_{gx}}_{a_{1u}}> = |\psi_1(2)\,\psi_2(2)\ldots\psi_{a_{1u}}(1)\,\psi_{e_{gy}}(1)\,\psi_{a_{2u}}(2)> \tag{11.20d}$$

$$(a_{2u}\ e_{gy}) = |\Psi^{e_{gx}}_{a_{1u}}> = |\psi_1(2)\,\psi_2(2)\ldots\psi_{a_{1u}}(2)\,\psi_{e_{gy}}(1)\,\psi_{a_{2u}}(1)> \tag{11.20e}$$

and so on. In this notation, (a_{1u} e_{gx}) refers to the determinantal wavefunction in this four-state basis set in which an electron has been promoted from the a_{1u} HOMO to the e_{gx} LUMO.

The Hamiltonian diagonalised in the configuration interaction procedure involves both parts of the Hamiltonian in Eq. (11.15). The Hamiltonian matrix can be simplified into two smaller matrices:

$$Hy = \begin{bmatrix} \langle a_{2u}e_{gy} \mid \hat{H} \mid a_{2u}e_{gy}\rangle & \langle a_{2u}e_{gy} \mid \hat{H} \mid a_{1u}e_{gx}\rangle \\ \langle a_{1u}e_{gx} \mid \hat{H} \mid a_{2u}e_{gy}\rangle & \langle a_{1u}e_{gx} \mid \hat{H} \mid a_{1u}e_{gx}\rangle \end{bmatrix} = \begin{bmatrix} E_1 - D_1 & C_{12} \\ C_{21} & E_2 - D_2 \end{bmatrix} \tag{11.21a}$$

$$Hx = \begin{bmatrix} \langle a_{2u}e_{gx} \mid \hat{H} \mid a_{2u}e_{gx}\rangle & \langle a_{2u}e_{gx} \mid \hat{H} \mid a_{1u}e_{gy}\rangle \\ \langle a_{1u}e_{gy} \mid \hat{H} \mid a_{2u}e_{gx}\rangle & \langle a_{1u}e_{gy} \mid \hat{H} \mid a_{1u}e_{gy}\rangle \end{bmatrix} = \begin{bmatrix} E_3 - D_3 & C_{34} \\ C_{43} & E_4 - D_4 \end{bmatrix} \tag{11.21b}$$

in which the subscripts 1, 2, 3, and 4 refer to the one-electron transitions (a_{2u} e_{gy}), (a_{1u} e_{gx}), (a_{2u} e_{gx}), and (a_{1u} e_{gy}), respectively, and the matrix elements are defined as

$$E_1 = \langle a_{2u}e_{gy} \mid \hat{H}^0 \mid a_{2u}e_{gy}\rangle = E_0 + \varepsilon(e_{gy}) - \varepsilon(a_{2u}) \tag{11.22a}$$

$$D_1 = \langle a_{2u}e_{gy} \mid \hat{H}' \mid a_{2u}e_{gy}\rangle \tag{11.22b}$$

$$C_{12} = \langle a_{2u}e_{gy} \mid \hat{H}' \mid a_{1u}e_{gx}\rangle \tag{11.22c}$$

E_0 is the ground state energy, and ε is the energy of the molecular orbital in parentheses determined in the Hückel calculation. The other terms can be written down similarly.

A useful starting assumption is that the system is dominated by the zero-order terms, and that the differences between the matrix elements of the $\hat{H}'$coupling operator are negligible. This approximation leads to

$$D_1 = D_2 = D_3 = D_4 = D \tag{11.23a}$$

$$C_{12} = C_{21} = C_{34} = C_{43} = C \tag{11.23b}$$

The resulting B band transition energies are given by

$$\Delta E_{B_x} = \left[\frac{(\varepsilon(e_{gx}) - \varepsilon(a_{2u})) + (\varepsilon(e_{gy}) - \varepsilon(a_{1u}))}{2}\right] + D + \sqrt{\left[\frac{(\varepsilon(e_{gx}) - \varepsilon(a_{2u})) - (\varepsilon(e_{gy}) - \varepsilon(a_{1u}))}{2}\right]^2 + C^2} \tag{11.24a}$$

$$\Delta E_{By} = \left[\frac{(\varepsilon(e_{gx}) - \varepsilon(a_{1u})) + (\varepsilon(e_{gy}) - \varepsilon(a_{2u}))}{2}\right] + D + \sqrt{\left[\frac{(\varepsilon(e_{gx}) - \varepsilon(a_{1u})) - (\varepsilon(e_{gy}) - \varepsilon(a_{2u}))}{2}\right]^2 + C^2} \tag{11.24b}$$

and the corresponding Q band transitions by

$$\Delta E_{Q_x} = \left[\frac{(\varepsilon(e_{gx}) - \varepsilon(a_{2u})) + (\varepsilon(e_{gy}) - \varepsilon(a_{1u}))}{2}\right] + D - \sqrt{\left[\frac{(\varepsilon(e_{gx}) - \varepsilon(a_{2u})) - (\varepsilon(e_{gy}) - \varepsilon(a_{1u}))}{2}\right]^2 + C^2} \tag{11.24c}$$

$$\Delta E_{Qy} = \left[\frac{(\varepsilon(e_{gx}) - \varepsilon(a_{1u})) + (\varepsilon(e_{gy}) - \varepsilon(a_{2u}))}{2}\right] + D - \sqrt{\left[\frac{(\varepsilon(e_{gx}) - \varepsilon(a_{1u})) - (\varepsilon(e_{gy}) - \varepsilon(a_{2u}))}{2}\right]^2 + C^2} \tag{11.24d}$$

If we further assume that the two HOMOs are perfectly degenerate, and the two LUMOs also perfectly degenerate, then these transition energies simplify to

$$\Delta E_{B_x^0} = \Delta E_{B_y^0} = (\varepsilon(e_g) - \varepsilon(a_u)) + D + C \tag{11.25a}$$

$$\Delta E_{Q_x^0} = \Delta E_{Q_y^0} = (\varepsilon(e_g) - \varepsilon(a_u)) + D - C \tag{11.25b}$$

where $\varepsilon(a_u)$ is the HOMO energy, and $\varepsilon(e_g)$ is the LUMO energy. The wavefunctions that correspond to these doubly degenerate energy levels can be written as

$$| B_x^0 > = \frac{1}{\sqrt{2}} [(a_{2u}\, e_{gx}) - (a_{1u}\, e_{gy})] \tag{11.26a}$$

$$| B_y^0 > = \frac{1}{\sqrt{2}} [(a_{2u}\, e_{gy}) + (a_{1u}\, e_{gx})] \tag{11.26b}$$

$$| Q_x^0 > = \frac{1}{\sqrt{2}} [(a_{2u}\, e_{gx}) + (a_{1u}\, e_{gy})] \tag{11.26c}$$

$$| Q_y^0 > = \frac{1}{\sqrt{2}} [(a_{2u}\, e_{gy}) - (a_{1u}\, e_{gx})] \tag{11.26d}$$

The intensity of the absorptions for these starting states are proportional to the transition dipole strengths. The superscript 0 is used to identify these states as coming from the maximum degeneracy situation, which is the starting point for further analysis using Gouterman's four-orbital model. The B^0 and Q^0 transition strengths are given by

$$R^2 = \frac{1}{2}(R_1 + R_2)^2 \tag{11.27a}$$

$$r^2 = \frac{1}{2}(R_1 - R_2)^2 \tag{11.27b}$$

respectively, where R_1 and R_2 are the dipole strengths of the individual one-electron excitations $a_{1u} \rightarrow e_g$ and $a_{2u} \rightarrow e_g$. Since $R_1 \cong R_2$, the excitations to the $|B^0>$ states are intense in the UV/Vis spectrum, and those to the $|Q^0>$ states are very weak. Alterations to the porphyrin electronic structure through metal coordination in the core or substitution around

the periphery by electron-donating or -withdrawing groups, for example, will result in altering the UV/Vis spectrum away from this fully mixed state. In a sense, these represent the idealised 'perfect' D_{4h} porphyrin states.

The mixing can be diagrammatically represented as shown in Figure 11.9. The one-electron excitations between the LCAO-MO Hückel orbitals that are labelled *y* mix to yield $|B_y^0>$ and $|Q_y^0>$, while those labelled *x* yield $|B_x^0>$ and $|Q_x^0>$ in an analogous manner. The doubly degenerate, idealised B^0 and Q^0 bands are centred at $(\varepsilon(e_g) - \varepsilon(a_{2u}) + D)$ and split by the configuration mixing element $2C$.

The classic example of a porphyrin in the strong configuration interaction, used by Gouterman in his original papers, is Zn tetraphenylporphyrin (ZnTPP) [29]. The intensity of the ZnTPP's Q band is relatively small, and occurs at low energy (e.g. separated widely from the position of the B band), and it thus appears that the a_{1u} and a_{2u} HOMOs are essentially degenerate. The B (Soret) band of ZnTPP appears at 23 200 cm^{-1} (430 nm) and the Q band very weakly at 16 000 cm^{-1} (625 nm). As depicted in Figure 11.9, the configuration interaction mixing element, C, can be determined from the energy separation between the Q and B bands; C = 3600 cm^{-1} in this example. D is related to the average position of the bands in the UV/Vis spectrum and the energy difference between the HOMOs. There is no experimental measure of this energy difference; however, the Hückel LCAO-MO calculations indicate that a reasonable value is D = 5400 cm^{-1}.

Many porphyrins do not exhibit the perfect degeneracy described in Figure 11.9. Metal coordination and axial ligation, peripheral substituent chemical nature and pattern, and the environment affect the molecular symmetry and degeneracy of the frontier orbitals. This will be explored more fully in the next section. Gouterman's four-orbital model treats these effects as perturbations from the ideal, zero-order starting point.

When the E_u symmetry transitions are not totally degenerate, for example, when the a_{1u} and a_{2u} energies are not equal, then the Q bands 'steal' intensity from the B bands (Soret). This can be thought of as unmixing the idealised transitions through unmixing coefficients γ_x and γ_y:

$$|B_x> = \cos\gamma_x\,|B_x^0> + \sin\gamma_x\,|Q_x^0> \tag{11.28a}$$

$$|B_y> = \cos\gamma_y\,|B_y^0> + \sin\gamma_y\,|Q_y^0> \tag{11.28b}$$

$$|Q_x> = \cos\gamma_x\,|Q_x^0> - \sin\gamma_x\,|B_x^0> \tag{11.28c}$$

$$|Q_y> = \cos\gamma_y\,|Q_y^0> - \sin\gamma_y\,|B_y^0> \tag{11.28d}$$

The magnitude of the unmixing coefficient is directly related to the difference in the energies of the (a_{1u} e_g) and (a_{2u} e_g) one-electron excitations, and is inversely proportional to the $1/r_{ij}$ configuration interaction coupling strength given by C.

For most porphyrins, γ is quite small, and the above expressions can be written as

$$|B_x> = |B_x^0> + \gamma_x\,|Q_x^0> \tag{11.29a}$$

$$|B_y> = |B_y^0> + \gamma_y\,|Q_y^0> \tag{11.29b}$$

$$|Q_x> = |Q_x^0> - \gamma_x\,|B_x^0> \tag{11.29c}$$

$$|Q_y> = |Q_y^0> - \gamma_y\,|B_y^0> \tag{11.29d}$$

In this limit, the unmixing coefficients are approximately

$$\tan(2\gamma_x) \cong 2\gamma_x \cong \frac{[(\varepsilon(e_{gx}) - \varepsilon(a_{2u})) - (\varepsilon(e_{gy}) - \varepsilon(a_{1u}))\,]}{2C_x} \tag{11.30a}$$

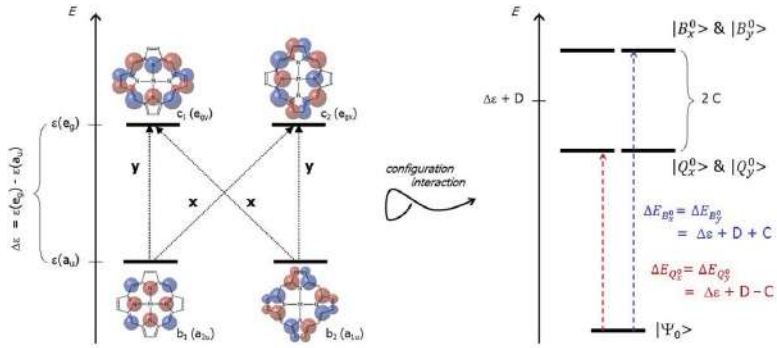

Figure 11.9 The starting point (zero-order condition) of Gouterman's four-orbital model. (a) The four frontier molecular orbitals and their one-electron excitations that give the four single configurations that form the basis set for the configuration interaction. x- and y-labels indicate the polarisation of the transition. (b) The results of mixing those four basis states through configuration interaction to form the $|B_x^0>$, $|B_y^0>$, $|Q_x^0>$, and $|Q_y^0>$ electronic excited states that dominate the porphyrin UV/Vis absorption spectrum. Note: The labels b_1, b_2, c_1, and c_2 have been included here because they are commonly encountered in the literature. They arise because the symmetry labels are only precisely accurate under D_{4h} symmetry, and many porphyrins are perturbed from square-planar geometries.

$$\tan(2\gamma_y) \cong 2\gamma_y \cong \frac{[(\varepsilon(e_{gy}) - \varepsilon(a_{2u})) - (\varepsilon(e_{gx}) - \varepsilon(a_{1u}))\,]}{2C_y} \tag{11.30b}$$

The transition energies can then be written in terms of these unmixing factors γ_x and γ_y:

$$\Delta E_{B_x} = \Delta E_{B_x^0} + 2C_x{\gamma_x}^2 \tag{11.31a}$$

$$\Delta E_{B_y} = \Delta E_{B_y^0} + 2C_y{\gamma_y}^2 \tag{11.31b}$$

$$\Delta E_{Q_x} = \Delta E_{Q_x^0} - 2C_x{\gamma_x}^2 \tag{11.31c}$$

$$\Delta E_{Q_y} = \Delta E_{Q_y^0} - 2C_y{\gamma_y}^2 \tag{11.31d}$$

Note that $C = C_x = C_y$ is the approximation made in Eqs. (11.23). These are conveniently written so that the perturbation arising from weakening the configuration interaction appears as an additive term ($2C\gamma^2$) to the ideal transition energy for the perfect D_{4h} model with degenerate HOMOs and LUMOs.

The B and Q band intensities can be predicted in the limit of small γ_x and γ_y as well:

$$q_{B_y}^2 = {R_y}^2 - {\gamma_y}^2{R_y}^2 + 2\gamma_y R_y r_y \tag{11.32a}$$

$$q_{q_y}^2 = (\gamma_y R_y - r_y)^2 \tag{11.32b}$$

where R_y and r_y are the transition dipoles of the B_y^0 and Q_y^0 bands, respectively; analogous terms can be written for the x-polarised bands. Since both ${r_y}^2$ and γ_y are small relative to ${R_y}^2$, the intensity of the Q_y band is expected to be much smaller than that of the B_y band, as is borne out experimentally.

As the states become less mixed, however, the Q_y band gains intensity at the expense of the B_y band. In the limit of complete unmixing, the above equations are no longer valid. The B and Q bands become dominated by the individual (a_{1u} e_g) and (a_{2u} e_g) transitions, respectively, and become more equal in intensity as predicted by the simple Hückel calculations.

11.2.5 Metals, Ligands, and Peripheral Substituents

The intuitive power of Gouterman's four-orbital model derives from its underlying starting assumption: the frontier electronic structure of a porphyrin or porphyrinoid is dominated by the consequences of delocalising its π-electrons about a very high symmetry (D_{4h}) macrocycle. In most cases, other important factors such as the type of metal (or other atom(s)) coordinated at the macrocycle centre, axial ligands to that metal, peripheral substituents, distortions from planarity, interactions with substrates and others can be treated, at least initially, as perturbations on this 'perfect' D_{4h} system. The frontier states dominate the molecule's interactions with light, with the solvent, with other molecules, macromolecules and materials, and drive most of its function. Thus, Gouterman's model affords chemists with a sound starting point from which to adapt their interpretation by predicting how their systems are perturbed, and the consequences of that perturbation on the behaviour of interest.

Two mechanisms by which the configurations become unmixed (i.e. γ becomes large and the UV/Vis spectrum is affected) are through (i) splitting of the a_{1u} and a_{2u} energies, and (ii) symmetry-lowering under which the LUMOs are no longer degenerate, and they split (Figure 11.10). Each of these leads to different characteristic signatures in the UV/Vis absorption spectra [27, 28, 32, 33].

If unmixing arises due to the separation of the a_{1u} and a_{2u} orbitals in energy, the x- and y polarisations remain equivalent (Figure 11.10a). The x- and y-polarised transitions are

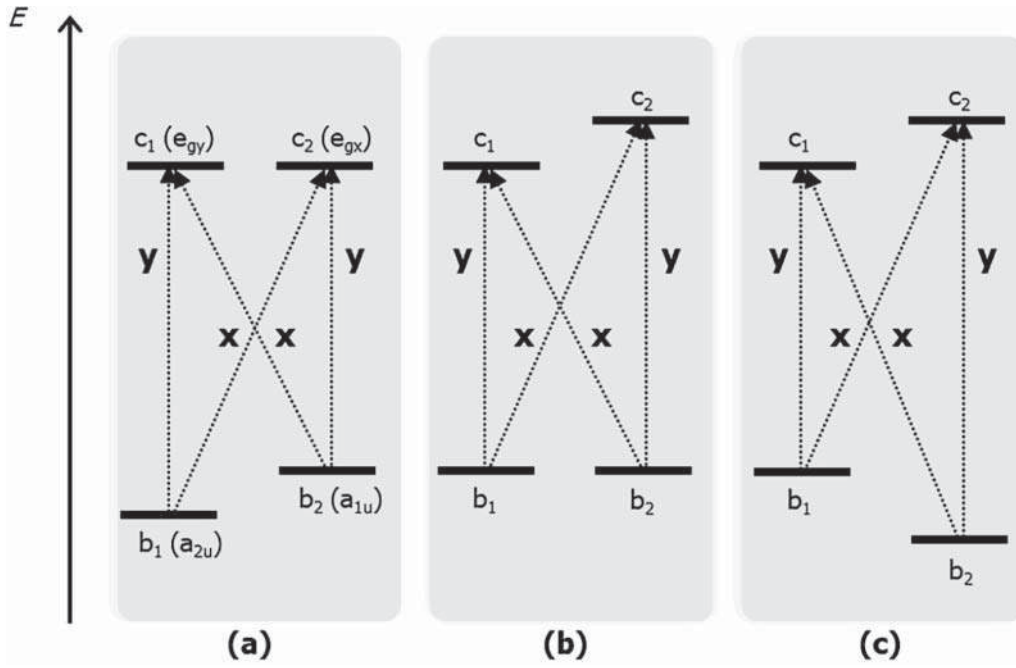

Figure 11.10 Types of unmixing of the porphyrin π-π* excitations through relieving either the accidental degeneracy or the symmetry-induced degeneracy of the HOMOs and LUMOs, respectively. Examples include (a) metal coordination; (b) and (c) symmetry breaking through peripheral substitution and/or out-of-plane distortion. See note in Figure 11.9 for information about labels.

equally affected as the a_{1u} – a_{2u} energy splitting increases. The ΔE_{B_x} and ΔE_{B_y} transition energies remain degenerate, as do the ΔE_{Q_x} and ΔE_{Q_y} transition energies. If the average energy of the a_{1u} and a_{2u} orbitals remains constant, the B and Q bands simply become more separated in energy as γ increases. Alternatively, the entire spectrum can be seen to shift in the same direction. This type of unmixing can be seen in the effect of metal ion coordination to the pyrrole nitrogens. The a_{1u} orbitals have very little electron density on the pyrrole nitrogens, in contrast to the a_{2u} orbital (Figure 11.8). Metal coordination thus tends to affect the a_{2u} orbital preferentially, and split it away from a_{1u} in energy.

Many metalloporphyrins behave similarly to ZnTPP, with small Q band intensities reflecting the perturbative nature of the metal–macrocycle interactions upon the porphyrin electronic structure. In this extremely weak perturbation limit, $\gamma \ll 1$ and Eqs. (11.31a–d) can be simplified to

$$\Delta E_{B_x} = \left[\frac{(\varepsilon(e_{gx}) - \varepsilon(a_{2u})) + (\varepsilon(e_{gy}) - \varepsilon(a_{1u}))}{2}\right] + D + C_x \tag{11.33a}$$

$$\Delta E_{Q_x} = \left[\frac{(\varepsilon(e_{gx}) - \varepsilon(a_{2u})) + (\varepsilon(e_{gy}) - \varepsilon(a_{1u}))}{2}\right] + D - C_x \tag{11.33b}$$

and the analogous y-polarised pair. The form of these equations is similar to Eqs. (11.25a, b) and to Figure 11.9, but with the $\Delta\varepsilon = (\varepsilon(e_g) - \varepsilon(a_u))$ for perfectly degenerate HOMOs replaced by the average of the HOMO and HOMO-1 to LUMO one-electron excitation energies. Under

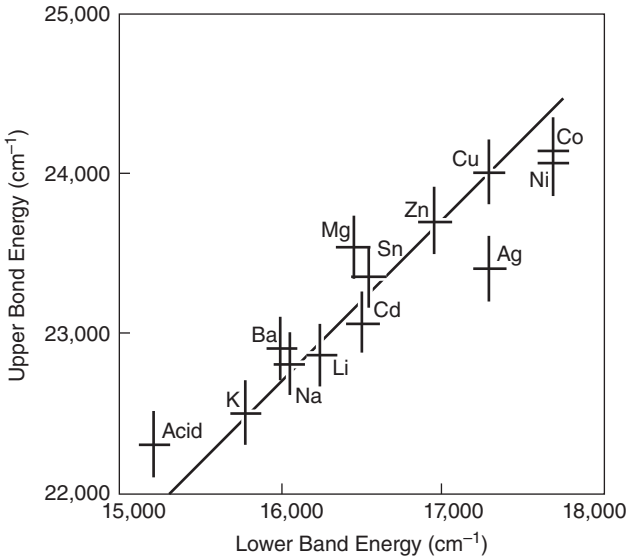

Figure 11.11 Linear relationship between the Q and B band energies for a series of metal TPPs demonstrates that configuration interaction is strong, and the uncoupling coefficient γ is small for these types of porphyrins. Source: From [27].

these conditions, addition, the following further approximations can be made as well:

$$\Delta E_B - \Delta E_Q = constant = 2C \tag{11.34a}$$

$$q_B^2 = constant = R^2 \tag{11.34a}$$

These results predict a linear relationship between the B and Q band transition energies, with a slope of 1; this was confirmed by experiment (Figure 11.11). In addition, the B band (Soret) oscillator strength does not vary much experimentally. Thus, it seems valid to approximate the interactions between the metal and the porphyrin macrocycle as relatively weak, for metals like zinc. Figure 11.11 shows the stronger blue shift that occurs with Cu, Ni, and Co, metals also commonly found in porphyrin cores.

Metal electronegativity, which can influence the porphyrin electronic structure through inductive and/or conjugative effects, correlates with the observed spectral changes. Conjugative effects dominate metal electronegativity-dependent behaviour through coupling of the p_π orbitals of the metal to the porphyrin π-system. As the electronegativity of the metal increases, electron density is withdrawn from the porphyrin macrocycle π-system through interactions with the a_{2u} orbital. The a_{2u} orbital is stabilised relative to the a_{1u} and e_g orbitals, the $(\varepsilon(e_g)–\varepsilon(a_{2u}))$ energy separation increases, and both the B and Q bands shift to higher energy. The value of γ also increases, though since $\gamma \ll 1$ this has little effect on the transition energies, and the expected increase in energetic splitting of the B and Q bands in the spectrum is usually quite small.

A second type of UV/Vis spectrum is observed when the e_g orbitals become non-degenerate, often in concert with a_{1u} and a_{2u} splitting (Figures 11.10b and c). Here, impact on the spectrum can affect the x- and y-polarised transitions differently. Both the B and Q bands will split into two transitions, though the splitting in the Soret band is often too small to be observed. Examples in which this behaviour is observed include free-base porphyrins (see

Figure 11.3), peripheral substitution and reduction of the metalloporphyrin ring (e.g. in chlorins) [28, 32].

The UV/Vis absorption spectrum of porphyrins and related compounds and its role as a window into functional properties has been extraordinarily thoroughly studied, for well over 100 years. For the last 60 or so of those years, Gouterman's four-orbital model has been the dominant lens through which the spectrum–structure–function axis was viewed. Literally thousands of papers have been published upon the absorption spectra of porphyrins and related compounds. Gouterman and his colleagues alone published over 40 papers in his 'Porphyrins' series, many of which explore in detail the effects of the above factors (and others) upon porphyrin and porphyrinoid electronic states and UV/Vis absorption spectra (see, for example, [25, 28, 29, 34, 35]). He and others have written comprehensive reviews on the absorption spectra of porphyrins and related systems as well [32, 33, 36–38]. For more detail or for more specific information to a particular porphyrin or class of porphyrins, the interested reader is advised to begin with those reviews.

11.2.6 Beyond Gouterman's Four Orbitals

The electron-on-a-ring, Hückel LCAO-MO, and Gouterman's four-orbital model were developed at a time when computational chemistry, the application of quantum mechanics to molecular systems, was in its infancy. These models do an excellent job at predicting the major features of the porphyrin electronic structure and UV/Vis absorption spectrum, and provide a framework for how those features change with when the structure is perturbed. They also give chemists a powerful intuitive tool for understanding and exploiting the structure–function relationship in this important class of molecules.

Given today's ease in applying user-friendly quantum chemical software to the computation of structures, energies, orbitals, states, and other important physical observables on basic and complex porphyrins and porphyrin systems, an important question arises: how do we merge the level of detail and complexity in the output from high-powered quantum chemistry calculations with the intuition afforded by the electron-on-a-ring, Hückel, and Gouterman's four-orbital pictures?

Many modern studies of porphyrin electronic states exploit the intuitive power of Gouterman's model by folding it into the analysis of high-level computational chemistry results. A few illustrations of how Gouterman's model can be used in conjunction with computational chemistry are presented here; ab initio computational approaches to porphyrin states and spectra are presented in more detail below. These examples focus upon the effects of peripheral substitution at the *meso*-carbon and β-carbon positions.

The first highlights porphyrins in molecular electronics, a field that has grown significantly since the key paper by Aviram and Ratner was published in 1974 [39, 40]. Porphyrins were quickly recognised for their high potential as electron donor-acceptor components (see [41–44] and references therein). Tsai and Simpson [45] used DFT and the four-orbital model to confirm that excited state energy transfer rates in porphyrin dimers are correlated with the ordering of the frontier orbitals and their contributions to the B- and Q band transitions [46, 47].

This study calculated orbital energies for several geometry-optimised, *meso*-substituted Zn(II) porphyrin derivatives. The substituents possessed varying electron-withdrawing and electron-donating strengths (Figure 11.12). As anticipated, electron-donating groups stabilised the a_{2u} orbital, and electron-withdrawing groups de-stabilised it. For example, the

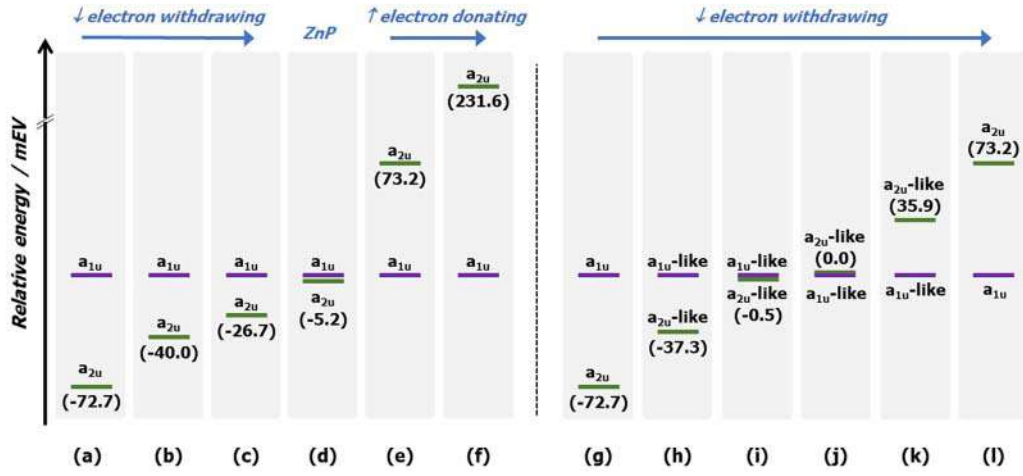

Figure 11.12 The relative energies of the occupied frontier orbitals for a series of *meso*-substituted Zn(II) porphyrin compounds based upon the ZnTPP core structure, calculated at the B3LYP/6-31G(d,p) level. (a)–(f): (a) ZnTPP-F_{20} (phenyl hydrogens replaced with fluorines); (b) ZnTPP-Cl_{20}; (c) ZnTPP-Br_{20}; (d) ZnP; (e) ZnTPP; and (f) ZnTPP with -NH_2 at phenyl *ortho* positions; (g)–(l): ZnTPP with different numbers of pentafluorinated phenyl groups (g) ZnTPP-F_{20}; (h) ZnTPP-F_{15}; (i) ZnTPP-F_{10} adjacent on macrocycle; (j) ZnTPP-F_{10} across macrocycle; (k) ZnTPP-F_5; and (l) ZnTPP. Energy levels from [45].

addition of each electron-withdrawing pentafluorophenyl group stabilised the a_{2u} orbital relative to the a_{1u} by ~0.85 kcal mol^{-1} [45].

The contributions of each orbital to the B and Q band states were then calculated as follows. The unmixing coefficient was determined by using the DFT-calculated frontier orbital energy differences and the configuration interaction strength C. The latter, $C_x = C_y = C$, was found by using the experimentally observed energy splitting of the B and Q bands (ΔE_B - ΔE_Q), with the equation

$$\Delta E_B - \Delta E_Q = 2\sqrt{\left[\frac{(\varepsilon_{eg} - \varepsilon_{a2u}) - (\varepsilon_{eg} - \varepsilon_{a1u})}{2}\right]^2 + C^2} \tag{11.35}$$

This expression has its origins in Eqs. (11.24a–d) above. Once the configuration interaction strength is known, the contributions of each one-electron excitation to the B and Q excited states can be computed and correlated with the experimentally measured excited state energy transfer rates reported in the literature. The results support the hypothesis that the ordering and degree of splitting of the porphyrin frontier molecular orbitals plays a pivotal role in the effectiveness of the electronic communication between porphyrins in arrays [45–47].

Lindsey, Holten, Bocian, and co-workers exploited the availability of new robust synthetic methods to study a series of free-base porphyrins [43] with 0, 1, 2, 3, or 4 phenyl groups attached to the *meso*-carbons, from H_2-porphine to H_2-TPP. In addition to density functional theoretical methods, they used Gouterman's four-orbital model to simulate UV/Vis absorption spectra, and experimentally measured the steady-state and time-resolved absorption and fluorescence spectra for the compounds in the series as well. They found that

(1) the HOMO and HOMO-1 in the D_{2h} free-base macrocycle remained a_{2u}-like and a_{1u}-like, respectively, throughout the series, and the a_{2u}-like was progressively destabilised by the addition of *meso*-phenyl groups, whereas the a_{1u}-like was relatively insensitive (Figure 11.13);

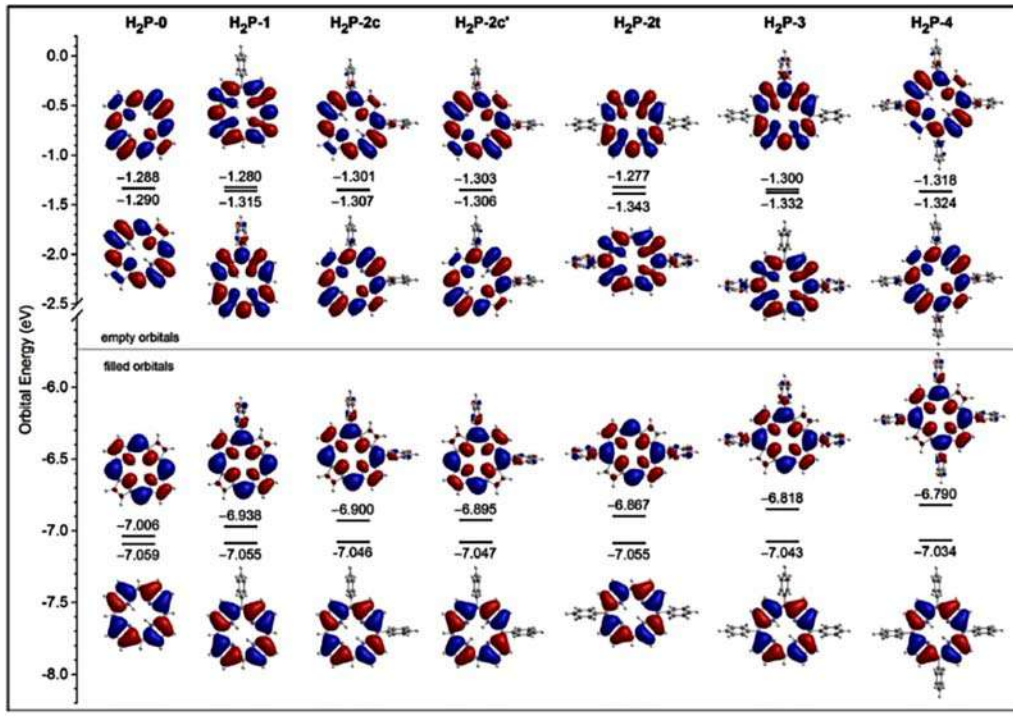

Figure 11.13 The frontier orbitals calculated by DFT. H_2P-X = porphine with X phenyl groups, as indicated on the diagram. The LUMOs are no longer degenerate by symmetry; they are not highly affected by phenyl substitution at the *meso*-positions and remain nearly degenerate and at constant energy. Source: From [43].

(2) the observed shifts in the static UV/Vis absorption spectra are qualitatively reproduced by both the time-dependent DFT and by Gouterman's four-orbital model;
(3) the polarisation of the S_1 transition is along the axis that contains the inner N-H protons, consistent with findings for chlorins, bacteriochlorins, and photosynthetic compounds; and
(4) the lifetimes and quantum yields for the excited state decay pathways from the S_1 excited state depend linearly upon the number of phenyls attached to the core porphine macrocycle ring.

They also have recently reported a similar computational and experimental study of the photophysics and electronic structure of the analogous series of Zn(II) porphyrins, from Zn(II)-porphine to Zn(II)-TPP [48]. The position and intensity changes in the UV/Vis absorption spectra can be explained well in terms of the orbital shapes and energies via Gouterman's four-orbital model. The results of these two studies lend insight into the prevalence of free-base and Zn(II) porphyrins in molecular arrays designed to study energy and electron transfer [43, 48].

Zhang et al. studied the effects of peripheral substitution of Zn porphyrins at the β-carbon positions, rather than at the *meso*-carbons, for the purpose of understanding and guiding the development of better solar energy conversion and photodynamic therapy systems as well [49]. Red-shifted Q band spectra are a key advantage for both of these applications, to facilitate energy harvesting's electron transfer and photodynamic therapy's singlet-oxygen

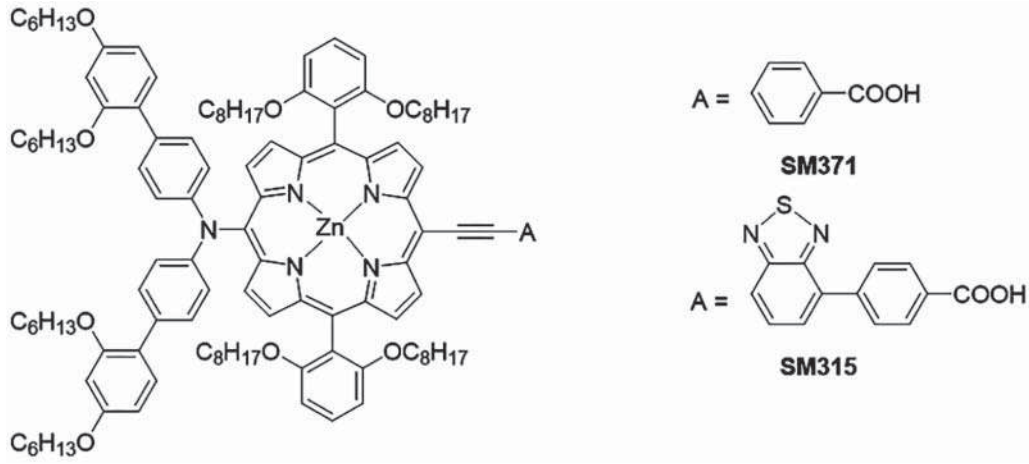

Figure 11.14 Structures of the two dyes used in the 2014 record-breaking study from M. Grätzel's group [51]. The donor is the bis(2′,4′-bis(hexyloxy)-[1,1′-biphenyl]-r-yl)amine, and the acceptor is either benzoic acid (SM317) or benzothiadiazole (SM315).

generation. With asymmetric substitution patterns, these authors observed nonsymmetric delocalisation on the pyrrole rings. The consequence is that the four Gouterman orbitals, both the HOMO and HOMO-1 pair and the LUMOs, can undergo energy splitting. For example, when an $-NO_2$ replaces a β-hydrogen, the LUMO loses formal degeneracy and is significantly split. The resulting Q band shifts significantly to lower energy [49].

The fourth example focuses upon creating high-performance solar energy harvesting sensitisers from porphyrins as well [50]. In a recent report, Grätzel's group used molecular engineering to broaden the B and Q band absorptions and 'fill in' the absorption spectrum between the two bands, while optimising the compatibility with their electrolyte [51, 52]. The core structure is a Zn porphyrin, with donor and acceptor groups joined across the macrocycle (Figure 11.14). The UV/Vis absorption spectrum shows significant broadening and splitting of the B band, which is explained using Gouterman's four-orbital model and point-dipole exciton coupling theory [51]. The donor and acceptor functional groups increase the conjugation and charge transfer character along the donor-acceptor access across the macrocycle, leading to significant electronic asymmetry and two distinct bands (B_x and B_y) in the Soret region of the spectrum. The Q band also broadens, intensifies, and red-shifts, particularly through the Q_x transition. The result was a pair of excellent sensitisers, one of which (SM315) demonstrated record-breaking 13% power conversion efficiency at full sun illumination [51].

In the early 2000s, Baerends and co-workers [53] published a key study in which they developed a model analogous to Gouterman's four-orbital model from computational chemistry results; their key paper has been cited over 300 times, to date. They employed DFT and time-dependent density functional theory (TDDFT) to calculate the molecular and electronic structures and UV/Vis transitions of Mg, Zn, and Ni complexes of porphine and porphyrazine (the porphine structure with N groups replacing the methine CH bridging units). Then, they bridged the complexity of the molecular orbital picture from computations with the significantly more simple Gouterman's model, with its isolated a_{1u} and a_{2u} HOMOs and the e_g LUMOs.

In the quantum chemistry results, the occupied region of the molecular orbital diagram is fairly congested [53]. Although the equivalents of Gouterman's four orbitals can be identified in every metalloporphine and metalloporphyrazine complex studied, each diagram presents a different overall pattern in its details. For example, Ni porphine exhibits a metal-related e_g- type orbital just below the HOMOs that is not present in the Mg and Zn coordinated systems. In the porphyazine complexes, the a_{1u} and a_{2u} HOMOs are quite split in energy, and several molecular orbitals appear in the gap between them, including those associated with the bridging nitrogens and metal-related orbitals.

The authors reconciled the significantly more complex results of these calculations with the intuition provided by simple models by proposing an approach based on the key structural fragments (pyrrole rings and bridging groups) that make up a porphyrin (Figure 11.15) [53]. The approach begins with cyclopentadiene rings perturbed by the presence of a nitrogen to make pyrroles with C_{2v} symmetry. Arranging four of these in a D_{4h} pattern, and adding two electrons to give the system a closed shell, leads to a set of π-based molecular orbitals for $(Py)_4^{2-}$. An analogous D_{4h} arrangement of CH groups generates a collection of π-orbitals for the bridging units. Mixing these together creates the delocalised π-molecular orbital diagram for the D_{4h} porphyrin dianion, in all its complexity. A similar treatment using a D_{4h} arrangement of N bridges creates the analogous diagram for the D_{4h} porphyrazine dianion [53].

The model explores the details of the contributions of the ring and bridge states to the key levels in the porphyrin π molecular orbitals. One key feature is the orbital amplitudes on the α-carbons in the pyrrole rings, where the rings will interact with the bridges. The 'e_y' and '$e_{x2\text{-}y2}$' orbitals have significant amplitudes on those carbons, whereas the 'e_x' orbital does not; so the former two orbitals interact strongly with the bridges, and the latter not so strongly, if at all [53].

The 'e_x' collection of pyrrole-based orbitals does not play a part in Gouterman's four-orbital model [53]. These are, however, recognisable as a $\{2b_{2u}, 3e_g, 3a_{2u}\}$ set of orbitals near the frontier in both porphyrin (P^{2-}) and metalloporphyrin molecular orbital diagrams. The Gouterman orbitals have their origins in the 'e_y' and '$e_{x2\text{-}y2}$' sets from the pyrroles and the collection of π orbitals from the bridging groups. The 'e_y' set contributes to the $1a_{1u}$ HOMO, and the '$e_{x2\text{-}y2}$' set to both the $4a_{2u}$ HOMO and 5 e_g LUMOs [53].

The fragment model provides useful rationalisation of the transition energies and intensities for the B and Q bands, and for those bands relative to the other π-π* transitions in the system as well. For example, a discussion of the nature of the orbitals involved leads to the conclusion that the π-π* excitations from the 'e_x' orbitals to the $5e_g$ LUMO are expected to be higher in energy and weaker than the B and Q bands. Finally, the configuration interaction predicted by Gouterman is borne out in the TDDFT findings as well, in the contributions of each configuration to the excited states [53].

11.2.7 Vibronic Coupling

As discussed above, the typical free-base or metalloporphyrin UV/Vis absorption spectrum consists of several characteristic peaks. Thus far, the theoretical approaches to understanding the B band and Q-band relative intensities, polarisations, and energy splitting have been discussed in some detail. However, some of the complexity in the porphyrin UV/Vis spectrum arises from coupling between electronic and vibrational degrees of freedom. This vibronic

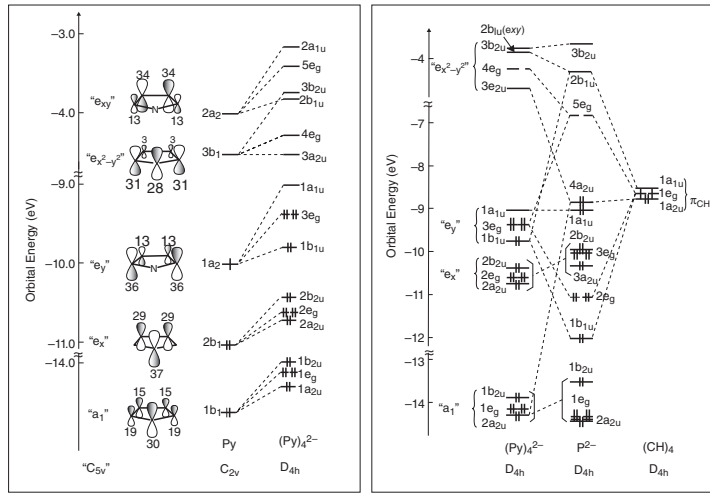

Figure 11.15 Orbital interaction diagrams for (left) the pyrrolic system to make up the D_{4h} collection of pyrrole rings as a structural component of porphine; and (right) the interaction between the pyrrolic system on the left and the four bridging methine CH groups to form the D_{4h} porphyrin dianion P^{2-}. Source: Adapted from Figures 11.4 and 11.5 in [53].

coupling leads to peaks in the absorption spectrum that originate from electronic and vibrational state changes [11, 32, 54–59].

Vibronic coupling is most evident in the Q band region of the free-base porphyrins spectrum, which shows four characteristic peaks (Figure 11.3a). The highest energy of the four is the vibronic $Q_y(1,0)$ transition, where the (1,0) indicates the vibrational excitation in the final excited state and the ground state, respectively. The next transition in energy is the $Q_y(0,0)$. The lower-energy pair is assigned to the $Q_x(1,0)$ and $Q_x(0,0)$ transitions, in that order. In metalloporphyrin spectra, the symmetry is higher and x- and y-polarised bands become more degenerate, leading to a simpler spectrum. The two peaks in the 500–600 nm region of the spectrum are assigned Q(1,0) and Q(0,0) (Figure 11.3b). The spacing between the (1,0) and (0,0) bands reflects the vibrational frequency(s) of the vibration(s) that couple to the electronic excitation. Although the bands are too broad to resolve at room temperature, multiple vibronic transitions contribute to the observed spectrum (Figure 11.16) [32, 60].

Most quantum mechanical treatments of molecules make a very important approximation to separate the nuclear and electronic degrees of freedom, so that the equations that describe the electronic and nuclear motions can be written as a product and the Hamiltonian as a sum of electronic and nuclear energy terms [5, 6, 8, 57]. The nuclear coordinates are parameters in the electronic wavefunction. The Born–Oppenheimer approximation can be described as imagining the electrons moving in the field of a static nuclear geometry, justification for which is often given by comparing the masses of the two types of atomic particles. Electrons are very light and moving so rapidly compared to the nuclei that the nuclei look static to them. Vibronic coupling occurs when that approximation breaks down. A book by Gad Fischer provides a clear, concise description of different ways to approximate the interaction between electronic and nuclear motion [57].

One way to put vibronic coupling back into the relevant equations is to use perturbation theory [56, 58]. Herzberg–Teller coupling mixes electronic states together through their molecular vibrations and allows the normally forbidden vibronic transitions to 'borrow' intensity from allowed ones. In porphyrins, the vibronic transitions in the Q band are ascribed to intensity borrowing from the B bands. Recall that the porphyrin has D_{4h} symmetry, and its B and Q band states both have E_u symmetry. A group theoretical analysis demonstrates that only in-plane vibrational modes of A_{1g}, A_{2g}, B_{1g}, and B_{2g} symmetry can vibronically couple these states [54, 61]. In addition to the already discussed effects observed in the UV/Vis absorption bands, the impact of vibronic coupling in porphyrins also is seen in the polarisation of fluorescence bands (for example, [55]), anomalous Zeeman behaviour ([54], and references therein) and resonance Raman scattering (for example, [33, 59, 61–66]). In porphyrin nanotubes, a detailed examination of excitonic and vibronic coupling showed that, though vibronic coupling is weak, it is essential to accurately understand the absorption spectrum, particularly in the Q band region [67].

Vibronic coupling, like configuration interaction, results from the high symmetry of the porphyrin macrocycle. The presence of these phenomena can make understanding the finer details of a given porphyrin spectrum challenging. However, the presence of these phenomena also means that they are quite well understood in porphyrins, and even relatively complex analysis can exploit simplifications using group theoretical arguments. Perhaps just as importantly, then, porphyrins have provided theoretically minded chemists and physicists with an excellent, challenging class of molecules for testing their ideas about electronic states, adiabatic approximations, and vibronic coupling.

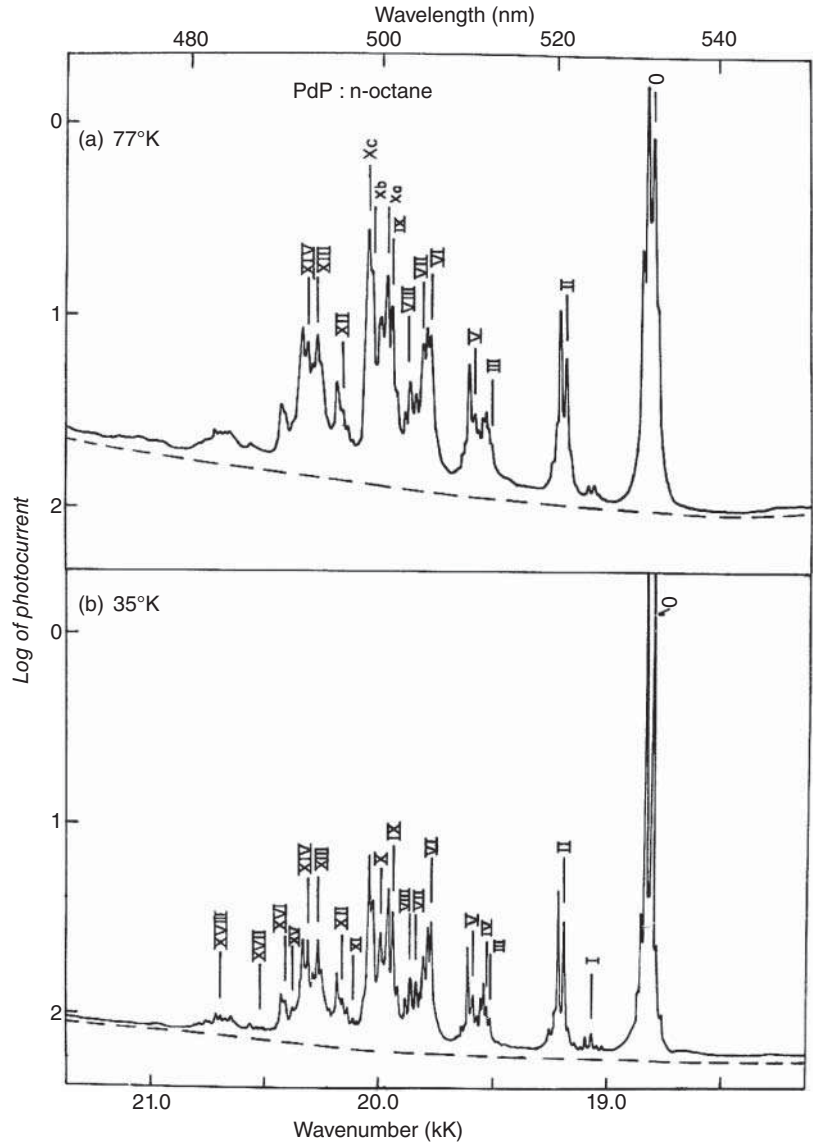

Figure 11.16 Shpol'skii spectra of Pd porphine in n-octane at a 77 K; and b 35 K. The Roman numerals identify the multiple vibronic transitions that contribute to the UV/Vis absorption spectrum. At room temperature, these broaden and are not individually resolved. Source: From [60].

11.3 Ab Initio Quantum Mechanics and Porphyrins

Today's modern computational capabilities (calculation speed, memory size and speed, and sophisticated quantum chemical software) allow porphyrin chemists to routinely employ ab initio quantum mechanics to calculate porphyrin electronic states. The two key ab initio methods we will discuss are (i) the wave mechanical, Schrödinger equation theory based upon the Hartree–Fock self-consistent field method (HF) and (ii) the DFT approach that

uses the Kohn–Sham orbitals.[1] We will particularly focus on the latter, as it offers significant advantages for predicting the states, energies, and spectroscopy of porphyrins and related compounds.

11.3.1 Hartree–Fock Theory and Porphyrins

HF is a wave mechanical method; it solves the Schrödinger equation in an iterative, self-consistent way to determine wavefunctions that describe the particles in the system. These solutions reflect the molecule's physical properties, including the electronic states and their energies. HF works well for many molecular systems, particularly now that readily available computational power allows the use of large, complex basis sets. In addition, the errors associated with HF tend to be systematic, so scaling types of corrections often can be used to compare results accurately with experiment (see, for example, [5, 6, 8]).

In wave mechanics, we can write down the exact form of the Hamiltonian operator, which is the part of the Schrödinger equation that governs the motions of the particles. The practical challenge with this method is that, unfortunately, we do not know how to solve the Schrödinger equation for the vast majority of interesting problems, so our solutions are approximations. The results of HF are made more accurate by improving the quality of the wavefunction through methods like Møller–Plesset perturbation theory (MP2, MP3, etc.), coupled-cluster theory, and configuration interaction [6]. In fact, complete configuration interaction can, in principle, yield an exact solution to the Schrödinger equation. The four-orbital configuration interaction approach outlined above is a simple example. An exact solution would include the full set of configurations associated with all one-electron, two-electron, three-electron, and so on, excitations, which is obviously impractical. These types of corrections to basic HF can provide high-quality results. However, they also are quite computationally expensive and do not scale favourably with the size of the system.

Unfortunately, although HF works quite well for many types of molecules, it does not work very well for porphyrins, because it does not include a sufficiently accurate treatment of electron correlation (for reviews, see [68, 69]). HF predicts significantly incorrect ground state geometries with alternating bond lengths around the macrocycle [70–72], and does not provide quantitatively accuracy of ionisation potentials in many cases [68, 69, 73–76]. For HF to work well for porphyrins and result in structures that reflect the delocalisation of electrons around the macrocycle, computationally expensive, higher-order methods like MP2 and others mentioned above must be included so that electron correlation is treated more correctly.

11.3.2 DFT and Porphyrins

Kohn–Sham DFT is an ab initio approach for formulating quantum mechanics that focuses upon the electron density, rather than upon the wavefunctions. Although the idea of using electron densities was proposed in the early days of quantum mechanics, it was not until key developments in the mid-1960s by people like Hohenberg, Kohn, and Sham that the implementation of DFT became practical and gave computational chemists a new tool for predicting the structures and physical properties of molecules and materials. Unlike with

1 Orbital-free DFT will not be discussed in this chapter. The abbreviations KS-DFT and DFT are equivalent here.

the Schrödinger equation, solving the DFT-density-formulated equation of motion exactly is well understood. Unfortunately, the exact density functional that governs the motions of the particles, the equivalent of the Hamiltonian in the wave mechanics approach, is not known. Theoretically, there exists a perfect functional that would yield exact answers for all systems; all other density functionals are approximations to that elusive perfect or universal one [77–79]. The component of the total density functional that cannot be written down in its complete form is the exchange-correlation part. All known density functionals today approximate this term in different ways.

The two biggest advantages of DFT over HF-based approaches are that (i) calculations are less computationally expensive and tend to scale more favourably with system size; and (ii) the Kohn–Sham orbitals are based on a one-electron potential that includes electron correlation even at the lowest levels of the theory. In addition, although it was not clear that this would be the case at the outset, the energies and other molecular properties that result from DFT calculations are accompanied by a physically meaningful molecular orbital picture that underpins interpretation and intuition [53, 80–82]. The Kohn–Sham orbitals that result from DFT calculations are arguably superior to the analogous results from HF-based calculations.

These qualities led to the successful rise of DFT in the late 1980s and 1990s to become the most popular quantum mechanical modelling approach for chemists today. That popularity holds for porphyrins and related classes of molecules as well; DFT is the 'go to' method for calculating the geometries, energies, and other physical properties of porphyrins and porphyrinoid compounds like phthalocyanines, corroles, chlorophylls, chlorins, etc.

The original Hohenberg–Kohn theorem was published in 1964 [83], which makes 2014 the 50th anniversary of DFT. A special issue of the *Journal of Chemical Physics* was published on that occasion [84, 85], including perspective by Becke, the 'B' in the widely used BLYP [86, 87] and B3LYP [87, 88] density functionals, designed to be both historical and educational [89]. Among recent advances in DFT are significant improvements in the treatment of non-covalent interactions [90, 91]. Other useful and interesting reviews from the last 10 years include [79, 92–94].

The quality of the result of a DFT calculation depends upon two key choices: (i) the size and type of basis set; and (ii) the density functional. The computational efficiency of DFT means that augmented triple-zeta and quadruple-zeta basis sets are commonly employed, even for relatively large molecules [79]. Most commonly used basis sets, for example, the split-valence double or triple family, 6-31G or 6-311G, respectively, with polarised and/or diffuse functions, perform well for atoms in the porphyrin macrocycle and peripheral substituents, like carbon, nitrogen, oxygen, and hydrogen. More care is needed in choosing a basis set for metals coordinated in the porphyrin core, especially for heavier ones. Effective core potential basis sets like LanL2DZ, a valence double zeta basis set, have been used with successful results. Finally, some basis sets are more appropriate when studying particular molecular or material properties and behaviours, such as non-bonding interactions and highly extended conjugation. Basis set choice will not be further discussed here; the reader is referred to [79, 95] and references therein.

The last 20 years have seen an explosion in the number and variety of density functionals available to chemists, and in the improvement of DFT's ability to accurately predict molecular and material structures, energies, and other properties. At this point, literally hundreds of density functionals exist from which to choose. Each differently approximates the exchange-correlation part of the functional, usually represented as the sum of exchange and correlation components. It is not the purpose of this chapter to provide a comprehensive

list of basis sets or functionals, their theoretical underpinnings, or their benchmark results, nor is it within our scope to discuss progress of the field towards the universal functional [78]. We refer the interested reader to recent reviews, and references therein (see below). A particularly useful review that ranks 200 functionals for their performance in 8 different categories across nearly 5000 datapoints was published in 2017 by Mardirossian and Head-Gordon [79].

Here, we summarise several sources of error in DFT and which types of functionals minimise them. We explore how DFT can be utilised with a strong focus upon understanding and predicting the behaviour of porphyrins, their structures, and their electronic states. Then, we briefly address TDDFT, a method for calculating porphyrin excited state structures, energies, and UV/Vis absorption spectra.

Unfortunately, there is no theoretically proven hierarchical or systematic way to improve the density functional. This is the most serious disadvantage of, and source of user dissatisfaction with, DFT [93]. In wave mechanics, successive extensions to each level of theory provide clearly anticipated improvements in performance. For example, adding MP2 theory to an HF energy calculation is straightforward way to generate a more exact result. In contrast, the path to an improved DFT functional is not so clear; the addition of more terms, changes in the functional form, more precise fitting of empirical components to experimental parameters, and so forth do not necessarily provide greater accuracy. The consequence is that thorough benchmarking of DFT functionals is needed to enable practitioners to make wise choices for a particular system.

Some guidance about how to improve DFT results can be found in a broad-strokes scaffold for different classes of DFT functionals that was introduced by Perdew and colleagues about 15 years ago (Figure 11.17) [96], and highlighted in several reviews including [79, 90]. In this 'Jacobs ladder', the distinction between successive 'rungs' is the inclusion of additional physics in the functional. For example, generalised gradient approximation (GGA) functionals generally perform better than do those that employ a local spin density (LSDA) approximation, because they include terms that account for inhomogeneity in the electron density; molecules, of course, have quite inhomogeneous electron densities. LSDA and GGA functionals form the two lowest tiers of the ladder. BLYP, PBE [135], and PW91 [136] are popular GGA-type exchange-correlation functionals. LSDA and GGA functionals, and those in the 3rd tier, meta-GGA functionals, suffer from (i) self-interaction error (SIE); (ii) long-range dynamic correlation error; and (iii) strong correlation error. Different types of terms are needed to overcome these.

SIE is essentially an overcounting error. DFT calculates the interaction of each electron with the electron density of the system, which includes that same electron. The well-known global hybrid functionals like B3LYP, B3PW91 [88, 136], and PBE0 include some non-local exchange, and they provide improvements to overcome SIE. For example, B3LYP contains 20% exact HF exchange, as does B3PW91. Global hybrid GGA and global hybrid meta-GGA functionals form the fourth and final tier that will be discussed here.

To improve upon SIE even further, range separation can be employed. In this method, the exact HF exchange is split into short- and long-range contributions, each contributing some percentage to the overall exact exchange part of the functional. For example, the relatively recent functionals ωB97X [145] and CAM-B3LYP [144] employ fractions of 15.77% and 19% short-range exact exchanges, respectively. The parameterisation of the exchange-correlation functional can become quite complicated.

Figure 11.17 Perdew's 'Jacob's Ladder' for density functionals with a focus upon examples of functionals used for DFT computational studies on porphyrins [79, 96]. See Table 11.1 for examples of studies employing various levels of functional. LSDA: VWN [133], PW92 [134]. GGA: PBE [135], BLYP [86, 87], PW91 [136], BP86 [86, 137]. meta-GGA: TPSS [138], PKZB, M06-L [139]. Hybrids: B3LYP [87, 88], PBE0 [140], B97 [141], TPSSh [142], M06 [143], M06-2X [143]. Range-separated hybrids: CAM-B3LYP [144], ωB97 [145], ωB97X [145]. Double hybrids: B2PYLP [146], SCAN0-2 [147], PWPB95 [148]; Range-separated and spin-component scaled double hybrids: ωB2PYPLP [149], ωB97M(2) [150], revDSD-PBEP86 [151]. Long-range dynamic correlation: -D3 [152], -D3(BJ) [153], -D3(CSO) [154], -VV10 [155].

Density functionals that do not account for long-range dynamic correlation, the second type of error mentioned above, are unable to treat non-bonding interactions very accurately. This was a significant challenge for DFT until relatively recently, when additive models that correct long-range interactions were developed [79, 90, 91]. One approach is to use the non-local correlation functionals like VV10 and vdW-DF2 [155]. This method introduces fewer adjustable parameters, yet can provide very accurate results. The more widely used method was developed by Grimme and co-workers, who have created three generations of DFT-D tails (D1, D2, and D3) that can be added to an existing functional to provide a path to accurately treat non-covalent behaviours [91, 152, 156–158]. The latest generation, -D3, can be used with a variety of damping functions (e.g. -D3(0) [152], -D3(BJ) [156], -D3M(BJ) [153], and -D3(CSO)) [154]. These types of dispersion corrections attempt to overcome underbinding in non-covalent interactions, and they can work very well, including in challenging porphyrin applications [91]. The addition of dispersion correction can improve benchmark calculations to bring them within errors of 1 kcal mol^{-1} or less (Figure 11.18) [79].

The third type of error, strong correlation, is still a significant challenge in DFT. This type of error is largest for systems that require multiple, strongly correlated determinants to accurately describe states. As discussed extensively above, an accurate description of porphyrin states requires multiple configurations. This is particularly true for the excited state manifold. No doubt, solving this problem in DFT will provide more quantitative accuracy for DFT

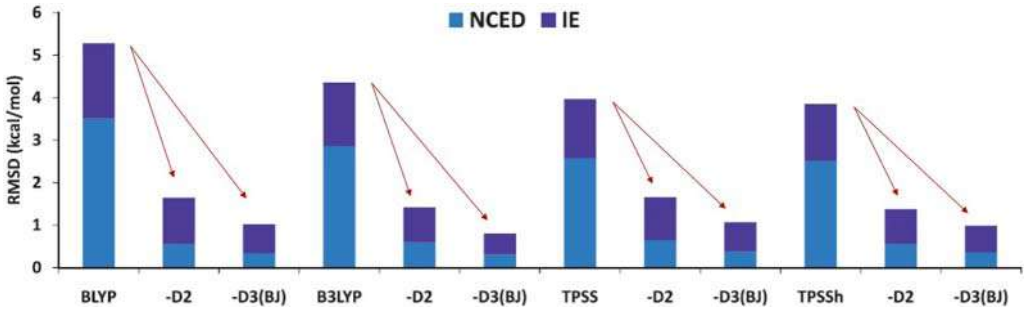

Figure 11.18 The improvement in benchmark performance (RMSD = root-mean-square deviation) for four functionals (BLYP, B3LYP, TPSS, and TPSSh) upon addition of dispersion correction (-D2, -D3(BJ)). BLYP (local GGA), B3LYP (hybrid GGA), TPSS (local meta-GGA), and TPSSh (hybrid meta-GGA). NCED = 1744 data points of 'easy' non-covalent dimers ('easy' = not very sensitive to self-interaction error or strong correlation); IE = 755 'easy' isomerisation energies. Source: Adapted from [79].

calculations in porphyrins. In the meantime, DFT provides an excellent resource for porphyrin chemists to obtain significant insight into porphyrin behaviour in a wide variety of situations.

Fifth tier density functionals are the last rung on the ladder, on the path to the 'heaven' of broad-spectrum, efficient, chemically accurate computational methods. Double-hybrid density functionals are one of the types of approaches on this rung [159, 160].

Happily, fourth tier global hybrid GGA functionals provide sufficiently accurate electronic structures and energies for most situations facing porphyrin chemists. The DFT workhorse of the porphyrin world has been B3LYP, which consists of Becke's 1993 three-parameter, gradient-corrected hybrid exchange functional [88] and Lee–Yang–Parr's gradient-corrected correlation functional [87]. The discussion below about DFT calculations of porphyrins is not meant to be comprehensive, but to provide a few illustrative examples.

One approach used to demonstrate the utility of the B3LYP functional for calculating basic porphyrin electronic structures and energies is to compare the calculated and experimental vibrational frequencies at the same level of theory. If the calculated vibrational spectrum cannot be well correlated with the experimental one, then the computed geometry and/or electronic structure is likely to be incorrect. Examples of this approach include early work by our group [127] and a more recent, extensive study by Dietzek and co-workers [126].

In the first example, BLYP/6-31G(d,p) and B3LYP/6-31G(d,p) were applied to Ni(II) porphine to calculate the optimised ground state geometry and harmonic vibrational frequencies. The results were compared to the experimental geometry [161] and previous B3LYP/6-31G(d),VTZ(Ni) calculations [162] (Figure 11.19). The B3LYP/6-31G(d,p) method gave the smallest RMS error in bond lengths and better accuracy for angles. The optimised structure is distorted out of plane in a ruffling geometry, as anticipated. Both in-plane and out-of-plane vibrational frequencies are well reproduced, with a systematic RMS error of just under 31 cm^{-1}. The BLYP functional reproduces the vibrational frequencies with a smaller overall error. However, our studies and others' [162] indicate that, once scaled for systematic errors, the B3LYP harmonic potential provides a superior harmonic potential surface. In Tsai and Simpson, the B3LYP harmonic potential and experimental vibrational frequencies were fit by classical force fields of varying complexity in which specific types of interactions were successively added [127]. The study showed that long-range force field cross terms are essential for accurate predictions of the porphyrin vibrational spectrum,

	Experiment[a]	BLYP/6-31G(d,p)[b]	B3LYP/6-31G(d,p)[b]	B3LYP/6-31G(d),VTZ(Ni)[c]
Bond Lengths (Å)				
Ni – N	1.951(2)	1.9394	1.9425	1.9659
C_α – N	1.379(2)	1.3960	1.3794	1.3778
C_α – C_β	1.435(4)	1.4467	1.4389	1.4400
C_α – C_m	1.371(3)	1.3901	1.3815	1.3823
C_β – C_β	1.347(3)	1.3700	1.3585	1.3587
rms error		*0.0168*	*0.0078*	*0.0099*
Bond Angles (deg)				
rms error		*0.42*	*0.26*	*0.17*
Out-of-plane distortion (deg)				
C_α – N – N – C_α	1.7	28.8	22.8	11.8

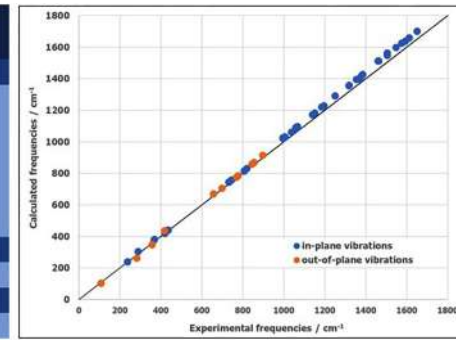

Figure 11.19 Full geometry optimisation and vibrational frequency calculation for Ni(II) porphine at the BLYP/6-31G(d,p), B3LYP/6-31G(d,p) and B3LYP/6-31G(d),VTZ(Ni) levels. (Left) Comparison of the experimental and calculated geometries. (Right) Comparison of experimental and B3LYP/6-31G(d,p) calculated vibrational frequencies [127], with in-plane (blue) and out-of-plane (orange) vibrations. The guideline has a slope of 1. (a) from [161]; (b) from [127]; (c) from [162].

including the isotopic shifts of vibrational frequencies. This finding reflects the importance of delocalisation of the π electron system across the macrocycle.

In 2018, Schindler et al. employed a slightly modified B3LYP functional, with 15% exact exchange rather than the normal 20%, called B3LYP(15) to study 18 different Ni(II) porphyrins, with methodically varying types and degrees of peripheral substitution [126]. They used a 6-31G(d) basis set for the macrocycle and peripheral substituents, and a 10-electron, non-relativistic effective core potential MDF-10 for the coordinated Ni(II). The goal of this study was to correlate the experimental resonance Raman spectrum with the degree of out-of-plane ruffling in the ground state structure. This type of distortion is very 'soft' or low energy, and the study also explored the importance of crystal packing forces upon the extent of ruffling distortion observed experimentally. The validity of the computational approach was confirmed in two ways. First, there was very good agreement between calculated and observed vibrational frequencies, though as in the previous studies the frequencies were systematically underestimated; these authors applied a correcting scaling factor of 0.98, as is commonly done. Second, the cosine dependence of the frequency shifts of key bands in the Raman spectrum on the ruffling angle was very similar in the experiments and calculations. This finding confirms that the B3LYP functional does a good job of accurately reproducing the ground state geometry and the harmonic potential energy surface around that geometry, for simple porphyrins [126].

Iron porphyrins present a much more difficult challenge to computational methods, particularly because of the myriad of spin states they can adopt. De Visser and colleagues have shown several examples of how effective the B3LYP functional can be in calculation the geometries and energies of several iron porphyrin systems [163]. In a recent example, they explored the electrochemical reduction of CO_2 to CO via an iron porphyrin using three functionals, B3LYP, BPE0, and B3LYP-D3 [115]. Geometry optimisations were performed with the 6-31G* basis set for everything except the iron, and the LANL2DZ basis for the iron. Then, single-point energy calculations were performed with significantly more complex basis sets to obtain higher-quality energies: 6-311+G* for everything except the iron, and LACV3P+ for the iron. The ground state geometries were relatively insensitive to the functional used. In contrast, the B3LYP-D3 functional did not perform as well as did B3LYP and BPE0 for calculating iron reduction potentials. This multistep reaction involves several transitions that

include multiple Fe(II) ions, ligand binding, electron and proton transfers, and ligand release. Interestingly, the authors conclude that the overall results were relatively insensitive to the type of functional employed, though clearly there were some differences in performance for individual steps [115].

This iron porphyrin example above illustrates the particular challenge of using DFT. It simply is not always clear how to improve the computational results. Including the Grimme dispersion tail in the calculation did not seem to improve the reaction step involving release of CO upon reduction, and it made the calculations of iron reduction potentials worse [115]. In some cases, it can be difficult to predict how a given functional will behave for a particular compound and application, and the implementation of DFT can become a bit experimental in approach.

Clearly, there is no single DFT functional that works well for all porphyrins or for all porphyrin behaviours. This conclusion merely reflects the general state of DFT today, and its aspirations for the future. Examination of the comparison tables in the extensive review by Mardirossian and Head-Gordon [79] shows that there are general trends in performance, but that even the best-performing functionals have different strengths and weaknesses. There is more to be accomplished in the search for a universal or perfect functional [78, 89]. Fortunately, there are benchmark studies to guide one's choices.

Some types of porphyrins are particularly challenging, including those with altered ring structures such as expansions, contractions, N-confused porphyrins, and porphyrazines. Similarly, highly substituted and distorted porphyrins and porphyrins coordinated to transition metals or other heavy elements can necessitate extra care in computing electronic structures and energies. Of rapidly growing interest in the field of porphyrinoid chemistry are the expanded porphyrins, whose aromaticity will be explored in more detail below. These systems provide an excellent example of the how the B3LYP functional can provide inadequate results. The larger, flexible ring system of the expanded porphyrins provides a challenge to computational chemistry, because of important long-range interactions and complicated topologies that can have relatively soft potential energy surfaces.

A systematic study examining the performance of a series of DFT functionals upon calculations of expanded porphyrins that act as topological switches was performed recently by Torrent-Sucarrat et al. [131] In this study, optimum geometries, energies, and magnetic properties were calculated for extended porphyrins with either six or seven pyrrole rings, and two molecular distortions were explored. Eleven different functionals were tested (B3LYP, BPE, BP86, M06-L, TPSSh, M05-2X [164], M06-2X, BH&HLYP [165], CAM-B3LYP, BMK [166], and ωB97XD [167]) using the 6-31G and 6-311G(d,p) basis sets. For five of the functionals, Grimme's D3 dispersion tail with Becke–Johnson damping (-D3(BJ)) was added. Notably, the B3LYP, PBE, BP86, ωB97XD, and TPSSh functionals performed quite poorly overall. A significant problem is overstabilisation of the Hückel aromatic structures, which has deleterious follow-on effects on the prediction of the correct minima and transition states associated with the potential energy surface. The ωB97XD functional, though highly rated in a recent extensive benchmarking exercise [79], gave significantly incorrect structures. Of particular concern is the poor performance of B3LYP in these extended topological switch systems, given its popularity in the literature (Figure 11.20) (see, for example, [93]).

The functionals that performed the best were the CAM-B3LYP, M05-2X, and M06-2X functionals. CAM-B3LYP [144] is a range-separated hybrid functional that culminates in 65% exact exchange at long distances. The Minnesota functionals M05-2X and M06-2X from Truhlar's group [143, 164] are global hybrid meta-GGA functionals, in tier four of the 'Jacob's

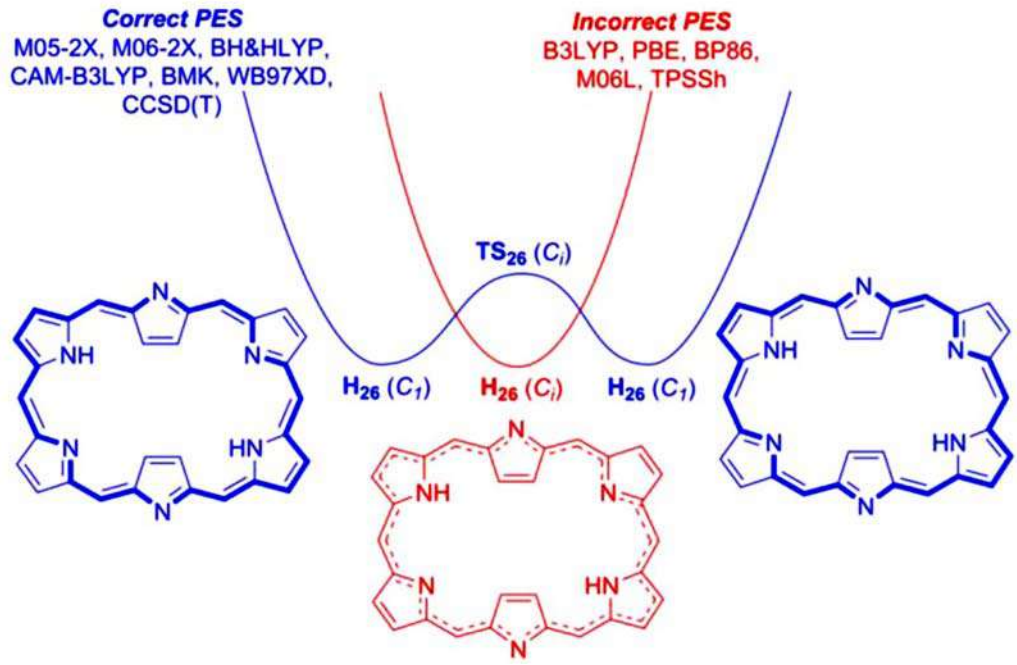

Figure 11.20 Schematic of the potential energy surfaces for the interconversion between two conjugation paths in [26]-hexaphyrin in its Hückel aromatic conformation. The authors used a coupled-cluster method (DLPNO-CCSD(T)) and tested 11 different density functionals: GGA (PBE, BP96), meta-GGA (M06L), hybrid GGA and meta-GGA (B3LYP, BMK, BH&HLYP, M05-2X, M06-2X, TPSSh), and range-separated hybrid GGA (CAM-B3LYP, ωB97XD). Source: From [131].

ladder' above (Figure 11.17). These functionals are not range separated, but they do have relatively high fractions of exact HF exchange, with 56% and 54%, respectively. Correcting for dispersion provided no systematic improvement on the relative energies of the conformers [131].

Though the M05-2X and M06-2X functionals are not as popular in the porphyrin literature as is B3LYP, they are beginning to appear more often. These functionals are semiempirical, with relatively large numbers of parameters that have been optimised against a large amount of chemical data. They are aimed at providing broad accuracy in main group chemistry and in systems with transition metals. Their benchmark results are mixed [79].

A recent benchmark study on switching among Hückel, Möbius, and twisted-Hückel conformers of extended porphyrins evaluated the performance of dozens of functionals from the second to the fifth rung of Jacob's ladder (Figure 11.17), including over 20 from the double-hybrid fifth rung (Table 11.1) [95]. The Minnesota meta-GGA functionals performed well in that study; range-separated double hybrids like B2GP-PLYP and ωB97M(2) performed even better. The inclusion of dispersion improved results for many of the functionals. Martin, Alonso et al. also compared the DFT results to HF-based methods, including Møller–Plesset perturbation and coupled cluster [95].

Table 11.1 presents a handful of illustrative examples of the application of DFT to porphyrins. No attempt is made to be comprehensive, though slight biases in favour of more highly cited and more recent papers was applied. The goal of this table is to provide an overview of how DFT is used today in porphyrin research, which is largely to support and

Table 11.1 Illustrative examples of DFT and TDDFT calculations of porphyrins.

Application	Density functional(s)	References
Dye-sensitised solar cells – porphyrin sensitisers		
Effect of peripheral substitution on Zn porphyrins: molecular orbitals, orbital energies, redox properties, UV/Vis spectra	B3LYP	[97, 98]
	B3LYP, CAM-B3LYP	[99]
	B3LYP, CAM-B3LYP, BH&HLYP, M06-2X, M06-HF	[100]
	M06-2X-D3	[101]
Optimising DSSC efficiency in Zn porphyrin sensitisers	B3LYP, M06	[51, 52]
Distorted push-pull Zn porphyrins; oxidation potentials; non-linear optical properties	B3LYP, BLYP, BH&HLYP, PBE0, PBEH7HPBE, mPWPW91, mPW1K, mPWH&HPW91, M06, M06-2X	[102]
Free-base porphyrins grafted to TiO_2 for light-driven water oxidation	B3LYP, PBE0, HSE06, BMK, TPSSh, M02-2X, MPW1K, CAM-B3LYP, ωB97X-D, LC-ωPBE	[103]
Light harvesting and charge separation in ZnTPP and free-base TPP with increasing *meso*-carbon phenyl substitution	B3LYP, ωB97XD	[43, 48]
Hemes (Fe porphyrins)		
CO deligation from heme	B3LYP, BLYP, SVWN	[104]
Geometries of Fe porphyrin complexes	BP86, PBE, TPSS, B3LYP, PBEO, TPSSH, B97-D	[105]
Spin states of Fe porphyrins using effective core potentials	B3LYP	[106]
Spin-forbidden binding of ligands to ferrous heme	B3LYP, B3PW91, B3P86 (open shell)	[107]
Mössbauer and NMR properties of S = 3/2 Fe porphyrins	B3LYP	[108, 109]
Porphyrins as catalysts or reaction intermediates		
Fe porphyrin carbenes Mössbauer and NMR properties	B3LYP, mPW1PW91, M06, B97D, ωB97XD	[110]
Bifunctional Mg porphyrin catalysis for synthesis of cyclic carbonates, mechanistic insight	B3LYP	[111]
Electrochemical reduction of CO_2 in water by Co porphyrin, mechanistic insight	B3LYP, BPE, BP86	[112]
Porphyrin-MOFs (metal organic framework) for light-driven processes, optical properties	PBE, PBE0, CAM-B3LYP, PBE0-XC-D3	[113]

Table 11.1 (Continued)

Application	Density functional(s)	References
CO_2 reduction with iron porphyrin catalysts, mechanistic insight	ωB97X-D, ωB97M-V, B97D, B3LYP-D3	[114]
CO_2 reduction with iron porphyrin catalysts, mechanistic insight, optimal functional	B3LYP, PBE0, B3LYP-D3	[115]
Asphaltene-metalloporphyrin aggregation, contribution of Ni porphyrins	PBE-D	[116]
Asphaltene-metalloporphyrin aggregation, contribution of Ni and V porphyrins	B3P86, B3PW91, BLYP, B3LYP, G96LYP, X3LYP, O3LYP, MPW1B85, mPW1PW1, PBE, PBE0, PW91, TPSS	[117]
Porphyrins and extended carbon structures (fullerenes, carbon nanotubes, graphene)		
Charge transfer excited states Zn porphyrin, Zn chlorin, and Zn bacteriochlorin complexes with fullerene for organic photovoltaics	B3LYP-D3, OT-RSH (80%PBE, 20% Fock exchange)	[118]
Free-base porphyrin-fullerene dyad, absorption, and electron transfer	SVWN, PBE, B3LYP, PBE0	[119]
Electronic communication in porphyrin-hexi-peri-hexabenzocoronene as a test case for graphene-based molecular electronics; quasi-optoelectronic electrodes	B3LYP	[41]
Non-covalent functionalisation of graphene with H_2-porphine and H_2-TPP, structures & intermolecular interaction energies	M05-2X	[120]
Non-covalent bonding of 3d metal phthalocyanines to single-walled carbon nanotubes, intermolecular interaction energies	PBE-D	[121]
Trends, comparisons, & other studies		
Metal–macrocycle interaction in metalloporphyrins and metallophthalocyanines	VWN-B-P	[36, 37]
Optical and redox properties of radially symmetric Zn porphyrins, porphyrinoids, and phthalocyanines	CAM-B3LYP	[122]
Chirogenesis in Zn porphyrin complexes, CD spectroscopy	RI-BP86-D3, PBE, BH&HLYP, B3LYP, M06, M06-2X, CAM-B3LYP, ωB97X-D, LC-ωHPBE	[123]
Zn porphyrin dimers linked by different bridges to study porphyrin-to-porphyrin conjugation	B3LYP	[124]

(*continued*)

Table 11.1 (Continued)

Application	Density functional(s)	References
Zn porphyrin-perylene diimide donor–bridge–acceptor systems, non-linear optical properties	B3LYP, PBE0, ωB97X, LC-BLYP, ωB97X*, LC-BLYP*	[125]
Steric out-of-plane distortions of Ni porphyrins	B3LYP(15) (15% exact exchange)	[126]
Long-range, cross-macrocycle interactions in Ni porphyrins	B3LYP	[127]
Ground and excited states of porphyrin and porphyrazine	SAOP	[53]
Charge transfer in porphyrins and chlorophylls, higher-energy (N) absorption bands, orbitals, orbital energies	B3LYP, CAM-B3LYP, SAOP, BP86	[128]
Porphyrin-related structures & extended porphyrins		
Free-base porphyrins in pyridine bridged covalent organic framework, stability and structural feasibility	PW-91, PZ	[129]
Stereochemical preferences in diboron porphyrazines and phthalocyanines	BP86-D3	[130]
Extended porphyrins, structures, and energies of conformers	B3LYP, BPE, BP86, M06L, TPSSh, M05-2X, M06-2X, BH&HLYP, CAM-B3LYP, BMK, and ωB97XD, some with -D3(BJ)	[131, 132]
	BLYP, PBE, revPBE, TM, TMTPSS, SCAN, TPSS, B3LYP, BHLYP, PBE0, revPBE0, SCAN0, PW6B95, TPSSh, M06, M06-2X, M08-HX, CAM-B3LYP, CAM-QTP00, CAMQTP01, M11, LC-ωPBE, ωB97XD, ωB97MV, ωB97XV, MN15, and 20+ double hybrid functionals	[95]

provide insight into aspects of the porphyrin structure–spectrum–function relationship, from both fundamental and applied perspectives.

11.3.3 Porphyrin Excited States and TDDFT

Today, DFT is the most widely used method for computing porphyrin ground state geometries, energies, and other properties, including the magnetic ones associated with ring currents and aromaticity. DFT can also be used to explore excited states and their properties through a method called TDDFT, a relatively young method that has its origin in a key 1984 paper by Runge and Gross [168]. For reviews of TDDFT for excited state calculations of large molecules, see [104, 169–174]

TDDFT is based upon the idea that the time-dependent properties of a system can be calculated from the time-evolving density. Such time-dependent properties include spectroscopy, in which the interaction of the system with light is inherently time dependent. Using TDDFT, one can calculate vertical electronic excitations (absorption, fluorescence, phosphorescence) and 0-0 transitions between the minima on ground and excited states. TDDFT can also be used to probe dynamical behaviours such as photochemical reactions and evolution of the system along the ground and/or excited state potential energy surfaces. Access to the excited state geometries and potential energy surfaces also provides for excited state absorption and vibrational spectroscopic information, and gives chemists a better understanding of molecular photochemistry and photophysics, excited state reactions, and other excited state dynamics.

TDDFT has some well-known areas in which it does not perform as well (see, for example, [169, 170, 175, 176] and references therein). These include long-range charge transfer, non-vertical excitations, double excitations, and Rydberg states. TDDFT also struggles with conical intersections, areas of degeneracy among potential energy surfaces where rapid nonradiative transitions to lower-energy states can occur. Many of these problems have their origin in the exchange-correlation functional, and research in this area continues.

Nonetheless, TDDFT can be a very powerful method for porphyrins and related systems. Consider one study by Rozzi et al. of the photodynamics of a classic carotenoid-porphyrin-fullerene light harvesting triad [177]. Here, the authors combine ultrafast spectroscopy and TDDFT to show that correlated, coherent motion of electrons and nuclei plays a key role in the charge transfer dynamics. Fuks later studied the origins of the success of TDDFT in this instance, compared to its failure for charge transfer dynamics in the small molecule LiCN, and found that the choice of initial conditions is important [175].

Table 11.1 highlights several examples in which TDDFT has been applied to porphyrin systems; often DFT and TDDFT are employed together, though not necessarily with the same functional and basis set. One early use of TDDFT for porphyrins explored Mg, Zn, and Ni complexes of porphyrin and porphyrazine [53]. Baerends et al. provide a thorough evaluation of TDDFT performance, and report that it performs quite well, particularly for the Q bands. There is functional-dependence error when comparing to experiments for the B band and higher-lying absorptions. Importantly, the detailed results from the TDDFT approach can be connected directly with the previous molecular orbital models for porphyrins, including Gouterman's four-orbital model, so the intuition afforded by those approaches is not lost. Others studies have since echoed this critical conclusion (see, for example, [45, 48, 122].

Recently, in a study focused upon porphyrin-based dye-sensitised solar cells, the lowest vertical excitation energies (VEE) and excitation energies from the ground state minimum to the lowest-energy excited state minimum ($E_{0\text{-}0}$) were computed at several different levels of DFT/TDDFT for seven free-base porphyrins with different substituent patterns [103]. Computations further explored the structure of one of the porphyrins adsorbed on a TiO_2 cluster, and assessed how well the energy levels between the porphyrin and substrate aligned, as well as the ground and excited state oxidation potentials. Different functionals performed better or worse for different parts of this set of calculations. B3LYP provided the best ground state geometries, while functionals that contained long-range corrections with range separation (CAM-B3LYP and ωB97X-D) performed better for the VEE and $E_{0\text{-}0}$ calculations (Figure 11.21). The only functional that gave the correct alignment of TiO_2 and porphyrin energy levels was B3LYP. Finally, the hybrid functional with significant exact HF exchange, M06-2X, gave superior results for the ground and excited state oxidation potentials. This study

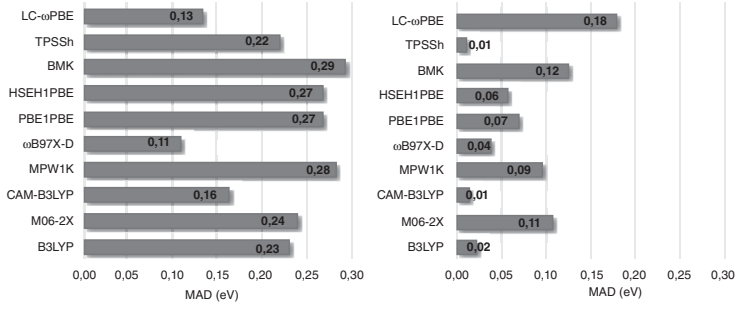

Figure 11.21 Comparison of experimental and TDDFT-calculated Q_x (left) and Q_y (right) bands with 10 different high-level (tier four) density functionals. MAD = mean absolute deviations from experiment in eV. The results are for six hybrid GGA and meta-hybrid GGA functionals (B3LYP, BMK, TPSSh, M06-2X, MPW1K, and PBE1PBE) and six hybrid range-corrected functionals (LC-ωPBE, ωB97X-D, CAM-B3LYP, HSEH1PBE). In addition, ωB97X-D includes a dispersion tail. Source: From [103].

provides an example of using different functionals for the individual parts of a complicated series of computations to achieve overall better performance [103].

TDDFT is not the only way to explore porphyrin excited states. A recent review of computational photochemistry by Mai and González highlights and compares the several theoretical approaches, including coupled-cluster, multi-configurational, hybrids, and dynamical frameworks [170]. These each have their strengths and weaknesses. The combination of TDDFT's efficiency, accuracy, and user-friendly software implementation has made TDDFT one of the most popular methods used for adding interpretative guidance and depth to experimental studies. This holds true for the porphyrin molecular family as well.

The use of DFT and TDDFT methods in porphyrin studies is growing exponentially. A snapshot using Google Scholar shows nearly 41 000 papers on DFT and porphyrins, nearly half of which have been published since 2015. The use of TDDFT is growing at an even faster rate; nearly 60% of the 5300+ studies that discussed both TDDFT and porphyrins were published over the last five years. Table 11.1 can only show a small fraction of these.

This rapid rise is partly due to great improvements in the computational power available at reasonable expense, and partly due to improvements in the quality of the functionals and our understanding of when and how best to use them. An excellent example is the relatively recent new collection of approaches for handling long-range dispersion forces that overcame an early limitation of DFT. With a judicious choice of functional, basis set, and mesh, DFT and TDDFT can give remarkable insight into the behaviour of porphyrins and their chemical relatives.

11.4 Aromaticity and Porphyrins

11.4.1 Aromaticity

Aromaticity has been a central concept in chemistry since the discovery of benzene (C_6H_6) in 1825 by Michael Faraday [178], a sample of which still exists [179], and it is still a topic of great interest today (see, for example, [180, 181]). One reason for this intellectual popularity is that, despite more than a century of focused scientific study, there still exists no precise definition for aromaticity today. Aromaticity is a term that is associated with cyclic π-electron systems that exhibit delocalised orbitals over multiple atoms that confer greater than expected energetic stability and uniformity in bond lengths [2]. Aromatic molecules tend to have longer wavelength UV/Vis absorptions, exhibit characteristic magnetic properties, and undergo (and not undergo) characteristic types of chemical reactions. This class of molecules is named for the distinctive –which some find attractive – odour of some of the earliest discovered members of the class, like benzene (discovered 1825), xylene (discovered 1850), and toluene (discovered 1838).

The notion of aromaticity predates the discoveries of electrons and orbitals by over 50 years. Patterns of isomers and homologues found for substituted benzenes supported August Kekulé's idea that the six unsaturated carbon–carbon bonds in benzene were equivalent, and led to two papers and the last section of a textbook between 1865 and 1866 [182–185], and another in 1872 [186] that ultimately outlined the famous Kekulé model

2 This chapter focuses upon 2D aromaticity of ring-compounds. 3D aromaticity is a very interesting topic that will not be discussed.

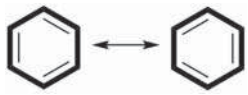

Figure 11.22 Kekulé model for benzene. In his model, these two structures represent the endpoints of rapid vibrations that create an average structure with sixfold rotation symmetry with six equivalent C—C bonds and six equivalent C—H bonds. The prevalent view that Kekulé proposed that these structures oscillate is incorrect [185, 187].

of vibrating conformations with alternating C—C and C=C bonds (Figure 11.22) (readers interested in the history are referred to [188–191] and references therein).

This is not the model for benzene that we use today, though the structures in Figure 11.22 can be found in modern organic chemistry textbooks as resonance structures for benzene. Nonetheless, the highly symmetric structure inspired by Kekulé's 1862 daydream of a 'snake eating its own tail' had an extraordinarily high impact. It was proposed at a time when the picture of molecular structures was still evolving, and it played a pivotal role in the way chemistry as a discipline unified its view of molecular bonding and structures, as well as providing 'the basis for the first satisfactory understanding of aromatic compounds' [190].

The Kekulé model accounted for the equivalency of the six carbons and high structural symmetry, but it took the advent of molecular orbital theory, particularly the Hückel LCAO-MO approach some 60 years later [22, 23], to provide chemists an explanation for the other features of aromaticity (readers interested in the history of Hückel and his molecular orbital theory are referred to [20, 21, 192] and references therein).

The key feature of molecular orbital theory that gives insight into aromaticity is orbital delocalisation. Recall from the above that the Hückel LCAO-MO model uses the individual atomic p_z-orbitals of the atoms in the aromatic ring to create a set of π-orbitals that are delocalised across the molecule. Delocalisation provides for the energetic stabilisation of the system that makes these aromatic rings planar and less chemically reactive than anticipated by their level of unsaturation. Further, the electrons in these π-orbitals are free to move over the full extent of the orbital, generating ring currents that account for the magnetic signatures of aromaticity observed for molecules like benzenes and porphyrins.

From the application of this approach to many molecules, a set of guidelines to establish whether a system is aromatic could be written: if the molecule is cyclic, conjugated, and obeys Hückel's rule of possessing $(4n + 2)$ π-electrons (where n is an integer), it will have a closed-shell configuration, exhibit uniform bond lengths, and will be aromatic. In contrast, a different class of cyclic, conjugated systems with $(4n)$ π-electrons will have an open shell configuration, be less stable, and more reactive. To relieve the instability, these molecules can 'break' the π-conjugation by becoming nonplanar and by adopting alternating 'single' – 'double' bond lengths. Such molecules are classed as anti-aromatic. Molecules that are not cyclic, not conjugated, or have other orbital configurations are non-aromatic [193, 194].

In this and related molecular orbital models, the delocalised π-orbitals arranged above and below the molecular plane are thought dominate the cause and effect of aromatic behaviour. Clearly, aromatic stability and anti-aromatic instability arise from the energetic consequences of delocalising the π-orbitals. Puzzling observations, however, suggest this is not an entirely satisfactory picture [195, 196]. Consider the molecule N_6, which is isoelectronic to benzene. Using the above guidelines for aromaticity, N_6 should be every

bit as aromatic as benzene, and should adopt a D_{6h} planar geometry with uniform N—N bond lengths. It does not. The N_6 molecule has not been synthesised. In calculations, it is unstable, despite its $(4n + 2)$ filled shell, and it adopts a D_{3h} structure with alternating bonds or dissociates into three N_2 molecules [196–202]. This example, along with other similar ones, points to there being something beyond delocalised π-orbitals with a filled shell of $(4n + 2)$ electrons to account for aromaticity.

In the last 30–40 years, supported by the ability to perform all-electron quantum chemical calculations, it has become well accepted that the σ-bonding architecture plays an important role in aromaticity, providing the driving force towards uniform bond lengths and high symmetry. The π-bonding system provides energetic stability through delocalisation, but the π-system also exhibits a net destabilising effect on the uniform geometry, driving the system towards alternating bond lengths and structures of lower symmetry. Early Hückel-type molecular orbital pictures do not account for the σ-bond system properly, and the intuition provided by that simple picture about delocalisation of the π-system providing a dominant stabilising effect towards a uniform geometry is unfortunately both compelling and misleading.

It is now understood that a cyclic, unsaturated molecule exhibits aromaticity as the result of a balance between the energies of a localised framework of uniform, pair-wise σ-bonds and a delocalised, stabilising, and distortive π-bond system. In aromatic molecules like benzenes, the σ-bonds energies dominate the π-bond distortivity, and these aromatic molecules exhibit uniform, symmetric geometries, characteristic ring currents that affect magnetic properties like the ^{1}H NMR spectrum, π-π* transitions in the UV/Vis spectrum and tendencies towards certain types of chemical reactions (e.g. substitution at the periphery of the ring is relatively facile, and electrophilic addition into the ring is not).

The tendency of N_6 to fragment is consistent with this picture. The N—N σ-bond (34 kcal mol^{-1}) is weaker than is the C—C σ-bond (80 kcal mol^{-1}), while the N—N π-bond is stronger (94 kcal mol^{-1}) than its C—C counterpart (70 kcal mol^{-1}). The σ-bond system in N_6 cannot keep the molecule in a uniform, D_{6h} hexagonal ring; the delocalising drive of the π-orbital system wins [203].

Many reviews, books, and journal special issues have been dedicated to aromaticity [191, 201, 204–214]. Two special issues of *Chemical Reviews* have been particularly highly regarded [187, 215]. More detailed treatments of aromaticity, separation of the σ- and π-bonding systems, π-distortivity, progress, and challenges in characterising and measuring aromaticity and more can be found there.

11.4.2 Aromaticity and Porphyrins

Porphyrins and their related compounds are aromatic. Though they do not have a high enough vapour pressure to be associated with a characteristic odour, they do exhibit the other characteristic aromatic behaviours. As with all aromatic compounds, the aromaticity of porphyrins determines many of their physical and chemical properties. Therefore, understanding them as aromatic macrocycles provides insight into their reactivity, stability, electronic structure, interactions with light, and magnetic properties. This section of the chapter first will discuss models and characterisation of porphyrin aromaticity, then out-of-plane (OOP) distortions of the macrocycle. In the following section, the relatively new approach of using extended porphyrin structures to study more exotic types of aromaticity,

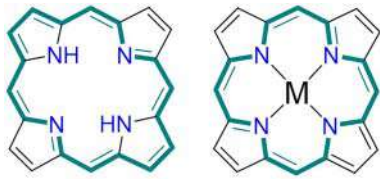

Figure 11.23 Main conjugation pathway in the diaza[18]annulene model of the porphyrin ring for the free-base porphyrin (left) and metalloporphyrin (right). These conjugation pathways have 18 π-electrons distributed over 18 and 16 atoms, respectively.

such as Möbius or twisted-Hückel aromaticity and aromaticity switching, will be explored. The section concludes with porphyrin aromaticity and excited states.

As the understanding of chemical aromaticity has evolved, the nature of aromaticity in porphyrins has also been debated [216–223]. The basic challenge involves reconciling two intuitively compelling pictures: (i) the 18 π-electron annulene-like (bridged diaza[18]annulene) model, which has its origins in the particle-on-a-ring approach [9, 17, 19]; and (ii) the Hückel LCAO-MO approaches, including Gouterman's four-orbital model, which transform the 24 atomic p_z-orbitals into π-orbitals delocalised over the entire molecule [24, 25, 27]. The aromaticity of porphyrin rings was historically attributed to the diaza[18]annulene structure, in which the outer CH=CH groups of two of the pyrrole rings and the inner NH moieties are bridges, and not included in conjugation pathway (Figure 11.23).

Although it is easy to describe aromaticity as the energetic stabilisation associated with delocalisation of electrons about a ringed system, it is much more difficult to quantitatively assess aromaticity, either experimentally or theoretically. Porphyrins add a layer of complexity in that they have both local and global aromaticity; a porphyrin is an aromatic ring constructed of bridged more or less aromatic rings.

11.4.3 Characterising Porphyrin Aromaticity

Several methods to quantify molecular aromaticity have been developed and applied to porphyrins and porphyrinoid compounds. These can be classified based upon whether they predominantly (i) evaluate molecular geometry, such as ring planarity or bond length alternation, one of the more successful of which is the harmonic oscillator model of aromaticity (HOMA); (ii) assess magnetic properties related to the ring currents from the mobile π-electrons, tested indirectly through altered chemical shifts in ^{1}H NMR spectra or predicted computationally using methods like the nucleus-independent chemical shift (NICS); and (iii) measure and/or calculate degrees of energy stabilisation terms using heats of formation, bond energies, overlap integrals, or thermodynamic stability metrics. Only a few examples of the many approaches to quantifying aromaticity will be provided here, with a focus on how they have been applied to porphyrins. New approaches are still being developed [224].

One of the hallmarks of aromatic molecular cycles is that the bond lengths are uniform (e.g. benzene) or are more uniform than expected by their Kekulé-like resonance structures (e.g. porphyrins) about the conjugation pathway, and these bond lengths have values between those of corresponding single and double bonds. Various geometric indices of aromaticity have been developed based upon this observation (see [212, 213] and references therein). The most widely used is the HOMA method by Krygowski and co-workers [225, 226]. This method assumes that molecular bonds are harmonic oscillators and the energy associated with their compression or extension depends upon their force constants and lengths. One of the advantages of HOMA is that it can be applied to subsystems in a larger macrocycle.

This simple approach starts with benzene as the chemical epitome of aromaticity, with a HOMA index of 1.0. Molecules with alternating bond lengths will have values less than 1,

according to the formula

$$\mathrm{HOMA} = 1 - \frac{\alpha}{n}\sum_{i=1}^{n}(R_i - R_{opt})^2 \tag{11.36}$$

in which α is a normalisation constant designed to make HOMA = 0 for model non-aromatic systems, n is the number of CC bonds in the ring, R_i is the ith CC bond in the ring, and R_{opt} is the optimal aromatic CC bond length. There now exist optimised parameters for carbon-only systems or for conjugated systems with heteroatoms, like porphyrins and many others. The HOMA succeeds as a simple, clear way of indexing aromaticity, and perhaps other types of systems as well [227].

The HOMA index can be split into two intuitively useful contributions: HOMA = 1 − (EN + GEO). EN is essentially an energetic destabilisation term that reflects the difference between the average bond length and the optimal aromatic bond length for a system. The GEO geometric term indicates the degree of bond length alternation in the molecule. Each of these terms reduces the aromaticity of the cyclic conjugated system. For systems with heteroatoms, application of this separation method incorporates bond orders.

A seminal examination of porphyrin aromaticity was performed by Krygowski and co-workers, who applied the HOMA method to a database of >450 porphyrins, plus some DFT-calculated optimised structures, across three structural classes: (i) free-base porphine, (ii) metalloporphyrins, and (iii) porphyrin dianions [228]. In this study, the authors evaluated the HOMA indices, as well as the EN and GEO contributions, for the whole macrocycle, for pairs of pyrrole rings (1,3 and 2,4) and for the internal cross shape consisting of 16 atoms and 18 π-electrons (Figure 11.24). The porphyrin macrocycles all exhibit significant molecular aromaticity, with HOMA indices for the free-base and metal complexes above 0.65, and slightly lower for the dianion (calculated), at 0.448. The magnitudes of the GEO and EN terms indicate that the loss of 'perfect' aromaticity in porphyrins has its origin more in the bond length alteration rather than in nonideal average bond lengths [228].

The highest aromaticity was found for the internal cross for all three classes, with HOMA values above 0.870 for experimental and above 0.90 for all three computed structures [228]. This finding indicates that all four N groups participate fully in the conjugated aromatic ring. In particular, this finding contradicts the diazo[18]annulene model for free-base porphine, in which the N—H groups are treated as bridges (Figure 11.24).

The HOMA indices of the pyrrole rings show distinct patterns, including indications that the outer CH=CH of rings(2,4) do act more as bridges in the free-base porphine (Figure 11.24). This distinction in the aromaticity between the pairs of rings disappears in the computed metal complex and dianion, but does not completely vanish in the experimental metalloporphyrins. In these latter systems, the ring(1,3) pair is still slightly more aromatic than the ring(2,4) pair [228]. The HOMA results were supported by NICS as a measure of the consequences of aromaticity on the porphyrin magnetic properties, which will be discussed more fully below.

This study concluded that all atoms participate in the aromaticity of metal coordinated porphyrins [228]. In contrast, the free-base porphyrin can be treated as a perturbed or slightly extended annulene model, with bridged pyrroles rings(1,3) and all four nitrogens in the internal cross involved in the aromaticity. The aromaticity of the dianion is described well by the internal cross, with significant loss of aromaticity in the individual pyrrole rings [228].

The π-electrons in a delocalised, aromatic system are free to move about the molecule in a cyclic path. When such molecules are put in a magnetic field, a ring current parallel to the

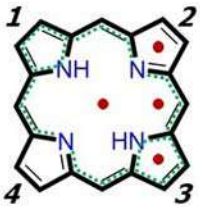

	HOMA[a]	HOMA[b]	EN[a]	GEO[a]	NICS[b]
H_2-Porphine	0.652	0.666	0.107	0.240	-16.5[c]
ring(1,3)	0.666	0.702	0.132	0.202	-15.2
ring(2,4)	0.452	0.381	0.175	0.373	-4.5
internal cross	0.880	0.932	0.075	0.045	-21.7

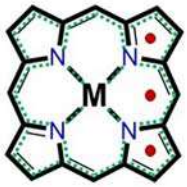

M-porphine	0.656	0.671	0.094	0.249	---[c]
ring(1,3)	0.566	0.556	0.158	0.276	-10.0
ring(2,4)	0.524	0.556	0.153	0.323	-10.0
internal cross	0.872	0.906	0.071	0.057	-21.0

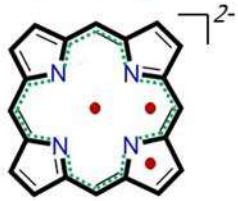

Porphine^{2-}		0.448			-14.9[c]
ring(1,2,3,4)		0.287			-4.0
internal cross		0.908			-17.5

Figure 11.24 Assessment of the aromaticity of H_2-porphine, metalloporphine, and the porphine dianion using HOMA and nucleus-independent chemical shifts (NICS), geometric measures, and ring current measures, respectively [228]. HOMA, EN, and GEO were calculated using (a) the 456 experimental geometries from the Cambridge Structural Database and (b) geometries calculated at the B3LYP/6-31G* level. NICS (ppm) values were calculated at the locations of the red dots on the diagrams to the left; and (c) the metalloporphine NICS cannot be calculated at the centre of the macrocycle. The green dashed lines indicate the resulting picture of delocalisation of the π-system.

plane of the molecule is induced that in turn creates its own magnetic field (Figure 11.25). For molecules that exhibit aromatic stabilisation, the ring magnetic field is aligned with the external magnetic field on the outside of the ring of circulating electrons and aligned against it inside the ring. In a ^{1H}NMR spectrum, protons on the outside of the aromatic ring (e.g. *meso* and *β* protons) are de-shielded and exhibit downfield chemical shifts relative to their positions for analogous non-aromatic systems. The internal N—H protons experience the opposite effect; they are strongly shielded and exhibit upfield chemical shifts. This pattern for aromatic systems is called a diatropic ring current. Anti-aromatic molecules also exhibit ring currents, but these are called paratropic ring currents, and they exhibit the opposite directionality and shielding/de-shielding effects in NMR spectroscopy.

Multiple methods have been developed to exploit the ring currents and magnetic properties of aromatic (and anti-aromatic) systems as a measure of their aromaticity (see [208, 209] and references therein). Like aromaticity itself, ring currents are not observables that can be directly measured. Experimentally, the impact of ring currents can be observed in diamagnetic susceptibility exaltation and in NMR chemical shifts, as mentioned above. Diamagnetic susceptibility exaltation depends on the size of the ring and suffers from the need for calibration. Today, NMR is more commonly used by those wishing to assess the effects of ring currents. Unfortunately, the relationship between NMR chemical shifts and aromaticity can

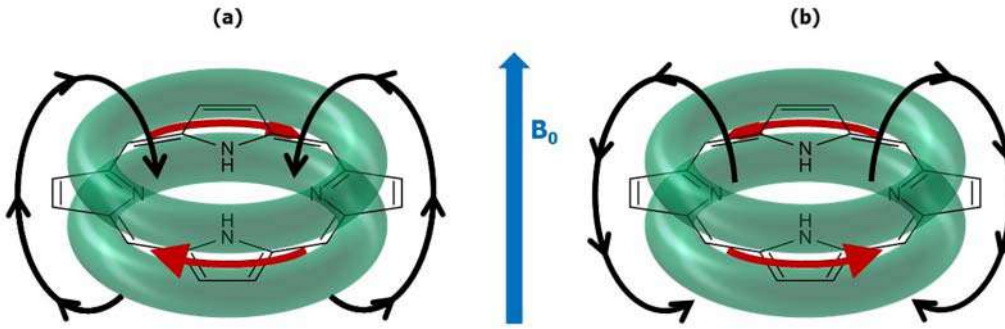

Figure 11.25 Illustration of porphyrin (a) aromatic and (b) anti-aromatic ring currents. The dark red arrows indicate the direction of the ring current. The blue arrow shows the direction of the applied magnetic field. The black circular arrows depict the induced magnetic field. The ring current is diatropic when the induced magnetic field is aligned with the applied field, and paratropic when it is aligned against the applied field. In aromatic rings, the inner protons experience shielding, and protons outside the ring are deshielded. In anti-aromatic rings, the converse holds true.

be difficult to predict, and there is debate about whether NMR chemical shifts should be used for quantifying molecular aromaticity [209].

High-quality quantitative assessments of ring currents and their effect on aromaticity can be made using computational methods [208, 209, 229, 230]. The NICS approach is widely used to calculate aromaticity for a molecule, and for sub-cyclical structures within that molecule [207]. This method was first proposed by von Ragué Schleyer and co-workers in 1996 in an influential paper that has now been cited >4500 times [231]. The method employs quantum chemical calculations of the magnetic shielding evaluated at the centre points of rings within a molecule. Negative values of NICS indicate aromaticity, and positive ones indicate anti-aromaticity.

The signatures of ring currents in NMR spectra of porphyrins have long been known (for example, [232, 233]). When NICS was applied to the porphyrin database in the study discussed above [228], the results gave further insight into the aromaticity of the overall porphyrin macrocycle, as well as the contributions to the aromaticity from the pyrrole rings (Figure 11.24). The NICS values for the pyrrole rings make the conclusions from the HOMA bond length calculations even more clear. In metalloporphyrins, the pyrrole rings exhibit moderate aromaticity with an NICS of −10.0 ppm; note that this is midway between the NICS values for ring(1,3) and ring(2,4), which are −15.2 ppm and −4.5 ppm, respectively. In the dianion they become less involved in the aromatic circulation of the porphyrin macrocycle (NICS = −4.0). In all three systems, the internal cross exhibits the strongest aromaticity, with the largest negative NICS results [228].

Another method for assessing aromaticity through its magnetic effects is current density analysis (CDA) [208]. Current density maps provide a pictorial view of the behaviour of the ring current that is induced within a cyclic compound that has delocalised electrons, though it has been found that obtaining quantitative results that allow comparisons of degree of aromaticity between systems can be challenging. There is no rigorous way to separate the delocalised electron density from the total electron density. Figure 11.26 shows some examples of current density maps for free-base porphyrin [234, 235].

The anisotropy of the induced current density (ACID) approach defines a quantum mechanical quantity that is associated with the delocalised electron density, and provides a method for assessing the current density that is free from adjustable parameters [208, 234].

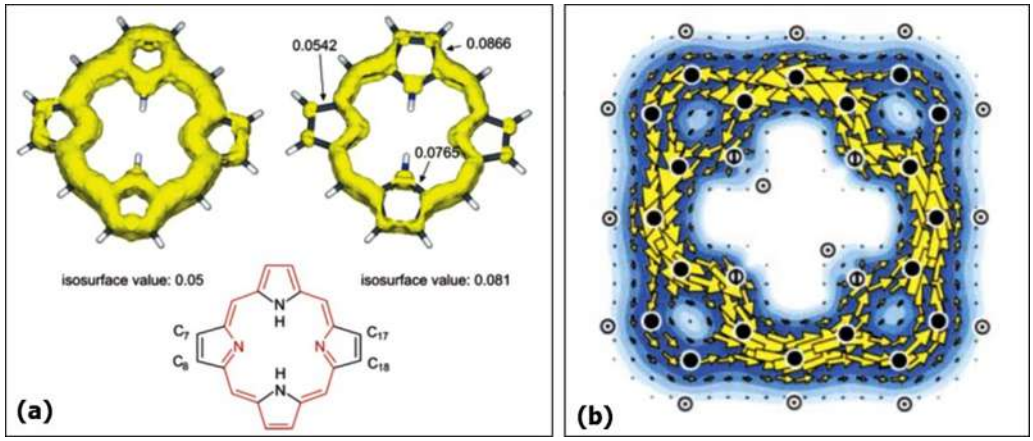

Figure 11.26 Ring current densities in free-base porphine. (a) ACID plots for H_2-porphine at two different isosurface values; the stronger part of the ring current involves the 18 atoms highlighted in red [234]; and (b) current density map from the CTOCD-DZ approach, showing a similarly shaped ring current over the same 18 atoms [235] (note the porphyrin in (b) is oriented −45° relative to the diagrams in (a)).

ACID plots are isosurfaces of a scalar field. Figure 11.26a shows examples of ACID plots for H_2-porphine. At the standard isosurface value of 0.05 (left), all bonds participate in the electron delocalisation that gives rise to the porphyrin's aromatic behaviour. However, when the isosurface value is increased to 0.081 (right), a diaza[18]annulene shape emerges with a strong diatropic ring current; two C_2H_2 and two NH bridging units are apparent.

The CTOCD-DZ method (continuous transformation of origin of current density diamagnetic zero) enables the separation of contributions of the σ and π orbitals to the electron density [208]. Steiner and Fowler have applied this method to porphyrins, including directly addressing the four-orbital model and ring currents [235–237]. The π electron distribution for H_2-porphine is shown in Figure 11.26b [235]. The bifurcation of the ring currents at the C_α positions is apparent, as is the diaza[18]annulene shape. In this same work, the authors also show that this strong ring current is largely due to the HOMO and HOMO-1 frontier orbitals, with limited contribution from the other π-electrons in the system [235].

A third current density method, gauge including magnetically induced current (GIMIC) [208, 238–240], has been utilised to explore the heterocyclic nature of porphyrins and heteroporphyrins (internal pyrrole nitrogens replaced by O, S, C, etc.). In this method, induced current strengths are calculated in individual chemical bonds to provide detailed information about electron delocalisation, aromatic character, and ring current pathways. The approach can reasonably predict aromaticity in porphyrins when used in conjunction with NICS. GIMIC is used to calculate gauge-origin independent current density susceptibility tensors to accurately determine the magnetic properties of porphyrins and to visualise current densities in the porphyrin.

Geometric and ring current methods of assessing aromaticity in porphyrins, and other molecules, have been discussed thus far. The third measure correlated with the degree of aromaticity is the aromatic stabilisation energy (ASE). Discussed above are the influential studies by Shaik, co-workers, and others that illustrated the distortive effect of the delocalised π-orbital system ([201, 211] and references therein). This approach explores the orthogonality of the σ- and π-orbitals that arises formally from symmetry considerations in molecular

orbital theory, and relative contributions of those systems to the overall energetics of the molecule. This σ-π separation underpins important facets of our chemical intuition, including the π-orbital delocalisation that leads to aromaticity and ring currents. Aromaticity results from a balance between the bond-equalising σ-bonding scaffold and the bond-alternating distortive π-bonding distributed across the molecule. That balance explains aromatic benzene with its uniform CC and CH bond lengths and the isoelectronic hexazine's tendency to break into diatomic N_2 molecules.

Various approaches to calculating the stabilisation energy have been developed, and often such computations are used in concert with geometric and magnetic measures. Other terminology one finds for ASE includes resonance energy and delocalisation energy, depending upon the underlying model employed.

An example of a detailed energy approach from Aihara and colleagues has been used explore porphyrinoid aromaticity [206, 217, 241–243]. The approach particularly addresses the multiple circuits of aromaticity in porphyrin molecules and their cousins, in a similar manner to NICS, identifying and evaluating local (pyrrole) and larger macrocycle contributions to aromaticity. This method calculates three types of energy associated with delocalised electrons in closed circuits: (i) topological resonance energy (TRE); (ii) bond resonance energy (BRE); and superaromatic stabilisation energy (SSE). BRE is the local aromatic term, and in porphyrins it is used to quantify the contributions of substructures such as the pyrrole rings and the central cross to the overall aromaticity (Figure 11.27). It reflects how a given π-bond substructure contributes to the TRE. TRE and SSE are global terms. SSE is the stabilisation energy afforded by conjugation across the macrocycle; and it forms a part of the TRE. TRE then reflects the molecule's global 'amount' of aromaticity. The analysis of energies can be coupled to ring current distribution calculations as well [217, 243]

Application of this method to 20+ porphyrin and porphyrinoid molecules indicates that these systems are only moderately aromatic [241]. The bridges linking the pyrroles into a larger, macrocyclic structure suppress local pyrrole aromaticities. Using the BRE to trace the dominant conjugation pathway, or the main macrocyclic conjugation pathway (MMCP), results in an 18 atom, 18 π-electron [18]annulene path for free-base porphine and the 16 atom, 18 π-electron internal cross for metalloporphine. However, these are just the dominant paths; all of the π-bonds were found to contribute to porphyrin aromaticity [217, 241, 243].

11.4.4 Anti-Aromatic Porphyrins

Hundreds of derivatives of the aromatic [18]annulene porphyrin are known. In contrast, porphyrins with 16 or 20 π-electrons are quite rare (Figure 11.28). These types of compounds should be anti-aromatic by the extended Hückel's rule with their [4n] π-electrons, and therefore much less stable. One way to add stability is to increase n; extended porphyrins are excellent systems for studying aromaticity, anti-aromaticity, and more exotic forms such as Möbius and twisted-Hückel aromaticity; aromaticity in extended porphyrins will be discussed in a later section. It is only in the last 15 years or so that a handful of [4n] π-electron porphyrins based upon the classic porphyrin macrocycle have been synthesised and studied. These include the 16 π-electron porphyrins from Yamamoto's [244–249] and Vaid's [250] groups, and 20 π-electron porphyrins from Vaid's [251–254], Chen's [255, 256], and Brothers' [257] groups.

In a very interesting study, Cissel et al. report a Ge^{II} (TPP) and $Ge^{IV}(TPP)(pyr)_2$ system in which the axial ligand induces a reversible oxidation state change in the germanium core,

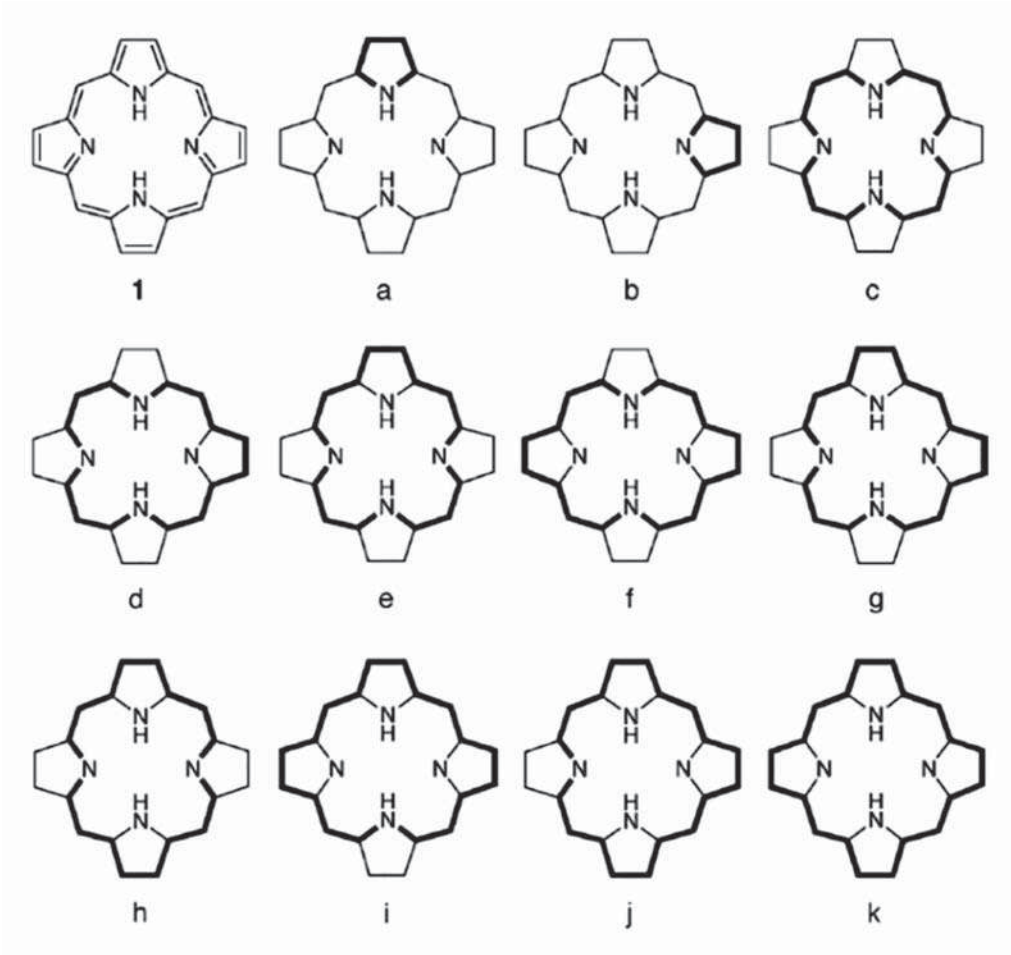

Figure 11.27 Measuring aromaticity using the details of the ASE through the contributions of all possible electron circuits to the overall aromaticity of the macrocycle. The 12 unique circuits in H_2-porphine are shown in bold. Source: From [243].

and thus a switch from aromatic to anti-aromatic in the macrocycle. The TPP macrocycle has the classic 18-electron, −2- oxidation state in Ge^{II} (TPP) and has a 20 π-electron, −4 oxidation state in the $Ge^{IV}(TTP)(pyr)_2$ compound [253]. This group also has studied the analogous 20-electron $Si^{IV}(TPP)(pyr)_2$ and $Si^{IV}(TPP)(THF)_2$ systems [252, 254].

The macrocycles of these 20 π-electron rings exhibit similar physical properties. They are distorted from planarity in a ruffled conformation and exhibit significant bond length alternation around the macrocycle. NICS calculations return positive values in the macrocycle core and pyrrole rings, indicating the paratropic ring current signatures of anti-aromaticity. NMR spectra are consistent with the assignment of these three compounds as anti-aromatic porphyrins. For example, the C_β hydrogens are shifted significantly upfield for $Si^{IV}(TPP)(THF)_2$ (1.3 ppm) and $Ge^{IV}(TTP)(pyr)_2$ (0.6 ppm), similar to earlier reports of the reduced $Zn(TTP)^{2-}$ shift of −0.9 ppm. 16 π-electron aromatic porphyrins exhibit downshifts for these hydrogens, for example, 9 ppm for $Ge^{II}(TPP)$ and 8.95 ppm for Zn(TTP). The UV/Vis absorption spectra of these compounds also exhibit characteristic patterns. The B and Q bands tend to broaden

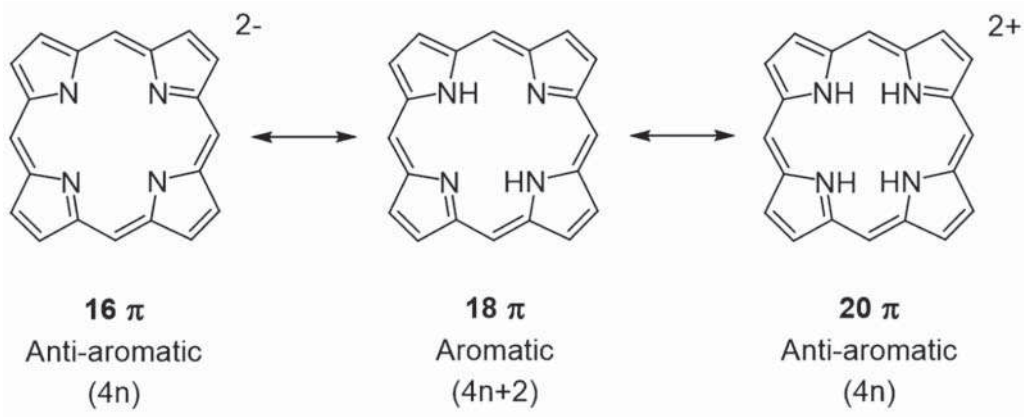

Figure 11.28 Reduction and oxidation of a porphyrin to achieve 16π, 18π, and 20π electron conjugation pathways.

and blue shift, and the relative intensity of the B band is significantly reduced (e.g. fivefold) compared to that of the Q bands [252, 253].

A detailed spectroscopic study of the anti-aromatic Si(TPP)$(pyr)_2$ revealed that the fluorescence quantum yield is very low, and the excited state lifetime is only a few picoseconds, approximately 750 times faster than that of the aromatic Si(TPP)Cl_2 analogue. The OOP conformation and presence of low-lying excited states are consistent with these phenomena [254, 257].

Vaid reported the successful synthesis and characterisation of a porphyrin with a -C=C- group in the centre of the macrocycle: (C=C)TTP [251]. This 20 π-electron molecule is anti-aromatic, while the dication (C=C)TPP^{2+} is aromatic. Both are distorted from planarity, as the -C=C- is smaller than the ~2 Å of the planar macrocycle core. Bond length alternation is observed for the neutral species, and the NCIS values were strongly positive as is consistent with a paratropic ring current. The NCIS values for the dication were negative, as expected.

A very unusual example of a 20 π-electron, anti-aromatic molecule is B_2(TPP) from the Brothers group. This compound ligates a pair of boron atoms in its core, leaving the macrocycle with a −4 oxidation state; it acts as a diboranyl(4) isophlorin. As with the Ge^{IV} and Si^{IV} porphyrins above, comparisons of the structure, NICS calculations, and experimental NMR shift patterns of B_2(TTP) with its aromatic, 18 π-electron partner $(B_2TTP)^{2+}$ are entirely consistent with the former molecule's being anti-aromatic.

Distortions from planarity and a tendency to alternating bond lengths break the conjugation of the delocalised π-system, and reduce the degree of molecular anti-aromaticity. In β-tetrakis(CF_3)-TPP, these distortions are sufficiently large that the 20 π-electron macrocycle becomes only very weakly anti-aromatic or even non-aromatic [255, 256]. The C_β hydrogens on the non-substituted pyrrole rings are shifted upfield to only 6.87 ppm. In addition, the UV/Vis spectrum of this molecule shows no Q bands and a broad B band at 418 nm, confirming the essentially different character of this 20 π-electron macrocycle from the others discussed above.

In their series of 16 π-electron molecules, Yamamoto and colleagues note three ways to stabilize anti-aromatic 16 π-electron porphyrins: (i) to deform the macrocycle core away from planarity and bond length uniformity; (ii) to metallate the porphyrin core; and (iii) to introduce electron-donating groups to the *meso*-positions of the porphyrin ring [244–249].

Table 11.2 16 π-electron porphyrins with varying degrees of anti-aromaticity.

	RMS nonplanarity (Å)[a)]	ΔN-C_a (Å)[b)]	NICS (ppm)[c)]	References
OiPTPP	1.078	0.109(4)		[246]
OiBTPP	0.921	0.114(3)	+2.40	[247, 248]
OETPP	0.836	0.114(3)	+2.83	[247, 248]
$[Li^{I}(TPP)]^{+}$ $[BF_4]^{-}$	0.381	0.092(3)	+36.5	[250]
$[Zn^{II}OEP(nBu)(H)_3]^{2+}$ $2(X^{-})$	0.339	0.090(4)	+19.71	[245]
$[Zn^{II}OEP(Me)(H)_3]^{2+}$ $2(X^{-})$	0.291	0.087(7)	+20.08	[245]
$[Zn^{II}(OEP)]^{2+}$ $2(X^{-})$	planar		+43.61	[244]

a) RMS nonplanarity is the root-mean-square of the distance of each atom from the mean plane defined by the 24 core atoms.
b) ΔN-C_α is the difference in the average bond distances of the N-C_α bonds.
c) NICS(ppm) is the NICS value calculated halfway between two N-C_α bonds (see Figure 11.24 for diagram).

The correlation between the degree of planarity and the strength of anti-aromaticity is nicely illustrated by the 16 π-electron porphyrins (Table 11.2; Figure 11.29). There is a clear relationship between larger positive NICS values, higher degree of planarity (smaller rms nonplanarity), and shifts in the ^{1}H-NMR spectra. For example, OiBTPP (octa-isobutyl tetraphenyl porphyrin) exhibits a strongly alternating pattern of bonds and an rms deviation from planarity of 0.921 Å. Its NICS calculated at a point halfway between the N-C_α bonds is +2.40 ppm, indicating that this molecule is only slightly anti-aromatic or non-aromatic. In contrast, $[(TPP)Li^1]^{+}$ $[BF]^{-}$ exhibits more moderate bond length alterations and an rms deviation from planarity of only 0.31 Å. It is clearly anti-aromatic, from the NICS at the same point of +36.5 ppm and its ^{1}H-NMR spectrum. This trend continues for the approximately planar $[(OEP)Zn^{II}]^{2+}$ $2(X^{-})$ species, which has an NICS at the same point of +43.61 ppm.

11.4.5 Porphyrin Aromaticity – Closing Comments

No chapter considering the electronic structure of porphyrins would be complete without addressing one of its central features: aromaticity. There is still controversy in the literature about porphyrin aromaticity. Can they really be considered as annulene-like compounds that follow the Hückel π-electron counting rules for aromatic, non-aromatic, and anti-aromatic behaviour? Or does their ring-of-rings structure require a more nuanced view, one that includes multiple conjugation pathways and involves all atoms to varying degrees? These disparate views are not new, and this chapter does not resolve them by making a case for one approach over another. After all, the first model for porphyrin electronic structure was Simpson's 18 electron ring model, inherently annulene-like, followed by molecular orbital pictures that involved all atoms and π-electrons, with states delocalised across the whole system.

Part of the challenge is that aromaticity is not an observable. There is no operator one can plug into the Hamiltonian to predict 'aromaticity', and there is no single physical measurement that can put it on an unambiguous quantitative scale. Attempts to describe and compare

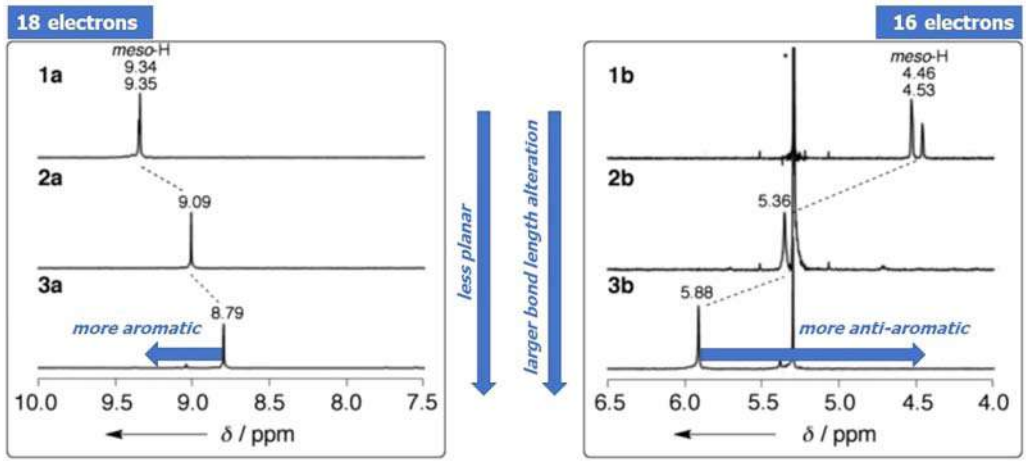

Figure 11.29 NMR spectra of aromatic (18 π-electrons; left panel) and reduced anti-aromatic (16 π-electrons; right panel) Ni(II)OEP with increasing numbers of nBu groups substituted at the *meso*-carbon positions. (1a, 1b) -$(nBU)_1$ -$(H)_3$; (2a, 2b) -$(nBu)_2$ -$(H)_2$; (3a, 3b) -$(nBu)_3$ -$(H)_1$. Source: Adapted from Y. Yamamoto et al. (2011) Chem Eur J. 17 :7768–7771 [245].

degrees of aromaticity in different molecules and across molecular systems thus depend on the goals of the comparison and the assumptions employed.

Bröring puts the debate down to the different disciplinary foci of the two sides [219]. Synthetic chemists seek simple, intuitive concepts, while physical chemists, particularly the theoretical and computational ones, are more comfortable with gaining precision at the cost of lost intuitive power. There is probably some truth to this assessment. The fact that chemists can make 16 and 20 π-electron analogues of porphyrin macrocycles that exhibit the hallmark behaviours of anti-aromaticity – instability, a tendency to seek stability through geometry changes like alternating bond lengths and OOP distortions, and paratropic ring currents – certainly provides support for the idea that the annulene picture works quite well as a first approximation for understanding aromaticity in porphyrin electronic states.

Nevertheless, the physical chemists have added intuitive value to our understanding of aromaticity in porphyrins, beyond the simple [18]annulene picture. For many porphyrins, the dominant conjugation pathway does appear to be annulene-like. However, to fully account for ring currents, and the impact of aromaticity on magnetically sensitive measurements like NMR, it is advantageous to include the ring current contributions more than just the dominant one when understanding the observed upfield and downfield shifts of atoms at different locations in the system. In addition, while simple free-base and metal coordinated porphyrins have electronic structures dominated by 18 π-electron rings, those conjugated macrocycles involve different pathways around the macrocycle. HOMA, graph theory, and NICS studies highlight an 18 atom, 18 π-electron annulene ring with bridging NH and ethylene groups for free-base porphyrins, while metalloporphyrin conjugation is dominated by an 'inner cross' pattern of 16 atoms and 18 π-electrons.

Perhaps the clearest conclusion is that porphyrins and porphyrinoid compounds provide an excellent class of compounds for studying and exploiting aromaticity, in all of its nuanced forms. Consider the recent report of experimental evidence for creating 3D aromaticity by π-stacking 2D anti-aromatic systems. Kowalczyk, Kim, Shinokubo, and co-workers formed anti-aromatic porphyrinoid compounds, Ni(II) diphenylnorcorrole, in stacks that

demonstrated reduced anti-aromaticity [258]. Similarly, expanded porphyrins and porphyrinoids have been used to explore more exotic forms of aromaticity such as Möbius and twisted-Hückel forms (see below).

11.4.6 OOP Distortions and the UV/Vis Spectrum

One of the key features of aromatic compounds is planarity, driven by the delocalisation of the π-orbitals across the molecule. As aromatic compounds, porphyrins tend to planarity as well. However, for porphyrins, distortions of the macrocycle from perfect planarity is a relatively soft degree of freedom. For example, Ni(II)OEP exists in three different crystal forms, two planar (triclinic A and triclinic B) [259, 260] and one ruffled (tetragonal) [261] form. In room temperature solution, ruffled and planar forms coexist in equilibrium [262–264]. Most biological porphyrins are nonplanar as well, influenced by the protein steric and electronic structure around them and by the spin- and axial-ligation state of the coordinated metal.

Porphyrin OOP distortions can be induced by the metal, the peripheral substituents, and/or by the environment (see reviews [69, 265–267] and references therein). The 'ideal' metal-N bond length for a planar porphyrin macrocycle core is about 2 Å. Smaller ions such as Ni and Co prefer shorter metal-N distances, so they tend to induce OOP twists in the macrocycle to accommodate those shorter bonds. Porphyrins with larger ions, such as Zn and Cu, are more likely to be planar. Even larger metals, heavy metals, can adopt positions above the macrocycle. Peripheral substituents can influence the planarity through electronic and/or through steric mechanisms. Electron-withdrawing or -donating groups can change the thermodynamic stability of different conformations by strengthening or weakening the aromatic delocalisation. Bulky substituents can drive OOP distortion of the macrocycle to relieve steric crowding at the edges. Crystal packing forces and local protein structures also can influence the porphyrin to adopt nonplanar conformations that can be simple and symmetric or complex.

Numerous studies provide support for the notion that distortions from planarity are functionally significant for porphyrins. For example, detailed classification of the types and extent of OOP distortion of the hemes in their heme protein crystal structures revealed characteristic distortions for similar proteins in different species, suggesting evolutionary conservation of function through OOP heme conformation via optimisation of the heme pocket [267–271].

A classic example of the functional importance of OOP distortion can be seen in the cooperative binding of O_2 by haemoglobin. Haemoglobin consists of four subunits, two α and two β, each of which contains an iron porphyrin. The iron (Fe(II)) in each heme is bound to the protein through axial ligation to a histidine moiety. The sixth coordination position is where the O_2 molecules bind (in the lungs) and release (in the tissues). When the O_2—Fe bond breaks, the Fe changes spin state, and its radius increases. It moves out of the plane of the heme by approximately 0.4 Å within 0.35–1 ps to form a domed structure [272]. As the Fe(II) moves OOP, it 'pulls' on the histidine [273], inducing a sliding and rotation of subunits relative to one another that ultimately (in microseconds) changes the O_2 binding constant at the other heme positions. Binding and release of ligands (O_2, CO) from the coordinated iron triggers a quaternary structure transformation, and enzymatic O_2-binding cooperativity, through motion of the central metal in and out of plane.

Doming *(dom)* and ruffling *(ruf)* are just two types of OOP deformed structures that porphyrins can adopt (Figure 11.30a). Others include the saddle *(sad)* and wave *(wav)* distortions. Porphyrins in crystals, proteins, or other inhomogeneous environments can

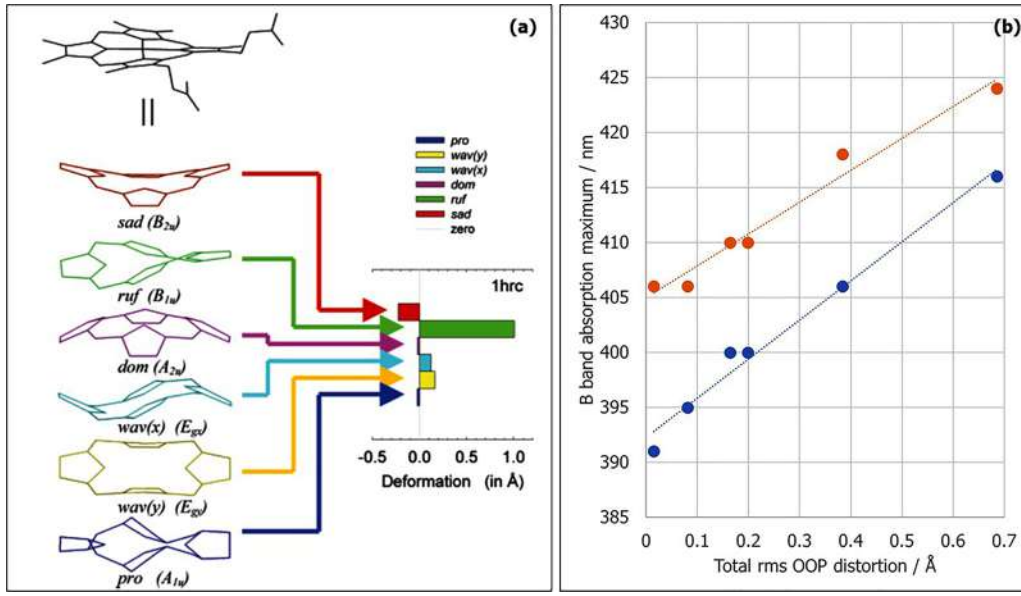

Figure 11.30 (a) The normal-coordinate structural decomposition approach, illustrating how any porphyrin can be described in terms of the displacements along the normal coordinates of porphine (only the six lowest-energy OOP ones are shown here). From [274]. (b) Example of the red shift observed with increasing magnitude of OOP distortion for a series of Ni(II) octaethyl-*meso*-nitroporphyrins in dichloromethane (blue) and piperidine (orange). Source: Data from [275].

take on quite complex OOP deformations. A significant step forward in porphyrin chemists' ability to characterise and quantify OOP deformations of porphyrins was made by the introduction of the normal-coordinate structural decomposition method (NSD) by Shelnutt's group [276–278] (and references therein). In this approach, illustrated diagrammatically in Figure 11.30a, the low-frequency OOP vibrational normal modes are used as a basis set with which to treat porphyrin OOP deformations from crystal structures and computational modelling. The method is routinely adopted for classifying porphyrin structures and correlating them with physical observables like UV/Vis absorption, redox potentials, and Raman spectra, and with molecular function [126, 267, 278]. One of its advantages is that the distortions are decomposed into different symmetry groups. When used with theoretical approaches like Gouterman's four-orbital model, symmetry rules can make the analysis more intuitive.

In the UV/Vis absorption spectrum, intuition about aromaticity suggests that ground state OOP distortions should shift the π-π^* transitions to lower energy, and experimental results are consistent with that prediction (Figure 11.30b). For haemoglobin, the CO-ligated, planar UV/Vis absorption lines appear at 420 nm (B band) and at 538 and 568 nm (Q bands). In the domed, deoxy conformer, the B band shifts to 428 nm, and the Q band becomes a red-shifted, broad band with a peak at 552 nm [26].

Gouterman's four-orbital model also supports this hypothesis. For the Ni(II)OEP example above, application of extended Hückel theory and Gouterman's model predicts that all four of the frontier molecular orbitals are destabilised by ruffling, with the a_{1u} and a_{2u} more so than the e_g [264]. This results in predicted B(0,0) and Q(0,0) bands for the ruffled conformer that red-shifted from their planar counterparts by 410 and 360 cm^{-1}, respectively. By measuring

the resonance Raman spectrum of Ni(II)OEP at multiple wavelengths across the broad B band, it can be seen that both ruffled and planar Ni(II)OEP are present in room temperature solution, and that the UV/Vis spectrum of the ruffled species is at longer wavelengths than the 393 nm position assigned to the planar conformer [264].

Between about 1995 and 2005, a controversy about the origin of the red shift in UV/Vis absorption bands that accompanies nonplanar distortions appeared in the literature. Largely on the basis of quantum calculations of UV/Vis transitions at geometries derived from constrained geometry optimisations, the experimental red shift could not be confirmed to have its origin in the OOP distortion (e.g. *ruf* or *sad*). It was proposed that in-plane nuclear reorganisation accompanying peripheral substitution was the dominant origin of the experimentally observed red shifts (see, for example, [279]).

Shelnutt and co-workers resolved this issue with an elegant study that used DFT, high-quality NSD, and a set of brindled porphyrins [274]. They showed that the OOP distortion is responsible for the UV/Vis absorption red shift observed in experimental spectra of crowded porphyrins. However, the phenomenon is very sensitive to the contributions of higher-energy OOP modes to the overall distortion. For example, the lowest-energy *ruf* deformation is not the only B_{1u} symmetry OOP distortion that contributes to the description of the experimental structure. Relatively small components of two higher-energy B_{1u} OOP distortions contribute as well, and these dominate the effect upon the absorption spectrum. Estimating their contribution accurately requires high-quality crystal structures and NSD analysis. Computations that constrain only along the lowest-energy OOP coordinates will miss the contributions of the higher-energy terms altogether, and provide misleading results [274].

The conclusion is that, as predicted by Gouterman's four-orbital model and intuition about aromaticity, the experimentally observed red-shifted patterns in the UV/Vis absorption spectrum that accompany distortions of the porphyrin macrocycle from planarity have their origin in the details (symmetry, extent, etc.) of the conformational displacement of the macrocycle out of the planar geometry.

11.4.7 Expanded Porphyrins and Möbius (Anti)Aromaticity

The Hückel [4n + 2] π-electron rule for aromaticity, and its cousin [4n] π-electron rule for anti-aromaticity, are based upon a planar conformation of a conjugated, closed ring in which the atomic p-orbitals can overlap with one another around the macrocycle. In 1964, Heilbronner applied a topological idea, first introduced a century earlier, to chemistry and proposed that π-systems could form in the shape of a Möbius strip [280]. Carrying through this idea using molecular orbital theory, he concluded that introducing a half-twist to an annulene-type system could create a conjugated π-system that is stabilised if the molecule has [4n] π-electrons, and destabilised if it has [4n + 2]. Introducing another half-twist would return the aromaticity rule to the Hückel's [4n + 2] (Figure 11.31).

Heilbronner further predicted that the strain energy engendered by the twist would only be small enough to allow realisation of these molecules for annulenes with $n > 20$. The different π-electron number rules for Hückel and Möbius (anti)aromatic systems reflects the fact that the molecular orbital diagrams depend upon this topology (Figure 11.32).

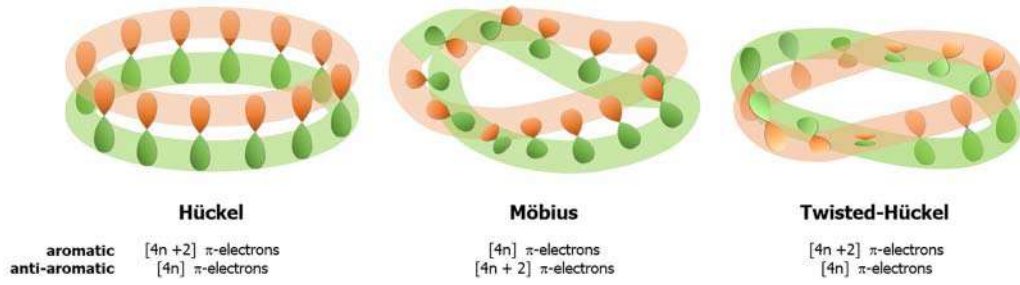

Figure 11.31 Orientation of the atomic p_z-orbitals for classic Hückel aromaticity (left), half-twisted Möbius aromaticity (centre), and full twisted Hückel aromaticity (right).

Figure 11.32 The (a) Hückel [4n + 2] π-electron and (b) Möbius [4n] π-electron molecular orbitals.

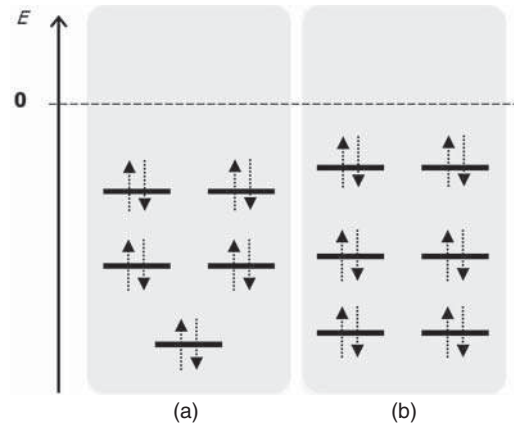

It was several decades before the first Möbius aromatic molecule was synthesised and its structure characterised. Attempts to synthesise Möbius annulenes were hampered by large ring strains in smaller systems, and too much conformational flexibility in larger ones. Finally, in 2003, Herges reported a [16]annulene with two rigid ring groups that exhibited clear evidence of Möbius aromaticity [281]. A few years after that, it became apparent that expanded porphyrins offered an excellent platform for exploring Möbius and other types of aromaticity (see [282–286] and references therein).

Expanded porphyrins are extended π-macrocycles that possess five or more pyrrolic or related rings linked together. They are an increasingly important class of compounds, recognised for their potential in numerous applications including applications as non-linear optical materials, photodynamic therapeutic and magnetic resonance imaging contrast agents, and as molecular switches. Some examples of expanded porphyrins are shown in Figure 11.33. The reader is referred to recent reviews for more detail on the synthesis, characterisation, and uses of these systems, and for insight into their chemical cousins, the contracted and isomeric porphyrins [284–293].

Expanded porphyrins offer several advantages over annulenes as systems for exploring Hückel, Möbius, and more complex types of aromaticity. These large, flexible macrocyclic systems possess considerable conformational flexibility, yet the potential energy surface has barriers high enough to confer stability to different conformers that can switch from one to

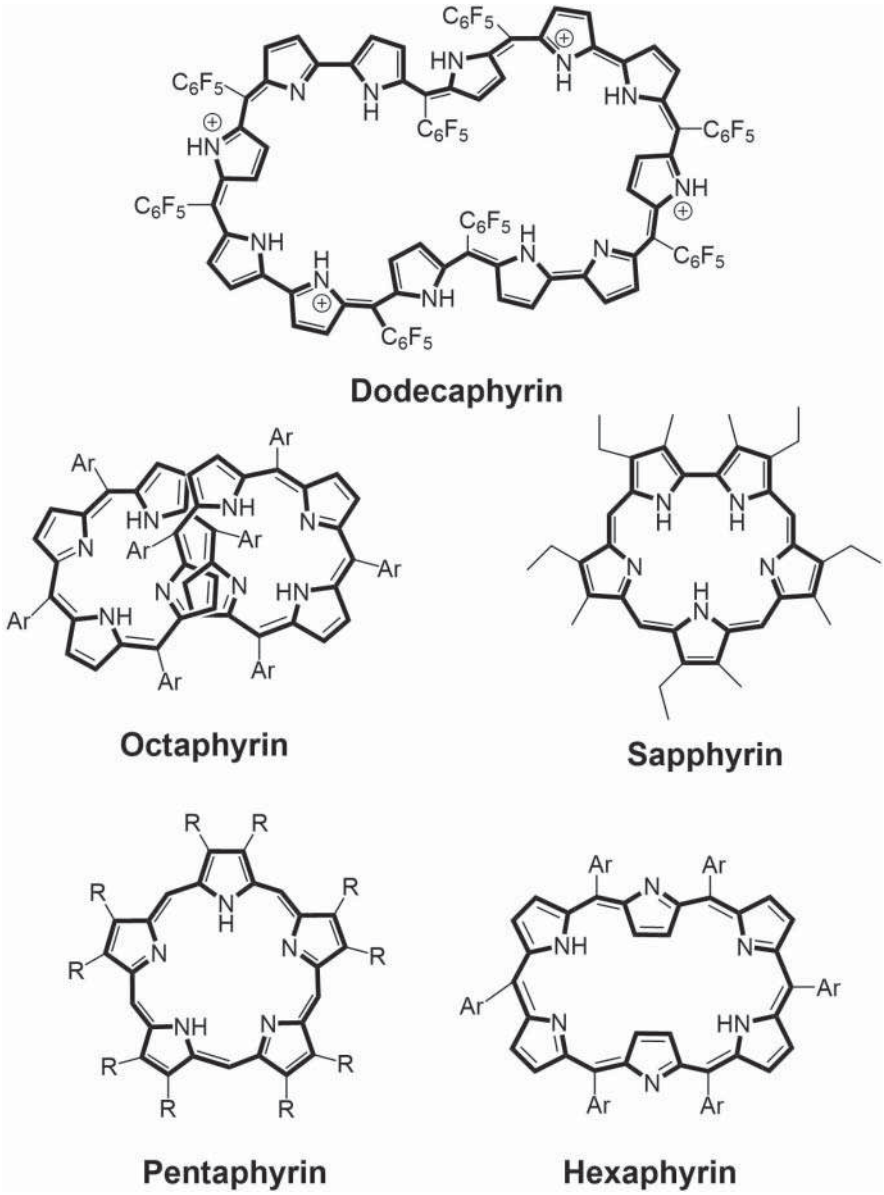

Figure 11.33 Some examples of extended porphyrins.

another. There are multiple ways in which this switching can occur, through pH, protonation, oxidation and reduction, metallation, and solvent conditions, for example. As potential switches for molecular electronics, extended porphyrins offer a powerful combination of mechanical (conformational) switching and electronic (π-electron aromaticity) switching [95, 132, 291, 292, 294, 295].

In 2007, Latos-Grażyński and co-workers described an expanded porphyrin, di-p-benzilhexaphyrin, with a 28 π-electron conjugation pathway that could switch between Hückel and Möbius topologies under different solvent and temperature conditions (Figure 11.34) [294].

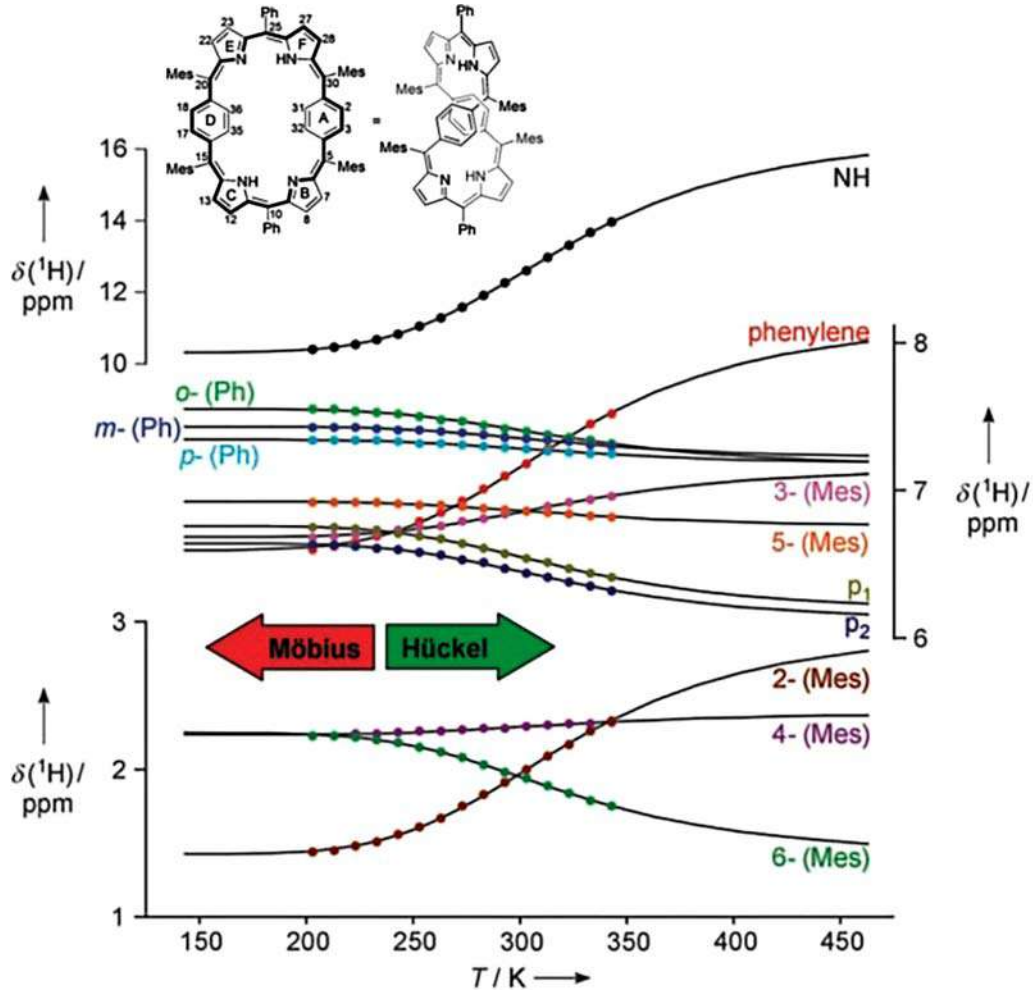

Figure 11.34 Temperature dependence of several ^{1}H NMR shifts in the spectrum of di-*p*-benzihexaphyrin (inset), showing the switch between Möbius and Hückel conformations. The Hückel conformation shows a paratropic shift, indicative of anti-aromaticity. Source: Adapted from [294].

^{1}H NMR chemical shifts were used to detect the switch from diatropic (Möbius) to paratropic (Hückel) ring currents in these systems (Figure 11.34b); though the paratropic ring current is evident, the diatropic one is not seen, presumably because of relatively inefficient p-orbital overlap in the twisted species. This was the first example of a π-system that was a continuous Möbius band with a half-twist. Since then, several aromatic Möbius [4n] π-electron expanded porphyrins have been observed.

Osuka and co-workers were the first to structurally characterise a Möbius anti-aromatic compound, stabilised through the insertion of two electron-withdrawing phosphamide groups into an expanded porphyrin, hexaphyrin in this case (Figure 11.35) [293]. ^{1}H NMR spectroscopy of the [28]hexaphyrin monophosphorus (V) and [30]hexaphyrin diphosphorus (V) complexes showed diatropic and paratropic ring currents, respectively. The first set of

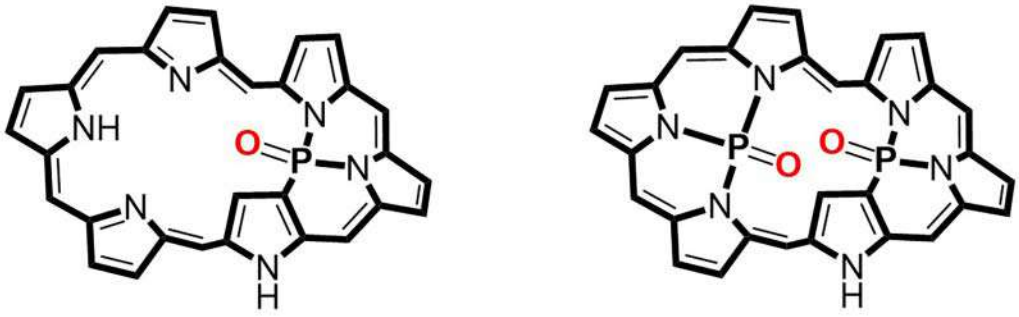

Figure 11.35 (Left) [28]hexaphyrin exhibits Möbius aromaticity with [4n] π-electrons. (Right) [30] hexaphyrin exhibits Möbius anti-aromaticity with [4n + 2] π-electrons [293].

these complexes exhibits [4n] π-electron Möbius aromaticity, and the second demonstrates [4n + 2] π-electron Möbius anti-aromaticity.

A quite different example of an extended porphyrin system that can be switched between states of aromaticity and anti-aromaticity is the porphyrin nanoring *c*-P6-T6 studied by Anderson et al. (Figure 11.36) [296]. This π-conjugated macrocycle possesses six porphyrins linked at their *meso*-positions by butadienes arranged in a ring, ligated through the Zn in each core to a central template. The (anti)aromaticity of this macrocycle is sensitive to its oxidation state, and it is stable in across a range of these, from −6 to +12. Calculations of NCIS at the centre of the nanoring (template removed) show that the neutral (84 electron) nanoring is non-aromatic, which is not unusual for these species. Oxidised and reduced species follow the Hückel's rules: the 4- (88 π-electron) and 4+ (80 π-electron) rings have very positive NICS values and are anti-aromatic, and the 6- (90 π-electron) and 6+ (78 π-electron) nanorings are moderately aromatic, results that are further confirmed by ACID calculations. ^{1}H NMR spectroscopy confirmed experimentally that the 90 π-electron compound is aromatic, and the 88 π-electron state is anti-aromatic.

As mentioned in the section on DFT calculations of porphyrins above, applying computational methods to extended systems can be tricky. These systems are replete with low-energy conformations and barriers and important long-range interactions. Several recent survey and benchmark studies on extended porphyrins and their conformational switching can provide guidance about the appropriate choice(s) of method to obtain reliable results [95, 131, 132].

11.4.8 Baird's Rule and Aromaticity Reversal in Excited States

Baird's rule refers to the simple perturbation theory prediction that the lowest-energy excited triplet state of a Hückel aromatic molecule should exhibit anti-aromatic character. Similarly, a [4n] π-electron Hückel molecule should exhibit anti-aromaticity in the ground state, and be aromatic in the first triplet state. The consequences of this aromaticity reversal are significant for the electronic properties and reactivity of aromatic molecules. Although Baird published his paper in 1972 [297], it was not until just a few years ago that this aromaticity reversal was demonstrated. Kim, Osuka, and co-workers exploited the advantages of expanded porphyrins and time-resolved spectroscopy in a series of hexaphyrins [292, 298–300].

The UV/Vis spectra of aromatic and anti-aromatic expanded porphyrins, confirmed by NICS and ACID, differ sufficiently that this measurement seems to be a good indicator

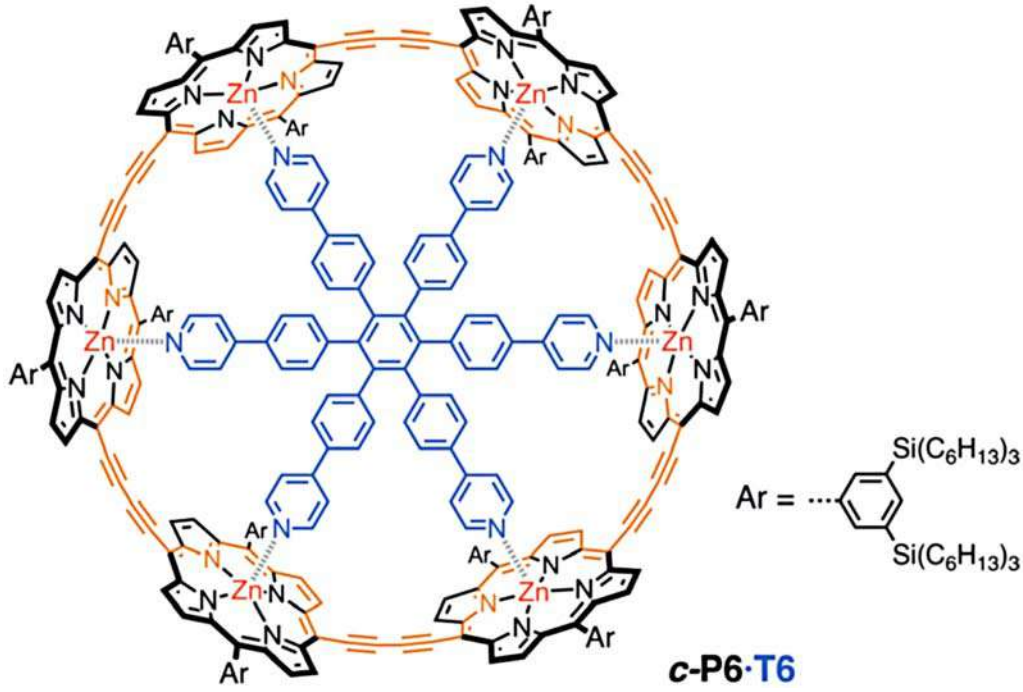

Figure 11.36 Six-porphyrin nanoring with the conjugation pathway indicated in orange. Source: From [296].

of the system's aromatic or anti-aromatic character. For example, Cho et al. examined the photophysics of a set of expanded porphyrins with between 20 and 26 π-electrons that obeyed Hückel's rules for (anti)aromaticity [301]. The UV/Vis spectrum of the aromatic compounds exhibited clear transitions similar to porphyrin Soret and Q bands, were strongly fluorescent, and the excited state lifetime was found to be several hundred picoseconds to nanoseconds. In contrast, the UV/Vis spectra of the anti-aromatic compounds are broad and indistinct, the compounds are very weakly or non-fluorescent, and their excited state lifetimes are ultrashort. Computational chemistry indicated that a dark state is the lowest-energy excited state for the anti-aromatic extended porphyrins, and that an additional deactivation pathway was postulated to account for the rapid excited state decay and the absence of fluorescence emission.

In an impressive series of studies, Kim and co-workers used femtosecond time-resolved optical spectroscopy across the UV/Vis and NIR regions of the spectrum and computational chemistry to examine the states and NCID values for the ground and electronic states of Hückel and Möbius expanded porphyrins to probe their ground state and first singlet and triplet excited states. Using matched pairs of hexaphryins, one with a Hückel aromatic $[4n + 2]$ π electron ground electronic state and the other with a $[4n]$ anti-aromatic one, they determined that Baird's rule applies to both the triplet and singlet excited states, and for ground states that are either aromatic or anti-aromatic. More recent studies have observed Baird aromaticity in annulene compounds [302, 303]. These results could have far-reaching consequences for our understanding of the photochemistry and photophysics of aromatic systems [288, 291, 292, 298–300], and references therein).

11.5 Conclusions

Porphyrins are an exceptional class of molecules, and a significant underpinning of that remarkable behaviour derives from their electronic structure. Their extended π-electron system gives them the ability to harness the energy carried by light into a myriad of important biological and chemical reactions. That same delocalised structure, coupled with their high symmetry and ring-of-rings structure, also makes them of deep interest to physicists and chemists trying out new ways to think about and model molecular structure, spectra, and functions. Hence, porphyrins and their electronic structure and spectra have been attractive targets of ground-breaking studies for well over 100 years. This chapter walks through how this has been true from the earliest days of the colour changes that accompany ligand binding to hemes to the newest approaches of the time in quantum mechanical descriptions of molecules to stretching our understanding of aromaticity and anti-aromaticity in porphyrins. No doubt this keen interest in the porphyrin electronic structure and spectrum, their functional consequences, and the intrinsic properties that make them suitable as test beds for new ideas and methods will continue for the next 100 years.

Acknowledgements

The authors would like to thank Liam Barber for his creative contributions to several of the figures, and Prof. Penny Brothers for insightful conversations and patience.

References

1 Tian, H., Oscarsson, J., Gabrielsson, E. et al. (2014). *Enhancement of p-type dye-sensitized solar cell performance by supramolecular assembly of electron donor and acceptor*. *Scientific Reports* 4: 4282.
2 Atkins, P. and Friedman, R. (2010). *Molecular Quantum Mechanics*, 5e. Oxford University Press.
3 Cotton, F.A. (1990). *Chemical Applications of Group Theory*, 3e. Wiley.
4 Hamermesh, M. (1989). *Group Theory and its Application to Physical Problems*, Dover Press (original work published 1954).
5 McQuarrie, D. (2007). *Quantum Chemistry*, 2e. University Science Books.
6 Szabo, A. and Ostlund, N.S. (1996). *Modern Quantum Chemistry: Introduction to Advanced Electronic Structure Theory*, Dover Press (original work published 1982).
7 Tinkham, M. (2003). *Group Theory and Quantum Mechanics*. Dover Press (original work published 1964).
8 Schatz, G. and Ratner, M. (2002). *Quantum Mechanics in Chemistry*. Dover Press (original work published 1993).
9 Platt, J.R. (1949). *Classification of spectra of cata-condensed hydrocarbons. The Journal of Chemical Physics* 17 (5): 484–495.
10 Platt, J.R. (1953). *Classification and assignments of ultraviolet spectra of conjugated organic molecules. Journal of the Optical Society of America* 43 (4): 252–257.
11 Platt, J.R. (1956). *Electronic structure and exctitation of polyenes and porphyrins*. In: *Radiation Biology* (ed. A. Hollaender), 71–123. New York: McGraw-Hill.

12 Klevens, H.B. and Platt, J.R. (1949). *Spectral resemblances of cata-condensed hydrocarbons. The Journal of Chemical Physics* 17 (5): 470–481.

13 Moffitt, W. (1954). *The electronic spectra of cata-condensed hydrocarbons. The Journal of Chemical Physics* 22 (2): 320–333.

14 Gamgee, A. (1896). *On the absorption of the extreme violet and ultra-violet rays of the solar spectrum by haemoglobin, its compounds, and certain of its derivatives. Proceedings. Royal Society of London* 59 (353–358): 276–279.

15 Soret, J.-L. (1878). *Researches sur l'Absorption des Rayons ultra-violets par diverses Substances. Archives des Sciences Physiques et Naturelles* 61 (Geneva): 322–359.

16 Soret, J.-L. (1879). *Recherches sur l'absorption des Rayons ultra-violets par diverses Substances. Journal of Physics Theoretical Applied* 8 (1): 145–158.

17 Kuhn, H. (1949). *A quantum-mechanical theory of light absorption of organic dyes and similar compounds. The Journal of Chemical Physics* 17 (12): 1198–1212.

18 Simpson, W.T. (1948). *Electronic states of organic molecules. The Journal of Chemical Physics* 16 (12): 1124–1136.

19 Simpson, W.T. (1949). *On the theory of the pi-electron system in porphines. The Journal of Chemical Physics* 17 (13): 1218–1221.

20 Kutzelnigg, W. (2006). *What I like about Hückel theory. Journal of Computational Chemistry* 28: 25–34.

21 Frenking, G. (2000). *Perspective on "Quantentheoretische Beiträge zum Benzolproblem. I. Die Elekronenkonfigurtion des Benzols und verwandter Beziehungen". Theoretical Chemistry Accounts* 103: 187–189.

22 Hückel, E. (1930). *Zur Quantentheorie der Doppelbindung. Zeitschrift für Physik* 60: 423–456.

23 Hückel, E. (1931). *Quantentheoretische Beiträge zum Benzolproblem. I. Die Elektronenkonfiguration des Benzols und verwandter Verbindungen. Zeitschrift für Physik* 70: 204–286.

24 Longuet-Higgins, H.C., Rector, C.W., and Platt, J.R. (1950). *Molecular orbital calculations on porphine and tetrahydroporphine. The Journal of Chemical Physics* 18 (9): 1174–1181.

25 Gouterman, M., Wagniére, G.H., and Snyder, L.C. (1963). *Spectra of porphyrins. Part II. Four orbital model. Journal of Molecular Spectroscopy* 11: 108–127.

26 Simpson, M.C. (1994). (published as Schneebeck, M. C.). *Functional dynamics in Metalloporphyrin systems*. PhD dissertation, University of New Mexico.

27 Gouterman, M. (1959). *Study of the effects of substitution on the absorption spectra of porphin. The Journal of Chemical Physics* 31 (5): 1139–1161.

28 Gouterman, M. (1961). *Spectra of porphyrins. Journal of Molecular Spectroscopy* 6: 138–163.

29 Weiss, C., Kobayashi, H., and Gouterman, M. (1965). *Spectra of porphyrins. Part III. Self-consistent molecular orbital calculations of porphyrin and related ring systems. Journal of Molecular Spectroscopy* 16: 415–450.

30 Citation counts from Web of Science. Accessed 6 Dec 2020.

31 Nesbet, R.K. (1955). *Configuration interaction in orbital theories. Proceedings of the Royal Society of London. Series A, Mathematical and Physical Sciences* 230 (1182): 312–321.

32 Gouterman, M. (1978). *Optical spectra and electronic structure of porphyrins and related rings*. In: *The Porphyrins* (ed. D. Dolphin), 1–165. New York: Academic Press.

33 Adar, F. (1978). *Electronic absorption spectra of hemes and hemoproteins*. In: *The Porphyrins* (ed. D. Dolphin), 167–209. New York: Academic Press.

34 Antipas, A. and Gouterman, M. (1983). *Porphyrins. 44. Electronic states of Co, Ni, Rh, and Pd complexes*. *Journal of the American Chemical Society* 105 (15): 4896–4901.

35 Gouterman, M., Hanson, L.K., Khalil, G.E. et al. (1975). *Porphyrins. XXXI. Chemical properties and electronic spectra of d0 transition-metal complexes*. *Journal of the American Chemical Society* 97 (11): 3142–3149.

36 Liao, M.-S. and Scheiner, S. (2001). *Electronic structure and bonding in metal phthalocyanines, metal= Fe, Co, Ni, Cu, Zn, Mg*. *The Journal of Chemical Physics* 114 (22): 9780–9791.

37 Liao, M.-S. and Scheiner, S. (2002). *Electronic structure and bonding in metal porphyrins, metal= Fe, Co, Ni, Cu, Zn*. *The Journal of Chemical Physics* 117 (1): 205–219.

38 Cárdenas-Jirón, G., Borges-Martínez, M., Mera-Adasme, R., and Pino-Rios, R. (2019). *Quantum chemical studies of porphyrin-and expanded porphyrin-based systems and their potential applications in nanoscience. Latin America research review*. *International Journal of Quantum Chemistry* 119 (2): e25821.

39 Aviram, A. and Ratner, M.A. (1974). *Molecular rectiviers*. *Chemical Physics Letters* 29 (2): 277–283.

40 Mirkin, C.A. and Ratner, M.A. (1992). *Molecular Electronics*. *Annual Review of Physical Chemistry* 43: 719–754.

41 Martin, M.M., Lungerich, D., Haines, P. et al. (2019). *Electronic communication across porphyrin hexabenzocoronene isomers*. *Angewandte Chemie, International Edition* 58: 8932–8937.

42 Jurow, M., Schuckman, A.E., Batteas, J.D., and Drain, C.M. (2010). *Porphyrins as molecular electronic components of functional devices*. *Coordination Chemistry Reviews* 254: 2297–2310.

43 Mandal, A.K., Taniguchi, M., Diers, J.R. et al. (2016). *Photophysical properties and electronic structure of porphyrins bearing zero to four meso-phenyl substitutents: new insights into seemingly well understood tetrapyrroles*. *The Journal of Physical Chemistry. A* 120: 9719–9731.

44 Hu, G., Kang, H.S., Mandal, A.K. et al. (2019). *Synthesis of arrays containing porphyrin, chlorin, and perylene-imide constituents for panchromatic light-harvesting and charge separation*. *RSC Advances* 8: 23854–23874.

45 Tsai, H.-H. and Simpson, M.C. (2002). *The role of frontier molecular orbital ordering on electronic communication in porphyrin arrays*. *Chemical Physics Letters* 353: 111–118.

46 Strachan, J.-P., Gentemann, S., Seth, J. et al. (1997). *Effects of orbital ordering on electronic communication in multiporphyrin arrays*. *Journal of the American Chemical Society* 119: 11191–11201.

47 Yang, S.I., Seth, J., Balasubramanian, T. et al. (1999). *Interplay of orbital tuning and linker location in controlling electronic communication in porphyrin arrays*. *Journal of the American Chemical Society* 121: 4008–4018.

48 Magdaong, N.C.M., Taniguchi, M., Diers, J.R. et al. (2020). *Photophysical properties and electronic structure of zinc(II) porphyrins bearing 0–4 meso-phenyl substituents: zinc porphine to zinc tetraphenylporphyrin (ZnTPP)*. *The Journal of Physical Chemistry. A* 124: 7776–7794.

49 Zhang, A., Kwan, L., and Stillman, M.J. (2017). *The spectroscopic impact of interactions with the four Gouterman orbitals from peripheral decoration of porphyrins with simple electron withdrawing and donating groups*. *Organic & Biomolecular Chemistry* 15: 9081–9094.

50 Li, L.-L. and Diau, E.W.-G. (2013). *Porphyrin-sensitized solar cells*. *Chemical Society Reviews* 42: 291–304.

51 Mathew, S., Yella, A., Gao, P. et al. (2014). *Dye-sensitized solar cells with 13% efficiency achieved through molecular engineering of porphyrin sensitizers*. *Nature Chemistry* 6: 242–247.

52 Ma, R., Guo, P., Cui, H. et al. (2009). *Substituent effect on the meso-substituted porphyrins: theoretical screening of sensitizer candidates for dye-sensitized solar cells*. *Journal of the American Chemical Society* 113: 10119–10124.

53 Baerends, E.J., Ricciardi, G., Rosa, A., and Van Gisbergen, S.J.A. (2002). *A DFT/TDDFT interpretation of the ground and excited states of porphyrin and porphyrazine complexes*. *Coordination Chemistry Reviews* 230 (1–2): 5–27.

54 Perrin, M.H., Gouterman, M., and Perrin, C. (1969). *Vibronic coupling. VI. Vibronic borrowing in cyclic polyenes and porphyrin*. *The Journal of Chemical Physics* 50: 4137–4150.

55 Weigl, J.W. (1957). *The polarization of the fluorescence of tetraphenylporphine*. *Journal of Molecular Spectroscopy* 1: 133–138.

56 Albrecht, A.C. (1960). *"Forbidden" character in allowed electronic transitions*. *The Journal of Chemical Physics* 33: 156–169.

57 Fischer, G. (1984). *Vibronic Coupling. The Interaction between the Electronic and Nuclear Motions*. London: Academic Press.

58 Hertzberg, G. and Teller, E. (1933). *Schwingungsstruktur der Elektronenübergänge bei mehratomigen Molekülen*. *Zeitschrift für Physikalische Chemie* 21B (1): 433–446.

59 Shelnutt, J.A. and O'Shea, D.C. (1978). *Resonance Raman spectra of copper tetraphenylporphyrin: effects of strong vibronic coupling on excitation profiles and the absorption spectrum*. *The Journal of Chemical Physics* 69: 5361–5374.

60 Aronowitz, Y.J. and Gouterman, M. (1977). *Effect of metal and substituents on the quasi-line spectra of some Metalloporphyrins*. *Journal of Molecular Spectroscopy* 64: 267–289.

61 Albrecht, A.C. (1960). *On the theory of Raman intensities*. *The Journal of Chemical Physics* 34: 1476–1484.

62 Unger, E., Bobinger, U., Dreybrodt, W., and Schweitzer-Stenner, R. (1993). *Vibronic coupling in Ni(II) porphine derived from resonant Raman excitation profiles*. *The Journal of Physical Chemistry* 97: 9956–9968.

63 Shelnutt, J.A. (1981). *A simple interpretation of Raman excitation spectra of metalloporphyrins*. *The Journal of Chemical Physics* 74: 6644–6657.

64 Friedman, J.M. and Hochstrasser, R.M. (1976). *Approximate selection rules for resonance Raman spectroscopy*. *Journal of the American Chemical Society* 98: 4043–4048.

65 Spiro, T.G. and Strekas, T.C. (1972). *Resonance Raman spectra of hemoglobin and cytochrome c: inverse polarization and vibronic scattering*. *Proceedings of the National Academy of Sciences of the United States of America* 69 (9): 2622–2626.

66 Friedman, J.M. and Hochstrasser, R.M. (1973). *A description of resonant Raman scattering in hemeproteins: cytochrome-c*. *Chemical Physics* 1: 457–467.

67 Stradomska, A. and Knoester, J. (2010). *Shape of the Q band int he absorption spectra of porphyrin nanotubes: Vibronic coupling or exciton effects?* *The Journal of Chemical Physics* 133: 094701.

68 Ghosh, A. (1998). *First-principles quantum chemical studies of porphyrins*. *Accounts of Chemical Research* 31 (4): 189–198.

69 Ghosh, A. (2000). *Quantum chemical studies of molecular structures and potential energy energy surfaces of porphyrins and hemes*. In: *The Porphyrin Handbook*, vol. 7 (ed. K.M. Kadish, K.M. Smith and R. Guilard), 1–38. Publisher Academic Press, Chapter 47.

70 Almlöf, J., Fischer, T.H., Gassman, P.G. et al. (1993). *Electron correlation in tetrapyrroles. Ab initio calculations on porphyrin and the tautomers of chlorin*. *The Journal of Physical Chemistry* 97: 10964–10970.

71 Piqueras, M.C. and Rohlfing, C.M. (1996). *Hartree-Fock symmetry-breaking in magnesium and nickel porphyrins*. *Journal of Molecular Structure (THEOCHEM)* 388: 293–297.

72 Piqueras, M.C. and Rohlfing, C.M. (1997). *An ab initio analysis of the electronic structure and harmonic frequencies of nickel porphyrin*. *Theoretical Chemistry Accounts* 97: 81–87.

73 Gassman, P.G., Ghosh, A., and Almlöf, J. (1992). *Electronic effects of peripheral substituents in porphyrins: X-ray photoelectron spectroscopy and ab initio self-consistent field calculations*. *Journal of the American Chemical Society* 114: 9990–10000.

74 Ghosh, A. and Almlöf, J. (1993). *The ultraviolet photoelectron spectrum of free-base porphyrin revisited. The performance of local density functional theory*. *Chemical Physics Letters* 213 (5, 6): 519–521.

75 Ghosh, A., Almlöf, J., and Gassman, P.G. (1991). *Ab initio SCF studies of basis set effects in free base porphin*. *Chemical Physics Letters* 186 (1): 113–118.

76 Ghosh, A. (1994). *Ab initio Hartree-Fock and local density functional calculations on prototype halogenated porphyrins. Do electrochemically measured substituent effects reflect gas phase trends?* *The Journal of Physical Chemistry* 98: 11004–11006.

77 Peverati, R. and Truhlar, D.G. (2014). *Quest for a universal density functional: the accuracy of density functionals across a broad spectrum of databases in chemistry and physics*. *Philosophical Transactions of the Royal Society A* 372 (2011): 20120476.

78 Medvedev, M.G., Bushmarinov, I.S., Sun, J. et al. (2017). *Density functional theory is straying from the path toward the exact functional*. *Science* 355: 49–52.

79 Mardirossian, N. and Head-Gordon, M. (2017). *Thirty years of density functional theory in computational chemistry: an overview and extensive assessment of 200 density functionals*. *Molecular Physics* 115 (19): 2315–2372.

80 Baerends, E.J. (2000). *Perspective on "Self-consistent equations including exchange and correlation effects"*. *Theoretical Chemistry Accounts* 103 (3–4): 265–269.

81 Baerends, E.J. and Gritsenko, O.V. (1997). *A quantum chemical view of density functional theory*. *The Journal of Physical Chemistry* 101 (30): 5383–5403.

82 Stowasser, R. and Hoffmann, R. (1999). *What do the Kohn-Sham orbitals and eigenvalues mean?* *Journal of the American Chemical Society* 121: 3414–3420.

83 Hohenberg, P. and Kohn, W. (1964). *Inhomogeneous electron gas*. *Physical Review* 136 (3B): B864–B871.

84 Yang, W. (2014). *Preface: special topic on advances in density functional theory*. *The Journal of Chemical Physics* 140: 18A101.

85 Kohn, W. and Sherrill, C.D. (2014). *Editorial: reflections on fifty years of density functional theory*. *The Journal of Chemical Physics* 140: 18A201.

86 Becke, A.D. (1988). *Density-functional exchange-energy approximation with correct asymptotic behavior*. *Physical Review A* 38 (6): 3098–3100.

87 Lee, C., Yang, W., and Parr, R.G. (1988). *Development of the Colic-Salvetti correlation-energy formula into a functional of the electron density*. *Physical Review B* 37 (2): 785–789.

88 Becke, A.D. (1993). *Density-functional thermochemistry. III. The role of exact exchange. The Journal of Chemical Physics* 98: 5648–5652.

89 Becke, A.D. (2014). *Perspective: fifty years of density-functional theory in chemical physics. The Journal of Chemical Physics* 140: 18A301.

90 Klimeš, J. and Michaelides, A. (2012). *Perspective: advances and challenges in treating van der Waals dispersion forces in density functional theory. The Journal of Chemical Physics* 137: 120901.

91 Erlich, S., Moellmann, J., and Grimme, S. (2013). *Dispersion-corrected density functional theory for aromatic interactions in complex systems. Accounts of Chemical Research* 46 (4): 916–926.

92 Yu, H.S., Li, S.L., and Truhlar, D.G. (2016). *Perspective: Kohn-Sham density functional theory descending a staircase. The Journal of Chemical Physics* 145: 130901.

93 Burke, K. (2012). *Perspective on density functional theory. The Journal of Chemical Physics* 136: 150901.

94 Jones, R.O. (2015). *Density functional theory: its origins, rise to prominence and future. Reviews of Modern Physics* 87 (3): 897–923.

95 Woller, T., Banerjee, A., Sylvetsky, N. et al. (2020). *Performance of electronic structure methods for the description of Huckel-Mobius interconversions in extended pi-systems. The Journal of Physical Chemistry. A* 124: 2380–2397.

96 Perdew, J.P., Ruzsinszky, A., Tao, J. et al. (2005). *Prescription for the design and selection of density functional approximations: more constraint satisfaction with fewer fits. The Journal of Chemical Physics* 123: 062201.

97 Lee, C.-W., Lu, H.-P., Lan, C.-M. et al. (2009). *Novel zinc porphyrin sensitizers for dye-sensitized solar cells: synthesis and spectral, electrochemical, and photovoltaic properties. Chemistry: A European journal* 15: 1403–1412.

98 Hseih, C.-P., Lu, H.-P., Chiu, C.-L. et al. (2010). *Synthesis and characterization of porphyrin sensitizers with various electron-donating substituents for highly efficient dye-sensitized solar cells. Journal of Materials Chemistry* 20: 1127–1134.

99 Yasin, A., Jose, R., and Yusoff, M.M. (2015). *Predicting larger absorption cross-section in porphyrin dyes using DFT calculations. Journal of Porphyrins and Phthalocyanines* 19 (12): 1270–1278.

100 Santhanamoorthi, N., Lo, C.-M., and Jiang, J.-C. (2013). *Molecular design of porphyrins for dye-sensitized solar cells: a DFT / TDDFT study. Journal of Physical Chemistry Letters* 4: 524–530.

101 Yang, L.-N., Lin, L.-G., Meng, A.L., and Li, Z.-J. (2019). *Theoretical insights into co-sensitization mechanism in Zn-porphyrin and Y123 co-sensitized solar cells. Journal of Photochemistry and Photobiology A: Chemistry* 369: 25–33.

102 Lee, M.-J., Balanay, M.P., and Kim, D.H. (2012). *Molecular design of distorted push-pull porphyrins for dye-sensitized solar cells. Theoretical Chemistry Accounts* 131: 1269.

103 Daoudi, S., Semmeq, A., Badawi, M. et al. (2019). *Electronic structure and optical properties of isolated and TiO_2-grafted free base porphyrins for water oxidation: a challenging test case for DFT and TDDFT. Journal of Computational Chemistry* 40: 2530–2538.

104 Dreuw, A. and Head-Gordon, M. (2005). *Single-reference ab initio methods for the calculation of excited states of large molecules. Chemical Reviews* 105: 4009–4037.

105 Rydberg, P. and Olsen, L. (2009). *The accuracy of geometries for iron porphyrin complexes from density functional theory. The Journal of Physical Chemistry. A* 113: 11949–11953.

106 Liu, Y.-P. (2001). *Applications of effective core potentials and density functional theory to the spin states of iron porphyrin*. *Journal of Chemical Information and Computer Sciences* 41 (1): 22–29.

107 Strickland, N. and Harvey, J.N. (2007). *Spin-forbidden ligand binding to the ferrous-heme group: ab initio and DFT studies*. *The Journal of Physical Chemistry. B* 111: 841–852.

108 Ling, Y. and Zhang, Y. (2009). *Mossbauer, NMR, geometric, and electronic properties in S= 3/2 iron porphyrins*. *Journal of the American Chemical Society* 131 (18): 6386–6388.

109 Godbout, N., Havlin, R., Salzmann, R. et al. (1998). *Iron-57 NMR chemical shifts and Mössbauer quadrupole splittings in metalloporphyrins, ferrocytochrome c, and myoglobins: a density functional theory investigation*. *The Journal of Physical Chemistry. A* 102 (13): 2342–2350.

110 Khade, R.L., Fan, W., Ling, Y. et al. (2014). *Iron porphyrin carbenes as catalytic intermediates: structures, Mössbauer and NMR spectroscopic properties, and bonding*. *Angewandte Chemie* 126 (29): 7704–7708.

111 Ema, T., Miyazaki, Y., Shimonishi, J. et al. (2014). *Bifunctional porphyrin catalysts for the synthesis of cyclic carbonates from epoxides and CO_2: structural optimization and mechanistic study*. *Journal of the American Chemical Society* 136: 15270–15279.

112 Nielsen, I.M.B. and Leung, K. (2010). *Cobalt-porphyrin catalyzed electrochemical reduction of carbon dioxide in water. 1. A density functional study of intermediates*. *The Journal of Physical Chemistry. A* 114: 10166–10173.

113 Ortega-Guerrero, A., Fumanal, M., Capano, G., and Smit, B. (2020). *From isolated porphyrin ligands to periodic Al-PMOF: a comparative study of the optical properties using DFT/TDDFT*. *Journal of Physical Chemistry C* 124: 21751–21760.

114 Loipersberger, M., Zee, D.Z., Panetier, J.A. et al. (2020). *Computational study of an iron(II) polypyridine electrocatalyt for CO_2 reduction: key roles for intramolecular interactions in CO_2 binding and proton transfer*. *Inorganic Chemistry* 59: 8146–8160.

115 Davethu, P.A. and de Visser, S.P. (2019). *CO_2 reduction on an iron-porphyrin center: a computational study*. *The Journal of Physical Chemistry. A* 123: 6527–6535.

116 Mousavi, M., Hosseinnezhad, S., Hung, A.M., and Fini, E.H. (2019). *Preferential adsorption of nickel porphyrin to resin to increase asphaltene precipitation*. *Fuel* 236: 468–479.

117 Stoyanov, S.R., Yin, C.-X., Gray, M.R. et al. (2010). *Computational and experimental study of the structure, binding preferences and spectroscopy of nickel(II) and vanadyl porphyrins in petroleum*. *The Journal of Physical Chemistry. B* 114: 2180–2188.

118 Ahmed, R. and Manna, A.K. (2020). *Molecular-scale engineering of the charge-transfer excited states in non-covalently bound Zn-porphyrin and carbon fullerene based donor0acceptor complex*. *Physical Chemistry Chemical Physics* 22: 14822–14831.

119 Cramariuc, O., Hukka, T., Rantala, T.T., and Lemmetyinen, H. (2006). *TD-DFT description of photoabsorption and electron transfer in a covaletly bonded porphyrin-fullerene dyad*. *The Journal of Physical Chemistry. A* 110: 12470–12476.

120 Karachevtsev, V.A., Stepanian, S.G., Karachevtsev, M.V., and Adamowicz, L. (2018). *Graphene induced molecular flattening of meso-5, 10, 15, 20-tetraphenyl porphyrin: DFT calculations and molecular dynamics simulations*. *Computational and Theoretical Chemistry* 1133: 1–6.

121 Basiuk, E.V., Huerta, L., and Basiuk, V.A. (2019). *Noncovalent bonding of 3d metal (II) phthalocyanines with single-walled carbon nanotubes: a combined DFT and XPS study*. *Applied Surface Science* 470: 622–630.

122 Mack, J., Stone, J., and Nyokong, T. (2014). *Trends in the TD-DFT calculations of porphyrins and phthalocyanine analogs. Journal of Porphyrins and Phthalocyanines* 18: 630–641.

123 Osadchuk, I., Borovkov, V., Aav, R., and Clot, E. (2020). *Benchmarking computational methods and influence of guest conformation on chirogenesis in zinc porphyrin complexes. Physical Chemistry Chemical Physics* 22: 11025–11037.

124 Rintoul, L., Harper, S.R., and Arnold, D.P. (2013). *A systematic theoretical study of the electronic structures of porphyrin dimers: DFT and TD-DFT calculations on diporphyrins linked by ethane, ethene, ethyne, imine and azo bridges. Physical Chemistry Chemical Physics* 15: 18951–18964.

125 Hu, Z., Sun, Z., and Sun, H. (2017). *Design of zinc porphyrin-perylene diimide donor-bridge-acceptor chromophores for large second-order nonlinear optical response: a theoretical exploration. International Journal of Quantum Chemistry* 118: e25536.

126 Schindler, J., Kupfer, S., Ryan, A.A. et al. (2018). *Sterically induced distortions of nickel (II) porphyrins–comprehensive investigation by DFT calculations and resonance Raman spectroscopy. Coordination Chemistry Reviews* 360: 1–16.

127 Tsai, H.-H. and Simpson, M.C. (2003). *HBFF-SVD force field treatment of Ni(II) porphine: important long range cross terms. The Journal of Physical Chemistry. A* 107: 526–541.

128 Cai, Z.-L., Crossley, M.J., Reimers, J.R. et al. (2006). *Density functional theory for charge transfer: the nature of the N-bands of porphyrins and chlorophylls revealed through CAM-B3LYP, CASPT2, and SAC-CI calculations. The Journal of Physical Chemistry. B* 110: 15624–15632.

129 Ghosh, S. and Singh, J.K. (2019). *Hydrogen adsorption in pyridine bridged porphyrin-covalent organic framework. International Journal of Hydrogen Energy* 44 (3): 1782–1796.

130 Tay, A.C.Y., Frogley, B.J., Ware, D.C. et al. (2019). *Tetrahedral pegs in square holes: stereochemistry of diboron porphyrazines and phthalocyanines. Angewandte Chemie, International Edition* 58: 3057–3061.

131 Torrent-Sucarrat, M., Navarro, S., Cossío, F.P. et al. (2017). *Relevance of the DFT method to study expanded porphyrins with different topologies. Journal of Computational Chemistry* 38 (32): 2819–2828.

132 Marcos, E., Anglada, J.M., and Torrent-Sucarrat, M. (2012). *Theoretical study of the switching between Huckel and Mobius topologies for expanded porphyrins. The Journal of Physical Chemistry. C* 116 (45): 24358–24366.

133 Vosko, S.H., Wilk, L., and Nusair, M. (1980). *Accurate spin-dependent electron liquid correlation energies for local spin density calculations: a critical analysis. Canadian Journal of Physics* 58 (8): 1200–1211.

134 Perdew, J.P. and Wang, Y. (1992). *Accurate and simple analytic representation of the electron-gas correlation energy. Physical Review B* 45: 13244.

135 Perdew, J.P., Burke, K., and Ernzerhof, M. (1996). *Generalized gradient approximation made simple. Physical Review Letters* 77 (18): 3865–3868.

136 Perdew, J.P., Chevary, J.A., Vosko, S.H. et al. (1992). *Atoms, molecules, solids, and surfaces: applications of the generalized gradient approximation for exchange and correlation. Physical Review B* 46 (11): 6671–6687.

137 Perdew, J.P. (1986). *Density-functional approximation for the correlation energy of the inhomogeneous electron gas. Physical Review B* 33 (12): 8822–8824.

138 Tao, J., Perdew, J.P., Staroverov, V.N., and Scuseria, G.E. (2003). *Climbing the density functional ladder: nonempirical meta–generalized gradient approximation designed for molecules and solids*. *Physical Review Letters* 91 (14): 146401.

139 Zhao, Y. and Truhlar, D.G. (2006). *A new local density functional for maingroup thermochemistry, transition metal bonding, thermochemical kinetics, and noncovalent interactions*. *The Journal of Chemical Physics* 125 (19): 194101.

140 Adamo, C. and Barone, V. (1999). *Toward reliable density functional methods without adjustable parameters: the PBE0 model*. *The Journal of Chemical Physics* 110 (13): 6158–6170.

141 Becke, A.D. (1997). *Density-functional thermochemistry. V. Systematic optimization of exchange-correlation functionals*. *The Journal of Chemical Physics* 107 (20): 8554–8560.

142 Staroverov, V.N., Scuseria, G.E., Tao, J., and Perdew, J.P. (2003). *Comparative assessment of a newnonempirical density functional: molecules and hydrogen-bonded complexes*. *The Journal of Chemical Physics* 119 (23): 12129–12137.

143 Zhao, Y. and Truhlar, D.G. (2008). *The M06 suite of density functionals for main group thermochemistry, thermochemical kinetics, noncovalent interactions, excited states, and transition elements: two new functionals and systematic testing of four M06-class functionals and 12 other functionals*. *Theoretical Chemistry Accounts* 120: 215–241.

144 Yanai, T., Tew, D.P., and Handy, N.C. (2004). *A new hybrid exchange–correlation functional using the Coulomb-attenuating method (CAM-B3LYP)*. *Chemical Physics Letters* 393 (1–3): 51–57.

145 Chai, J.-D. and Head-Gordon, M. (2008). *Systematic optimization of long-range corrected hybrid density functionals*. *The Journal of Chemical Physics* 128 (8): 084106.

146 Grimme, S. (2006). *Semiempirical hybrid density functional with perturbative second-order correction*. *The Journal of Chemical Physics* 124 (3): 034108.

147 Hui, K. and Chai, J.-D. (2016). *SCAN-based hybrid and double-hybrid density functionals from models without fitted parameters*. *The Journal of Chemical Physics* 144 (4): 044114.

148 Goerigk, L. and Grimme, S. (2011). *Efficient and accurate double-hybrid-meta-GGA density functionals-evaluation with the extended GMTKN30 database for general main group thermochemistry, kinetics, and noncovalent interactions*. *Journal of Chemical Theory and Computation* 7: 291–309.

149 Casanova-Páez, M., Dardis, M., and Goerigk, L. (2019). *wB2PLYP and wB2GPPLYP: the first two double-hybrid density functionals with long-range correction optimized for excitation energies*. *Journal of Chemical Theory and Computation* 15: 4735–4744.

150 Mardirossian, N. and Head-Gordon, M. (2018). *Survival of the most transferable at the top of Jacob's ladder: defining and testing the wB97M(2) double hybrid density functional*. *The Journal of Chemical Physics* 148 (24): 241736.

151 Kozuch, S. and Martin, J.M.L. (2013). *Spin-component-scaled double hybrids: an extensive search for the best fifth-rung functionals blending DFT and perturbation theory*. *Journal of Computational Chemistry* 34: 2327–2344.

152 Grimme, S., Antony, J., Erlich, S., and Krieg, H. (2010). *A consistent and accurate ab initio parametrization of density functional dispersion correction (DFT-D) for the 94 elements H-Pu*. *The Journal of Chemical Physics* 132: 154104.

153 Smith, D.G.A., Burns, L.A., Patkowski, K., and Sherrill, C.D. (2010). *Revised damping parameters for the D3 dispersion correction to density functional theory*. *Journal of Physical Chemistry Letters* 7 (12): 2197–2203.

154 Schröder, H., Creon, A., and Schwabe, T. (2015). *Reformulation of the D3(Becke–Johnson) dispersion correction without resorting to higher than C_6 dispersion coefficients*. *Journal of Chemical Theory and Computation* 11: 3163–3170.

155 Vydrov, O.A. and Voorhis, T.V. (2010). *Nonlocal van der Waals density functional: the simpler the better*. *The Journal of Chemical Physics* 133: 244103.

156 Grimme, S., Erlich, S., and Goerigk, L. (2011). *Effect of the damping function in dispersion corrected density functional theory*. *Journal of Computational Chemistry* 32: 1456–1465.

157 Grimme, S. (2006). *Semiempirical GGA-type density functional constructed with a long-range dispersion correction*. *Journal of Computational Chemistry* 27: 1787–1799.

158 Grimme, S. (2004). *Accurate description of van der Waals complexes by density functional theory including empirical correction*. *Journal of Computational Chemistry* 25: 1463–1473.

159 Martin, J.M.L. and Santra, G. (2020). *Empirical double-hybrid density functional theory: A 'Third Way' in between WFT and DFT*. *Israel Journal of Chemistry* 60: 787–804.

160 Sancho-García, J.C. and Adamo, C. (2013). *Double-hybrid density functionals: merging wavefunctiona dn density approaches to get the best of both worlds*. *Physical Chemistry Chemical Physics* 15: 14581–14594.

161 Jentzen, W., Turowska-Tyrk, I., Scheidt, W.R., and Shelnutt, J.A. (1996). *Planar solid-state and solution structures of (porphinato)nickel(II) as determined by X-ray diffraction and resonance Raman spectroscopy*. *Inorganic Chemistry* 35: 3559–3567.

162 Kozlowski, P.M., Rush, T.S.I., Jarzecki, A. et al. (1999). *DFT-SQM force field for nickel porphine: intrinisic ruffling*. *The Journal of Physical Chemistry. A* 103: 1357–1366.

163 de Visser, S.P. and Stillman, M.J. (2016). *Challenging density functional theory calculations with hemes and porphyrins*. *International Journal of Molecular Sciences* 17: 519.

164 Zhao, Y., Schultz, N.E., and Truhlar, D.G. (2006). *Design of density Functionals by combining the method of constraint satisfaction with parametrization for thermochemistry, thermochemical kinetics, and noncovalent interactions*. *Journal of Chemical Theory and Computation* 2: 364–382.

165 Becke, A.D. (1993). *A new mixing of Hartree–Fock and local density-functional theories*. *The Journal of Chemical Physics* 98 (2): 1372–1377.

166 Boese, A.D. and Martin, J.M.L. (2004). *Development of density functionals for thermochemical kinetics*. *The Journal of Chemical Physics* 121 (8): 3405–3416.

167 Chai, J.-D. and Head-Gordon, M. (2008). *Long-range corrected hybrid density functionals with damped atom–atom dispersion corrections*. *Physical Chemistry Chemical Physics* 10: 6615–6620.

168 Runge, E. and Gross, E.K.U. (1984). *Density-functional theory for time-dependent systems*. *Physical Review Letters* 52 (12): 997–1000.

169 Adamo, C. and Jacquemin, D. (2013). *The calculations of excited-state properties with time-dependent density functional theory*. *Chemical Society Reviews* 42 (3): 845–856.

170 Mai, S. and González, L. (2020). *Molecular photochemistry: recent developments in theory*. *Angewandte Chemie, International Edition* 59: 16832–16846.

171 Maitra, N.T. (2016). *Perspective: fundamental aspects of time-dependent density functional theory*. *The Journal of Chemical Physics* 144: 220901.

172 Laurent, A.D. and Jacquemin, D. (2013). *TD-DFT benchmarks: a review*. *International Journal of Quantum Chemistry* 113: 2019–2039.

173 Casida, M.E. and Huix-Rotllant, M. (2012). *Progress in time-dependent density-functional theory*. *Annual Review of Physical Chemistry* 63: 287–323.

174 Santoro, F. and Jacquemin, D. (2016). *Going beyond the vertical approximation with time-dependent density functional theory. WIREs Computational Molecular Science* 6: 460–486.

175 Fuks, J.I. (2016). *Time-dependent density functional theory for charge-transfer dynamics: review of the causes of failure and success. European Physical Journal B* 89: 236.

176 Zhou, P. (2018). *Why the lowest electronic excitations of rhodamines are overestimated by time-dependent density functional theory. International Journal of Quantum Chemistry* 118: e25780.

177 Rozzi, C.A., Falke, S.M., Spallanzani, N. et al. (2013). *Quantum coherence controls the charge separation in a prototypical artificial light-harvesting system. Nature Communications* 4: 1602.

178 Faraday, M. (1825). *On new compounds of carbon and hydrogen, and on certain other products obtained during the decomposition of oil by heat. Philosophical Transactions. Royal Society of London* 115: 440–466.

179 *Michael Faraday's sample of benzene, The Royal Institution*. [cited 2020 28 December]; https://www.rigb.org/our-history/iconic-objects/iconic-objects-list/faraday-benzene (accessed 17 November 2021).

180 Liu, Y., Kilby, P., Frankcombe, T.J., and Schmidt, T.W. (2020). *The electronic structure of benzene from a tiling of the correlated 126-dimensional wavefunction. Nature Communications* 11: 1210.

181 Furukawa, S., Fujita, M., Kanatomi, Y. et al. (2018). *Double aromaticity arising from sigma- and pi-rings. Communications Chemistry* 1: 60.

182 Kekulé, A. (1865). *Sur la constitution des substances aromatiques. Bulletin de la Société Chimique de France* 3: 98–110.

183 Kekulé, A. (1866). *Untersuchungen über aromatische Verbindungen. I. Ueber die Constitution der aromatischen Verbindungen. Justus Liebigs Annalen der Chemie* 137: 129–196.

184 Kekulé, A. (1866). *Lehrbuch der organischen Chemie*, vol. 2. Erlangen: Verlag von Ferdinand Enke.

185 Balaban, A.T., von Rague Schleyer, P., and Rzepa, H.S. (2005). *Crocker, not Armit and Robinson, begat the six aromatic electrons. Chemical Reviews* 105 (10): 3436–3447.

186 Kekulé, A. (1872). *Ueber Einegen Condesationsproducte des Aledhyds. Justus Liebigs Annalen der Chemie* 162 (1): 77–123.

187 von Ragué Schleyer, P. (2005). *Introduction: delocalization - pi and sigma. Chemical Reviews* 105 (10): 3433–3435.

188 Rocke, A.J. (2015). *It began with a daydream: the 150th anniversary of the Kekulé benzene structure. Angewandte Chemie, International Edition* 54: 46–50.

189 Rocke, A.J. (1981). *Kekulé, Bulterov, and the historiography of the theory of chemical structure*; brit. *The British Journal for the History of Science* 14 (46): 27–57.

190 Rocke, A.J. (1988). *Kekulé's benzene theory and the appraisal of scientific theories*. In: *Scrutinizing Science: Empirical Studies of Scientific Change* (ed. A. Donovan and R. Laudan), 145–161. Springer Netherlands; Kluwer Academic Publishers.

191 Merino, G. and Solà, M. (2016). *Celebrating the 150th anniversary of the Kekulé benzene structure. Physical Chemistry Chemical Physics* 18: 11587–11588.

192 Berson, J. A. (1999). Erich Hückel and the theory of aromaticity: reflections on theory and experiment. In: *Chemical Creativity: Ideas from the Work of Woodward, Hückel, Meerwein, and Others*. 33–75. Wiley-VCH.

193 Dewar, M.J.S. and de Llano, C. (1969). *Ground states of conjugated molecules. Journal of the American Chemical Society* 91 (4): 789–795.

194 Breslow, R. (1973). *Antiaromaticity. Accounts of chemical research* 6 (12): 393–398.

195 Heilbronner, E. (1989). *Why do some molecules have symmetry different from that expected? Journal of Chemical Education* 66 (6): 471–478.

196 Hiberty, P.C., Danovich, D., Shurki, A., and Shaik, S. (1995). *Why does benzene possess a D6h symmetry? A quasiclassical state approach for probing pi-bonding and delocalization energies. Journal of the American Chemical Society* 117: 7760–7768.

197 Huber, H. (1982). *Is hexazine stable? Angewandte Chemie, International Edition* 21 (1): 64–65.

198 Ha, T.-K., Cimiraglia, R., and Nguyen, M.T. (1981). *Can hexazine (N_{6-}) be stable? Chemical Physics Letters* 83 (2): 317–319.

199 Glukhovtsev, M.N. and von Rague Schleyer, P. (1992). *Structures, bonding and energies of N_6 isomers. Chemical Physics Letters* 198 (6): 547–554.

200 Saxe, P. and Schaeffer, H.F.I. (1983). *Cyclic D_{6h} hexaazabenzene - a relative minimum on the N_6 potential energy hypersurface? Journal of the American Chemical Society* 105 (7): 1760–1764.

201 Shaik, S., Shurki, A., Danovich, D., and Hiberty, P.C. (2001). *A different story of pi-delocalization - the distortivity of pi-electrons and its chemical modifications. Chemical Reviews* 101: 1501–1539.

202 Chong, D.P. (2019). *Computational study of the structures and photoelectron spectra of 12 azabenzenes. Canadian Journal of Chemistry* 97: 697–703.

203 Kutzelnigg, W. (1984). *Chemical bonding in higher main group elements. Angewandte Chemie, International Edition* 23: 272–295.

204 Garratt, P.J. (1986). *Aromaticity*. Wiley-Interscience; John Wiley & Sons.

205 Martín, N. and Scott, L.T. (2015). *Challenges in aromaticity: 150 years after Kekulé's benzene. Chemical Society Reviews* 44: 6397–6400.

206 Aihara, J.-i. (2008). *Dimensionality of aromaticity. Bulletin of the Chemical Society of Japan* 81 (2): 241–247.

207 Chen, Z., Wannere, C.S., Corminboeuf, C. et al. (2005). *Nucleus-independent chemical shifts (NICS) as an aromaticity criterion. Chemical Reviews* 105: 3842–3888.

208 Gershoni-Poranne, R. and Stanger, A. (2015). *Magnetic criteria of aromaticity. Chemical Society Reviews* 44: 6597–6615.

209 Gomes, J.A.N.F. and Mallion, R.B. (2001). *Aromaticity and ring currents. Chemical Reviews* 101: 1349–1383.

210 De Proft, F. and Geerlings, P. (2001). *Conceptual and computational DFT in the study of aromaticity. Chemical Reviews* 101: 1451–1464.

211 Jug, K., Hiberty, P.C., and Shaik, S. (2001). *Sigma-pi energy separation in modern electronic theory for ground states of conjugated systems. Chemical Reviews* 101: 1477–1500.

212 Krygowski, T.M. and Cyrañski, M.K. (2001). *Structural aspects of aromaticity. Chemical Reviews* 101: 1385–1419.

213 Krygowski, T.M., Szatylowicz, H., Stasyuk, O.A., and Dominikowska, J. (2014). *Aromaticity from the viewpoint of molecular geometry: application to planar systems. Chemical Reviews* 114: 6383–6422.

214 Mulder, J.J.C. (1998). *The pi-electron-system of monocyclic polyenes $C_{2n}H_{2n}$ with alternating single and double bonds. Journal of Chemical Education* 75 (5): 594–595.

215 von Ragué Schleyer, P. (2001). *Introduction: aromaticity. Chemical Reviews* 101 (5): 1115–1117.

216 Wu, J.I., Fernández, I., and Schleyer, P.v.R. (2012). *Description of aromaticity in porphyrinoids. Journal of the American Chemical Society* 135 (1): 315–321.

217 Aihara, J.-I., Nakagami, Y., Sekine, R., and Makino, M. (2012). *Validity and limitations of the bridged annulene model for porphyrins. The Journal of Physical Chemistry. A* 116 (47): 11718–11730.

218 Vogel, E. (2011). *From small carbocyclic rings to porphyrins: a personal account of 50 years of research. Angewandte Chemie, International Edition* 50: 4278–4287.

219 Bröring, M. (2011). *How should aromaticity be described in porphyrinoids? Angewandte Chemie, International Edition* 50: 2436–2438.

220 Ghosh, A., Larsen, S., Conradie, J., and Foroutan-Nejad, C. (2018). *Local versus global aromaticity in azuliporphyrin and benziporphyrin derivatives. Organic & Biomolecular Chemistry* 16 (42): 7964–7970.

221 Lash, T.D. (1999). *Carbaporphyrinoids: taking the heterocycle out of nature's [18] annulene. Synlett* 3: 279–295.

222 Lash, T.D. (2011). *Origin of aromatic character in porphyrinoid systems. Journal of Porphyrins and Phthalocyanines* 15 (11n12): 1093–1115.

223 Vogel, E. (1993). *The porphyrins from the 'annulene chemist's' perspective. Pure & Applied Chemistry* 65 (1): 143–152.

224 Casademont-Reig, I., Woller, T., Contreras-García, J. et al. (2018). *New electron delocalization tools to describe the aromaticity in porphyrinoids. Physical Chemistry Chemical Physics* 20 (4): 2787–2796.

225 Kruszewski, J. and Krygowski, T.M. (1972). *Definition of aromaticity basing on the harmonic oscillator model. Tetrahedron Letters* 36: 3839–3842.

226 Krygowski, T.M. and Cyrañski, M.K. (1996). *Separation of the energetic and geometric contributions to the aromaticity of pi-electron carbocyclics. Tetrahedron* 32 (5): 1713–1722.

227 Dobrowolski, J.C. (2019). *Three queries about the HOMA index. ACS Omega* 4: 18699–18710.

228 Cyrañski, M.K., Krygowski, T.M., Wisiorowski, M. et al. (1998). *Global and local aromaticity in porphyrins: an analysis based on molecular geometries and nucleus-independent chemical shifts. Angewandte Chemie International Edition* 37 (1–2): 177–180.

229 Havenith, R.W.A., Meijer, A.J.H.M., Irving, B.J., and Fowler, P.W. (2009). *Comparison of ring currents evaluated consistently at density functional and Hartree-Fock levels. Molecular Physics* 107 (23–24): 2591–2600.

230 Merino, G., Heine, T., and Seifert, G. (2004). *The induced magnetic field in cyclic molecules. Chemistry: A European Journal* 10: 4367–4371.

231 von Ragué Schleyer, P., Maerker, C., Dransfeld, A. et al. (1996). *Nucleus-independent chemical shifts: a simple and efficient aromaticity probe. Journal of the American Chemical Society* 118: 6317–6318.

232 Ellis, J., Jackson, A.H., Kenner, G.W., and Lee, J. (1960). *Porphyrin nuclear magnetic resonance spectra. Tetrahedron Letters* 2: 23–27.

233 Becker, E.D. and Bradley, R.B. (1959). *Effects of "Ring Currents" on the NMR spectra of porphyrins. The Journal of Chemical Physics* 31 (5): 1413–1414.

234 Geuenich, D., Hess, K., Köhler, F., and Herges, R. (2005). *Anisotropy of the induced current density (ACID), a general method to quantify and visualize electronic delocalization*. *Chemical Reviews* 105 (10): 3758–3772.

235 Steiner, E. and Fowler, P.W. (2002). *Ring currents in the porphyrins: a four-orbital model*. *ChemPhysChem* 3 (1): 114–116.

236 Steiner, E. and Fowler, P.W. (2004). *Diamagnetic and paramagnetic ring currents in expanded porphyrins*. *Organic & Biomolecular Chemistry* 2: 34–37.

237 Steiner, E. and Fowler, P.W. (2006). *The shell structure of pi ring currents in the expanded porphyrin amethyrin*. *Organic & Biomolecular Chemistry* 4: 2473–2476.

238 Fliegl, H., Özcan, N., Mera-Adasme, R. et al. (2013). *Aromatic pathways in thieno-bridged porphyrins: understanding the influence of the direction of the thiophene ring on the aromatic character*. *Molecular Physics* 111 (9–11): 1364–1372.

239 Fliegl, H., Sundholm, D., Taubert, S. et al. (2009). *Magnetically induced current densities in aromatic, antiaromatic, homoromatic, and nonaromatic hydrocarbons*. *The Journal of Physical Chemistry. A* 113: 8668–8676.

240 Fliegl, H., Taubert, S., Lehtonen, O., and Sundholm, D. (2011). *The gauge including magnetically induced current method*. *Physical Chemistry Chemical Physics* 13: 20500–20518.

241 Aihara, J.-i. (2008). *Macrocyclic conjugation pathways in porphyrins*. *The Journal of Physical Chemistry. A* 112 (23): 5305–5311.

242 Aihara, J.-i., Kimura, E., and Krygowski, T.M. (2008). *Aromatic conjugation pathways in porphyrins*. *Bulletin of the Chemical Society of Japan* 81 (7): 826–835.

243 Aihara, J.-i. and Makino, M. (2010). *Prediction of the main macrocyclic conjugation pathway for porphyrinoids from the ring current distribution*. *Organic & Biomolecular Chemistry* 8: 261–266.

244 Hiramatsu, S., Sugawara, S., Kojima, S., and Yamamoto, Y. (2013). *Synthesis of the most-anti-aromatic 16pi porphyrin: an octaethylporphyrin zinc(II) complex with no meso-substituents*. *Journal of Porphyrins and Phthalocyanines* 17: 1183–1187.

245 Kakui, T., Sugawara, S., Hirata, Y. et al. (2011). *Anti-aromatic 16pi porphyrin-metal complexes with meso-alkyl substituents*. *Chemistry: A European Journal* 17: 7768–7771.

246 Sugawara, S., Kodama, M., Hirata, Y. et al. (2011). *Synthesis and characterization of the most distorted 16π porphyrin: 16π octaisopropyltetraphenylporphyrin (OiPTPP)*. *Journal of Porphyrins and Phthalocyanines* 15 (11n12): 1326–1334.

247 Yamamoto, Y., Hirata, Y., Kodama, M. et al. (2010). *Synthesis, reactions, and electronic properties of 16 pi-electron octaisobutyltetraphenylporphyrin*. *Journal of the American Chemical Society* 132: 12627–12638.

248 Yamamoto, Y., Yamamoto, A., Furuta, S.-y. et al. (2005). *Synthesis and structure of 16 pi-octaalkyltetraphenylporphyrins*. *Journal of the American Chemical Society* 127: 14540–14541.

249 Sugawara, S., Hirata, Y., Kojima, S. et al. (2012). *Synthesis, characterization and spectroscopic analysis of antiaromatic benzofused metalloporphyrins*. *Chemistry: A European Journal* 18: 3566–3581.

250 Cissell, J.A., Vaid, T.P., and Yap, G.P.A. (2006). *The doubly oxidized, antiaromatic tetraphenylporphyrin complex [Li(TPP)][BF_4]*. *Organic Letters* 8 (11): 2401–2404.

251 Vaid, T.P. (2011). *A porphyrin with a C=C unit at its center*. *Journal of the American Chemical Society* 133: 15838–15841.

252 Cissell, J.A., Vaid, T.P., and Rheingold, A.L. (2005). *An antiaromatic porphyrin complex: tetraphenylporphyrinato(silicon)(L)$_2$ (L = THF or pyridine)*. *Journal of the American Chemical Society* 127: 12212–12213.

253 Cissell, J.A., Vaid, T.P., and Yap, G.P.A. (2007). *Reversible oxidation state change in germanium(tetraphenylporphyrin) induced by a dative ligand: aromatic Ge^{II}(TPP) and antiaromatic Ge^{IV}(TPP)(pyridine)$_2$*. *Journal of the American Chemical Society* 129: 7841–7847.

254 Song, H.-e., Cissell, J.A., Vaid, T.P., and Holten, D. (2007). *Photophysics of reduced silicon tetraphenylporphyrin*. *The Journal of Physical Chemistry. B* 111: 2138–2142.

255 Chen, X.-G., Liu, C., Shen, D.-M., and Chen, Q.-Y. (2009). *N-substitution reactions of 20-pi-electron beta-tetrakis(trifluoromethyl)-meso-tetraphenylporphyrin*. *Synthesis* 22: 3860–3868.

256 Liu, C., Shen, D.-M., and Chen, Q.-Y. (2007). *Synthesis and reactions of 20 pi-electron beta-tetrakis(trifluoromethyl)-meso-tetraphenylporphyrins*. *Journal of the American Chemical Society* 129: 5814–5815.

257 Weiss, A., Hodgson, M.C., Boyd, P.D.W. et al. (2007). *Diboryl and diboranyl porphyrin complexes: synthesis, structural motifs, and redox chemistry: diborenyl porphyrin or diboranyl isophlorin*. *Chemistry: A European Journal* 13: 5982–5993.

258 Nozawa, R., Tanaka, H., Cha, W.-Y. et al. (2016). *Stacked antiaromatic porphryins*. *Nature Communications* 7: 13620.

259 Brennan, T.D., Scheidt, W.R., and Shelnutt, J.A. (1988). *New crystalline phase of (octaethylporphinato)nickel(II). Effects of pi-pi interactions on molecular structure and resonance Raman spectra*. *Journal of the American Chemical Society* 110 (12): 3919–3924.

260 Cullen, D.L. and Meyer, E.F.J. (1974). *Crystal and molecular structure of the triclinic form of 1,2,3,4,5,6,7,8-octaethylporphinatonickel(II). A comparison with the tetragonal form*. *Journal of the American Chemical Society* 96 (7): 2095–2102.

261 Meyer, E.F.J. (1972). *The crystal and molecular structure of nickel(II)octaethylporphyrin*. *Acta Crystallographica, Section B: Structural Science* 28 (7): 2162–2167.

262 Anderson, K.K., Hobbs, J.D., Luo, L. et al. (1993). *Planar-nonplanar conformational equilibrium in metal derivatives of octaethylporphyrin and meso-nitrooctaethylporphyrin*. *Journal of the American Chemical Society* 115: 12346–12352.

263 Jentzen, W., Unger, E., Karvounis, G. et al. (1996). *Conformational properties of nickel(II) octaethylporphyrin in solution. 1. Resonance excitation profiles and temperature dependence of structure-sensitive Raman lines*. *The Journal of Physical Chemistry* 100: 14184–14191.

264 Alden, R.G., Crawford, B.A., Doolen, R. et al. (1989). *Ruffling of nickel(II) octaethylporphyrin in solution*. *Journal of the American Chemical Society* 111: 2070–2072.

265 Golubchikov, O.A., Pukhovskaya, S.G., and Kuvshinova, E.M. (2005). *Structures and properties of spatially distorted porphyrins*. *Russian Chemical Reviews* 74 (3): 249–264.

266 Senge, M.O. (2006). *Exercises in molecular gymnastics - bending, stretching and twisting porphyrins*. *Chemical Communications* 2006: 243–256.

267 Senge, M.O., MacGowan, S.A., and O'Brien, J.M. (2015). *Conformational control of cofactors in nature - the influence of protein-induced macrocycle distortion on the biological function of tetrapyrroles*. *Chemical Communications* 51: 17031–17063.

268 Jentzen, W., Ma, J.-G., and Shelnutt, J.A. (1998). *Conservation of the conformation of the porphyrin macrocycle in hemoproteins*. *Biophysical Journal* 74: 753–763.

269 Huang, Q., Medforth, C.J., and Schweitzer-Stenner, R. (2005). *Nonplanar heme deformations and excited state displacements in nickel porphyrins detected by Raman spectroscopy at Soret excitation. The Journal of Physical Chemistry. A* 109: 10493–10502.

270 Hobbs, J.D. and Shelnutt, J.A. (1995). *Conserved nonplanar heme distortions in cytochromes c. Journal of Protein Chemistry* 14 (1): 19–25.

271 Shelnutt, J.A., Song, X.-Z., Ma, J.-G. et al. (1998). *Nonplanar porphyrins and their significance in proteins. Chemical Society Reviews* 27: 31–41.

272 Franzen, S., Lambry, J.C., Bohn, B. et al. (1994). *Direct evidence for the role of haem doming as the primary event in the cooperative transition of haemoglobin. Nature Structural Biology* 1 (4): 230–233.

273 Friedman, J.M., Rousseau, D.L., Ondrias, M.R., and Stepnoski, R.A. (1982). *Transient Raman study of hemoglobin: structural dependence of the iron-histidine linkage. Science* 218: 1244–1246.

274 Haddad, R.E., Gazeau, S., Pecaut, J. et al. (2003). *Origin of the red shifts in the optical absorption bands of nonplanar tetraalkylporphyrins. Journal of the American Chemical Society* 125: 1253–1268.

275 Hobbs, J.D., Majumder, S.A., Luo, L. et al. (1994). *Structural heterogeneity and coordination chemistry of nickel(II) octaethyl-meso-nitroporphyrins. Journal of the American Chemical Society* 116: 3161–3270.

276 Jentzen, W., Simpson, M.C., Hobbs, J.D. et al. (1995). *Ruffling in a series of nickel (II) meso-tetrasubstituted porphyrins as a model for the conserved ruffling of the heme of cytochromes c. Journal of the American Chemical Society* 117 (45): 11085–11097.

277 Jentzen, W., Song, X.-Z., and Shelnutt, J.A. (1997). *Structural characterization of synthetic and protein-bound porphyrins in terms of the lowest-frequency normal coordinates of the macrocycle. The Journal of Physical Chemistry B* 101: 1684–1699.

278 Shelnutt, J.A. (1999). *Molecular simulations and normal-coordinate structural analysis of porphyrins and heme proteins.* In: *The Porphyrin Handbook* (ed. K.M. Kadish, K.M. Smith and R. Guilard), 167–224. Academic Press.

279 Wertsching, A.K., Koch, A.S., and DiMagno, S.G. (2001). *On the negligible impact of ruffling on the electronic spectra of porphine, tetramethylporphyrin, and perfluoroalkylporphyrins. Journal of the American Chemical Society* 123: 3932–3939.

280 Heilbronner, E. (1964). *Huckel molecular orbitals of Mobius-type conformations of annulenes. Tetrahedron Letters* 29: 1923–1928.

281 Ajami, D., Oeckler, O., Simon, A., and Herges, R. (2003). *Synthesis of Mobius aromatic hydrocarbon. Nature* 426: 819–821.

282 Herges, R. (2006). *Topology in chemistry: designing Mobius molecules. Chemical Reviews* 106: 4820–4842.

283 Rzepa, H.S. (2005). *Möbius aromaticity and delocalization. Chemical Reviews* 105 (10): 3697–3715.

284 Jux, N. (2008). *The porphyrin twist: Hückel and Möbius aromaticity. Angewandte Chemie International Edition* 47 (14): 2543–2546.

285 Osuka, A. and Saito, S. (2011). *Expanded porphyrins and aromaticity. Chemical Communications* 47 (15): 4330–4339.

286 Yoon, Z.S., Osuka, A., and Kim, D. (2009). *Möbius aromaticity and antiaromaticity in expanded porphyrins. Nature Chemistry* 1 (2): 113.

287 Alka, A., Shetti, V.S., and Ravikanth, M. (2019). *Coordination chemistry of expanded porphyrins. Coordination Chemistry Reviews* 401: 21063.

288 Lim, J.M., Yoon, Z.S., Shin, J.-Y. et al. (2009). *The photophysical properties of expanded porphyrins: relationships between aromaticity, molecular geometry and non-linear optical properties. Chemical Communications* 2009: 261–273.

289 Roznyatovskiy, V.V., Lee, C.-H., and Sessler, J.L. (2013). *pi-Extended isomeric and expanded porphyrins. Chemical Society Reviews* 42: 1921–1933.

290 Sessler, J.L., Gross, Z., and Furata, H. (2017). *Introduction: expanded, contracted, and isomeric porphyrins. Chemical Reviews* 117: 2201–2202.

291 Shin, J.-Y., Kim, K.S., Yoon, M.-C. et al. (2010). *Aromaticity and photophysical properties of various topology-controlled expanded porphyrins. Chemical Society Reviews* 39 (8): 2751–2767.

292 Sung, Y.M., Oh, J., Cha, W.-Y. et al. (2016). *Control and switching of aromaticity in various all-aza-expanded porphyrins: spectroscopic and theoretical analyses. Chemical Reviews* 117: 2257–2312.

293 Tanaka, T. and Osuka, A. (2016). *Chemistry of meso-aryl-substituted expanded porphyrins: aromaticity and molecular twist. Chemical Reviews* 117 (4): 2584–2640.

294 Stępień, M., Latos-Grażyński, L., Sprutta, N. et al. (2007). *Expanded porphyrin with a split personality: a Hückel–Möbius aromaticity switch. Angewandte Chemie International Edition* 46 (41): 7869–7873.

295 Stuyver, T., Perrin, M., Geerlings, P. et al. (2018). *Conductance switching in expanded porphyrins through aromaticity and topology changes. Journal of the American Chemical Society* 140: 1313–1326.

296 Peeks, M.D., Jirasek, M., Claridge, T.D.W., and Anderson, H.L. (2019). *Global aromaticity and antiaromaticity in porphyrin nanoring anions. Angewandte Chemie, International Edition* 58: 15717–15720.

297 Baird, N.C. (1972). *Quantum organic photochemistry. II. Resonance and aromaticity in the lowest ^{3}pi-pi* state of cyclic hydrocarbon. Journal of the American Chemical Society* 94 (14): 4941–4948.

298 Ottosson, H. and Borbas, K.E. (2015). *A light-switched yin and yang pair. Nature Chemistry* 7: 373–375.

299 Sung, Y.M., Oh, J., Kim, W. et al. (2015). *Switching between aromatic and antiaromatic 1,3-Phenylene-strapped [26]- and [28]Hexaphyrins upon passage to the singlet excited state. Journal of the American Chemical Society* 137: 11856–11859.

300 Sung, Y.M., Yoon, M.-C., Lim, J.M. et al. (2015). *Reversal of Hückel (anti)aromaticity in the lowest triplet states of hexaphyrins and spectroscopic evidence for Baird's rule. Nature Chemistry* 7: 418–422.

301 Cho, S., Yoon, Z.S., Kim, K.S. et al. (2010). *Defining spectroscopic features of heteroannulenic antiaromatic porphyrinoids. Journal of Physical Chemistry Letters* 1: 895–900.

302 Hong, Y., Oh, J., Sung, Y.M. et al. (2017). *The extension of Baird's rule to twisted heteroannulenes: aromaticity reversal of singly and doubly twisted molecular systems in the lowest triplet state. Angewandte Chemie* 129 (11): 2978–2982.

303 Ueda, M., Jorner, K., Sung, Y.M. et al. (2017). *Energetics of Baird aromaticity supported by inversion of photoexcited chiral [4n]annulene derivatives. Nature Communications* 8: 346.

12

Photoinduced Electron and Energy Transfer

Eugeny A. Ermilov[1,2] *and Beate Röder*[1]

[1] *Institut für Physik, Photobiophysik, Humboldt-Universität zu Berlin, Berlin, Germany*
[2] *PicoQuant GmbH, Berlin, Germany*

12.1 Introduction

Sunlight is the basis for life on Earth. It is worth emphasizing that any photochemical and photophysical processes starts with absorption of light photons followed by formation of photoexcited species. Photoinduced electron and energy transfer processes are ubiquitous phenomena in nature as well as in physics, chemistry, and biology. Both transfer processes are efficiently utilized in photosynthesis, which is one of the most important events responsible for the genesis, development, and sustenance of all life on our planet [1–4]. After photon absorption by light-harvesting complexes, the electronic excitation energy is efficiently funneled to the photosynthetic reaction center, where a multi-step electron transfer reaction is initiated, leading eventually to the splitting of water and fixation of carbon dioxide.

Inspired by natural photosynthesis, great efforts have been made during the last few decades to develop artificial photosynthetic systems and devices with the goal of maximizing the total amount of solar energy that can be converted into electrical or chemical energy. Both the rational design of artificial photosynthetic systems and an in-depth knowledge of photoinduced processes within these systems are of great importance for increasing the "sunlight–electric current" conversion efficiency by organic photovoltaics [5–10].

Porphyrin-based molecular systems that can undergo efficient photoinduced energy and/or electron transfer have attracted much current interest not only for the development of solar energy conversion systems but also for the rational design of fluorescent sensors [11, 12], photocatalysts [13], novel drugs for photodynamic therapy (PDT) [12, 14], and optoelectronic devices [15, 16]. In these molecular systems, building blocks are covalently linked to each other or coupled via noncovalent intermolecular interactions. Energy and/or electron transfer processes are used to design and ensure the desired functionality. There is no doubt that a comprehensive understanding of energy and electron transfer processes is essential for further progress in the development of such novel functional materials and devices.

In this chapter, the emphasis will be on recent developments in porphyrin-based systems with photoinduced energy and/or electron transfer processes. The review will start with the basic principles of excitation energy transfer (EET) as well as photoinduced electron transfer (PET). Subsequently, representative examples of covalently linked and self-assembled

Fundamentals of Porphyrin Chemistry: A 21st Century Approach, Volume 2, First Edition.
Edited by Penelope J. Brothers and Mathias O. Senge.
© 2022 John Wiley & Sons Ltd. Published 2022 by John Wiley & Sons Ltd.

porphyrin-based molecular systems displaying interesting functional properties based on energy and/or electron transfer phenomena will be discussed. Of course, as more than 3000 papers dealing with photoinduced transfer processes in molecular systems containing porphyrin chromophores have been published during the last five years, it is impossible to mention all of them in the present chapter. The most fundamental aspect is to understand how one can manipulate the photoinduced energy and/or charge transfers in porphyrin-based molecular systems. This, in turn, can deepen our understanding of the factors that govern these fundamental processes and enable the design of sophisticated systems for the development of novel functional materials and devices.

12.2 Theoretical Background

Many texts give comprehensive accounts of the current theories of photoinduced charge and energy transfer processes [17–20]. Thus, in this section only some basic theoretical approaches to understanding EET and PET will be given.

12.2.1 EET

In general, the EET process between initially photoexcited energy donor (D^*) and energy acceptor (A) in its ground state can be described by the following scheme:

$$D^* + A \xrightarrow{EET} D + A^*. \tag{12.1}$$

One desired requirement for EET is that the emission spectrum of the donor must partially overlap the absorption spectrum of acceptor.

The electronic excitation energy can be transferred between molecules by either radiative or non-radiative processes. In the former case, the excited donor emits a photon, which is absorbed by the acceptor. The donor and acceptor molecules do not interact with each other, and the lifetime of the first excited singlet state of the donor molecule is not affected by the transfer process. The distance and mutual orientation of the donor and acceptor determine the probability of radiative EET, which follows an inverse square dependency on their separation distance [21]. Compared to non-radiative EET, the radiative energy transfer process occurs at much longer donor–acceptor separation distances and normally plays the dominant role in dilute solutions.

For non-radiative EET, besides overlap of the emission spectrum of the donor with the absorption spectrum of the acceptor, an additional condition is that the corresponding states of the donor and acceptor are coupled by suitable donor–acceptor interactions. This coupling can be strong, intermediate, or weak [22, 23]. The strong coupling plays an important role in many photophysical systems where chromophores are arranged in close proximity (e.g., in light-harvesting systems of bacteria [24], dendrimers [22], molecular aggregates [23], and arrays [25]). When the electronic coupling is strong, molecular excitons are the primary excited states of the donor–acceptor system. The molecular exciton model first proposed by Frenkel [26] was further developed for molecules by Davydov [27] and Kasha [28]. By means of dipole–dipole interactions and assuming that the overlap of the electronic wave functions of donor and acceptor is small, the wave functions and energies of the donor–acceptor pair were calculated applying first-order perturbation theory [28]. In the strong coupling case, the donor and acceptor electronic states mix strongly to produce new delocalized states. As result,

the optical spectra of strongly coupled donor and acceptor are very different from the corresponding spectra of individual chromophores: Depending on the mutual orientation of the donor and acceptor transition dipoles, the UV/Vis absorption bands may be split and shifted to shorter or longer wavelengths. The EET time between donor and acceptor moieties is faster than the vibrational relaxation time (i.e., $<10^{-14}$ s). The excitation energy is delocalized over the donor and acceptor, and the exciton is able to move freely through the strongly coupled molecular system as a quantum mechanical wave packet. The phase relations between excited state wave functions of donor and acceptor molecules are fixed [18].

A particularly challenging problem has been to model EET dynamics in the intermediate coupling case [29–31]. In this case, the interaction between donor and acceptor is not strong enough to form an exciton state, but is still sufficiently strong that EET occurs before thermal equilibrium is achieved in the intermediate state [29]. The excitation energy is first localized at the energy donor's site and is subsequently transferred coherently to the acceptor moiety (the transfer rate is 10^{11} to 10^{13} s^{-1}). It should be mentioned that for both strong and intermediate coupling regimes, the probability of EET diminishes with the cube of donor–acceptor separation distance R_{DA}.

The weak coupling regime differs fundamentally from the excitonic interactions discussed above. After photoexcitation of the donor molecule, the thermal equilibrium with the surrounding medium occurs on a time scale that is considerably faster than that of EET. In solution or in other condensed systems, this thermal equilibrium occurs over 10^{-13} to 10^{-12} s. Moreover, the coupling to the surrounding medium is much stronger than the electronic coupling between donor and acceptor. This latter condition ensures that EET is incoherent and irreversible [31].

The theory of EET in the weak coupling case was first described by Theodor Förster in the 1940s [32–34] and is based on an equilibrium *Fermi Golden Rule* approach with a perturbation theory treatment of the electronic coupling between donor and acceptor. In this case, the rate of EET $D^* \rightarrow A$, k_{EET}, could be written as

$$k_{EET} = \left(\frac{2\pi}{\hbar}\right) |V_{DA}|^2 FC, \tag{12.2}$$

where V_{DA} is the electronic coupling between donor and acceptor (defined as the effective electronic Hamiltonian matrix element that couples the initial and final states of the donor–acceptor system), and FC is the Franck–Condon weighted density of states, which accounts for the conservation of energy and describes the influence from the nuclear modes of the system. It is assumed that V_{DA} does not depend on the vibrational coordinates (Condon approximation).

The electronic coupling matrix V_{DA} consists of two parts, namely, the Coulomb, V_{COUL}, and the exchange, V_{EXCH}, part:

$$V_{DA}^2 = V_{COUL}^2 + V_{EXCH}^2. \tag{12.3}$$

When the Coulomb part dominates, the EET is described in terms of Förster theory, whereas Dexter theory of EET takes into account the exchange interactions between the energy donor and acceptor. In general, the Coulomb part can be considered as a sum of dipole–dipole, dipole–quadrupole, quadrupole–quadrupole, and so on, interactions, but the dipole–dipole interaction has a dominant contribution for allowed donor and acceptor transitions in the optical range. The exchange term depends on the degree of overlap between the wave functions of the donor and acceptor, and can be neglected if the donor and the acceptor are well separated.

As already mentioned, Förster theory assumes that $V_{DA} \approx V_{COUL}$. Moreover, it is also assumed that only the dipole–dipole interaction between transition dipole moments of the donor and acceptor chromophores contribute to the Coulombic coupling. In this case, the so-called Förster (or fluorescence) resonance energy transfer (FRET), the coupling V_{DA} can be written in the following form [32–34]:

$$V_{DA} = \frac{1}{4\pi\varepsilon_0} \frac{|k|\mu_D\mu_A}{R_{DA}^3}, \tag{12.4}$$

where μ_D and μ_A are the oscillator strengths of the donor and acceptor transition, R_{DA} is the center-to-center donor–acceptor separation distance, and k is the orientation factor, which is defined by

$$|k| = |\cos\theta_{DA} - 3\cos\theta_D \cos\theta_A| \tag{12.5}$$

where θ_{DA} is the angle between the emission transition dipole moment of the donor and the absorption transition dipole of the acceptor, and θ_D and θ_A are the angles between these dipoles and the center-to-center vector joining the donor and acceptor, respectively. Depending on the relative orientation of the donor and acceptor chromophores, the orientation factor can range from 0 to 4. For example, for randomly distributed, freely rotating donor and acceptor molecules in liquid solution, k^2 was calculated to be equal to 2/3. When rotational diffusion is frozen, then $k^2 = 0.563$ [17]. For covalently linked donor–acceptor systems, the value of the orientation factor depends strongly on the length and flexibility of the linker, as well as its coupling position in the donor and acceptor chromophores.

As it stands, Förster theory is accurate provided that four conditions are satisfied: (i) a dipole–dipole (or convergent multipole–multipole) approximation for the electronic coupling can be employed appropriately for the donor–acceptor interaction; (ii) neither the donor fluorescence lifetime, emission line shape, acceptor absorption line shape, or oscillator strength is perturbed due to donor–acceptor interactions; (iii) static disorder (inhomogeneous line broadening) is absent in the donor and acceptor line shapes; and (iv) the energy transfer dynamics are incoherent [31].

Combining Eqs. (12.2) and (12.4), Förster obtained the expression for the FRET rate, where only measurable quantities are present [34]:

$$k_{FRET} = \frac{1}{\tau_0^D}\left(\frac{R_0}{R_{DA}}\right)^6 \tag{12.6}$$

where τ_0^D is the donor's excited state lifetime in the absence of the acceptor, and R_0 is the Förster radius of EET:

$$R_0^6 = \frac{9000\,(\ln 10)\,k^2\Phi_{fl}}{128\,\pi^5 n^4 N_a} \int I_{fl}^n(\tilde{\nu})\,\varepsilon(\tilde{\nu})\frac{d\tilde{\nu}}{\tilde{\nu}^4} \tag{12.7}$$

N_a is Avogadro's number; n is the refractive index of the solvent used; Φ_{fl} is the fluorescence quantum yield of the energy donor in the absence of the acceptor; k is the orientation factor, which is calculated according to Eq. (12.5); $\varepsilon(\tilde{\nu})$ is the molar absorptivity of the acceptor at wavenumber $\tilde{\nu}$; and $I_{fl}^n(\tilde{\nu})$ is the donor's normalized fluorescence spectrum.

From Eqs. (12.4)–(12.7), it is seen that the FRET rate will be high if (i) both donor and acceptor transitions are allowed; (ii) the overlap integral (the last term in Eq. (12.7)) is high, meaning that there is good spectral overlap between the emission spectrum of the donor and the absorption spectrum of the acceptor, and the latter spectrum has high extinction; (iii) the

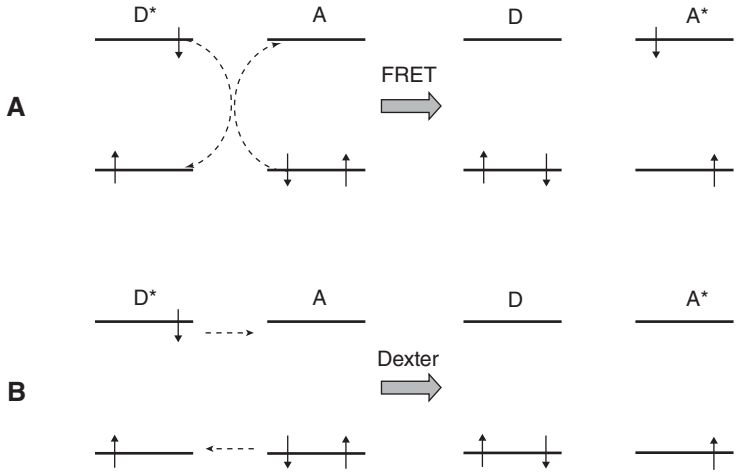

Figure 12.1 Schematic representation of (A) Förster and (B) Dexter energy transfer processes.

corresponding transition dipole moments of donor and acceptor have such an orientation that the orientation factor $k^2 \neq 0$; and (iv) the donor–acceptor distance $R_{DA} \leq R_0$.

Taking a more general approach, Dexter derived, in additional to the Coulomb term, an expression for the EET rate due to the exchange mechanism, Eq. (12.8) [35]:

$$k_{EET}^{EXCH}(R_{DA}) = \frac{2\pi}{\hbar} z^2 \int I_D(\nu)\varepsilon_A^n(\nu)d\nu \tag{12.8}$$

with

$$z^2 = K^2 \exp(-2R_{DA}/L) \tag{12.9}$$

where I_D and ε_A^n are the normalized fluorescence and absorption spectra of the donor and acceptor, respectively, R_{DA} is the donor–acceptor center-to-center separation distance, K is a constant with the dimension of energy, and L is the effective orbital radius, which for organic molecules was estimated to be 1.1–1.9 Å [36]. The direct exchange interaction is short range (<10 Å), whereas FRET can occur over quite large distances (<100 Å). The main difference between Förster and Dexter EET mechanisms can be clearly seen in Figure 12.1.

One additional remark must be made here. For donor–bridge–acceptor molecular systems, the electronic coupling between donor and acceptor can be mediated via the connecting intervening bonds, thus promoting EET over relatively large donor–acceptor distances. Such long-range electronic couplings have received wide attention in the area of electron transfer studies, but there is growing experimental evidence to suggest that triplet-triplet as well as singlet–singlet EET may be mediated by such a mechanism over distances where through-space overlap of wave functions is negligible [37, 38]. The theoretical treatment of such systems is based on the through-bond mechanism used to explain intramolecular electron transfer [39–41], and the bridge-mediated EET rate, k_{EET}^{Med}, can be expressed in the following form [31, 38]:

$$\left(k_{EET}^{Med}\right)^{1/2} \propto V_{DA}^{Med} \propto \frac{V_{DB}V_{DB}}{\Delta E_{DB}}, \tag{12.10}$$

where V_{DB} and V_{BA} are the electronic couplings of donor–bridge and bridge–acceptor, respectively, and ΔE_{DB} is the energy gap between the donor absorption and the bridge absorption.

If EET is only the process that quenches the excited state of the donor, then the efficiency of EET, E_{EET}, can be calculated using experimental data measured with steady-state or time-resolved spectroscopic techniques:

$$E_{EET} = 1 - \frac{\tau_D}{\tau_D^0} = 1 - \frac{\Phi_D}{\Phi_D^0} \tag{12.11}$$

where τ_D, τ_D^0, Φ_D, and Φ_D^0 are the lifetimes and luminescence quantum yields of the donor in the presence and absence of the acceptor, respectively.

12.2.2 PET

A PET process between an electron donor, D, and an electron acceptor, A, can be presented according to the following equation (see also Figure 12.2):

$$D^* + A \xrightarrow{PET} D^+ + A^- \text{ or } D + A^* \xrightarrow{PET} D^+ + A^- \tag{12.12}$$

and principally occurs when either the donor or acceptor is photoexcited initially (see below).

Note that PET can occur between donor and acceptor chromophores freely distributed in solution (the so-called diffusion-limited electron transfer) as well as in donor–acceptor systems where chromophores are covalently linked to each other or held together via self-assembling interactions. Donor–acceptor systems that can undergo efficient PET have attracted significant current interest for the development of solar energy conversion systems, optoelectronic devices, and various sensors. Moreover, such model donor–acceptor systems allow one to study in detail the factors that govern the PET process and learn how to manipulate them. Therefore, in this chapter, we have omitted diffusion-limited PET and discuss only PET in donor–acceptor systems held together by covalent bonds or self-assembly mechanisms.

The electron transfer theory was originally proposed by Marcus in 1956 [42], and over the past decades has been developed and successfully applied to explain PET in different molecular systems [43–46]. The classical Marcus theory formulates electron transfer as the transition from a reactant state, R (D^*-A in the case of donor excitation or D-A^* when the acceptor is initially excited), to a product state, P, (D^+-A^-). In an absolute rate formalism, potential energy curves of the PET reaction for the R and P states of the system are represented by parabolic functions (potential energy vs. the reaction coordinate, which includes the coordinates of all nuclei involved) (Figure 12.3). Charge transfer occurs at the crossing point of the R and P energy curves, which can be regarded as a transient photoexcited complex. The rate constant for PET process, k_{PET}, can be expressed as

$$k_{PET} = \nu_N \kappa_{el} \exp\left(-\frac{\Delta G^*}{k_B T}\right) \tag{12.13}$$

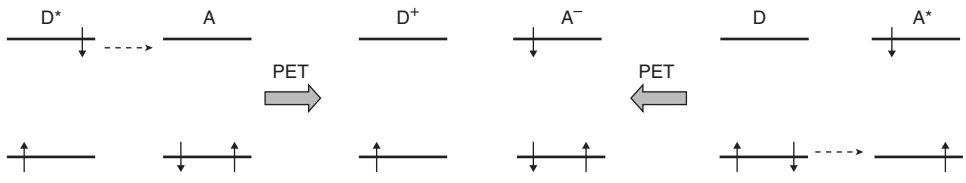

Figure 12.2 Schematic representation of PET upon initial excitation of an electron donor (left) or an electron acceptor (right).

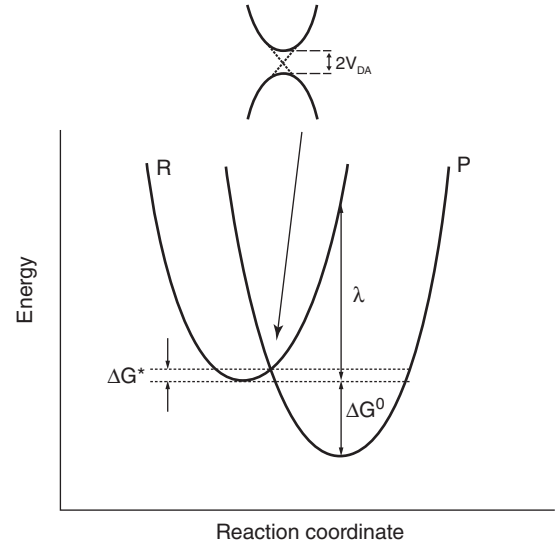

Figure 12.3 Potential energy surfaces of the reactant (R) and product (P) states in harmonic approximation versus a single reaction coordinate.

where ν_N is the average nuclear frequency (it can range from $\sim 10^{12}$ to $\sim 10^{14}$ s^{-1}), κ_{el} is the electronic transmission factor, k_B is the Boltzmann constant, and ΔG^* is the free activation energy. The free activation energy of the PET reaction can be expressed by the Marcus quadratic relationship:

$$\Delta G^* = \frac{(\Delta G^0 + \lambda)^2}{4\lambda} \tag{12.14}$$

where ΔG^0 is the free energy of activation for the PET, and λ is the total reorganization energy (Figure 12.3).

Equations (12.13) and (12.14) predict that for a homogeneous series of reactions (i.e., for reactions having the same λ and κ_{el} values), a plot of $\ln(k_{PET})$ versus ΔG^0 will be bell-shaped (Figure 12.4A) involving two regions: (i) a "normal" region ($-\Delta G^0 < \lambda$) in which the PET is thermally activated and the rate of PET, k_{PET}, increases with increasing ΔG^0, and (ii) an "inverted" region ($-\Delta G^0 > \lambda$) in which the rate of the PET process decreases with increasing ΔG^0 (this was originally predicted by Marcus [47] and first experimentally observed by Miller, Calcaterra, and Closs [48]). In the middle of these regions is the point at which $-\Delta G^0 = \lambda$ and k_{PET} reaches a maximum. In the "normal" region, the electron transfer barrier (ΔG^*) is positive (Figure 12.4B) and its value continuously decreases with increasing ΔG^0 until it reaches zero (Figure 12.4C; in this case $-\Delta G^0 = \lambda$). In the "inverted" region, ΔG^* is again positive, and its value increases with larger ΔG^0 (Figure 12.4D).

The feasibility of electron transfer between donor and acceptor chromophores is dictated by the free energy of charge separation, ΔG^0, and the condition of exothermicity ($\Delta G^0 < 0$) is a major requirement for this process to occur. Note that what has been presented thus far is valid not only for PET but also for electron transfer between donor and acceptor molecules in their ground states. In the latter case, the ΔG^0 value in the gas phase (this simple situation will be discussed for clarity) is given by [46]:

$$\Delta G^0 = IP_D - EA_A \tag{12.15}$$

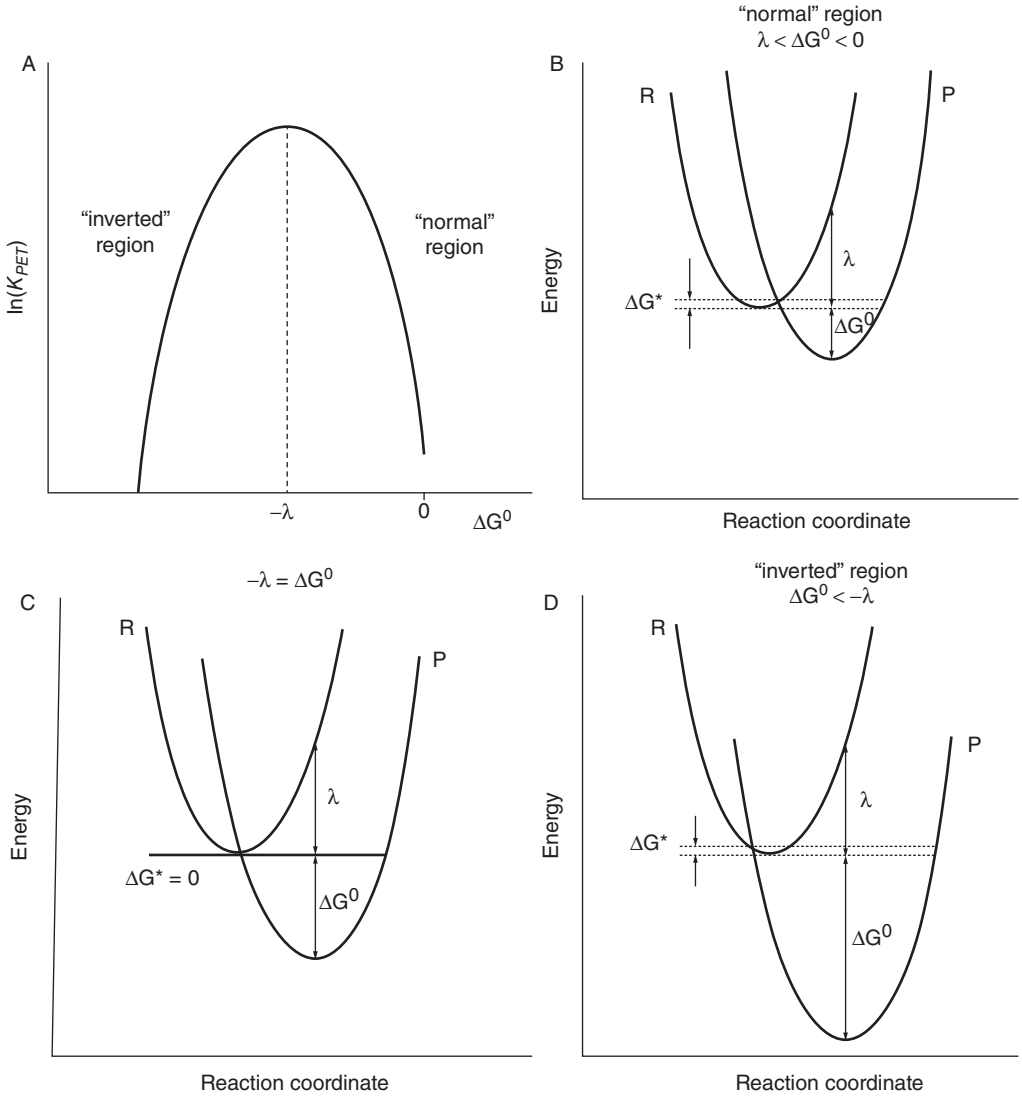

Figure 12.4 Free energy dependence of (A) PET rate and (B) potential energy surfaces for the "normal" region, (C) maximal k_{PET}, and (D) "inverted" region.

where IP_D is the ionization potential of a donor, and EA_A is the electron affinity of an acceptor. When the donor or acceptor is photoexcited, Eq. (12.15) takes the form

$$\Delta G^0_{D(A)} = IP_D - EA_A - E^{D(A)}_{0,0} \tag{12.16}$$

where $E^{D(A)}_{0,0}$ is the energy of the $S_0 \rightarrow S_1$ transition of the donor or acceptor [46]. It is clearly seen that photoexcitation reduces the value of ΔG^0, thus making the electron transfer reaction more exothermic and energetically more favorable. Since IP_D and EA_A are one-electron properties obtained in the gas phase and do not properly describe electron transfer processes in solution, Eqs. (12.15) and (12.16) are used here only for comparison and will not be used in further discussions.

The free energy of charge separation ΔG^0 of the PET process in solution can be calculated only from experimental data by means of the Rehm–Weller equation [49, 50], which accounts for Coulombic and solvent effects:

$$\Delta G^0_{D(A)} = e\left(E^{oxd}_{1/2}(D/D^+) - E^{red}_{1/2}(A/A^-)\right) - E^{D(A)}_{0,0} - \frac{e^2}{4\pi\varepsilon_0\varepsilon_s R_{DA}} - \frac{e^2}{8\pi\varepsilon_0}\left[\frac{1}{r_{D^+}} + \frac{1}{r_{A^-}}\right]\left[\frac{1}{\varepsilon_{ec}} - \frac{1}{\varepsilon_s}\right], \tag{12.17}$$

where $\Delta G^0_{D(A)}$ is the change in free energy of charge separation (in eV) with selective excitation of the electron donor D or the electron acceptor A, e is the charge of the transferred electron, $E^{oxd}_{1/2}$ and $E^{red}_{1/2}$ are the half-wave oxidation and reduction potentials of the donor D/D^+ and acceptor A/A^- couple (in V), R_{DA} is the donor–acceptor separation distance (in Å), ε_s is the dielectric constant of the solvent, ε_0 is the vacuum permittivity, ε_{ec} is the dielectric constant of the solvent used in the electrochemical studies, and r_D and r_A are the effective radii of the cationic and the anionic radicals, respectively. Eq. (12.17) is a powerful tool that can be used to find out if PET is a thermodynamically favorable process ($\Delta G^0_{D(A)} < 0$) using experimentally measurable parameters.

The total free reorganization enthalpy λ can be separated into two terms. The "inner-sphere" reorganization enthalpy (λ_{in}) refers to changes in bond lengths and angles during PET. The "outer-sphere" (λ_{out}) reorganization enthalpy describes the solvent reorientation around the reactants:

$$\lambda = \lambda_{in} + \lambda_{out}. \tag{12.18}$$

The inner reorganization energy is given by the following equation [19, 43]:

$$\lambda_{in} = \sum_i \left(\frac{f(\mathrm{R})_i f(\mathrm{P})_i}{f(\mathrm{R})_i + f(\mathrm{P})_i}\right)[\Delta q_i]^2 \tag{12.19}$$

where Δq_i is the difference in equilibrium bond distance between the reactant and product state corresponding to the i-th vibration, and $f(\mathrm{R})_i$ and $f(\mathrm{P})_i$ are the force constants for this vibration. It is assumed that λ_{in} is temperature independent. It should be mentioned that the values of λ_{in} are comparably small and vary between 0.1 and 0.3 eV [51].

The outer reorganization energy, which is often the predominant term in PET processes, is the result of differences in orientation of the solvent molecules in the vicinity of the reactant and product. Using a spherical charge distribution of the transferred electron on the donor as well as the acceptor, λ_{out} is expressed in terms of the ionic radii of donor (r_D) and acceptor (r_A), the D-A center-to-center distance (R_{DA}), the optical ($\varepsilon_{op} = n^2$, where n is the refraction index) and static (ε_s) dielectric constants of the solvent, and the charge transferred (e) [42–44]:

$$\lambda_{out} = \frac{e^2}{4\pi\varepsilon_0}\left[\frac{1}{r_{D^+}} + \frac{1}{r_{A^-}} - \frac{1}{R_{DA}}\right]\left[\frac{1}{n^2} - \frac{1}{\varepsilon_s}\right] \tag{12.20}$$

It is seen that λ_{out} is particularly large for reactions between well-separated donor and acceptor chromophores in polar solvents.

The electronic transmission coefficient κ_{el} (Eq. (12.13)) is related to the probability of crossing the intersection region (Figure 12.3) and can be expressed as [52]

$$\kappa_{el} = \frac{2[1 - \exp(-\nu_{el}/\nu_N)]}{2 - \exp(-\nu_{el}/\nu_N)} \tag{12.21}$$

with

$$\nu_{el} = \frac{2\pi}{\hbar} \frac{|V_{DA}|^2}{\sqrt{4\pi\lambda k_B T}} \tag{12.22}$$

where V_{DA} is the matrix element for electronic interaction (see inset in Figure 12.3).

In the so-called adiabatic regime of PET, the electronic transmission coefficient $\kappa_{el} \approx 1$; that is, PET occurs at the intersection point of two potential curves. In this case, $\nu_{el} >> \nu_N$ and the PET rate can be calculated according to Eq. (12.13) with $\kappa_{el} = 1$. In the non-adiabatic regime, the V_{DA} value is small and $\nu_{el} << \nu_N$. Combining Eq. (12.13) with Eqs. (12.21) and (12.22), the rate of PET can be calculated according to Eq. (12.23):

$$k_{PET} = \frac{2\pi}{\hbar} \frac{|V_{DA}|^2}{\sqrt{4\pi\lambda k_B T}} \exp\left\{-\frac{(\Delta G^0 + \lambda)^2}{4\lambda k_B T}\right\} \tag{12.23}$$

For values of $V_{DA} \gtrsim 200\ \text{cm}^{-1}$, the pre-exponential factor of Eq. (12.23) approaches $\sim 10^{14}\ \text{s}^{-1}$, so that PET reaction becomes adiabatic. As the V_{DA} value falls below $200\ \text{cm}^{-1}$, the reaction becomes increasingly non-adiabatic [19]. Note that a similar expression for the PET rate can be obtained using a quantum mechanical approach [18, 19].

The coupling matrix V_{DA} depends exponentially on the separation distance between the electron donor and the electron acceptor:

$$V_{DA} = V_{DA}^0 \exp[-\beta(R_{DA} - r_D - r_A)] \tag{12.24}$$

where β is an attenuation factor, and its values range typically from 0.8 to $3\ \text{Å}^{-1}$. Eq. (12.24) is frequently used when examining the effect of the separation distance on the PET efficiency in donor–acceptor systems where the electron donor and acceptor are geometrically fixed relative to one other.

In donor–bridge–acceptor systems, the PET process can be influenced by the nature and number of bonds in the molecular bridge. The electron or the hole may actually "hop" via successive jumps from the adjoining molecules to occupied (electron) or unoccupied (hole) orbitals of the bridge. Alternatively, the bridge can provide the electronic coupling between the donor and acceptor, and the "virtual" orbitals localized on the bridge promote PET from donor and acceptor, despite the fact that the spacer does not figure as a real intermediate in the PET process. This type of interaction is commonly termed as the "super-exchange" mechanism [19, 38–41, 52] and has been widely used as the basis for understanding long-range PET in multicomponent molecular systems. Super-exchange theory predicts that the donor–acceptor coupling V_{DA} is related to the energy gap (ΔE_{DB}) between relevant orbitals on the donor and bridge as well as on the coupling donor–bridge (V_{DB}) and bridge–acceptor (V_{BA}) (see Eq. (12.10)) [39–41]. If the bridge is composed of n identical units, then Eq. (12.10) should be modified and V_{DA} is given by [53]:

$$V_{DA} = \frac{V_{DB} V_{BA}}{\Delta E_{DB}} \left(\frac{V_{BB}}{\Delta E_{DB}}\right)^{n-1} \tag{12.25}$$

where V_{BB} is the coupling between nearest neighbors of the bridge.

PET mediation by the bridge is characterized by the attenuation factor β (see Eq. (12.24)), which depends not only on the bridge structure but also on the donor and acceptor; that is, the same bridge can either be poorly or strongly conducting depending on the donor and acceptor [53]. It is worth emphasizing that this is valid for both EET and PET processes in donor–bridge–acceptor systems.

The efficiency of PET can experimentally be estimated – as just discussed for EET – using steady-state or time-resolved fluorescence data according to Eq. (12.11).

12.3 Photoinduced Energy and Charge Transfer in Covalently Linked Porphyrin-Based Donor–Acceptor Molecular Systems

Two different approaches are widely employed to construct porphyrin-based molecular arrays: covalent bonding and supramolecular chemistry concepts. A bridge in the donor–bridge–acceptor system serves as a spacer between donor and acceptor and provides geometrical constraints in the molecular system. Moreover, the bridge can alter donor–acceptor coupling and mediate EET as well as PET. The nature of the bridge (its chemical structure as well as length) can be rationally manipulated in order to study its effect on the photoinduced transfer processes. The design of sophisticated covalently linked porphyrin-based molecular systems with EET and/or PET was reported in several resent reviews [54–60]. Here, we discuss only a couple of examples of such systems to demonstrate different transfer mechanisms that occur in covalently linked porphyrin-based donor–acceptor arrays and how the probability of these processes can be manipulated by rational modification of the structure of the molecular system.

Albinsson and Mårtensson reviewed the mechanisms by which the interactions responsible for EET and PET are attenuated by oligo(phenylene-ethynylene)-type bridges in a series of bisporphyrin molecular systems and discussed the attenuation factors β for both EET and PET processes (Figure 12.5) [53]. For example, it was shown for the ZnP-AB-H_2P system that the EET rate measured was larger by a factor of 3.7 than the calculated Förster rate (Eq. (12.6)) and is due to two simultaneously operating mechanisms, namely, the through-space mechanism according to Förster and the Dexter-type through-bond-mediated mechanism [38, 53]. The mediating contribution is correlated with the inverse energy splitting between excitation energies of the donor and bridge chromophores, in accordance with Eq. (12.10). It was also

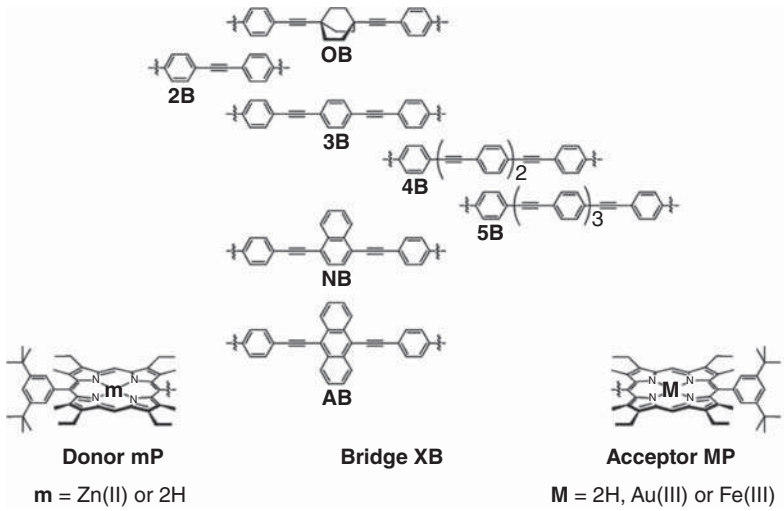

Figure 12.5 mP-XB-MP donor–bridge–acceptor molecular systems Source: Albinsson and Mårtensson [53]. Copyright 2008, with permission from Elsevier.

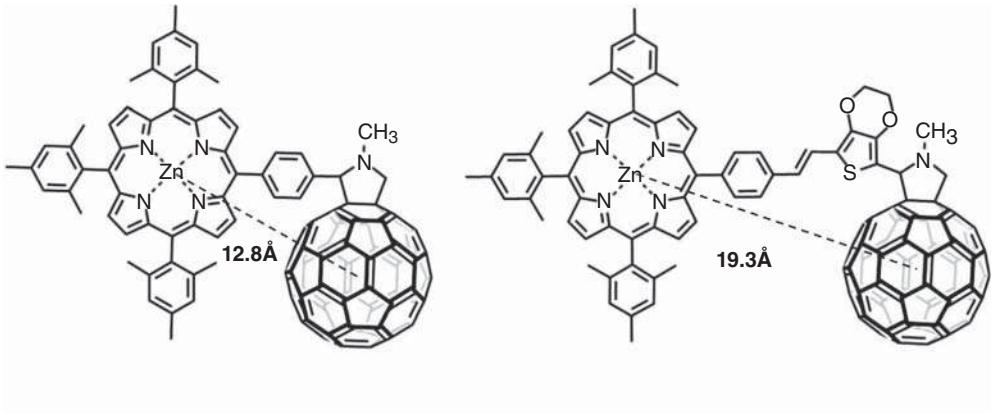

Figure 12.6 Chemical structures of ZnP-Ph-C_{60} (left) and ZnP-EDOTV-C_{60} (right) donor–acceptor dyads. The donor–acceptor center-to-center separation distances are also shown Source: Pelado et al. [61]. With permission from Wiley.

shown that sequential and direct super-exchange-mediated PET can occur in parallel if the bridge has a sufficient small reduction potential (this was only provided by the AB bridge for the donor–bridge–acceptor systems presented in [53]). The sequential pathway is efficiently turned off in solvents of low polarity and at low temperatures.

The role of π-conjugated molecular bridges in through-space and through-bond PET was studied by Pelado et al. by comparing two Zn(II) porphyrin–fullerene(C_{60}) dyads with either a phenyl or 3,4-ethylenedioxythienylvinylene (EDOTV) bridge (Figure 12.6) [61]. The EDOTV unit increased the distance between the donor and acceptor chromophores, but at the same time provided increased electronic donor–acceptor communication. As result, faster charge recombination, as well as the disappearance of the intramolecular exciplex, which mediated photoinduced charge separation in the ZnP-Ph-C_{60} dyad, was observed. In polar benzonitrile, the photophysics of the ZnP-EDOTV-C_{60} dyad was presented by a linear chain reaction as $ZnP^* - C_{60} \xrightarrow{4\ ps} ZnP - C_{60}^* \xrightarrow{12\ ps} ZnP^+ - C_{60}^- \xrightarrow{68\ ps} ZnP - C_{60}$, whereas for the ZnP-Ph-C_{60} dyad the reaction followed the path $ZnP^* - C_{60} \xrightarrow{1.3\ ps} (ZnP - C_{60})^* \xrightarrow{12\ ps} ZnP^+ - C_{60}^- \xrightarrow{75\ ps} ZnP - C_{60}$. In nonpolar toluene, population of the first excited singlet state of C_{60} (or exciplex (ZnP-C_{60})* excitation) was followed by intersystem crossing to the triplet state C_{60}^T, which decayed to the ground state within the sub-millisecond time domain [61].

A great deal of attention has been paid to designing donor–acceptor systems with a long-lived charge-separated state. This is important for the development of novel materials, for example, for the dye-sensitized solar cells. One example is a $[Cu(phen)_2]^+$-based rotaxane, featuring Zn(II) porphyrin (ZnP) and ferrocene (Fc) as electron donors and fullerene C_{60} as the electron acceptor (Figure 12.7) [62]. It was found that photoexcitation of the rotaxane triggers a cascade of multi-step EET and PET events, ultimately leading to remarkably long-lived charge-separated states featuring a C_{60}^- radical anion and either ZnP^+ or Fc^+ radical cations with lifetimes up to 61 μs. In addition, shorter-lived charge-separated states involving a one-electron oxidized copper complex $[Cu(phen)_2]^{2+}$ and C_{60}^- (with lifetime <100 ns) or ZnP^+ and C_{60}^- (lifetime ca. 2 μs) were identified as intermediates (see the energy level diagram in Figure 12.7).

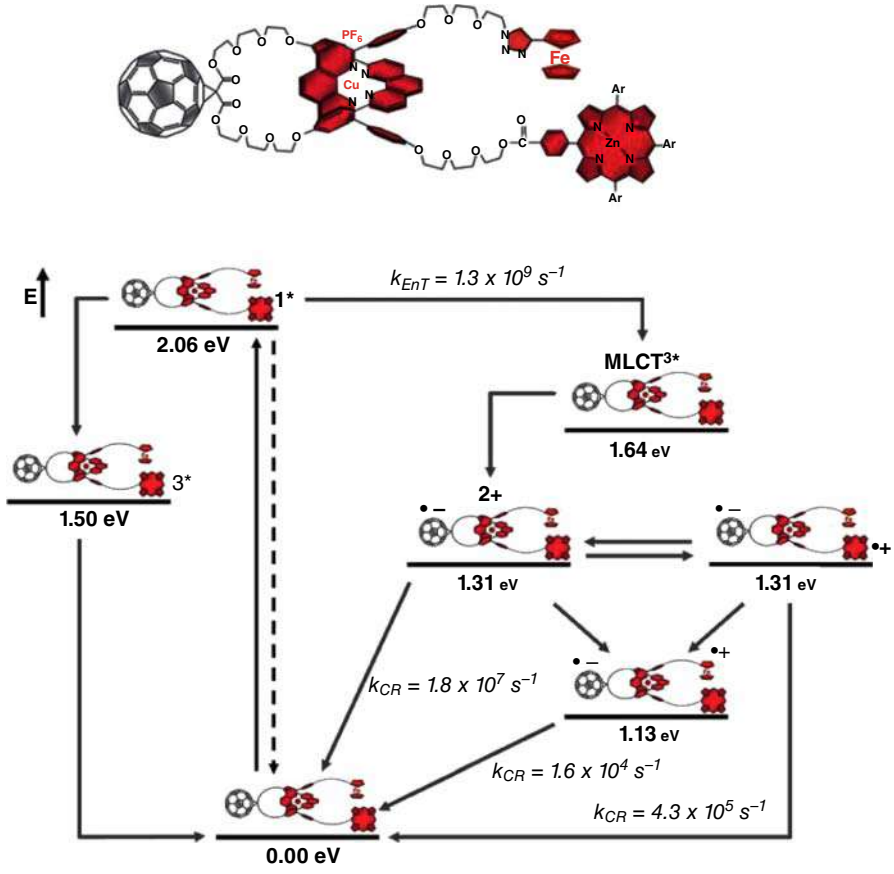

Figure 12.7 Fc-ZnP-$[Cu(phen)_2]^+$-C_{60} rotaxane and schematic energy level diagram with decay pathways and rate constants upon excitation at 425 nm. k_{EnT} = EET rate; k_{CR} = charge recombination rate Source: Kirner et al. [62]. Published by The Royal Society of Chemistry. Licensed under CC BY 3.0.

12.4 Photoinduced Transfer Processes in Self-Assembled Porphyrin-Based Systems

As already emphasized above, a vast number of covalently linked porphyrin-based molecular systems have been prepared and studied with regard to their photophysical properties and the electronic interactions between the chromophore components. Supramolecular chemistry provides an alternative and perhaps a more powerful approach to the assembling process. This strategy has been widely used to build sophisticated porphyrin scaffolds for the collection, conduction, and conversion of light energy [63–69]. Here, we will present and discuss some representative examples of self-assembled multicomponent porphyrin-based molecular systems that undergo EET and PET.

Menting et al. showed the formation of mixed host–guest supramolecular complexes consisting of a β-cyclodextrin-conjugated subphthalocyanine (SubPc), a tetrasulfonated porphyrin, and a series of Si(IV) phthalocyanines axially substituted with two β-cyclodextrins via different spacers (SiPc1-SiPc3) (Figure 12.8) [70]. The three components form

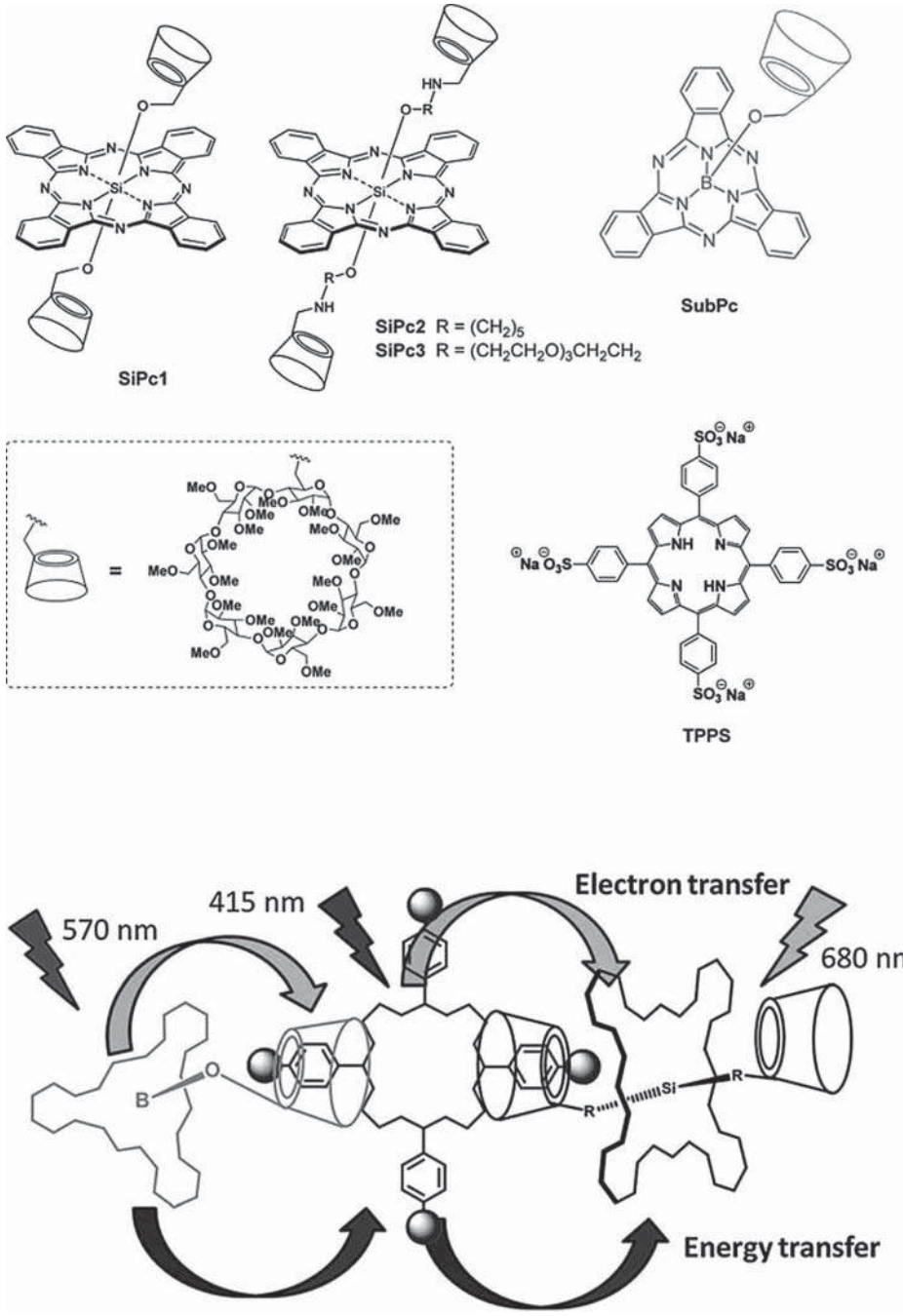

Figure 12.8 Chemical structures of Si(IV) phthalocyanines (SiPc1-SiPc3), subphthalocyanine (SubPc), and tetrasulfonated porphyrin (TPPS) as well as illustration of sequential EET and PET processes in the self-assembled SubPc-SiPc1-TPPS supramolecular complex Source: Menting et al. [70]. With permission from the PCCP Owner Societies.

supramolecular complexes held by host–guest interactions in aqueous solution. Upon excitation of the SubPc part of the complexes, the excitation energy was efficiently delivered to the SiPc unit via long-range FRET, and TPPS acted as an energy transfer bridge enabling this process. A sequential PET process from the TPPS unit to the SiPc moiety and, subsequently, from the SubPc moiety to the TPPS unit occurred (Figure 12.9), and the probability of this process was controlled by the linker between β-cyclodextrin and phthalocyanine. The lifetimes of the charge-separated state SubPc-TPPS^{+}-SiPc^{-}, as determined by means of pump-probe experiments, were ca. 100 ps. At the same time, formation of the SubPc^{+}-TPPS-SiPc^{-} charge-separated state was observed in the SubPc-TPPS-SiPc1 complex, and its lifetime was determined as 1.7 ns (due to the increased separation distance between the electron donor (SubPc) and the electron acceptor (SiPc)) [70].

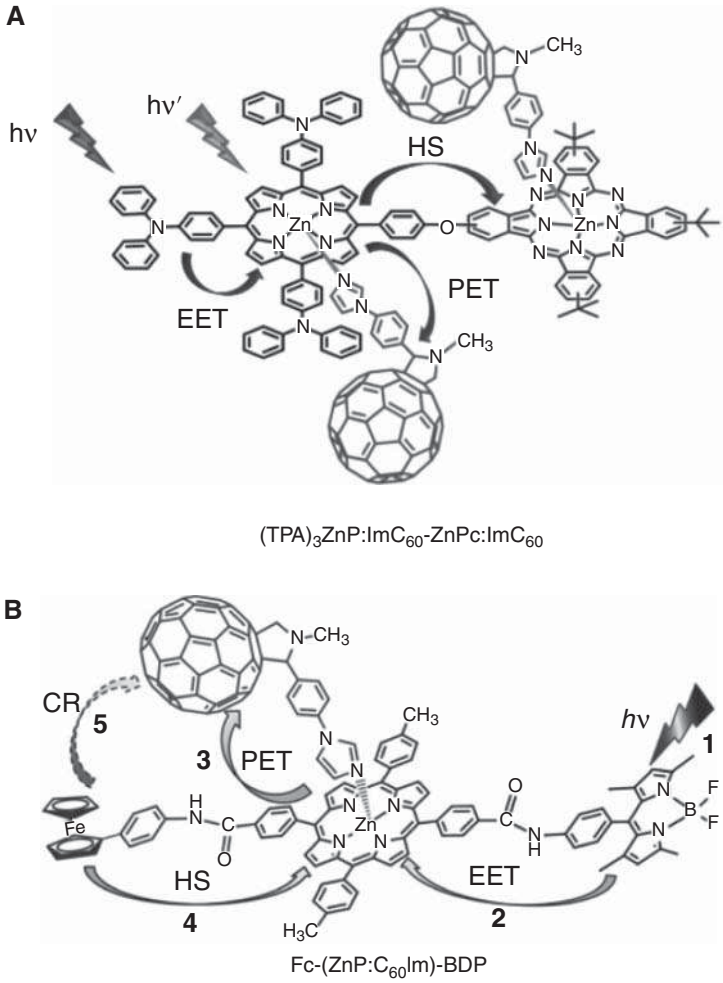

Figure 12.9 (A) Structure and photoinduced transfer processes in $(TPA)_3$ZnP: C_{60}Im-ZnPc: C_{60}Im supramolecular complex. Source: Adapted from Chandra et al. [71]. With permission of The Royal Society of Chemistry. (B) Fc-(ZnP: C_{60}Im)-BDP supramolecular tetrad featuring a ZnP as primary electron donor, BDP as energy-transferring antenna, Fc as charge-stabilizing agent, and C_{60}Im as terminal electron acceptor. The photochemical events occurring in the chronological order upon selective excitation of the BDP moiety are shown with the numbers. HS = hole shift Source: Adapted from Lim et al. [72]. With permission from Wiley.

A relatively long-lived charge-separated state can be achieved in artificial photosynthetic systems by appending a hole-shifting agent to the primary electron donor–acceptor pair. For example, D'Souza and co-workers achieved this in a tris(triphenylamine)-zinc porphyrin-zinc phthalocyanine-fullerene $(TPA)_3ZnP$:C_{60}Im-ZnPc:C_{60}Im supramolecular system (see Figure 12.9A) [71]. Very efficient EET from initially photoexcited triphenylamine (TPA) to zinc porphyrin (ZnP) was followed by PET, resulting in the formation of $[(TPA)_3ZnP]^+$:C_{60}^-Im-ZnPc:C_{60}Im. The latter compound yielded the $(TPA)_3ZnP$:C_{60}^-Im-$ZnPc^+$:C_{60}Im radical ion pair via a hole transfer mechanism. Due to the distant location of the radical cation and radical anion (ZnP acting as a spacer), the charge recombination process was slowed down, and the lifetime of the final charge-separated state was ~100 ns. An even longer charge separation lifetime was observed in a tetrad composed of ferrocene (Fc), ZnP, and BF_2-chelated dipyrromethene (BDP) coordinated to phenylimidazole-functionalized fulleropyrrolidine (C_{60}Im) (Figure 12.9B) [72]. Selective excitation of BDP resulted in efficient EET to the ZnP moiety, followed by ultrafast PET to the coordinated fullerene and formation of the Fc-(ZnP^+:C_{60}^-Im)-BDP radical ion pair. Subsequent hole migration to the Fc entity resulted in the Fc^+-(ZnP:C_{60}^-Im)-BDP radical ion pair, whose lifetime was determined via nanosecond transient absorptions studies as 7–15 μs, depending upon the solvent conditions [72].

12.5 Implication of Electron and Energy Transfer Processes in Biology and Sensing

Porphyrin-based molecular systems have found numerous phototheranostic applications [11, 14, 73, 74]. Already years ago the PDT was proposed to be a powerful treatment against cancer and other diseases [75], and porphyrins are one of the most widely used classes of photosensitizers (PSs) in PDT of tumors [14, 73–76]. Irradiation of PS at a specific wavelength leads to population of its excited triplet state (T_1) by intersystem crossing (ISC) from the first excited singlet state (S_1) followed by EET (via the Dexter mechanism) to $^3O_2$, resulting in production of highly reactive singlet oxygen, $^1O_2$ (see the Jablonski diagram in Chapter 14), a highly cytotoxic species. For EET to occur, the PS's T_1-state energy should be ≥0.98 eV [77]. It is commonly accepted that a high singlet oxygen quantum yield Φ_Δ is a fundamental requirement for successful PDT treatment. The value of Φ_Δ can be calculated using experimentally measured parameters according to Eq. (12.26) [78]:

$$\Phi_\Delta = \Phi_{ISC}\tau_{T,O_2}k_{EET}, \tag{12.26}$$

where Φ_{ISC} is the ISC quantum yield, τ_{T,O_2} is the lifetime of the T_1-state of the PS in the presence of oxygen, and k_{EET} is the EET rate constant. Up to now many approaches have been used to develop porphyrin-based PSs with high singlet oxygen quantum yield. For example, Jsasinski et al. synthesized a cycloketoporphyrin (Figure 12.10) [79] that showed a remarkably high efficiency in the generation of singlet oxygen, the quantum yield being $\Phi_\Delta = 0.85$. Moreover, its absorption underwent a bathochromic shift to 689 nm, and the Q-band extinction was more than two times higher compared to that of H_2TPP, making such compounds promising candidates for use in PDT.

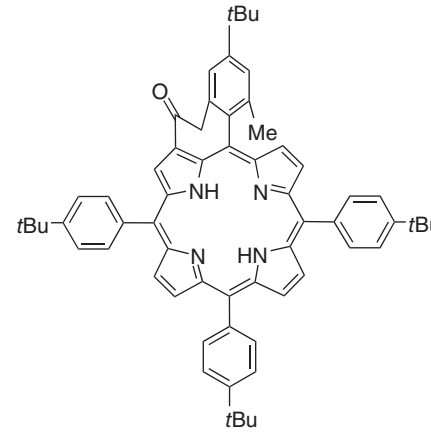

Figure 12.10 Structure of cycloketoporphyrin
Source: Reproduced with permission from Jasinski et al. [79].

Upon interaction with molecular oxygen, the photoexcited triplet state of the PS will be quenched, and this quenching can be described by the Stern–Volmer equation [80]. This effect is used to construct various sensors, whose luminescence intensity as well as luminescence lifetime strongly depend on the molecular oxygen concentration in their environment [81]. Among others, Pt(II) and Pd(II) porphyrin-based dyes have been widely used as oxygen sensors due to their high phosphorescence quantum yield, relatively long triplet lifetime, near-infrared (NIR) excitation and emission wavelengths, and high photochemical stability [82]. Doping of such porphyrin-based oxygen-sensing systems into appropriate materials opens the door for *in vivo* oxygen sensing. For example, an intracellular O_2-sensing probe made from a cationic polymer, Eudragit RL-100, and (5,10,15,20-tetrakis(pentafluorophenyl)porphyrinato)platinum(II) was developed and studied by means of time-resolved fluorescence spectroscopy, confocal microscopy, and flow cytometry. The intracellular oxygen concentration was monitored by measuring the changes in the phosphorescence lifetime of the nanosensor [83].

Porphyrin-based molecular systems with EET and/or PET have been successfully used for other sensing applications. For example, a CO_2 sensor incorporated in plastic matrix was developed for potential use in food packaging applications [84]. In this sensor, a Pt(II) porphyrin phosphorescent dye was used as a reporter, whereas α-naphtholphthalein was used as a colorimetric pH indicator. Good spectral overlap between porphyrin emission and α-naphtholphthalein provided efficient FRET from the porphyrin, thus reducing its phosphorescence lifetime. The use of a long-decay phosphorescent indicator dye and an absorbance pH indicator dye provided an accurate readout of the CO_2 content with relatively simple instrumentation. Likewise, a BDP-porphyrin ratiometric fluorescence sensor for Ag^+ was proposed (Figure 12.11A) [85]. Upon excitation of the BDP moiety at 470 nm, efficient FRET to porphyrin (with efficiency of ca. 99%) occurred, resulting in strong quenching of the BDP fluorescence at 513 nm and rising of the porphyrin emission at 654 nm. When Ag^+ was selectively bound in the porphyrin core, the FRET efficiency was diminished and the porphyrin fluorescence was quenched, leading to an increase in the F_{513}/F_{654} ratio with increasing Ag^+ concentration (Figure 12.11B).

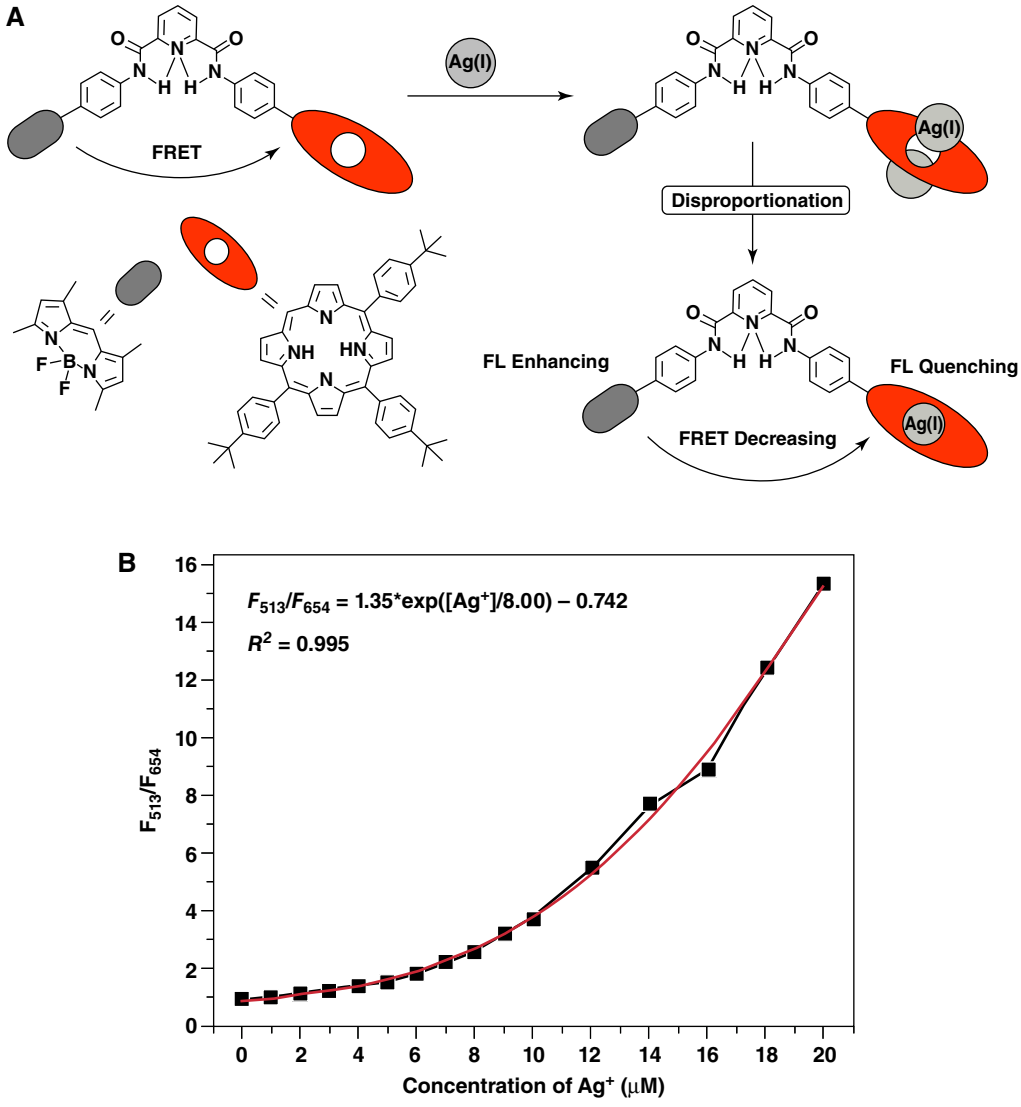

Figure 12.11 (A) Sensing mechanism of a BDP-porphyrin dyad toward Ag^+. (B) Fluorescence intensity ratio (F_{513}/F_{654}) of the BDP-porphyrin dyad as function of Ag^+ concentration Source: With permission from Zhu et al. [85]. Copyright 2014 American Chemical Society.

Another approach was used in NIR fluorescent sensing of the for sulfide anion S^{2-} [86]. For this purpose, a dyad constructed of a hydroxyl porphyrin (TPP-OH) covalently linked to a 2,4-dinitrobenyenesulfonyl group was prepared (Figure 12.12A). The latter unit acted not only as a porphyrin fluorescence quencher through very efficient PET, but also served as a leaving group in the presence of S^{2-}. Upon addition of S^{2-}, the 2,4-dinitrobenyenesulfonate ester group was cleaved by the sulfide anion, thus turning the sensor into fluorescent TPP-OH. As a result, the sensor fluorescence at 653 nm gradually increased (Figure 12.12B).

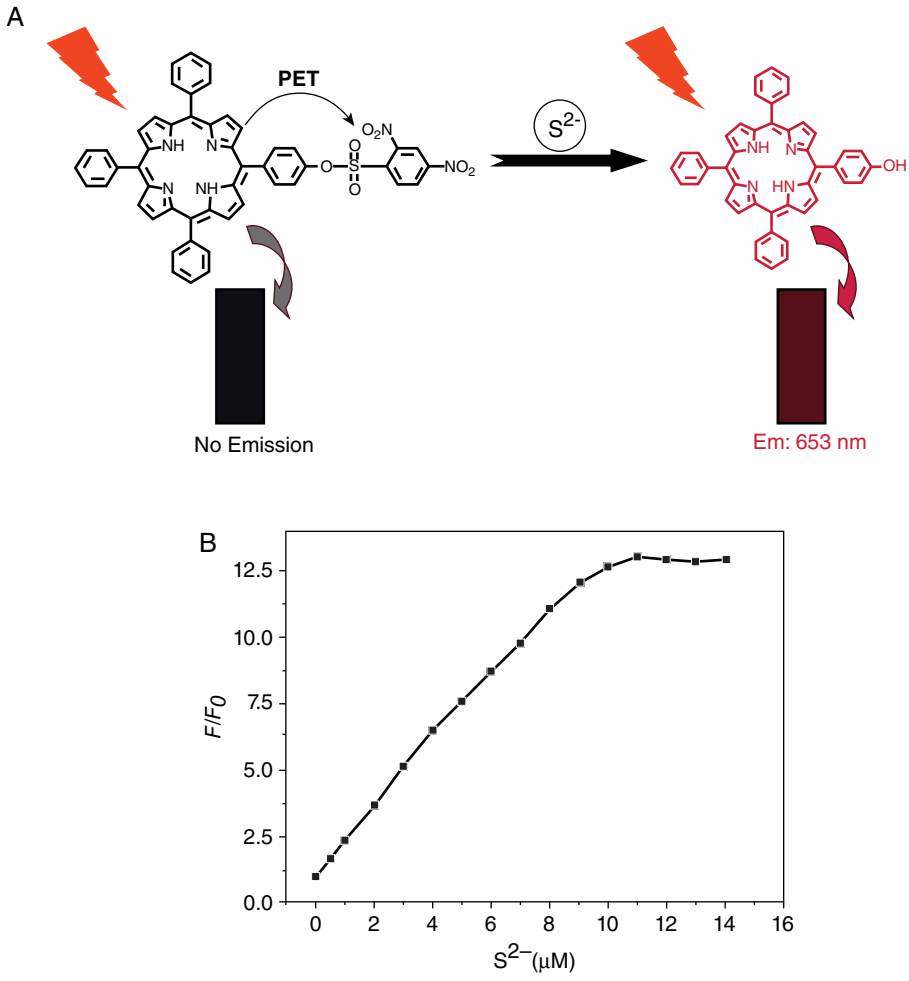

Figure 12.12 (A) Sensing mechanism of porphyrin-based dyad toward S^{2-}. (B): Fluorescence intensity ratio (F/F_0) of the dyad solution (10 μM) as function of the S^{2-} concentration Source: Cheng et al. [86]. Copyright 2016, with permission from Elsevier.

12.6 Conclusions

Photoinduced energy and electron transfer are ubiquitous phenomena in nature and play a key role in contemporary studies in life sciences and technology. Understanding these photoinduced transfer processes is of crucial importance for the development of sophisticated porphyrin-based molecular systems for various applications. In this chapter, the fundamental principles of EET as well as PET processes were reviewed. Förster and Dexter, as well as excitonic mechanisms of EET including the influence of the bridge connecting donor and acceptor chromophores, were discussed. Quantum mechanical and Marcus theories of PET were presented, allowing an estimation of the PET rate and probability as a function of the physicochemical properties of a particular donor–acceptor molecular system

and its environment. Subsequently, several representative examples of covalently linked and self-assembled porphyrin-based molecular systems displaying interesting functional properties based on energy and/or electron transfer phenomena were discussed. It was demonstrated that rationally designed porphyrin-based molecular systems with EET and PET are excellent candidates for the development of novel functional materials for solar energy harvesting and transformation, optoelectronics, sensing, and phototheranostics.

References

1 Deisenhofer, J. and Norris, J.R. (ed.) (1993). *The Photosynthetic Reaction Center*. San Diego: Academic Press.
2 Cogdell, R. and Mullineaux, C. (ed.) (2008). *Photosynthetic Light Harvesting, Springer*. Dordrecht: Netherlands.
3 Fleming, G.R., Schlau-Cohen, G.S., Amarnath, K., and Zaks, J. (2012). Design principles of photosynthetic light-harvesting. *Faraday Discuss.* 155: 27–41.
4 Loll, B., Kern, J., Saenger, W. et al. (2005). Towards complete cofactor arrangement in the 3.0 Å resolution structure of photosystem II. *Nature* 438: 1040–1044.
5 Gust, D., Moore, T.A., and Moore, A.L. (2009). Solar fuels via artificial photosynthesis. *Acc. Chem. Res.* 42: 1890–1898.
6 House, R.L., Iha, N.Y.M., Coppo, R.L. et al. (2015). Artificial photosynthesis: where are we now? Where can we go? *J. Photochem. Photobiol. C Photchem. Rev.* 25: 32–45.
7 Wasielewski, M.R. (1992). Photoinduced electron transfer in supramolecular systems for artificial photosynthesis. *Chem. Rev.* 92: 435–461.
8 Balzani, V., Credi, A., and Venturi, M. (2008). Photochemical conversion of solar energy. *ChemSusChem* 1: 26–58.
9 Benniston, A.C. and Harriman, A. (2008). Artificial photosynthesis. *Mater. Today* 11: 26–34.
10 Berardi, S., Drouet, S., Francas, L. et al. (2014). Molecular artificial photosynthesis. *Chem. Soc. Rev.* 43: 7501–7519.
11 Ishihara, S., Labuta, J., Rossom, W.V. et al. (2014). Porphyrin-based sensor nanoarchitectonics in diverse physical detection modes. *Phys. Chem. Chem. Phys.* 16: 9713–9746.
12 Ng, K.K., Lovell, J.F., Vedadi, A. et al. (2013). Self-assembled porphyrin nanodiscs with structure-dependent activation for phototherapy and photodiagnostic applications. *ACS Nano* 7: 3484–3490.
13 Chen, Y., Li, A., Huang, Z.-H. et al. (2016). Porphyrin-based nanostructures for photocatalitic applications. *Nanomaterials* 6: 51.
14 Pandey, R.K. and Zheng, G. (2000). Porphyrins as photosensitizers in photodynamic therapy. In: *The Porphyrin Handbook*, vol. 6, Chapter 43 (ed. K.M. Kadish, K.M. Smith and R. Guilard), 157–230. New York: Academic Press.
15 Chou, J.-H., Kosal, M.E., Nalwa, H.S. et al. (2000). Applications of porphyrins and metalloporphyrins to materials chemistry. In: *The Porphyrin Handbook*, vol. 6, Chapter 41 (ed. K.M. Kadish, K.M. Smith and R. Guilard), 43–131. New York: Academic Press.
16 Jurow, M., Schuckman, A.E., Batteas, J.D., and Drain, C.M. (2010). Porphyrins as molecular electronic components of functional devices. *Coord. Chem. Rev.* 254: 2297–2310.

17 Agranovich, V.M. and Galanin, M.D. (1982). *Electronic Excitation Energy Transfer in Condensed Matter*. North-Holland, Amsterdam, New York.

18 May, V. and Kühn, O. (2011). *Charge and Energy Transfer Dynamics in Molecular Systems*. Weinheim: Wiley-VCH Verlag GmbH.

19 Kavarnos, G.J. (1993). *Fundamentals of Photoinduced Electron Transfer*. New York: VCH Publishers, Inc.

20 Balzani, V. (2001). *Electron Transfer in Chemistry*. Weinheim: Wiley-VCH Verlag GmbH.

21 Avery, J.S. (1966). Resonance energy transfer and spontaneous photon emission. *Proc. Phys. Soc.* 88: 1–8.

22 Ermilov, E.A., Helmreich, M., Jux, N., and Röder, B. (2007). Novel pyropheophorbide fullerene conjugates as part of modular carrier systems in PDT and as promising units in artificial photosynthesis. In: *Chemical Physics Research Trends Horizons in World Physics*, vol. 252 (ed. B.V. Arnold), 215–246. Nova Science Publishers.

23 Kameyama, K., Morisue, M., Satake, A., and Kobuke, Y. (2005). Highly fluorescent self-coordinated phthalocyanine dimers. *Angew. Chem. Int. Ed.* 44: 4763–4766.

24 van Amerongen, H., Valkunas, L., and van Grondelle, R. (2000). *Photosynthetic Excitons*. Singapore: World Scientific.

25 Aratani, N., Osuka, A., Cho, H.S., and Kim, D. (2002). Photochemistry of covalently-linked multi-porphyrinic systems. *J. Photochem. Photobiol. C Photchem. Rev.* 3: 25–52.

26 Frenkel, J. (1931). On the transformation of light into heat in solids. I. *Phys. Rev.* 37: 17–44.

27 Davydov, A.S. (1962). *Theory of Molecular Excitons*. New York: McGraw-Hill.

28 Kasha, M., Rawls, H.R., and Ashraf el-Bayoumi, M. (1965). The exciton model in molecular spectroscopy. *Pure Appl. Chem.* 11: 371–392.

29 Kakitani, T., Kimura, A., and Sumi, H. (1999). Theory of excitation transfer in the intermediate coupling case. *J. Phys. Chem. B.* 103: 3720–3726.

30 Kimura, A., Kakitani, T., and Takahisa, Y. (2000). Theory of excitation energy transfer in the intermediate coupling case. II. Criterion for intermediate coupling excitation energy transfer mechanism and application to the photosynthetic antenna system. *J. Phys. Chem. B.* 104: 9276–9287.

31 Scholes, G.D. (2003). Long-range resonance energy transfer in molecular systems. *Annu. Rev. Phys. Chem.* 54: 57–87.

32 Förster, T. (1948). Zwischenmolekulare Energiewanderung und Fluoreszenz. *Ann. Phys.* 437: 55–75.

33 Förster, T. (1949). Experimentelle und theoretische Untersuchung des zwischenmolekularen Übergangs von Elektronenanregungsenergie. *Zeitschrift für Naturforschung* 4a: 321–327.

34 Förster, T. (1959). 10th Spiers memorial lecture. Transfer mechanisms of electronic excitation. *Discuss. Faraday Soc.* 27: 7–17.

35 Dexter, D.L. (1953). A theory of sensitized luminescence in solids. *J. Chem. Phys.* 21: 836–850.

36 Inokuti, M. and Hirayama, F. (1965). Influence of energy transfer by the exchange mechanism on donor luminescence. *J. Chem. Phys.* 43: 1978–1989.

37 Closs, G.L., Piotrowiak, P., MacInnes, J.M., and Fleming, G.R. (1988). Determination of long-distance intramolecular triplet energy-transfer rates. Quantitative comparison with electron transfer. *J. Am. Chem. Soc.* 110: 2652–2653.

38 Kilså, K., Kajanus, J., Mårtensson, J., and Albinsson, B. (1999). Mediated electronic coupling: singlet energy transfer in porphyrin dimers enhanced by the bridging chromophore. *J. Phys. Chem. B.* 103: 7329–7339.

39 McConnell, H.M. (1961). Intramolecular charge transfer in aromatic free radicals. *J. Chem. Phys.* 35: 508–515.

40 Scholes, G.D. and Ghiggino, K.P. (1995). Rate expressions for excitation transfer. IV. Energy migration and superexchange phenomena. *J. Chem. Phys.* 103: 8873–8883.

41 Clayton, A.H.A., Scholes, G.D., Ghiggino, K.P., and Paddon-Row, M.N. (1996). Through-bond and through-space coupling in photoinduced electron and energy transfer: an *ab initio* and semiempirical study. *J. Phys. Chem.* 100: 10912–10918.

42 Marcus, R.A. (1956). On the theory of oxidation-reduction reactions involving electron transfer. I. *J. Chem. Phys.* 24: 966–978.

43 Marcus, R.A. (1965). On the theory of electron transfer reactions. VI. Unified treatment for homogeneous and electrode reactions. *J. Chem. Phys.* 43: 679–701.

44 Marcus, R.A. (1968). Theoretical relations among rate constants, barriers, and Brønsted slopes of chemical reactions. *J. Phys. Chem.* 72: 891–899.

45 Nelsen, S.F., Adamus, J., and Wolff, J.J. (1994). Comparison of intramolecular electron transfer rate constant with hush theory for an organic intervalence compound. *J. Am. Chem. Soc.* 116: 1589–1590.

46 Kavarnos, G.J. and Turro, N.J. (1986). Photosensitization by reversible electron transfer: theories, experimental evidence, and examples. *Chem. Rev.* 86: 401–449.

47 Marcus, R.A. (1964). Chemical and electrochemical electron-transfer theory. *Annu. Rev. Phys. Chem.* 15: 155–196.

48 Miller, J.R., Calcaterra, L.T., and Closs, G.L. (1984). Intramolecular long-distance electron transfer in radical anions. The effect of free energy and solvent on the reaction rates. *J. Am. Chem. Soc.* 106: 3047–3049.

49 Rehm, D. and Weller, A. (1970). Kinetics of fluorescence quenching by electron and hydrogen-atom transfer. *Israel J. Chem.* 8: 259–271.

50 Weller, A. (1982). Photoinduced electron transfer in solution: exciplex and radical ion pair formation, free enthalpies and their solvent dependence. *Zeitschrift für Physikalische Chem.* 133: 93–98.

51 Bolton, J.R. and Archer, M.D. (1991). Basic electron-transfer theory. In: *Electron Transfer in Inorganic, Organic and Biological Systems*, Advances in Chemistry Series, vol. 228, Chapter 2 (ed. J.R. Bolton, N. Mataga and G. McLendon), 7–23. Washington: ACS.

52 Ceroni, P. and Balzani, V. (2012). Photoinduced energy and electron transfer processes. In: *The Exploration of Supramolecular Systems and Nanostructures by Photochemical Techniques*, Lecture Notes in Chemistry 78 (ed. P. Ceroni), 21–38. Dordrecht, Heidelberg, London, New York: Springer.

53 Albinsson, B. and Mårtensson, J. (2008). Long-range electron and excitation energy transfer in donor-bridge-acceptor systems. *J. Photochem. Photobiol. C Photchem. Rev.* 9: 138–155.

54 Osuka, A. (2015). Towards *meso-meso*-linked porphyrin arrays and *meso*-aryl expanded porphyrins. *Chem. Rec.* 15: 143–159.

55 Kang, Y.K., Iovine, P.M., and Therien, M.J. (2011). Electron transfer reactions in rigid, cofacially compressed, π-stacked porphyrin-bridge-quinone systems. *Coord. Chem. Rev.* 255: 804–824.

56 Kesters, J., Verstappen, P., Kelchtermans, M. et al. (2015). Porphyrin-based bulk heterojunction organic photovoltaics: the rise of the colors of life. *Adv. Energy Mater.* 5: 1500218.

57 Fukuzumi, S., Honda, T., and Kojima, T. (2012). Structures and photoinduced electron transfer of protonated complexes of porphyrins and metallophthalocyanines. *Coord. Chem. Rev.* 256: 2488–2502.

58 Khan, T.K., Bröring, M., Mathur, S., and Ravikanth, M. (2013). Boron dipyrrin-porphyrin conjugates. *Coord. Chem. Rev.* 257: 2348–2387.

59 Yang, J., Yoon, M.-C., Yoo, H. et al. (2012). Excitation energy transfer in multiporphyrin arrays with cyclic architectures: towards artificial light-harvesting antennae complexes. *Chem. Soc. Rev.* 41: 4808–4826.

60 Yan, Q., Luo, Z., Cai, K. et al. (2014). Chemical designs of functional photoactive molecular assemblies. *Chem. Soc. Rev.* 43: 4199–4221.

61 Pelado, B., Abou-Chanine, F., Calbo, J. et al. (2015). Role of the bridge in photoinduced electron transfer in porphyrin-fullerene dyads. *Chem. A Eur. J.* 21: 5814–5825.

62 Kirner, S.V., Henkel, C., Guldi, D.M. et al. (2015). Multistep energy and electron transfer processes in novel rotaxane donor-acceptor hybrids generating microsecond-lived charge separated state. *Chem. Sci.* 2015: 7293–7304.

63 Lo, P.-C., Leng, X., and Ng, D.K.P. (2007). Hetero-arrays of porphyrins and phthalocyanines. *Coord. Chem. Rev.* 251: 2334–2353.

64 Chitta, R. and D'Souza, F. (2008). Self-assembled tetrapyrrole-fullerene and tetrapyrrole-carbon nanotube donor–acceptor hybrids for light induced electron transfer applications. *J. Mater. Chem.* 18: 1440–1471.

65 Panda, M.K., Ladomenou, K., and Coutsolelos, A.G. (2012). Porphyrins in bio-inspired transformations: light-harvesting to solar cells. *Coord. Chem. Rev.* 256: 2601–2627.

66 Bottari, G., Trukhina, O., Ince, M., and Torres, T. (2012). Towards artificial photosynthesis: supramolecular, donor-acceptor, porphyrin- and phthalocyanine/carbon nanostructure ensembles. *Coord. Chem. Rev.* 256: 2453–2477.

67 Chandra, B.K. and D'Souza, F. (2016). Design and photochemical study of supramolecular donor-acceptor systems assembled via metal-ligand axial coordination. *Coord. Chem. Rev.* 322: 104–141.

68 de la Torre, G., Bottari, G., Sekita, M. et al. (2013). A voyage into the synthesis and photophysics of homo- and heterobinuclear ensembles of phthalocyanines and porphyrins. *Chem. Soc. Rev.* 42: 8049–8105.

69 Chakrabarty, R., Mukherjee, P.S., and Stang, P.J. (2011). Supramolecular coordination: self-assembly of finite two- and three-dimensional ensembles. *Chem. Rev.* 111: 6810–6918.

70 Menting, R., Ng, D.K.P., Röder, B., and Ermilov, E.A. (2012). Sequential energy and charge transfer processes in mixed host-guest complexes of subphthalocyanine, porphyrin and phthalocyanine chromophores. *Phys. Chem. Chem. Phys.* 14: 14573–14584.

71 Chandra, B.K., Lim, G.N., and D'Souza, F. (2015). Multi-modular, tris(triphenylamine) zinc porphyrin-zinc phthalocyanine-fullerene conjugate as a broadband capturing, charge stabilizing, photosynthetic "antenna-reaction center" mimic. *Nanoscale* 7: 6813–6826.

72 Lim, G.N., Maligaspe, E., Zandler, M.E., and D'Souza, F. (2014). A supramolecular tetrad featuring covalently linked ferrocene-zinc porphyrin-BODIPY coordinated to fullerene: a charge stabilizing, photosynthetic antenna-reaction center mimic. *Chem. Eur. J.* 20: 17089–17099.

73 Ethirajan, M., Patel, N.J., and Pandey, R.V. (2010). Porphyrin-based multifunctional agents for tumor-imaging and photodynamic therapy. In: *Handbook of Porphyrin Science*, vol. 4, Chapter 20 (ed. K.M. Kadish, K.M. Smith and R. Guilard), 249–323. Singapore: World Scientific Publishing Co. Pte. Ltd.

74 Jux, N. and Röder, B. (2010). Targeting strategies for tetrapyrrole-based photodynamic therapy. In: *Handbook of Porphyrin Science*, vol. 4, Chapter 20 (ed. K.M. Kadish, K.M. Smith and R. Guilard), 325–401. Singapore: World Scientific Publishing Co. Pte. Ltd.

75 Dolphin, D. (1994). 1993 Syntex award lecture: photomedicine and photodynamic therapy. *Can. J. Chem.* 72: 1005–1013.

76 Ormond, A.B. and Freeman, H.S. (2013). Dye sensitizers for photodynamic therapy. *Materials* 6: 817–840.

77 Ochsner, M. (1997). Photophysical and photobiological processes in the photodynamic therapy of tumors. *J. Photochem. Photobiol. B Biol.* 39: 1–18.

78 Hackbarth, S., Bornhütter, T., and Röder, B. (2016). Singlet oxygen in heterogeneous systems. In: *Singlet Oxygen: Applications in Biosciences and Nanosciences*, vol. 2, Chapter 26 (ed. S. Nonell and C. Flors), 27–42. Cambridge: Royal Society of Chemistry.

79 Jasinski, S., Ermilov, E.A., Jux, N., and Röder, B. (2007). Novel synthetic cycloketo-tetraphenylporphyrins. *Eur. J. Org. Chem.* 1075–1084.

80 Turro, N.J. (1991). *Modern Molecular Photochemistry*. Sausalito, CA, USA: University Science Books.

81 Feng, Y., Cheng, J., Zhou, L. et al. (2012). Ratiometric optical oxygen sensing: a review in respect of material design. *Analyst* 137: 4885–4901.

82 Papkovsky, D.B., Ponomarev, G.V., Trettnak, W., and O'Leary, P. (1995). Phosphorescent complexes of porphyrin ketones: optical properties and application to oxygen sensing. *Anal. Chem.* 67: 4112–4117.

83 Fercher, A., Borisov, S.M., Zhdanov, A.V. et al. (2011). Intracellular O_2 sensing probe based on cell-penetrating phosphorescent nanoparticles. *ACS Nano* 5: 5499–5508.

84 Borchert, N.B., Kerry, J.P., and Papkovski, D.B. (2013). A CO_2 sensor based on Pt-porphyrin dye and FRET scheme for food packaging applications. *Sens. Actuators B* 176: 157–165.

85 Zhu, M., Zhou, Y., Yang, L. et al. (2014). Synergetic coupling of fluorescent "turn-off" with spectral overlap modulated FRET for ratiometric Ag^+ sensor. *Inorg. Chem.* 53: 12186–12190.

86 Cheng, F., Wu, X., Liu, M. et al. (2016). A porphyrin-based near-infrared fluorescent sensor for sulfur ion detection and its application in living cells. *Sens. Actuators B* 228: 673–678.

13

NMR Spectroscopy of Porphyrins

Craig J. Medforth

LAQV-REQUIMTE, Department of Chemistry and Biochemistry, University of Porto, Porto, Portugal

13.1 Introduction

NMR spectroscopy is widely used to study porphyrins and related tetrapyrroles, and a vast amount of literature has been published in this area. The applications of NMR range from the routine (e.g., obtaining a spectrum to confirm the structure and purity of a porphyrin) to exquisite studies of the structures and dynamics of supramolecular porphyrin arrays and heme proteins. Several comprehensive reviews of NMR spectroscopy of porphyrins have been published since the first NMR spectrum of a porphyrin was reported in 1959 [1]. The first review was published in 1975 as part of the classic textbook *Porphyrins and Metalloporphyrins* [2]. Four years later, the area was reviewed again as part of a seven-volume set, *The Porphyrins*, where coverage was divided into separate chapters for diamagnetic [3] and paramagnetic [4] porphyrins. More than 20 years passed before NMR spectroscopy of porphyrins was comprehensively reviewed once more as part of a 20-volume series, *The Porphyrin Handbook*, which included chapters on NMR spectroscopy of diamagnetic [5] and paramagnetic [6] porphyrins and heme proteins [7, 8].

This chapter provides an overview of NMR spectroscopy of porphyrins and related tetrapyrroles, beginning with a description of the proton NMR features of simple symmetrical diamagnetic porphyrins (Section 13.2.1). It continues with NMR spectroscopy of porphyrins with unsymmetrical substituent patterns or complex substituents and with the techniques that are used to assign the spectra of these molecules (Section 13.2.2). Proton NMR spectra of porphyrins with modified macrocycles are then discussed with an emphasis on how the structure influences the ring current of the macrocycle (Section 13.2.3). Section 13.3 introduces heteronuclear NMR spectroscopy of diamagnetic porphyrins and describes some of the nuclei that have been investigated. Examples of NMR studies of the structures and dynamics of porphyrins are discussed in Section 13.4. The final sections describe proton NMR spectroscopy of paramagnetic metalloporphyrins (Section 13.5) and solid-state NMR (SSNMR) spectroscopy of porphyrins (Section 13.6).

Fundamentals of Porphyrin Chemistry: A 21st Century Approach, Volume 2, First Edition.
Edited by Penelope J. Brothers and Mathias O. Senge.
© 2022 John Wiley & Sons Ltd. Published 2022 by John Wiley & Sons Ltd.

13.2 Proton NMR Spectroscopy of Diamagnetic Porphyrins

13.2.1 Simple Symmetrical Porphyrins

The proton NMR spectra of symmetrical molecules such as porphine (H_2P) [9], 2,3,7,8,12,13,17,18-octaethylporphyrin (H_2OEP) [10], and 5,10,15,20-tetraphenylporphyrin (H_2TPP) [5] (Figure 13.1, Table 13.1) serve as a useful starting point for exploring NMR spectroscopy of porphyrins. The molecules display only single signals for each type of proton due to rapid exchange of the inner hydrogen atoms between the four nitrogen atoms (NH tautomerism). The proton signals are also seen over a very large chemical shift range (+11 to −4 ppm). In the case of H_2P, the chemical shifts of the signals (NH −3.76 ppm, β protons +9.74 ppm) are very different from those of pyrrole (NH 7–12 ppm, β protons +6.05 ppm) [11].

The chemical shift observed for a proton is the result of several effects including a diamagnetic contribution from the magnetic field generated by electron density in the s orbital and anisotropic effects from groups such as carbonyls, hydrogen bonding shifts, and aromatic ring currents [12]. The unusual chemical shifts seen in porphyrins are due in large part to the large ring current of the porphyrin macrocycle. This can be viewed as an induced magnetic field generated by the circulation of delocalized π-electrons around the molecular framework due to an applied magnetic field (B_0) [13] as illustrated for the benzene molecule in Figure 13.2 [14]. The β and meso protons are outside the ring and in the plane of the porphyrin, so the induced and applied (B_0) fields are aligned, and large downfield shifts are

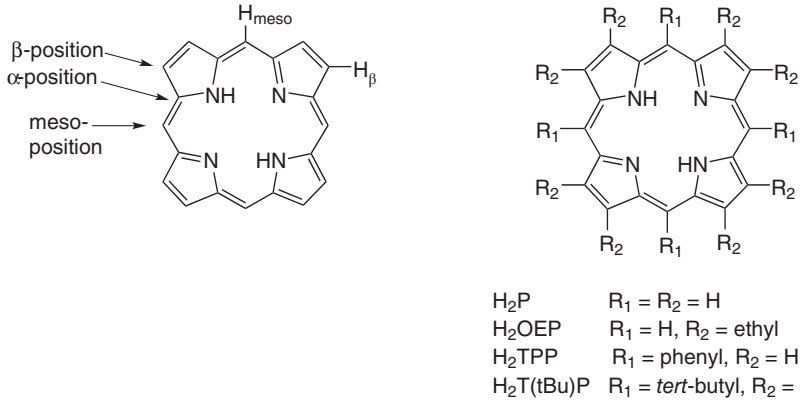

Figure 13.1 Porphyrin nomenclature and the structures of some symmetrically substituted free-base porphyrins.

Table 13.1 Proton chemical shifts for simple symmetrical porphyrins.

Porphyrin	H_{meso}	Hβ	NH	Δδ (H_{meso}-NH)
H_2P	10.58	9.74	−3.76	14.34
H_2OEP	10.18	n/a	−3.74	13.92
H_2TPP	n/a	8.75	−2.76	

Spectra were measured in $CDCl_3$ and referenced to TMS.

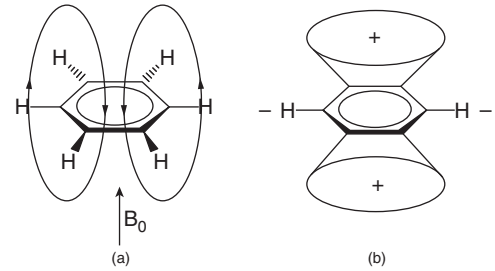

Figure 13.2 The ring current effect in benzene: (a) induced magnetic field of benzene resulting from a magnetic field (B_0) applied perpendicular to the ring plane, and (b) shielding regions (indicated by a plus sign) and deshielding regions (minus sign). Source: From Baranac-Stojanovic [14] with permission of The Royal Society of Chemistry.

seen (Figure 13.2b). In contrast, the NH protons are inside the porphyrin core where the applied and induced magnetic fields oppose each other, so large upfield shifts are observed. The difference between the chemical shifts of the meso (or β) and NH protons (Δδ, Table 13.1) can be used an approximate measure of the ring current.

The presence of a signal for the NH protons in the region from −2 to −4 ppm is generally a useful indicator that a free-base porphyrin has been successfully synthesized. However, occasionally this "fingerprint" is shifted, as seen for $H_2T(t\text{Bu})P$ (Figure 13.1), where the NH proton signal is at +1.58 ppm [15]. This large downfield shift is a result of the *tert*-butyl substituents deforming the macrocycle into a nonplanar structure that favors intramolecular hydrogen bonding.

For diamagnetic metal complexes of OEP there is a downfield shift of the meso proton signal as the oxidation state of the central metal increases [5]. This is consistent with an electron withdrawing effect from the central metal ion. Depending upon the metal ion complexed to the porphyrin, there is also the possibility of observing signals for axial anions or ligands. The signals for these protons are often far upfield of where they are normally observed due to their position in the shielding region of the porphyrin ring current (Figure 13.2b). For example, the chemical shift for the *ortho* protons of pyridine is 8.6 ppm [11], but the signal for these protons is seen at 0.0 ppm in the diamagnetic complex $Co^{III}OEP(pyridine)_2$ [16].

A number of empirical models have been developed to allow the calculation of ring current shifts for porphyrins [16, 17]. One model uses the flow of electrons in wire loops positioned above and below the plane of the porphyrin macrocycle (representing the location of the π-orbitals) [17]. Another uses equivalent dipoles to represent the current loops [16] and has eight dipoles on each face of the porphyrin (four for the pyrrole rings and four for the "hexagons" that sit between the pyrrole rings). The ring currents in several porphyrins were investigated using the dipole model [16, 18] and found to decrease by approximately 5% between adjacent members of the series $Co^{III}OEP < Co^{III}TPP < Co^{III}T(t\text{Bu})P$.

13.2.2 Porphyrins with Unsymmetrical Substitution or Complex Substituents

In the early days of proton NMR spectroscopy, assignment of the spectra of this class of porphyrins could be challenging. For example, assignment of the spectrum of protoporphyrin IX dimethyl ester (Figure 13.3a) was problematic as there is no *J*-coupling between the substituents at the porphyrin periphery. Developments such as nuclear Overhauser effect (NOE) spectroscopy [19] solved this problem by allowing the establishment of *through-space* connectivities. Together with other NMR techniques that have been developed (e.g., two-dimensional NMR spectroscopy), it is now possible to completely assign virtually all proton NMR spectra of porphyrins and related molecules.

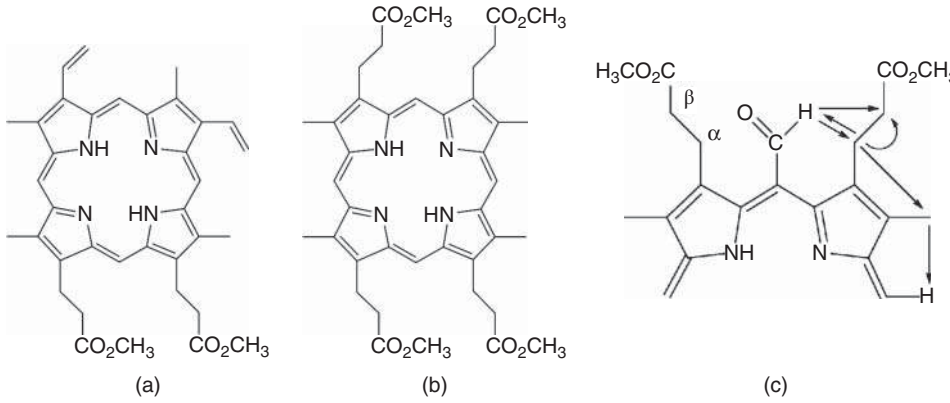

Figure 13.3 Structures of (a) protoporphyrin IX dimethyl ester and (b) coproporphyrin II tetramethyl ester. Nuclear Overhauser effect (NOE) connectivities determined for the formylated side product of coproporphyrin II are shown in (c). The tail of the arrow indicates the proton(s) irradiated during the NOE experiment, and the head shows the signals with an NOE enhancement detected by difference spectroscopy.

The use of NOE difference spectroscopy to solve a simple structural problem is illustrated in Figures 13.3b,c [20]. A formylated by-product was obtained during the synthesis of coproporphyrin II tetramethyl ester (Figure 13.3b), but it was not clear if formylation had occurred between the methyl or propionate substituents. NOE difference experiments involving irradiation of the signal for the formyl protons revealed through-space connections with the α and β methylene protons of the adjacent propionate groups (Figure 13.3c). Irradiation of the signal for the α-methylene protons also gave enhancements of signals for the formyl, methyl, and β-methylene protons. This clearly show that formylation occurs between the propionate substituents even though this is the more sterically hindered position [20].

The NMR spectrum of the cyclic trimer of Ga(III) 2-hydroxy-5,10,15,20-tetraphenylporphyrin $[Ga^{III}(2\text{-O-TPP})]_3$ (Figure 13.4a) is extremely complicated (Figure 13.4c) [21, 22]. However, the spectrum could be assigned using two-dimensional NMR spectroscopy [23]. Nuclear Overhauser enhancement (NOESY) and *through-bond* correlation spectroscopy (COSY) experiments for this molecule are shown in Figure 13.4c. Assignments for two of the porphyrin phenyl groups are given in the COSY spectrum, and complete assignments for the porphyrin rings are provided in Figure 13.4b. Note that signals for the three β-protons next to the oxygen substituents are strongly shielded by the ring current of an adjacent porphyrin and are seen between 1.5 and 3 ppm (Figure 13.4c).

13.2.3 Porphyrins with Modified Macrocycles

A large number of porphyrins with modified macrocycles have been synthesized, which provide insights into the effect of structural changes on the ring current and other properties of the macrocycle. A selection of modified macrocycles is shown in Figure 13.5, and proton NMR data for some of these molecules are summarized in Table 13.2.

Reduction of a peripheral double bond to produce H_2OEC [24] results in a downfield shift for the signal from the NH protons and an upfield shift for the meso proton signal. These changes are consistent with a decrease in the ring current for the chlorin macrocycle even though porphyrins and chlorins both have an 18 π-electron delocalization pathway. Changes in the ring current for up to three reductions at the porphyrin periphery have been quantified using a dipole model of the ring current [25].

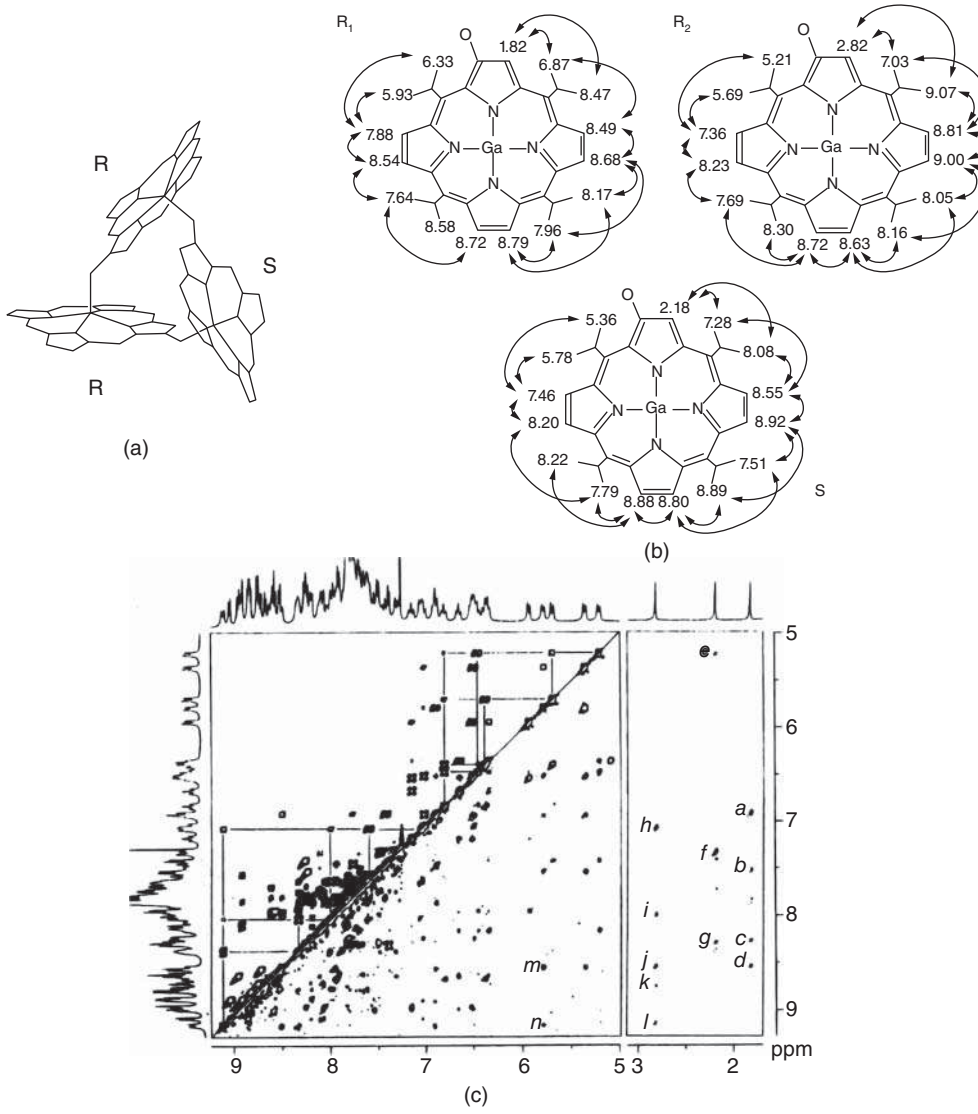

Figure 13.4 (a) Structure of the cyclic trimer of Ga(III) 2-hydroxy-5,10,15,20-tetraphenylporphyrin $[Ga^{III}(2\text{-O-TPP})]_3$ with the phenyl groups omitted for clarity, (b) assignments of the proton NMR signals for the three TPP subunits with their NOE connectivities, and (c) correlation spectroscopy (COSY) (upper left triangle) and Nuclear Overhauser enhancement (NOESY; lower right triangle) spectra for the trimer. Source: Adapted with permission from Wojaczynski and Latos-Grazynski [21] and Wojaczynski et al. [22]. Copyright 1995 and 1997 American Chemical Society.

For Ex-H_2OEP [26] the extra meso carbon atoms increase the delocalization pathway to 26 π-electrons from the 18 π-electrons in H_2OEP, which is expected to increase the ring current. The chemical shifts for the respective diprotonated species (H_4OEP^{2+} and Ex-H_2OEP^{2+}) confirm that the ring current is significantly increased, with Δδ changing from 15.62 to 20.12 ppm.

A comparison of the NMR spectrum of Iso-H_2P with H_2P reveals only small upfield shifts for the meso and β-protons. However, there is a large downfield shift for the NH proton signal,

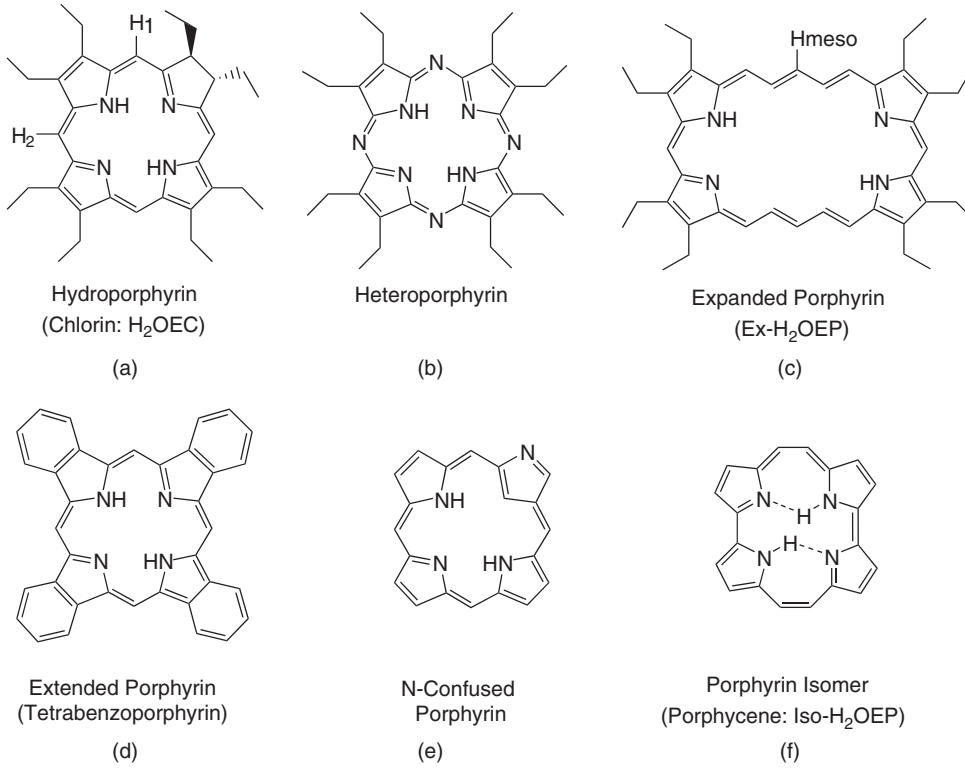

Figure 13.5 Structures of porphyrins with modified macrocycles. Structures (a)–(c) are related to H_2OEP, and structures (d)–(f) are related to H_2P.

Table 13.2 Proton chemical shifts for some porphyrins with modified macrocycles.

Porphyrin	H_{meso}	Hβ	NH	Δδ (H_{meso}-NH)	Solvent
H_2OEP	10.18	n/a	−3.74	13.92	$CDCl_3$
H_2OEC	8.95 (H_1) 9.80 (H_2)	n/a	−2.46	11.41 12.26	$CDCl_3$
$[H_4OEP^{2+}][CF_3CO_2]_2$	11.22	9.92	−4.40	15.62	$CDCl_3$/ CF_3CO_2D
$[Ex\text{-}H_4OEP^{2+}][CF_3CO_2]_2$	14.35		−5.77	20.12	CF_3CO_2D
H_2P	10.58	9.74	−3.76	14.34	$CDCl_3$
Iso-H_2P (Porphycene)	9.83	9.67, 9.23	+3.15	6.68	$CDCl_3$

Spectra are referenced to TMS.

which is seen at +3.15 ppm [27]. This is the result of strong intramolecular hydrogen bonding made possible by the unusual geometry of Iso-H_2P (see Figure 13.5f).

13.3 Heteronuclear NMR Spectroscopy of Diamagnetic Porphyrins

NMR spectra have been obtained for a large number of heteronuclei in diamagnetic porphyrins including ^{2}H, ^{3}H, ^{7}Li, ^{11}B, ^{13}C, ^{15}N, ^{17}O, ^{19}F, ^{27}Al, ^{29}Si, ^{31}P, ^{59}Co, ^{77}Se, ^{113}Cd, ^{119}Sn,

Table 13.3 Chemical shifts for some heteronuclei in TPP complexes.

Nucleus	Porphyrin	Chemical shift	Solvent	Chemical shift standard
^{19}F	$Si^{IV}(TPP)F_2$	−122.5	$CDCl_3$	$CFCl_3$
^{31}P	$[P^{V}(TPP)Cl_2]Cl$	−176.7	$CDCl_3$	H_3PO_4
^{59}Co	$[Co^{III}(TPP)(Im)_2]BF_4$	8300	CH_3OH	$K_3Co(CN)_6$
^{119}Sn	$Sn^{IV}(TPP)Cl_2$	−590	$CDCl_3$	$Sn(Me)_4$
^{195}Pt	$Pt^{II}TPP$	1235	$CDCl_3$	a)
^{195}Pt	$Pt^{IV}TPPCl_2$	4215	$CDCl_3$	a)

a) Chemical shifts were referenced using an absolute frequency equal to 0.214 times the ^1H frequency of TMS.

^{195}Pt, and ^{205}Tl [5]. The feasibility of obtaining an NMR spectrum depends upon several factors, including the relative sensitivity of the nucleus, its natural abundance, and its spin (nuclei with $I \geq 1$ have electric quadrupole moments, which can lead to broadening or complete loss of the NMR signal) [13]. Using ^1H as a reference (natural abundance 99.98%, relative sensitivity 1.00, absolute sensitivity 1.00), the heteronuclei listed above have absolute sensitivities ranging from 3.9×10^{-6} (for ^{15}N) to 0.83 (for ^{19}F) [13]. The most commonly studied heteronucleus is ^{13}C, which has an absolute sensitivity of only 1.8×10^{-4}. However, the sensitivity of this and other heteronuclei can be increased by the use of indirect detection techniques [28] and also by isotopic enrichment.

The chemical shift ranges for heteronuclei are usually much larger than those observed in proton NMR spectroscopy due to the presence of a paramagnetic contribution to the chemical shifts. This arises from the magnetic fields generated by electron density in orbitals that are not spherically symmetrical (e.g., p-orbitals) and the presence of low-lying paramagnetic states [12]. This paramagnetic contribution should not be confused with the paramagnetic shifts arising from the unpaired electrons of a metal complexed to the porphyrin, which are discussed in Section 13.5. Note that the ring current effect is the same (when measured in ppm) for different nuclei, so its contribution to the chemical shifts of heteronuclei is usually small.

Table 13.3 shows the chemical shifts of ^{19}F, ^{31}P, ^{59}Co, ^{119}Sn, and ^{195}Pt in some TPP complexes [5]. Note that the chemical shifts vary over hundreds or even thousands of ppm due to the paramagnetic contribution. Large chemical shift differences are also observed for the same nucleus in different oxidation states, as shown by the chemical shifts for Pt(II) and Pt(IV) (1235 and 4215 ppm, respectively).

The chemical shifts for the three nuclei present in almost all porphyrins (^1H, ^{13}C, and ^{15}N) are listed in Table 13.4 for H_2OEP. Some non-porphyrin compounds are also shown for comparison [11, 29]. The ^{13}C [30] and ^{15}N [31] spectra were measured at low temperatures, where NH tautomerism is slow on the NMR timescale. Under these conditions, it is possible to observe signals for "pyridine" type (C—N=C) and "pyrrole" type (C—NH—C) rings of the porphyrin. In the ^{13}C NMR spectra, the α-positions show a downfield shift (+17.0 ppm) for the "pyridine" rings versus the "pyrrole" rings. A downfield shift is also seen for the reference compounds pyridine and pyrrole (+31.8 ppm) [11]. In the ^{15}N spectrum of H_2OEP, there is also a very large downfield shift for C—N=C versus C—NH—C nitrogen atoms (+104 ppm), which is again similar to that seen in model systems (+110 ppm).

Table 13.4 Chemical shifts for different nuclei present in H_2OEP.

Nucleus	Chemical shift	Reference(temperature)	Non-porphyrin compound
^{1}H	10.18 (Hmeso)	TMS	
^{13}C	95.8 (Cmeso) 150.6 (Cα, C—N=C), 133.6 (Cα, C—NH—C) 143.6 (Cβ, C—N=C) 138.3 (Cβ, C—NH—C)	TMS (193 K)	 149.8 (Cα, pyridine) 118.0 (Cα, pyrrole) 123.6 (Cβ, pyridine) 107.7 (Cβ, pyrrole)
^{15}N	−143 (C—N=C) −247 (C—NH—C)	External nitromethane (227 K)	−126 (1-methylimidazole) −236 (pyrrole)

Spectra were measured in $CDCl_3$ or CD_2Cl_2.

Two-dimensional heteronuclear NMR spectroscopy is a powerful tool for assigning the NMR spectra of porphyrins. For example, heteronuclear single quantum coherence (HSQC) spectroscopy can be used to detect one-bond connections between ^{1}H and ^{13}C, and heteronuclear multiple-bond correlation (HMBC) spectroscopy can detect ^{1}H and ^{13}C connections over 2–4 bonds. These experiments are often used in combination with ^{1}H—^{1}H experiments such as COSY and NOESY to assign complicated NMR spectra. An example of this approach is shown in Figure 13.6 [32] for the trimer of a porphyrin tetramer (molecular weight 14.7 kDa). The region of the ^{13}C NMR spectrum displayed in Figure 13.6b contains signals for the pyrrole protons (125–135 ppm) and the *ortho*-aryl (110–115 ppm) and *para*-aryl (100–105 ppm) protons. A total of 24 pyrrole signals are observed, consistent with the parallel stacked structure shown in Figure 13.6a. NOESY was used to establish through-space interactions between the porphyrins in the tetramer and between the tetramer units (arrows in Figure 13.6a).

13.4 Structures and Dynamics of Diamagnetic Porphyrins

NMR spectroscopy has long been used to study the structures and dynamics of porphyrins [2, 3, 5]. Earlier in this chapter, the effect of core modification on aromaticity was discussed (Section 13.2.3), and the structure determination of a trimer of porphyrin tetramers was described (Section 13.3). Some examples of other structural studies include the self-aggregation of porphyrins [33, 34] or chlorophylls [35, 36], stacking of porphyrins with non-porphyrinic π-systems [37], binding of ligands to metalloporphyrins [16, 38–40], and the formation of inclusion complexes stabilized by porphyrin–guest hydrogen bonds [41].

Figure 13.7 shows several examples of porphyrin–guest pairs that have been investigated using proton NMR spectroscopy. Exchange between amine ligands and zinc porphyrins is usually fast on the NMR timescale at room temperature. However, exchange of imidazole is slow on the NMR timescale for the doubly capped porphyrin host shown in Figure 13.7a [39]. This is due to favorable interactions between the ligand and the porphyrin cap. Note that bulky amines such as 4-*t*-butylpyridine do not bind to the porphyrin because the cavity is too small. The porphyrin shown in Figure 13.7b is optimized for the binding of barbital by the formation of six hydrogen bonds between the host and the guest [41]. A large upfield

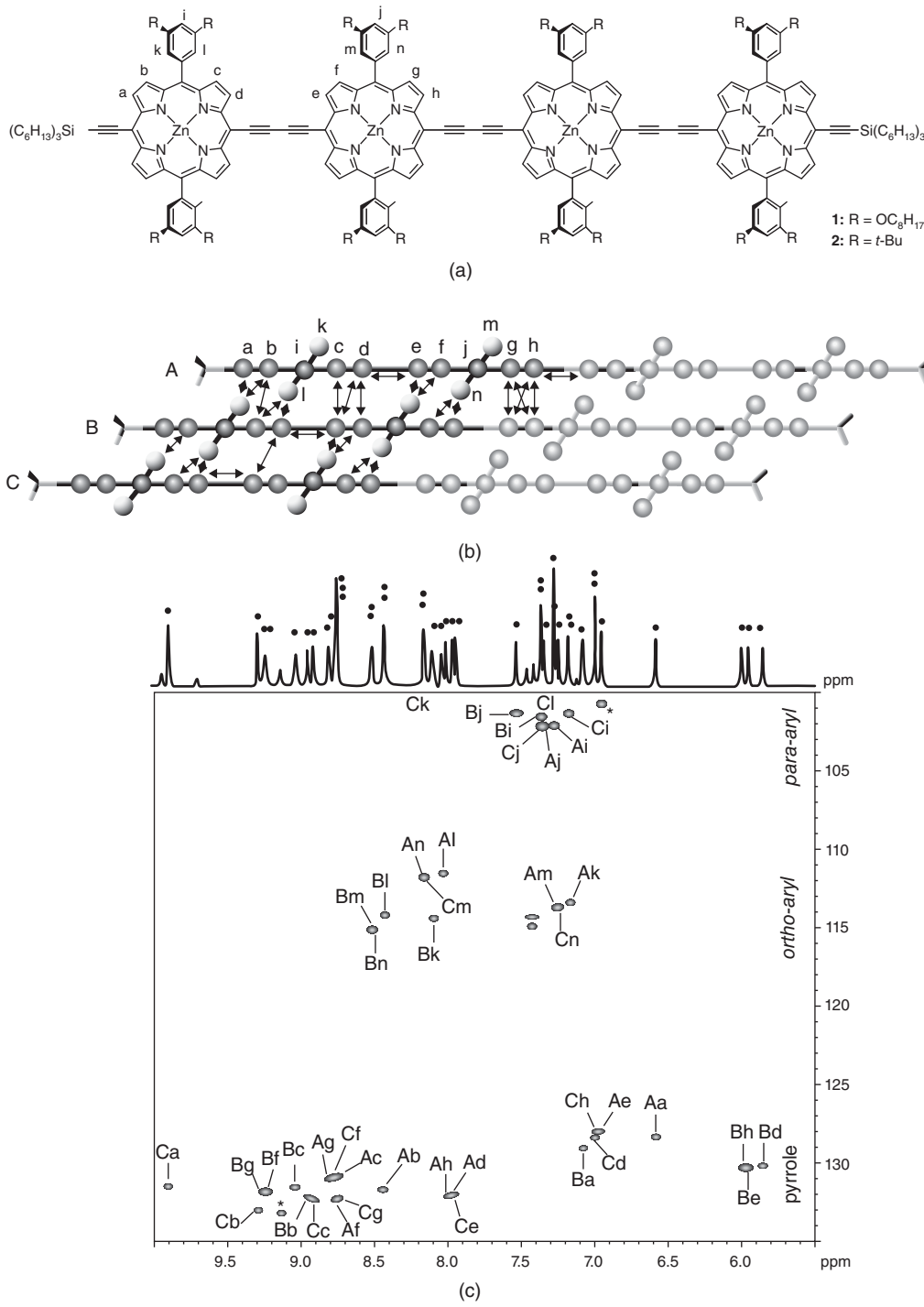

Figure 13.6 (a) Structure of a porphyrin tetramer and its trimeric structure in solution (NOE connectivities shown by arrows) and (b) partial $^{1}H-{}^{13}C$ HSQC spectrum. Source: Adapted with permission from Hutin et al. [32]. Copyright 2013 American Chemical Society.

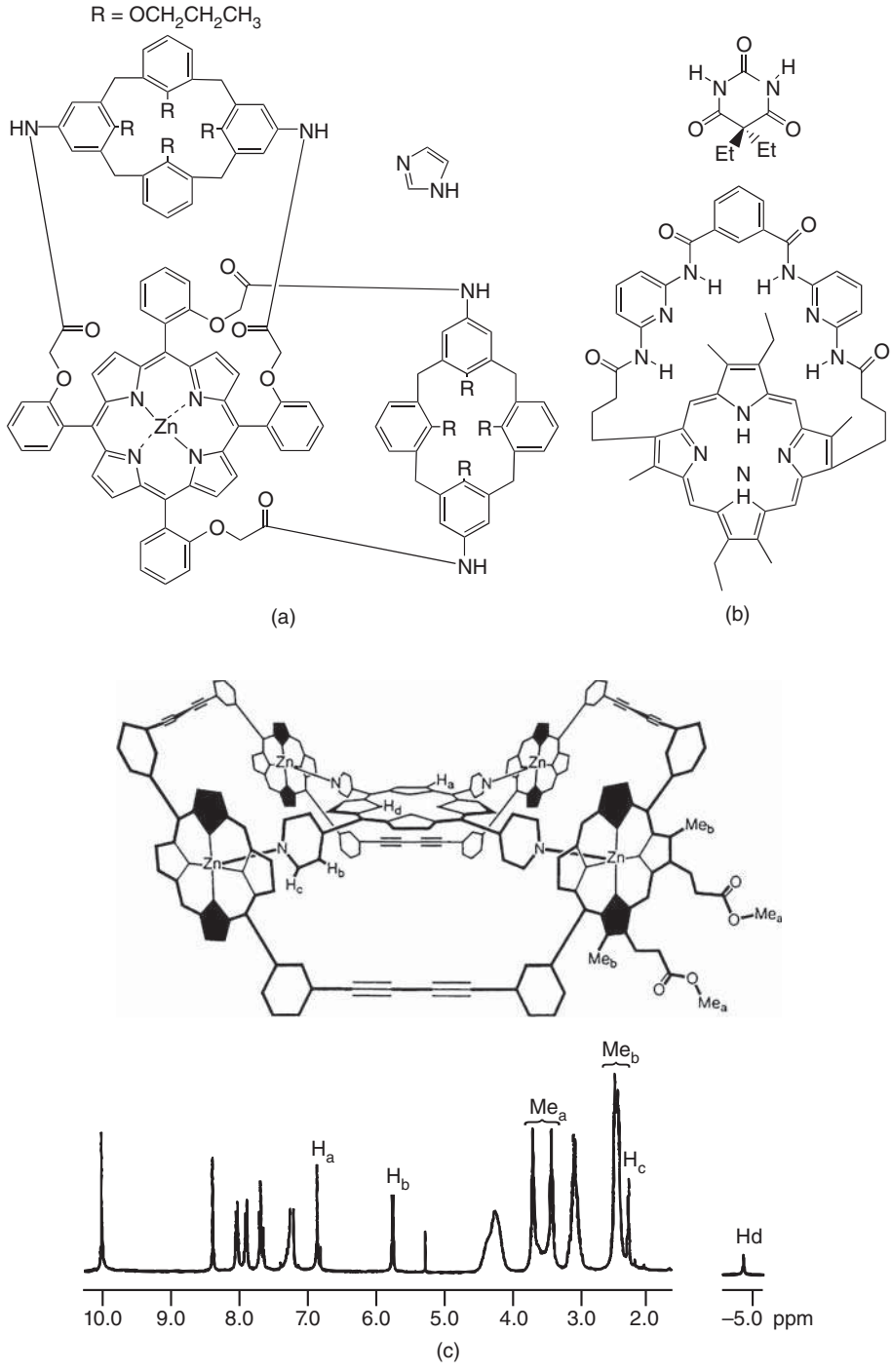

Figure 13.7 Structures of some porphyrin host–guest complexes. Source: Figure (c) reproduced from Anderson et al. [40] with permission of The Royal Society of Chemistry.

shift (6.1 ppm) is observed for the methylene protons of the guest molecule, as binding places them in the shielding region of the porphyrin ring current. An unusual example of a porphyrin host complexing a porphyrin guest is shown in Figure 13.7c [40]. In this case, a cyclic zinc porphyrin tetramer binds a metal-free 5,10,15,20-tetrapyridylporphyrin. A large upfield shift is observed for the signal from protons adjacent to the pyridine nitrogen atom of the guest molecule, confirming that its pyridyl substituents are acting as axial ligands for the zinc porphyrins that form the host.

Activation energies for some dynamic processes seen in porphyrins are shown in Table 13.5. NH tautomerism (Figure 13.8a) has been studied in a large number of systems [5] since it was first reported in 1972 [42]. The NH tautomerism process in porphyrins is best described by (i) a transition state where a proton is bridging two nitrogen atoms, (ii) an intermediate state where the NH protons are on adjacent rings, and (iii) proton tunneling (which leads to nonlinear Arrhenius behavior at low temperatures [43] and a significant increase in the activation energy upon deuteration).

Table 13.5 Activation energies for some dynamic processes in porphyrins.[a)]

Porphyrin	Process	$\Delta G^{\ddagger}$ (kJ mol^{-1})
H_2P	NH Tautomerism	49
D_2P	ND Tautomerism	55
H_2TPP	NH Tautomerism	51
$H_2T(3\text{-OMe-P})P$	Aryl-porphyrin rotation	45
$H_2T(3\text{-OMe-P})OPP$	Aryl-porphyrin rotation	65
$Ni^{II}OETPP$	Porphyrin inversion	55
$[H_4OETPP][CF_3CO_2]_2$	Porphyrin inversion	>84

a) Calculated at the coalescence temperature except for NH(D) tautomerism, which was calculated at 298 K.

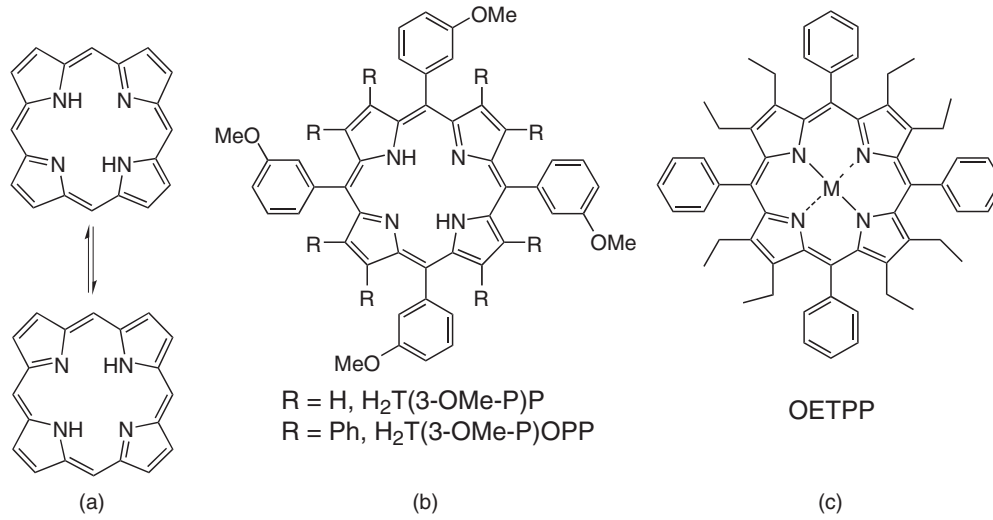

Figure 13.8 (a) NH tautomerism in porphyrins, (b) and (c) structures of some of the porphyrins in Table 13.5.

Rotational processes have been extensively investigated, including porphyrin-substituent rotation [44, 45], porphyrin-axial ligand rotation [46, 47], and porphyrin-porphyrin rotation in face-to-face dimers [48, 49]. For meso aryl groups with one *meta* substituent such as H_2T(3-OMe-P)P (Figure 13.8b, Table 13.5), the activation energy can be obtained by NMR spectroscopy [45], whereas aryl groups with *ortho* substituents usually have rotational barriers that are too high [44]. As expected, the addition of buttressing phenyl rings on the adjacent pyrrole rings to produce T(3-OMe-P)OPP [45] increases the rotational barrier.

Many exchange processes have been studied including anion exchange (in Tl^{III} porphyrins) [50], ligand exchange (in Co^{III} porphyrins) [51], and proton exchange (between the free base and dication of TPP) [52]. More unusual processes that have been investigated include the inversion of nonplanar porphyrins [53] or hydroporphyrins [54]. For the sterically crowded porphyrin OETPP (Figure 13.8(c)), the activation energy for inversion of the nonplanar macrocycle depends strongly on the substituent in the porphyrin core (Table 13.5) [53] and is much higher for the dication than for the nickel complex.

13.5 Proton NMR Spectroscopy of Paramagnetic Metalloporphyrins

NMR studies have been reported for many paramagnetic metalloporphyrins, including porphyrins where the same metal is present in different oxidation states, spin states, or ligation states [6]. As iron porphyrins are present as cofactors in a large number of proteins, it is not surprising that they have been extensively investigated [4, 6]. The proton NMR spectrum of a chloro(porphyrinato)iron(III) complex is shown in Figure 13.9 [55]. There is a large downfield shift and broadening of the signal for the protons of the β-methyl groups resulting from interactions with the paramagnetic metal center. In addition, two signals are observed for the *ortho* protons, indicating that rotation of the phenyl rings and exchange of the chloride anion are slow on the NMR timescale.

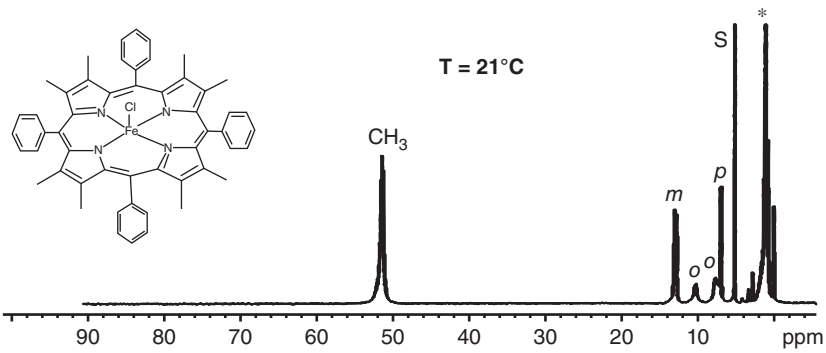

Figure 13.9 Proton NMR spectrum of the iron(III) chloride complex of 2,3,7,8,12,13,1,7,18-octamethyl-5,10,15,20-tetraphenylporphyrin. Source: Adapted with permission from Yatsunyk et al. [55]. Copyright 2005 American Chemical Society.

Table 13.6 Isotropic shifts for paramagnetic metalloporphyrins.

Metalloporphyrin complex	OEP H_{meso}	TPP or TTP[a] Hβ
Fe^{II} 5-coordinate with 2-MeIm (d^6, high spin, S = 2)	−6.7	43.4 (TPP)
Fe^{III} 5-coordinate with chloride anion (d^5, high spin, S = 5/2)	−55.6	
Fe^{III} 6-coordinate ($CF_3SO_3^-$ salt in DMSO) (d^5, high spin, S = 5/2)	40.1	
Co^{II} 4-coordinate complex (d^7, low spin, S = 1/2)	19.0	7.0 (TTP)
Dipolar Contribution (Contact Contribution)	15.0 (4.0)	9.4 (−2.4)

a) TTP = 5,10,15,20-tetra(4-methylphenyl)porphyrin.

The paramagnetic metal ion affects the chemical shifts of nearby protons by two mechanisms: (i) a contact effect that arises from scalar coupling between electron spins and proton nuclei and (ii) a dipolar effect that arises from dipole coupling of the nuclear and electron magnetic moments [6]. The contact contribution is a "through-bond" effect, whereas the dipolar contribution is a "through-space" effect. The paramagnetic shift (or isotropic shift) for a proton can be estimated using a diamagnetic reference such as the nickel complex. Isotropic shifts for protons in some paramagnetic metalloporphyrins are shown in Table 13.6.

Analysis of isotropic shifts for the meso or β-protons and substituents provides information about the contact and dipolar effects and how the unpaired electrons on the metal are delocalized via the σ- and π-orbitals of the porphyrin [6]. For example, the large positive shift seen for Hβ in the high-spin (S = 2) 5-coordinate Fe^{II}TPP complex with a 2-methylimidazole ligand arises from a σ-spin delocalization mechanism. In contrast, the large negative shift seen for the meso protons of the five-coordinate (S = 5/2) Fe^{III}OEP chloride complex results from a π−spin delocalization mechanism (Fe → P backbonding). The remarkable change in the isotropic shift of the meso proton when the Fe^{III}OEP complex becomes six coordinate (−55.6 to +40.1 ppm) indicates a significant increase in σ spin delocalization and/or a decrease in π spin delocalization. In the case of low-spin cobalt(II) porphyrins, the dipolar and contact components have been estimated [6] and are shown in Table 13.5.

Paramagnetic states are seen for hemes in a wide variety of proteins, including those involved in oxygen transport and storage (hemoglobin and myoglobin) and electron transport (cytochrome *c*) [7]. Figure 13.10 shows the proton NMR spectrum of horse cytochrome *c* where the heme is present as the low-spin iron(III) complex (d^5, S = 1/2) [56]. The 0–10 ppm region is crowded with signals from the protein, but a significant number of well-resolved signals are seen outside this window. Some of these signals arise from the substituents of the heme molecule such as the methyl groups (labeled A, B, and C) or propionate groups (b, e). Other signals are from the axial histidine ligand (protons H2 and H4, labeled i and a, respectively) or from other protein residues close to the paramagnetic center (e.g., signals k and F from Met-80).

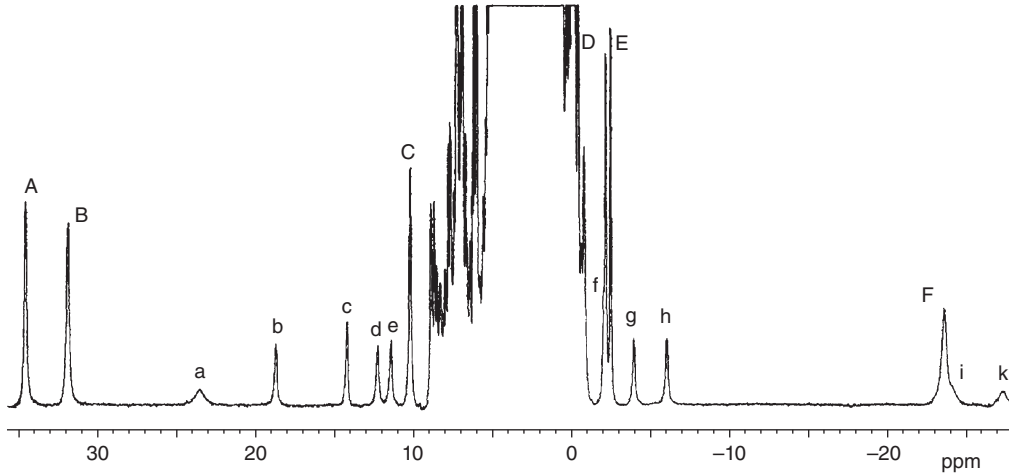

Figure 13.10 300 MHz proton NMR spectrum of 2 mM ferricytochrome *c* in D_2O at 30 °C and pH 6.8. Source: Reproduced from Santos and Turner [56]. Reproduced by permission of Wiley Publishing.

13.6 Solid-State NMR (SSNMR) Spectroscopy

SSNMR spectra have been obtained for porphyrins using cross-polarization magic angle spinning (CP-MAS). SSNMR has been used to investigate the structures and packing of porphyrins in the solid state [57, 58] and to measure the activation energies of dynamic processes such as NH tautomerism [43].

The ^{13}C spectra of a porphyrin in the solid state and in solution are shown in Figure 13.11 [57]. The SSNMR spectrum has line widths of approximately 1 ppm (100 Hz). These are at least an order of magnitude larger than those seen in the solution experiments. Many of the signals in the SSNMR spectrum can be assigned by comparison with the solution spectrum. However, there is a doubling of the carbonyl signals in the SSNMR spectrum, something that is also seen for a number of related porphyrins. SSNMR spectra of porphyrins where the alkyne groups are *para* to the porphyrin ring show up to *four* carbonyl signals together with splitting of the signals for other carbons. Crystal structures were determined for the *meta* and *para* alkyne-substituted porphyrins, and the structures were found to be consistent with the symmetries determined from the SSNMR spectra [57]. SSNMR has proved useful in other areas such as the identification of polymorphs of Cu(II) phthalocyanine ($Cu^{II}Pc$) (Figure 13.12) [58]. $Cu^{II}Pc$ is a tetrapyrrole with applications in dyes, inks, and molecular electronics. Finally, detailed ^{15}N SSNMR studies have shown that for ^{15}N-enriched H_2P, the rate constant for NH tautomerism and the kinetic isotope effect are remarkably similar in the solid (crystalline) state and in solution (toluene-d_8) [43].

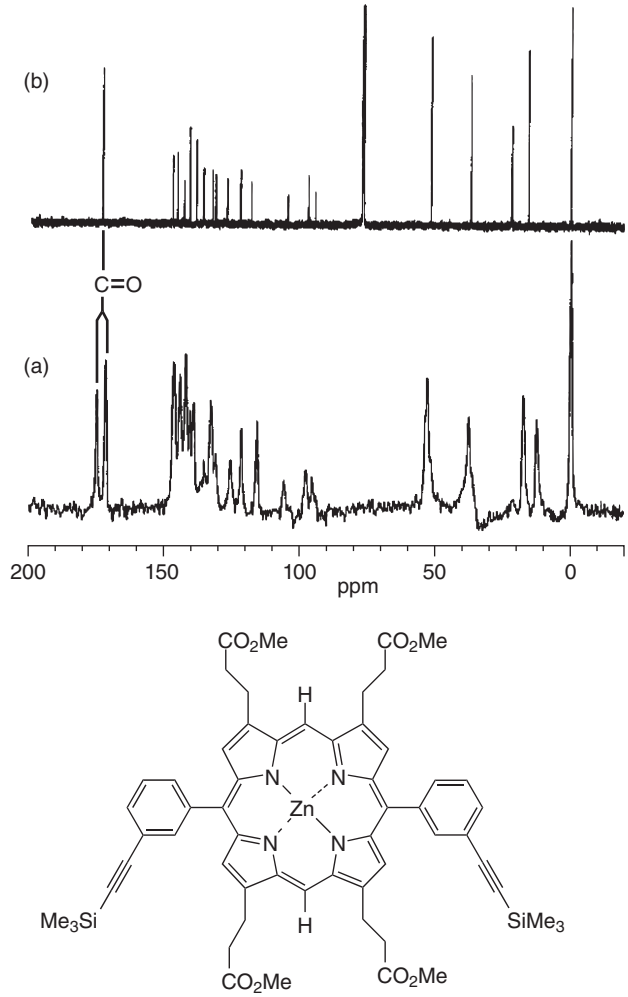

Figure 13.11 ^{13}C NMR spectra in (a) the solid state (CPMAS) and (b) in solution for the porphyrin shown. The intense signals seen at approximately 80 ppm in the solution spectrum but not in the solid-state NMR (SSNMR) spectrum are from $CDCl_3$. Source: Reproduced from Bampos et al. [57] with permission of The Royal Society of Chemistry.

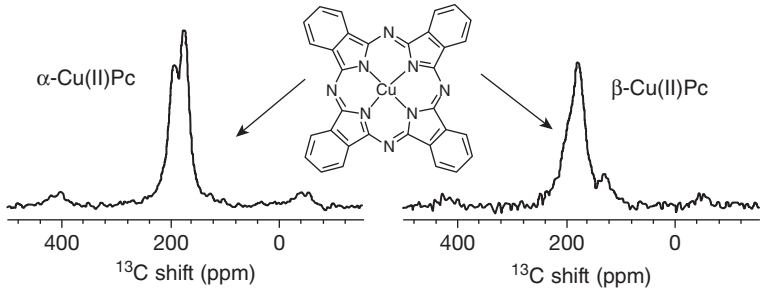

Figure 13.12 SSNMR ^{13}C NMR spectra of the α and β forms of $Cu^{II}Pc$ showing their different spectroscopic signatures. Source: Adapted with permission from Shaibat et al. [58]. Copyright 2010 American Chemical Society.

Acknowledgments

The author acknowledges financial support from the Fundação para a Ciência e a Tecnologia (Grant IF/00873/2013).

References

1 Becker, E.D. and Bradley, R.B. (1959). Effects of "ring currents" on the NMR spectra of porphyrins. *J. Chem. Phys.* 31: 1413–1414.
2 Scheer, H. and Katz, J.J. (1975). Nuclear magnetic resonance spectroscopy of porphyrins and metalloporphyrins. In: *Porphyrins and Metalloporphyrins* (ed. K.M. Smith), 399–524. Amsterdam: Elsevier.
3 Janson, T.R. and Katz, J.J. (1979). Nuclear magnetic resonance spectroscopy of diamagnetic porphyrins. In: *The Porphyrins*, vol. IV (ed. D. Dolphin), 1–59. New York: Academic Press.
4 La Mar, G.N. and Walker, F.A. (1979). Nuclear magnetic resonance of paramagnetic metalloporphyrins. In: *The Porphyrins*, vol. IV (ed. D. Dolphin), 61–157. New York: Academic Press.
5 Medforth, C.J. (2000). NMR spectroscopy of diamagnetic porphyrins. In: *The Porphyrin Handbook*, vol. 5 (ed. K.M. Kadish, K.M. Smith and R. Guilard), 1–80. Boston: Academic Press.
6 Walker, F.A. (2000). Proton NMR and EPR spectroscopy of paramagnetic metalloporphyrins. In: *The Porphyrin Handbook*, vol. 5 (ed. K.M. Kadish, K.M. Smith and R. Guilard), 81–184. Boston: Academic Press.
7 La Mar, G.N., Satterlee, J.D., and De Ropp, J.S. (2000). Nuclear magnetic resonance of hemoproteins. In: *The Porphyrin Handbook*, vol. 5 (ed. K.M. Kadish, K.M. Smith and R. Guilard), 185–298. Boston: Academic Press.
8 Banci, L., Bertini, I., Luchinat, C., and Turano, P. (2000). Solution structure of hemoproteins. In: *The Porphyrin Handbook*, vol. 5 (ed. K.M. Kadish, K.M. Smith and R. Guilard), 323–350. Boston: Academic Press.
9 Solov'ev, K.N., Mashenkov, V.A., Gradyushko, A.T. et al. (1970). High resolution NMR spectra of porphin and of porphin derivatives. *J. Appl. Spectrosc.* 13: 1106–1111.
10 Inhoffen, H.H., Fuhrhop, J.H., Voight, H., and Brockmann, H. (1966). Zur Weiteren Kenntnis des Chlorophylls und des Hämins, VI. Formylierung der meso-Kohlenstoffatome von Alkyl-substituierten Porphyrinen. *Liebigs Annal. Chem.* 695: 133–143.
11 Pretsch, E., Simon, W., Seibl, J., and Clerc, T. (1989). *Spectral Data for Structural Determination in Organic Compounds*. Berlin: Springler-Verlag.
12 Gunther, H. (1994). *NMR Spectroscopy. Basic Principles, Concepts, and Applications in Chemistry*. Chichester: Wiley.
13 Abraham, R.J., Fisher, J., and Loftus, P. (1988). *Introduction to NMR Spectroscopy*. Chichester: Wiley.
14 Baranac-Stojanovic, M. (2014). New insight into the anisotropic effects in solution-state NMR spectroscopy. *RSC Adv.* 4: 308–321.
15 Somma, M.S., Medforth, C.J., Nelson, N.Y. et al. (1999). Evidence for unusually strong intramolecular hydrogen-bonding in highly nonplanar porphyrins. *Chem. Commun.* 1221–1222.

16 Abraham, R.J. and Medforth, C.J. (1988). The NMR spectra of the porphyrins. 36 – ring currents in octaethylporphyrin, *meso*-tetraphenylporphyrin and phthalocyanine complexes. *Magn. Reson. Chem.* 26: 803–812.

17 Janson, T.R., Kane, A.R., Sullivan, J.F. et al. (1969). The ring-current effect of the phthalocyanine ring. *J. Am. Chem. Soc.* 91: 5210–5214.

18 Medforth, C.J., Muzzi, C.M., Shea, K.M. et al. (1997). Ring currents in cobalt(III) nonplanar porphyrins. *J. Chem. Soc. Perkin Trans.* 839–844.

19 Noggle, J.H. and Schirmer, R.E. (1971). *The Nuclear Overhauser Effect; Chemical Applications*. New York: Academic Press.

20 Cavaleiro, J.A.S., Graca, M., Neves, P.M. et al. (1994). Some new porphodimethene chemistry: synthesis of *meso*-formylporphyrins. *Heterocycles* 37: 213–218.

21 Wojaczynski, J. and Latos-Grazynski, L. (1995). Synthesis and characterization of gallium(III) 2-Hydroxy-5,10,15,20-tetraphenylporphyrin. A novel example of a cyclic gallium(III) porphyrin trimer. *Inorg. Chem.* 34: 1054–1062.

22 Wojaczynski, J., Latos-Grazynski, L., Olmstead, M.M., and Balch, A.L. (1997). Cyclic metalloporphyrin trimers: H-1 NMR identification of trimeric teterometallic (iron(III), gallium(III), manganese(III)) 2-hydroxy-5,10,15,20-tetraphenylporphyrins and X-ray crystal structure of the iron(III) 2-hydroxy-5,10,15,20-tetra-p-tolylporphyrin trimer. *Inorg. Chem.* 36: 4548–4554.

23 Claridge, T.D.W. (2016). *High-Resolution NMR Techniques in Organic Chemistry*. Amsterdam: Elsevier.

24 Wolf, H. and Scheer, H. (1973). Photochemical hydrogenation of pheoporphyrins – 7,8-cis-theophorbides. *Liebigs Ann. Chem.* 1710–1740.

25 Abraham, R.J., Medforth, C.J., Smith, K.M. et al. (1987). Ring currents in hydroporphyrins. *J. Am. Chem. Soc.* 109: 4786–4791.

26 Wessel, T., Franck, B., Moller, M. et al. (1993). Porphyrins with aromatic 26-π-electron systems. *Angew. Chem. Int. Ed.* 32: 1148–1151.

27 Vogel, E., Kocher, M., Schmickler, H., and Les, J. (1986). Porphycene – a novel porphyrin isomer. *Angew. Chem. Int. Ed.* 25: 257–259.

28 Bax, A., Griffey, R.H., and Hawkins, B.L. (1983). Correlation of proton and N-15 chemical-shifts by multiple quantum NMR. *J. Magn. Resn.* 55: 301–315.

29 Witanowski, M., Stefaniak, L., and Webb, G.A. (1981). *Nitrogen NMR Spectroscopy Volume 11B*. London: Academic Press.

30 Frydman, L., Olivieri, A.C., Diaz, L.E. et al. (1988). A variable-temperature solid-state carbon-13 CPMAS NMR analysis of *meso*-tetrapropylporphyrin and of octaethylporphyrin. *J. Am. Chem. Soc.* 110: 5651–5661.

31 Kawano, K., Ozaki, Y., Kyogoku, Y. et al. (1977). ^{15}N nuclear magnetic resonance spectra of octaethylporphyrin. *Chem. Commun.* 226–227.

32 Hutin, M., Sprafke, J.K., Odell, B. et al. (2013). A discrete three-layer stack aggregate of a linear porphyrin tetramer: solution-phase structure elucidation by NMR and X-ray scattering. *J. Am. Chem. Soc.* 135: 12798–12807.

33 Abraham, R.J., Eivazi, F., Pearson, H., and Smith, K.M. (1976). π–π aggregation in metalloporphyrins: causative factors. *Chem. Commun.* 699–701.

34 Abraham, R.J., Evans, B., and Smith, K.M. (1978). The NMR spectra of porphyrins – 14: self-aggregation of zinc(II) *meso*-nitro and *meso*-dinitro octaethylporphyrins. *Tetrahedron* 34: 1213–1220.

35 Abraham, R.J. and Smith, K.M. (1983). NMR spectra of porphyrins. 21. Applications of the ring-current model to porphyrin and chlorophyll aggregation. *J. Am. Chem. Soc.* 105: 5734–5741.

36 Abraham, R.J. (1985). Aggregation of a bacteriochlorophyllide d: direct evidence for a nonsymmetric aggregate in solution. *J. Am. Chem. Soc.* 107: 1085–1087.

37 Helaja, J., Tauber, A.Y., Kilpeläinen, I., and Hynninen, P.H. (1997). Novel model compounds for photoinduced electron transfer: structures of the folded conformers of zinc(II)–pyropheophytin – anthraquinone dyads. *Magn. Reson. Chem.* 35: 619–628.

38 Abraham, R.J., Bedford, G.R., and Wright, B. (1983). The NMR spectra of the porphyrins: 23 – metalloporphyrins as diamagnetic shift reagents, chemical applications. *Org. Magn. Reson.* 21: 637–642.

39 Rudkevich, D.M., Verboom, W., and Reinhoudt, D.N. (1995). Capped biscalix[4]arene-Zn-porphyrin: metalloreceptor with a rigid cavity. *J. Org. Chem.* 60: 6585–6587.

40 Anderson, H.L., Anderson, S., and Sanders, J.K.M. (1995). Ligand binding by butadiyne-linked porphyrin dimers, trimers and tetramers. *J. Chem. Soc. Perkin Trans.* 1: 2231–2245.

41 Slobodkin, G., Fan, E., and Hamilton, A.D. (1992). Molecular recognition: porphyrin containing receptors as analogs of barbiturate induced cytochrome P450. *New J. Chem.* 16: 643–645.

42 Storm, C.B. and Teklu, Y. (1972). Nitrogen-hydrogen tautomerism in porphyrines and chlorines. *J. Am. Chem. Soc.* 94: 1745–1747.

43 Braun, J., Schlabach, M., Wehrle, B. et al. (1994). NMR study of the tautomerism of porphyrin including the kinetic HH/HD/DD isotope effect in the liquid and solid state. *J. Am. Chem. Soc.* 116: 6593–6604.

44 Crossley, M.J., Field, L.D., Forster, A.J. et al. (1987). Steric effects on atropisomerism in tetraaryl porphyrins. *J. Am. Chem. Soc.* 109: 341–348.

45 Medforth, C.J., Muzzi, C.M., Dooley, N.R. et al. (2003). Unusual aryl-porphyrin rotational barriers in peripherally crowded porphyrins. *Inorg. Chem.* 42: 2227–2241.

46 Saitoh, T., Ikeue, T., Ohgo, Y., and Nakamura, M. (1997). Barriers to rotation of axially coordinated imidazole ligands in nonplanar *meso*-tetraalkylporphyrinato-cobalt(III) complexes. *Tetrahedron* 53: 12487–12496.

47 Shokhirev, N.V., Shokhireva, T.K., Polam, J.R. et al. (1997). 2D NMR investigations of the rotation of axial ligands in six-coordinate low-spin iron(III) and cobalt(III) tetraphenylporphyrinates having 2,6-disubstituted phenyl rings: quantitation of rate constants from ^{1}H EXSY cross-peak intensities. *J. Phys. Chem. A* 101: 2778–2786.

48 Collman, J.P., Garner, J.M., Hembre, R.T., and Ha, Y. (1992). Relative strength of 4d vs. 5d δ-bonds: rotational barriers of isostructural molybdenum and tungsten porphyrin dimers. *J. Am. Chem. Soc.* 114: 1292–1301.

49 Kim, J.C., Goedken, V.L., and Lee, B.M. (1996). Synthesis and rotational barrier of tungsten(II) porphyrin dimer, [W(TPP)]2 (TPP = tetraphenylporphyrin). *Polyhedron* 15: 57–62.

50 Chou, L.-F. and Chen, J.-H. (1996). Molecular structure of $[Tl(tpp)(O_2CCF_3)]$ and ^{19}F dynamic nuclear magnetic resonance of it and $[Tl(tmpp)(O_2CCF_3)]$[tpp = 5,10,15,20-tetraphenylporphyrinate, tmpp = 5,10,15,20-tetra(4-methoxyphenyl)porphyrinate]. *J. Chem. Soc. Dalton Trans.* 3787–3792.

51 Nakamura, M. (1995). Effects of ortho-methyl substituents on the rate of dissociation of imidazole ligands in tetraarylporphyrinatocobalt(III) complexes. *B. Chem. Soc. Jpn.* 68: 197–203.

52 Abraham, R.J., Hawkes, G.E., and Smith, K.M. (1974). Rate processes in *meso*-tetraphenylporphyrin. Slow exchange between *meso*-tetraphenylporphyrin and its diprotonated form. *Tetrahedron Lett.* 71–74.

53 Barkigia, K.M., Berber, M.D., Fajer, J. et al. (1990). Nonplanar porphyrins. X-ray structures of (2,3,7,8,12,13,17,18-octaethyl- and -octamethyl-5,10,15,20-tetraphenylporphinato)zinc(II). *J. Am. Chem. Soc.* 112: 8851–8857.

54 Waditschatka, R., Kratky, C., Jaun, B. et al. (1985). Chemistry of pyrrocorphins: structure of nickel(II)ccccc-octaethyl-pyrrocorphinate in the solid state and in solution. Observation of the inversion barrier between enantiomorphically ruffled conformers. *Chem. Commun.* 1604–1607.

55 Yatsunyk, L.A., Shokhirev, N.V., and Walker, F.A. (2005). Magnetic resonance spectroscopic investigations of the electronic ground and excited states in strongly nonplanar iron(III) dodecasubstituted porphyrins. *Inorg. Chem.* 44: 2848–2866.

56 Santos, H. and Turner, D.L. (1987). Proton NMR studies of horse ferricytochrome-C – completion of the assignment of the well resolved hyperfine shifted resonances. *FEBS Lett.* 226: 179–185.

57 Bampos, N., Princel, M.R., He, H. et al. (1998). ^{13}C CPMAS NMR spectroscopy as a probe for Porphyrin–Porphyrin and host–guest interactions in the solid state. *J. Chem. Soc. Perkin Trans.* 2: 715–723.

58 Shaibat, M.A., Casabianca, L.B., Siberio-Perez, D.Y. et al. (2010). Distinguishing polymorphs of the semiconducting pigment copper phthalocyanine by solid-state NMR and Raman spectroscopy. *J. Phys. Chem. B* 114: 4400–4406.

14

Spin States in Iron Porphyrins

Mikio Nakamura

Department of Chemistry, Faculty of Science, Toho University, Chiba, Japan

Abbreviations

DMAP	(*N*,*N*-dimethylamino)pyridine
4-MePy	4-methylpyridine
4-CNPy	4-cyanopyridine
HIm	imidazole
2-MeIm	2-methylimidazole
4,5-Cl_2Im	4,5-dichloroimidazole
*t*BuNC	*tert*-butylisocyanide
PyNO	pyridine *N*-oxide
4-MePyNO	4-methylpyridine *N*-oxide
3,5-Me2PyNO	3,5-dimethylpyridine *N*-oxide
Por	dianion of porphyrin
TPP	dianion of 5,10,15,20-tetraphenylporphyrins
TArP	dianion of 5,10,15,20-tetraarylporphyrins
TRP	dianion of 5,10,15,20-tetraalkylporphyrins where R is ethyl (Et), propyl (Pr), or isopropyl (*i*Pr)
ORTPP	dianion of 2,3,7,8,12,13,17,18-octaalkyl-5,10,15,20-tetraphenylporphyrins where R is methyl(M) or ethyl(E)
Fe(Por)X and $[Fe(Por)L_2]^+$	iron(III) porphyrin where X is an anionic ligand and L is a neutral ligand
Por•	porphyrin radical cation with total charge −1
$Fe(Por•)X^+$, Fe(Por•)XY, and $[Fe(Por•)L_2]^{2+}$	iron(III) porphyrin radical cation where X and Y are anionic ligands and L is a neutral ligand (Fe = O) (Por), oxo-iron(IV) porphyrins
$Fe(Por)X_2$	iron(IV) porphyrins with anionic ligand X.

Fundamentals of Porphyrin Chemistry: A 21st Century Approach, Volume 2, First Edition.
Edited by Penelope J. Brothers and Mathias O. Senge.
© 2022 John Wiley & Sons Ltd. Published 2022 by John Wiley & Sons Ltd.

14.1 Introduction

Iron porphyrin complexes have attracted wide attention from chemists and biochemists because they exist at the reaction centers of heme proteins and play central roles in various aspects of biological processes such as oxygen storage in myoglobin, oxygen transport in hemoglobin, electron transfer in cytochromes, and oxidation of organic substrates in peroxidases and cytochromes P450 [1–4]. In order to understand the functions and catalytic processes of heme proteins, much effort has been made to elucidate their electronic and magnetic properties. In parallel, a wide variety of synthetic iron porphyrin complexes as well as other metal–porphyrin complexes have been prepared to reveal the catalytic mechanisms of heme proteins and also to develop artificial enzymes whose activities are similar to or even superior to those of the naturally occurring heme proteins [5]. Since the catalytic activities of metal–porphyrin complexes are closely connected with their electronic and magnetic structures, it is quite important to elucidate them by using various spectroscopic, magnetic, and crystallographic techniques together with theoretical calculations.

In biological systems, the oxidation state of iron is either iron(II) or iron(III). In some specific cases, iron exists even as iron(IV). Each oxidation state has various spin states and electron configurations. For example, iron(III) complexes can adopt high-spin ($S = 5/2$), intermediate-spin ($S = 3/2$), and low-spin ($S = 1/2$) states. Furthermore, each spin state can have different electron configurations. Low-spin complexes can adopt either the $(d_{xy})^2(d_{xz}, d_{yz})^3$ or the $(d_{xz}, d_{yz})^4(d_{xy})^1$ configuration [6–8]. The electronic and magnetic structures of iron porphyrin complexes become further complicated because porphyrin is not an innocent ligand; it can easily be oxidized to form a π-cation radical [9]. Thus, the electronic and magnetic structures of each iron porphyrin complex can be expressed by the combination of its oxidation state, spin state, and electron configuration of iron as well as the oxidation state of the porphyrin ring. Recent studies have revealed that iron porphyrin complexes exist in many cases as a mixture of the limiting states mentioned above. Thus, in order to obtain detailed information on the electronic and magnetic structure of iron porphyrin complexes, combined analysis using various methods such as UV–Vis, NMR, EPR, resonance Raman, MCD, Mössbauer, EXAFS, SQUID, X-ray crystallography, and theoretical calculations are often necessary. In solution, ^{13}C and ^{1}H NMR methods are particularly useful because they exhibit the proton and carbon signals in specific regions that are closely correlated with their electronic and magnetic structures [6–9]. In this chapter, iron porphyrin complexes will first be classified on the basis of the oxidation state of iron, after which the spin state, electron configuration, and metal–porphyrin orbital interactions together with the factors that determine such properties will be described.

14.2 Iron(II) Complexes

Iron(II) porphyrin complexes possess six electrons in 3d orbitals. Therefore, there are three kinds of spin states – low-spin ($S = 0$), high-spin ($S = 2$), and intermediate-spin ($S = 1$) states – as shown in Figure 14.1a. These complexes are relevant to biological systems such as hemoglobin and myoglobin since these proteins contain iron(II) porphyrins in their active sites.

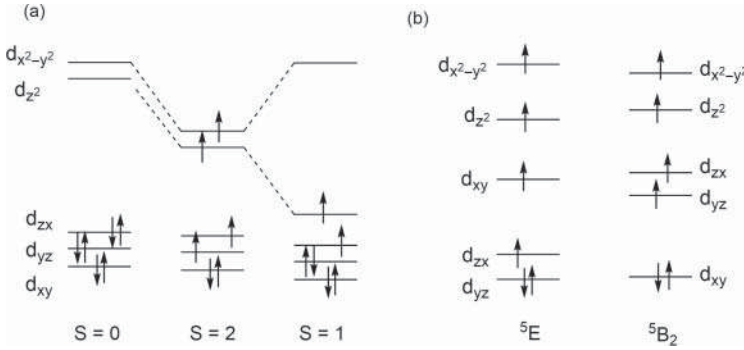

Figure 14.1 (a) Spin states of iron(II) porphyrin complexes. (b) Two different electronic states in high-spin iron(II) hemes.

14.2.1 Six-Coordinate Complexes

Six-coordinate iron(II) porphyrins usually adopt the low-spin (S = 0) state and are therefore diamagnetic. The iron atom is placed in-plane or nearly in-plane relative to the porphyrin ring even if the axial ligands are nonequivalent. Because of their diamagnetic nature, the ^{1}H NMR spectra exhibit sharp signals in the so-called diamagnetic region, 0–10 ppm A typical example is $[Fe^{II}(TPP)(1\text{-MeIm})_2]$, where Fe-$N_P$ = 1.998(3) Å, Fe-N_{Im} = 1.9970(12) Å, and the ^{1}H NMR chemical shift of the pyrrole-H signal is 8.33 ppm at −21 °C [6, 10].

14.2.2 Five-Coordinate Complexes

Five-coordinate iron(II) porphyrin complexes usually adopt the high-spin (S = 2) state. Since these complexes are good models for deoxy-Hb, deoxy-Mb, the reduced form of peroxidase, and so on, extensive studies have been done to reveal the detailed electronic structure. The electron configuration was originally reported to be $(d_{xy})^2(d_{xz}, d_{yz})^2(d_z{}^2)^1(d_x{}^2{}_{-y}{}^2)^1$. However, recent studies by Mössbauer spectroscopy have suggested that the electronic structures of these complexes are not that simple. Scheidt and co-workers have reported that these complexes have two distinct high-spin states with different electron configurations [11, 12]. Complexes having neutral ligands such as imidazole have a low-symmetry, doubly occupied d_{xz} or d_{yz} orbital, that is, the ^{5}E state with the $(d_{xz}, d_{yz})^3(d_{xy})^1(d_z2)^1(d_x2_{-y}2)^1$ electron configuration as shown in Figure 14.1b, and exhibit negative quadrupole splitting in the Mössbauer spectra. In contrast, complexes with anionic ligands such as imidazolate have a high-symmetry, doubly occupied d_{xy} orbital, that is, the $^5B_2$ state with the $(d_{xy})^2(d_{xz}, d_{yz})^2(d_z2)^1(d_x2_{-y}2)^1$ electron configuration, and exhibit positive quadrupole splitting. Importantly, the molecular structures are different depending on the electronic structures: the former complexes have a smaller out-of-plane displacement of iron(II) ion than the latter ones. Figure 14.2 shows the molecular structures of the imidazole and imidazolate complexes. It is clearly shown that the out-of-plane displacement of the iron(II) ion increases and the Fe-N_{ax} bond length decreases on going from (a) to (d) and, correspondingly, the electronic structure changes from the ^{5}E state in (a) to the $^5B_2$ state in (d). It should be noted that the hydrogen bonding to the imidazole N—H increases the imidazolate character and thus increases the contribution of the $^5B_2$ state [11, 12]. Yamamoto and co-workers have observed thermal equilibrium between the

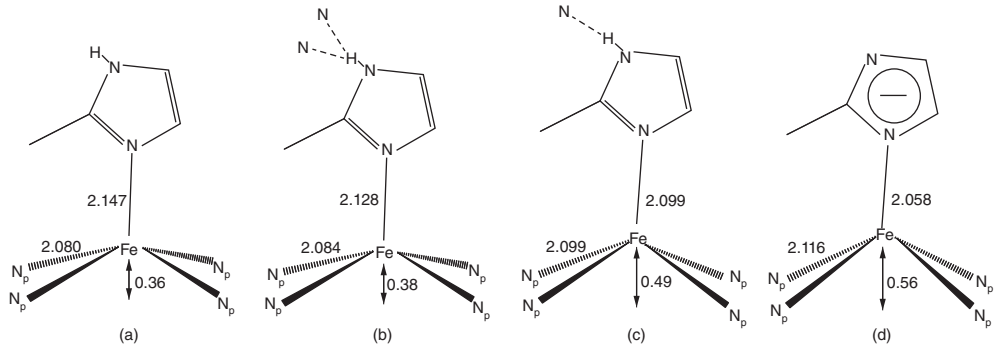

Figure 14.2 Structural differences in five-coordinate high-spin iron(II) porphyrinates. (a) 2-methylimidazole, (b) and (c) 2-methylimidazole hydrogen-bonded with 1,10-phenanthroline and 3-methylimidazole, respectively, (d) 2-methylimidazolate. Source: From Hu et al. [12] with permission of the Royal Society of Chemistry.

$^5B_2$ and ^5E states in sperm whale deoxymyoglobin reconstituted with CF_3 substituted heme and determined the thermodynamic parameters corresponding to the equilibrium [13].

Five-coordinate complexes can also take the low-spin (S = 0) state if they have strong-field axial ligands such as alkyl anions. A typical example is $[Fe(TPP)(CH_2CH_2CH_3)]^-$, which exhibits a pyrrole-H signal at 8.1 ppm in the ^1H NMR spectrum [6].

14.2.3 Four-Coordinate Complexes

In four-coordinate iron(II) porphyrins, the d_z2 orbital is stabilized due to the lack of the axial ligands. Consequently, these complexes adopt the intermediate-spin (S = 1) state (Figure 14.1a). Possible ground states in an unsubstituted D_{4h} complex are $^3A_{2g}$ $(d_{xy})^2(d_z2)^2(d_{xz}, d_{yz})^2$, ^3E_g $(d_{xy})^2(d_{xz}, d_{yz})^3(d_z2)^1$, and $^3B_{2g}$ $(d_{xz}, d_{yz})^4(d_{xy})^1(d_z2)^1$. Typical examples are Fe(TPP) and Fe(OEP). Because of the lack of unpaired electrons in the $d_x2_{-y}2$ orbital, the ^1H NMR isotropic shift of the pyrrole-H signal in Fe(TPP) is negative and that of the pyrrole-CH_2 signal in Fe(OEP) is positive. Here, the isotropic shift of the signal (δ_{iso}) is defined by $\delta_{iso} = \delta_{obs} - \delta_{dia}$, where δ_{obs} and δ_{dia} are the observed chemical shift and the chemical shift of the corresponding signal in an analogous diamagnetic complex, respectively. Among the possible ground states mentioned above, the $^3A_{2g}$ state is assigned to be the real ground state on the basis of the Mössbauer, ^1H NMR, and theoretical calculations [14].

14.3 Iron(III) Complexes

Iron(III) porphyrin complexes possess five electrons in 3d orbitals and can show three spin states depending on the number and nature of the axial ligands. The six-coordinate complexes with strong-field ligands prefer the low-spin (S = 1/2) state, whereas those with weak-field ligands tend to adopt the high-spin (S = 5/2) state. The intermediate-spin (S = 3/2) state is quite rare and is observed when the complex has a weak-field axial ligand together with a deformed porphyrin ring. Five-coordinate complexes tend to adopt the high-spin state, although intermediate spin is possible if the axial ligand has an extremely weak field strength such as ClO_4^- and SbF_6^- or the porphyrin ring is highly deformed.

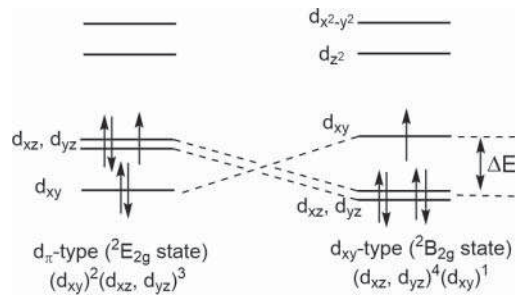

Figure 14.3 Electronic ground states in low-spin iron(III) complexes.

14.3.1 Low-Spin Iron(III)

It is now well established that there are two types of electronic ground states in low-spin iron(III) porphyrins: the ^2E_g state with a $(d_{xy})^2(d_{xz}, d_{yz})^3$ electron configuration and the $^2B_{2g}$ state with a $(d_{xz}, d_{yz})^4(d_{xy})^1$ electron configuration [6–8]. These two states are referred to as the d_π-type and d_{xy}-type ground state, respectively (Figure 14.3). Although they have the same spin state, these complexes exhibit quite different physicochemical properties.

14.3.1.1 The d_π-Type Ground State

This type of low-spin complex is commonly observed in six-coordinate complexes having nitrogen bases as axial ligands. Typical examples are $[Fe(TPP)(Py)_2]^+$ and $[Fe(OEP)(HIm)_2]^+$. In biological systems, most heme proteins have at least one histidyl imidazole as the axial ligand. Thus, heme proteins with a ferric low-spin state adopt the d_π-type ground state as shown in the oxidized forms of cytochrome b and cytochrome c.

Characteristic features of ^1H NMR spectra are the considerable upfield and downfield shifts of the pyrrole-H and pyrrole-CH_2 signals in $[Fe(TPP)(Py)_2]^+$ and $[Fe(OEP)(HIm)_2]^+$, respectively. The large isotropic shifts of these signals are ascribed to the interaction between the half-occupied iron d_{xz} or d_{yz} orbital and the porphyrin $3e_g$ orbital in D_{4h} porphyrin. Since the $3e_g$ orbital has large coefficients at the pyrrole β carbon atoms, the interaction produces a sizable amount of spin density on these carbon atoms, resulting in the large isotropic shifts of the protons signals mentioned above [15].

EPR spectroscopy is another powerful method of determining the electronic ground state of low-spin complexes. The d_π-type complexes exhibit so-called rhombic type spectra with three different g values: g_x, g_y, and g_z. If axial ligands are linear as in the case of cyanide, so-called large g_{max} type spectra are observed where one broad signal is observable at $g > 3.2$. Large g_{max} type spectra are also observed if two planar ligands such as imidazole and pyridine are perpendicularly aligned. Thus, $[Fe(OEP)(Py)_2]^+$ and $[Fe(OETPP)(Py)_2]^+$ exhibit the rhombic and large g_{max} type spectra, respectively, since the axial ligands are nearly parallel in the former and perpendicular in the latter complex [16, 17].

14.3.1.2 The d_{xy}-Type Ground State

The d_{xy}-type low-spin complexes are less common. The existence of this type was first reported by Walker, Scheidt, and co-workers in 1992 [18, 19]. Since then, extensive studies have been done to determine the factors that control the electronic ground state of low-spin iron(III) complexes [6–8]. If low-spin complexes satisfy the following conditions, the complexes are expected to adopt the d_{xy}-type ground state. They are (i) axial ligands with low-lying π* orbitals such as *tert*-butyl isocyanide and 4-cyanopyridine [18]; and (ii) strongly ruffled porphyrin rings where the *meso* carbon atoms are deviated up-down-up-down from

the mean porphyrin plane [20]. The former condition stabilizes the iron d_π (d_{xz} and d_{yz}) orbitals due to the interaction with the low-lying ligand π* orbitals. The strong d_π–p_{π^*} interactions reverse the d orbital ordering and stabilize the d_{xy}-type ground state. The latter condition destabilizes the d_{xy} orbital due to the interaction with the porphyrin a_{2u} orbital in a highly ruffled structure; note that both a_{2u} and d_{xy} orbitals in D_{4h} porphyrin change to b_2 orbital in D_{2d} ruffled porphyrin complexes [21, 22]. In addition to these conditions, some additional factors such as the electron-donating *meso*-substituents and the porphyrin ring with its low-lying π* orbital contribute to further stabilization of the d_{xy}-type ground state [23, 24]. Thus, the complexes that satisfy these conditions have a d_{xy} orbital that is much higher than the d_π orbitals, leading to the stabilization of the d_{xy}-type ground state. Since porphyrin is a flexible macrocycle, it can easily be ruffled in the d_{xy}-type complexes to gain further stabilization due to the d_{xy}–a_{2u} interaction. Therefore, the low-spin complexes with the d_{xy}-type ground state tend to exhibit a ruffled porphyrin core [19].

Typical examples that adopt the d_{xy}-type ground state are $[Fe(TPP)(^tBuNC)_2]^+$ and $[Fe(T^iPrP)(HIm)_2]^+$. The former adopts the d_{xy}-type ground state because the axially coordinating ^{t}BuNC ligand has low-lying π^* orbitals [19]. The latter exhibits the d_{xy}-type ground state because T^iPrP ring is intrinsically ruffled because of the presence of bulky substituents at the *meso* positions [25]; note that most of the low-spin iron(III) complexes having imidazole as axial ligands exhibit the d_π-type ground state. The characteristic feature in ^{1}H NMR spectra of the d_{xy}-type low-spin complexes is a small isotropic shift of the pyrrole-H signal. The results suggest that the spin densities on the β pyrrole carbon atoms are fairly small compared to those of the d_π-type complexes. In contrast, the *meso* carbon atoms have large spin densities due to the d_{xy}–a_{2u} interaction mentioned above. Consequently, the d_{xy}-type complexes always exhibit the *meso* carbon signals extremely downfield; they are 997 and 332 ppm at −50 °C for $[Fe(TPP)(^tBuNC)_2]^+$ and $[Fe(T^iPrP)(HIm)_2]^+$, respectively [25].

The d_{xy}-type complexes commonly exhibit the axial type EPR spectrum where the $g_\perp$ and $g_{||}$values are less than 2.6 and 2.0, respectively. If the energy gap between the d_{xy} and d_π orbitals increases, both the $g_\perp$and $g_{||}$values approach 2.0. Thus, it is possible to estimate the energy gap between the d_{xy} and d_π orbitals on the basis of the EPR g values [26]. Figure 14.4 shows the energy gaps in a series of $[Fe(OETArP)(^tBuNC)_2]^+$ complexes determined on the basis of the EPR g values. The data clearly indicate that the energy gap decreases as the *meso* substituent changes from the electron-donating 4-methoxyphenyl group to the electron-withdrawing 2,6-dichlorophenyl group [27]. In the case of the complex with strongly electron-withdrawing 3,5-bis(trifluoromethyl)phenyl group, the energy level of the d_{xy} and d_π orbitals is reversed, and the complex adopts a rare d_π-type low-spin state in spite of the coordination of ^{t}BuNC ligand.

14.3.1.3 Interconversion Between the d_π-Type and d_{xy}-Type Complexes

As mentioned, there are two types of low-spin iron(III) complexes. Complexes such as $[Fe(TPP)(HIm)_2]^+$ and $[Fe(T^iPrP)(^tBuNC)_2]^+$ are two limiting cases; they adopt essentially pure d_π-type and d_{xy}-type ground states, respectively. However, most of the low-spin complexes exist as an equilibrium mixture of two isomers, that is, electron configurational isomers, as shown in Eq. (14.1) [28–31]:

$$(d_{xy})^2(d_{xz}, d_{yz})^3 \rightleftharpoons (d_{xz}, d_{yz})^4(d_{xy})^1 \tag{14.1}$$

Table 14.1 lists the ^{1}H NMR, ^{13}C NMR, and EPR data for a series of $[Fe(T^nPrP)L_2]^\pm$. These data indicate that both the pyrrole-H and C_{meso} signals move continuously downfield as the

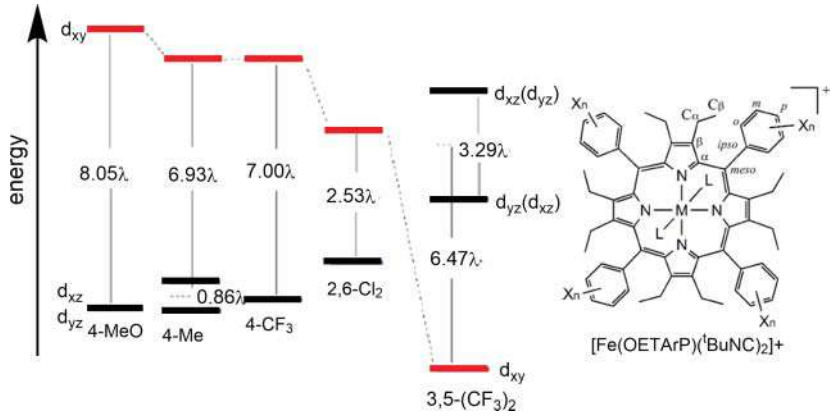

Figure 14.4 Relative energy levels of the d_{xy}, d_{xz}, and d_{yz} of $[Fe(OETArP)(^tBuNC)_2]^+$ determined on the basis of the EPR g values taken in frozen CH_2Cl_2 solution at 4.2–20 K, where λ is a spin-orbit coupling constant. Source: From Ohgo et al. [27] with permission of the American Chemical Society.

Table 14.1 ^1H and ^{13}C NMR chemical shifts (CD_2Cl_2, 223 K) and EPR g values (CH_2Cl_2, 4.2 K) of $[Fe(T^nPrP)L_2]^{\pm}$.

	^1H NMR		^{13}C NMR			EPR		
L	**Py-H**	***meso*-CHα**	**C_{meso}**	**C_α**	**C_β**	**g_1**	**g_2**	**g_3**
HIm	−21.5	1.7	73.1	0.0	73.6	2.90	2.35	1.45
DMAP	−16.7	9.7	130.5	−2.2	84.3	3.10	2.10	—
2-MeIm	−8.2	21.3	a)	a)	a)	2.85	2.85	—
CN^-	−3.5	30.9	336.1	−72.7	61.2	2.51	2.51	—
3-MePy	4.5	51.4	470.0	−88.5	77.0	a)	a)	—
Py	7.1	57.9	526.5	−108.2	74.3	2.55	2.55	—
4-CNPy	13.0	88.5	814.7	−267.2	66.0	2.46	2.46	1.68
^{t}BuNC	12.7	118.5	b)	−449.7	84.2	2.16	2.16	1.95

a) Not determined
b) Too broad to detect.
Source: Data from Ref. [25, 32]

axial ligand changes from HIm to ^{t}BuNC [25, 32]. The results suggest that the population of the d_{xy}-type isomer in Eq. (14.1) increases on going from HIm to ^{t}BuNC. Although it is difficult to observe two kinds of low-spin complexes directly by NMR spectroscopy due to a very small barrier to interconversion, it is possible for suitable complexes examined by EPR spectroscopy at extremely low temperatures. In fact, the EPR spectrum of $[Fe(TArP)(CN)_2]^-$ (Ar = 2,4,6-triethylphenyl) taken in frozen acetonitrile solution at 4.2 K showed two types of signals, a large g_{max} type at g = 3.65 and an axial type signal at $g_\perp$ = 2.50, suggesting that the complex exists as an equilibrium mixture under these conditions [28].

14.3.1.4 Relevance to Biological Systems

Bren et al. examined how the ruffling of heme in wild-type *Pseudomonas aeruginosa* cytochrome c_{551} and its point mutant as well as in wild-type *Hydrogenobacter thermophilus*

cytochrome c_{552} and its variants affects the physicochemical properties of the enzymes [33, 34]. The ^{1}H and ^{13}C NMR studies revealed that as the ruffling of heme increases, the spin densities on the β-pyrrole carbons decrease, whereas those on the α-pyrrole and *meso* carbons increase. Thus, the ruffling controls the spin density and spin distribution on the heme, which is consistent with the conclusions obtained from the model heme systems [35].

Heme oxygenase is a heme degradation enzyme and catalyzes the oxygen-dependent degradation of heme to biliverdin with the release of carbon monoxide and iron. Rivera et al. examined the ^{13}C NMR chemical shifts of the hydroxide complex of *P. aeruginosa* heme oxygenase (Fe^{III}-OH), which is considered to be the reactive intermediate model in the heme oxygenase catalytic cycle [29, 30]. The study revealed that the heme hydroxide exists partially as a low-spin complex with the d_{xy}-type ground state. The result suggests that the real reactive intermediate in the catalytic cycle of heme oxygenase, Fe^{III}-OOH, could also adopt the d_{xy}-type ground state and consequently increase the spin density at the *meso* carbon positions to activate the *meso* hydroxylation.

Recently, a novel family of heme degradation enzymes, IsdG and IsdI, has been identified in *Staphylococcus aureus* [36]. These enzymes similarly catalyze heme degradation and convert heme to staphilobilin (not biliverdin), formaldehyde, and iron as shown in Figure 14.5. Another heme degradation enzyme obtained from *Mycobacterium tuberculos* is called MhuD (mycobacterial heme utilization, degrader), which converts heme to mycobilin and iron [37]. Thus, the *meso* carbon atom is retained as a formyl group in the case of the MhuD enzyme as shown in Figure 14.5 [38].

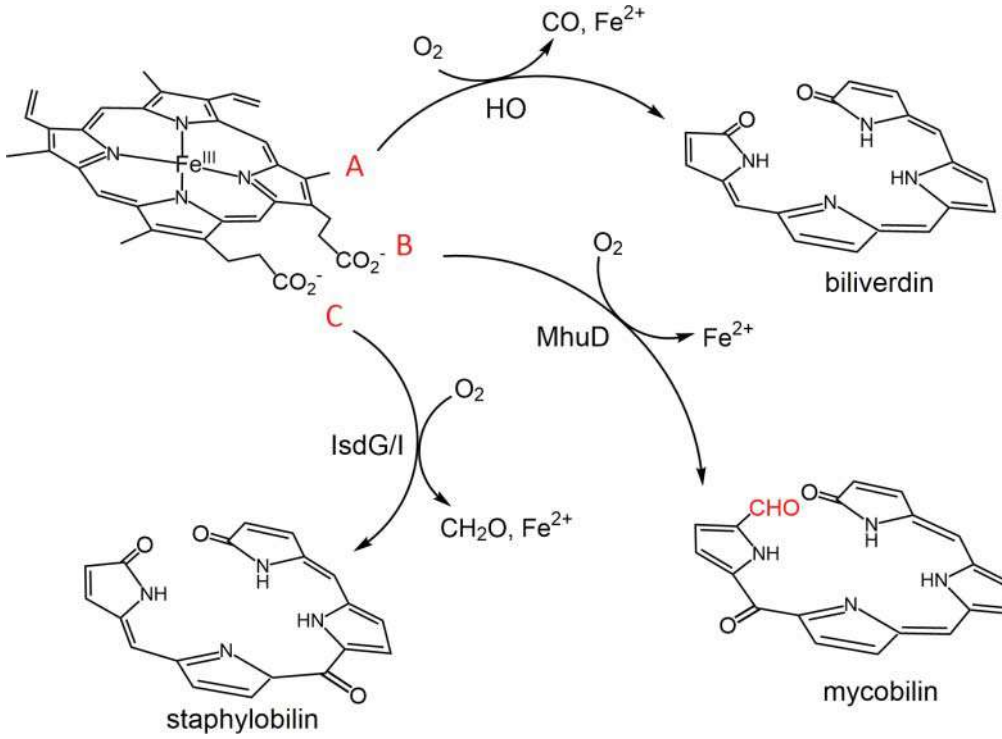

Figure 14.5 Reaction products of heme degrading proteins. (a) Canonical heme oxygenase (HO). (b) and (c) Noncanonical bacterial MhuD and IsdG/I HOs, respectively. The peripheral substituents have been omitted for simplicity. Source: From Wilks and Ikeda-Saito [38] with permission of the American Chemical Society.

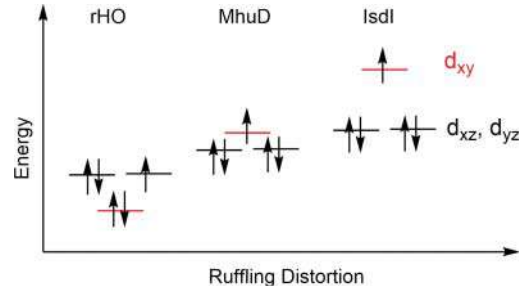

Figure 14.6 Relative energy levels of iron d_{xy}, d_{xz}, and d_{yz} orbitals. As the degree of ruffling increases from rHO to MhuD, and then to IsdI, the electronic ground state changes from ^2E_g to $^2B_{2g}$. Source: From Graves et al. [40] with permission of the American Chemical Society.

Mauk et al. reported the X-ray crystal structure of cyanide-inhibited IsdI (IsdI-heme-CN) and found that the out-of-plane distortions determined by the normal-coordinate structural decomposition (NSD) reached as much as 2.3 Å [39]. Thus, the values are by far the largest among all the heme proteins reported previously. The hemes in MhuD also exhibit ruffling. Liptak et al. reported the X-ray crystal structure of cyanide-inhibited MhuD (MhuD-heme-CN) and found that the ruffled distortions of the hemes increased to 1.4 and 1.5 Å as compared with that of native MhuD-diheme (0.7 Å) [40]. Since the magnitude of heme ruffling is only 0.5 Å in cyanide-inhibited rat heme oxygenase (rHO-heme-CN), it is clear that the ruffling of the bound heme increases on going from rHO to MhuD, and then to IsdI. Thus, the electronic ground state of low-spin iron(III) is considered to change from the d_π-type (^2E_g) to the d_{xy}-type ($^2B_{2g}$) ground state, as shown in Figure 14.6 [40].

In fact, IsdI-heme-CN exhibited an unprecedented shift of the heme *meso*-H signals more than 10 ppm upfield, whereas the corresponding rHO showed no upfield shifted signals. The large upfield shift suggests the presence of large spin densities on the *meso* carbon atom, which in turn indicates that the low-spin iron(III) of IsdI-heme-CN adopts the d_{xy}-type electronic ground state. This situation should hold even if cyanide is replaced by hydroperoxide to form histidine-coordinated Fe(III)-OOH, which is supposed to be the reactive intermediate in these heme degradation enzymes. Thus, it is possible to ascribe the difference in products in these heme degradation reactions to the degree of ruffling of the porphyrin ring and/or electronic ground state of low-spin iron(III).

14.3.2 High- and Intermediate-Spin State

Five-coordinate iron(III) complexes carrying an anionic ligand (X) at the axial position such as Fe(TPP)X and Fe(OEP)X adopt the mixed high- and intermediate-spin state, ranging from a pure high-spin (S = 5/2) to a pure intermediate-spin (S = 3/2) state depending on the field strength of the anionic ligand. Since each complex has a different amount of contribution from the S = 5/2 and S = 3/2 states, spectroscopic properties such as NMR chemical shifts continuously change toward one direction on going from the pure high-spin to the pure intermediate-spin state [8, 35].

Six-coordinate iron(III) complexes having nitrogen bases such as pyridine and imidazole adopt the low-spin state. However, if the axial ligands are weak-field oxygen ligands such as pyridine N-oxides, DMSO, DMF, THF, and so on, the resulting complexes adopt the mixed high- and intermediate-spin state depending on the field strength of the oxygen ligands [41]. An exceptional case is $[Fe(tn\text{-}OEP)(Py)_2]^+$ (**1**) as shown in Figure 14.7a, which adopts the high-spin state in spite of the bis-coordination of the nitrogen base [42].

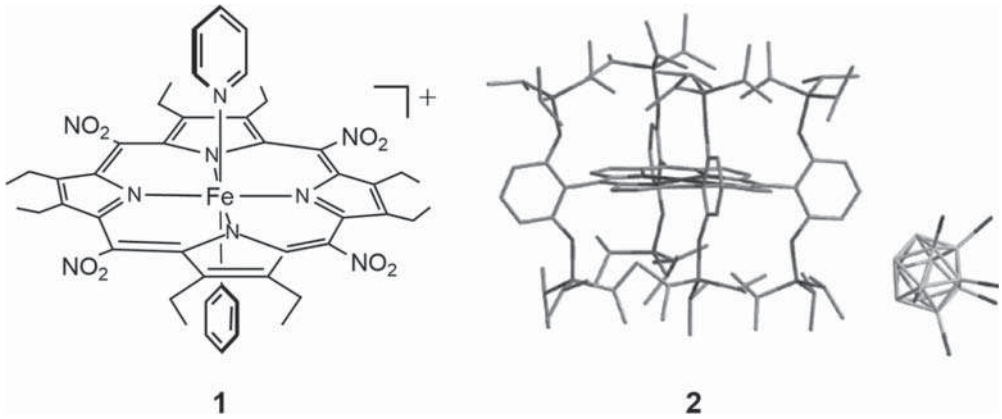

Figure 14.7 (a) High-spin (S = 5/2) $[Fe(tn\text{-}OEP)(Py)_2]^+$ (**1**) with pyridine as axial ligands [42]. (b) X-ray single-crystal structure of intermediate-spin (S = 3/2) $[Fe(TipsiPP)][CB_{11}H_6Br_6]$ (**2**). Source: From Fang et al. [43] with permission of the American Chemical Society.

Four-coordinate iron(III) complexes should adopt the S = 3/2 state, although they are difficult to obtain. This is because even very weakly coordinating counter anions still interact with the iron(III) center as the fifth ligand. Suslick et al. were successful in preparing such a complex by placing the anionic ligand far away from the iron(III) center in Fe(TipsiPP)X (**2**), in which all the *meso* phenyl groups bear bulky bis(triisopropylsiloxy)phenyl groups at the 2,6-positions [43]. Thus, the iron center is extremely hindered with a pocket opening of only 2 Å. Consequently, bulky anionic ligands such as $CB_{11}H_6Br_6^-$, SbF_6^-, and ClO_4^- are located outside the cavity. The spectroscopic and magnetic properties of **2** (X = $CB_{11}H_6Br_6^-$) are as follows: EPR ($g_\perp = 4.2$), ^{1}H NMR (pyrrole-H, $\delta = -81$ ppm), Mössbauer ($\delta = 0.33\ mm\ s^{-1}$, $\Delta E_q = 5.16\ mm\ s^{-1}$), and effective magnetic moment ($\mu_{eff} = 4.1\ \mu_B$).

14.3.3 Conditions to Obtain Essentially Pure Intermediate-Spin Complexes

The intermediate-spin state can be stabilized if the complexes have (i) a weak-field axial ligand, (ii) a highly deformed porphyrin ring, and (iii) a small N4 cavity. Factor (i) stabilizes the d_z2 orbital, while factors (ii) and (iii) destabilize the $d_{x^2-y^2}$ orbital. If the field strengths of the axial ligands are extremely weak and/or if the porphyrin ring is highly deformed, then the complexes should exhibit close to a pure intermediate-spin state.

14.3.3.1 Axial Ligands with Weak Field Strengths

In five-coordinate high-spin complexes such as Fe(TPP)Cl, the iron(III) ion is pulled out of the N4 plane by the chloride ion. The deviation of the iron(III) ion from the N4 plane should be decreased as the field strength of the axial ligand is weakened. Consequently, the d_z2 orbital is stabilized while the $d_{x^2-y^2}$ orbital is destabilized, resulting in stabilization of the intermediate-spin state [44, 45]. Reed et al. ordered the weakness of the anionic ligands on the basis of the pyrrole-H chemical shifts in a series of five-coordinate complexes, Fe(TPP)X, and called the hierarchy given in Eq. (14.2) the magnetochemical series [46, 47].

$$\begin{aligned} Br_6CB_{11}H_6^- &< CB_{11}H_{12}^- < SbF_6^- < Co(C_2B_9H_{11})_2^- \\ &< AsF_6^- < ClO_4^- < C(CN)_3^- < CF_3SO_3^- < BF_4^- \\ &< ONC(CN)_2^- < ReO_4^- < OTeF_3^- < I^- < Br^- < Cl^- \end{aligned} \tag{14.2}$$

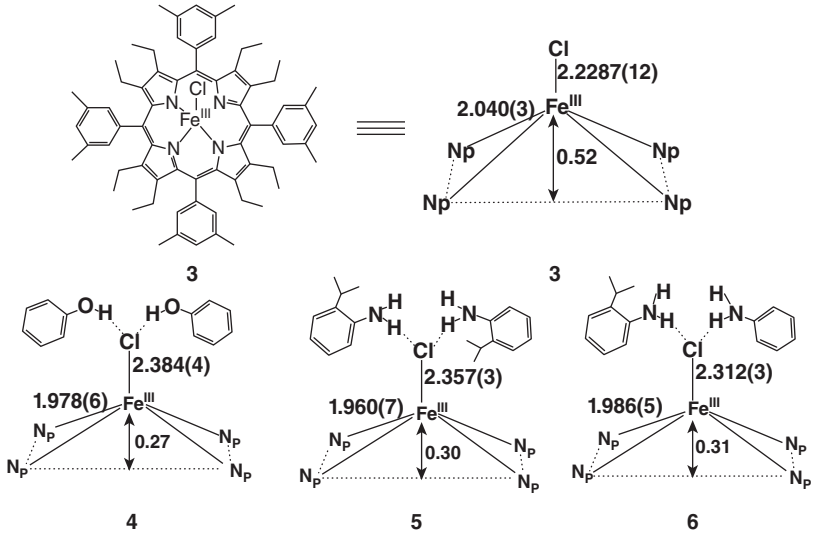

Figure 14.8 Schematic representation of the complexes (**3–6**) together with some structural parameters obtained from the X-ray crystallographic analysis. Source: From Sahoo et al. [49] with permission of Wiley.

This is possible because the chemical shifts of the pyrrole-H signals differ greatly between the high-spin and intermediate-spin complexes: they are +81 ppm for high-spin Fe(TPP)Cl and −62 ppm for intermediate-spin Fe(TPP)($Br_6CB_{11}H_6$), at 298 K. A similar magnetochemical series was reported for oxygen ligands on the basis of the ^1H and ^{13}C NMR chemical shifts of $[Fe(TPP)L_2]^+$, $[Fe(T^iPrP)L_2]^+$, and $[Fe(OETPP)L_2]^+$ as shown in Eq. (14.3) [41].

$$\begin{aligned} &\text{THF} < \text{MeOH} < \text{DMF} < \text{DMSO} < 4-\text{ClPyNO} < \text{PyNO} < 3{,}5 \\ &\quad -\text{Me2PyNO} \sim 4-\text{MePyNO} \end{aligned} \tag{14.3}$$

Although the axial ligand giving "intermediate-spin complex" and "weak-field ligands" are not synonyms [48], the magnetochemical series proposed by Reed et al. is quite convenient for evaluating the weakness of the anionic ligands.

The spin state can easily be converted between high-spin and intermediate-spin state by subtle external perturbations. A good example is the saddle-shaped Fe(OETArP)Cl (**3**) as shown in Figure 14.8 [49]. As expected, this complex adopts a typical high-spin state. The iron(III) ion deviates from the mean porphyrin plane by 0.52 Å. However, the structural and spectroscopic parameters of **3** were drastically changed by the addition of hydrogen bond donors. Figure 14.8 shows some structural parameters of **4**, **5**, and **6** having hydrogen-bonded phenol, 2-isopropylaniline, and aniline, respectively. Because of the hydrogen bonding, both the out-of-plane deviation of iron(III) and the Fe-N_P bond lengths showed a sizable decrease. The results suggest that the hydrogen bonding weakens the field strength of the chloro ligand. Consequently, all these complexes exhibit the intermediate-spin state as confirmed by UV–Vis, ^1H NMR, EPR, and Mössbauer spectroscopy as well as SQUID magnetometry.

14.3.3.2 Highly Deformed Complexes

Cheng et al. pointed out that the deformation of the porphyrin ring should stabilize the intermediate-spin state [50]. In fact, highly saddle-shaped complexes Fe(OETPP)X

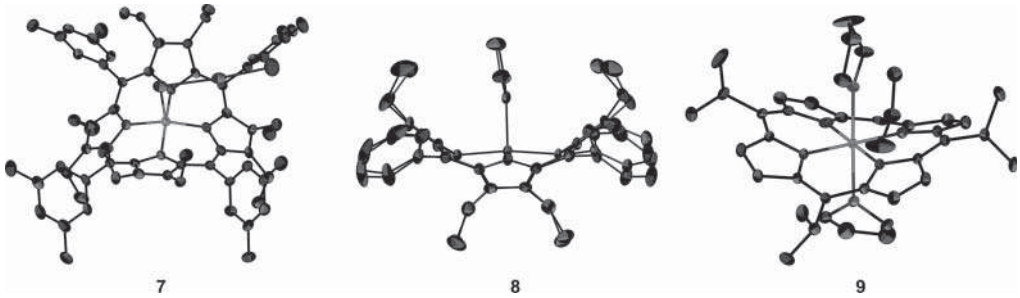

Figure 14.9 X-ray crystal structures of the intermediate-spin complexes with deformed porphyrin ring. Saddled Fe(OETArP)I_3 (**7**) where Ar is 3,5-xylyl. Source: Adapted from Sahoo and Rath [54] with permission of The Royal Society of Chemistry. Saddled [Fe(OETPP)(HIm)]ClO_4 (**8**). Source: Adapted from Ikezaki et al. [55] with permission of Wiley. ruffled [Fe(T^iPrP)$(THF)_2$]ClO_4 (**9**) Source: Adapted from Ohgo et al. [56].

($X = I^-, ClO_4^-$) adopt an essentially pure intermediate-spin state though the corresponding Fe(TPP)I adopts a high-spin state [51–53]. Figure 14.9 shows the molecular structures of intermediate-spin Fe(OETArP)I_3 (**7**, Ar = 3,5-dimethylphenyl) and Fe(OETPP)(HIm) (**8**). The average Fe-N_P lengths in these highly saddled **7** and **8** are as short as 1.947(8) Å [54] and 1.969(3) Å [55], respectively. Figure 14.9 shows the molecular structure of ruffled [Fe(T^iPrP)$(THF)_2$]ClO_4 (**9**), [56]. The average Fe-N_P length is also quite short, 1.967(12) Å. These results indicate that the intermediate-spin state is stabilized by the short Fe-N_P lengths caused by the saddled or ruffled deformation of the porphyrin ring.

14.3.3.3 Porphyrinoids Having a Small N4 Cavity

As mentioned earlier, complexes with intrinsically deformed porphyrin rings stabilize the intermediate-spin state due to their short Fe-N_P bonds. Thus, we can expect the stabilization of the intermediate-spin state even in planar complexes if the N4 cavity of the porphyrin ring is smaller than that of a typical porphyrin ring. We can see such cases in porphyrin analogues.

A typical example is the tetraazaporphyrin known as porphyrazine, where the *meso* carbons are completely replaced by nitrogen atoms [57]. Fitzgerald et al. reported that the octaethyltetraazaporphyrin complex Fe(OETAP)Cl (**10**) shown in Figure 14.10, where the

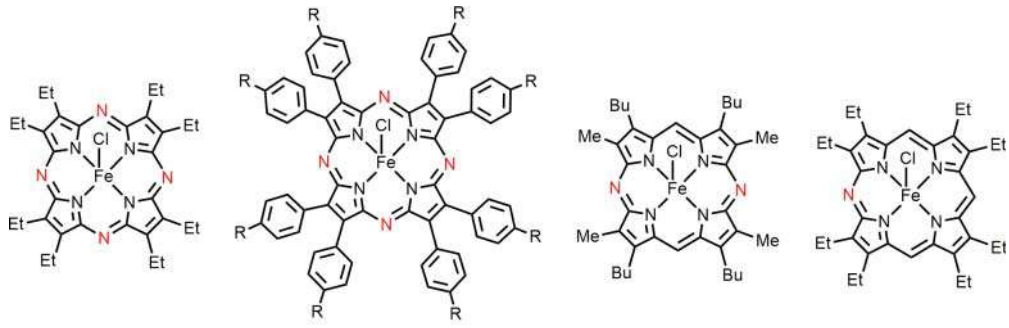

Figure 14.10 Tetraazaporphyrins (**10–12**), diazaporphyrin (**13**), and monoazaporphyrin (**14**).

Fe-N_P bond length is only 1.929 Å, exhibits a rather pure intermediate-spin state on the basis of the EPR ($g_\perp$ = 3.98), Mössbauer (ΔE_q = 3.07 and 3.00 mm s^{-1} for two iron sites), and magnetic susceptibility (μ_B = 3.9 B.M.) data [58]. Analogous complexes such as **11** and **12** are also in the intermediate-spin state [59–61]. Stuzhin et al. examined the spin state of the diazaporphyrin complex (**13**), which shows interesting magnetic behavior due to the existence of two *meso* nitrogen atoms and two *meso* carbon atoms [62]. The crystal is built up from two nonequivalent molecules containing Fe1 and Fe2. The Fe—N_p bond lengths are 1.992 and 1.954 Å for Fe1 and Fe2, and the corresponding out-of-plane deviations are 0.385 and 0.290 Å, respectively. Thus, the structural parameters suggest that Fe1 is in the mixed high-spin and intermediate-spin state, while Fe2 is in the pure intermediate-spin state. In solution, the spin state of **13** shows solvent dependence. While the complex exhibits the high-spin state in CCl_4, C_6D_6, THF-d_8, and acetone-d_6 solutions, the intermediate-spin state predominates in CD_2Cl_2 and $CDCl_3$ solutions due to the weak C-H···Cl^- hydrogen bonding. As expected, octaethylmonoazaporphyrin complex (**14**) shows a high-spin state [63]. The average Fe-N_P bond length and the out-of-plane deviation of iron are 2.044 and 0.49 Å, respectively, which are slightly shorter than the corresponding values of high-spin Fe(TPP)Cl, that is, 2.070 and 0.57 Å [64].

Porphyrin isomers such as hemiporphycene (HPc), corrphycene (Cn), and porphycene (Pc) shown in Figure 14.11 are suitable models to reveal the size effect of the N4 cavity on the electronic and magnetic structure of iron porphyrins. The cavity sizes of Fe(EtioP)I (**15**), Fe(EtioHPc)I (**16**), Fe(EtioCn)I (**17**), and Fe(EtioPc)I (**18**) determined by X-ray crystallography are 8.094, 7.897, 7.882, and 7.355 $Å^2$, respectively [65, 66]. Correspondingly, the effective magnetic moments determined by SQUID at 300 K are 5.66, 5.68, 5.68, and 4.21 μ_B, respectively. The quadrupole splitting values (ΔE_q) in their Mössbauer spectra are 1.14, 1.34, 1.52, and 3.25 mm s^{-1} at 77 K, respectively. These data clearly indicate that the small cavity size of porphycene stabilizes the intermediate-spin state.

It is quite natural that iron(III) complexes of corrole and triazacorrole with neutral axial ligand(s) adopt the intermediate-spin state due to the small N4 cavity (see Figure 14.12). In fact, the octaethylcorrole (OEC) complex, [Fe(OEC)Py] (**19**), is known to adopt the intermediate-spin state [67–69]. The average Fe-N_P bond length is only 1.893(2) Å [70]. Similarly, the five-coordinate iron(III) complex of triazacorrole known as corrolazine [71], [Fe(Ar)$_8$Cz(Py)] (**20$_e$**), where Ar is 4-*tert*-butylphenyl, adopts the intermediate-spin state [72]. Ikeue et al. have examined the spin states of a series of five-coordinate corrolazine complexes [Fe(Ar)$_8$Cz(L)] (**20$_{a–g}$**) with various axial ligands(L). Spectroscopic studies have revealed that these complexes adopt the intermediate-spin state at 298 K regardless of the

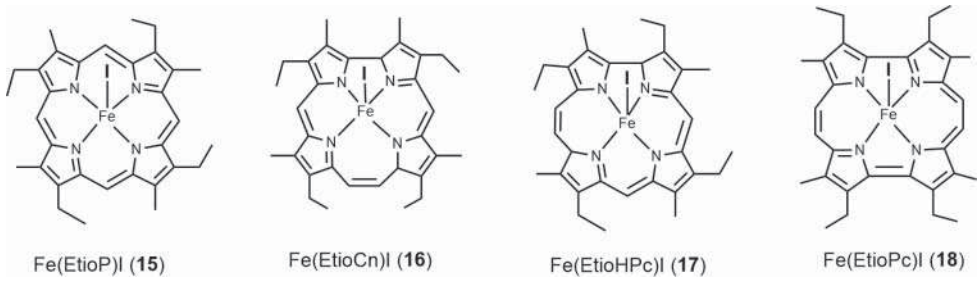

Figure 14.11 Five-coordinate iron(III) iodide complexes of etioporphyrin (**15**), etiocorrphycene (**16**), ethiohemiporphycene (**17**), and etioporphycene (**18**).

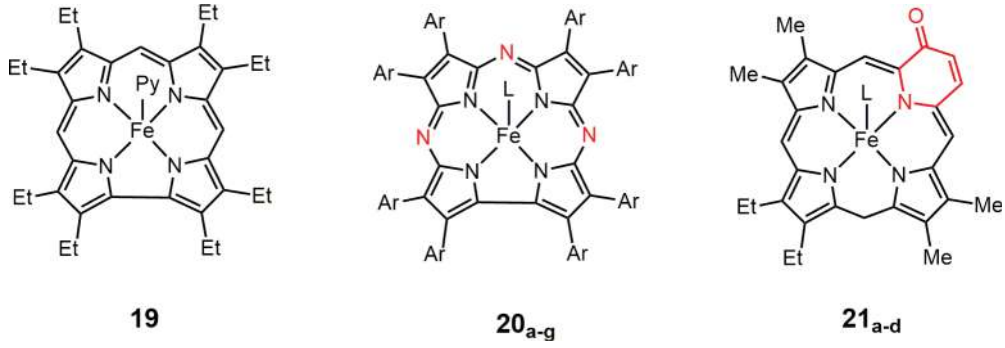

Figure 14.12 Iron(III) complexes of corrole (**19**), corrolazines (**20**), and oxypyriporphyrin (**21**), where Ar is 4-tert-butylphenyl and axial ligands(L) are (a) CN^-, (b) DMAP, (c) HIm, (d) 1-MeIm, (e) Py, (f) 4-CNPy, and (g) ^{t}BuNC.

kind of axial ligands [73]. Stable formation of five-coordinate iron(III) corrolazine complexes with neutral axial ligands is quite different from the corresponding iron(III) porphyrin complexes. In contrast, six-coordinate $[Fe(Ar)_8Cz(L)_2]$ are obtained only in the presence of a large excess of nitrogen bases such as HIm, 1-MeIm, and DMAP at very low temperature, that is, 200 K [73]. These complexes exhibit a low-spin state with a $(d_{xy})^2(d_{xz}, d_{yz})^3$ electron configuration.

Oxypyriporphyrin, which was first synthesized by Lash and Chaney [74], is a unique porphyrin analogue in that the N4 cavity size is supposed to be larger than that in porphyrin due to the replacement of a five-membered pyrrole ring by a six-membered pyridone ring [74]. Although structural data of these complexes have not been reported, quantum chemical calculations for Fe(OxyPyP)Cl have shown that the average Fe—N bond length is 2.139 Å as compared with 2.065 Å in Fe(OEP)Cl [75]. The electronic structure of a series of six-coordinate iron(III) complexes ($\mathbf{21_{a–d}}$) where the axial ligands are strong-field ligands such as CN^- (**a**), DMAP (**b**), Him (**c**), and 1-MeIm (**d**) have been examined [76]. The ^{1}H NMR chemical shifts and effective magnetic moments have shown that the spin state changes from the low-spin state in $\mathbf{21_a}$ to the intermediate-spin state in $\mathbf{21_d}$. The unexpected spin state of the bis(1-MeIm) complex ($\mathbf{21_d}$) could be ascribed to the weak equatorial field strength caused by the wide N4 cavity intrinsic to the oxypyriporphyrin ring.

14.4 Oxidation Products of Iron(III) Porphyrin Complexes

Oxidized products in iron(III) porphyrin complexes are of great interest since some of them are considered to be the reactive intermediates in biological oxidation reactions catalyzed by cytochromes P450, peroxidase, and so on. Figure 14.13 shows possible one-electron and two-electron oxidation products of iron(III) porphyrins. As shown in Figure 14.13, either the iron(III) porphyrin radical cation (**A**) or iron(IV) porphyrin (**B**) is formed by one-electron oxidation. Further one-electron oxidation of **A** and **B** could produce the iron(III) porphyrin dication (**C**), iron(IV) porphyrin radical cation (**D**), or iron(V) porphyrin (**E**) [77, 78].

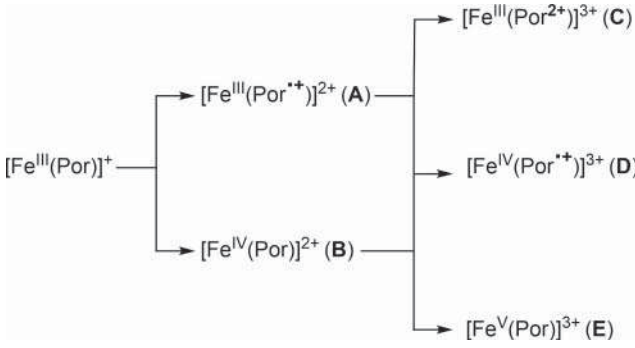

Figure 14.13 Oxidation products of iron(III) porphyrin complexes.

14.4.1 Iron(III) Porphyrin Radical Cations (A)

One-electron oxidation of iron(III) porphyrin usually produces an iron(III) porphyrin radical cation. Radical spin in the porphyrin HOMO, either the a_{2u} or a_{1u} orbital, can interact with the unpaired electron in the paramagnetic iron(III) ion [79–82]. The interactions should be affected by the spin state and electron configuration of iron(III) as well as the structure and peripheral substituents of the porphyrin. Thus, it is convenient to classify iron(III) porphyrin radical cations into three categories depending on the spin state of the central iron(III) ion.

14.4.1.1 Low-Spin Iron(III) Porphyrin Radical Cations

As shown in Figure 14.3, there are two types of electronic ground states in low-spin iron(III) porphyrins: d_π-type and d_{xy}-type. Typical examples are $[Fe^{III}(TMP)(HIm)_2]^+$ and $[Fe^{III}(TMP)(^tBuNC)_2]^+$, respectively. Thus, it is interesting to reveal how the electron configuration of low-spin iron(III) affects the interaction with the porphyrin radical in one-electron oxidized $[Fe^{III}(TMP^{\bullet+})(HIm)_2]^{2+}$ and $[Fe^{III}(TMP^{\bullet+})(^tBuNC)_2]^{2+}$.

In the case of $[Fe^{III}(TMP^{\bullet+})(HIm)_2]^{2+}$, both the pyrrole-H and *meta*-H signals appeared extremely upfield (−53.2 ppm) and downfield (52.1 ppm), respectively, in the ^{1}H NMR spectrum at 213 K; see entry 7 in Table 14.2. The large downfield shift of the *meta*-H signal suggests the formation of the a_{2u} radical cation. The large upfield shift of the pyrrole-H signal suggests the absence of the unpaired electron in the $d_{x^2-y^2}$ orbital. Thus, the electronic structure of the complex should be expressed as $S = 1$ $(d_{xy})^2(d_{xz}, d_{yz})^3(a_{2u})^1$ as shown in Figure 14.14a [83, 84].

In contrast, $[Fe^{III}(TMP^{\bullet+})(^tBuNC)_2]^{2+}$ showed all the signals in 2–7 ppm region at 213 K, which indicates that the complex is diamagnetic; see entry 9 in Table 14.2. The effective magnetic moment is 0.45 μ_B at 173 K. The diamagnetism in this complex should be ascribed to the antiferromagnetic coupling between half-filled iron d_{xy} and half-filled a_{2u}-like orbital in the ruffled porphyrin framework to form an overall $S = 0$ ground state as shown in Figure 14.14b. An equivalent expression should be $S = 0$ $(d_{xz}, d_{yz})^4(d_{xy}, a_{2u})^2$ as proposed by Ghosh et al. [22]. In $[Fe^{III}(TMP^{\bullet+})(4,5\text{-}Cl_2Im)_2]^{2+}$, all the signals are located between the corresponding signals of $[Fe^{III}(TMP^{\bullet+})(HIm)_2]^{2+}$ and $[Fe^{III}(TMP^{\bullet+})(^tBuNC)_2]^{2+}$, indicating that the electronic structure of low-spin iron(III) is a mixture of $(d_{xy})^2(d_{xz}, d_{yz})^3$ and $(d_{xz}, d_{yz})^4(d_{xy})^1$ due to the presence of the low-lying π^* orbital in 4,5-Cl_2Im; see entry 8. Therefore,

Table 14.2 Comparison of ^{1}H NMR chemical shifts of iron(III) porphyrin radical cations and iron(IV) porphyrins.

			pyrrole		*meso*[a]						
					o-H	*m*-H	*p*-H				
Entry	**Complexes**	**T(K)**	**H**	***α*-CH**	**α-H**	**β-H**		**Spin state of iron**	**Spin–spin interaction**	**Total spin**	**Reference**
1	$[Fe^{III}(TPP^{\cdot+})(HIm)_2]^{2+}$	235	−40.1	—	−31.7	30.4	−22.1	$S = 1/2(d_x)$	Ferro	S = 1	[80]
2	$[Fe^{III}(TDP^{\cdot+})(HIm)_2]^{2+}$	217	−49.1	—	(19.0)	(2.2)	−1.8	$S = 1/2(d_x)$	Ferro	S = 1	[84]
3	$[Fe^{III}(TDP^{\cdot+})(2\text{-}MeIm)_2]^{2+}$	217	−49.5[b]	—	(22.8)[b]	(1.8)[b]	−1.6[b]	$S = 1/2(d_x)$	Ferro	S = 1	[84]
4	$[Fe^{III}(TEtP^{\cdot+})(HIm)_2]^{2+}$	223	−36.0	—	230.9	15.5	—	$S = 1/2(d_x)$	Ferro	S = 1	[85]
5	$[Fe^{III}(TPrP^{\cdot+})(HIm)_2]^{2+}$	223	−34.1	—	232.6	14.4	—	$S = 1/2(d_x)$	Ferro	S = 1	[85]
6	$[Fe^{III}(T^iPrP^{\cdot+})(HIm)_2]^{2+}$	223	−20.4	—	42.4	9.0	—	$S = 1/2(d_x)$ $S = 1/2(d_{xy})$	Ferro Antiferro	S = 1 S = 0	[85]
7	$[Fe^{III}(TMP^{\cdot+})(HIm)_2]^{2+}$	213	−53.2	—	(20.1)	52.1	(7.0)	$S = 1/2(d_x)$	Ferro	S = 1	[83]
8	$[Fe^{III}(TMP^{\cdot+})(4,5\text{-}Cl_2Im)_2]^{2+}$	213	−25.6	—	n.d.	24.8	(4.0)	$S = 1/2(d_x)$, $S = 1/2(d_{xy})$	Ferro Antiferro	S = 1 S = 0	[83]
9	$[Fe^{III}(TMP^{\cdot+})(^tBuNC)_2]^{2+}$	213	4.6	—	(2.7)	6.8	(2.2)	$S = 1/2(d_{xy})$	Antiferro	S = 0	[83]
10	$[Fe^{III}(OEP^{\cdot+})Cl]^+$	298	—	30.5 29.6	−18[c]	—	—	S = 5/2	Antiferro	S = 2	[79]
11	$[Fe^{III}(TPP^{\cdot+})Cl]^+$	298	66.1	—	37.6 34.4	−12.3	29.5	S = 5/2	Antiferro	S = 2	[79]
12	$[Fe^{III}(T^iPrP^{\cdot+})Cl]^+$	298	64.6	—	−38.1	−9.6	—	S = 5/2	Antiferro	S = 2	[86]
13	$[Fe^{III}(OETPP^{\cdot+})Cl]^+$	298	—	42.2[b]	36.3[b]	−10.8[b]	28.8	S = 5/2	Antiferro	S = 2	[86]
14	$[Fe^{III}(TMP^{\cdot+})(F)_2]$	193	123.3	—	(40.7)	112.2	(21.2)	S = 5/2	Ferro	S = 3	[93]
15	$[Fe^{III}(TPP^{\cdot+})(SO_3CF_3)_2]$	298	43.9	—	−17.1	31.3	−11.3	S = 5/2	Ferro	S = 3	[81]
16	$[Fe^{III}(TPP^{\cdot+})(ClO_4)_2]$	298	25.6	—	−16.2	32.4	−9.2	S = 5/2	Ferro	S = 3	[81]
17	$[Fe^{III}(TMP^{\cdot+})(ClO_4)_2]$	195	−22.5	—	(32.2)	90.9	(19.7)	S = 5/2 S = 3/2	Ferro Ferro	S = 3 S = 2	[91]

18	$[Fe^{III}(T^iPrP^{\bullet+})(ClO_4)_2]$	298	−64.1	—	109.7	23.8	—	S = 3/2	Ferro	S = 2	[86]
19	$[Fe^{III}(OETPP^{\bullet+})(ClO_4)_2]$	298	—	91.4 23.8	33.5	−7.7	26.9	S = 5/2	Antiferro	S = 2	[86]
20	$[Fe^{III}(TMP^{\bullet+})(N_3)_2]$	213	−42.1	—	(11.6)	34.3	(5.4)	S = 1/2(d_z)	Ferro	S = 1	[96]
21	$[Fe^{III}(p\text{-}OCH_3\text{-}TPP^{\bullet+})(N_3)_2]$	213	−36.3	—	−22.9	30.4	—	S = 1/2(d_z)	Ferro	S = 1	[96]
22	$[Fe^{III}(p\text{-}CF_3\text{-}TPP^{\bullet+})(N_3)_2]$ ⇅ $[Fe^{IV}(p\text{-}CF_3\text{-}TPP)(N_3)_2]$	213	−40.1	—	0.4	16.5	—	Fe^{III}, S = 1/2(d_z) ⇅ Fe^{IV}, S = 1	Ferro —	S = 1 S = 1	[96]
23	$[Fe^{IV}(TMP)(OMe)_2]$	195	−37.5	—	(2.4)	7.7	(2.9)	S = 1	—	S = 1	[91]
24	$[(Fe^{IV}{=}O)(TMP)]$	195	5.9	—	(3.4) (1.1)	6.8 6.2	(2.6)	S = 1	—	S = 1	[88]
25	$[(Fe^{IV}{=}O)(TMP)(1\text{-}MeIm)]$	243	4.6	—	(3.2) (1.6)	7.4	(2.7)	S = 1	—	S = 1	[92]
26	$[(Fe^{IV}{=}O)(TPP)(1\text{-}MeIm)]$	193	5.1	—	9.2	7.9	7.9	S = 1	—	S = 1	[92]
27	$[(Fe^{IV}{=}O)(TPP)(OCD_3)]$	243	0.1	—	(1.5)		(2.7)	S = 1	—	S = 1	[92]
28	$[(Fe^{IV}{=}O)(TMP^{\bullet+})Cl]$	196	−27	—	(26) (24)	68	(11)	S = 1	Ferro	S = 3/2	[97]

a) Values in parentheses are the chemical shifts of methyl signals
b) Averaged value
c) Chemical shift of *meso*-H.

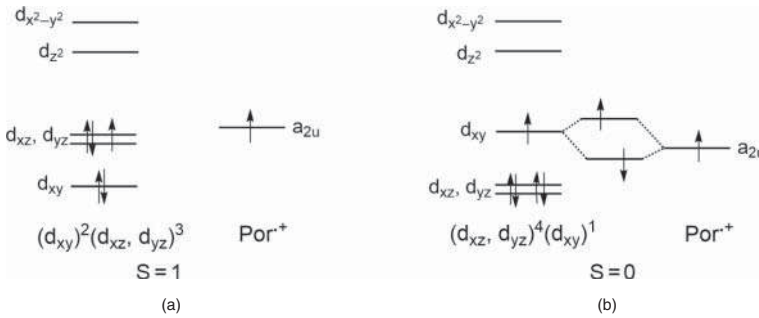

Figure 14.14 Electron configurations of low-spin iron(III) porphyrin cation radicals: (a) $[Fe^{III}(TMP^{\bullet+})(HIm)_2]^{2+}$ and (b) $[Fe^{III}(TMP^{\bullet+})(^tBuNC)_2]^{2+}$.

$[Fe^{III}(TMP^{\bullet+})(4,5\text{-}Cl_2Im)_2]^{2+}$ is best described as a mixture of the $(d_{xz}, d_{yz})^4(d_{xy}, a_{2u})^2$ (S = 0) and $(d_{xy})^2(d_{xz}, d_{yz})^3(a_{2u})^1$ (S = 1) spin states. In other words, all the low-spin iron(III) porphyrin cation radicals should be expressed as an equilibrium mixture given by Eq. (14.4):

$$(d_{xy})^2(d_{xz}, d_{yz})^3(a_{2u})^1 \text{ (S = 1)} \rightleftarrows (d_{xz}, d_{yz})^4(d_{xy}, a_{2u})^2 \text{ (S = 0)} \quad (14.4)$$

The equilibrium constant can be determined by the nature of the axial ligands, electronic effects of the peripheral substituents, deformation mode and degree of the porphyrin ring, and so on. The ^{1}H NMR chemical shifts of low-spin iron(III) porphyrin radical cations are summarized in Table 14.2; see entries 1–9 among them, $[Fe^{III}(T^iPrP^{\bullet+})(HIm)_2]^{2+}$ exhibits the pyrrole-H signal relatively downfield, $\delta = -20.4$ ppm, as compared with other bis(HIm) complexes. The results indicate that the contribution of the S = 0 in this complex is larger than that in the other bis(HIm) complexes due to the highly ruffled structure of the porphyrin ring [85].

14.4.1.2 High-Spin Iron(III) Porphyrin Radical Cations

It is well known that one-electron oxidation of the five-coordinate high-spin iron(III) complex Fe^{III}(TPP)Cl produces the corresponding five-coordinate high-spin iron(III) porphyrin radical cation, $[Fe^{III}(TPP^{\bullet+})Cl]^+$ (Table 14.2, entry 11). Because the complex is deformed in a saddled fashion, the radical spin in the porphyrin a_{2u} orbital couples antiferromagnetically with the half-occupied $d_z{}^2$ and $d_{x^2-y^2}$ orbitals to form the complex with total spin S = 2 [78, 80]. The a_{2u}-$d_z{}^2$ and a_{2u}-$d_{x^2-y^2}$ interactions induce spin flip of the a_{2u} radical spin as shown in Figure 14.15a, resulting in a large negative spin density on the *meso* carbon atoms and inducing a large upfield shift of the *meta*- and large downfield shifts of the *ortho*- and *para*-proton signals.

In contrast, the six-coordinate iron(III) porphyrin cation radicals such as $Fe^{III}(TPP^{\bullet+})(ClO_4)_2$ (Table 14.2, entry 16), are produced by one-electron oxidation of $Fe^{III}(TPP)(ClO_4)$ using $Fe(ClO_4)_3$ as the oxidant. Because the complex is supposed to adopt planar D_{4h} symmetry in solution, the a_{2u} radical orbital is orthogonal to any of the iron d orbitals and therefore the complex should adopt the S = 3 configuration as shown in Figure 14.15b. Consequently, the *meta* proton signal appears downfield, whereas the *ortho*- and *para*-proton signals appear upfield [81, 82]. The chemical shifts of the relevant complexes are given in Table 14.2, entries 10–17.

14.4.1.3 Intermediate-Spin Iron(III) Porphyrin Radical Cations

As mentioned earlier, highly deformed iron(III) porphyrins carrying a weak-field axial ligand such as saddled $Fe^{III}(OETPP)ClO_4$ and ruffled $Fe^{III}(T^iPrP)ClO_4$ adopt essentially pure

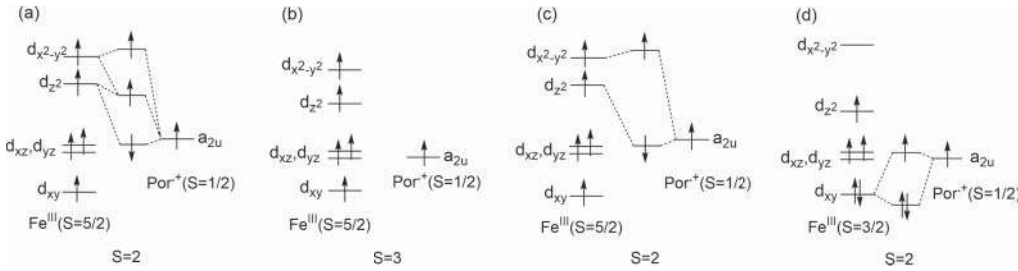

Figure 14.15 Electron configurations of iron(III) porphyrin radical cation: (a) $[Fe(TPP^{\bullet+})Cl]^{+}$, a high-spin iron(III) with antiferromagnetically coupled planar porphyrin radical, (b) $[Fe^{III}(TPP^{\bullet+})(ClO_4)_2]$, a high-spin iron(III) with ferromagnetically coupled planar porphyrin radical, (c) $[Fe^{III}(OETPP^{\bullet+})(ClO_4)_2]$, a high-spin iron(III) with antiferromagnetically coupled saddle-shaped porphyrin radical, and (d) $[Fe^{III}(T^{i}PrP^{\bullet+})(ClO_4)_2]$, an intermediate-spin iron(III) with ferromagnetically coupled ruffle-shaped porphyrin radical.

intermediate-spin states [50–54]. By one-electron oxidation using $Fe(ClO_4)_3$, these complexes are converted to the corresponding iron(III) porphyrin radical cations $Fe^{III}(OETPP^{\bullet+})(ClO_4)_2$ and $Fe^{III}(T^{i}PrP^{\bullet+})(ClO_4)_2$. The question is whether these oxidized complexes maintain the intermediate-spin state. NMR studies of $Fe^{III}(OETPP^{\bullet+})(ClO_4)_2$ have shown the spin flip of the a_{2u} radical spin, which suggests that the a_{2u} radical spin interacts antiferromagnetically with the iron spin in the $d_x2_{-y}2$ orbital. Thus, the complex adopts the S = 2 $(d_{xy})^1(d_{xz})^1(d_{yz})^1(d_z2)^1(d_{x2-y2}, a_{2u})^2$ electron configuration as shown in Figure 14.15c. The result suggests that removal of an electron from the porphyrin a_{2u} orbital weakens the coordination ability of the porphyrin ring. Thus, the iron $d_x2_{-y}2$ orbital is stabilized, resulting in the change in iron(III) spin state from intermediate spin to high spin [54, 86]. In contrast, ruffled $[Fe^{III}(T^{i}PrP^{\bullet+})(ClO_4)_2]$ maintains the intermediate-spin iron(III) with a ferromagnetically coupled porphyrin radical to form the S = 2 $(d_{xy})^2(d_{xz})^1(d_{yz})^1(d_z2)^1(a_{2u})^1$ electron configuration as shown in Figure 14.15d. The d_{xy} orbital should be doubly occupied since no spin flip was observed in the porphyrin radical. The results can be explained in terms of the intrinsically small N4 cavity of the $T^{i}PrP$ ring. The chemical shifts of the relevant complexes are given in Table 14.2, entries 18 and 19.

Thus, iron(III) porphyrin cation radicals can adopt various spin states ranging from S = 0 to S = 3 depending on the field strength of axial ligands and the deformation modes of porphyrin ring: S = 0 as in $[Fe^{III}(TMP^{\bullet+})(^{t}BuNC)_2]^{2+}$ (S = 1/2, S = 1/2, antiferro), S = 1 as in $[Fe^{III}(TMP^{\bullet+})(HIm)_2]^{2+}$ (S = 1/2, S = 1/2, ferro), S = 2 as in $[Fe^{III}(TPP^{\bullet+})Cl]^{+}$ (S = 5/2, S = 1/2, antiferro), $[Fe^{III}(OETPP^{\bullet+})(ClO_4)_2]^{+}$ (S = 5/2, S = 1/2, antiferro), and $[Fe^{III}(T^{i}PrP^{\bullet+})(ClO_4)_2]$ (S = 3/2, S = 1/2, ferro) or S = 3 as in $[Fe^{III}(TMP^{\bullet+})(F)_2]$ (S = 5/2, S = 1/2, ferro).

14.4.2 Iron(IV) Porphyrin

Iron(IV) porphyrins are in general very unstable and difficult to obtain experimentally. Since the iron(IV) ion has four electrons in the d orbitals, the possible spin states are S = 0, S = 1, and S = 2. However, all the iron(IV) porphyrin complexes reported to date adopt the S = 1 spin state and most contain an Fe^{IV}=O bond.

14.4.2.1 Oxo-Iron(IV) Porphyrin Complexes

Iron porphyrins with an Fe^{IV}=O bond are frequently seen in biological systems and are known as compound II in peroxidase and catalase [87, 88]. In model systems, the first

example of this type of complex (Fe^{IV}=O)(Por)(1-MeIm) was reported by LaMar and Balch's group in 1980, where Por is the dianion of tetrakis(3-methylphenyl)porphyrin [89]. The spectroscopic and magnetic data revealed that the complex adopts the S = 1 $(d_{xy})^2(d_{xz}, d_{yz})^2$ electron configuration. Although the complex has no unpaired electron in the $d_x2_{-y}2$ orbital, the pyrrole-H signal was observed in the so-called diamagnetic region. Theoretical studies have revealed that the unpaired electrons on the iron(IV) ion are localized in the Fe^{IV}=O bond [90]. As a result, the spin density on the porphyrin ring is negligibly small. The chemical shifts of the relevant complexes are given in Table 14.2, entries 24–27.

14.4.2.2 Iron(IV) Complexes Without Oxo-Iron(IV) Bond

These complexes are quite rare. The only well-characterized example is $[Fe^{IV}(TMP)(OMe)_2]$, obtained by the addition of methoxide to a CD_2Cl_2 solution of $[Fe^{III}(TMP^{\cdot+})(ClO_4)_2]$ [91]. The isomer shift (δ) and quadrupole splitting (ΔE_q) values in the Mössbauer spectrum in frozen methanol solution at 77 K were − 0.025 and 2.104 mm s^{-1}, respectively, suggesting the iron(IV) oxidation state. The ^{1}H NMR spectrum of $[Fe^{IV}(TMP)(OMe)_2]$ is, however, quite different from that of (Fe^{IV}=O)(TMP)(1-MeIm) in their pyrrole-H chemical shifts; the former occurs at −37.5 ppm, whereas the latter is at 5.9 ppm at 195 K [92]; compare the chemical shifts of entries 23 and 24 in Table 14.2. Thus, the unpaired electrons in the iron d_{xz} and d_{yz} orbitals are delocalized onto the porphyrin ring by the d_π–$3e_g$ interactions. On the basis of the spectroscopic and magnetic data, the complex is best described as an S = 1 $(d_{xy})^2(d_{xz}, d_{yz})^2$ electron configuration. One can expect that $[Fe(TMP)(F)_2]$ is another example of an iron(IV) complex since the fluoride is a strong anionic base like methoxide. ^{1}H NMR and Mössbauer studies have revealed, however, that $[Fe(TMP)(F)_2]$ adopts high-spin iron(III) with a ferromagnetically coupled porphyrin radical cation to form $[Fe^{III}(TMP^{\cdot+})(F)_2]$ with total spin S = 3 as shown in Table 14.2, entry 14 [93–95].

14.4.2.3 Conversion of Iron(III) Porphyrin Radical Cation to Iron(IV) Porphyrin

Is it possible to convert low-spin iron(III) porphyrin cation radical to the corresponding iron(IV) porphyrin by manipulating the electronic nature of the axial ligand and peripheral substituents of porphyrin ring as shown in Eq. (14.5)?

$$[Fe^{III}(Por^{\cdot+})(L)_2] + 2L\prime \rightleftarrows [Fe^{IV}(Por)(L\prime)_2] + 2L \tag{14.5}$$

Such a conversion was observed in the azido complexes $[Fe(TMP)(N_3)_2]$ and $[Fe(p\text{-X-TPP})(N_3)_2]$. As shown in Table 14.2, the ^{1}H NMR signal of each proton in $[Fe(TMP)(N_3)_2]$ (entry 20) is located between the corresponding signals of $[Fe^{III}(TMP^{\cdot+})(HIm)_2]$ (entry 7) and $[Fe^{IV}(TMP)(OMe)_2]$ (entry 23). Furthermore, the ^{1}H NMR signals in a series of $[Fe(p\text{-X-TPP})(N_3)_2]$ complexes move closer to those of $[Fe^{IV}(TMP)(OMe)_2]$ as the *para* substituent changes from an electron-donating methoxy (entry 21) to an electron-withdrawing trifluoromethyl group (entry 22). Thus, the *p*-methoxyphenyl complex exists mainly as $[Fe^{III}(p\text{-}CH_3O\text{-}TPP^{\cdot+})(N_3)_2]$, while the *p*-trifluoromethyl complex exists mainly as $[Fe^{IV}(p\text{-}CF_3\text{-}TPP)(N_3)_2]$ at 195 K. The electron-withdrawing substituent at the *meso* positions should destabilize the porphyrin cation radical state and lead to the formation of an iron(IV) state in Eq. (14.5) [96].

14.4.3 Two-Electron Oxidation Products of Iron(III) Porphyrins

Two-electron oxidation of iron(III) porphyrins produces iron(IV) porphyrin cation radicals rather than iron(V) porphyrins. As in the case of the iron(IV) complexes, these species

usually contain an oxo-iron group, Fe^{IV}=O. Thus, the second electron is removed from the porphyrin ring to form an oxo-iron(IV) porphyrin cation radical $[(Fe^{IV}=O)(Por^{\bullet+})]^+$. The first example to show this electronic structure was reported by Groves et al. in 1981, who prepared $[(Fe^{IV}=O)(TMP^{\bullet+})Cl]$ (Table 14.2, entry 28) by the oxidation of Fe(TMP)Cl with *m*-chloroperoxybenzoic acid in dichloromethane solution at 195 K [97]. Since then, extensive studies have been done on the electronic and magnetic structures of these complexes because they are regarded as reactive intermediate (Compound I) models of oxidation enzymes such as cytochrome P450 and peroxidase. In these complexes, iron adopts the $(d_{xy})^2(d_{xz}, d_{yz})^2$ configuration and the porphyrin has an unpaired electron in an a_{2u} or a_{1u} orbital to form an S = 3/2,either $(d_{xy})^2(d_{xz}, d_{yz})^2(a_{2u})^1$ or $(d_{xy})^2(d_{xz}, d_{yz})^2(a_{1u})^1$ electronic structure depending on the peripheral substituents [9].

Recently, a different type of two-electron oxidized complex was observed in a biological system. The enzyme in question is MauG, which catalyzes the final steps in biosynthesis of the catalytic tryptophan tryptophylquinone cofactor of methylamine dehydrogenase [98–103]. As shown in Figure 14.16, MauG possesses two c-type hemes together with a Trp93 residue located between the two hemes [101]. In the resting di-iron(III) state, MauG has a five-coordinate high-spin (S = 5/2) heme ($Heme_{5c}$) with an axial histidine coordination and a six-coordinate low-spin (S = 1/2) heme ($Heme_{6c}$) with an unusual histidine-tyrosine coordination. The two heme iron ions are separated by 21.1 Å, and the edge-to-edge distance between hemes is 14.5 Å.

Upon oxidation with H_2O_2, the enzyme is oxidized to form the unprecedented bis-iron(IV) intermediate, where $Heme_{5c}$ and $Heme_{6c}$ are converted to $(Fe^{IV}=O)$(Por)(His) and Fe^{IV}(Por)(Tyr)(His), respectively, as shown in Figure 14.17 [102]. In the oxidation reaction, the five-coordinate high-spin heme ($Heme_{5C}$) is converted to the Fe^{IV}=O porphyrin cation radical, to which an electron is transferred from the second heme ($Heme_{6C}$) to form a bis-iron(IV) intermediate. The intermediate has been characterized by crystallographic and spectroscopic studies.

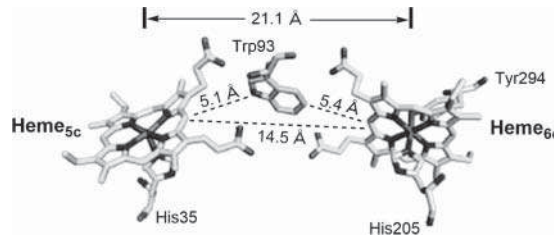

Figure 14.16 Structural orientation of the hemes and the intervening tryptophan residue in MauG (PDB entry: 3L4M). The distance between the two iron ions and the edge-to-edge distances between the aromatic moieties are labeled. Source: From Geng et al. [101] with permission of Wiley.

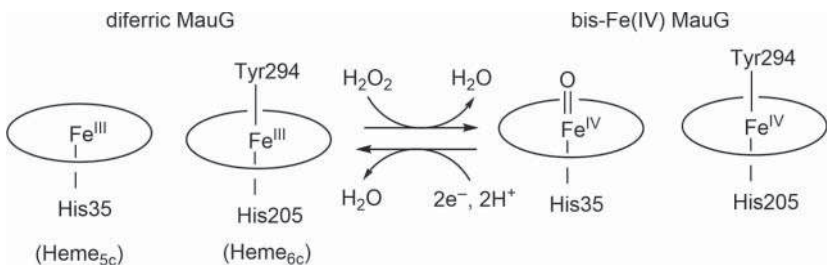

Figure 14.17 Chemical conversion between di-iron(III) and di-iron(IV) MauG. Source: Geng et al. [102] with permission of PNAS.

In the Mössbauer spectra, the isomer shift (δ) and the quadrupole splitting (ΔE_Q) of the (Fe^{IV}=O)(Por)(His) species are 0.06 and 1.70 mm s^{-1}, respectively, while those of Fe^{IV}(Por)(Tyr)(His) are 0.17 and 2.56 mm s^{-1}, respectively. The large ΔE_Q value in the latter heme is quite unusual for an iron(IV) complex in a biological system and supports the formation of a six-coordinate iron(IV) complex without an Fe^{IV}=O bond. It is considered that the long-range electron transfer from one heme to the other is mediated by the reversible oxidation and reduction of Trp93 located between two hemes as shown in Figure 14.16 [101].

14.5 Summary

In order to understand the physicochemical properties of heme proteins in biological systems, the author has introduced in this chapter a wide variety of iron porphyrin complexes showing characteristic properties ascribed to their oxidation states, spin states, and electron configurations.

Acknowledgments

The author would like to thank Dr. Takahisa Ikeue of Shimane University and Dr. Akira Ikezaki of Toho University for valuable discussions.

References

1 Sono, M., Roach, M.P., Coulter, E.D., and Dawson, J.H. (1996). Heme-containing oxygenases. *Chemical Reviews* 96: 2841–2888.
2 Denisov, I.G., Makris, T.M., Sligar, S.G., and Schlichting, I. (2005). Structure and chemistry of cytochrome P450. *Chemical Reviews* 105: 2253–2278.
3 Ortiz de Montellano, P.R. (2010). Hydrocarbon hydroxylation by cytochrome P450 enzymes. *Chemical Reviews* 110: 932–948.
4 Mansuy, D. and Battioni, P. (2000). Diversity of reactions catalyzed by heme-thiolate proteins. In: *The Porphyrin Handbook*, vol. 4 (ed. K.M. Kadish, K.M. Smith and R. Guilard), 1–15. New York: Academic Press.
5 Liu, W. and Groves, J.T. (2015). Manganese catalyzed C–H Halogenation. *Accounts of Chemical Research* 48: 1727–1735.
6 Mansuy, D. and Battioni, P. (2000). Proton NMR and EPR spectroscopy of paramagnetic metalloporphyrins. In: *The Porphyrin Handbook*, vol. 5 (ed. K.M. Kadish, K.M. Smith and R. Guilard), 81–83.
7 Nakamura, M., Ohgo, Y., and Ikezaki, A. (2008). Electronic ground states of low-spin iron (III) porphyrinoids. *Journal of Inorganic Biochemistry* 102: 433–445.
8 Nakamura, M., Ohgo, Y., and Ikezaki, A. (2010). Electronic and magnetic structures of iron porphyrin complexes. In: *Handbook of Porphyrin Science*, vol. 7 (ed. K.M. Kadish, K.M. Smith and R. Guilard), 1–146. New York: World Scientific.
9 Fujii, H. (2002). *Coordination Chemistry Reviews* 226: 51–61.

10 Guan, Y., Powell, D.R., and Richter-Addo, G.B. (2015). Crystal structure of bis (1-methyl-1H-imidazole-κN3)(5, 10, 15, 20-tetraphenylporphyrinato-κ4N) iron (II)–1-methyl-1H-imidazole (1/2). *Acta Crystallographica Section E* 71: m57–m58.

11 Hu, C., Noll, B.C., Piccoli, P.M.B. et al. (2008). Hydrogen bonding effects on the electronic configuration of five-coordinate high-spin iron (II) porphyrinates. *Journal of the American Chemical Society* 130: 3127–3136.

12 Hu, C., Schulz, C.E., and Scheidt, W.R. (2015). All high-spin (S = 2) iron(II) hemes are NOT alike. *Dalton Transactions* 44: 18301–18310.

13 Shibata, T., Kanai, Y., Nishimura, R. et al. (2016). Characterization of ground state electron configurations of high-spin quintet ferrous heme iron in deoxy myoglobin reconstituted with trifluoromethyl group-substituted heme cofactors. *Inorganic Chemistry* 55: 12128–12136.

14 Kozlowski, P.M., Spiro, T.G., Berces, A., and Zgierski, M.Z. (1998). Low-lying spin states of iron(II) porphine. *The Journal of Physical Chemistry. B* 102: 2603–2608.

15 La Mar, G.N. and Walker, F.A. (1979). NMR studies of paramagnetic metalloporphyrins. In: *The Porphyrins*, vol. IV (ed. D. Dolphin), 61–157. New York: Academic Press.

16 Walker, F.A., Reis, D., and Balke, V.J. (1984). Models of the cytochromes *b*. 5. EPR studies of low-spin iron(III) tetraphenylporphyrins. *Journal of the American Chemical Society* 106: 6888–6898.

17 Walker, F.A., Huynh, B.H., Scheidt, W.R., and Osvath, S.R. (1986). Models of the cytochromes *b*. Effect of axial ligand plane orientation on the EPR and Mössbauer spectra of low-spin ferrihemes. *Journal of the American Chemical Society* 108: 5288–5297.

18 Safo, M.K., Gupta, G.P., Watson, C.T. et al. (1992). Models of the cytochromes *b*. Low-spin bis-ligated (porphinato)iron(III) complexes with unusual molecular structures and NMR, EPR, and Mössbauer spectra. *Journal of the American Chemical Society* 114: 7066–7075.

19 Walker, F.A., Nasri, H., Turowska-Tyrk, I. et al. (1996). π-Acid ligands in iron(III) porphyrinates. Characterization of low-spin Bis(*tert*-butylisocyanide)(porphyrinato)iron(III) complexes having $(d_{xz},d_{yz})^4(d_{xy})^1$ ground states. *Journal of the American Chemical Society* 118: 12109–12118.

20 Nakamura, M., Ikeue, T., Fujii, H., and Yoshimura, T. (1997). Change in electron configuration of Ferric Ion in Bis(cyanide)(*meso*-tetraalkylporphyrinatoiron(III)), $[Fe(TRP)(CN)_2]^-$, caused by the nonplanarity of the porphyrin ring. *Journal of the American Chemical Society* 119: 6284–6291.

21 Cheng, R.-J., Chen, P.-Y., Lovell, T. et al. (2003). Symmetry and bonding in metalloporphyrins. A Modern Implementation For The Bonding Analyses Of Five- And Six-Coordinate High-Spin iron(III)–porphyrin complexes through density functional calculation and NMR spectroscopy. *Journal of the American Chemical Society* 125: 6774–6783.

22 Conradie, J. and Ghosh, A. (2003). Do the one-electron oxidized derivatives of some six-coordinate low-spin Iron (III) porphyrins feature strong metal– ligand ferromagnetic coupling? *The Journal of Physical Chemistry B* 107: 6486–6490.

23 Ikezaki, A., Ikeue, T., and Nakamura, M. (2002). Electronic effects of *para*-substituents on the electron configuration of dicyano[*meso*-tetrakis(*p*-substituted phenyl) porphyrinato]iron(III) complexes. *Inorganica Chimica Acta* 335: 91–99.

24 Ikeue, T., Handa, M., Chambarin, A. et al. (2011). Benzoannelation stabilizes the d_{xy}^1 state of low-spin iron(III) porphyrinates. *Inorganic Chemistry* 50: 3567–3581.

25 Ikeue, T., Ohgo, Y., Saitoh, T. et al. (2001). Factors affecting the electronic ground state of low-spin iron (III) porphyrin complexes. *Inorganic Chemistry* 40: 3423–3434.

26 Palmer, G. (1983). Electron paramagnetic resonance of hemoproteins. In: *Iron Porphyrins, Part II*, Physical Bioinorganic Chemistry Series 2 (ed. A.B.P. Lever and H.B. Gray), 43–88. Reading, MA: Addison-Wesley.

27 Ohgo, Y., Hoshino, A., Okamura, T. et al. (2007). Metal–porphyrin orbital interactions in highly saddled low-spin iron(III) porphyrin complexes. *Inorganic Chemistry* 46: 8193–8207.

28 Ikezaki, A. and Nakamura, M. (2002). Effects of solvents on the electron configurations of the low-spin Dicyano[*meso*-tetrakis(2,4,6-triethylphenyl)porphyrinato]iron(III) complex: importance of the C–H···N weak hydrogen bonding. *Inorganic Chemistry* 41: 2761–2768.

29 Caignan, G.A., Deshmukh, R., Zeng, Y.A. et al. (2003). The hydroxide complex of *Pseudomonas aeruginosa* heme oxygenase as a model of the low-spin iron(III) hydroperoxide intermediate in heme catabolism: ^{13}C NMR spectroscopic studies suggest the active participation of the heme in macrocycle hydroxylation. *Journal of the American Chemical Society* 125: 11852.

30 Zeng, Y., Caignan, G.A., Bunce, R.A. et al. (2005). Azide-inhibited bacterial heme oxygenases exhibit an $S = 3/2$ $(d_{xz},d_{yz})^3(d_{xy})^1(d_{z^2})^1$ spin state: mechanistic implications for heme oxidation. *Journal of the American Chemical Society* 127: 9794–9807.

31 Li, J., Noll, B.C., Schulz, C.E., and Scheidt, W.R. (2015). Bis(cyano) iron(III) porphyrinates: what is the ground state? *Inorganic Chemistry* 54: 6472–6485.

32 Ikeue, T., Ohgo, Y., Saitoh, T. et al. (2000). Spin distribution in low-spin (*meso*-Tetraalkylporphyrinato)iron(III) complexes with $(d_{xz},d_{yz})^4(d_{xy})^1$ configuration. Studies by ^{1}H NMR, ^{13}C NMR, and EPR spectroscopies. *Journal of the American Chemical Society* 122: 4068–4076.

33 Liptak, M.D., Wen, X., and Bren, K.L. (2010). NMR and DFT investigation of heme ruffling: functional implications for cytochrome *c*. *Journal of the American Chemical Society* 132: 9753–9763.

34 Kleingardner, J.G., Bowman, S.E.J., and Bren, K.L. (2013). The influence of heme ruffling on spin densities in ferricytochromes *c* probed by heme core ^{13}C NMR. *Inorganic Chemistry* 52: 12933–12946.

35 Nakamura, M. (2006). Electronic structures of highly deformed iron (III) porphyrin complexes. *Coordination Chemistry Reviews* 250: 2271–2294.

36 Skaar, E.P., Gaspar, A.H., and Schneewind, O. (2004). IsdG and IsdI, heme-degrading enzymes in the cytoplasm of *Staphylococcus aureus*. *The Journal of Biological Chemistry* 279: 436–443.

37 Chim, N., Iniguez, A., Nguyen, T.Q., and Goulding, C.W. (2010). Unusual diheme conformation of the heme-degrading protein from *Mycobacterium tuberculosis*. *Journal of Molecular Biology* 395: 595–608.

38 Wilks, A. and Ikeda-Saito, M. (2014). Heme utilization by pathogenic bacteria: not all pathways lead to biliverdin. *Accounts of Chemical Research* 47: 2291–2298.

39 Takayama, S.J., Ukpabi, G., Murphy, M.E.P., and Mauk, A.G. (2011). Electronic properties of the highly ruffled heme bound to the heme degrading enzyme IsdI. In: *Proceedings of National Academy of Sciences of United States of America (PNAS)*, vol. 108, 13071–13076.

40 Graves, A.B., Morse, R.P., Chao, A. et al. (2014). Crystallographic and spectroscopic Insights into heme degradation by *Mycobacterium tuberculosis* MhuD. *Inorganic Chemistry* 53: 5931–5940.

41 Hoshino, A., Ohgo, Y., and Nakamura, M. (2005). Electronic structures of six-coordinate ferric porphyrin complexes with weak axial ligands: usefulness of ^{13}C NMR chemical shifts. *Inorganic Chemistry* 44: 7333–7344.

42 Patra, R., Bhowmik, S., Ghosh, S.K., and Rath, S.P. (2010). Effects of axial pyridine coordination on a saddle-distorted porphyrin macrocycle: stabilization of hexa-coordinated high-spin Fe(III) and air-stable low-spin iron(II) porphyrinates. *Dalton Transactions* 39: 5795–5806.

43 Fang, M., Wilson, S.R., and Suslick, K.S. (2008). A four-coordinate Fe(III) porphyrin cation. *Journal of the American Chemical Society* 130: 1134–1135.

44 Scheidt, W.R. and Lee, Y.J. (1987). Recent advances in the stereochemistry of metallotetrapyrroles. *Structure and Bonding* 64: 1–70.

45 Scheidt, W.R. (2008). Explorations in metalloporphyrin stereochemistry, physical properties and beyond. *Journal of Porphyrins and Phthalocyanines* 12: 979–992.

46 Reed, C.A. and Guiset, F. (1996). A "Magnetochemical" series. Ligand field strengths of weakly binding anions deduced from $S = {}^3/_2, {}^5/_2$ spin state mixing in iron(III) porphyrins. *Journal of the American Chemical Society* 118: 3281–3282.

47 Evans, D.R. and Reed, C.A. (2000). Reversal of H_2O and OH^- ligand field strength on the magnetochemical series relative to the spectrochemical series. Novel 1-equiv water chemistry of iron(III) tetraphenylporphyrin complexes. *Journal of the American Chemical Society* 122: 4660–4667.

48 Cirera, J. and Alvarez, S. (2013). Stereospinomers of pentacoordinate iron porphyrin complexes: the case of the $[Fe(porphyrinato)(CN)]^-$ anions. *Dalton Transactions* 42: 7002–7008.

49 Sahoo, D., Quesne, M.G., de Visser, S.P., and Rath, S.P. (2015). Hydrogen-bonding interactions trigger a spin-flip in iron(III) porphyrin complexes. *Angewandte Chemie, International Edition* 54: 4796–4800.

50 Cheng, R.-J., Chen, P.-Y., Gau, P.-R. et al. (1997). Control of spin state by ring conformation of iron(iii) porphyrins. A novel model for the quantum-mixed intermediate spin state of ferric cytochrome *c*′ from photosynthetic bacteria. *Journal of the American Chemical Society* 119: 2563–2569.

51 Ikeue, T., Saitoh, T., Yamaguchi, T. et al. (2000). Formation of pure intermediate spin complexes in highly nonplanar iron(III) porphyrins. *Chemical Communications* 36: 1989–1990.

52 Barkigia, K.M., Renner, M.W., and Fajer, J. (2001). Molecular structure of Fe(III) 2,3,7,8,12,13,17,18-octaethyl-5,10,15,20-tetraphenylporphyrin perchlorate: a saddle-shaped porphyrin with an intermediate S = 3/2 spin state. *Journal of Porphyrins and Phthalocyanines* 5: 415–418.

53 Nakamura, M., Ikeue, T., Ohgo, Y. et al. (2002). Highly saddle shaped (porphyrinato)iron(III) iodide with a pure intermediate spin state. *Chemical Communications* 38: 1198–1199.

54 Sahoo, D. and Rath, S.P. (2015). Controlled generation of highly saddled (porphyrinato)iron(III) iodide, tri-iodide and one-electron oxidized complexes. *Chemical Communications* 51: 16790–16793.

55 Ikezaki, A., Takahashi, M., and Nakamura, M. (2009). Models for cytochromes *c*′: observation of an extremely labile spin state in monoimidazole complexes of saddle-shaped iron(III) porphyrinates. *Angewandte Chemie, International Edition* 48: 6300–6303.

56 Ohgo, Y., Saitoh, T., and Nakamura, M. (2001). Bis (tetrahydrofuran-κ*O*)(*meso*-5, 10, 15, 20-tetraisopropylporphyrinato-κ^4*N*) iron (III) perchlorate. *Acta Crystallographica Section C* 57: 233–234.

57 Kobayashi, N. (2000). *The Porphyrin Handbook, Volume 2*, vol. 2 (ed. K.M. Kadish, K.M. Smith and R. Guilard), 301–360. New York: Academic Press.

58 Fitzgerald, J.P., Haggerty, B.S., Rheingold, A.L. et al. (1992). Iron octaethyltetraazaporphyrins: synthesis, characterization, coordination chemistry, and comparisons to related iron porphyrins and phthalocyanines. *Inorganic Chemistry* 31: 2006–2013.

59 Stuzhin, P.A., Hamdush, M., and Ziener, U. (1995). Iron octaphenyltetraazaporphyrins: synthesis and characterization of the five-coordinate complexes of iron(III) (XFe^{III}OPTAP; X=F, Cl, Br, I, HSO_4). *Inorganica Chimica Acta* 236: 131–139.

60 Fitzgerald, J.P., Lebenson, J.R., Wang, G. et al. (2008). Iron tetraanthracenotetraazaporphyrins: synthesis, structural characterization, ligand binding properties, and unexpected selectivity of a bis-"bowl" tetraazaporphyrin. *Inorganic Chemistry* 47: 4520–4530.

61 Ikeue, T., Kurahashi, S., Handa, M. et al. (2008). Electronic structure of five- and six-coordinate iron(III) tetraazaporphyrin complexes: pyrrole-C_α chemical shift as a useful probe. *Journal of Porphyrins and Phthalocyanines* 12: 1041–1049.

62 Stuzhin, P.A., Nefedov, S.E., Kumeev, R.S. et al. (2010). Effects of solvation on the spin state of iron(III) in 2,8,12,18-Tetrabutyl-3,7,13,17-tetramethyl-5,10-diazaporphyrinatoiron(III) Chloride. *Inorganic Chemistry* 49: 4802–4813.

63 Balch, A.J., Olmstead, M.N., and Safari, N. (1993). (Octaethylazaporphyrinato)iron(III) chloride: its structure in the solid state and in solution. *Inorganic Chemistry* 32: 291–296.

64 Scheidt, W.R. and Finnegan, M.G. (1989). Structure of monoclinic chloro(*meso*-tetraphenylporphyrinato)iron(III). *Acta Crystallographica Section C* 45: 1214–1216.

65 Ohgo, Y., Neya, S., Ikeue, T. et al. (2002). Molecular structures of five-coordinated halide ligated iron(III) porphyrin, porphycene, and corrphycene complexes. *Inorganic Chemistry* 41: 4627–4629.

66 Ohgo, Y., Neya, S., Ikeue, T. et al. (2003). Iodo(etiohemiporphycenato)iron(III). Unexpected difference in magnetic behavior in solution and solid. *Chemistry Letters* 32: 526–527.

67 Caemelbecke, E.V., Autret, S.W.M., Adamian, V.A. et al. (1996). Electrochemical and spectral characterization of iron corroles in high and low oxidation states: first structural characterization of an iron(IV) tetrapyrrole π cation radical. *Inorganic Chemistry* 35: 184–192.

68 Simkhovich, L., Mahammed, A., Goldberg, I., and Gross, Z. (2001). Synthesis and characterization of germanium, Tin, Phosphorus, Iron, and Rhodium complexes of Tris(pentafluorophenyl)corrole, and the utilization of the iron and rhodium corroles as cyclopropanation catalysts. *Chemistry – A European Journal* 7: 1041–1055.

69 Simkhovich, L., Goldberg, I., and Gross, Z. (2002). Iron(III) and iron(IV) corroles: synthesis, spectroscopy, structures, and no indications for corrole radicals. *Inorganic Chemistry* 41: 5433–5439.

70 Erben, C., Will, S., and Kadish, K.M. (2000). Metallocorroles: Molecular structure, spectroscopy and electronic states (chapter 12). In: *The Porphyrin Handbook, Volume 2*, vol. 2 (ed. K.M. Kadish, K.M. Smith and R. Guilard), 233–300. New York: Academic Press.

71 Ramdhanie, B., Stern, C.L., and Goldberg, D.P. (2001). Synthesis of the first corrolazine: A new member of the porphyrinoid family. *Journal of the American Chemical Society* 123: 9447–9448.

72 Kerber, W., Ramdhanie, B., and Goldberg, D.P. (2007). H_2O_2 oxidations catalyzed by an iron(III) corrolazine: avoiding high-valent iron–oxido species? *Angewandte Chemie, International Edition* 46: 3718–3721.

73 Kurahashi, S., Ikeue, T., Handa, M. et al. (2012). Formation and characterization of five- and six-coordinate iron(III) corrolazine complexes. *Journal of Porphyrins and Phthalocyanines* 16: 518–529.

74 Lash, T.D. and Chaney, S.T. (1996). Oxypyriporphyrin, the first fully aromatic porphyrinoid macrocycle with a pyridine subunit. *Chemistry – A European Journal* 2: 944–948.

75 Neya, S., Suzuki, M., Ode, H. et al. (2008). Functional evaluation of iron oxypyriporphyrin in protein heme pocket. *Inorganic Chemistry* 47: 10771–10778.

76 Eguchi, H., Ohgo, Y., Ikezaki, A. et al. (2008). Bis(1-methylimidazole) complex of iron(III) oxypyriporphyrin adopting an intermediate-spin state. *Chemistry Letters* 37: 768–769.

77 Ikezaki, A., Ohgo, Y., and Nakamura, M. (2009). NMR studies on the electronic structure of one-electron oxidized complexes of iron(III) porphyrinates. *Coordination Chemistry Reviews* 253: 2056–2069.

78 Nakamura, M., Ikezaki, A., and Takahashi, M. (2013). Metal-porphyrin orbital interactions in paramagnetic iron complexes having planar and deformed porphyrin ring. *Journal of the Chinese Chemical Society* 60: 9–21.

79 Phillippi, M.A. and Goff, H.M. (1982). Electrochemical synthesis and characterization of the single-electron oxidation products of ferric porphyrins. *Journal of the American Chemical Society* 104: 6026–6034.

80 Goff, H.M. and Phillippi, M.A. (1983). Imidazole complexes of low-spin iron(III) porphyrin π-cation radical species. models for the compound I π-cation radical state of peroxidases. *Journal of the American Chemical Society* 105: 7567–7571.

81 Boersma, A.D. and Goff, H.M. (1984). Electrochemical oxidation of spin-admixed S= 5/2, 3/2 iron(III) porphyrins: in situ characterization by deuterium NMR spectroscopy. *Inorganic Chemistry* 23: 1671–1676.

82 Gans, P., Buisson, G., Duee, E. et al. (1986). High-valent iron porphyrins: synthesis, x-ray structures, π-cation radical formulation, and notable magnetic properties of chloro(meso-tetraphenylporphinato)iron(III) hexachloroantimonate and bis(perchlorato)(meso-tetraphenylporphinato)iron(III). *Journal of the American Chemical Society* 108: 1223–1234.

83 Ikezaki, A., Tukada, H., and Nakamura, M. (2008). Control of electronic structure of a six-coordinate iron(III) porphyrin radical by means of axial ligands. *Chemical Communications* 2257–2259.

84 Nakamura, M. and Kawasaki, Y. (1996). Formation and ^{1}H NMR spectra of low spin ferric porphyrin radical cations with orientationally fixed imidazole ligands. *Chemistry Letters* 25: 805–806.

85 Ikeue, T., Ohgo, Y., and Nakamura, M. (2003). Effects of a nonplanar porphyrin rings on the spin–spin interactions in low-spin ferric porphyrin radical cations. *Chemical Communications* 220–221.

86 Kouno, S., Ikezaki, A., Ikeue, T., and Nakamura, M. (2011). Spin–spin interactions in iron(III) porphyrin radical cations with ruffled and saddled structure. *Journal of Inorganic Biochemistry* 105: 718–721.

87 Groves, J.T. (2006). High-valent iron in chemical and biological oxidations. *Journal of Inorganic Biochemistry* 100: 434–447.

88 Groves, J.T., Gross, Z., and Stern, M.K. (1994). Preparation and reactivity of oxoiron(IV) porphyrins. *Inorganic Chemistry* 33: 5065–5072.

89 Chin, D.H., Balch, A.L., and La Mar, G.N. (1980). Formation of porphyrin ferryl (FeO^{2+}) complexes through the addition of nitrogen bases to peroxo-bridged iron(III) porphyrins. *Journal of the American Chemical Society* 102: 1446–1448.

90 Dey, A. and Ghosh, A. (2002). "True" iron(V) and iron(VI) porphyrins: a first theoretical exploration. *Journal of the American Chemical Society* 124: 3206–3207.

91 Groves, J.T., Quinn, R., McMurry, T.J. et al. (1985). Preparation and characterization of a dialkoxyiron(IV) porphyrin. *Journal of the American Chemical Society* 107: 354–360.

92 Balch, A.L., Chan, Y.-W., Cheng, R.-J. et al. (1984). Oxygenation patterns for iron (II) porphyrins. Peroxo and ferryl ($Fe^{IV}O$) intermediates detected by ^{1}H nuclear magnetic resonance spectroscopy during the oxygenation of (oetramesitylporphyrin)iron(II). *Journal of the American Chemical Society* 106: 7779–7785.

93 Ikezaki, A., Takahashi, M., and Nakamura, M. (2011). One-electron oxidized product of difluoroiron(III) porphyrin: is it iron(IV) porphyrin or iron(III) porphyrin π-cation radical? *Dalton Transactions* 40: 9163–9168.

94 Ghosh, A. and Taylor, P.R. (2005). Iron(IV) porphyrin difluoride does not exist: implications for DFT calculations on heme protein reaction pathways. *Journal of Chemical Theory and Computation* 1: 597–600.

95 Panchmatia, P.M., Ali, M.E., Sanyal, B., and Oppeneer, P.M. (2010). Halide ligated iron porphines: A DFT+*U* and UB3LYP study. *Journal of Physical Chemistry. A* 114: 13381–13387.

96 Ikezaki, A., Takahashi, M., and Nakamura, M. (2013). Equilibrium between Fe(IV) porphyrin and Fe(III) porphyrin radical cation: new insight into the electronic structure of high-valent iron porphyrin complexes. *Chemical Communications* 49: 3098–3100.

97 Groves, J.T., Haushalter, R.C., Nakamura, M. et al. (1981). High-valent iron-porphyrin complexes related to peroxidase and cytochrome P-450. *Journal of the American Chemical Society* 103: 2884–2886.

98 Davidson, V.L. (2007). Protein-derived cofactors. Expanding the scope of post-translational modifications. *Biochemistry* 46: 5283–5292.

99 Wilmot, C.M. and Yukl, E.T. (2013). MauG: a di-heme enzyme required for methylamine dehydrogenase maturation. *Dalton Transactions* 42: 3127–3135.

100 Ma, Z., Williamson, H.R., and Davidson, V.L. (2015). Roles of multiple-proton transfer pathways and proton-coupled electron transfer in the reactivity of the *bis*-Fe^{IV} state of MauG. *Proceedings of National Academy of Sciences of United States of America (PNAS)* 112: 10896–10901.

101 Geng, J., Davis, I., and Liu, A. (2015). Probing Bis-FeIV MauG: experimental evidence for the long-range charge-resonance model. *Angewandte Chemie, International Edition* 54: 3692–3696.

102 Geng, J., Dornevil, K., Davidson, V.L., and Liu, A. (2013). Tryptophan-mediated charge-resonance stabilization in the bis-Fe(IV) redox state of MauG. *Proceedings of National Academy of Sciences of United States of America (PNAS)* 110: 9639–9644.

103 Sil, D., Dey, S., Kumar, A. et al. (2016). Oxidation triggers extensive conjugation and unusual stabilization of two di-heme dication diradical intermediates: role of bridging group for electronic communication. *Chemical Science* 7: 1212–1223.

15

Electrochemical Properties of Porphyrin-Type Complexes

Tebello Nyokong

Institute for Nanotechnology Innovation, Rhodes University, Grahamstown, South Africa

Abbreviations

Ac	acetate
AFM	atomic force microscopy
CV	cyclic voltammetry
DCE	dichloroethane
DCM	dichloromethane
DMF	dimethylformamide
DMSO	dimethylsulfoxide
DPV	differential pulse voltammetry
GCE	glassy carbon electrode
HOMO	highest occupied molecular orbital
HOPG	highly oriented pyrolytic graphite
ITO	indium tin oxide
LUMO	lowest unoccupied molecular orbital
MPc	metallophthalocyanine
Mpy	mercapro pyridine
OBTPc	octabutylthio phthalocyanine
ODTPc	octa decylthio phthalocyanine
OPG	ordinary pyrolytic graphite
OPhTPc	octa phenylthio phthalocyanine
OTE	optically transparent electrode
OTTLE	optically transparent thin layer electrode
Por	porphyrin
Pc	phthalocyanine
SAM	self-assembled monolayer
SECM	scanning electrochemical microscopy
SPAuE	screen-printed Au electrode
STM	scanning tunneling microscopy
SWCNT	single-walled carbon nanotube
SWV	square wave voltammetry
TBAP	tetrabutyl ammonium perchlorate

Fundamentals of Porphyrin Chemistry: A 21st Century Approach, Volume 2, First Edition.
Edited by Penelope J. Brothers and Mathias O. Senge.
© 2022 John Wiley & Sons Ltd. Published 2022 by John Wiley & Sons Ltd.

$TBABF_4$	tetrabutylammonium tetrafluoroborate
UME	ultramicro electrode
XPS	X-ray photoelectron spectroscopy

15.1 Introduction to Porphyrin-Type Complexes

15.1.1 Structure and General Applications

Phthalocyanines (Pc, **1**) and porphyrins (Por, **4**) (Figure 15.1a) belong to a class of compounds known as tetrapyrrolic macrocycles, which includes porphyrazines (tetraazaporphyrins) (**2**) and tetrabenzoporphyrins (**3**), among others. The macrocycles are structurally similar except that **1** and **2** have imino nitrogen atoms at each of the four *meso* positions, while **3** and **4** have methine bridges [1]. Macrocycles **1** and **3** have in addition four benzo groups attached to the ring. Metal-free porphyrins (H_2Por, **4**) or phthalocyanines (H_2Pc, **1**) are of D_{2h} symmetry. Most metal ions fit inside the cavity of the ring, thus increasing the symmetry from D_{2h} (of metal-free Por or Pc) to D_{4h} (of metalloporphyrin, MPor or metallophthalocyanines, MPc).

For phthalocyanines (which will be used as examples for electrochemistry), the non-peripheral positions on the Pc ring are located at 1, 4, 8, 11, 15, 18, 22, and 25 and are designated as α–substituents, while those located at positions 2, 3, 9, 10, 16, 17, 23, and 24 are designated as β-substituents (Figure 15.1b).

For large metal ions (e.g., Pb), the molecular symmetry is decreased to C_{4v} (i.e., square pyramidal for MPc), and the metal ions tend to lie above the ring to adopt a "shuttlecock-shaped" configuration (Figure 15.2) [2], which affects their electrochemical properties.

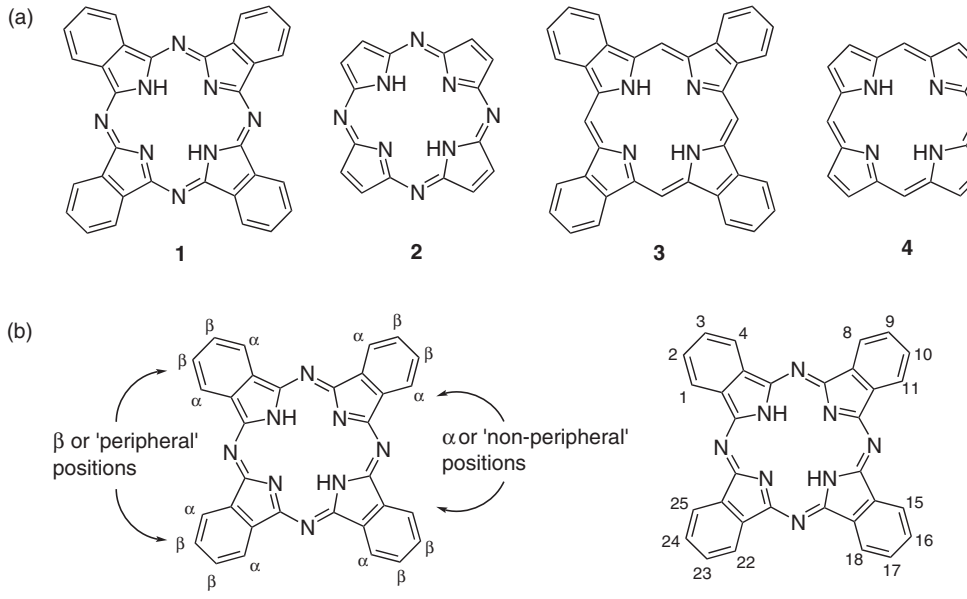

Figure 15.1 (a) Structure of tetrapyrrolic macrocycles: **1** = phthalocyanine, **2** = porphyrazine, **3** = tetrabenzoporphyrin, and **4** = porphyrin. (b) Representation of the non-peripheral (α) and peripheral (β) positions as well as the numbering of the phthalocyanine ring.

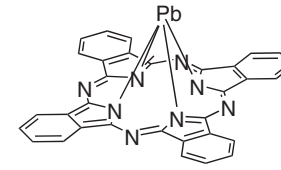

Figure 15.2 Structure of lead phthalocyanine, showing the shuttlecock shape.

Applications of porphyrin-type complexes include their use as dyes and pigments [3–5], photoconducting materials in laser printers and photocopiers [3], in nonlinear optics [6], in photodynamic therapy (PDT) [7], and as electrochemical and chemical sensors [8, 9]. Specificity in the applications can be introduced by modification of the phthalocyanine/porphyrin rings or by changes in the central metal or axial ligands.

15.1.2 Spectra

In Gouterman's four-orbital model, the first two allowed π-π* bands for porphyrin-type complexes arise from transitions from a_{1u} and a_{2u} to e_g. For phthalocyanines, a_{1u} lies well above a_{2u}, whereas for many porphyrins a_{1u} and a_{2u} are close together (Figure 15.3a), resulting in considerable configuration interaction. Thus, phthalocyanines exhibit a red-shifted and intense Q band compared to the weak Q bands for porphyrins in general (Figure 15.3b).

The spectra of MPc complexes consist of an intense absorption band in the visible region traditionally near 670 nm (for most Pcs) called the Q band and a generally weaker band near 340 nm called the Soret or B band (Figure 15.3b). Both are $\pi \rightarrow \pi^*$ transitions. Transition from the HOMO (the highest occupied molecular orbital) with a_{1u} symmetry to the LUMO (the lowest unoccupied molecular orbital) with e_g symmetry results in the Q-band absorption, while transitions from a_{2u} and b_{2u} to e_g give the B-band absorptions (see Figure 15.3a for energy levels). The B band consists of two transitions, B1 and B2. At higher energies, additional $\pi \rightarrow \pi^*$ transitions (N, L, and C, in order of increasing energy) may be observed [10] in UV-transparent solvents.

Porphyrins are characterized by an intense band called the Soret or B band at about 400 nm. The Q bands are observed between 500 and 700 nm. Metal-free porphyrins contain four Q bands that collapse into two on metalation (Figure 15.3c). The two Q bands of metalated porphyrins are called α (high-energy band) and β (low-energy band) [11]. The relative intensities of these bands have been associated with the stability of the metal complex. When $\alpha > \beta$, the metal forms a stable square-planar porphyrin complex [11].

The propensity of phthalocyanines/porphyrins to form aggregates due to the strong interactions between these planar macrocyclic rings in solution is well known [1, 12]. Both porphyrins and phthalocyanines exhibit J- and H-aggregates. H-aggregates result from cofacial arrangement (face to face) of the rings, resulting in blue shifting of the spectra relative to the monomer band. H-aggregation is common in most Pcs (Figure 15.4), whereas an edge-to-edge arrangement (J-aggregation) is rare in Pc aggregates and occurs more frequently in porphyrins, yielding a red-shifted absorption. For phthalocyanines, the H-aggregate arrangement is primarily due to the hydrophobic nature of the benzene rings, which readily allows macrocycles to stack on top of each other, thus leading to a stabilized overlap of their π electron cloud. Aggregation strongly affects the electrochemistry of phthalocyanines, as will be discussed later.

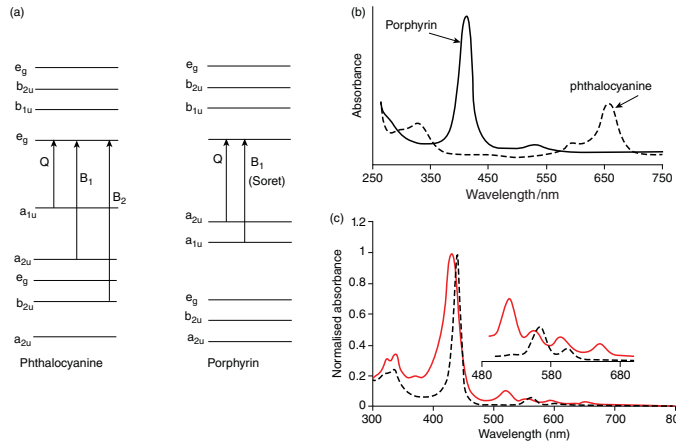

Figure 15.3 (a) Electronic energy levels for metalated phthalocyanines and porphyrins; (b) overlay of typical metallophthalocyanine and metalloporphyrin electronic absorption spectra, and (c) electronic absorption spectra with expanded Q band region (insert) of a metalated (black line) and metal-free (blue line) porphyrin (solvent = DMF, dimethylformamide). Unpublished work.

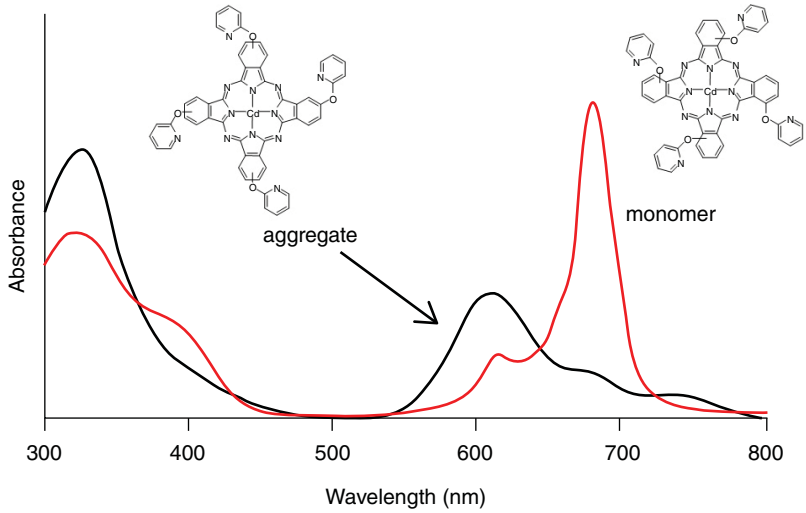

Figure 15.4 UV–Vis spectra of aggregated and nonaggregated phthalocyanines showing the effects of the position of substituents. Unpublished work.

15.1.3 General Electrochemistry

Porphyrin-type complexes are electroactive. The electrochemistry of these compounds is similar. They can undergo multiple one-electron redox processes. The exact number of the redox processes depends on the potential range of the solvent/electrolyte system, the type of macrocycle, and the nature of the central metal ion. The potentials at which these redox processes occur as well as the site of electron transfer itself (whether it at the metal or ring) depends on the nature of the porphyrin-type complex, the nature and oxidation state of the central metal, the axial ligand, and the solvent and electrolyte.

In general, porphyrin-type complexes containing electro-inactive central metals such as Zn only undergo redox reactions involving the π-ring system, but both metal- and ring-centered redox processes are observed in the case of electroactive metals such as Fe, Co, or Mn.

Porphyrin-type complexes have also been extensively studied as electrocatalysts for many reactions. They transform non-selective, unmodified surfaces into sensitive and selective sensors. The choice of these complexes as suitable electrocatalysts is based on their ability to change their oxidation states but retain their stability during electrocatalysis. Modification of the ring by attaching different substituents and varying the nature of the central metal ion will affect their electrocatalytic behavior. Complexes containing electroactive central metals are usually the most electroactive, the potential at which catalytic currents are observed being closely related to the redox potentials of the central metals in these complexes.

This chapter will focus on electrochemistry of phthalocyanines as an example of porphyrin-type complexes, since the electrochemical behavior of these complexes is similar.

15.2 Introduction to Electrochemistry of Phthalocyanines

15.2.1 Origin of Electrochemical Behavior

The deprotonated Pc exists as a dianion, that is, Pc^{2-}, which may be oxidized or reduced in successive steps. The Pc ring redox activity is directly related to the frontier orbitals in the

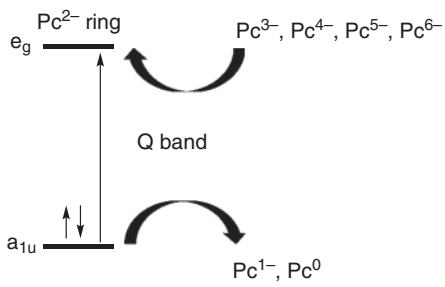

Figure 15.5 Reduction and oxidation of the phthalocyanine ring.

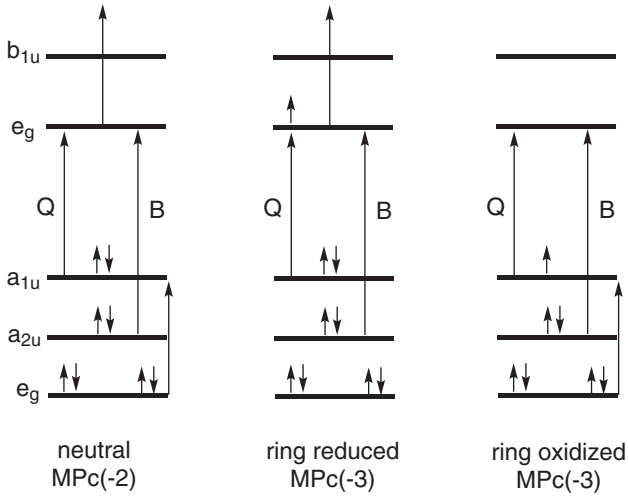

Figure 15.6 Energy level diagrams of neutral, one-electron ring-reduced, and one-electron ring-oxidized MPc complex.

molecule where oxidation is the removal of electron(s) from the highest occupied molecular orbital (HOMO, a_{1u}), while reduction is the addition of electron(s) to the LUMO (e_g). Up to four electrons can be successively added to the doubly degenerate e_g orbitals of the LUMO to form Pc^{3-}, Pc^{4-}, Pc^{5-}, and Pc^{6-} reduced complexes, and two electrons can be removed from the HOMO to form Pc^{1-} and Pc^{0} oxidized complexes (Figure 15.5). The redox activity of MPc complexes containing central metals that are not electroactive occurs only at the ring. For main group phthalocyanine complexes, the first ring oxidation is separated from the first ring reduction by energy that is approximately equal to the HOMO–LUMO gap. Hence, the study of the electrochemistry of main group Pc molecules may be linked to their spectra. Redox processes for MPc complexes occurring at the central metal or ring often result in color changes, with ring redox processes showing more drastic color changes. New electronic absorption peaks are formed on oxidation or reduction of the Pc ring due to the transitions shown in Figure 15.6.

The nature of the central metal, axial ligands, and solvents and the substituents on the ring periphery determine the redox properties of a given complex. Electron-donating substituents such as alkyl-thio groups increase the electron density on the ring, thereby making it easier to oxidize and harder to reduce MPc complexes. In particular, electrochemistry of alkyl- or aryl-thio substituted MPc complexes is often different from that of other substituted MPc complexes. Irreversible ring reductions for the thio-Pcs have been reported [13–15],

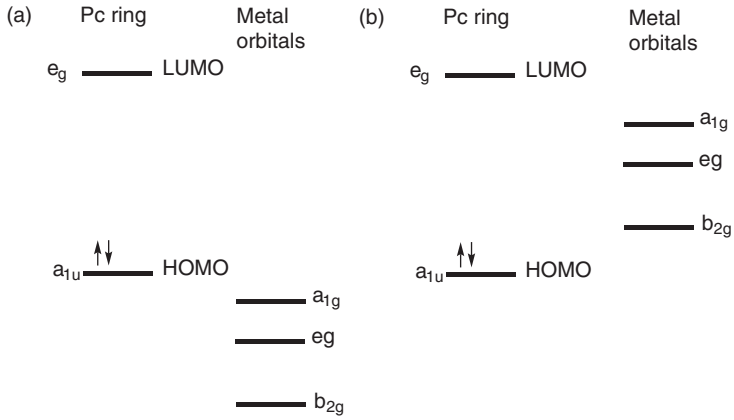

Figure 15.7 (a) Metal orbitals lying below the HOMO of the Pc and (b) metal orbitals lying between the HOMO and the LUMO of the Pc.

often coupled with chemical reactions and adsorption of the reduction products. Overlap of reduction couples to form one peak, and single step (irreversible) multi-electron oxidation accompanied by decomposition have also been reported [15].

Oxidation or reduction of MPcs with redox-active metals (i.e., with vacant or partially occupied orbitals) may occur both at the metal and at the ring, depending on the relative energies and proximity of metal d and Pc ring π orbitals. When metal orbitals lie between the HOMO and the LUMO (Figure 15.7b), the electrochemical behavior is greatly affected. The presence of the electroactive central metal (such as Cr, Co, Fe, Mn) results in additional redox processes occurring at the central metal, with unique electronic spectral behavior. When metal orbitals lie below the HOMO (Figure 15.7a), only ring-based processes occur.

15.2.2 Voltammetry Techniques Often Used for Studies of Phthalocyanines

Cyclic voltammetry (CV) is a versatile and effective electroanalytical technique commonly used to study the electrochemistry of phthalocyanines. The technique provides a rapid and simple way of acquiring information about the rate of electron transfer, stability of analyte, and adsorption processes as well as electrode kinetics and mechanisms. In an electrochemical study, CV is generally the first experiment to be performed. It is often accompanied by differential pulse voltammetry (DPV) or square wave voltammetry (SWV). The latter two techniques are more sensitive than CV. Figure 15.8 shows a typical example of a cyclic voltammogram of a phthalocyanine (MnPc derivative) accompanied by SWV.

When phthalocyanines are aggregated, the redox processes are overlapped as shown in Figure 15.9a [15] (peaks labeled **I′** and **I**). Evidence of aggregation can be provided by dilution of the solution used for CV, the peak due to the aggregate (process **I′**) will disappear, with only one process remaining (process **I**), in Figure 15.9a.

Cyclic voltammograms sometimes show peculiar behavior as observed for a non-peripherally substituted $OTiPc(SC_5H_{11})_8$ derivative with a broad pre-peak followed by a sharp peak typical of adsorption [16] (Figure 15.9b(i)). The cyclic voltammograms obtained for the second and subsequent scans showed additional sharp peaks that were attributed to polymer formation following cycling of the monomer in solution (Figure 15.9b(ii)).

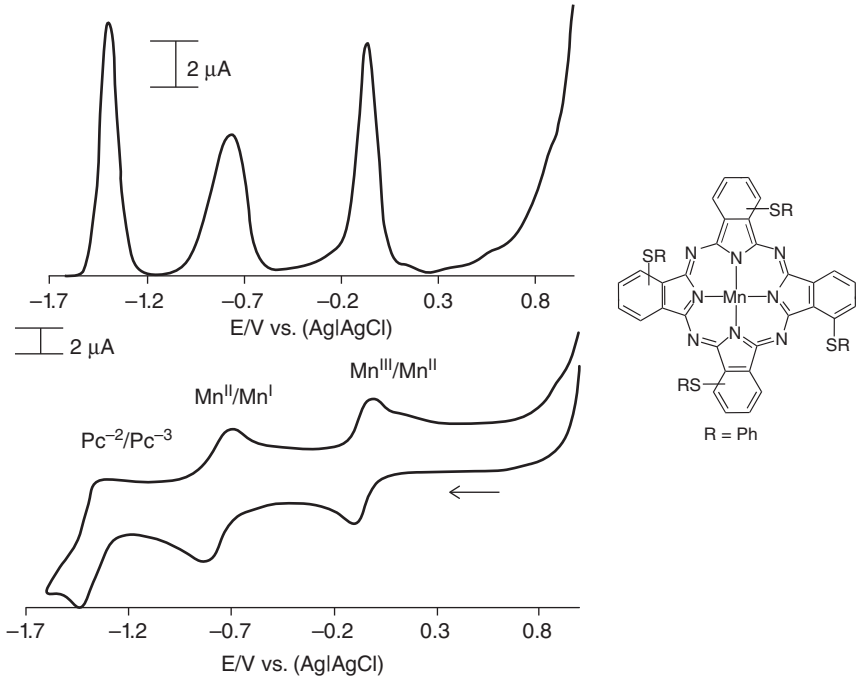

Figure 15.8 Typical cyclic voltammogram (bottom) and SWV (top) of hydroxy manganese tetraphenylthio phthalocyanine, in DMF containing 0.1 M $TBABF_4$; scan rate = 100 mV s^{-1}. Source: Reproduced with permission from Mbambisa et al. [13]. Ph = Phenyl.

The common working electrodes employed for CV of phthalocyanines include metals such Pt, Au, and carbon electrodes. Carbon exists in a variety of physical and chemical forms, for example, graphite single crystal (GSC), pyrolytic graphite (PG), highly oriented pyrolytic graphite (HOPG), glassy (vitreous) carbon (GCE), and so on, and many of these forms of carbon have been used in developing electrodes for characterization or electrode modification using phthalocyanines. Different types of solvents and electrolytes may be used for phthalocyanine electrochemistry depending on the solubility. Table 15.1a lists the estimated potential ranges for some solvents often used for phthalocyanine electrochemistry [17]. It is clear from this table that acetonitrile shows favorable limits both in the cathodic and anodic limits. Table 15.1b shows that the use of tetrabutylammonium ion $[(n\text{-}C_4H_9)_4N]^+$ in combination with ClO_4^- would favor a wide potential range [17]. Other anions with favorable potentials are BF_4^- and PF_6^- [17].

15.2.3 Spectroelectrochemistry

Electroanalytical methods such as voltammetry, amperometry, and coulometry are not able to directly identify intermediates and products formed during a redox reaction. The assignments of the spectra following oxidation or reduction of Pcs are based on spectroelectrochemistry, which is the combination of UV–vis spectroscopic measurements with electrochemistry. In MPc complexes, metal-based redox processes during spectroelectrochemistry are characterized by the shifting of the Q band either to the red or blue region of the spectrum [18], without much change in intensity. Ring- or ligand-based processes

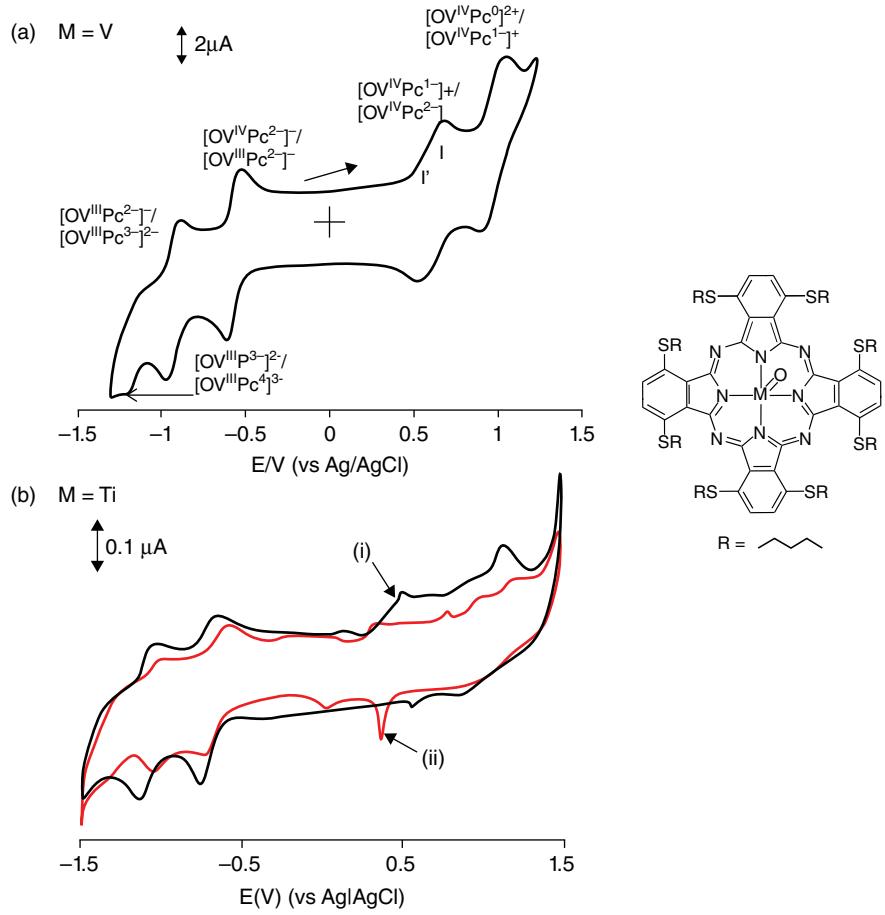

Figure 15.9 Cyclic voltammograms of 1,4,8,11,15,18,22,25-octapentylthio phthalocyanine ($Pc^{\alpha}(SC_5H_{11})_8$) containing (a) M = V(IV) (Source: Reproduced with permission from Mbambisa and Nyokong [14]) and (b) M = Ti(IV) (Source: Reproduced with permission from Mbambisa et al. [15]); (i) first scan and (ii) 20th scan, in dichloromethane (DCM) containing $TBABF_4$; scan rate = 100 mV s^{-1}.

are characterized by the disappearance of the Q band and formation of weak bands in the 500–600 nm region for the MPcs [18].

The field of spectroelectrochemistry dates back to 1964, when the first work was reported by Kuwana et al. [19]. Comparative analysis of the spectral properties of the starting complex and that of the electro-generated species provides valuable information on the nature of redox processes. A diverse number of species can be formed following oxidation or reduction of the phthalocyanine ring. Each oxidation or reduction product has a distinct spectrum that may be used for its characterization.

Many spectroelectrochemical techniques rely on the existence of electrodes that are transparent to light in a particular spectral range. An ideal optically transparent electrode (OTE) combines the characteristics of high optical transparency with low electrical resistivity. Tin oxide (or Zn oxide) films on glass or quartz, for example, show good optical transparency and high electrical conductivity [20–22].

Table 15.1 Electrode potential limits for common electrolytes and solvents used for MPcs on Pt working electrodes (V vs. saturated calomel electrode). (a) Cathodic/anodic limits in tetrabutylammonium perchlorate in different solvents and (b) potential limits of common electrolytes in acetonitrile.

(a)			(b)	
Solvent	**Cathodic limit (V)**	**Anodic limit (V)**	**Ion**	**Potential limit (V)**
Acetonitrile	−2.3	+2.1	Cl^-	+1.1
DMF	−2.6	+1.3	ClO_4^-	+2.1
DCM	−1.7	+1.4	K^+	−2.0
DMSO	−2.7	+1.2	NH_4^+	−1.8
Pyridine	−2.1	+1.2	$(n\text{-}C_4H_9)_4N^+$	−2.3

Source: Data from Chang et al. [17].

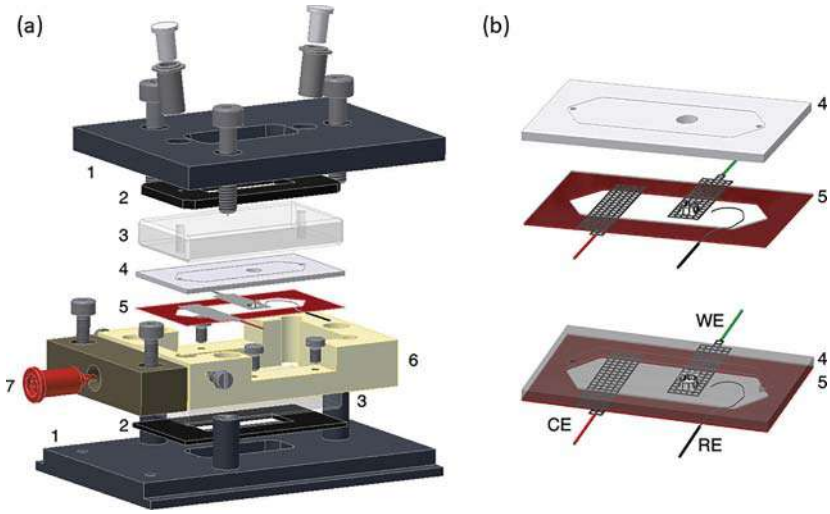

Figure 15.10 (a) Expanded OTTLE cell: 1, metal cover plates (with filling ports); 2, rubber gasket; 3, CaF_2 window; 4, custom polytetrafluoroethylene (PTFE) spacer (1 mm thick) with a circular aperture (4 mm diameter); 5, custom polyethylene-electrode spacer (enhanced view in (b)); 6, protective frame; 7, electrode plug. Source: Reproduced with permission from Domingos et al. [31].

Several different OTEs have been reported for spectroelectrochemistry of phthalocyanines, with the most common type being indium tin oxide (ITO) coated glass [23–30]. Optically transparent thin layer electrode (OTTLE) cells are often employed and may contain Pt minigrid working and counter electrodes, and a Ag wire reference electrode. OTTLE cells of the type shown in Figure 15.10 are commonly employed [31]. The attractive features of OTTLE cells include the high sensitivity that can be achieved with very small volumes, and the ability to achieve bulk electrolysis in a few seconds [32, 33].

In order to elucidate the mechanism occurring during spectroelectrochemistry, the number of electrons transferred at each oxidation or reduction step needs to be calculated by using

Faraday's equation (Eq. 15.1) [32]:

$$Q = nFVC \tag{15.1}$$

where V is the volume, n is the number of electrons transferred, F is Faraday's constant, C = concentration, and Q is the charge.

The next subsections will discuss the CV and spectroelectrochemistry of a selection of metallophthalocyanines. The most studied electrochemically are Mn, Fe, and Co phthalocyanines. These will be discussed individually. Other MPc complexes that have been studied are those containing V, Ti, Mo, Zr, Ru, and Pd, but their studies are limited, and hence these will be discussed in groups. Initially, main group phthalocyanines and other redox-inactive metal containing phthalocyanines are discussed. Ball-type and bis-phthalocyanines will be discussed separately.

15.2.3.1 Redox-Inactive (Main Group) Metallophthalocyanines

Ring-based redox processes often result in color changes, while metal-based redox processes exhibit less dramatic color changes [18]. Monitoring spectral changes of MPc during spectroelectrochemistry gives information on the nature of the redox process. For example, a shift in the Q band is due to oxidation/reduction of the central metal [1], whereas a decrease in the Q band intensity, accompanied by an increase in intensity in the 500–600 nm region, is due to oxidation/reduction of the ring [18]. New peaks are formed on oxidation or reduction of the Pc ring due to the transitions shown in Figure 15.6. Only ring-based processes are observed in the main group metal phthalocyanines.

Figure 15.11 shows typical spectroelectrochemical changes observed during the first ring reduction and oxidation of dialkylaminophenoxy-substituted zinc phthalocyanine [34]. Typical of phthalocyanines containing electro-inactive central metal (Zn in this case, but main group metals in general), there is a collapse of the Q band. As stated earlier, the electronic spectra observed in MPc complexes are due to transitions originating in the π orbitals of the ring. Any removal (or addition) of electrons from (or to) the ring will result in drastic changes in the electronic absorption spectra. Reduction or oxidation of the ring results in a considerable reduction in the intensity of the Q band, as observed in Figure 15.11a,b. The peaks in the 450 nm region and those to the red (longer wavelength) of the Q band are assigned to the Pc^{1-} radical (Figure 15.11b) [18]. The electronic absorption spectra can thus be used to differentiate between ring- and metal-based redox processes and to characterize the products of ring oxidation or reduction. Collapse of all bands in Figure 15.11c indicates decomposition during further oxidation. Solutions containing ring-oxidized phthalocyanines show a distinct purple color. Ring-reduced Pcs show a purplish blue color.

PbPc derivatives may show reversible redox processes during the voltammetric measurements (Figure 15.12a), but get demetalated (to the metal-free phthalocyanine) during spectroelectrochemical measurements [35–38], because of the large metal out-of-plane displacement resulting in the shuttlecock geometry (shown in Figure 15.12). During the first reduction (Figure 15.12b(ii)) the Q band is split due to demetalation. The final spectrum in Figure 15.12b(ii) is a characteristic spectrum of the metal-free phthalocyanine, thus confirming the demetalation of the PbPc complex. The spectral changes observed on further reduction (Figure 15.12b[iii and iv]) are similar to those observed for metal-free Pc [35].

Oxidation and reduction occur exclusively at the phthalocyanine ring in $(OH)_2Zr^{IV}Pc$, $Ru^{II}Pc$, and $Pd^{II}Pc$ complexes, suggesting that the metal orbitals in these complexes are buried inside the filled phthalocyanine levels [39].

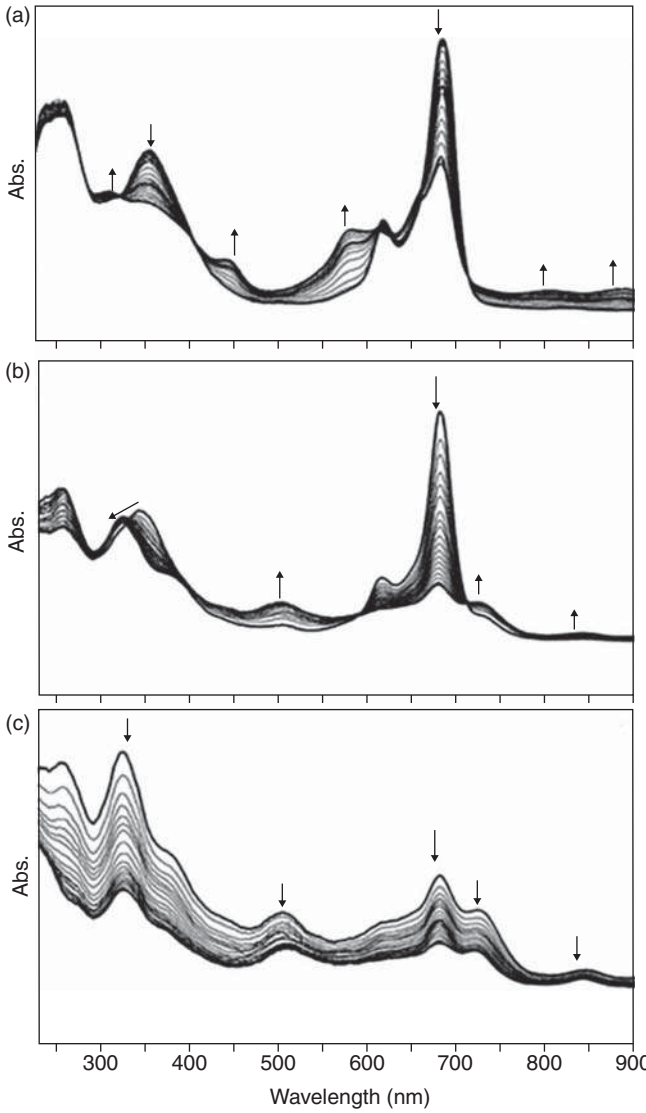

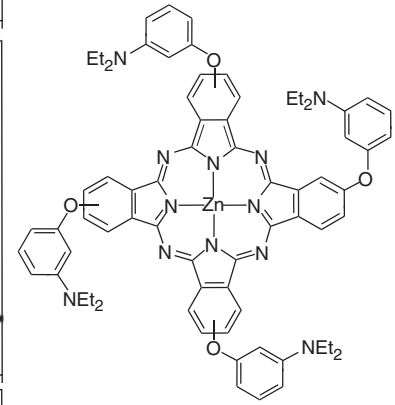

Figure 15.11 In situ UV–Vis spectroscopic changes in dialkylaminophenoxy-substituted zinc phthalocyanine (Et = ethyl). (a) $E_{app} = -0.90$ V (first reduction); (b) $E_{app} = 0.70$ V (first oxidation); and (c) $E_{app} = 1.00$ V, second oxidation in DCM/TBAP. Source: Reproduced with permission from Atsay et al. [34].

15.2.3.2 Cobalt Phthalocyanines

Cobalt exhibits three oxidation states: Co^{I}, Co^{II}, and Co^{III}. Co^{I} does not bind any axial ligands and hence exists as a square-planar complex. Co^{II} does bind axial ligands but with low affinity. Co^{III} has high affinity for axial ligands and is usually stabilized by two axial ligands; hence, it exists predominantly in an octahedral environment [40]. Axial ligation has a direct effect on the solution electrochemistry of $(X)Co^{III}Pc$ complexes (X = negatively charged axial ligand). $[Co^{I}Pc^{2-}]^{-}$ and $Co^{II}Pc^{2-}$ species can be observed in both coordinating and non-coordinating solvents. $[Co^{III}Pc^{2-}]^{+}$ species are normally observed in coordinating solvents such as DMSO

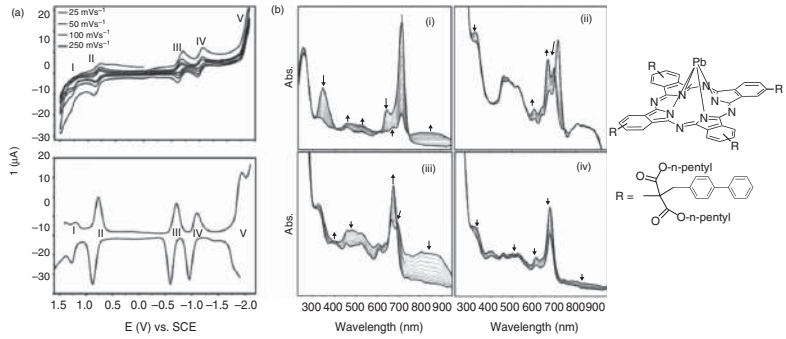

Figure 15.12 (a) Cyclic voltammograms at various scan rates and corresponding DPV of a PbPc derivative shown on a Pt working electrode in DCM/TBAP with DPV parameters: pulse width, 50 ms; pulse height, 100 mV; step height, 5 mV; step time, 100 ms; scan rate, 50 mV s^{-1}; and (b) in situ UV–vis spectral changes of the PbPc derivative during the reduction processes (i) at the beginning of the first reduction process during the potential application at $E_{app} = -0.70$ V; (ii) the second part of the spectral changes during the potential application at $E_{app} = -0.70$ V; (iii) the final part of the spectral changes during the potential application at $E_{app} = -0.70$ V; (iv) spectral changes during the potential application at $E_{app} = -1.10$ V (the second reduction process). Source: Reproduced with permission from Dinçer et al. [35].

and pyridine. These solvents coordinate axially to Co^{III}, offering stability to this oxidation state and hence the possibility of observing $[Co^{III}Pc^{2-}]^+$ species in solution. Apart from coordinating solvents, the Co^{III} ion can also be stabilized through axial ligation of anionic species in the supporting electrolyte. This suggests that the type of electrolyte in solution may have a significant impact on the electrochemical properties of CoPc complexes. The formation of $[Co^{III}Pc^{2-}]^+$ species is usually followed by the first ring oxidation (formation of $[Co^{III}Pc^{-}]^{2+}$ species), while the first ring reduction (formation of $[Co^{I}Pc^{3-}]^{2-}$ species) is preceded by the formation of $[Co^{I}Pc^{2-}]^{-}$ species [40]. Apart from shifts in cyclic voltammogram peak potentials, the spectra of CoPc derivatives do not change much with the nature of substituents.

Figure 15.13b shows the spectral changes observed during spectroelectrochemical studies of phenylthio-substituted cobalt(II) phthalocyanine [41]. The corresponding CV/SWV are shown in Figure 15.13a. During the first reduction, the Q band shifts from 673 to 711 nm while a new band appears at 478 nm (Figure 15.13b(i)). The band at 478 nm is typical of central metal reduction of $Co^{II}Pc^{2-}$ to $[Co^{I}Pc^{2-}]^{-}$. The Q band does not collapse as was observed for ring-based redox process in Figure 15.11. A shift in the Q band to longer wavelengths, typical of metal oxidation, can be seen in Figure 15.13b(ii), consistent with the oxidation of $Co^{II}Pc^{2-}$ to $[Co^{III}Pc^{2-}]^+$ [1]. Figure 15.13b(iii) shows the collapse of the Q band and a small increase in absorbance near 450 nm, due to a combination of ring-based processes and degradation.

15.2.3.3 Manganese Phthalocyanines

The electrochemical properties of manganese phthalocyanine (MnPc) complexes have also generated considerable interest [13, 15, 42–56]. The variable oxidation states of Mn (Mn^{I}, Mn^{II}, Mn^{III}, and Mn^{IV}) make MnPc complexes attractive for electrocatalytic purposes. The shape and reversible behavior of cyclic voltammograms for MnPc derivatives are highly dependent on the substituents. For manganese tetra(2-mercapto)pyrimidyl phthalocyanine, irreversible peaks (**V**, **VI** in Figure 15.14) were obtained together with reversible processes **I** to **IV** [47]. The structure of the complex is shown as an insert in Figure 15.15.

In MnPc complexes, the electronic absorption spectrum may consist of three absorption bands corresponding to three different species in solution (Figure 15.15), hence complicating the electrochemistry. This is typical of MnPc species in equilibrium in the presence of oxygen [50]. In the presence of O_2, $Mn^{II}Pc$ is known to form an oxygen adduct (Eq. 15.2), which has been described as a $(O_2^{-})Mn^{III}Pc$ species [47, 51], with subsequent formation of the species shown by Eqs. (15.3)–(15.5), and the net result shown by Eq. (15.6).

$$PcMn^{II} + O_2 \rightleftharpoons PcMn^{III}(O_2) \tag{15.2}$$

$$PcMn^{III}(O_2) + PcMn^{II} \rightleftharpoons PcMn^{III} - O_2 - Mn^{III}Pc \tag{15.3}$$

$$PcMn^{III} - O_2 - Mn^{III}Pc \rightleftharpoons 2PcMn^{IV}O \tag{15.4}$$

$$2\,PcMn^{IV}O + 2\,PcMn^{II} \rightleftharpoons 2PcMn^{III} - O - Mn^{III}Pc \tag{15.5}$$

$$\text{net: } 4\,PcMn^{II} + O_2 \longrightarrow 2\,PcMn^{III} - O - Mn^{III}Pc \tag{15.6}$$

In Figure 15.15, the absorption band at 719 nm is due to $[Mn^{III}Pc]^+$ [47], the peak at 626 nm was assigned to μ-oxo MnPc species and the peak at 686 nm to $Mn^{II}Pc$ [47]. When the solution was deaerated with dry N_2, the peak due to $[Mn^{III}Pc]^+$ at 719 nm decreased in intensity accompanied by an increase in the intensity of the peaks characteristic of $Mn^{II}Pc$ species at 686 nm, while the μ-oxo MnPc species 626 nm decreased in intensity.

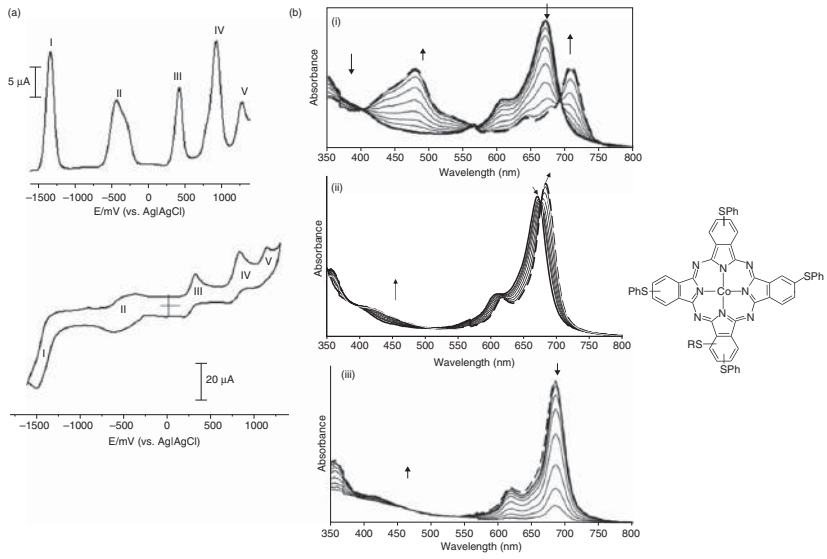

Figure 15.13 (a) Square wave (top) and cyclic (bottom) voltammograms of cobalt tetraphenylthio phthalocyanine in DMF containing 0.1 M $TBABF_4$, scan rate = 100 mV s^{-1}; (b) UV–vis spectral changes of the complex in DMF containing 0.1 M $TBABF_4$ observed during application of controlled potentials (i) **II** (−0.6 V), (ii) **III** (+0.4 V), and (iii) **IV** (+0.8 V); the first scan in (iii) is the same as the last scan in (ii). Ph = phenyl. Source: Reproduced with permission from Nombona and Nyokong [41].

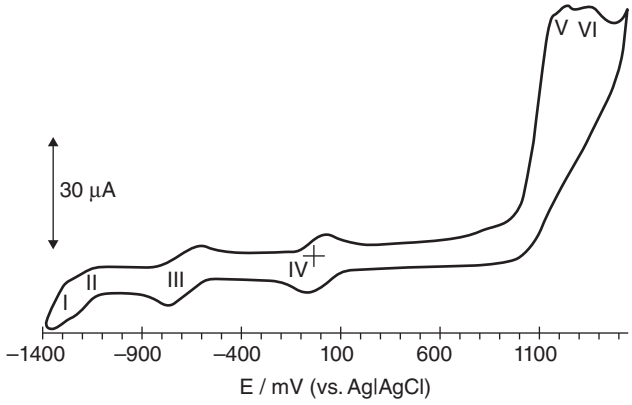

Figure 15.14 Cyclic voltammograms of ~1.5 mM manganese tetra(2-mercapto)pyrimidyl phthalocyanine (structure shown in Figure 15.15) in DMF containing 0.1 M $TBABF_4$. Scan rate: 100 mV s^{-1}. Source: Reproduced with permission from Obirai and Nyokong [47].

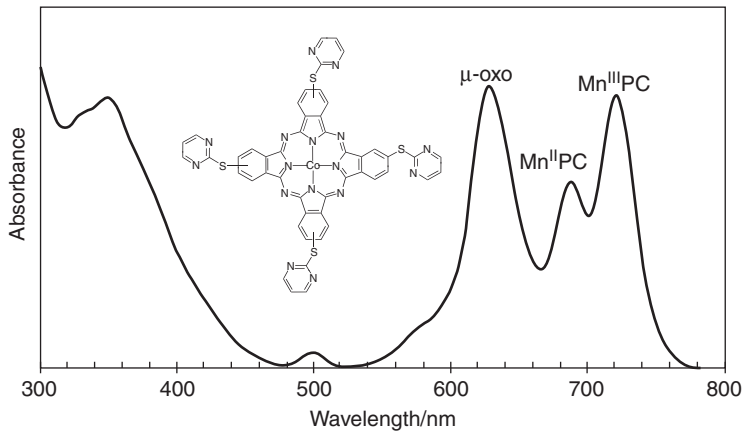

Figure 15.15 Electronic absorption spectra of manganese tetra(2-mercapto)pyrimidyl phthalocyanine in DMF. Concentrations: 5×10^{-6} mol dm^{-3}. Source: Reproduced with permission from Obirai and Nyokong [47].

Due to the ease of oxidation of $Mn^{II}Pc^{2-}$ to $[Mn^{III}Pc^{2-}]^+$, the latter is the stable species isolated during synthesis [53]. $[Mn^{III}Pc^{2-}]^+$ is easily reduced back to $Mn^{II}Pc^{2-}$ at moderate potentials ranging from −0.08 to −0.15 V or by using mild reducing agents, as shown in Figure 15.16 [53]. The confirmation of metal-based redox processes in Figure 15.16 is provided by the lack of decrease in the Q band with only a shift to higher energies. The spectral changes observed in Figure 15.16 result in the change of the color from brown of $[Mn^{III}Pc^{2-}]^+$ (Figure 15.16(i)) to green $Mn^{II}Pc^{2-}$ (Figure 15.16(ii)). Apart from a few reports [54], oxidation of $[Mn^{III}Pc^{2-}]^+$ to $[Mn^{IV}Pc^{2-}]^{2+}$ rarely occurs. Its rare occurrence was evidenced by a shift in the Q band rather that its collapse on oxidation of $[Mn^{III}Pc^{2-}]^+$ [54]. Conversion of $[Mn^{III}Pc^{2-}]^+$ to $[Mn^{III}Pc^{1-}]^{2+}$ is normally favored over $[Mn^{III}Pc^{2-}]^+$ to $[Mn^{IV}Pc^{2-}]^{2+}$. Reduction of $Mn^{II}Pc^{2-}$ species is still a subject of debate; ring reduction (formation of $[Mn^{II}Pc^{3-}]^-$) [54] and reduction of the central metal (formation of $[Mn^{I}Pc^{2-}]^-$) [18] have been reported. The reduction of $Mn^{II}Pc^{2-}$ to $[Mn^{I}Pc^{2-}]^-$ species results in a distinct broad absorption at

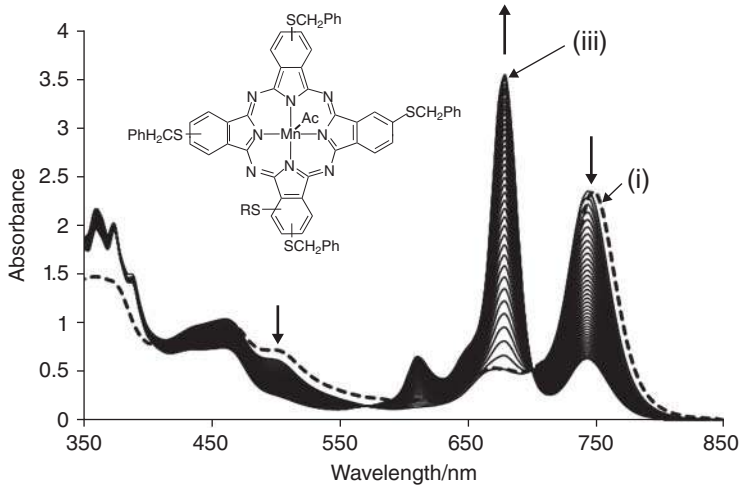

Figure 15.16 Reduction of (acetate)$Mn^{III}Pc$ (structure shown as an insert) in DMSO using nitrite (Ph = phenyl); (i) (acetate)$Mn^{III}Pc^{2-}$ and (ii) $Mn^{II}Pc^{2-}$. Reproduced with permission from Agboola and Nyokong [53].

575 nm (Figure 15.17b) [55]. The cyclic voltammogram in Figure 15.17a shows irreversible behavior for the oxidation process **I**, typical of MnPc complexes as discussed above.

15.2.3.4 Iron Phthalocyanines

Like the cobalt analogues, electrochemical properties of iron phthalocyanine (FePc) complexes have been extensively investigated [52, 53, 56, 57]. The $Fe^{II}Pc^{2-}$ species is predominantly an octahedral complex in coordinating solvents such as pyridine and DMSO [1]. The ease of oxidation of $Fe^{II}Pc^{2-}$ to $[Fe^{III}Pc^{2-}]^{+}$ is dependent on the anions in solution. This process is more energetically feasible (occurs at less positive potential) in the presence of Cl^{-} or OH^{-}, which offer more stability than ClO_4^{-} as coordinating anions [40]. Further oxidation occurs on the ring in FePc complexes, forming the $[Fe^{III}Pc^{1-}]^{2+}$ species. Two reduction processes are usually observed for $Fe^{II}Pc^{2-}$. Metal reduction (formation of penta-coordinate $[Fe^{I}Pc^{2-}]^{-}$ species) is normally followed by ring reduction (Pc^{2-} to Pc^{3-}) [56]. The spectroelectrochemical changes are thus similar to those of CoPc derivatives.

15.2.3.5 Titanium, Vanadium, and Molybdenum Phthalocyanines

Oxotitanium phthalocyanine (OTiPc) complexes exhibit variable oxidation states. Oxidation of OTi(IV)Pc is expected to occur only at the ring, whereas reduction is expected to occur at both the central metal and the ring. Spectroelectrochemistry was employed to confirm the redox processes for the OTiPc derivative shown in Figure 15.9b [15]. The mechanism in Eqs. (15.7)–(15.9) is proposed for the reduction and oxidation of $OTiPc(SC_5H_{11})_8$. Eq. (15.9) is proposed based on the fact that electrochemical oxidation of the complexes resulted in degradation, as judged by collapse of all bands with no new peaks forming.

$$OTi^{IV}Pc + e^{-} \rightarrow \left[OTi^{III}Pc\right]^{1-} \tag{15.7}$$

$$\left[OTi^{III}Pc\right]^{-} + e^{-} \rightarrow \left[OTi^{II}Pc\right]^{2-} \tag{15.8}$$

$$OTi^{IV}Pc \rightarrow \text{oxidation products} + e^{-} \tag{15.9}$$

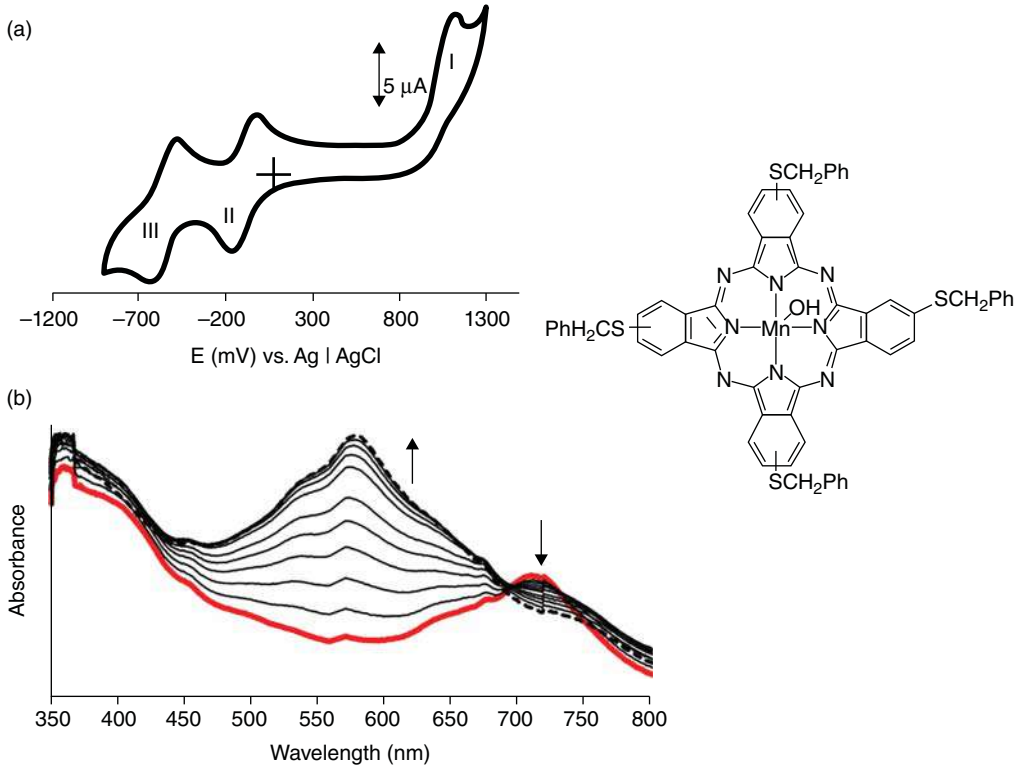

Figure 15.17 (a) Cyclic voltammogram and (b) UV–vis spectral changes for hydroxyl manganese Pc (structure as in inset) observed using controlled potential electrolysis at the potential of process **III** (−700 mV) in DMF containing 0.1 M $TBABF_4$; electrolysis time was 30 min for each redox process. Source: Reproduced with permission from Sehlotho et al. [55].

Vanadium phthalocyanine complexes exhibit variable oxidation states, II to V, which makes them useful as potential electrocatalysts. The OVPc derivatives show ring-based processes as well as metal reduction [14] as shown by Eqs. (15.10)–(15.14). The cyclic voltammogram of the OVPc is shown in Figure 15.9a.

$$OV^{IV}Pc^{2-} \rightarrow \left[OV^{IV}Pc^{1-}\right]^{+} + e^{-} \tag{15.10}$$

$$\left[OV^{IV}Pc^{1-}\right]^{+} \rightarrow \left[OV^{IV}Pc^{0}\right]^{2+} + e^{-} \tag{15.11}$$

$$OV^{IV}Pc^{2-} + e^{-} \rightarrow \left[OV^{III}Pc^{2-}\right]^{-} \tag{15.12}$$

$$\left[OV^{III}Pc^{2-}\right]^{1-} + e^{-} \rightarrow \left[OV^{III}Pc^{3-}\right]^{2-} \tag{15.13}$$

$$\left[OV^{III}Pc^{3-}\right]^{2-} + e^{-} \rightarrow \left[OV^{III}Pc^{4-}\right]^{3-} \tag{15.14}$$

$OMo^{V}(OH)Pc$ shows metal redox activity before any oxidation or reduction can be observed at the ring [39], as shown in Eqs. (15.15)–(15.18).

$$OMo^{V}(OH)Pc^{2-} + e^{-} \rightarrow \left[OMo^{IV}(OH)Pc^{2-}\right]^{-} \tag{15.15}$$

$$\left[OMo^{IV}(OH)Pc^{2-}\right]^{1-} + e^{-} \rightarrow \left[OMo^{IV}(OH)Pc^{3-}\right]^{2-} \tag{15.16}$$

$$OMo^{V}(OH)Pc^{2-} \rightarrow \left[OMo^{VI}(OH)Pc^{2-}\right]^{+} + e^{-} \tag{15.17}$$

$$\left[OMo^{VI}(OH)Pc^{2-}\right]^{1+} \rightarrow \left[OMo^{VI}(OH)Pc^{1-}\right]^{2+} + e^{-} \tag{15.18}$$

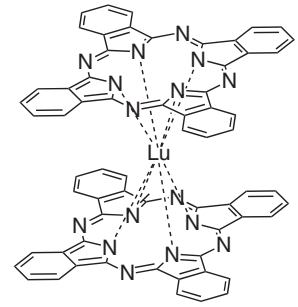

Figure 15.18 Molecular structure of a typical sandwich (bis)phthalocyanine.

15.2.3.6 Sandwich- and Ball-Type Phthalocyanines

Sandwich Pcs, as their name implies, contain a metal ion encapsulated between two Pc rings (Figure 15.18) [27]. As is the case with mono Pcs in general, the electrochemical properties of sandwich phthalocyanines determine their possible technological applications. In Eqs. (15.19)–(15.23), all redox processes are Pc ring based because the lutetium(III) metal center is redox inactive and the processes occur through one-electron reduction or oxidation of the Pc ring [58].

$$\left[Pc^{2-}Lu^{III}Pc^{1-}\right] \rightarrow \left[Pc^{1-}Lu^{III}Pc^{1-}\right]^{1+} + e^{-} \tag{15.19}$$

$$\left[Pc^{1-}Lu^{III}Pc^{1-}\right]^{1-} \rightarrow \left[Pc^{0}Lu^{III}Pc^{1-}\right]^{2+} + e^{-} \tag{15.20}$$

$$\left[Pc^{2-}Lu^{III}Pc^{1-}\right] + e^{-} \rightarrow \left[Pc^{2-}Lu^{III}Pc^{2-}\right]^{1-} \tag{15.21}$$

$$\left[Pc^{2-}Lu^{III}Pc^{2-}\right]^{1-} + e^{-} \rightarrow \left[Pc^{3-}Lu^{III}Pc^{2-}\right]^{2-} \tag{15.22}$$

$$\left[Pc^{3-}Lu^{III}Pc^{2-}\right]^{2-} + e^{-} \rightarrow \left[Pc^{3-}Lu^{III}Pc^{3-}\right]^{3-} \tag{15.23}$$

Ball-type Pcs have four bridged substituents on the periphery of each benzene ring of the two Pc units, resulting in a ball-like structure as shown in Figure 15.19a. The electronic properties of ball-type Pcs can change dramatically depending on the bridging compounds or the central metal [59]. Ball-type Pcs containing Co exhibit metal- and ring-based redox processes typical of cobalt phthalocyanine complexes (Figure 15.19b).

Two-electron processes were observed in ball-type 2′,10′,16′,24′-[tetrakis(4,4′-(1,1′-binaphthyl-8,8′-diyl(oxy))diphenyl)]bis-phthalocyaninato dicobalt(II) complex (Figure 15.19a), suggesting that there is no significant interaction between the two Pc rings and that the two rings are reduced and oxidized at the same potentials [59].

15.3 Phthalocyanines Confined to Electrode Surfaces

MPcs are well known as electrode modifiers for various applications, including as electrocatalysts. This section presents electrode modification using phthalocyanines. The characterization of the modified electrodes is also presented.

15.3.1 Methods of Electrode Modification

There are several methods for modifying electrodes using phthalocyanines, some of which will be discussed in the following sections.

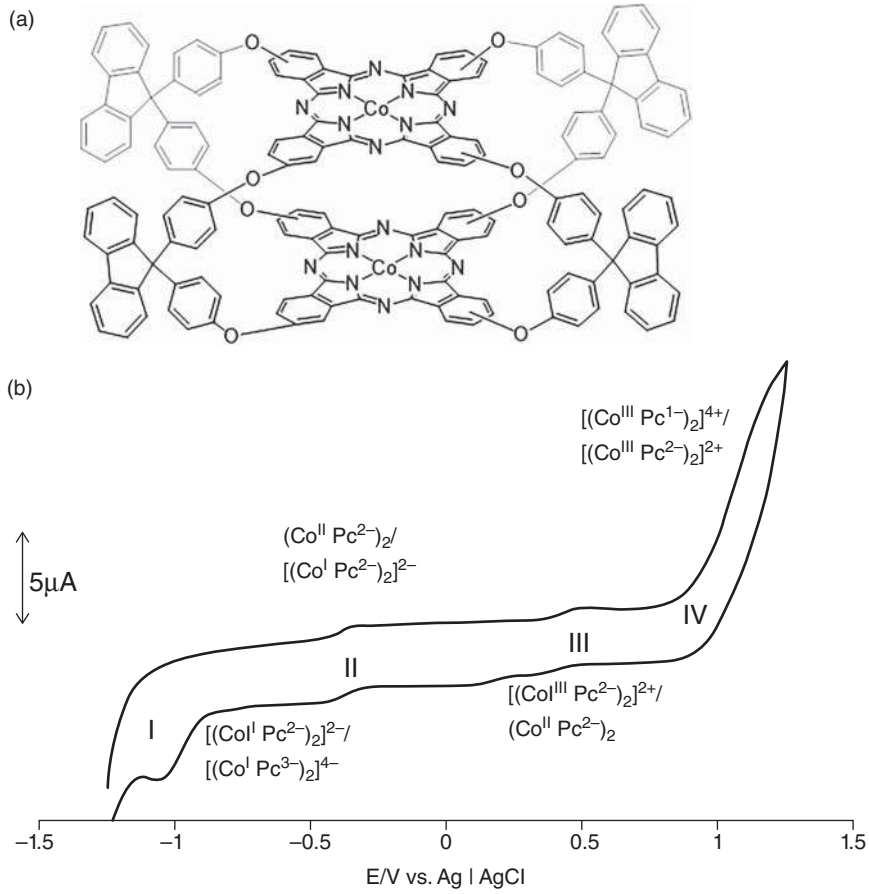

Figure 15.19 (a) Structure of a ball-type Pc (2′,10′,16′,24′-[tetrakis(4,4′-(1,1′-binaphthyl-8,8′-diyl(oxy))diphenyl)]bis-phthalocyaninato dicobalt(II)) and (b) cyclic voltammogram of the complex in DMSO containing 0.1 M $TBABF_4$. Source: Reproduced with permission from Canlica et al. [59].

15.3.1.1 Dip-Dry or Drop-Dry

As the name suggests, the species that is used to modify the electrode is dropped on the electrode surface (or dipped in the solution containing the Pc) and left to dry to form a film on the electrode surface [60–63]. It is a noncovalent method of electrode modification, where simple intermolecular forces such as electrostatic attraction and π-π interactions (between the Pc and carbon-based electrodes, for example) are used to hold a thin layer of modifying species on a surface (Figure 15.20). The modified electrode will show the cyclic voltammogram of the adsorbed Pc as shown in Figure 15.21. The problem with this method is that the film that is formed on the surface of the electrode is not stable. However, the method is commonly used because it is a fast way of modifying an electrode.

15.3.1.2 Electrodeposition

The MPc is adsorbed onto the electrode by CV without polymer formation [60]. The first scan is generally similar to the second and subsequent CV scans, in terms of potential values, but

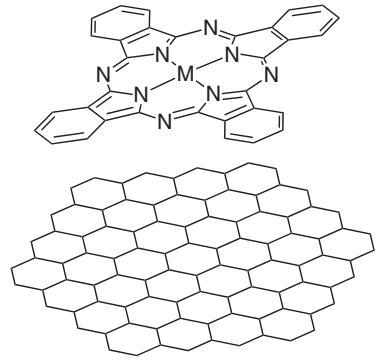

Figure 15.20 Schematic representation of π–π interactions between carbon electrodes and a phthalocyanine.

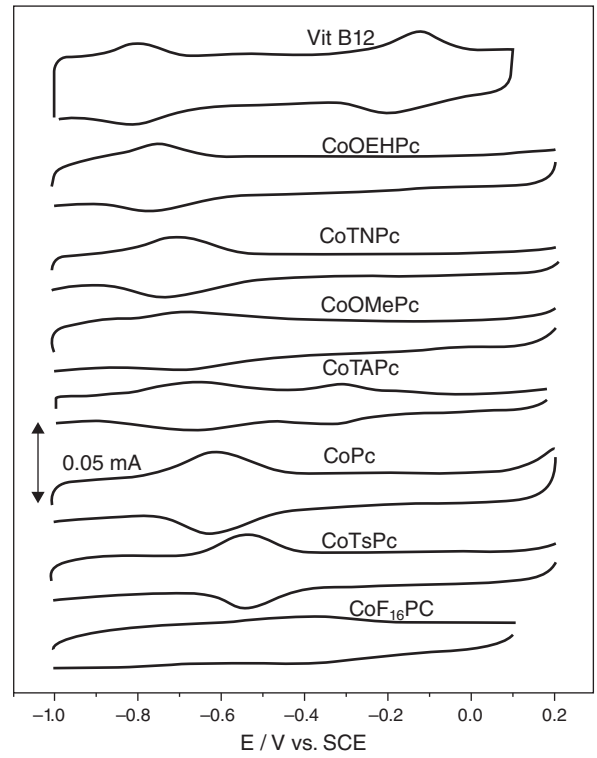

Figure 15.21 Cyclic voltammograms of an ordinary pyrolytic graphite (OPG) electrode modified with adsorbed cobalt phthalocyanine derivatives in deaerated 0.1 M NaOH aqueous solution, scan rate 0.1 Vs^{-1}. TAPc, tetraamino phthalocyanine; TsPc, tetrasulfonatophthalocyanine; OMePc, octamethoxyphthalocyanine; TNPc, tetranitro phthalocyanine; OEHPc, octaethylhexyloxyphthalocyanine; Vit B12, vitamin B12. Source: Reproduced with permission from Claußen et al. [61].

the current increases with scan number, as seen in Figure 15.22 [64]. The amount of catalyst on the surface may be controlled by the number of CV scans.

15.3.1.3 Electropolymerization

Polymerization is effected by scanning the electrode in the solution of the monomer within a well-defined potential range [60]. Electropolymerization is evidenced by the first voltammetric scan being different from the second and subsequent scans (Figure 15.23) [52]. The shifts and formation of new peaks confirm the formation of an electroactive polymer on the electrode surface. Most studies have concentrated on the electrochemical polymerization of $MPc(NH_2)_4$ complexes [65–68], with a few other examples as shown in Figure 15.23 [52].

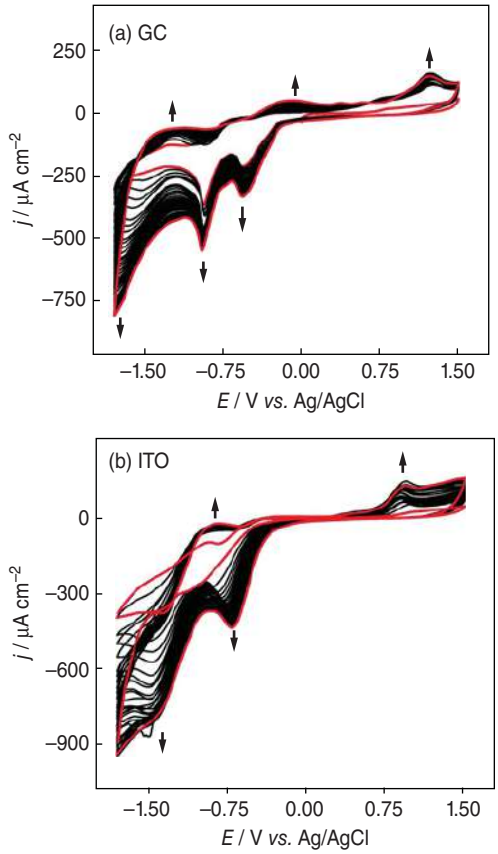

Figure 15.22 Cyclic voltammetric response for the electrodeposition of 1.0 mmol l^{-1} FePc in 0.1 mol l^{-1} TBAP/DCE (dichloroethane) on (a) GC and (b) ITO electrodes, applying 30 potential cycles between −1.8 and +1.5 V vs. Ag/AgCl at 50 mV s^{-1}. Source: Reproduced with permission from Martin et al. [64].

15.3.1.4 Carbon Paste Electrode

These are prepared by thoroughly mixing paraffin oil, the solid MPc, and graphite powder to form a paste [69], which is then packed into Teflon™ or glass tubes as shown in Figure 15.24 [70]. The advantage of a carbon paste is that a fresh electrode surface may be achieved by pushing the paste out of the electrode.

15.3.1.5 Self-Assembled Monolayer (SAM)

SAMs are highly ordered molecular assemblies that are formed by the adsorption of the compound onto the electrode surface [71–75]. SAMs form without any external factors that control the organization of the molecules on the surface of the electrode. SAMs may form as a result of the chemical bond that forms between the substrate (the electrode surface) and the compound. An example of this is the self-assembly of alkanethiols on gold in which a strong chemical bond is formed between the gold surface and the sulfur group of the alkanethiol. The method involves the immersing of a clean electrode in a millimolar or micromolar solution of a particular modifier (that has been purged with N_2 or argon).

Alkylthio ring-substituted MPcs may be self-assembled on gold electrodes (Figure 15.25a) [75]. Thiol-substituted Pcs are ideal for the formation of SAMs, but these Pcs are hard to synthesize due to the unwanted formation of S—S bonds. The formation of SAMs using MPcs axially substituted with thiol groups has been reported [74]. The use of preformed SAMs

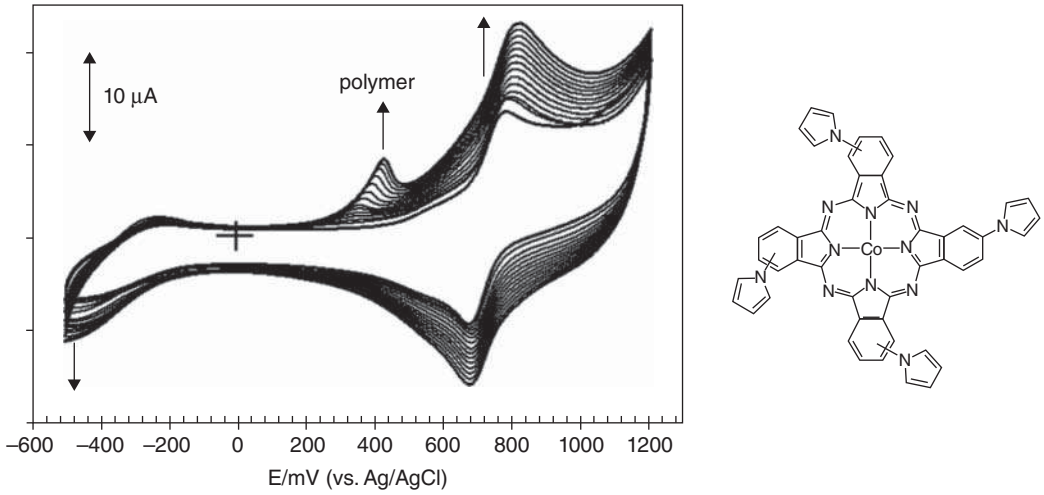

Figure 15.23 Evolution of the cyclic voltammograms of complex Co tetrakis-4-(pyrrol-1-yl)phenoxy phthalocyanine in DCM containing 0.1 mol dm^{-3} $TBABF_4$ during repeated successive scans (only 15 scans are shown); scan rate = 200 mV s^{-1}, concentration ~3×10^{-3} mol dm^{-3}, electrode = glassy carbon. Source: Reproduced with permission from Obirai et al. [52].

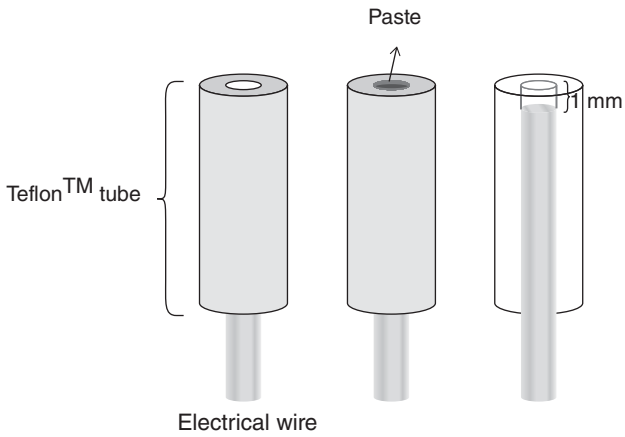

Figure 15.24 Representation of a carbon paste electrode. Source: Reproduced from Lowinsohn et al. [70].

using thiols followed by coordination of the Pc to the preformed SAM [56] has been reported (Figure 15.25b).

15.3.1.6 Grafting of Diazonium Salts

Grafting is the term used for the covalent linkage of diazonium salts to a conductive surface by electrochemical or chemical reduction [76–83]. Grafting proceeds by the reaction shown in Figure 15.26a (step A) on glassy carbon as an example [76–78]. MPcs containing appropriate functional groups (such as amino groups) can then be linked to grafted electrodes (containing aldehyde groups in this case), Figure 15.26b [79].

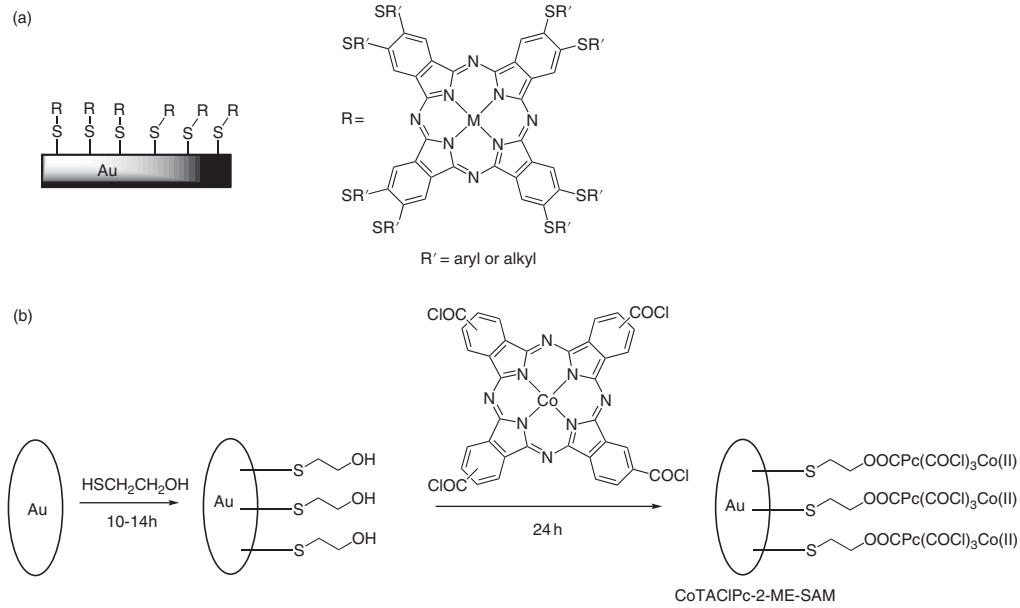

Figure 15.25 (a) Schematic representation of a SAM of a sulfur-containing Pc on Au; (b) attachment of a simple Pc to a preformed SAM; ME = mercaptoethanol, TAClPc = tetraacid chloride phthalocyanine. Source: Part (b) reproduced with permission from Mashazi et al. [56].

15.3.1.7 Click Chemistry

A good example of a click chemistry reaction is the Huisgen 1,3-dipolar cycloaddition of azides and alkynes to give triazole linkages [84, 85]. The general scheme for click chemistry is shown in Figure 15.26a (step B). Phthalocyanines may then be attached to the clicked electrode axially as shown in Figure 15.26a (step C). In the particular case in Figure 15.26a, a simple unsubstituted MPc was linked to the electrode by taking advantage of the linkage of Fe central metal to pyridine. The synthesis of phthalocyanines containing alkyl or azide groups is quite challenging. However, the attachment of phthalocyanines ring-substituted with an alkyl group is possible, as shown in Figure 15.27 [86].

15.3.2 Methods of Characterization of Phthalocyanine-Modified Electrodes

Modified electrodes can be characterized by electrochemical and spectroscopic methods (such as X-ray photoelectron spectroscopy, XPS), and microscopy methods (such as atomic force microscopy [AFM] and scanning electrochemical microscopy [SECM]). These techniques when combined give a good idea of the effectiveness of the modification, the properties of the layer, and the integrity of the surface coverage.

15.3.2.1 CV

The uniformity of the surface coverage – whether the layer is pinhole and defect free, and whether the layer is tightly packed – as well as its orientation may be determined by recording the cyclic voltammogram of the modified electrode using known redox probes such as $[Fe(CN)_6]^{3+/4+}$ (Figure 15.28a).

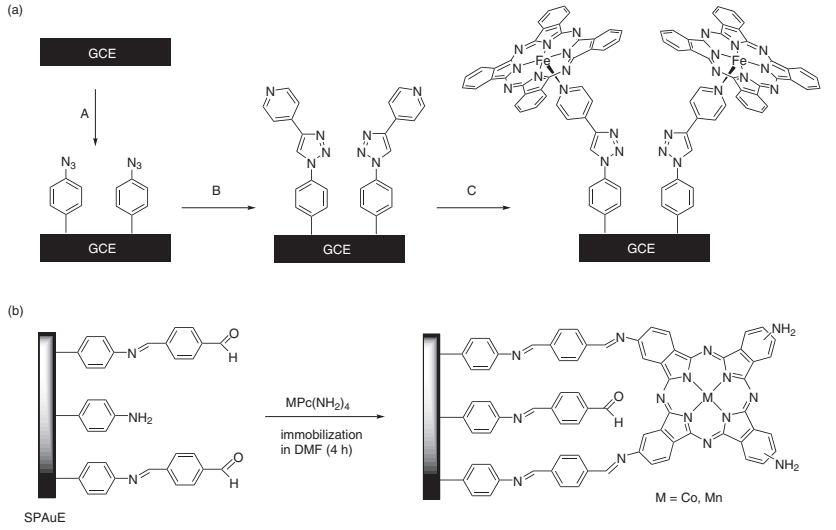

Figure 15.26 Schematic representation of (a) a diazonium salt grafting onto a glassy carbon electrode (GCE) upon electrochemical reduction (A), followed by clicking (B) and axial ligand attachment of a phthalocyanine to the clicked electrode (C). Source: With permission from Coates and Nyokong [83]. (b) Attachment of a substituted MPc onto a screen-printed Au electrode (SPAuE). Source: With permission from Mashazi and Nyokong [79].

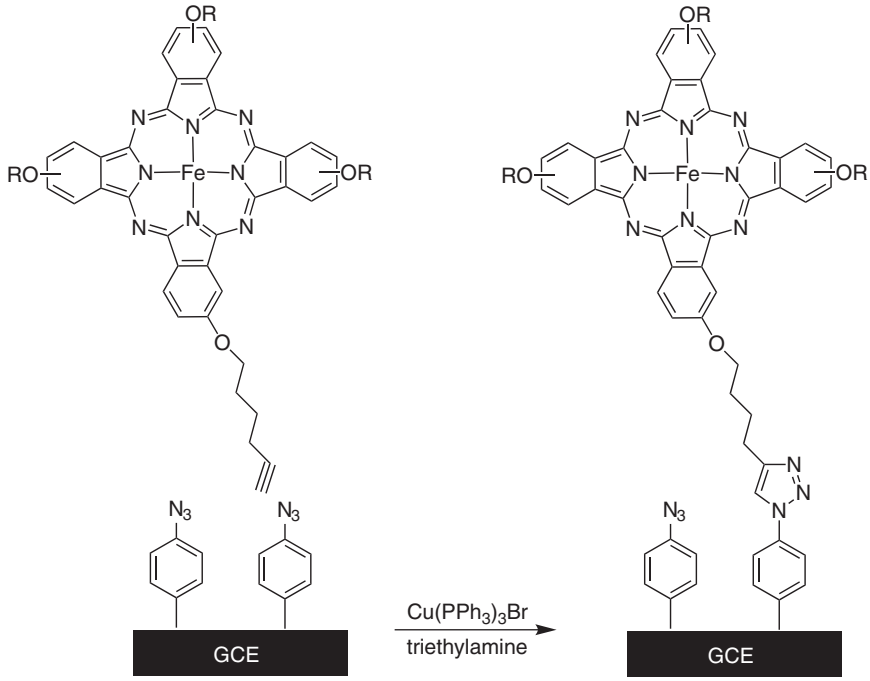

Figure 15.27 Click reaction using Pc-substituted peripherally with alkyl groups. Source: Reproduced with permission from Nxele et al. [86].

Where Nernstian behavior is observed, Eq. (15.24) or Eq. (15.25) can be used to calculate the surface coverage (Γ) [32, 87, 88]:

$$I_p = \frac{n^2F^2\Gamma A\nu}{4RT} \tag{15.24}$$

$$Q = nFA\Gamma \tag{15.25}$$

where Ip = the peak current, Q = total charge, n = number of electrons transferred, F = Faraday's constant, A = real surface area, ν = scan rate, R = gas constant, and T = temperature. The real surface area of the electrode can be calculated using a redox-active probe with a known diffusion constant (D) and the Randles–Ševčík equation, Eq. (15.26) [32, 87, 88]:

$$I_p = \left(2.69 \times 10^5\right)\ n^{3/2}ACD^{1/2}\upsilon^{1/2} \tag{15.26}$$

the parameters are as described above, and C is the concentration of a probe such as $[Fe(CN)_6]^{3+/4+}$. The cathodic to anodic peak differences (ΔE) for this process are usually larger for electrodes modified with MPc complexes compared to bare Au (Figure 15.28a) [89].

The points of interest that can be determined using voltammetry are the surface coverage, Γ_{MPc}, and ion barrier factor, Γ_{ibf}. The surface coverage can be determined using various methods, including by (i) using Eqs. (15.24) and (15.25) and (ii) using the charge difference that exists between the bare electrode and the SAM modified electrode in basic media [90] as shown in Figure 15.29. For MPc-SAMs, a surface coverage that is approximately 1×10^{-10} mol cm^{-2} confirms monolayer formation on the electrode [74].

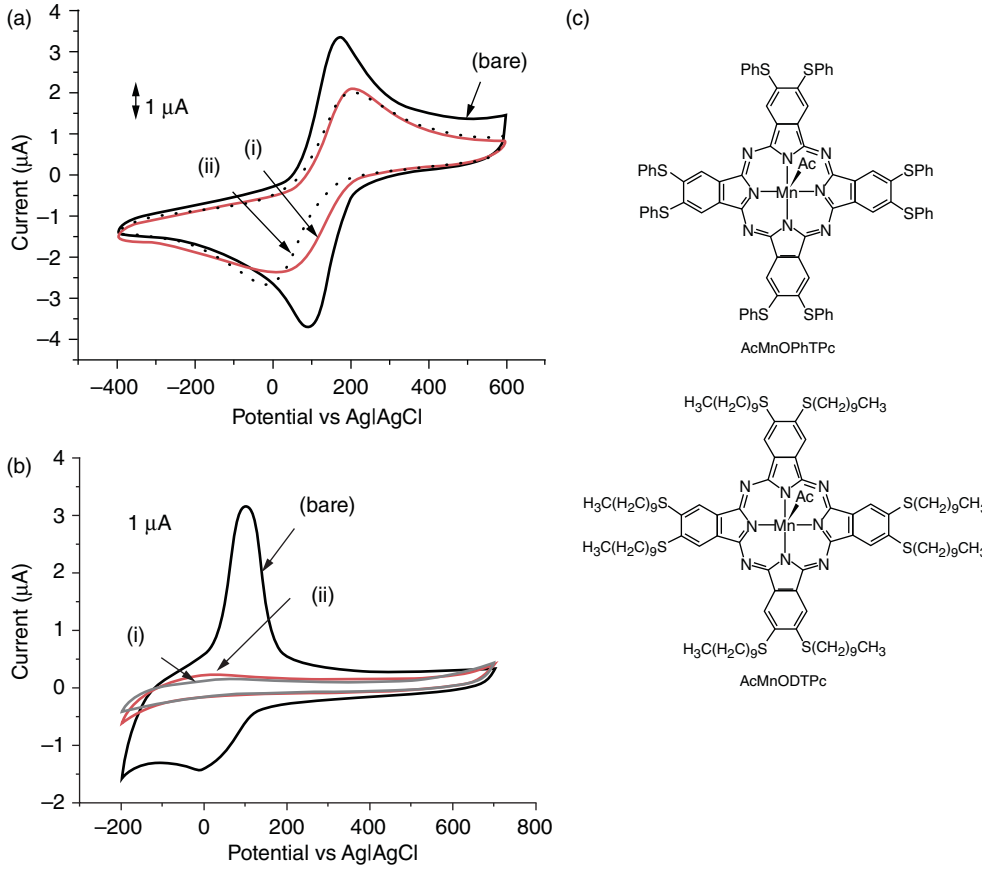

Figure 15.28 Cyclic voltammograms for bare Au, (i) octakis(decylthio) phthalocyaninato manganese(III)(acetate) (AcMnODTPc) and (ii) octakis(phenylthio) phthalocyaninato manganese (III)(acetate) (AcMnOPhTPc) in (a) 1 mM $K_3[Fe(CN)_6]$ in 0.1 M KCl, (b) 1 mM $CuSO_4$ in pH 4 buffer solution, and (c) the structure of the complexes; scan rate = 50 mV s^{-1} versus Ag|AgCl. Source: Reproduced with permission from Coates et al. [89].

Another important aspect of the characterization of SAMs is the determination of the ion barrier factor (Γ_{ibf}), which is the measure of the MPc-SAM effectiveness in preventing the interaction of the surface with the electrolyte.

The Γ_{ibf} is determined using Eq. (15.27):

$$\Gamma_{ibf} = 1 - \left(Q_{SAM}/Q_{BARE}\right) \tag{15.27}$$

where Q_{SAM} is the charge using MPc-SAM, and Q_{BARE} is the charge for the bare electrode in basic media as shown in Figure 15.29. The voltammogram of MPc-SAM is supposed to show the blockage of the gold redox process, in comparison to the bare gold electrode in basic media. For example, Γ_{ibf} values of ~0.9 were obtained for $OV(Pc(SC_5H_{11})_8)$ and $OTi(Pc(SC_5H_{11})_8)$ complexes shown in Figure 15.9, suggesting that SAMs of these molecules are able to act as efficient barriers for the electrolyte.

There are other methods used to determine the integrity of the SAMs on gold electrodes, including the blockage of the underpotential deposition of copper using $CuSO_4$ (Figure 15.28b) [89]. This is evidenced by the absence of peaks for the SAMs of Pcs, showing

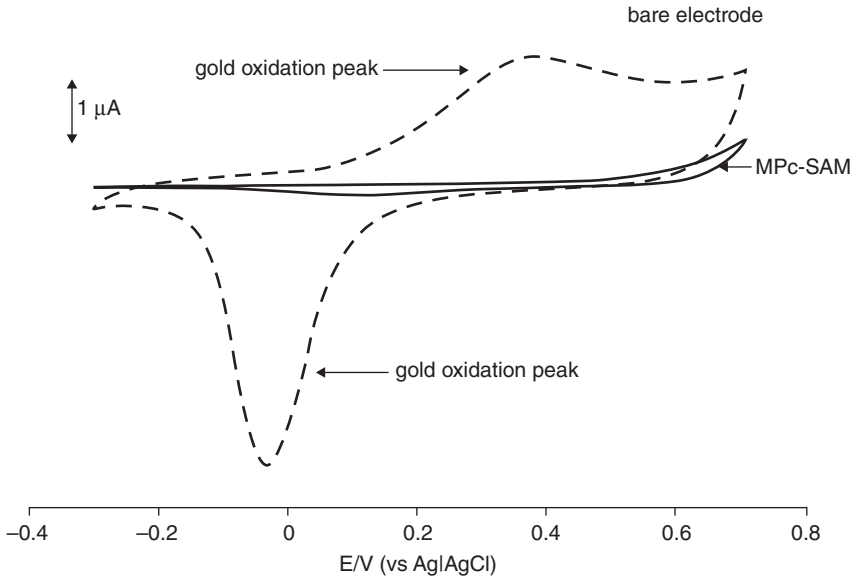

Figure 15.29 Cyclic voltammogram of the bare and modified Au electrode in basic media; SAM = self-assembled monolayer. Unpublished work.

the layers to be almost completely pinhole free. Grafting of diazonium salts has been shown to have a blocking effect on the electrode, particularly when the layer is well packed [78]. This blocking effect can thus be used to determine whether the layer is pinhole free, or if there are any defects in the coverage [78].

15.3.2.2 Electrochemical Impedance Spectroscopy (EIS)

Two plots are commonly used to show impedance behavior [91], the Nyquist and Bode plots, which are shown in Figure 15.30 [92]. The Nyquist plot (Figure 15.30a) is divided into two frequency regions, the kinetically controlled (high-frequency) region, where a semicircle is observed, and the diffusion-controlled (low-frequency) region, where the Warburg line is observed. On a Nyquist plot, the infinite Warburg impedance appears as a diagonal line. Parameters such as the electrolyte resistance (R_e), charge transfer resistance (R_{CT}), double-layer capacitance (C_{DL}), and constant phase element (CPE) capacitance can be determined from Nyquist plots (Figure 15.30a). A high R_{CT} signifies that the electrodes have low conductivity. The increase in R_{CT} values (compared to bare electrode) after modification with the phthalocyanine could be attributed to the presence of the surface-confined phthalocyanine films that impedes electron transport.

A complementary plot is the Bode plot (Figure 15.30b), where the phase angle is plotted against frequency. In the Bode phase-angle plot, a phase angle close to −90° implies pure capacitive behavior [93].

15.3.2.3 Scanning electrochemical microscopy (SECM)

SECM is a useful tool in elucidating the conductivity of a substrate, and has applications in areas such as corrosion science, fuel cells, and biotechnology [94–96]. SECM gives information on the conductivity of a surface, and allows the creation of images or maps of the substrate [94–96]. In SECM, an ultramicro electrode (UME) is used as the probe (Figure 15.31).

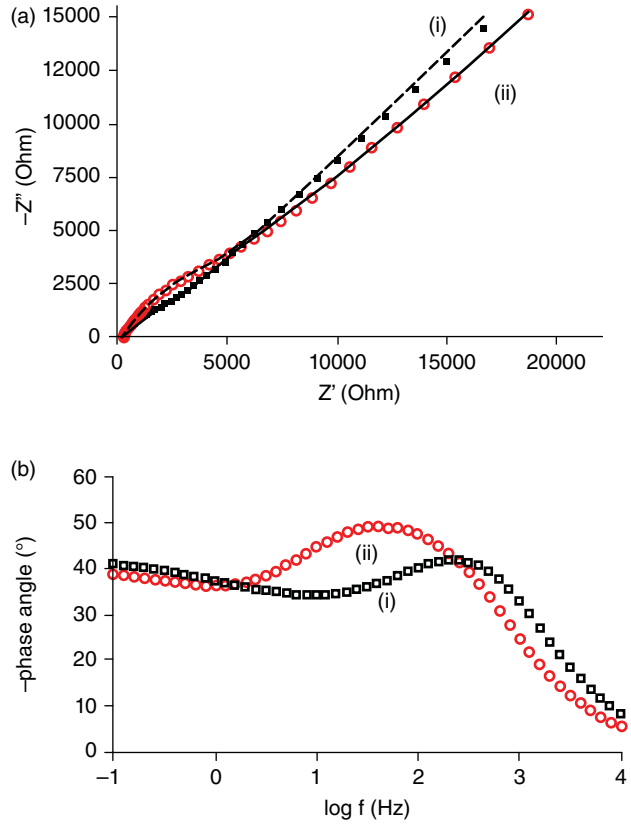

Figure 15.30 Examples of (a) Nyquist and (b) Bode plots of modified electrodes, for (i) bare electrodes, (ii) poly$Co(NH_2)_4$ (polymerized Co tetraamino phthalocyanine) in (1:1) 1 mM $K_4/K_3[Fe(CN)_6]$ solution containing 0.1 M KCl, Au working electrode; applied potential corresponds to $E_{1/2}$ of ferricyanide redox couple. Source: Reproduced with permission from Mashazi et al. [92].

The tip current is dependent on the electroactive redox probe in solution, the conductive nature of the substrate, and on the tip–substrate distance [94]. The feedback mode is most commonly used. When in close proximity to an insulating surface, the diffusion of electroactive material from the solution to the tip is blocked and the current decreases, whereas close proximity to a conducting surface results in regeneration of the electroactive species, and thus the current increases [94–96].

Figure 15.32 shows examples of approach curves to both a conductive and an insulating surface. The redox probe used was $K_3[Fe(CN)_6]$. The bare GCE plate illustrated by Figure 15.32(i) appeared to be conducting. However, the grafted and clicked GCE plates, illustrated by Figure 15.32(ii) and (iii), respectively, proved to be insulating toward the $K_3[Fe(CN)_6]$ solution, which was expected.

Images of the different electrode surfaces may also be obtained using SECM (Figure 15.33). Figure 15.33a shows that lower currents are observed after grafting compared to the unmodified section of the GCE plate. This observation corresponds with the results obtained from the approach curves. Figure 15.33b illustrates the surface after grafting and click chemistry.

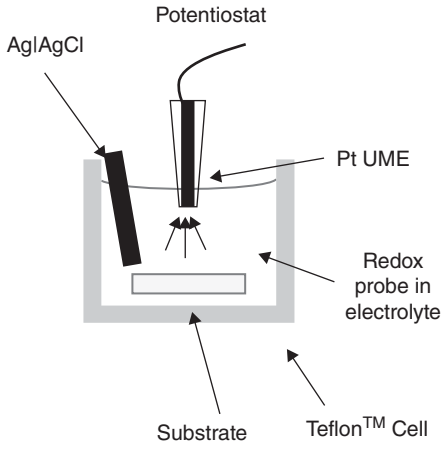

Figure 15.31 Representation of the scanning electrochemical microscopy (SECM) electrochemical cell.

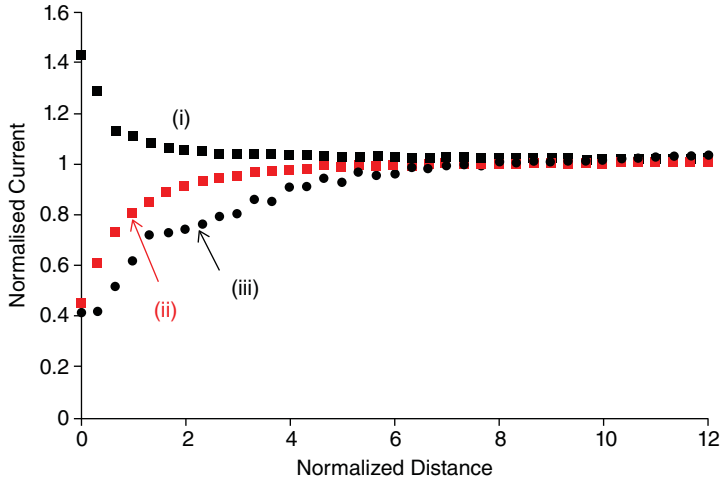

Figure 15.32 Scanning electrochemical microscopy (SECM) approach curves of (i) bare glassy carbon electrode (GCE), (ii) grafted GCE, and (iii) grafted GCE after click chemistry of alknyl FePc shown in Figure 15.27; 2 mM $K_3[Fe(CN)_6]$ in 0.1 M KCl at 0.15 V versus Ag/AgCl. Reproduced with permission from Nxele et al. [86].

The currents are still lower for grafting and clicked electrode compared to the unmodified section, Figure 15.33b, confirming the observation from the approach curves.

15.3.2.4 XPS

XPS can be used to characterize the modified surfaces [97–99]. For the SAM formation using aryl- or alkyl-thio (SR) Mn phthalocyanines, the question as to whether the R group remains intact following SAM formation was resolved using XPS (Figure 15.34), which showed that some RS bond remains intact [89].

The ratio of the relative areas of the bound (at 161.9 and 161.5 eV for the SAMs of AcMnODTPc and AcMnOPhTPc, respectively, Figure 15.34) to unbound (163.6 and 163.4 eV for AcMnODTPc-SAM and AcMnOPhTPc-SAM, respectively) thiolate RS peaks was used to determine the amount of bound sulfur groups. Approximately 60% of the sulfur groups in the AcMnOPhTPc-SAM surface were bound to gold through the cleavage of the C—S bond,

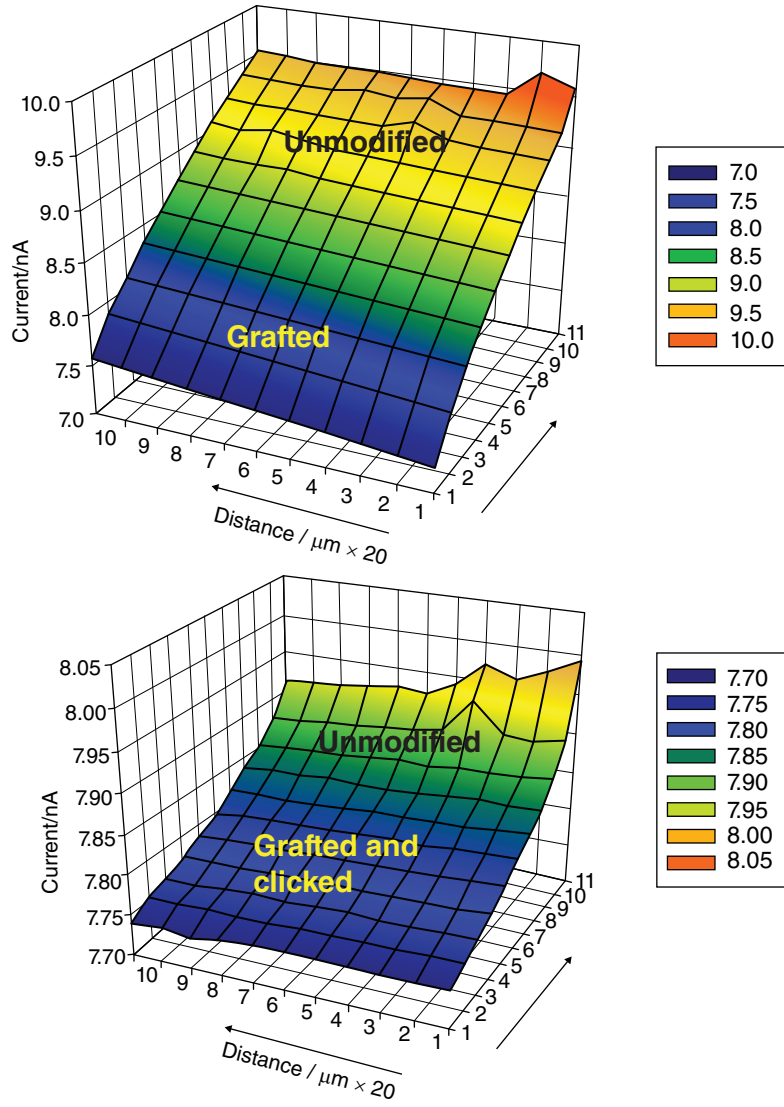

Figure 15.33 Scanning electrochemical microscopy (SECM) images of (a) glassy carbon electrode (GCE) after grafting and (b) GCE after grafting and click chemistry with FePc; image obtained with 15 μm diameter UME Pt tip in 2 mM $K_3[Fe(CN)_6]$ in 0.1 M KCl at 0.15 V versus Ag/AgCl. Source: Reproduced with permission from Nxele et al. [86].

as opposed to only 37% for the AcMnODTPc-SAM. It was concluded [89] that the longer alkyl chain in AcMnODTPc causes more steric hindrance to SAM formation than the aryl substituents in AcMnPhTPc, as also the fact that the former containing a poorer leaving group.

XPS was also used to confirm click reaction and attachment of the FePc on the clicked electrode. The survey scan (Figure 15.35a) shows all the expected elements following grafting and clicking on the carbon plate [83]. The high-resolution scan of the N(1 s) region of the XPS spectrum shows the characteristic peak for the central nitrogen of the azide group at

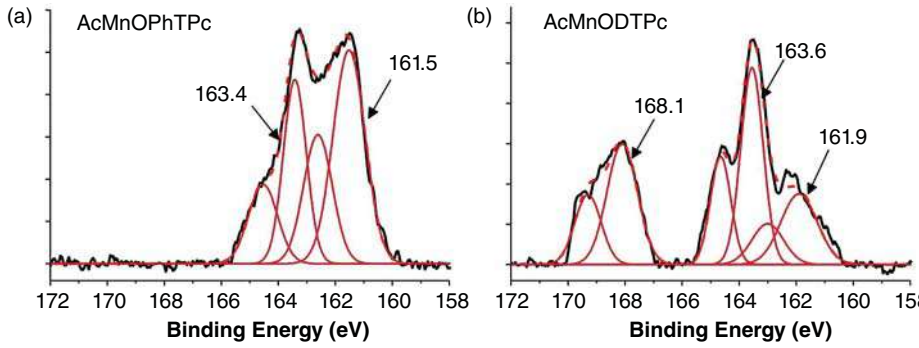

Figure 15.34 High-resolution XPS spectra of the S(2p) region of (a) AcMnOPhTPc-SAM and (b) AcMnODTPc-SAM; pass energy 40 eV, number of scans 5; the structures of the Pcs are shown in Figure 15.28. Source: Reproduced with permission from Coates and Nyokong [99].

404 eV for the grafted electrode, which is greatly reduced after the click step, showing that the majority of the azide groups reacted to form the triazole (Figure 15.35b).

15.3.2.5 AFM and Scanning Tunneling Microscopy (STM)

AFM can be used to indicate clearly whether there is complete coverage by looking at the changes in the electrode surface after modification. AFM images of the preformed SAM containing single-walled carbon nanotubes (SWCNTs) linked to $CoPc(NH_2)_4$ modified electrode (represented in Figure 15.36b) [100] clearly proved that the SAM lies perpendicular to the gold surface with needle-like protrusions (Figure 15.36a).

A difference in terms of surface roughness values for AFM images may be used to confirm different compositions of the hybrid electrodes. The AFM image of CoPc adsorbed on GCE (Figure 15.37b) shows the island-like structure corresponding to CoPc cluster on the GC electrode [101]. It is observed from Figure 15.37c that the SWCNTs are randomly distributed. The mean roughness factor increases with different stages of the modification and are often used to confirm electrode modification.

STM is so sensitive that that the four-leaf clover-like shape of the MPc molecules is clearly apparent for the mixed CoPc/CuPc assembled on Au 111 (Figure 15.38) [102]. In Figure 15.38, some molecules have an intense bright (high) area in the center, whereas others have a pronounced dark region (hole). The STM image of mixed CoPc/CuPc showed that for CuPc, the central metal appears as a hole in the molecular image, while for CoPc, the cobalt atom appears as the highest point in the molecular image (Figure 15.38). The benzene ring regions of CoPc and CuPc appear to have the same height. Thus, it may be possible to chemically identify the different metal phthalocyanines simply by their appearance on the STM images.

15.4 Electrocatalysis

15.4.1 Background

An electrocatalyst is a molecule that is able to increase the rate at which an electrochemical reaction takes place and in turn lowers the applied potentials and increases the current produced. A good electrocatalyst must lower the redox potential, increase the sensitivity and selectivity (Figure 15.39), and show stability.

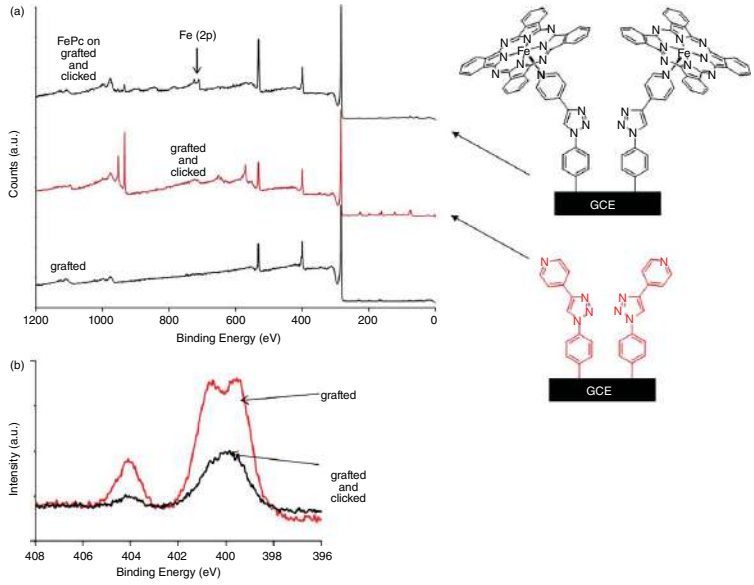

Figure 15.35 Wide scan (a) and high N 1s resolution (b) XPS spectra for grafted GCE, grafted GCE following click chemistry with ethynylpyridine and grafted GCE after click chemistry followed by linking of FePc (the latter only for wide scans). Source: Reproduced with permission from Coates and Nyokong [83].

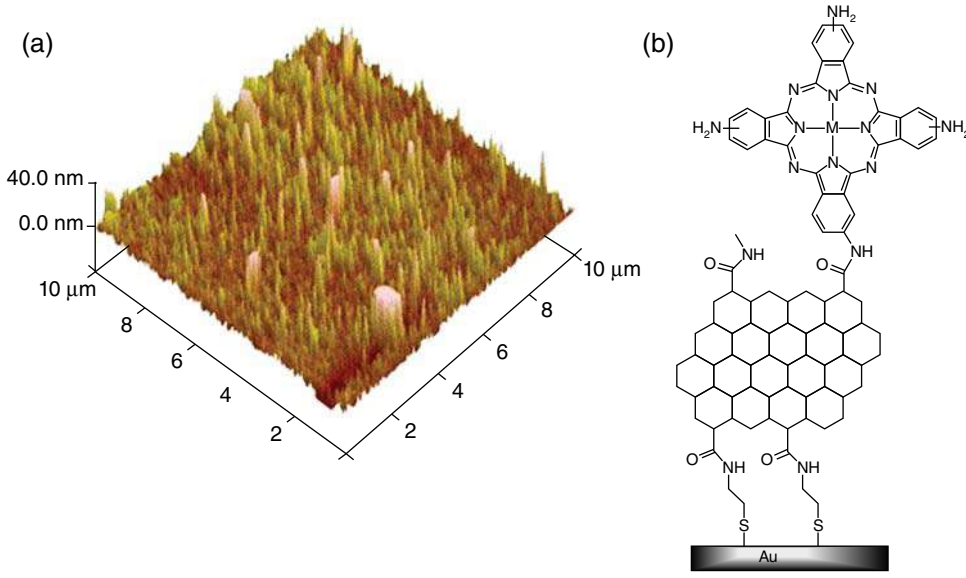

Figure 15.36 Atomic force microscopy (AFM) image (a) of SAM formed as represented in (b). Source: Reproduced with permission from Ozoemena et al. [100].

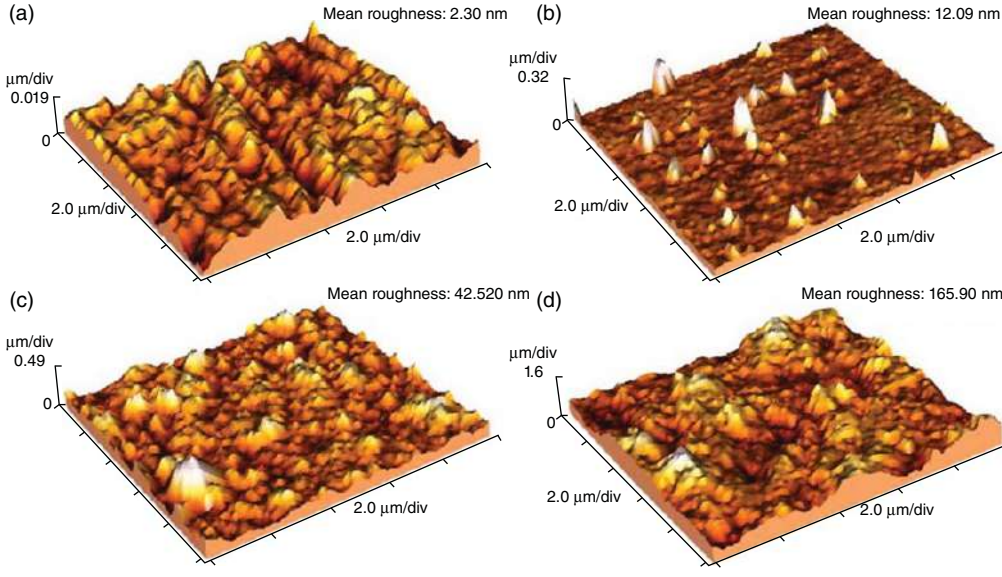

Figure 15.37 Atomic force microscopy (AFM) images of the surface of (a) bare GC electrode; (b) GC/$CoPc_{ads}$; (c) GC/SWCNT; and (d) GC/SWCNT+CoPc. Source: Reproduced with permission from Geraldo et al. [101].

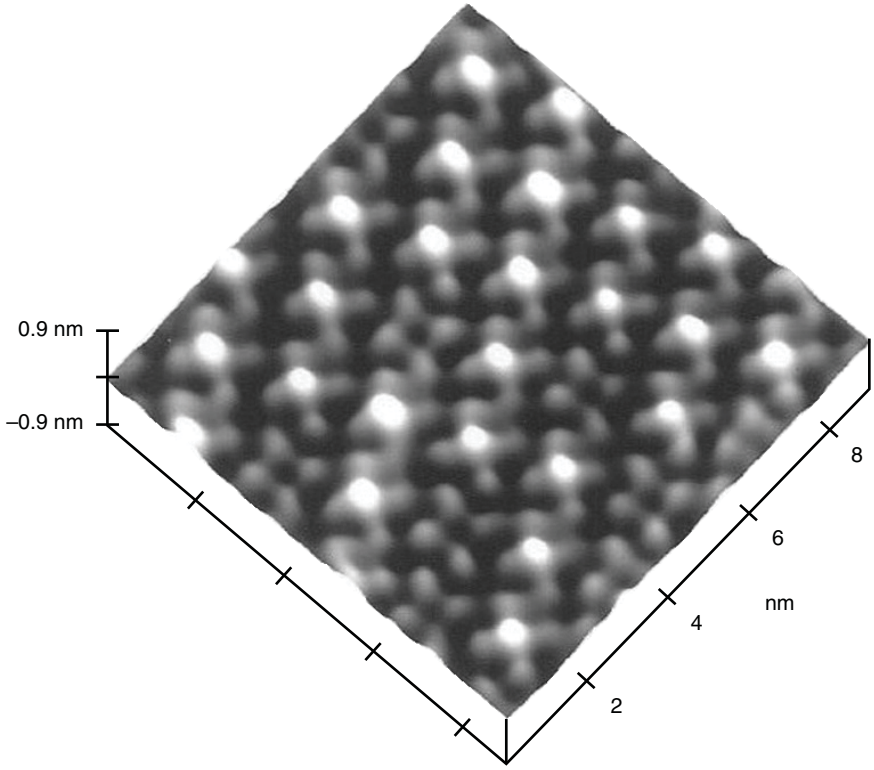

Figure 15.38 Surface plot of a mixed CoPc and CuPc monolayer on Au(111); the gray scale extends over a range of 0.5 nm, and the image was Fourier filtered. Source: Reproduced with permission from Hipps et al. [102].

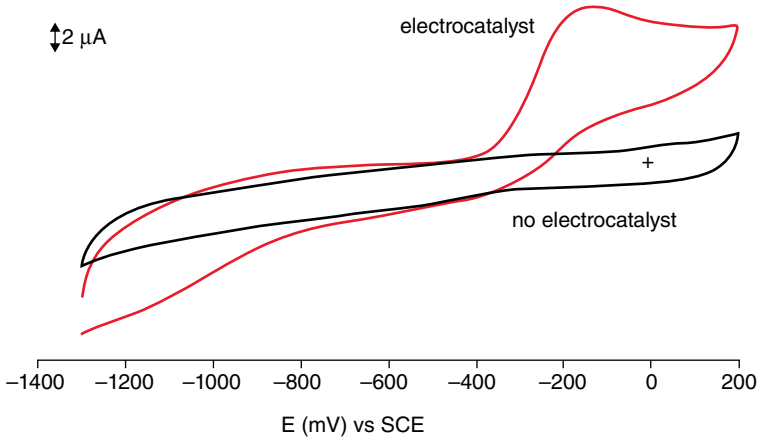

Figure 15.39 Cyclic voltammograms illustrating the enhancement of current by an electrocatalyst. Unpublished work.

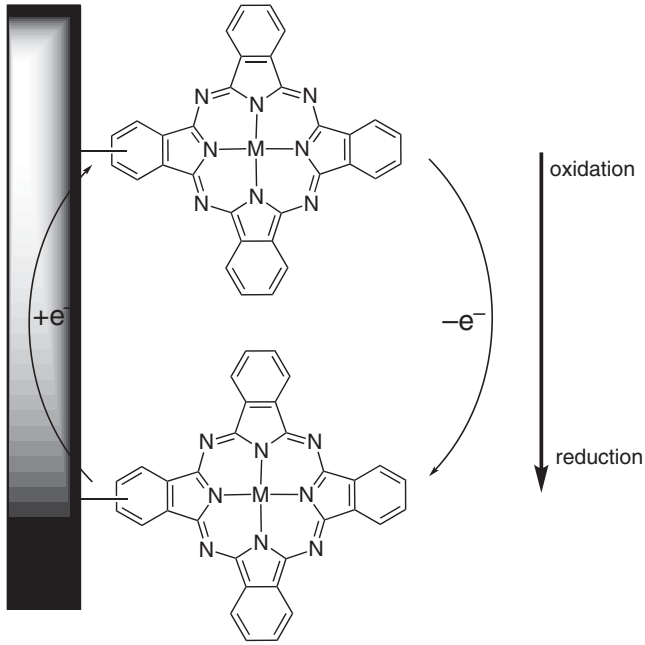

Figure 15.40 Typical electrocatalytic process of metallophthalocyanines immobilized on electrodes.

MPcs have been confirmed as good electrocatalysts for various analytes [60, 62, 64, 66, 68, 69, 101, 103–106]. This is partly due to their good thermal and chemical stability. During electrocatalysis (using reduction as an example), the central metal (Eqs. 15.28 and 15.29) or the Pc ring (Eqs. 15.30 and 15.31) can undergo redox processes before they act as mediators between the analyte and the electrode. After the reaction, it is expected that the MPc will go back to its original oxidation state as illustrated in Eqs. (15.29) and (15.31) (A = analyte, P = product).

$$M^{II}Pc^{2-} + e^- \rightarrow \left[M^{I}Pc^{2-}\right]^- \tag{15.28}$$

$$\left[M^{I}Pc^{2-}\right]^- + A \rightarrow M^{II}Pc^{2} + P \tag{15.29}$$

or

$$M^{II}Pc^{2-} + e^- \rightarrow M^{II}\,Pc^{3-}\big]^- \tag{15.30}$$

$$\left[M^{II}Pc^{3-}\right]^- + A \rightarrow M^{II}Pc^{2-} + P \tag{15.31}$$

Figure 15.40 illustrates how MPcs work as electrocatalysts when immobilized on an electrode. During electrocatalytic oxidation reactions, assuming the starting MPc to contain a metal in its 2^+ oxidation state, the central metal is generally oxidized to its 3^+ state and is in turn reduced to its 2^+ state by the analyte.

15.4.2 Examples of Electrocatalysis Using MPcs

15.4.2.1 Adsorbed MPcs

Figure 15.41 shows that the catalytic activity for hydrazine oxidation on CoPc alone or with SWCNTs. Catalytic currents are higher in the presence of CoPc and even much higher on GC/SWCNT + CoPc as a result of the synergistic effect produced by the use of SWCNT

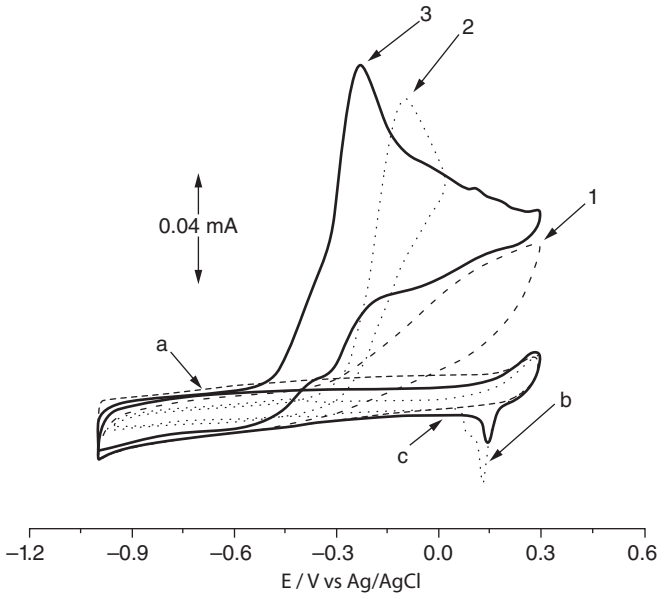

Figure 15.41 Cyclic voltammograms of N_2H_4 (2.6 mM) in 0.2 M NaOH aqueous solution at different GC electrodes. Curve 1, GC/SWCNT; curve 2, GC/CoPc adsorbed; and curve 3, GC/SWCNT + CoPc. Curves a, b, and c correspond to the background for GC/SWCNT, GC/CoPc, and GC/SWCNT + CoPc, respectively, in the presence of the electrolyte but without hydrazine; scan rate: 50 mV s^{-1}. Source: Reproduced with permission from Geraldo et al. [101].

functionalized with CoPc. There is also a large reduction in overpotential for GC/SWCNT + CoPc [101].

15.4.2.2 MPcs as SAMs

SAMs of 2,3,9,10,16,17,23,24-octabutylthiophthalocyaninato iron (II) were used as electrocatalysts for the detection of the thiols L-cysteine (Figure 15.42a) and penicillamine (Figure 15.42b) with detection limits in the 10^{-7} to 10^{-6} M range [103].

MnPc-SAMs have been employed for the detection of thiocyanate [104]. The SAM was formed by coordination of MPc complexes to pre-formed SAMs. On MnPc-4-MPy-SAM (MPy = mercapro pyridine), the oxidation of SCN^- occurred at 0.50 V. Analysis of SCN^- in the presence of possible interfering species (uric acid, oxalic acid, and ascorbic acid) in biological samples revealed insignificant effects from these compounds [104]. Thus, SCN^- can be analyzed in the presence of ascorbic acid. Analysis of urine samples from a smoker and a nonsmoker showed clearly that the SAM electrode could be used to differentiate between the two groups (Figure 15.43) [104].

15.4.2.3 Electropolymerized MPcs

Nitrite oxidation occurred at 0.63 V on polymerized $OTiPc(NH_2)_4$ [105] and 0.65 V on polymerized $AcMnPc(NH_2)_4$ (Ac = acetate) [105]. Thus, the overpotential was lowered from 0.92 V at the bare electrode to 0.65 and 0.63 V at the polymerized $AcMnPc(NH_2)_4$ and $OTiPc(NH_2)_4$ modified electrodes, respectively. The effect of central metal (Mn or Ti) on the oxidation potential for nitrite oxidation was insignificant. Also there was no significant influence on the point of substitution (i.e., peripheral $OTiPc^{\beta}(NH_2)_4$ versus non-peripheral

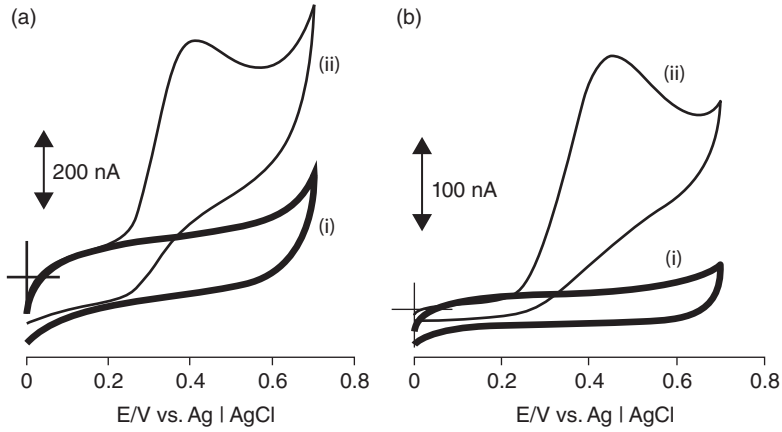

Figure 15.42 Cyclic voltammograms for the oxidation of (a) L-cysteine (1×10^{-5} mol dm^{-3}) and (b) penicillamine (1×10^{-5} mol dm^{-3}) on SAM of 2,3,9,10,16,17,23,24-octa butylthiophthalocyaninato iron(II); (i) buffer (pH 4) alone and (ii) in the presence of the analyte; scan rate = 25 mV s^{-1}. Source: Reproduced with permission from Ozoemena et al. [103].

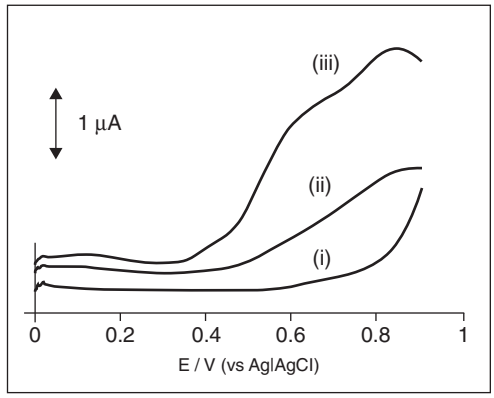

Figure 15.43 Comparative Osteryoung square wave voltammograms obtained for urine samples of (ii) nonsmoker and (iii) smoker. Curve (i) is pH 4.0 phosphate buffer solution alone. Scan rate = 25 mV s^{-1}. Reproduced with permission from Ozoemena and Nyokong [104].

$OTiPc^{\alpha}(NH_2)_4$) on the oxidation potential of nitrite [13]. The proposed mechanism for the electrocatalytic oxidation of nitrite on MnPc is as given by Eqs. (15.32)–(15.34) (Ac = acetate) [105]:

$$AcMn^{III}Pc^{2-} + NO_2^- \rightarrow \left[\left(AcMn^{III}Pc^{2-}\right)\left(NO_2^-\right)\right]^{1-} \quad (15.32)$$

$$\left[\left(AcMn^{III}Pc^{2-}\right)\left(NO_2^-\right)\right]^{1-} \rightarrow \left(AcMn^{III}Pc^{1-}\right)\left(NO_2^-\right) + e^- \quad (15.33)$$

$$\left(AcMn^{III}Pc^{1-}\right)\left(NO_2^-\right) + H_2O \rightarrow AcMn^{III}Pc^{2-} + NO_3^- + 2H^+ + e^- \quad (15.34)$$

For OTiPc derivatives where only ring-based oxidation processes are possible, the following mechanism was proposed [105], Eqs. (15.35)–(15.37):

$$OTi^{IV}Pc^{2-} + NO_2^- \rightarrow \left[\left(OTi^{IV}Pc^{2-}\right)\left(NO_2^-\right)\right]^{1-} \quad (15.35)$$

$$\left[\left(OTi^{IV}Pc^{2-}\right)\left(NO_2^-\right)\right]^{1-} \rightarrow \left(OTi^{IV}Pc^{1-}\right)\left(NO_2^-\right) + e^- \quad (15.36)$$

$$\left(OTi^{IV}Pc^{1-}\right)\left(NO_2^-\right) + H_2O \rightarrow OTi^{IV}Pc^{2-} + NO_3^- + 2H^+ + e^- \quad (15.37)$$

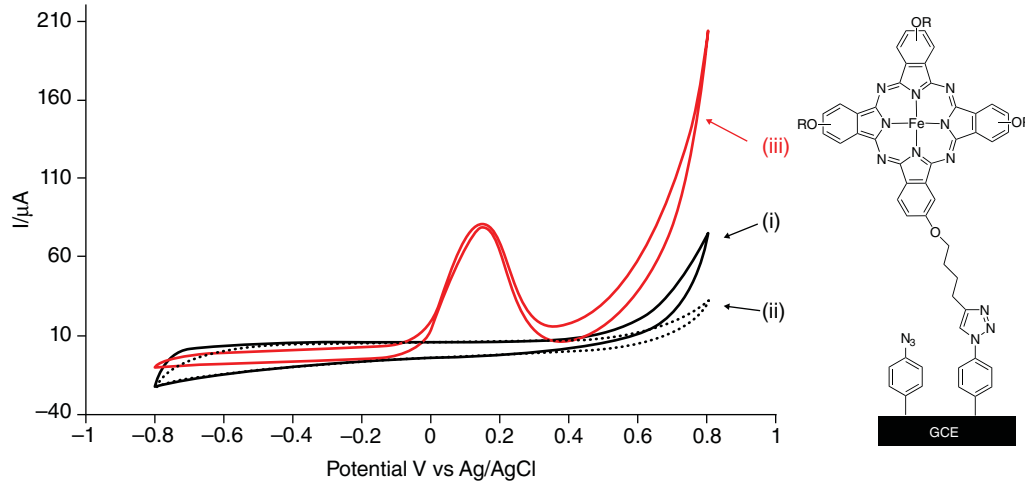

Figure 15.44 Cyclic voltammograms of (i) bare glass carbon electrode (GCE), (ii) grafted GCE, and (iii) grafted GCE after click chemistry with alkynyl FePc in 5 mM hydrazine in 0.1 M NaOH; scan rate 100 mV s^{-1}. Source: Reproduced with permission from Nxele et al. [86].

15.4.2.4 Clicked MPc

For the electrocatalysis of hydrazine oxidation, the electrode modified by click chemistry was employed. Figure 15.44 shows comparative CVs for (i) the bare GCE, (ii) grafted GCE, and (iii) grafted GCE after click chemistry with alkynyl FePc in the presence of hydrazine (5 mM in 0.1 M NaOH). The adsorbed (without clicking, CV not shown) alkynyl FePc was able to oxidize hydrazine with double oxidation being observed at 0.3 V with a maximum peak current of 40 μA. The grafted GCE clicked with alkynyl FePc also showed a double oxidation peak at approximately 0.1 V with a maximum peak current of 76.8 μA (Figure 15.44). This shows evidence of improved currents and lowered potentials following clicking. The electro-oxidation of hydrazine is due to the Fe(II)Pc as the active electrocatalyst [86].

15.5 Conclusion

The chapter summarizes the CV and spectroelectrochemical behavior of phthalocyanines, which are similar to other porphyrin-type complexes. The central metal plays a huge role in the electrochemical behavior of porphyrin-type complexes. MPcs containing main group metals only show redox processes centered on the Pc ring, whereas transition metals show both ring- and metal-based processes. Spectroelectrochemistry plays a crucial role in determining if ring or metal processes are involved, and if there is disaggregation, demetalation, or decomposition of the complex. Pcs may also be used to modify electrodes for various applications. The chapter describes methods of electrode characterization such as XPS/ AFM/STM, and various electrochemical techniques. The use of the modified electrodes for electrocatalysis is discussed with a few examples.

Acknowledgments

This work was supported by the Department of Science and Technology (DST) and National Research Foundation (NRF), South Africa through DST/NRF South African Research Chairs

Initiative for Professor of Medicinal Chemistry and Nanotechnology (NRF 62620) as well as Rhodes University.

References

1 Stillman, M.J. and Nyokong, T. (1989). Absorption and magnetic circular dichroism spectral properties of phthalocyanines Part 1: complexes of the dianion Pc(-2). In: *Phthalocyanine Properties and Applications*, vol. 1 (ed. C.C. Leznoff and A.B.P. Lever), 133–289. New York: VCH Publishers.

2 Kalugasalam, P. and Ganesan, S. (2010). Surface morphology of annealed lead phthalocyanine. *Thin Films* 2: 1773–1779.

3 McKeown, N.B. (1998). *Phthalocyanine Materials: Synthesis, Structure and Function*. Cambridge, U.K.; New York: Cambridge University Press.

4 Gregory, P. (1991). *High-Technology Applications of Organic Colourants*. New York: Springer.

5 Gregory, P. (1999). Steamrollers, sports cars and security: Phthalocyanine progress through the ages. *Journal of Porphyrins Phthalocyanines* 3: 468–476.

6 Dini, D. and Hanack, M. (2003). Phthalocyanines: properties and materials. In: *The Porphyrin Handbook*, vol. 17, Chapter 107 (ed. K.M. Kadish, K.M. Smith and R. Guilard), 1–36. New York: Academic Press.

7 Okura, I. (2000). *Photosensitization of Porphyrins and Phthalocyanines*. London: CRC Press.

8 Zagal, J.H., Bedioui, F., and Dodelet, J.P. (ed.) (2006). *N_4-Macrocyclic complexes*. New York: Springer.

9 Snow, A.W. and Barger, W.R. (1989). Phthalocyanine films in chemical sensors. In: *Phthalocyanine Properties and Applications*, vol. 1 (ed. C.C. Leznoff and A.B.P. Lever), 341s. New York: VCH Publishers.

10 Mack, J. and Stillman, M. (2003). Optical spectra and electronic structure of metallophthalocyanines and metalloporphyrins. In: *The Porphyrin Handbook*, vol. 16 (ed. K.M. Kadish, K.M. Smith and R. Guilard), 43–116. New York, Chapter 103: Academic Press.

11 Giovannetti, R. (2012). The use of spectrophotometry UV-Vis for the study of porphyrins. In: *Macro to Nano Spectroscopy* (ed. J. Uddin), 87–108. London, Chapter 6: IntechOpen.

12 Chidawanyika, W. and Nyokong, T. (2009). Spectroscopic and photophysicochemical behaviour of novel cadmium phthalocyanine derivatives tetra-substituted at the alpha and beta positions. *Journal of Photochemistry and Photobiology A: Chemistry* 202: 99–106.

13 Mbambisa, G., Nombona, N., and Nyokong, T. (2009). The formation of self-assembled monolayers of thiophthalocyanine complexes of titanium, vanadium and manganese and their use in l-cysteine electrocatalysis. *Microchemical Journal* 93: 60–66.

14 Mbambisa, G. and Nyokong, T. (2008). Synthesis and electrochemical characterisation of a near infrared absorbing oxo vanadium(IV) octapentylthio-phthalocyanine. *Polyhedron* 27: 2799–2804.

15 Mbambisa, G., Tau, P., Antunes, E., and Nyokong, T. (2007). Synthesis and electrochemical properties of purple manganese(III) and red titanium(IV) phthalocyanine complexes octa-substituted at non-peripheral positions with pentylthio groups. *Polyhedron* 26: 5355–5364.

16 Kissinger, P.T. and Heinman, W. (1984). *Laboratory Techniques in Electroanalytical Chemistry*. New York: Marcel Dekker.

17 Chang, J., Large, R.F., and Popp, G. (1971). Electrochemical methods. In: *Techniques in Chemistry*, Physical Methods in Chemistry, part IIB, vol. 1 (ed. A.W. Weissberger and B.W. Rossiter), 74–75. New York: Wiley.

18 Stillman, M.J. (1993). Absorption and magnetic circular dichroism spectral prpoerties of phthalocyanines. Part 2: Ring oxidized and ring-reduced complexes. In: *Phthalocyanine Properties and Applications*, vol. 3 (ed. C.C. Leznoff and A.B.P. Lever), 227–296. New York: VCH Publishers.

19 Kuwana, T., Darlington, R.K., and Leedy, D.W. (1964). Electrochemical studies using conducting indicator electrodes. *Analytical Chemistry* 36: 2023–2025.

20 Mousa, A.O., Habubi, N.F., and Nema, N.A. (2015). Substrate effects on structural and optical properties of ZnO thin films deposited by chemical spray pyrolysis. *International Letters of Chemistry, Physics and Astronomy* 51: 69–77.

21 Huang, Y., Li, D., Feng, J. et al. (2010). Transparent conductive tungsten-doped tin oxide thin films synthesized by sol–gel technique on quartz glass substrates. *Journal of Sol-Gel Science and Technology* 54: 276–281.

22 Babar, A.R., Shinde, S.S., Moholkar, A.V. et al. (2011). Physical properties of sprayed antimony doped tin oxide thin films: The role of thickness. *Journal of Semiconductors* 32: 053001.

23 Demir, F., Erdogmus, A., and Koca, A. (2013). Oxygen reduction reaction catalyzed with titanyl phthalocyanines in nonaqueous and aqueous media. *Physical Chemistry Chemical Physics* 15: 15926–15934.

24 Salan, Ü., Altindal, A., Özkaya, A.R. et al. (2012). Photovoltaic and electrocatalytic properties of novel ball-type phthalocyanines bridged with four dicumarol. *Dalton Transactions* 41: 5177–5187.

25 Karadağ, S., Bozoğlu, C., Şener, K.M., and Koca, A. (2014). Synthesis and electrochemical properties of a double-decker lutetium(III) phthalocyanine bearing electropolymerizable substituents on non-peripheral positions. *Dyes and Pigments* 100: 168–176.

26 Zheng, W., Wang, B.B., Lai, J.C. et al. (2015). Electrochromic properties of novel octa-pinene substituted double-decker Ln(III) (Ln = Eu, Er, Lu) phthalocyanines with distinctive near-IR absorption. *Journal of Materials Chemistry C* 3: 3072–3080.

27 Arıcı, M., Bozoğlu, C., Erdoğmus, A. et al. (2013). Electrochemical and spectroelectrochemical properties of novel lutetium(III) mono- and bis-phthalocyanines. *Electrochimica Acta* 113: 668–678.

28 Smolenyak, P.E., Peterson, R.A., Dunphy, D.R. et al. (1999). Formation and spectroelectrochemical characterization of multilayer and submonolayer thin films of 2,3,9,10,16,17,23,24-octa(2-benzyloxy-ethoxy) phthalocyninato copper ($CuPc(OC_2OBz)_8$). *Journal of Porphyrins and Phthalocyanines* 3: 620–633.

29 Maldonado, S., Smith, T.J., Williams, R.D. et al. (2006). Surface modification of indium tin oxide via electrochemical reduction of aryldiazonium cations. *Langmuir* 22: 2884–2891.

30 Senthilkumar, M., Mathiyarasu, J., Joseph, J. et al. (2008). Electrochemical instability of indium tin oxide (ITO) glass in acidic pH range during cathodic polarization. *Materials Chemistry and Physics* 108: 403–407.

31 Domingos, S.R., Luyten, H., van Anrooij, F. et al. (2013). An optically transparent thin-layer electrochemical cell for the study of vibrational circular dichroism of chiral redox-active molecules. *Review of Scientific Instruments* 84: 033103.

32 Bard, A.J. and Faulkner, L.R. (1996). *Electrochemical Methods, Fundamentals and Applications*. New York: Wiley.

33 Hartl, F., Luyten, H., Nieuwenhuis, H.A., and Schoemaker, G.C. (1994). Versatile cryostated optically transparent thin-layer electrochemical (OTTLE) cell for variable-temperature UV-Vis/IR spectroelectrochemical studies. *Applied Spectroscopy* 48: 1522–1528.

34 Atsay, A., Koca, A., and Koçak, M.B. (2009). Synthesis, electrochemistry and *in situ* spectroelectrochemistry of water-soluble phthalocyanines. *Transition Metal Chemistry* 34: 877–890.

35 Dinçer, H.A., Şener, M.K., Koca, A. et al. (2008). Synthesis, electrochemistry and in situ spectroelectrochemistry of soluble lead phthalocyanines. *Electrochimica Acta* 53: 3459–3467.

36 Nas, A., Kantekin, H., and Koca, A. (2015). Electrochemical and spectroelectrochemical analysis of 4-(4-(5-phenyl-1,3,4-oxadiazole-2-yl)phenoxy)-substituted cobalt(II), lead(II) and metal-free phthalocyanines. *Electroanalysis* 27: 1602–1609.

37 Kantekin, H., Sarkı, G., Koca, A. et al. (2015). Synthesis, structural characterizations, and electrochemical and spectroelectrochemical properties of novel peripherally octa-substituted metallophthalocyanines. *Journal of Organometalic Chemistry* 789–790: 53–62.

38 Demirbaş, Ü., Akyüz, D., Mermer, A. et al. (2016). The electrochemical and spectroelectrochemical properties of metal free and metallophthalocyanines containing triazole/piperazine units. *Spectrochimica Acta Part A: Molecular and Biomolecular Spectroscopy* 153: 478–487.

39 Nyokong, T. (1995). Electrochemistry of some second-row transition-metal phthalocyanine complexes. *South African Journal of Chemistry* 48: 23–29.

40 Lever, A.B.P., Milaeva, E.R., and Speier, G. (1993). The redox chemistry of metallophthalocyanines. In: *Phthalocyanine Properties and Applications*, vol. 3 (ed. C.C. Leznoff and A.B.P. Lever), 1–69. New York: VCH Publishers.

41 Nombona, N. and Nyokong, T. (2009). Synthesis, cyclic voltammetry and spectroelectrochemical studies of Co(II) phthalocyanines tetra-substituted at the α and β positions with phenylthio groups. *Dyes and Pigments* 80: 130–135.

42 Arıcı, M., Arıcan, D., Uğur, A.L. et al. (2013). Electrochemical and spectroelectrochemical characterization of newly synthesized manganese, cobalt, iron and copper phthalocyanines. *Electrochimica Acta* 87: 554–566.

43 Sevim, A.M., Yenilmez, H.Y., Aydemir, M. et al. (2014). Synthesis, electrochemical and spectroelectrochemical properties of novel phthalocyanine complexes of manganese, titanium and indium. *Electrochimica Acta* 137: 602–615.

44 Özçeşmeci, İ., Burat, A.K., İpek, Y. et al. (2013). Synthesis, electrochemical and spectroelectrochemical properties of phthalocyanines having extended π-electrons conjugation. *Electrochimica Acta* 89: 270–277.

45 Burat, A.K., Bayir, Z.A., and Koca, A. (2012). Synthesis and electrochemical and *in situ* spectroelectrochemical characterization of chloroindium(III) and chloromanganese(III) phthalocyanines bearing 4-([4′-trifluoromethyl]phenoxy)phenoxy substituents. *Electroanalysis* 24: 338–348.

46 Arican, D., Arici, M., Ugur, A.L. et al. (2013). Effects of peripheral and nonperipheral substitution to the spectroscopic, electrochemical and spectroelectrochemical properties of metallophthalocyanines. *Electrochimica Acta* 106: 541–555.

47 Obirai, J. and Nyokong, T. (2005). Synthesis, spectral and electrochemical characterization of mercaptopyrimidine-substituted cobalt, manganese and Zn (II) phthalocyanine complexes. *Electrochimica Acta* 50: 3296–3304.

48 Duruk, E.G., Yenilmez, H.Y., Koca, A., and Bayır, Z.A. (2015). Synthesis, electrochemical and spectroelectrochemical properties of thiazole-substituted phthalocyanines. *Synthetic Metals* 209: 361–368.

49 Sevim, M., Yaraşir, M.N., Koca, A., and Kandaz, M. (2014). Novel scorpion type phthalocyanine chemosensors for detection of selective-metal ion by inducing H- and J-aggregations in solution; synthesis, characterization and electrochemistry. *Dyes and Pigments* 111: 190–201.

50 Lever, A.B.P., Wilshire, J.P., and Quan, S.K. (1981). Oxidation of manganese(II) phthalocyanine by molecular oxygen. *Inorganic Chemistry* 20: 761–768.

51 Janczak, J., Kubiak, R., Śledź, M. et al. (2003). Synthesis, structural investigations and magnetic properties of dipyridinated manganese phthalocyanine, $MnPc(py)_2$. *Polyhedron* 22: 2689–2697.

52 Obirai, J., Pereira Rodrigues, N., Bedioui, F., and Nyokong, T. (2003). Synthesis, spectral and electrochemical properties of a new family of pyrrole substituted cobalt, iron, manganese, nickel and zinc phthalocyanine complexes. *Journal of Porphyrins and Phthalocyanines* 7: 508–520.

53 Agboola, B. and Nyokong, T. (2007). Comparative electrooxidation of nitrite by electropolymerised Co(II), Fe(II) and Mn(III) tetrakis benzylmercapto and dodecylmercapto metallophthalocyanines on gold electrodes. *Analytica Chimica Acta* 587: 116–123.

54 Leznoff, C.C., Black, L.S., Hiebert, A. et al. (2006). Red manganese phthalocyanines from highly hindered hexadecaalkoxy phthalocyanines. *Inorganica Chimica Acta* 359: 2690–2699.

55 Sehlotho, N., Durmuş, M., Ahsen, V., and Nyokong, T. (2008). The synthesis and electrochemical behaviour of water soluble manganese phthalocyanines: anion radical versus Mn(I) species. *Inorganic Chemistry Communictions* 11: 479–483.

56 Mashazi, P.N., Westbroek, P., Ozoemena, K.I., and Nyokong, T. (2007). Surface chemistry and electrocatalytic behaviour of tetra-carboxy substituted iron, cobalt and manganese phthalocyanine monolayers on gold electrode. *Electrochimica Acta* 53: 1858–1869.

57 Kadish, K.M., Bottomley, L.A., and Cheng, J.S. (1978). Electrochemical characterization of iron(II) and iron(I) phthalocyanine-amine derivatives. *Journal of the American Chemistry Society* 100: 2731–2737.

58 L'Her, M. and Pondaven, A. (2003). Electrochemistry of phthalocyanines. In: *The Porphyrin Handbook*, vol. 16 (ed. K.M. Kadish, K.M. Smith and R. Guilard), 117–170. New York, Chapter 104: Academic Press.

59 Canlica, M., Booysen, I.N., and Nyokong, T. (2011). Synthesis and electrochemical behaviour of novel peripherally and non-peripherally substituted ball-type cobalt phthalocyanine complexes. *Polyhedron* 30: 522–528.

60 Nyokong, T. (2006). *N_4-Macrocyclic Metal Complexes* (ed. J.H. Zagal, F. Bedioui and J.P. Dodelet), 315–347. New York: Springer.

61 Claußen, J.A., Ochoa, G., Páez, M.G. et al. (2008). Volcano correlations for the reactivity of surface-confined cobalt N4-macrocyclics for the electrocatalytic oxidation of 2-mercaptoacetate. *Journal of Solid State Electrochemistry* 12: 473–481.

62 Magdesieva, T.V., Yamamoto, T., Tryk, D.A., and Fujishima, A. (2002). Electrochemical reduction of CO_2 with transition metal phthalocyanine and porphyrin complexes supported on activated carbon fibers. *Journal of the Electrochemical Society* 149: D89–D95.

63 Sehlotho, N., Nyokong, T., Zagal, J.H., and Bedioui, F. (2006). Electrocatalysis of oxidation of 2-mercaptoethanol, L-cysteine and reduced glutathione by adsorbed and electrodeposited cobalt tetra phenoxypyrrole and tetra ethoxythiophene substituted phthalocyanines. *Electrochimica Acta* 51: 5125–5130.

64 Martin, C.S., Gouveia-Caridade, C., Crespilho, F.N. et al. (2016). Iron phthalocyanine electrodeposited films: characterization and influence on dopamine oxidation. *Journal of Physical Chemistry C* 120: 15698–15706.

65 Brown, K.L., Shaw, J., Ambrose, M., and Mottola, H.A. (2002). Voltammetric, chronocoulometric and spectroelectrochemical studies of electropolymerized films based on Co(III/II)- and Zn(II)-4,9,16,23-tetra aminophthalocyanine: Effect of high pH. *Microchemical Journal* 72: 285–298.

66 Trollund, E., Ardiles, P., Aguirre, M.J. et al. (2000). Spectroelectrochemical and electrical characterization of poly(cobalt-tetraaminophthalocyanine)-modified electrodes: electrocatalytic oxidation of hydrazine. *Polyhedron* 19: 2303–2312.

67 Alpatova, N.M., Ovsyannikova, E.V., Tomilova, L.G. et al. (2001). Anodic doping of electropolymerized copper 2,9,16,23-tetra aminophthalocyanine. *Russian Journal of Electrochemistry* 37: 1012–1016.

68 Goux, A., Bedioui, F., Robbiola, L., and Pontie, M. (2003). Nickel tetraaminophthalocyanine based films for the electrocatalytic activation of dopamine. *Electroanalysis* 15: 969–974.

69 Shahrokhian, S., Amini, M.K., Mohammadpoor-Baltork, I., and Tangestaninejad, S. (2000). Potentiometric detection of 2-mercaptobenzimidazole and 2-mercaptobenzothiazole at cobalt phthalocyanine modified carbon-paste electrode. *Electroanalysis* 12: 863–867.

70 Lowinsohn, D., Lee, P.T., and Compton, R.G. (2014). Electrocatalytic detection of glutathione – the search for new mediators. *Journal of the Brazilian Chemical Society* 25: 1614–1620.

71 Somashekarappa, M.P. and Sampath, S. (2002). Orientation dependent electrocatalysis using self-assembled molecular films. *Chemical Communications* 1262–1263.

72 Somashekarappa, M.P., Keshavayya, J., and Sampath, S. (2002). Self-assembled molecular films of tetraamino metal (Co, Cu, Fe) phthalocyanines on gold and silver. Electrochemical and spectroscopic characterization. *Pure and Applied Chemistry* 74: 1609–1620.

73 Revell, D.J., Chambrier, I., Cook, M.J., and Russell, D.A. (2000). Formation and spectroscopic characterization of self-assembled phthalocyanine monolayers. *Journal of Materials Chemistry* 10: 31–37.

74 Li, Z., Lieberman, M., and Hill, W. (2001). XPS and SERS study of silicon phthalocyanine monolayers: Umbrella versus octopus design strategies for formation of oriented SAMs. *Langmuir* 17: 4887–4894.

75 Ozoemena, K., Westbroek, P., and Nyokong, T. (2002). Cyclic voltammetric studies of octabutylthiophthalocyaninatocobalt(II) and its self-assembled monolayers (SAMs) on gold electrode. *Journal of Porphyrins and Phthalocyanines* 6: 98–106.

76 Delamar, M., Hitmi, R., Pinson, J., and Savéant, J.M. (1992). Covalent modification of carbon surfaces by grafting of functionalized aryl radicals produced from electrochemical reduction of diazonium salts. *Journal of the American Chemical Society* 114: 5883–5884.

77 Allongue, P., Delamar, M., Desbat, B. et al. (1997). Covalent modification of carbon surfaces by aryl radicals generated from the electrochemical reduction of diazonium salts. *Journal of the American Chemical Society* 119: 201–207.

78 Saby, C., Ortiz, B., Champagne, G.Y., and Bélanger, D. (1997). Electrochemical modification of glassy carbon electrode using aromatic diazonium salts. 1. Blocking effect of 4-nitrophenyl and 4-carboxyphenyl groups. *Langmuir* 13: 6805–6813.

79 Mashazi, P. and Nyokong, T. (2010). Electrocatalytic studies of covalently immobilized metal tetra-amino phthalocyanines onto derivatized, screen-printed gold electrodes. *Microchimica Acta* 171: 321–332.

80 Stewart, M.P., Maya, F., Kosynkin, D.V. et al. (2004). Direct covalent grafting of conjugated molecules onto Si, GaAs, and Pd surfaces from aryldiazonium salts. *Journal of the American Chemical Society* 126: 370–378.

81 Paulik, M.G., Brooksby, P.A., Abell, A.D., and Downard, A. (2007). Grafting aryl diazonium cations to polycrystalline gold: insights into film structure using gold oxide reduction, redox probe electrochemistry, and contact angle behavior. *Journal of Physical Chemistry C* 111: 7808–7815.

82 Bélanger, D. and Pinson, J. (2011). Electrografting: a powerful method for surface modification. *Chemical Society Reviews* 40: 3995–4048.

83 Coates, M. and Nyokong, T. (2012). Electrode modification using iron metallophthalocyanine through click chemistry and axial ligation with pyridine. *Journal of Electroanalytical Chemistry* 687: 111–116.

84 Kolb, H.C., Finn, M.G., and Sharpless, K.B. (2001). Click chemistry: diverse chemical function from a few good reactions. *Angewandte Chemie International Edition* 40: 2004–2021.

85 Rostovtsev, V.V., Green, L.G., Fokin, V.V., and Sharpless, K.B. (2002). A stepwise Huisgen cycloaddition process: Copper(I)-catalyzed regioselective "ligation" of azides and terminal alkynes. *Angewandte Chemie International Edition* 41: 2596–2599.

86 Nxele, S.R., Mashazi, P., and Nyokong, T. (2015). Electrode modification using alkynyl substituted Fe(II) phthalocyanine via electrografting and click chemistry for electrocatalysis. *Electroanalysis* 27: 2468–2478.

87 Wang, J. (2000). *Analytical Electrochemistry*, 2e. New York: Wiley-VCH.

88 Brett, C.M.A. and Brett, A.M.O. (1993). *Electrochemistry: Principles, Methods, and Applications*. Oxford: Oxford University Press.

89 Coates, M., Antunes, E., and Nyokong, T. (2010). Electrochemical, spectroscopic and microscopic studies of new manganese phthalocyanine complexes: in solution and as self-assembled monolayers on gold. *Journal of Porphyrins and Phthalocyanines* 14: 568–581.

90 Juodkazis, K., Juodkazyte, J., Šebeka, B., and Lukinskas, A. (1999). Cyclic voltammetric studies on the reduction of a gold oxide surface layer. *Electrochemistry Communications* 1: 315–318.

91 Macdonald, J.R. and Johnson, W.B. (2005). Fundamentals of impedance spectroscopy. In: *Impedance Spectroscroscopy Theory, Experiment and Application*, 2e (ed. E. Barsoukov and J.R. Macdonald), 1–26. Hoboken: Wiley-Interscience.

92 Mashazi, P., Togo, C., Limson, J., and Nyokong, T. (2010). Comparison of gold and glassy carbon electrodes modified with polymerized metal tetraaminophthalocyanines towards the detection of hydrogen peroxide. *Journal of Porphyrins and Phthalocyanines* 14: 252–263.

93 Lakshminarayanan, V. and Sur, U.K. (2003). Hydrophobicity-induced drying transition in alkanethiol self-assembled monolayer–water interface. *Pramana Journal of Physics* 61: 361–371.

94 Wittstock, G., Burchardt, M., and Pust, S.E. (2007). Applications of scanning electrochemical microscopy (SECM). In: *Applied Scanning Probe Methods VII: Biomimetics and Industrial Applications* (ed. B. Bhushan and H. Fuchs), 259–299. Springer.

95 Mirkin, M.V. and Horrocks, B.R. (2000). Electroanalytical measurements using the scanning electrochemical microscope. *Analytical Chimica Acta* 406: 119–146.

96 Nagy, G. and Nagy, L. (2000). Scanning electrochemical microscopy: a new way of making electrochemical experiments. *Fresenius Journal of Analytical Chemistry* 366: 735–744.

97 Schulze, R.K., Boyd, D.C., Evans, J.F., and Gladfelter, W.L. (1990). A variable temperature X-ray photoelectron spectroscopic study of the surface conversion of diethylaluminum azide to AlN. *Journal of Vacuum Science and Technology* 8: 2338–2343.

98 Watts, J.F. and Wolstenholme, J. (2003). *An Introduction to Surface Analysis by XPS and AES*. Chichester, UK: Wiley.

99 Coates, M. and Nyokong, T. (2013). X-ray photoelectron spectroscopy analysis of the effect of alkyl- and arylthio substituents on manganese phthalocyanines for self-assembled monolayer formation on gold. *Electrochemistry Communications* 31: 104–107.

100 Ozoemena, K.I., Nkosi, D., Nyokong, T. et al. (2007). Insights into the cyclic voltammetry and impedance spectroscopy of single-walled carbon nanotube – cobalt(II) tetra-aminophthalocyanine self-assembled on gold electrode. *Electrochimica Acta* 52: 4132–4143.

101 Geraldo, D., Togo, C., Limson, J., and Nyokong, T. (2008). Electrooxidation of hydrazine catalyzed by noncovalently functionalized single-walled carbon nanotubes with CoPc. *Electrochimica Acta* 53: 8051–8057.

102 Hipps, K.W., Lu, X., Wang, X.D., and Mazur, U. (1996). Metal *d*-orbital occupation-dependent images in the scanning tunneling microscopy of metal phthalocyanines. *Journal of Physical Chemistry* 100: 11207–11210.

103 Ozoemena, K., Westbroek, P., and Nyokong, T. (2003). Self-assembled monolayers of cobalt and iron phthalocyanine complexes on gold electrodes: comparative surface electrochemistry and electrocatalytic interaction with thiols and thiocyanate. *Electroanalysis* 15: 1762–1770.

104 Ozoemena, K.I. and Nyokong, T. (2005). Surface electrochemistry of iron phthalocyanine axially ligated to 4-mercaptopyridine self-assembled monolayers at gold electrode: applications to electrocatalytic oxidation and detection of thiocyanate. *Journal of Electroanalytical Chemistry* 579: 283–289.

105 Nombona, N., Tau, P., Sehlotho, N., and Nyokong, T. (2008). Electrochemical and electrocatalytic properties of α -substituted manganese and titanium phthalocyanines. *Electrochimica Acta* 53: 3139–3148.

106 Matemadombo, F., Griveau, S., Bedioui, F., and Nyokong, T. (2008). Electrochemical characterization of self-assembled monolayer of a novel manganese tetra benzyl thio-substituted phthalocyanine and its use in nitrite oxidation. *Electroanalysis* 20: 1863–1872.

16

Heme Proteins – Structure and Function

Sk Amanullah, Chandradeep Ghosh, Somdatta Ghosh Dey and Abhishek Dey

School of Chemical Sciences, Indian Association for the Cultivation of Science, Kolkata, India

Abbreviations

Arg	arginine
Asp	aspartic acid
ATP	adenosine triphosphate
CcO	cytochrome c oxidase
CCP	cytochrome c peroxidase
Cys	cysteine
Cyt	cytochrome
DNA	deoxyribonucleic acid
EPR	electron paramagnetic resonance
Glu	glutamic acid
Gly	glycine
Hb	hemoglobin
His	histidine
HO	heme oxygenase
HRP	horseradish peroxidase
Mb	myoglobin
NADH	reduced form of nicotinamide adenine dinucleotide
NADPH	reduced form of nicotinamide adenine dinucleotide phosphate
NHE	normal hydrogen electrode
NiR	nitrite reductase
NOR	nitric oxide reductase
PDB	Protein Data Bank
pO_2	partial pressure of oxygen
ROS	reactive oxygen species
Tyr	tyrosine

16.1 Introduction

Heme, a commonly found cofactor in various biomolecules, consists of the tetrapyrrole protoporphyrin IX, which encapsulates a single iron atom. The iron is coordinated to the four

Fundamentals of Porphyrin Chemistry: A 21st Century Approach, Volume 2, First Edition.
Edited by Penelope J. Brothers and Mathias O. Senge.
© 2022 John Wiley & Sons Ltd. Published 2022 by John Wiley & Sons Ltd.

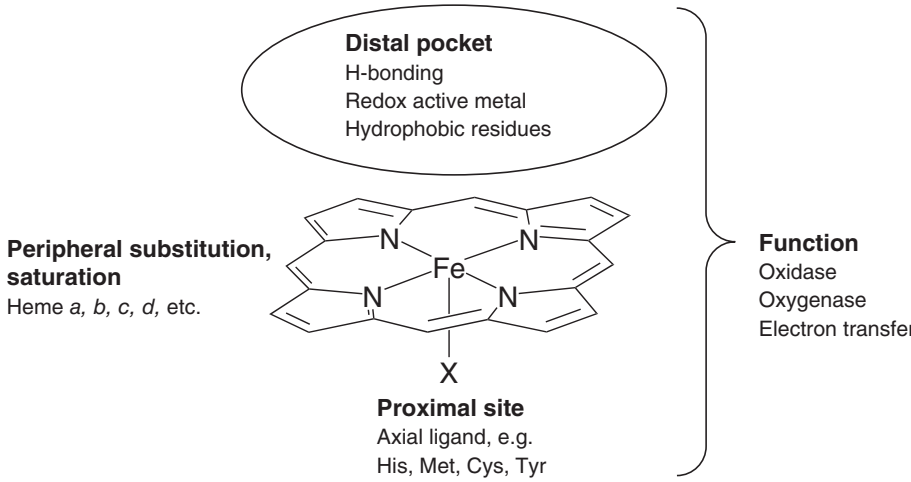

Figure 16.1 The basic organization of the active site of different heme proteins found in nature.

porphyrin nitrogen atoms, while one or both of the axial sites are ligated to an amino acid residue that links the heme to the protein. The porphyrin macrocycle skeleton itself is modified in different heme proteins. Six-coordinate heme units with two amino acid residues as the axial ligands are usually found in electron transfer proteins, like the cytochromes. Oxygen binding or substrate binding heme proteins either have a vacant sixth axial site or a weakly bound sixth ligand that can be easily displaced by oxygen or a substrate (Figure 16.1).

Heme cofactors are quite ubiquitous and are present in almost all known higher life forms. The best-known heme protein is hemoglobin, the protein that carries oxygen for cellular function and gives blood its characteristic red color [1]. Another well-known heme protein is cytochrome P450. The cytochrome P450 superfamily is involved in the biosynthesis of steroids and hormones, catabolism of organic food, and breakdown of drugs in the liver [2]. These transformations involve oxidation of inert organic molecules using O_2, which is activated by cytochrome P450. Similarly, the heme enzyme catalase acts to induce the disproportionation of the reactive oxygen species (ROS) H_2O_2, thereby protecting living cells against oxidative damage [3]. Cytochrome P450 and heme dioxygenases are both capable of performing facile oxidations of organic molecules using molecular oxygen [2, 4]. Cytochrome c oxidase (CcO) is another important heme protein that catalyzes the reduction of O_2 to H_2O in the mitochondria [5–7]. The energy obtained during oxygen reduction is utilized to produce ATP through oxidative phosphorylation, and it is because of this that mitochondria are known as the powerhouses of cells. The electrons needed for the reduction of oxygen are delivered by yet another important heme protein, cytochrome c (cyt c) [8, 9]. cyt c, an electron transfer protein, is an important signaling protein that controls respiration and signals apoptosis (programmed cell death) [10, 11]. The critical physiological roles played by these enzymes are of interest to the chemical and pharma industries, which seek to develop systems that replicate their selectivity and activity. The last century has witnessed substantial research on understanding how these enzymes work, with the goal of either intercepting their function to control biological processes for drug development or to emulate their function in artificial systems via the development of new catalysts or reagents.

Heme cofactors exhibit substantial variations in the structure of the basic tetrapyrrole macrocycles. These variations include different peripheral substituents as well as different extents of saturation of the tetrapyrrole core. In addition to the basic hemes *a*, *b,* and *c*, shown in Figure 16.2, several more variants of heme are found in nature. Apart from the

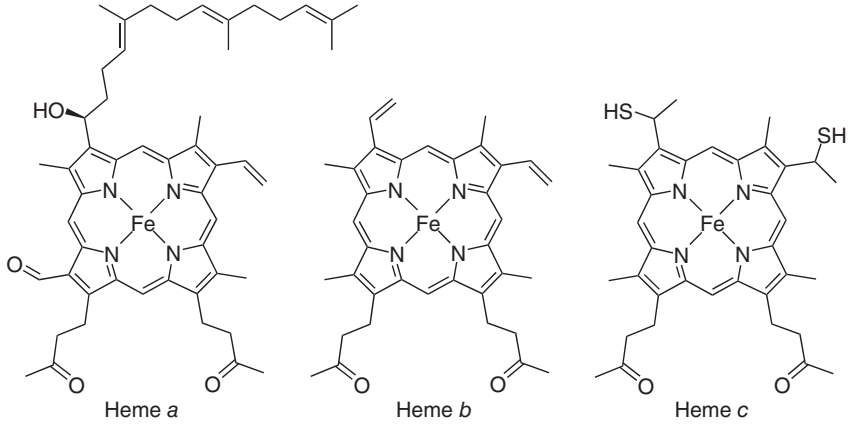

Figure 16.2 Heme *a*, *b*, and *c* cofactors.

fully unsaturated derivatives, which are found in the oxygen-activating enzymes mentioned earlier, partially saturated analogues are abundant in microbes and bacteria and have facilitated chemical transformations involved in maintaining the ecological balance in the environment [12]. For example, sulfite reductases and nitrite reductases are key enzymes in the global sulfur and nitrogen cycles, respectively [13, 14]. These proteins are generally found in organisms that grow in oxygen-free anoxic environments, and thus they were difficult to identify and purify. As a result, very little is known about this large class of heme proteins, which are vital for maintaining the ecological balance on our planet.

The fact that the same cofactor can catalyze such a diverse set of chemical reactions has fascinated researchers and sparked much of the research into their structure and function. Structurally subtle variations in the axial ligand and variations of weak interactions beyond the immediate iron coordination sphere, commonly referred to as second sphere interactions, are responsible for this diversity in reactivity [15, 16]. This has prompted investigations into the differences in electronic structure that also contribute to the diversity of chemical reactivity. The heme cofactor with an intense Soret band and a paramagnetic iron center at the middle is very amenable to spectroscopic investigations using an array of techniques. These include absorption spectroscopy, X-ray absorption spectroscopy (XAS), resonance Raman (rR) spectroscopy, electron paramagnetic resonance (EPR) spectroscopy, Mossbauer spectroscopy, and nuclear magnetic resonance (NMR) spectroscopy. In fact, there are no other known metalloproteins that can be probed with so many distinct spectroscopic tools. As a result, the literature on heme enzymes is substantially larger than any other metalloenzymes and can be overwhelming. The goal of this chapter is to summarize the structure–function correlations discovered for a few important heme enzymes to serve as exemplars.

16.2 Myoglobin and Hemoglobin

16.2.1 Function and Structure

Oxygen has poor solubility in aqueous media (40 mg L^{-1} at 25 °C) and therefore cannot be carried to tissues in sufficient quantity if it is simply dissolved in blood serum. The diffusion of oxygen through tissues is also insufficient to serve the cellular demand. The evolution of complex multicellular organisms led to the evolution of proteins that could transport and store oxygen. Hemoglobin (Hb, molecular weight 64 500 g mol^{-1} = 64.5 kDa) is the protein that carries oxygen from the lungs through the arteries to the tissues, and on the return trip,

takes the carbon dioxide that has been produced in the cells, as a result of cellular respiration, through the veins back to the lungs. Hemoglobin is found in the red blood cells. Each red blood cell contains about 280 million Hb units, comprising approximately one third of the mass of a mammalian red blood cell. Myoglobin (Mb, 16.7 kDa) is a relatively simple oxygen-binding protein found in almost all mammals, primarily in muscle tissue. In the late 1950s, the first X-ray crystal structures of Mb and Hb were solved, and currently crystal structures of Mb are available in several ligation states and conformations.

Hb is a tetrameric protein and consists of four polypeptide chains (Figure 16.3a), two alpha globin subunits, (α1 and α2 chains), and two beta globin subunits, or (β1 and β2 chains), while Mb is a monomeric protein (Figure 16.3b). Each subunit binds one heme. The alpha and beta globin subunits are composed of 141 and 146 amino acids, respectively. The alpha and beta chains have very similar secondary and tertiary structures, and fold into eight or nine α-helical segments. Hydrophobic interactions predominate at the α1β1 and α2β2 interfaces, but there are also many hydrogen bonds and a few ion pairs or salt bridges [19–21]. Mb is a single polypeptide of 153 amino acid residues and one heme.

The oxygen binding sites in Hb and Mb are very similar. In its deoxygenated form (Figure 16.3c), the ferrous ion of the heme (heme *b*; see Figure 16.2) is in a five-coordinate,

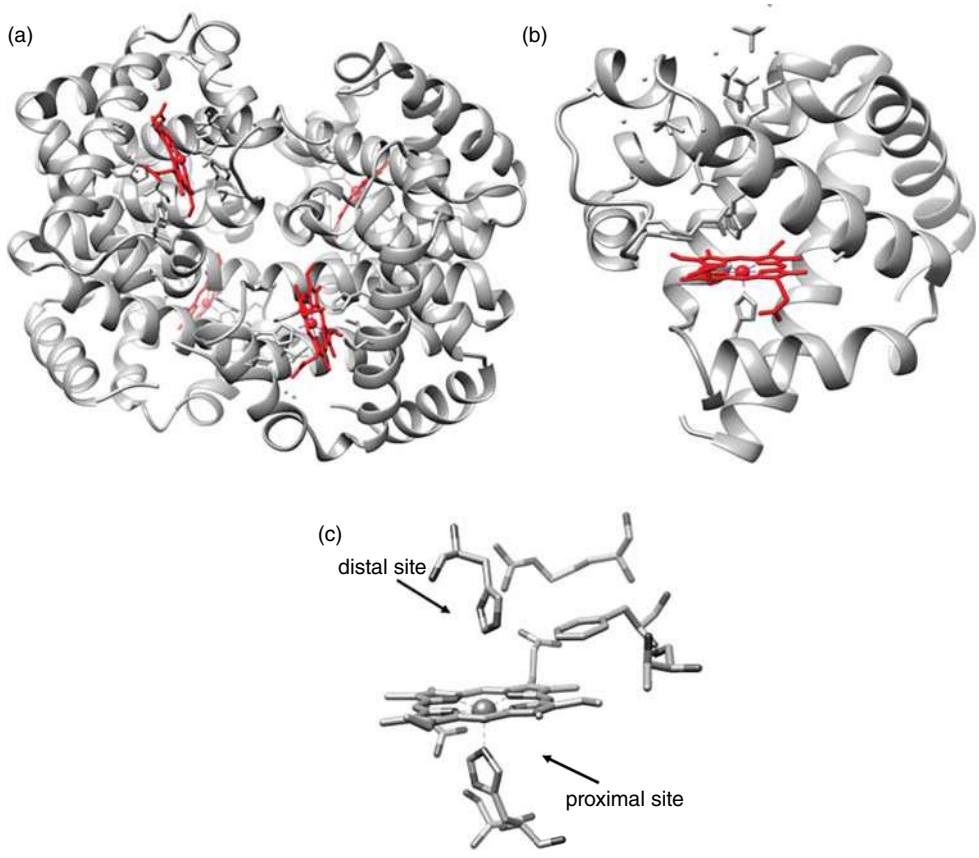

Figure 16.3 Tertiary structure of (a) hemoglobin (PDB id: 1A3N); (b) myoglobin (PDB id: 1A6N); and (c) active site environment of the heme center in both the proteins (drawn using Chimera 1.12rc software). Source: Based on Tame and Vallone [17]; Vojtechovsky et al. [18].

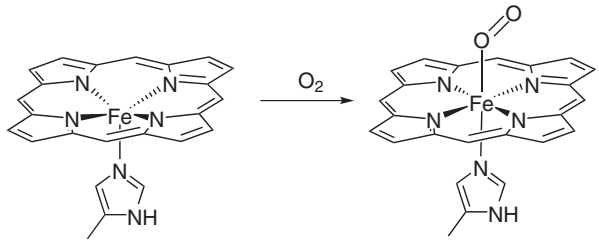

Figure 16.4 Schematic diagram of the oxy-adduct and the deoxy form of hemoglobin and myoglobin.

high-spin state ($S = 2$), with histidine serving as the axial ligand. The ligand attached directly to the heme from the protein backbone is termed the proximal ligand. The ferrous ion is displaced 0.5 Å out of the heme mean 24-atom plane toward the proximal histidine. In the oxygenated form, dioxygen binds at the sixth (distal) vacant coordination site [22] with the Fe-O-O angle in the range 115–130° (Figure 16.4). The six-coordinate iron atom lies in the heme plane and is diamagnetic ($S = 0$) with a controversial electronic structure [23]. Some experimental studies define the electronic structure of the heme iron oxygen complex as a low-spin Fe^{3+} ($S = ½$) species antiferromagnetically coupled to a superoxide ion (O_2^-, $S = ½$). This has been supported by the IR stretching frequency of the FeO-O bond, which has been measured at 1105 cm^{-1}. Some theoretical calculations define the system as having an intermediate ferrous species ($S = 1$) antiferromagnetically coupled to oxygen (O_2, $S = 1$), while more recent calculations define it as a combination of the above two. Experimentally, this has not been very accessible to the usual physical methods, and theoretically it has been challenging to calculate due to electron delocalization over the heme porphyrin ring.

16.2.2 Oxygen Binding to Hemoglobin

Iron in the Fe^{2+} state reversibly binds oxygen, and the oxidized Fe^{3+} state, also known as the met form, is toxic [22]. When oxygen binds, the electronic properties of heme iron change. There is a change in color of oxygen-depleted venous blood from dark purple to the bright red of oxygen-rich arterial blood. The globin chains in Hb are folded around the heme molecule in such a way that they prevent two heme molecules from coming together in the presence of oxygen to form an irreversible undesirable μ-oxo dinuclear compound. Since each Hb molecule has four globins and four heme groups, it can carry up to four molecules of oxygen. There are two major conformations of hemoglobin, the R state and the T state, which originally denoted "tense" and "relaxed," respectively [24]. Although O_2 binds to hemoglobin in either state, O_2 binding stabilizes the R state, and it has a significantly higher affinity for hemoglobin in the R state. The T state is more stable in the absence of oxygen and is thus the predominant conformation of deoxyhemoglobin [25]. The binding of O_2 to the T state of hemoglobin induces a change in conformation to the R state. During the transition from the T to the R state, there is no drastic change in the structures of the individual subunits, but in this process, some of the ion pairs that stabilize the T state are broken and some new ones are formed. Max Perutz proposed that the T to R transition is triggered by changes in the positions of key amino acid side chains surrounding the heme. In the T state, the Fe of the heme protrudes out of the porphyrin plane toward the proximal His.

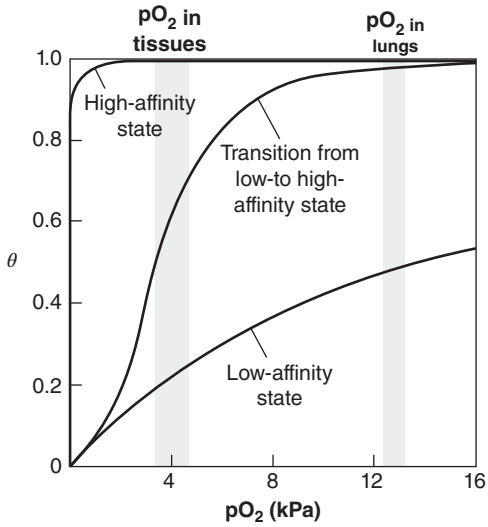

Figure 16.5 A sigmoid (cooperative) binding curve; θ is the fraction of the ligand binding sites that are occupied by the ligand. Source: Diagram reproduced with permission from Nelson and Cox [1].

On binding O_2, the Fe is pulled into the plane of the porphyrin to assume a more planar conformation.

Mb or any protein that binds oxygen with a hyperbolic binding curve is not well suited for the function of delivering O_2 from the lungs to the tissues [26]. A protein with a high affinity for O_2 would bind it efficiently in the lungs, but would not release much of it in the required tissues. On the other hand, a protein with a low affinity for O_2 would release the bound O_2, but would not bind much oxygen in the lungs. Hb, which efficiently binds O_2 in the lungs where the pO_2 is about 13.3 kPa, and releases O_2 in the tissues where the pO_2 is about 4 kPa, is well suited for this function. The transition from the low-affinity T state to the high-affinity R state structure in the presence of O_2 enables efficient O_2 binding and transfer in Hb. This results in a hybrid S-shaped or sigmoid O_2 binding curve for Hb (Figure 16.5).

When O_2 binds to one subunit of Hb, it alters the affinity of the remaining three subunits for O_2. The first O_2 molecule weakly binds to the heme of one Hb subunit, initially in the deoxy T state form. This leads to conformational changes in which the T state undergoes a transition into the R state so that binding of subsequent O_2 molecules to the remaining three Hb subunits becomes easier. When the fourth O_2 molecule binds, the heme is already in the R state, and hence it binds O_2 with a much higher affinity. This phenomenon is called cooperative binding. Hb is an allosteric protein, where binding of a ligand to one site affects the binding properties of another site on the same protein. This type of cooperative binding of a ligand to a protein is a form of allosteric binding often observed in multimeric proteins. Because of the sigmoidal relationship characteristic of the cooperative binding phenomenon, hemoglobin not only responds quickly but also very effectively to small changes in oxygen demand [27].

Cooperative binding of oxygen by hemoglobin that has later been generalized for ligand binding to multi-subunit proteins was first analyzed by Archibald Hill in 1910 [28, 29]. A sigmoid binding curve can be viewed as a hybrid curve reflecting a transition from a low-affinity to a high-affinity state. Cooperative binding, as manifested by a sigmoid binding curve, renders hemoglobin more sensitive to the small differences in O_2 concentration between the tissues and the lungs, allowing hemoglobin to bind oxygen in the lungs (where pO_2 is high)

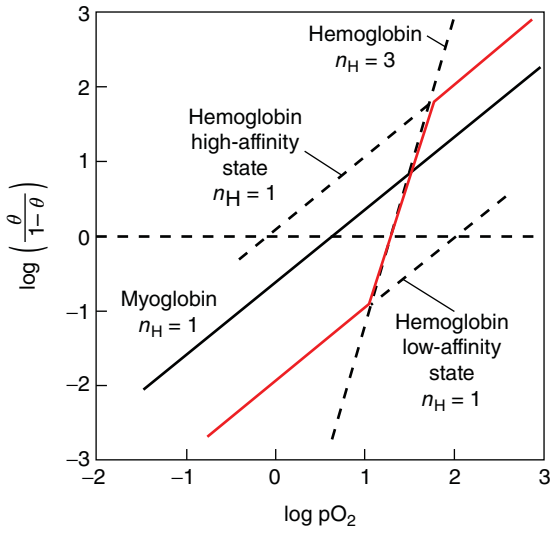

Figure 16.6 Hill plots for the binding of oxygen to myoglobin and hemoglobin. Source: Diagram reproduced with permission from Nelson and Cox [1].

and release it in the tissues (where pO_2 is low).

$$\log\left[\theta/(1-\theta)\right] = n\ \log\ [\mathrm{L}] - \log\ \mathrm{K_d} \tag{16.1}$$

$$\log\left[\theta/(1-\theta)\right] = n\ \log\ pO_2 - n\ \log\ P^{n}{}_{50} \tag{16.2}$$

Equations 16.1 and 16.2 shows the Hill equation, where θ is the fraction of the ligand binding sites that are occupied by the ligand, [L] is the concentration of the free ligand, n is the number of ligand binding sites, and K_d is the ligand dissociation constant. Expressed in terms of pressure (Eq. 16.2), $P^{n}{}_{50}$ is the partial pressure of oxygen at which half of the ligand binding sites are occupied. A plot of log θ/(1- θ) versus log[L] is called a Hill plot, where n can be obtained from the slope of the plot (Figure 16.6). However, the experimentally obtained value of n from the slope of the Hill plot does not reflect the number of binding sites but the degree of interaction between them. Thus, the slope of a Hill plot is depicted by n_H, the Hill coefficient, which is a measure of the degree of cooperativity [28].

When ligand binding is not cooperative, $n_H = 1$, as is observed in the case of Mb. In proteins with multiple subunits, $n_H = 1$ if the subunits do not communicate. Values of $n_H > 1$ indicate a positive cooperative effect, as observed in hemoglobin, in which the binding of one molecule of ligand facilitates the binding of subsequent ones. Theoretically, the maximum value of $n_H = n$, when the binding is completely cooperative. In this case, all binding sites on the protein would simultaneously bind ligands. Values of $n_H < 1$ indicates negative cooperative binding, where binding of one molecule of ligand hinders the binding of subsequent ligands [1]. Hemoglobin exhibits allosteric binding behavior with a maximum degree of cooperativity of $n_H = 3$.

There are several chemical factors that contribute to the ability of hemoglobin to release oxygen, for example, the presence of CO, CO_2 and 2,3-diphosphoglycerate in the blood. Hemoglobin, like other proteins, is also sensitive to changes in pH and temperature.

16.2.3 Carbon Monoxide Binding to Hemoglobin

Carbon monoxide (CO) is a colorless, odorless gas. CO has an approximately 250 times greater affinity for Hb than does oxygen. CO combines with Hb to form a stable complex known

as carboxyhemoglobin, or COHb. When CO binds to Hb, it cannot be released as easily as oxygen. The slow release rate of CO causes an accumulation of COHb in the blood as exposure to CO continues. Because of this, fewer Hb molecules are available to bind and deliver oxygen. Consequently, gradual suffocation is associated with CO poisoning. In healthy individuals, on average 1% or less of the total Hb is complexed as COHb. When less than 10% of the total Hb exists as COHb, symptoms are rarely observed because Hb and Mb are clearly designed by nature to transport and store oxygen in the presence of the endogenous poisonous gasses like CO. Steric, electrostatic, and H-bonding properties of the distal pocket appear to assist Mb and Hb to discriminate between CO and oxygen. The distal oxygen in oxy-Hb is stabilized by a hydrogen-bonding interaction from the distal His residue. A distal valine residue on top of the heme cofactor disfavors binding of CO, as metal carbonyl complexes prefer a linear geometry and favor binding of O_2 as the Fe-O-O angle is bent (115°–130°). As a result, the binding of CO to the heme active site of Hb is not as strong as that of free heme. When 15% of the total Hb is complexed as COHb, the individual experiences mild headaches. At 20%–30%, the headache is severe and is generally accompanied by nausea, dizziness, confusion, disorientation, and some visual disturbances. However, if the individual is exposed to oxygen, these symptoms are generally reversed. At COHb levels of 30%–50%, the neurological symptoms become more severe, and at levels near 50% the individual loses consciousness and may go into coma and may suffer from respiratory failure. Normally death occurs when COHb levels rise above 60%. It is important to note that CO not only binds to Hb but also to other heme proteins and a variety of other metalloproteins.

16.2.4 Carbon Dioxide and Proton Transport by Hemoglobin

In addition to carrying oxygen, Hb also carries the two products of respiration: CO_2 and H^+. Since CO_2 is not very soluble in aqueous media, it is converted to bicarbonate, which leads to an increase in the H^+ ion concentration or a decrease in pH in the tissues ($CO_2 + H_2O \leftrightharpoons H^+ + HCO_3^-$). The binding of oxygen by Hb depends on the pH and CO_2 concentration [30]. At high CO_2 concentration and at a relatively low pH, the oxygen affinity of Hb is low, and it readily releases O_2 to the tissues. In contrast, CO_2 gets excreted from the lungs, as a result of which the pH of the blood increases, increasing the affinity of Hb for oxygen, which will be transported to the tissues. This effect of CO_2 and pH on the binding and release of oxygen by Hb is called the Bohr effect and is crucial in removing CO_2 from the tissue as well as in regulating oxygen delivery to the tissues that are in need of oxygen [31]. Temperature does not have as much of an effect as the previously described factors, although hyperthermia (low body temperature) causes a rightward shift and hypothermia (high body temperature) causes a leftward shift in the oxygen dissociation curve of Hb.

Fetal hemoglobin (HbF) is structurally different from normal Hb. Typically, fetal arterial oxygen pressures are lower than adult arterial oxygen pressures (Figure 16.7). Hence, higher affinity is required to bind oxygen at lower levels of partial pressure (pO_2) in the fetus to allow diffusion of oxygen across the placenta. The fetal dissociation curve is shifted to the left relative to the curve for the normal adult.

Several genetic variations of Hb are known to occur in human beings. The variant genes are called alleles. The effects of the genetic variations on the structure and function of Hb are often minor, but can sometimes be devastating. Sickle-cell anemia is a genetic disease caused by a single amino acid substitution (Val6Glu in the two β chains), in which an individual has inherited the allele for sickle-cell hemoglobin from both parents. The normal erythrocytes are

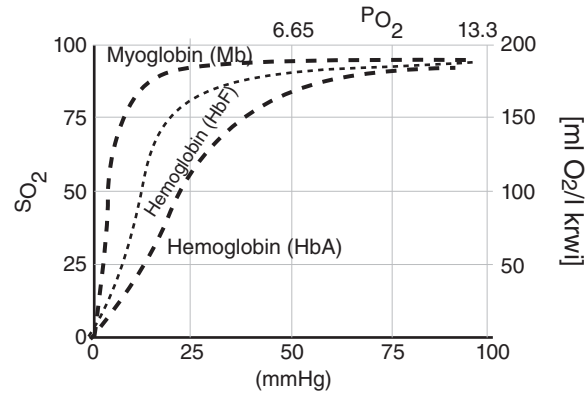

Figure 16.7 Difference in oxygen affinity between myoglobin (Mb), hemoglobin (HbA), and fetal hemoglobin (HbF). P_{O2} and S_{O2} are the partial pressure and saturation of oxygen, respectively.

fewer. There many long, thin crescent-shaped erythrocytes that look like the blade of a sickle, called hemoglobin S. Deoxygenated hemoglobin S is insoluble and tends to form aggregates because of increased hydrophobic interactions introduced due to the mutation of negatively charged glutamate to hydrophobic valine residue. Sickle-cell anemia is a life-threatening and painful disease. Without medical treatment, people with sickle-cell anemia usually die in their childhood [32]. People with sickle-cell anemia cannot tolerate physical exertion. They become weak, dizzy, and short of breath and experience heart murmurs and an increased pulse rate. The Hb content of their blood is only about half the normal value, as sickled cells are very fragile and rupture easily, resulting in anemia. Additionally, the capillaries become blocked by the long, sickle-shaped red blood cells, causing severe pain and interfering with the normal functioning of the body [32].

16.3 Cytochrome c

16.3.1 Function and Structure

Cytochrome c (cyt c) is a heme protein that is localized in the compartment between the inner and outer mitochondrial membranes, where its function is to transfer electrons between complex III (Coenzyme Q – cytochrome c reductase) and complex IV (CcO) of the respiratory chain. It is critical for sustaining cellular life through an elaborate electron–proton energy transduction mechanism that is responsible for the synthesis of ATP, the major energy currency molecule in living organisms [8]. This small heme protein (mol. wt. 12000) is found loosely associated with the inner membrane of the mitochondrion in plants, animals, and many unicellular organisms [33]. It is a unique protein capable of undergoing redox reactions, but does not bind oxygen. The protein gets its name ("cyto"–"chrome") from its characteristic intense red color that resembles the color of the cell [33]. The term *cytochrome* dates back to 1925, when Keilin introduced it to describe a group of heme proteins undergoing oxidation/reduction reactions, characterized in the reduced form by intense absorption bands in the 510–615 nm range [34]. Since then, the gradual build-up of knowledge on cytochromes increasingly suggested that their diversity would make it extremely difficult to find a simple basis for a complete classification of these proteins. As a result, no systematic nomenclature of cytochromes has yet been fixed, beyond their deep-rooted designation as cytochrome a, b, c, or d depending on the type and the binding mode of the heme moiety (see Figure 16.2).

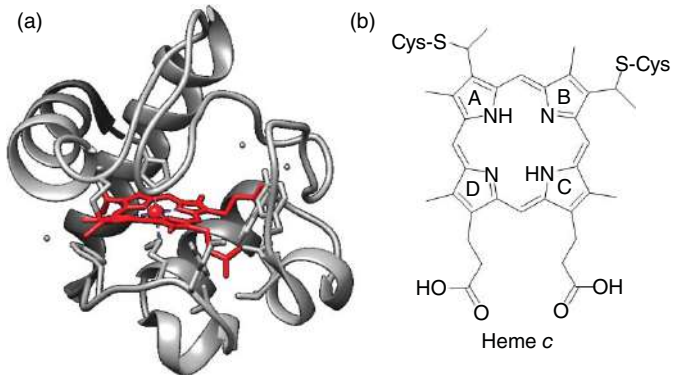

Figure 16.8 (a) Active site structure of cytochrome c (PDB id: 1HRC) [36] (drawn using Chimera 1.12rc software); and (b) heme *c* showing A, B, C, and D pyrrole rings.

Within the cyt c group, two main nomenclatures have been used to label the experimentally characterized subgroups, using subscripts. In the first system, a progressive numbering of the subscripts has been used to identify different functional classes (such as cytochrome c1, c2, and so on), but this has not been applied consistently over the years. In the second system, subscripts are assigned based on the experimental wavelength (in nanometers) of the so-called α-band in the visible absorption spectrum of the reduced protein (such as cytochrome c550, c551, and so on) [35]. The four pyrrole rings of the heme *c* are in different chemical environments because they are adjacent to different protein amino acid residues, and hence these four rings have been assigned as A, B, C, and D, respectively (Figure 16.8) [37]. The heme is buried inside the protein pocket, and the Fe is coordinatively saturated with a histidine and methionine axial ligands that makes the protein unable to carry out small molecule activation like O_2 or NO or act as a O_2 transport protein (Figure 16.9). Alternatively, the low reorganization energy owing to efficient delocalization of the charge acquired or lost during reduction or oxidation into the porphyrin ring allows this protein to work efficiently as electron transfer proteins, where the oxidation state of the central iron cycles between the Fe^{III}/Fe^{II} states. The reduction potential of cytochromes can vary between 300 mV to 150 mV versus NHE.

The three-dimensional structure of mitochondrial cyt c was first solved in the 1970s [38]. Most of the monohemic cyt c domains display a single Cys-Xaa-Xaa-Cys-His (CXXCH) motif for covalent attachment of the heme through the cysteines and axial coordination of the iron through the histidine side chain [39]. The typical cyt c fold consists of five α-helices of different length interconnected by extended Ω loops, in addition to a couple of very short two-stranded antiparallel β-sheets. The heme group is almost completely buried inside a hydrophobic pocket with only the edge of pyrrole B partially solvent exposed. The two propionate substituents from rings C and D are shielded from the bulk solvent and stabilized by interactions with polar side chains of amino acids. Four highly conserved residues are responsible for the tight binding and primary electronic properties of the heme: Cys14, Cys17, and His18 belonging to the CXXCH motif and Met80 (amino acid sequence numbering of horse heart cyt c). The two cysteines form covalent thioether bonds with the vinyl substituents of pyrrole rings A and B, while His18 and Met80 are the proximal and distal axial ligands of the heme iron. Only in a few cases is the heme attached via a single thioether bond [40, 41].

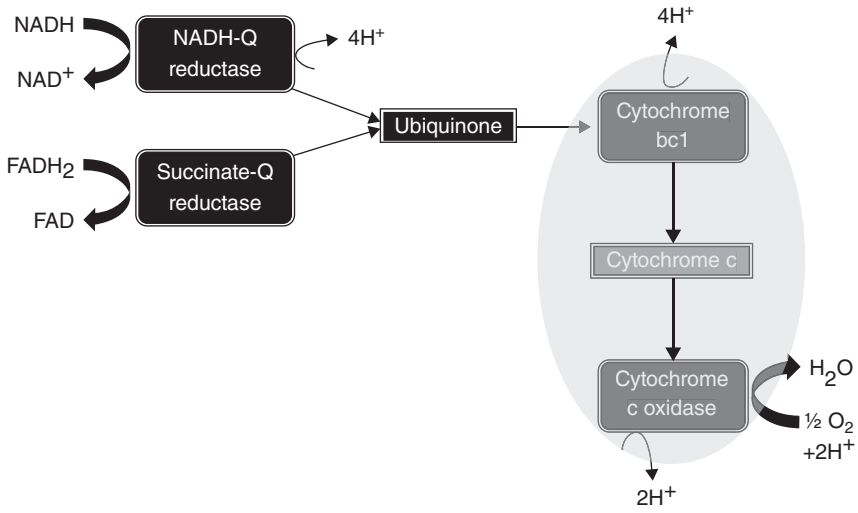

Figure 16.9 Schematic diagram of the electron flow by cyt c.

The heme group is slightly saddled, with the vinyl-substituted rings A and B exhibiting the strongest deviations from the average tetrapyrrole plane [42, 43].

16.3.2 Alternative Functions of Cytochrome c

The cyt c functions essentially as an electron transfer protein that is mainly involved in aerobic as well as anaerobic respiration. In mammalian cells, cyt c is also involved in apoptosis [11]. Owing to the more recent discovery of the involvement of cyt c in the latter process, there are still several important questions to be answered, such as how widespread the cyt c dependent pathway of cell death is. Very recently, it has been reported that in mammalian mitochondria, the enzyme p66Shc can oxidize cyt c to generate reactive oxygen species, which act as signaling molecules for apoptosis [10]. Mitochondrial cyt c appears to be necessary for the assembly of the membrane protein CcO [9]. A minor but interesting role for cytochrome c in Eukaryota is in the pathway of hydrogen peroxide scavenging [44]. Cyt c is also widespread in the bacterial world, where it takes part in biochemical processes such as respiration and H_2O_2 scavenging, as well as in a number of other pathways. In particular, it is not uncommon for cyt c to be fused to redox enzymes and constitute an entry/exit point for electrons in the catalytic cycle of several enzymes.

16.4 CcO

16.4.1 Function and Structure

CcO is the terminal enzyme in the respiratory electron transport chain of the mitochondria (or bacteria) located in the mitochondrial (or bacterial) membrane. It reduces oxygen to water in a process called oxidative phosphorylation. During oxygen reduction, it translocates four protons across the membrane, helping to establish a trans-membrane proton electrochemical gradient that the ATP synthase then utilizes to synthesize ATP. The electrons for $4e^-/4H^+$ O_2

reduction are obtained from cyt c (Section 16.3). Thus, CcO catalyzes the reduction of dioxygen to water and converts the released energy into an electrochemical proton gradient that subsequently drives the synthesis of ATP [6, 7, 45]. The overall reaction can be summarized in Eq. (16.3).

$$4\ Fe^{II}\text{-Cyt C} + O_2 \xrightarrow[CcO]{8\ H^+ \quad 4\ H^+} 4\ Fe^{III}\text{-Cyt C} + 2\ H_2O \tag{16.3}$$

CcO was discovered in 1924, and in 1995 the X-ray structures of both bovine and bacterial CcO's were reported at 2.8 Å resolution [46, 47], which subsequently was improved to 1.8 Å in 2010 [7]. Crystal structures of CcO reveal that it contains four redox-active metal sites, designated as Cu_A, heme *a*, Cu_B, and heme a_3 (Figure 16.10a). The largest subunit (subunit I), contains heme *a*, heme a_3, and Cu_B. Another copper site, Cu_A, is located in the third largest subunit (subunit II). A magnesium ion bridges Glu198 of subunit II and His368 of subunit I [49]. The second largest subunit (subunit III) contains three phospholipids that define the O_2 channel [50]. The Cu_A is a binuclear copper site where the two coppers are bridged by two cysteine residues present in a cupredoxin-type fold. The Cu_A is the site that initially accepts an electron from the donor, cyt *c* [6, 51–53]. There exists an electron transfer pathway from Cu_A to heme *a* via His204, one of the ligands of Cu_A. The amide carbonyl group of His204 is coordinated to the peptide NH group of R^{438}, which in turn hydrogen-bonds to one of the propionate groups of heme *a* [49]. There is no direct experimental evidence suggesting direct electron transfer from Cu_A to heme a_3. The copper atoms in Cu_A shuttle between a mixed-valent Cu^{2+}-Cu^+ redox state to a fully reduced Cu^+-Cu^+ state on accepting an electron from cytochrome *c*.

Unlike heme *b* in hemoglobin and myoglobin, the two heme *a* and heme a_3 centers have different structures: one of the methyl groups is replaced by a formyl group and one vinyl group is replaced by a hydroxyfarnesylethyl group (Figure 16.2) [54]. Heme *a* and heme a_3 are connected through their axial histidine ligands (His-Phe-His linker) having an interplanar angle of 104° and a Fe···Fe distance of 13.4 Å. The electron transferred from the Cu_A site to the heme *a* is subsequently transferred to the heme a_3 site. So the electron flow is cyt c to Cu_A to heme *a* to binuclear heme a_3-Cu_B site [55].

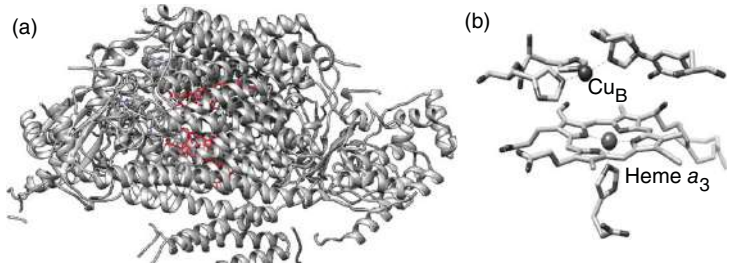

Figure 16.10 (a) Crystal structure of CcO from bovine heart (PDB id: 1OCR); and (b) structure of the binuclear active site for dioxygen activity from fully reduced (Fe^{II}…Cu^I) bovine heart cytochrome c oxidase (drawn using Chimera 1.12rc software). Source: Based on Yoshikawa et al. [48].

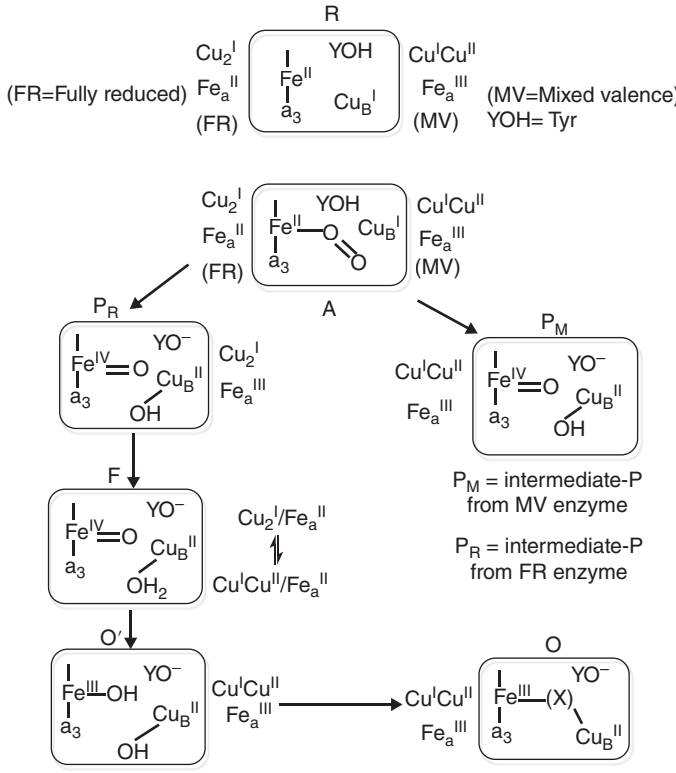

Figure 16.11 Schematic diagram for the intermediates involved in O_2 reduction.

16.4.2 Mechanism of the O_2 Reduction Reaction

A variety of biochemical and spectroscopic methods have been applied to study the O_2 reduction chemistry of CcO, occurring at the binuclear heme a_3-Cu_B center [56–58]. Three different redox states are accessible, as shown below and in Figure 16.11.

Fully reduced (FR)	$\{Cu^ICu^I\}_A$	Fe_a^{II}	Fe_{a3}^{II}	Cu_B^I	TyrOH
Mixed-valence (MV)	$\{Cu^ICu^{II}\}_A$	Fe_a^{III}	Fe_{a3}^{II}	Cu_B^I	TyrOH
Fully oxidized	$\{Cu^{II}Cu^{II}\}_A$	Fe_a^{III}	Fe_{a3}^{III}	Cu_B^I	TyrOH
Intermediate P from FR (P_R)	$\{Cu^ICu^{II}\}_A$	Fe_a^{III}	Fe_{a3}^{IV}=O	Cu_B^{II}	TyrOH
Intermediate P from MV (P_M)	$\{Cu^ICu^{II}\}_A$	Fe_a^{III}	Fe_{a3}^{IV}=O	Cu_B^{II}	TyrO·

Fully reduced CcO can donate four electrons; the mixed-valence form can donate two more electrons relative to the fully oxidized enzyme. For the investigation of the intermediates involved in the catalytic reaction cycle, absorption spectroscopy is inadequate for providing structural information. Resonance Raman was applied to investigate the structural changes in heme *a* and heme a_3 during the course of O_2 reduction by CcO. Isotope-sensitive bands at different delay times after the initiation of the reaction were obtained upon exciting the fully reduced bovine heart CcO using 423 nm laser at 4°C [59].

From the detailed analysis of the intermediate species, the plausible mechanism of oxygen reduction is proposed as follows: fully reduced and mixed-valent enzymes react with molecular O_2 to give a Fe-oxy intermediate (intermediate-A), which is more likely to be an end-on-peroxo, Fea_3^{III}-O_2^{2-}-Cu_B^{II} intermediate, where two electrons are assumed to be given from both Fea_3^{II} and Cu_B^{I} centers. Intermediate-A readily undergoes O-O bond cleavage to give a high-valent "ferryl-oxo" intermediate (intermediate P), accepting one electron from Fea_3^{III}. For the fully reduced enzyme, the fourth electron likely comes from heme *a*, but in the case of mixed-valent species, it has been suggested that it comes from the cross-linked Tyr^{244} residue. Subsequently there is a partial electron transfer between heme *a* and Cu_A, generating an equilibrium mixture of two redox states of sites. Here, the "ferryl-oxo" undergoes a change in H-bonding network after taking up an additional proton (intermediate-F), and finally, it goes to a strongly H-bonded high-spin Fe_{a3}^{III}–OH state (intermediate-O′). Release of one of the OH group leads to the fully oxidized enzyme (O), and the catalytic cycle continues [6, 45].

16.5 Nitric Oxide Reductase

16.5.1 Function and Structure

In biology, nitric oxide (NO), which acts as a signaling agent, is produced by the endothelial cells lining the arteries. It penetrates the underlying smooth muscles and acts as a potent vasodilator that relaxes the arteries. Therefore, NO plays a critical role in blood pressure and overall circulation. It is mainly synthesized by NO-synthases (utilizing L-arginine oxidative chemistry) and reduction of nitrite by nitrite reductases (NiR) [60]. Since NO is a potent inhibitor, the cellular balance of NO is very important, and is regulated by nitric oxide reductase (NOR), which couples two molecules of NO to give one molecule of N_2O and one molecule of water, involving $2e^-/2H^+$ reduction [61] and NO-dioxygenase (NOD), which produces nitrate as a benign NO oxidation product [60]. The overall reaction by NOR can be written as shown in Eq. (16.4):

$$2NO + 2H^+ + 2e^- \rightarrow N_2O + H_2O \tag{16.4}$$

Based on the similarity of the amino acid sequence of the core portion of NOR to the catalytic subunit of the aerobic respiratory enzyme CcO, which catalyzes the reduction of O_2, in 1994, NOR was classified as a member of the heme-copper oxidase (HCO) superfamily [62, 63]. Also, NOR and CcO are known to show cross-reactivity with respective substrates [64–66]. The possible evolutionary link between NOR and CcO suggests that after a drastic increase in the O_2 concentration on Earth (ca. 3 billion years ago), a part of the ancient respiratory enzyme survived as the NO reducing enzyme, NOR, while another respiratory enzyme was functionally converted via some structural modifications into the O_2 reducing enzyme CcO to utilize O_2 as a substrate [67]. Recently, the crystal structures of two distinct types of bacterial NORs have been successfully determined: cNOR from the gram-negative *Pseudomonas aeruginosa* in 2010 [68] and qNOR from the gram-positive *Geobacillus stearothermophilus* in 2012 [69].

cNOR, a cytochrome c dependent NOR found only in denitrifying bacteria, consists of two subunits, NorB and NorC [70]. The NorC subunit contains a heme c with His and Met residues as axial ligands, which accepts electrons from an external protein electron donor (either cytochrome c_{551} or the blue copper protein, azurin). The larger subunit of cNOR is

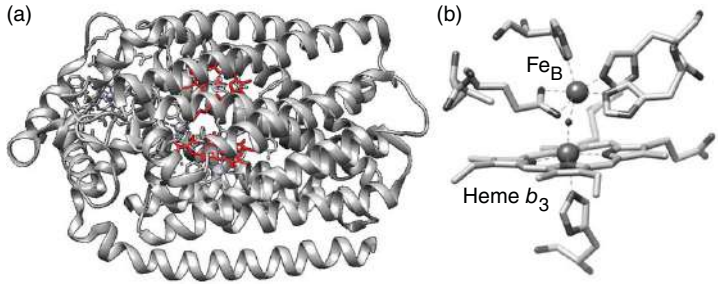

Figure 16.12 (a) The structure of cNOR (PDB id: 3O0R) and (b) the active site structure of cNOR (drawn using software Chimera 1.12rc). Source: Based on Hino et al. [68].

NorB, which contains three iron centers, heme *b*, heme b_3, and one non-heme iron (Fe_B). (Figure 16.12a) The low-spin heme *b* mediates the electron transfer from the heme c in the NorC subunit to the binuclear catalytic center, which consists of heme b_3 and Fe_B.

qNOR is related to single-subunit enzymes that are observed in non-denitrifying pathogenic bacteria as well as in denitrifying bacteria and archaea [70, 71]. Although there are differences in the subunit composition between qNOR and cNOR, the structural characteristics at the active site of qNOR consist of heme *b*, heme b_3, and non-heme Fe_B, which are intrinsically conserved between cNOR and qNOR. Five Glu residues in the same spatial positions in both cNOR and qNOR are all known to be important in the catalytic NO reduction reaction [72–75]. Three residues are located in close proximity to Fe_B, while the other two are positioned near the water cluster, which is located around the Ca^{2+} binding site. The structures of the binuclear centers are quite similar in cNOR and qNOR; one His is the axial ligand for heme b_3, three His residues are ligands for the non-heme Fe_B site, and the heme b_3 and non-heme Fe_B are bridged by one oxygen atom (Figure 16.12b).

16.5.2 Mechanism of NO Reduction

For the reduction of NO by bacterial NOR, two NO molecules must be accommodated in the heme b_3 and Fe_B binuclear center [76], while in the case of CcO, only one O_2 molecule binds to the binuclear site. The binuclear site of cNOR is highly sterically hindered, and there is no room to accommodate two NO molecules, likely because of the binding of Glu^{211} residue to the Fe_B site [68]. Therefore, conformational changes are required for reasonable NOR activity. In contrast to cNOR, qNOR is comparatively less crowded, because the Glu^{512} is not coordinated to Fe_B; rather, a water molecule is coordinated to the Fe_B center [69]. From the structures, it is assumed that during the catalytic turnover of the enzyme, a Glu residue may dissociate from Fe_B site, thereby giving room to the incoming second equivalent of NO [67]. As suggested by the rR and crystallographic data, in the resting state, the heme b_3 and Fe_B are bridged by O, leading to the formation of a μ-oxo-bridged structure (Figure 16.13, **1**) [77, 78].

From the structures, it is assumed that during the catalytic turnover of the enzyme, a Glu residue may dissociate from Fe_B site, thereby giving room for the incoming second equivalent of NO [67]. The pathway is summarized in Figure 16.13. As suggested by the rR and crystallographic data, in the resting state, the heme b_3 and Fe_B are bridged by O, leading to the formation of a μ-oxo-bridged structure (**1**) [77, 78]. In a single turnover study with cNOR, an EPR signal with g = 6 is obtained, which corresponds to a five-coordinated high-spin heme

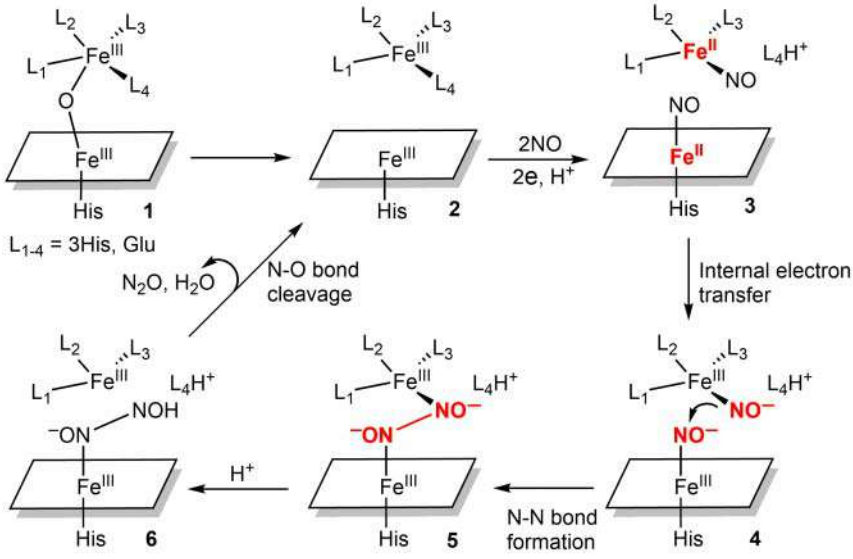

Figure 16.13 Schematic diagram for the proposed mechanistic cycle of NO reduction by NOR.

b_3 species designated as the fully oxidized state (**2**) [79]. It is suggested that each Fe center binds one NO (trans-mechanism), and possibly the Glu residue cleaves off the reduced Fe_B site, allowing NO binding (**3**) [79]. After electron transfer from Fe^{II} to the bound NO molecules, two NO molecules on the heme b_3 and Fe_B undergo N-N bond formation via a transient hyponitrite intermediate (**4**), leading to a hyponitrite-bridged diiron intermediate (**5**) [80]. Protons are transferred from bulk water via (**6**) to facilitate hyponitrite N-O bond cleavage to produce N_2O and H_2O. The dissociated Glu side chain could function as a shuttle for catalytic protons from another Glu to the hyponitrite [67].

In summary, the bacterial NOR contains a binuclear diiron active site, which at its fully reduced state binds two molecule of NO in a *trans* manner. It undergoes N-N bond formation and goes through a hyponitrite-bridged binuclear site, which upon addition of protons from the bulk water, generates N_2O and H_2O, and the fully oxidized form is regenerated for continuation of the catalytic cycle.

16.6 Peroxidases

16.6.1 Function and Structure

Peroxidases are extensively distributed in nature, especially in animal and plant cells. These enzymes utilize hydrogen peroxide or alkyl peroxides as the oxidants to catalyze the oxidation of a variety of organic and inorganic compounds [81]. Phenols and anilines are generally recognized as substrates of the heme peroxidases, often via free-radical intermediates [82, 83]. Nonphenolic compounds, such as indole-3-acetic acid, phenylenediamines, ferrocenes, phenothiazines, and phenoxazines, have also been investigated as peroxidase substrates [82, 84]. Steady-state kinetics of peroxidase action has been described as a ping-pong scheme with Compound I and Compound II formation. Rapid reactions of the resting peroxidases

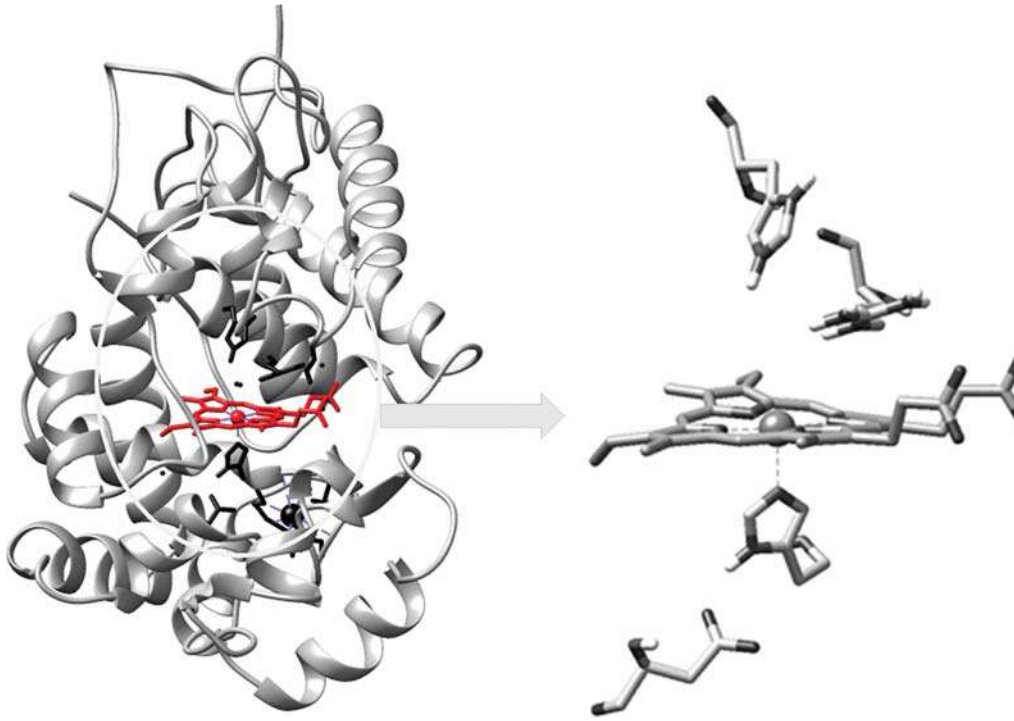

Figure 16.14 Active site structure of horseradish peroxidase (PDB id: 1ATJ) (drawn using Chimera 1.12rc software).

with peroxides to form Compound I discriminate the peroxidases from other classes of hemoproteins.

The peroxidase superfamily has been divided into three classes [85]. Class I includes yeast cytochrome c peroxidase (CCP), cytosol and chloroplast ascorbate peroxidases (APXs), and gene-duplicated bacterial peroxidases. Class II includes peroxidases of fungal origin, the most prominent examples being lignin and manganese peroxidases from *Phanerochaete chrysosporium* and the inkcap peroxidase from *Coprinus cinereus*. Plant peroxidases, such as the well-known enzyme from horseradish root (HRP C), comprise class III of the superfamily (Figure 16.14).

The structure of yeast CCP was solved in 1980 and represented both the first peroxidase and the first heme enzyme structure to be solved [86]. Most of the peroxidases contain a heme at the active site that is invariably bound to a histidine residue at the proximal pocket. In most cases, the distal pocket remains vacant or loosely bound to a solvent molecule. Two important amino acid residues are present close to the distal pocket [2]. The first is a histidine residue that helps H_2O_2 to bind to the heme center and, with the help of a solvent molecule, acts as proton channel that relays H^+ from the α-O to the β-O of the heme-bound peroxide [87–89]. The second residue is an arginine that acts as an H-bond donor to the heme-bound peroxide to facilitate the heterolytic O-O bond cleavage to form the oxy-ferryl complex [90]. On the proximal side, there is an Asp residue H-bonded to the histidine that increases the imidazolate character of the His, rendering it a stronger electron donor and in turn assisting the formation of the Fe=O double bond in Compound I. This influence of the Asp residue is known as the "push effect" [91, 92].

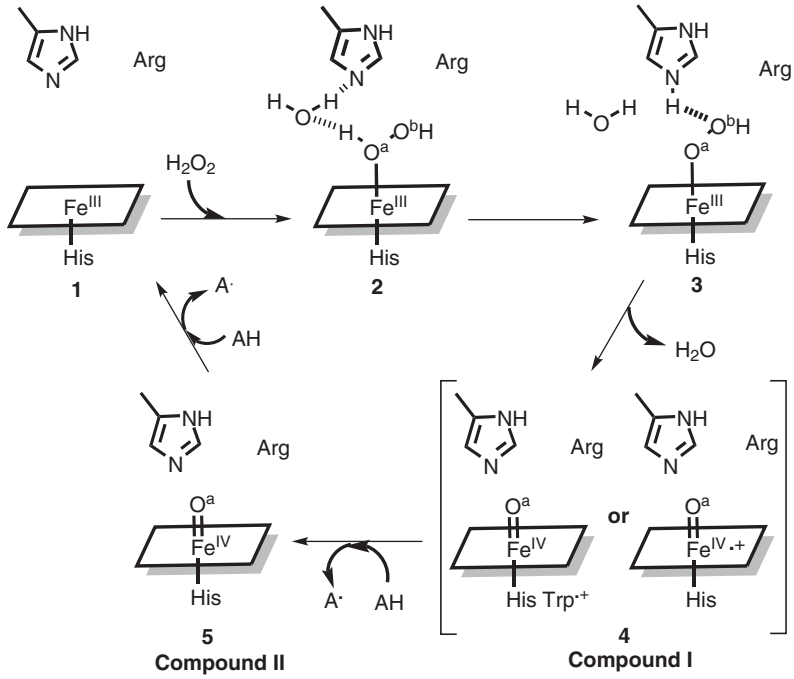

Figure 16.15 Catalytic cycle of peroxidase (AH = substrate).

16.6.2 Reaction Mechanism of the H_2O_2 Reduction Pathway

The catalytic cycle is summarized in Figure 16.15. The resting state of the enzyme contains Fe^{III} (**1**). A peroxide molecule binds to the heme center to form a heme-peroxide adduct (**2**), which then loses an H_2O molecule vis (**3**) to form a high-valent oxy-ferryl complex, Compound I (**4**), which has a characteristic green color [93]. This is now formulated as an Fe^{IV}=O porphyrin π-cation radical. In many of the peroxidases, it has been found that the π-cation radical, previously mentioned to stay over the porphyrin ring, may also reside over a tryptophan residue present near the proximal pocket of the heme center. This intermediate then oxidizes one substrate molecule and converts it to another intermediate, Compound II (**5**) (red). This species has a Fe=O double bond similar to that of the Compound I, but lacks the π-cation radical on the porphyrin ring. This species then oxidizes another substrate molecule to return to the Fe(III)-porphyrin resting state (**1**). The high-valent Fe(IV) = O species is thought to be stabilized by the Arg residue (responsible for showing a pull effect), through the donation of a hydrogen bond [94].

16.7 Cytochrome P450

16.7.1 Function and Structure

Until 1955 it was believed that the sole role of dioxygen in biological systems was as an electron acceptor in dioxygen-utilizing oxidase or dehydrogenase reactions. In that year, Mason [95] and Hayaishi [96] independently reported that dioxygen can be directly incorporated into organic molecules following enzymatic oxidation of 3,4-dimethylphenol by phenolase and

catechol by pyrocatechase, respectively. Hayaishi designated those enzymes as "oxygenases," which incorporates oxygen atoms from dioxygen in such reactions [97]. Two years later, Klingenberg [98] and Garfinkel [99] independently described the presence of a CO-binding pigment in liver microsomes having an unusual absorption band maximum near 450 nm (from the difference spectrum of ferrous-CO and ferrous species). Six years later, Omura and Sato identified this unusual pigment as a heme protein containing protoheme IX and assigned it as "cytochrome P450" (cyt P450) despite the lack of knowledge about its function [100]. It is now known that oxygenases are extensively distributed in nature throughout the plant, animal, and microorganism kingdoms. One of the major roles of cyt P450 in the body is xenobiotic detoxification. Drugs and other xenobiotics are hydroxylated by various cyt P450s in the liver, rendering them more soluble and susceptible to further modification for easier elimination. For example, cyt P450 34A (known as CYP3A4) is one of the drug-metabolizing P450s responsible for metabolizing about half of all currently used drugs. A series of diverse reactions catalyzed by cyt P450 are listed in Figure 16.16. In addition to these catabolic functions, cyt P450s also play a critical role in the biosynthesis of important compounds, with steroids topping the list [2]. Although it eliminates insoluble hydrocarbons, a desirable process, the oxidative chemistry of cyt P450s has a downside. It can also form epoxides, which are generally highly electrophilic, and hence the macromolecular nucleophiles such as DNA are susceptible to covalent modification. Aromatic epoxides can undergo intercalation into the double-stranded DNA, where they can modify the genetic material with deleterious downstream consequences. A classic example is aflatoxin, which is activated by cyt P450 oxidation, resulting in selective modification of the P53 tumor suppressor gene [101].

Cyt P450s are single polypeptides ranging from 40 to 55 kDa, and the overall protein folding in all known cyt P450s is similar (Figure 16.17). The I helix lies over the surface of the heme and contributes groups that interact with both the substrate and dioxygen [2]. The local structure around the Cys ligand (which is the axial ligand, bound to Fe), however, is much more highly conserved. The Cys ligand is situated at the C-terminal end of the L helix where the Cys sulfur accepts a H-bond from a peptide NH group. This type of H-bonding is very common in iron-Cys proteins for two reasons. First, it modulates the iron redox potential [103–106], as without such H-bonds the redox potential would be too low for physiological reductants. Second, in Fe-Cys proteins there is a possibility of valence tautomerism between Fe^{III}-thiolate and Fe^{II}-thiyl radical. In the latter form, the protein would not be stable in presence of O_2; the H-bonds stabilize the Fe^{III}-thiolate form, rendering it stable under aerobic conditions [106].

Cyt P450s are sufficiently flexible to allow substrates to enter and products to leave. In general, there are two extreme forms: substrate-bound (closed) and substrate-free (open). In the open form, the substrate pocket is filled with solvent molecules that are displaced when the substrate binds, which is presumed to be an entropically favored process [107]. In the closed substrate-bound form, there may be substantial variation in active site volume. One common feature in all cyt P450s is that the atom to be hydroxylated is usually within 4–5 Å of the iron. Hence, during the catalysis, the ferryl O atom of compound I (which is a reactive intermediate represented as $Fe^{IV}{=}O(Por^{+\cdot})$ with a porphyrin cation radical) can directly interact with the correct carbon atom for regio- and stereoselective hydroxylation [2].

Cyt P450s are very diverse and can involve various combinations of flavin and iron–sulfur proteins [108]. In any biological electron transfer system, the two redox partners must recognize one another via complementary surfaces to enable the donor and acceptor redox partners to properly align with respect to distance and the intervening protein matrix [109, 110].

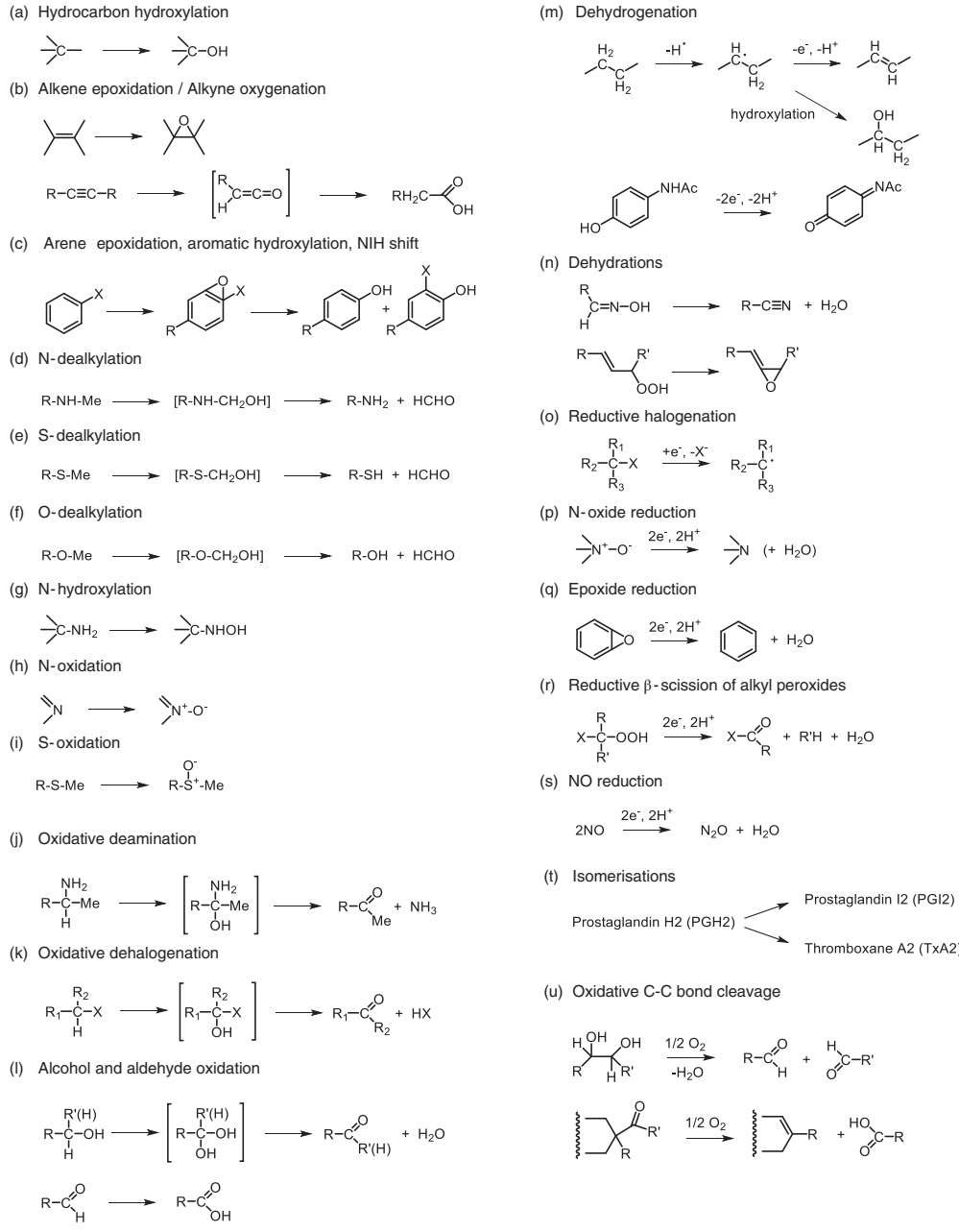

Figure 16.16 Schematic summary of the diverse P450-catalyzed reactions.

There are three crystal structures of P450 redox complexes: in the first structure, P450BM3 complexed with the flavin mononucleotide (FMN) domain of the reductase [111]; in the second structure, P450scc (CYP11A1) complexed with adrenodoxin [112]; and in the third structure, P450cam complexed with putidaredoxin (Pdx) [113]. As expected in all cases, the redox partner docks on the proximal side (Cys ligand side) of the heme, which is the closest approach of the heme to the surface.

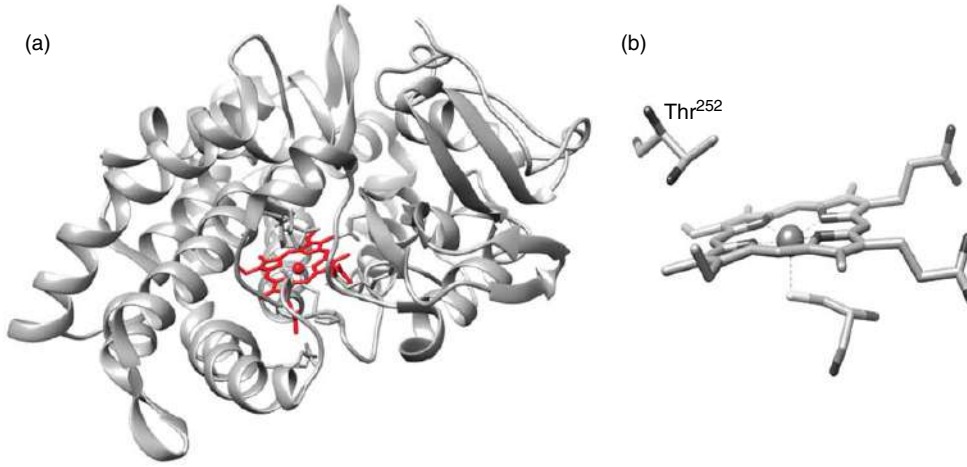

Figure 16.17 (a) Crystal structure of P450cam (pdb id: 2CPP) and (b) active site structure of P450cam (pdb id: 2CPP) (drawn using Chimera 1.12rc software). Source: Based on Poulos et al. [102].

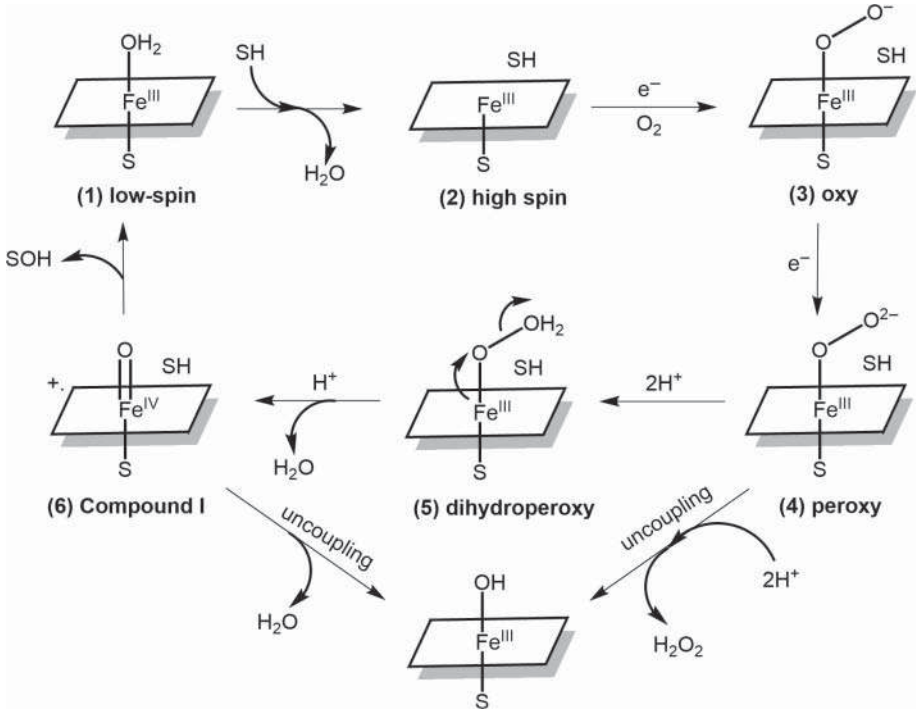

Figure 16.18 Schematic diagram of general mechanistic cycle of substrate oxidation by P450.

16.7.2 Catalytic Mechanism

The overall catalytic cycle of cyt P450 is illustrated in Figure 16.18. The resting state is hexa-coordinated and low-spin heme (**1**). When the substrate approaches, the axial water ligand and other water molecules occupying the active site pocket are displaced, rendering a penta-coordinated high-spin heme (**2**) that possesses a relatively higher potential. The

electron donors usually contain a flavin or FeS cofactor whose redox potential thermodynamically favors electron transfer to the higher-potential substrate-bound cyt P450. This shift in redox potential due to the change in spin state actually ensures the electron transfer only to the substrate-bound enzyme, thereby avoiding the wasteful consumption of NADH/NADPH-derived reducing equivalents to the substrate-free enzyme, and consequently it prevents dioxygen reduction chemistry to generate peroxide and/or water. When peroxide or water is released instead of the oxidized product, it is referred to as "uncoupling." After getting reduced by the redox partner, Fe^{II}-heme binds O_2 to form a Fe^{III}-superoxide complex (**3**). The second electron transfer gives the peroxy intermediate (**4**), which, after protonation, results in heterolytic cleavage of the O–O bond and thereby generates the active hydroxylating agent, compound I (**6**). Due to the strong push effect from the cysteine axial ligand, the pKa of the conjugate acid of Compound I, which is a Fe(IV)-hydroxide species (termed as Compound II), is quite high [114]. Hence, compound I can abstract H from the substrate, making a bound radical species [115]. After rebinding to Compound II, the substrate can be hydrolyzed, leading the enzyme to its resting state.

It is worth mentioning that, unlike peroxidases, cyt P450 can oxidize C—H bonds. This is for three reasons: (i) the strong push effect of the Cys in cyt P450 decreases the ability of Compound I to serve as an electron acceptor; (ii) the Cys push helps to increase the Fe–O bond length, which increases the pKa of the ferryl O atom in Compound II, thus also increasing the H atom abstraction ability of Compound I; and (iii) the greater polarity of the peroxidase distal pocket compared to cyt P450 lowers the proton affinity of the ferryl O atom in peroxidases relative to cyt P450s [2]. The generally accepted mechanism for substrate hydroxylation is the radical rebound mechanism initially proposed by Groves [116]. In this mechanism, Compound I abstracts an H atom from the substrate to form a carbon radical followed by radical recombination to give the C–OH product. However, there is also a provision to go through a cationic intermediate or follow a concerted mechanism. To differentiate between the possible mechanisms of C–H bond hydroxylation, cyclopropyl radical clocks have been developed [117–119]. The rate of ring opening in a strained ring of a substrate, such as cyclopropyl, along with the product analysis can provide information on the mechanism of C–OH bond formation. For example, formation of a radical α to the ring could result in ring opening, thus generating predictable products, whereas in a concerted mechanism there will not be any ring opening. These experiments support the radical rebound process [120], although experiments with different cyt P450s and other substrates indicate a cationic intermediate rather than a radical [121]. Again, ultrafast radical clocks are not consistent with a radical mechanism [122]. However, density functional (DFT) calculations [123, 124] have provided important insights that may help to clarify some of the complications in the interpretation of radical clock experiments. The key result is that the process of C–OH bond formation is dependent on the spin state of the ferryl center. In the low spin state, there is no energetic barrier to radical recombination, so the reaction is effectively concerted; whereas in the high spin state, there is a substantial barrier and hence the reaction proceeds in the more traditional stepwise fashion. Therefore, in spite of the fact that both concerted and stepwise processes use Fe^{IV}=O, they can give different product profiles as well as deceptively short estimates of radical lifetimes.

In summary, P450s are a class of enzymes present in nature throughout the plant, animal, and microorganism kingdoms. They can catalyze a series of oxidation reactions using molecular oxygen, through a high-valent Fe^{IV}=O intermediate.

16.8 Heme Oxygenase

16.8.1 Function and Structure

The degradation of heme proteins releases free heme in the body. Hemoglobin is the major source of heme, and approximately 6–8 g of hemoglobin is degraded daily, releasing about 300 mg of heme per day. Since accumulation of free heme has toxic effects, it needs to be removed from the body. Free heme is degraded to biliverdin with subsequent release of CO and iron. This iron is stored in the body because our bodies acquire <3% of the required iron from dietary sources [125, 126]. A family of enzymes, called heme oxygenases (HOs), is responsible for the degradation of heme [127, 128]. Mammalian HOs are a membrane-bound enzyme, anchored to the microsomal membranes through C-terminal hydrophobic tails [129]. They exist in two major isoforms, inducible 33 kDa HO-1 and constitutive 36 kDa HO-2, which are differently regulated and have different roles. The HO-1 is induced by chemical agents and a variety of stress conditions, and is found in high concentrations in the spleen and liver. In contrast, HO-2 is not induced by exogenous stimuli, and is found in the brain and testes in high concentrations. The primary functions of HO-1 are excess heme catabolism and antioxidant defense, while HO-2 is proposed to generate CO as a physiological messenger molecule [130–133]. The final product of HO-mediated heme degradation is biliverdin, which is converted to bilirubin by bilirubin reductase [134].

The activity of HO was first described in 1968–1969 [134, 135]. The first crystal structure of HO was human HO-1, published in 1999 [136]. Since then, several structures of other HOs from different sources, including bacterial HOs [137–139], rat HO [140], and human HO-2 [141] have been reported, that are structurally related to human HO-1. The overall protein fold of these HOs is unique and distinctly different from other known protein structures. The heme is sandwiched between the proximal and distal helices, where a His residue from the proximal helix is axially ligated with the heme (Figure 16.19a). The HO holds the overall fold, even in the absence of the substrate, heme (Figure 16.19b). In the substrate-free form, substantial conformational changes occur to make the "proximal" and "distal" helices (which sandwich the heme group during the successive oxygenation processes) move farther apart to facilitate the substrate (heme) binding [142]. Unlike other heme enzymes, in the case of HOs, heme itself is the substrate. As a result, in the active site, flexibility is likely to be required for

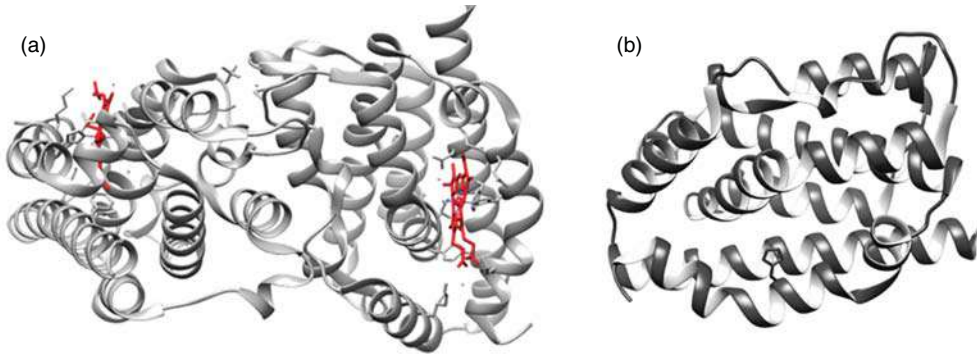

Figure 16.19 (a) Ribbon diagram of substrate-bound human HO-1 (PDB id: 1N45) and (b) ribbon diagram of substrate-free human HO-1 (PDB id: 1NI6) (drawn using Chimera 1.12rc software). Source: Based on Lad et al. [142].

substrate binding and product release, because the substrate heme is a comparatively large molecule. The distal helix, just over the heme, consists of a glycine-rich segment to make the arrangement flexible [2].

16.8.2 Mechanism of Heme Degradation

Heme degradation takes place via three self-mono-oxygenation reactions (Figure 16.20). In the first step, heme activates molecular O_2 for the regiospecific self-hydroxylation of the porphyrin α-meso-carbon atom. In the second step, the resulting α-meso-hydroxyheme reacts with another O_2 to yield verdoheme and CO. The third O_2 activation by verdoheme cleaves the porphyrin macrocycle to afford biliverdin and free ferrous iron.

The initial O_2 activation of HO is similar to cyt P450. In both HO and cyt P450, the initial step is the reduction of the ferric heme to the ferrous state, which binds O_2 (Figure 16.20). Subsequent one-electron reduction and protonation of the ferrous-oxy heme gives a ferric hydroperoxy species (FeOOH). Unlike cyt P450 (where due to the "pull" effect of the thiolate axial ligand, it undergoes O—O bond cleavage to form Compound I with release of a water molecule), in HO the heme group is tightly bound between the proximal and distal helices, where a His ligand from the proximal helix is bound to heme, which does not exert "pull" effect. The distal helix of HO is kinked above the heme plane around the two conserved Gly residues and is in close contact with the heme group, which creates steric restriction to all of the meso-positions except for the α-meso-carbon and upon hydroxylation leads to the formation of α-meso-hydroxyheme [144]. As a surrogate of O_2 and two electrons, H_2O_2 efficiently forms the α-meso-hydroxyheme, whereas most alkyl and acyl hydroperoxides afford the inactive ferryl hemes [145]. A small peroxide (ethyl hydroperoxide), was reported to produce α-meso-ethoxyheme in a relatively lower yield, suggesting an intramolecular ethoxy

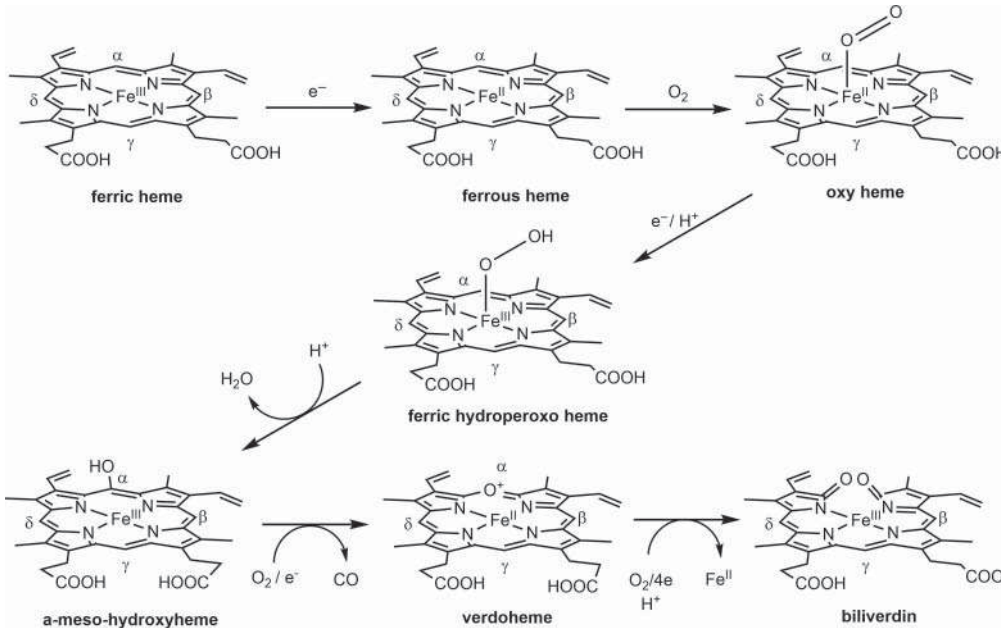

Figure 16.20 Schematic diagram of heme oxygenase catalytic intermediates. Source: Based on Yoshida and Migita [143].

transfer by an FeOOEt intermediate [146]. Also, from the crystal structure of the ferrous-oxy complex of HmuO, it is evident that steric constraints imposed by the distal helix make the Fe-O-O angle in oxy-HO unusually acute (~110°) and directs the terminal oxygen atom of the ferrous-O_2 complex toward the heme α-meso-carbon [147]. Another feature is that the terminal oxygen atom of the heme-bound O_2 interacts with a water molecule, which is a part of the hydrogen-bonding network containing a water cluster and a catalytically critical distal Asp residue.

The next step in the reaction is the conversion of α-meso hydroxyheme to verdoheme along with the release of CO. There is a controversy about whether Fe^{III} gets reduced to Fe^{II} via an external electron donor or not [148, 149]. Actually, in one of the resonance structures of α-meso-hydroxyheme, Fe is in +2 oxidation state along with a radical in the macrocycle. In fact, a g = 2.004 EPR signal has been observed when O_2 is added to an anaerobic solution of HO-1-α-meso hydroxyheme, which has been attributed to a porphyrin radical [148]. It has been reported that prior reduction of Fe^{III} is not strictly required for the conversion of α-meso-hydroxyheme to verdoheme [150]. However, different mechanisms have been proposed that may be equally valid, depending on the experimental conditions because up to now no intermediate has been isolated for this step. The conversion of mesohydroxyheme to verdoheme is a spontaneous process in the presence of O_2, and the protein might not play a significant role [151].

In the third stage of heme degradation, Fe^{II}-verdoheme is cleaved to afford biliverdin and the free ferrous ion with the consumption of one O_2 molecule and four reducing equivalents (Figure 16.20). This third step is considered to be the rate determining step to regulate the enzyme activity *in vivo* [152]. Among the three steps, this step is difficult to unravel. The verdoheme-HO complex was originally reported to not react with H_2O_2 and to utilize exclusively O_2 for biliverdin formation, which makes this step mechanistically different from the first step because it can also proceed if H_2O_2 is added instead of O_2 [145, 153]. Although Fe^{III}-verdoheme does not react with H_2O_2, Fe^{II}-verdoheme readily reacts with H_2O_2 to give biliverdin under reducing conditions [154]. O_2 as well as H_2O_2 may bind either at the verdoheme iron or on a radical generated at the α-pyrrole carbon because of the possible resonance structures of Fe^{II}-verdoheme, generating Fe^{III}OOH or ring-OOH-verdoheme complexes that may be deprotonated to form a bridged intermediate. From the product analysis of the experiment taking CH_3OOH instead of H_2O_2, it was found that methoxybiliverdin forms exclusively, which suggests that Fe^{III}OOH verdoheme is likely to transfer its terminal OH group into the α-pyrrole carbon in a similar fashion to the first step [155]. Cleavage of the O–O bond results in a high-valent Fe^{IV}=O intermediate that is subject to attack by an active site water/hydroxide. This initiates the process of ring opening followed by electron transfer to give the final biliverdin product.

In summary, HOs are a family of enzymes that catalyze the degradation of free heme into biliverdin, iron, and CO via a three-step mechanism involving three molecules of O_2 and seven electrons.

16.9 Summary

Heme enzymes continue to enthrall biologists and chemists alike. After almost 100 years of research into their structure and function, a lot has been learned. The effect of axial ligand and second sphere residues have been broadly understood, both using experimental and

theoretical methods. Substantial work remains to be done on the heme enzymes involved in sulfur and nitrogen cycles, which are important for global ecology. Moving forward, the structure function correlations discovered need to be emulated in artificial systems. A catalyst designed based on these principles has the potential to outperform most other catalysts designed ab initio. Such an effort is bound to be challenging, but also promises to be extremely rewarding.

References

1 Nelson, D. and Cox, M. (2005). *Lehninger Principles of Biochemistry*, 4e. New York: W.H. Freeman.
2 Poulos, T.L. (2014). Heme enzyme structure and function. *Chemical Reviews* 114: 3919–3962.
3 Alfonso-Prieto, M., Biarnés, X., Vidossich, P., and Rovira, C. (2009). The molecular mechanism of the catalase reaction. *Journal of the American Chemical Society* 131: 11751–11761.
4 Sono, M., Roach, M.P., Coulter, E.D., and Dawson, J.H. (1996). Heme-containing oxygenases. *Chemical Reviews* 96: 2841–2888.
5 Wikström, M., Krab, K., and Sharma, V. (2018). Oxygen activation and energy conservation by cytochrome c oxidase. *Chemical Reviews* 118: 2469–2490.
6 Yoshikawa, S. and Shimada, A. (2015). Reaction mechanism of cytochrome c oxidase. *Chemical Reviews* 115: 1936–1989.
7 Muramoto, K., Ohta, K., Shinzawa-Itoh, K. et al. (2010). Bovine cytochrome c oxidase structures enable O_2 reduction with minimization of reactive oxygens and provide a proton-pumping gate. *Proceedings of the National Academy of Sciences* 107: 7740–7745.
8 Scott, R.A. and Mauk, A.G. (ed.) (1996). *Cytochrome c - a Multidisciplinary Approach*. Sausalito, CA: University Science Books.
9 Pearce, D.A. and Sherman, F. (1995). Degradation of cytochrome oxidase subunits in mutants of yeast lacking cytochrome c and suppression of the degradation by mutation of *yme1*. *Journal of Biological Chemistry* 270: 20879–20882.
10 Giorgio, M., Migliaccio, E., Orsini, F. et al. (2005). Electron transfer between cytochrome c and p66Shc generates reactive oxygen species that trigger mitochondrial apoptosis. *Cell* 122: 221–233.
11 Jiang, X. and Wang, X. (2004). Cytochrome c-mediated apoptosis. *Annual Review of Biochemistry* 73: 87–106.
12 Battersby, A.R. (2000). Tetrapyrroles: the pigments of life. *Natural Product Reports* 17: 507–526.
13 Maia, L.B. and Moura, J.J.G. (2014). How biology handles nitrite. *Chemical Reviews* 114: 5273–5357.
14 Parey, K., Warkentin, E., Kroneck, P.M.H., and Ermler, U. (2010). Reaction cycle of the dissimilatory sulfite reductase from *Archaeoglobus fulgidus*. *Biochemistry* 49: 8912–8921.
15 Chatterjee, S., Sengupta, K., Mondal, B. et al. (2017). Factors determining the rate and selectivity of 4e–/4H+ electrocatalytic reduction of dioxygen by iron porphyrin complexes. *Accounts of Chemical Research* 50: 1744–1753.
16 Poulos, T.L. (1996). The role of the proximal ligand in heme enzymes. *Journal of Biological Inorganic Chemistry* 1: 356–359.

17 Tame, J.R. and Vallone, B. (2000). The structures of deoxy human haemoglobin and the mutant Hb Tyralpha42His at 120 K. *Acta Crystallographica. Section D, Biological Crystallography* 56: 805–811.

18 Vojtechovsky, J., Chu, K., Berendzen, J. et al. (1999). Crystal structures of myoglobin-ligand complexes at near-atomic resolution. *Biophysical Journal* 77: 2153–2174.

19 Van Beekvelt, M.C.P., Colier, W.N.J.M., Wevers, R.A., and Van Engelen, B.G.M. (2001). Performance of near-infrared spectroscopy in measuring local O_2 consumption and blood flow in skeletal muscle. *Journal of Applied Physiology* 90: 511–519.

20 Schechter, A.N. (2008). Hemoglobin research and the origins of molecular medicine. *Blood* 112: 3927–3938.

21 http://www.bio.davidson.edu/Courses/Molbio/MolStudents/spring2005/Heiner/hemoglobin.html

22 Linberg, R., Conover, C.D., and Shum, K.L. (1998). Hemoglobin based oxygen carriers: how much methemoglobin is too much? *Artificial Cells, Blood Substitutes, and Biotechnology* 26: 133–148.

23 Bren, K.L., Eisenberg, R., and Gray, H.B. (2015). Discovery of the magnetic behavior of hemoglobin: a beginning of bioinorganic chemistry. *Proceedings of the National Academy of Sciences* 112: 13123–13127.

24 Berg, J.M., Tymoczko, J.L., and Stryer, L. (2002). *Biochemistry*, 5e. New York: W. H. Freeman.

25 Mihailescu, M.-R. and Russu, I.M. (2001). A signature of the T→R transition in human hemoglobin. *Proceedings of the National Academy of Sciences* 98: 3773–3777.

26 Collman, J.P., Brauman, J.I., Halbert, T.R., and Suslick, K.S. (1976). Nature of O_2 and CO binding to metalloporphyrins and heme proteins. *Proceedings of the National Academy of Sciences* 73: 3333–3337.

27 Chou, K.-C. (1989). Low-frequency resonance and cooperativity of hemoglobin. *Trends in Biochemical Sciences* 14: 212.

28 Hill, A.V. (1910). The possible effects of the aggregation of the molecules of hæmoglobin on its dissociation curves. *The Journal of Physiology* 40, January 22, 1910: iv–vii.

29 Stefan, M.I. and Le Novère, N. (2013). Cooperative binding. *PLoS Computational Biology* 9: e1003106.

30 Hall, J. and Guyton, A. (2005). *Textbook of Medical Physiology*, 11e, 511. Saunders.

31 Voet, D., Voet, J.G., and Pratt, C.W. (2016). *Fundamentals of Biochemistry: Life at the Molecular Level*, 5e. Hoboken: John Wiley & Sons.

32 Lanzkron, S., Strouse, J.J., Wilson, R. et al. (2008). Systematic review: hydroxyurea for the treatment of adults with sickle cell disease. *Annals of Internal Medicine* 148: 939–955.

33 Hüttemann, M., Pecina, P., Rainbolt, M. et al. (2011). The multiple functions of cytochrome c and their regulation in life and death decisions of the mammalian cell: from respiration to apoptosis. *Mitochondrion* 11: 369–381.

34 Theorell, H. and Åkesson, Å. (1941). Studies on cytochrome c. III. Titration curves. *Journal of the American Chemical Society* 63: 1818–1820.

35 Bertini, I., Cavallaro, G., and Rosato, A. (2006). Cytochrome c: occurrence and functions. *Chemical Reviews* 106: 90–115.

36 Bushnell, G.W., Louie, G.V., and Brayer, G.D. (1990). High-resolution three-dimensional structure of horse heart cytochrome c. *Journal of Molecular Biology* 214: 585–595.

37 Alvarez-Paggi, D., Hannibal, L., Castro, M.A. et al. (2017). Multifunctional cytochrome c: learning new tricks from an old dog. *Chemical Reviews* 117: 13382–13460.

38 Swanson, R., Trus, B.L., Mandel, N. et al. (1977). Tuna cytochrome c at 2.0 A resolution. I. Ferricytochrome structure analysis. *Journal of Biological Chemistry* 252: 759–775.

39 Bowman, S.E.J. and Bren, K.L. (2008). The chemistry and biochemistry of heme c: functional bases for covalent attachment. *Natural Product Reports* 25: 1118–1130.

40 Fülöp, V., Sam, K.A., Ferguson, S.J. et al. (2009). Structure of a trypanosomatid mitochondrial cytochrome c with heme attached via only one thioether bond and implications for the substrate recognition requirements of heme lyase. *FEBS Journal* 276: 2822–2832.

41 Jasion, V.S. and Poulos, T.L. (2012). *Leishmania major* peroxidase is a cytochrome c peroxidase. *Biochemistry* 51: 2453–2460.

42 Shelnutt, J.A., Song, X.-Z., Ma, J.-G. et al. (1998). Nonplanar porphyrins and their significance in proteins. *Chemical Society Reviews* 27: 31–42.

43 Liptak, M.D., Wen, X., and Bren, K.L. (2010). NMR and DFT investigation of heme ruffling: functional implications for cytochrome c. *Journal of the American Chemical Society* 132: 9753–9763.

44 Pettigrew, G.W. and Moore, G.R. (1987). *Cytochromes C - Biological Aspects*, Springer Series in Molecular Biology. Berlin: Springer.

45 Kim, E., Chufán, E.E., Kamaraj, K., and Karlin, K.D. (2004). Synthetic models for heme–copper oxidases. *Chemical Reviews* 104: 1077–1134.

46 Tsukihara, T., Aoyama, H., Yamashita, E. et al. (1995). Structures of metal sites of oxidized bovine heart cytochrome c oxidase at 2.8 Å. *Science* 269: 1069–1074.

47 Iwata, S., Ostermeier, C., Ludwig, B., and Michel, H. (1995). Structure at 2.8 Å resolution of cytochrome c oxidase from *Paracoccus denitrificans*. *Nature* 376: 660–669.

48 Yoshikawa, S., Shinzawa-Itoh, K., Nakashima, R. et al. (1998). Redox-coupled crystal structural changes in bovine heart cytochrome c oxidase. *Science* 280: 1723–1729.

49 Tsukihara, T., Aoyama, H., Yamashita, E. et al. (1996). The whole structure of the 13-subunit oxidized cytochrome c oxidase at 2.8 Å. *Science* 272: 1136–1144.

50 Shinzawa-Itoh, K., Aoyama, H., Muramoto, K. et al. (2007). Structures and physiological roles of 13 integral lipids of bovine heart cytochrome c oxidase. *The EMBO Journal* 26: 1713–1725.

51 Hill, B.C. (1991). The reaction of the electrostatic cytochrome c-cytochrome oxidase complex with oxygen. *Journal of Biological Chemistry* 266: 2219–2226.

52 Pan, L.P., Hibdon, S., Liu, R.Q. et al. (1993). Intracomplex electron transfer between ruthenium-cytochrome c derivatives and cytochrome c oxidase. *Biochemistry* 32: 8492–8498.

53 Malatesta, F., Nicoletti, F., Zickermann, V. et al. (1998). Electron entry in a CuA mutant of cytochrome c oxidase from *Paracoccus denitrificans*. Conclusive evidence on the initial electron entry metal center. *FEBS Letters* 434: 322–324.

54 Lübben, M. and Morand, K. (1994). Novel prenylated hemes as cofactors of cytochrome oxidases. Archaea have modified hemes A and O. *Journal of Biological Chemistry* 269: 21473–21479.

55 Winkler, J.R., Malmström, B.G., and Gray, H.B. (1995). Rapid electron injection into multisite metalloproteins: intramolecular electron transfer in cytochrome oxidase. *Biophysical Chemistry* 54: 199–209.

56 Ferguson-Miller, S. and Babcock, G.T. (1996). Heme/copper terminal oxidases. *Chemical Reviews* 96: 2889–2908.

57 Michel, H., Behr, J., Harrenga, A., and Kannt, A. (1998). Cytochrome c oxidase: structure and spectroscopy. *Annual Review of Biophysics and Biomolecular Structure* 27: 329–356.

58 Kitagawa, T. and Ogura, T. (2007). Oxygen activation mechanism at the binuclear site of heme–copper oxidase superfamily as revealed by time-resolved resonance raman spectroscopy. *Progress in Inorganic Chemistry* 45: 431–479.

59 Ogura, T., Hirota, S., Proshlyakov, D.A. et al. (1996). Time-resolved resonance raman evidence for tight coupling between electron transfer and proton pumping of cytochrome c oxidase upon the change from the Fe^{V} oxidation level to the Fe^{IV} oxidation level. *Journal of the American Chemical Society* 118: 5443–5449.

60 Lehnert, N., Berto, T.C., Galinato, M.G.I., and Goodrich, L.E. (2011). 63 The role of heme-nitrosyls in the biosynthesis, transport, sensing, and detoxification of nitric oxide (NO) in biological systems: enzymes and model complexes. In: *Handbook of Porphyrin Science*, vol. 14 (ed. K.M. Kadish, K.M. Smith and R. Guilard), 1–247. Singapore, Ch. 63: World Scientific.

61 Braun, C. and Zumft, W.G. (1991). Marker exchange of the structural genes for nitric oxide reductase blocks the denitrification pathway of *Pseudomonas stutzeri* at nitric oxide. *Journal of Biological Chemistry* 266: 22785–22788.

62 Saraste, M. and Castresana, J. (1994). Cytochrome oxidase evolved by tinkering with denitrification enzymes. *FEBS Letters* 341: 1–4.

63 van der Oost, J., De Boer, A.P.N., de Gier, J.-W.L. et al. (1994). The heme-copper oxidase family consists of three distinct types of terminal oxidases and is related to nitric oxide reductase. *FEMS Microbiology Letters* 121: 1–9.

64 Hayashi, T., Lin, M.T., Ganesan, K. et al. (2009). Accommodation of two diatomic molecules in cytochrome bo_3: insights into NO reductase activity in terminal oxidases. *Biochemistry* 48: 883–890.

65 Fujiwara, T. and Fukumori, Y. (1996). Cytochrome cb-type nitric oxide reductase with cytochrome c oxidase activity from *Paracoccus denitrificans* ATCC 35512. *Journal of Bacteriology* 178: 1866–1871.

66 Giuffrè, A., Stubauer, G., Sarti, P. et al. (1999). The heme-copper oxidases of *Thermus thermophilus* catalyze the reduction of nitric oxide: evolutionary implications. *Proceedings of the National Academy of Sciences* 96: 14718–14723.

67 Shiro, Y. (2012). Structure and function of bacterial nitric oxide reductases: nitric oxide reductase, anaerobic enzymes. *Biochimica et Biophysica Acta - Bioenergetics* 1817: 1907–1913.

68 Hino, T., Matsumoto, Y., Nagano, S. et al. (2010). Structural basis of biological N_2O generation by bacterial nitric oxide reductase. *Science* 330: 1666–1670.

69 Matsumoto, Y., Tosha, T., Pisliakov, A.V. et al. (2012). Crystal structure of quinol-dependent nitric oxide reductase from *Geobacillus stearothermophilus*. *Nature Structural & Molecular Biology* 19: 238–245.

70 Zumft, W.G. (2005). Nitric oxide reductases of prokaryotes with emphasis on the respiratory, heme–copper oxidase type. *Journal of Inorganic Biochemistry* 99: 194–215.

71 Hendriks, J., Oubrie, A., Castresana, J. et al. (2000). Nitric oxide reductases in bacteria. *Biochimica et Biophysica Acta - Bioenergetics* 1459: 266–273.

72 Flock, U., Thorndycroft, F.H., Matorin, A.D. et al. (2008). Defining the proton entry point in the bacterial respiratory nitric-oxide reductase. *Journal of Biological Chemistry* 283: 3839–3845.

73 Butland, G., Spiro, S., Watmough, N.J., and Richardson, D.J. (2001). Two conserved glutamates in the bacterial nitric oxide reductase are essential for activity but not assembly of the enzyme. *Journal of Bacteriology* 183: 189–199.

74 Thorndycroft, F.H., Butland, G., Richardson, D.J., and Watmough, N.J. (2007). A new assay for nitric oxide reductase reveals two conserved glutamate residues form the entrance to a proton-conducting channel in the bacterial enzyme. *Biochemical Journal* 401: 111–119.

75 Flock, U., Lachmann, P., Reimann, J. et al. (2009). Exploring the terminal region of the proton pathway in the bacterial nitric oxide reductase. *Journal of Inorganic Biochemistry* 103: 845–850.

76 Moenne-Loccoz, P. (2007). Spectroscopic characterization of heme iron-nitrosyl species and their role in NO reductase mechanisms in diiron proteins. *Natural Product Reports* 24: 610–620.

77 Moënne-Loccoz, P., Richter, O.-M.H., Huang, H.-W. et al. (2000). Nitric oxide reductase from *Paracoccus denitrificans* contains an oxo-bridged heme/non-heme diiron center. *Journal of the American Chemical Society* 122: 9344–9345.

78 Moënne-Loccoz, P. and de Vries, S. (1998). Structural characterization of the catalytic high-spin heme b of nitric oxide reductase: a resonance Raman study. *Journal of the American Chemical Society* 120: 5147–5152.

79 Kumita, H., Matsuura, K., Hino, T. et al. (2004). NO reduction by nitric-oxide reductase from denitrifying bacterium *Pseudomonas aeruginosa*: characterization of reaction intermediates that appear in the single turnover cycle. *Journal of Biological Chemistry* 279: 55247–55254.

80 Watmough, N.J., Field, S.J., Hughes, R.J.L., and Richardson, D.J. (2009). The bacterial respiratory nitric oxide reductase. *Biochemical Society Transactions* 37: 392–399.

81 Altschul, A.M., Abrams, R., and Hogness, T.R. (1940). Cytochrome c peroxidase. *Journal of Biological Chemistry* 136: 777–794.

82 Candeias, L.P., Folkes, L.K., and Wardman, P. (1997). Factors controlling the substrate specificity of peroxidases: kinetics and thermodynamics of the reaction of horseradish peroxidase compound I with phenols and indole-3-acetic acids. *Biochemistry* 36: 7081–7085.

83 Howes, B.D., Brissett, N.C., Doyle, W.A. et al. (2005). Spectroscopic and kinetic properties of the horseradish peroxidase mutant T171S. *FEBS Journal* 272: 5514–5521.

84 Kulys, J. and Ziemys, A. (2001). A role of proton transfer in peroxidase-catalyzed process elucidated by substrates docking calculations. *BMC Structural Biology* 1: 3.

85 Welinder, K.G. (1992). Superfamily of plant, fungal and bacterial peroxidases. *Current Opinion in Structural Biology* 2: 388–393.

86 Poulos, T.L., Freer, S.T., Alden, R.A. et al. (1980). The crystal structure of cytochrome c peroxidase. *Journal of Biological Chemistry* 255: 575–580.

87 Poulos, T.L. and Kraut, J. (1980). A hypothetical model of the cytochrome c peroxidase · cytochrome c electron transfer complex. *Journal of Biological Chemistry* 255: 10322–10330.

88 Goodin, D.B. and McRee, D.E. (1993). The Asp-His-iron triad of cytochrome c peroxidase controls the reduction potential electronic structure, and coupling of the tryptophan free radical to the heme. *Biochemistry* 32: 3313–3324.

89 Vidossich, P., Fiorin, G., Alfonso-Prieto, M. et al. (2010). On the role of water in peroxidase catalysis: a theoretical investigation of HRP compound I formation. *The Journal of Physical Chemistry B* 114: 5161–5169.

90 Howes, B.D., Rodriguez-Lopez, J.N., Smith, A.T., and Smulevich, G. (1997). Mutation of distal residues of horseradish peroxidase: influence on substrate binding and cavity properties. *Biochemistry* 36: 1532–1543.

91 Chang, C.K. and Traylor, T.G. (1973). Neighboring group effect in heme-carbon monoxide bonding. *Journal of the American Chemical Society* 95: 8475–8477.

92 Valentine, J.S., Sheridan, R.P., Allen, L.C., and Kahn, P.C. (1979). Coupling between oxidation state and hydrogen bond conformation in heme proteins. *Proceedings of the National Academy of Sciences* 76: 1009–1013.

93 Dolphin, D., Forman, A., Borg, D.C. et al. (1971). Compounds I of catalase and horse radish peroxidase: π-Cation radicals. *Proceedings of the National Academy of Sciences* 68: 614–618.

94 Berglund, G.I., Carlsson, G.H., Smith, A.T. et al. (2002). The catalytic pathway of horseradish peroxidase at high resolution. *Nature* 417: 463–468.

95 Mason, H.S., Fowlks, W.L., and Peterson, E. (1955). Oxygen transfer and electron transport by the phenolase complex 1. *Journal of the American Chemical Society* 77: 2914–2915.

96 Hayaishi, O., Katagiri, M., and Rothberg, S. (1955). Mechanism of the pyrocatechase reaction. *Journal of the American Chemical Society* 77: 5450–5451.

97 Hayaishi, O. (1974). *Molecular Mechanisms of Oxygen Activation*. New York: Academic Press.

98 Klingenberg, M. (1958). Pigments of rat liver microsomes. *Archives of Biochemistry and Biophysics* 75: 376–386.

99 Garfinkel, D. (1958). Studies on pig liver microsomes. I. Enzymic and pigment composition of different microsomal fractions. *Archives of Biochemistry and Biophysics* 77: 493–509.

100 Omura, T. and Sato, R. (1964). The carbon monoxide-binding pigment of liver microsomes: I. Evidence for its hemoprotein nature. *Journal of Biological Chemistry* 239: 2370–2378.

101 Smela, M.E., Currier, S.S., Bailey, E.A., and Essigmann, J.M. (2001). The chemistry and biology of aflatoxin B1: from mutational spectrometry to carcinogenesis. *Carcinogenesis* 22: 535–545.

102 Poulos, T.L., Finzel, B.C., and Howard, A.J. (1987). High-resolution crystal structure of cytochrome P450cam. *Journal of Molecular Biology* 195: 687–700.

103 Adman, E., Watenpaugh, K.D., and Jensen, L.H. (1975). NH···S hydrogen bonds in *Peptococcus aerogenes* ferredoxin, *Clostridium pasteurianum* rubredoxin, and *Chromatium* high potential iron protein. *Proceedings of the National Academy of Sciences* 72: 4854–4858.

104 Langen, R., Jensen, G.M., Jacob, U. et al. (1992). Protein control of iron-sulfur cluster redox potentials. *Journal of Biological Chemistry* 267: 25625–25627.

105 Ueyama, N., Yamada, Y., Okamura, T.-A. et al. (1996). Structure and properties of $[Fe_4S_4\{2,6\text{-bis(acylamino)benzenethiolato-}S\}_4]^{2-}$ and

$[Fe_2S_2\{2,6\text{-bis(acylamino)benzenethiolato-}S\}_4]^{2-}$: protection of the Fe–S bond by double NH···S hydrogen bonds. *Inorganic Chemistry* 35: 6473–6484.

106 Das, P.K., Samanta, S., McQuarters, A.B. et al. (2016). Valence tautomerism in synthetic models of cytochrome P450. *Proceedings of the National Academy of Sciences* 113: 6611–6616.

107 Stoll, S., Lee, Y.-T., Zhang, M. et al. (2012). Double electron–electron resonance shows cytochrome P450cam undergoes a conformational change in solution upon binding substrate. *Proceedings of the National Academy of Sciences* 109: 12888–12893.

108 Hannemann, F., Bichet, A., Ewen, K.M., and Bernhardt, R. (2007). Cytochrome P450 systems — biological variations of electron transport chains. *Biochimica et Biophysica Acta - General Subjects* 1770: 330–344.

109 Gray, H.B. and Winkler, J.R. (1996). Electron transfer in proteins. *Annual Review of Biochemistry* 65: 537–561.

110 Gray, H.B. and Winkler, J.R. (2010). Electron flow through metalloproteins. *Biochimica et Biophysica Acta - Bioenergetics* 1797: 1563–1572.

111 Sevrioukova, I.F., Li, H., Zhang, H. et al. (1999). Structure of a cytochrome P450–redox partner electron-transfer complex. *Proceedings of the National Academy of Sciences* 96: 1863–1868.

112 Strushkevich, N., MacKenzie, F., Cherkesova, T. et al. (2011). Structural basis for pregnenolone biosynthesis by the mitochondrial monooxygenase system. *Proceedings of the National Academy of Sciences* 108: 10139–10143.

113 Tripathi, S., Li, H., and Poulos, T.L. (2013). Structural basis for effector control and redox partner recognition in cytochrome P450. *Science* 340: 1227–1230.

114 Yosca, T.H., Rittle, J., Krest, C.M. et al. (2013). Iron(IV)hydroxide pKa and the role of thiolate ligation in C-H bond activation by cytochrome P450. *Science* 342: 825–829.

115 Rittle, J. and Green, M.T. (2010). Cytochrome P450 compound I: capture, characterization, and C-H bond activation kinetics. *Science* 330: 933–937.

116 Groves, J.T. and McClusky, G.A. (1976). Aliphatic hydroxylation via oxygen rebound. Oxygen transfer catalyzed by iron. *Journal of the American Chemical Society* 98: 859–861.

117 Ortiz de Montellano, P.R. and Stearns, R.A. (1987). Timing of the radical recombination step in cytochrome P-450 catalysis with ring-strained probes. *Journal of the American Chemical Society* 109: 3415–3420.

118 Bowry, V.W. and Ingold, K.U. (1991). A radical clock investigation of microsomal cytochrome P-450 hydroxylation of hydrocarbons. Rate of oxygen rebound. *Journal of the American Chemical Society* 113: 5699–5707.

119 Newcomb, M., Manek, M.B., and Glenn, A.G. (1991). Ring opening and hydrogen-atom transfer trapping of the bicyclo[2.1.0]pent-2-yl radical. *Journal of the American Chemical Society* 113: 949–958.

120 Cryle, M.J., Ortiz de Montellano, P.R., and De Voss, J.J. (2005). Cyclopropyl containing fatty acids as mechanistic probes for cytochromes P450. *The Journal of Organic Chemistry* 70: 2455–2469.

121 Newcomb, M., Shen, R., Lu, Y. et al. (2002). Evaluation of norcarane as a probe for radicals in cytochome P450- and soluble methane monooxygenase-catalyzed hydroxylation reactions. *Journal of the American Chemical Society* 124: 6879–6886.

122 Newcomb, M. and Toy, P.H. (2000). Hypersensitive radical probes and the mechanisms of cytochrome P450-catalyzed hydroxylation reactions. *Accounts of Chemical Research* 33: 449–455.

123 Shaik, S., de Visser, S.P., Ogliaro, F. et al. (2002). Two-state reactivity mechanisms of hydroxylation and epoxidation by cytochrome P-450 revealed by theory. *Current Opinion in Chemical Biology* 6: 556–567.

124 Shaik, S., Lai, W., Chen, H., and Wang, Y. (2010). The valence bond way: reactivity patterns of cytochrome P450 enzymes and synthetic analogs. *Accounts of Chemical Research* 43: 1154–1165.

125 Foresti, R. and Motterlini, R. (1999). The heme oxygenase pathway and its interaction with nitric oxide in the control of cellular homeostasis. *Free Radical Research* 31: 459–475.

126 Uzel, C. and Conrad, M.E. (1998). Absorption of heme iron. *Seminars in Hematology* 35: 27–34.

127 Kikuchi, G. and Yoshida, T. (1983). Function and induction of the microsomal heme oxygenase. *Molecular and Cellular Biochemistry* 53: 163–183.

128 Maines, M.D. (1988). Heme oxygenase: function, multiplicity, regulatory mechanisms, and clinical applications. *The FASEB Journal* 2: 2557–2568.

129 Yoshida, T., Ishikawa, K., and Sato, M. (1991). Degradation of heme by a soluble peptide of heme oxygenase obtained from rat liver microsomes by mild trypsinization. *European Journal of Biochemistry* 199: 729–733.

130 Maines, M.D. (1997). The heme oxygenase system: a regulator of second messenger gases. *Annual Review of Pharmacology and Toxicology* 37: 517–554.

131 Yoshida, T. and Kikuchi, G. (1978). Reaction of the microsomal heme oxygenase with cobaltic protoporphyrin IX, and extremely poor substrate. *Journal of Biological Chemistry* 253: 8479–8482.

132 Yoshida, T., Biro, P., Cohen, T. et al. (1988). Human heme oxygenase cDNA and induction of its mRNA by hemin. *European Journal of Biochemistry* 171: 457–461.

133 Poss, K.D. and Tonegawa, S. (1997). Reduced stress defense in heme oxygenase 1-deficient cells. *Proceedings of the National Academy of Sciences* 94: 10925–10930.

134 Tenhunen, R., Marver, H.S., and Schmid, R. (1968). The enzymatic conversion of heme to bilirubin by microsomal heme oxygenase. *Proceedings of the National Academy of Sciences* 61: 748–755.

135 Tenhunen, R., Marver, H.S., and Schmid, R. (1969). Microsomal heme oxygenase: characterization of the enzyme. *Journal of Biological Chemistry* 244: 6388–6394.

136 Schuller, D.J., Wilks, A., Ortiz de Montellano, P.R., and Poulos, T.L. (1999). Crystal structure of human heme oxygenase-1. *Nature Structural & Molecular Biology* 6: 860–867.

137 Friedman, J., Lad, L., Li, H. et al. (2004). Structural basis for novel δ-regioselective heme oxygenation in the opportunistic pathogen *Pseudomonas aeruginosa*. *Biochemistry* 43: 5239–5245.

138 Hirotsu, S., Chu, G.C., Unno, M. et al. (2004). The crystal structures of the ferric and ferrous forms of the heme complex of HmuO, a heme oxygenase of *Corynebacterium diphtheriae*. *Journal of Biological Chemistry* 279: 11937–11947.

139 Schuller, D.J., Zhu, W., Stojiljkovic, I. et al. (2001). Crystal structure of heme oxygenase from the gram-negative pathogen *Neisseria meningitidis* and a comparison with mammalian heme oxygenase-1. *Biochemistry* 40: 11552–11558.

140 Sugishima, M., Omata, Y., Kakuta, Y. et al. (2000). Crystal structure of rat heme oxygenase-1 in complex with heme. *FEBS Letters* 471: 61–66.

141 Bianchetti, C.M., Yi, L., Ragsdale, S.W., and Phillips, G.N. (2007). Comparison of apo- and heme-bound crystal structures of a truncated human heme oxygenase-2. *Journal of Biological Chemistry* 282: 37624–37631.

142 Lad, L., Schuller, D.J., Shimizu, H. et al. (2003). Comparison of the heme-free and -bound crystal structures of human heme oxygenase-1. *Journal of Biological Chemistry* 278: 7834–7843.

143 Yoshida, T. and Migita, C.T. (2000). Mechanism of heme degradation by heme oxygenase. *Journal of Inorganic Biochemistry* 82: 33–41.

144 Matsui, T., Iwasaki, M., Sugiyama, R. et al. (2010). Dioxygen activation for the self-degradation of heme: reaction mechanism and regulation of heme oxygenase. *Inorganic Chemistry* 49: 3602–3609.

145 Wilks, A. and Ortiz de Montellano, P.R. (1993). Rat liver heme oxygenase. High level expression of a truncated soluble form and nature of the meso-hydroxylating species. *Journal of Biological Chemistry* 268: 22357–22362.

146 Wilks, A., Torpey, J., and Ortiz de Montellano, P.R. (1994). Heme oxygenase (HO-1). Evidence for electrophilic oxygen addition to the porphyrin ring in the formation of alpha-meso-hydroxyheme. *Journal of Biological Chemistry* 269: 29553–29556.

147 Unno, M., Matsui, T., Chu, G.C. et al. (2004). Crystal structure of the dioxygen-bound heme oxygenase from *Corynebacterium diphtheriae*: implications for heme oxygenase function. *Journal of Biological Chemistry* 279: 21055–21061.

148 Matera, K.M., Takahashi, S., Fujii, H. et al. (1996). Oxygen and one reducing equivalent are both required for the conversion of -hydroxyhemin to verdoheme in heme oxygenase. *Journal of Biological Chemistry* 271: 6618–6624.

149 Taiko Migita, C., Fujii, H., Mansfield Matera, K. et al. (1999). Molecular oxygen oxidizes the porphyrin ring of the ferric α-hydroxyheme in heme oxygenase in the absence of reducing equivalent. *Biochimica et Biophysica Acta (BBA) – Protein Structure and Molecular Enzymology* 1432: 203–213.

150 Liu, Y., Moënne-Loccoz, P., Loehr, T.M., and de Montellano, P.R.O. (1997). Heme oxygenase-1, intermediates in verdoheme formation and the requirement for reduction equivalents. *Journal of Biological Chemistry* 272: 6909–6917.

151 Morishima, I., Fujii, H., Shiro, Y., and Sano, S. (1995). Studies on the iron(ii) meso-oxyporphyrin π-neutral radical as a reaction intermediate in heme catabolism. *Inorganic Chemistry* 34: 1528–1535.

152 Liu, Y. and Ortiz de Montellano, P.R. (2000). Reaction intermediates and single turnover rate constants for the oxidation of heme by human heme oxygenase-1. *Journal of Biological Chemistry* 275: 5297–5307.

153 Ortiz de Montellano, P.R. (1998). Heme oxygenase mechanism: evidence for an electrophilic, ferric peroxide species. *Accounts of Chemical Research* 31: 543–549.

154 Matsui, T., Nakajima, A., Fujii, H. et al. (2005). O_2- and H_2O_2-dependent verdoheme degradation by heme oxygenase: reaction mechanisms and potential physiological roles of the dual pathway degradation. *Journal of Biological Chemistry* 280: 36833–36840.

155 Matsui, T., Omori, K., Jin, H., and Ikeda-Saito, M. (2008). Alkyl peroxides reveal the ring opening mechanism of verdoheme catalyzed by heme oxygenase. *Journal of the American Chemical Society* 130: 4220–4221.

17

Chlorophylls

Hitoshi Tamiaki

Graduate School of Life Sciences, Ritsumeikan University, Kusatsu, Shiga, Japan

17.1 Molecular Structures and Names

Chlorophylls are cyclic tetrapyrrole pigments in photosynthetic organisms and function in light-harvesting, energy-transferring, and charge-separating processes at the initial stages of photosynthesis. Natural chlorophylls are estimated to be biosynthesized at an amount of about 10 billion tons per year on Earth [1]. Their annual metabolic (biosynthesized and degraded) turnover is the largest of all pigments produced in the world. A variety of chlorophylls are observed in natural systems, including photosynthetically active pigments and metabolic intermediates.

Chlorophyll *a* was the first recognized pigment [2, 3] with green color from natural leaves: *chloros* (Greek) = green, *phyllon* (Greek) = leaf, and a = the alphabetically first character. In this chapter, the term "chlorophyll *a*" is used, while others are also observed in the literature: chlorophyll a, chlorophyll **a**, chlorophyll-*a*, and so on. Here, chlorophyll *a* is abbreviated as Chl *a*, where the first character is always the capital letter "C," the last "*a*" is in italics, and a space (but not a hyphen) separates "Chl" and "*a*."

17.1.1 Basic Structures and Nomenclature

Chl *a* is the most used and abundant pigment of the chlorophylls (Figure 17.1). The representative Chl *a* is a neutral magnesium(II) complex of a square planar tetradentate ligand, pheophytin *a* (Pheo *a*). Pheo *a* is a cyclic tetrapyrrole linked by four methine groups, and its dianion utilizes four nitrogen donors as the ligand. Pheo *a* has a chlorin π-skeleton – that is, it is a dihydroporphyrin – and one of the pyrrole rings (C-ring) is condensed with a cyclopentanone ring (E-ring). The reduced pyrrole (pyrroline) ring (D-ring) neighboring the E-ring is produced by stereospecific *trans*-hydrogenation of a porphyrin precursor to give a single bond, C17(*S*)–C18(*S*). All peripheral positions of the chlorin moiety are substituted with several functional groups except three meso-positions (5-, 10-, and 20-positions). The 13-substituent of a Chl *a* precursor (a methoxycarbonylethyl group of magnesium protoporphyrin IX monomethyl ester) is cyclized at the 15-position [4], and thus atoms in the fused E-ring are numbered as C13, $C13^1$, $C13^2$, C15, and C14 (not C13, $C13^1$, $C15^1$, C15, and C14).

For substituents on the A- to E-rings, Chl *a* has four methyl groups at the 2-, 7-, 12-, and 18-positions, and vinyl, ethyl, oxo, methoxycarbonyl, and 2-(phytyloxycarbonyl)ethyl

Fundamentals of Porphyrin Chemistry: A 21st Century Approach, Volume 2, First Edition.
Edited by Penelope J. Brothers and Mathias O. Senge.
© 2022 John Wiley & Sons Ltd. Published 2022 by John Wiley & Sons Ltd.

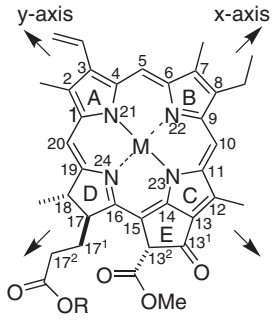

Figure 17.1 Molecular structures of chlorophyll *a* (Chl *a*), its demetalated pheophytin *a* (Pheo *a*), and its hydrolyzed chlorophyllide *a* (Chlide *a*).

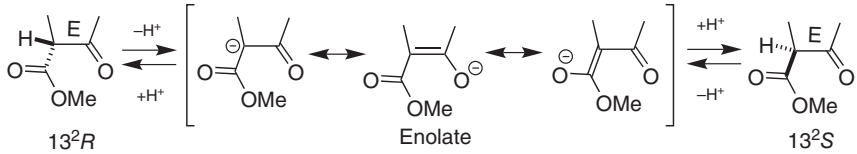

Figure 17.2 Epimerization at the 13^2-position of chlorophylls: (13^2R) "normal" and (13^2S) "prime" forms.

groups at the 3-, 8-, 13^1-, 13^2-, and 17-positions, respectively. In modern nomenclature, use of the term *methoxycarbonyl group* is highly recommended, and the term *carbomethoxy group* should be avoided. The methoxycarbonyl group is connected to the 13^2-position to make a chiral center, and the stereochemistry is an (*R*)-configuration. The formal name of the 17-substituent is so long that it is often simply called the 17-propionate residue.

In Chl *a*, the 17- and 18-substituents are situated in a chemically stable *trans*-form, with a (17*S*,18*S*)-configuration, and dehydrogenation at the C17H–C18H is too difficult to form the fully conjugated porphyrin π-system under ambient conditions. In contrast, the 13^2-proton is located at the α-position of a β-ketoester and is easily removed from the 13^2-carbon atom. The resulting anion (enolate) can be protonated to reproduce the original β-ketoester, and conversion from the (13^2R) to (13^2S)-configuration partly occurs during the protonation of the planar enolate (Figure 17.2). This stereoinversion is an epimerization process of the Chl *a* molecule with multiple chiral centers to give the 13^2-epimer. The diastereomer is called the prime form of Chl *a*, and is shown as chlorophyll *a*′ and Chl *a*′.

Chl *a* is biosynthesized through hydrogenation of the C17=C18 double bond of a precursor of Chl *a* [4, 5], and thus the dehydrogenated Chl *a* derivative possessing a porphyrin π-skeleton is called protochlorophyll *a*. The prefix "proto" was also used for other 17,18-didehydrogenated compounds of chlorophyll derivatives in the older nomenclature. Another Chl *a* derivative demethoxycarbonylated at the 13^2-position via pyrolysis is called pyrochlorophyll *a*; the prefix "pyro" was utilized for 13^2-demethoxycarbonylated chlorophylls. Note that the 13^2-demethoxycarbonylation makes the C13^2-position an achiral center, where no more epimerization occurs.

The phytyl ester of Chl *a* is hydrolyzed to give the corresponding carboxylic acid, which is often observed in metabolic processes of Chl *a* [6, 7]. The free carboxylic acid is called chlorophyllide *a*, Chlide *a* (Figure 17.1). The carboxy group of Chlide *a* is enzymatically

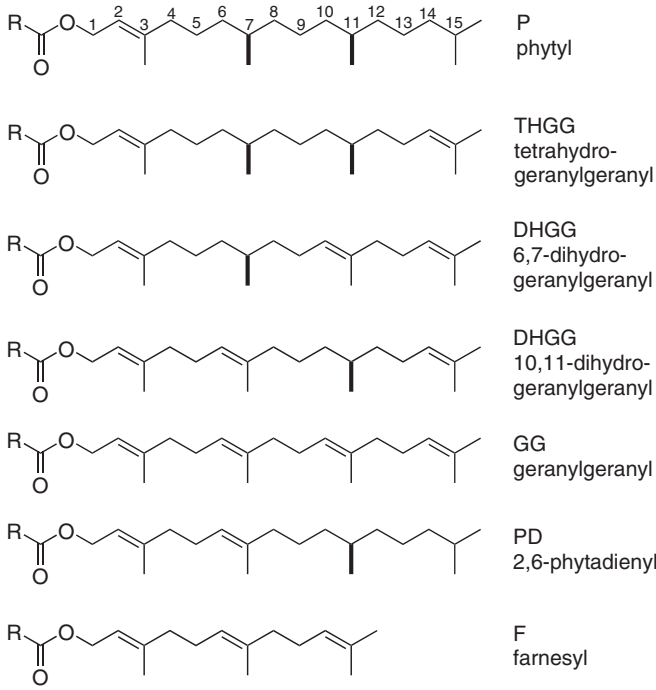

Figure 17.3 Esterifying groups in the 17-propionate residue of chlorophylls.

esterified with phytyl diphosphate to afford Chl *a*, and hence Chlide *a* is a biosynthetic precursor of Chl *a* as well as its degradation product. Other precursors, such as geranylgeranyl (GG, 6,7,10,11,14,15-hexadehydrophytyl), 6,7- or 10,11-dihydrogeranylgeranyl (DHGG) and 6,7,10,11-tetrahydrogeranylgeranyl (THGG) esters of Chlide *a* are found during the greening process of etiolated angiosperm species (Figure 17.3) [5]. For differentiation of the ester moieties in Chl *a*, the following suffix is added as a subscript face. Chls *a* esterified with GG, DHGG, and THGG groups are shown as Chl a_{GG}, Chl a_{DHGG}, and Chl a_{THGG}, while standard phytylated Chl *a* is Chl a_P. In the reaction center (RC) of green sulfur bacteria and a chloracidobacterium, another isomeric Chl a_{THGG} is observed, which is esterified with 10,11,14,15-tetrahydrogeranylgeranyl (6,7-didehydrophytyl or 2,6-phytadienyl = PD) and abbreviated as Chl a_{PD} [8, 9]. Additionally, unnatural esters of Chlide *a* with methyl (M), ethyl (E), and farnesyl groups (F) are depicted as Chl a_M, Chl a_E, and Chl a_F, respectively. Substitution of the phytyl group with a hydrogen atom (H) can be described as Chl a_H, which is equal to Chlide *a*.

Substitution of the central magnesium(II) ion in Chl *a* with two protons afforded Pheo *a*. Similar substitution with zinc(II) ion gives zinc chlorophyll *a* (Zn-Chl *a*) via zinc metalation of Pheo *a*. Removal of the central Mg(II) in Chlide *a* generates its free-base form, the so-called pheophorbide *a*, Pheo a_H.

Hydrogenation of the 3-vinyl group in Chl *a* gives mesochlorophyll *a* possessing the 3-ethyl group, formally called $3^1,3^2$-dihydrochlorophyll *a* (Figure 17.4). Dehydrogenation of the 8-ethyl group in Chl *a* affords divinyl-chlorophyll *a* (DV-Chl *a*) bearing two vinyl groups at the 3- and 8-positions. DV-Chl *a* is a naturally occurring and photosynthetically active

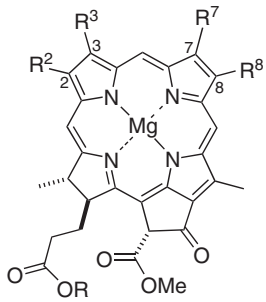

Chl *a*: $R^2 = R^7 = Me$, $R^3 = vinyl$, $R^8 = Et$
DV-Chl *a*: $R^2 = R^7 = Me$, $R^3 = R^8 = vinyl$
Chl *b*: $R^2 = Me$, $R^3 = vinyl$, $R^7 = CHO$, $R^8 = Et$
Chl *d*: $R^2 = R^7 = Me$, $R^3 = CHO$, $R^8 = Et$
Chl *f*: $R^2 = CHO$, $R^3 = vinyl$, $R^7 = Me$, $R^8 = Et$
mesochlorophyll *a*: $R^2 = R^7 = Me$, $R^3 = R^8 = Et$

Figure 17.4 Photosynthetically active chlorophylls possessing a chlorin π-system and their related derivative (R = phytyl).

pigment in specific cyanobacteria [10], and is 8^1,8^2-didehydrochlorophyll *a*. Additionally, oxidation of peripheral substituents of Chl *a* leads to other natural chlorophyll pigments. Transformation of the 2-methyl, 3-vinyl, or 7-methyl group to a formyl group yields Chl *f*, Chl *d*, or Chl *b*, respectively.

17.1.2 Chlorophylls

Chlorophyll is the term used for cyclic tetrapyrrole pigments found in oxygenic organisms and four Chls, *a*, *b, c*, and *d*, were found in order. Chl *b*, 7-demethyl-7-formyl-chlorophyll *a*, is an accessory pigment in Chl-*a*-producing phototrophs including green plants. Chl *c* is a group name for other accessory pigments in chromophyta including diatoms and brown algae (vide infra). Chl *d*, 3-devinyl-3-formyl-chlorophyll *a*, was originally found in some red algae and reported in 1943 [11], but later was recognized as an artifact of Chl *a* due to its fluctuating amount in some phototrophic cells. About 50 years later, Chl *d* was again observed in a cyanobacterium, *Acaryochloris marina* [12], and unambiguously accepted as a naturally occurring pigment. Chl *e* was tentatively used for a pigment with specific visible absorption maxima in the 1950s [13]. It has not been found yet and might be an artifact produced from Chl *a* [14]. However, Chl *f*, 2-demethyl-2-formyl-chlorophyll *a*, was recently found in *Halomicronema hongdechloris*, one of the cyanobacteria. Since the first report in 2010 [15], Chl *f* has also been observed in some cyanobacterial cells cultured under far-red light conditions [16, 17].

Although Chls *a*, *b*, *d*, and *f* have a chlorin π-skeleton and a propionate residue with a phytyl ester [2-(phytyloxycarbonyl)ethyl], Chl *c* has a fully π-conjugated porphyrin moiety and a free acrylate residue without a long esterifying hydrocarbon chain (2-carboxyethenyl) (Figure 17.5). As mentioned above, Chl *c* is primarily divided into three pigments: Chl c_1, possessing methyl and ethyl groups at the 7- and 8-positions, respectively; Chl c_2, possessing the 7-methyl and 8-vinyl groups; and Chl c_3, bearing the 7-methoxycarbonyl and 8-vinyl groups. Chl c_1 corresponds to 17^1,17^2-didehydro-protochlorophyllide *a*. In Chls *c*, all the acrylate residues have a *trans*-configuration, and the diene moieties at C18=C17–$C17^1$=$C17^2$ take a *cisoid* (s-*cis*) conformation [18]. Other related Chl *c* pigments have been found in natural Chl c_2-producing phototrophs: Chl c_2 esterified with monogalactosyldiglyceride at the 6-hydroxy group of the galactose [19], 17,18-dihydrogenated Chl c_2 (divinyl-protochlorophyllide *a*), and 8^1,8^2-dihydrogenated Chl c_3 (monovinyl-chlorophyll c_3) [20] among others.

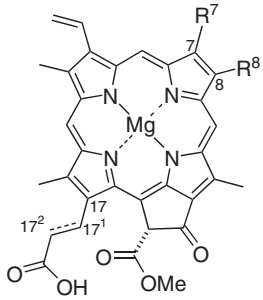

protochlorophyllide *a*: R^7 = Me, R^8 = Et, $C17^1H_2$–$C17^2H_2$
divinyl-protochlorophyllide *a*: R^7 = Me, R^8 = vinyl, $C17^1H_2$–$C17^2H_2$
Chl c_1: R^7 = Me, R^8 = Et, $C17^1H$=$C17^2H$
Chl c_2: R^7 = Me, R^8 = vinyl, $C17^1H$=$C17^2H$
Chl c_3: R^7 = COOMe, R^8 = vinyl, $C17^1H$=$C17^2H$
monovinyl-chlorophyll c_3: R^7 = COOMe, R^8 = Et, $C17^1H$=$C17^2H$

Figure 17.5 Natural chlorophylls possessing a porphyrin π-system.

17.1.3 Bacteriochlorophylls

A variety of bacteriochlorophylls are found as photoactive pigments in anoxygenic photosynthetic bacteria, and bacteriochlorophyll is abbreviated as BChl. Seven types of BChls have been identified: BChls *a* to *g*. BChl *a* is isolated from purple and green bacteria. It has a bacteriochlorin (tetrahydroporphyrin) π-skeleton and is equal to 3-acetyl-*trans*-7,8-dihydrochlorophyll *a* with the (7*R*,8*R*)-configuration (Figure 17.6, left). Zinc-substituted BChl *a* (Zn-BChl *a*) was recently found in specific purple bacteria grown in acidic environments [21] and a thermophilic chloracidobacterium [22, 23]. BChl *b* found in some purple bacteria is $8,8^1$-didehydrogenated BChl *a* and possesses an (*E*)-ethylidene group at the 8-position (Figure 17.6, right). Both BChls *a* and *b* usually are esterified with phytol, but in purple bacteria some of them have other ester groups including GG, DHGG, and THGG [24]. Additionally, BChl a_{GG} and BChl $b_{2,10\text{-PD}}$ (2,10-phytadienyl or 10,11-didehydrophytyl) are exclusively found in specific purple bacteria [19].

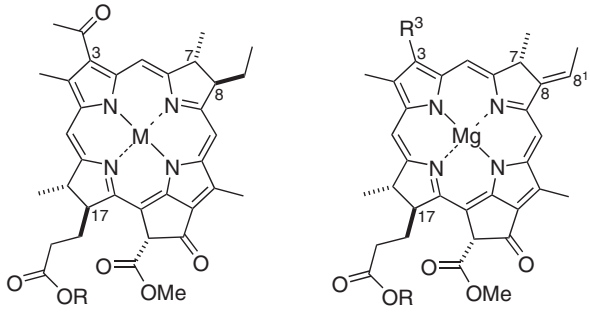

BChl *a*: M = Mg, R = phytyl, etc.
Zn-BChl *a*: M = Zn, R = phytyl
BChl *b*: R^3 = COMe, R = phytyl, etc.
BChl *g*: R^3 = vinyl, R = farnesyl

Figure 17.6 Natural bacteriochlorophylls possessing a bacteriochlorin π-system.

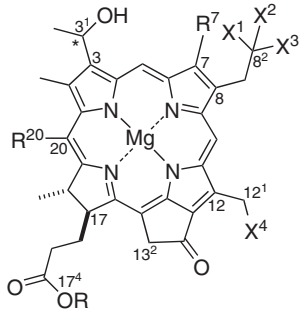

BChl *c*: $R^7 = R^{20}$ = Me
BChl *d*: R^7 = Me, R^{20} = H
BChl *e*: R^7 = CHO, R^{20} = Me
BChl *f*: R^7 = CHO, R^{20} = H
X^1, X^2, X^3, X^4 = H or Me,
R = farnesyl, stearyl, etc.

Figure 17.7 Natural bacteriochlorophylls possessing a chlorin π-system.

Heliobacteria always produce BChl *g*, which is 3-vinyl-bacteriochlorophyll *b* esterified with farnesol (Figure 17.6, right). Phytylated BChl *g* has not been found in natural species yet. The BChl *g* molecule is an isomer of farnesylated Chl *a*, whose C7=C8 double bond is shifted to C8=C8^1 or whose hydrogen atom at the 8^1-position moves to the 7-position to form BChl *g* [= farnesylated 7-hydro-8^1-dehydro-chlorophyll *a* with the (7*R*,8*E*)-configuration].

BChls *a*, *b*, and *g* have a bacteriochlorin π-skeleton, while BChls *c*, *d*, *e*, and *f* have the same chlorin π-skeleton as Chl *a*. Each BChl *c*, *d*, *e*, or *f* represents not a single molecular structure but comprises 3^1-stereochemical mixtures possessing various substituents at the 8-, 12-, and 17^4-positions (Figure 17.7). BChls *c*–*f* have a 1-hydroxyethyl group at the 3-position and lack a methoxycarbonyl group at the 13^2-position. One of the BChl *d* species is prepared by hydration of pyrochlorophyll *a* in a Markovnikov fashion at the 3-vinyl group. BChl *c* is 20-methylated BChl *d*, and BChls *e* and *f* are 7-formylated BChls *c* and *d*, respectively. BChls *c*–*e* are observed in wild-type cells of green photosynthetic bacteria, while BChl *f* has not yet been found in natural species, only in genetic mutants of BChl-*e*-producing bacteria [25]. In green sulfur bacteria, BChls *c*–*f* generally possess a farnesyl (C_{15}) group as the esterifying moiety, and also various hydrocarbon moieties with C_{10} to over C_{20} are present in some green bacteria and a chloracidobacterium. These natural BChl molecules are a mixture of (3^1R)- and (3^1S)-epimers, and also mixtures of 8- and 12-homologs that are methylated at the 8^2- and 12^1-positions: 8-ethyl (E), propyl (P), isobutyl (I), and neopentyl groups (N) as well as 12-methyl (M) and ethyl groups. For example, stearylated (3^1R)-8-ethyl-12-methyl-bacteriochlorophyll *c* and farnesylated (3^1S)-8-isobutyl-12-ethyl-bacteriochlorophyll *e* are abbreviated as R[E,M]BChl c_S and S[I,E]BChl e_F, respectively [26].

17.1.4 Axial Coordination

Chlorophylls are magnesium (rarely zinc) complexes of cyclic tetrapyrroles, and their molecular structures are usually drawn as square planar complexes without any axial ligands at the central metal. However, the central Mg has one axial ligand in solution, in a polypeptide matrix, and in the solid state. The Mg atom is always five-coordinated in natural systems, whereas four-coordinated complexes lacking the axial ligand have never been observed. Conventional six-coordinated (6c) complexes with two axial ligands have not been reported in naturally occurring (B)Chl–peptide systems, while two highly coordinating pyridine molecules can equally ligate to the central Mg at both the axial positions in a neat solvent. In natural systems, a pseudo six-coordination can be observed. Here, two ligands

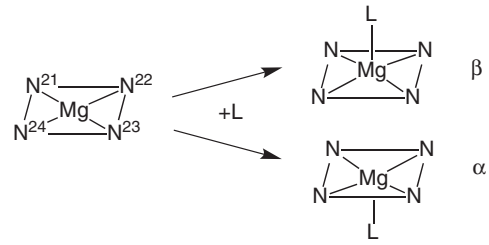

Figure 17.8 Schematic drawing for singly axial coordination of chlorophylls to form five-coordinated species with chirality at the central magnesium.

are axially ligated to the Mg in an asymmetric fashion, with one axial coordination having the usual bond length and the other having a weaker coordination with a longer Mg–ligand distance [27].

The dianionic forms of pheophytins are unsymmetric due to various substituents at the peripheral positions, and the four nitrogen atoms N_4 are chemically different. A magnesium dication is coordinated with the pheophytinato ligand to form planar MgN_4, to which one more ligand L coordinating from the axial side is added to give five-coordinated (5c) $LMgN_4$ (Figure 17.8). The ligand L coordinated from the upper or lower side affords mirror-imaged enantiomers around the Mg, and hence the 5c Mg center produces an asymmetric center. As the pheophytins are chiral molecules, the two 5c chlorophylls are diastereomers. Such stereochemistry has been recently investigated from the crystallographic structural analysis of many chlorophyll–protein complexes [28–30]. The ligand L coordinates to MgN_4 from the bottom and upper sides (see Figures 17.1/4–7) to form 5c complexes $LMgN_4$, called α- and β-complexes, respectively (Figure 17.8).

X-ray crystallographic analyses of various chlorophyll–proteins containing the diastereomerically different 5c complexes showed that α-complexes are observed more often than β-complexes. This stereochemical preference may be due to the fact that the α-complexes are energetically more stable than the β-complexes, which is supported by molecular modeling calculations. The energy difference is small and axial coordination is a relatively weak bonding, and hence stereochemically pure α/β-complexes have not yet been identified in solution. In related Ga(III) and In(III) complexes of chlorophylls, the equilibrium reaction between the α/β-complexes slows down in solution, and they could be differentiated using NMR spectroscopy at room temperature [31]. Recently, Sn(IV) complexes of Chl *a* derivatives with two axial halides were prepared, and their fluorides ligating the 6c tin(IV) centers gave different chemical shifts of the ^{19}F NMR peaks, indicating the differentiation of α/β-ligands in solution [32].

17.1.5 Minor Chlorophylls

In photosynthetic RCs, unique chlorophylls are observed as charge transfer pigments. These chlorophylls are important for the process, but their content is low in phototrophic cells. Based on advancements in modern analytic techniques, several were recently identified and characterized physicochemically. Their biosynthetic pathways have also been investigated.

RCs in photosystem I (PS I) of oxygenic phototrophs and PS I-type RCs of three anoxygenic bacteria, green sulfur bacteria, heliobacteria, and a chloracidobacterium, have (13^2S)-epimers (prime forms) of chlorophylls as a primary electron-donating component [33]. Typically, Chl *a* and Chl *a*′ molecules form a dimeric structure and play the role of a primary electron donor in the RC of PS I. Phototrophs producing DV-Chl *a*, Chl *d*, (Zn-)BChl

a, and BChl *g* also contain the corresponding prime forms in their PS I (or PS I-type) RCs. The epimerization readily occurs in solution (see Figure 17.2 and Section 17.3.1), but the natural prime forms are supposed to be enzymatically biosynthesized from the corresponding normal chlorophylls, although the specific epimerases have not been identified yet. (DV-)Chl *b*′, Chl *c*′, Chl *f*′, and BChl *b*′ have not been detected in natural phototrophic cells, which is comparable to the absence of their (13^2R)-epimers in the PS I(-type) RCs. Note, that there are no prime forms of BChls *c*–*f* as they lack the 13^2-methoxycarbonyl group.

Oxygenic RCs in photosystem II (PS II) and anoxygenic PS II-type RCs of purple bacteria and green filamentous (gliding) bacteria (recently renamed filamentous anoxygenic phototrophs) contain free bases (metal-free forms) of chlorophylls, that is, pheophytins: (DV-)Pheo *a* and BPheos *a*/*b*. These molecules function as a primary electron acceptor in the RCs. Demetalation of the chlorophylls (pheophytinization) would occur by unknown enzymes, while it smoothly proceeds under acidic conditions (see Section 17.3.3). Such pheophytins possess two hydrogen atoms at the N21 and N23 positions along the molecular y-axis. Moreover, Chl a_{PD} (see Section 17.1.1) and farnesylated (8^1R)-hydroxy-chlorophyll *a* are found in green sulfur bacteria or a chloracidobacterium and heliobacteria, respectively, and function as primary electron acceptors in their PS I-type RCs.

17.1.6 Inconsistency of Molecular Structures with Names

Natural chlorophylls possess three π-skeletons, porphyrin, chlorin (17,18-dihydroporphyrin), and bacteriochlorin (7,8,17,18-tetrahydroporphyrin). The names of (B)Chls do not always reflect on their composite π-skeletons. Chl *c* is one of the porphyrins, and BChls *c*–*f* have a chlorin moiety, while other Chls and BChls possess chlorin and bacteriochlorin π-systems, respectively. Chls are called chlorophyll pigments of oxygenic phototrophs, not for chlorin-type macrocycles, and BChls are also named for major chlorophyll pigments found in anoxygenic photosynthetic bacteria. Please do not confuse the inconsistency of the names with their molecular structures.

17.2 Optical Properties

All chlorophylls have intense electronic absorption bands in the visible region, which sometimes reaches into the near-infrared region. Therefore, chlorophylls can absorb sunlight efficiently and are used as light-harvesting pigments in photosynthesis. Here, the relationship of their molecular structures with optical properties including electronic absorption spectra is discussed [8, 34–36].

Chlorophylls have two main absorption bands, the Q and B (Soret) bands in the red and blue regions, respectively, which is similar to the other porphyrinoids. Since chlorophylls are unsymmetrical molecules, the two bands are split to give Q_y, Q_x, B_y, and B_x bands from longer to shorter wavelengths. The transition moments of the Q_y/B_y and Q_x/B_x bands are parallel to the perpendicular molecular y- and x-axes, respectively (see Figure 17.1), which are situated nearly along the N21–N23 (through the A to C rings) and N22–N24 lines (through the B to D rings). Furthermore, the main (0,0) peaks of the four bands are associated with the minor vibronic bands, (0,1), (0,2), and so on, in their blue sides.

The absorption bands of chlorophylls in natural systems are complex, so their absorption spectra in an organic solvent are first described in their monomeric states.

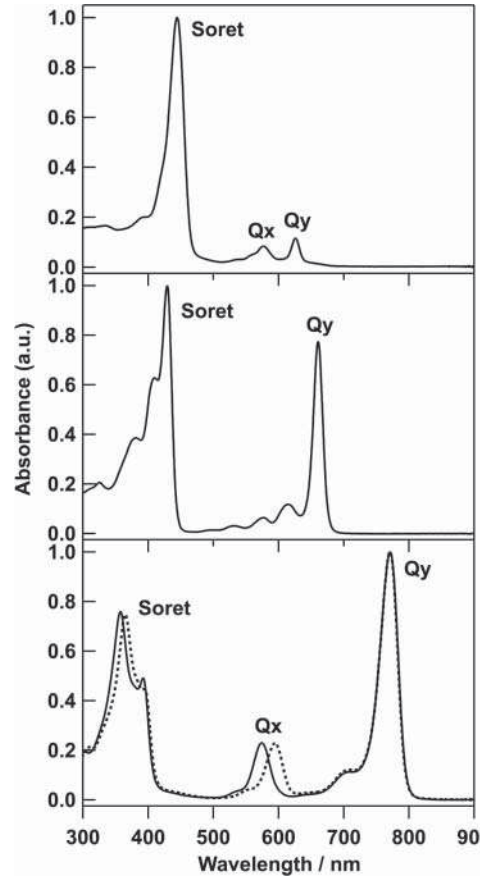

Figure 17.9 Electronic absorption spectra of Chl c_1 (top), Chl *a* (middle), and BChl *a* (bottom) in diethyl ether (solid) and tetrahydrofuran (dotted) at room temperature.

17.2.1 π-Conjugation

Chl *a*, possessing a chlorin π-system, is readily dissolved in diethyl ether to give sharp absorption bands in the visible region (Figure 17.9, middle). The visible spectrum shows intense Q_y and Soret bands, while relatively weak Q_x bands are observed between the two main bands. BChl *a*, having a bacteriochlorin π-skeleton, affords absorption bands in a wider range from the ultraviolet to near-infrared regions (Figure 17.9, bottom). The changes in the electronic absorption spectra of Chl *a* to BChl *a* are (i) a red shift of the Q_y band, (ii) an increase in Q_x absorbance, and (iii) a blue shift of the Soret band. It is noteworthy that less π-conjugation, for example, going from a chlorin to a bacteriochlorin through the 7,8-dihydrogenation, bathochromically shifts the longest (Q_y) absorption maximum. This observation is unique, since a decrease of π-conjugation usually moves an absorption edge to a shorter wavelength: blue shifts in butadiene to ethylene and in naphthalene to benzene. This reverse tendency is explained by the reduction of the C7=C8 double bond in a chlorin π-system generating a more localized π-electron circuit along the y-axis of the resulting bacteriochlorin, giving a red-shifted Q_y band.

In a similar manner, oxidation of the C17H–C18H single bond of Chl *a* to the C17=C18 double bond of protochlorophyll *a* blue-shifts the Q_y maximum. The increased π-conjugation degree going from a chlorin to a porphyrin moiety disfavors localization of the π-system along the y-axis, leading to such a hypsochromic shift. Additional dehydrogenation of the

17-propionate to the 17-acrylate residue in Chl *c* results in a small red shift of the Q_y maximum due to the π-elongation along the x-axis. All Chls *c* have relatively less intense Q_y bands as well as the aforementioned weak Q_x bands (Figure 17.9, top), which is characteristic of visible spectra for fully π-conjugated porphyrin compounds [34–38].

17.2.2 Peripheral Substituents

The electronic absorption spectra of chlorophylls are dependent on their peripheral substituents as well as their π-conjugated cores (see Section 17.2.1). Oxidation of the 7-methyl group in Chl *a* to the 7-formyl group in Chl *b* induces a blue-shifted and less intense Q_y band and a red-shifted Soret band (Table 17.1). The 7^1-oxidation elongates the π-conjugation pathway along the x-axis, and hence π-conjugation along the y-axis decreases relatively to give the blue shift of the Q_y maximum, which is consistent with the effect of the oxidation of the C7H–C8H of bacteriochlorins to the C7=C8 of chlorins. The same changes are observed in BChl *c* (7-methyl) to BChl *e* (7-formyl) and in BChl *d* (7-methyl) to BChl *f* (7-formyl) possessing a chlorin chromophore. The Soret band is produced by both the B_x and B_y bands, so the Soret maximum of Chl *b* is bathochromically shifted by a red-shifted B_x band based on an increase of the π-conjugation along the x-axis.

In contrast, oxidation of a methyl to a formyl group at the 2-position of Chl *a* to Chl *f* moves both the Q_y and Soret maxima to longer wavelengths (Table 17.1). The 2^1-oxidation enhances the π-conjugation along the y-axis to afford the above red shifts, as expected. The oxidative cleavage of the 3-vinyl group in Chl *a* to the 3-formyl group in Chl *d* also leads to bathochromic shifts of the Q_y and Soret maxima. As the electronegativity of a formyl group is larger than that of a vinyl group [39], the substitution increases the delocalization to the π-circuit at the y-axis to give such red shifts. A similar substitution effect at the 3-position is observed in BChl *g* (3-vinyl) to BChl *b* (3-acetyl). The blue shifts of both Q_y and Soret maxima by hydration of the 3-vinyl group in Chl *a* to the 3-(1-hydroxyethyl) group as in BChl *d*, are also explained by less π-conjugation along the y-axis and reduction in the group's electronegativity, because 13^2-demethoxycarbonylation in Chl *a* to BChl *d* only slightly affects the visible spectra due to the lack of its π-conjugation with the chlorin moiety.

The less π-conjugation of the 3-substituent blue-shifts the Q_y maxima of monomeric chlorophylls in solution. A similar effect is observed in natural systems. In the light-harvesting antenna systems of purple bacteria, light-harvesting 1, 2, and 3 (LH1, LH2, and LH3) complexes, the light-absorbing components are composed of protein-bound BChl *a* molecules [40]. The specific bonding of BChl *a* with one of the peptides rotates the 3-acetyl group from coplanarity with the bacteriochlorin π-system toward a perpendicular orientation. The rotation reduces the π-conjugation along the y-axis and moves some of the red-most absorption maxima in LH3 to a shorter wavelength.

Methylation at the 20-position of BChls *d* and *f* to BChls *c* and *e*, respectively, red-shifts both the Q_y and Soret maxima (Table 17.1). The bathochromic shifts are partially due to the electronic effect of the methyl group and primarily ascribable to its steric effect. The 20-methyl group interacts with the neighboring 2- and 18-methyl groups to disturb the planarity of the chlorin π-system. This sterically induced distortion of the π-plane affects the electronic levels of the chlorin chromophores to give the aforementioned red shifts. Methylation at other positions, including 8^2- and 12^1-methylation of BChls *c*/*d*/*e*/*f*, does not alter their absorption spectra, due to the lack of their direct conjugation with the chlorin π-system and less steric interactions. Note that any peripheral substituents lacking direct π-conjugation

Table 17.1 Electronic absorption spectral data of naturally occurring and photosynthetically active chlorophylls in diethyl ether.

	λ_{max}/nm[a] (relative intensity[b])		
Chlorophylls	**Soret**	**Q_x**	**Q_y**
Chl a_P	409/430*	616 (0.12)	661 (0.77)
Chl a'_P	410/429*	614 (0.12)	661 (0.79)
DV-Chl a_P	436	615 (0.10)	660 (0.71)
Pheo a_P	409	534 (0.09)	667 (0.50)
Chl b_P	429/453*	593 (0.07)	642 (0.36)
Chl c_1	444	576 (0.08)	626 (0.12)
Chl c_2	448	579 (0.09)	626 (0.08)
Chl c_3	451	584 (0.11)	623 (0.07)
PChlide a[c]	432	570 (0.05)	622 (0.13)
Chl d_P	391/446*	638 (0.14)	686 (1.18)
Chl f_P	396*/440	–	695 (1.44)
BChl a_P	357*/392	574 (0.31)	771 (1.35)
BChl a_{GG}	357*/392	574 (0.31)	771 (1.33)
Zn-BChl a_P	354*/390	559 (0.30)	763 (1.27)
BPheo a_P	357*/384	524 (0.24)	750 (0.64)
BChl b_P	369*/408	579 (0.30)	795 (1.43)
BChl c_F[d]	412/432*	624 (0.10)	660 (0.66)
BChl d_F[d]	405/425*	611 (0.11)	650 (0.83)
BChl e_F[d]	435/459*	594 (0.05)	646 (0.27)
BChl f_F[d]	426/450*	586 (0.07)	633 (0.36)
BChl g_F	365*/405	565 (0.33)	767 (1.06)

a) The lowest energy bands Q(0,0) are shown. In Mg-chlorins, the second longest maxima are given as values of the Q_x column. When more than two Soret peaks were measured, the second intense maximum is cited, too.
b) Based on the intense Soret peak (*).
c) Protochlorophyllide *a*.
d) (3^1R)-Epimeric 8,12-diethyl homolog.

hardly change the visible absorption spectra of chlorophylls, for example, the stereochemistry at the 3^1- and 13^2-positions and esterifying hydrocarbons in the 17-substituent.

17.2.3 Intermolecular Interactions Including Coordination

Axial coordination to the central metal of chlorophylls affects the electronic absorption bands. As mentioned in Section 17.1.4, the central magnesium carries one axial ligand, at least in proteins and solutions, and the coordination strength is dependent on the binding ability of the ligand. A ligand weakly coordinates to the magnesium, which slightly moves to the axial direction out of the cyclic tetrapyrrole π-plane. Strongly coordinating ligands tightly coordinate to the Mg to form an apparent pyramidal complex with a large distortion

of the π-system. Increased displacement of the Mg from the tetrapyrrole plane gives a more largely π-distorted 5c complex and shifts the absorption bands to shorter wavelengths. Two strongly coordinating ligands can form the 6c species, where the Mg is more in the in-plane position. Such a complex, with two equivalent axial ligands, has less π-distortion and the abovementioned hypsochromic shifts are reduced. The absorption shifts via coordination are most notable for the Q_x bands. The relatively intense Q_x band in bacteriochlorin π-systems, including the BChls *a*/*b*/*g*, is shifted remarkably upon changing from five- to six-coordination: $\lambda_{max} = 574$ (5c in diethyl ether) → 594 (6c in tetrahydrofuran) for Q_x maxima of BChl *a* (Figure 17.9, bottom).

Substitution of the central magnesium ion of chlorophylls with two protons gives pheophytins, showing largely different absorption spectra. The spectral changes are dependent on the chlorophyll species. For example, pheophytinization of Chl *a* to Pheo *a* in solution induces red shifts of the Q_x bands and blue shifts of the Q_y and Soret maxima (Table 17.1). The red-shifted Q_x bands are intensified, so the green-colored solution is darkened by the pheophytinization. Metalation of Pheo *a* with divalent cations, for example, Mg^{2+} and Zn^{2+}, changes the solution to bright green, and this color change is useful for following such metalations. Pheophytins are readily protonated at the imino nitrogen atoms under acidic conditions. The stepwise protonation produces their mono and dications, giving spectra different from the neutral species. For example, treatment of Chl *a* in diethyl ether with aqueous acid results in spontaneous demetalation and protonation with a color change from green to black.

Other intermolecular interactions affect the electronic absorption spectra of chlorophylls as well. For example, the carbonyl groups directly conjugated with a tetrapyrrole π-system, including the 2,3,7-formyl, 3-acetyl, and 13-keto-carbonyl groups, can hydrogen-bond with other moieties accompanied by a change in the absorption bands. In contrast, carbonyl groups in the 13^2-methoxycarbonyl group and 17-propionate residue are not π-conjugated with the porphyrinoid core, and their hydrogen bonding hardly alters the absorption spectra in the monomeric state. Electronic absorption spectra are dependent on the environment around the chlorophyll molecules, that is, homogeneous solvents, heterogeneous peptides, and so on. Especially polar functional groups, including charged moieties, can specifically interact with the excited states of chlorophylls in peptides to significantly change the absorption spectra. Note that relatively rigid peptides can distort the tetrapyrrole π-plane and perturb the chlorophyll spectra [41, 42].

17.2.4 Aggregation

Chlorophylls often self-aggregate to form large oligomers due to their extended π-systems. Such aggregates are readily formed in less polar organic solvents as well as in an aqueous solution, while in coordinating solvents they are axially ligated by solvent molecules, which suppresses formation of self-aggregates via π–π interaction. It is very difficult to control self-aggregation of chlorophylls in solution; hence, disordered aggregates with a range of sizes and supramolecular structures are produced. An increase in the aggregation number reduces the solubility of self-aggregates, and very large aggregates are insoluble and precipitate. Self-aggregates of submicrometer size are heterogeneous supramolecular structures, showing broadened absorption spectra and also an increase in the absorbance at the shorter wavelengths due to the light scattering in the region of several hundred nanometers.

In photosynthetic apparatuses, some chlorophyll molecules self-aggregate in an ordered fashion to give specific functions such as light harvesting, energy transfer, and charge

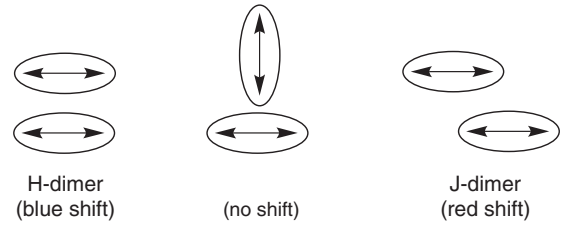

Figure 17.10 Schematic drawings of chlorophyll dimers and their spectral changes.

separation. Their absorption spectra are dependent on the supramolecular structures. When two chlorophyll π-planes are interacted along the same molecular axis to form a completely overlapping dimer, they form H-aggregates (Figure 17.10). In the H-dimer, the electronic absorption maxima are shifted to shorter wavelengths due to the exciton coupling of the molecular transition moments [43]. When one of the components in the H-dimer is rotated 90° around the center-to-center axis, the transition moments are perpendicular and no longer interact in the dimer, resulting in the same spectra as those of the monomers. If one component in the H-dimer is moved along the molecular axis to form a J-dimer whose absorption band corresponds to the transition moment, the spectrum is red-shifted.

In J-type self-aggregates, composite chlorophylls are situated more closely to each other and their exciton-coupling interaction is enhanced; hence, the absorption bands based on the slipped transition moments are shifted to longer wavelengths. The red-shifted value of the absorption maxima increases with the aggregation number. For example, the special pair of BChls in bacterial photosynthetic RCs is a J-type dimer nearly along the y-axis, and the Q_y maximum is red-shifted from the monomeric peak. LH1 complexes, the core antennas of purple bacteria [40], and chlorosomes, the main peripheral antenna systems of green bacteria [44, 45], are composed of J-type self-aggregates of the composite bacteriochlorophyll molecules, which have largely red-shifted Q_y maxima.

17.2.5 Circular Dichroism

All naturally occurring and photosynthetically active chlorophylls possess chiral centers, and dichroism spectral bands are observed in pigment solutions. The circular dichroism (CD) spectra are dependent on the stereochemistry. Chl *a* has three chiral carbon atoms at the 13^2-, 17-, and 18-positions except an asymmetric phytyl group with the (2*E*,7*R*,11*R*)-stereochemistry. All chiral positions are not directly included in the chlorin π-system, and hence its CD spectrum is less intense in the visible region (Figure 17.11, upper, solid line). 13^2-Epimeric Chl *a*′ is partly distorted in the π-plane through the steric repulsion of the (13^2R)-methoxycarbonyl group with the (17*S*)-propionate residue to give relatively larger CD bands (Figure 17.11, upper, dotted line). The epimerization barely affects the visible absorption bands (Table 17.1), but Chl *a*′ shows a different CD spectrum from that of Chl *a*. Measuring the CD spectra is useful for detection of the epimerization.

The CD spectra of monomeric chlorophylls are not so intense, but those of their exciton-coupled self-aggregates are relatively intense. For example, large CD couplets of the aforementioned LH1 and chlorosome are observed in the red-shifted Q_y regions (Figure 17.11, lower). Additionally, chlorophylls give intense CD bands upon specific interaction with peptides.

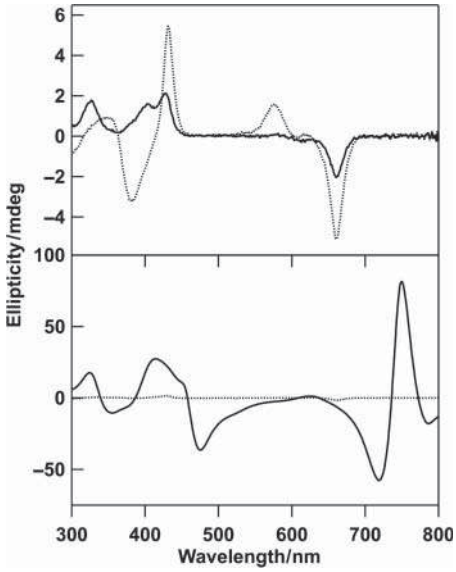

Figure 17.11 Circular dichroism spectra of (upper) Chl *a* (solid) and its 13^2-epimeric Chl *a*′ (dotted) in diethyl ether and (lower) BChl *c* in an aqueous chlorosome solution (self-aggregates, solid) and diethyl ether (monomer, dotted).

17.2.6 Fluorescence Emission

Chlorophylls are highly fluorescent in their monomeric state. When a solution of monomeric chlorophyll species in organic solvents is irradiated with visible light, the fluorescence emission is observed in regions of longer wavelengths than the red-most Q_y band. The emission spectral shape is nearly a mirror image of the Q_y bands. The fluorescence emission behavior of some chlorophylls in aerated diethyl ether at room temperature, that is, axially ligated with a single solvent molecule to form their monomeric 5c species (see Section 17.2.3), is described below [8, 35–37]. Note that fluorescence data are independent of the excited wavelength due to Kasha's rule. Usually, the intense Soret maxima are excited in fluorescence measurements. The light scatter at the half energy level of the excited light (= twice the wavelength of excited light) must be carefully considered for their discussion.

Chlorophylls possessing a chlorin or porphyrin π-system typically exhibit the main emission peaks at a wavelength longer by about 5 nm than the red-most Q_y maximum. The difference between the absorption and emission peak positions is called the Stokes shift. The Stokes shift values in solution are dependent on the structural and solvation energy differences between the ground (S_0) and singlet excited (S_1) states, that is, their difference in electronic distribution and atomic positions. The small Stokes shifts indicate that the conformations of their S_1 states are not largely different from their S_0 states in solution. The singlet excited energy is estimated from the visible absorption and fluorescence emission spectra. In their normalized spectra, the crossing point corresponds to the singlet excited energy (Figure 17.12). In the case of small Stokes shifts, the singlet excited energy is comparable to the red-most Q_y maximum. Therefore, the Q_y maxima of chlorophylls can be used for their singlet excited energies and these are called site energies in solutions as well as protein complexes.

The fluorescence emission lifetime of Chl *a* is about 5 ns at room temperature, and other chlorophylls with a chlorin moiety have similar lifetimes. Fluorescence emission quantum yields of (DV-)Chl *a* and Chls *d*/*f* are about 30%, while those of Chl *b* and Pheo *a* are smaller with about 20%. The 8-vinylation and chemical modification on the A-ring hardly affect the

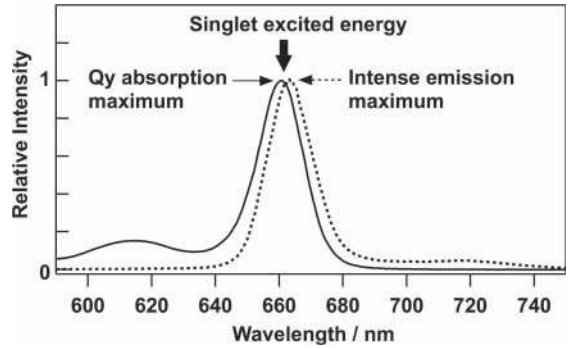

Figure 17.12 Normalized visible absorption (solid) and fluorescence emission spectra (dotted, excited at the Soret maximum) of Chl *a* in diethyl ether.

quantum yields, but 7-formylation and pheophytinization apparently decrease the values. Chls *c* have about 20% emission quantum yields, and dehydrogenation on the D-ring suppresses the values substantially.

BChl *a*, bearing a bacteriochlorin π-skeleton, shows about 10 nm as its Stokes shift. Even considering it at the energy unit, the observed value is larger than those of the above chlorins and porphyrins. Its singlet excited states give about 2 ns and 20% for the lifetime and quantum yield, respectively. These values are also smaller than those of Chl *a*. The differences might be ascribable to the higher flexibility of its π-system. Additionally, pheophytinization and zinc metalation suppress both values. This reduction might be explained by the former having a more flexible π-skeleton lacking the coordinated central Mg and the latter experiencing a heavy metal effect.

17.3 Chemical Reactivities

Naturally occurring chlorophylls are usually magnesium complexes of cyclic tetrapyrroles with a variety of functional groups at the peripheral positions. Monomeric states of chlorophylls are labile in solution, while they are chemically stable in the photosynthetic apparatus. Especially, external stimuli including irradiation with visible light, thermal treatment, and exposure to air (molecular oxygen) can transform them to other compounds. Such chemical modifications of reactive chlorophylls are described below.

17.3.1 Epimerization

Most chlorophylls have a β-ketoester moiety on the E-ring, which is the most reactive of the peripheral substituents. Under basic conditions, deprotonation at the 13^2-position readily occurs to form the anion stabilized by two adjacent carbonyl groups (Figure 17.2). The resulting carbanion is protonated in a less stereoselective fashion to give a mixture of the original (13^2R)-chlorophyll and its (13^2S)-epimer. This 13^2-stereoinversion (epimerization) produces the prime form, which is less thermodynamically stable. For example, under equilibrium conditions, Chl *a* in pyridine is transformed to Chl *a*′ in about 20% yield [46]. In the prime form, the 13^2-methoxycarbonyl group is situated toward the same direction of the 17-propionate residue, so the steric repulsion destabilizes the stereoisomer.

The enol forms of β-ketoesters are generally observed in solution under neutral conditions, as they are thermodynamically stabilized by intramolecular hydrogen bonding. In contrast,

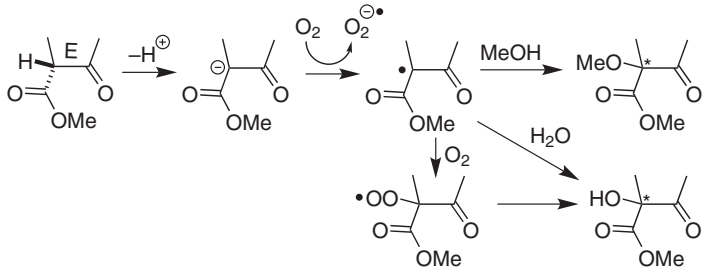

Figure 17.13 Allomerization of chlorophylls to form epimeric mixtures of 13^2-methoxy- and hydroxy-substitutes.

the enol forms of chlorophylls are not detected in neutral solvents due to the lower stability of the enol form [47]. Therefore, chlorophylls always take the keto forms in natural systems as well as in conventional organic solvents, except for specific basic [48] or chelating conditions [49].

17.3.2 Allomerization

During the extraction of chlorophylls from natural phototrophs using methanol, 13^2-methoxy- and hydroxy-substituted products are sometimes obtained. These products and reactions are called allomers and allomerizations, respectively, and must be avoided in order to obtain pure samples of chlorophylls efficiently. The undesired allomerization of chlorophylls occurs as follows (Figure 17.13). If a trace amount of base is present in methanol as the extraction solvent, the 13^2-proton of chlorophylls is removed to form the corresponding anions (see Section 17.3.1). The carbanion loses one electron to produce its radical species, which reacts with methanol to give a methoxy-substituted allomer. The allomer is a stereochemical mixture of the 13^2-epimers due to the less stereoselective attack, similar to the aforementioned epimerization. The radical species reacts with an oxygen molecule to afford the corresponding peroxide radical, which is transformed to a hydroxy-substituted allomer. The hydroxy allomer is also produced by the reaction of the radical with a water molecule. This allomerization during the extraction of chlorophylls is promoted by an electron transfer induced by irradiation with visible light and accelerates at high temperature; thus, the extraction procedures should be performed in the dark and at a low temperature [50].

17.3.3 Pheophytinization

The central magnesium cation of chlorophylls is easily replaced by two protons under acidic conditions to give pheophytins. This pheophytinization is initiated by the attack of a proton on one of the four coordinating nitrogen atoms. The protonation proceeds through a direct attack of H^+ from the environment around the chlorophyll molecule or an intramolecular attack of a proton species bound to an axially coordinated ligand, such as water or alcohols. The *in vivo* pheophytinization is catalyzed by Mg-dechelatases, which were very recently implicated in stay-green processes of plants and green algae [51]. During degradation of chlorophylls, such enzymatic pheophytinizations are preferable, but non-enzymatic demetalation during the biosynthesis of photosynthetically active pheophytins (see Section 17.1.5) cannot be ruled out at present.

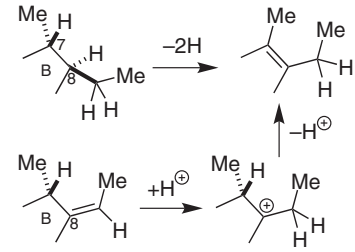

Figure 17.14 Dehydrogenation of 7,8-dihydro-bacteriochlorin (BChl *a*) and isomerization of 8-ethylidene-bacteriochlorins (BChls *b*/*g*) to chlorins, Chl *a* and its 3-acetyl derivative.

Electron-withdrawing substituents at the peripheral positions of the chlorophyll π-system suppress the electron density of the nitrogen atoms in cyclic tetrapyrroles and make attack by a proton and pheophytinization less likely. For example, Chl *b* (with a formyl group at the 7-position) is pheophytinized less quickly than Chl *a* (with the 7-methyl group) [52], and a Mg-dechelatase active for Chl *a* did not catalyze the same reaction with Chl *b* in *in vitro* experiments [51].

Likewise, zinc chlorophylls are more tolerant to acid than the corresponding magnesium complexes, and are often used as chemically more stable and more easily handled biomimetic models thereof. Zinc-substituted BChl *a* was found in specific photosynthetic bacteria grown in acidic environments (see Section 17.1.3) [21], and the use of such a pigment might be related to its relatively slow pheophytinization by an acid.

17.3.4 Alteration of Core π-System

(B)Chls are biosynthesized through successive hydrogenation of a porphyrin to a bacteriochlorin via a chlorin π-skeleton. These reductions are catalyzed in nature by reductases and proceed regio- and stereoselectively in a *trans*-dihydrogenation manner [5]. Such regioselective hydrogenations are possible in a flask [53, 54], but stereoselective hydrogenations have not been performed yet using artificial chiral systems.

Reverse dehydrogenations (oxidations) are readily performed *in vitro*. BChl *a* was oxidized gradually in air and rapidly by treatment with 2,3-dichloro-5,6-dicyanobenzoquinone (DDQ) in acetone to give 3-acetyl-chlorophyll *a* through regioselective didehydrogenation at the 7,8-positions (Figure 17.14) [55]. The B-ring is more reactive for air- and DDQ-oxidations than the D-ring. The chlorin product was also obtained by acid-induced isomerization at the B-ring of BChl *b* (Figure 17.14) [56]. This is because 3-acetyl-chlorophyll *a* is more π-conjugated and thermodynamically more stable than BChl *b* bearing the 8-ethylidene group.

Chl *a* can be reacted with excess DDQ to afford protochlorophyll *a* possessing a fully conjugated porphyrin π-skeleton after didehydrogenation at the 17,18-positions. Chl *a* bearing the 3-vinyl group is oxidized more readily than 3-acetyl-chlorophyll *a* with an electron-withdrawing acetyl group (see Section 17.3.5), so further oxidation of the latter was not observed in the aforementioned oxidation of BChl *a* with a smaller amount of DDQ for a short period. Similarly to the transformation of BChl *b* to 3-acetyl-chlorophyll *a*, 8-ethylidene-bacteriochlorin, BChl *g* bearing the 3-vinyl group, was isomerized in acid to 8-ethyl-chlorin, Chl *a*, which was more rapid than the isomerization of BChl *b* due to the less electron-withdrawing 3-vinyl group [57]. Note that natural BChl *g* is a farnesyl ester in the 17-propionate reside, and its isomerized product Chl *a* is a farnesyl ester, not the phytyl ester that is found in natural systems [19].

17.3.5 Electrochemical Oxidation and Reduction

Chlorophylls are macrocyclic and π-conjugated molecules, and hence they are electrochemically active in solution as well as in protein complexes such as the photosynthetic RCs. Their electrochemical oxidation and reduction are observed in solution, and the one-electron redox potentials are available in the literature [8]. The redox potentials depend on the peripheral substituents as follows. Chl *a* is more oxidized and less reduced than Chl *b*, because the former possesses the 7-methyl group and the latter has a more electron-withdrawing formyl group at the 7-position. Chl *a* bearing the 8-ethyl group is slightly more oxidized and less reduced than DV-Chl *a* with the 8-vinyl group, which is consistent with the fact that an ethyl group is slightly less electron withdrawing than a vinyl group [58]. Similarly, the oxidation and reduction potentials of mesochlorophyll *a* bearing the 3-ethyl group are lower than those of Chl *a* with the 3-vinyl group. Oxidation of the 3-vinyl group of Chl *a* to the formyl group of Chl *d* enhances the redox potentials, and oxidation of the 2-methyl group of Chl *a* to the formyl group of Chl *f* increases the redox potentials even more. These observations are explained by the functional group's electronegativities: formyl > vinyl > methyl ≈ ethyl [39].

Chlorophylls with a magnesium at the central position are more oxidized and less reduced than the corresponding free bases, pheophytins. This may explain why (bacterio)pheophytins are utilized as primary electron acceptors in PS II(−type) RCs (see Section 17.1.5). Moreover, BChl *a* with a bacteriochlorin π-system and the 3-acetyl group is more reduced and oxidized than Chl *d* with a chlorin skeleton and the 3-formyl moiety. Bacteriochlorins are more labile to one-electron oxidation and reduction than chlorins.

The above redox potentials are observed in the monomeric states of chlorophylls, and self-aggregation affects the values significantly. For example, dimerization of Chl *a* through π–π stacking decreased the one-electron oxidation potential [59]. This facile oxidation is ascribable to the π-extension in the dimer. This is reminiscent of the fact that dimers of (bacterio)chlorophylls are used as primary electron donors in photosynthetic RCs.

17.4 Chemical Syntheses

Natural chlorophylls are obtained by their extraction from phototrophs and their purification by chromatography including HPLC since the pioneering work by Tsvet [60]. Some (bacterio)chlorophylls are prepared by chemical modification of natural chlorophyll molecules by *in vitro* enzymatic reactions and organic synthetic procedures. Chemical modifications of chlorophyll derivatives have been extensively reported in the previous review [34].

17.4.1 Total Synthesis of Chl *a*

Woodward and his collaborators reported the total synthesis of Chl *a* through preparation of composite pyrroles (pyrroles A to D), their cyclization, and the reduction to a pyrroline ring in the D-ring. The precise route is summarized in the reports [61, 62] and is briefly described below. Its stereoselective course is beautiful, and this excellent research resulted in the single award of the Nobel Prize in Chemistry in 1965.

17.4.1.1 Ring A

Ethyl 3-oxobutanoate (acetoacetate) was coupled in the presence of sodium nitrite and zinc powder to give substituted pyrrole **1** [step (i) of Figure 17.15]. The ethyl ester at

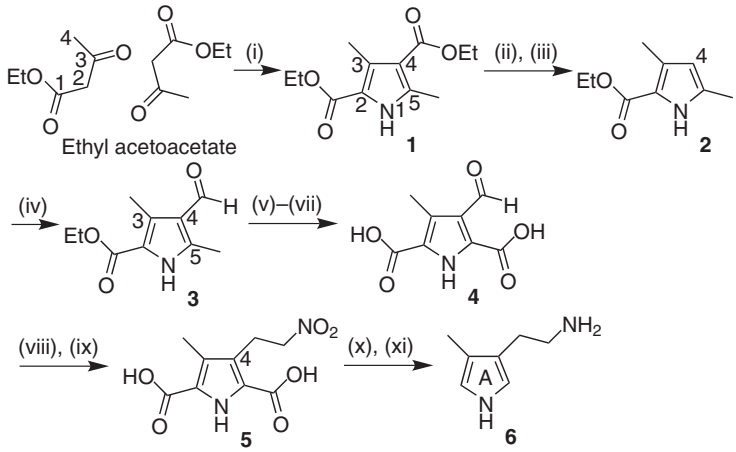

Figure 17.15 Synthesis of ring A: (i) $NaNO_2$, Zn AcOH, H_2O; (ii) H_2SO_4; (iii) $HO(CH_2)_2NH_2$, Δ; (iv) $POCl_3$, DMF; (v) $CH_2(CN)_2$, Et_2NH, EtOH, Δ; (vi) Br_2, MeOH, Δ; (vii) aq. NaOH, Δ; (viii) $MeNO_2$, Et_2NH, EtOH, Δ; (ix) $NaBH_4$, aq. $NaHCO_3$; (x) $NaOAc{\cdot}3H_2O$, KOAc, Δ; (xi) H_2, Pt_2O, MeOH.

the 4-position of **1** was regioselectively hydrolyzed under acidic conditions (ii), and the carboxylic acid was pyrolyzed (iii, decarboxylation) to afford 4-unsubstituted pyrrole **2**. After Vilsmeier formylation at the 4-position of **2** (iv) and Knoevenagel condensation of aldehyde **3** with malononitrile ((v), protection of the 4-formyl group), the sole 5-methyl group was transformed to the methoxycarbonyl group by one-pot reaction with bromine and methanol (vi) through $H \rightarrow Br \rightarrow OMe$ (three times) and removal of Me_2O. The regioselectivity is ascribable to the fact that the α(5)-methyl group of a pyrrole ring is more reactive than its β(3)-methyl group. Hydrolysis of ethyl and methyl esters and retro-Knoevenagel reaction (deprotective reproduction of the 4-formyl group) under basic conditions (vii) yielded **4**. Henry reaction of aldehyde **4** with nitromethane (viii) and olefin reduction of the 2-nitroethenyl group at the 4-position with sodium borohydride (ix) gave **5**. Dicarboxylic acid **5** was pyrolyzed with sodium acetate trihydrate and potassium acetate without any solvents (x), and the nitro group was catalytically hydrogenated (xi) to afford **6**.

17.4.1.2 Ring B

Pyrrole **2** was acetylated at the 4-position [step (i) of Figure 17.16] and Wolff–Kishner reduction of the 4-acetyl group (ii), and concomitant hydrolysis of the 2-ethyl ester and decarboxylation gave 2-unsubstituted 4-ethyl-pyrrole **7**. After Vilsmeier formylation at the 2-position (iii) and Knoevenagel condensation of the 2-formyl group with malononitrile (iv), the 5-methyl group was exclusively mono-chlorinated (v) to give **8**. The regioselectivity is due to the high reactivity of the α-methyl group of a pyrrole ring (vide supra).

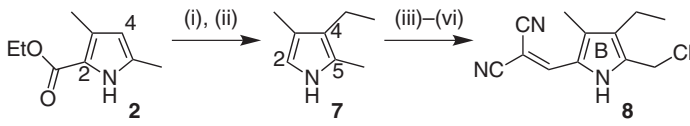

Figure 17.16 Synthesis of ring B: (i) AcCl, $AlCl_3$, CH_2Cl_2, Δ; (ii) $H_2NNH_2{\cdot}H_2O$, NaOH, $HO(CH_2CH_2O)_3H$, Δ; (iii) $POCl_3$, DMF; (iv) $CH_2(CN)_2$, Et_2NH, EtOH, Δ; (v) SO_2Cl_2, AcOH.

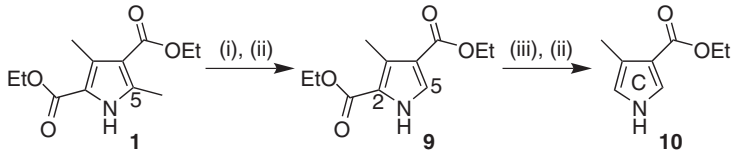

Figure 17.17 Synthesis of ring C: (i) Br_2, SO_2Cl_2, AcOH, Ac_2O, then H_2O; (ii) Cu-Sn powder, Δ; (iii) KOH, aq. EtOH, Δ.

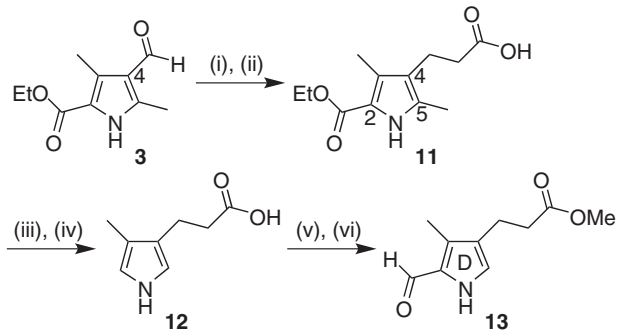

Figure 17.18 Synthesis of ring D: (i) $CH_2(COOH)_2$, $C_6H_5NH_2$, EtOH, Δ; (ii) H_2, Raney-Ni, aq. NaOH; (iii) SO_2Cl_2, Et_2O, then H_2O; (iv) aq. NaOH, Δ; (v) CH_2N_2-Et_2O, MeOH; (vi) $POCl_3$, DMF, $ClCH_2CH_2Cl$.

17.4.1.3 Ring C

Regioselective oxidation of the 5-methyl group of **1** [step (i) of Figure 17.17], and the resulting carboxylic acid was pyrolyzed (ii) to give 5-unsubstituted pyrrole **9**. The regioselectivity is similar to that in the aforementioned oxidation of a derivative of **3** in Figure 17.15. The ethyl ester at the 2-position of **9** was regioselectively hydrolyzed under basic conditions (iii), and the obtained 2-carboxylic acid was pyrolyzed (ii) to afford **10**.

17.4.1.4 Ring D

Knoevenagel condensation of aldehyde **3** with malonic acid [step (i) of Figure 17.18], followed by decarboxylation (i) and hydrogenation of the acrylic acid moiety at the 4-position (ii) gave **11**. The 5-methyl group of **11** was regioselectively oxidized (iii; see also the oxidation of **1** in Figure 17.17), the 2-ethyl ester was hydrolyzed (iv), and the 2,5-dicarboxylic acid was pyrolyzed (iv) to yield **12**. After treatment of diazomethane (v), regioselective formylation (vi) afforded **13**. The regioselectivity is ascribable to the steric factor: Me is smaller in size than $CH_2CH_2CO_2Me$.

17.4.1.5 Rings A–D (Left Half)

Acid-catalyzed condensation of **6** with **13** gave **14** in a regioselective manner [step (i) of Figure 17.19]. The regioselectivity is controlled by the steric (see the formylation of **12** in Figure 17.18) and electronic factors (Me vs. $CH_2CH_2NH_3^+Br^-$). The coupling product **14** was reduced (ii) to give dipyromethane **15**.

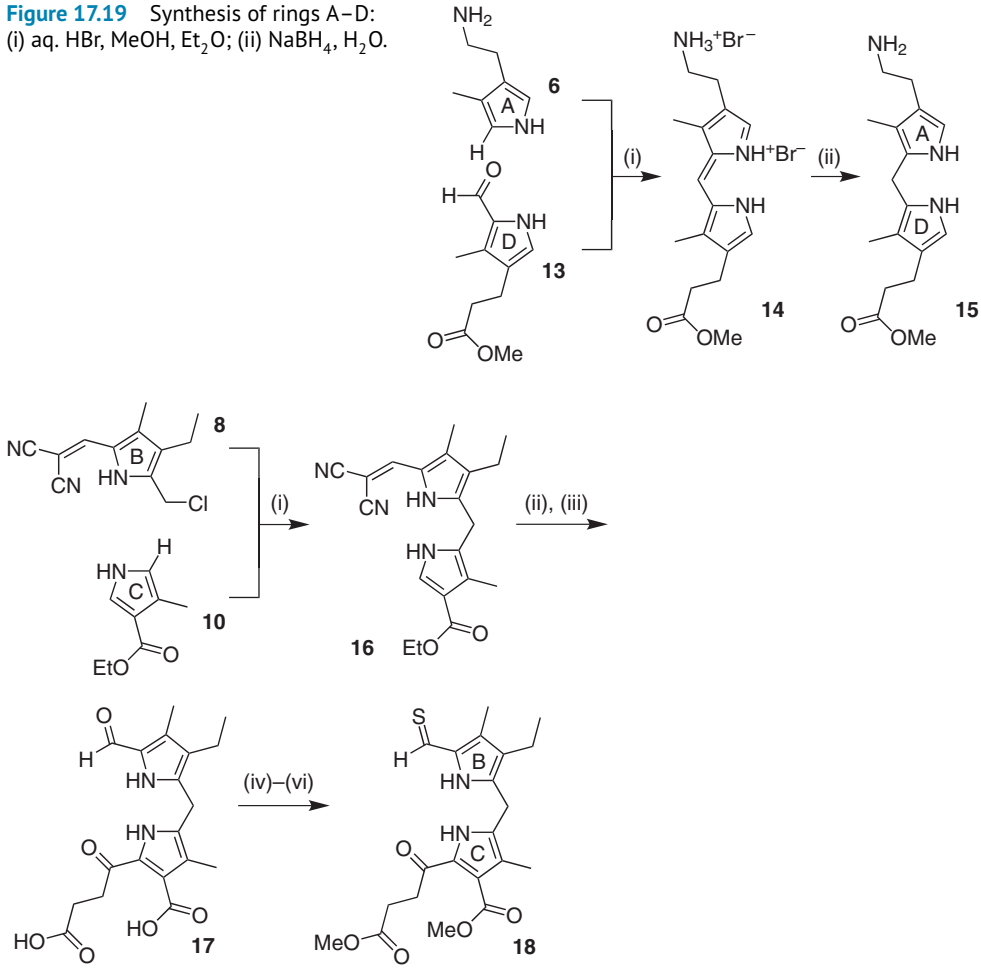

Figure 17.19 Synthesis of rings A–D: (i) aq. HBr, MeOH, Et_2O; (ii) $NaBH_4$, H_2O.

Figure 17.20 Synthesis of ring B–C: (i) aq. HCl, EtOH, Δ; (ii) $MeO_2C(CH_2)_2COCl$. $ZnCl_2$, CH_2Cl_2, Δ; (iii) aq. NaOH, Δ; (iv) CH_2Cl_2, Et_2O, MeOH; (v) $EtNH_2$, AcOH, then aq. HBr, CH_2Cl_2; (vi) H_2S, C_6H_6, MeOH and NaOAc, MeOH.

17.4.1.6 Rings B–C (Right Half)

Friedel–Crafts alkylation of **10** with **8** gave predominantly **16** [step (i) of Figure 17.20]. The regioselectivity is ascribable to the steric (Me vs. CO_2Et) and electronic factors (standard electrophilic substitution of a pyrrole ring). Further Friedel–Crafts acylation of **16** with methoxycarbonylpropanoyl chloride (ii) and basic hydrolysis and retro-Knoevenagel reaction (iii) afforded **17**. The two carboxy groups of **17** were methyl-esterified (iv), the formyl group was condensed with ethylamine (v), and the Schiff base was transformed to thioaldehyde **18** (vi).

17.4.1.7 Porphyrin

Coupling of amine **15** with thioaldehyde **18** gave Schiff base [step (i) of Figure 17.21], which was rearranged and cyclized under acidic conditions (ii). The product was oxidized (iii) to afford porphyrin **19**. After protection of amine with acetic anhydride (iv), the 15-propionate residue was dehydrogenated (v) to the 15-acrylate residue of **20**.

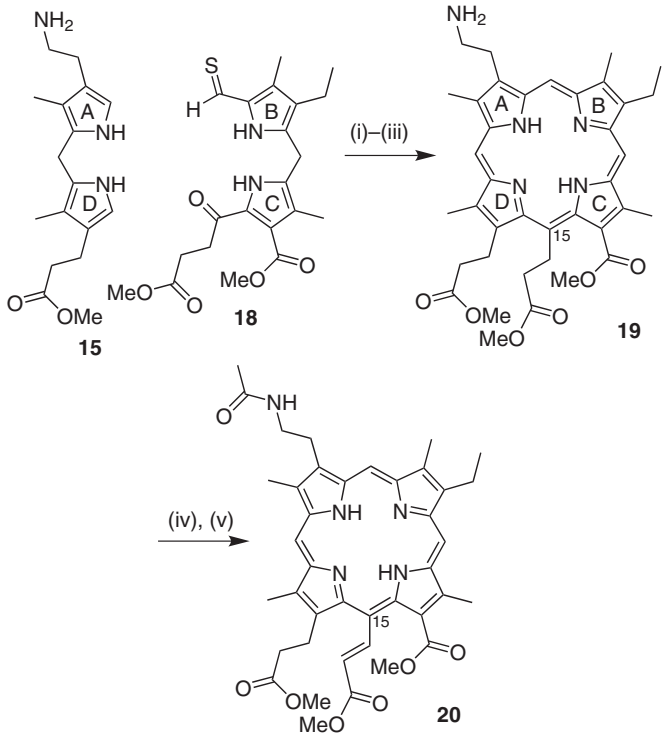

Figure 17.21 Synthesis of porphyrin: (i) CH_2Cl_2; (ii) HCl, MeOH; (iii) I_2; (iv) Ac_2O, C_5H_5N; (v) O_2, AcOH.

17.4.1.8 Chlorin

The 15-acrylate residue of **20** was cyclized under acidic conditions to the 17-position [step (i) of Figure 17.22]. Due to the protonation at the C18 atom from the less sterically demanding direction, the cyclization proceeded stereoselectively to form a *trans*-configuration between the 17-propionate residue and 18-methyl group. The resulting chlorin was the racemic mixture of (17*S*,18*S*)-form **21** shown in Figure 17.22 and its enantiomeric (17*R*,18*R*)-form. The mixture containing acetamide **21** was hydrolyzed (ii), and the amino group was removed under Hofmann elimination conditions (iii) to give the 3-vinyl analog of **21**. When the 3-vinyl-chlorin in air-saturated dichloromethane was irradiated with visible light (iv), the $C15^1$=$C15^2$ double bond was oxidatively cleaved to afford **22** and its enantiomer.

17.4.1.9 Chlorin e_6 Trimethyl Ester

Treatment of **22** and its enantiomer with methoxide [step (i) of Figure 17.23] induced removal of the 17-methoxalyl group with stereochemical retention through retro-Claisen condensation (to methyl oxalate and C17H–C16=N24) and cyclization of the 13-methoxycarbonyl and 15-formyl groups to form methyl ether of a lactol derivative. The 15^1-methyl ether and 17^2-methyl ester moieties were basically cleaved (ii) to lactol **23** and its enantiomer. The stereochemically mixed 17,18-*trans*-products were separated by fractionated crystallization with (-)-quinine to yield optically pure (17*S*,18*S*)-**23**. Separated lactol **23** was ring-opened, and the dicarboxylic acid was methyl-esterified (iii) to give **24**. Addition of hydrogen cyanide to the 15-formyl group of **24** and successive lactonization of the resulting cyanohydrin with the 13-methoxycarbonyl group (iv) afforded **25**. Cyanolactone **25** was

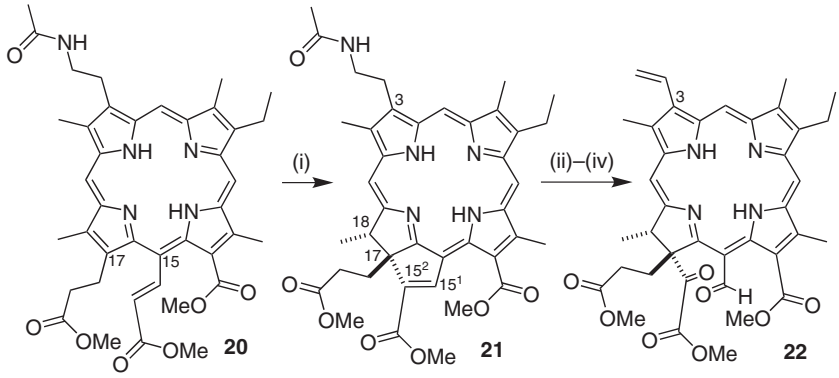

Figure 17.22 Synthesis of chlorin: (i) AcOH, Δ; (ii) conc. HCl, MeOH, Δ; (iii) Me_2SO_4, NaOH, MeOH, Δ; (iv) O_2, CH_2Cl_2, hν.

hydrogenolyzed with zinc and acetic acid (v) to give 13-carboxy-15-cyanomethyl-chlorin [13-COO–CH(CN)-15 → 13-COOH +15-CH_2CN], and concomitantly zinc was inserted into the chlorin core during the reduction. The central zinc was removed by an action of an acid (vi), and the resulting free base was methyl-esterified (vii). Finally, the 15^1-cyano group was methanolyzed (viii) to give chlorin e_6 trimethyl ester. Note that Woodward and his collaborators reported the synthesis of chlorin e_6 trimethyl ester from various low-molecular-weight organic compounds (vide supra) and had never examined the following steps to Chl *a* that were available in some previous reports (vide infra).

17.4.1.10 Chl *a*

Base-catalyzed Dieckmann cyclization of the 13-methoxycarbonyl group with the 15-methoxycarbonylmethyl group in chlorin e_6 trimethyl ester [step (i) of Figure 17.24] [63] gave a mixture of methyl pheophorbide *a* (Pheo a_M) and its (13^2S)-epimer, methyl pheophorbide *a*′ (Pheo a'_M). The major product, Pheo a_M was separated by chromatography.

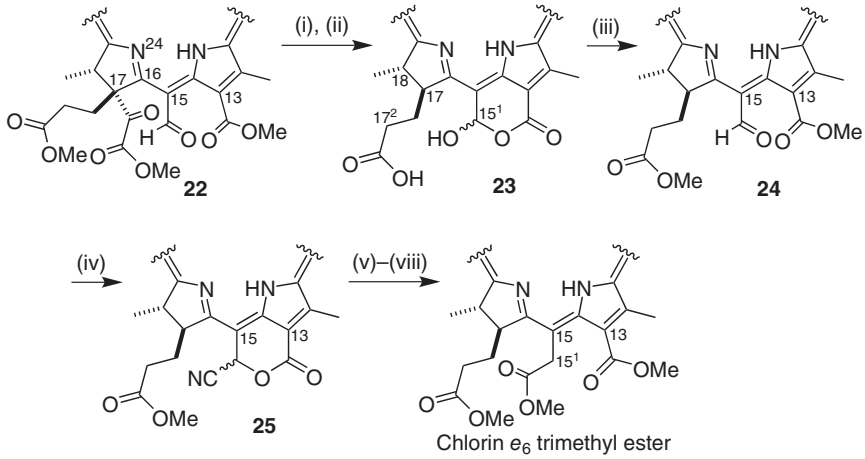

Figure 17.23 Synthesis of chlorin e_6 trimethyl ester: (i) KOH, MeOH, CH_2Cl_2; (ii) aq. NaOH, $O(CH_2CH_2)_2O$; (iii) CH_2N_2-Et_2O, MeOH; (iv) HCN, Et_3N, CH_2Cl_2; (v) Zn, AcOH, CH_2Cl_2; (vi) aq. HCl, CH_2Cl_2, Et_2O; (vii) CH_2N_2-Et_2O, CH_2Cl_2, MeOH; (viii) aq. HCl, MeOH.

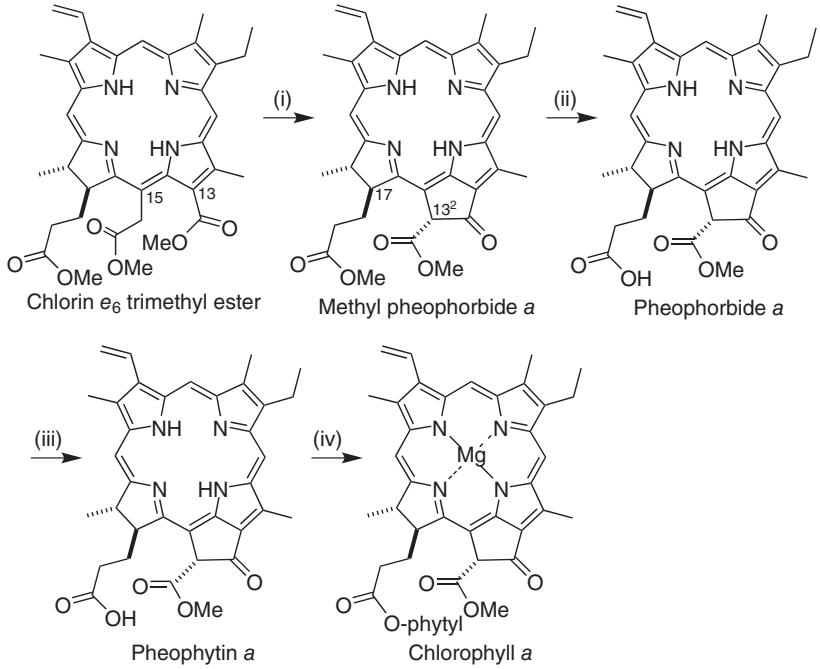

Figure 17.24 Synthesis of chlorophyll *a*: (i) *t*BuOK, *t*BuOH, C_5H_5N; (ii) conc. HCl; (iii) phytol, $COCl_2$, C_5H_5N; (iv) MgI[OC_6H_2(2,6-*t*Bu_2–4-Me)], CH_2Cl_2, Et_2O.

The methyl ester in the 17-propionate residue was hydrolyzed under acidic conditions (ii), and pheophorbide *a* (Pheo a_H) was esterified with phytol (iii) [64]. Pheophytin *a* (Pheo *a*) was magnesium-metalated (iv) to give Chl *a* [64].

17.4.2 Partial Synthesis of Chl *d*

Natural Chl *d* is supposed to be biosynthesized by oxidation of the 3-vinyl group of chlorophyllide *a* (Chlide *a*, Chl a_H) to the 3-formyl and successive esterification of a phytyl group to the 17^2-carboxy group. The former enzymatic oxidation has not been determined yet. The oxidation was reproduced by the following chemical step.

The direct oxidation of Chl *a* to Chl *d* was reported as follows [65]. Chl *a* in aerated tetrahydrofuran was treated with thiophenol and acetic acid to give Chl *d* (31% yield) with a smaller amount of its epimer Chl *d*′. The undesired pheophytinization of Chls *a*/*d* was not observed, not even when one equivalent of acetic acid was used. The reaction mechanism has not been clarified, but a radical species produced by phenylthiyl radical (PhS·) and dioxygen (·O–O·) would be important for the thiol-olefin co-oxidation. A similar radical process was proposed for the biosynthetic route in the oxidation of the 3-vinyl to the 3-formyl group [4, 66].

17.4.3 Partial Synthesis of Chl *b*

Chl *b* bearing the 7-formyl group is biosynthesized by oxidation of the 7-methyl group of chlorophyllide *a* (Chlide *a*, Chl a_H) and phytyl esterification or by the direct oxidation of Chl *a*. Oxidation of 7-Me to 7-CHO proceeds via an enzyme, chlorophyll(ide) *a* oxidase (CAO)

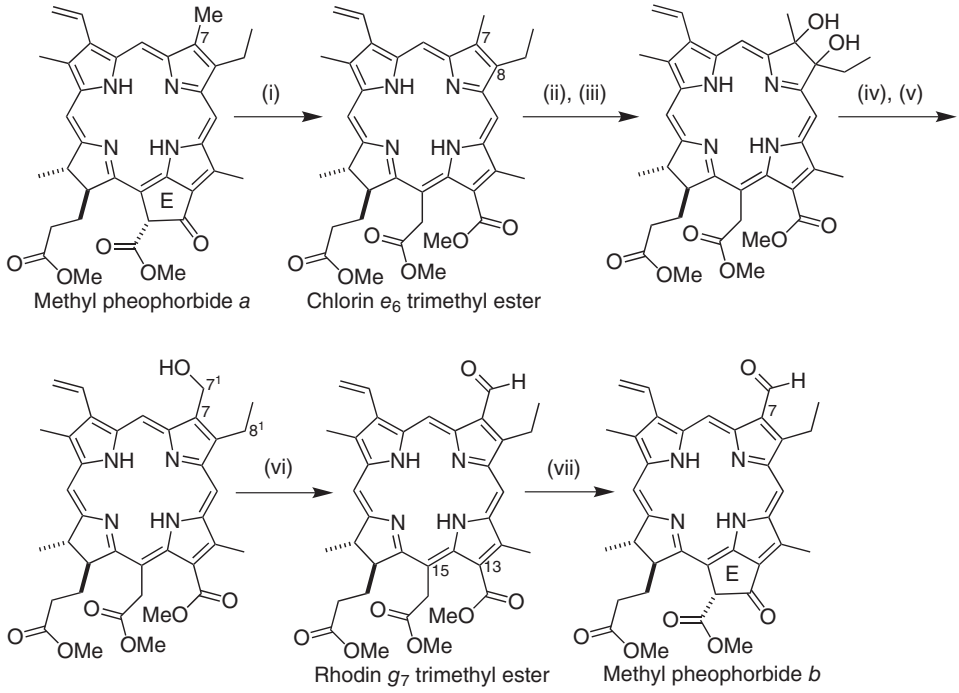

Figure 17.25 Transformation of methyl pheophorbide *a* (7-Me) to methyl pheophorbide *b* (7-CHO): (i) NaOMe, MeOH, $CHCl_3$; (ii) electrochemical reduction, $O(CH_2CH_2)_2O$; (iii) O_2, aq. sat. H_3BO_3, hν; (iv) aq. HCl, $O(CH_2CH_2)_2O$, Δ; (v) chromatographic separation; (vi) Me_2SO, Ac_2O; (vii) *t*BuOK, *t*BuOH, C_5H_5N.

[67]. The enzyme catalyzes the oxidation with full regioselectivity, which is very difficult to achieve with conventional oxidizing reagents. Here, artificial transformation of the 7-methyl group of a chlorophyll derivative to the 7-formyl group is shown below (Figure 17.25) [68].

Methyl pheophorbide *a* (Pheo a_M) was prepared by acidic pheophytinization of Chl *a* and transesterification of the phytyl to methyl ester [60] and used as the starting material. The E-ring of Pheo a_M was cleaved by sodium methoxide in methanol [step (i) of Figure 17.25] to give chlorin e_6 trimethyl ester. The C7=C8 olefin was regioselectively oxidized by electrochemical reduction (ii) and photo-oxidation (iii). The resulting diol was mono-dehydrated (iv), and the 7^1- and 8^1-hydroxy-chlorins in the obtained mixture were separated by preparative layer chromatography (v). The 7-hydroxymethyl group of the regioisomer isolated was oxidized (vi, Albright–Goldman oxidation). The resulting rhodin g_7 trimethyl ester was anaerobically treated with *tert*-butoxide (vii), and the E-ring was cyclized [Dieckmann condensation; see also step (i) of Figure 17.24] to afford methyl pheophorbide *b* (Pheo b_M). The total chemical yield of methyl pheophorbide *a* to *b* was quite low (<1%). Oxidation succeeded after removal of reactive moieties: the central Mg, phytyl group, and β-ketoester on the E-ring. Methyl pheophorbide *b* (Pheo b_M) can be transesterified to a phytyl ester and metalated to a magnesium complex, allowing generation of Chl *b* (see Figure 17.24).

17.4.4 Partial Synthesis of BChl *c*

The 20-methyl group of BChl *c* is introduced by *S*-adenosylmethionine (SAM) as a methyl source and 20-methyltransferase (called BchU) as an enzyme [4]. The 20-methylation of 20-unsubstituted bacteriochlorophyllide *d* (BChlide *d*, BChl d_H) prepared via basic hydrolysis of BChl *d* was performed using SAM and BchU *in vitro* [69]. The resulting bacteriochlorophyllide *c* (BChlide *c*, BChl c_H) was esterified with farnesol to give BChl *c*.

The non-enzymatic 20-methylation succeeded in the following two pathways. Methyl pyropheophorbide *a*, one of the Chl *a* derivatives, was prepared by demethoxycarbonylation of Pheo a_M (see Section 17.4.3) in refluxing collidine [60]. The vinyl group at the 3-position of the pyrolyzed product was treated with thallium nitrate in methanol to be transformed to the 2,2-dimethoxyethyl group [step (i) in Figure 17.26]. The dimethyl acetal was hydrolyzed under acidic conditions (ii), the aldehyde (3-CH_2CHO) was reduced by sodium borohydride (iii), the alcohol (3-CH_2CH_2OH) was chlorinated by benzoyl chloride in *N*,*N*-dimethylforamide (iv), and the resulting free base was copper-metalated at the central position (v) to give **26**. Friedel–Crafts alkylation at the 20-position of **26** with methylsulfanylmethyl chloride (vi) and the reductive demethylsulfurization of the product bearing 20-CH_2SMe (vii) gave 20-methyl-chlorin **27**. Acidic demetalation of the central Cu(II) (viii) and basic removal of hydrogen chloride in the 3-substituent (ix) afforded methyl 20-methyl-pyropheophorbide *a*. For the 20-methylation, protection of the reactive 3-vinyl

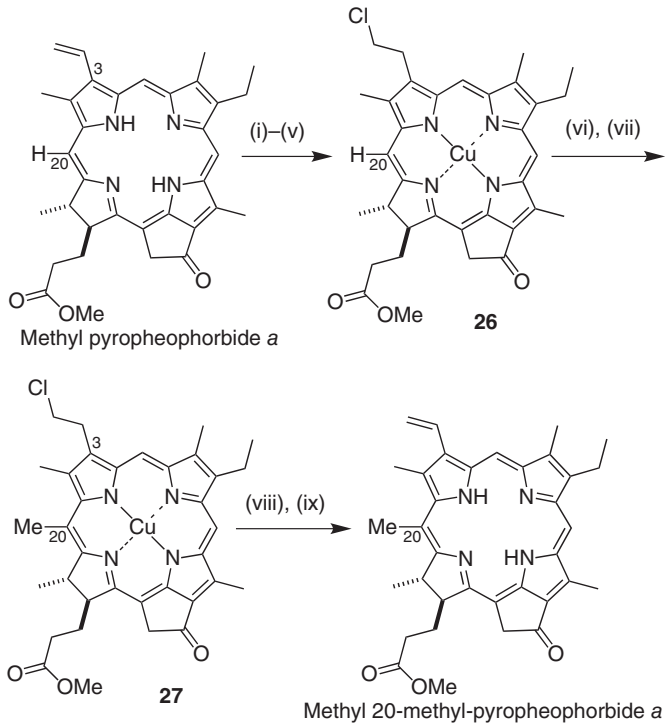

Figure 17.26 20-Methylation of methyl pyropheophorbide *a* (20-H): (i) $Tl(NO_3)_3 \cdot 3H_2O$, MeOH, CH_2Cl_2, then SO_2, conc. HCl; (ii) conc. HCl, CH_2Cl_2, THF, Δ; (iii) $NaBH_4$, MeOH, CH_2Cl_2; (iv) C_6H_5COCl, DMF; (v) $Cu(OAc)_2 \cdot H_2O$, MeOH, CH_2Cl_2; (vi) $MeSCH_2Cl$, $TiCl_4$, CH_2Cl_2; (vii) Raney-Ni, Me_2CO; (viii) HCl (g), CH_2Cl_2; (ix) aq. NaOH, C_5H_5N.

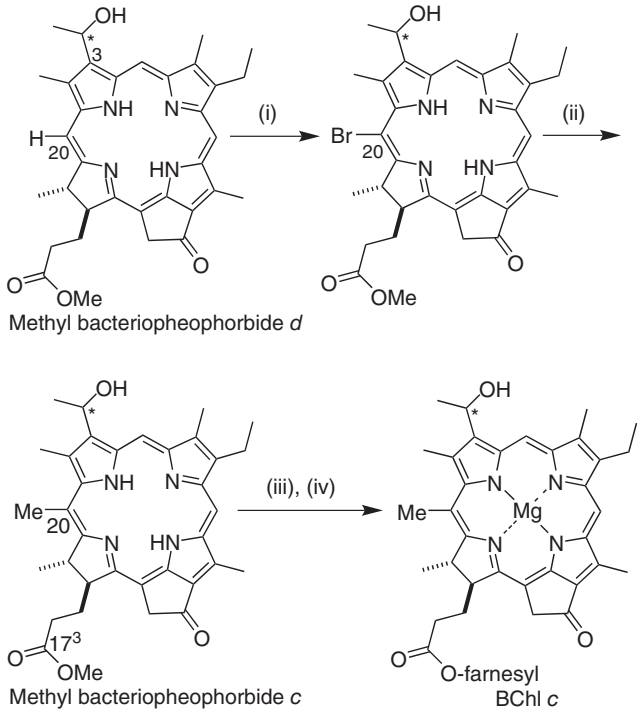

Figure 17.27 Transformation of methyl bacteriopheophorbide *d* (20-H) to methyl bacteriopheophorbide *c* (20-Me) followed by production of BChl *c*: (i) $C_5H_5NH^+Br_3^-$, CH_2Cl_2; (ii) $MeB(OH)_2$, $PdCl_2(dppf)$, Cs_2CO_3, THF; (iii) farnesol, $(Bu_2ClSn)_2O$, C_6H_5Me, Δ; (iv) $Mg(ClO_4)_2$, C_5H_5N, Δ.

group and insertion of Cu(II) are necessary, and multi-step synthesis is required. The total chemical yield of methyl pyropheophorbide *a* to its 20-methyl derivative was at most 8% [70].

Methyl bacteriopheophorbide *d* (BPheo d_M) prepared by hydration of the 3-vinyl group of methyl pyropheophorbide *a* was brominated at the 20-position [step (i) of Figure 17.27]. The 20-bromide was reacted with methyl boronic acid in the presence of palladium catalyst (ii) to give methyl bacteriopheophorbide *c* (BPheo c_M). The two steps for the 20-methylation proceeded smoothly, and the total chemical yield for the regioselective bromination and Suzuki–Miyaura cross-coupling was 70% [71]. The synthetic route is efficient without any protection of the peripheral substituents and useful for the 20-methylation. The resulting 20-methyl-chlorin was transesterified with farnesol (iii) and metalated with magnesium (iv) to give BChl *c* [71].

17.4.5 Partial Synthesis of BChl *f*

BChl *f* possessing the 7-formyl group is biosynthesized in the mutant cell of a green sulfur bacterium producing BChl *e* by oxidation of the 7-methyl group of bacteriochlorophyllide *d* (BChlide *d*, BChl d_H) and esterification with a farnesyl group. Oxidation is carried out by an oxidase (BciD) *in vitro* [72]. The double hydroxylation at the 7-methyl group followed by spontaneous dehydration of the geminal diol affords the 7-formyl group. The single hydroxylation at the 7-CH_3 and successive dehydrogenation of the resulting 7-CH_2OH alternatively

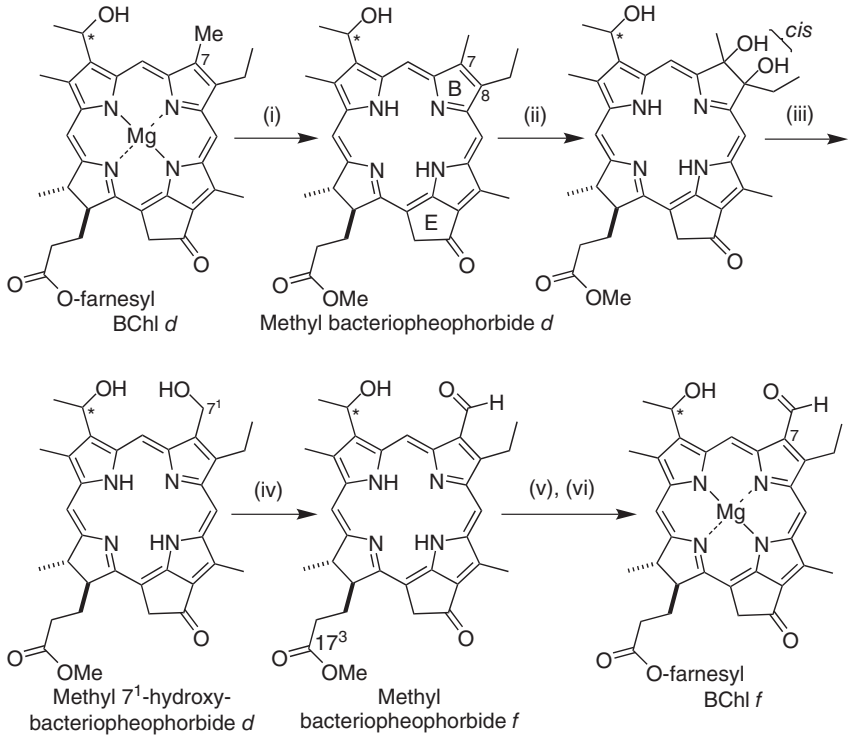

Figure 17.28 Transformation of BChl *d* (7-Me) to BChl *f* (7-CHO): (i) H_2SO_4, MeOH; (ii) OsO_4, C_5H_5N, CH_2Cl_2, then H_2S, MeOH; (iii) aq. HCl. $O(CH_2CH_2)_2O$, Δ, then silica gel chromatographic separation; (iv) $(C_5H_5NH^+)_2Cr_2O_7^{2-}$ (PDC, Cornforth reagent), C_6H_6; (v) farnesol, $(Bu_2ClSn)_2O$, C_6H_5Me, Δ; (vi) $Mg(ClO_4)_2$, C_5H_5N, Δ.

produces the 7-CHO. The BciD-catalyzed oxidation is similar to the CAO-catalyzed oxidation in Chl *a* to Chl *b* (see Section 17.4.3), while the former oxidation conditions are strictly anoxygenic and different from the latter oxygenic conditions.

The C7=C8 double bond of methyl bacteriopheophorbide *d* (BPheo d_M) was oxidized by osmium tetroxide, and the resulting osmate was cleaved by hydrogen sulfide to give the corresponding *cis*-diol [step (ii) in Figure 17.28]. After acidic mono-dehydration and chromatographic separation (iii), methyl 7^1-hydroxy-bacteriopheophorbide *d* was obtained [73]. The primary alcohol was oxidized by pyridinium dichromate (iv), the methyl ester was transesterified with farnesol (v), and the free base was magnesium-metalated (vi) to give BChl *f* [74]. This part of the synthetic procedure is similar to those for the transformation of Chl *a* to Chl *b* (Figure 17.25), but the present oxidation at the B-ring cleanly occurred without protection of the reactive E-ring due to the lack of a reactivity-enhancing methoxycarbonyl group neighboring to a keto-carbonyl moiety at the 13-position.

Alternatively, methyl 7^1-hydroxy-bacteriopheophorbide *d* was produced as the precursor of BChl *f* [10, 75]. A pigment mixture including Chls *a* and *b* was obtained by extraction from spinach with methanol. The extracted mixture was treated with sulfuric acid to give methyl pheophorbides *a*/*b* (Pheo a/b_M). The mixed products were pyrolyzed in refluxing collidine and regioselectively reduced by *tert*-butylamine borane in dichloromethane to give a mixture of methyl pyropheophorbide *a* (see Figure 17.26) and its 7^1-hydroxy-derivative. The products

(7-Me/7-CH_2OH) were easily separated by chromatography due to their larger polarity difference. The 3-vinyl group of methyl 7^1-hydroxy-pyropheophorbide *a* was hydrated to yield methyl 7^1-hydroxy-bacteriopheophorbide *d*.

17.5 Concluding Remarks

Chlorophylls are porphyrinoids, but their optical properties are different from those of usual porphyrins including commercially available, (in)expensive, and synthetic *meso*-tetraphenylporphyrin and octaethylporphyrin, which is ascribable to their molecular structures. Most chlorophylls have chlorin or bacteriochlorin π-skeletons (*trans*-17,18-dihydroporphyrin or *trans*,*trans*-7,8,17,18-tetrahydroporphyin) conjugated with an electron-withdrawing carbonyl group at the 13-position on an *exo*-five-membered ring along the molecular y-axis, while conventional porphyrins are symmetric and fully π-conjugated molecules. Structurally unsymmetric chlorophylls give intense Q_y bands at red or near-infrared region, which are useful for directional excited energy transfer inside and between photosynthetic apparatuses.

Chlorophylls are naturally produced in large amounts in phototrophs and can be used as starting materials for preparation of several (bacterio)chlorins. In particular, the 3-vinyl group of Chl *a* and the 3-acetyl group of BChl *a* are readily modified to various functional groups [34, 60]. Such chlorophyll derivatives are promising for elucidation of the photosynthetic mechanisms, production of functional materials (e.g., photodynamic therapeutic reagents), and construction of environmentally friendly (green) photo-driven systems, including artificial photosynthesis.

Acknowledgment

I thank Prof. Tadashi Mizoguchi of Ritsumeikan University for the preparation of spectral drawings.

References

1 Kräutler, B. (2008). Chlorophyll breakdown and chlorophyll catabolites in leaves and fruit. *Photochemical & Photobiological Sciences* 7: 1114–1120.
2 Niedzwiedzki, D.M., Liu, H., Chen, M., and Blankenship, R.E. (2014). Excited state properties of chlorophyll *f* in organic solvents at ambient and cryogenic temperatures. *Photosynthesis Research* 121: 25–34.
3 de Oliveira, K.T., Momo, P.B., de Assis, F.F. et al. (2014). Chlorins: natural sources, synthetic developments and main applications. *Current Organic Synthesis* 11: 42–58.
4 Bryant, D.A., Hunter, C.N., and Warren, M.J. (2020). Biosynthesis of the modified tetrapyrroles—the pigments of life. *The Journal of Biological Chemistry* 295: 6888–6925.
5 Tamiaki, H., Teramura, M., and Tsukatani, Y. (2016). Reduction processes in biosynthesis of chlorophyll molecules: chemical implication of enzymatically regio- and stereoselective hydrogenations in the late stages of their biosynthetic pathway. *Bulletin of the Chemical Society of Japan* 89: 161–173.

6 Teramura, M. and Tamiaki, H. (2018). Semi-synthesis and HPLC analysis of (bacterio)chlorophyllides possessing a propionic acid residue at the C17-position. *Journal of Porphyrins and Phthalocyanines* 22: 423–436.

7 Lin, Y.-P. and Charng, Y.-Y. (2021). Chlorophyll dephytylation in chlorophyll metabolism: a simple reaction catalyzed by various enzymes. *Plant Science* 302: 110682.

8 Kobayashi, M., Sorimachi, Y., Fukayama, D. et al. (2016). Physicochemical properties of chlorophylls and bacteriochlorophylls. In: *Handbook of Photosynthesis*, 3rd edition (ed. M. Pessarakli), 95–147. Boca Raton, FL, chap. 6: CRC Press.

9 Zill, J.C., He, Z., Tank, M. et al. (2018). ^{15}N photo-CIDNP MAS NMR analysis of reaction centers of *Chloracidobacterium thermophilum*. *Photosynthesis Research* 137: 298–305.

10 Tamiaki, H., Tsuji, K., Kim, K., and Miyatake, T. (2016). Preparation of mono-vinylated and formylated chlorophyll derivatives and their optical properties. *Tetrahedron* 72: 4368–4376.

11 Manning, W.M. and Strain, H.H. (1943). Chlorophyll d, a green pigment of red algae. *The Journal of Biological Chemistry* 151: 1–19.

12 Miyashita, H., Ikemoto, H., Kurano, N. et al. (1996). Chlorophyll *d* as a major pigment. *Nature* 383: 402.

13 Allen, M.B. (1966). Distribution of the chlorophylls. In: *The Chlorophylls* (ed. L.P. Vernon and G.R. Seely), 514–515. New York: Academic Press.

14 Sorimachi, Y., Kanjoh, T., Komatsu, H. et al. (2015). Chlorophyll *e* is 15^1-OH-lactone chlorophyll *a* or chlorophyllide *a*? *Photomedicine and Photobiology* 37: 31–34.

15 Chen, M., Schliep, M., Willows, R.D. et al. (2010). A red-shifted chlorophyll. *Science* 329: 1318–1319.

16 Ho, M.-Y., Shen, G., Canniffe, D.P. et al. (2016). Light-dependent chlorophyll f synthase is a highly divergent paralog of PsbA of photosystem II. *Science* 353: 886. https://doi.org/10.1126/science.aaf9178.

17 Tros, M., Mascoli, V., Shen, G. et al. (2021). Breaking the red limit: efficient trapping of long-wavelength excitations in chlorophyll-*f*-containing photosystem I. *Chem* 7: 155–173.

18 Mizoguchi, T., Kimura, Y., Yoshitomi, T., and Tamiaki, H. (2011). The stereochemistry of chlorophyll-c_3 from the haptophyte *Emiliania huxleyi*: the (13^2*R*)-enantiomers of chlorophylls-*c* are exclusively selected as the photosynthetically active pigments in chromophyte algae. *Biochimica et Biophysica Acta - Bioenergetics* 1807: 1467–1473.

19 Tamiaki, H., Shibata, R., and Mizoguchi, T. (2007). The 17-propionate function of (bacterio)chlorophylls: biological implication of their long esterifying chains in photosynthetic systems. *Photochemistry and Photobiology* 83: 152–162.

20 Álvarez, S., Zapata, M., Garrido, J.L., and Vaz, B. (2012). Characterization of [8-ethyl]-chlorophyll c_3 from *Emiliania huxleyi*. *Chemical Communications* 48: 5500–5502.

21 Wakao, N., Yokoi, N., Isoyama, N. et al. (1996). Discovery of natural photosynthesis using Zn-containing bacteriochlorophyll in an aerobic bacterium *Acidiphilium rubrum*. *Plant & Cell Physiology* 37: 889–893.

22 Tsukatani, Y., Romberger, S.P., Golbeck, J.H., and Bryant, D.A. (2012). Isolation and characterization of homodimeric type-I reaction center complex from *Candidatus* chloracidobacterium thermophilum, an aerobic chlorophototroph. *The Journal of Biological Chemistry* 287: 5720–5732.

23 Charles, P., Kalendra, V., He, Z. et al. (2020). Two-dimensional ^{67}Zn HYSCORE spectroscopy reveals that a Zn-bacteriochlorophyll a_p' dimer is the primary donor (P_{840}) in

the type-1 reaction centers of *Chloracidobacterium thermophilum*. *Physical Chemistry Chemical Physics* 22: 6457–6467.

24 Mizoguchi, T., Isaji, M., Harada, J. et al. (2015). The 17-propionate esterifying variants of bacteriochlorophyll-*a* and bacteriopheophytin-*a* in purple photosynthetic bacteria. *Journal of Photochemistry and Photobiology B: Biology* 142: 244–249.

25 Harada, J., Mizoguchi, T., Tsukatani, Y. et al. (2012). A seventh bacterial chlorophyll driving a large light-harvesting antenna. *Scientific Reports* 2: 671. https://doi.org/10.1038/srep00671.

26 Smith, K.M. (1994). Nomenclature of the bacteriochlorophylls *c*, *d*, and *e*. *Photosynthesis Research* 41: 23–26.

27 Frolov, D., Marsh, M., Crouch, L.I. et al. (2010). Structural and spectroscopic consequences of hexacoordination of a bacteriochlorophyll cofactor in the *Rhodobacter sphaeroides* reaction center. *Biochemistry* 49: 1882–1892.

28 Oba, T. and Tamiaki, H. (2002). Which side of the π-macrocycle plane of (bacterio) chlorophylls is favored for binding of the fifth ligand? *Photosynthesis Research* 74: 1–10.

29 Balaban, T.S., Fromme, P., Holzwarth, A.R. et al. (2002). Relevance of the diastereotopic ligation of magnesium atoms of chlorophylls in photosystem I. *Biochimica et Biophysica Acta - Bioenergetics* 1556: 197–207.

30 Oba, T. and Tamiaki, H. (2014). Asymmetry of chlorophylls in photosynthetic proteins: from the viewpoint of coordination chemistry. *Journal of Porphyrins and Phthalocyanines* 18: 919–932.

31 Sasaki, S., Mizoguchi, T., and Tamiaki, H. (2006). Gallium(III) complexes of methyl pyropheophorbide-*a* as synthetic models for investigation of diastereomerically controlled axial ligation towards chlorophylls. *Bioorganic & Medicinal Chemistry Letters* 16: 1168–1171.

32 Kawamoto, Y., Kinoshita, Y., and Tamiaki, H. (2020). Synthesis of tin(IV) complexes of chlorophyll-*a* derivatives with two halides as axial ligands and their optical properties in solution. *Tetrahedron* 76: 130948.

33 Orf, G.S. and Redding, K.E. (2021). Perturbation of the primary acceptor chlorophyll site in the heliobacterial reaction center by coordinating amino acid substitution. *Biochimica et Biophysica Acta - Bioenergetics* 1862: 148324.

34 Tamiaki, H. and Kunieda, M. (2011). Photochemistry of chlorophylls and their synthetic analogs. In: *Handbook of Porphyrin Science*, vol. 11 (ed. K.M. Kadish, K.M. Smith and R. Guilard), 223–290. Singapore: World Scientific.

35 Blankenship, R.E. (2014). *Molecular Mechanisms of Photosynthesis*, 2nd edition. West Sussex: Wiley Blackwell.

36 Taniguchi, M. and Lindsey, J.S. (2021). Absorption and fluorescence spectral database of chlorophylls and analogues. *Photochemistry and Photobiology* 97: 136–165.

37 Scheer, H. (ed.) (1991). *Chlorophylls*. Boca Raton, Florida: CRC Press.

38 Matsubara, S. and Tamiaki, H. (2018). Synthesis and self-aggregation of π-expanded chlorophyll derivatives to construct light-harvesting antenna models. *The Journal of Organic Chemistry* 83: 4355–4364.

39 Inamoto, N. and Masuda, S. (1982). Revised method for calculation of group electronegativities. *Chemistry Letters* 11: 1003–1006.

40 Cogdell, R.J., Gall, A., and Köhler, J. (2006). The architecture and function of the light-harvesting apparatus of purple bacteria: from single molecules to *in vivo* membranes. *Quarterly Reviews of Biophysics* 39: 227–324.

41 Senge, M.O., MacGowan, S.A., and O'Brien, J.M. (2015). Conformational control of cofactors in nature – the influence of protein-induced macrocycle distortion on the biological function of tetrapyrroles. *Chemical Communications* 51: 17031–17063.

42 Bednarczyk, D., Dym, O., Prabahar, V. et al. (2016). Fine tuning of chlorophyll spectra by protein-induced ring deformation. *Angewandte Chemie International Edition* 55: 6901–6905.

43 Takagi, S., Eguchi, M., Tryk, D.A., and Inoue, H. (2006). Porphyrin photochemistry in inorganic/organic hybrid materials: clays, layered semiconductors, nanotubes, and mesoporous materials. *Journal of Photochemistry and Photobiology C: Photochemistry Reviews* 7: 104–126.

44 Miyatake, T. and Tamiaki, H. (2010). Self-aggregates of natural chlorophylls and their synthetic analogues in aqueous media for making light-harvesting systems. *Coordination Chemistry Reviews* 254: 2593–2602.

45 Matsubara, S. and Tamiaki, H. (2020). Supramolecular chlorophyll aggregates inspired from specific light-harvesting antenna "chlorosome": static nanostructure, dynamic construction process, and versatile application. *Journal of Photochemistry and Photobiology C: Photochemistry Reviews* 45: 100385.

46 Ogasawara, S. and Tamiaki, H. (2015). Synthesis of methyl ($13^2R/S$)-alkyl-pyropheophorbide *a* and a non-epimerized chlorophyll *a* mimic. *Bioorganic & Medicinal Chemistry* 23: 6612–6621.

47 Kunieda, M., Nakato, E., and Tamiaki, H. (2007). Optical properties of synthetic porphyrins bearing or lacking an exo-five-membered ring and a keto carbonyl group on it, both of which are present in naturally occurring chlorophylls. *Journal of Photochemistry and Photobiology A: Chemistry* 185: 321–330.

48 Hynninen, P.H., Kavakka, J.S., and Mesilaakso, M. (2005). Electronic structure of the enolate anion of chlorophyll *b*. *Tetrahedron Letters* 46: 1145–1147.

49 Scheer, H. and Katz, J.J. (1975). New peripheral metal complexes related to chlorophyll. *Journal of the American Chemical Society* 97: 3273–3275.

50 Hynninen, P.H. and Hyvärinen, K. (2002). Tracing the allomerization pathways of chlorophylls by ^{18}O-labeling and mass spectrometry. *The Journal of Organic Chemistry* 67: 4055–4061.

51 Shimoda, Y., Ito, H., and Tanaka, A. (2016). Arabidopsis *STAY-GREEN*, Mendel's green cotyledon gene, encodes magnesium-dechelatase. *The Plant Cell* 28: 2147–2160.

52 Saga, Y. and Tamiaki, H. (2012). Demetalation of chlorophyll pigments. *Chemistry & Biodiversity* 9: 1659–1683.

53 Tamiaki, H., Watanabe, T., and Kunieda, M. (2007). Self-aggregation of synthetic zinc 3^1-hydroxy-13^1-oxo-17,18-*cis*-chlorin in a non-polar organic solvent. *Research on Chemical Intermediates* 33: 161–168.

54 Tamiaki, H., Xu, M., Tanaka, T., and Mizoguchi, T. (2013). Photoreduction of zinc 8-vinylated chlorophyll derivative to bacteriochlorophyll-*b*/*g* analog possessing an 8-ethylidene group. *Bioorganic & Medicinal Chemistry Letters* 23: 2377–2379.

55 Smith, J.R.L. and Calvin, M. (1966). Studies on the chemical and photochemical oxidation of bacteriochlorophyll. *Journal of the American Chemical Society* 88: 4500–4506.

56 Kobayashi, M., Yamamura, M., Akutsu, S. et al. (1998). Successfully controlled isomerization and pheophytinization of bacteriochlorophyll *b* by weak acid in the dark in vitro. *Analytica Chimica Acta* 361: 285–290.

57 Kobayashi, M., Hamano, T., Akiyama, M. et al. (1998). Light-independent isomerization of bacteriochlorophyll *g* to chlorophyll *a* catalyzed by weak acid in vitro. *Analytica Chimica Acta* 365: 199–203.

58 Kim, K., Tsuji, K., Kinoshita, Y. et al. (2017). Synthesis of monovinyl- and divinyl-chlorophyll analogs and their physical properties. *Tetrahedron* 73: 313–321.

59 Wasielewski, M.R., Svec, W.A., and Cope, B.T. (1978). Bis(chlorophyll)cyclophanes. New models of special pair of chlorophyll. *Journal of the American Chemical Society* 100: 1961–1962.

60 Tamiaki, H., Machida, S., and Mizutani, K. (2012). Modification of 3-substituents in (bacterio)chlorophyll derivatives to prepare 3-ethylated, methylated, and unsubstituted (nickel) pyropheophorbides and their optical properties. *The Journal of Organic Chemistry* 77: 4751–4758.

61 Woodward, R.B., Ayer, W.A., Beaton, J.M. et al. (1960). The total synthesis of chlorophyll. *Journal of the American Chemical Society* 82: 3800–3802.

62 Woodward, R.B., Ayer, W.A., Beaton, J.M. et al. (1990). The total synthesis of chlorophyll *a*. *Tetrahedron* 46: 7599–7659.

63 Smith, K.M., Bisset, G.M.F., and Bushell, M.J. (1980). Partial syntheses of optically pure methyl bacteriopheophorbides *c* and *d* form methyl pheophorbide *a*. *The Journal of Organic Chemistry* 45: 2218–2224.

64 Smith, K.M. and Lewis, W.M. (1981). Partial synthesis of chlorophyll-a from rhodochlorin. *Tetrahedron* 37 (supplement 1): 399–403.

65 Fukusumi, T., Matsuda, K., Mizoguchi, T. et al. (2012). Non-enzymatic conversion of chlorophyll-*a* into chlorophyll-*d* in vitro: a model oxidation pathway for chlorophyll-*d* biosynthesis. *FEBS Letters* 586: 2338–2341.

66 Chen, M. and Blankenship, R.E. (2011). Expanding the solar spectrum used by photosynthesis. *Trends in Plant Science* 16: 427–431.

67 Tanaka, R. and Tanaka, A. (2011). Chlorophyll cycle regulates the construction and destruction of the light-harvesting complexes. *Biochimica et Biophysica Acta - Bioenergetics* 1807: 968–976.

68 Inhoffen, H.H., Jäger, P., and Mählhop, R. (1971). Partialsynthese von Rhodin-g_7-trimethylester aus Chlorin-e_6-trimethylester, zugleich Vollendung der Harvard-Synthese des Chlorophylls a zum Chlorophyll b. *Justus Liebigs Annalen der Chemie* 749: 109–116.

69 Harada, J., Saga, Y., Yaeda, Y. et al. (2005). In vitro activity of C-20 methyltransferase, BchU, involved in bacteriochlorophyll *c* biosynthetic pathway in green sulfur bacteria. *FEBS Letters* 579: 1983–1987.

70 Smith, K.M., Goff, D.A., and Simpson, D.J. (1985). *Meso* substitution of chlorophyll derivatives: direct route for transformation of bacteriopheophorbides *d* into bacteriopheophorbides *c*. *Journal of the American Chemical Society* 107: 4946–4954.

71 Sasaki, S., Mizoguchi, T., and Tamiaki, H. (2007). A facile synthetic method for conversion of chlorophyll-*a* to bacteriochlorophyll-*c*. *The Journal of Organic Chemistry* 72: 4566–4569.

72 Thweatt, J.L., Ferlez, B.H., Golbeck, J.H., and Bryant, D.A. (2017). BciD is a radical-SAM enzyme that completes bacteriochlorophyllide *e* biosynthesis by oxidizing a methyl group into a formyl group at C-7. *The Journal of Biological Chemistry* 292: 1361–1373.

73 Tamiaki, H., Omoda, M., Saga, Y., and Morishita, H. (2003). Synthesis of homologously pure bacteriochlorophyll-*e* and *f* analogues from BChls-*c*/*d* via transformation of the 7-methyl to formyl group and self-aggregation of synthetic zinc methyl bacteriopheophorbides-*c*/*d*/*e*/*f* in non-polar organic solvent. *Tetrahedron* 59: 4337–4350.

74 Tamiaki, H., Komada, J., Kunieda, M. et al. (2011). In vitro synthesis and characterization of bacteriochlorophyll-*f* and its absence in bacteriochlorophyll-*e* producing organisms. *Photosynthesis Research* 107: 133–138.

75 Tamiaki, H., Kubo, M., and Oba, T. (2000). Synthesis and self-assembly of zinc methyl bacteriopheophorbide-*f* and its homolog. *Tetrahedron* 56: 6245–6257.

18

Vitamin B_{12} and Cofactor F430

Bernhard Kräutler[1] *and Bernhard M. Jaun*[2]

[1] *Institute of Organic Chemistry & Center of Molecular Biosciences (CMBI), University of Innsbruck, Innsbruck, Austria*
[2] *Laboratory of Organic Chemistry, ETH-Zürich, Zürich, Switzerland*

Abbreviations and Symbols

Ado	5′-deoxy-adenosyl
AdoCba	5′-deoxy-adenosylcobamide
AdoCbl	5′-deoxy-adenosylcobalamin, coenzyme B_{12}
ANME	anaerobic methanotrophic archaea
AOM	anaerobic oxidation of methane
Cba	cobamide
Cbi	cobinamide
Cbl	cobalamin (DMBCba)
CNCbl	cyanocobalamin
CoB-SH	coenzyme B, 7-mercaptoheptanoylthreoninephosphate
DFT	density functional theory
DMB	5,6-dimethylbenzimidazole
F430	cofactor F430
$F430Me_5$	F430 pentamethyl ester
GM	glutamate mutase
H_2OCbl	aquocobalamin
HOCbl	hydroxocobalamin
HS-CoM	coenzyme M, 2-mercaptoethanesulfonate
IBC	isobacteriochlorin
MeS-CoM	*S*-methyl-coenzyme M
MCM	methylmalonyl-CoA mutase
MCR	methyl-coenzyme M reductase
MeCbl	methylcobalamin
MeS-F430	(17^2S)-17^2-methylthio-F430
NHE	normal hydrogen electrode
QM/MM	quantum mechanics combined with molecular mechanics
RNR	ribonucleotide reductase
SAM	*S*-adenosylmethionine (= AdoMet)

Fundamentals of Porphyrin Chemistry: A 21st Century Approach, Volume 2, First Edition.
Edited by Penelope J. Brothers and Mathias O. Senge.
© 2022 John Wiley & Sons Ltd. Published 2022 by John Wiley & Sons Ltd.

S_N2	nucleophilic substitution with 2nd order kinetics
SRB	sulfate reducing bacteria

18.1 Introduction

Cobalt-corrinoids (such as vitamin B_{12}) and nickel-corphinoids (such as cofactor F430) are natural porphyrinoids that enrich the arsenal of the "pigments of life" with unique structures and biologically exceptional chemical reactivity [1, 2]. Both cobalt-corrins and nickel-hydrocorphins are among the less easily noticed members of the porphyrinoid "pigments of life," which are more prominently represented by the very visible structural and biosynthetic relatives, chlorophyll and heme. The discovery of the red cobalt complex vitamin B_{12} dates back to the 1940s, and was the result of extensive studies on the cause of "pernicious anemia," which is cured by vitamin B_{12} [3].

The yellow Ni-hydrocorphin F430 was identified around 1980 as a cofactor involved in methane formation by methanogenic archaea [4] and later identified as the prosthetic group of the key enzyme of methanogenesis, methyl-coenzyme reductase (MCR). More recently, in 2000, consortia between anaerobic methanotrophic archaea (ANME) and sulfate reducing bacteria (SRB) carrying out the reverse process, namely anaerobic oxidation of methane (AOM), were discovered in the oceans [5, 6]. ANME archaea involved in AOM contain close homologues of MCR with either cofactor F430 (ANME-2 + 3) or a structural variant, 17^2-methylthio-F430, (ANME-1) as the prosthetic group.

Both of the natural porphyrinoids, vitamin B_{12} and cofactor F430, feature exceptional, chiral, and inherently nonplanar reduced tetrapyrrolic ligands tightly binding the transition metal ions cobalt or nickel, respectively (Figure 18.1). The corrins are also uniquely "contracted" porphyrinoids, presumably an evolutionary adaptation of their coordination hole to the size of the bound cobalt-ions, and resulting in proper tuning of their redox reactivity and axial coordination. Ni-hydrocorphins, like F430, are strongly nonplanar when tetra-coordinate and diamagnetic, a feature related to their redox and axial coordination behavior [7]. Thus, in the natural cobalt-corrinoids and nickel-corphinoids, a specific ligand properly tunes the reactivity of their respective redox-active transition metal centers (see below).

The hexahydroporphyrin uroporphyrinogen III (Uro'gen III), the key tetrapyrrolic biosynthetic precursor of all natural porphyrinoids, arises from enzyme-controlled tetramerization of the biological pyrrole porphobilinogen [8]. The particular biosynthetic lines of cobalt-corrins and nickel-corphinoids split off as the initially common "cobalt- and nickel"- branch from the ones toward heme and chlorophyll (see Figure 18.2). Only certain prokaryotes have the capacity for the de novo biosynthesis of corrinoids. Two separate biosynthetic pathways have been fully elucidated [8, 9]. B_{12}-biosynthesis depends characteristically upon the ability of the microorganisms to grow as (facultative) aerobes or as anaerobes. In the aerobic biosynthesis path, the metal-free corrin hydrogenobyrinic acid is assembled first, and incorporation of cobalt occurs "late," at the stage of hydrogenobyrinic acid *a,c*-diamide. In contrast, anaerobic formation of the corrin ring depends upon the redox reactivity of the cobalt ion, which is incorporated "early," at the stage of the porphyrinoid sirohydrochlorin, an isobacteriochlorin [10]. At the very same stage (sirohydrochlorin), the (anaerobic) biosynthesis line toward the nickel-hydrocorphins branches off by incorporation of a Ni(II)-ion [11] (see Figure 18.2 and Section 18.6.2).

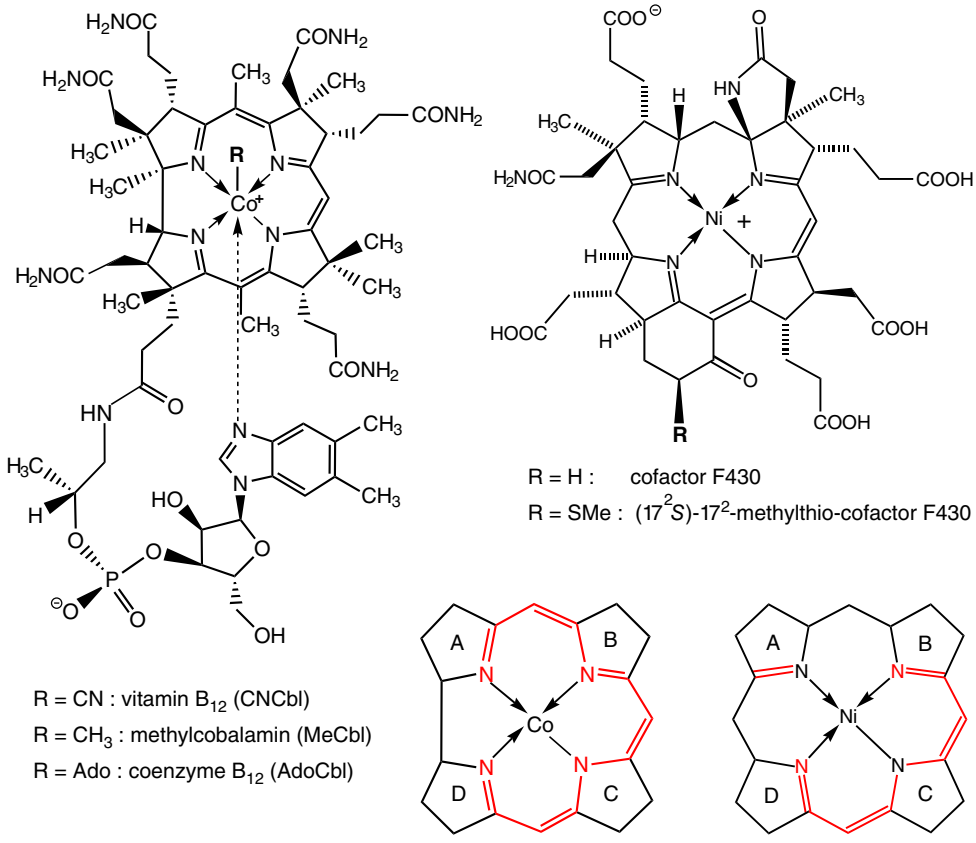

Figure 18.1 Structural formulas of important cobalamins and natural nickel-hydrocorphins, and symbols for the corrin and hydrocorphin ligands of vitamin B_{12} and of cofactor F430, highlighting their respective π-systems.

Cobalt-corrinoids and Ni-corphinoids play key roles in the specific biological catalysis of essential life processes, often depending upon biological redox processes. In fact, cobalt-corrins and cofactor F430 represent the only naturally occurring tetrapyrroles with known biological roles of these two transition metals. Cobalt-corrins are mostly used as cofactors in enzymatic organometallic reactions, in which highly reactive "organic" intermediates are key components. Such reactive species (e.g., radicals) require activation for their formation, as well as tight control of their reaction space for further enzymatic use. These are typical tasks of the proteinaceous environment of the apo-enzymes, not only of the group of the B_{12}-dependent enzymes [12], but also of those that contain cofactor F430.

The class of the natural cobalt-corrinoids is often referred to in a more general way as "B_{12}" [12–15]. Vitamin B_{12} is the traditional specific name of the compound cyanocobalamin (CNCbl), a crystalline early isolation form of the cobalamins (Cbl's). In the popular medicinal literature, however, "vitamin B_{12}" often refers to Cbl's in general, as several Cbl's are B_{12}-vitamin forms, which help to cure B_{12}-deficiency (or Cbl deficiency) [16]. CNCbl is not directly physiologically active in humans and other mammals; the specific important metabolic roles as B_{12}-cofactors are played by two light-sensitive organometallic Cbl's, named coenzyme B_{12} (5′-deoxyadenosylcobalamin, AdoCbl) and methylcobalamin (MeCbl), discovered in the 1960s (see Figure 18.1) [12–15, 17].

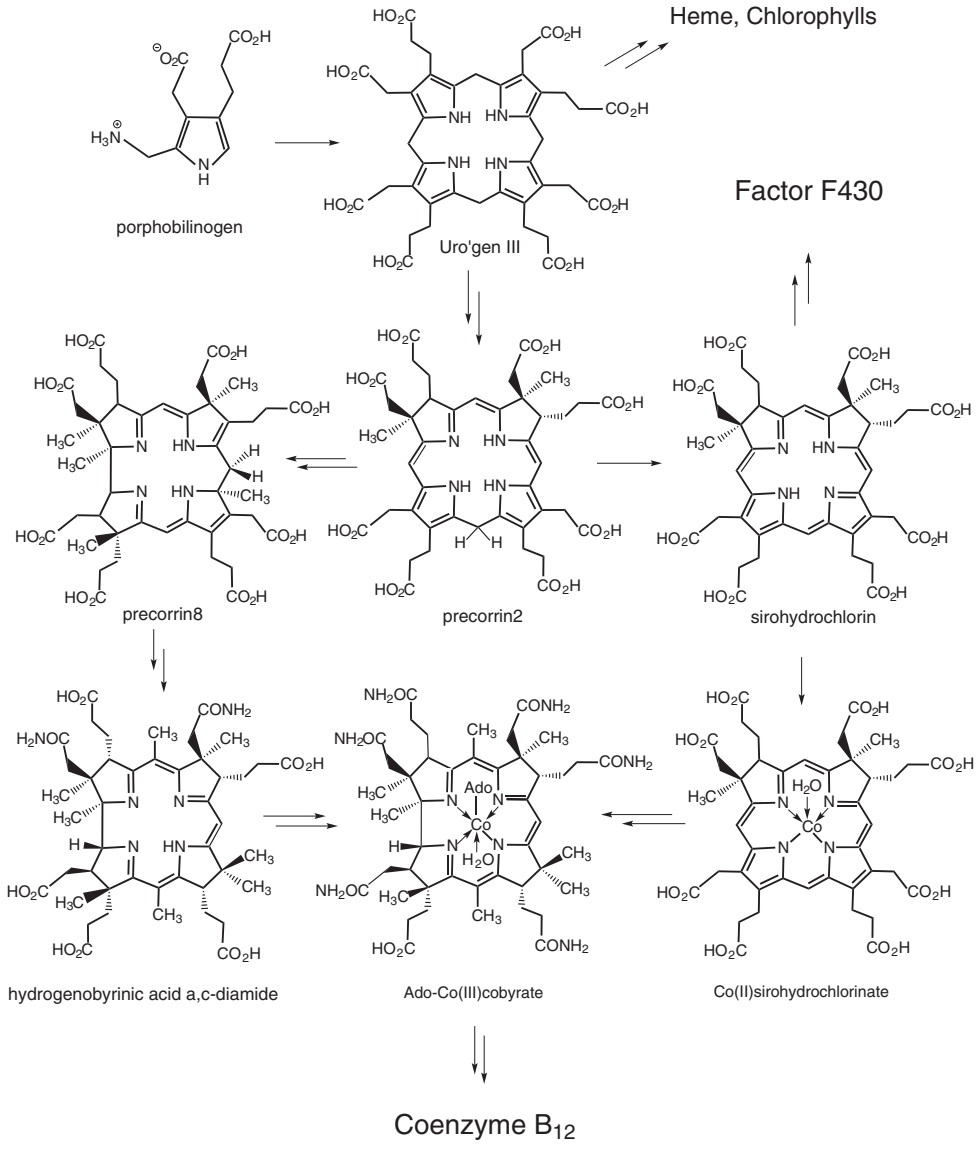

Figure 18.2 A short structural outline of B_{12}-biosynthesis, highlighting the structures of the aerobic and anaerobic paths (at the lower left and right, respectively), and including the branching point (sirohydrochlorin) in anaerobes toward the cofactor F430 biosynthetic line.

Cofactor F430 (Figure 18.1) is the only naturally occurring nickel-containing tetrapyrrole with a known biological function, and by far the most reduced one: All peripheral β-carbons, three α-carbons, and two of the four meso-positions are sp^3-centers. The chromophore is linear as in corrins, but extends only over three of the central nitrogens (rings B-C-D). Because it exhibits the carbon skeleton of a porphyrin and a linearly conjugated chromophore like a corrin, factor F430 is often called a hydrocorphin, a reference to the term *corphin* coined by A. Eschenmoser [18].

The focus areas of this short chapter on "vitamin B_{12} and F430" are – with emphasis on recent developments published before 2017 – structure, biological formation, chemical reactivity, biomolecular binding, mode of action and metabolic relevance as cofactors of the biologically most important cobalt-corrinoids and nickel-corphinoids.

18.2 B_{12}: Synthesis, Structure, and Reactivity

18.2.1 Synthesis

Microbial biosynthesis, boosted by enormous biotechnological developments, provides the major commercial sources of vitamin B_{12}, which is produced nowadays in amounts of several 10 000 metric tons per year (most of it is used as a food additive for feeding livestock). The total synthesis of small amounts of the structurally complex vitamin B_{12} (CNCbl) was achieved in the 1970s as an absolute synthesis highlight in the laboratories of Eschenmoser (ETH, Switzerland) and of Woodward (Harvard University, United States) [1, 19].

18.2.2 Structure

X-ray crystal structure analysis, pioneered by the laboratory of D. C. Hodgkin in Oxford, revealed the molecular structures of several crystalline vitamin B_{12}-derivatives and their previously unknown corrin ligand [20]. In more recent times, high-field heteronuclear NMR-studies have provided detailed insights into the (dynamic) structures of diamagnetic Co(III)corrins in solution [21, 22]. The Cbl's exist in a unique "base-on" structure, in which the 5,6-dimethylbenzimidazole (DMB) pseudo-nucleotide appendage is coordinated to the "lower" face of the cobalt-bound Co(III)-center in an intramolecular fashion (Figure 18.3) [12, 17]. Therefore, CNCbl, AdoCbl, or MeCbl carry their CN-, Ado- or Me-group as axial ligand at the opposite (the "upper") face of the hexa-coordinate Co(III)center. Co(II)corrins, such as Co(II)cobalamin (Co^{II}Cbl), the product of homolysis of the Co—C bond of organometallic Cbl's, feature a low-spin paramagnetic, penta-coordinate Co(II)center. Co(I)corrins, such as Co(I)cobalamin (Co^{I}Cbl), are diamagnetic and are presumed to have their tetra-coordinate Co(I)center bound in a square planar fashion by the corrin ligand (only). The corrin ligand is inherently asymmetric and is nonplanar (due to the direct trans-junction between its rings A and D). The resulting "folding" of the corrin ligand is a much-studied parameter characteristic of the geometric influence of the DMB base and other axial groups at the cobalt center on the structure of the corrin ligand [20, 23].

18.2.3 Reactivity and Redox Chemistry

Vitamin B_{12} (CNCbl) is a remarkably robust Co(III)-complex. The corrin ring of cobalt-corrins remains practically unaffected by typical redox reactions, which take place at the cobalt center. The cobalt oxidation state and the pattern of axial coordination of DMB and other ligands go hand in hand (see above and Figure 18.4) [24]. Thus, redox processes at cobalt are coupled with coordination/de-coordination at the metal center. The biologically crucial Co(II)/Co(I) redox couple occurs at −0.61 V versus NHE, that is, at a slightly more negative potential than the typical range of biological redox systems. Co(I)-corrins are inferred – but hardly observed – in biosynthetic and other enzymatic processes (see below), as their formation is generally coupled metabolically with follow-up processes that trap the

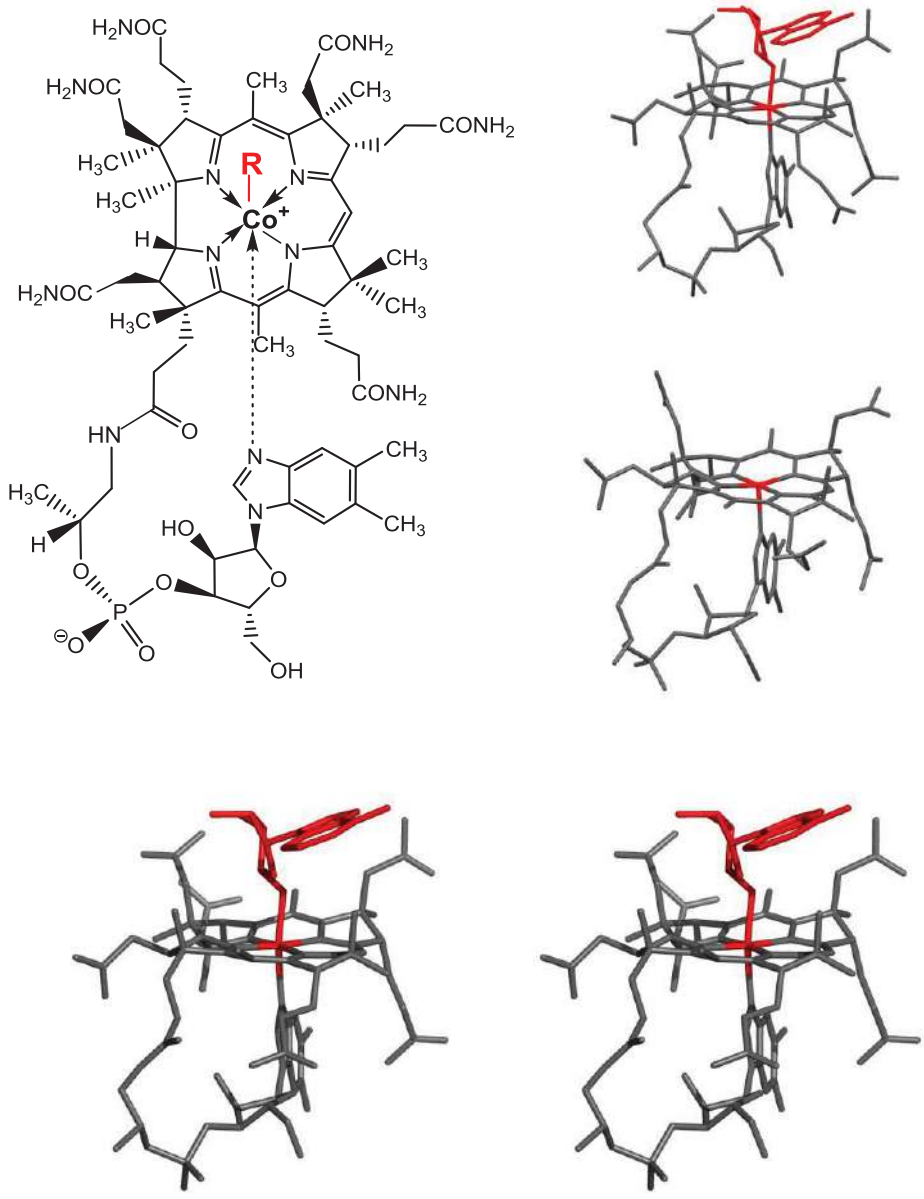

Figure 18.3 Structural formulas (top left) and models (top right) of the crystal structures of coenzyme B_{12} (AdoCbl) and of Co(II)cobalamin (Co^{II}Cbl), featuring B_{12} "base-on" forms with a six-coordinate Co(III)- and a five-coordinate Co(II)center, respectively, and a stereoscopic model of AdoCbl (bottom).

strongly reducing Co(I) form and generate corresponding organometallic Co(III)-corrins [25]. Organometallic Co(III)corrins are particularly difficult to reduce, and their typical reduction potentials are even more negative than the one of the Co(II)/Co(I) redox couple (the half-wave potential of MeCbl was estimated to be near −1.35 V vs. NHE) [24, 26]. Most organometallic Co(III)corrins are very sensitive to visible light, which cleaves their Co—C

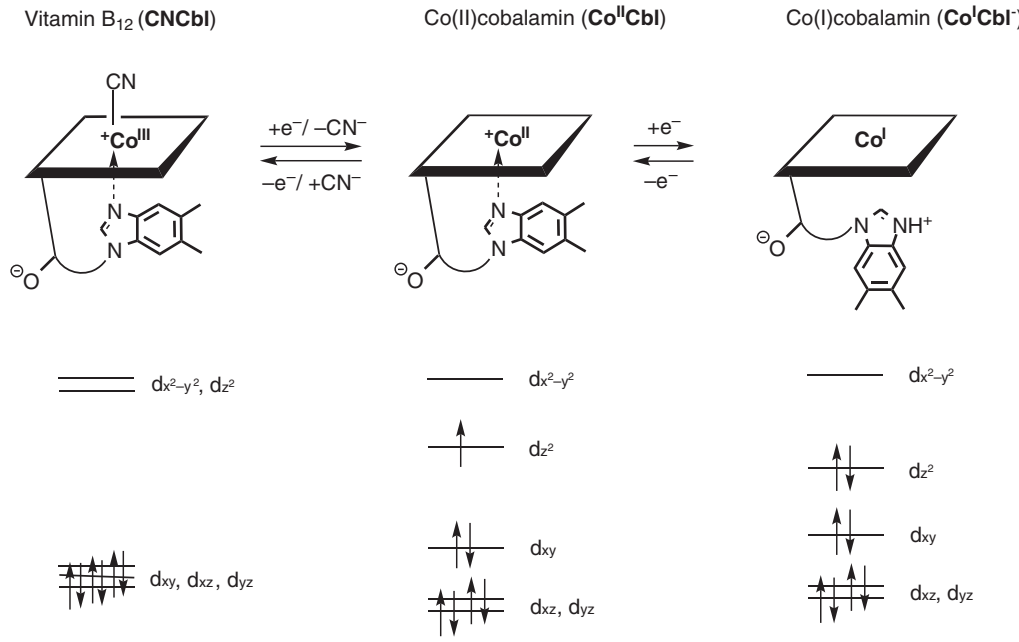

Figure 18.4 Basic correlation between the formal redox state of the cobalt ion and pattern of axial coordination at cobalt in corrins, represented by vitamin B_{12} (CNCbl) with a six-coordinate, diamagnetic d^6-Co(III)-center, Co(II)cobalamin ($Co^{II}Cbl$) with a five-coordinate, low-spin d^7-Co(III)-center, and Co(I)cobalamin ($Co^{I}Cbl$) with a four-coordinate, diamagnetic d^8-Co(III)-center. The electronic ground state configuration is qualitatively specified in a corresponding d-orbital scheme.

bond with high quantum efficiency [27]. Alkynyl-Cbl's (such as 2-phenylethynyl-Cbl) are exceptionally photostable, as is CNCbl [28].

18.2.4 Organometallic Chemistry

Most of the biologically important organometallic chemistry of cobalt-corrins is associated with adenosyl- and methyl-corrins, the two classes of B_{12}-cofactors that are represented by AdoCbl and MeCbl (see below for other natural cobamides). The crucial reactivity of AdoCbl (or coenzyme B_{12}) centers on the thermally activated, reversible homolysis of its weak Co—C bond, which features a homolytic Co—C bond dissociation energy of about 30 kcal mol^{-1} [29]. The Co—C bond of MeCbl, the simplest organo-Cbl, appears to be slightly stronger. It is cleaved by attack of a nucleophile (nucleophile-induced "heterolysis" by an S_N2-mechanism) or of a radical (radical abstraction), to which the methyl group is then attached [30]. After absorption of light, the Co—C bonds of AdoCbl or of MeCbl are also readily cleaved homolytically [27]. Conversely, the Co—C bonds of organo-Cbl's are typically formed either by reaction of the highly nucleophilic ("supernucleophilic") $Co^{I}Cbl$ with an alkylation agent, or by the very fast reaction of the persistent radical trap $Co^{II}Cbl$ with organic radicals (Figure 18.5) [12, 17].

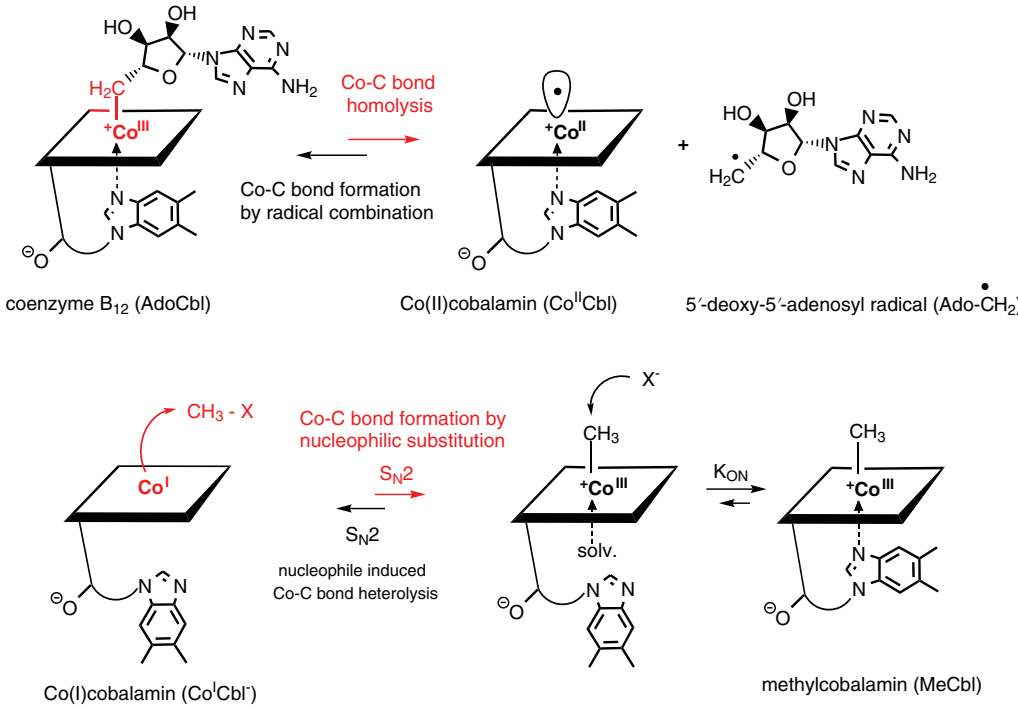

Figure 18.5 Two biologically broadly relevant basic mechanisms of formation and of cleavage of the Co–C bond of organometallic corrinoids, exemplified with homolytic, organometallic chemistry of AdoCbl (top) and organometallic, heterolytic chemistry of MeCbl (bottom).

18.2.5 Natural Corrinoids

With few exceptions [31], natural corrinoids have a completely conserved structure of their corrin moiety and differ by their pseudo-nucleotide group extending from their f-side chain. The corrinoids lacking the nucleotide moiety are called "incomplete" and are generally considered (potential) biosynthetic intermediates en route to their "completion" by attachment of the nucleotide function [10, 32]. Cbl's are "complete" natural corrinoids, in which the pseudo-nucleotide group harbors a DMB "base": they are also called 5,6-dimethylbenzimidazolyl-cobamides (DMBCba's; see [33] for B_{12}-nomenclature). Alternatively, "complete" natural corrinoids may contain other benzimidazole bases, certain purines (mostly adenine and modified adenine), as well as non-coordinating phenol ethers [12, 32]. The remarkable diversity of the natural "complete" corrinoids is the result of the specific biosynthetic capacity of B_{12}-producing organisms for the respective nucleotide heterocycles. Recently, natural "complete" corrinoids have become biomarkers, to monitor the populations of natural microbial communities in the human gut and in other natural habitats (in animals, on land, in lakes, and in the ocean) [34, 35].

The diverse "complete" natural corrinoids differ in their capacity to form the unique B_{12} "base-on" forms. The characteristic purine bases found in the ubiquitous adeninyl-cobamides (also called "pseudocobalamins") give the respective Cba's a considerably lower tendency to from their "base-on" forms [36]. Such differences are likely to be biologically relevant, as "complete corrinoids" may bind to their biomolecular partners (proteins and oligonucleotides) in the characteristic "base-on" form or, alternatively, in

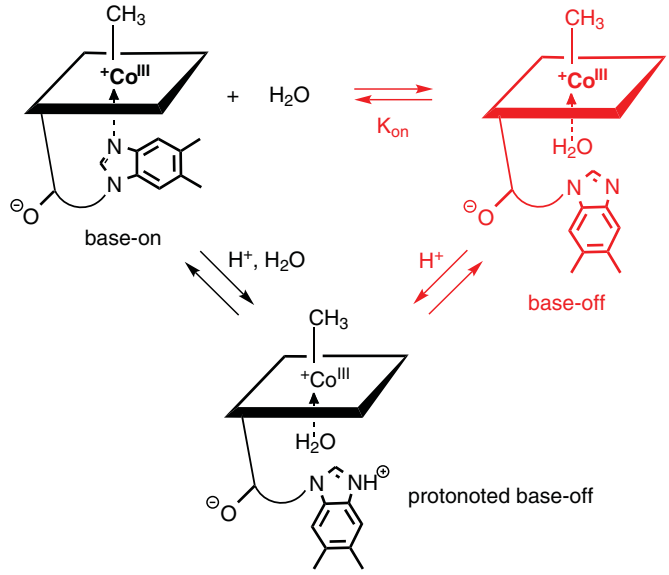

Figure 18.6 The characteristic B_{12} base-on/base-off switch of "complete" corrinoids exemplified with MeCbl. The base-off form of MeCbl is a minor component in aqueous solution, which is not directly observable. It is estimated to be about 2.8 kcal.mol^{-1} less stable than the base-on form of MeCbl from determination of the pK_a of the protonated base-off-form (pK_a = 2.89 at 25 °C).

corresponding "base-off" forms. The base-off forms of Co(III)cobalamins are generally much less stable than their base-on isomers and thus not directly observed. The switch from base-on to base-off of Co^{III}Cbl's can be characterized indirectly by determining their tendency to become protonated at the DMB--nitrogen to give the observable protonated "base-off" form (see Figure 18.6). For example, in aqueous solution at 25 °C, MeCbl is calculated from the pKa = 2.89 of its protonated base-off form to be stabilized in the base-on form with K_{ON} = 93 [17]. The base-on/base-off switch not only leads to an exceptional restructuring of "complete" corrinoids, but also to a pronounced adaptation of their reactivity as cofactors [12, 17, 37].

18.2.6 Unnatural Cobamides – Antivitamins B_{12}

B_{12}-using microorganisms may be able to "remodel" the nucleotide parts of "foreign" natural corrinoids to generate their "own complete" cobamides [38], an important capacity for survival in marine communities in which access to functional B_{12}-forms may be a fundamental resource [39]. Cobalamins are the only class of "complete" corrinoids used by mammals. However, Cbl's with specific artificial structural modifications appear to be tolerated by the (highly structure-sensitive) mammalian cellular uptake systems, and they may be used for drug transport in animal studies (see below) [40, 41]. In contrast, the typical further B_{12}-dependent metabolism of mammals is incapacitated by chemical modifications that prevent Cbl's from fulfilling the roles of (metabolic sources of) B_{12}-cofactors. Hence, they may act as B_{12}-antimetabolites [40, 42]. The metabolically inert unnatural organometallic aryl- and alkynyl-Cbl's appear to represent particularly effective B_{12}-antimetabolites, classified as "antivitamins B_{12}" (see Figure 18.7) [42]. The aryl-Cbl 4-ethylphenyl-Cbl (EtPhCbl) [43] and the

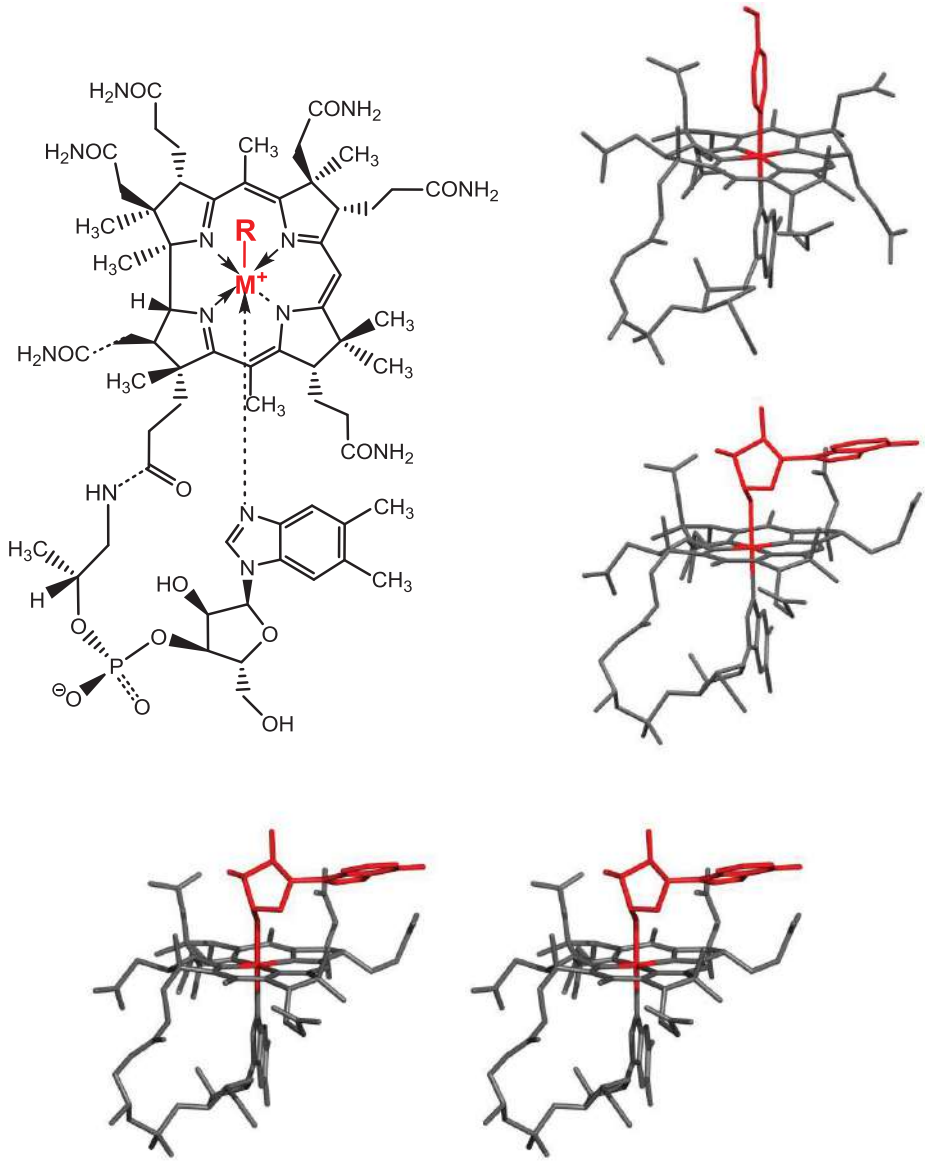

Figure 18.7 Generalized structural formula (top left) and crystal structures (top right) of 4-ethylphenyl-Cbl (EtPhCbl, M = Co(III), L = 4-ethylphenyl) and of adenosylrhodibalamin (AdoRhbl, M = Rh(III), L = Ado), two potential "antivitamins B_{12}," and stereoscopic structure of AdoRhbl (bottom).

alkynyl-Cbl 2-phenylethynyl-Cbl (PhEtyCbl) [44] have been synthesized recently by radical chemistry and were revealed to represent promising "antivitamin B_{12}" candidates.

The biological roles of natural corrinoids are intimately connected with their tightly bound cobalt center. Transition metal analogues of the cobalt-based Cba's have hardly become accessible, as the cobalt ion could not be replaced directly by other metal ions in natural corrins. However, thanks to insights into B_{12}-biosynthesis and advances in biotechnology [45], adenosylrhodibalamin (AdoRhbl, the rhodium-homologue of AdoCbl, right) was recently prepared

by combined biological and chemical synthesis. AdoRhbl was shown to be structured similar to AdoCbl and to behave as a very effective "antivitamin B_{12}" [46]. Surprisingly, the crystal structure suggested that the Rh(III)-ion has a better fit in AdoRhbl than has the Co(III)-ion in AdoCbl. Other unnatural transition metal analogues of the cobalt-based Cba's with structures similar to the natural B_{12}-cofactors would, likewise, be expected to play the roles of effective "antivitamins B_{12}" and to also represent B_{12}-antimetabolites capable of inhibiting B_{12}-dependent enzymes [42].

"Antivitamins B_{12}" are "vitamin B_{12} dummies" that do not function as (metabolic sources of) natural B_{12}-cofactors, but have structures similar to the natural "complete corrinoids" [42]. Hence, they may have the capacity to simulate natural corrinoids in "non-canonical" B_{12}-regulatory roles, such as those of the recently discovered B_{12}-riboswitches (see below) [47]. Via their interaction with B_{12}-riboswitches, "antivitamins B_{12}" may signal the presence of the metabolically important corrinoids. However, they do not support B_{12}-dependent metabolism. Thus, when applied to B_{12}-dependent microorganisms, "antivitamins B_{12}" are expected to inhibit microbial growth strongly, [46] and they would, therefore, function as antibiotics [48].

18.3 B_{12}: Biological Roles

In the course of evolution, cobalt-corrinoids have acquired a broad spectrum of biological roles in most spheres of life on Earth [12, 15, 17, 49, 50]. B_{12}-derivatives are particularly important as catalysts in the basic metabolism of a variety of anaerobic microorganisms, such as acetogens and methanogens. Cbl's also have an important, but remarkably specific role in the metabolism of humans and other mammals, where MeCbl and AdoCbl are the Cbl-cofactors in the enzymes methionine synthase (MetH) and methylmalonyl-CoA mutase (MCM), respectively.

18.3.1 B_{12}-Dependent Methyl Group Transfer

Methyl group transferases are key enzymes in all life forms, and B_{12}-dependent methyl group transfer is one of the major biological tasks of the natural corrinoids [51]. B_{12}-dependent methyl group transferases using the heterolytic methyl group transfer modes play fundamental roles, for example, in methionine biosynthesis, in microbial methanogenesis and acetogenesis, as well as in many other uses of methyl-group-based C1-units [52]. B_{12}-dependent methionine synthase is the most thoroughly representative of this class of enzymes (see below). Interestingly, a range of organisms can (also) rely on the typically less active B_{12}-independent methionine synthases.

Class B radical S-adenosyl-methionine (SAM) methyl transferases (class BRSMTs) are a second and still less established group of B_{12}-dependent methyl group transferases [53]. They appear to employ a homolytic methyl group transfer mode [30] to achieve methylation reactions at "unactivated" positions (carbon and phosphorous centers), important in the biosynthesis of natural products in microorganisms (see below) [53].

18.3.1.1 B_{12}-Dependent Methionine Synthase

B_{12}-dependent methionine synthase (MetH) is a thoroughly investigated methyl group transferase [54], essential in the metabolism of humans and other mammals. MetH uses the

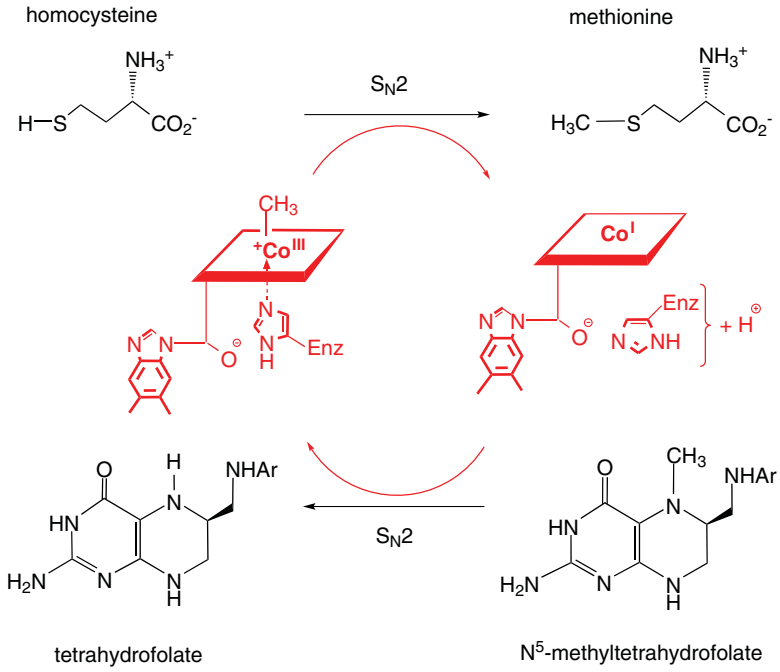

Figure 18.8 Cbl-dependent methionine synthase (MetH) catalyzes methylation of homocysteine to give methionine, using the methyl group of N-methyl tetrahydrofolate. Methyl group transfer in MetH takes place through a "ping-pong" mechanism and occurs via two nucleophilic substitution (S_N2) steps, that is, with overall stereochemical retention. Stereoelectronics of S_N2-steps require both the demethylating nucleophile and the methylating agent to adopt a precise position with respect to the cobalt center of the protein-bound MeCbl cofactor. The latter is bound in a base-off/His-on structure, in which the imidazole ring of His759 of MetH replaces the DMB base. Presumably, His759 is de-coordinated from Co^{I}Cbl, assisting in the demethylation of the protein-bound MeCbl cofactor. Alternatively, it has been suggested that a "molecular juggling act" by the respective domains of MetH is needed to position activated forms of homocysteine or N^5-methyltetrahydrofolate.

heterolytic mode of methyl group transfer and catalyzes methylation of homocysteine, furnishing methionine, in a process coupled with demethylation of *N*-methyl-tetrahydrofolate to tetrahydrofolate. In the course of this enzyme reaction, enzyme-bound MeCbl donates its "organometallic" methyl group to the methylation substrate, the (weakly) nucleophilic homocysteine, furnishing MetH with a protein-bound Co^{I}Cbl. This highly nucleophilic, strongly reducing Co(I)corrin is methylated rapidly by the properly placed, activated methyl group donor *N*-methyl tetrahydrofolate, regenerating MeCbl and restoring the typical resting state of the B_{12}-dependent methionine synthase. Both enzyme-catalyzed methyl group transfer steps are thus considered to follow the mechanism of S_N2-processes. The intriguing base-off/his-on mode of the cofactor MeCbl was discovered in the crystal structure of the B_{12}-binding domain of MetH (see Figure 18.8) [55]. MetH consists of four major domains, each enabling one of the four crucial processes relevant for the proper function of this B_{12}-dependent methyl group transferase [51]. The complex dynamic interplay between these domains of MetH [56] in achieving the controlled methyl group transfer is still a matter of current investigations.

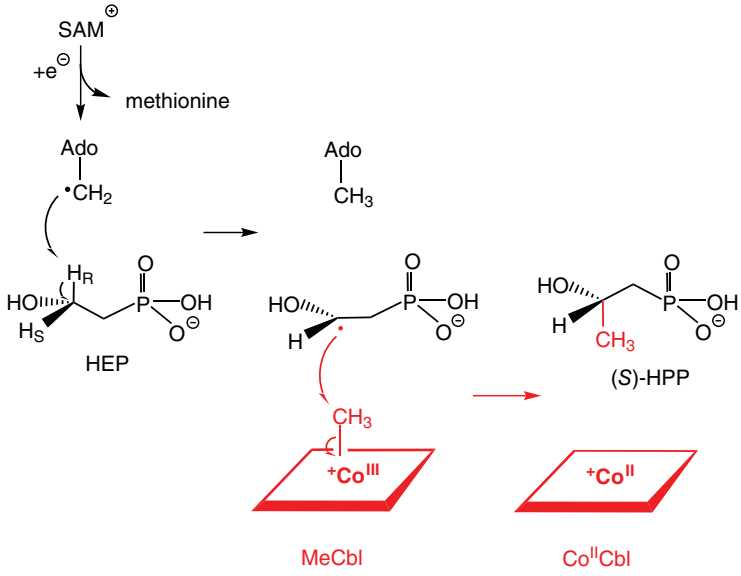

Figure 18.9 During the course of the biosynthesis of the antibiotic fosfomycin, 2-hydroxyethyl-phosphonate (HEP) is methylated stereospecifically to (*S*)-2-hydroxypropylphosphonate (HPP). The enzyme reaction is proposed to occur by abstraction of H_R by the 5′-deoxy-5′-adenosyl radical (Ado-CH_2·), derived from SAM, and methylation of the intermediate hydroxyethyl-2-phosphonate radical via abstraction of the cobalt-bound methyl group of properly positioned MeCbl. In support of this mechanism, the methyl group transfer from SAM to HPP occurs with overall retention of the configuration of the methyl group.

18.3.1.2 B_{12}-Radical SAM Enzymes

A still less well-documented, second role of cobalt-corrinoids in biological methyl group transfer is based on the participation of Me-Co(III)corrins in the so-called class B radical SAM methyl transferases (class BRSMTs) [57]. These use SAM (or AdoMet), the "poor man's AdoCbl" [58, 59], as a source of adenosyl radicals that generate a substrate radical by H-abstraction, as well as a methylating agent for regenerating MeCbl (in an overall stoichiometric amount) in the course of the methylation reaction. BRSMTs are presumed to rely on a bound Me-Co(III)-corrin as the second cofactor as the direct source of the methyl group (that is found in the respective product). In this path, the methyl group of the bound Me-Co(III)-corrin may be abstracted by a substrate radical that is made available by the previous H-atom abstraction by the adenosyl radical [30]. This pathway introduces an intact methyl group in biosynthesis intermediates and appears to be relevant for the biosynthesis of the antibiotic fosfomycin by methylation at "inactivated" carbon (Figure 18.9) and of the tripeptidic herbicide bialaphos by P-methylation of a phosphinate precursor. Consistent with the proposed two-transfer mechanism, the methyl group of SAM is incorporated into the products with overall retention of configuration [53, 57].

18.3.2 Coenzyme B_{12}-Dependent Radical Enzymes

Adenosyl-corrins, such as AdoCbl, are crucial cofactors in the catalysis of a range of enzymatic radical reactions [49, 50, 60, 61]. Among these are skeletal rearrangements of metabolic substrates, such as of methylmalonyl-CoA in the C-skeleton mutases MCM [60]

Table 18.1 Reactions catalyzed by AdoCba-dependent carbon skeleton mutases.

a) Acyl-CoA mutases

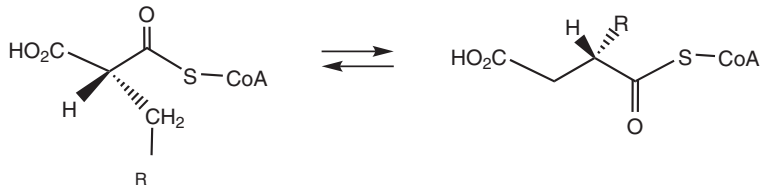

R = H: (*R*)-methylmalonyl-CoA / succinyl-CoA

R = CH_3: (*R*)-ethylmalonyl-CoA / (2S)-2-methyl-succinyl-CoA

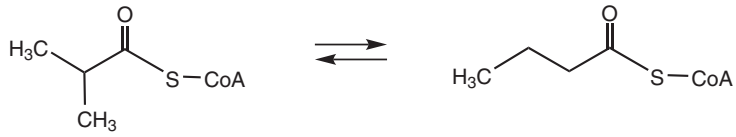

Isobutyryl-CoA / n-butyryl-CoA

b) Glutamate mutase

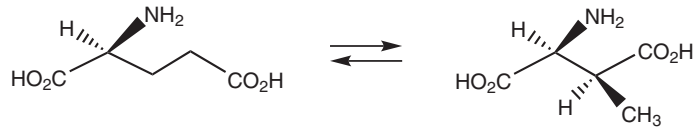

(S)-glutamic acid / (2S,3S)-3-methylaspartic acid

c) Methylene glutarate mutase

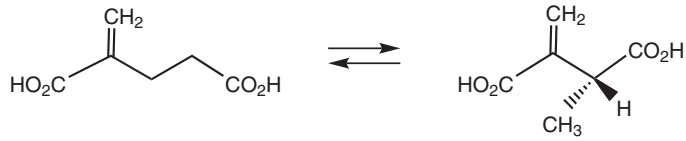

2-methyleneglutarate / (R)-3-methylitaconate

or of glutamate in glutamate mutase (GM) (see Table 18.1) [62]. The C-skeleton mutases appear to depend specifically upon the AdoCba cofactors, and B_{12}-independent counterparts are unknown [50].

A second class of AdoCbl-dependent isomerases catalyze either overall substrate dehydration (as in B_{12}-dependent diol-dehydratases) [63] or rearrangements with intramolecular transport of an amino group (in the amino-mutases) (see Table 18.2) [58]. In this group of isomerases, B_{12}-independent versions are known, too [49].

Reduction of RNA to DNA by ribonucleotide reductases (RNRs) is a process that is essential in the biosynthetic generation of DNA. RNRs are found in all organisms, and

Table 18.2 Reactions catalyzed by AdoCba-dependent isomerases.

Amino mutases

D-ornithine / (2*R*,4*S*)-2.4-diaminovaleric acid

D-(α)-lysine / 2.5-diaminohexanoic acid

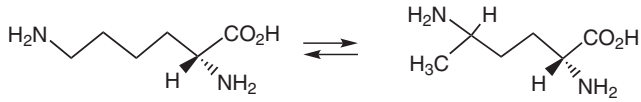

L-(β)-lysine / (3*S*,5*S*)-3.5-diaminohexanoic acid

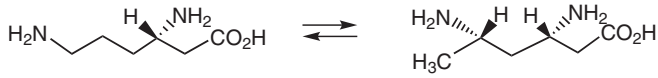

Diol dehydratases

R = H : 1.2-propanediol / propanal
R = OH : glycerol / 3-hydroxypropanal

Ethanolamine deaminase

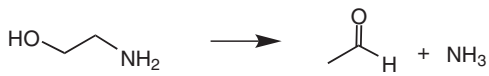

ethanolamine / acetaldehyde

four classes of RNRs are now known that all catalyze overall reduction of nucleotides to 2′-deoxynucleotides via radical steps [64]. AdoCbl-dependent RNRs have been categorized as class II RNRs [65]. The four classes of RNRs differ by the initiation mechanisms in which an H-atom is abstracted from a cysteine residue of the protein (and the corresponding cysteine radical is generated) and appear to follow the same sequence of subsequent radical steps.

18.3.2.1 Methylmalonyl-CoA mutase (MCM)

MCM is an important AdoCbl-dependent enzyme in humans, in higher animals, and other organisms, where it converts (*R*)-methylmalonyl-CoA (e.g., from degradation of uneven numbered fatty acids) to succinyl-CoA, a metabolite and a key intermediate of the tricarboxylic acid cycle [60]. MCM and several related C-skeleton mutases have been thoroughly studied, and their basic radical mechanisms appear to be largely established (see Figure 18.10) [60]. An enzyme-bound 2′-methylmalonyl-CoA radical isomerizes to the

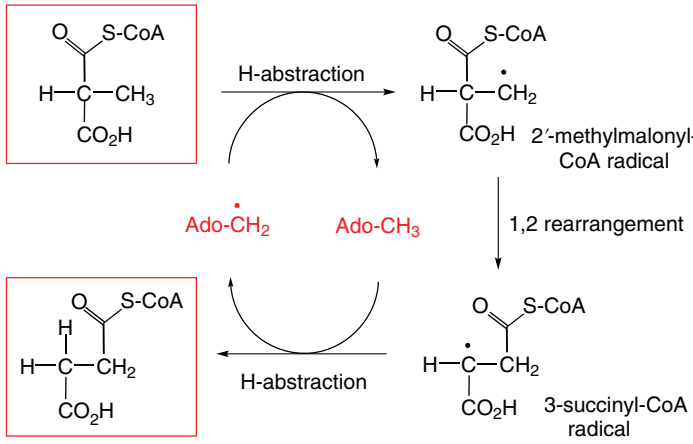

Figure 18.10 Methylmalonyl-CoA mutase (MCM) interconverts (*R*)-methylmalonyl-CoA and succinyl-CoA, induced by a 5′-deoxyadenosyl radical (Ado-CH_2·) that is generated by (Co—C)-homolysis of protein-bound AdoCbl. The proposed mechanism involves an initial H-atom abstraction by a tightly controlled Ado-CH_2· radical. This furnishes a 2′-methylmalonyl-CoA radical, which undergoes fast carbon skeleton rearrangement to the 3′-succinyl-CoA radical. H-Atom abstraction by this "product radical" from 5′-deoxyadenosine (Ado-CH_3) provides succinyl-CoA and regenerates Ado-CH_2 (the sequence of steps of this reversible enzyme reaction is only shown in the "forward" direction).

corresponding 3′-succinyl-CoA radical in the proper rearrangement step of MCM [50, 60]. However, the particular mode(s) of activation of the protein-bound "pre-catalyst" AdoCbl toward homolysis of its Co—C bond that furnishes the catalytically active, tightly controlled 5′-deoxyadenosyl radical still remain to be clarified [61].

18.3.2.2 B_{12}-Dependent Ribonucleotide Reductase

As do the other RNRs, AdoCbl-dependent (or class II) RNR uses radical chemistry to reduce off the 2′-hydroxyl group of the ribose part of a nucleotide, furnishing the corresponding 2′-deoxyribonucleotides [65]. Selectivity for reduction by RNR of a particular nucleotide is achieved by an intriguing mode of allosteric specificity regulation. The crystal structure of an AdoCbl-dependent ribonucleotide-triphosphate reductase revealed the use of the base-on form of AdoCbl in this enzyme, supported the function of a protein-bound catalytically active cysteinyl radical, and helped localize the binding site for the allosteric effectors (ATP, dNTP) [66]. According to the established mechanism, the cysteinyl radical starts the enzyme reaction by abstraction of an H-atom at the 3′-position of the ribonucleotide substrate. Subsequent elimination of water, H-atom abstraction form a cysteine, one-electron reduction by a proposed intermediate disulfide anion followed by H-atom back transfer to the C3′ of the ribose moiety, furnish the corresponding 2′-deoxyribonucleotide (and a disulfide link in the protein) (see Figure 18.11) [64].

18.3.3 B_{12}-Dependent Reductive Dehalogenases

Certain anaerobes can make use of B_{12}-dependent dehalogenases to reduce organic waste by dehalogenation, a process that is useful, in turn, for a type of respiration by these anaerobes with the help of oxidizing (halogenated) substrates. B_{12}-dependent processes play the

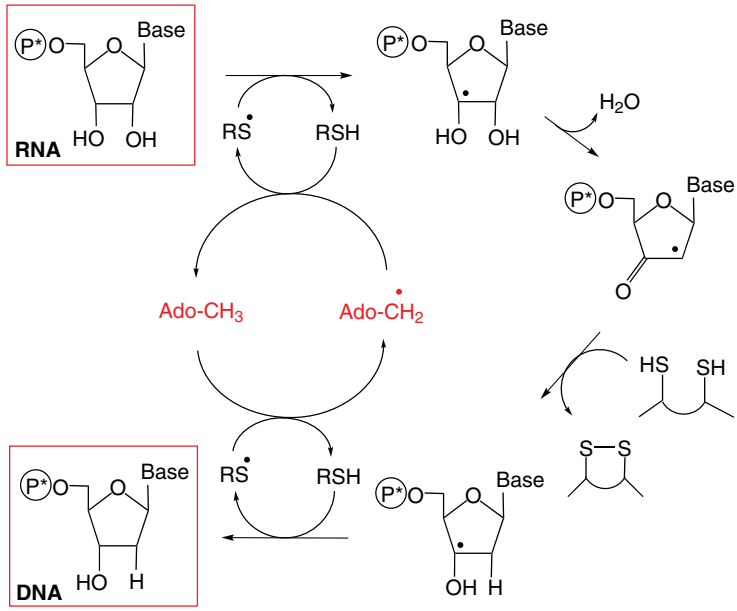

Figure 18.11 AdoCbl-dependent ribonucleotide reductase (RNR) reaction. The proposed mechanism involves generation of the cysteinyl radical (RS·) via H-atom abstraction by a 5′-deoxy-5′-adenosyl radical (Ado-CH_2·), which is available from homolysis of the (Co—C)-bond of AdoCbl (not displayed). Subsequent abstraction of an H-atom from the 3′-position of the ribonucleotide (P* stands for di- or triphosphate) activates loss of water at the 2′-position of the latter. Back transfer of an H-atom from a protein-bound thiol and successive one-electron reduction generate the 2′-deoxyribonucleotide radical and a protein disulfide unit. Abstraction of an H-atom from cysteine furnishes the reduced 2′-deoxyribonucleotide. The cysteinyl radical may now abstract an H-atom from Ado-CH_3, giving Ado-CH_2· (ready for recombination with Cbl^{II}Cbl and reconstitution of protein-bound AdoCbl – not shown).

central role in the dehalogenase reductions. Perchloroethylene (PCE) is a well-suited substrate of the thoroughly studied enzyme PCE dehalogenase in the anaerobe *Sulfurospirillum multivorans* [67]. PCE-reductase reduces PCE to *cis*-dichloroethene. PCE dehalogenase of the anaerobe *S. multivorans* carries the remarkable adeninyl-norcobamides as cofactor, an uncommon norcorrinoid that lacks the methyl group at carbon-176 of the isopropanol linker of typical Cba's. Such norcobamides appear to be better catalysts in this dehalogenase than (the more "conventional") cobamides, a finding rationalized by the slightly lesser negative reduction potentials of norcobamides [31].

18.3.4 B_{12}-Derivatives in Gene Regulation

Vitamin B_{12}-derivatives may interact directly with the "aptamer part" of B_{12}-binding "riboswitches." Riboswitches are newly discovered components in the 5′-untranslated region of mRNA that may operate as gene regulatory elements and effect gene regulation via control of transcription or translation [47]. Riboswitches, in which a bound metabolite controls downstream transcription or translation of the mRNA involved, are widespread in microorganisms. A B_{12}-dependent riboswitch or B_{12}-riboswitch from *Escherichia coli* (that helps control expression of the B_{12}-uptake protein BtuB) was the first riboswitch to be discovered [47]. In this B_{12}-riboswitch, specific binding of the "ligand" AdoCbl induces a conformational

change in the (aptamer segment of) bound RNA, leading to inhibition of ribosome binding and to repression of translation of the btuB mRNA [47, 68]. AdoCbl is the most tightly bound ligand of the btuB riboswitch, and other related B_{12}-derivatives interact more weakly with this B_{12}-riboswitch [69]. Other B_{12}-riboswitches may have a different selectivity for their B_{12}-ligands [70].

Remarkably, light-sensitive AdoCbl is also used as a ligand in protein-based photoregulation of gene expression [71]. AdoCbl regulates the biosynthesis of photo-protecting carotenoids in a group of bacteria, for example, in *Myxococcus xanthus*, by binding to the DNA-binding protein CarH, a B_{12}-based photoreceptor [72]. Upon exposure to light, the Ado-group of CarH-bound AdoCbl is cleaved off, resulting in a strongly reduced affinity of CarH for the promoter region of the dsDNA. Crystallographic work has provided detailed insights into the structural basis of the light-induced transformations of AdoCbl-dependent CarH from *Thermus thermophilus* [73]. The light-induced cleavage of the organometallic bond of AdoCbl provides the chemical basis of the novel role of AdoCbl as a remarkable, irreversibly functioning natural photoswitch. Thus, Nature makes use of the notorious light sensitivity of AdoCbl in a remarkable way.

18.4 B_{12}: Uptake, Transport, and Biosynthetic Remodeling in Humans and Mammals

Vitamin B_{12} and other Cbl's are very scarce natural products that are very valuable components of our nutrition [74]. Humans and most other organisms that use corrinoids for their metabolism have intricate machineries for efficient uptake, selection, and biosynthetic modification of vitamin B_{12} derivatives [75, 76]. Humans and other vertebrates require the complete Cbl-structure, but may convert natural Cbl's into the two Cbl-cofactors AdoCbl and MeCbl [77]. The human B_{12}-uptake system relies on transport by the B_{12}-binding proteins haptocorrin (HC), intrinsic factor (IF), and transcobalamin (TC), which bind typical Cbl's with astoundingly high affinities [75]. Attachment of Cbl strongly restructures these B_{12}-binding proteins, which is important for recognition of the Cbl-binding proteins by their receptors. Indeed, B_{12} uptake in humans depends upon receptor-mediated entry into cells. Thus, IF bound by a Cbl ligand, is docked at cubam specifically, a receptor complex located at the membrane of enterocytes in the ileum [78]. In this way, Cbl's are imported from ingested nutrition into the bloodstream, where they are bound to TC and/or HC. Likewise, Cbl bound to TC is taken up from the blood into all cells via interaction of Cbl-bound holo-TC with TC-receptor [79] and liberation by subsequent endocytosis [75].

Upon delivery to human cells, natural Cbl's are remodeled ("tailored") by the recently discovered and characterized enzyme CblC (a Cbl-deligase, also called the MMACHC protein) [80], which de-coordinates the DMB-nucleotide reversibly and cleaves off the "upper" axial ligand [77]. Hence, vitamin B_{12} (CNCbl) loses its CN-ligand by enzymatic reduction, and natural organometallic Cbl's (such as MeCbl and AdoCbl) are dealkylated by CblC-bound glutathione (presumably by an S_N2-process). CblC releases Co^{II}Cbl as the cellular biosynthesis precursor for MeCbl and AdoCbl, the two B_{12}-cofactors of the B_{12}-dependent enzymes MetH and MCM (see Figure 18.12) [77]. The known "antivitamins B_{12}" resist tailoring by CblC and cannot be transformed into the two B_{12}-cofactors AdoCbl and MeCbl [42]. Hence, their presence induces "functional B_{12} deficiency" in experiments with laboratory animals and cell cultures, allowing studies of the physiological consequences of B_{12} deficiency [81].

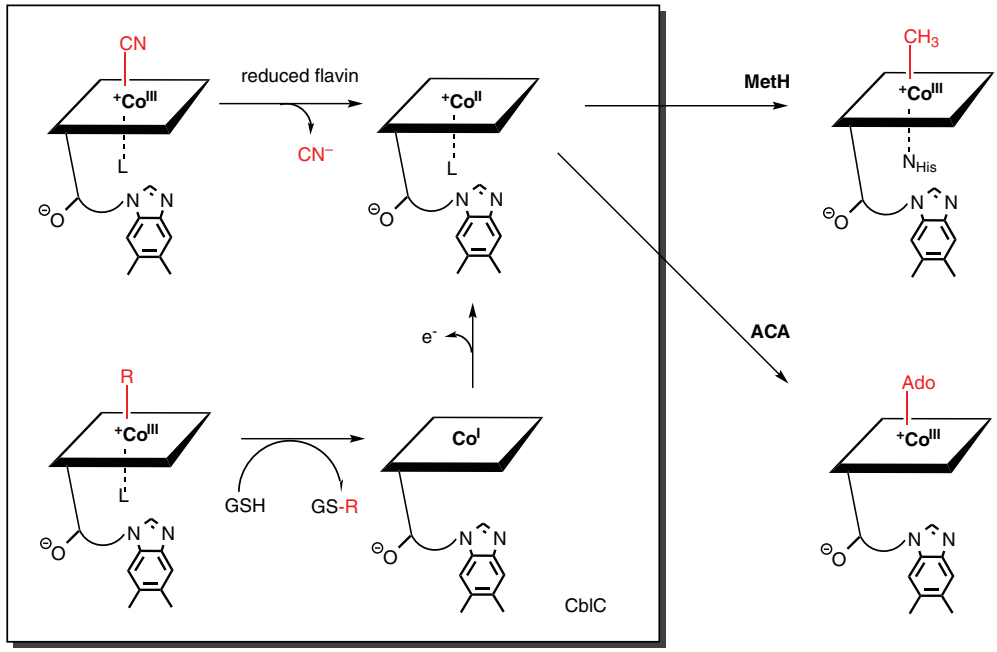

Figure 18.12 The CblC protein binds incoming Cbl's in an activated base-off form and "tailors" them to Co^{II}Cbl, thanks to its dual reactivity as a reducing and de-alkylating enzyme. Its product, Co^{II}Cbl, is formed either by reductive decyanation of CNCbl or by nucleophilic substitution of alkylcobalamins followed by oxidation of the resulting Co^{I}Cbl species. Co^{II}Cbl is subsequently converted intracellularly into the physiologically relevant B_{12} derivatives MeCbl (by methionine synthase, MetH) and AdoCbl (by ATP:cob(I)alamin adenosyl-transferase, ACA). GSH = glutathione; L = a tentative cobalt-coordinating ligand.

Clearly, EtPhCbl and other "antivitamins B_{12}," such as AdoRhbl, are to be classified as poisons and need to be handled with appropriate precautions.

18.5 B_{12}: Applications in Biology and Medicine

Vitamin B_{12} (CNCbl) is, first of all, a common vitamin supplement for food and health and safe pharmaceutical product [74]. It is important to know that 100-fold "overdoses" of CNCbl appear to be harmless [82]. In a standard treatment of patients with B_{12}-deficiency, CNCbl and several other Cbl's are applied intravenously [83]. Aquo- or hydroxocobalamin (HOCbl) also serve as antidotes to acute cyanide poisoning [40]. However, the highly specific and effective machinery employed for B_{12} uptake and transport in mammals has also become useful for application of Cbl's as carriers of specific molecular loads into cells and subsequent delivery there [41, 84, 85]. Hence, fluorescent or radiolabeled covalent Cbl conjugates have been developed for the purpose of imaging cell-specific B_{12}-transport and for tissue diagnosis in animals [85, 86]. B_{12} conjugates have also been designed to carry pharmacologically active peptides [87] and single-stranded DNA [88]. Along the same lines, covalent Cbl conjugates may serve as "Trojan horses" for the selective delivery of toxic loads into cancerous human cells and animal tissues, potentially helping in tumor therapy [85, 86].

B_{12} deficiency leads to degeneration of the human peripheral and central nervous system [89]. It is common among a large fraction of elderly people, where it affects the development of atrophy of the brain's gray matter [82], and it also results in particularly devastating neurological defects in developing embryos [90]. Thus, serious neurological consequences of B_{12} deficiency are indicated that arise through still largely unknown mechanisms, calling for experimental studies of (functional) B_{12} deficiency in healthy animals [89].

18.6 Cofactor F430 and Its Role in Anaerobic Methane Formation and Oxidation by Archaea

18.6.1 Structure [91]

Cofactor F430 was first reported as a yellow, non-fluorescent component in cell extracts of methanogens in 1978 by Wolfe and co-workers, who also showed that F430 is tightly but not covalently bound to the methyl-coenzyme M reductase enzyme. The insight that this factor (named F430 because of its UV/VIS maximum at 430 nm) is a tetrapyrrole containing nickel is mainly due to the group of R. K. Thauer. Using isotope labeling (^{14}C and ^{63}Ni), they showed that eight units of δ-amino-levulinic acid, one Ni atom, and two methyl groups originating from SAM are incorporated into F430. This indicated that uroporphyrinogen III and sirohydrochlorin (or, alternatively, dihydrosirochlorin = precorrin 2) were common biosynthetic precursors to both B_{12} and F430 in methanogens, which was confirmed by further tracer studies and formed the basis of the full structure elucidation carried out in a collaboration of the groups of R.K. Thauer (MPI Marburg) and A. Eschenmoser (ETH Zurich) [92–94]. (*Note:* In [92], the relative configuration at C17-C18-C19 (ring D) was left open, but a tentative assignment was shown in the formula. The question of the configuration at ring D was answered only nine years later, and the tentative assignment had to be revised to the one shown in Figure 18.1 [95]. Unfortunately, the wrong stereochemistry in ring D is depicted not only in the literature before 1992 but also in some recent publications.)

All side chains of uroporphyrinogen III are intact in F430. The two acetic acid side chains at C2 and C7 are amidated, and two form additional rings: the C7-acetic acid side chain forms a γ-lactam to C6, and the propionic acid side chain at C17 has acylated meso-position C15 to give a cyclohexenone ring with a keto group that is in conjugation with the chromophore.

18.6.2 Biosynthesis – From Sirohydrochlorin to F430

The discovery of a second nickel-containing yellow factor in methanogens, the elucidation of its structure as 15,17^3-seco-F430–17^3-acid, and its conversion to F430 by cell extract showed that the last step of F430 biosynthesis is the formation of the cyclohexenone ring (Figure 18.13) [96]. However, the biosynthetic steps between sirohydrochlorin (or dihydrosirohydrochlorin = precorrin 2) and 15,17^3-*seco*-F430–17^3-acid remained unknown until very recently, when Zheng et al. reported on the identification of five cofactor F430 biosynthesis (cfb) genes in the methanogen *Methanosarcina acetivorans* by comparative genomics. These include a nickel chelatase, a Ni-sirohydrochlorin *a*,*c*-diamide synthetase, a primitive homologue of nitrogenase mediating a six-electron reduction and formation of the lactam ring, and a homologue of Mur ligase, which forms the six-membered carbocyclic ring in the final step after activating the C-17^3-carboxylate group with ATP via formation of an acyl phosphate [11].

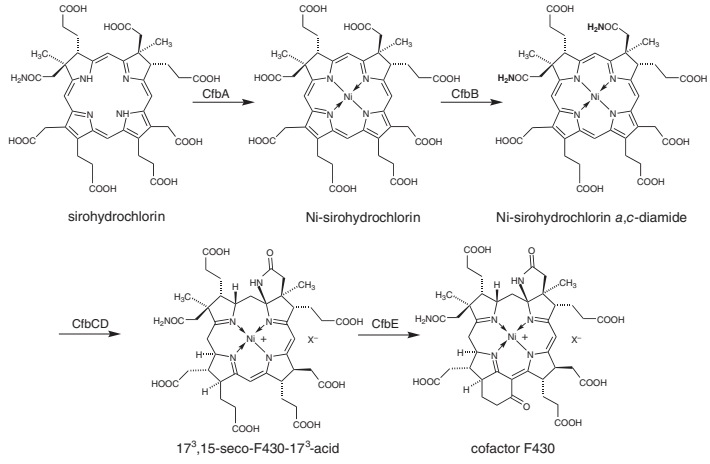

Figure 18.13 Biosynthetic steps from sirohydrochlorin to cofactor F430. Source: Based on Zheng et al. [11].

18.6.3 Redox Chemistry of F430 [7]

Because cofactor F430 is a pentacarboxylic acid, the investigation of its redox chemistry is rendered difficult by competing reductions of H^+ to molecular hydrogen except at very high pH (>10). Therefore, most redox studies of the Ni-hydrocophinoid system of F430 were carried out with F430 pentamethyl ester ($F430Me_5$), which is soluble in non-protic solvents and does not have acidic hydrogens.

Metal- versus ligand-centered reduction/oxidation. $Ni(II)F430Me_5$ can be reduced and oxidized reversibly by one electron. As demonstrated by EPR spectroscopy, the reduction product has most of the spin density on the central metal, in contrast to Ni-porphyrins and Ni-chlorins, which are reduced to ligand π-radical anions. Thus, the one-electron reduction product is best described as $Ni(I)F430Me_5$, an $S = 1/2$ species with the unpaired electron in the d_{x2-y2}-type orbital of the nickel. With E° at about –0.6 V versus NHE, the potential of the $Ni(II)F430Me_5/Ni(I)F430Me_5$ redox couple is very low, lower than the about –0.5 V limit generally estimated to by reachable in anaerobic cells and similar to the Co(II)/Co(I) couple in base-on B_{12} systems. Chemical reduction of $F430Me_5$ without over-reduction can be achieved by ZnHg or decamethylcobaltocene and, for native F430, by Ti(III)citrate at pH > 10 [97]. It is well established by now that, in order to be active, the enzyme MCR must contain cofactor F430 in the Ni(I) valence state (see below).

One-electron oxidation of $F430Me_5$ in non-coordinating or weakly coordinating solvents is also metal centered and leads to $Ni(III)F430Me_5$ with a $(d_{z2})^1$ ground configuration. With E° = 1.45 V versus NHE, $Ni(III)F430Me_5$ is a very strong oxidant, unlikely to survive inside a protein or cell.

18.6.3.1 Influence of the Hydrocorphinoid Ligand on the Redox Properties

Ni-isobacteriochlorins (e.g., NiOEIBC), which also exhibit metal-centered reduction, have Ni(II)/Ni(I) redox potentials of about –1.3 V versus NHE, about 0.70 V lower than $Ni(II/I)F430Me_5$. Considering that the Ni(I) valence state is required for catalysis in MCR, it is of interest to understand which structural features of F430 are responsible for the much easier reduction of F430 compared to Ni-isobacteriochlorins. Comparison of the Ni(II/I) potentials of a series of partial synthetic derivatives of F430 (see Figure 18.14) reveals two main factors: (i) mono-anionic (F430) versus dianionic (IBC) ligand (ΔE ca. +0.3 V) and (ii) the electron withdrawing effect of the C=O group in conjugation with the chromophore (ΔE ca. +0.3 V).

Interestingly, the very short chromophore of F430, extending only over three of the four central nitrogen atoms, is neither a prerequisite for metal-centered reduction nor for reduction at relatively high potential. The corphinoid nickel complex 19,20-didehydro-$F430Me_5$ (see Figure 18.14), the pentamethyl ester of a minor component obtained from crude F430 isolates, exhibits the full chromophore of a corrin ("rotated" by 90°). The one-electron reduction of 19,20-didehydro-$F430Me_5$ is metal centered, leading to a Ni(I) species (EPR), and its Ni(II)/Ni(I) redox potential is approximately 0.15 V higher than that of $Ni(II)F430Me_5$ [98].

18.6.3.2 Reactivity of the Nickel Center in F430

Low-spin and high-spin Ni(II): $Ni(II)F430Me_5$ in non-coordinating solvents is diamagnetic (low-spin d^8, $S = 0$) with four-coordinate nickel, but has a strong tendency to add axial ligands to give paramagnetic (high-spin d^8) five- and six-coordinate complexes. Ligands such as Cl^-, CN^-, pyridine, imidazole, and thiolates were found to give five- and six-coordinate

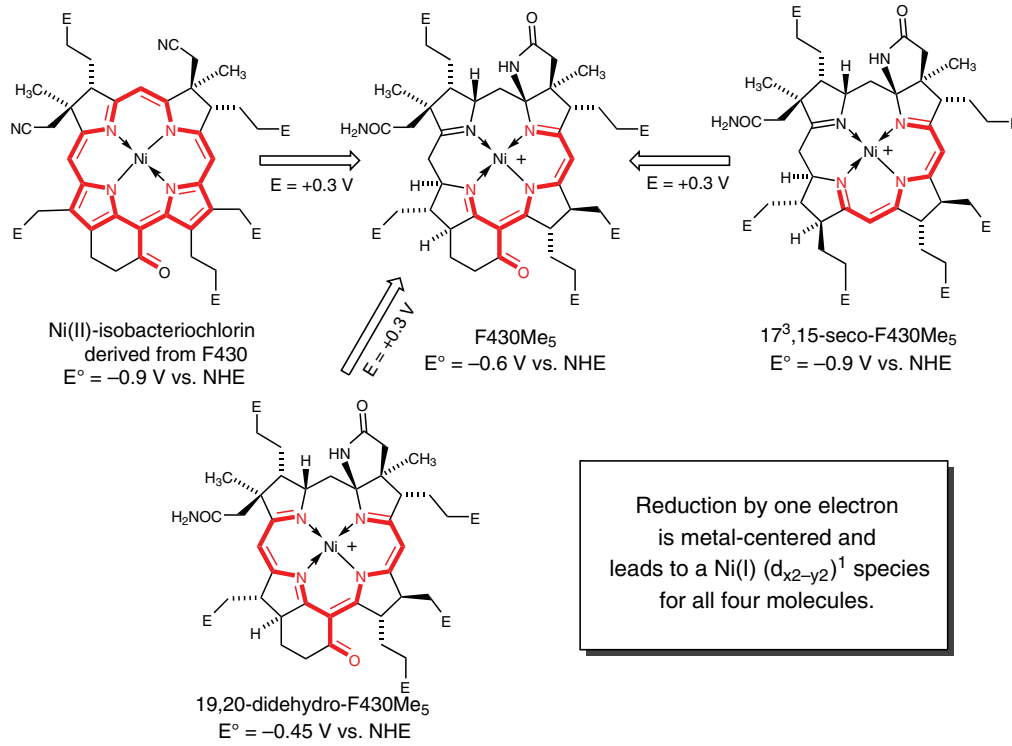

Figure 18.14 Comparison of redox potentials in $F430Me_5$ and partial synthetic derivatives.

complexes, whereas for thiols and thioethers (such as methyl-coenzyme M, the natural substrate of MCR) no axial coordination could be demonstrated. The ionic radius of low-spin Ni(II) is too small for the large coordination hole of the hydrocorphinoid ligand of F430 with its seven single bonds in the inner 16-membered macrocycle. The equatorial macrocyclic ligand adjusts through a saddle-shaped out-of-plane deformation and concomitant shortening of the Ni—N distances. However, this ligand-hole contraction by ruffling is opposed by induced steric strain between the side chains at neighboring rings and at the sp^3-centers in the α-positions.

The ionic radii of high-spin Ni(II) (d^8, $S = 1$) and Ni(I) (d^9, $S = 1/2$) are similar, both about 0.2 Å larger than low-spin Ni(II). Release of the steric strain induced by out-of-plane ruffling and the concomitant expansion of the coordination hole is therefore not only the driving force for the addition of axial ligands and transition to high-spin d^8 but also contributes to the relatively high reduction potential of four-coordinate Ni(II)$F430Me_5$. The fact that the Ni(II)/Ni(I) redox potential of $F430Me_5$ is about 50 mV more negative in the presence of axial pyridine or imidazole ligands is in keeping with this interpretation. In the X-ray structures of inactive enzyme (see below), the Ni(II) ion of F430 is five- or six-coordinate, and the hydrocorphinoid ligand shows only a small saddle deformation. This implies that the reduction to Ni(I)F430 in the enzyme is even more difficult (ca. –0.65 V vs. NHE) than judged from the reduction potential of four-coordinate Ni(II)$F430Me_5$.

Ni(I). In the presence of weak acids (HA) such as thiols, alcohols, or ammonium ions, Ni(I)$F430Me_5$ reacts with electrophilic methyl donors CH_3-X (X = I, Br, S^+R_2, O-Ts) to give

methane according to the overall equation

$$2\,\mathrm{Ni\,(I)\,F430Me_5} + \mathrm{CH_3\_X} + \mathrm{HA} \rightarrow \mathrm{CH_4} + 2\,\mathrm{Ni\,(II)\,F430Me_5} + \mathrm{X^-} + \mathrm{A^-} \quad (18.1)$$

Mechanistic studies indicate an S_N2-type attack of the Ni(I) center at methyl carbon leading to CH_3–Ni(III) and CH_3–Ni(II) intermediates and introduction of the fourth hydrogen in CH_4 as a proton, not a hydrogen atom [99]:

$$\mathrm{Ni\,(I)\,F430Me_5} + \mathrm{CH_3-X} \rightarrow \mathrm{CH_3-Ni\,(III)\,F430Me_5} + \mathrm{X^-} \quad (18.2)$$

$$\mathrm{CH_3-Ni\,(III)\,F430Me_5} + \mathrm{Ni\,(I)\,F430Me_5} \rightarrow \mathrm{CH_3-Ni\,(II)\,F430Me_5} + \mathrm{Ni\,(II)\,F430Me_5} \quad (18.3)$$

$$\mathrm{CH_3-Ni\,(II)\,F430Me_5} + \mathrm{HA} \rightarrow \mathrm{CH_4} + \mathrm{Ni\,(II)\,F430Me_5} + \mathrm{A^-} \quad (18.4)$$

In a catalytic system where Ni(I)F430Me_5 was constantly regenerated by stirring with liquid ZnHg, over 100 equivalents (rel. to F430Me_5) of methane were formed from methyl-sulfonium ions.

Me-Ni(II/III)-F430. Of the postulated metal–organic intermediates in (18.2, 18.4), Me-Ni(II)F430Me_5 could be generated in solution by stoichiometric reaction of Ni(II)F430Me_5 with $(CD_3)_2Mg$ at low temperature [99]. It is a paramagnetic species with an axial Ni—C bond, as demonstrated by the extreme high-field shift of the ^{2}H-NMR signal of the CD_3 group with $\delta = -485$ ppm at −40 °C, similar to Me-Ni(II)-*N,N,N,N*-tetramethylcyclam ($\delta = -380$ ppm at −40 °C), for which an X-ray structure is available [100].

The first postulated intermediate, CH_3-Ni(III)F430Me_5, has not been accessible in solution from free F430 or F430Me_5 so far, but it could be generated in the active site of the of the enzyme Ni(I)MCR by reaction with CH_3I or CH_3Br and was characterized by advanced EPR methods [101, 102].

A reaction of Ni(I)F430Me_5 with methyl thioethers, including methyl-coenzyme M, the natural substrate of MCR, could never be detected. Nevertheless, the proof of existence of methyl nickel derivatives of F430 described above inspired the mechanistic hypothesis that methane formation in the enzyme might proceed via such intermediates with a carbon-nickel bond (see below) [103, 104].

18.6.4 The Catalytic Role of F430 in the Active Site of Methyl-Coenzyme M Reductase

18.6.4.1 Importance of the Formation and Anaerobic Oxidation of Methane by Archaea in the Global C_1-Cycle

Each year, about 1.5 Gt of methane is generated on Earth geochemically (serpentinization) and by methanogenic archaea. About 1 Gt/a is re-oxidized to CO_2, either by methanotrophic archaea within the anoxic layer of the biosphere (0.3 Gt/a) or by bacteria with O_2 in the oxic layer (ca. 0.6 Gt/a). The excess escapes into the troposphere, where current CH_4 concentrations are 1.8 ppm (an increase from 1.1 ppm in 1950). There, CH_4 acts a potent greenhouse gas (ca. 25× stronger than CO_2/mass; average lifetime 12.5 years). This global methane cycle is connected to huge methane deposits (>10 000 Gt), either in the form of natural gas or of methane clathrates (methane hydrates) found in the oceans on the continental slopes at depths >500 m. For a scheme of the global C_1-cycle, see Figure 1 in [105].

Methanogens. Methanogens are strictly anaerobic microorganisms belonging to the domain of archaea. They produce methane from H_2 and CO_2 or from acetate (in some

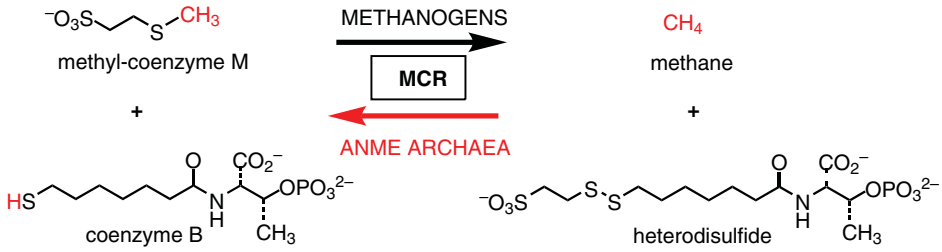

Figure 18.15 Structures of the substrates and reaction catalyzed by methyl-coenzyme M reductase (MCR).

cases, also from methanol or other methylated substrates) as a means of generating their energy (ATP). Methanogens live in anoxic habitats such as lake sediments, tundra, swamps, and rice paddies, as well as in the rumen or intestine of animals and humans, and are the microorganisms responsible for methane production in biogas plants or the anaerobic stage of sewage plants. The sequence of biochemical transformations, the involved enzymes, bioenergetics, and the associated genetics of methanogenesis have been thoroughly studied over the last 60 years and are reviewed in [106]. The key step, methane formation proper, consists of the reaction of a thiol (coenzyme B) with a thioether (methyl-coenzyme M) to give methane and a heterodisulfide (Figure 18.15):

This transformation, which has no known analogue in non-enzymatic chemistry, is catalyzed by MCR, the enzyme containing cofactor F430 in its active site. All methanogens and methanotrophic archaea (see below), but no other known organisms, contain this enzyme and cofactor F430.

ANME methanotrophs. Studies of marine methanotrophic archaea (ANME) carrying out the AOM [107] are rendered difficult because they live in syntrophic association with other microorganisms, such as SRB, and could not be grown in pure cultures so far. However, metagenomic analysis revealed that ANME archaea have close homologues to all methanogen genes involved in methane formation. Two close homologues of MCR could indeed be isolated from microbial mats carrying out AOM. One of these proteins (later attributed to ANME-2 + 3) contained cofactor F430 and the other (attributed to ANME-1) was a structural variant with a CH_3-S- substituent at position 17[2] (see Figure 18.1) [108, 109]. This led to the hypothesis that ANME archaea oxidize methane using the same reaction steps as methanogens but in the reverse direction, which was confirmed by the demonstration that MCR isolated from a methanogen can indeed convert CH_4 to CH_3-S-CoM [110]. However, ANME archaea do not produce H_2, and hence their catabolism is not exactly the reverse of methanogenesis from H_2 and CO_2. In syntrophy with SRB, the overall process is

$$CH_4 + SO_4^{2-} + 2\,H^+ \rightarrow CO_2 + H_2S + 2\,H_2O \quad \Delta G^{\circ\prime} = -21\ \text{kJ.mol}^{-1} \tag{18.5}$$

This requires that ANME transfer the reduction equivalents generated by the oxidation of methane to CO_2 to the SRB for the reduction of SO_4^{2-} to H_2S. Recent results point to direct interspecies electron transfer rather than to a small, reduced molecule as the carrier of the reduction equivalents [111]. Other species of ANME use the reduction equivalents to reduce NO_3^- (ANME-2d) [112] or, perhaps indirectly via other bacteria, metal oxides such as MnO_2 and $Fe(OH)_3$ [113].

18.6.4.2 MCR [114]

In cells of *Methanothermobacter marburgensis* two isoenzymes of MCR (MCR I and II) are expressed at different levels depending on the growth conditions in the cells of methanogens. Practically all biochemical and biophysical studies reported in the literature and discussed here were carried out with isoenzyme MCR I. Since active MCR contains Ni(I), the preparation of homogeneous and highly active MCR requires strictly anaerobic procedures for all steps, including growth and lysis of cells, centrifugation, and chromatographic purification (separation of the two isoenzymes) [115, 116]. No procedure was known to reactivate the pure enzyme from the EPR-silent Ni(II)MCR states generated upon contact with O_2 to active Ni(I)MCR_{red} until the recent discovery that a multicomponent protein isolated from the methanogenic cell achieves this long-sought reactivation under reducing conditions [117].

X-ray crystal structures of several inactive (Ni(II)MCR) forms of MCR from methanogens, and of MCR of the ANME-1 methanotroph, have been determined [118–121]. MCR (ca. 300 kDa) is composed of three different subunits arranged as a $\alpha_2\beta_2\gamma_2$ heterohexamer. The α-chain contains post-translationally modified amino acids, among them a conserved thioglycine with a C=S moiety. Two symmetry-equivalent active sites contain one molecule of F430 (resp. MeS-F430 in ANME-1) each. They are buried deep in the protein, accessible only through a narrow channel that leads from the protein surface to a hydrophobic dome on the proximal side of the hydrocorphinoid plane. The distal axial coordination site of the Ni is occupied by the amide carbonyl oxygen of a glutamine side chain (Figure 18.16).

18.6.4.3 Proposed Catalytic Reaction Mechanisms [122]

In the following discussion, the reaction is described in the methane-forming direction. According to the principle of microscopic reversibility, the reverse reaction, C—H activation of CH_4 as observed in AOM, has to proceed through the same intermediates and transition states. The early observation of EPR signals (MCR_{red1}) in methanogen cells that were almost identical to those in the spectrum of Ni(I)F430Me_5, and the fact that the pure enzyme in its active form shows EPR- and UV/VIS spectra typical of Ni(I)F430, led to the conclusion that the catalytic cycle for (18.5)) starts and ends with Ni(I)F430.

S_N2 at methyl carbon. The reactivity of free Ni(I)F430Me_5 and the formation of CH_3-Ni(II/III) species, together with the known organometallic chemistry of Co(I/II) in B_{12}, prompted proposals of mechanisms proceeding via methyl-Ni intermediates, like mechanism I depicted in Figure 18.17. Ni-hydride species as well as (CH_3)(H)-Ni and (σ-CH_3-H)Ni complexes (Figure 18.17, Ib) were also discussed as intermediates in variants of this two-electron, non-radical class of mechanisms.

S_RN at the thioether sulfur. Based on the differences in the bond strengths of CH_3-Ni(III)F430 and RS-Ni(II)F430, as predicted by quantum mechanical calculations (DFT), Siegbahn and Crabtree and co-workers proposed a mechanism that is based on a radical substitution by Ni(I) on the thioether sulfur of Me-S-CoM. In the original proposal, the first step led to the formation of a free methyl radical and the CoM-S-Ni(II)F430 thiolate complex [123]. This would be inconsistent with the net inversion of the configuration at the methyl carbon reported earlier [124]. In later studies, using higher-quality DFT calculations, a reaction profile was predicted in which the methyl radical is no longer an intermediate, as hydrogen transfer from CoB-SH to the methyl carbon is concerted with the cleavage of the CH_3–SCoM bond (mechanism II in Figure 18.17) [125–127].

Both types of proposed mechanisms close the catalytic cycle by electron transfer from the heterodisulfide radical anion to Ni(II)F430 to regenerate Ni(I)F430. In the reaction profile

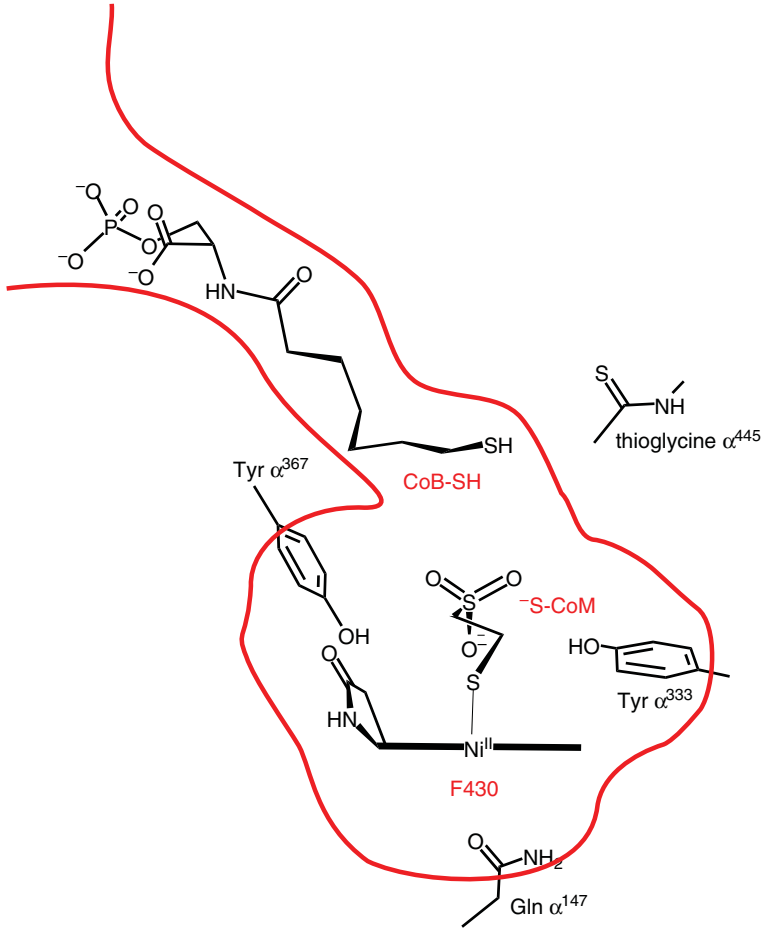

Figure 18.16 Illustration of the active site of MCR as found in the X-ray structure of the inactive Ni(II) form $MCR_{ox1\text{-}silent}$, in which the two thiols CoB-SH (substrate) and HS-CoM (not substrate: the natural substrate would be MeS-CoM) are bound to the enzyme.

calculated by DFT, this second part of the reaction proceeds through a single transition state, and electron transfer to Ni(II) is synchronous with the formation of the heterodisulfide S—S bond [127]. For attack of the Co-S• radical at the thiolate sulfur coordinated to Ni(II)F430, the methane molecule generated in the first, rate-limiting step would have to move out of the way. In the DFT calculation of the second step reported in [127], CH_4 was simply removed from the model. A full QM/MM calculation taking into account the protein residues lining the active site and their noncovalent interactions with substrates and products would be required to make predictions about the fate of the methane molecule inside the active site.

Experimental evidence in favor of mechanism I or II. Isotope exchange studies showed that the MCR-catalyzed reaction proceeds via at least one intermediate between the substrates-ternary complex and the products-ternary complex. All four C—H bonds of the product CH_4 are present and equivalent in this intermediate. This would be consistent with either methane bound in the active site by non-bonded hydrophobic interactions (mechanism II) or by σ-(CH_3-H)Ni or (CH_3)(H)Ni complexes with rapid exchange between

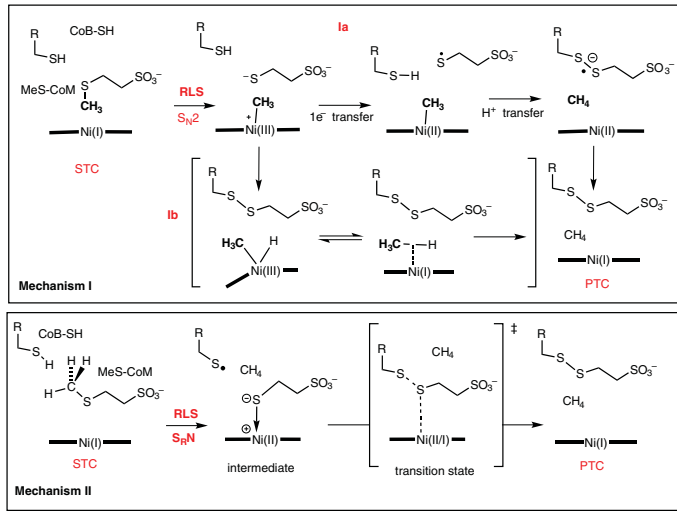

Figure 18.17 Proposed mechanisms for catalysis by F430 in MCR. Shown are the steps proposed between the substrates-ternary complex (STC) and the products-ternary complex (PTC). RLS = rate-limiting step. The hydrocorphin ligand of F430 is displayed as a horizontal bold line.

the C—H bonds (mechanism I), but not with CH_3-Ni(III) as the intermediate [128]. A large $^{13}C/^{12}C$ isotope effect ($k_{12}/k_{13} = 1.04$) with $^{13/12}CH_3$-S-CoM indicates that the cleavage of the carbon-sulfur bond between the substrates-ternary complex and the intermediate is rate limiting. The α-secondary isotope effect for CH_3/CD_3-S-CoM is large ($k_H/k_D = 1.19/D$), consistent with a planar geometry of the CH_3 moiety in the transition state and is significantly larger than expected for an S_N2 reaction [129, 130]. With CoB6-SH, the CoB-SH analogue with a -$(CH_2)_6$-SH instead of -$(CH_2)_7$-SH chain, methane formation in the MCR reaction is about 1000 times slower than with the natural substrate CoB-SH. Using this substrate analogue and rapid freeze-quench or stopped-flow techniques, Ragsdale and co-workers were recently able to show by EPR that the intermediate state does not contain a Ni(III) or Ni(I) $S = 1/2$ species [131]. The UV/VIS and magnetic circular dichroism spectra of the intermediate resemble those of $MCR_{ox1\text{-}silent}$, a high-spin CoM-S-Ni(II)F430 form that had been also characterized by X-ray structure analysis.

The large α-secondary H/D-isotope effect and the absence of $S = 1/2$ Ni(I/III) species in the intermediate point to the radical mechanism (II), rather than to an organo-nickel mechanism (I). However, if the intermediate state contains CoM-S-Ni(II)F430 and CH_4, a high-energy species must be present at the same time to allow formation of the heterodisulfide in the following step(s) that is(are) not rate limiting. According to the reaction profile proposed by Siegbahn and co-workers, this high-energy species would be the CoB-S• radical. Detection and unequivocal identification of this radical in stoichiometric amounts is the missing link that would allow the question of the basic catalytic mechanism of MCR to be considered solved.

18.6.4.4 Open Questions

None of the mechanisms discussed above considers direct involvement of the thioglycine residue that is conserved in all the methanogens and ANME methanotrophs investigated so far by reliable techniques. Thioglycines α^{445} and α'^{445} are located near the channels binding CoB-SH (Figure 18.16). The following roles have been discussed speculatively for thioglycine α^{445}: (i) prevention of a hydrogen bond (thioglycine is a weaker donor and acceptor of hydrogen bonds than glycine), (ii) electron-transfer mediator, for example, in the reactivation of Ni(II) to Ni(I), (iii) reversible formation of an adduct with CoBS• to "park" this radical in form of a more stable radical, and (iv) in conjunction with (ii) or (iii): "sensor" for transmission of state information from one active site to the other via the α and α′-chains connecting the two active sites, for example, through a conformational change.

Speculation (iv) leads to another important open question: whether the two identical active sites in MCR are mechanistically coupled or not. A "two-stroke engine" mode of action has been proposed [132], but no experimental evidence for or against mechanistic or regulatory coupling between the two active sites is available so far.

Another unanswered question is the order of release of the products methane and heterodisulfide (or the order of substrate binding in the AOM process). Kinetic studies clearly show that MeS-CoM has to enter the active site before CoB-SH to give a reactive ternary complex in the methane-forming direction. This is consistent with the single, extremely narrow access channel observed in the X-ray structures and leads to the presumption that the heterodisulfide product has to leave the enzyme before methane can be released – unless there is a second, so far unrecognized exit/entry channel for the small molecule CH_4.

18.7 Outlook

Present-day knowledge of the biological chemistry of cobalt-corrins and nickel-corphinoids as cofactors still is far from sufficient. Therefore, profound biochemical and biostructural investigations will be welcome to clarify open questions, such as the ones mentioned above. It will be of particular interest to learn more about the detailed biological radical processes catalyzed by these transition metal porphyrinoids, which provide an exceptional means for extending the range of the biological enzymatic chemistry. Along these lines, the question of the hypothetical roles of cobalt-corrinoids and nickel-corphinoids in the emergence of life on Earth, resulting from their unique reactivity, will continue to fascinate [133].

Due to the importance of Cbl's and of B_{12}-dependent metabolic processes in human health, studies of the pathological consequences of Cbl deficiency will continue to engage scientists in the biomedical field. The importance of cobalt-corrinoids in the microflora of the digestive tracts of humans and many animals begins to elicit interest of the health sciences and zoology [35]. Expanding expertise on the use of Cbl's as drug carriers may open the door to cell- and organ-specific delivery of B_{12}-based "Trojan horses" as anticancer agents [41]. Our increasing knowledge of gene regulatory functions of B_{12}-derivatives may furnish new tools (as antibiotics) and projects in the control and combat of (highly resistant) bacterial strains [48]. In this respect, the advances in bio- and gene-technology may provide new avenues to tailor-made semisynthetic corrinoids [46] as molecular carriers of diagnostic signals, such as by easily traced luminescent, radioactive, and paramagnetic transition metal analogues of the cobalt-corrins. The recently discovered need of large marine microbial communities for specific "complete" cobalt-corrinoids will increase research interest in B_{12}-based ecological topics [34]. Enzymological advances may pave the way for new biotechnology based on B_{12}-dependent enzymes and organisms.

From a more chemical perspective, the excellent commercial supply with the complex vitamin B_{12} and with related Cbl-based fine chemicals may increase interest in synthetic studies with Cbl's or other chemically modified and "incomplete" corrinoids. Such corrins may be particularly attractive chiral catalysts in photoinduced or redox-triggered organic transformations. The unique redox reactivity of corrins may find more extensive analytical use in the detection and controlled manipulation of natural or artificial bio-conjugates. Likewise, the high affinity and rapid rates of binding of a range of "inorganic" ligands to the Co(III) center of vitamin B_{12} derivatives may find (further) application in the detection and detoxification of chemical poisons in food, such as cyanide and nitrite, and so on [41].

The activation of C—H bonds under mild conditions is currently a hot topic in chemistry [134]. Methyl-coenzyme M reductase of ANME archaea achieves activation of the very strong C—H bond of methane (BDE[CH_3-H] = 105 kcal mol^{-1}) using the Ni-hydrocorphin F430 as catalyst. Understanding the enzymatic mechanism of MCR in detail would certainly contribute to the development of new catalysts for C—H activation, regardless of whether a mechanism with organometallic or radical intermediates turns out to be the correct one.

Direct spectroscopic evidence for stoichiometric formation of CoB-S• in the first step of methane formation would put MCR in the class of radical enzymes depending on metal tetrapyrrole cofactors such as B_{12} in the enzymes discussed above (see Section 18.3.2) or heme in cytochrome P450. Accepting mechanism II would imply that in the methane-activating direction (AOM), a thiyl radical abstracts a hydrogen atom from CH_4 in a highly endothermic reaction (ΔH = ca. 17 kcal mol^{-1}). Such a reaction is impossible in solution because competing pathways (such as disulfide formation) are much faster. In the absence of diffusion, inside the active site of an enzyme, a thiyl radical might survive long enough to allow such an uphill reaction to proceed if no more easily abstractable hydrogen

atoms are within reach in the active site. The fact that the active site of MCR is lined with aromatic residues (BDE[C_{ar}—H] > 110 kcal mol^{-1}) may signify that Nature has selected this strategy for MCR.

The increasing levels of the strong greenhouse gas methane in the atmosphere (see Section 18.6.4.1) have been largely attributed to human activity such as cattle farming. Feeding livestock with inhibitors of methanogenesis has been discussed as a countermeasure and prompted research on strong inhibitors of MCR. The newly discovered enzymes for F430 biosynthesis would be promising targets because they are specific for methanogenesis.

Dedication

We dedicate this work to Professor Albert Eschenmoser.

Acknowledgments

Research in Innsbruck has been generously supported by the Austrian National Science Foundation (FWF, current project No. P-28892).

References

1 Eschenmoser, A. (1988). Vitamin-B_{12} – experiments concerning the origin of its molecular-structure. *Angewandte Chemie International Edition* 27: 5–39.
2 Eschenmoser, A. (1986). Chemistry of Corphinoids. *Annals of the New York Academy of Sciences* 471: 108–129.
3 Folkers, K. (1982). History of vitamin B_{12}: pernicious anemia to crystalline cyanocobalamin. In: *B_{12}* (ed. D. Dolphin), 1–15. New York: Wiley.
4 Ellefson, W.L., Whitman, W.B., and Wolfe, R.S. (1982). Nickel-containing factor F430: chromophore of the methylreductase of Methanobacterium. *Proceedings of the National Academy of Sciences USA* 79: 3707–3710.
5 Hinrichs, K.U., Hayes, J.M., Sylva, S.P. et al. (1999). Methane-consuming archaebacteria in marine sediments. *Nature* 398: 802–805.
6 Boetius, A., Ravenschlag, K., Schubert, C.J. et al. (2000). A marine microbial consortium apparently mediating anaerobic oxidation of methane. *Nature* 407: 623–626.
7 Jaun, B. (1993). Methane formation by methanogenic bacteria – redox chemistry of coenzyme-F430. *Metal Ions in Biological Systems* 29: 287–337.
8 Battersby, A.R. (2000). Tetrapyrroles: the pigments of life. *Natural Product Reports* 17: 507–526.
9 Warren, M.J., Raux, E., Schubert, H.L., and Escalante-Semerena, J.C. (2002). The biosynthesis of Adenosylcobalamin (vitamin B_{12}). *Natural Product Reports* 19: 390–412.
10 Leeper, F.J., Warren, M.J., Kelly, J.M., and Lawrence, A.D. (2012). Biosynthesis of vitamin B_{12}. In: *Handbook of Porphyrin Science*, vol. 25 (ed. K.M. Kadish, K.M. Smith and R. Guilard), 2–83. World Scientific.
11 Zheng, K., Ngo, P.D., Owens, V.L. et al. (2016). The biosynthetic pathway of coenzyme F430 in methanogenic and methanotrophic archaea. *Science* 354: 339.
12 Kräutler, B. and Puffer, B. (2012). Vitamin B12-derivatives: organometallic catalysts, cofactors and ligands of bio-macromolecules. In: *Handbook of Porphyrin Science*, vol. 25 (ed. K.M. Kadish, K.M. Smith and R. Guilard), 133–265. World Scientific.
13 Dolphin, D. (ed.) (1982). *B_{12}*, vol. I. Chichester: Wiley, New York.

14 Kräutler, B., Arigoni, D., and Golding, B.T. (ed.) (1998). *Vitamin B_{12} and B_{12}-Proteins*. John Wiley VCH: Weinheim.

15 Banerjee, R. (ed.) (1999). *Chemistry and Biochemistry of B_{12}*. New York, Chichester: Wiley.

16 O'Leary, F. and Samman, S. (2010). Vitamin B_{12} in health and disease. *Nutrients* 2: 299–316.

17 Brown, K.L. (2005). Chemistry and enzymology of vitamin B_{12}. *Chemical Reviews* 105: 2075–2149.

18 Johnson, A.P., Wehrli, P., Fletcher, R., and Eschenmoser, A. (1968). Corphin, ein corrinoid-porphinoides Ligandsystem. *Angewandte Chemie* 80: 622–625.

19 Woodward, R.B. (1979). Synthetic Vitamin B12, in Vitamin B12. In: *Proceedings of the Third European Symposium on Vitamin B12 and Intrinsic Factor* (ed. B. Zagalak and W. Friedrich), 37. Berlin: Walter de Gruyter.

20 Randaccio, L., Geremia, S., Nardin, G., and Würges, J. (2006). X-ray structural chemistry of cobalamins. *Coordination Chemistry Reviews* 250: 1332–1350.

21 Konrat, R., Tollinger, M., and Kräutler, B. (1998). New NMR structural and dynamical probes of organometallic B_{12} derivatives. In: *Vitamin B_{12} and B_{12}-Proteins* (ed. B. Kräutler, D. Arigoni and B.T. Golding), 349–368. Weinheim: Wiley-VCH.

22 Summers, M.F., Marzilli, L.G., and Bax, A. (1986). Complete ^{1}H and ^{13}C assignments of coenzyme-B_{12} through the use of new two-dimensional NMR experiments. *Journal of the American Chemical Society* 108: 4285–4294.

23 Kratky, C. and Kräutler, B. (1999). Molecular structure of B12 cofactors and other B12 derivatives. In: *Chemistry and Biochemistry of B12* (ed. R. Banerjee), 9–41. New York: Wiley.

24 Lexa, D. and Savéant, J.M. (1983). The electrochemistry of vitamin B_{12}. *Accounts of Chemical Research* 16: 235–243.

25 Matthews, R.G. (2009). Cobalamin- and crrinoid-dependent enzymes. In: *Metal-Carbon Bonds in Enzymes and Cofactors, Metal Ions in Life Sciences*, vol. 6 (ed. A. Sigel, H. Sigel and R.K.O. Sigel), 53–114. Cambridge: RSC Publishing.

26 Kräutler, B. (1999). Electrochemistry and organometallic electrochemical synthesis. In: *Chemistry and Biochemistry of B_{12}* (ed. R. Banerjee), 315–339. New York: Wiley.

27 Rury, A.S., Wiley, T.E., and Sension, R.J. (2015). Energy cascades, excited state dynamics, and photochemistry in Cob(III)alamins and ferric porphyrins. *Accounts of Chemical Research* 48: 860–867.

28 Miller, N.A., Wiley, T.E., Spears, K.G. et al. (2016). Toward the design of Photoresponsive conditional antivitamins B_{12}: a transient absorption study of an arylcobalamin and an alkynylcobalamin. *Journal of the American Chemical Society* 138: 14250–14256.

29 Halpern, J. (1985). Mechanisms of coenzyme B_{12}-dependent rearrangements. *Science* 227: 869–875.

30 Mosimann, H. and Kräutler, B. (2000). Methylcorrinoids methylate radicals – their second biological mode of action? *Angewandte Chemie International Edition* 39: 393–200.

31 Kräutler, B., Fieber, W., Ostermann, S. et al. (2003). The cofactor of tetrachloroethene reductive dehalogenase of *Dehalospirillum multivorans* is Norpseudo-B_{12}, a new type of a natural corrinoid. *Helvetica Chimica Acta* 86: 3698–3716.

32 Renz, P. (1999). Biosynthesis of the 5,6-dimethylbenimidazole moiety of cobalamin and of cobalamin and of the other bases found in natural Corrinoids. In: *Chemistry and Biochemistry of B_{12}* (ed. R. Banerjee), 557–576. New York: Wiley.

33 Kräutler, B. (1998). B_{12}-nomenclature and a suggested atom-numbering. In: *Vitamin B_{12} and B_{12}-Proteins* (ed. B. Kräutler, D. Arigoni and B.T. Golding), 517–521. Weinheim: Wiley VCH.

34 Croft, M.T., Lawrence, A.D., Raux-Deery, E. et al. (2005). Algae acquire vitamin B_{12} through a symbiotic relationship with bacteria. *Nature* 438: 90–93.

35 Seth, E.C. and Taga, M.E. (2014). Nutrient cross-feeding in the microbial world. *Frontiers in Microbiology* 5: 350.

36 Fieber, W., Hoffmann, B., Schmidt, W. et al. (2002). Pseudocoenzyme B_{12} and adenosyl-factor a: electrochemical synthesis and spectroscopic analysis of two natural B_{12} coenzymes with predominantly base-off constitution. *Helvetica Chimica Acta* 85: 927–944.

37 Gruber, K., Puffer, B., and Kräutler, B. (2011). Vitamin B_{12}-derivatives – enzyme cofactors and ligands of proteins and nucleic acids. *Chemical Society Reviews* 40: 4346–4363.

38 Yi, S., Seth, E.C., Men, Y.J. et al. (2012). Versatility in corrinoid salvaging and remodeling pathways supports Corrinoid-dependent metabolism in Dehalococcoides mccartyi. *Applied and Environmental Microbiology* 78: 7745–7752.

39 Helliwell, K.E., Lawrence, A.D., Holzer, A. et al. (2016). Cyanobacteria and eukaryotic algae use different chemical variants of vitamin B_{12}. *Current Biology* 26: 999–1008.

40 Zelder, F. (2015). Recent trends in the development of vitamin B_{12} derivatives for medicinal applications. *Chemical Communications* 51: 14004–14017.

41 Zelder, F. and Alberto, R. (2012). Vitamin B12 derivatives for Spectroanalytical and medicinal applications. In: *Handbook of Porphyrin Science*, vol. 25 (ed. K.M. Kadish, K.M. Smith and R. Guilard), 84–132. World Scientific.

42 Kräutler, B. (2015). Antivitamins B_{12} – a structure- and reactivity-based concept. *Chemistry – A European Journal* 21: 11280–11287.

43 Ruetz, M., Gherasim, C., Fedosov, S.N. et al. (2013). Radical synthesis opens access to organometallic aryl-Cobaltcorrins – 4-ethylphenyl-cobalamin, a potential "antivitamin B_{12}". *Angewandte Chemie International Edition* 52: 2606–2610.

44 Ruetz, M., Salchner, R., Wurst, K. et al. (2013). Phenylethynylcobalamin: a light-stable and thermolysis-resistant organometallic vitamin B_{12} derivative prepared by radical. *Angewandte Chemie International Edition* 52: 11406–11409.

45 Deery, E., Schroeder, S., Lawrence, A.D. et al. (2012). An enzyme-trap approach allows isolation of intermediates in cobalamin biosynthesis. *Nature Chemical Biology* 8: 933–940.

46 Widner, F.J., Lawrence, A.D., Deery, E. et al. (2016). Total synthesis, structure, and biological activity of adenosylrhodibalamin, the non-natural rhodium homologue of coenzyme B_{12}. *Angewandte Chemie International Edition* 55: 11281–11286.

47 Winkler, W.C. and Breaker, R.R. (2005). Regulation of bacterial gene expression by riboswitches. *Annual Review of Microbiology* 59: 487–517.

48 Guzzo, M.B., Nguyen, H.T., Pham, T.H. et al. (2016). Methylfolate trap promotes bacterial thymineless death by sulfa drugs. *PLoS Pathogens* 12: e1005949.

49 Frey, P.A. and Hegeman, A.D. (2007). *Enzymatic Reaction Mechanisms*. New York: Oxford University Press.

50 Buckel, W. and Golding, B.T. (2008). Chemistry of B12-dependent enzyme reactions. In: *Encyclopedia of Life Sciences*, 159. Wiley.

51 Matthews, R.G., Koutmos, M., and Datta, S. (2008). Cobalamin-dependent and cobamide-dependent methyltransferases. *Current Opinion in Structural Biology* 18: 658–666.

52 Sauer, K. and Thauer, R.K. (1999). The role of corrinoids in methanogenesis. In: *Chemistry and Biochemistry of B_{12}* (ed. R. Banerjee), 655–679. New York, Chichester: Wiley.

53 Woodyer, R.D., Li, G., Zhao, H., and van der Donk, W.A. (2007). New insight into the mechanism of methyl transfer during the biosynthesis of fosfomycin. *Chemical Communications* 359–361.

54 Matthews, R.G., Drummond, J.T., and Webb, H.K. (1998). Cobalamin-dependent methionine synthase and serine hydroxymethyltransferase: targets for chemotherapeutic intervention? *Advances in Enzyme Regulation* 38: 377–392.

55 Drennan, C.L., Matthews, R.G., and Ludwig, M.L. (1994). Cobalamin-dependent methionine synthase – the structure of a methylcobalamin-binding fragment and implications for other B_{12}-dependent enzymes. *Current Opinion in Structural Biology* 4: 919–929.

56 Bandarian, V., Ludwig, M.L., and Matthews, R.G. (2003). Factors modulating conformational equilibria in large modular proteins: a case study with cobalamin-dependent methionine synthase. *Proceedings of the National Academy of Sciences USA* 100: 8156–8163.

57 Zhang, Q., van der Donk, W., and Liu, W. (2012). Radical-mediated enzymatic methylation: a tale of two SAMS. *Accounts of Chemical Research* 45: 555–564.

58 Frey, P.A. and Magnusson, O.T. (2003). *S*-Adenosylmethionine: a wolf in sheep's clothing, or a rich man's adenosylcobalamin? *Chemical Reviews* 103: 2129–2148.

59 Stubbe, J. (2011). The two faces of SAM. *Science* 332: 544–545.

60 Banerjee, R. and Ragsdale, S.W. (2003). The many faces of vitamin B_{12}: catalysis by cobalamin-dependent enzymes. *Annual Reviews of Biochemistry* 72: 209–247.

61 Marsh, E.N.G., Patterson, D.P., and Li, L. (2010). Adenosyl radical: reagent and catalyst in enzyme reactions. *ChemBioChem* 11: 604–621.

62 Gruber, K. and Kratky, C. (2002). Coenzyme B_{12} dependent glutamate mutase. *Current Opinion in Chemical Biology* 6: 598–603.

63 Toraya, T. (2014). Cobalamin-dependent dehydratases and a deaminase: radical catalysis and reactivating chaperones. *Archives of Biochemistry and Biophysics* 544: 40–57.

64 Stubbe, J. and van der Donk, W.A. (1998). Protein radicals in enzyme catalysis. *Chemical Reviews* 98: 705–762.

65 Stubbe, J. (2000). Ribonucleotide reductases: the link between an RNA and a DNA world? *Current Opinion in Structural Biology* 10: 731–736.

66 Sintchak, M.D., Arjara, G., Kellogg, B.A. et al. (2002). The crystal structure of class II ribonucleotide reductase reveals how an allosterically regulated monomer mimics a dimer. *Nature Structural Biology* 9: 293–300.

67 Bommer, M., Kunze, C., Fesseler, J. et al. (2014). Structural basis for organohalide respiration. *Science* 346: 455–458.

68 Peselis, A. and Serganov, A. (2012). Structural insights into ligand binding and gene expression control by an adenosylcobalamin riboswitch. *Nature Structural and Molecular Biology* 19: 1182–1184.

69 Gallo, S., Oberhuber, M., Sigel, R.K.O., and Kräutler, B. (2008). The corrin moiety of coenzyme B_{12} is the determinant for switching the btuB riboswitch of *E. coli*. *ChemBioChem* 9: 1408–1414.

70 Johnson, J.E., Reyes, F.E., Polaski, J.T., and Batey, R.T. (2012). B_{12} cofactors directly stabilize an mRNA regulatory switch. *Nature* 492: 133–137.

71 Elias-Arnanz, M., Padmanabhan, S., and Murillo, F.J. (2011). Light-dependent gene regulation in nonphototrophic bacteria. *Current Opinion in Microbiology* 14: 128–135.

72 Ortiz-Guerrero, J.M., Polanco, M.C., Murillo, F.J. et al. (2011). Light-dependent gene regulation by a coenzyme B_{12}-based photoreceptor. *Proceedings of the National Academy of Sciences USA* 108: 7565–7570.

73 Jost, M., Fernandez-Zapata, J., Polanco, M.C. et al. (2015). Structural basis for gene regulation by a B_{12}-dependent photoreceptor. *Nature* 526: 536–541.

74 Friedrich, W. (1988). *Vitamins*. Berlin: Walter de Gruyter.

75 Fedosov, S.N. (2012). Physiological and molecular aspects of cobalamin transport. In: *Subcellular Biochemistry*, vol. 56 (ed. O. Stanger), 347–368. Springer.

76 Seetharam, B. and Yammani, R.R. (2003). Cobalamin transport proteins and their cell-surface receptors. *Expert Reviews in Molecular Medicine* 5: 1–18.

77 Banerjee, R., Gherasim, C., and Padovani, D. (2009). The tinker, tailor, soldier in intracellular B_{12} trafficking. *Current Opinion in Chemical Biology* 13: 484–491.

78 Nielsen, M.J., Rasmussen, M.R., Andersen, C.B.F. et al. (2012). Vitamin B_{12} transport from food to the body's cells-a sophisticated, multistep pathway. *Nature Reviews Gastroenterolology and Hepatology* 9: 345–354.

79 Alam, A., Woo, J.-S., Schmitz, J. et al. (2016). Structural basis of transcobalamin recognition by human CD320 receptor. *Nature Communications* 7: 12100.

80 Lerner-Ellis, J.P., Tirone, J.C., Pawelek, P.D. et al. (2006). Identification of the gene responsible for methylmalonic aciduria and homocystinuria, cblC type. *Nature Genetics* 38: 93–100.

81 Mutti, E., Ruetz, M., Birn, H. et al. (2013). 4-Ethylphenyl-cobalamin impairs tissue uptake of vitamin B_{12} and causes vitamin B_{12} deficiency in mice. *PLoS One* 8: e75312.

82 Douaud, G., Refsum, H., De Jager, C.A. et al. (2013). Preventing Alzheimer's disease-related gray matter atrophy by B-vitamin treatment. *Proceedings of the National Academy of Sciences USA* 110: 9523–9528.

83 Green, R. and Miller, J.W. (2014). Vitamin B_{12}. In: *Handbook of Vitamins*, 5e (ed. J. Zempleni), 447–489.

84 Clardy, S.M., Allis, D.G., Fairchild, T.J., and Doyle, R.P. (2011). Vitamin B_{12} in drug delivery: breaking through the barriers to a B_{12} bioconjugate pharmaceutical. *Expert Opinion on Drug Delivery* 8: 1–14.

85 Hogenkamp, H.P.C., Collins, D.A., Grissom, C.B., and West, F.G. (1999). Diagnostic and therapeutic analogues of cobalamin. In: *Chemistry and Biochemistry of B_{12}* (ed. R. Banerjee), 385–410. New York: Wiley.

86 Tran, M.T.Q., Stürup, S., Lambert, I.H. et al. (2015). Cellular uptake of metallated cobalamins. *Metallomics* 8: 298–304.

87 Clardy-James, S., Chepurny, O.G., Leech, C.A. et al. (2013). Synthesis, characterization and pharmacodynamics of vitamin-B_{12}-conjugated glucagon-like Peptide-1. *ChemMedChem* 8: 582–586.

88 Hunger, M., Mutti, E., Rieder, A. et al. (2014). Organometallic B_{12}-DNA-conjugate: synthesis, structure analysis and studies of binding to human B_{12}-transporter proteins. *Chemistry – A European Journal* 20: 13103–13107.

89 Scalabrino, G. (2009). The multi-faceted basis of vitamin B_{12} (cobalamin) neurotrophism in adult central nervous system: lessons learned from its deficiency. *Progress in Neurobiology* 88: 203–220.

90 Moreno-Garcia, M.A., Rosenblatt, D.S., and Jerome-Majewska, L.A. (2013). Vitamin B_{12} metabolism during pregnancy and in embryonic mouse models. *Nutrients* 5: 3531–3550.

91 Telser, J. (1998). Nickel in F430. *Structure and Bonding* 91: 31–63.

92 Pfaltz, A., Jaun, B., Fässler, A. et al. (1982). On factor-F430 from methanogenic bacteria – structure of the porphinoid ligand system. *Helvetica Chimica Acta* 65: 828–865.

93 Livingston, D.A., Pfaltz, A., Schreiber, J. et al. (1984). Factor-F430 from methanogenic bacteria – structure of the protein-free factor. *Helvetica Chimica Acta* 67: 334–351.

94 Fässler, A., Kobelt, A., Pfaltz, A. et al. (1985). Zur Kenntnis des Faktors F430 aus methanogenen Bakterien: absolute konfiguration. *Helvetica Chimica Acta* 68: 2287–2298.

95 Färber, G., Keller, W., Kratky, C. et al. (1991). Coenzyme F430 from methanogenic bacteria – complete assignment of configuration based on an X-ray-analysis of 12,13-Diepi-F430 pentamethyl ester and on Nmr-spectroscopy. *Helvetica Chimica Acta* 74: 697–716.

96 Pfaltz, A., Kobelt, A., Hüster, R., and Thauer, R.K. (1987). Biosynthesis of coenzyme F430 in methanogenic bacteria. *European Journal of Biochemistry* 170: 459–467.

97 Holliger, C., Pierik, A.J., Reijerse, E.J., and Hagen, W.R. (1993). A spectroelectrochemical study of factor F430 nickel(II/I) from methanogenic bacteria in aqueous solution. *Journal of the American Chemical Society* 115: 5651–5656.

98 Jaun, B. (1994). Coenzyme F430 from methane bacteria – correlation of the structure of the hydroporphinoid ligand and redox chemistry of the nickel center. *Chimia* 48: 50–55.

99 Lin, S.-K. and Jaun, B. (1992). Coenzyme F430 from methanogenic bacteria: mechanistic studies on the reductive cleavage of sulfonium ions catalyzed by F430 pentamethyl ester. *Helvetica Chimica Acta* 75: 1478–1490.

100 Ram, M.S., Riordan, C.G., Yap, G.P.A. et al. (1997). Kinetics and mechanism of alkyl transfer from Organocobalt(III) to nickel(I): implications for the synthesis of acetyl coenzyme a by CO dehydrogenase. *Journal of the American Chemical Society* 119: 1648–1655.

101 Yang, N., Reiher, M., Wang, M. et al. (2007). Formation of a nickel–methyl species in methyl-coenzyme M reductase, an enzyme catalyzing methane formation. *Journal of the American Chemical Society* 129: 11028–11029.

102 Dey, M., Telser, J., Kunz, R.C. et al. (2007). Biochemical and spectroscopic studies of the electronic structure and reactivity of a methyl–Ni species formed on methyl-coenzyme M reductase. *Journal of the American Chemical Society* 129: 11030–11032.

103 Jaun, B. and Thauer, R.K. (2009). Nickel-alkyl bond formation in the active site of methyl-coenzyme M reductase. In: *Metal-Carbon Bonds in Enzymes and Cofactors*, vol. 6 (ed. A. Sigel, H. Sigel and R.K.O. Sigel), 115–132. Cambridge: RSC Publishing.

104 Grabarse, W., Mahlert, F., Duin, E.C. et al. (2001). On the mechanism of biological methane formation: structural evidence for conformational changes in methyl-coenzyme M reductase upon substrate binding. *Journal of Molecular Biology* 309: 315–330.

105 Thauer, R.K. (2011). Anaerobic oxidation of methane with sulfate: on the reversibility of the reactions that are catalyzed by enzymes also involved in methanogenesis from CO_2. *Current Opinion in Microbiology* 14: 292–299.

106 Thauer, R.K. (1998). Biochemistry of methanogenesis: a tribute to Marjory Stephenson. *Microbiology* 144: 2377–2406.

107 Knittel, K. and Boetius, A. (2009). Anaerobic oxidation of methane: progress with an unknown process. *Annual Review of Microbiology* 63: 311–334.

108 Krueger, M., Meyerdierks, A., Gloeckner, F.O. et al. (2003). A conspicuous nickel protein in microbial mats that oxidize methane anaerobically. *Nature* 426: 878–881.

109 Mayr, S., Latkoczy, C., Kruger, M. et al. (2008). Structure of an F430 variant from archaea associated with anaerobic oxidation of methane. *Journal of the American Chemical Society* 130: 10758–10767.

110 Scheller, S., Goenrich, M., Boecher, R. et al. (2010). The key nickel enzyme of methanogenesis catalyses the anaerobic oxidation of methane. *Nature* 465: 606–608.

111 Scheller, S., Yu, H., Chadwick, G.L. et al. (2016). Artificial electron acceptors decouple archaeal methane oxidation from sulfate reduction. *Science* 351: 703.

112 Haroon, M.F., Hu, S., Shi, Y. et al. (2013). Anaerobic oxidation of methane coupled to nitrate reduction in a novel archaeal lineage. *Nature* 500: 567–570.

113 Beal, E.J., House, C.H., and Orphan, V.J. (2009). Manganese- and iron-dependent marine methane oxidation. *Science* 325: 184–187.

114 Grabarse, W., Shima, S., Mahlert, F. et al. (2001). Methyl-coenzyme M reductase. In: *Handbook of Metalloproteins*, vol. 2, 897–914. Wiley.

115 Mahlert, F., Grabarse, W., Kahnt, J. et al. (2002). The nickel enzyme methyl-coenzyme M reductase from methanogenic archaea: in vitro interconversions among the EPR detectable MCR-red1 and MCR-red2 states. *Journal of Biological Inorganic Chemistry* 7: 101–112.

116 Duin, E.C., Prakash, D., and Brungess, C. (2011). Chapter nine – methyl-coenzyme M reductase from methanothermobacter marburgensis. In: *Methods in Enzymology* (ed. C.R. Amy and W.R. Stephen), 159–187. Academic Press.

117 Prakash, D., Wu, Y., Suh, S.-J., and Duin, E.C. (2014). Elucidating the process of activation of methyl-coenzyme M reductase. *Journal of Bacteriology* 196: 2491–2498.

118 Ermler, U., Grabarse, W., Shima, S. et al. (1997). Crystal structure of methyl-coenzyme M reductase: the key enzyme of biological methane formation. *Science* 278: 1457–1462.

119 Wagner, T., Kahnt, J., Ermler, U., and Shima, S. (2016). Didehydroaspartate modification in methyl-coenzyme M reductase catalyzing methane formation. *Angewandte Chemie International Edition* 55: 10630–10633.

120 Cedervall, P.E., Dey, M., Pearson, A.R. et al. (2010). Structural insight into methyl-coenzyme M reductase chemistry using coenzyme B analogues. *Biochemistry* 49: 7683–7693.

121 Shima, S., Krueger, M., Weinert, T. et al. (2012). Structure of a methyl-coenzyme M reductase from Black Sea mats that oxidize methane anaerobically. *Nature* 481: 98–101.

122 Ermler, U. (2005). On the mechanism of methyl-coenzyme M reductase. *Dalton Transactions* 3451–3458.

123 Pelmenschikov, V., Blomberg, M.R.A., Siegbahn, P.E.M., and Crabtree, R.H. (2002). A mechanism from quantum chemical studies for methane formation in methanogenesis. *Journal of the American Chemical Society* 124: 4039–4049.

124 Ahn, Y., Krzycki, J.A., and Floss, H.G. (1991). Steric course of the reduction of ethyl coenzyme M to ethane catalyzed by methyl coenzyme M reductase from Methanosarcina barkeri. *Journal of the American Chemical Society* 113: 4700–4701.

125 Chen, S.-L., Blomberg, M.R.A., and Siegbahn, P.E.M. (2014). An investigation of possible competing mechanisms for Ni-containing methyl-coenzyme M reductase. *Physical Chemistry Chemical Physics* 16: 14029–14035.

126 Chen, S.-L., Pelmenschikov, V., Blomberg, M.R.A., and Siegbahn, P.E.M. (2009). Is there a Ni-methyl intermediate in the mechanism of methyl-coenzyme M reductase? *Journal of the American Chemical Society* 131: 9912–9913.

127 Pelmenschikov, V. and Siegbahn, P.E.M. (2003). Catalysis by methyl-coenzyme M reductase: a theoretical study for heterodisulfide product formation. *Journal of Biological Inorganic Chemistry* 8: 653–662.

128 Scheller, S., Goenrich, M., Mayr, S. et al. (2010). Intermediates in the catalytic cycle of methyl-coenzyme M reductase: isotope exchange is consistent with formation of a σ-alkane Ni complex. *Angewandte Chemie International Edition* 49: 8112–8115.

129 Scheller, S., Goenrich, M., Thauer, R.K., and Jaun, B. (2013). Methyl-coenzyme M reductase from methanogenic archaea: isotope effects on label exchange and ethane formation with the homologous substrate ethyl-coenzyme M. *Journal of the American Chemical Society* 135: 14985–14995.

130 Scheller, S., Goenrich, M., Thauer, R.K., and Jaun, B. (2013). Methyl-coenzyme M reductase from methanogenic archaea: isotope effects on the formation and anaerobic oxidation of methane. *Journal of the American Chemical Society* 135: 14975–14984.

131 Wongnate, T., Sliwa, D., Ginovska, B. et al. (2016). The radical mechanism of biological methane synthesis by methyl-coenzyme M reductase. *Science* 352: 953.

132 Goenrich, M., Duin, E.C., Mahlert, F., and Thauer, R.K. (2005). Temperature dependence of methyl-coenzyme M reductase activity and of the formation of the methyl-coenzyme M reductase red2 state induced by coenzyme B. *Journal of Biological Inorganic Chemistry* 10: 333–342.

133 Eschenmoser, A. (2011). Etiology of potentially primordial biomolecular structures: from vitamin B_{12} to the nucleic acids and an inquiry into the chemistry of life's origin – a retrospective. *Angewandte Chemie International Edition* 50: 12412–12472.

134 Gensch, T., Hopkinson, M.N., Glorius, F., and Wencel-Delord, J. (2016). Mild metal-catalyzed C-H activation: examples and concepts. *Chemical Society Reviews* 45: 2900–2936.

Index

Fundamentals of Porphyrin Chemistry: A 21st Century Approach, Volume 2, First Edition.
Edited by Penelope J. Brothers and Mathias O. Senge.
© 2022 John Wiley & Sons Ltd. Published 2022 by John Wiley & Sons Ltd.

b

C

d

e

f

g

i

k

l

m

n

O

p

u